The Van Allen Probes Mission

Nicola Fox • James L. Burch
Editors

The Van Allen Probes Mission

Previously published in *Space Science Reviews* Volume 179,
Issues 1–4, 2013

Springer

Editors
Nicola Fox
Johns Hopkins University
Laurel, MD, USA

James L. Burch
Southwest Research Institute
San Antonio, TX, USA

ISBN 978-1-4899-7432-7
ISBN 978-1-4899-7433-4 (eBook)
DOI 10.1007/978-1-4899-7433-4
Springer New York Heidelberg Dordrecht London

Library of Congress Control Number: 2013957701

Cover illustration: NASA.

Printed on acid-free paper

Springer is part of Springer Science+Business Media (www.springer.com)

Contents

Preface
N.J. Fox · J.L. Burch **1**

Science Objectives and Rationale for the Radiation Belt Storm Probes Mission
B.H. Mauk · N.J. Fox · S.G. Kanekal · R.L. Kessel · D.G. Sibeck · A. Ukhorskiy **3**

Mission Overview for the Radiation Belt Storm Probes Mission
J.M. Stratton · R.J. Harvey · G.A. Heyler **29**

Radiation Belt Storm Probes—Observatory and Environments
K. Kirby · D. Artis · S. Bushman · M. Butler · R. Conde · S. Cooper · K. Fretz · C. Herrmann · A. Hill · J. Kelley · R. Maurer · R. Nichols · G. Ottman · M. Reid · G. Rogers · D. Srinivasan · J. Troll · B. Williams **59**

The Electric and Magnetic Field Instrument Suite and Integrated Science (EMFISIS) on RBSP
C.A. Kletzing · W.S. Kurth · M. Acuna · R.J. MacDowall · R.B. Torbert · T. Averkamp · D. Bodet · S.R. Bounds · M. Chutter · J. Connerney · D. Crawford · J.S. Dolan · R. Dvorsky · G.B. Hospodarsky · J. Howard · V. Jordanova · R.A. Johnson · D.L. Kirchner · B. Mokrzycki · G. Needell · J. Odom · D. Mark · R. Pfaff Jr. · J.R. Phillips · C.W. Piker · S.L. Remington · D. Rowland · O. Santolik · R. Schnurr · D. Sheppard · C.W. Smith · R.M. Thorne · J. Tyler **127**

The Electric Field and Waves Instruments on the Radiation Belt Storm Probes Mission
J.R. Wygant · J.W. Bonnell · K. Goetz · R.E. Ergun · F.S. Mozer · S.D. Bale · M. Ludlam · P. Turin · P.R. Harvey · R. Hochmann · K. Harps · G. Dalton · J. McCauley · W. Rachelson · D. Gordon · B. Donakowski · C. Shultz · C. Smith · M. Diaz-Aguado · J. Fischer · S. Heavner · P. Berg · D.M. Malsapina · M.K. Bolton · M. Hudson · R.J. Strangeway · D.N. Baker · X. Li · J. Albert · J.C. Foster · C.C. Chaston · I. Mann · E. Donovan · C.M. Cully · C.A. Cattell · V. Krasnoselskikh · K. Kersten · A. Brenneman · J.B. Tao **183**

The Relativistic Proton Spectrometer (RPS) for the Radiation Belt Storm Probes Mission
J. Mazur · L. Friesen · A. Lin · D. Mabry · N. Katz · Y. Dotan · J. George · J.B. Blake · M. Looper · M. Redding · T.P. O'Brien · J. Cha · A. Birkitt · P. Carranza · M. Lalic · F. Fuentes · R. Galvan · M. McNab **221**

Radiation Belt Storm Probes Ion Composition Experiment (RBSPICE)
D.G. Mitchell · L.J. Lanzerotti · C.K. Kim · M. Stokes · G. Ho · S. Cooper · A. Ukhorskiy · J.W. Manweiler · S. Jaskulek · D.K. Haggerty · P. Brandt · M. Sitnov · K. Keika · J.R. Hayes · L.E. Brown · R.S. Gurnee · J.C. Hutcheson · K.S. Nelson · N. Paschalidis · E. Rossano · S. Kerem **263**

Erratum to: Radiation Belt Storm Probes Ion Composition Experiment (RBSPICE)
D.G. Mitchell · L.J. Lanzerotti · C.K. Kim · M. Stokes · G. Ho · S. Cooper · A. Ukhorskiy · J.W. Manweiler · S. Jaskulek · D.K. Haggerty · P. Brandt · M. Sitnov · K. Keika · J.R. Hayes · L.E. Brown · R.S. Gurnee · J.C. Hutcheson · K.S. Nelson · C.M. Hammock · N. Paschalidis · E. Rossano · S. Kerem **309**

Science Goals and Overview of the Radiation Belt Storm Probes (RBSP) Energetic Particle, Composition, and Thermal Plasma (ECT) Suite on NASA's Van Allen Probes Mission
H.E. Spence · G.D. Reeves · D.N. Baker · J.B. Blake · M. Bolton · S. Bourdarie · A.A. Chan · S.G. Claudepierre · J.H. Clemmons · J.P. Cravens · S.R. Elkington · J.F. Fennell · R.H.W. Friedel · H.O. Funsten · J. Goldstein · J.C. Green · A. Guthrie · M.G. Henderson · R.B. Horne · M.K. Hudson · J.-M. Jahn · V.K. Jordanova · S.G. Kanekal · B.W. Klatt · B.A. Larsen · X. Li · E.A. MacDonald · I.R. Mann · J. Niehof · T.P. O'Brien · T.G. Onsager · D. Salvaggio · R.M. Skoug · S.S. Smith · L.L. Suther · M.F. Thomsen · R.M. Thorne **311**

The Relativistic Electron-Proton Telescope (REPT) Instrument on Board the Radiation Belt Storm Probes (RBSP) Spacecraft: Characterization of Earth's Radiation Belt High-Energy Particle Populations
D.N. Baker · S.G. Kanekal · V.C. Hoxie · S. Batiste · M. Bolton · X. Li · S.R. Elkington · S. Monk · R. Reukauf · S. Steg · J. Westfall · C. Belting · B. Bolton · D. Braun · B. Cervelli · K. Hubbell · M. Kien · S. Knappmiller · S. Wade · B. Lamprecht · K. Stevens · J. Wallace · A. Yehle · H.E. Spence · R. Friedel **337**

The *Magnetic Electron Ion Spectrometer* (MagEIS) Instruments Aboard the Radiation Belt Storm Probes (RBSP) Spacecraft
J.B. Blake · P.A. Carranza · S.G. Claudepierre · J.H. Clemmons · W.R. Crain Jr. · Y. Dotan · J.F. Fennell · F.H. Fuentes · R.M. Galvan · J.S. George · M.G. Henderson · M. Lalic · A.Y. Lin · M.D. Looper · D.J. Mabry · J.E. Mazur · B. McCarthy · C.Q. Nguyen · T.P. O'Brien · M.A. Perez · M.T. Redding · J.L. Roeder · D.J. Salvaggio · G.A. Sorensen · H.E. Spence · S. Yi · M.P. Zakrzewski **383**

Helium, Oxygen, Proton, and Electron (HOPE) Mass Spectrometer for the Radiation Belt Storm Probes Mission
H.O. Funsten · R.M. Skoug · A.A. Guthrie · E.A. MacDonald · J.R. Baldonado · R.W. Harper · K.C. Henderson · K.H. Kihara · J.E. Lake · B.A. Larsen · A.D. Puckett · V.J. Vigil · R.H. Friedel · M.G. Henderson · J.T. Niehof · G.D. Reeves · M.F. Thomsen · J.J. Hanley · D.E. George · J.-M. Jahn · S. Cortinas · A. De Los Santos · G. Dunn · E. Edlund · M. Ferris · M. Freeman · M. Maple · C. Nunez · T. Taylor · W. Toczynski · C. Urdiales · H.E. Spence · J.A. Cravens · L.L. Suther · J. Chen **423**

The Engineering Radiation Monitor for the Radiation Belt Storm Probes Mission
J.O. Goldsten · R.H. Maurer · P.N. Peplowski · A.G. Holmes-Siedle · C.C. Herrmann · B.H. Mauk **485**

The Balloon Array for RBSP Relativistic Electron Losses (BARREL)
R.M. Millan · M.P. McCarthy · J.G. Sample · D.M. Smith · L.D. Thompson · D.G. McGaw · L.A. Woodger · J.G. Hewitt · M.D. Comess · K.B. Yando · A.X. Liang · B.A. Anderson · N.R. Knezek · W.Z. Rexroad · J.M. Scheiman · G.S. Bowers · A.J. Halford · A.B. Collier · M.A. Clilverd · R.P. Lin · M.K. Hudson **503**

The Radiation Belt Storm Probes (RBSP) and Space Weather
R.L. Kessel · N.J. Fox · M. Weiss **531**

Dynamics of Radiation Belt Particles
A.Y. Ukhorskiy · M.I. Sitnov **545**

AE9, AP9 and SPM: New Models for Specifying the Trapped Energetic Particle and Space Plasma Environment
G.P. Ginet · T.P. O'Brien · S.L. Huston · W.R. Johnston · T.B. Guild · R. Friedel · C.D. Lindstrom · C.J. Roth · P. Whelan · R.A. Quinn · D. Madden · S. Morley · Y.-J. Su **579**

Radiation Belt Storm Probes (RBSP) Education and Public Outreach Program
D. Turney · A. Matiella Novak · K. Beisser · N. Fox **617**

DOI 10.1007/978-1-4899-7433-4_1
Reprinted from *Space Science Reviews* Journal, DOI 10.1007/s11214-013-9997-2

Preface

N.J. Fox · J.L. Burch

Received: 21 May 2013 / Accepted: 23 May 2013 / Published online: 1 June 2013

The discovery of the Van Allen radiation belts in 1958, starting with data from the United States' first two successful orbiting spacecraft, Explorer's I and III, was an astounding surprise and represented the founding of what we now call magnetospheric physics. Since that time many spacecraft have traversed the radiation belts en route to other more distant parts of Earth's magnetosphere and other worlds beyond Earth's orbit. After initial climatological models of the radiation belts were obtained in the 1960's and early 1970's, the main concern about them was the ability of spacecraft and astronauts to survive their intense radiation. And yet there were true scientific mysteries to be solved, glimpses of which came in the 1990's from spacecraft like CRRES and SAMPEX. CRRES observed the unexpected creation of a brand new radiation belt and also a variety of unanticipated features including peculiar distributions of strong electric fields deep within the belts during geomagnetic storms. SAMPEX, observed the slot region between the inner and outer belts to contain anomalous cosmic rays and also observed high cadence variations in the energetic electrons within that region that were unanticipated from known radiation belt drivers. In addition, measurements by spacecraft transiting the radiation belts showed them to contain a rich variety of strong plasma waves with frequencies from mHz to 10's of kHz, known to interact resonantly with the various periodicities of the charged particles, transporting them, scattering them, and causing them to precipitate into the atmosphere. But the mechanisms of those interactions, for example whether they are principally linear or strongly non-linear, and how robustly they influence the belts, are poorly determined. While new discoveries will always be made by spacecraft visiting new places, improved measurements made in old places can make equally exciting discoveries and also lead to deep understanding. The radiation belts have clearly become a place ripe for renewed exploration.

N.J. Fox
The Johns Hopkins University, Laurel, MD 20723, USA

J.L. Burch (✉)
Southwest Research Institute, San Antonio, TX 78228-0510, USA
e-mail: jburch@swri.edu

With the advent of the National Space Weather (NSW) and Living With a Star (LWS) programs, there was renewed interest in the radiation belts and other near-Earth space phenomena, especially those that affect technological systems. The 2002 Solar and Space Physics Decadal Survey gave high priority to a Geospace Network mission, which comprised a radiation-belt component (called then the Radiation Belt Storm Probes, RBSP) and an ionospheric component (Ionospere-Thermosphere Storm Probes, ISTP). That report noted critical gaps in understanding of space weather, including the fact that the strongest effects of severe magnetospheric storms are produced by radiation belt particles, which often appear and disappear in unexpected ways. Noting that changes in the particle distribution functions and electric and magnetic fields in the inner magnetosphere are measured at satellite orbital periods rather than at particle drift periods, the report called for a multiple-spacecraft RBSP mission.

The start of the Vision for Space Exploration program in 2004 lent particular urgency toward understanding the radiation hazards presented to astronauts travelling beyond Earth orbit. In response to this concern, RBSP was started by NASA in 2005 but with ITSP left for future implementation. As part of the NASA LWS program, NASA assigned the implementation of RBSP to the Johns Hopkins University Applied Physics Laboratory for implementation and spacecraft development, and solicited instrument proposals from the science community with an Announcement of Opportunity in August 2005. Following selection of instruments in 2006, RBSP underwent timely and successful development toward a launch on August 30, 2012. After launch and commissioning the mission was appropriately renamed the Van Allen Probes.

This special issue of Space Science Reviews describes the design, development, calibration and testing of all aspects of RBSP leading up to its launch. Numerous new measurement capabilities were developed for the mission including extensions of the electron and ion measurements to both much higher and lower energies than ever before with the addition of ion composition to both plasma and energetic particle measurements. In addition, more comprehensive wave measurements are included. And, as prescribed, the use of two identical spacecraft in nearly the same orbit increases the time cadence of the measurements substantially and allows for the separation of spatial and temporal effects over various spatial scales. In addition to the on-board instrumentation an extensive campaign involving balloon-borne energetic particle measurements maps the precipitation zones in the upper atmosphere.

DOI 10.1007/978-1-4899-7433-4_2
Reprinted from *Space Science Reviews* Journal, DOI 10.1007/s11214-012-9908-y

Science Objectives and Rationale for the Radiation Belt Storm Probes Mission

B.H. Mauk · N.J. Fox · S.G. Kanekal · R.L. Kessel · D.G. Sibeck · A. Ukhorskiy

Received: 1 February 2012 / Accepted: 2 June 2012 / Published online: 7 September 2012

Abstract The NASA Radiation Belt Storm Probes (RBSP) mission addresses how populations of high energy charged particles are created, vary, and evolve in space environments, and specifically within Earth's magnetically trapped radiation belts. RBSP, with a nominal launch date of August 2012, comprises two spacecraft making in situ measurements for at least 2 years in nearly the same highly elliptical, low inclination orbits (1.1×5.8 RE, 10°). The orbits are slightly different so that 1 spacecraft laps the other spacecraft about every 2.5 months, allowing separation of spatial from temporal effects over spatial scales ranging from ∼0.1 to 5 RE. The uniquely comprehensive suite of instruments, identical on the two spacecraft, measures all of the particle (electrons, ions, ion composition), fields (**E** and **B**), and wave distributions ($d\mathbf{E}$ and $d\mathbf{B}$) that are needed to resolve the most critical science questions. Here we summarize the high level science objectives for the RBSP mission, provide historical background on studies of Earth and planetary radiation belts, present examples of the most compelling scientific mysteries of the radiation belts, present the mission design of the RBSP mission that targets these mysteries and objectives, present the observation and measurement requirements for the mission, and introduce the instrumentation that will deliver these measurements. This paper references and is followed by a number of companion papers that describe the details of the RBSP mission, spacecraft, and instruments.

Keywords Radiation belt · Magnetosphere · Geomagnetic storms · NASA mission

B.H. Mauk (✉) · N.J. Fox · A. Ukhorskiy
Applied Physics Laboratory, The Johns Hopkins University, Laurel, MD 20723, USA
e-mail: Barry.Mauk@jhuapl.edu

S.G. Kanekal · D.G. Sibeck
Code 674, NASA Goddard Space Flight Center, Greenbelt, MD 20771, USA

D.G. Sibeck
e-mail: david.g.sibeck@nasa.gov

R.L. Kessel
SMD, Heliophysics Division, NASA Headquarters, 300 E St. SW, Washington, DC 20546, USA
e-mail: mona.kessel@nasa.gov

1 Introduction

The science objectives for the Radiation Belt Storm Probes Mission (RBSP) were first articulated by the NASA-sponsored Geospace Mission Definition Team (GMDT) report published in 2002, refined within the NASA RBSP Payload Announcement of Opportunity issued in 2005, and finalized in the RBSP Program Level (Level 1) requirements document signed by NASA's Associate Administer for Science in 2008. The fundamental objective of the RBSP mission is to:

Provide understanding, ideally to the point of predictability, of how populations of relativistic electrons and penetrating ions in space form or change in response to variable inputs of energy from the Sun.

This broad objective is parsed into three overarching science questions:

1. Which physical processes produce radiation belt enhancements?
2. What are the dominant mechanisms for relativistic electron loss?
3. How do ring current and other geomagnetic processes affect radiation belt behavior?

The purpose of this paper is to provide the background and context for these overarching questions and to break them down to reveal the most compelling scientific issues regarding the behavior of the radiation belts. We then describe how the characteristics and capabilities of the RBSP mission enable the resolution of these issues. This introductory paper is followed by a number of companion papers that describe the details of the mission, spacecraft, instrument investigations, and instrument hardware. Also, background on present understandings of some mathematical tools used in the study of radiation belts is provided in Ukhorskiy and Sitnov (this issue), and the importance of the RBSP science in mitigating the societal impacts of space weather is described by Kessel et al. (this issue).

2 Background and Context

It has now been over 50 years since observations from the first spacecraft in the late 1950's were used to discover the radiation belts and reveal their basic configuration (e.g. Ludwig 2011; Zavidonov 2000). Those discoveries lead to an explosion of investigations into the nature of the belts over the next two decades, including studies of the behavior of the transient belts created artificially with nuclear explosions (Ludwig 2011; Van Allen 1983; Walt 1997). Textbooks like those written by Hess (1968), Roederer (1970) and Schulz and Lanzerotti (1974) captured the fundamental physics of the radiation belts discovered during the first decade of study, including such important breakthroughs as the initial development of the magnetospheric coordinate systems needed to understand particle behavior (e.g. McIlwain 1961). By the middle of the 1970's, interest in studying the radiation belts had dwindled, and the focus of those who continued to work on the belts shifted to characterizing their properties for engineering and space environment applications. The proton and electron radiation belts were popularly viewed as being relatively static structures (Fig. 1). Key features of interest have always been the electron slot region centered near equatorial radial distances of ~2–3 R_E and the electron horn structures at high latitudes (Fig. 1).

During the epoch described above, time averaged and modeled distributions of particle intensities were generated to estimate the long-term debilitating influences of penetrating electron and ions on spacecraft and astronauts. The examples presented in Fig. 2 shows equatorial distributions of omnidirectional particle fluxes. Modern particle

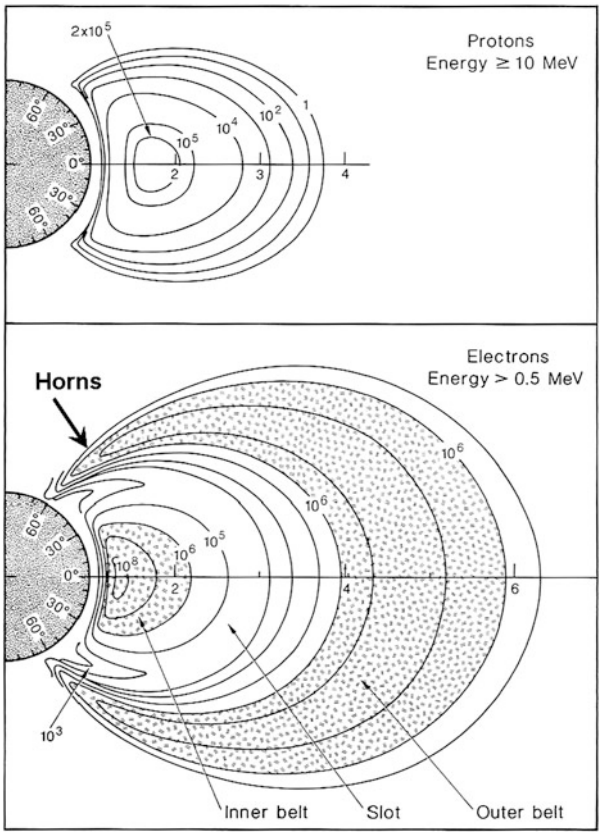

Fig. 1 Time averaged radiation belt omnidirectional fluxes for >10 MeV protons (*top*) and >0.5 MeV electons (*bottom*). See, for example, Kivelson and Russell (1995)

spectrometers measure the directional differential particle intensities: $I[E, \alpha]$ with units ($\text{sec}^{-1}\,\text{cm}^{-2}\,\text{sr}^{-1}\,\text{MeV}^{-1}$), where E is energy in MeV and α is pitch angle, the angle between the particle velocity vector **V** and the local magnetic field vector **B**. The intensity I is related to the omnidirectional flux $F_{Om}(>E)$ in Fig. 2 through integration, specifically:

$$F_{Om}[>E] = \int_0^{\pi} 2\pi \sin[\alpha] d\alpha \int_E^{\infty} I\left[E', \alpha\right] dE' \tag{1}$$

$F_{Om}(>E)$ is most useful from the engineering perspective because for a specific level of shielding, just one of the profiles in each of Figs. 2(a) and 2(b) provides an estimate of the electron and proton radiation fluxes that penetrate into the shielded volume. For example, for 100 mils of aluminum (0.25 cm corresponding to $\sim$0.67 g/cm^2) the relevant profiles would be the red one labeled with the electron energy 1.5 MeV in Fig. 2(b), and the red one labeled with the proton energy 20–30 MeV in Fig. 2(a).

In the early 1990's, several observations revealed that the behavior of the Earth's radiation belts were far more dynamic and interesting than previously thought. Specifically, the observations of the CRRES mission, flying in a highly elliptical geosynchronous transfer orbit, revealed the sudden creation of a brand new radiation belt that filled the electron slot region (Fig. 3; Blake et al. 1992; color figures like that shown here are reviewed by Hudson et al. 2008). Also in the early 1990's the SAMPEX mission was launched into a low altitude polar orbit with the science goals of studying cosmic rays, radiation belts, and other energetic particles (Mason et al. 1990). The two-decade-long ongoing extended SAMPEX

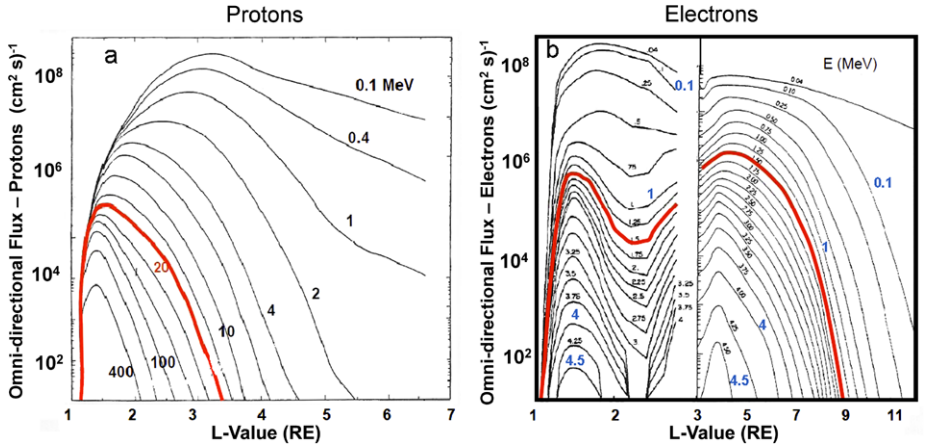

Fig. 2 (**a**) Proton radiation belt distribution from Sawyer and Vette (1976). The *red profile* added to this display corresponds to those protons (>20 MeV) that just penetrate about 100 mils (0.25 cm) aluminum. NASA publication. (**b**) Electron radiation belt figure generated by combining 2 of the standard plots provided in the Handbook of Geophysics and the Space Environment (edited by Jursa 1985), the right-hand portion generated by Singley and Vette (1972). The inner electron belt fluxes are more uncertain because it is difficult to measure energetic electrons in an environment of very energetic protons. The *red profile* corresponds to those electrons (>1.5 MeV) that just penetrate about 100 mils (0.25 cm) aluminum. Air Force publication

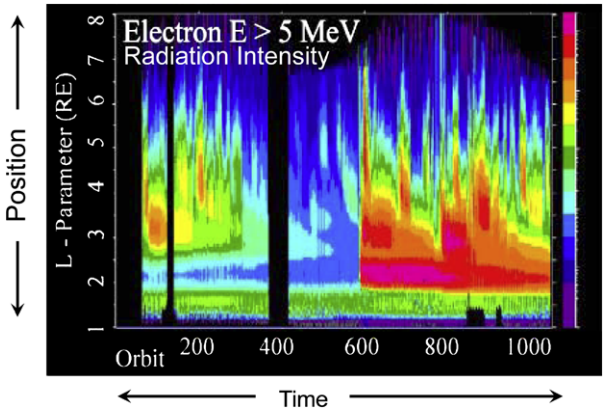

Fig. 3 CRRES spacecraft observation of the creation of a new electron radiation belt that filled the slot region between 2 and 3 R_E (Blake et al. 1992; figure discussed by Hudson et al. 2008). The new belt (*bright red*) is thought to be the result of an interplanetary shock wave impinging on Earth's magnetosphere

mission has enabled studies of the dynamics of the low altitude, high latitude extensions of the Earth's radiation belts, the so-called radiation belt "horns" (Fig. 1, bottom). SAMPEX revealed that the radiation belts change dramatically over multiple time scales for reasons that are not always readily apparent (Fig. 4; Baker et al. 2004; Li et al. 2011).

The work that was performed in conjunction with and following the CRRES and SAMPEX missions has convinced the scientific community that we are far from having a predictive understanding of the behavior of the Earth's radiation belts, as discussed below. Present understanding of aspects of radiation belt physics is captured in several monographs and reviews. Lemaire et al. (1996) document the mid-1990's understanding of the belts; and Hudson et al. (2008), Thorne (2010), and a series of papers in the *Journal of Atmospheric and Solar-Terrestrial Physics* edited by Ukhorskiy et al. (2008), review more recent understanding.

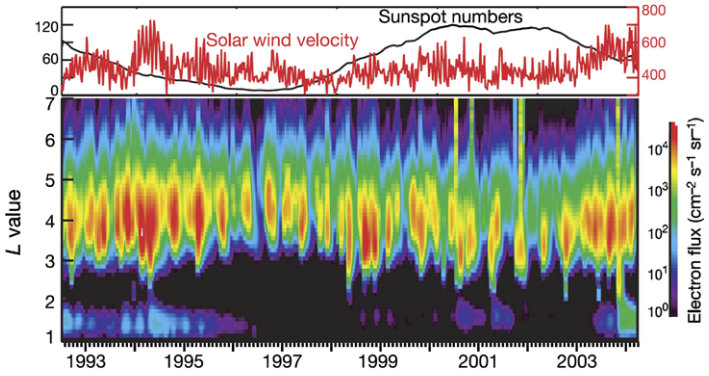

Fig. 4 Electron intensity (*color scale*) versus magnetospheric L-parameter (*vertical axis*) versus time (*horizontal axis*) for 2–6 MeV electrons as measured by the low altitude, polar orbit SAMPEX mission for over an entire ∼11-year solar cycle (Baker et al. 2004; these measurements have continued for a second solar cycle; see Li et al. 2011)

In parallel with the new findings and interest in the radiation belts of Earth, extraterrestrial planetary probes have revealed robust radiation belts at all of strongly magnetized planets, despite the huge differences between the respective planets and despite the huge differences in how the space environments of these different planets are powered (Mauk and Fox 2010, and references therein). The creation of trapped populations of relativistic and penetrating charged particles is clearly a universal characteristic of strongly magnetized space environments and not just a characteristic of the special conditions that prevail at Earth. For example, the solar wind, thought to be the overwhelming driver for energization of Earth's radiation belts, has only a marginal influence at Jupiter on the creation of Jupiter's dramatic, and much more energetic, radiation belts (Ibid).

3 Radiation Belt Science Mysteries

After over 50 years of study, we know a lot about the Earth's radiation belts. Many of the fundamental processes (e.g. Fig. 5) that control radiation belt behaviors have been studied both observationally and theoretically. A good example would be the influence of strong interplanetary shock waves on the radiation belts (Fig. 5), one of which instigated the dramatic creation of a new radiation belt observed by CRRES (Fig. 3; e.g. Blake et al. 1992; Li et al. 1993). However, we are still far from having a predictive understanding of the radiation belts. Our ignorance resides both in the complexity about how the various processes combine together to produce a variety of radiation belt disturbances, and in the characteristics and complex behaviors of some of the specific mechanisms. Here we provide some illustrative examples of the most easily articulated of scientific mysteries regarding the behaviors of the Earth's radiation belts, which we pose in the form of questions. Many other sample questions than those selected here could have been chosen, and indeed would have been chosen by other authors with different scientific perspectives.

Sample Question 1 Why do the radiation belts respond so differently to different dynamic magnetic storm events?

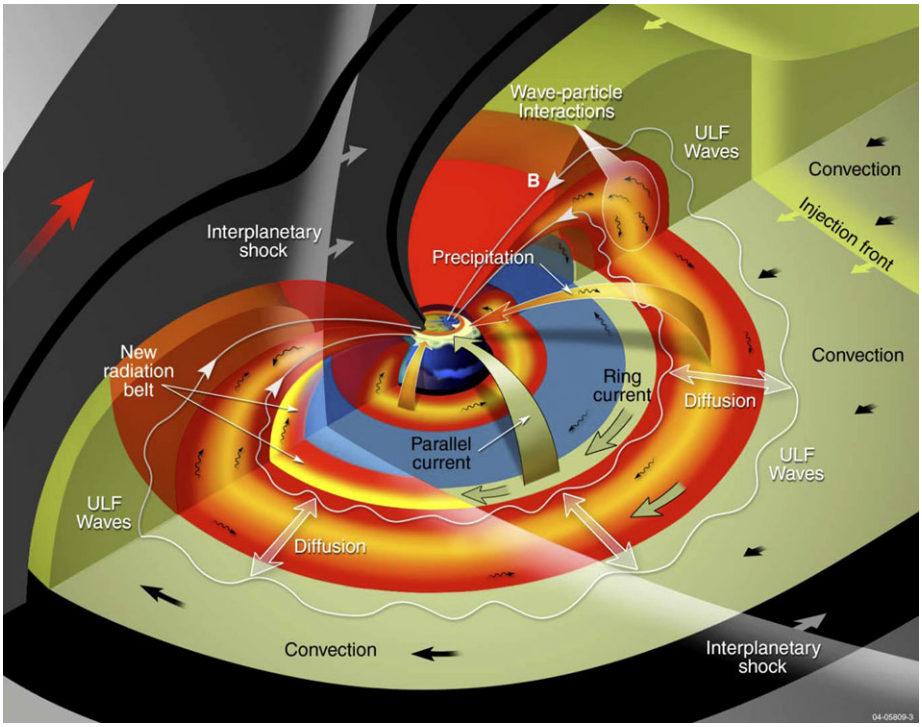

Fig. 5 Schematic of some of the physical processes affecting the behaviors of Earth's radiation belts

It has long been conventional wisdom that the radiation belts dramatically intensify in association with geomagnetic storms. Such storms are often created by the impact of solar coronal mass ejections with the Earth's magnetosphere and also the passage of high speed solar wind streams. Storms last for 1 to several days, occur roughly a dozen times a year, and cause dramatic increases in the flux of hot ion populations at geocentric distances between 2 and 6 R_E. Currents associated with these 'ring current' ion populations distort inner magnetospheric magnetic fields and depress equatorial magnetic fields on the surface of the Earth. The so-called storm time disturbance (Dst) index, a measure of these depressions, is generally taken to provide a direct measurement of the ring current energy content according to the Dessler-Parker-Sckopke relationship (Dessler and Parker 1959; Sckopke 1966; however, there are caveats—Liemohn 2003).

Reeves et al. (2003) published a now classic paper that showed that radiation belt responses to storms can contradict conventional wisdom. At times the Earth's outer radiation belt populations do increase during magnetic storms (decreases in Dst), but at other times they remain largely unchanged by magnetic storms or even decrease dramatically (Fig. 6). We do not know why the outer electron belt responds so differently during individual magnetic storm events, and these results highlight our lack of predictive understanding about radiation belts.

Sample Question 2 Why do observed global electric field patterns behave so differently than expected?

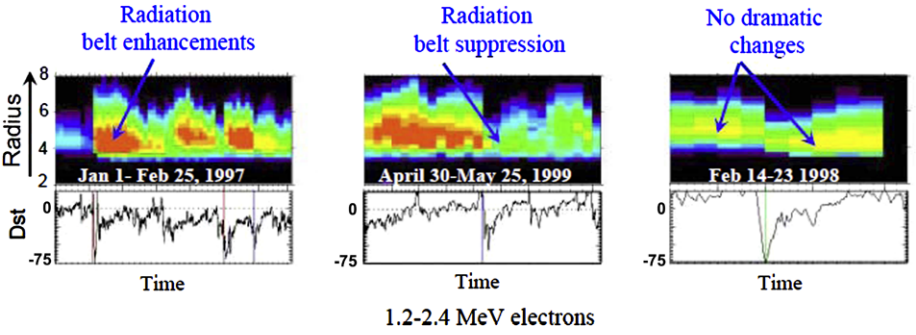

Fig. 6 Variable responses of Earth's outer electron belt (*top of each panel*) to magnetospheric storms as diagnosed with the *Dst* parameter (*bottom*). After Reeves et al. (2003). © The American Geophysical Union

A critical element in the control of the radiation belts is the distribution of other plasma populations relative to the radiation belt populations. Cold, warm, and hot plasma populations provide both the free energy needed for the generation and growth of various plasma waves and the media through which these waves propagate. The plasma waves can scatter and energize radiation belt particles. To a substantial degree, it is thought that large scale global electric field patterns within the inner and middle magnetosphere control the locations where the cold, warm, and hot plasma populations occur within the radiation belts. Here we are making a distinction between the quasi-steady (hours) global electric fields and the transient electric fields (minutes) associated with injections and other fast processes.

Classical models for inner and middle magnetospheric global electric fields often employ a so-called Volland-Stern type configuration (e.g. reviewed by Burke et al. 2007) with an electric potential: $\Phi = \Phi_0 L^\gamma \cos[LT]$, where Φ_0 is the electric potential at some outer boundary position, L is the standard magnetospheric distance parameter (equatorial radial position in R_E for a magnetic dipole field), LT is the angle that corresponds to local time, and γ is the so-called shielding parameter. The idea of this configuration is that the global electric field is applied "externally" by the interaction between the solar wind and the outer boundaries of the magnetosphere, and that the trapped inner region populations respond to partially shield out that electric field from the inner regions.

It therefore came as a shock when Rowland and Wygant (1998) published their statistical distribution of electric field measurements from the CRRES mission (Fig. 7). Inner magnetospheric electric fields increase dramatically with increasing geomagnetic activity with an L-dependence that is contrary to expectations. This result has been highly controversial. Part of the debate is stimulated by the fact that CRRES measured only the dawn-dusk component, so that different functional forms can be hidden in the missing component due to distortions in the geometry.

However, the absence of any significant increase in quasi-stationary electric fields at larger radial distances (e.g. 7–8 RE in Fig. 7) as geomagnetic activity increases represents an equally significant result. Conventional wisdom proclaims that the "cross-tail" electric fields at these radial distances increase with increasing geomagnetic activity, and thereby drive the transport of magnetotail plasmasheet populations into the inner regions. Global models for ring current and radiation belt transport invariably include this effect (e.g. Fok et al. 2001a, 2001b, Khazanov et al. 2003), even when they invoke inductive electric fields to explain rapid enhancements in inner magnetospheric electron fluxes. However, the absence of any increase in the quasi-stationary cross-tail electric field that transports plasmasheet

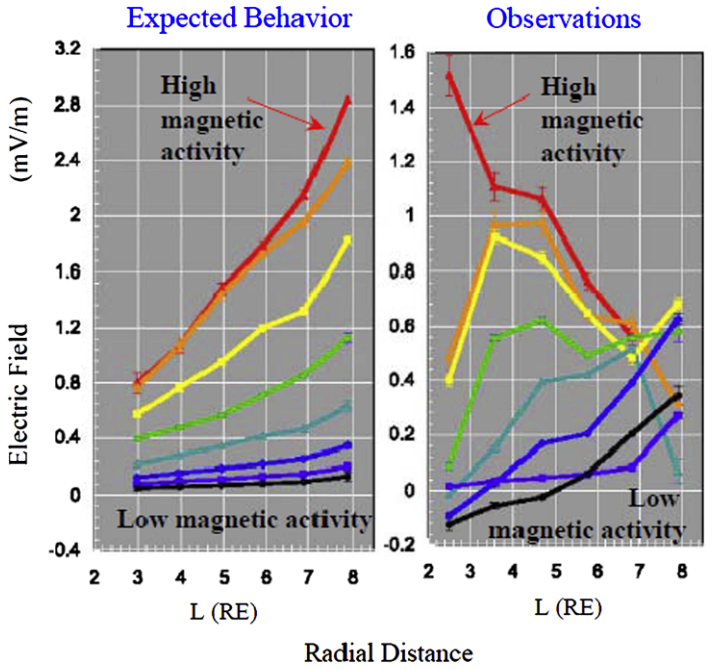

Fig. 7 Time averaged dawn-dusk global, non-transient electric field as a function of geomagnetic conditions ($Kp = 0, 1, 2, 3, 4, 5, 6, 7$) as determined by CRRES measurements (*right*) and compared with expectations from the standard Volland-Stern model (*left*). After Rowland and Wygant (1998). © The American Geophysical Union

plasma into the middle and inner regions has been confirmed independently by Hori et al. (2005; see Fig. 8 and caption).

Clearly some fundamental issues concerning the generation and configuration of the global electric field patterns remain to be solved.

Sample Question 3 How are such large intensities of radiation belt electrons energized to multi-MeV energies?

The ultimate sources of radiation belt electrons are the ionosphere and the solar wind. Ionospheric electron temperatures are less than 0.1 eV. Temperatures of the core population in the solar wind are on the order 10 eV, while temperatures of the halo (heated) population in the solar wind are on the order of 60 eV (Feldman et al. 1975; Lin 1998). Auroral and related magnetospheric interaction processes extract and energize ionospheric electrons, providing them to the outer magnetosphere (generally at distances beyond 9 R_E) at energies ranging from 1 to 10's of keV. Processes occurring at the Earth's bow shock and magnetopause both energize and transport electrons into the magnetosphere. Reconnection and other processes within the Earth's dynamic magnetotail magnetic current sheet then accelerate electrons of both ionospheric and solar wind origins still further. The resulting plasmasheet populations have temperatures of order 5 keV but often exhibit very substantial high energy tails (Christon et al. 1991).

One might then assume that Earth's radiation belts result from the transport of these plasmasheet electrons into the inner magnetosphere in a fashion that conserves the first and

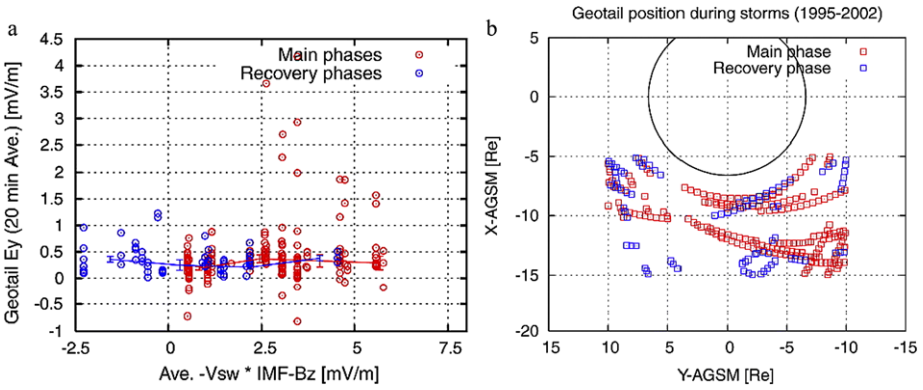

Fig. 8 (*Left*) Dawn-dusk electric fields from Geotail measured as a function storm-time conditions during periods that include both the main phase of the storms (first several hours during the strengthening of the ring current) and the recovery phase where the ring current is relaxing back to nominal, pre-storm levels (1–2 days). (*Right*) Positions where the measurements were made. After Hori et al. (2005). The key point is that during the more disturbed conditions the quasi-static field remains at the level observed during the more undisturbed conditions, while the occurrence of transient electric fields become prevalent. © The American Geophysical Union

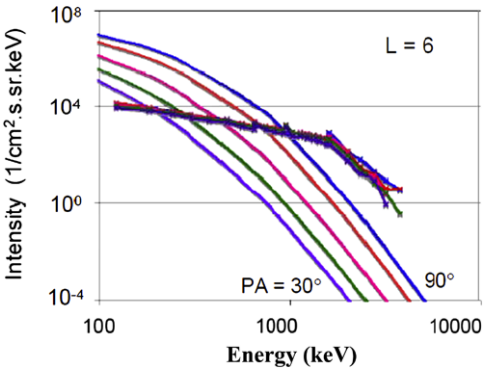

Fig. 9 Comparison between a CRRES-measured electrons spectra during a very strong magnetic storm with the maximized expectations from the most intense spectra observed within the magnetotail ($R = 11\ R_E$) after transporting the magnetotail spectrum adiabatically to the measurement position by conserving the adiabatic invariants of gyration and bounce. The adiabatically transported spectra cannot explain the >1 MeV portion of the spectra measured within the inner magnetosphere. From Fox et al. (2006). © The American Geophysical Union

possibly the second adiabatic invariants, those associated with gyration and bounce motion. Conservation of the first adiabatic invariant requires the energies of core and tail populations to increase by a factor of perhaps 40 as particles are transported Earthward from regions in the magnetotail where magnetic field strengths are on the order of 5 nT to regions of the inner magnetosphere where field strengths are on the order of 200 nT.

However, recent results indicate that adiabatic energization of plasma populations is not sufficient to account for the >1 MeV component of Earth's outer electron radiation belt (see Fig. 9, Fox et al. 2006). We have also learned that at least some of that unaccounted-for

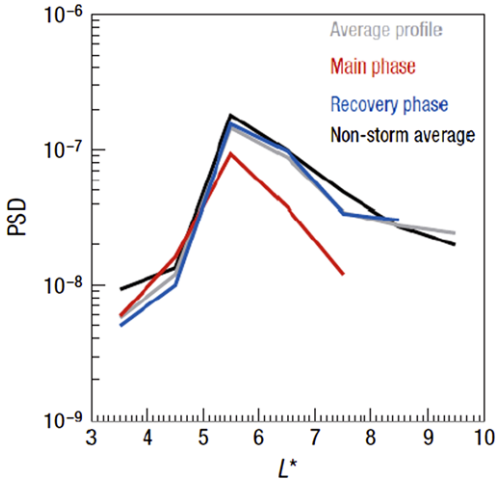

Fig. 10 Phase Space Density (PSD) of energetic electrons for a constant value of the adiabatic invariants of gyration and bounce plotted as a function of L^*, the L-shell value of a purely dipolar magnetic field that would contain the same magnetic flux as would the particle drift orbit within the true distorted magnetic field configuration. L^* is equivalent to what is called the third adiabatic invariant (Roederer 1970). Note that for a storm-time magnetic field configuration, $L^* = 5.5$ correspond to an equatorial radial position of some higher value of the standard L-parameter, perhaps 6 R_E. The key feature is the peak at $L^* \sim 5.5$ R_E. Under present understanding of transport processes, a peak in the PSD profile suggests that a local, invariant-violating acceleration is occurring at that position (Ukhorskiy and Sitnov this issue). This figure is from Chen et al. (2007), whose findings solidified previous indications such as those from Green and Kivelson (2004) and Iles et al. (2006). © The Nature Publishing Group

energization occurs within the regions of the radiation belts themselves (see Fig. 10, Chen et al. 2007). And so the question is, how does that additional energization come about?

Quasi-linear interactions with whistler mode plasma waves may provide the additional energization, effectively by transferring energy from low to high energy electrons (Horne and Thorne 1998; Summers et al. 1998; Horne et al. 2005a, 2005b). The idea is illustrated in Fig. 11, showing a notional distribution of energetic electrons as a function of momentum parallel and perpendicular to the local magnetic field direction. Whistler waves that propagate parallel to the magnetic field establish a cyclotron resonance with gyrating electrons along the nearly vertical black lines (2 of a continuum of resonance curves are shown on the right side). In response to the interaction, electrons diffuse along curves like those shown in red. Diffusion down the slopes of the gradients in the blue-contoured Phase Space Density distribution take energy away from the particles for low energies (the lower portion of the plot) and add energy to the particles for high energies (the upper portion of the plot). This process represents a quasi-linear mechanism of transporting energy from low to high energy particles (Horne and Thorne, 2003). The time scale for high energy particle energization via this mechanism has been modeled and compared with observed energization time scales, and a reasonable match has been achieved (Horne et al. 2005a, 2005b). However, this and other hypotheses need further testing. In view of recent observations of very large amplitude waves like that shown in Fig. 12 (e.g., Cattell et al. 2008) and in view of recent theoretical studies (Bortnik et al. 2008; Kellogg et al. 2010), the role of large amplitude waves interacting in a highly non-linear fashion with the particles must be considered. Theoretical modeling indicates that other wave modes, for example the so-called fast magnetosonic waves (Horne et al. 2007), must

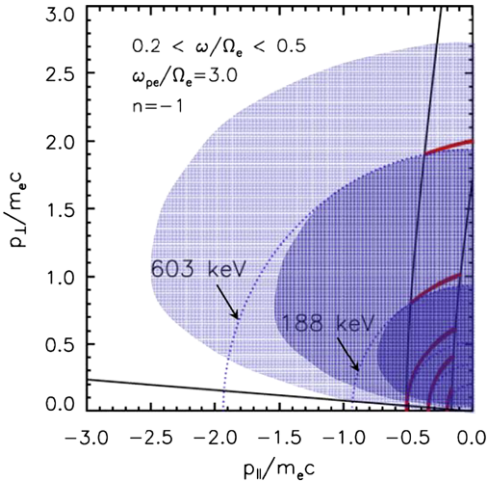

Fig. 11 A notional distribution of energetic electrons (*blue contours*) as a function of momentum parallel and perpendicular to the local magnetic field direction. Whistler waves that propagate parallel to the magnetic field establish a cyclotron resonance with gyrating electrons on the *nearly vertical black lines on the right side* (2 of a continuum of resonance curves are shown). In response to the interaction, electrons diffuse along curves like those shown in *red*. The majority of particles move (diffuse) in the direction that takes them down the slope of the gradients in the blue-contoured electron phase space density distributions. On the plot, ω is wave frequency (radians/sec), Ω_e is electron cyclotron frequency, Ω_p is plasma frequency. See Horne et al. (2003) for other details. © The American Geophysical Union

Fig. 12 Very large amplitude whistler waves observed by the STEREO spacecraft in Earth's inner magnetosphere. After Cattell et al. (2008). © The American Geophysical Union

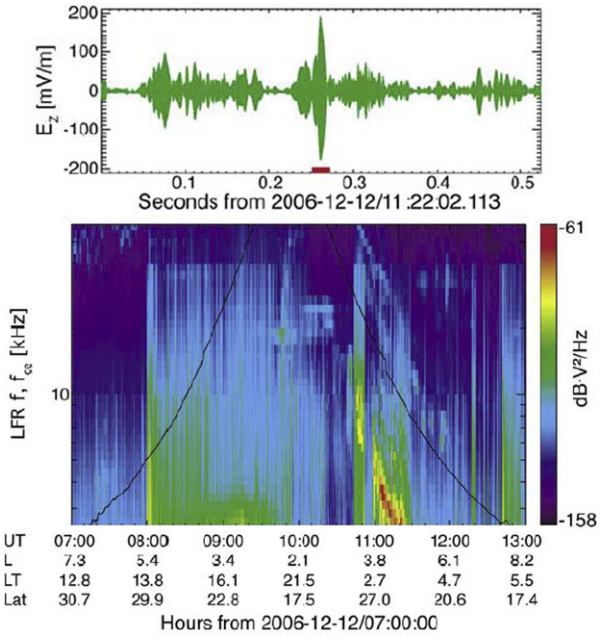

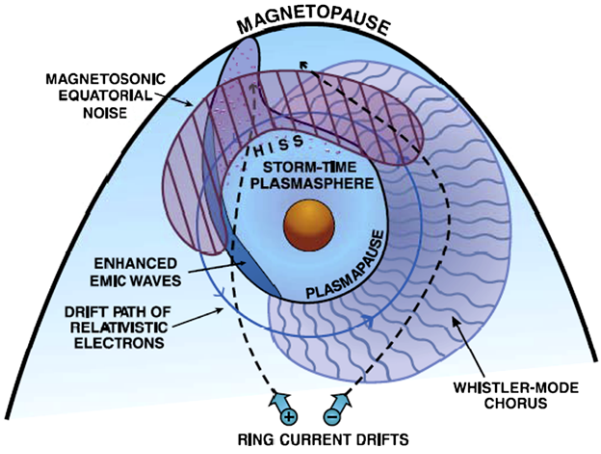

Fig. 13 A now standard schematic of the regions of the influence of plasma waves on the radiation belts. After Thorne (2010) and references therein. © The American Geophysical Union

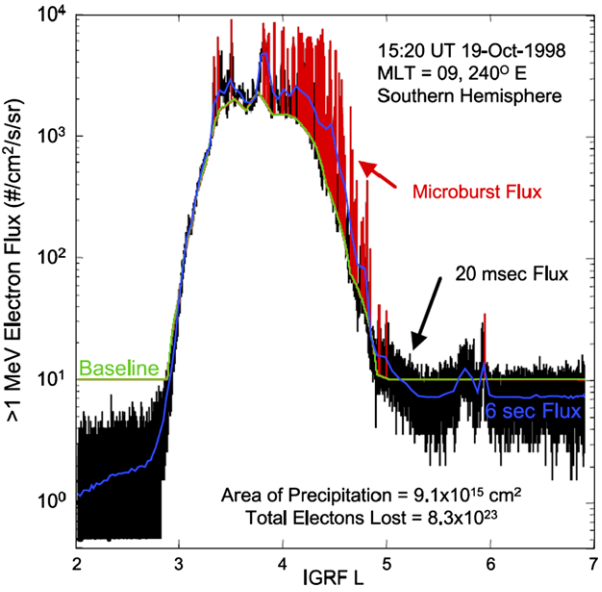

Fig. 14 SAMPEX observations of so-called microburst precipitation of relativistic electrons into the belts with transient time scales of <20 milliseconds. From O'Brien et al. (2004). © The American Geophysical Union

also be considered. Figure 13 shows the regions in which the various proposed wave interactions are thought to occur (Thorne 2010). Understanding how and when particles are locally accelerated is very important for understanding how the radiation belts are formed.

Sample Question 4 What causes "microbursts" and how important are they for the loss of particles from the radiation belts?

One of the most intriguing phenomena related to Earth's radiation belts are the so-called microbursts observed at low altitudes (Nakamura et al. 2000; Lorentzen et al. 2001). In the case of the features shown in Fig. 14, these events correspond to radiation belt electron precipitation spikes with time scales less than 20 milliseconds. O'Brien et al. (2004) have

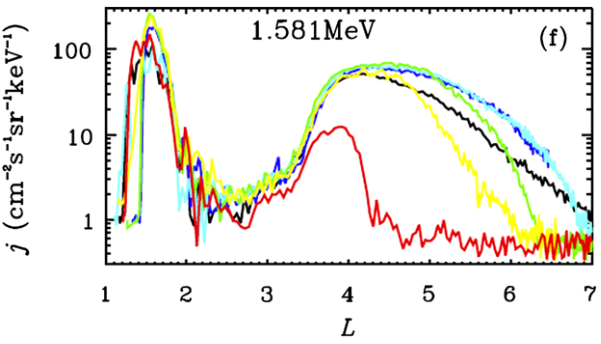

Fig. 15 CRRES observations of the sudden (*red trace*) dropout of outer zone radiation belt electrons on the time scale of a single orbit of the spacecraft. From Su et al. (2011). © The American Geophysical Union

combined measurements with assumptions to suggest that microbursts may represent a very significant fraction of the losses that come from the active radiation belts.

Since microbursts occur in the dawn-morning quadrant (O'Brien et al. 2004), where chorus/whistler waves are active (Fig. 13), it seems natural to assume that the bursts correspond to strong whistler-mode wave-particle interactions (Thorne et al. 2005). Strong wave phase trapping of the particles could be involved, again, given the now-recognized presence of very large amplitude whistler waves (Kersten et al. 2011; again see Fig. 12). We anticipate that the RBSP mission will resolve the uncertainties.

Sample Question 5 What causes the dramatic, sudden, large-scale dropout of radiation belt particles as near to Earth as $L = 4\ R_E$?

Closely related to the issue of the variable responses of the radiation belts to magnetic storms (Question 1) are the surprising observations of very sudden dropouts of particle fluxes in the outer electron radiation belt (Fig. 15; Su et al. 2011) for L values as close to Earth as 4 R_E. Su et al. (2011) have modeled the particular dropout depicted in Fig. 15 as an amalgamation of multiple processes acting simultaneously, all making significant contributions. The processes included are Magnetopause Shadowing (MS), Adiabatic Transport (AT), Radial Diffusion (RD), and Wave-Particle scattering losses associated with the so-called plasmasheric plumes (PW, comprising losses due to electromagnetic ion cyclotron waves [EMIC] and whistler hiss waves). Multiple processes (magnetopause shadowing and wave scattering) were also invoked by Millan et al. (2010) to explain a similar depletion. For another observed depletion, Turner et al. (2012) invoked magnetopause shadowing followed by modeled outward radiation diffusion.

A common element in all of the most recent proposed ideas is the robust participation of magnetopause shadowing, whereby initially closed magnetic drift paths encounter the magnetopause because of changes in the global magnetic field configuration. Ukhorskiy et al. (2006) have shown that the partial ring current can distort trajectories in the middle magnetosphere to a greater extent that previously appreciated, even to the extent of generating isolated drift path islands (Fig. 16). These strong distortions can substantially enhance the magnetopause shadowing losses. This idea remains highly controversial, and so it and other ideas need to be tested with a mission like RBSP that can separate spatial from temporal processes.

Sample Question 6 How important is the role of substorm injections in generating the radiation belts?

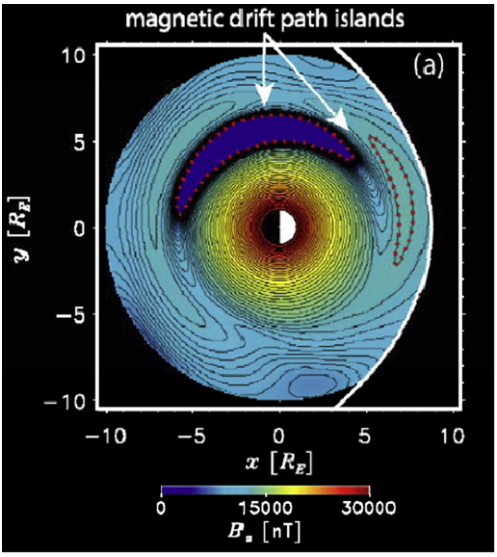

Fig. 16 A model of magnetic configurations that accompany the evacuation of the outer radiation belts based on stronger than anticipated partial ring currents. The partial ring current is strong enough to even generate topological changes in the electron drift orbits. The contours show drift orbits and the colors indicate the perturbation magnetic field strengths. After Ukhorskiy et al. (2006). © The American Geophysical Union

On <1 hour time scales of substorm injections themselves, injections are thought to only modestly perturb the distribution of MeV class electrons in the outer radiation belts. Their importance has traditionally been viewed as helping in the transport of the source populations, specifically by providing a "seed" population for the subsequent transport and energization that occurs during the generation of the radiation belts (Baker et al. 1979, 1981; Fok et al. 2001b). The uncertainties about the configuration of the global electric field configuration, and whether or not enhanced global electric fields move magnetotail plasma sheet particles Earthward during geomagnetic storms (Question 2) raises the importance of establishing the fundamental role that substorm injections may play in the transport of particles to the middle and inner magnetosphere. The relative importance of that role needs to be explored and resolved.

Evidence has been presented that substorms are critical to the fundamental processes that energize radiation belt electrons (Meredith et al. 2002, 2003). It is even suggested that substorms increase radiation belt intensities while storms reduce intensities (Li et al. 2009). Substorm injections disturb the structure of medium energy electron pitch angle distributions, making them highly conducive to the generation of strong whistler/chorus mode emissions. The waves in turn can accelerate the higher energy electrons in the manner described in the discussion of Question 3 (Fig. 11). The evidence in favor of this scenario is based on observed correlations between magnetic storms and substorms as diagnosed with magnetic indices, observations of whistler/chorus mode emissions, and observations of radiation belt intensities over a wide range of energies and extended periods of time. It is of interest that a similar scenario has been proposed for Jupiter's dramatic radiation belt (Horne et al. 2007). Despite the absence of solar wind forcing, injection-like processes occur at Jupiter, associated with the shedding by Jupiter's magnetosphere of the materials dumped into the magnetosphere by the volcanic moon Io. These Jovian injections are observed to be correlated with the generation of strong whistler mode emissions.

Because we are so uncertain as to the role of substorms in the processes of transporting particles from the magnetotail to the middle and inner magnetosphere, much work remains to be done in testing the ideas discussed above and in generally understanding the role of substorms in the generation of Earth's radiation belts.

The sample science questions discussed in this section are intended to give a sense of the many fundamental scientific mysteries that presently pervade our understanding of the behavior of Earth's radiation belts. Their purpose is specifically to confront the longstanding notion that developing a predictive understanding of Earth's radiation belts is simply one of characterization or modeling, and to emphasize the need for comprehensive measurements of both particles and waves.

4 Science Implementation

There are two aspects of the RBSP Mission design that are critical to resolving the science issues illustrated above. RBSP must first deliver simultaneous multipoint sampling at various spatial and temporal scales. Secondly, RBSP must deliver very high quality, integrated in situ measurements with identical instrumentation on the multiple spacecraft.

Simultaneous multipoint sampling has become a mantra for all in situ studies of space phenomena, but it is worth presenting a specific example relevant to the Earth's inner magnetosphere. Figure 17 (Lui et al. 1986) shows oxygen measurements from the AMPTE mission in the form of radial profiles of the particle Phase Space Density (PSD) at a given value of the first adiabatic invariant of gyration (note that PSD[**p**] is derived from $I[E,\alpha]/p^2$, where $I[E,\alpha]$ was defined in the Introduction, and **p** is particle momentum; see the paper by Ukhorskiy and Sitnov in this issue). The kind of presentation in Fig. 17 will be standard for the RBSP mission representation of energetic electron and ion data (e.g. Fig. 10). The figure shows two PSD profiles taken 31 hours apart (before and during a storm period). Two features are of particular interest. First, there is a "shoulder" on the PSD profile that appears to simply move inward from about 5.5 to 3.5 R_E. Did a global increase of inner magnetospheric electric fields drive a coherent adiabatic earthward motion of this shoulder? The other feature of interest is the "bump" centered near $L = 7.5\ R_E$. Does this bump provide

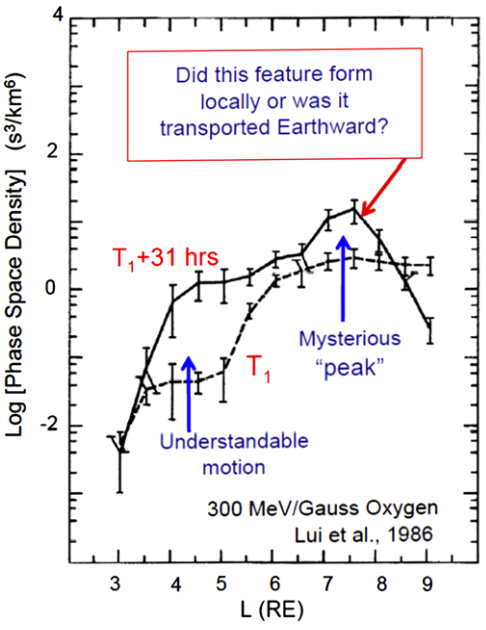

Fig. 17 Pre-storm and storm-time radial phase space density profiles of energetic oxygen ions showing some perhaps understandable and some possibly mysterious changes caused by the storm. The figure is intended to support the need for simultaneous multisatellite sampling over a spectrum of spatial and temporal scales. From Lui et al. (1986). © The American Geophysical Union

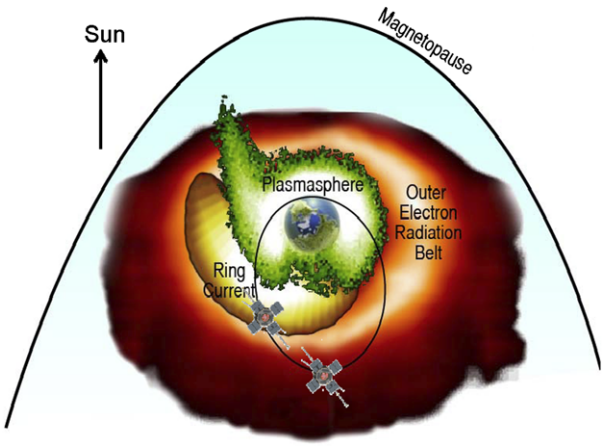

Fig. 18 A snapshot of the orbits of the 2 RBSP spacecraft in the context of structures within Earth's inner magnetosphere

evidence for local acceleration or is it the result of a structure that has propagated inward from adjacent or more distant regions? We simply cannot tell from the available single point measurements. Multipoint sampling over a wide range of time and spatial scales is needed to resolve these kinds of questions.

4.1 RBSP Mission Design

The RBSP mission design that accomplishes the needed multipoint sampling over multiple spatial and temporal scales is illustrated in Fig. 18. The RBSP mission design has the following characteristics.

(1) It comprises two identically instrumented spacecraft.
(2) The two spacecraft are in nearly identical orbits with perigee of ~600 km altitude, apogee of 5.8 R_E geocentric, and inclination of 10°. These orbits allow RBSP to access all of the most critical regions of the radiation belts (Figs. 18 and 19).
(3) The lines of apogee for the two spacecraft precess in local time at a rate of about 210° per year in the clockwise direction (looking down from the north). The 2 year nominal mission lifetime (~4 years of expendables are available) allows all local times to be studied. By starting the mission with lines of apogee at dawn (a Program Level mission requirement), the nightside hemisphere will be accessed twice within the nominal 2 year mission lifetime.
(4) Slightly different (~130 km) orbital apogees cause one spacecraft to lap the other every ~75 days, corresponding to about twice for every quadrant of the magnetosphere visited by the lines of apogee during the two year mission.
(5) Because the spacecraft lap each other, their radial spacing varies periodically between ~100 km and ~5 R_E; and resampling times for specific positions vary from minutes to 4.5 hours.
(6) The orbital cadence (9 hour periods; an average of 4.5 hours between inbound and outbound sampling for each spacecraft) is faster than the relevant magnetic storm time scales (day).
(7) The low inclination (10°) allows for the measurements of most of the magnetically trapped particles; while the precession of the line of apogee and the tilt of the Earth's magnetic axis enables nominal sampling to magnetic latitudes of $0 \pm 21°$ (Fig. 20).

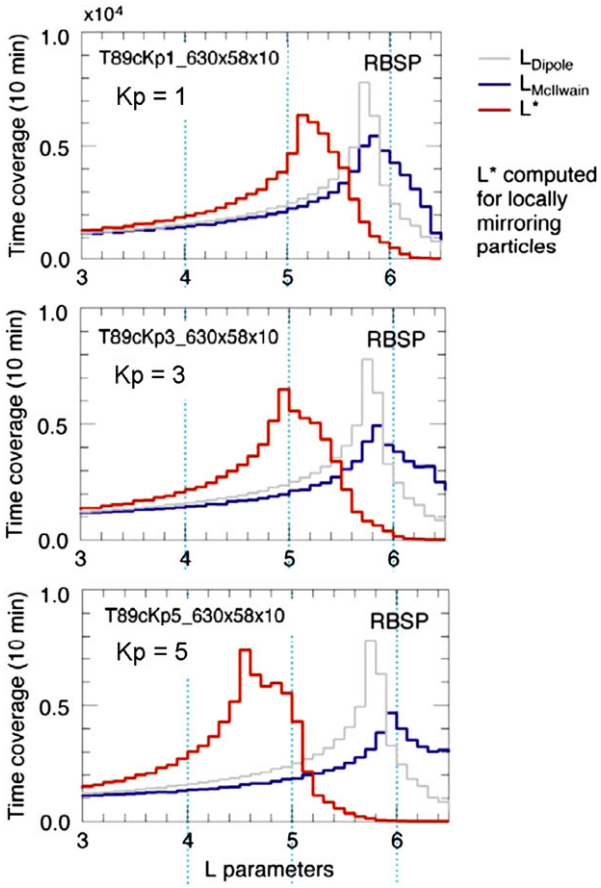

Fig. 19 Modeled, RBSP mission-summed sampling of uniform time samples (10 minutes) of various values of the radial magnetospheric L-parameter (in R_E) for various magnetospheric dynamic conditions as characterized by the activity parameter Kp for inactive conditions ($Kp = 1$), modestly active conditions ($Kp = 3$) and relatively active conditions ($Kp = 5$). The *grey curve* shows the Kp-independent result for sampling the McIlwain L-parameter in a purely dipole field, and the *blue curves* show the sampling of that same parameter for the Kp-dependent TS89 magnetic field model (Tsyganenko 1989). The *red curve* shows the sampling of the so-called L^* parameter, which is the L-shall value of the purely dipolar magnetic field configuration that contains the same magnetic flux as would the particle drift orbit within the true distorted magnetic field configuration. L^* is equivalent to the 3rd adiabatic invariant of particle motion. The McIlwain L-parameter and the L^* parameter are defined, for example, by Roederer (1970); see Ukhorskiy and Sitnov (this issue). L^* has become an increasingly important standard parameter for ordering radiation belt measurements (e.g. Fig. 10)

(8) Spacecraft spin axes point roughly Sunward. Due to orbit precession, the spin axis must be re-aligned with respect to the sun periodically once each ~21 days. The spin axis is always maintained to lie within 27° of the sun's direction.

(9) The 5 RPM spin period of the spacecraft, the nominal sunward orientation of the spin axis, and the positioning of the spacecraft near the magnetic equator of the quasi-dipolar magnetic configuration, combine to enable the particle detectors to obtain fairly complete pitch angle distributions twice for every spin of the spacecraft and the electric field instrument to make excellent measurements of the crucial dawn/dusk electric field.

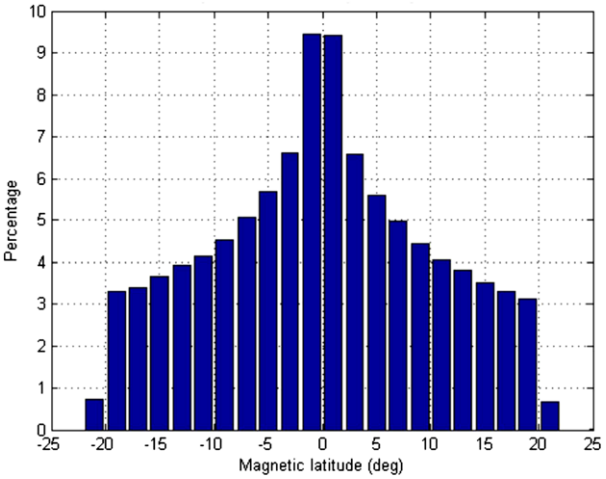

Fig. 20 RBSP mission-averaged sampling of magnetic latitude calculated using a tilted dipole magnetic field model

RBSP is expected to see perhaps 2 dozen magnetic storms during its nominal 2-year lifetime. During critical events (e.g. the several hours that comprise "main phase" periods of magnetic storms), the two spacecraft will perform radial cuts through the inner regions with separation times that vary from minutes to several hours. For each quadrant of Earth's magnetosphere, perhaps 6 storms will be observed within the first 20 months, and again specific features will be sampled with a distribution of separation distances and times. In this way, a range of spatial and temporal scales will be examined by the RBSP mission. To the extent that features such as the "bump" displayed in Fig. 17 characterize radiation belt responses to storms and other processes, as we know they do (Fig. 10), the RBSP mission will definitively distinguish the spatial from temporal structures and establish how they are generated.

Members of the RBSP team will employ modeling and partnerships with other missions to infer details concerning some crucial processes. For example, some strong whistler mode interactions that may energize electrons can occur at relatively high magnetic latitudes, particularly on the dayside (Horne et al. 2005a, 2005b; Bortnik et al. 2008). In the absence of other assets, RBSP will infer the characteristics of such interactions by observing the low-latitude consequences of such interactions and combining those observations with the sophisticated models that are now being brought to bear on the problem (e.g. Bortnik et al. 2008). Additionally, although the RBSP instruments do not have the pitch angle resolution to measure particle fluxes within the atmospheric loss cone, such particles are precisely those that will be measured by the Mission of Opportunity BARREL mission, which focuses upon the radiation belt particles precipitating into the atmosphere (Millan et al. this issue). BARREL will launch a series of balloon-borne X-ray sensors from the Antarctic during two month-long phases of the RBSP mission. Sensors on the SAMPEX, DMSP, and POES spacecraft can also be used to address this particle population. Third, the RBSP team will work with other missions such as THEMIS and geosynchronous spacecraft capable of measuring source populations outside the 5.8 R_E apogee of the RBSP mission. Finally, ACE and other missions will supply information concerning the interplanetary drivers such as the interplanetary magnetic field, and prevailing solar wind conditions.

4.2 RBSP Observations and Instruments

The observation requirements for the RBSP mission and spacecraft payload are delineated in the Program Level (Level-1) requirements document. The verifiable requirements in that document are expressed in the form of specific parameter measurements (e.g. energy ranges, energy resolution, frequency ranges, time cadences, etc.). The "observations" from which these verifiable requirements are derived are in paragraphs that express the "intent" of the mission measurements. Those intended "observations" are paraphrased in the table provided here in Table 1. A survey of these intended observations and their purposes provides an appreciation for the comprehensive measurements provided by the RBSP payload.

The parameter measurement requirements for the RBSP payload, derived by putting the observational needs (Table 1) into the context of the characteristics of Earth's inner and middle magnetosphere, are shown in the Level-1 document tables reproduced in Fig. 21. The instruments and instrument suites that will provide these measurements are summarized here in Table 2. This table also shows the PSBR Investigation, which includes the RPS instrument, a contributed, but not required, element that will fly as part of the RBSP payload on each spacecraft. It targets the inner proton belt by measuring proton energies up to 2 GeV. Additionally, the figure includes the BARREL Mission of Opportunity investigation (mentioned above) which involves balloon payloads flown in the Antarctic in conjunction with the RBSP mission. Each of the entries in Table 2 has one or more chapters in this special issue describing the details and capabilities of the instrumentation.

The particle energy and species coverage requirements versus payload capabilities are shown graphically in Fig. 22. Similarly, the electric and magnetic fields frequency range requirements versus payload capabilities are shown in Fig. 23. These graphical displays demonstrate the comprehensive and coordinated nature of the RBSP payload elements. As an additional requirement within the Program Level requirements document, the "fields" payload elements must be capable of taking concurrent full 3 dimensional (3D) magnetic and 3D electric waveforms with at least 20 k samples/s to determine the propagation characteristics of waves up to 10 kHz. This capability is implemented as a burst capability within the EFW and EMFISIS instruments (Table 2; see Wygant et al. this issue, and Kletzing et al. this issue). What is not apparent from Fig. 22 regarding the particle measurement is the fact that, because of the use of multi-parameter sensing techniques for both electrons and ions, the RBSP particle measurements will be, as a set, the cleanest measurements yet taken in this harsh environment relative to the contamination from penetration radiation (Baker et al. this issue; Blake et al. this issue; Funsten et al. this issue; Lanzerotti et al. this issue; Mazur et al. this issue).

5 Closing Remarks

The high level objectives of the RBSP mission are articulated in Sect. 1. To achieve those objectives it is necessary to develop science questions, like those presented in Sect. 2, that are specific enough to invite the generation of testable hypotheses. The RBSP mission design has many of the capabilities that are needed to discriminate between and test these hypotheses. Most critical is the ability of RBSP to perform simultaneous multipoint sampling over a broad spectrum of spatial and temporal scales, combined with extremely capable and highly coordinated instrumentation. These capabilities will enable researchers to discriminate between time and space variations. With such capabilities one may compare the time scales for the generation of local particle acceleration features with the theoretical expectations

Table 1 RBSP program level (Level-1) observations

Observations	Purposes
Determine spatial/temporal variations of medium & high energy electron & proton angle & energy distributions, faster than drift times, interior & exterior to acceleration events	Determine time history of energization, loss, & transport for hazardous particles. Understand/quantify source of these particles & source paths. Enable improved particle models
Derive electron & proton radial phase space density profiles for medium & high-energy electrons & protons on timescales short compared to storm times	Distinguish between candidate processes of acceleration, transport, & loss, & statistically characterize these processes versus solar input conditions
Determine spatial/temporal variations of charged particle partial pressures & their gradients within the inner magnetosphere with fidelity to calculate pressure-driven currents	Understand how large-scale magnetic & electric fields in the inner magnetosphere are generated & evolve, their role in the dynamics of radiation belt particles, & their role in the creation & evolution of the plasma environments for other processes
Determine spatial/temporal variations of low-to-medium energy electron & ion energy, composition, & angle distributions on timescales short compared to drift periods	Understand/quantify the conditions that control the production & propagation of waves (e.g. EMIC, whistler-mode chorus and hiss); & determine the wave propagation medium
Determine the local steady & impulsive electric & magnetic fields with fidelity to determine the amplitude, vector direction, and time history of variations on a timescale short compared times required for particle measurements	Determine convective & impulsive flows causing particle transport & energization; determine propagation properties of shock-generated propagation fronts; & inferring total plasma densities
Determine spatial/temporal variations of electrostatic & electromagnetic field amplitudes, frequencies, intensities, directions & temporal evolutions with fidelity to calculate wave energy, polarization, saturation, coherence, wave angle, and phase velocity for (A) VLF, and ELF waves, & (B) random, ULF, and quasi-periodic fluctuations	Determine the types/characteristics of plasma waves causing particle energization & loss: including wave growth rates; energization & loss mechanisms; diffusion coefficients & loss rates; plasma densities; ULF waves versus irregular fluctuations effects on radial transport; and statistical maps of wave fields versus position and conditions
Provide concurrent, multipoint measurements sufficient to constrain global convective electric field & storm-time electric and magnetic field models	Covert particle measurements to invariant coordinate systems; infer loss cone sizes; & model effects of global electric & magnetic field variations on particle distributions
Track/characterize transient structures propagating through the inner magnetosphere with fidelity to determine amplitude, arrival times, and propagation directions	Determine which shock-related pressure pulses produce significant acceleration, & provide estimate of their significance relative to other energization mechanisms

based on the measurements of the static and dynamic fields. With such capabilities one may measure rather than just infer the gradients that generate currents and the gradients that reveal electric potential distributions. With the capabilities of the RBSP instrumentation, one may determine the detailed characteristics of resonant interactions between particle and waves.

An important element in achieving complete science closure for some of the science objectives is the utilization of sophisticated models and simulations to place the RBSP multipoint measurements into the broader 3-dimensional picture. Strong coordination between

Particle Measurements

REQ#	Measurement	Cadence	Energy Range	Angular Res.	Energy Res.	No. of platforms
4.1.1.1	High energy electrons	1 distribution per minute	1 – 10 MeV	30°	30% at 3 MeV	2
4.1.1.2	Medium energy electrons	1 distribution per minute	0.05 – 1 MeV	20°	30% at 0.3 MeV	2
4.1.1.3	High energy protons	1 distribution per minute	20 – 75 MeV	30°	40% at 30 MeV	2
4.1.1.4	Medium energy protons	1 distribution per minute	0.1 – 1 MeV	20°	40% at 0.3 MeV	2
4.1.1.5	Medium energy ion composition	1 distribution per minute	0.02 – 0.3 MeV	30°	40% at 0.05 MeV	2
4.1.1.6	Low-Energy ion/electron composition	1 distribution per minute	50 ev – 0.05 MeV	30°	40% at 0.01 MeV	2

Field and Wave Measurements

REQ#	Measurement	Cadence	Frequency Range	Frequency Res.	No. of platforms
4.1.1.7	3-D magnetic Field	20 vectors/s	DC – 10 Hz	n/a	2
4.1.1.8	3-D Wave magnetic field	6s	10 Hz – 10 kHz	20 channels per decade	2
4.1.1.9	3-D Wave electric field	6s	10 Hz – 10 kHz	20 channels per decade	2
4.1.1.10	3-D electric field	20 vectors/s	DC – 10 Hz	n/a	2
4.1.1.11	Plasma Density	10s	n/a	n/a	2

Fig. 21 RBSP measurement parameter requirements as specified in the RBSP Program Level requirements document. These measurement requirements are derived from the observation needs summarized in Table 1

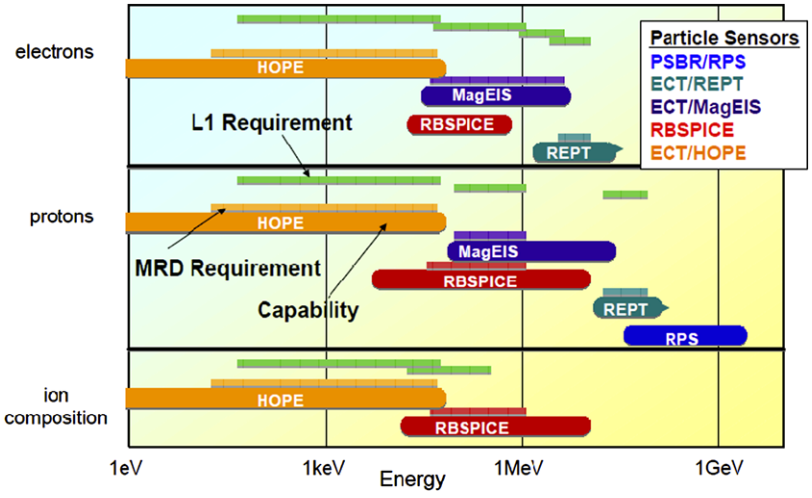

Fig. 22 Comparison between the RBSP particle measurement requirements and instrument capabilities for the range of energies and species to be measured

data analysts and model builders is described in each of the investigation reports in this special issue, and specifically in the articles by Spence et al., Kletzing et al., Lanzerotti et al., Wygant et al., and Ginet et al.

Table 2 RBSP investigations

Instrument/Suites	Science teams	Science investigation
Energetic Particle, **C**omposition and **T**hermal Plasma Suite (**ECT**)	*Harlan Spence*, PI University of New Hampshire *Key partners*: LANL, SwRI, Aerospace, LASP	Measure near-Earth space radiation belt particles to determine the physical processes that produce enhancements and loss
Electric and **M**agnetic **F**ield **I**nstrument **S**uite and **I**ntegrated **S**cience (**EMFISIS**)	*Dr. Craig Kletzing*, PI University of Iowa *Key partners*: NASA/GSFC, University of New Hampshire	Understand plasma waves that energize charged particles to very high energies; measure distortions to Earth's magnetic field that control the structure of the radiation belts
Electric **F**ield and **W**aves Instrument (**EFW**)	*John Wygant*, PI University of Minnesota *Key partners*: University of California, Berkeley, LASP	Study electric fields and waves that energize charged particles and modify the inner magnetosphere
Radiation **B**elt **S**torm **P**robes **I**on **C**omposition **E**xperiment (**RBSPICE**)	*Louis Lanzerotti*, PI New Jersey Institute of Technology *Key partners*: APL, Fundamental Technologies	Understand the creation of the "storm time ring current" and the role of the ring current in the creation of radiation belt populations
Proton **S**pectrometer **B**elt **R**esearch (**PSBR**)	*David Byers*, PSBR PI National Reconnaissance Office *Key partners*: Aerospace Corp. MIT Lincoln Lab.	Specification models of the high-energy particles in the inner radiation belt
Relativistic **P**roton **S**pectrometer (**RPS**)	*Joseph Mazur*, RPS PI Aerospace Corp.	
Balloon **A**rray for **RBSP** **R**elativistic **E**lectron **L**osses (**BARREL**)	*Robyn Millan*, PI Dartmouth College	Measure, study, and understand electron loss processes from Earth's outer electron belt

A distinction is made in the structure of this special issue on the RBSP mission between the instrument investigations and the instruments themselves. The papers cited at the end of the last paragraph describe the instrument investigation for the ECT, EMFISIS, RBSPICE, EFW, and PSBR investigations (see Table 2). These papers describe in various degrees the science objectives of the individual team investigations, the science teams involved, the data processing, analysis, and archiving plans, the role of theory and modeling in resolving the targeted science issues, and the role of modeling in synthesizing the limited two point measurements that are made by the RBSP instruments. The instrumentation associated with these instrument investigations are in some cases described within the same instrument investigation papers (EMFISIS: Kletzing et al.; RBSPICE: Lanzerotti et al.; and EFW: Wygant et al.). In other cases the instrumentation is described in separate papers (ECT-HOPE: Funsten et al.; ECT-MagEIS: Blake et al.; ECT-REPT: Baker et al.; PSBR-RPS: Mazur et al.; again see Table 2).

Other papers in this special issue describe engineering details of the RBSP mission (Stratton et al.), the RBSP spacecraft (Kirby et al.), the RBSP contributions to the practical issues of space weather (Kessel et al.), the overarching RBSP data processing, analysis, dissemination, and archiving plans (Science Operations: Fox et al.), and the RBSP Education and

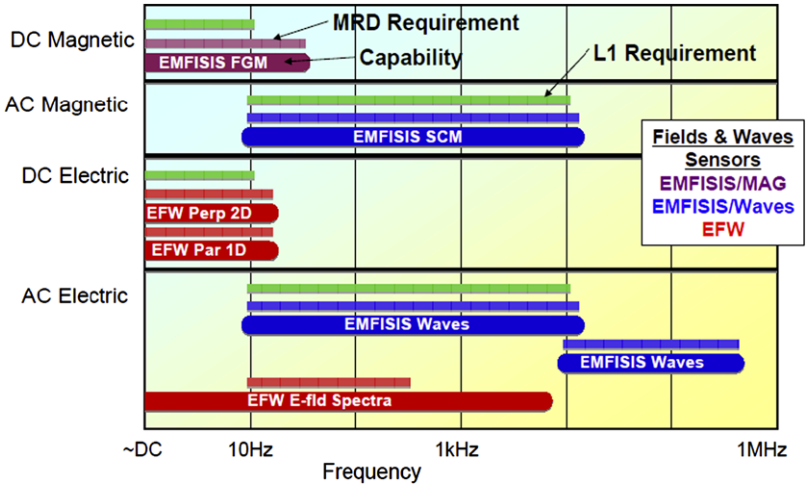

Fig. 23 Comparison between the RBSP fields measurement requirements and instrument capabilities for the range of frequencies and fields types to be measured

Public Outreach plan (EPO: Fox et al.). Additionally, Ukhorskiy and Sitnov review present understanding regarding the definitions and calculations of various parameters that order the radiation belts and the mathematical tools that are used to manipulate those parameters; and Millan et al. describe the Mission of Opportunity Antarctic high-altitude balloon program called BARREL that will make measurements of precipitated electrons in coordination with the RBSP mission. Finally, Goldsten et al. describe an engineering sub-system, the Environmental Radiation Monitor that measures total radiation dose under various shielding thickness and monitors the potential for deep dielectric discharge by measuring the penetrating electron current delivered to two deeply buried conductors.

Acknowledgements We very much appreciate the efforts of Thomas Sotirelis, Kazue Takahashi, and Gene Heyler in generating several of the important plots and analyses for this paper, most specifically, Figs. 19 and 20.

References

D.N. Baker, R.D. Belian, P.R. Higbie, E.W. Hones Jr., J. Geophys. Res. **84**(A12), 7138–7154 (1979). doi:10.1029/JA084iA12p07138

D.N. Baker, E.W. Hones Jr., P.R. Higbie, R.D. Belian, P. Stauning, J. Geophys. Res. **86**(A11), 8941–8956 (1981). doi:10.1029/JA086iA11p08941

D.N. Baker, S.G. Kanekal, X. Li, S.P. Monk, J. Goldstein, J.L. Burch, Nature **432**, 878 (2004). doi:10.1038/nature03116

D.N. Baker et al., The relativistic electron-proton telescope (REPT/ECT) instrument on board the radiation belt storm probes (RBSP) spacecraft: characterization of Earth's radiation belt high-energy particle populations, this issue

J.B. Blake, W.A. Kolasinski, R.W. Fillius, E.G. Mullen, Geophys. Res. Lett. **19**(8), 821–824 (1992). doi:10.1029/92GL00624

J.B. Blake et al., The MagEIS/ECT instrument on the RBSP mission, this issue

J. Bortnik, R.M. Thorne, U.S. Inan, Geophys. Res. Lett. **35**, L21102 (2008). doi:10.1029/2008GL035500
W.J. Burke, L.C. Gentile, C.Y. Huang, J. Geophys. Res. **112**, A07208 (2007). doi:10.1029/2006JA012137
C. Cattell et al., Geophys. Res. Lett. **35**, L01105 (2008). doi:10.1029/2007GL032009
Y. Chen, G.D. Reeves, R.H.W. Friedel, *Nature Physics*, 1 July 2007. doi:10.1038/nphys655
S.P. Christon, D.J. Williams, D.G. Mitchell, C.Y. Huang, L.A. Frank, J. Geophys. Res. **96**(A1), 1–22 (1991). doi:10.1029/90JA01633
A.J. Dessler, E.N. Parker, Hydromagnetic theory of geomagnetic storms. J. Geophys. Res. **64**(12), 2239–2252 (1959). doi:10.1029/JZ064i012p02239
W.C. Feldman, J.R. Asbridge, S.J. Bame, M.D. Montgomery, S.P. Gary, J. Geophys. Res. **80**(31), 4181–4196 (1975). doi:10.1029/JA080i031p04181
M.-C. Fok, T.E. Moore, W.N. Spjeldvik, J. Geophys. Res. **106**, 3873–3881 (2001a). doi:10.1029/2000JA000150
M.-C. Fok, R.A. Wolf, R.W. Spiro, T.E. Moore, J. Geophys. Res. **106**, 8417–8424 (2001b). doi:10.1029/2000JA000235
N.J. Fox, B.H. Mauk, J.B. Blake, Geophys. Res. Lett. **33**, L18108 (2006). doi:10.1029/2006GL026598
N.J. Fox, M. Weiss, R. Barnes, The RBSP science operations plans, this issue
H.O. Funsten et al., The HOPE/ECT instrument on the RBSP mission, this issue
G.P. Ginet et al., AE9/AP9/SPM: models for specifying the trapped energetic particle and space plasma environment, this issue
J.O. Goldsten, R.E.H. Maureer, P.N. Peplowski, A. Holmes-Siedle, C.C. Herrmann, B.H. Mauk, The RBSP engineering radiation monitor, this issue: doi:10.1007/s11214-012-9917-x
J.C. Green, M.G. Kivelson, J. Geophys. Res. **109**, A03213 (2004). doi:10.1029/2003JA010153
W.N. Hess, *The Radiation Belt and Magnetosphere* (Blaisdell, Boston, 1968)
T. Hori, A.T.Y. Lui, S. Ohtani, P. Cson Brandt, B.H. Mauk, R.W. McEntire, K. Maezawa, T. Mukai, Y. Kasaba, H. Hayakawa, J. Geophys. Res. **110**, A04213 (2005). doi:10.1029/2004JA010449
R.B. Horne, R.M. Thorne, Geophys. Res. Lett. **25**(15), 3011–3014 (1998). doi:10.1029/98GL01002
R.B. Horne, R.M. Throne, N.P. Meredith, R.R. Anderson, J. Geophys. Res. **108**(A7), 1290 (2003). doi:10.1029/2002JA009736
R.B. Horne et al., Nature **437**, 227–230 (2005a). doi:10.1038/nature03939
R.B. Horne, R.M. Thorne, S.A. Glauert, J.M. Albert, N.P. Meredith, R.R. Anderson, J. Geophys. Res. **110**, A03225 (2005b). doi:10.1029/2004JA010811
R.B. Horne, R.M. Thorne, S.A. Glauert, N.P. Meredith, D. Pokhotelov, O. Santolík, Geophys. Res. Lett. **34**, L17107 (2007). doi:10.1029/2007GL030267
M.K. Hudson, G.T. Kress, H.-R. Mueller, J.A. Zastrow, J.B. Blake, J. Atmos. Sol.-Terr. Phys. **70**, 708–729 (2008)
R.H.A. Iles, N.P. Meredith, A.N. Fazakerley, R.B. Horne, J. Geophys. Res. **111**, A03204 (2006). doi:10.1029/2005JA011206
A.S. Jursa, *Handbook of Geophysics and the Space Environment* (Air Force Geophysics Laboratory, Hanscom, 1985)
P.J. Kellogg, C.A. Cattell, K. Goetz, S.J. Monson, L.B. Wilson III, Geophys. Res. Lett. **37**, L20106 (2010). doi:10.1029/2010GL044845
K. Kersten, C.A. Cattell, A. Breneman, K. Goetz, P.J. Kellogg, J.R. Wygant, L.B. Wilson III, J.B. Blake, M.D. Looper, I. Roth, Geophys. Res. Lett. **38**, L08107 (2011). doi:10.1029/2011GL046810
R.L. Kessel, N.J. Fox, M. Weiss, RBSP and space weather, this issue
G.V. Khazanov, K.V. Gamayunov, V.K. Jordanova, J. Geophys. Res. **108**(A12), 1419 (2003). doi:10.1029/2003JA009856
K.W. Kirby et al., Radiation belt storm probe spacecraft and environments, this issue
M.G. Kivelson, C.T. Russell, *Introduction to Space Physics* (Cambridge University Press, Cambridge, 1995)
C. Kletzing et al., The electric and magnetic field instrument suite and integrated science (EMFISIS) on RBSP, this issue
L.J. Lanzerotti et al., Radiation belt storm probes ion composition experiment (RBSPICE), this issue
J.F. Lemaire, D. Heynderickx, D.N. Baker, *Radiation Belts, Models and Standards*, Geophysical Monograph, vol. 97 (American Geophysical Union, Washington, 1996)
X. Li, I. Roth, M. Temerin, J.R. Wygant, M.K. Hudson, J.B. Blake, Geophys. Res. Lett. **20**(22), 2423–2426 (1993). doi:10.1029/93GL02701
L.Y. Li, J.B. Cao, G.C. Zhou, X. Li, J. Geophys. Res. **114**, A12214 (2009). doi:10.1029/2009JA014333
X. Li, M. Temerin, D.N. Baker, G.D. Reeves, J. Geophys. Res. **116**, A11207 (2011). doi:10.1029/2011JA016934
M.W. Liemohn, J. Geophys. Res. **108**(A6), 1251 (2003). doi:10.1029/2003JA009839
R.P. Lin, Space Sci. Rev. **86**, 61–78 (1998)

K.R. Lorentzen, M.D. Looper, J.B. Blake, Relativistic electron microbursts during the GEM storms. Geophys. Res. Lett. **28**(13), 2573–2576 (2001). doi:10.1029/2001GL012926
G.H. Ludwig, *Opening Space Research, Dreams, Technology, and Scientific Discovery* (Geopress, American Geophysical Union, Washington, 2011)
A.T.Y. Lui, R.W. McEntire, S.M. Krimigis, E.P. Keath, in *Ion Acceleration in the Magnetosphere and Ionosphere*. Geophysical Monograph, vol. 38 (American Geophysical Union, Washington, 1986), pp. 149–152
G.M. Mason, D.N. Baker, J.B. Blake, L.B. Callis, D.C. Hamilton, D. Hovestadt, B. Klecker, R.A. Mewaldt, M. Scholer, E.C. Stone, T.T. von Rosenvinge, SAMPEX mission overview, in *Particle Astrophysics: the NASA Cosmic Ray Program for the 1990s and Beyond*. AIP Conference Proceedings, vol. 203 (American Institute of Physics, New York, 1990), pp. 44–47
B.H. Mauk, N.J. Fox, J. Geophys. Res. **115**, A12220 (2010). doi:10.1029/2010JA015660
J. Mazur et al., The relativistic proton spectrometer (RPS) sensor for the radiation belt storm probes mission, this issue
C.E. McIlwain, J. Geophys. Res. **66**(11), 3681–3691 (1961). doi:10.1029/JZ066i011p03681
N.P. Meredith, R.B. Horne, R.H.A. Iles, R.M. Thorne, D. Heynderickx, R.R. Anderson, J. Geophys. Res. **107**(A7), 1144 (2002). doi:10.1029/2001JA900146
N.P. Meredith, M. Cain, R.B. Horne, R.M. Thorne, D. Summers, R.R. Anderson, J. Geophys. Res. **108**(A6), 1248 (2003). doi:10.1029/2002JA009764
R.M. Millan, K.B. Yando, J.C. Green, A.Y. Ukhorskiy, Geophys. Res. Lett. **37**, L20103 (2010). doi:10.1029/2010GL044919
R. Millan et al., The BARREL mission of opportunity investigation for the RBSP mission, this issue
R. Nakamura, M. Isowa, Y. Kamide, D.N. Baker, J.B. Blake, M. Looper, J. Geophys. Res. **105**(A7), 15,875–15,885 (2000). doi:10.1029/2000JA900018
T.P. O'Brien, M.D. Looper, J.B. Blake, Geophys. Res. Lett. **31**, L04802 (2004). doi:10.1029/2003GL018621
G.D. Reeves, K.L. McAdams, R.H.W. Friedel, T.P. O'Brien, Geophys. Res. Lett. **30**(10), 1529 (2003). doi:10.1029/2002GL016513
J.G. Roederer, *Dynamics of Geomagnetically Trapped Radiation* (Springer, Berlin, 1970)
D.E. Rowland, J.R. Wygant, J. Geophys. Res. **103**(A7), 14,959–14,964 (1998). doi:10.1029/97JA03524
D.M. Sawyer, J.I. Vette, AP-8 trapped proton environment for solar maximum and solar minimum, NSSDC/WDC-A-R&S 76-06, NASA-GSFC TMS-72605 (1976)
M. Schulz, L.J. Lanzerotti, *Particle Diffusion in the Radiation Belts* (Springer, Berlin, 1974)
N. Sckopke, J. Geophys. Res. **71**, 13 (1966). doi:10.1029/JZ071i013p03125
G.W. Singley, J.I. Vette, The AE-4 model of the outer radiation zone electron environment, NSSDC 72-06 (1972)
H.E. Spence et al., The ECT investigation on the RBSP mission, this issue
J.M. Stratton, R.J. Harvey, G.A. Heyler, Mission overview for the radiation belt storm probes mission, this issue: doi:10.1007/s11214-012-9933-x
Z. Su, F. Xiao, H. Zheng, S. Wang, Geophys. Res. Lett. **38**, L06106 (2011). doi:10.1029/2011GL046873
D. Summers, R.M. Thorne, F. Xiao, J. Geophys. Res. **103**(A9), 20,487–20,500 (1998). doi:10.1029/98JA01740
R.M. Thorne, Geophys. Res. Lett. **37**, L22107 (2010). doi:10.1029/2010GL044990
R.M. Thorne, T.P. O'Brien, Y.Y. Shprits, D. Summers, R.B. Horne, J. Geophys. Res. **110**, A09202 (2005). doi:10.1029/2004JA010882
N.A. Tsyganenko, A magnetospheric magnetic field model with a warped tail current sheet. Planet. Space Sci. **37**, 5 (1989)
D.L. Turner, Y. Shprits, M. Hartinger, V. Angelopoulos, Nature Phys. **8**, 208 (2012). doi:10.1038/NPhysics2185
E.D. Turney, A.M. Novak, K. Beisser, N. Fox, Radiation belt storm probes (RBSP) education and public outreach program, this issue
A.Y. Ukhorskiy, M. Sitnov, Dynamics of radiation belt particles, this issue
A.Y. Ukhorskiy, B.J. Anderson, P.C. Brandt, N.A. Tsyganenko, J. Geophys. Res. **111**, A11S03 (2006)
A. Ukhorskiy, P. O'Brien, D. Sibeck, Special issue: dynamic variability of Earth's radiation belts. J. Atmos. Sol.-Terr. Phys. **70**(14), 1679–1846 (2008)
J.A. Van Allen, *Origins of Magnetospheric Physics* (Smithsonian Inst., Washington, 1983)
M. Walt, in *Discovery of the Magnetosphere*, ed. by C.S. Gillmaor, J.R. Spreiter. History of Geophysics, vol. 7 (American Geophysical Union, Washington, 1997), pp. 253–264
J.R. Wygant et al., The EFW investigation and instruments on the RBSP mission, this issue
I.V. Zavidonov, Sputniks, explorers, and propaganda: the discovery of the Earth's radiation belts. Hist. Technol. **17**, 99–124 (2000)

DOI 10.1007/978-1-4899-7433-4_3
Reprinted from *Space Science Reviews* Journal, DOI 10.1007/s11214-012-9933-x

Mission Overview for the Radiation Belt Storm Probes Mission

J.M. Stratton · R.J. Harvey · G.A. Heyler

Received: 5 June 2012 / Accepted: 23 August 2012 / Published online: 4 January 2013

Abstract Provided here is an overview of Radiation Belt Storm Probes (RBSP) mission design. The driving mission and science requirements are presented, and the unique engineering challenges of operating in Earth's radiation belts are discussed in detail. The implementation of both the space and ground segments are presented, including a discussion of the challenges inherent with operating multiple observatories concurrently and working with a distributed network of science operation centers. An overview of the launch vehicle and the overall mission design will be presented, and the plan for space weather data broadcast will be introduced.

Keywords NASA · Space weather · Radiation belt · Magnetosphere · Geomagnetic storm

1 Introduction

The Radiation Belt Storm Probes (RBSP) Mission is part of NASA's Living With a Star program and is being implemented by the Johns Hopkins University Applied Physics Laboratory (APL) in Laurel, MD. The organizational structure of the mission is presented below in Fig. 1. The fundamental purpose of the mission is to provide a better understanding of the processes that drive changes within the Earth's radiation belts. The flight segment of the mission consists of two nearly-identical observatories, each instrumented with a set of eight instruments (in five instrument suites) that measure particle intensities over a wide range of energy and species, as well as the magnetic and electric fields over a wide range of frequencies. The Science Objectives and rationale for the mission are provided by Mauk et al. (this issue), and details of the spacecraft design are provided by Kirby et al. (2012, this issue). The details of each of the RBSP instruments are described in companion papers within this special issue. In the sections that follow we describe the mission requirements, describe mission design, summarize the observatory configuration, describe the mission operations and facilities, and describe the unique challenges that had to be overcome to implement this unique mission.

J.M. Stratton (✉) · R.J. Harvey · G.A. Heyler
Applied Physics Laboratory, The Johns Hopkins University, Laurel, MD 20723, USA
e-mail: James.Stratton@jhuapl.edu

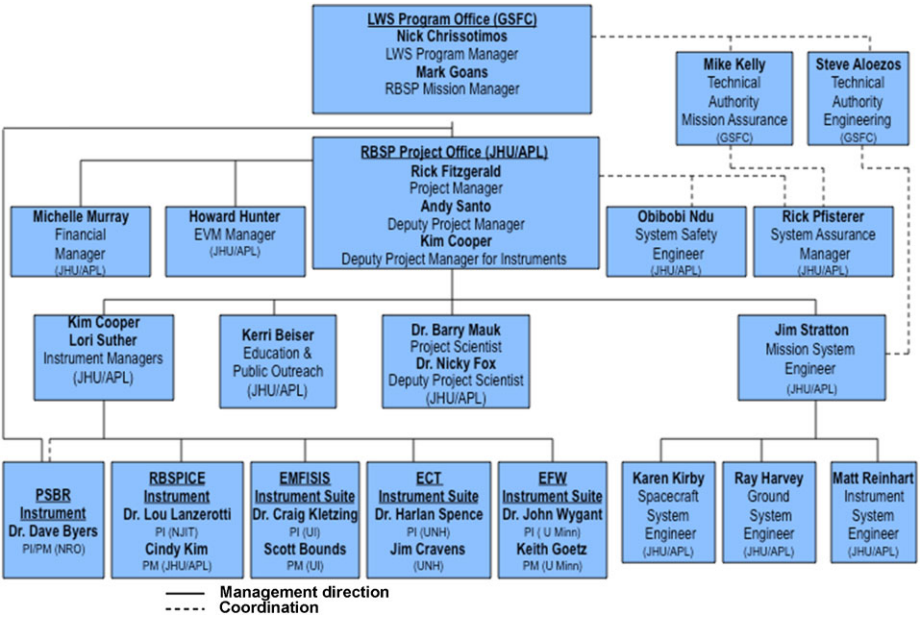

Fig. 1 RBSP program organization (RBSP 2012)

2 Mission Requirements

The science goals drive certain key requirements that define the rest of the mission system. Here we describe selected requirements for the RBSP mission, with an emphasis on those requirements that had the greatest impacts on the mission design (the driving requirements).

2.1 Orbit Definition & Mission Life

The science goals drive certain key requirements that define the rest of the mission system. The most fundamental of these requirements is that the mission fly two functionally equivalent observatories in orbits that take them through the various regions of the Earth's radiation belts. Specifically, the orbits are required to have an apogee altitude between 30,050 km and 31,250 km, a perigee altitude between 500 km and 675 km, and an orbital inclination of $10° \pm 0.25°$. These constraints place the observatories in orbits that cut through both the inner and outer radiation belts, and which sweep through all local Solar times as the orbit precesses over time.

Regions of particular interest to the science community occur between local Solar dawn (06:00) and dusk (18:00), as shown below in Fig. 2. Thus, the mission is designed such that the apogee of each observatory passes through all local Solar times in this region during the first year of the mission after commissioning. The baseline mission life is two years (plus commissioning), allowing the local Solar dawn region—which is of particular interest—to be studied twice in full. Lastly, per NASA's orbital debris mitigation requirements, both observatories must be disposed of at the end of the mission.

Fig. 2 RBSP mission design

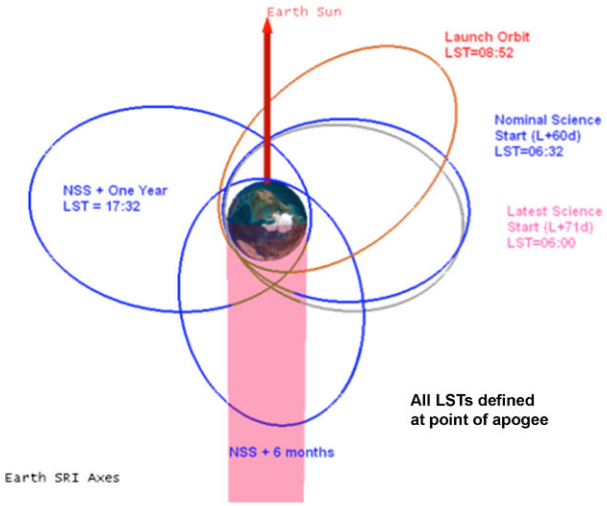

2.2 Operate—Through "Storm" Events

As this is a mission to study radiation belt science, the observatories must continue to operate in the harsh radiation environment. One key goal of the investigation is to observe the effects and the processes at work during a Solar storm, so the observatories must continue to collect science data through the worst expected storm environment. This requirement, particularly on a mission that is categorized as Risk Category C and thus contains only limited hardware redundancy, significantly drove the design of the flight system. The impacts this requirement imposes on the design of the system are discussed in greater detail below.

2.3 Electromagnetic Cleanliness and Control

The RBSP science investigation relies on an accurate understanding of the ambient environment in which the various measurements are being made. This drives the need for both magnetic and electric (differential charging) cleanliness of the observatories. Each observatory is required to have a residual magnetic field (as measured at the magnetometer locations) of less than 5 nT, with dynamic variations of this residual field of less than 0.1 nT. Similarly, the observatory-generated electric field as measured at the tip of the EFW axial booms is required to be less than 4 mV/m, even in the worst-case charging environments. Again, the effect of these requirements on the design of the flight system is discussed in more detail below.

2.4 Inter-instrument Requirements

The use of a suite of multiple instruments to capture the various data products required for the investigation dictates the need for significant coordination between these instruments and with the spacecraft bus itself. The ability to correlate the relative time of measurements from different instruments is required to allow the science team to distinguish temporal behavior within the radiation belts, and this in turn drives the need for accurate time knowledge between the instruments and also with the spacecraft avionics. The value of the science gathered can also be significantly enhanced if the instruments have the ability to share some

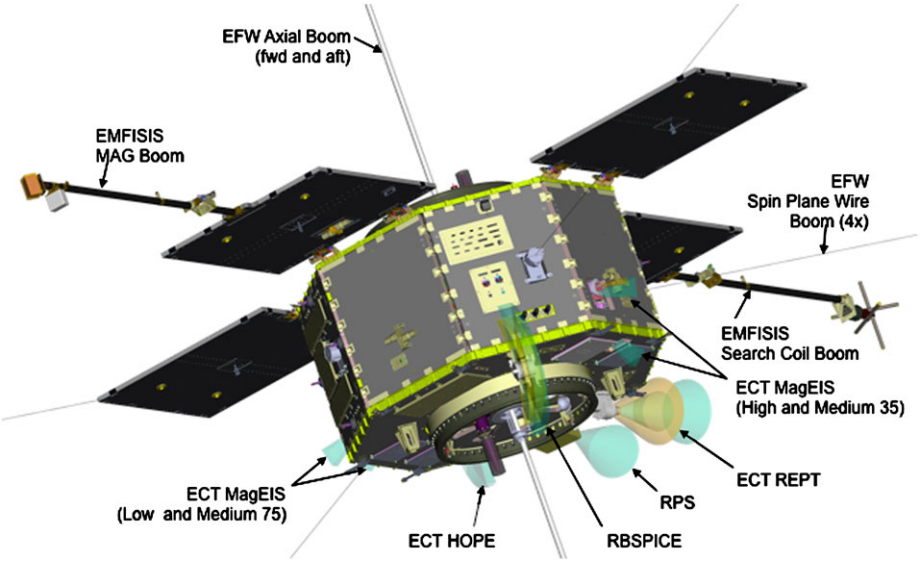

Fig. 3 RBSP observatory deployed configuration

amount of data in real-time. For example, an instrument can send out a "flag" that a significant even is occurring, and other instruments can then trigger off this signal and increase capture data rates or switch instrument modes to better investigate the event. This provides the best possible chance of capturing the high-value data associated with storm events.

2.5 Attitude Determination & Control

As with most spacecraft, attitude knowledge plays an important role for this mission. The science investigation requires a post-processed attitude knowledge of $\leq$3 degrees (3-sigma). Both observatories are nominally Sun-pointing and spin stabilized. To maintain the observatory's Sun sensors within the operational range and to ensure sufficient power system margins, the total off-pointing angle between each observatory and the Sun-Earth line is required to remain within the range of 15–27 degrees. Further, each observatory is required to operate within the spin range of 4–6 RPM during normal operations, and to maintain the spin rate within 0.25 RPM once the nominal spin rate is established.

3 Mission Design

In order to achieve the mission science objectives, the RBSP flight segment includes two nearly-identical observatories operating in highly elliptical Earth orbits. The two observatories are launched from Kennedy Space Center aboard a single Atlas V 401 launch vehicle. One of the observatories is shown in its deployed flight configuration below in Fig. 3. After launch ascent into a 167 km by 598 km parking orbit, the launch vehicle coasts for nearly a one-half orbit revolution, and then performs a maneuver to raise the apogee of its orbit. The vehicle then initiates an attitude maneuver that points the nose of the vehicle towards the Sun, which is in a direction that is nearly orthogonal to the flight direction. The first observatory (known as RBSP-A) is separated and the launch vehicle slews back to pointing in

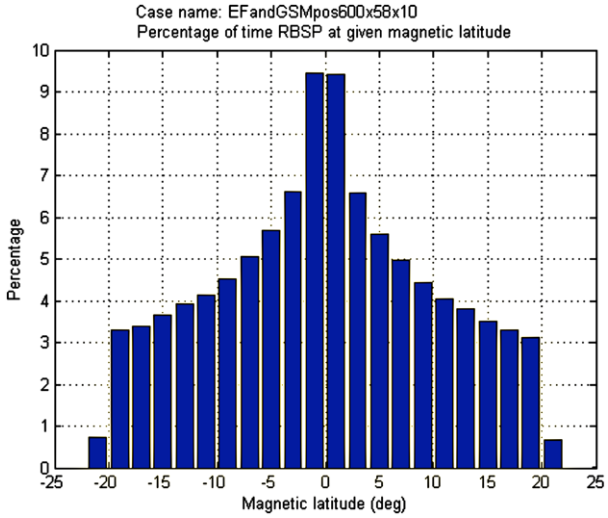

Fig. 4 RBSP magnetic latitude coverage

its flight direction. It then performs a small settling burn as a setup for its upcoming deorbit burn. This maneuver serves two purposes: it forces propellants to the bottom of the tanks, and it raises the apogee of the instantaneous orbit by 130 km to the desired altitude. The launch vehicle then slews back to pointing towards the Sun and then separates the second observatory (RBSP-B).

The nominal injection orbits of the two observatories are approximately 600 km × 30,500 km, which results in an orbit period of approximately 9 hours and 3 minutes, and as stated previously the orbit is at a 10° inclination. The difference in apogee between RBSP-A and RBSP-B causes RBSP-A to continually "lap" RBSP-B, with a lapping rate of approximately four times per year. That is, over a period of 90 days, RBSP-A evolves 239 orbits while RBSP-B evolves 238 orbits. Thus, throughout the mission the two observatories are constantly changing their relative positions, allowing the mission science team ample opportunity to study both the temporal and spatial effects of changes in the radiation belts.

The current manifested launch date for the RBSP observatories is 23 August 2012, though the mission design allows for a launch opportunity on any day of the year. The launch injection point is chosen such that the apogee of each observatory orbit, expressed in Local Solar Time (LST), will pass through local Solar dawn approximately 71 days after launch. This allows the observatories to proceed through their 60-day commissioning period with some margin before the required start of nominal science operations. The apogee LSTs then precess through all local Solar times between dawn and dusk over the course of the first year of nominal science operations, and the apogee LSTs will pass through all local Solar times in the two year nominal mission.

Because of varying declinations of the Sun throughout the year, the rate at which apogee LSTs precess from their initial launch value to local Solar dawn also varies; that is, the precession rate is dependent on launch date. To hold the 71-day precession requirement, the varying precession rates require the design of multiple launch trajectories that have various initial apogee LSTs relative to local Solar dawn. This in turn requires a varying daily launch time throughout the year.

Because of acceptable granularity in the desired initial LSTs, it is possible to group several adjacent launch days to have the same targeted LST. The 366 day year was condensed into 32 unique daily LSTs, and then reverse propagated to find their associated launch times.

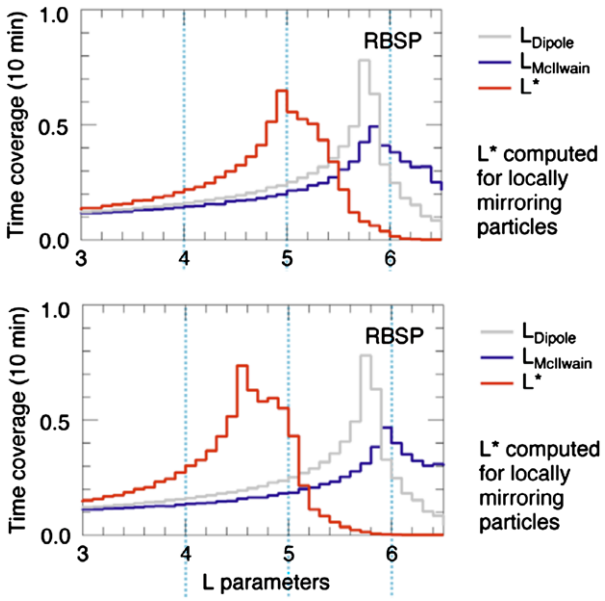

Fig. 5 RBSP L parameter coverage computed using T89c for Kp1 (*top*) and Kp5 (*bottom*)

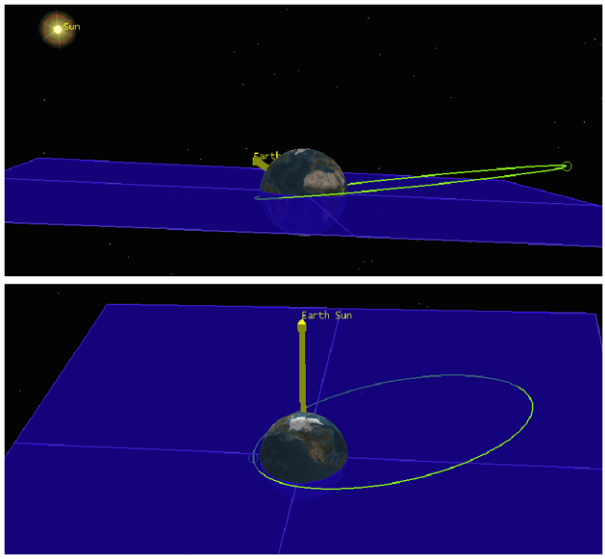

Fig. 6 Two limiting cases for orbit variation with changes in Argument of Perigee (AOP)

The earliest launch time was found to be 08:05 UTC for 29–31 August and 6–9 September, while the latest launch time was found to be 08:54 UTC for 28–29 April and 8 May.

This mission design results in an orbit with a period of approximately nine hours, and the low inclination means that most orbits include periods of eclipse. The maximum eclipse time the observatories will see is approximately 114 minutes when the orbit apogee LST is passing through local midnight, though most eclipses are of significantly shorter duration. This in turn drives the design of both the power generation and thermal management systems. This orbit design also provides for multiple ground contact opportunities for each

Fig. 7 Stacked observatories in the Atlas V 401 launch vehicle fairing

observatory on most days, and at least one ground contact opportunity for each observatory on each day.

The RBSP orbit configuration was designed to provide coverage near the magnetic equator (Fig. 4) in order to well sample the particle population, and to cover a range of radial distances most important to radiation belt physics (Fig. 5). The Argument of Perigee (AOP) cycles through all values every ∼14 months. The two limiting cases—which occur every 3.5 months—are shown in Fig. 6.

4 Launch Vehicle Overview and Interfaces

As mentioned previously, the observatories will be launched together aboard a single Atlas V 401 launch vehicle. An illustration of the observatories in their stacked configuration in the 4 m launch vehicle fairing is shown below in Fig. 7. The observatories mate to the launch vehicle via a standard EELV 937 mm. interface, and are attached using a RUAG Lightband separation system. The launch vehicle provides umbilical power, telemetry and purge services to both observatories via T-0 interfaces that are active until just prior to launch. The umbilical services for RBSP B (the "bottom" observatory in the stacked configuration) are routed up from the launch vehicle adapter and across the launch vehicle/observatory interface plane, whereas the umbilical services for RBSP A are provided via a "flyaway boom" that extends from the launch vehicle fairing to the side of the observatory. The air in the fairing is conditioned from the time of encapsulation until shortly before launch to maintain observatory-specified temperature and humidity requirements.

The Atlas V 401 launch vehicle is a two-stage rocket that does not have any solid rocket motors. Approximately 4 minutes after liftoff the Centaur second stage of the launch vehicle separates from the first stage and begins the first of two long burns. Fairing jettison occurs 8 seconds after the start of the first second stage burn, and the burn lasts for just under 10 minutes. The vehicle then enters a coast phase of approximately 55 minutes to achieve the desired geometry prior to final injection. After performing an approximately 5 minute second burn of the second stage, the launch vehicle turns to a near-Sun pointing attitude, spins up to 5 RPM and releases RBSP A approximately 79 minutes after liftoff. The launch vehicle then performs a short maneuver to raise the apogee of RBSP B, orients to the desired separation attitude, spins to 5 RPM and then separates the second observatory approximately 91 minutes after launch. Finally, the Centaur second stage performs a controlled de-orbit maneuver and reenters the atmosphere over the southern Atlantic Ocean approximately 12 hours after liftoff.

5 Instrument Payload & Data Management

Each RBSP observatory carries four instrument suites and one instrument contributed to the mission by the National Reconnaissance Office (NRO). The instruments are designed to observe a broad spectrum of energetic particles while measuring the in-situ magnetic and electric field environments in which the observations are taken. The top-level science requirements are provided below in Tables 1 and 2, and the capabilities of the instruments are shown in Figs. 8 and 9. Lastly, a brief introduction to each of the instrument suites is included. The telemetry allocations by instrument suite are shown in Table 3.

5.1 Electric and Magnetic Field Instrument Suite and Integrated Science (EMFISIS)

This investigation will provide the observations needed to determine the origin of important plasma wave classes and their role in particle acceleration and loss processes. EMFISIS will provide calculations of on board spectra, including spectral matrices, making it possible to determine wave normal angles and Poynting fluxes for the plasma waves of interest. In addition, EMFISIS provides information for wave mode identification and propagation modeling which are essential for understanding and modeling of radiation particle physics. EMFISIS will also measure the upper hybrid frequency, permitting accurate determination of the electron plasma density required for analysis of wave propagation and instability growth

Table 1 Baseline particle measurement requirements

Measurement	Cadence	Energy range	Angular resolution	Energy resolution	Number of platforms
High energy electrons	1 distribution per minute	1–10 MeV	30°	30 % at 3 MeV	2
Medium energy electrons	1 distribution per minute	0.05–1 MeV	20°	30 % at 0.3 MeV	2
High energy protons	1 distribution per minute	20–75 MeV	30°	40 % at 30 MeV	2
Medium energy protons	1 distribution per minute	0.1–1 MeV	20°	40 % at 0.3 MeV	2
Medium-energy ion composition	1 distribution per minute	0.02–0.3 MeV	30°	40 % at 0.05 MeV	2
Low-energy ion/electron composition	1 distribution per minute	20 eV–0.05 MeV	20°	40 % at 0.01 MeV	2

Table 2 Baseline fields and waves requirements

Measurement	Cadence	Frequency range	Frequency resolution	Number of platforms
3-D magnetic field	20 vectors/s	DC–10 Hz	n/a	2
3-D wave magnetic field	6 s	10 Hz–10 kHz	20 channels per decade	2
3-D wave electric field	6 s	10 Hz–10 kHz	20 channels per decade	2
3-D electric field	20 vectors/s	DC–10 Hz	n/a	2
Plasma density	1 s	n/a	n/a	2

Table 3 Average daily data rate and volume

Instrument	Daily average data rate (kbps)	Average daily data volume (Gb)
Instrument data		
ECT	20.4	1.763
EFW	12.0	1.037
RPS	2.0	0.173
RBSPICE	5.4	0.467
EMFISIS waves survey	6.7	0.579
EMFISIS mag survey	2.3	0.199
EMFISIS burst (downlink allocation)	23.2	2.004
Housekeeping	3.5	0.309
Total	75.5	6.530

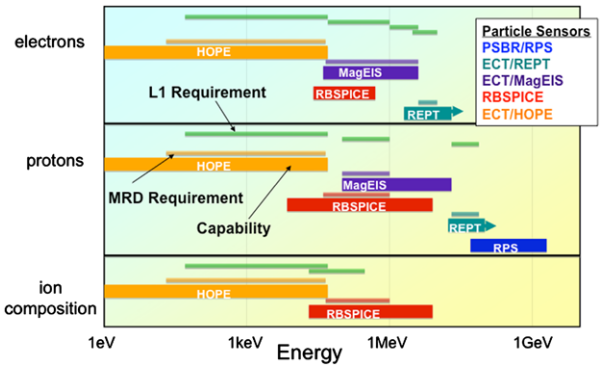

Fig. 8 Particle measurement capability

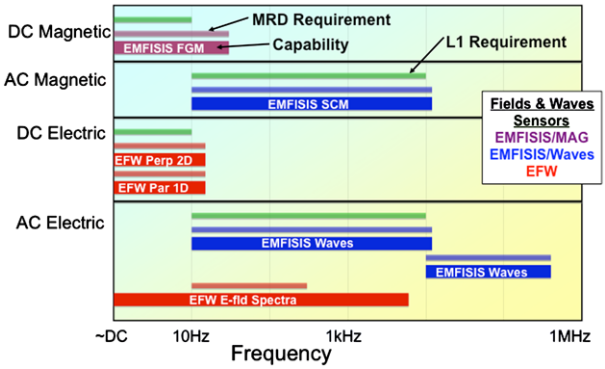

Fig. 9 Fields measurement capability

Fig. 10 Fluxgate magnetometer

rates. The EMFISIS suite includes two magnetometer instruments mounted on booms: the Magnetic Search Coil (MSC) to sense AC magnetic fields, and the Fluxgate Magnetometer (MAG) to measure low frequency and DC magnetic fields. EMFISIS also makes use of electric field observations from EFW. EMFISIS DC magnetic field observations will provide the basic coordinate system controlling the structure of the radiation belts and the storm-time ring current. The EMFISIS sensors are shown below in Figs. 10 and 11.

5.2 Electric Field and Waves (EFW) Instrument

The investigation will provide the observations needed to understand the electric field properties associated with particle energization, scattering and transport, and the role of the large-scale convection electric field in modifying the structure of the inner magnetosphere. EFW measurements of the observatory potential will be used to infer the ambient plasma density.

Fig. 11 Magnetic search coil

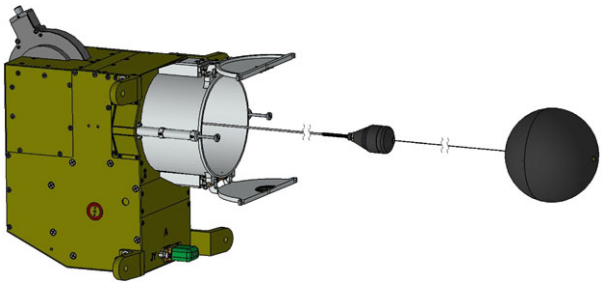

Fig. 12 EFW spin plane boom and sensor

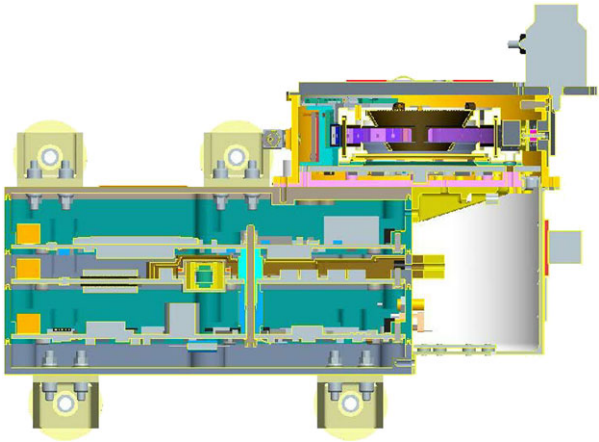

Fig. 13 RBSPICE

The EFW instrument sensors are mounted on booms that deploy out from the observatory, thereby minimizing influence of the observatory noise signature ion the measured electric fields. These sensors are deployed in six orthogonal axes, with the two $\pm W$ axis (i.e. the observatory spin axis) sensors deployed to approximately 12 meters tip-to-tip, and the $\pm U$ and V axis sensors deployed to approximately 100 meters tip-to-tip. One of the EFW Spin Plane Booms is shown below in Fig. 12.

5.3 Radiation Belt Storm Probes Ion Composition Experiment (RBSPICE)

This investigation will provide observations that accurately resolve the ring current pressure distribution needed to understand how the inner magnetosphere changes during geomagnetic storms. RBSPICE then determines how that storm environment supplies and supports the acceleration and loss processes involved in creating and sustaining hazardous radiation particle populations. The RBSPICE instrument is shown below in Fig. 13.

Fig. 14 HOPE

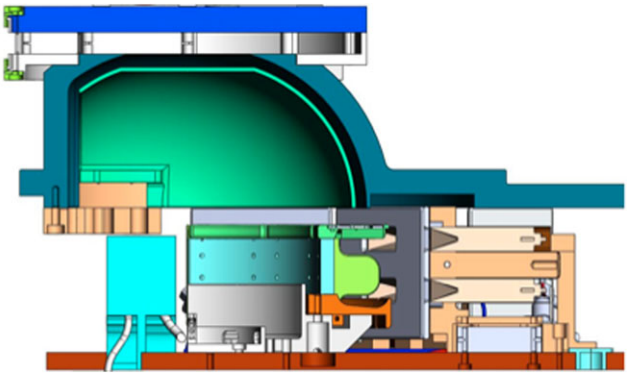

Fig. 15 MagEIS

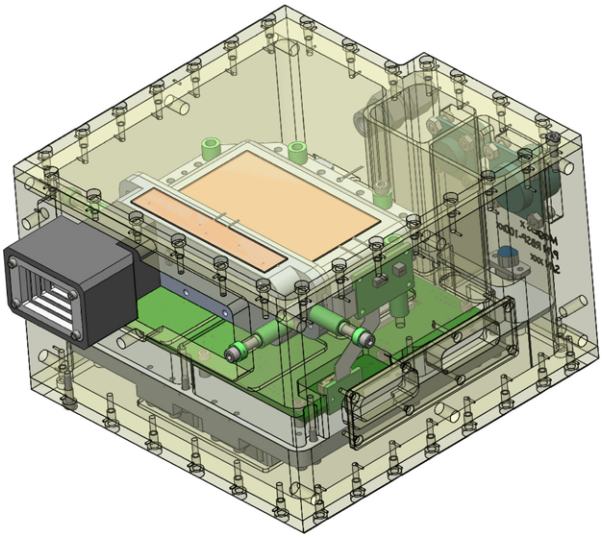

5.4 Energetic Particle, Composition and Thermal Plasma Suite (ECT)

This investigation will determine the spatial, temporal, and pitch angle distributions of electrons and ions over a broad and continuous range of energies, from a few eV to >10 MeV for electrons, and from a few eV to many 10's of MeV for ions. It differentiates the causes of particle acceleration mechanisms, understand the production of plasma waves, determine how the inner magnetospheric plasma environment controls particle acceleration and loss, and characterize source particle populations and their transport. The investigation will provide a complete complement of data analysis techniques, case studies, theory, and modeling, along with expertise to define particle acceleration mechanisms, radiation belt particle enhancement and loss, and determine how the near-Earth environment controls those acceleration and loss processes. The ECT suite is comprised of three instruments: Magnetic Electron Ion Spectrometer (MagEIS), Relativistic Electron Proton Telescope (REPT) and

Fig. 16 REPT

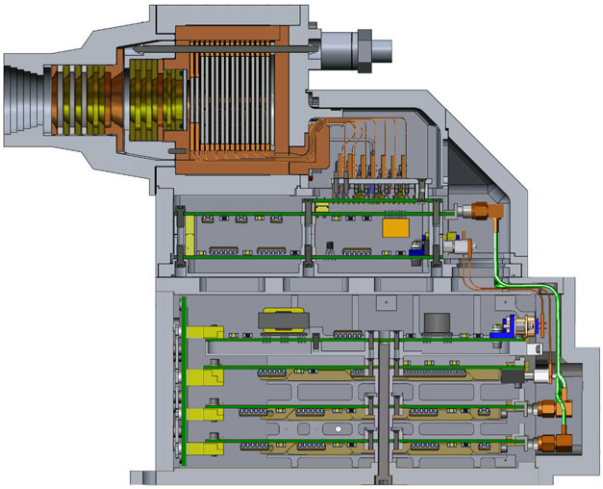

Helium, Oxygen, Proton and Electron Mass Spectrometer (HOPE). The ECT instruments are shown below in Figs. 14, 15 and 16.

5.5 Proton Spectrometer Belt Research (PSBR)

This investigation will determine the upper range of proton fluxes, up to ~2 GeV, in the inner magnetosphere and develop and validate models of the Van Allen radiation belts. The flight instrument on board each observatory is known as the Relativistic Proton Spectrometer (RPS). This instrument, its operations and the analysis of its data are contributed to the mission by the NRO. The RPS instrument is shown below in Fig. 17.

5.6 Data Management

The mission science requirements dictate that an average of 5.9 Gb of science data be returned from each observatory per day during normal science operations. The nominal op-

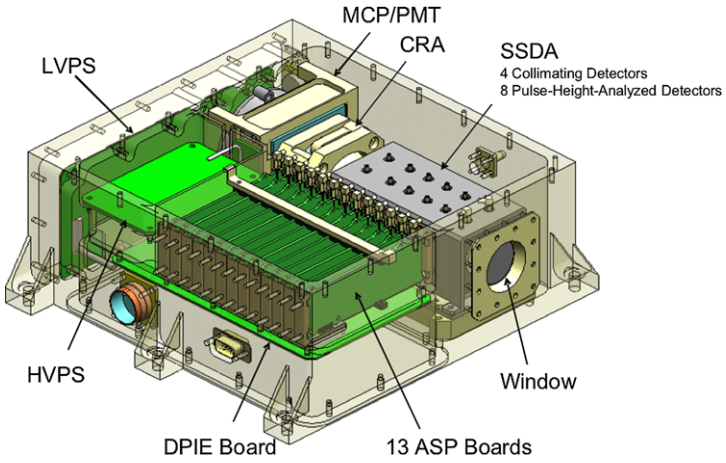

Fig. 17 RPS

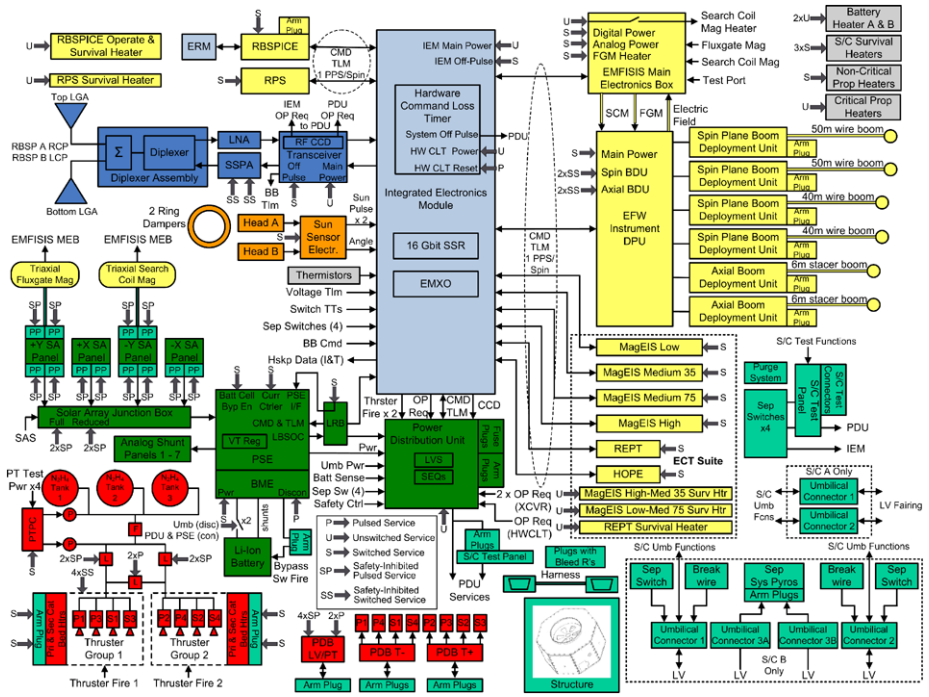

Fig. 18 RBSP observatory block diagram

erations plan calls for daily contacts with the observatory to allow this data volume to be downlinked every day, but the observatory solid state recorders are sized to allow the observatory to miss a day of contacts without losing any science data. Each instrument has the ability to set its own data recording rate, but data storage is managed by the spacecraft flight software and this software will begin to overwrite science data (starting with the oldest data from that instrument suite) should a given suite overrun its onboard storage allocation. An indication of the percentage of a given instrument suite's current data usage is downlinked via standard housekeeping telemetry and provided to each Science Operations Center. The responsibility for managing science data storage within allocations therefore falls on each of the instrument operations teams. The average daily data rates and resulting average daily data volume for each instrument suite is presented below in Table 3. Note that the total daily data volume includes instrument and spacecraft housekeeping data, and is therefore greater than the 5.9 Gb of required daily science data.

6 Spacecraft Overview

A complete description of the spacecraft is provided by Kirby et al. (2012, this issue); a brief introduction is presented here. The observatory block diagram is shown below in Fig. 18. The avionics for the system are contained in the Integrated Electronics Module (IEM), and include a RAD750-based single board computer, a 16 GB solid state recorder (SSR), the EMXO precision oscillator, and the Actel RTAX2000-based spacecraft interface (SCIF) card that handles all data connections with the instruments and other spacecraft electronics.

Power generation and storage is achieved respectively via four solar arrays and an eight cell 50 AHr Lithium-ion battery. In addition to these, the Power Generation System (PGS) includes the Power Switching Electronics (PSE), which limits the maximum bus current, limits the battery voltage and provides the telemetry and command interfaces to operate and monitor the PGS components. The Power Distribution Unit (PDU) provides power switching functionality, and contains circuit breakers and fuses for all non-critical loads.

The RF communications system contains a single transceiver, an 8 Watt solid-state power amplifier (SSPA), a diplexer, and two broadbeam, near-hemispherical antennas. The system provides S-band uplink, downlink and radiometric tracking capability. It supports both 1/2 turbo and convolutional encoding, and it uses coherent downlink to allow for Doppler navigation. The system provides a downlink rate of 1 kbps to 2 Mbps, and an uplink rate of 125 bps (emergency rate) to 2 kbps.

Attitude determination is accomplished by two means. The Flux-Gate Magnetometer sensor is the primary sensor for determining definitive observatory attitude. The data from this sensor is not processed on-board, so additional sensing is required to allow for autonomous attitude sense for observatory health and safety. The on-board attitude determination is accomplished via two Sun sensors. These sensors provide coarse observatory attitude information that is sufficient for autonomous monitoring of health and safety. This data is also sent to the ground where it is used in the estimation of definitive observatory attitude used for science processing. Each observatory also includes two passive nutation dampers that help maintain a stable system attitude and damp out any "wobble" after propulsive maneuvers.

The propulsion system is a simple monopropellant blowdown system. Three Inconel tanks store the 56 kg of hydrazine propellant onboard, and feed the eight 0.9 N thrusters. The position and orientation of these eight thrusters allow for spin up and spin down about the primary spin axis, positive and negative precession about the spin-plane axes, and velocity change toward and away from the sun. These thrusters are the only active attitude control mechanisms on board the observatories, and provide the full set of capability required to maintain the system attitude and spin rate and perform orbit corrections, collision avoidance maneuvers as required, and the final de-orbit burn at the end of the mission.

The spacecraft structure consists of a primary load-bearing central cylinder and aluminum honeycomb decks with aluminum facesheets for mounting instruments and spacecraft components. The two Observatories are held together by a RUAG-supplied Lightband low-shock separation system. This same separation system is also used between the stacked Observatories and the launch vehicle.

The spacecraft also includes diagnostic instrumentation—termed the Engineering Radiation Monitor (ERM)—to monitor the in-situ radiation environment. The long-term health and operability of observatory electronics and materials are directly affected by the total incident radiation dose. The ERM will measure this incident dose, and will provide a means for correlating upsets in observatory electronics with the environment present at that time. This monitor will also allow refinement of the standard total dose curves that are traditionally used for the design of spacecraft that operate in the Earth's radiation belts.

6.1 Fault Protection

Each observatory also includes robust Fault Protection and Autonomy systems that work together to maintain the overall health and safety of the flight segment. Because the observatories includes limited hardware redundancy, the Fault Protection and Autonomy systems are of particular importance on RBSP. The architecture uses a layered response approach to

maximize science data collection in the event of a fault. The system protects against the extended loss of communications by way of both software and hardware command loss timers. It also monitors the Sun angle of a given observatory, and can safe the system and notify the ground in case of an exceedance of the minimum or maximum sun angle. Similarly, the Fault Protection system monitors the bus voltage and battery state of charge, and can safe the system in case of a Low Voltage Sense (LVS) or a Low Battery State of Charge (LBSOC) where the bus voltage or battery state of charge drop below a minimum preset level.

The system also monitors the current condition and the health of observatory components, and it has the ability to individually off-pulse the primary unswitched loads (the IEM, the PDU and the transceiver) to restore those systems to a known startup configuration and presumably to clear any faults that my be present. In addition to monitoring and managing spacecraft bus health and safety, the system can also monitor instrument currents and heartbeats and can power off instruments in the case of a fault, and they can also individually power off the instruments based on a turn off request generated by that instrument.

Lastly, the fault protection system manages the separation sequence after launch, deploying the solar arrays and powering on the RF downlink (uplink is enabled by default at launch).

7 Mission Operations

7.1 Mission Operations Overview

The mission operations concept is designed for mostly unattended observatory operations, with distributed science operations. Because the observatories are spin-stabilized and nominally sun-pointing, they are inherently in a safe state and the need for constant monitoring is minimized. All critical activities—including commissioning activities and all propulsive maneuvers—are performed in contact with the ground. Nominal science operations are not constrained to occur during "staffed" periods of time. Similarly, the instrument operations are performed "offline" of the MOC, and instrument commands are queued up at the MOC remotely from the SOCs, then uploaded to the observatory during the next regular contact. This approach of unattended, decoupled operations greatly reduces the cost of the operational phase of the mission, and it has been successfully demonstrated at APL on the STEREO mission.

The mission operations center (MOC) is located at APL, and serves as the central hub through which all commands and telemetry flow. Figure 19 shows the distributed nature of the operations architecture. APL's Satellite Control Facility (SCF), with its 18-meter antenna, serves as the primary ground station for the mission. Supplemental contacts using the Near Earth Network (NEN) will be used to ensure sufficient daily data download to maintain data volume margin on the observatory solid-state recorders. The observatories will also utilize the TDRSS system for communications shortly after launch and during early operations, and also rely on TDRSS for emergency communications. Immediately after launch the observatories enter what is called the Launch and Early Ops (LEOPs) or "commissioning" phase of the mission. During this time the observatories are configured into their fully deployed state, and then the spacecraft subsystems and instruments are checked out in turn to ensure that they are in good health and operating as expected. After the initial deployment of the solar arrays and commissioning of the RF communications system, the next task is to deploy the EMFISIS magnetometer booms and check out those systems. Shortly thereafter, the EFW booms—both the ∼7 m axial booms and the 40–50 m spin plane booms are

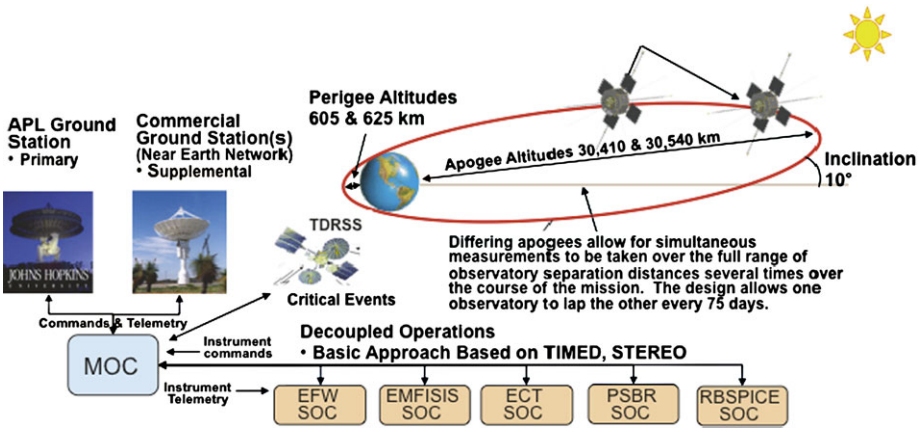

Fig. 19 RBSP distributed ground system, MOC and SOC architecture

deployed. After the EFW booms deploy, both observatories have achieved their nominal deployed configuration, and the full characterization of the attitude determination system can begin. Similarly, this point also marks the gate whereby the commissioning of the energetic particle instruments can begin in earnest.

Operational data rates vary for each instrument suite with the nominal rates ranging between 2 and 33 Kbps. The system also accommodates a "burst" data collection mode from the EMFISIS instrument suite of just over 1 Mbps. Each observatory is required to downlink an average of at least 5.9 Gb of science data per day during the nominal science mission.

The observatory's stable, sun-relative attitude drifts with the motion of the Earth, but the attitude of the observatories is set such that an East-West precession maneuver to maintain Sun on the arrays is only required about once every three weeks. Similarly, a North-South precession maneuver is required once per year to adjust for seasonal drift relative to the ecliptic plane. Apart from any initial orbit injection correction and the end-of-mission deorbit maneuver, these are the only propulsive maneuvers required during the mission.

As mentioned above, the observatory system does include two Sun sensors for onboard attitude determination to support observatory health and safety, but the primary method of attitude determination is performed during post-processing on the ground. The measurement of the local magnetic field from the Flux Gate Magnetometer (Mag) is transmitted from the observatory to the ground system as part of the normal science data downlink during each ground pass. This data is then processed by the Guidance & Control (G&C) system's ground software and compared to the reference standard model for the Earth's magnetic field. The accuracy of this model, and the general stability of the Earth's magnetic field, allow this method to provide an accurate prediction of the observatory attitude. A "quick-look" version of this attitude estimation is provided within 24 hours of receipt of data, and the estimate is further refined after calibration and post-processing of the magnetometer data by the science team. This final attitude estimate is provided within one week of receipt of the data, and is used for final processing of all science data.

Per NASA requirements, the mission is obligated to dispose of both observatories at the end of the mission lifetime. Although the observatories carry sufficient propellant to do so, they have insufficient thrust levels to perform a controlled reentry burn that would deposit the observatories reliably in a targeted broad ocean area. As-designed approximately 1/3 of the mission propellant budget is designated to disposal of the observatories. The deorbit

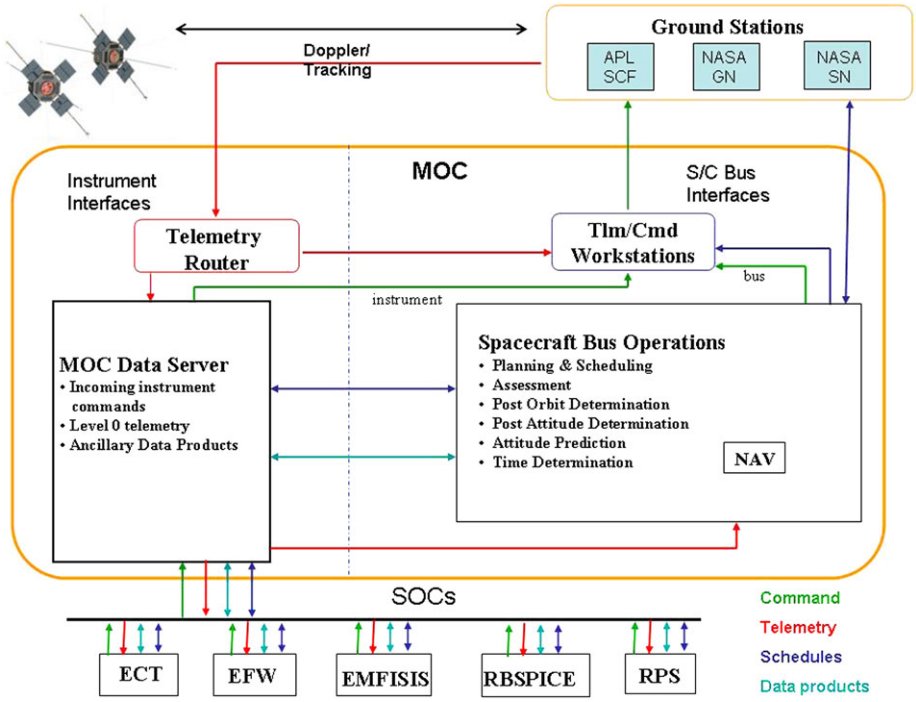

Fig. 20 RBSP ground segment functions and data flow

plan calls for performing a maneuver to lower the perigee of the observatories, and then rotating each spacecraft to have the solar arrays nearly edge-on to the Sun such that as the observatory continues to naturally precess the arrays will point away from the sun and the battery will slowly drain over time. At the completion of this precession maneuver, the team will perform a net-zero propulsive maneuver to drain the propellant reserves from the tanks, thus eliminating any stored energy onboard the observatory. This leaves the spacecraft in a safe, passivated state where they remain as the orbit naturally decays. Approximately six months after these decommissioning activities occur the atmospheric drag takes over and the observatories reenter Earth's atmosphere.

7.1.1 Ground Segment

The Ground Segment supporting the RBSP Mission include the hardware and software in the Mission Operations Center (MOC), the Science Operations Centers (SOC), the MOC Data Server (MDS), the Ground Stations, the Navigation Function (NAV), and the Guidance & Control (G&C) Function. Figure 20 shows the general flow of data between these entities of the Ground Segment. This section will go into more detail of the various Ground Segment components.

7.1.2 Mission Operations Center

Housed in one of the newest and largest buildings on the APL campus, the RBSP Mission Operations Center (MOC) is located in a new Multi-Mission Operations Center. The room

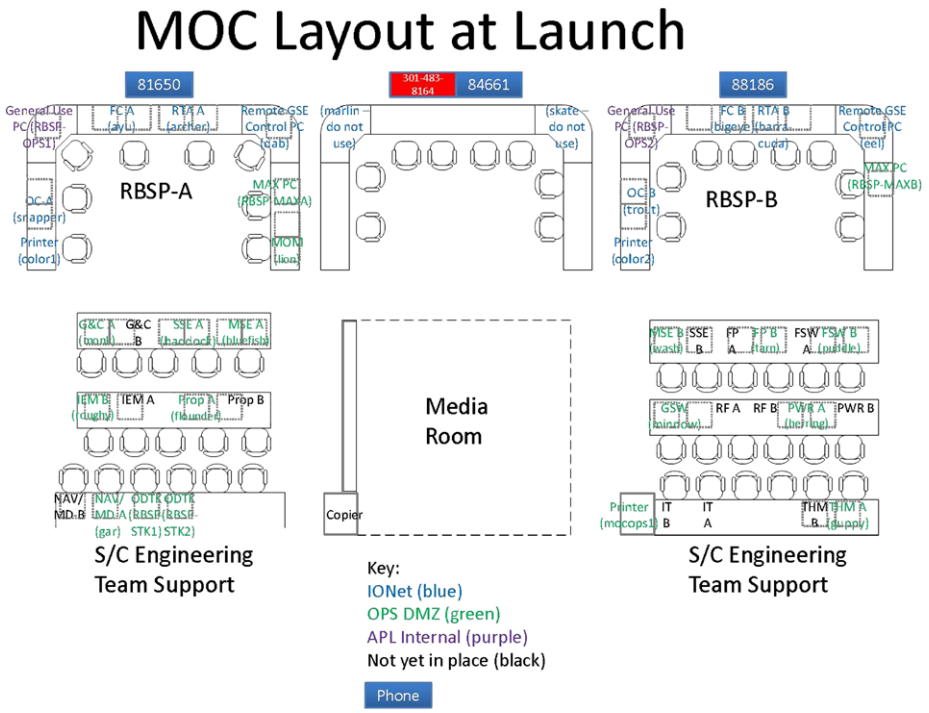

Fig. 21 Personnel seating and hardware placement in the MOC for launch

is sized to allow the operation of up to three multi-spacecraft missions at a time. With three large "command pit" areas as shown in Fig. 21, the facility can support two missions in "launch" phase and one in a well-established "post-launch" phase. Being the first and only mission for up to six months after launch, the RBSP Mission will initially utilize the entire room. As shown in Fig. 21, the RBSP A command pit is furthest from the entrance and RBSP B command pit is on the other side. The middle command pit is used for overflow and is anticipated to be the space the mission will occupy six months after launch. The large areas behind the RBSP A and B command pits are areas for the Engineering Teams required for launch and special critical activities. Figure 21 also indicates were Subsystem personnel are stationed for launch as well as names of hardware workstations.

7.1.3 Features of the MOC Facility

Figure 22 shows the floor plan of the larger area surrounding the MOC. Contained within the MOC area is a glass enclosed Media Room where VIPs and others can congregate to observe the activities taking place within the MOC. In addition to the MOC area, and as shown in Fig. 22, the facility houses a large Network room, an ESD Compliant Hardware Simulator Room, a Control Room for Instrument Operators, two Situation Rooms, a library space, and a kitchen area. The RBSP Instrument Teams will be hosted in the adjacent Instrument Control Room and will communicate with the MOC personnel over the facility's voice system. The Mission Operations Team is also located around the MOC Facility in the surrounding office space as well as in the larger "Office Overflow Space" down the hall.

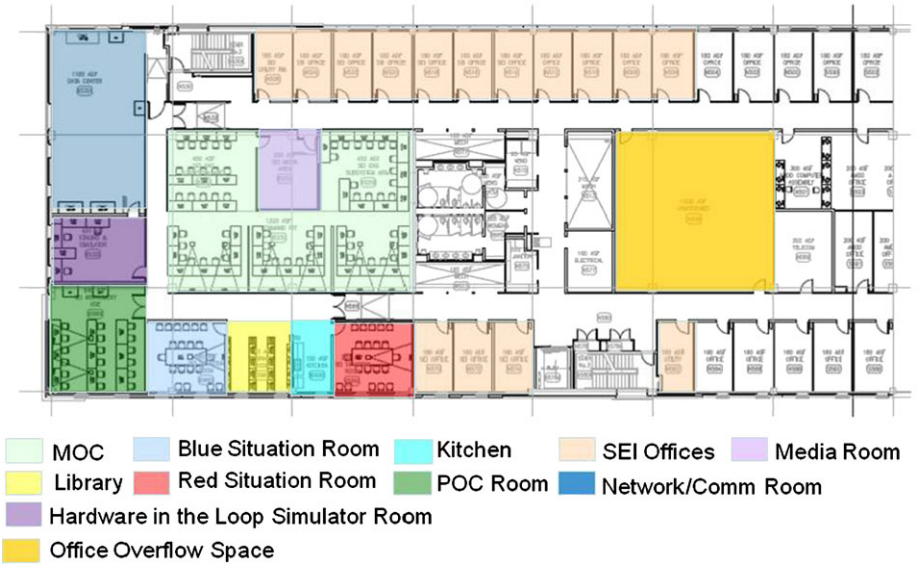

Fig. 22 Floor plan layout showing MOC and surrounding facilities

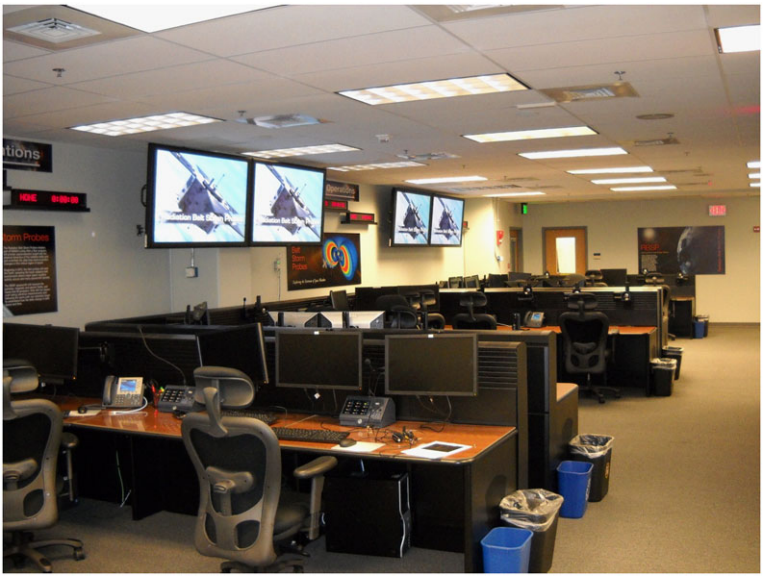

Fig. 23 Picture inside the MOC

Additional features of the facility include 65 inch LCDs for heads-up displays and clocks for displaying GMT and countdown information as seen in Fig. 23. The A-V system within the MOC allows any of the workstations along the front row to be shown on any one of ten 65 inch LCDs positioned around the MOC. The Countdown clocks are used to provide a countdown to the start of a contact and once inside the contact, a countdown to the end

of the contact. In addition, small monitors in the Situation Rooms and on the hallway side of the Media Room, display upcoming contact information for the different observatories, similar to an airport's flight schedule.

The Ground System Hardware architecture used on the RBSP Mission is client/server based. The PC-based computers acting as clients are running the Linux operating system. Servers are housed in the network room separate from the MOC.

The Ground System software includes L-3's InControl, the primary command and control system for RBSP, and contains interfaces with the planning and assessment software and real-time tools developed by APL.

7.1.4 Science Operations Centers (SOC)

The Science Operations Centers (SOCs) are owned and operated by the Instrument teams to control the Instrument Operations. Each of the Instrument Suites has both a Test SOC and a Flight SOC. The Test SOCs are located at APL in a room adjacent to the MOC. This facility is used during some of the pre-launch testing and during the Commissioning Phase. During the Commissioning Phase it is desired to have the Instrument Teams in close proximity to the Mission Operations Team because of the possibility of a dynamic timeline of activities required to occur throughout the Commissioning Phase. During that time is it highly desirable to be able to have face to face communications as much as possible to reduce the risk of possible miscommunications amongst the various teams. The Flight SOCs reside at a facility of the Instrument Team's choice. In many cases, they have chosen their home organizations. The details of the Instrument Operations and Instrument SOCs are provided in the instrument investigation papers within this special issue.

7.1.5 MOC Data Server

The MOC Data Server is the "hub" of data product transfer and resides in the MOC area. The various data products produced for the day to day operations are placed on the MOC Data Server for access by the various teams, especially the SOC Teams. In addition, the Level 0 Telemetry files are place there after their processing is complete.

7.1.6 Ground Stations

The primary ground station is the 18 m antenna on the APL campus shown in Fig. 24. It is controlled by the Satellite Communications Facility (SCF) in Bldg. 36. The 18 m dish should support the majority of contact time required to bring down the desired 5.9 Gbits of data per day per observatory. However, there are periods throughout the year when the orbital geometry does not allow that support. During those periods, the Universal Space Network's South Point, Hawaii and Dongara, Australia stations will be utilized. For Navigation purposes, short contacts with the Dongara station will be required on a weekly basis due to its proximity in the Southern Hemisphere. In addition to these ground stations, the RBSP project will also utilize communications with the TDRSS system. Downlink rates of 1 kbps are all that is possible for RBSP with TDRSS spacecraft, so these contacts will only be used to support launch, commissioning, and critical activities.

7.1.7 Navigation Function

The Navigation function for RBSP is produced by a team at APL. Doppler data is received from contacts with the various ground station antennas and that is used to produce the definitive orbit on the ground. The Navigation team will also produce predicted orbit products that are used in the Mission Operations Planning function.

Fig. 24 18 m (60 ft) antenna on the campus of JHU/APL in Laurel, MD

7.1.8 Guidance and Control on the Ground

The Guidance & Control (G&C) function on the ground is used to produce predicted and definitive attitude solutions for use in the Planning functions as well as data processing. In the G&C Component within the MOC, the attitude data products are based on the sun sensor data and the Magnetometer data transmitted from the RBSP observatories.

7.2 Mission Operations Functionality

The Mission Operations System (MOS) includes the team, hardware, software, and facilities involved in operating the RBSP observatories on a daily basis. The primary tasks are to maintain healthy spacecraft and obtain the science data placed on the Solid State Recorder (SSR) by the Science Instruments. Mission Operations functionality is broken down into the Planning and Scheduling, the Real-time Control, and the Performance Assessment functions. Each of these functions feed into the other in order to conduct a safe and efficient mission.

7.2.1 Mission Operations Team

At the heart of the Mission Operations System is the Mission Operations Team. The team is comprised of Mission Operations Analysts and Flight Controllers. The Mission Operations Analysts are lead engineers who conduct all of the functions within Mission Operations, while Flight Controllers are less experienced and focus on the Real-time Control aspect. During the Launch and Commissioning Phase of the mission, the team is sized in order to be able to perform 24/7 operations; which may be required in order to conduct all of the required activities during the 60 day period. Once into the nominal science operations Phase of the mission, the majority of contacts will be run in an “Unattended” sense. This eliminates the need for Flight Controllers and the team remains staffed with the Analysts. The team is still required to staff contacts during which critical activities are performed. The majority of

those activities are the propulsive maneuvers. The team of Mission Operations Analysts will rotate through positions on the Mission Operations team and will switch between operating RBSP A and B as part of the rotation.

7.2.2 Mission Operations Concept

The RBSP Mission Operations Concept is based on the Decoupled Operations approach. The Decoupled approach is enabled by the mission itself and the spacecraft design. The relative observatory attitude remains constant and the power system is sized to allow 100 % duty cycle of the instruments. The decoupled operations concept is implemented by distributing the Science Instrument Operations amongst the teams that developed those Instruments. While the Mission Operations Team operates the spacecraft bus, the teams within the Science Operations Centers (SOC) operate their individual instruments independent of the bus operations and the operation of the other Instruments. The SOCs send instrument commands into the MOC where they are stored in command queues until a ground station contact, when the queues are opened and the commands are transmitted to the Instrument on-board the observatory. The SOCs may receive housekeeping telemetry during the contacts by connecting to the MOC and will receive the Science data after contacts by retrieving the Level 0 telemetry files from the MOC Data Server (MDS). Additionally, the MDS will store many data products the various teams will need to conduct routine operations. The Mission Operations management of the SSR is simplified on RBSP because of the on-board file system and the use of CCSDS File Delivery Protocol (CFDP). Using the closed loop CFDP functionality, the ground system and observatory will communicate autonomously to ensure the data has been received on the ground prior to the data being deleted on-board. While closed loop CFDP will be employed when in contact with the APL Ground Station, during contacts with a USN station, an open loop version of CFDP will be employed due to the lack of the ability of exchanging the CFDP communications in real-time. Initially, the SSR will be configured in a simple “dump and delete” mode during USN operations; however, if an alternate solution would benefit, that concept may be adjusted after some experience is gained.

7.2.3 Mission Operations Planning Function

The RBSP Planning function is used for scheduling observatory activities necessary for safe and efficient operations. These activities include RF Control for Ground Station Contact, SSR Control, Eclipse entry and exit notifications, various Housekeeping functions, and Maneuvers. The activities, also known as Events, are comprised of repeatable command sequences which may have various instantiations depending on the specific scheduling criteria. All Events are classified as either routine or sporadic. Routine events are scheduled on regular intervals, whether it is based on time or per contact. A web-based tool known as “Scheduler” is a ground software tool used by the Mission Operations Team for developing the weekly schedule of events. The Scheduler tool schedules routine events automatically based on their pre-defined scheduling criteria. Sporadic events are placed in the schedule by the Mission Operations Team at the appropriate time. Due to gradual observatory precession throughout the orbit, the Mission Operations Team is required to schedule an Attitude adjustment maneuver every 21 days to keep the spin-axis within specifications. While this is a routine event, it also is classified as a Critical Event and therefore must be scheduled during a ground station or TDRSS contact that will be staffed. For this reason, these maneuvers are scheduled more on a manual basis every three weeks.

The Planning function is begun three weeks out in the Contact Scheduling process. Each successive week, the timeline of activities that occur on the contacts are firmed up to the point where commands are generated the week prior to planned execution. The primary tool used in the planning process is the Scheduler tool. Scheduler itself is an APL-developed web-based platform independent tool that makes use of user-generated templates mapped to each event type. Each template is designed to make use of a repeatable command sequence that allows arguments to be input for definition of specific instances each time it is scheduled. Based on its architecture, the "Scheduler" tool allows the Mission Operations Team to conduct planning or view all related planning information from their office, the MOC, or a remote location.

Also in the Planning process, Simulators are used to verify proper command sequencing for particular observatory activities. There are two types of Simulators employed by the RBSP Mission Operations Team. One type is hardware based (RBSP Operations Simulator, or RBOPS) and the other is software based (Flight Accelerated Simulation Tool, or FAST).

There are three hardware-in-the-loop simulators of various fidelities. The high fidelity RBOPS includes versions of the spacecraft IEM, PDU, and Transceiver. The other less fidelity RBOPSes have only a spacecraft IEM. Surrounding the RBOPS Simulators is a Testbed which is used to emulate the remaining virtual spacecraft components. The Software Simulator is used as the primary method of constraint checking of spacecraft command sequences prior to uplink.

The final part of the Planning process involves the final creation of Contact Plans and associated procedures and scripts. These are transferred to the MOC for execution during the Contact.

7.2.4 Real-time Contact Operations

The Real-time Control Function is the aspect of Mission Operations where communications occur between the ground and observatories during the Ground Station Contacts. During the Launch and Commissioning phase, the contacts taken will be staffed by members of the Mission Operations Team, Engineering Team, and Instrument Team members. This is because the majority of commissioning activities will be conducted in real-time during a contact. Once the mission enters the Routine Science Phase, the majority of contacts will be taken on an unattended basis. Unattended contact operations are planned for all contacts except for those during which critical activities will take place. During the Routine Science Phase, the instruments are powered and constantly sending data to the SSR. The majority of observatory activities are not critical and can be scheduled during unattended contacts. The only critical activities in this phase are maneuvers and possible anomaly recovery activities. Those will be scheduled during staffed contacts. During all contacts, including unattended, the spacecraft housekeeping telemetry is evaluated for state of health and the ground system is setup to provide remote notification of specific alarms to the Mission Operations Team for spacecraft alarms and to the Instrument/SOC teams for specific instrument alarms. Following the initial state-of-health evaluation, the SSR downlink is initiated. Spacecraft commanding is then performed, followed by the opening of the different SOC Command Queues, so that Instrument commands that had been waiting will be uplinked. Following notification of an alarm, the remote Mission Operations Team members may log in and begin evaluation of the urgency of the situation. If urgent, they can remotely schedule additional contact time and alert other members of the team to begin troubleshooting the anomaly. If the situation is not urgent, the team members choose a course of action less pressing that maintains the health and safety of the observatories and science objectives.

In order to downlink the amount of science data acquired on the SSR on a daily basis, the Mission Operations Team will schedule approximately three hours of contact time per day per observatory. In order to obtain this much contact time as well as to obtain the contact time for maneuvers and other necessary activities to be done outside of SSR downlinks, the project will utilize three different networks. The primary antenna is the APL 18 m (60 foot) antenna.

With the 18 m, the MOC will communicate with the Satellite Control Facility (SCF) to initiate observatory commands and receive telemetry. If necessary for a data rate change during a contact, the MOC initiates scripted commands to configure both the observatories and the ground station properly for a given change. Also, during the contacts with the APL station, the closed loop CFDP communications will occur.

To supplement the ability to obtain all of the Science data on the SSR, in particularly during times of year when communication opportunities with the primary station are minimal, two stations from the Universal Space Network will be used—those in South Point, Hawaii and in Dongara, Australia. The data throughput from the USN stations to the MOC is insufficient for real-time communication, therefore, the SSR data return path to APL from the USN stations is a store and forward method after the contact. This also prohibits the use of the closed loop CFDP. During data rate changes necessary for USN contacts, a communication will be made ahead of time for the Ground Station to make the change at the coordinated time.

Use of the TDRSS Space Network (SN) will take place during times where contact is required and ground station visibility and/or availability is not possible. This occurs mostly during periods of time during the Launch and Commissioning phase and during maneuvers and possible times of contingency operations during the Routine Science Phase. During TDRSS contact the downlink rate for RBSP is limited to 1 kpbs and therefore SSR downlink is not scheduled.

7.2.5 Performance Assessment

The Performance Assessment function is broken down into two classifications. One type is Routine Assessment which involves alarm processing and trending. The other type is anomaly investigation and resolution. Routine Assessment consists of determining the status, configuration, and performance of each spacecraft Subsystem. Alarm processing is performed on all observatory housekeeping data that is collected via the SSR as well as real-time. The Alarm processing software notifies the MOT of an unusual occurrence or condition of the observatory. Each alarm is evaluated by the team to determine a proper course of action to understand the cause and if necessary, remedy the alarm condition. Trending is the periodic monitoring of critical bus components, including those components that are known to degrade over time. Trend Analysis software automatically generates plots that are produced on routine intervals—on a daily, weekly, monthly, quarterly, and annual basis. Various data averaging is used for each time interval. The Mission Operations Team reviews the plots on a daily basis to monitor for any usual occurrences or possible trends.

The other function within Performance Assessment is the investigation and resolution of anomalous behavior identified either during real-time contact or during off-line assessment of performance. Anomaly Reports are written when an anomalous condition is first identified. The Performance Assessment function within Mission Operations further investigates to understand the cause and to determine a path of resolution. In some cases, the resolution may involve changes to processes, procedures, command sequences, and possibly alarms. These changes are documented as part of the anomaly closeout process.

The Performance Assessment function closes the loop within the Mission Operations Process by feeding changes necessary because of issues uncovered during the Real-time or Assessment aspects, onto the Planning function, to continue to try to improve Operations efficiency.

8 Space Weather

During normal science operations, the observatories will only require approximately 2.5 hours of ground contact time per day to downlink the stored science and housekeeping data. When the observatories aren't in primary ground contacts they will be broadcasting space weather data intended to be received by participating ground stations throughout the world. This space weather data is a subset of the full science data normally being collected by the instruments, and all of the RBSP instruments contribute to the space weather data products. The data subset will include particle fluxes at a variety of energies as well as electric and magnetic fields. The science operations teams also have a goal of providing "quick look" data products that will fill in the gaps of space weather data that occur when the observatories are in primary ground contact, thus providing essentially continuous 24 hour coverage of space weather data. The space weather broadcast is performed using the observatory's primary S-band RF communications system.

9 Unique Challenges for RBSP

The demanding science requirements and the routine operation of the observatories in the radiation belts create some unique design challenges for the RBSP mission.

9.1 Radiation

The most obvious effect of operating in the radiation belts is, of course, the constant bombardment by damaging high-energy electrons and ions. This can lead to the well-known effect of displacement and ionizing damage in electronic parts, but it also causes two other effects that must be mitigated to ensure observatory health and mission success. Internal Charging and Deep Dielectric Discharge are both caused by high-energy electrons and ions penetrating the observatory structure and coming to rest in the spacecraft. These particles ultimately cause internal surfaces to charge until they exceed the breakdown or gap voltage, at which point it discharges to the local ground. This discharge can result in damage to electronic circuits, or can cause upsets or noise in spacecraft subsystems or instruments.

The launch vehicle selected for this mission has a great deal of lift capability to the RBSP orbit, and as such the project was in the enviable position of being able to use mass to solve some technical problems early in the design phase. This allowed the project to dictate that all observatory electronics (including on the instruments) be shielded by an equivalent of 350 mils of aluminum, thus effectively eliminating the internal charging and DDD effects within electronics boxes. Filtering circuits were also added to the inputs of each box to mitigate the effects of discharge-induced noise on signal lines.

A challenge related to this is the need for RBSP to operate through significant storm events, despite being a single-string architecture. This means that, to the extent possible, science data collection should continue through events such as spacecraft processor resets—events which can be common occurrences in the radiation belts. As a final measure of protection against radiation-induced upsets and to ensure that the system can operate through

significant storm events, the observatory design includes an "off-pulse" architecture in which the primary bus electronics boxes (the IEM, the PDU and the transceiver) can be power cycled either by ground command or autonomously as the situation may warrant. This enables many potential faults to be cleared by removing power from the box and then restoring it to its known power-on condition. In all cases except the IEM power-off reset this also allows the spacecraft to continue recording science data, and therefore maximizes the potential for operating through a storm event.

9.2 Magnetic Cleanliness

Another key challenge for the mission is the need for both static and dynamic magnetic cleanliness. The magnetometers (both the DC Flux Gate Magnetometer and the AC Search Coil Magnetometer) are positioned away from the observatory body by means of deployable booms, but they are still sensitive to a static offset of the magnetic field (i.e. a shift in the Earth's apparent field due to the magnetic signature of the observatory) and to dynamic changes in the apparent field, such as from periodic magnetic fields caused by unbalanced current loops within the observatory structure or electronics. This latter effect is very difficult to compensate for, and consequently great care was taken during the design of the observatory to minimize current loops in the structure and electronics regardless of the observatory's operating mode. Static magnetic cleanliness drove materials selection—such as the use of Inconel propellant tanks, and it has also had a significant effect on ground processing, both for the integration and test of the observatories and for the integration and ground processing of the launch vehicle.

9.3 Surface Charging

In much the same way that the observatory can induce a bias in the magnetic field measured by the magnetometers, any differential charging of observatory surfaces will introduce a bias on the measurement of the ambient electrical field by the EFW instruments. To prevent this from occurring, the spacecraft and instruments are designed such that there are no (or very minimal) surfaces on the exterior of the observatories that can build up charge. In essence, all exterior surfaces are either conductive or are at least static-dissipative. This was particularly challenging in the design and manufacture of the solar arrays, which normally contain substantial areas of non-conductive grouting material. Similarly, many of the adhesives and tapes frequently used in spacecraft manufacturing are non-conductive materials, so great care had to be taken both in the design of the Observatories and in ensuring that these materials don't find their way into the final assembled hardware.

9.4 Magnetometer as the Primary Attitude Sensor

The use of one of the science instruments as the primary attitude sensor did provide some level of program cost savings, and it minimizes the onboard hardware and removes at least one spacecraft hardware interface, but it also leads to some unique challenges. Perhaps the most difficult of these challenges is ensuring that the system can still meet attitude estimation requirements during periods of Solar storms. As discussed previously, the primary method of determining observatory attitude is by comparing the measured magnetic field to the standard model of the Earth's magnetic field. During times of Solar storms the Earth's magnetic field can be significantly perturbed, meaning that the *actual* field no longer matches the models for the Earth's field, and the resulting measurement of the field results in an attitude estimation error. This approach also removed the "ownership" of the primary attitude

determination sensor from the Guidance & Control team, and thereby replaced a hardware interface with an organizational interface. The end result is a design that is efficient and will meet mission needs, but it did impose some engineering and management challenges along the way.

9.5 Operating Multiple Observatories Simultaneously

There are also unique challenges in operating multiple observatories simultaneously. The most obvious of these is staffing mission operations and engineering teams for both observatories. For the most part, operations are designed to be sequential, though for significant periods of time—particularly during launch and commissioning—the operations of both observatories occur simultaneously. To accommodate this, dedicated teams of operators and engineers are in place for each observatories, and the operations of both spacecraft occur in separate spaces of the common RBSP Mission Operations Center. The two observatories are designed to be functionally identical and this aids in making the operation of each essentially interchangeable. This simultaneous operation is tested repeatedly prior to launch through mission simulations and other dedicated tests.

9.6 Working with a Distributed SOC System

Another challenge of the operational system is working with distributed Science Operation Centers. This approach allows convenience and reduction of cost for each of the science teams, but it requires numerous additional interfaces and relies on networks to reliably flow data to and from the MOC. One key to making this approach work was specifying a single operating system (GSEOS) for all of the SOCs to use. This greatly simplified the definition of the interface between the MOC and SOCs, and reduced the testing required to ensure that this interface works. A single MOC-to-SOC Interface Control Document (ICD) was used to define these interfaces, and a SOC working group meets regularly to discuss design, implementation and interface details. A phased set of testing that began long before the delivery of any of the instruments also helped ensure a working interface when it was needed. APL's test-as-you-fly approach was extended here as well, as the instrument teams run much of their instrument testing during Observatory I&T from their remote SOCs.

10 Conclusions

The RBSP mission is set to explore the fundamental physics that drive changes within the Earth's radiation belts, and the selected instrumentation and the mission design will enable an investigation of both the spatial and temporal components of these changes. The ambitious science goals and the unique environment in which the observatories operate led to some significant challenges for the design and operation of the RBSP mission, but the observatories and the ground system have been designed to overcome these challenges and meet the requirements of the mission. The science obtained by this mission will greatly enhance the community's understanding of the processes at work in the Earth's radiation belts, and it will allow for the development of new models that better predict the both the radiation environment and its effects on observatory hardware.

References

J.M. Stratton, N.J. Fox, Radiation belt storm probes (RBSP) mission overview, in *IEEE Aerospace Conference*, vol. 2 (2012), p. 0503

K.W. Kirby et al., Radiation belt storm probe spacecraft and impact of environment on spacecraft design, in *IEEE Aerospace Conference*, vol. 2 (2012), p. 0504

Radiation Belt Storm Probes (RBSP), Space Weather Interface Control Document, 7417-9100 (2012)

DOI 10.1007/978-1-4899-7433-4_4
Reprinted from *Space Science Reviews* Journal, DOI 10.1007/s11214-012-9949-2

Radiation Belt Storm Probes—Observatory and Environments

Karen Kirby · David Artis · Stewart Bushman · Michael Butler · Rich Conde · Stan Cooper · Kristen Fretz · Carl Herrmann · Adrian Hill · Jeff Kelley · Richard Maurer · Richard Nichols · Geffrey Ottman · Mark Reid · Gabe Rogers · Dipak Srinivasan · John Troll · Bruce Williams

Received: 18 May 2012 / Accepted: 3 November 2012 / Published online: 14 December 2012

Abstract The National Aeronautics and Space Administration's (NASA's) Radiation Belt Storm Probe (RBSP) is an Earth-orbiting mission that launched August 30, 2012, and is the latest science mission in NASA's Living with a Star Program. The RBSP mission will investigate, characterize and understand the physical dynamics of the radiation belts, as well as the influence of the Sun on the Earth's environment, by measuring particles, electric and magnetic fields and waves that comprise geospace. The mission is composed of two identically instrumented spinning observatories in an elliptical orbit around earth with 600 km perigee, 30,000 km apogee and 10° inclination to provide full sampling of the Van Allen radiation belts. The twin RBSP observatories (recently renamed the Van Allen Probes) will follow slightly different orbits and will lap each other four times per year, offering simultaneous measurements over a range of observatory separation distances. A description of the observatory environment is provided along with protection for sensitive electronics to support operations in the harsh radiation belt environment. Spacecraft and subsystem key characteristics and instrument accommodations are included that allow the RBSP science objectives to be met.

Keywords Heliophysics · NASA · Mission · Observatory · RBSP · Radiation · Science · Space · Spacecraft · Van Allen probes

1 Introduction

The National Aeronautics and Space Administration's (NASA's) RBSP mission is a dual observatory mission depicted in Fig. 1 that will study variations in solar activity and how this affects the earth's environment as well as human activities in space and on the ground. This will improve our overall knowledge of the radiation belts and how they respond to solar

Portions of this paper reprinted from Kirby et al. (2012), with permission.

K. Kirby (✉) · D. Artis · S. Bushman · M. Butler · R. Conde · S. Cooper · K. Fretz · C. Herrmann · A. Hill · J. Kelley · R. Maurer · R. Nichols · G. Ottman · M. Reid · G. Rogers · D. Srinivasan · J. Troll · B. Williams
Applied Physics Laboratory, The Johns Hopkins University, Laurel, MD 20723, USA
e-mail: karen.kirby@jhuapl.edu

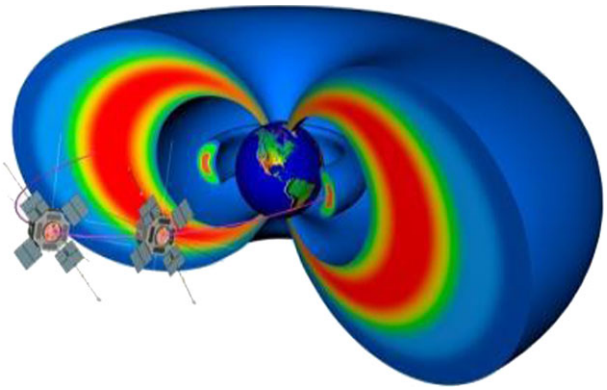

Fig. 1 RBSP is a low-risk and affordable mission, consisting of two identical observatories, built to survive in the radiation belt environment and to fully achieve all of the RBSP science objectives

storms and events. Particles are accelerated to form the radiation belts in unpredictable ways, and scientists need better observations to develop new and improved models of this important aspect of the Earth's environment. The observatory instruments will measure high- and low-energy electrons and protons, ion composition, and electric and magnetic fields using the Energetic Particle Composition and Thermal Plasma Suite (ECT), the Electric and Magnetic Field Instrument Suite (EMFISIS), the RBSP Proton Spectrometer (RPS), the Electric Field and Waves Instrument (EFW) and the RBSP Ion Composition Experiment (RBSPICE).

The sections that follow describe the baseline RBSP observatory designed by engineers at the Johns Hopkins University Applied Physics Laboratory (APL). Key mission and Observatory design drivers include the following.

Mission Requirements

- Orbit with an apogee of 30,500 km and perigee of 600 km, maximizing time in the radiation belts.
- Provide twin observatories identically instrumented.
- Launch both observatories on a single launch vehicle.
- Design for a mission life of 2.25 years with a goal of 5 years.
- Provide near-continuous transmission of space weather.

Observatory Requirements

- Operate through the challenging radiation environment.
- Provide attitude control through spin stabilization to provide required instrument fields of view; observatory is nearly Sun pointed, with nominal spin rate of 5.5 revolutions per minute (rpm).
- Provide power system to operate through eclipses up to 114 min.
- Downlink an average daily data volume of at least 6.61 Gbits of recorded plus real-time data per day during the operational phase of the mission.
- Accommodate significant payload mass (130 kg) and average power (149 W).
- Provide deployed science booms for fluxgate and search coil magnetometers.
- Provide deployed axial and wire radial booms for electric field measurements.

The two observatories are positioned and phased such that one will lap the other approximately four times per year. Each observatory is designed for an on-orbit life of 2 years and 74 days. This encompasses a 60-day commissioning period post launch, a 2-year science

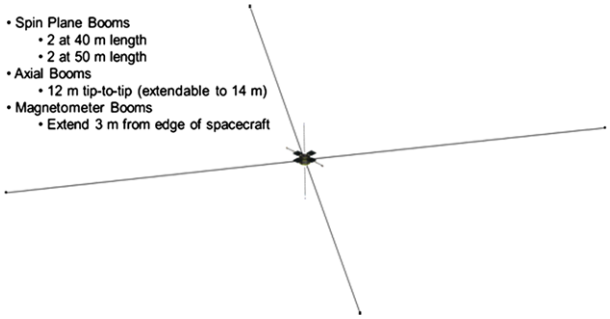

Fig. 2 RBSP observatory in fully deployed configuration

mission, and 14 days at the end of the mission to passivate the observatories. Observatory passivation includes a delta-velocity (ΔV) maneuver to lower the perigee and a precession maneuver to orient the solar arrays away from the Sun; each observatory will be disposed of via uncontrolled atmospheric re-entry within 5 months. The 2-year science mission lifetime provides sufficient local time, altitude, and event coverage to improve the understanding of, and determine the relative significance of, the various mechanisms that operate within the radiation belts and their individual and collective effects.

The RBSP observatories (renamed the Van Allen Probes by NASA on November 9, 2012) were launched together on a single Atlas V-401 Evolved Expendable Launch Vehicle (EELV) from Kennedy Space Center on August 30, 2012. The launch vehicle spun up, oriented each observatory so that the solar arrays pointed toward the Sun, and released each observatory separately. Both observatories are operating in highly elliptical orbits that will spend a substantial part of the mission life in the Van Allen radiation belts. The two orbits have apogee altitudes between 30,050 and 31,250 km, perigee altitudes between 500 and 675 km, and inclinations of 10° (Stratton and Fox 2012).

Each RBSP observatory operates independently in a spin-stabilized mode at a 4–6 rpm nominal spin rate with the spin axis nearly Sun pointed and maintained between 15° and 27° off pointing from the Sun, with 4 deployed solar array panels and 8 deployed instrument booms. Four 50-m spin plane booms provide AC and DC electric field measurements, two 6-m axial booms (12-m tip-to-tip) provide three-dimensional electric field measurements, and two magnetometer booms extend an additional 2 m beyond the solar array panels. Figure 2 shows the observatory in a fully deployed configuration, and Figs. 3 and 4 depict the observatory bus with accommodation of the instruments and their respective fields of view (FOVs). The spinning observatory sweeps the instrument apertures and sensors on the booms through 360° to obtain measurement samples as a function of angular direction.

1.1 Payload Accommodation

The RBSP science objective is to investigate how populations of relativistic electrons and ions in the radiation belts form and change in response to variable inputs of energy from the Sun. The mission targets the fundamental processes that energize, transport, and cause the loss of these charged-particle populations. These particles are in and around the Earth's radiation belts and are hazardous to observatory and astronauts. The investigations and instruments selected by NASA for each RBSP observatory measure particle distributions, fields, waves, densities, and other parameters with sufficient fidelity to answer the most pressing outstanding scientific questions regarding the behavior of the radiation belts (Sibek et al. 2006; Ukhorskiy et al. 2011). Each observatory will carry a hardware complement

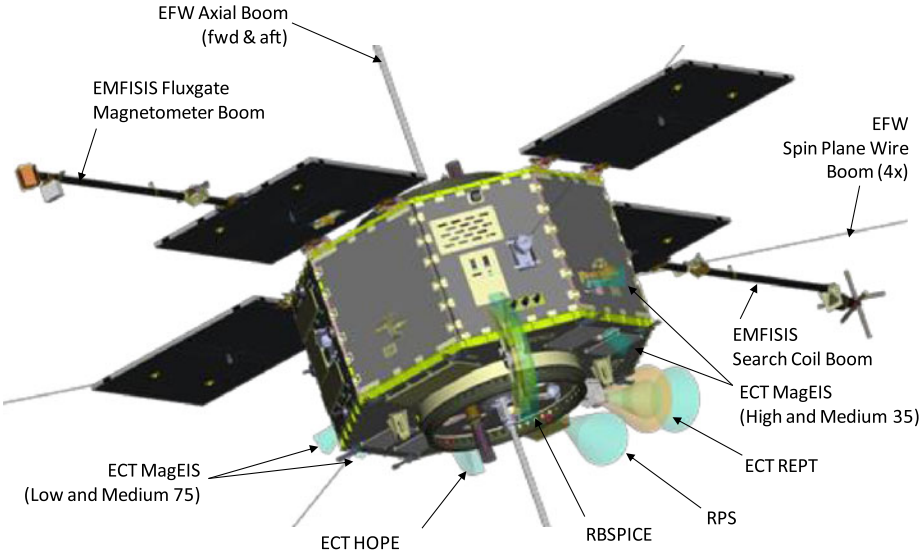

Fig. 3 Observatory configuration showing instrument fields of view

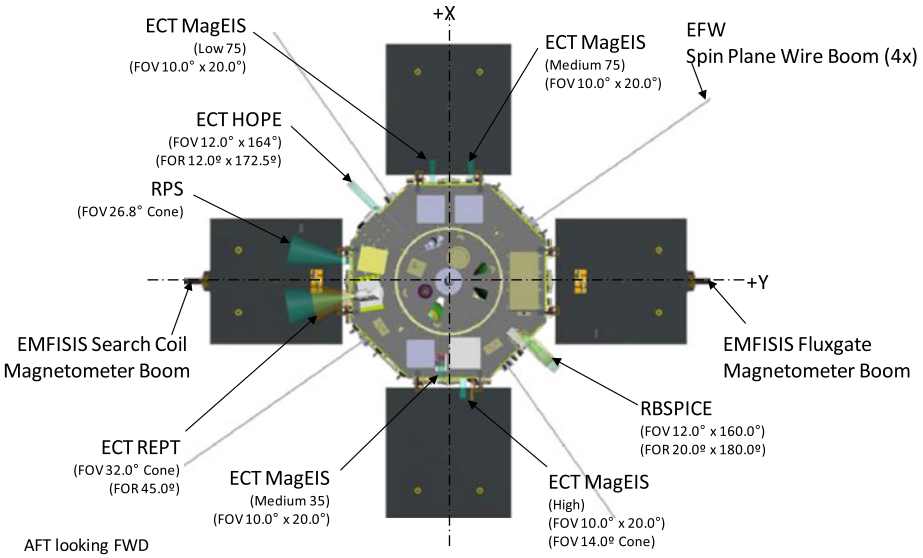

Fig. 4 Detailed instrument fields of view from observatory aft perspective

to support five science investigations and instrument suites identified in Table 1, along with their associated payload resource allocations. A detailed description of these instrument suites and their components and measurements is provided elsewhere. The main focus of this paper is to describe the spacecraft and accommodations for these science instruments.

Table 1 RBSP science payload

Science instruments	Name	Mass (kg)	Power allocation (W)	Avg daily data rate (kbps)
Energetic particle composition and thermal plasma suite	ECT	65.6	89.7	20.4
ECT—helium-oxygen-proton-electron spectrometer	HOPE	18.1	26.3	9.32
ECT—magnetic electron ion spectrometer	MagEIS	34.1	53	9.5
ECT—relativistic electron proton telescope	REPT	13.4	10.4	1.58
Electric field and waves	EFW	27.4	15.5	12
RB proton spectrometer	RPS	9.2	14.4	2
RBSP ion composition experiment	RBSPICE	6.6	7.1	5.4
Electric and magnetic field instrument suite	EMFISIS	20.9	22.5	32.2
TOTALs for science payload		129.7	149.2	72

Table 2 RBSP observatory resources

Observatory resource	Current best estimate	Specification	Margin
Observatory dry mass (SCB)	609.4 kg	743 kg	22 %
Propellant	56 kg	56 kg	
Power consumption			
Normal 15–27°	277 W	350 W	26 %
Safe 27–33°	233 W	332 W	43 %
Thermal bus environment	0 to +30 °C	−20 to +45 °C	+15/−20 deg
Delta V	183.4 m/s	151.4 m/s	21 %
G&C—total attitude knowledge (SC-GND)	2.87 deg	3 deg	
Spin axis control	3.1 deg (3σ)	3.1 deg (3σ)	
Spin rate control	±0.25 rpm	±0.25 rpm	
Average instrument data rate (kbps)	72 kbps	78 kbps	8 %
Data storage	16 Gbits	16 Gbits	

1.2 Observatory and Spacecraft Configuration

A description of the observatory with a focus on spacecraft subsystems is included below and addresses how key mission characteristics and the environment drove the design solution. The observatory resources including mass and power are summarized in Table 2 and demonstrate a design that meets RBSP science needs and provides margin for observatory contingencies. Figure 5 provides an overview of the functional elements including interfaces and connectivity between the spacecraft and instrument components. The RBSP observatory onboard avionics computer is based on a radiation-hardened RAD-750 single board computer manufactured by BAE Systems with 16 megabytes (MB) of random access memory (RAM) plus a 16 gigabit (Gb) synchronous dynamic random-access memory

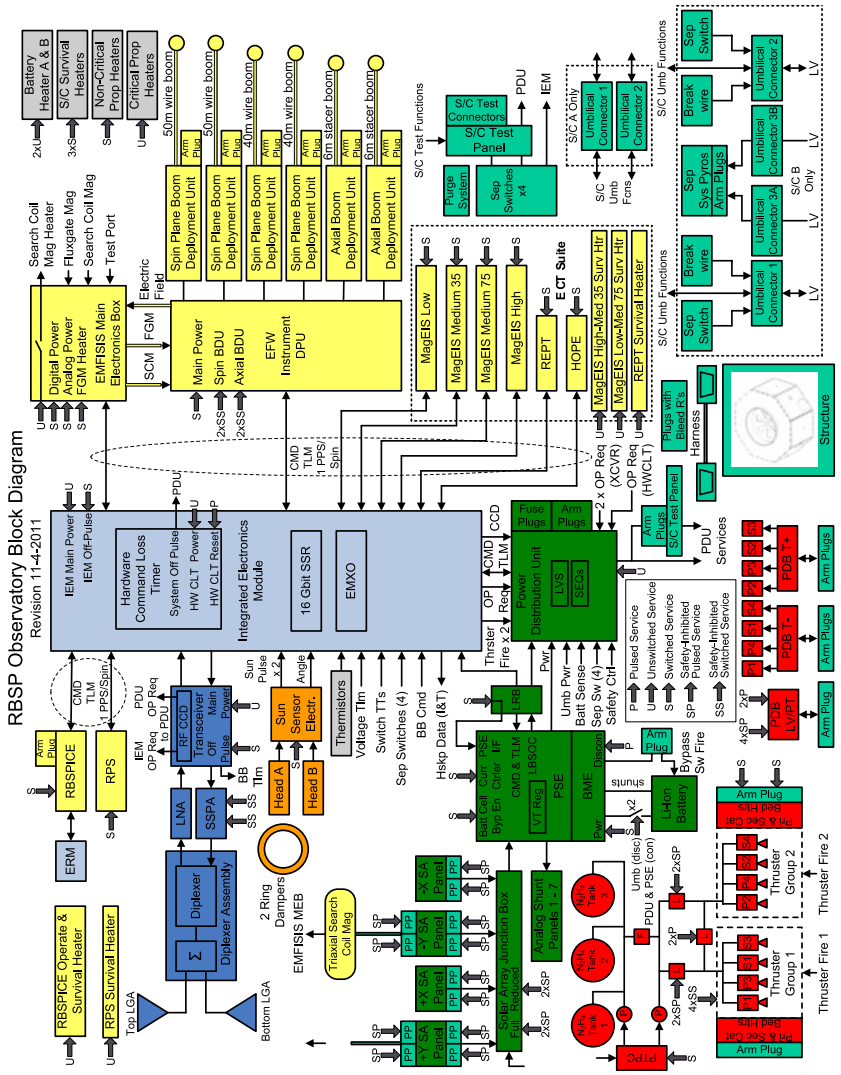

Fig. 5 RBSP observatory block diagram

(SDRAM) data recorder. The observatory interfaces are controlled by an RTAX2000 field-programmable gate array (FPGA).

The observatory supports continuous operations of all of the instruments. Power is supplied by four deployable solar panels, supplemented by an eight-cell lithium ion battery. The observatory will support the critical loads for at least 7 days in safe mode to provide sufficient time for the mission operations team to diagnose and resolve faults. The extreme radiation environment, combined with project cost constraints and the NASA risk classification (Class C), drove several unique features within the RBSP fault management system which is discussed in detail in the fault management section below.

The design philosophy for each observatory is to keep the observatory as simple as possible to reduce cost and to reduce the development and test schedules while meeting the science objectives. This philosophy is enabled by the mission science requirements, which drive the observatory to be a Sun-pointed spinner. Attitude knowledge and ephemeris are not required onboard. There is no onboard closed-loop guidance control system. Maneuvers and attitude adjustments are performed via thruster commands. Attitude determination is performed on the ground, after post-processing of downlinked Sun sensor and EMFISIS fluxgate magnetometer data. To support this ground-based attitude determination, the observatory components are placed and balance masses are located so that the observatory will produce less than 1° error of spin axis relative to the observatory frame. The measured uncertainty of the Sun direction relative to the observatory frame is $\leq 1.024°$ (3σ, single axis). This includes sensor and alignment errors, but not timing and processing errors, which are addressed separately. Contributions to alignment uncertainty knowledge include static alignment knowledge $<0.2°$ (3σ) and dynamic alignment knowledge $<0.09°$ (3σ). The attitude knowledge budget is shown in Table 3. Due to the spin and offset communications antennas, RBSP also has the redundant capability of using RF Doppler data to provide spin axis estimations (Srinivasan et al. 2012). Each RBSP observatory has the means (i.e., hardware, software, and expendables) to support orbital maneuvers throughout the commissioning, operational, and disposal phases of the mission, with a total ΔV of more than 150 m/s. This provides for translational maneuvers (collision avoidance, observatory separation distances/lapping rates, de-orbit), as well as for precession maneuvers that will be performed to keep the spin axis oriented towards the Sun with an overall attitude knowledge of 3°.

The observatory provides a broadcast message of observatory spin phase and spin period to each instrument at a frequency of 1/s. The observatory provides a spin pulse, from the Sun sensor when available, or a spin pulse based on a hardware timer, when Sun sensor pulse is unavailable, to each instrument approximately once per spin. This is described in Sect. 10, which goes into detail about the Guidance and Control System.

Table 3 Attitude knowledge budget

Term	Quiet time value (°)	Worst cast magnetic storm value (°)
Sun sensor alignment & measurement accuracy	0.546	0.546
Mag sensor alignment & measurement accuracy	1.197	1.197
Ground processing errors	0.707	2.062
Timing errors	1.500	1.5
RSS—all terms	2.117	2.869
Overall knowledge specified	3	3

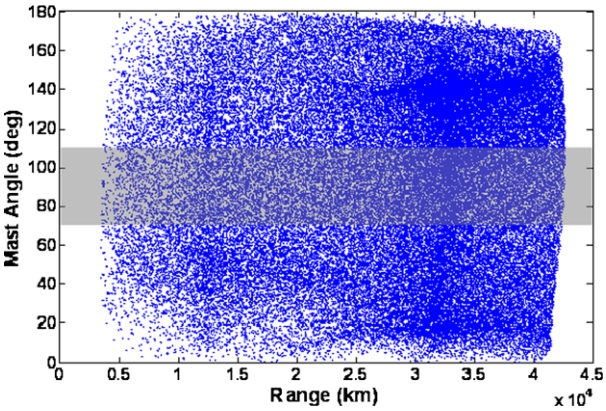

Fig. 6 Antenna boresight (mast) angle vs. range; each point represents 15 min of contact time The National Aeronautics and Space Administration's

The observatory solar array 3.2-m^2 total area will provide adequate power over the life of the mission to operate all onboard science instruments as long as the observatory is oriented with the arrays pointed to the Sun at an angle between 15° and 27° of normal. The observatory is spin stabilized to maintain this configuration, and the guidance and control systems will provide attitude correction maneuvers to maintain the spin axis and the arrays toward the Sun within these limits.

The observatory design includes a 50 Ah onboard battery that provides power to the observatory during the 2.5-h launch eclipse duration before the solar arrays deploy. The battery also is sized to provide observatory power during the mission to support full science operation through daily orbit eclipses that will vary throughout the mission for a given launch date. The longest eclipse duration is 114 min for the RBSP orbit, assuming launch any day of the year. The observatories will operate autonomously during solar eclipses and will continue to collect science data, transmit during scheduled contacts, and continuously transmit space weather data. Onboard fault management functions will monitor and transition the observatory to safe mode if needed as discussed in detail in Sect. 3 on fault management below.

The radio frequency (RF) system includes an APL-built Frontier radio transceiver and solid-state power amplifier that provides 8 W S-band RF transmitter power. The observatory RF system includes an S-band antenna on top ($+Z$) and bottom ($-Z$) observatory decks transmitting simultaneously. Because the antennas have broadbeam patterns, there is an interferometer pattern around the observatory in which no communications are planned. This exclusion zone is shown in Fig. 6; the observatory will transition through these short exclusion zones (hours) during each orbit. The observatory-to-ground communication link provides the capability to transmit all science and housekeeping data with a 1-hour pass per day for each observatory after commissioning. Therefore the impact is minimal to work around those portions of the orbit that do not support communication with the RBSP observatory. The system supports operation at up to 2 Mbps and is described below in Sect. 5.

The observatory coordinate system is shown in Fig. 7 and is defined as follows. The X–Y plane is parallel with and contains the launch adapter interface. The Z-axis extends from the center of the adaptor ring, normal to the X–Y plane and runs through the central cylinder. The $+Y$ direction extends from the Z-axis in the direction of the centerline of the solar array supporting the EMFISIS fluxgate magnetometer. The $+X$ direction is set relative to the other axes by the application of the right-hand rule. For the nominal mission attitude the $+Z$ direction will be pointed close to the Sun line and the direction of positive rotation for each observatory is defined by the application of the right-hand rule about the Z axis.

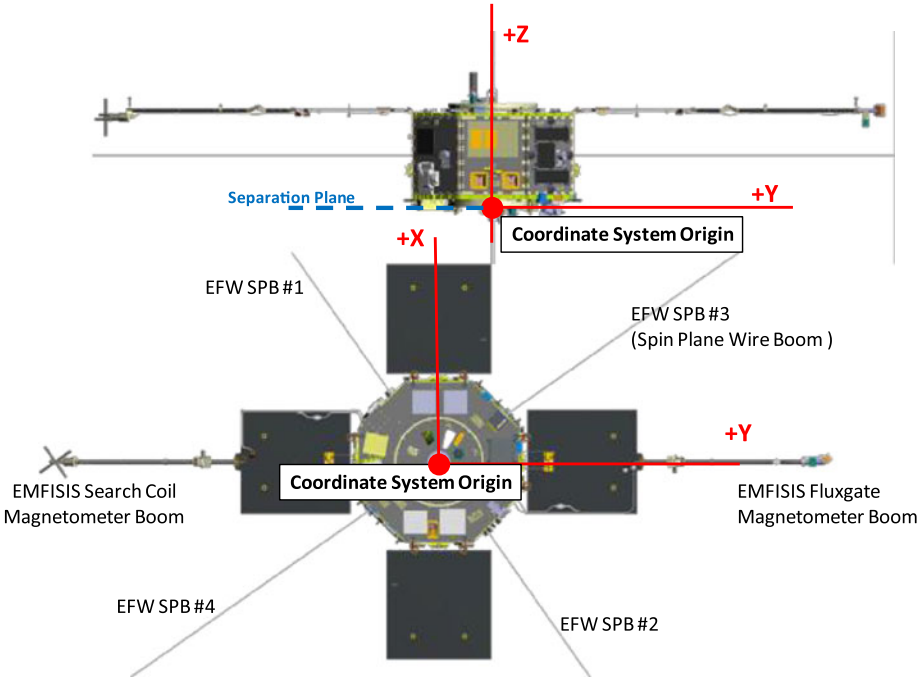

Fig. 7 Spacecraft coordinate system

The EMFISIS search coil and magnetometer field of views are shown in Fig. 8 relative to the observatory XYZ coordinate system for reference.

There is also a science UVW coordinate system defined for the mission that is related to the observatory XYZ coordinate system as a $-35°$ rotation about the observatory $+Z$ axis, with the $+W$ direction aligned with the observatory $+Z$ direction. The origin of the UVW coordinate system lies in the plane of the EFW spin plane booms (SPBs) at the intersection point of the EFW axial boom (AXB) deployment axis. The $+W$ direction is aligned with the center line of the forward EFW AXB. The $+U$ direction is aligned with the nominal location of EFW SPB #1. The $+V$ direction is relative to the other axes by the application of the right-hand rule, aligning it with the nominal location of EFW SPB #3. The science coordinate system is shown in Fig. 9. This figure also depicts the instrument field of views for the observatory body-mounted instruments including the HOPE, RBSPICE, REPT, RPS, and MagEIS instruments. The relative instrument views are shown in Fig. 10.

2 Observatory Environment

An RBSP design driver is the severe environment in which the RBSP observatories will spend the majority of their time: each observatory is designed for the challenging environmental requirements imposed by its orbit in the Van Allen Radiation Belts. The risk to electronic hardware is high. The environment causes high total ionizing dose and single event effects due to radiation as well as surface charging and deep dielectric charging/discharging on electrical hardware. Since RBSP is mostly single-string, several passive fault management features are designed into the system to deal with these environmental effects. First,

Instrument	Alignment Requirements	Defined FOV	Orientation	FOV Clear	Defined FOR/FOE	FOR/FOE Clear	Intrusions Coordinated	Plume Impingement Intrusion	Mechanical Mount	Thermal Mount	Radiator FOV Accomdated	Purge	Covers
EMFISIS													
Mag	Static: 1.0° Dynamic: 0.25°	None	Aligned w/ SPB - 3m from body	N/A	None	N/A	N/A	None	Boom	Isolated	N/A	No	No
Search Coil	Static: 1.0° Dynamic: 0.5°	None	Aligned w/ SPB - 3m from body	N/A	None	N/A	N/A	None	Boom	Isolated	N/A	No	No
MEB		N/A	N/A	N/A	N/A	N/A	N/A	None	Deck	Conductive	N/A	No	N/A

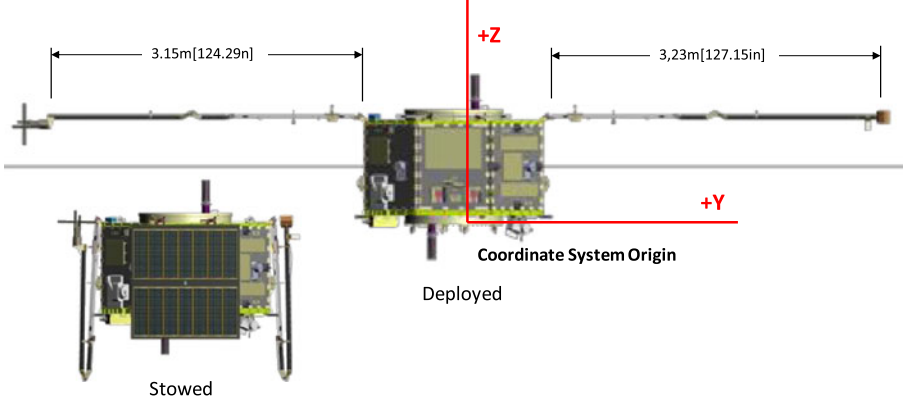

Fig. 8 EMFISIS instrument fields of view and boom-mounted locations

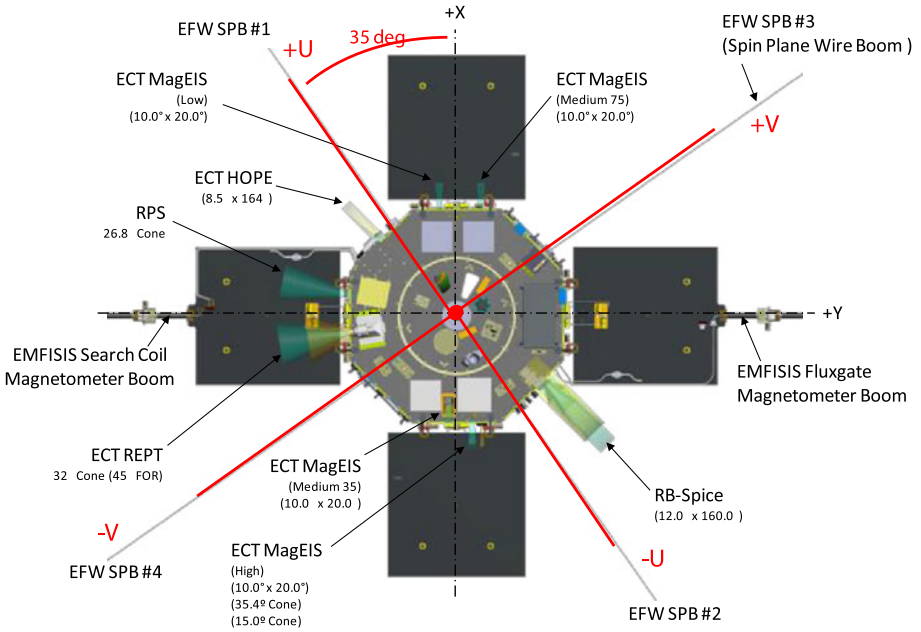

Fig. 9 Science coordinate system

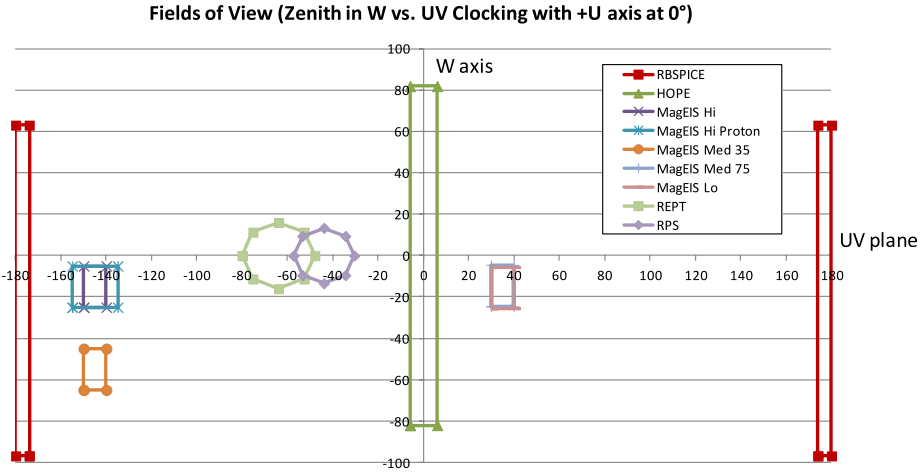

Fig. 10 Relative instrument fields of view

additional shielding is utilized around electronics boxes. Second, a radiation-hard parts program is employed in which devices were tested to at least 50 krad (Si), with the required hardness based on chassis wall thickness and use of spot shielding. All integrated circuits were required to be latch-up immune. Third, first circuit interfaces are hardened to survive deep dielectric discharge pulses in the observatory harness. Fourth, in order to enable sensitive RBSP science measurements, the observatory is designed using techniques to reduce observatory internal and surface charging so that the observatory-generated fields will not

contaminate the electric fields and magnetic fields that the science instruments will be measuring.

Significant effort was expended in the design of the observatory to minimize nonconductive external surfaces that could charge up and generate electric fields contaminating EFW measurements or experience discharges that could damage observatory electronics. Also magnetic material was restricted and current loops were either eliminated of minimized to avoid generating magnetic fields that could contaminate EMFISIS measurements. The required error due to the observatory-generated electric field at the tip of the axial booms is $\leq$4 mV/m. To meet this requirement, all exposed surfaces of the observatory are grounded, and internal to the observatory there are no floating metal conductors or large dielectric surfaces. Electromagnetic interference (EMI) backshells are used on all internal harness connectors, and all harnesses are wrapped with an aluminum tape outer wrap. In selective cases lead overwrap was added to electrical harnesses that connect to components that are sensitive to deep dielectric discharge events. Unused pins in the observatory harness are grounded and bleed resistors are included for umbilical and launch vehicle connections that would be left floating after the observatory disconnects from the launch vehicle. Special care was given to the design of the solar arrays, as these extend from the observatory body and are closer to the boom-mounted sensors. The solar arrays use solar cells with a grounded indium tin oxide (ITO)—coated coverglass and also incorporate a double layer of insulating grout covered by conductive grout and dissipative black Kapton tape over solar array interconnects. To reduce the magnetic signature of the solar array, the strings were designed carefully to reverse adjacent polarities and thereby cancel out magnetic fields for each panel. The RBSP solar arrays provide the necessary observatory power while nearly eliminating extraneous electric and magnetic fields. SAIC completed a study for APL, which predicted a spurious electric field contribution of less than 1.6 mV/m generated at the EFW axial boom sensors, assuming 8 % of the solar array area would be nonconductive. Since the solar array design actually achieved a performance of less than 1 % nonconductive array area, the expected array-generated spurious electric field will be significantly below the predicted 1.6 mV/meter (Davis et al. 2007). Electromagnetic Compatibility (EMC) tests were conducted on each observatory demonstrating that the observatory generated electric field is below 24 μV/m over the frequency range of 30 Hz to 400 kHz.

The RBSP observatory-generated time domain magnetic field is required to be less than 5 nT static and 0.1 nT dynamic over the frequency range of 50 Hz to 15 kHz at the EMFISIS fluxgate and search coil magnetometer locations on the booms. To meet this requirement the use of magnetic material was restricted and care was taken in all designs to minimize current loops and other effects that could generate magnetic fields. A test program was instituted consisting of testing at the part, box, and observatory levels. Magnetic cleanliness was a high priority throughout the development effort. The static magnetic field produced by the solar array has been measured and is $\ll$1 nT at 0.5 m thus it is well below the required performance to support mission science measurements. The static magnetic field of each observatory was measured during the observatory magnetic swing test performed at APL in the environmental test facility in January 2012 and again just prior to launch in July 2012. This testing provided a measured static magnetic field below 4 nT and dynamic magnetic field below 0.1 nT.

2.1 Radiation Environment

The observatory and instrument subsystems and components are required to operate continuously while the RBSP observatory transits through the heart of the inner trapped-proton

Table 4 Total ionizing dose (RDM = 2)

Observatory assembly	Max total dose (krads)
Boom electronics	12.6
Top deck RF antenna	14.4
Sun sensor electronics	12.9
RB spice	15.4
ECT/REPT	14.6
RPS	14.4
ECT/MAGEIS electronics	12.6
ECT/HOPE electronics	14.2
RPS	14.4
EFW DPU	12.4
Power distribution unit	13.2
Battery	12.8
Transceiver	10.2
Solid state power amplifier	10.8
Integrated electronics module	12
Power supply electronics	12.4
Solar array junction box	13.6

Van Allen belt twice every ~9-h orbit for the nominal 2-year + 74-day mission. These energetic protons (up to hundreds of megaelectron volts (MeV)) provide the majority of the penetrating dose and all of the displacement damage. The second major contribution to the total radiation dose is from the outer belt trapped electrons that bombard the observatory during the long exposures near apogee. An analysis was done to determine the corresponding total dose versus shield depth for the RBSP mission from SHIELDOSE box-level generic geometry results. All parts used in the RBSP observatories were specified to survive a total ionizing dose of at least 34 krad (Si) [23 krad (Si) for the integrated electronics module (IEM)] without parametric or functional failure. This value is based on a 2-year (plus 74-day) life, with a radiation design margin (RDM) factor of 2, and a nominal shield depth of 350 mils (500 mils for the IEM) of aluminum. As mentioned previously, radiation parts testing was performed at an even higher level, 50 krad, on parts that were not already specified by the vendor to handle that level of radiation.

After the RBSP observatory mechanical configuration was designed and defined, a detailed radiation transport ray trace analyses using NOVICE code gave specific results for individual electronics boxes and locations. The maximum dose for any box was 15,400 rad (RDM = 2). Table 4 shows predicted results for RBSP observatory mounted assemblies. The large number of 350-mil wall boxes provides substantial shielding for nearest neighbors on the observatory and reduce the electronics box doses to minimal levels from the most penetrating protons.

Connector cutouts in the chassis were shielded to prevent localized high ionizing doses inside electronics boxes. This shielding was inside or outside of the electronics box. The expected low to moderate accumulated total doses of 23–34 krad (Si) behind 500 mils and 350 mils aluminum, respectively, eliminated the need for enhanced low dose rate (ELDRS) testing.

Solar panels and instrument optics or exposed detectors must withstand displacement damage associated with the trapped proton fluence. For the 2-year + 74-day RBSP mission

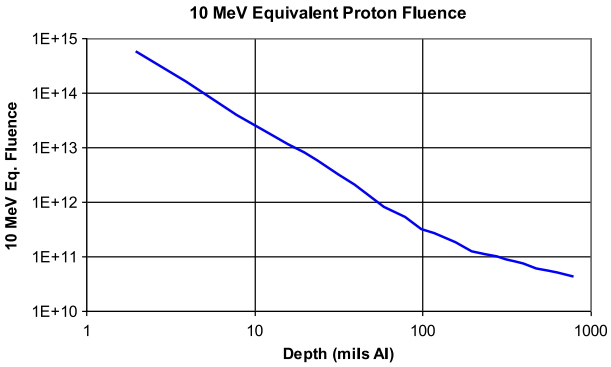

Fig. 11 Equivalent 10 MeV proton fluence vs. shield depth

the equivalent 1-MeV electron fluence is 1.35×10^{15} e/cm^2 behind 20-mil cover glass thicknesses for the maximum power parameter on the solar cells. Figure 11 shows the expected 10 MeV equivalent proton fluence as a function of shield depth in aluminum. For the box wall thicknesses of 350–500 mils, the fluences are in the range of 5×10^{10} to 8×10^{10} p/cm^2.

The estimated deep space cosmic ray integral linear energy transfer (LET) spectra for the RBSP orbit were used to estimate the upset rates of single event effects (SEEs) for the mission. The deep space spectra are relevant but conservative for the RBSP mission, since the observatories spend the vast majority of the time at or near geosynchronous altitudes, where the deep space environment applies. The "Worst Week" environment curve is generally used in upset rate calculations. It must be combined with the experimentally determined upset cross-section for a given device to calculate the upset rate.

Parts susceptible to single event latch-up with linear energy transfer threshold less than 80 MeV cm^2/mg were not used in RBSP systems. A failure modes and effects analysis (FMEA) was performed to demonstrate that other single event upsets (SEUs) in parts would not cause mission critical failures. SEUs in parts of noncritical systems were not allowed to compromise flight system health or mission performance.

Critical digital parts (i.e., programmable devices, memories, and microprocessors) were evaluated for susceptibility to SEU effects, such as single- and double-bit errors, functional interrupt and stuck bits. Critical linear and mixed signal devices were evaluated for proton-induced single event transients (SETs). Power devices were analyzed for single event burnout (SEB) and single event gate rupture (SEGR).

The peak proton flux expected in the RBSP orbit has been calculated and is 1.0×10^6 protons/cm^2 s with energy greater than 10 MeV; the peak electron flux is 3.7×10^7 electrons/cm^2 s with energy greater than 1 MeV. These peak fluxes produce the maximum dose rates and noise caused by charged particle hits during the RBSP orbit, which may affect dynamic integrated circuit performance, guidance and control sensors, and science instrument resolution. Hardware must operate through these levels.

2.2 RBSP Parts and Materials Radiation Test and Evaluation

An extensive parts radiation test program was implemented as part of the RBSP project to evaluate radiation performance of key radiation sensitive components. Parts were evaluated for total ionizing dose based on the predicted mission dose levels and SEEs were predicted based on single event latch-up and single event functional interrupt performance (Tipton et al. 2009).

Total ionizing dose (TID) testing was performed at 18–25 rad/s in the APL cobalt 60 Irradiator on about 50 part types that were proposed for use in the RBSP flight hardware. The remaining part types were either purchased as radiation-hardened devices or evaluated to be hard to the TID requirements by manufacturers or third party data. Displacement damage testing of optocouplers and linear regulators was carried out at the Indiana University Cyclotron Facility (IUCF) with 200 MeV protons in October 2007, October 2008, and June 2009. No passive parts testing was performed. Bipolar transistor screening in March 2009 showed that only the 2N2222 needed to be purchased as a radiation-certified part. Six other bipolar transistors passed 100 krad: 2N2369, 2N4957, 2N2857, 2N2907, 2N3501, and 2N3700.

SEE testing was conducted using heavy ion runs for latch-up, SEFIs, SEUs, and transients in July 2008, December 2008, and March 2009 at the Brookhaven National Laboratory Tandem van de Graaff accelerator. Several digital-to-analog converters (DACs) and frequency synthesizers were evaluated for use in the APL RF transceiver. Proton upset of the RTAX2000 FPGA static random access memory (SRAM) was completed at IUCF in August 2009, and the components for the RF transceiver were evaluated in June 2009. Upset rates for the RF transceiver and solid-state recorder (SSR) were computed and deemed acceptable. Proton transient tests for linear regulators and power converters were also conducted at IUCF in October 2008, June 2009, and April 2011.

In addition to the supporting the testing of observatory components, APL supported evaluation and testing of the following parts and materials for the science instruments:

- Total dose testing for materials on the EFW booms.
- Proton-induced radioactivity in shield materials for RBSPICE and ECT.
- Bipolar transistor results for several instruments.
- Consultation on HV801 optocoupler/driver for ECT.
- Displacement damage work on optocouplers for ECT.
- Single event testing for latch-up and transients for ECT and EFW.
- The results of SEU testing of FPGA SRAM blocks were provided to the instrument teams.

Materials investigations included several total dose evaluations and conclusions:

- ITO-coated silverized Teflon in a self-supporting thermal blanket configuration lost all mechanical integrity and was in pieces after 10 Mrad, which was the estimated surface total dose.
- The same material when structurally supported by a plate of aluminum in a radiator configuration passed the 10-Mrad level with respect to mechanical integrity. However, the ITO coating's electrostatic discharge (ESD) conductivity was destroyed.
- Germanium black Kapton in the thermal blanket configuration survived the 10-Mrad exposure with only some minor discoloration in isolated locations and no visible degradation in mechanical integrity and surface conductivity and was chosen for thermal control applications.
- External wire insulation for solar panel wire and the EFW SPB passed testing successfully.
- EFW AXB cable from Gore and the EFW painted and plated external materials all passed testing successfully.
- Purge tubing passed radiation exposure test successfully.
- Silicone oil for the nutation damper showed $\sim$7 % increase in viscosity at -20° C temperature after radiation exposure.
- Several RF antenna mockups with coax cable performed well under radiation exposure test.

Tungsten/copper, tantalum, and 364 stainless steel disc samples were exposed by the Laboratory for Space Physics (LASP) ECT team for induced radioactivity at Brookhaven National Lab to a simulated RBSP orbit proton spectrum. 90/10, 80/20 tungsten/copper and tantalum had no sustained significant radioactivity. The 364 stainless steel had only a minor long-term response.

2.3 Electromagnetic Environment

The electromagnetic environment (EME) for RBSP includes all effects of the environment from initial design and parts selection through mission operation. This includes the normal observatory electromagnetic compatibility with launch radar and other equipment. It also includes magnetic control for the magnetic field measurements, electrostatic control for the charged particle detectors, and low-frequency electric field measurements, as well as internal charging control to assure all devices survive and operate properly in the radiation belt plasma environment. Of these four EME areas, the internal charging issue was the most critical to the observatory design, since electrical discharges due to internal charging of dielectrics or floating conductors could actually damage electrical hardware and cause mission failure.

High-energy electrons and ions in the radiation belts will penetrate the outer structure of the observatory and come to rest inside the spacecraft. The flux of ions that penetrate the observatories is small and gives rise to radiation issues discussed previously. However, the electron flux in the energy range of 0.1 to 10 MeV in particular is large enough to accumulate substantial charge in dielectric materials and floating conductors. Figure 12 shows an integrated spectrum plot of the log of the number of electrons that strike every square centimeter of the observatory every second verses the energy of these electrons. If the charged particle stops in an active circuit, the operational current will carry the charge to ground. However, when the charged particle stops in an insulator or floating conductor, the charge cannot return to ground and accumulates. If the observatory is not properly designed, both conductor and dielectric material can charge up to several thousand volts. When sufficient charge accumulates in an object so that the local voltage exceeds the breakdown voltage of the dielectric or the gap voltage of a floating conductor, a discharge to the local ground occurs. A discharge is a flow of electrons that results in a negative pulse when the discharge is directly into a circuit, but circuit properties or the movement of image charges can cause a positive or ringing pulse. If the local ground is a trace on a circuit board connected to an ESD-sensitive circuit, damage can occur. But even if damage does not occur, the electric discharge creates an electric field pulse inside the device that can upset circuits, inject noise in communications, or contaminate low voltage signals.

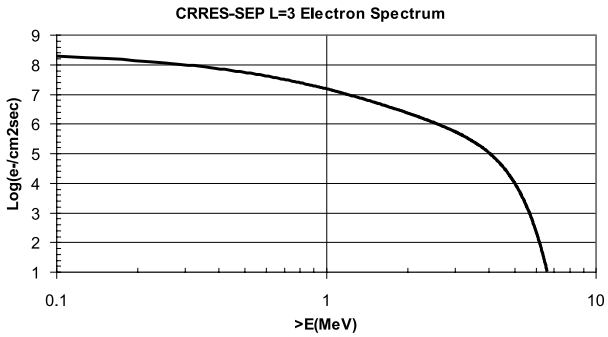

Fig. 12 Electron spectrum

Floating conductors will neutralize the entire charged volume of the conductor in one discharge, producing a high-voltage, high-energy pulse that can easily damage circuits and upset distant circuits from the large electric field pulse. Large exposed dielectric surfaces will also discharge most if not all exposed surface in one discharge. For this reason, floating metal and large dielectric surfaces were not allowed anywhere on the observatory unless shielded with enough metal to prevent charging.

Dielectrics covered with thin layers of conductors or in immediate contact with a conductor (such as the insulation on a wire) can discharge and cause ESD-like damage and can also create EMI noise. But the discharge is limited to a local volume of dielectric due to the high relative resistivity preventing electrons from moving through the material to sustain the discharge. This limits the energy of the discharge, producing a lower voltage and larger resistance for the discharge. All devices and harnesses had to be specially designed with extra shielding and discharge protection to not only survive these discharges but to operate while these multitudes of discharges are occurring. Special care was taken to assure no segment of harness was left open, causing the wire to become floating metal. All of this required special circuitry in some situations, additional shielding over some cables, and the use of large drain resistors to connect to ground in other circuits.

Since discharges in the harness are unavoidable, all first circuit interfaces have to survive these discharges. A test program was instituted to evaluate a variety of interface ICs and protection circuits. The test program utilized standard ESD testing using the Human Body Model ESD event, since this ESD test is more damaging than the expected deep dielectric discharge pulses in the observatory harness. A unique aspect of this test was that devices were tested in the powered and unpowered states. First circuit interfaces were selected based on this testing or in some cases based on analysis. The selected interfaces will survive deep dielectric pulses; however, most input interfaces will pass the pulse to the next stage of electronics. To ensure that this pulse did not affect operability (e.g., be detected as a command, or corrupt a command in transit), the use of a pulse rejection circuit was required. These circuits were typically located in an FPGA for digital interfaces.

Low-energy particles in the radiation belt plasma stop and accumulate on the outer surface of the observatory, causing the second EME issue of observatory charging. Surfaces in sunlight emit electrons due to the photoelectric effect. These two effects come to equilibrium by charging the observatory to a voltage different from that of the local plasma until the two currents balance. If sections of the observatory are not electrically connected, large potential differences can develop. These potential differences can lead to discharges, but at a much lower value they contaminate both the electric field and particle measurements required by the mission. The observatory must be a "grounded" local reference frame in the plasma so that the science instruments can measure the DC and low-frequency electric fields and low-energy particle spectra. This required all outer surfaces to be conductive and bonded together, as well as surfaces inside the observatory, since a multitude of medium-energy electrons make it through the observatory body but lose enough energy to stop on the inside surfaces. One of the crucial requirements was to find conductive black paint and conductive adhesives that would meet the electrical, thermal, and mechanical requirements of the observatory.

A detailed charging model of the observatory was developed and used to finalize surface charging requirements as the development of the observatory progressed. Major effort was put into the development of the solar panels, since they represent a very large area close to the sensitive instruments. Extreme care had to be taken to make sure that the conductivity requirements did not interfere with the function and isolation requirements of the arrays.

To perform the mission, the observatories had to survive assembly, integration, and testing in environments where static electricity is possible. Standard ESD control procedures for

assembly and testing of deliverable hardware and minimum standards for ESD safeguards related to observatory assembly, inspection, test, transport, and storage of flight and spare hardware were defined for the project.

The third EME issue is magnetic control. As part of the science instruments, each RBSP observatory carries a triaxial fluxgate magnetometer (MAG) which measures the Earth's vector magnetic field and a triaxial search coil magnetometer (SCM) which measures the magnetic field associated with plasma waves in the radiation belt. MAG and SCM are extremely sensitive devices with wide dynamic range necessary to measure both small deviations in the field and off-axis fields to determine field and propagation direction. Due to the wide dynamic range, the MAG and SCM instruments are sensitive to magnetic fields generated by the observatory. Of particular concern is the increasing use of low-voltage parts that pull substantial currents when active. These circuits will turn on for a while, drawing large currents with possible high-frequency modulation, and then turn off. This on–off cycle can create low-frequency magnetic fields that can interfere with science measurements. The feed and return circuits on circuit boards had to be carefully laid out and inspected to minimize the area inside the closed current loop from the power supply to the part and back. Special segmentation of power and return planes was necessary to minimize magnetic emissions by reducing the loop area.

Any electrical interfaces with an unbalanced current flow would generate magnetic fields that could interfere with science measurements. Therefore single-ended electrical interfaces were not allowed; only balanced differential interfaces were used, generally with a shielded twisted pair harness configuration. Digital interfaces between observatory electronics used low-noise low voltage differential signaling (LVDS) circuits. There would have been some advantages to using a MIL-STD-1553 bus, but the high level of emissions that have been measured on MIL-STD-1553 interfaces precluded its use.

Another major magnetic control area was the solar arrays, especially the $+Y$ solar array, because the MAG was attached to this panel. A piece-wise linear magnetic circuit model based on a model from Goddard Space Flight Center (GSFC) and an APL magnetic moment model were used to guide the design. All the solar cells were laid out in U-shaped strings with the return current loop on the back surface of the panel back-tracking the current flow through the solar cells to achieve magnetic compensation. To further reduce the magnetic emissions, neighboring strings were wired in opposite directions, i.e., one string clockwise and the adjacent strings counter-clockwise. Measurements were made of every string individually to verify that the front and back currents were in the proper direction and relation to adjacent strings. A final test where the entire array was driven with a realistic square wave current was performed to verify the total cancelation of the design. For all panels, the measured magnetic field amplitude was at or below the 1-nT detection threshold. The solar arrays are shown in Fig. 13 during observatory integration and test with solar array protective covers installed for use during ground processing.

Since magnetic cleanliness was a major concern, magnetic measurements of every device began during the development stage which identified some materials that were replaced with nonmagnetic alternatives. This testing continued as components were installed on the spacecraft, and culminated in a final observatory-level test to determine the total signature of the assembled observatory. Of particular concern were motors, latch valves, and strong magnets in particle instruments. Because the Earth's magnetic field varies by a factor of about 200 over the orbit, the use of magnetic shielding material had to be carefully controlled, as this material would drag the Earth's field along with the observatory and contaminate the science measurements. Early measurements during development identified that the particle instruments did not need the shielding due to their careful design. The SPB motors did need

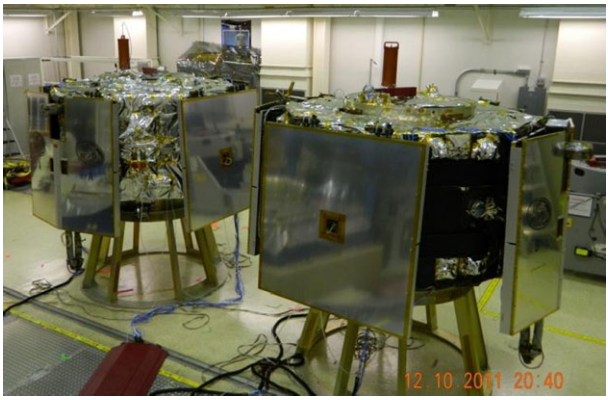

Fig. 13 RBSP Observatory A and Observatory B side by side in APL test facility with solar array protective covers

the shielding, but again, careful design eliminated any problem. Latch valves are necessary in the propulsion system and they must have a magnet to function; early measurements identified the need for a compensating magnet to be installed in the observatory near the latch valves to reduce the field to acceptable levels at the science instrument.

The final EME area of concern is meeting the standard EMC requirements for the observatory. No device may interfere with the operation of any other device or with the launch vehicle, and all devices must also survive interaction with launch radars and radios. These requirements were assigned to every device. Verification started in the development stage and continued to measurements made when each device was installed on the spacecraft, with a final observatory-level EMC test which finished with a "plugs out" test of the fully operating observatory in a configuration as close to flight-like as possible.

The MIL-STD-461-C test requirements were tailored for this mission and every device type went through full qualification testing as well as a reduced set of acceptance tests. Because two observatories were built, there were at least two of every device plus (for many devices) a flight-like engineering model (EM) was built. When the EM was nearly identical to the flight model (FM), the qualification testing was done on the EM so that any identified problem could be fixed in the FM and re-tested. This greatly helped to avoid scheduling issues, preventing a flurry of activity on a device just before delivery if an EMC problem was identified.

Since magnetic cleanliness was so important, the radiated emissions RE-01 tests were tailored for the measurement requirements and for the distance a device was from the SCM on the observatory. The RE-01 magnetic field emissions test limits are shown in Fig. 14 for a distance of 3–5 m from the observatory. Because distance was not a major factor in the low-frequency electric field tests there was one specification for all devices, which was tailored to the measurement requirements of the science instruments. A critical problem in RBSP science is that electric fields in the plasma vary from DC to hundreds of kilohertz, requiring electric field measurements below the normal minimum RE-02 frequency of 14 kHz. The APL EMC chamber was specially modified to make measurements down to 50 Hz, and most devices had to use this facility since commercial chambers could not make the measurement below 14 kHz. To control emissions at these low frequencies, conducted emissions CE-01 measurements were acquired on breadboards and power supplies to aid in the device design and tailor filter and board designs. CE-01 and CE-03 measurements were acquired on every device before delivery and again after installation on the observatory to look for interaction problems with actual harness and power systems. Identified problems were reworked and retested.

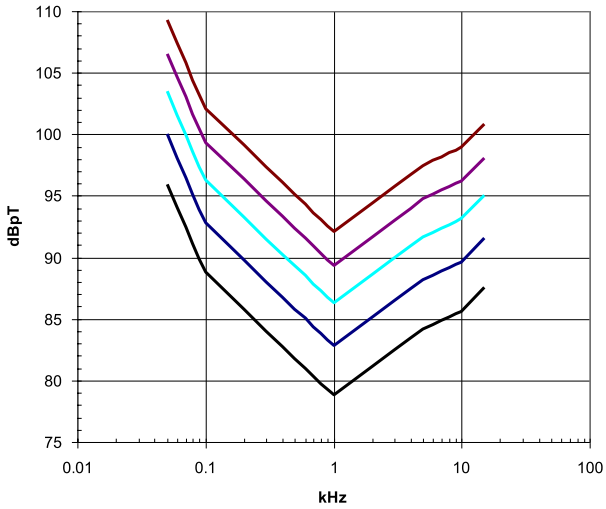

Fig. 14 Radiated emissions RE-01 magnetic field emissions limits for 3 to 5 m

Conducted and radiated susceptibility (RS) tests were also performed to tailored limits for the RBSP Mission. RS levels were specified at one level for operation and at a higher level for survival. Many devices opted to test for operation at the survival level to reduce test time and only a few had any problem, but everything did pass both levels. Due to the probability of ESD from internal charging, every device at the prototype level was tested for susceptibility to nearby ESD discharges and passed; however, not all the ground support equipment operated properly during the test.

2.4 Magnetic Testing

During observatory development, significant care was taken to ensure the magnetic cleanliness of all observatory components, either procured or developed for RBSP. All observatory electronics boxes were measured and found to be acceptable prior to installation on the observatory. Magnetic materials were prohibited for use on RBSP, and all components were tested prior to installation to ensure that they did not carry a residual magnetic field. The only component on the observatory that is magnetic is the latch valve in the propulsion system, for which there was no non-magnetic alternative. Compensation magnets were installed on each observatory to cancel the latch valve magnetic field.

A magnetic swing test was conducted during observatory-level integration and test to measure the static magnetic fields of the fully integrated RBSP observatory bus in an unpowered configuration. The purpose of this test was to confirm the residual magnetic field in order to separate the observatory-induced field from the natural in-space environment. The test configuration is shown in Fig. 15. Magnetic field data were collected and the observatory magnetic moments determined to confirm that the residual permanent magnetization is within the observatory allocation. The solar panels were measured separately and their performance was also verified as acceptable.

The RBSP total observatory generated time domain magnetic field is required to be less than 5 nT static and 0.1 nT dynamic (from 15 Hz to 15 kHz) at the boom-mounted magnetometers which extend 3 m each from the observatory main body. The static magnetic field produced by the solar array panels was measured to be $\ll$1 nT at 0.5 m and is well below the required performance to support mission science measurements. The solar array magnetic

Fig. 15 Observatory magnetic swing test configuration

testing was performed jointly with the APL EMC engineers and the GSFC magnetometer team. The solar array strings were driven with a square wave current, either separately, or together, to facilitate identification of a magnetic field due to the solar arrays (string plus compensation loop) in the presence of a variable environmental field. The test demonstrated that the RBSP solar array is very well compensated, with little or no statistically significant field observed as close as 0.5 m from the array. This indicated that the solar arrays will well exceed requirements, particularly allowing for the separation of the arrays and the flight sensor positions.

To test the observatory main body, each RBSP observatory was suspended from a crane in the APL high bay facility for a magnetic swing test using only verified nonmagnetic materials in the mechanical test configuration. Simultaneous measurements with sensors at different locations permit the first order removal of background variations. Two magnetometers were used in gradiometer mode for each measurement to subtract the Earth's field and background noise by taking the difference of the readings between the two magnetometers. An initial translational measurement was made to measure the dependence of the observatory magnetic field with distance and then a rotational measurement was made to determine the angular dependence of the static field. During the test each observatory was suspended from the crane directly under the hook and allowed to swing back and forth with a translational motion, and later rotated about a fixed axis at a fixed position such that measurements were acquired continuously over a 360° rotation.

The observatory magnetic swing tests verified that there were no major sources of magnetic field other than the latch valves and the compensation magnet on each observatory at the time of the test. The test also verified that the compensation magnets for both observatories were installed properly so that they cancel the magnetic field of the propulsion system latch valve at the EMFISIS magnetometer sensors. The EMFISIS sensors are located on booms that extend approximately 3 m from the body of the observatory. Based on the magnetic field measurements made during the swing test at 1.5 m, combined with the measurements done on the solar arrays, the magnitude field at the location of the sensor is estimated to be 3.71 nT for Observatory A and 3.63 nT for Observatory B, both are below

the stated DC goal for magnetic cleanliness of 5 nT. Based on analysis, the dynamic magnetic field is determined to be less than 0.1 nT over the frequency range of 50 Hz to 15 kHz. Additional measurements were made just before launch to verify the observatory magnetic cleanliness in the final flight configuration after shipment to the launch site.

3 Fault Management

The RBSP observatories have a single-string fault tolerant architecture. Critical single-string spacecraft components use un-switched power and have the ability to be power cycled (or "off-pulsed") in the event that a radiation induced failure causes a fault that requires removal of power. Critical boxes can be off-pulsed individually or as a group. Both software and hardware command loss timers are part of this off-pulse architecture and result in a power cycle of observatory electronics if a specific command is not received for a defined duration. The off-pulse architecture is described in more detail below.

The RBSP fault management system is a distributed system with allocations to observatory hardware, flight software, rule-based autonomy, and ground/mission operations as depicted in the fault protection operational modes diagram in Fig. 16. The RBSP fault management design uses both "active" and "passive" features to deal with potential faults. Some of these features were included to mitigate faults induced by the environment. Active features include actions taken onboard the observatory that are implemented with hardware, software, or a combination of the two, whereas passive features include design decisions and development practices to minimize the probability that a fault occurs. The overall goal was for the onboard fault management system to be as simple as possible while ensuring that (1) the observatory is capable of detecting, correcting, and recovering from any single, recoverable anomaly that affects the health and safety of the observatory and (2) the observatory meets the overall mission concept and mission goals.

While allocations were made to hardware, flight software, ground/mission operations, many of the onboard fault detection and responses were allocated to autonomy. The RBSP rule-based autonomy system uses a traditional monitor-response style architecture. It consists of over 70 monitors and responses that autonomously address observatory faults. The type of protection varies, such as powering off loads that draw excessive current (software circuit breakers) to more complex system-level responses such as initiating a safe mode sequence if a pre-defined failure is detected autonomously. The latter response involves a series of load-shedding actions wherein the observatory is configured into a power-conserving state that supports emergency RF communications with the Earth. The autonomy system is also used for selected operational responses not directly tied to faults. These include sensing observatory separation from the launch vehicle and commencing the critical post-separation sequence which enables safety-inhibited observatory buses, powers on the RF system, and deploys the solar panels to acquire power. Although the autonomy system executes within the flight software, the individual monitors and responses can be modified without changing the underlying flight code. Since the observatory is operating in a dynamic radiation environment, this approach provides the engineering team with flexibility to quickly modify or augment the autonomy system in response to unexpected behavior that may be observed in flight.

While the RBSP fault management design takes advantage of inherent mission design characteristics to reduce complexity, a number of design drivers also influence the design. The near-Sun pointed, spin-stabilized design offers a number of advantages, while the extreme radiation environment, project cost constraints, and the NASA risk classification drive

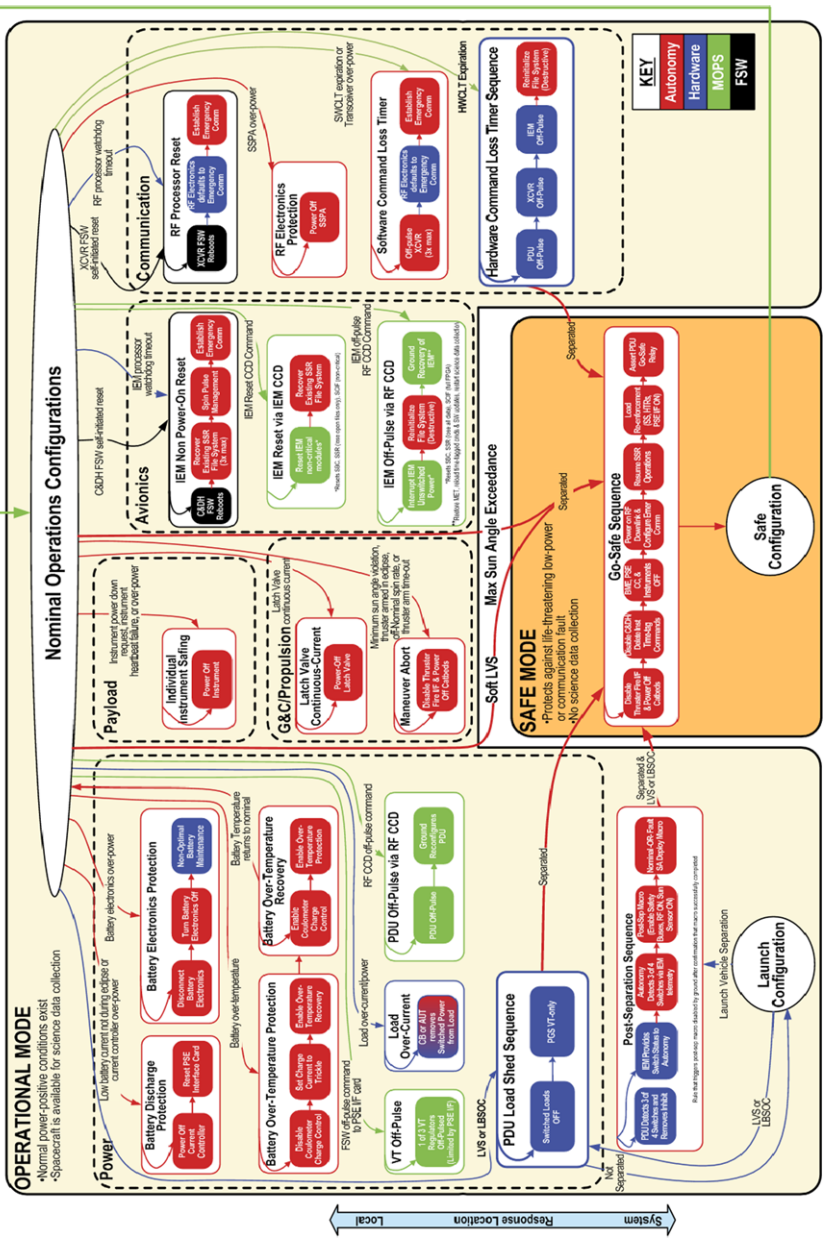

Fig. 16 Fault protection modes diagram

several unique features within the fault management system. These influences on the design resulted in five high-level principles that governed the overall RBSP fault management design and from which lower-level fault management concepts and requirements were derived. These high-level principles include selective fault tolerance, minimized onboard fault management, layered fault management for maximum science, limited instrument fault management, and off-pulse capability for unswitched electronics. The result of applying these five principles was a simplified observatory with a fault management design aimed at reducing complexity while at the same time increasing the probability of success.

The NASA risk classification for the mission, as defined by the *Risk Classification for NASA Payloads* (NASA 2008) influenced several of the high-level principles. The RBSP mission is categorized as a Class C mission, which is defined as a medium-to-low cost mission, with medium-to-low complexity, and accepts a medium level of risk. In addition, Class C missions may use single string and selectively redundant design approaches, and critical single point failures (for Level 1 Requirements) may be permitted but are mitigated by use of high-reliability parts, additional testing, or other means. The Class C designation drove both the overall system design and the fault management system, with the program adopting a *selective fault tolerance* philosophy to maximize reliability while minimizing cost and complexity. This resulted in a single-string architecture for RBSP, incorporating passive fault management measures to increase the reliability of critical sequences and to reduce the use of parts with high risk of failure, with failure modes that are more likely due to the environment, or parts with movable components. Table 5 summarizes the selective fault tolerance implemented on RBSP.

In addition to the use of passive features such as the radiation-hard parts program, additional box shielding, etc. to protect against the harsh radiation belt environment, a unique active fault management feature was devised to mitigate against the effects of discharges inside boxes. Since RBSP uses a single-string architecture, critical components [i.e., the IEM, Power Distribution Unit (PDU), and Transceiver (XCVR)] are powered using unswitched power services so that they cannot be turned off once the observatory is powered (devices on switched power can be power cycled by ground command). These components are described in more detail later in this paper. However, the extreme mission radiation environment can induce faults in these components that can only be cleared by the removal and re-application of power (termed off-pulsing). The fault management system implements an *off-pulsing capability for unswitched electronics* to clear faults in the XCVR, IEM, and PDU. Mechanisms were provided to allow off-pulsing of any single component as well as simultaneous faults in all three of these components. As shown in Fig. 17, all off-pulse requests are routed through the PDU, with the PDU implementing a specific hardware command sequence for each off-pulse type. The off-pulse mechanism was designed to be fault-tolerant with a single fault resulting in, at most, a single off-pulse cycle.

The fault management architecture utilizes the following off-pulse requests: IEM request to off-pulse transceiver (via software command loss timer [SWCLT]), transceiver request to off-pulse IEM (via RF critical command decoder (CCD) command), transceiver request of off-pulse PDU (via RF CCD command), and hardware command loss timer (HWCLT) request to off-pulse PDU, IEM, and transceiver. Both the software and hardware command loss timers are reset using a specific command; if that command is not received for a defined duration, an off-pulse of the transceiver occurs (in the case of SWCLT expiration) and an off-pulse of the PDU, IEM, and transceiver (in the case of HWCLT expiration). Table 6 summarizes the components to be off-pulsed, the source of the off-pulse request, and the trigger for the off-pulse.

The severe environment and mission science requirements also influenced the design principle *layered fault management for maximum science data collection*. An important

Table 5 RBSP selective fault tolerance

Function	Redundancy/fault tolerance	Description
Separation indication	Fault tolerant separation switches	3 of 4 separation switches required
Deployments	Redundant deployment for mag boom and search coil	1 of 2 actuators required (for each)
	Redundant deployment for solar panel	1 of 2 actuators required (for each)
	Redundant EFW AXB and SPB deployment enables	1 of 2 boom enables required (for each)
Data storage	Fault tolerant SSR memory banks	Failure of an SSR memory bank impacts the amount of data stored (half the recorder lost), but SSR would still function
	Failed SSR	IEM continues to function without SSR; mission severely degraded
Latch valves	Cross-over latch valve	2 of 3 latches valves required
Maneuvers	Redundant catbed heaters	1 thruster control group could fail and still perform nominal or degraded manuever
	Redundant thruster groups	
Sun sensor	Redundant sensor heads	1 of 2 heads needed for spin pulse
Sun sensor	Back-up sun pulse from spin timer (not adequate for full science)	Mitigates spurious pulses on Sun Sensor output
Communication	Antennas	Failure of antenna reduces availability by 50 %
PDU	Redundant safety enabled buses	Redundant operation of actuators, thrusters, SSPA, and SAJB
	Redundant wires for select loads	Redundant wires for HOPE, REPT, RPS, IEM, PDU, XCVR, thruster valves, and latch valves
Power generation	Spare solar string	Power design is tolerant of one failed solar string without loss in mission performance
Power generation	Battery cell	Power design is tolerant of one failed battery cell with possible degraded performance
Power management	Spare shunt	Power design is tolerant of one failed shunt without loss in mission performance
	Redundant relays to connect battery to power bus	1 of 2 relays needed to connect battery to bus
	Fault tolerant VT controllers	2 of 3 VT controllers required for majority voter
Power management	PSE interface card	Power system has reduced functionality and battery performance may be affected if PSE I/F Card, BME, or Current Controller fail
	Battery management electronics	
	Current controller	
Flight software	Two copies	Identical copies of the image stored in EEPROM
Thermal control	Fully redundant dual element battery heaters with series redundant thermostats	1 of 2 battery heaters needed; series redundant thermostats protect against thermostat failed closed condition
	Fault tolerant heaters and layout	Protects against heater failing open
	Unswitched instrument heaters with series redundant thermostats	Series redundant thermostats protect against thermostat failed closed condition
Fluxgate mag data for attitude determination	Backup path for analog fluxgate magnetometer data	EFW instrument can packetize mag data if digital section of EMFISIS MEB fails

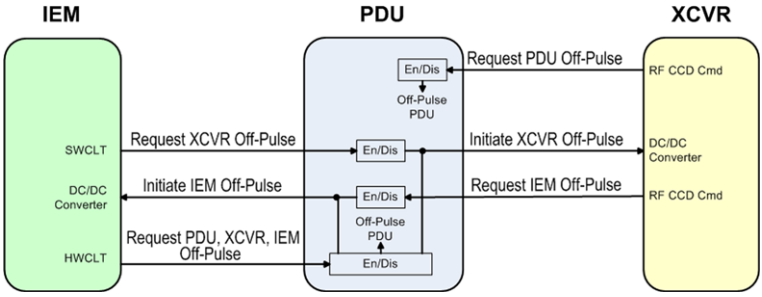

Fig. 17 Top-level off-pulsing architecture

Table 6 Sources and targets of off-pulsing

Component(s) to be off-pulsed	Off-pulse requestor	Off-pulse trigger
XCVR	IEM	SWCLT (autonomy rule)
IEM	XCVR	RF CCD command initiated by MOPs
PDU	XCVR	RF CCD command initiated by MOPs
PDU, IEM, & XCVR	HWCLT	HWCLT command not received for 3.58 days

aspect of the science measurements is to obtain simultaneous observations over a range of observatory separations to distinguish between spatial and temporal variations. To meet these science measurement goals, the RBSP fault management system, in the event of a fault, utilizes a layered fault management design for maximum science data collection, which ultimately defines the fault management modes. Faults are categorized by severity with the goal of quickly detecting and responding to less severe, isolated faults with minimum interruption to science data collection (i.e., remain in operational mode) and ensuring a power-safe and communication-safe observatory for more severe, time-critical faults through a system-wide response (i.e., demote to safe mode).

While the design philosophy for the observatory and fault management is to keep the observatory as simple as possible to reduce cost, as influenced by the risk classification, this philosophy is made feasible by the mission requirements for the observatory to be pointed toward the Sun and to be spin-stabilized. The near-Sun pointed attitude is the only attitude required to collect the prime science measurements and maintaining it requires only periodic precession maneuvers every $\sim$21 days for the duration of the mission. The periodic precession maneuvers are dictated by the Earth's orbital motion around the Sun, with maneuvers being performed when the total Sun offset angle reaches a maximum value. This orbit offers a number of design advantages: (1) when combined with antenna coverage out to 70° from both sides of the spin-axis, frequent ground contacts (more than one per day) with negligible communication delays are possible; (2) the near-Sun pointed attitude ensures adequate power generation when attitude is maintained within the maximum offset angle; and (3) the inherently stable spin state requires infrequent adjustments to maintain the observatory's orientation, allowing for open-loop attitude control. The inherently stable observatory with open-loop attitude control system and frequent ground contacts allow for a *minimized onboard fault management system* (as compared with more complicated missions with 3-axis stabilized attitude control), with the burden for fault correction and recovery to be placed on the ground. This design principle encompasses the overall safing concept for

the mission and defines the fault management modes. To reduce the complexity of the fault management system, the goal was to have the least number of modes possible to safely perform the RBSP mission. By design, the RBSP observatories are in a "safe" state: they are inherently stable, near-Sun pointing spinners which require only periodic attitude precession maneuvers performed via an open-loop attitude control system.

Two modes have been identified for RBSP, operational mode and safe mode, which is consistent with the fault management philosophy principle of layered fault management for maximum science data collection. Operational mode is the primary mode for the observatory and is used from launch through the end of the mission unless the observatory encounters a life-threatening fault condition. When possible, the observatory "flies through" faults or "fails operational," meaning that noncritical faults leave the observatory in operational mode. These faults are handled by the onboard fault management system or by the ground during subsequent ground passes. The occurrence of a critical fault [defined as a hardware or software low voltage sense (LVS), low battery state of charge (LBSOC), violation of the maximum Sun angle, or extended loss of communication (HWCLT)] causes a transition to safe mode. The goal of safe mode is to autonomously place the observatory into a known communication-safe, power-preserving configuration so that the ground has time to identify and recover from the fault. The transition from safe mode back to operational mode is performed by ground command only.

Finally, onboard fault management is also significantly reduced because there is no onboard capability for the guidance and control subsystem to autonomously point the observatory, and the observatory and science instruments are decoupled. When possible, fault management measures are allocated to hardware to reduce the size of the onboard rule-based autonomy. When fault management measures are allocated to autonomy, the dedicated rules take simple actions such as powering off a component or resetting a component. This leads to the last design principle: *limited instrument fault management*. The RBSP observatory fault management is decoupled from the science instruments, with instrument fault management limited to the monitoring of instrument power draw, power down request, and heartbeat. In the event of an instrument fault, the instrument is immediately powered off with no advanced warning; however, all other instruments remain powered on to maximize the science data collection.

4 Power System

Each RBSP observatory utilizes a direct energy transfer (DET) power system topology which simplifies observatory electronics and minimizes power system–generated EMI. The power bus voltage varies with the eight-cell Li-ion battery voltage. The RBSP power system consists of the power system electronics (PSE), the battery management electronics (BME), the solar array junction box (SAJB), the 50-Ah Li-ion battery, and four deployed solar array panels. A simplified block diagram of the power system is shown in Fig. 18.

The power system electronics consist of a single fault-tolerant 16-stage sequential analog voltage control shunt regulator with maximum battery current limit. The loads are connected to the single 8-cell, 50-Ah Li-ion battery via the PDU. The nominal bus voltage is 30 V and can vary between 24 and 32 V depending on the state of charge (SOC) and temperature of the battery. Each battery cell can be by-passed with a bypass switch, activated by ground command, to remove a single cell from the battery in case of a pending cell failure. If bypass switch activation has occurred, the corresponding bus voltage range becomes 21 to 28 V. The primary battery charge control method is constant current followed by a constant voltage

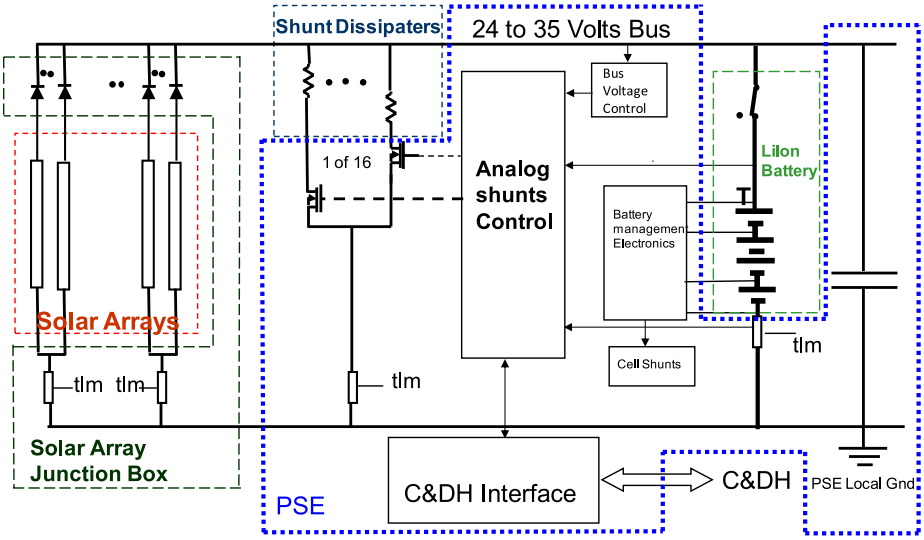

Fig. 18 Simplified block diagram of the RBSP power system

taper charge (CC/CV). The battery is charged at a high rate, limited to $C/5$, where C is the battery capacity, using the available solar array power that is not used by the loads until the battery SOC reaches 60 %. The onboard coulometer then reduces the battery charge current to $C/10$. The battery maximum voltage is controlled to preset safe levels via voltage (V) limits that are implemented in the single fault tolerant voltage regulator. Whenever the battery voltage reaches the V limit, the V control loop will force the charge current to taper.

The battery management electronics consists of an interface board and a cell shunt board. Each battery cell has a parallel-connected analog shunt used during the mission to balance the end of charge voltage of each Li-ion battery cell. Each cell shunt is limited to 0.75 A maximum current bypassed around the cell in order to limit the amount of power dissipated in the BME. The BME contains eight relays that allow the battery cells to be disconnected from cell shunts to limit leakage current during ground operations or whenever the BME is not powered. During safe mode operation, the current controller and BME are not powered and the system relies on the single fault tolerant voltage limit regulator. The average observatory load power during flight is expected to be 277 W.

4.1 Solar Array

The RBSP solar array consists of four deployed panels with a total active area of 3.2 m^2. Each panel is approximately 0.739 m wide and 1.26 m long. The panel substrates are 25.4-mm-thick aluminum honeycomb with composite face sheets. The panel front cell side is insulated with Kapton, co-cured with the graphite fiber face sheet. The back face sheet is not painted. Three different solar cell sizes are used to maximize the cell packing density. Each panel contains 12 strings of 24 series connected 28.3-cm^2 solar cells. The panels without booms panels (two panels of the four) contain an additional two strings of 22 series connected 26.62-cm^2 solar cells and four strings of 22 series connected 11.5-cm^2 solar cells. The panels with booms (two panels of the four) contain an additional string of 22 series connected 26.62-cm^2 solar cells and two strings of 22 series connected 11.5-cm^2 solar cells.

Fig. 19 RBSP solar array panels ready for observatory integration

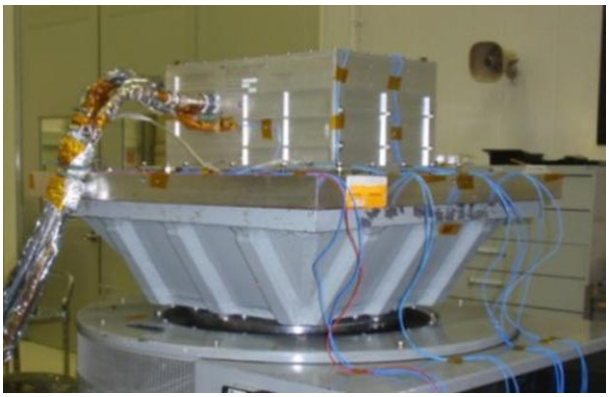

Fig. 20 Flight battery after completed vibration testing in preparation for observatory integration

The solar cells are triple junction cells with a minimum efficiency of 28.5 % (BTJ), from EMCORE Photovoltaics. The cover glass on each cell is 0.5-mm-thick cerium-doped microsheet, from Qioptiq with ITO coating. Figure 19 shows the solar array panels for both RBSP observatories ready for observatory integration.

The RBSP mission instruments required that more than 85 % of all array surfaces be conductive with exposed potentials at spacecraft ground. To achieve this, the cell side is grouted with two-layer grout and two-layer tape over all interconnects. The wires on each panel backside are shielded. The shields were connected to the face sheet at regular intervals using conductive adhesive and are electrically connected to the aluminum honeycomb core with conductive epoxy at the connector bracket. The wiring on the cell side is not shielded but is covered with conductive grout. The solar panel temperatures are sensed using PT103 platinum wire sensors, placed beneath the solar-cell-side face sheet in small bored cavities. To minimize the magnetic field induced by the currents in the strings, the strings are laid down in a U pattern and back wired. Roughly, every other string is placed with the current polarity in the opposite direction to further cancel any residual magnetic field.

4.2 Battery

The RBSP observatory battery as shown in Fig. 20 was designed and built at APL. The battery contains eight Li-ion cells, LSE-50, that were manufactured by GS YUASA. Bypass

switches from NEA, Inc., were placed across each cell to eliminate the potential of an observatory failure caused by a cell where the performance is diverging from the majority of the pack. The bypass switch is a make-before-break design with the switch performed activated ground command. The battery is required during launch, eclipses, and maneuvers, and to support the solar array power during peak power transients and guidance and control (G&C) Sun off-pointing anomalies. The battery package includes connect relays and temperature transducers. The voltage of each cell is monitored with the voltage and temperature signals reported by the BME.

4.3 Power Distribution

The power distribution unit provides switched, unswitched, and pulsed power to the observatory components; the allocations of the switched, unswitched, and pulsed power services and rate power levels are shown in Table 7 (spacecraft components) and Table 8 (instrument components). The PDU receives primary power from the PSE and has a serial universal asynchronous receiver/transmitter (UART) command/telemetry interface with the IEM. The PDU box is a modular slice design. Each slice consists of a printed circuit board housed in a mechanical frame, and the slices stack and bolt together. The slices are electrically connected using internal rigid-flex connectors for signals. A wiring harness external to the box is used for power connections. A solid 350-mil-thick aluminum chassis and solid 150-mil aluminum radiation shields (located in thinned areas of the PDU chassis) are used to mitigate the effects of radiation on the electronics parts and allow the PDU to function nominally in a high radiation environment.

The PDU is shown in Fig. 21 as installed on the interior of an observatory side panel. The PDU includes power metal–oxide–semiconductor field-effect transistor (MOSFET) switches for the load power services. For hazardous functions, such as thrusters, deployment actuators, and RF transmitters, electromechanical relays are used to "arm" the safety-critical power busses. Additional power MOSFETs are used in series to provide a sufficient quantity of inhibits to meet range safety requirements. Majority-voting of separation signals is used to control one of the inhibits. Mechanical safe/arm plugs were employed during integration and test. Switched power services include a circuit breaker function implemented in the switch control circuit that makes use of current monitors and power MOSFET switches. The circuit breakers can be individually enabled and disabled. To protect the main power bus, each load power service also has an upstream fuse. These fuses are type FM12A, which are of solid-body construction and have no cavity. These high-reliability fuses have significant spaceflight heritage and are rugged with respect to mechanical vibration and shock.

The PDU functions are shown in a bock diagram in Fig. 22 and include the fault protection hardware sequences. The PDU has eight hardware sequences stored in programmable read-only memory (PROM), which are utilized by the fault management system; these sequences contain the hardware responses to critical observatory faults and off-pulse requests. Both the LVS and LBSOC detections result in load shedding via hardware sequence. In addition, the off-pulse architecture is implemented by the PDU with a specific hardware command sequence for each off-pulse type. If a fault is detected in any critical observatory component (i.e., PDU, IEM, or XCVR); an off-pulse request can be issued by the nominally functioning component to off-pulse (power cycle) the component with the fault. This off-pulsing architecture also includes the capability to off-pulse all three critical components via HWCLT expiration in the unlikely event that all three are simultaneously subjected to fault conditions. Finally, the PDU also features a power-on-reset circuit

Table 7 RBSP observatory power services

Subsystem	Power service	Service type	Maximum pulse current; N/A for switched and unswitched services	Nominal pulse duration; N/A for switched and unswitched services	Configured pulse duration; N/A for switched and unswitched services	Flight fuse rating
C&DH	IEM	Unswitched	N/A	N/A	N/A	Jumper
	Hardware Cmd loss timer reset	Pulsed	0.25 A	200 ms	200 ms	2.0 A
	Hardware command loss timer	Unswitched	N/A	N/A	N/A	2.0 A
	Off-pulse IEM	Pulsed	0.25 A	8 s	1.024 s	2.0 A
G&C	Sun sensor electronics unit	Switched	N/A	N/A	N/A	2.0 A
Mechanical	Solar array deploy $+X$ axis A	Pulsed	10.0 A	1.0 s	1.0 s	10.0 A
	Solar array deploy $+Y$ axis A	Pulsed	10.0 A	1.0 s	1.0 s	10.0 A
	Solar array deploy $-X$ axis A	Pulsed	10.0 A	1.0 s	1.0 s	10.0 A
	Solar array deploy $-Y$ axis A	Pulsed	10.0 A	1.0 s	1.0 s	10.0 A
	Solar array deploy $+X$ axis B	Pulsed	10.0 A	1.0 s	1.0 s	10.0 A
	Solar array deploy $+Y$ axis B	Pulsed	10.0 A	1.0 s	1.0 s	10.0 A
	Solar array deploy $-X$ axis B	Pulsed	10.0 A	1.0 s	1.0 s	10.0 A
	Solar array deploy $-Y$ axis B	Pulsed	10.0 A	1.0 s	1.0 s	10.0 A
	Magnetometer boom deploy A	Pulsed	10.0 A	1.0 s	1.0 s	10.0 A
	Magnetometer boom deploy B	Pulsed	10.0 A	1.0 s	1.0 s	10.0 A
	Search coil boom deploy A	Pulsed	10.0 A	1.0 s	1.0 s	10.0 A
	Search coil boom deploy B	Pulsed	10.0 A	1.0 s	1.0 s	10.0 A
Power dist.	PDU	Unswitched	N/A	N/A	N/A	Jumper
Power generation	BME battery cell bypass	Pulsed*	10.0 A	100 ms	Switch	10.0 A
	PSE interface card	Switched	N/A	N/A	N/A	2.0 A
	Battery relay 1 & 2 connect pulse	Pulsed	0.5 A	100 ms	104 ms	2.0 A
	PSE battery interface electronics	Switched	N/A	N/A	N/A	3.0 A
	PSE current controller	Switched	N/A	N/A	N/A	2.0 A

Table 7 (*Continued*)

Subsystem	Power service	Service type	Maximum pulse current; N/A for switched and unswitched services	Nominal pulse duration; N/A for switched and unswitched services	Configured pulse duration; N/A for switched and unswitched services	Flight fuse rating
	PSE disable BEB cell balancing	Pulsed	1.0 A	100 ms	104 ms	2.0 A
	SAJB relay—SA reduced current A	Pulsed	1.0 A	100 ms	104 ms	2.0 A
	SAJB relay—SA full current A	Pulsed	1.0 A	100 ms	104 ms	2.0 A
	SAJB relay—SA reduced current B	Pulsed	1.0 A	100 ms	104 ms	2.0 A
	SAJB relay—SA full current B	Pulsed	1.0 A	100 ms	104 ms	2.0 A
Propulsion	Latch valve 1 open	Pulsed	1.0 A	100 ms	104 ms	2.0 A
	Latch valve 1 close	Pulsed	1.0 A	100 ms	104 ms	2.0 A
	Latch valve 2 open	Pulsed	1.0 A	100 ms	104 ms	2.0 A
	Latch valve 2 close	Pulsed	1.0 A	100 ms	104 ms	2.0 A
	Crossover latch valve open	Pulsed	1.0 A	100 ms	104 ms	2.0 A
	Crossover latch valve close	Pulsed	1.0 A	100 ms	104 ms	2.0 A
	Catbed heaters group 1 (Pri)	Switched	N/A	N/A	N/A	3.0 A
	Catbed heaters group 1 (Red)	Switched	N/A	N/A	N/A	3.0 A
	Catbed heaters group 2 (Pri)	Switched	N/A	N/A	N/A	3.0 A
	Catbed heaters group 2 (Red)	Switched	N/A	N/A	N/A	3.0 A
	Pressure transducers	Switched	N/A	N/A	N/A	2.0 A
	Thruster valve select P1	Switched	N/A	N/A	N/A	2.0 A
	Thruster valve select P3	Switched	N/A	N/A	N/A	2.0 A
	Thruster valve select S1	Switched	N/A	N/A	N/A	2.0 A
	Thruster valve select S3	Switched	N/A	N/A	N/A	2.0 A
	Thruster valve select P2	Switched	N/A	N/A	N/A	2.0 A
	Thruster valve select P4	Switched	N/A	N/A	N/A	2.0 A
	Thruster valve select S2	Switched	N/A	N/A	N/A	2.0 A
	Thruster valve select S4	Switched	N/A	N/A	N/A	2.0 A

Table 7 (*Continued*)

Subsystem	Power service	Service type	Maximum pulse current; N/A for switched and unswitched services	Nominal pulse duration; N/A for switched and unswitched services	Configured pulse duration; N/A for switched and unswitched services	Flight fuse rating
RF	S-band transceiver	Unswitched	N/A	N/A	N/A	Jumper
	SSPA (PDU switch A)	Switched	N/A	N/A	N/A	Jumper
	SSPA (PDU switch B)	Switched	N/A	N/A	N/A	Jumper
	Off-pulse tranceiver	Pulsed	0.25 A	8s	1.024 s	2.0 A
Thermal	Bus survival heaters 1	Switched	N/A	N/A	N/A	7.5 A
	Bus survival heaters 2	Switched	N/A	N/A	N/A	7.5 A
	Bus survival heaters 3	Switched	N/A	N/A	N/A	7.5 A
	Non-critical prop module heaters	Switched	N/A	N/A	N/A	7.5 A
	Critical propulsion module heaters	Unswitched	N/A	N/A	N/A	Jumper
	Battery heater A	Unswitched	N/A	N/A	N/A	6.0 A
	Battery heater B	Unswitched	N/A	N/A	N/A	6.0 A

Table 8 RBSP instrument power services

Suite	Power service	Service type	Maximum pulse current; N/A for switched and unswitched services	Maximum pulse duration; N/A for switched and unswitched services	Configured pulse duration; N/A for switched and unswitched services	Flight fuse; rating is higher for short duration pulses
ECT	ECT—REPT	Switched	N/A	N/A	N/A	3.0 A
	ECT—MagEIS Low	Switched	N/A	N/A	N/A	3.0 A
	ECT—MagEIS Med35	Switched	N/A	N/A	N/A	3.0 A
	ECT—MagEIS Med75	Switched	N/A	N/A	N/A	3.0 A
	ECT—MagEIS high	Switched	N/A	N/A	N/A	3.0 A
	ECT—HOPE	Switched	N/A	N/A	N/A	6.0 A
	ECT survival heaters—high & mid 35	Unswitched	N/A	N/A	N/A	6.0 A
	ECT survival heaters—low & mid 75	Unswitched	N/A	N/A	N/A	6.0 A
	ECT survival heaters—REPT	Unswitched	N/A	N/A	N/A	2.0 A
EFW	EFW main power	Switched	N/A	N/A	N/A	6.0 A
	EFW AxB deploy enable A	Switched	N/A	N/A	104 ms***	10.0 A
	EFW SPB deploy enable A	Switched	N/A	N/A	104 ms***	10.0 A
	EFW AxB deploy enable B	Switched	N/A	N/A	104 ms***	10.0 A
	EFW SPB deploy enable B	Switched	N/A	N/A	104 ms***	10.0 A
EMFISIS	EMFISIS analog power	Switched	N/A	N/A	N/A	2.0 A
	EMFISIS digital power	Switched	N/A	N/A	N/A	3.0 A
	Search coil mag survival heater	Unswitched	N/A	N/A	N/A	2.0 A
	Fluxgate mag heater	Switched	N/A	N/A	N/A	2.0 A
PSBR	RPS main power	Switched	N/A	N/A	N/A	3.0 A
	RPS survival heaters	Unswitched	N/A	N/A	N/A	3.0 A
RBSPICE	RBSPICE main power	Switched/Pulsed**	1.0 A	100 ms	Switch	3.0 A
	RBSPICE operate & survival heaters	Unswitched	N/A	N/A	N/A	2.0 A

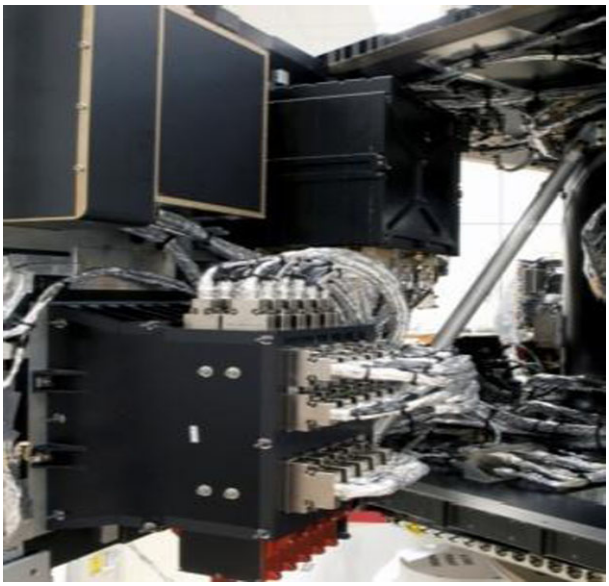

Fig. 21 Power distribution unit (PDU) installed on Observatory A panel

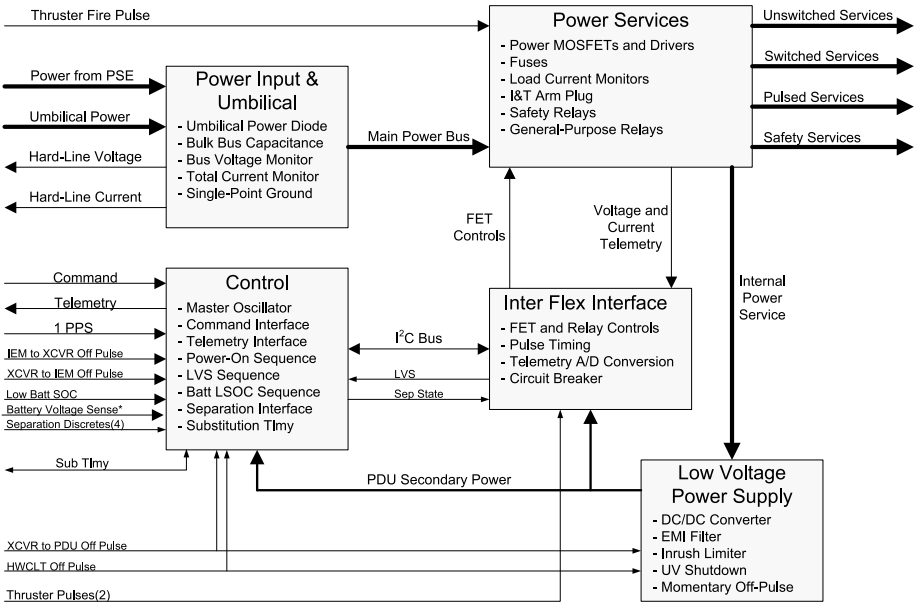

Fig. 22 PDU block diagram

with an autonomous initialization sequence to ensure that loads are in an appropriate predefined power state following bus voltage recovery in the unlikely event of a bus undervoltage.

5 Telecommunications system

The RBSP RF telecommunication system has three primary functions: (1) provide a downlink for science data and observatory telemetry return, (2) provide an uplink for observatory commanding, and (3) provide highly accurate Doppler data for observatory navigation (Srinivasan et al. 2009). The RF system operates at S-band, with separate uplink and downlink frequencies for observatories A and B. The RF system is sized to enable downlinking of at least 6.7 Gbits of data per day per observatory, including real-time housekeeping telemetry and adequate margins, during the operational phase of the mission. To meet data return requirements given the constraints of the mission system, the RF system provides data rates up to 2 Mbps. The data rate is optimized during a ground contact as the link parameters change due to the changing observatory range to the ground station.

The 10° inclination of the RBSP orbit places the ground track in the region indicated in Fig. 23. To provide adequate ground tracking of the observatory, three geographically diverse stations are used. The APL 18-m dish in Laurel (APL-18), Maryland, USA, is the primary ground antenna (Copeland et al. 2010). This ground station provides sufficient performance and view periods to adequately downlink the required mission science data nominally on a daily basis. At S-band, the 18-m dish provides 49.5 dB of antenna gain with a system noise temperature of 135 K. To augment these contacts, secondary ground antennas are selected to provide additional coverage for circumstances such as launch and early operations, emergencies, and periods of poor geometry to APL-18. These antennas are the Universal Space Network (USN) 13-m ground stations at South Point, Hawaii, USA, and Dongara, Australia. The telecommunications system is also compatible with the Tracking and Data Relay Satellite System (TDRSS).

A block diagram of the S-band RF communication system is shown in Fig. 24. The major components include two low-gain antennas, a power combiner/divider, a diplexer, an 8-W solid-state power amplifier (SSPA), and a Frontier radio transceiver (XCVR) to interface with the observatory avionics subsystem. The antennas, SSPA, and Frontier radio were all designed and built by APL. Conical bifilar helix antennas (Stilwell 1991) provide the broad-beam −4 dBic gain coverage required for the mission and are shown in Fig. 25. The S-band Frontier radio, shown in Fig. 26, consists of four slices: an exciter, receiver, Digital Signal Processor (DSP), and power converter. The receiver and exciter slices contain

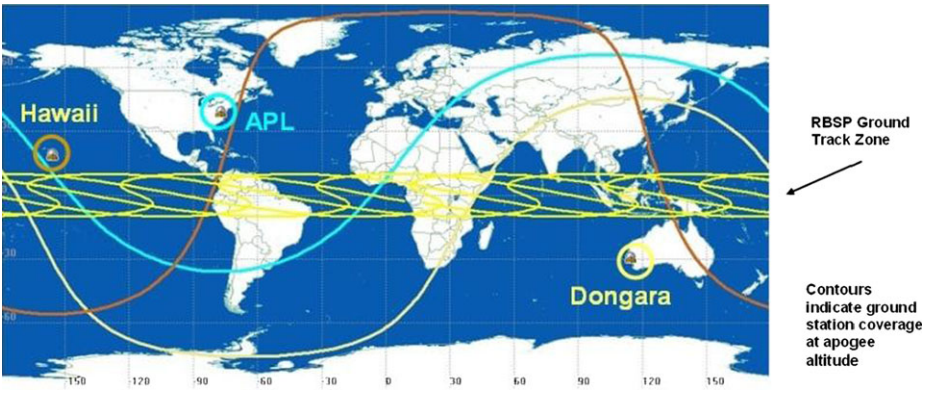

Fig. 23 Ground station locations and their fields of view at the RBSP apogee distance. At closer distances the coverage area diminishes; however, the closer distance enables a higher downlink rate for increased data volume throughput

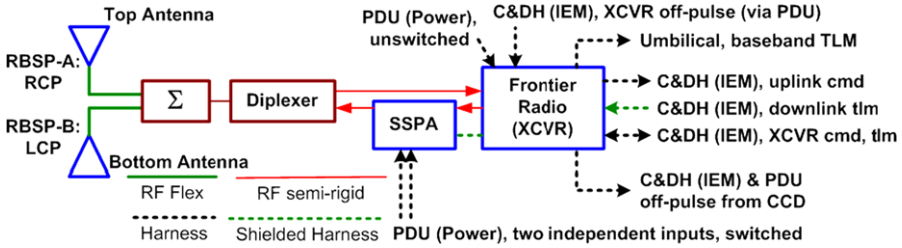

Fig. 24 RBSP RF subsystem block diagram

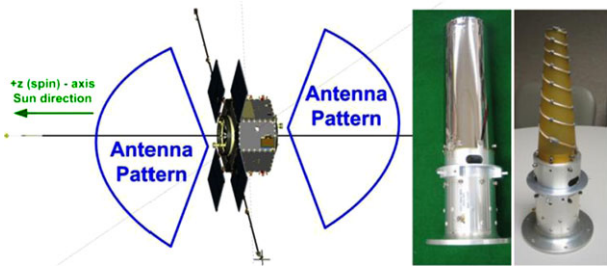

Fig. 25 The RBSP mission requires broad-beam antenna coverage from boresight to 70° for each antenna. The antenna is shown on the right with and without a radome

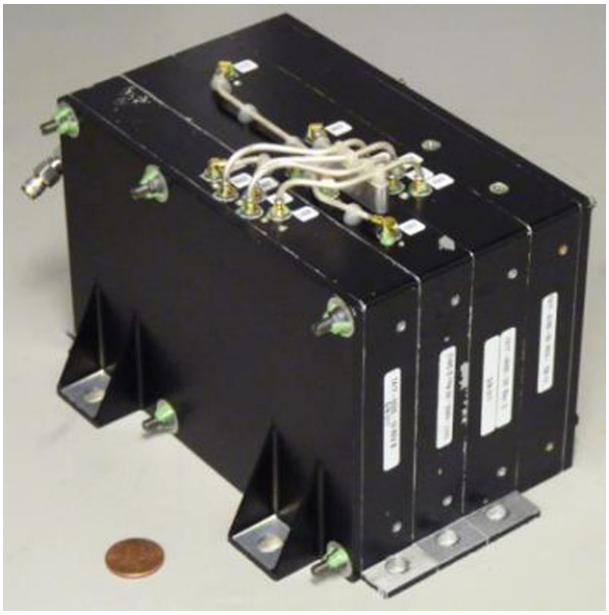

Fig. 26 The RBSP flight Frontier radio transceiver

the RF hardware for the uplink and downlink respectively. The DSP slice supplies the central control of the transceiver and enables the transceiver to function as a software-defined radio. This compact design provides state-of-the-art mass (1.8 kg) and power (<9 W full duplex) for the offered capability (Haskins and DeBoy 2007; Haskins et al. 2006, 2010; Haskins and Millard 2010; Crowne et al. 2011; Millard and Haskins 2011).

The RBSP XCVR includes special protections to mitigate the extreme radiation environment. There is 350-mil shielding around all the radio and SSPA electronics to minimize the total dose experienced by the internal electronic, electrical and electromechanical (EEE) components. Further, several risk reduction techniques are employed in the radio firmware to mitigate single-event upsets including register refreshing, error checking and correcting, device resetting, safe control circuit design, and watchdog timers. Further, system-level communication protocols such as Command Operations Protocol Number 1 (COP-1) and Consultative Committee for Space Data Systems (CCSDS) File Delivery Protocol (CFDP) are employed to optimize proper data transmission.

The various communications modes used in the communications system are described in Table 9. Uplink bit rates include 2,000 bps (nominal) and 125 bps (emergency). Since there is more than 20 dB margin at the nominal uplink bit rate, emergency communications to ground stations are not an issue assuming nominal ground station and observatory antenna performance. Downlink bit rates include 2,000, 1,000, 500, 250, and 125 kbps (science) and 1000 bps (emergency and space weather). Specific parameters are provided in Table 9.

Each RBSP observatory includes two S-band RF antennas: a forward (FWD) antenna, located on the top deck, and a back (AFT) antenna located on the bottom deck to provide coverage in both observatory hemispheres as shown in Fig. 27. There is a 40° gap in coverage around the observatory center caused by the interferometer pattern between the antennas. The FWD and AFT RF antennas are fixed, mounted at a radius of 9 in. (23 cm) from observatory spin axis, and they extend 10.15 in. (25.8 cm) above the separation interface plane. The antenna field of view (FOV) is 70° half angle. The two observatory antennas use different polarization which allows for tracking from a single ground station at the same time and simplifies ground operations; Observatory A uses right hand circular polarization (RHC) and Observatory B uses left hand circular polarization (LHC). The antennas are located off-center of the spacecraft, which allowed the two spacecraft to stack on top of each other for launch without mechanical clearance issues.

Figure 28 and Table 10 show how the supportable downlink bit rate changes as a function of range. Because the downlink data rate is continuously optimized to account for the widely changing range, only the fixed parameters are presented in Table 10. Three encoding modes are utilized: APL-18 (turbo encoding only), and USN-13 (turbo and convolutional encoding). The baseline plan is to use turbo encoding (rate $= 1/2$) for all science downlink passes to ground stations. The observatory supports rate $= 1/2$ convolutional encoding as a backup mode. There is no ranging requirement for RBSP. For all science modes (lowest rate of 125 kbps), a minimum downlink margin of 3 dB is required. Assuming similar ground station and observatory antenna performance, the margin for the emergency rate of 1 kbps is well above the 3-dB requirement to ground stations.

The RBSP observatories are navigated via processing of the RF Doppler data acquired during all ground contacts with the APL 18-m and the USN 13-m ground antennas. In all downlink modes, the observatory XCVR emits a coherent S-band downlink, the frequencies of which are recorded by the ground station Cortex receivers. The frequency measurement meets the required navigation accuracy of 5 mm/s over a 10-s integration period. This performance was ultimately verified during observatory-level thermal-vacuum compatibility testing with both the APL and USN ground networks.

6 Observatory Avionics

The avionics subsystem comprises the hardware command and data handling (C&DH) functions in a single spacecraft bus component, the Integrated Electronics Model (IEM). The

Table 9 RBSP mission communications mode presets

Preset state number	Uplink bit rate	Downlink							Description
		Downlink bit rate (bps)	NRZ-L Biphase	Conv $r = 1/2$ Turbo $r = 1/2$	PM, QPSK	I/Q calibration set	Coherency on/off	Exciter enabled	
0	–	–	–	–	–	–	–	–	Custom
1	125	1000	Bi-f	Conv	PM	1	On	Yes	Emergency power on default
2	125	N/A	N/A	N/A	N/A	N/A	N/A	No	Low power (Rx only)
3	125	1000	Bi-Φ	Conv	PM	3	N/A	Yes	Space weather
4	2000	125000	Bi-Φ	Conv	PM	1	On	Yes	Backup
5	2000	250000	Bi-Φ	Conv	PM	1	On	Yes	Backup
6	2000	500000	Bi-Φ	Conv	PM	1	On	Yes	Backup
7	2000	1000000	NRZ-L	Conv	PM	1	On	Yes	Backup
8	2000	2000000	NRZ-L	Conv	QPSK	2	On	Yes	Backup
9	2000	125000	Bi-Φ	Turbo	PM	1	On	Yes	Science
10	2000	250000	Bi-Φ	Turbo	PM	1	On	Yes	Science
11	2000	500000	Bi-Φ	Turbo	PM	1	On	Yes	Science
12	2000	1000000	NRZ-L	Turbo	PM	1	On	Yes	Science
13	2000	2000000	NRZ-L	Turbo	QPSK	2	On	Yes	Science
14	125	N/A	N/A	N/A	N/A	1	On	Yes	CW downlink

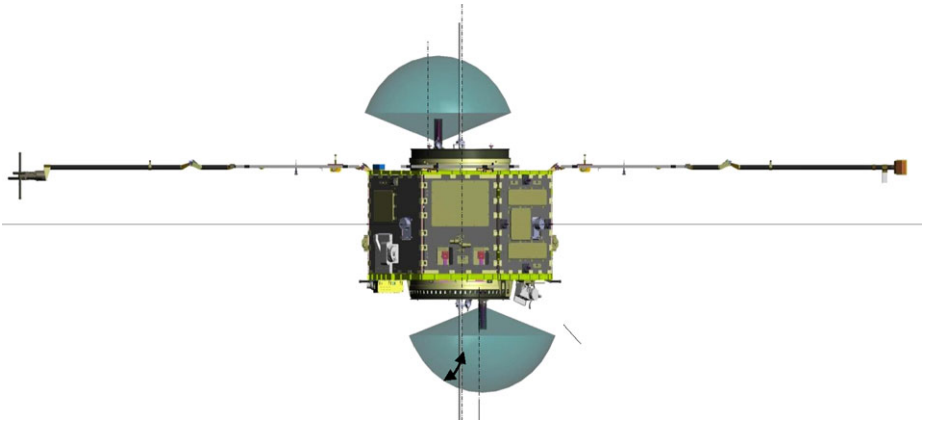

Fig. 27 Antenna field of view

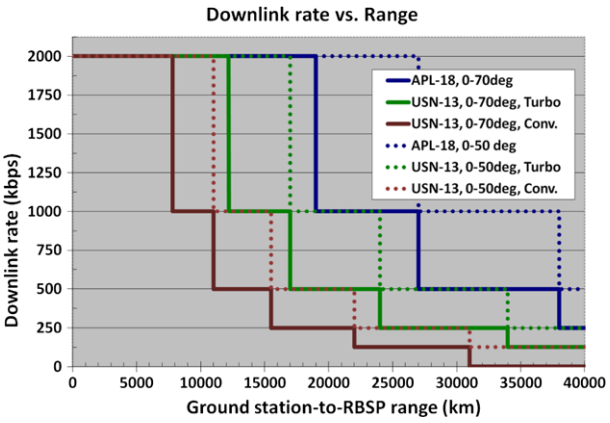

Fig. 28 Supportable science downlink rate vs. range assuming a 3-dB downlink margin. *Solid curves* represent the downlink rate with the specified antenna gain of −4 dBic over the entire field of view. *Dotted line* represents the enhanced downlink capability when the antennas are used from 0° to 50° from their boresights

Table 10 Maximum ranges for given downlink rate for each link condition

Bit rate (kbps)	APL		USN	
	0–50 deg (km)	50–70 deg (km)	0–50 deg (km)	50–70 deg (km)
2000	27000	19000	17000	12200
1000	apogee	27000	24000	17000
500	n/a	apogee	34000	24000
250	n/a	n/a	apogee	34000
125	n/a	n/a	n/a	apogee
1	apogee	apogee	apogee	apogee

IEM is a card cage design based upon the 6U Compact PCI (cPCI) form factor. The IEM chassis and external radiation shields encase the box electronics in aluminum at 500 mils (nominal) thickness. A detailed block diagram of the IEM and its external interfaces is shown in Fig. 29.

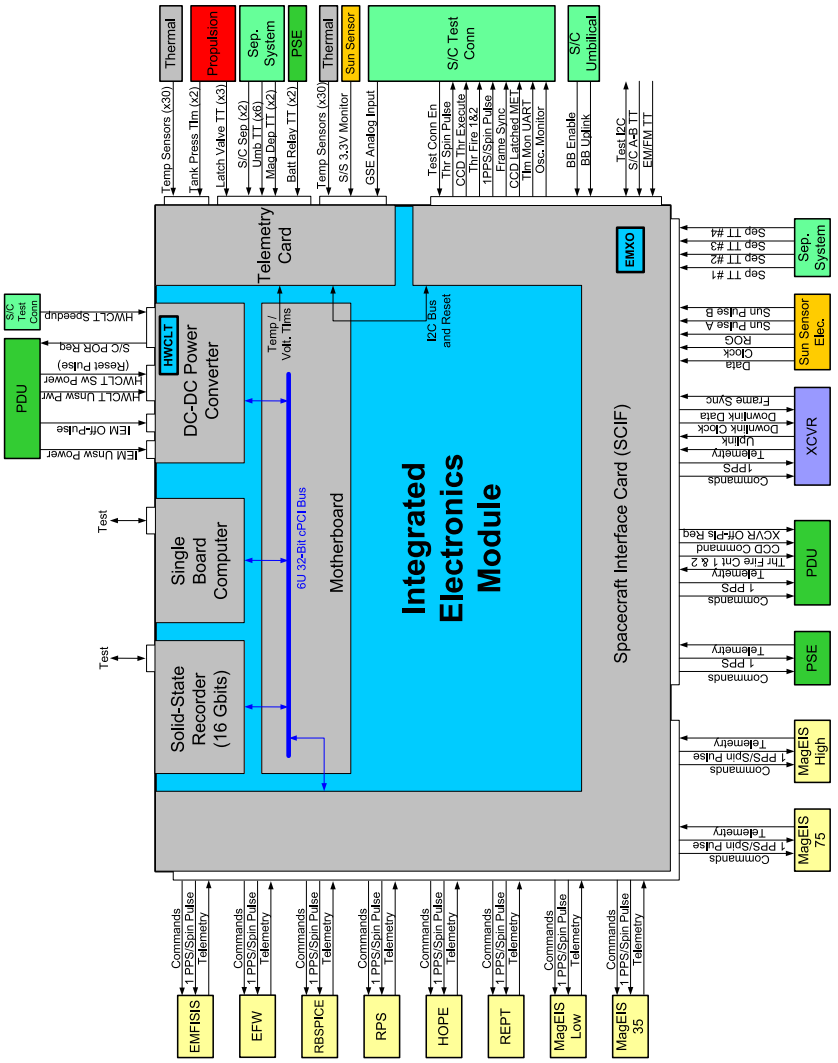

Fig. 29 Integrated electronics module (IEM) block diagram

The IEM consists of five cards connected across a common backplane. A 32-bit PCI bus, clocked at 16.5 MHz, connects the single board computer (SBC), solid-state recorder (SSR), spacecraft interface card (SCIF), DC-to-DC converter, and telemetry cards for flow of commands and telemetry. The SBC is a BAE RAD750-based design clocked at 33 MHz for 50 MIPS (nominal) with 16 MBytes of SRAM, 4 Mbytes of electrically erasable read-only memory (EEPROM) and 64 Kbytes of PROM. The SSR contains 16 Gbits of synchronous dynamic random access memory (SDRAM) with error detection and correction (EDAC) and hardware scrubbing. The selected SDRAM has a low upset rate (even in the RBSP environment); the few SDRAM errors that are expected will be corrected by SSR EDAC. The SCIF card contains a custom FPGA design that implements interface logic and thruster control. The board also houses the observatory precision oscillator, which is used for generation of mission elapsed time (MET). The DC–DC converter card provides regulated secondary voltages derived from the spacecraft primary power bus and implements the box off-pulse capability. The telemetry card gathers temperature, analog, and discrete data and is connected to the SCIF card via an internal I2C bus.

While the RAD750 is not expected to reset as a result of environmental effects, there have been cases where processors have reset due to unexpected uncorrectable errors. If no mitigation steps were taken, a processor reset could result in the loss of data stored on the SSR and a halt in the recording of science data. To prevent this, the fault management system includes autonomy rules that will preserve SSR contents and re-enable the recording of science data in the event of a processor reset.

The IEM handles both commands to each instrument and telemetry and science data flow from each instrument via 115.2 kbaud UART links. The UARTs are synchronized to the observatory timekeeping system via a one pulse-per-second (1 PPS) interface. Commands to the instruments and other spacecraft bus components are sent out via two sequenced transmission buffers with the delay from 1 PPS dependent upon the prior command buffer usage. The two groupings are PDU, PSE, XCVR, EMFISIS, EFW, RBSPICE and RPS; and HOPE, REPT, MAGEIS Low, MagEIS 35, MagEIS 75, MagEIS High and the spacecraft real-time telemetry monitor (telemetry output for ground use only). The peak instrument science and telemetry data rate is permitted up to the full 115.2 kbaud rate, effectively 83 kbps per instrument. The IEM is shown installed on the observatory in Fig. 30.

An electrically-isolated function within the IEM is the hardware command-loss timer (HWCLT) utilized as part of the fault management off-pulse architecture. This is a discrete, logic-based circuit that maintains a countdown between successive “reset” pulses from the ground. If the HWCLT is not “reset” by a specific command sent from the ground within 3.58 days, a logic pulse is sent to the PDU which initiates a PDU sequence to off-pulse the PDU and then off-pulse the IEM and XCVR. As with all off-pulse implementations, there are multiple levels of protection on this action including an inhibit feature within the PDU itself and two physical interfaces to each box being off-pulsed. The 3.58 day duration is set based upon other fault management mitigation events such as a software based command loss-timer and specific actions initiated through the ground.

7 Flight Software

The APL-developed custom RBSP command and data handling (C&DH) software consists of a set of functional applications and libraries that are designed to be used with the GSFC core Flight Executive software, which provides standard application services, and the VxWorks operating system, hosted by the RBSP observatory IEM single-board computer (Reid and Monaco 2012).

Fig. 30 IEM installed on Observatory A

The onboard RBSP flight software provides the following functionality: command uplink, spacecraft command management, autonomy rule processing, command macro management, spacecraft time-tag command management, SSR management, telemetry management, downlink management and managing the hardware interfaces to instrument and observatory hardware.

Telecommand code blocks are received at a data rate of 2 kbps during normal operations or at a rate of 125 bps for emergency operations. The C&DH software retrieves these code blocks from the SCIF over the PCI bus and reconstructs telecommand packets from the code blocks. Telecommand packets are distributed to the instruments via the SCIF hardware or to the C&DH command management software based on the telecommand packet's application identifier.

Observatory command packets that are received by the C&DH command management software are validated, prioritized, and sent for execution to the appropriate C&DH software application. Command sources are real-time commands, commands from a real-time command to execute a macro, commands that execute as a result of a time-tagged rule firing, and commands that execute as a result of an autonomy rule firing. Allowed priorities for spacecraft commands are 0 (highest) to 15 (lowest). One command can execute every 40 ms (25 Hz). The command that executes in a given cycle is the highest priority command awaiting execution. Commands execute chronologically within a particular priority level. Before a command is executed by the C&DH software, its parameters are validated.

The C&DH software manages the loading and memory management of command macros. Command macros are a sequence of stored commands that execute in response to a real-time command, the firing of an autonomy rule or the firing of a spacecraft time-tagged rule.

The C&DH autonomy rule engine manages loading and processing autonomy rules, computed telemetry equations, and storage variables. Autonomy rules are evaluated each second

and provide the ability to execute a command when a logical expression evaluates to "true" for "n of m" seconds. The logical expressions consist of operands and operators where the operands are either constants or entries in the data collection buffer (DCB). Similarly, computed telemetry equations are logical expressions that are evaluated once per second where the results of the evaluation (numeric or boolean values) are made available as inputs to autonomy rules (through the DCB). Finally, storage variables are a means of providing memory to the autonomy system.

The C&DH spacecraft time-tag command management software provides the ability to load, store, and evaluate time-tagged rules. Once per second, the MET associated with each rule is compared to the spacecraft MET; if the rule MET is greater than or equal to the spacecraft MET, the command associated with the rule is delivered to the C&DH command management software for execution. The C&DH subsystem provides storage for instrument time-tagged commands. As instrument commands are received by the C&DH subsystem, time-tagged instrument commands are recognized and stored in a buffer. Once per second the C&DH subsystem checks the instrument command buffer for commands ready to be sent to the instrument. At the appropriate time the CCSDS command packet is transferred to the instrument. The C&DH telemetry management software outputs all spacecraft telemetry in variable length CCSDS-formatted telemetry packets. These packets contain the MET of packet generation. The software provides modifiable tables that control the rates and prioritization of real-time spacecraft and instrument telemetry packets sent to the downlink software.

8 SSR Data Management

The RBSP observatory is capable of simultaneous data collection, recording, and playback/downlink, and includes a 16 Gbit SDRAM data recorder. The SSR is designed to retain data during a non-power-cycling (i.e., soft) reset. Flight software SSR management functions are designed to automate data collection and storage and to minimize operations complexity for configuring the system to control the downlink of stored science and engineering data.

The flight software uses a file system to store data on the SSR. Each instrument and spacecraft component has been assigned an onboard data storage allocation. Because instruments for the most part produce data at a continuous data rate (despite some variation based on orbit position or radiation belt activity), each instrument is given an SSR data volume allocation corresponding to the amount of data produced per day based on the daily average bit rate. An exception is the burst data produced by the EMFISIS instrument when a significant radiation belt event is detected. While the concept of operations is to downlink 24 hours of science survey data each day, burst data is instead stored in a 3.5 Gb buffer that is downlinked at a lower priority than other science data over the course of up to 7 days. Data allocations are given in Table 11.

Under nominal operations, 24 hours of stored science data are downlinked every day. However the SSR is sized to provide the capability to store observatory housekeeping data for the number of days equivalent to the time-out duration of the HWCLT heartbeat monitor, which provides a time-out period of 3.58 days. Similarly, the SSR allocations for instrument data are sized to store data for 2.5 days to preserve science and housekeeping data until ground contact is successfully reestablished. This meets the requirement to provide instrument data storage sufficient to account for at least 1 day of missed ground contacts.

All instruments and spacecraft components natively produce science and housekeeping data in the form of CCSDS packets. The C&DH flight software collects the packets and

Table 11 Observatory data allocations

	Instrument	Daily average data rate (kbps)	Average daily data volume (Gb)
Instrument data	ECT	20.4	1.763
	EFW	12.0	1.037
	RPS	2.0	0.173
	RB-SPICE	5.4	0.467
	EMFISIs waves survey	6.7	0.579
	EMFISIS mag survey	2.3	0.199
	EMFISIS burst (downlink allocation)	23.2	2.004
	Spacecraft housekeeping	4.4	0.380
	Total	75.5	6.61

routes them into files on the SSR that are stored in one of three directories which in turn represent downlink priority. Uploadable tables and parameters configure the flight software to specify which packets are stored in each file, the directory it is to be stored in, the maximum size for each file type, and the maximum data volume allowed for each source. This allows for completely automated onboard data collection and storage. For normal operations, flight software also automatically creates the file names, incorporating observatory time into the name as well. As the software routes packets into a file, it monitors the file size and closes it when the maximum size is reached, then automatically opens a new file of that type to continue storing packets without interruption. Flight software limits the maximum SSR data volume for each source by monitoring the total current volume for all stored files (science + housekeeping). If a data source reaches its maximum quota, flight software will delete the oldest stored file from that source upon opening a new one. Reported in status telemetry provided to each instrument is the current percent utilization of its SSR data volume quota. Thus, if so desired, an instrument can be configured to cease producing packets when the data quota limit is reached, thereby allowing for a "stop when full" behavior rather than having old data get discarded and overwritten.

Flight software provides additional automation to simplify downlink operations, in the form of an SSR playback manager. Upon the start of a ground contact, stored commands enable the playback manager. This software scans the directories on the SSR and automatically selects for downlink the oldest file in the highest priority directory, moving onto the next file in priority order as required to keep the downlink bandwidth fully utilized. The three directories containing files to be downlinked represent, in priority order: (1) spacecraft housekeeping, events and history, instrument housekeeping, and EMFISIS MAG data; (2) survey science data from all instruments; and (3) EMFISIS burst data. Once a file has been successfully downlinked, it is automatically deleted to recover SSR space.

To minimize data loss or the need to retransmit data lost due to RF dropouts, the flight software utilizes the CCSDS File Delivery Protocol (CFDP) during the downlink of files from the SSR. This protocol provides an "FTP in space" capability and is managed by CFDP client software resident in both the flight software and the ground system software. Flight software packs SSR file data into protocol data units which in turn are placed into CCSDS frames for transmission to the ground system via the spacecraft downlink hardware. A virtual channel identifier indicates to the ground that the received frames contain SSR file data. CFDP client software in the ground system recognizes if any protocol data units

have been lost during downlink, and in turn automatically generates control directives on the uplink that are received by the flight CFDP client. The flight software then retransmits only the missing protocol data units. This two-way handshaking between flight and ground software is automatic within the CFDP clients, and apart from the ACK/NAK of protocol data units, also provides an indication of when the downlink of a file is finished and it is fully intact. Flight software then deletes the source SSR file. The flight software supports the downlink of telemetry frames at nominal rates of up to 2,000,000 bps. If the Mission Operations Center (MOC) is using a ground station with insufficient bandwidth to support two-way handshaking on the ground links, CFDP can be configured to downlink files in a best-effort mode. In either event, the ground system receives data files in the exact native format used when they were stored on the spacecraft SSR. Thus a simple Level-0 ground software processing step readily prepares files with packets sorted in time order. The files are placed on a server in the MOC and made available to each of the instrument Science Operations Centers.

9 Observatory Time Management

The RBSP timekeeping system provides knowledge of the correlation between time onboard the observatory and time on the ground. Central to this task is the principle of providing an onboard time reference to which the times of all other events on the observatories are referred, including the times of observations by the science instruments. Since the two RBSP observatories do not communicate with each other in any way, there is a separate timekeeping system associated with each observatory. The two observatory timekeeping systems are identical except for behavioral parameters such as clock drift rate.

Time is represented onboard the RBSP observatory using a composite hardware counter called mission elapsed time (MET). This is the standard term that has been used on many APL missions such as MESSENGER, New Horizons, STEREO, Solar Probe Plus, and NEAR. Non-APL missions often use other terminology to refer to this function, such as the SOHO on board time (OBT). Other terms in common use include spacecraft clock (SCLK). However, RBSP and other APL missions use the term “spacecraft clock” to refer to the time that is supplied by the C&DH subsystem to the science instruments. The RBSP MET composite counter consists of two parts. One part, called iMET or IMET, represents the integer number of seconds since the start epoch of midnight (00:00:00 UTC) on January 1st, 2010. The second part, called vMET or VMET, represents sub-seconds in units of clock “ticks,” each such tick lasting 1/50,000th of an IMET second, or about 20 ms. This tick interval is an ad hoc APL standard being used on New Horizons and Solar Probe Plus, as well as on RBSP, so that the same software algorithms can be used from mission to mission.

The RBSP avionics subsystem provides IMET or “spacecraft clock” to each of the science instruments. From the point of view of the instrument teams, however, the terms spacecraft clock and MET are interchangeable, even though the MET that the instruments “see” is really IMET. The VMET value is used on the ground by Mission Operations in the process of correlating onboard time to Earth time, but VMET is not seen or employed by any of the instrument teams. When $\mathrm{VMET} = 0$, the IMET value represents the time of the onboard time reference. In other words, IMET is a label for the time of the time reference, which can be correlated on the ground to Earth time. The onboard time reference for RBSP is the time of the trailing edge of a 1-Hz signal called the one-pulse-per-second signal (1 PPS).

The observatory onboard timing system is maintained through the distribution of a 1-PPS timing signal from the observatory avionics to observatory components and to instru-

Table 12 RBSP post-processing absolute time knowledge accuracy requirements

Instrument	Post-processing accuracy (3σ) compared to UTC
EMFISIS	±50 ms
EFW	±50 ms
RBSPICE	±50 ms
ECT—MagEIS	±100 ms
ECT—HOPE	±100 ms
ECT—REPT	±100 ms

ments with a timing uncertainty within ±30 ms (3σ) to support the observatory-level timing accuracy requirements which define how well the time of a science observation (i.e., the instrument data time tag) or ancillary observatory data can be correlated to UTC after post-processing.

9.1 Time Accuracy Requirements

A primary need for science is to be able to correlate observations of an instrument on one observatory with observations of the same instrument on the other observatory and this is met by imposing requirements on each observatory to correlate the times of science observations to Earth time. These requirements are referred to as "absolute" time requirements and expressed as the allowed 3σ deviation from "true" UTC of the post-processing correlation between the spacecraft clock and UTC. In other words, the science observation time stamp that is based on the spacecraft clock is converted to an estimate of UTC, and that estimate must differ from true UTC by no more than the specified absolute time accuracy requirement. Table 12 lists the requirements on each of the science instruments. The RPS instrument is not listed because no absolute time requirement has been imposed on RPS.

Relativity does affect the time accuracy but to a negligible extent (a few microseconds) for RBSP. The science observations are taken in the frame of reference of the observatory but UTC is defined in a frame of reference on the Earth. In addition to the requirements of Table 12, the relative timing between instruments on the same observatory is of interest. The post-processing 3σ error in the MET-based time stamps of each instrument relative to the EMFISIS flux gate magnetometer time stamp is specified. Table 13 lists these requirements.

Finally, the accuracy of the prediction of when each instrument command will be executed is specified as absolute accuracy of the time of execution of each command relative to UTC. The requirement is that command execution times shall be predictable 1 month in advance with an accuracy of ±5 s 3σ for all instrument and observatory time-tagged commands.

9.2 Implementation

Each observatory provides a 48-bit MET, latched at a known time in a transmitted frame that has an accuracy of ±70 ms 3σ relative to the 1 PPS and is placed in the frame secondary header. This accuracy includes uncertainties due to the frame pulse from the transceiver, the IEM hardware that latches the (downlink frame) MET, and the error contributed by software computation of some MET values. This supports the absolute mission-level measurement time knowledge accuracy that is needed to support the science measurements. The generation of MET and 1-PPS signals is undisturbed by processor resets. This helps to ensure that

Table 13 RBSP post-processing relative time knowledge accuracy requirements

Instrument	Post-processing accuracy (3σ) relative to EMFISIS MAG
EFW	5 ms
RBSPICE	8 ms
RPS	100 ms goal
ECT—MagEIS	10 ms
ECT—HOPE	10 ms
ECT—REPT	10 ms

timekeeping requirements continue to be satisfied even if the IEM processor resets due to environmental or other effects.

The absolute time accuracy requirements are addressed by providing to the science teams and other users of time information two products (for each observatory) that relate the spacecraft clock to Earth time and that also provide other information relevant to that correlation. These products are generated routinely by Mission Operations and are called the Operations SCLK Kernel and the Time History File. The relative time knowledge requirements of Table 13 are addressed by limiting the time uncertainty contributed by each instrument itself to its MET-based time stamp. For example, the 5-ms EMFISIS/EFW relative time requirement is addressed by limiting the uncertainty contributed by each instrument to 1 ms which, together with a small allowance for the uncertainty in distribution of time from the C&DH to the instruments plus an allowance for margin, adds up to less than 5 ms.

The RBSP observatory is designed to achieve absolute time accuracy of ± 50 ms for post-processing time accuracy to support the EMFISIS, EFW, and RBSPICE science instruments. This is satisfied with the use of a low-mass onboard clock oscillator. The evacuated miniature crystal oscillator (EMXO) used for this mission exhibits ± 50 parts per billion (ppb) frequency–temperature stability over the full range of oscillator temperature.

An IEM off-pulse or power cycle results in the value in the MET counter being reset to zero. Once the cause of the problem is evaluated on the ground, the MET counter is restored to its original timeline by ground command. To aid in analysis of the problem and also to ensure that data generated after the off-pulse are not confused with data from earlier in the mission, the MET is set on the launch pad to a very large value. Specifically, MET is set to the number of seconds since 00:00:00 UTC on January 1, 2010.

Note that the same Operations SCLK Kernel is used before the off-pulse event and after the MET counter is restored to the original timeline. That SCLK Kernel cannot be used to examine data that occurred between those two events. The plan is to place post-off-pulse packets that contain low values of MET into a separate telemetry archive associated with that specific off-pulse event. Access to that data will require a manually generated Off-pulse SCLK Kernel unique to that off-pulse archive. It is expected that the off-pulse archive will not contain data from the science instruments.

As shown in Fig. 31, time from the observatory, together with information provided by the receiving ground station and with the predictive ephemeris provided by the navigation team, is used by Mission Operations to determine the correlation between the spacecraft clock and Earth time and to provide that and related information in the Operations SCLK Kernel and in the Time History File.

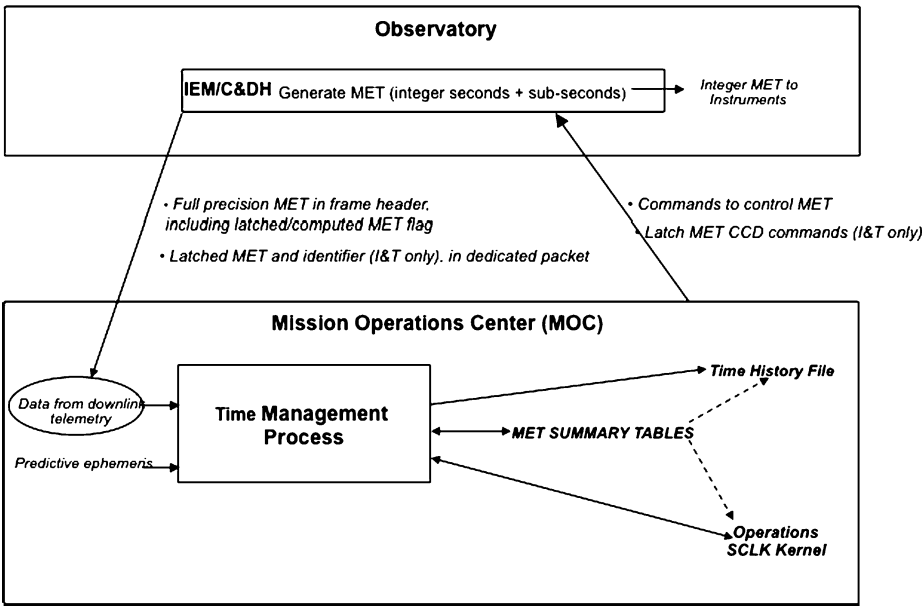

Fig. 31 Framework of the RBSP timekeeping system

9.3 The Operations SCLK Kernel

The RBSP ground system uses a set of navigation-related software developed by the Jet Propulsion Laboratory Navigation and Ancillary Information Facility (NAIF) called SPICE. SPICE provides tools for a variety of applications, including time conversions. Operation of SPICE depends on a collection of parameter files called kernels. One such kernel is the SCLK kernel, a text file containing a table that provides correlations between observatory time (IMET in our case) and Earth time. UTC is not used in SCLK kernels because of the discontinuities introduced by leap seconds. Instead, SPICE offers a choice between two continuous time systems. For RBSP, the continuous time system Terrestrial Dynamical Time (TDT or TT) is used; a TDT second is the same as a UTC second.

The particular flavor of SPICE SCLK kernel used for RBSP is called an Operations SCLK Kernel, with the following structure. Whenever the Operations SCLK Kernel is updated by Mission Operations to provide the most recent correlation between IMET and TDT, that correlation information is added to the end of the table in the kernel as a new time record. The new time record consists of three components: (1) an encoded SCLK that represents MET, (2) a corresponding TDT and (3) a predicted rate of change of the clock that we call "predicted TDTRATE," the predicted rate of change of TDT for a unit change in MET. Another way of looking at TDTRATE is that it represents how long in TDT or UTC seconds a MET second lasts.

The predicted TDTRATE can be used by Mission Operations or by the instrument teams to determine the MET needed in a time-tagged command to cause that command to execute at specified future UTC. Mission Operations uses UTC exclusively for specifying command execution times. When another time record is added to the Operations SCLK Kernel, the TDTRATE of the previous kernel is recomputed to provide a more accurate estimate of the actual rate of change of TDT that has occurred for a unit change in MET, referred to

as "interpolated TDTRATE." To satisfy the post-processing absolute time requirements of Table 12, the interpolated TDTRATE should be used. In other words, when mapping the time stamp of a science observation to TDT, that mapping may not be sufficiently accurate if the predicted TDTRATE is used because that prediction does not fully account for the actual observed past behavior of the clock. The use of interpolated TDTRATE is what distinguishes the APL Operations SCLK Kernel from the standard SPICE SCLK kernel.

For each time record added to the Operations SCLK Kernel, a corresponding record (line) is added to the Time History File that contains information relevant to the SCLK Kernel time record and metrics related to that. For RBSP, those fields include

- Encoded SCLK
- The corresponding IMET
- TDT(G), the ground estimate of the TDT that corresponds to IMET
- The predicted TDTRATE, in TDT seconds per MET second
- The rate of drift of MET, in milliseconds per day
- A temperature related to EMXO temperature
- The method used to compute predicted TDTRATE
- The interval of data used to compute predicted TDTRATE
- The estimated error in the Operations SCLK Kernel correlation since the previous time record was added
- The average error in milliseconds per day since the previous time record was added
- The number of days since the previous time record was added
- The identification of the ground station that received the data used to update the Operations SCLK Kernel
- The computed one-way-light-time from the observatory to the receiving ground station
- The SCLK Kernel partition (should always be 1 for this mission)
- The presumed RF downlink encoding method (turbo or convolutional coding)
- The estimated downlink bit rate
- The observatory identification (A or B)

9.4 Concept of Operations

Maintenance of the Operations SCLK Kernel and of the Time History File is accomplished in the MOC by running custom timekeeping system ground software, called tk_automation, nominally once a day. Up to 4 days of downlink contacts can be missed without compromising the accuracy of the MET–UTC correlations provided by the Operations SCLK Kernel.

Data used for tk_automation will be taken only from downlinks received at the APL Satellite Communications Facility (SCF) and at the NASA Near Earth Network (NEN) USN ground stations in Hawaii and Dongara, Australia. All downlink data used for tk_automation will be turbo coded data at the operational downlink bit rates 125, 250, 500, 1000 and 2000 kilobits per second (kbps). In an extreme emergency, data at the emergency 1 kbps downlink rate can be used by tk_automation but with possibly reduced accuracy. Figure 32 illustrates the flow of data used by the MOC to support timekeeping.

10 Guidance and Control

The RBSP guidance and control (G&C) subsystem is responsible for determining the attitude of each observatory and performing propulsive maneuvers to maintain each observatory in an attitude, spin rate, and orbit consistent with the mission's objectives. The two RBSP

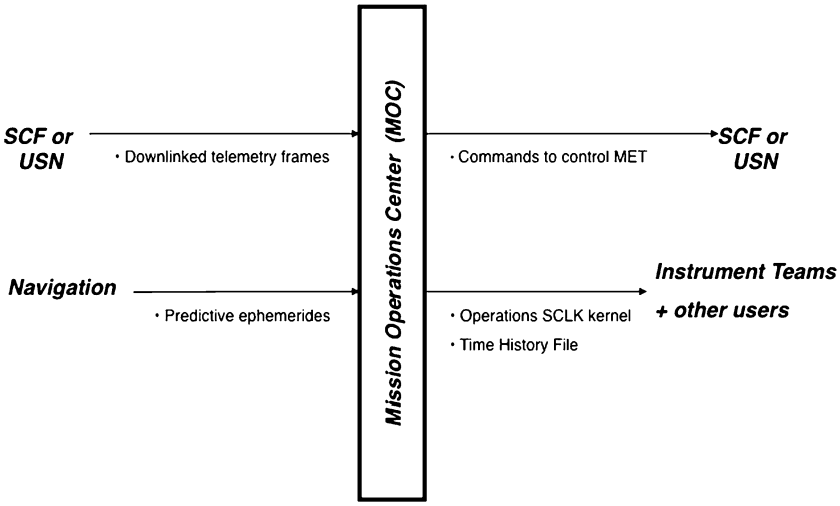

Fig. 32 Mission Operations Center (MOC) external timekeeping interfaces

observatories are major-axis spinners with no onboard software to estimate or control their attitude or orbits. Each observatory carries a blowdown monopropellant propulsion system with eight 0.9-N thrusters used to change attitude, spin rate, or orbit. These adjustment maneuvers will be designed and commanded from the ground. Onboard G&C flight software is limited to processing Sun sensor data and relaying this information to the instruments via a spin pulse or via the 1-Hz time and status message. Attitude prediction and determination are also performed using ground software tools.

10.1 Flight Sensors

The G&C sensors consist of a Sun sensor assembly and the Electric and EMFISIS fluxgate magnetometer. The Sun sensors, purchased from Adcole Corp., consist of two Sun sensor heads (SSH) spaced 180° apart from each other about the spin axis, and a single Sun sensor electronics box (SSE). The SSH boresights are oriented such that the active fields of view do not overlap and cover an area roughly 2° to approximately 85° from the spin axis. Each head, when not in eclipse, will produce a Sun pulse, head ID, and Sun offset angle. The angular resolution of the Sun sensor assembly is 0.125°, and provides accurate Sun pulse and aspect angle data only when the observatory is spinning positively about its $+Z$ axis. The assembly has been tested to operate between 3 to 15 rpm. The Sun sensor data are used by flight software to provide a spin pulse, observatory spin rate, phase angle, and Sun offset angle to onboard instruments and to autonomy when the observatory is not in eclipse. The data are also used in the timing for some of the open-loop propulsive maneuvers and are downlinked to the ground for attitude determination.

The EMFISIS fluxgate magnetometer data are also downlinked to ground for input to software that combines the magnetic field readings with Sun sensor data to produce an estimated observatory attitude. There are three different formats of fluxgate magnetometer data (compressed, uncompressed, and 1-Hz failsafe) from the EMFISIS instrument. There is also one pass-through format from the EFW instrument that can be downlinked in the event the digital section of the EMFISIS main electronics box fails.

10.2 Flight Actuators

Each type of propulsive maneuver will use a pair of the eight 0.9-N thrusters on the observatory. The length of the pulses for each maneuver will be chosen to minimize the amount of nutation and spin plane boom deflection during and after the maneuvers. The maneuvers will be used to maintain the spin axis to within 3.1° 3σ and the spin rate to within ± 0.25 rpm of their desired values. They will also adjust the orbit of the observatory as requested. The ΔV activities only use the pro-Sun and anti-Sun thrusters and are continuous, non-pulsed maneuvers. There is no plan to execute ΔV maneuvers in all inertial directions.

Thruster commands are decoded and executed directly by IEM hardware. The fault management system uses autonomy rules (executed in the IEM processor) to detect several unexpected conditions (such as a spin rate violation, maneuver in eclipse, and Sun angle violation) due to a maneuver error resulting from a command with incorrect timing, FPGA upset, or other causes. If one of these unexpected conditions is detected an autonomy rule will abort the maneuver so that mission operations can resolve the issue.

In addition, each observatory contains two ring nutation damper units, with the plane of the ring position normal to the X and Y axes of the spacecraft. These dampers are metal tubes fully filled with a silicon oil fluid and are located inside the spacecraft structure. They were designed at APL and are as large as feasible within the geometrical constraints of the observatory. They are intended to damp out the core spacecraft nutation oscillatory mode that is introduced after an observatory propulsive maneuver and after separation from the launch vehicle.

10.3 G&C Flight Software

For RBSP the traditional G&C functions are implemented as ground software tools and procedures. G&C flight software is limited to sampling Sun sensor data and providing spin pulses and spin period, rate, phase angle, and Sun offset angle information to the instruments and autonomy. The spin rate data are passed through a low-pass filter, and there are also several validity flags which indicate if the data are valid for use. The software also allows operators or autonomy to set eclipse flags, indicating if it is producing the spin pulse by receiving valid pulses from the Sun sensor assembly, or if the spin pulse is being driven by a hardware timer which used the last valid Sun pulse and derived spin rate to set the spin period.

Spin Pulse Accuracy The requirement of the Sun sensor assembly is to provide a Sun pulse to an accuracy of within $\pm 0.25/\cos(\alpha)$ degrees, where α is defined by the vendor as the Sun vector relative to the perpendicular to the spin axis. For this reason the pulse angle accuracy will change as a function of Sun offset angle. The actual accuracy varies from SSH-to-SSH. The timing accuracy of the pulse is then dependent not only on the Sun offset angle, but also any misalignments of the sensor heads, spin rate of the observatory, and timing delays between the SSH, SSE, and the IEM. Accuracy is not a function of altitude above the Earth. Table 14 presents an example of the variability in timing accuracy.

The orbit defined for the RBSP mission will cause each observatory to periodically go into eclipse. During these times the spin pulse will be driven by a 20-µs-resolution hardware spin timer. When commanded, the flight software will initialize the hardware timer using a Sun pulse combined with the most recently computed spin rate. Because there is uncertainty in the spin rate, the accuracy of the hardware spin pulse timing will degrade as a function of time in eclipse mode.

Table 14 Example Sun pulse timing accuracy assuming no misalignments, timing delays, and $\pm 0.25/\cos(\alpha)$ degree Sun pulse accuracy per SSH. Actual performance will vary

Spin rate (RPM)	Sun offset angle (degrees)	Spin pulse accuracy (ms)
3	15	53.7
5	15	32.2
15	15	10.7
3	27	30.6
5	27	18.4
15	27	6.1

10.4 Ground Software

The ground software tools include the Maneuver Design Suite, the Attitude Determination Software, and the Attitude Prediction Software. Each of these tools will be run either automatically or by G&C team members and the results will be provided to the mission operations or science teams. The Maneuver Design Suite software is a set of computer software components (CSCs) which (in conjunction with the high-fidelity simulator) take information on the desired maneuver target (change to spin axis direction, rate, or velocity), the current observatory state, selection of thrusters, and firing profile to produce commands needed to execute the maneuver. The Attitude Determination Software CSCs use the Sun sensor and EMFISIS fluxgate magnetometer data to generate estimates of observatory attitude. The Attitude Prediction Software CSCs will produce a nominally 42-day predicted attitude using the current observatory attitude, future maneuver schedules, and observatory configuration information. Both the attitude history and predicted attitude will be provided to the engineering and science teams in the form of SPICE C-kernel files.

Attitude Knowledge Uncertainty The requirement of the attitude determination ground software is to ensure that the attitude knowledge uncertainty for each observatory coordinate frame relative to the inertial frame is $\leq 3^\circ$ 3σ per axis. This assumes that EMFISIS in-flight calibration activities have been conducted and that attitude knowledge is not guaranteed at times when magnetometer data are not available or for daily solutions during severe magnetic storms. When a storm does occur the quality of the solution will degrade as a direct effect of the measured magnetic field deviating from the reference magnetic field model. Methods were implemented in the software to use data before and after a storm to bound the attitude excursions, and possibly use a "snap shot" attitude solution at or very near perigee and then use Sun sensor spin pulse and spin rate information to propagate the attitude over the higher altitudes.

Ground Software-Generated Maneuvers The Maneuver Design Suite software can generate three types of maneuvers: spin axis adjustments, spin rate adjustments, and orbit adjustments. For these different maneuvers the IEM is commanded via the ground with parameters that determine how the PDU will fire each thruster. The thruster control parameters indicate if the maneuver will use the Sun sensor pulses or the hardware timer, which Sun sensor head should be used, which thrusters should be used, and information that determines the on and off times of each thruster set. When the parameters are loaded and locked into the IEM a separate "start burn" command is sent to the IEM CCD to start the maneuver. Both ground software and autonomy do have the ability to terminate thruster firings using the normal thruster fire interface or via CCD command.

11 Propulsion

The RBSP propulsion subsystem is a blowdown monopropellant hydrazine system that provides precession capability, spin rate adjustments, and ΔV for each observatory (Bushman 2012). The system consists of eight 0.9-N (0.2 lbf) Aerojet MR-103G thrusters and components required to control the flow of propellant and monitor system health and performance. The propellant and pressurant are stored in the three identical tanks, without diaphragms, which are spaced equally around the observatory spin axes. The spinning of the observatory positions the propellant over the outlets at the spherical tanks' midplanes. As propellant is expelled, the pressure of the pressurant decreases; therefore the thrust and specific impulse of the thrusters decrease as the mission progresses. All valves possess heaters to maintain temperatures above 5 °C to protect the soft seals. The propulsion system schematic is shown in Fig. 33.

The baseline usable propellant load for RBSP is 56 kg of hydrazine per observatory (see Table 15). For a launched wet mass of 665 kg, this translates to 183.4 m/s of ΔV. The propellant tanks are 25.6 liter (1560 in^3) Inconel 718 tanks manufactured by ARDÉ. These 18.4 cm (7.25 in.) ID, vacuum-rated spherical tanks contain cruciform vortex suppressors, which aid in propellant expulsion at the outlet. The tanks have flight heritage on the THEMIS observatory. The maximum expected operating pressure and temperature for the RBSP mission is 400 psi at 50 °C.

The thrusters on the RBSP observatory are of the catalytic monopropellant hydrazine type. When the dual-seat thruster valves are opened, propellant flows through the capillary tube into a catalyst bed, where the hydrazine spontaneously decomposes into hot gases, which then expand through a nozzle and exit the thruster, producing thrust. The MR-103G has substantial flight heritage including Iridium and Lockheed Martin A2100 spacecraft. The actual steady-state thrust produced on RBSP will vary from 0.97 N at beginning of life (BOL) to 0.25 N at end of life (EOL) as the tank pressure decreases. The specific impulse will range from 222.3 s at BOL to 205.7 s at EOL. The thrusters also possess redundant catalyst bed heaters. The remaining subsystem components—latch valve, filter, orifice, and pressure and temperature transducers—have substantial heritage. The propulsion diode boxes (PDBs), required to mitigate back-EMF (Electromotive Force) from valve closings, were designed by APL/Aerojet and built by Aerojet. They contain suppression and blocking diodes as well as test interfaces to support ground operations. The pressure transducer power conditioner (PTPC) slows the inrush current to the pressure transducers to ensure they operate properly during the RBSP mission.

12 Mechanical

The two observatories are nearly identical. In addition to differences such as spacecraft ID, RF operating spectrum allocations, and umbilical connections, the major difference is the accommodation of the separation systems. Observatory B has the hardware required for separation of the top Observatory A (from Observatory B) and the bottom Observatory B from the launch vehicle. All separation is controlled by the launch vehicle. Specifically Observatory B, at its forward end, houses the intra-spacecraft separation system for Observatory A and the pyros to initiate separation of Observatory A. At its aft end, it supports the top of the launch vehicle interface and the separation switches to indicate Observatory B separation from the launch vehicle. Observatory B also provides the telemetry interfaces to the launch vehicle for Observatory A separation from Observatory B.

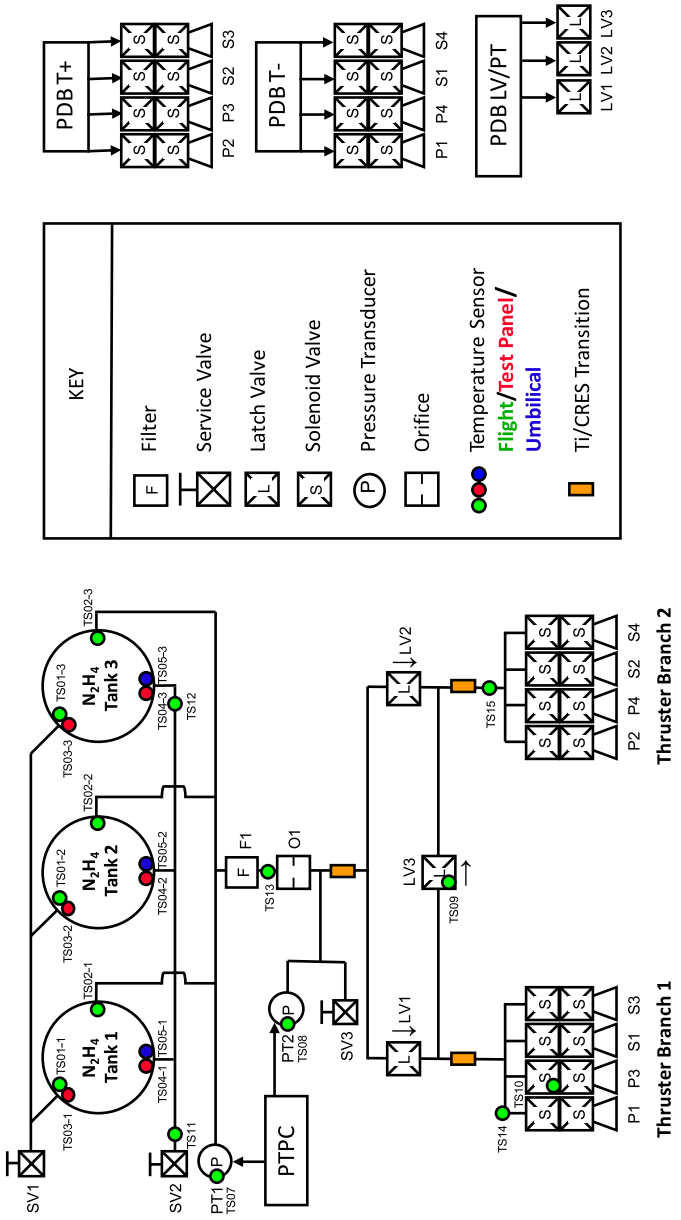

Fig. 33 Propulsion system schematic

Table 15 Propellant budget

Propellant budget	ΔV	Propellant
Mission—Phasing/Collision Avoidance	2.4 m/s	0.8 kg
G&C—Precession		13.3 kg
G&C—Spinup/Spindown		0.3 kg
Mission—Deorbit	59.6 m/s	18.3 kg
Additional N2H4 to fill tanks		23.3 kg
Residual propellant		0.5 kg
Total propellant mass		56.5 kg
Total GN2 pressurant mass		0.5 kg

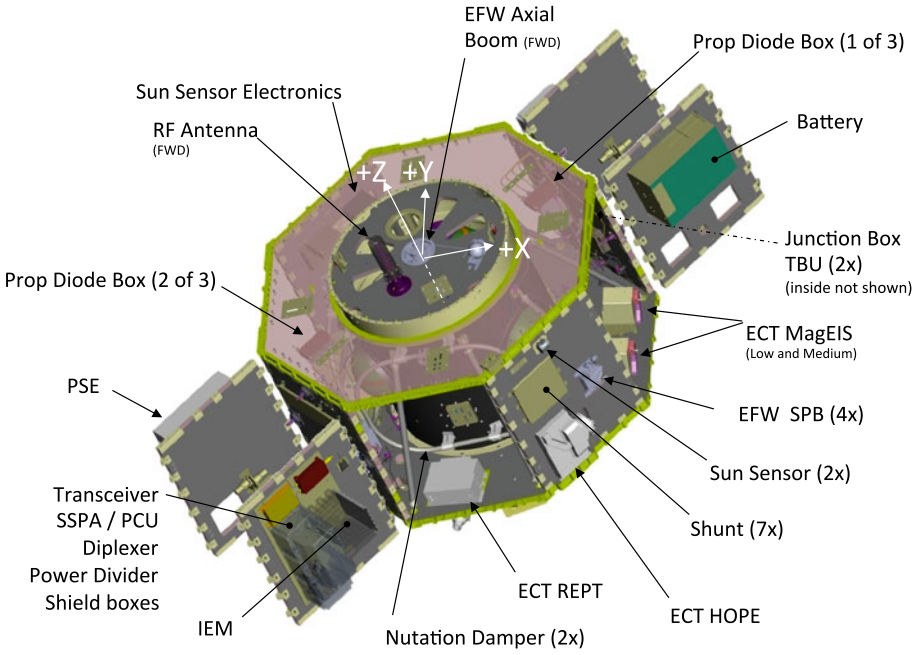

Fig. 34 RBSP observatory layout with side panels in a non-flight "open" orientation

The observatory mechanical design and configuration were selected to optimize for ease of access as well as to meet the launch vehicle loads and to fit both observatories stacked into a 4-m launch vehicle fairing. A single RBSP observatory with panels open is depicted in Fig. 34, which shows the placement of spacecraft electronics, instrument sensors, and instrument electronics boxes. The layout and packaging of these components provides the required fields of view for the instrument sensors and takes into account thermal needs as well as protection against radiation. The RBSP mission includes the first APL observatory to be completely tested at the APL environmental test facility, so care was taken to ensure each observatory would fit into the APL thermal vacuum chambers. The detailed observatory layout is shown in Figs. 35 and 36.

The mechanical subsystem includes primary and secondary structure (central cylinder and structural panels), mechanisms, deployables, and a separation system. The primary

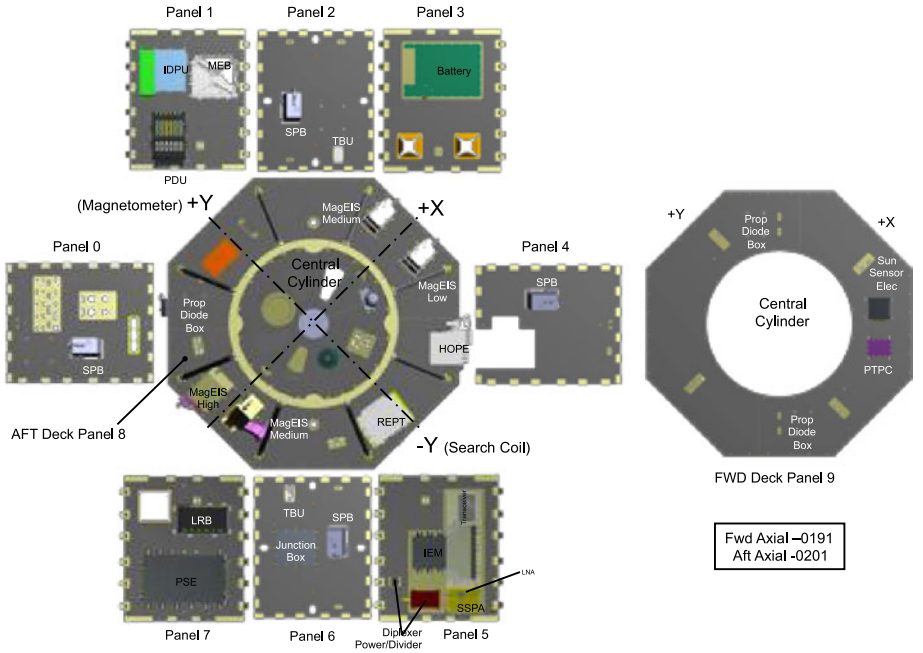

Fig. 35 Observatory component layout (forward looking aft)

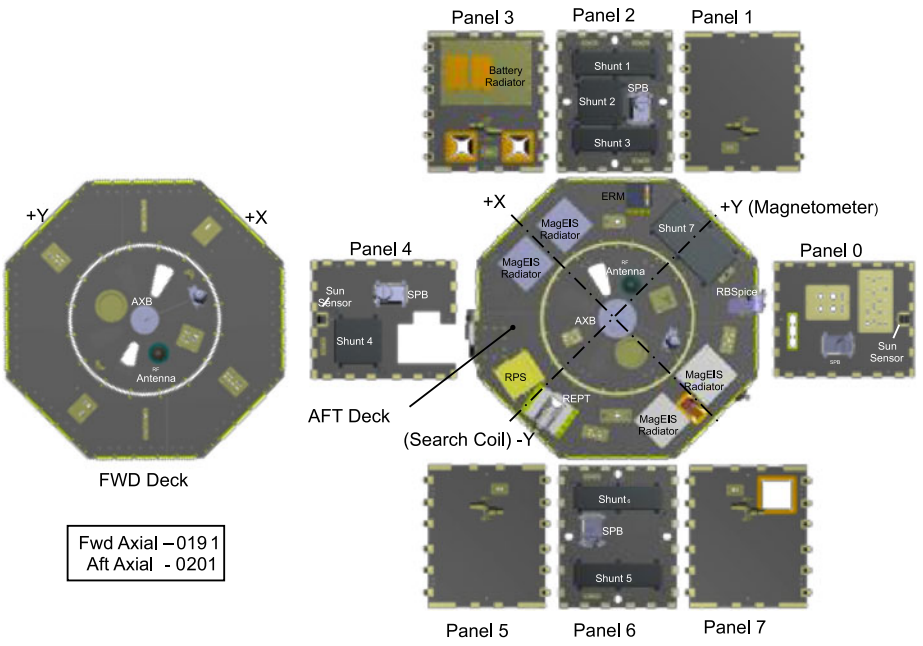

Fig. 36 Observatory component layout (aft looking forward)

Fig. 37 RBSP observatory stacked in launch configuration for system test (Photo: Lee Hobson, JHU/APL)

structure is an aluminum-forged cylinder and the panels and decks are honeycomb with aluminum face sheet. The mechanical design incorporates the use of hinged panels to provide easy access for installation and integration of observatory components. The observatory is shown in stacked configuration in Fig. 37 in preparation for observatory vibration testing.

Each observatory was designed to provide an offset of the maximum principal axis relative to the geometric $+Z$ axis of less than 0.5° (3σ, single axis) which provides a highly stable spinning platform. Nutation dampers are included to passively control nutation growth to maintain the offset of the observatory instantaneous angular velocity vector from the observatory $+Z$ body axis at $<0.5^\circ$ during the operational phase of the mission. Observatory mass properties and spin balance testing were performed as part of the test program to verify that there will be less than 1° error of spin axis relative to the observatory frame. The observatory test configuration for spin balance and moment of inertia (MOI) testing to validate mass properties is shown in Fig. 38.

The RBSP external surfaces are conductive or static dissipative to maintain ground continuity throughout the structure and to preclude surface charging. This was done to reduce the effect of the observatory on the electric field and particle science measurements. External surfaces are painted with a black conductive paint and the outermost blanket layer incorporates a conductive Kapton material. Thermal radiators for RBSP are constructed of Germanium Black Kapton based on material testing performed to measure radiation tolerance.

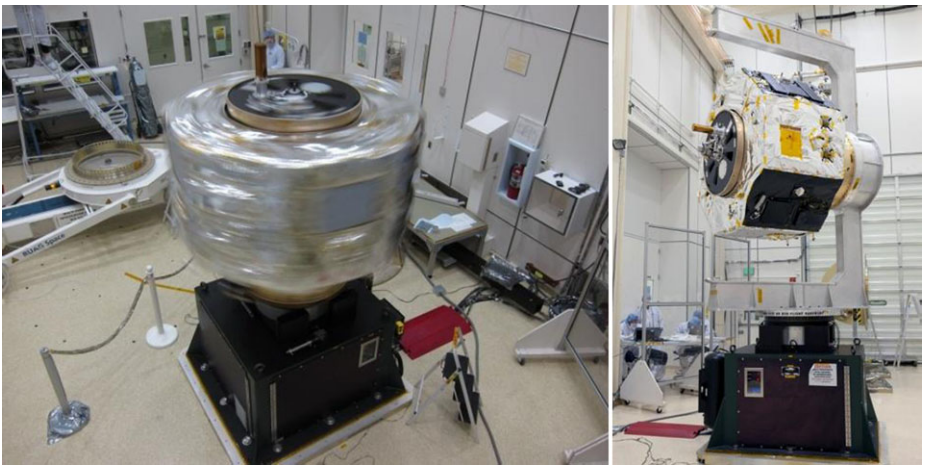

Fig. 38 Observatory spin balance and moment of inertia (MOI) testing were performed to validate mass properties (Photo: Ed Whitman, JHU/APL)

Fig. 39 In-air deployment test of solar array wing (Photo: Ed Whitman, JHU/APL)

Each observatory is equipped with four deployable hinged solar arrays and two deployable hinged instrument booms. Two EMFISIS sensors [a magnetic search coil (MSC) and a fluxgate magnetometer (MAG)], are mounted to the tip of the $-Y$ boom and the $+Y$ boom, respectively. Solar array panel and EMFISIS boom deployment testing was conducted to verify the performance of the APL-designed hinge and release mechanisms. The first set of tests was performed on the G-negation stand; the second set was performed on the observatory after its environmental tests. A final test was performed just prior to launch. All test subjects were in the final flight configuration for this set of tests, including the thermal blankets, the harnesses, and the EMFISIS magnetic sensors. Figure 39 shows one of the initial in-air deployment tests that was conducted with a solar array wing and its magnetometer boom.

13 Thermal Management

The two RBSP observatories utilize a cold-biased passive thermal control design system to maintain the onboard electronics and instruments within their required temperature limits. The majority of the electronics boxes are hard-mounted to the inside of the spacecraft panels and decks, with their internal heat going into the main structure. Local radiators on the side panels and bottom deck control the amount of heat lost to the space. Multi-layer insulation blankets cover the majority of the outside of the observatory, especially on the top deck to provide insulation from the Sun as RBSP is a near Sun-pointed spinning observatory. Heater circuits on all the panels and decks are installed to protect the observatory from getting too cold. Very little heater power is expected to be needed on orbit, and the heater circuits are provided as a fail-safe device. A few observatory components, such as the lithium-ion battery and several instruments, are thermally isolated and have their own radiators, blankets, and heaters. Table 16 shows the test temperature limits for all the major components on the observatory. The observatory will be maintained on orbit inside of the test limits specified for the typical electronics boxes of +55 and −25 °C.

The observatory thermal design was validated by the thermal balance test and by thermal vacuum hot and cold cycle testing performed at APL from February 14, 2012, to April 3, 2012. The test configuration is shown in Fig. 40 with the two RBSP observatories side by side in their respective thermal vacuum chambers in the Space Simulation Laboratory (SSL) at APL. All temperature and heater margins were found to be acceptable based on the results of the thermal vacuum testing. The predicted instrument survival temperatures are shown in Tables 17 and 18 for Observatory A and Observatory B based on the results of this

Table 16 Observatory component test temperature limits

	Survival		Operating	
	Max (°C)	Min (°C)	Max (°C)	Min (°C)
Battery	40	0	35	5
Propulsion module	55	5	50	10
Solar array	110	−130	110	−130
Typical electronics boxes	60	−30	55	−25
Shunts	200	−150	200	−150

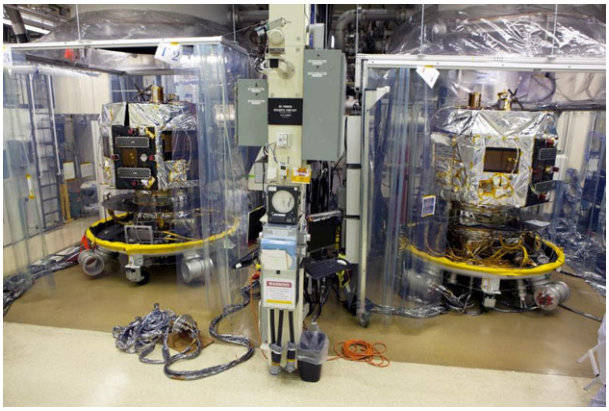

Fig. 40 RBSP Observatories A and B side by side prepared to lift into thermal vacuum chambers at JHU/APL (Photo: Ed Whitman, JHU/APL)

Table 17 Observatory A instrument survival temperatures

Component	Test temperature (°C)		Temperature predict (°C)		Margin (°C)		Heater power duty cycle (%)	
	Hot	Cold	T_{max}	T_{min}	Hot	Cold	Hot	Cold
RPS	60	−43.7	−28.13	−36.32	88.13	7.4	48 %	72 %
REPT electronics box	55	−45	−28.24	−37.01	83.24	8.0	0 %	20 %
HOPE—LVPS board	60	−30	−6.01	−18.79	66.01	11.2	0 %	0 %
IDPU	60	−30	2.0	−19.2	58.0	10.8	0 %	0 %
EMFISIS MEB	60	−30	1.2	−19.8	58.8	10.2	0 %	0 %
MagEIS HI DPU Brd	55	−40	1.12	−16.10	53.88	23.90	0 %	0 %
MagEIS HI	55	−40	−20.27	−30.34	75.27	9.7	0 %	0 %
MagEIS HI yoke rear	55	−40	−20.20	−31.08	75.20	8.9	12 %	19 %
MagEIS Med35 DPU Brd	55	−40	1.37	−15.17	53.63	24.83	0 %	0 %
MagEIS Med35 yoke rear	55	−40	−20.82	−30.72	75.82	9.3	48 %	72 %
MagEIS Med75 DPU Brd	55	−40	2.05	−14.42	52.95	25.58	0 %	0 %
MagEIS Med75 yoke rear	55	−40	−20.74	−29.32	75.74	10.7	50 %	73 %
MagEIS low DPU Brd	55	−40	−0.94	−15.96	55.94	24.04	0 %	0 %
MagEIS low yoke rear	55	−40	−21.98	−31.41	76.98	8.6	44 %	67 %
RBSPICE detector	60	−40	−16.86	−25.37	76.86	14.63	41 %	74 %
Mag sensor PCB	70	−35	16.70	9.29	53.30	44.29	29 %	36 %

Table 18 Observatory B instrument survival temperatures

Component	Test temperature (°C)		Temperature predict (°C)		Margin (°C)		Heater power duty cycle (%)	
	Hot	Cold	T_{max}	T_{min}	Hot	Cold	Hot	Cold
RPS	60	−40.2	−26.89	−36.31	86.89	3.9	45 %	71 %
REPT electronics box	55	−45	−23.96	−37.00	78.96	8.0	1 %	19 %
HOPE—LVPS board	60	−30	0.93	−17.25	59.07	12.7	0 %	0 %
IDPU	60	−30	8.8	−19.3	51.2	10.7	0 %	0 %
EMFISIS MEB	60	−30	7.5	−19.8	52.5	10.2	0 %	0 %
MagEIS HI DPU Brd	55	−40	8.32	−15.00	46.68	25.00	0 %	0 %
MagEIS HI	55	−40	−22.18	−29.62	77.18	10.4	0 %	0 %
MagEIS HI yoke rear	55	−40	−22.29	−30.64	77.29	9.4	11 %	19 %
MagEIS Med35 DPU Brd	55	−40	8.89	−14.04	46.11	25.96	0 %	0 %
MagEIS Med35 yoke rear	55	−40	−20.73	−30.62	75.73	9.4	44 %	70 %
MagEIS Med75 DPU Brd	55	−40	9.73	−13.06	45.27	26.94	0 %	0 %
MagEIS Med75 yoke rear	55	−40	−16.19	−29.10	71.19	10.9	47 %	72 %
MagEIS low DPU Brd	55	−40	6.87	−14.48	48.13	25.52	0 %	0 %
MagEIS low yoke rear	55	−40	−20.18	−31.18	75.18	8.8	39 %	65 %
RBSPICE detector	60	−40	−16.56	−25.31	76.56	14.69	37 %	72 %
Mag sensor PCB	70	−35	16.64	9.26	53.36	44.26	29 %	36 %

system-level thermal testing. All highlighted areas were evaluated and determined to have acceptable margins as they are either protected by heaters or actively controlled by heaters.

14 Integration and Test

The RBSP observatories were built and tested at APL. The observatory-level testing ensured that these two spacecraft and their payloads would withstand the launch and also operate successfully throughout their on-orbit environment. Significant spacecraft and observatory testing was conducted at APL and included the typical suite of environmental testing including vibration, shock, and thermal vacuum testing (Kirby and Stratton 2013).

The two RBSP observatories are shown proceeding through the integration and test phase of development in Fig. 41, side by side in one of the spacecraft integration and test high bays at APL. After the completion of environmental testing, the observatories were shipped to Astrotech, located nearby the Kennedy Space Center, for final integration and test and integration with the launch vehicle. The stacked observatories were successfully launched from Cape Canaveral Air Force Station on an Atlas V 401 launch vehicle on August 30, 2012.

14.1 Environmental Testing

Dynamics testing was performed in the APL Vibration Test Laboratory (VTL). The first test performed in this sequence was direct-field acoustic testing. In this test the stacked spacecraft were subjected to a simulated launch acoustic environment created by stacks of speakers that surrounded the spacecraft. The field was controlled to a specified profile through the use of control microphones set up in the sound field, and the response of the spacecraft was measured by accelerometers (Maahs 2012). Next, the RBSP spacecraft stack was exposed to a three-axis sine vibration test at protoflight levels to verify that the spacecraft stack fundamental frequencies meet the interface agreed to with the launch vehicle. The test also verified that the spacecraft assemblies demonstrate proper workmanship as integrated for flight. The tests were conducted without any issues. The spacecraft stack fundamental frequencies were shown to be 14.6, 14.4, and 30.2 Hz in the X, Y, and Z axes, respectively which are all above the minimum launch vehicle defined interface requirements.

Shock testing was performed on each spacecraft to verify that the shock induced by the launch vehicle separation would not cause any damage to the spacecraft or spacecraft components. The launch vehicle-provided payload separation ring was used initiate the shock event at the bottom of the spacecraft stack. The spacecraft-provided inter-separation system between the Observatory A and Observatory B spacecraft was used to initiate the shock

Fig. 41 Two RBSP observatories in cleanroom at JHU/APL (Photo: Lee Hobson, JHU/APL)

event for the top spacecraft. Both spacecraft passed the shock testing and the responses (as measured by onboard accelerometers) matched the predictions of the spacecraft dynamic analysis.

Initial spin balance testing was conducted on each spacecraft bus at rates up to 70 rpm. This testing provides data that is used to verify the spacecraft mass properties and balance mass placement on each spacecraft that are needed to meet the stability requirements on orbit. The nominal spacecraft spin rate on orbit is 5.5 rpm; however, the spacecraft was to be exposed to higher rates up to 15 rpm as part of the deployment of the spin plane booms. The solar arrays and magnetometer booms underwent spin balance testing to verify that they were properly balanced for flight. Deployment testing was performed on each solar array panel and on each of the magnetometer booms. All of this testing was performed at the APL Integration and Test facility.

The Environmental Test Facility at APL has side-by-side vacuum chambers that were used to test the two RBSP observatories in parallel as shown previously in Fig. 40. All instruments were integrated onto the spacecraft for this 6-week long test at APL. Initially a thermal balance test was conducted to demonstrate the thermal performance of the spacecraft at four thermal balance cases. This was followed by four thermal cycles including transitions from hot to cold cycling the temperature between -15 and $+45$ °C. The thermal cycle testing demonstrated that the RBSP spacecraft, assemblies, and instruments performed as expected over the operating temperature range that they will be exposed to in flight with margin. The RBSP integration and test team performed an observatory level comprehensive performance test (CPT) verifying that all spacecraft subsystems and the seven unique instruments operated successfully at hot and cold temperature extremes. Mission simulation testing was conducted during environmental testing by the mission operations team, exercising the command and control interfaces between the spacecraft and the ground systems. Finally ground station compatibility testing between the spacecraft and the APL SCF ground station, the USN ground stations, and the TDRSS network was performed over temperature to test all communication paths between the spacecraft and the ground system that will be used once the observatories are on orbit.

14.2 Processing at Astrotech

After the successful completion of the environmental testing at APL, the RBSP observatories were transported to Titusville, Florida, where final assembly, test, and propellant loading were completed at the Astrotech Facility. A final spin balance test was completed for each spacecraft to ensure that the final mass properties of each spacecraft were accurately modeled. A spacecraft-level magnetic swing test was conducted which verified that the residual magnetic field of the spacecraft was well understood. This is important so that instrument science measurements will not be adversely affected during the mission by spacecraft-generated magnetic fields contaminating the measured fields in space.

The RBSP solar array wings consist of solar array panels as well as instrument magnetometer booms. These were assembled in Florida at Astrotech and then all were installed on their respective spacecraft. Solar array flood testing was conducted to verify that all solar array cells were working properly and magnetic phasing testing was conducted to verify the magnetic cleanliness of the solar arrays in their final configuration. The RBSP mission includes two spacecraft and each has four solar array panels and two magnetometer booms, which made this an extensive effort. Deployment testing was completed on all deployables before they were stowed for launch.

Propellant loading is one of the final steps in preparing the spacecraft for launch. The RBSP spacecraft each carry 56 kg of hydrazine propellant onboard for use in orbit trimming

Fig. 42 RBSP onboard the Atlas V 401 launch vehicle ready for launch (Photo: Ed Whitman, JHU/APL)

maneuvers and spacecraft attitude adjustment during the life of the mission. Hydrazine is a hypergolic fuel and therefore propellant loading is a hazardous operation and is performed by trained personnel in Self-Contained Atmospheric Protection Ensemble (SCAPE) suits. The RBSP spacecraft underwent this final fueling procedure at Astrotech a few weeks before launch.

The payload launch adapter and launch vehicle fairing were mated with the stacked RBSP spacecraft at the Astrotech facility in preparation for integration onto the launch vehicle. The electrical interfaces were connected so that the launch vehicle would be able to send the signals needed to release the spacecraft once on orbit. Final inspections and closeout were completed and the spacecraft stack was completely encapsulated in the launch vehicle payload fairing. A transporter vehicle was used then used to move the encapsulated fairing out to the Atlas V processing facility where the launch vehicle was being assembled.

14.3 Atlas V Processing

Once at the Atlas V Vehicle Integration Facility (VIF) located on Cape Canaveral Air Force Station, the RBSP launch vehicle and the spacecraft underwent final preparations for launch. The spacecraft flight batteries were charged for launch. The clampbands that would be used to release the spacecraft from the launch vehicle were tensioned and checked. All safe plugs were replaced with arming plugs. In Fig. 42 the Atlas V 401 with the RBSP observatories onboard is shown at the launch pad, ready for launch.

15 Conclusion

The Radiation Belt Storm Probe (RBSP) mission includes two observatories designed and built at the Johns Hopkins University Applied Physics Laboratory (APL), for NASA's Living with a Star heliophysics program. The purpose of the RBSP mission is to collect data about the Earth's Van Allen radiation belts and the response of these belts to solar activity. The twin RBSP spacecraft and the payload they house are hardened to survive and operate in the harsh radiation belt environment for the initial 2-year mission life. It will take 2 years for both observatories to explore all regions of both the inner and the outer Van Allen belts. By using two observatories that will fly through different parts of the radiation belts at the same time, the data returned from the instruments can be combined to provide information about

how the environment changes in both space and time. So far these two Van Allen Probes are meeting all expectations for working well beyond the initial 2 years. The observatories each have consumables onboard to continue to return valuable science data for over 5 years while in orbit and traversing through the Earth's radiation belts.

Acknowledgements The authors thank the NASA Living With a Star program and the Science Mission Directorate for support of this work, as well as the efforts of the many RBSP team members whose work will contribute to the success of this mission.

References

S.S. Bushman, Design, fabrication, and testing of the Radiation Belt Storm Probes propulsion systems, in *48th Joint Propulsion Conf.*, AIAA Paper 10.2514/6.2012-4332, Atlanta, GA, USA, July (2012)

D.J. Copeland, C.C. DeBoy, D.W. Royster, W.C. Dove, D.K. Srinivasan, J.R. Bruzzi, A. Garcia, The APL 18.3 m station upgrade and its application to lunar missions, in *Proc. 2010 IEEE Aerospace Conf.*, Big Sky, MT, USA, March (2010)

M.J. Crowne, C.B. Haskins, R.E. Wallis, D.W. Royster, Demonstrating TRL-6 on the JHU/APL Frontier Radio for the Radiation Belt Storm Probe Mission, in *Proc. 2011 IEEE Aerospace Conf.*, Big Sky, MT, USA, March (2011)

V.A. Davis, M.J. Mandell, R.H. Maurer, Preliminary Surface and internal charging analysis of the Radiation Belt Storm Probes Observatory, in *10th Int. Observatory Charging Technol. Conf.*, June (2007)

C.B. Haskins, C.C. DeBoy, Deep-space transceivers—an innovative approach to observatory communications. Proc. IEEE **95**(10) (2007)

C. Haskins, W. Millard, Multi-band software defined radio for spaceborne communications, navigation, radio science and sensors, in *IEEE Aerospace Conf.*, Big Sky, MT, USA, March (2010)

C.B. Haskins, W.P. Millard, J.R. Jensen, Flexible, coherent digital transceiver for low power space missions, in *Proc. 2006 IEEE Aerospace Conf.*, Big Sky, MT, USA, March (2006)

C. Haskins, W. Millard, N. Adams, D. Srinivasan, M. Angert, The frontier software-defined radio: mission-enabling, multi-band, low-power performance, in *61st Int. Astronaut. Congr.*, Prague, CZ, September (2010)

K. Kirby, J. Stratton, Van Allen Probes: a successful launch campaign and early operations in Earth's radiation belts. in *Proc. of the 2013 IEEE Aerospace Conf.*, Big Sky, MT, USA, March (2013) 2.0401/2066

K. Kirby et al., Radiation Belt Storm Probes (RBSP) spacecraft and impact of environment on spacecraft design, in *Proc. 2012 IEEE Aerospace Conf.*, Big Sky, MT, USA, March (2012). doi:10.1109/AERO.2012.6187020

G. Maahs, Direct field acoustic test (DFAT) development and flight testing of Radiation Belt Storm Probe (RBSP) satellites, in *27th Aerospace Testing Seminar*, The Johns Hopkins University Applied Physics Laboratory, Laurel, MD, October (2012)

W. Millard, C. Haskins, The Frontier radio: common software defined radio processing platform for multiple space mission classes, in *The 62nd Int. Astronaut. Congr.*, Cape Town, South Africa, October (2011)

NASA, Risk classification for NASA payloads, NPR 8705.4 (Revalidated July 9, 2008). http://nodis3.gsfc.nasa.gov/displayDir.cfm?Internal_ID=N_PR_8705_0004_&page_name=main. Accessed 24 October 2012

W.M. Reid, C.A. Monaco, Flight software application framework simplifies development for RBSP observatory, in *Proc. IEEE Aerospace Conf.*, Big Sky, MT, USA, March (2012)

D.G. Sibeck, B.H. Mauk, J.M. Grebowsky, N.J. Fox, The living with a Star Radiation Belt Storm Probes mission and related missions of opportunity, in *American Geophysical Union, Fall Meeting* (2006)

D.K. Srinivasan, D.A. Artis, R.B. Baker, R.K. Stilwell, R.E. Wallis, RF communications subsystem for the Radiation Belt Storm Probes. Acta Astron. **65**(11–12), 1639–1649 (2009)

D. Srinivasan, G. Heyler, T. McGee, Spin-axis estimation of the Radiation Belt Storm Probes mission using RF Doppler data. Acta Astron. **73**, 30–37 (2012)

R.K. Stilwell, Satellite applications of the Bifilar Helix Antenna. Johns Hopkins APL Tech. Dig. **12**(1) (1991)

J. Stratton, N. Fox, Radiation Belt Storm Probes (RBSP) mission overview, in *Proc. 2012 IEEE Aerospace Conf.*, Big Sky, MT, USA, March (2012). doi:10.1109/AERO.2012.6187019

A.D. Tipton, C.H. Pham, R.H. Maurer, D.R. Roth, Radiation test results of candidate observatory parts for the Applied Physics Laboratory, in *IEEE Radiation Effects Data Workshop*, Montreal, July (2009), pp. 39–41

A. Ukhorskiy, B. Mauk, N. Fox, D. Sibek, J. Grebowsky, Radiation belt storm probes: resolving fundamental physics with practical consequences. J. Atmos. Sol.-Terr. Phys. **73**(11–12), 1417–1424 (2011)

DOI 10.1007/978-1-4899-7433-4_5
Reprinted from *Space Science Reviews* Journal, DOI 10.1007/s11214-013-9993-6

The Electric and Magnetic Field Instrument Suite and Integrated Science (EMFISIS) on RBSP

C.A. Kletzing · W.S. Kurth · M. Acuna · R.J. MacDowall · R.B. Torbert · T. Averkamp · D. Bodet · S.R. Bounds · M. Chutter · J. Connerney · D. Crawford · J.S. Dolan · R. Dvorsky · G.B. Hospodarsky · J. Howard · V. Jordanova · R.A. Johnson · D.L. Kirchner · B. Mokrzycki · G. Needell · J. Odom · D. Mark · R. Pfaff Jr. · J.R. Phillips · C.W. Piker · S.L. Remington · D. Rowland · O. Santolik · R. Schnurr · D. Sheppard · C.W. Smith · R.M. Thorne · J. Tyler

Received: 30 August 2012 / Accepted: 9 May 2013 / Published online: 1 June 2013

Abstract The Electric and Magnetic Field Instrument and Integrated Science (EMFISIS) investigation on the NASA Radiation Belt Storm Probes (now named the Van Allen Probes) mission provides key wave and very low frequency magnetic field measurements to understand radiation belt acceleration, loss, and transport. The key science objectives and the contribution that EMFISIS makes to providing measurements as well as theory and modeling are described. The key components of the instruments suite, both electronics and sensors,

C.A. Kletzing (✉) · W.S. Kurth · T. Averkamp · S.R. Bounds · D. Crawford · J.S. Dolan · R. Dvorsky · G.B. Hospodarsky · J. Howard · R.A. Johnson · D.L. Kirchner · B. Mokrzycki · J.R. Phillips · C.W. Piker · S.L. Remington
Department of Physics & Astronomy, University of Iowa, Iowa City, IA, USA
e-mail: craig-kletzing@uiowa.edu

M. Acuna · R.J. MacDowall · J. Connerney · J. Odom · R. Schnurr · D. Sheppard
Solar System Exploration Division, Goddard Space Flight Center, Greenbelt, MD, USA

R.B. Torbert · D. Bodet · M. Chutter · G. Needell · C.W. Smith · J. Tyler
Physics Department and Space Science Center, University of New Hampshire, Durham, NH, USA

R.M. Thorne
Atmospheric and Oceanic Sciences, University of California, Los Angeles, CA, USA

V. Jordanova
Space Science and Applications, Los Alamos National Laboratory, Los Alamos, NM, USA

O. Santolik
Department of Space Physics, Institute of Atmospheric Physics, Prague, Czech Republic

O. Santolik
Faculty of Mathematics and Physics, Charles University, Prague, Czech Republic

D. Mark
Bison Aerospace Inc., Newcastle, WY, USA

R. Pfaff Jr. · D. Rowland
Heliophysics Science Division, Goddard Space Flight Center, Greenbelt, MD, USA

including key functional parameters, calibration, and performance, demonstrate that EMFISIS provides the needed measurements for the science of the RBSP mission. The EMFISIS operational modes and data products, along with online availability and data tools provide the radiation belt science community with one the most complete sets of data ever collected.

Keywords Radiation belt physics · Wave measurements · Magnetometer measurements · Space flight instruments · RBSP · Radiation belt storm probes · Van Allen probes · Whistler waves · Geomagnetic storms · Space weather

1 Introduction

Radiation belt electrons are distributed in two distinct zones: the inner zone that is relatively stable and the outer zone that is very dynamic. The flux of energetic electrons in the Earth's outer radiation belt can vary by several orders of magnitude over time scales less than a day in response to changes in properties of the solar wind instigated by solar activity. Variability in the radiation belts is due to an imbalance between the dominant source and loss processes that are caused by a violation of one or more of the adiabatic invariants. For radiation belt electrons, non-adiabatic behavior is primarily associated with energy and momentum transfer during interactions with various magnetospheric waves (Thorne 2010). The most dramatic variations in the outer belt occur during magnetic storms, when the enhancement in the ring current causes a global decrease in the ambient magnetic field (e.g., Tsyganenko and Stern 1996). Reduced magnetic field affects the adiabatic drifts of radiation belt particles and causes an outward motion of radiation belt electrons with an accompanying loss of energy, which in turn causes an adiabatic decrease in radiation belt flux (e.g., Kim and Chan 1997) in addition to loss by scattering into the atmosphere (Millan and Thorne 2007) and transport to the magnetopause (Ukhorskiy et al. 2006). To differentiate between adiabatic and non-adiabatic changes in the radiation belts a simultaneous study of the radiation belts and ring current dynamics is needed (Jordanova 2012).

There are three adiabatic invariants (Roederer 1970) associated with the three basic periodic motions: gyromotion, the bounce motion in the Earth's magnetic mirror field, and the azimuthal drift due to magnetic gradients. Each invariant can be violated when the system is subject to fluctuations on timescales comparable to or shorter than the associated periodic motion (Schulz and Lanzerotti 1974). ULF waves, with periods comparable to tens of minutes, cause a violation of the third invariant, resulting in radial diffusion. Since the power in ULF waves is considerably enhanced during magnetic storms (Mathie and Mann 2000), radial diffusion is a potentially important mechanism for energetic electron acceleration (Rostoker et al. 1998; Elkington et al. 1999; Hudson et al. 2001; O'Brien et al. 2001; Shprits and Thorne 2004) or loss (Shprits et al. 2006; Jordanova et al. 2008; Loto'aniu et al. 2010) during storm conditions, dependent on the radial gradient in phase space density. Higher frequency ELF and VLF waves cause violation of the first two invariants and lead to pitch angle scattering loss to the atmosphere (Thorne and Kennel 1971; Lyons et al. 1972; Abel and Thorne 1998a, 1998b) or local stochastic energy diffusion (Horne and Thorne 1998; Summers et al. 1998; Horne et al. 2005; Miyoshi et al. 2003).

During storm conditions, the power spectral density of ELF and VLF waves is also strongly enhanced (Meredith et al. 2003a; Li et al. 2009b). Consequently, during disturbed conditions, all three adiabatic invariants can be violated simultaneously, and multidimensional diffusion models (Jordanova and Miyoshi 2005; Jordanova et al. 2008; Fok et al. 2008; Tao et al. 2008, 2009; Varotsou et al. 2008; Albert et al. 2009; Shprits et al. 2009;

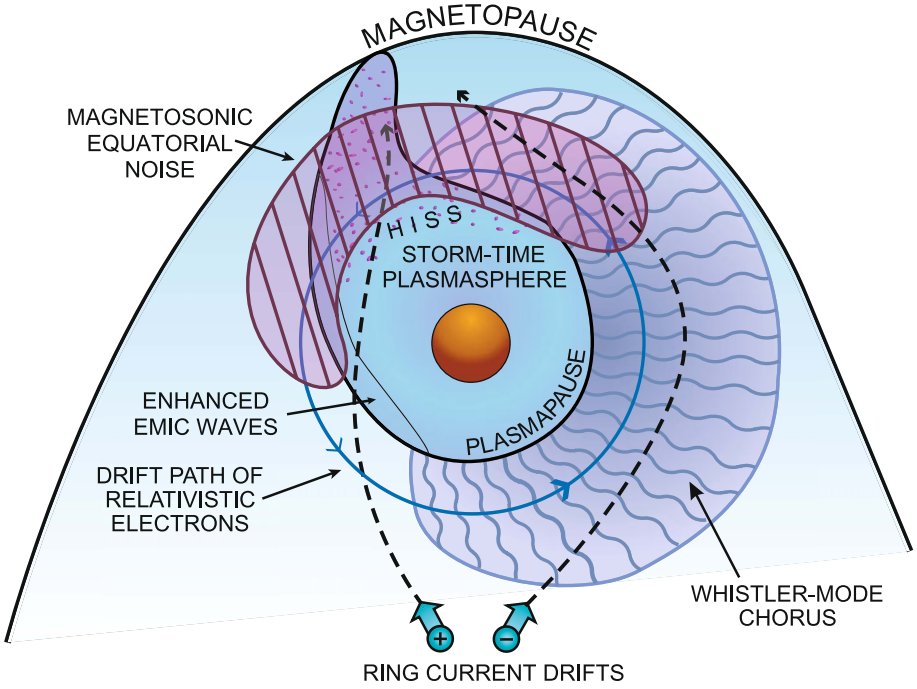

Fig. 1 A schematic diagram of the equatorial magnetosphere illustrating the spatial regions for wave-particle interactions between relativistic electrons and important plasma waves. Whistler-mode chorus can induce microburst precipitation (Thorne et al. 2005) and local stochastic acceleration (Summers et al. 1998; Horne et al. 2005) along a broad portion of the electron drift path between midnight and noon. Equatorial magnetosonic waves contribute to local electron acceleration. Strong pitch angle scattering by EMIC waves along the duskside plasmapause can cause intense but localized precipitation in the dusk sector Jordanova et al. (2008). Electrons are also subject to weak diffusion scattering on the dayside during resonance with plasmaspheric hiss. Relativistic electron drift times are typically less than 10 minutes and the average rate of precipitation loss or stochastic acceleration must be averaged over both the bounce and drift motions in this highly variable environment

Subbotin and Shprits 2009; Tu et al. 2009) are required to differentiate between the different source and loss processes. Such codes require accurate specification of the rate of radial diffusion D_{LL}, pitch angle scattering $D_{\alpha\alpha}$, and energy (or momentum) diffusion D_{EE}. Each diffusion coefficient requires a global specification of the power spectral density of all relevant plasma waves. A schematic model for the regions where some of these waves are excited is given in Fig. 1. The excited waves cause particle scattering, which modifies the particle pitch angle distribution and leads to loss in the atmosphere. During resonant scattering, energy can also be transferred from the low energy population (which provides the source of the waves) to the high energy tail population, causing in situ local acceleration (Horne and Thorne 2003). The variability of such scattering during geomagnetically active periods requires precise measurement of the intensity of all important magnetospheric waves. Accurate measurement of the large scale magnetic fields is needed to determine the evolution of ring current as well as the source population and/or the adiabatic effects on energetic electrons. The magnetospheric waves responsible for radiation belt dynamics have recently been reviewed by Thorne (2010). A brief summary of our current understanding of these waves is given below.

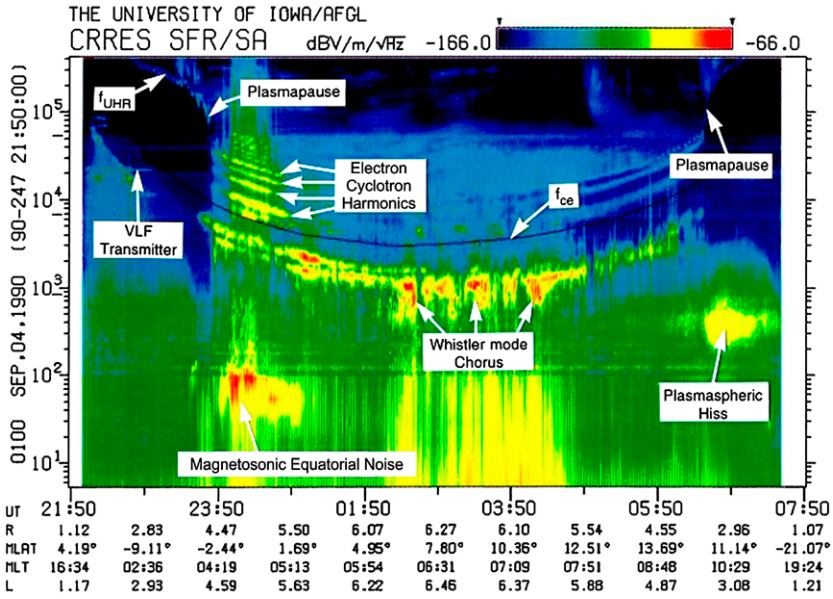

Fig. 2 Spectrogram of waves observed on Combined Release and Radiation Effects Satellite (CRRES), showing various magnetospheric waves which resonate with energetic electrons

Ultra Low Frequency Waves (*2–100 mHz*) are excited at the magnetopause boundary in response to velocity shear (Claudepierre et al. 2008) or solar wind pressure fluctuations (Ukhorskiy et al. 2006; Claudepierre et al. 2009). Hydromagnetic waves may also be excited internally by natural instability of the magnetospheric plasma. These ULF waves cause radial diffusion transport and associated energy change in the trapped particle population. The rate of radial transport is dependent on the power spectral density of the waves and tends to be much faster in the outer magnetosphere.

Chorus Emissions (*0.1–0.7* f_{ce}) are discrete coherent whistler mode waves, which occur in two distinct bands above and below one-half the electron cyclotron frequency f_{ce} as shown in Fig. 2 (Tsurutani and Smith 1974). Chorus is important because it plays a dual role in both the loss and local acceleration of radiation belt electrons (Bortnik and Thorne 2007) and is the dominant scattering process leading to diffuse auroral precipitation (Ni et al. 2008; Nishimura et al. 2010; Thorne et al. 2010). Recent statistical analyses of the global distribution of chorus observed on the THEMIS spacecraft indicates that the power spectral density is highly variable and responds to geomagnetic activity Li et al. (2009b). Chorus is enhanced over a broad spatial region (Hayosh et al. 2010) exterior to the plasmapause (see Fig. 1) associated with cyclotron resonant excitation during the convective injection of plasma sheet electrons into the magnetosphere (Li et al. 2008, 2009a; Jordanova et al. 2010a). Nightside chorus is strongest inside $L = 8$, and is also confined to latitudes below 15°, due to strong Landau damping of oblique waves during their propagation towards higher latitude from the equatorial source region (Bortnik et al. 2007). In contrast, dayside chorus is found over a broad range of latitudes, is most intense in the outer ($L \approx 8$) magnetosphere, and shows less dependence on geomagnetic activity (Tsurutani and Smith 1977; Li et al. 2009b). The wave normal distribution of chorus is required to accurately evaluate resonant electron energies and quantify the associated rates of scattering (Shprits and Ni

2009). Unfortunately, recent satellite observations (Chum et al. 2007; Breneman et al. 2009; Santolik et al. 2009; Haque et al. 2010) indicate a wide range of values for this key property, which adds uncertainty to modeling studies.

Equatorial Magnetosonic Waves ($< f_{lh}$) are highly oblique whistler-mode emissions excited within a few degrees of the equatorial plane at frequencies between the proton cyclotron frequency and the lower hybrid (e.g., Santolik et al. 2004). The waves are observed both inside and outside the plasmapause and are excited by a cyclotron resonant instability with a ring distribution of injected ring current ions (Horne et al. 2000; Meredith et al. 2008; Chen et al. 2010b). MS waves also undergo a Landau resonance with radiation belt (100 keV to a few MeV) electrons, and the spectral properties of intense MS waves observed on Cluster have been used to demonstrate that the timescale for energy diffusion (∼day) can be comparable to that due to chorus scattering (Horne et al. 2007). Test particle scattering of electrons in a finite amplitude MS wave have confirmed the rate of Landau resonant scattering (Bortnik and Thorne 2010) and demonstrated additional non-resonant transit time scattering due to the equatorial confinement of MS wave power.

Plasmaspheric Hiss (*100 Hz–(∼2) kHz*) is an incoherent whistler-mode emission mostly confined within the dense plasmasphere and within dayside plasmaspheric plumes, which is mainly responsible for the formation of the quiet time electron slot between the inner and outer radiation belt (Lyons and Thorne 1973; Abel and Thorne 1998a). Recent ray trace modeling has shown that hiss originates from a subset of chorus emissions that avoid Landau damping during propagation from the equatorial source region to higher latitude. Such waves also propagate to lower L where they enter and are trapped within the plasmasphere, where the discrete chorus emissions merge together to form incoherent hiss (Bortnik et al. 2008b, 2009a). The unexpected association between hiss and chorus has been confirmed by simultaneous observations on two THEMIS spacecraft (Bortnik et al. 2009b) and differences in the statistical MLT distribution of the two emissions has been explained by 3D ray tracing (Chen et al. 2009b).

Electromagnetic Ion Cyclotron Waves (*EMIC, <1–2 Hz*) are discrete electromagnetic emissions, which occur in distinct frequency bands separated by multiple ion gyrofrequencies. The EMIC source region is typically confined within ≈10 degrees of the geomagnetic equatorial plane, and the Poynting flux at higher latitude is always directed away from the equator, dispelling the long-standing bouncing wave packet model (Loto'aniu et al. 2005). EMIC waves are enhanced during magnetic storms (Fraser et al. 2010), as anisotropic energetic ring current ions are injected into the inner magnetosphere (Jordanova et al. 2001a). EMIC waves can cause rapid scattering and loss for ring current ions (Jordanova et al. 2001b, 2006) and relativistic electrons above 0.5 MeV (Thorne and Kennel 1971; Lyons and Thorne 1973; Albert 2003; Summers and Thorne 2003; Meredith et al. 2003b). Favored regions for EMIC excitation include the overlap between the ring current and the plasmasphere (Pickett et al. 2010), dayside drainage plumes (Morley et al. 2009), and the outer dayside magnetosphere in association with solar wind pressure fluctuations (Arnoldy et al. 2005; Usanova et al. 2008; McCollough et al. 2009). Theoretical global modeling of EMIC wave excitation has confirmed the plasmapause and plume as favored regions of cyclotron resonant instability (Jordanova et al. 2007; Chen et al. 2010a) and demonstrated that the wave excitation can also be enhanced by density fluctuations within a plume (Chen et al. 2009a). Hybrid codes have recently been used to evaluate the spectral properties and ultimate saturation amplitudes of EMIC waves (Hu and Denton 2009; Omidi et al. 2010).

Electron Cyclotron Harmonic (*ECH*, $f_{ce}(n + 1/2)$) waves are electrostatic emissions, which occur in harmonic bands between multiples of the electron cyclotron frequency. These waves are excited by the loss cone instability of injected plasma sheet electrons (e.g., Horne and Thorne 2000). The global distribution of ECH emission intensity and its dependence on geomagnetic activity has been analyzed by Meredith et al. (2009) and shown to be similar to that of chorus. Although ECH emissions contribute to the scattering loss of plasma sheet electrons below a few keV at larger L ($L > 8$) (Ni et al. 2011) ECH waves play little role in energetic (>30 keV) radiation belt dynamics.

The Electric and Magnetic Field Instrument Suite and Integrated Science (EMFISIS) investigation provides the key wave and DC (defined as 0–30 Hz for EMFISIS) magnetic field observations which, together with the EFW electric field measurements and the RBSP particle measurements, will allow us to identify the origin of all plasma waves important for radiation belt physics, as well as the evolution of the storm-time ring current, and to quantify their influences on the variability of trapped radiation belt particles.

On November 9, 2012 after the completion of commissioning of the instruments for RBSP, NASA renamed the Radiation Belt Storm Probes (RBSP) mission the Van Allen Probes mission. In what follows, we use the RBSP acronym to maintain consistency with other Van Allen Probes instrument papers, but future work of EMFISIS investigation will use the new name.

2 Science Goals and Objectives

The EMFISIS wave and magnetic field observations will address several key science objectives for the RBSP mission. Specifically, EMFISIS addresses the three overarching Level 1 Science questions:

2.1 Which Physical Processes Produce Radiation Belt Enhancement Events?

An essential unanswered question of inner magnetospheric dynamics is how electrons are accelerated to relativistic (MeV) energies following some magnetic storms. Comprehensive studies at geosynchronous orbit have indicated that acceleration in that region is correlated with enhanced ULF waves (Mathie and Mann 2000; O'Brien et al. 2001; Green and Kivelson 2001). However, the heart of the radiation belts lies well inside geosynchronous orbit, in the region near 3–5 RE. Theoretical calculations suggest that ULF acceleration mechanisms should be substantially reduced in efficiency at lower L, compared to geosynchronous orbit (Fälthammar and Walt 1969; Elkington et al. 2003). On the other hand, local acceleration involving VLF waves, particularly lower-band chorus, becomes most efficient in the region just outside the plasmapause, which corresponds to the radial range 3–5 RE for storm conditions (Summers et al. 1998; Meredith et al. 2003b).

Radial Transport and Acceleration by ULF Waves The global distribution and variability of low frequency Pc4 and Pc5 waves can be monitored by ground-based magnetometers and by satellites (Liu et al. 2009), and the observed wave spectral characteristics have been used to evaluate radial diffusion coefficients (Brautigam et al. 2005; Perry et al. 2005; Ukhorskiy et al. 2005; Huang et al. 2010) and employed in dynamic modeling of the outer radiation belt (Loto'aniu et al. 2006; Ukhorskiy et al. 2009; Chu et al. 2010). The properties of magnetospheric ULF waves, excited in response to solar wind variability, have also been obtained from global MHD simulations and used

to study the dynamic variability of radiation belt electrons (Fei et al. 2006; Kress et al. 2007). Although radial diffusion transport is able to simulate several important features of radiation belt dynamics, it fails to describe the rapid flux variation and the prolonged duration of electron acceleration observed during individual storms (Miyoshi et al. 2001; Subbotin and Shprits 2009). The ability of ULF waves to cause effective radial diffusion depends on the amplitude and the poloidal or toroidal properties of the waves and their modal structure (Perry et al. 2005). The azimuthal, radial, and field-aligned mode structure of ULF waves in space will be determined by multipoint EMFISIS measurements of magnetic fields on the two RBSP spacecraft.

Local Acceleration by Whistler-Mode Waves Persistent peaks in energetic electron phase space density have been identified in the heart of the outer radiation zone ($L \approx 5$) (Green and Kivelson 2004; Chen et al. 2006b, 2007), which support earlier theoretical studies of the importance of local stochastic acceleration (Summers et al. 1998; Horne and Thorne 1998). Potential mechanisms responsible for the local acceleration to relativistic energies during the recovery phase of a storm include cyclotron resonant interactions with VLF chorus in the low-density region just outside the plasmapause (Horne et al. 2005) and Landau resonance with equatorial magnetosonic waves (Horne et al. 2007). The rate of acceleration is strongly dependent on plasma density, specifically, on the ratio between the electron cyclotron frequency and the plasma frequency.

The EMFISIS wave instruments provide measurements of the power spectral density of VLF waves every 6 s, and a full 3D spectral matrix with the same cadence along with a selection of burst modes which include full waveforms from all three axes of the electric and magnetic field sensors. This information, together with our measurements of plasma density, are critical for understanding the effectiveness of local acceleration. Our observations, in conjunction with RBSP electron observations and detailed theoretical modeling, will allow us to determine whether the electron distribution evolves in a manner consistent with local acceleration or by inward radial diffusion.

Prompt Acceleration by Drift Resonance New radiation belts have been observed to be created on time scales of minutes, as interplanetary shocks compress the magnetosphere and resonantly accelerate energetic seed populations in the inner magnetosphere (Vampola and Korth 1992; Blake et al. 1992; Wygant et al. 1994). The new belts can persist from months to years after their formation. The mechanism involved is compression of the magnetosphere by an interplanetary shock, which drives a compressional wave deep into the inner magnetosphere. The azimuthal electric fields associated with this shock can be tens to hundreds of mV/m, on timescales of seconds to minutes. As these compressional waves propagate through the inner magnetosphere, they resonantly accelerate high-energy electrons and protons whose drift periods are commensurate with the wave period (Hudson et al. 1997; Li et al. 1993).

The magnetic field variations in the compressional wave are the direct drivers that energize the seed populations to form the new radiation belt. These quantities must be measured on timescales appropriate to the wave propagation, which requires at least one-second resolution in order to resolve the fast rise time of the initial compressional pulse. At present we have only a basic understanding of this type of event, but with the RBSP mission having two well-instrumented spacecraft at different local times and/or radial distances, we will be able to measure the magnetic and electric field variations at two spatial locations for the first time, and better understand the propagation of the compressional wave.

2.2 What Are the Dominant Mechanisms for Relativistic Electron Loss?

Nearly every magnetic storm begins with a dramatic decrease in relativistic electron fluxes over much of the inner magnetosphere. Some of this drop is the result of reversible adiabatic effects (Kim and Chan 1997), while the remainder represents real loss through wave scattering into the atmosphere, magnetopause shadowing, and demagnetization on highly stretched field lines.

Pitch-angle Scattering and Loss to the Atmosphere Energetic radiation belt electrons can be scattered into the loss cone and lost by collisions in the atmosphere during resonant interactions with whistler-mode chorus emissions (Thorne et al. 2005), plasmaspheric hiss (Lyons et al. 1972; Abel and Thorne 1998a) and electromagnetic ion cyclotron waves (Albert 2003; Summers and Thorne 2003; Jordanova et al. 2008). Although significant advances have been made recently in the theory and modeling of wave-particle scattering (Millan and Thorne 2007), the theoretical calculations need to be thoroughly tested against in situ observations. Our measurements of local electric and magnetic fields and wave power spectral density and angular distribution will enable unprecedented progress in our physical understanding of relativistic electron losses from the inner magnetosphere.

Magnetopause Shadowing and Current Sheet Scattering Electrons can be lost from the radiation belts as they drift through the magnetopause or as they get scattered into the loss cone by current sheet scattering. Both these processes are important at larger L-shells during disturbed geomagnetic conditions, when the magnetosphere is compressed on the dayside and stretched on the nightside. During the main phase of the storm a strong ring current will distort the magnetic field and allow current sheet scattering to move to lower L-shells. Similarly, the outward motion of the radiation belt particles due to the adiabatic effect causes electrons to move to larger L, thus increasing the losses through the magnetopause (Shprits et al. 2006; Jordanova et al. 2008; Loto'aniu et al. 2010). Accurate measurements of magnetic field distortions during geomagnetic storms are required to compute the effectiveness of such loss.

2.3 How Do Ring Current and Other Geomagnetic Processes Affect Radiation Belt Behavior?

There are several aspects in which the temporal and spatial evolution of the ring current influences radiation belt dynamics that will be investigated using EMFISIS data. The development of a strong ring current during the main phase of a geomagnetic storm inflates the magnetic field at near-Earth distances. This changes the adiabatic drifts of the charged particles as well as the losses through the magnetopause. Large magnetic field depressions have been measured at distances as small as 3–4 Earth radii (R_E) during major geomagnetic storms (Dst < 250 nT) and have been associated with the storm time ring current enhancement (e.g., Cahill 1966; Tsyganenko et al. 2003). Sophisticated physics-based models (e.g., Chen et al. 2006a; Jordanova et al. 2006, 2010b; Zaharia et al. 2006, 2010) have been developed to investigate the effect of plasma pressure on the magnetic field in the inner magnetosphere during magnetic storms. The computed magnetic field and electric currents showed that plasma pressure strongly affects the B-field, even very close to Earth, and large field depressions develop near Earth at the storm peak. Magnetic field data from EMFISIS will be used to verify these computations and validate the models.

Ring current dynamics are also closely related to the development of intense sub-auroral electric fields involved in the magnetosphere-ionosphere (MI) coupling phenomenon known

as sub-auroral polarization streams (SAPS). The asymmetric ring current closes via field-aligned currents through the ionosphere and may be responsible for the penetrating electric fields at mid-latitudes. While the general characteristics of SAPS are well-documented and understood from ionospheric and low-altitude observations (e.g., Foster and Vo 2002; Mishin et al. 2003), the magnetospheric signature has not been as extensively investigated.

During geomagnetic storms ring current distributions are anisotropic and become unstable to excitation of plasma waves which cause the further acceleration or loss of radiation belt particles (see discussion of RBSP objectives in Sects. 2.1 and 2.2). The ion distributions can generate electromagnetic ion cyclotron (EMIC) waves (e.g., Cornwall et al. 1970; Jordanova et al. 1997, 2001b) and magnetosonic waves (e.g., Horne et al. 2000; Chen et al. 2010b), while the electron distributions can excite whistler-mode waves (e.g., Kennel and Thorne 1967; Horne et al. 2003). The wave distributions during various storms will depend on storm strength and ion composition; for example, Thorne and Horne (1997) have shown that increased O^+ content favors the generation of waves below the O^+ cyclotron frequency and damps waves above it. Using theoretical modeling (described in Sect. 2.4) together with EMFISIS wave and field observations and RBSP particle measurements, we will identify the evolution of the storm-time ring current and quantify its effects on the radiation belt particles.

EMFISIS will provide measurements of the large-scale magnetic field to place in context the EFW measurements of the convection electric field, an essential quantity for studying ring current evolution during a magnetic storm. Enhanced convection transports moderately energetic particles (ions and electrons) into the inner magnetosphere and accelerates them to form a strong storm-time ring current (e.g., Lyons and Williams 1980; Wolf et al. 1997), while time-dependent variations in the large-scale electric field traps particles on closed drift trajectories (e.g., Ejiri 1978). Kinetic model simulations (Jordanova et al. 2001a, 2003; Liemohn et al. 2001; Zaharia et al. 2010) of ring current development during storms have shown reasonable agreement with the Dst index, indicating the dominant role of magnetospheric convection in ring current energization and trapping. Detailed comparison of modeled ring current distributions, however, showed significant differences at low L, depending on the electric field model being used (Jordanova et al. 2003; Yu et al. 2012) and highlight the importance of measuring the large-scale electric field.

Other mechanisms that contribute to ring current flux intensification during the main phase of the storm are radial diffusion (e.g., Chen et al. 1994; Jordanova and Miyoshi 2005) and substorm-induced electric fields (e.g., Wolf et al. 1997; Fok et al. 1999). Radial diffusion affects mostly the local time variations of higher energy (>100 keV) particles, which have drift periods shorter than those of the typical storm main phase and thus drift several times around the Earth during the period of enhanced electric field. Ganushkina et al. (2000) found that plasma sheet ions rapidly penetrate deep into the inner magnetosphere, well inside $L = 4$, due to short-lived intense electric fields that are formed in connection with substorm onset. Detailed measurements and simulations are needed to clarify the extent to which these two processes contribute to ring current buildup. EMFISIS measurements of VLF wave properties combined with EFW electric field measurements will clarify the effect of wave-particle interactions and time-varying electric fields on ring current dynamics during geomagnetic storms.

2.4 Theory and Modeling

Radiation belt particles are influenced by the global distribution of magnetospheric plasma waves, as well as the global magnetospheric electric and magnetic fields, but the properties

of such waves and fields will only be monitored along the orbit of the two RBSP satellites. Theory and modeling must be employed to place the spatially-limited observations in a global context. Below, we describe how the EMFISIS theory and modeling team will utilize the available observations to address the primary RBSP science objectives.

Quantifying the Effects of Diffusion on the Radiation Belt Population Measurements made by the EMFISIS wave instruments can only be used to evaluate local rates of radial, pitch-angle and energy diffusion. However, over the two-year duration of the mission, statistical models for the global distribution of all relevant waves will be constructed, as a function of MLT, L-shell, latitude, and geomagnetic activity. This unique RBSP data source will allow us to develop statistical models for the global distribution of particle scattering, which can be used in a Fokker Planck equation to solve for the temporal variability of phase space density.

Ring Current and Radiation Belt Modeling A newly-developed coupled ring current-radiation belt model (Jordanova and Miyoshi 2005; Jordanova et al. 2006, 2010a, 2010b; Zaharia et al. 2006, 2010) will be used as a powerful tool to understand the dynamics of energetic electrons and ions in the inner magnetosphere. This model represents an extension of our ring current-atmosphere interactions model (RAM) to relativistic energies and electrons. RAM solves numerically the bounce-averaged kinetic equation for H^+, O^+, and He^+ ions and electrons in the Solar Magnetic (SM) equatorial plane and is two-way coupled with a 3-D equilibrium code (SCB) that calculates the magnetic field in force balance with the anisotropic ring current distributions. The electric field model represents the gradient of an ionospheric convection potential (mapped to the SM equatorial plane along SCB field lines) and a corotation potential. The RAM-SCB model can be driven either by empirical electric fields (e.g., Weimer 2001) and boundary conditions or by those provided from a global magnetohydrodynamics (MHD) model, e.g. BATSRUS (Powell et al. 1999) self-consistently coupled with an electric field model (RIM) (Ridley and Liemohn 2002) and driven by dynamic solar wind input. Figure 3 shows RAM-SCB simulations during the 22 April 2001 storm indicating significant depressions in the magnetic field intensity on the nightside during the storm main phase when the ring current pressure intensifies. The location of the pressure peak, as well as the peak magnitude depends strongly on the strength of the convection and the magnetic field morphology. The EMFISIS measurements of the large-scale electric and magnetic fields will be used to test and improve the physics-based models.

The RAM-SCB model is coupled with a time-dependent 2-D plasmasphere model (Rasmussen et al. 1993). Initially, electron losses due to scattering by plasma waves inside and outside the plasmasphere were included using a simplified loss term (F/τ_{wp}) with an appropriate timescale τ_{wp}. Pitch angle scattering by EMIC waves was incorporated, within regions of EMIC instability predicted by the anisotropic ring current ion populations, using quasilinear diffusion coefficients (Jordanova et al. 2008). The diffusion properties of the model will be updated as RBSP data become available. We will perform simulations of geomagnetic storms and compute the electron scattering within the spatial regions of EMIC, magnetosonic, and whistler mode waves using quasilinear theory. This global modeling will allow us to differentiate among the changes of the phase space density from transport and those from local acceleration and loss of energetic particles (RBSP science objectives 1 and 2 discussed in Sects. 2.1 and 2.2).

To assess the changes of the radiation belts due to scattering by various plasma waves, knowledge of the global wave distributions is needed. One of our approaches will be to simulate the wave excitation by the anisotropic ring current distributions using our RAM-SCB

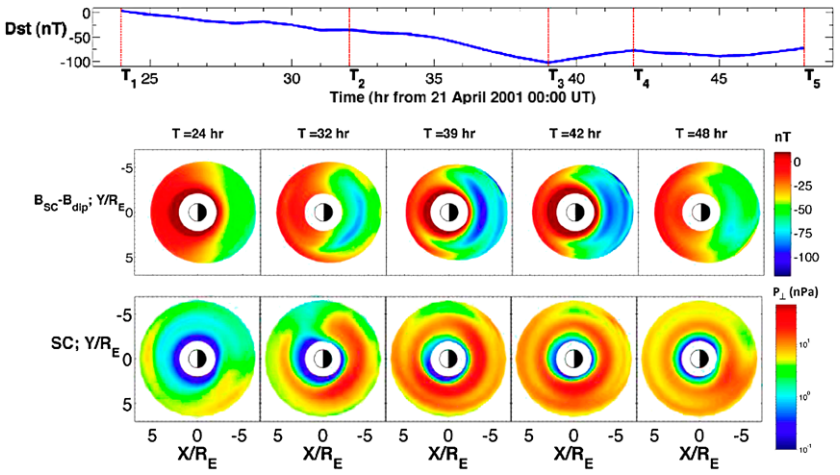

Fig. 3 (*Top*) Dst index during the April 2001 storm; (*Middle*) difference between the self-consistently calculated magnetic field intensity and the Earth dipolar field (after Zaharia et al. 2006); (*bottom*) ring current pressure calculations in the SM equatorial plane with RAM-SCB. Position is given in units normalized to an Earth radius

model (Jordanova et al. 2012) and to compare the wave growth predicted by our model with EMFISIS observations to estimate the wave amplitudes. Another approach will be to use the statistical models for the global distribution of all relevant waves constructed from RBSP data as a function of geomagnetic activity. A valuable test to our model will be provided by comparisons of ion and electron fluxes predicted by RAM-SCB with the pitch-angle distributions measured by the RBSP particle instruments.

Physical Understanding of Wave Excitation To develop a physics-based predictive model of the radiation belts, physical understanding of the most important transport, acceleration, and loss processes is required. Our kinetic ring current model (RAM-SCB) will provide global simulations of the equatorial distribution of all plasma waves important for radiation belt dynamics. We will calculate EMIC and magnetosonic wave excitation by the anisotropic ring current ion distributions during storm time. Figure 4 shows the equatorial growth rate of EMIC waves with frequencies between the oxygen and helium gyrofrequencies obtained with three different model formulations during the November 2002 storm. Intense EMIC waves are generated in the postnoon high-density plasmaspheric drainage plumes by the anisotropic ring current distributions that develop due to drift-shell splitting in realistic non-dipolar magnetic fields (Jordanova et al. 2010b). We will perform similar simulations and compare the regions of large wave growth with EMFISIS observations. The global patterns of intense ion and electron precipitation will be compared to energetic particle data from the RBSP mission. In addition, we will simulate with our kinetic model the injection of plasma sheet electrons into the inner magnetosphere by enhanced convection electric fields; this will provide a seed population of electrons. We will calculate the growth rate of whistler-mode waves due to the anisotropic ring current electron population using the dispersion relation for whistler waves and plasmaspheric densities from the coupled plasmasphere model. Global simulations of whistler instability during a geomagnetic storm were performed for the first time by Jordanova et al. (2010a) indicating significant wave growth in the dawnside MLT region outside the plasmasphere. Detailed comparisons with the EMFISIS wave data will be

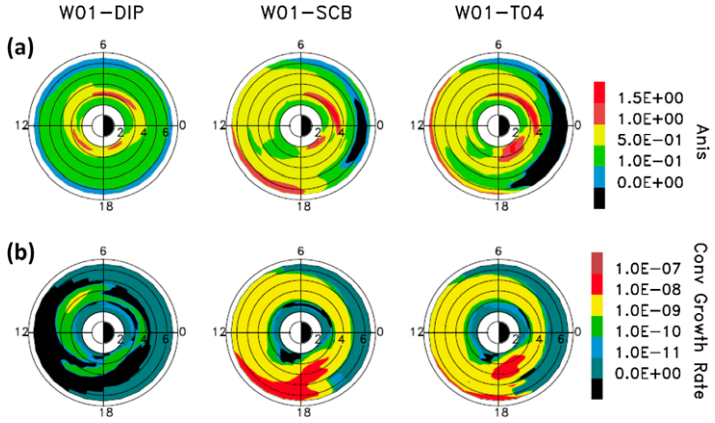

Fig. 4 (**a**) Proton ring current anisotropy obtained with RAM-SCB at 20 UT 20 November 2002 using W01 electric field and either dipolar (DIP), self-consistent (SCB), or T04 magnetic field, and (**b**) the corresponding convective growth rate of EMIC waves (after Jordanova et al. 2010b)

made to verify the location of whistler-mode growth and estimate the wave amplitudes. We will investigate the effect of these waves on the local acceleration and loss of radiation belt electrons and compare it to the effects of inward radiation belt transport and acceleration.

Non-linear Wave-Particle Interactions Extremely intense chorus emissions are occasionally observed (Cattell et al. 2008; Tsurutani et al. 2009) with amplitudes (>100 mV/m) far in excess of those where quasi-linear scattering is valid. Non-linear test particle scattering of resonant electrons in such large amplitude waves (Bortnik et al. 2008a) indicates that resonant electrons tend to exhibit advective transport towards the loss cone rather than the stochastic diffusive behavior. Such advective scattering could dramatically increase the average rate of resonant electron loss, and may thus be related to the observed electron dropouts (Onsager et al. 2007; Morley et al. 2010) during the main phase of magnetic storms. Non-linear phase trapping of electrons in large amplitude chorus can also lead to non-diffusive acceleration at relativistic energies (Albert 2002; Furuya et al. 2008; Summers and Omura 2007). Such processes will be treated with test particle scattering codes and the effects will be incorporated into the RAM code simulations.

3 Suite Overview

The EMFISIS instrumentation suite provides measurements of DC magnetic fields and a comprehensive set of wave electric and magnetic field measurements (the Waves instrument) covering the frequency range from 10 Hz up to 12 kHz (to 400 kHz for single-axis electric field) for the RBSP mission. EMFISIS comprises two sensors: a tri-axial fluxgate magnetometer (MAG) and a tri-axial magnetic search coil magnetometer (MSC). Additionally, to measure wave electric fields, the Waves instrument uses signals from the EFW experiment. Signals from these sensors are detected with receivers in a Main Electronics Box (MEB) which collects and processes all of the measurements.

Figure 5 shows a block diagram of the EMFISIS electronics and sensors. The majority of the electronics are contained within the Main Electronics box comprised of seven printed circuit boards.

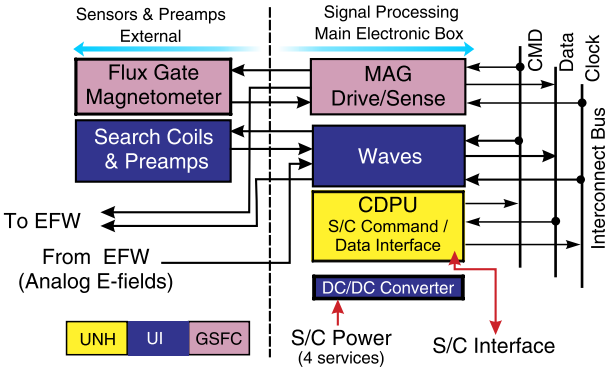

Fig. 5 EMFISIS System Block Diagram

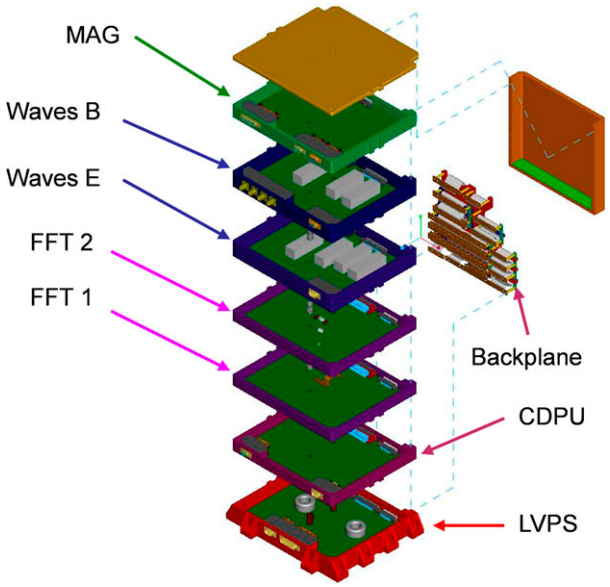

Fig. 6 Exploded view of the EMFISIS Main Electronics Box (MEB) showing board positions

As shown in the exploded view in Fig. 6, from bottom to top, is, first, the Low Voltage Power Supply (LVPS) which converts primary spacecraft power to voltages used by the rest of the suite, followed by the Central Data Processing Unit which controls the suite and handles data transfer to and from the central spacecraft systems. Above this are the four boards of the Waves instrument of the EMFISIS system: two FFT engine boards and the wave electric field and wave magnetic field receivers. Completing the stack is the MAG drive, sampling, and heater control board. Total dose, SEU, and deep dielectric charging issues were carefully considered in the design of all EMFISIS electronics, and these issues are further minimized by placing the MEB deep within the spacecraft bus.

The EMFISIS magnetic field sensors are mounted on booms as shown in Fig. 7. This figure shows the mounting of the various instruments and illustrates the spacecraft XYZ coordinate system and the UVW scientific coordinate system. All of the field instruments, that is, the EFW electric field booms and EMFISIS MAG and MSC sensors, are nominally mechanically co-aligned with the UVW coordinate system. This has the distinct advantage that phasing between these instruments is more easily verified and the data can be used

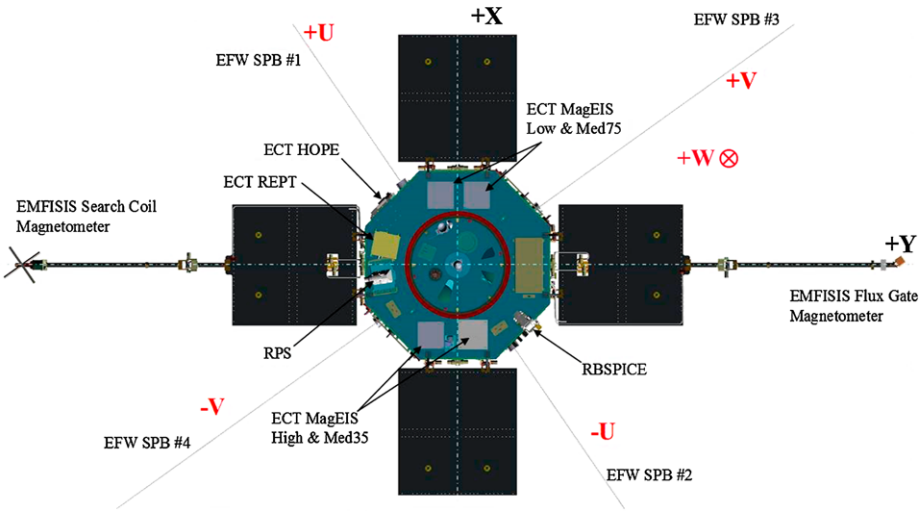

Fig. 7 Bottom view of the RBSP spacecraft layout showing the orientation of the field sensors. Both EMFISIS sensors, MSC and MAG, have their sensor axes nominally aligned with the EFW wire booms. This defines the UVW coordinate system used for analyzing science data. Note that the W direction is into the page. The figure also shows the orientation of the spacecraft XYZ coordinate system

with good success without needing to perform large rotations. However, the final, calibrated EMFISIS data products corrects for any minor misalignments (which less than one degree).

As Fig. 7 illustrates, the EMFISIS magnetic field sensors are mounted on booms which extend from two of the solar panels. These magnetometer booms place the sensors 3 m from the spacecraft body and a little under 4 m from the center of the spacecraft. This is done to minimize interference from the spacecraft systems in these measurements. Additionally, the magnetometer boom materials and design have been controlled to minimize or eliminate the use of permeable materials that can produce a magnetic signature. Similarly, the solar panel wiring layout has been controlled to ensure that currents from the solar cell strings cancel and do not produce a significant magnetic signature.

The electric field signals are supplied to the EMFISIS MEB from the EFW experiment. These measurements are made using spherical sensors at the ends of long booms to reduce the effects of the spacecraft at the sensors. In the spin-plane, the sensors are at the ends of wire booms for a tip-to-tip separation of 100 m. Along the spin axis, rigid booms are used which provide a tip-to-tip separation of up to 14 m. The difference in length is included in calculations of the EMFISIS flight software to normalize the signals to each other. Although the length is included, the shorter axial boom on the side of the spacecraft pointing away from the Sun is periodically shadowed (twice per ≈5.5 s spin) by the magnetometer booms. This shadowing produces a pulse of approximately 0.3 s in the E_W component of the electric field due to the sudden change in photoelectron current from the probe. The pulse provides low frequency contamination of the survey E_W component which must be taken into account when using the data.

3.1 Details of the Instrument Design

The science drivers for the EMFISIS design are the need to measure wave properties across the relevant frequency ranges and to measure the DC magnetic field both for background

field determination as well as to measure very low frequency waves. In both cases this drives the design to measure 3D vector quantities. For waves between 10 Hz and 12 kHz, EMFISIS makes 3D measurements of both the electric and the magnetic field. Below 10 Hz, EMFISIS measures only the magnetic field. However, this measurement can be combined with the 3D EFW electric field data to have a full set of electromagnetic vector quantities. Above 12 kHz, only a single electric component is measured from 10 to 500 kHz with decreasing response above 400 kHz due frequency roll-off in the EFW signals.

The highest frequency for the EMFISIS 3D wave measurements is set by the desire to fully measure both lower and upper band whistler-mode chorus. This sets the upper frequency response at 12 kHz. The desire to measure the upper hybrid line and the intensity of electron cyclotron harmonics drives the requirement to measure the electric field up to at least 400 kHz. A single electric field component is sufficient to satisfy this. Any of the three EFW dipole pairs can be used for the high frequencies, but it is expected that one of the spin-plane dipoles will provide the best sensitivity and lowest noise. The high frequency receiver is designed to measure up to 500 kHz, but the signal provided by EFW rolls off, significantly, above 400 kHz.

3.2 Mechanical Design

The EMFISIS mechanical design is implemented to both support the sensors and electronics for ascent vibration and acoustic loads as well as to provide good thermal conductivity to the spacecraft bus and shielding from penetrating radiation.

The mechanical implementation of the MEB is shown in an exploded view in Fig. 6 which illustrates how the seven boards are stacked and interconnected with a flexible backplane. Each board is contained within its own frame with an EMI cover to prevent cross-coupling of signals between adjacent layers. The boards are also thermally coupled to the frames to provide a conductive heat path for power dissipated on each board. Additionally, connectors are mounted in a "vault" to prevent penetrating radiation from entering through the connectors themselves.

3.3 Power System

The Low Voltage Power Supply (LVPS) converts primary spacecraft power to the various DC voltages required by the EMFISIS electronics. The LVPS is implemented as two separate supplies on a single board, one for the analog parts of the system (E and B receiver, MAG electronics) and one for the digital parts of the system (CDPU and FFT engines). This scheme was developed to simplify transformer design as well as to provide resiliency in the event of faults occurring on the digital side of the MEB. If this were to occur, the analog side can be powered separately maintaining MSC and MAG signals that are fed to the EFW experiment, thereby providing a redundant data path.

The analog side of the LVPS provides a set of secondary voltages which are filtered and then regulated by linear regulators to provide very low noise and stable voltages for the analog electronics. Because the power required for these parts of system is quite low, the somewhat lower efficiency of linear regulators is not significant. The digital side of the EMFISIS design consumes the majority of the power and consequently, several radiation hardened switching regulators are used.

4 The Fluxgate Magnetometer (MAG)

The EMFISIS magnetometer on RBSP measures 3D vector magnetic fields essential for our understanding of particle distributions that are critically dependent on the local and global magnetic fields and their time variation. Additionally, the fast measurement capability and wide dynamic range of the MAG together with the MSC search coil allows the detection and measurement of ULF electromagnetic waves that produce particle acceleration and transport in the magnetosphere. The EMFISIS investigation will allow the simultaneous measurement of the ambient magnetic field and its variation at two points within the magnetosphere. This makes possible the development of statistical descriptions of the large-scale dynamics of the magnetic field as well as monitoring the intensity of the quiet and storm-time ring current and the explosive release of energy stored in the geomagnetic tail during substorms. The MAG data also enables comparison of adiabatic invariants and particle phase space density at two points, providing key tests of energetic particle transport in the inner magnetosphere.

4.1 Heritage

The EMFISIS magnetometer is the latest in a series of magnetic field investigations developed by the magnetometry group at GSFC. This group has a long and successful track record of development and implementation of complex magnetic field investigations for planetary exploration, earth observing, and space physics missions. The EMFISIS sensors and analog electronics are designs similar to those flown on numerous NASA missions including Juno, MESSENGER, and STEREO. Modifications include changes to the mechanical, power and data interfaces for compatibility with the EMFISIS suite and RBSP spacecraft designs as well as added radiation tolerance through parts selection and shielding. The STEREO instruments were themselves based on more than fifty magnetometers previously developed for space missions, from Voyager (still operational after more than 35 years in space), ISPM, GIOTTO, WIND, ACE, CLUSTER I & II (more than 10 instruments), DMSP (11 instruments) to the more recent Lunar Prospector and Mars Global Surveyor instruments. They represent state of the art instruments with unparalleled performance.

4.2 Principle of Operation

The EMFISIS fluxgate magnetometer is a wide-range, high performance triaxial fluxgate magnetometer system. The signal processing, analog-to-digital converter (A/D) and interface electronics are implemented on a single electronics card shown in Fig. 8 and integrated in the MEB as discussed in Sect. 3. A block diagram is illustrated in Fig. 9. This configuration makes optimal use of limited spacecraft resources and takes full advantage of miniaturization made possible by contemporary technology and the maturity of the magnetometer design.

The wide dynamic range of the instrument covers ambient fields from 0.008 nT to 65,536 nT in three ranges selected automatically by the CDPU or ground command. The upper limit measurement capability is designed to make possible operation and testing in the Earth's surface field and also provides the appropriate range for RBSP perigee measurements. The magnetometer electronics include three 16-bit high resolution A/D converters to easily resolve small amplitude fluctuations of the field. The total power consumption (for zero field) is $\approx$0.9 W (excluding heater power). High reliability and radiation tolerance is obtained by the use of efficient, conservative design. The principal instrument characteristics are summarized in Table 1. The sensor assembly consists of an orthogonal triaxial arrangement of ring core fluxgate sensors shown in Fig. 10 plus additional elements required for

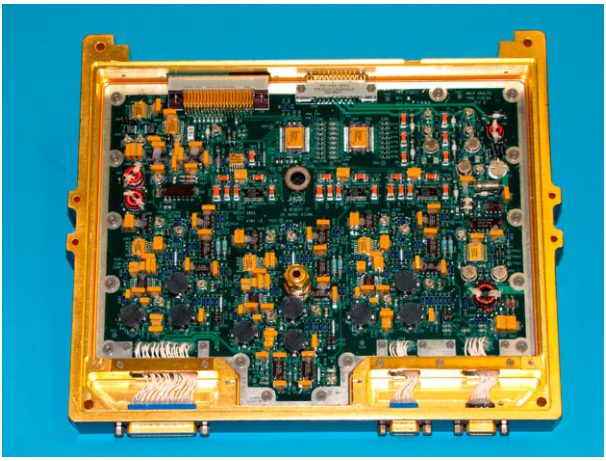

Fig. 8 EMFISIS Magnetometer electronics card in its frame

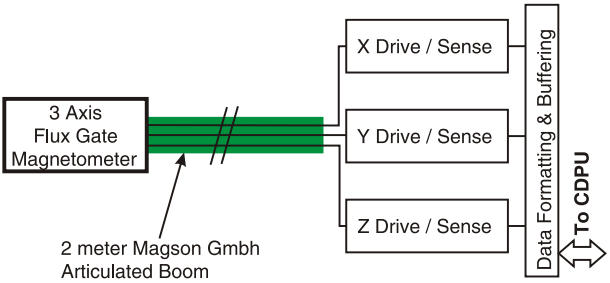

Fig. 9 EMFISIS Magnetometer (MAG) Block Diagram

Table 1 Key Magnetometer (MAG) operating parameters

Magnetometer Specifications (three ranges)	
Data Rate	~3 kbs, depending on compression number
Sampling Cadence	64 vectors/s
Ranges	Range 3: −65536 nT to 65536 nT
	Range 1: −4096 nT to 4096 nT
	Range 0: −256 nT to 256 nT
Resolution	2 nT (65536 nT range)
	0.125 nT (4096 nT range)
	0.0078 nT (256 nT range)
Accuracy	0.1 nT (sensor)
Frequency Range	0–30 Hz

thermal control. The fluxgate sensors are the latest in a series developed for space magnetic field measurements by Acuna (1974, 2002) with excellent performance and low power consumption. Total mass is ≈400 g, including the harness pigtail, cover, and thermal blanket.

The fluxgate sensors are driven cyclically to saturation by a 15.625 kHz signal derived from the CDPU master clock. The sensor drive signals are derived from an efficient high energy storage system which is capable of driving the ring core sensors to peak excitations which are more than 100 times the coercive saturation force of the cores. This type of excita-

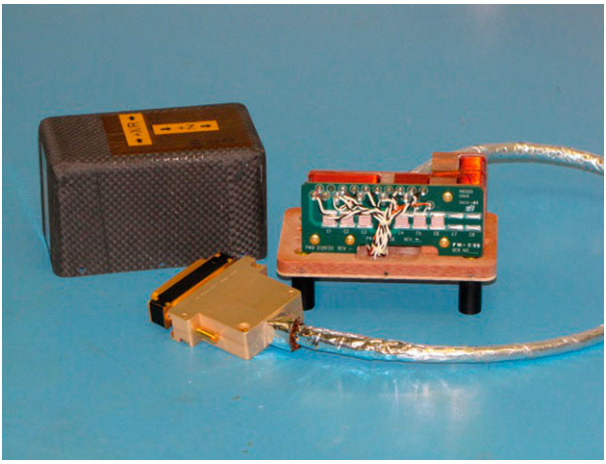

Fig. 10 EMFISIS Magnetometer sensor with cover and connector

tion eliminates from consideration many "perming" problems which have been attributed to fluxgate sensors in the past. In the absence of an external magnetic field, the fluxgate sensors are "balanced" and no signal appears at the output terminals.

When an external field is applied, the sensor balance is disturbed and a signal containing only even harmonics of the drive frequency appears at the output of the sensors. After amplification and filtering, this signal is fed to a synchronous detector and high gain integrating amplifier used to generate a current proportional to the magnitude of the applied field. This signal is fed back to the sensor to null the effective magnetic field. The output of a single axis magnetometer is then a voltage proportional to the magnitude, direction, and polarity of the ambient magnetic field with respect to the sensor axis orientation. A triaxial magnetometer is created when three single-axis sensors are arranged orthogonally and three sets of signal processing electronics are used to produce three output voltages proportional to the orthogonal components of the ambient magnetic field. For additional information the reader is referred to Ness (1970) and Acuna (1974, 2002).

4.3 Sensor Functional and Key Design Elements

The main components of the MAG system are the MEB electronics board, which contains drive, digitization, heater control, and interface circuitry; the MAG sensor which is mounted at the end of a boom; and the harness between the MEB and the sensor.

4.3.1 MAG Electronics in the MEB

CDPU Interface The CDPU software tasks perform all required operations: data manipulation and formatting, compression, and packetization for the MAG sensors. All core operations performed by the system are carried out under the control of interrupt driven software synchronized to the telemetry system clock. All default parameter values for the system are stored in tables in CDPU non-volatile memory and mapped into RAM during initialization, and can later be modified by commands to update calibrations, alignments, sampling rates, zero levels, etc. No burst data collection exists for the MAG system; data is always collected at the highest rate possible of 64 vectors/sec.

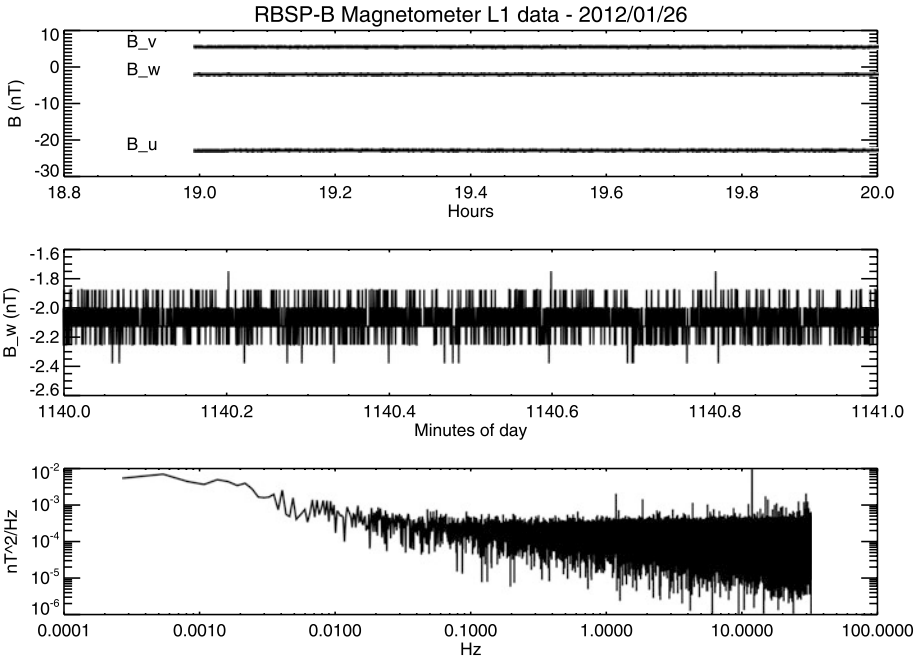

Fig. 11 EMFISIS magnetometer data (RBSP spacecraft B) from the Comprehensive Performance Test of Jan. 26, 2012 while in the ±4096 range. Magnetometer data from all three axes (*top*). The sensor was in a high-quality, mu-metal shield can, so the magnetic field levels are very low. Sixty second data interval from the W axis sensor (*middle*). Fluctuations over a range of less than 0.6 nT are due to residual noise from the test environment. Power spectral density of B_W data shown in *top panel* (*bottom*)

Power and Thermal Control The MAG system is powered by the analog side of the MEB LVPS. There is an additional, isolated power service passed straight through the MEB which provides power to the MAG sensor heater electronics. This power service is only switchable by the spacecraft power system and is not under EMFISIS CDPU control.

To maintain the fluxgate sensors within their optimum operating temperature range, particularly during eclipses (longest is ≈24 hours in duration) on the RBSP orbit, it is necessary to provide heater power to the boom mounted triaxial sensor assembly. This heater prevents thermal cycling of the sensor which could be detrimental to sensor performance as well as maintaining the sensor within the optimum calibrated range.

Since it is extremely difficult to reduce the stray magnetic field associated with the operation of DC powered foil heaters to acceptable levels, a pulse width modulator operating at ≈50 kHz is used to obtain automatic, proportional control of AC power supplied to the heating elements. The nominal power required to maintain the sensors at the desired temperatures is determined by modeling to lie in the range of 0.40 to 0.55 watts.

4.3.2 MAG Sensor Response and Characteristics

The performance of the MAG fluxgate sensors is shown in Fig. 11. Total RMS noise level over the 0.001–10 Hz band does not exceed 0.01 nT^2/Hz. This noise level is well below the required sensitivity for the RBSP mission and is more than adequate to properly detect and identify all magnetic field phenomena of interest.

The MAG system uses a single-pole low-pass filter with a 3 dB point at 30 Hz on all three axes. This provides a gentle roll-off for anti-aliasing and removes any differences between sensor cores as a function of frequency. The nominal operating temperature of the sensor and electronics is ≈15 °C and this has been achieved in flight. Very little temperature variation is experienced by the MAG electronics which are inside the spacecraft and essentially no variation is seen across the three MAG ranges. The sensor heater maintains the sensor within a few degrees of the nominal temperature, well within its well-calibrated range.

The three analog signals generated by the magnetometer are digitized by the 16 bit A/D converter. The 16 bit resolution allows the recovery of a very large dynamic range of signals. To further increase the measurement dynamic range and to accommodate simplified integration and test requirements during spacecraft testing, the dynamic range of the magnetometer can be changed automatically if the magnitude of the measured signals exceeds or drops below established, programmable digital thresholds. In this fashion, the MAG instrumentation can cover seven orders of magnitude in magnetic field measurement capability, from 0.008 nT to 65536 nT per axis. The operation of the automatic ranging system is controlled by the EMFISIS CDPU and has hysteresis to prevent overly frequent range changes. It is not expected that the 256 nT range will be used because the Earth's field only falls into this range near apogee and is quite variable. This would likely result in frequent range changes for geomagnetically interesting times which is not desirable. Consequently, range changes will typically occur only twice per orbit, once on the outbound leg as the Earth field drops and once on the inbound leg as the field increases. These range changes occur at approximately 2 R_E where the Earth's equatorial field decreases below 4000 nT.

Data compression is used in the CDPU to reduce the "raw" data rate (64 samples/s) to a value compatible with spacecraft resources and science objectives and is described in more detail in the section on the CDPU. The CDPU also controls calibration sequences that provide the necessary currents to determine the scale factor of each of the magnetometer axes for the two dynamic ranges.

4.4 Calibration

The MAG instrument calibration involves several traditional steps that were performed first at the laboratory level and later at the GSFC magnetics test facility. Initial calibrations are performed during electronics tuning and adjustment, and after each environmental test. The instrument incorporates a high accuracy internal calibration source that allows monitoring of trends or anomalies in performance in an end-to-end fashion. After the electronics and sensors are fully integrated a high accuracy scale factor and alignment test is performed using an absolute standard proton precession magnetometer. Parameters such as frequency response, zero levels, analog-to-digital conversion calibration and calibration sources are established with high accuracy in the laboratory using high accuracy sources and magnetic shields.

The spacecraft magnetic field signature is required to be less than 5 nT at the sensor. Prior to launch, this is verified by performing a "swing test" of the spacecraft in which the spacecraft is hung from a hoist and very gently swung back and forth in a direction aligned with a pair of external magnetometers. These magnetometers are operated in "gradient" mode which removes much of the background Earth field and allows the identification of the oscillating field from the swinging spacecraft.

The alignment of the sensor to the spacecraft reference is first done via control of the mechanical tolerances of the mounting and boom and allows an alignment determination of ≈1°. Final calibration and alignment analyses are performed in flight. A spinning spacecraft is an ideal platform to determine, from the modulation of the ambient field, the precise

value of the alignment of the spin axis to the magnetometer as well as the axes parallel to the spin plane. In addition, the spin-modulated magnetic signal allows the estimation of spin plane zero levels to an accuracy approaching the noise level of the measurements. Final calibration and alignment, now underway, is expected to be better than ≈0.1 nT and ≈0.1° respectively. Details of how the calibrations are applied to the magnetometer data are given in Sect. 8.1

5 The Waves Instrument

The primary objective of the Waves instrument is to provide sufficient information on plasma waves in the radiation belts to quantitatively determine the effect of these waves on radiation belt particles. Specifically, the Waves instrument measures all 3 components of the electric and all 3 components of the magnetic field for waves in the frequency range between ≈10 Hz and 12 kHz. The basic data returned is a set of spectral matrices including the auto- and cross-correlations between the sensors which, either on the ground or in the CDPU allow for the determination of spectral densities and various wave propagation characteristics. In burst mode, a primary data set includes full digitized waveforms from all six sensors to enable all types of wave analyses to be performed on the ground for a select fraction of times. The Waves instrument in concert with the CDPU also includes the ability to measure propagation characteristics of the waves such as the wave normal angle and Poynting flux for electromagnetic waves such as whistler-mode hiss and chorus within the constraints of limited telemetry. Measuring both the electric and magnetic components of the waves also allows one to distinguish between electromagnetic and electrostatic waves.

The instrument also measures a single electric field component of waves from 10 kHz to 500 kHz (with limited response above 400 kHz due to roll-off of the EFW signals) in order to determine the spectrum of electron cyclotron harmonic emissions and to measure the frequency of the upper hybrid resonance band, thereby providing an accurate determination of the electron density. Any of the three EFW dipoles can be selected by command to do this, but typically it is one of the spin plane booms will be used for optimum sensitivity upon evaluation in orbit. Figures 12 and 13 show the frequency range and amplitudes for the wave phenomena relevant to the RBSP objectives. The Waves instrument has a suitable dynamic range to cover all of these wave phenomena.

The Waves instrument also includes a set of four FPGA-based floating point accelerators called FFT engines to allow efficient digital signal processing of the Waves measurements onboard. The FFT engines can be considered computational resources controlled by the Leon III CDPU which assigns tasks to the engines and collects the results when the tasks are complete, as signaled by an interrupt. The multiple engines allows the CDPU to orchestrate complex modes requiring various computational tasks to be performed in concert or independently without having to wait for this resource to become available. While the engines are optimized for floating point fast Fourier transforms, they also control the Waves analog-to-digital converters to acquire waveforms; can Rice compress waveforms for transmission to the ground for burst modes; can calibrate, bin and average spectra; and be used to compute spectral matrices.

5.1 Waves Sensors

The Waves magnetic sensors consist of three identical search coil antennas mounted in a tri-axial configuration with each antenna oriented parallel to one of the spacecraft scientific

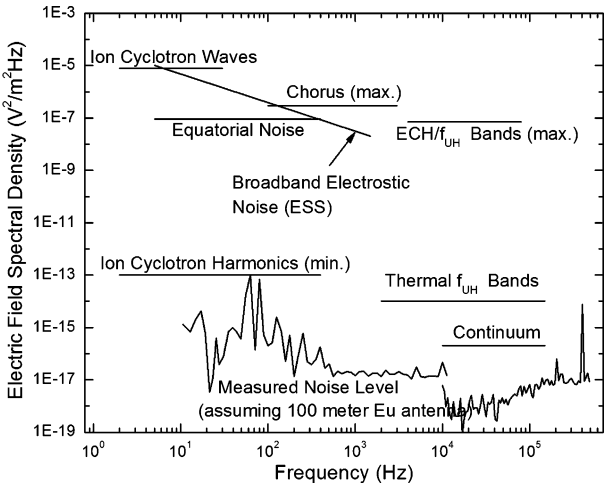

Fig. 12 Comparison of electric field wave phenomena important for RBSP science objectives with EMFISIS Wave frequency coverage and noise level measured during ground testing. The noise level at the lower frequencies is better in orbit due to the absence of 60 Hz interference

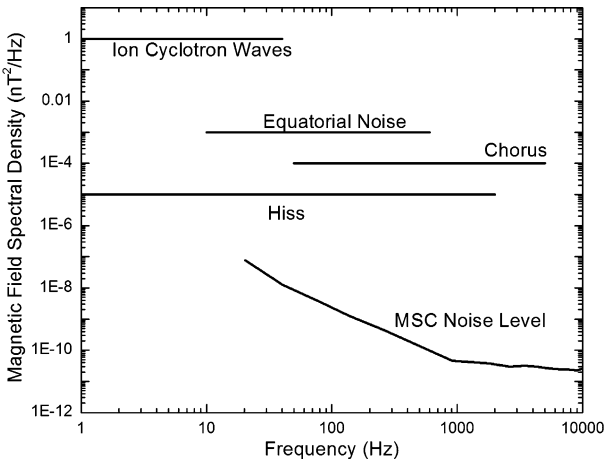

Fig. 13 Comparison of magnetic field wave phenomena important for RBSP science objectives with EMFISIS Wave frequency coverage and noise level

(UVW coordinates) axes. Two are parallel to the two spin-plane EFW electric field double probes and the third is parallel to the spin axis double probe. The search coils are mounted on the boom opposite from the magnetometer boom approximately 3 m from the spacecraft body to reduce any interference from the spacecraft. To enable the measurement of small amplitude signals, the spacecraft systems and other instruments have been designed and built with sound engineering practices that minimize electromagnetic interference.

The electric field signals for the Waves instrument are provided to the EMFISIS instrumentation from the EFW experiment. These signals consist of differential voltages from opposing EFW spherical sensors. Two of these signals, E_U and E_V, are derived from long wire booms in the spin-plane of the spacecraft. The third signal E_W is provided by rigid booms aligned along the spacecraft spin axis. Likewise, Waves provides analog signals from the triaxial search coils to the EFW instrument.

The magnetic search coil (MSC) design is based on previous sensors designed and built at the University of Iowa, including those for Hawkeye, ISEE, DE, CRRES, Polar, Wind, and Juno. Each search coil utilizes a mu-metal core approximately 40 cm in length and is wound with 10,000 turns of wire. The MSC sensors have a usable frequency range from

Fig. 14 The Magnetic Search Coil (MSC) sensor assembly and preamplifiers

below 10 Hz to 12 kHz. A flux feedback system is used to flatten the frequency response over the range of about 30 Hz to 12 kHz to provide a more easily calibrated output. The transfer function in this range is about 1.2 V/nT. The preamplifiers are mounted in a housing adjacent to the sensors in cylindrical housings on the end of the MSC boom. The search coils and preamplifiers are designed to operate within calibration between −70 and +30 °C and with a thermal design which does not require heaters during operation. A survival heater is provided for periods when the sensor is turned off. The MSC preamplifiers are specifically designed with radiation tolerant parts and spot shielding so as to operate in the RBSP radiation environment. The same design is also used on the Juno mission headed to Jupiter. A photo of the RBSP search coil and preamplifier assembly is shown in Fig. 14.

5.1.1 MSC Calibration and Performance

The calibration philosophy for the Waves instrument was to first calibrate the receivers and sensors individually, then perform a calibration of the combined sensors and receivers system (end-to-end), and verify that the results match.

The MSC sensor coil and pre-amplifier sub-systems were each calibrated (amplitude and phase from ≈1 Hz to ≈15 kHz) in a single axis mode just prior to assembly in the three-axis housing using a solenoid calibration coil inside a cylindrical mu-metal shield (to reduce 60 Hz interference). The calibrations were performed at the expected maximum temperature extremes of the sensors (−70 to 30 °C) and at room temperature (+22 °C). Following final assembly of the MSC sensors and preamplifiers into the tri-axial configuration (see Fig. 14), the MSC units were re-calibrated using a three-axis square stimulus coils in a large square mu-metal shield box to verify that the calibration had not changed. Because of the size of the tri-axial sensor unit and the square mu-metal shielding box, these tests were only performed at room temperature (+22 °C).

The tri-axial MSC unit was then attached to the EMFISIS MEB and the calibration tests were repeated to measure the response of the complete system (sensors + receivers). After

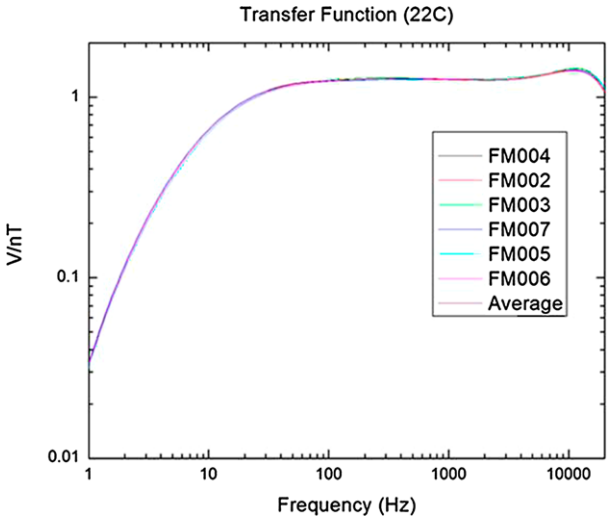

Fig. 15 The transfer function for each of the six single axis search coil sub-assemblies. As can be seen, the six units are nearly identical, allowing the use of a single table to calibrate the gain of the sensors

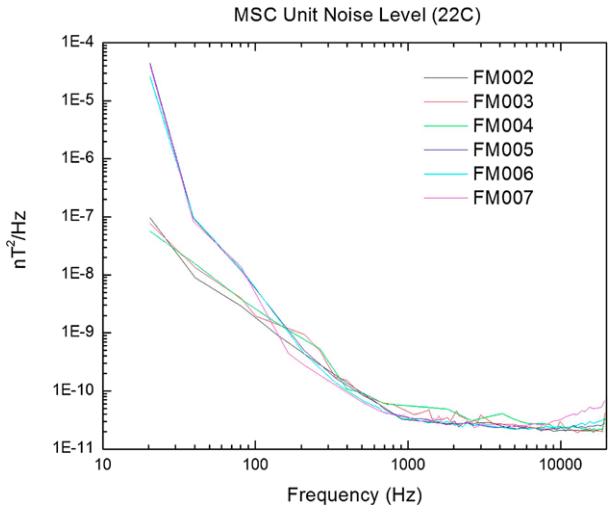

Fig. 16 The measured noise level in the lab at 22 °C of the six single-axis search coil sub-assemblies

delivery to the spacecraft the calibrations were repeated using the flight harness. During a series of interface tests with the EFW instrument, the calibrations were again repeated to verify the interfaces between the EMFISIS and EFW instruments.

Figure 15 shows the resulting transfer functions of all six of the individual, single-axis MSC sense coil and preamp sub-assemblies as well as the average of all six. As can be seen, the six units are very similar (within a fraction of a dB).

Figure 16 shows the Noise Levels measured for of all six MSC units. The difference between the units for Spacecraft A (FM 2, 3, & 4) and Spacecraft B (FM 5, 6, & 7) below about 100 Hz is due to a change in the test setup which provided better grounding of the test equipment during the testing of the units for Spacecraft A and a decrease in background 60 Hz noise, and not due to a differences between the sensors. The in-flight noise levels at low frequency are better than is shown here.

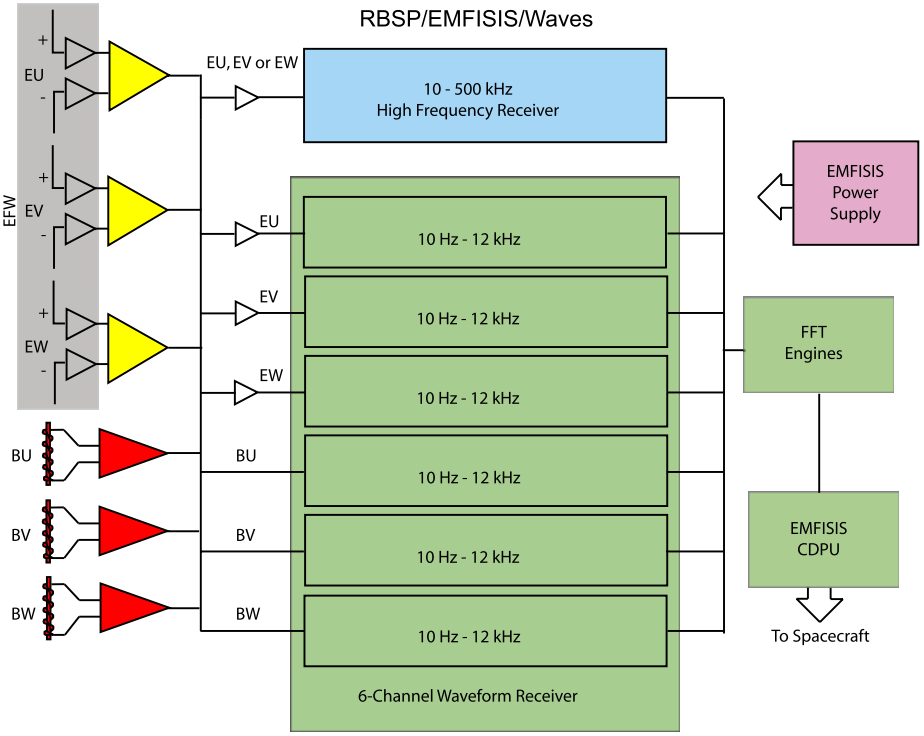

Fig. 17 Waves System Block Diagram

5.2 Waves Receivers

Figure 17 shows a block diagram of the Waves instrument. The six inputs from the sensors are shown on the left. In the middle, the various receivers are shown. The six receivers are identical waveform receivers with flat (to within 1 dB) response from 10 Hz to 12 kHz. Together, they constitute the six-channel Waveform Receiver (WFR). Each receiver consists of a variable gain amplifier followed by a bandpass filter (10 Hz–12 kHz). A 16 bit A/D converter is used to digitize each signal at a sampling rate of 35 kHz.

The primary output of the WFR is a set of six phase-matched waveforms which can be processed in various ways. These continuous waveform samples of a selectable (of up to 6 s) duration can be losslessly compressed by a factor of between 2 and 4 in the Waves FFT Engine coprocessors and stored for transmission to the ground.

The waveform time series comprise the primary burst mode of the Waves instrument. These data can be used for spectrum analysis, spectral matrices, wave normal analysis, and Poynting flux calculations on the ground. Second, the waveforms can be analyzed in the Waves FFT Engine coprocessors to produce spectral matrices similar to those computed on the Cluster STAFF instrument (Cornilleau-Wehrlin et al. 2003) which can be generalized to other instances (Santolik et al. 2001).

The spectral matrix is generated from 468 ms waveforms captured every 6 s and is telemetered to the ground as a regular survey data product, allowing computations of wave normals, Poynting flux, and other propagation characteristics. Another burst mode provides a set of spectral matrices every 30 ms, commensurate with the typical time scale of discrete

chorus elements. All of these data sets include spectral densities as a function of frequency. These can be losslessly compressed and stored for transmission to the ground. These data provide information that will be used for determining the effectiveness of the waves in acceleration, heating, and pitch-angle scattering of radiation belt particles.

The top receiver in the middle of the block diagram in Fig. 17, the High Frequency Receiver (HFR) is designed to provide spectral information from any one of the three EFW electric dipole antennas for the frequency range from 10 kHz to 500 kHz. Typically, one of the spin-plane pair is be used and will be selected on the basis of optimal noise level and sensitivity once on orbit. The HFR consists of a bandpass filter, followed by a variable gain amplifier with two discrete gain settings based on the input signal strength and a 14-bit A/D converter. The bandpass filter covers the range from 10 to 500 kHz, acting as an anti-aliasing filter at 500 kHz. The effective upper frequency response is limited to 400 kHz by the response of the EFW pre-amps driving the series resistance and capacitance of the long cables which connect them to the EFW electronics on the spacecraft. Digitized waveforms from this channel are spectrum analyzed by the digital signal processing electronics in the Waves FFT engines. It is also possible to compress and pass along the waveforms as a burst mode option for storage and eventual transmission to the ground, if desired.

In the plasmasphere and along the plasmapause this high frequency receiver will measure the frequency of the upper hybrid resonance band at f_{uh} which, in turn, provides an accurate measure of the electron plasma frequency, hence, electron density by $n_e = (f_{uh}^2 - f_{ce}^2)/8980^2$ where n_e is in cm^{-3} and the frequencies are in Hz. The electron density is a crucial plasma parameter for modeling and ray tracing. It is also most easily and accurately measured by means of resonances and cutoffs in the wave spectrum rather than particle detector measurements which are subject to spacecraft charging and other complicating factors. Beyond the plasmapause where the f_{uh} band is less distinct or absent, the low-frequency cutoff of nonthermal continuum radiation can be used to determine f_{pe}. The Waves instrument has the capability to determine the electron density along the spacecraft trajectory where densities are $2000/\mathrm{cm}^3$ or lower which covers much of the RBSP orbit. The EFW investigation's spacecraft potential measurements will also provide electron densities, especially at lower altitudes where the electron densities exceed $2000/\mathrm{cm}^3$. The two techniques are complementary and provide an excellent set of tools by which to make this very important measurement.

The primary output of the HFR will be spectral information at a rate of one spectrum every 6 s. However, it is possible to return higher cadence spectra as well waveforms in a burst mode.

5.2.1 Waves Receiver Calibration and Performance

An extensive series of calibrations and instrument performance checks were carried out on the EMFISIS Waves receivers, both before and after integration on the spacecraft. The Waves receivers were calibrated both individually and combined with the MSC sensors (end-to-end) at the University of Iowa. After delivery to the spacecraft, a series of interface tests were performed with the EFW instrument to verify the electrical performance and calibrations through the EFW antenna and preamplifiers, and also through the MSC sensors to EFW. These end-to-end calibrations were compared to the individual sensors and receiver calibrations to verify that the results matched. For both the MSC and the EFW signals, essentially the same end-to-end frequency and phase response was found. However, the EFW axial signal does have a smaller separation and consequently the effects of coupling to the plasma can lead to different response depending on the plasma environment.

Amplitude calibrations for each of the receivers were accomplished by providing an input signal of fixed frequency. The amplitude of the stimulus was decreased in 2 dB increments to

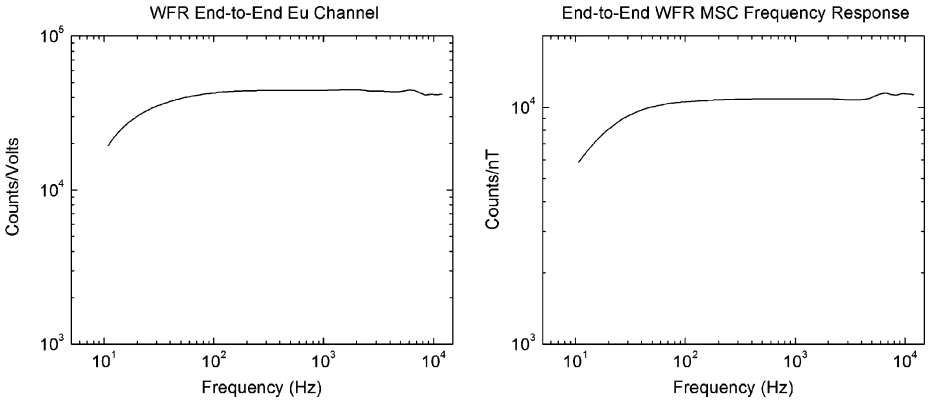

Fig. 18 WFR Electric and Magnetic Channel Frequency Response

cover the full amplitude range of the receiver. Amplitude calibrations were also performed with an input of white noise that was flat over the frequency range of the receiver. Frequency and phase calibrations were accomplished by sweeping an input signal of known amplitude and phase over the frequency range of the receivers. For the WFR receivers, additional calibrations were performed by applying the same white noise and a pseudo-random noise signal to the six receivers. These calibrations are used to construct lookup tables that convert the telemetry data value to the true input signal strength and phase.

Six-Channel Waveform Receiver Calibration The response of the six-channel waveform receivers was determined by applying signals of known frequency, amplitude and phase (sine waves, white noise, and pseudo-random noise) to the receiver inputs, and determining the gain factors required to convert the telemetry values into physical units. These gain factors provide calibrations for the time-series waveform, the onboard spectral matrix calculations, and the spectrum produced by a Fourier transform of the waveform on the ground. The amplitude and frequency response of the six-channel waveform receivers was determined for each attenuator state, and for the two EMFISIS to EFW MSC filter modes. End-to-end calibration checks were performed by repeating the frequency response test and by applying an input signal of white noise with known spectral properties to the input of the electric and magnetic preamplifiers. Figure 18 shows the average frequency response of the three electric (left panel) and three magnetic (right panel) channels of the six-channel waveform receiver for both spacecraft.

High Frequency Receiver Calibration The response of the HFR receiver was determined by applying signals of known frequency and amplitude (both sine waves and white noise) to the receiver inputs, and determining the gain factors required to convert the telemetry values into physical units. These gain factors provide calibrations for the time-series waveform, the onboard spectrum, and the spectrum produced by a Fourier transform of the waveform on the ground. The amplitude response of the HFR receivers was determined for each attenuation state. End-to-end calibration checks were performed by repeating the frequency response test and by applying an input signal of white noise with known spectral properties to the input of the EFW electric preamplifiers and to the MSC sensors. Figure 19 shows the average frequency response of HFR receiver.

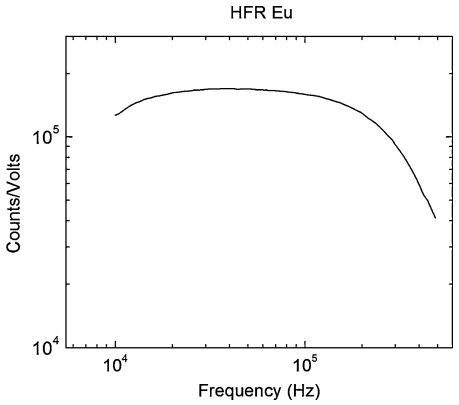

Fig. 19 HFR Frequency Response

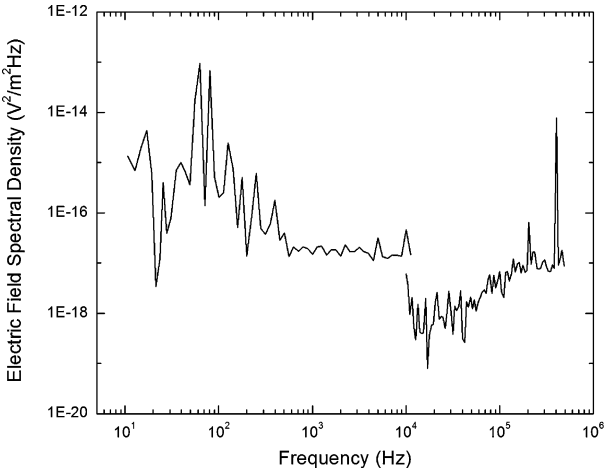

Fig. 20 WFR and HFR Noise Level (E_U–100 meter antenna)

WFR and HFR Receiver Performance Figure 20 shows the noise level of the WFR and HFR receivers attached to the E_U antenna and assuming an antenna length of 100 meters that was obtained on the spacecraft during interface testing with EFW. The noise lines at lower frequencies are believed to be primarily interference from GSE equipment (60 Hz). The overall noise level is much better in flight. The noise line at 400 kHz is a power supply interference line from EFW.

5.3 Waves FFT Engines

The Waves instrument includes four custom designed digital signal co-processors to address the large amount of computationally intensive signal processing required, called the Waves FFT Engine (WvFE) co-processors. These co-processors have been implemented in an Actel field programmable gate array (FPGA) that provides a high level of radiation tolerance, high performance and low power consumption. Nearly identical implementations of this co-processor design have been flown on the Juno Waves investigation as well.

The WvFE co-processors work in tandem with the CDPU, whom manages the scheduling of tasks across the co-processors and reads back the data produced by these tasks. The CDPU performs this management by selecting an available co-processor from the set, writing a task descriptor to the selected co-processor, and then waits for an interrupt to signal the

completion of the task. Once an interrupt is received, the CDPU will read back the results produced by the co-processor and then take subsequent action.

The logical design of the WvFE co-processor is described in a hardware description language (HDL) as a 'system on a chip', where multiple cores (logic elements) are connected together via an internal on-chip bus fabric. These cores are responsible for a number of tasks including the collection of science data, application of digital signal processing techniques and the compression of waveform data. All of the cores in a co-processor are able to access a shared working memory, known as waveform memory, through the on-chip system bus fabric. The waveform memory is used as a storage area for captured waveforms, program code, and partial/final products. The waveform memory is eight megabytes in size and is specific to a co-processor, where each co-processor has its own independent complement of memory to increase overall system bandwidth.

One type of core found in the WvFE co-processor, the A/D controller, is responsible for capturing and pre-processing waveform data. Each co-processor interfaces with the six ADCs on the waveform receiver and a single ADC on the high frequency receiver through its set of A/D controllers. To capture a waveform, an A/D controller core is programmed with the needed size and sample rate of the capture, once initiated the controller begins to sample the waveform channel(s) and converts each sample to a two's complement numbering notation. These pre-processed samples are saved in the co-processors' waveform memory.

Once waveform data is available, several other cores in the WvFE co-processor can now be used to further process the waveform. A Rice compression core capable of losslessly compressing 12-bit or 16-bit integer data provides a method for compressing raw waveforms. To apply signal processing techniques to the captured waveform, the UI's custom designed DSP processor architecture will be used, this is called the Waves FFT Engine core.

The WvFE core is a programmable general-purpose digital signal processor that performs DSP calculation in IEEE 754 single precision floating point arithmetic. The processor is capable of executing two instructions per clock cycle with at a peak performance of 21 million floating-point operations per second (MFLOPS) and 10.5 million integer operations per sec (MIPS) at 21 MHz. The processor's floating-point unit has been implemented as a multiply-accumulate operation that greatly aides in the acceleration of common vector calculations. Several signal processing algorithms have been implemented in programs specific to the WvFE core's instruction set architecture, including waveform windowing, the fast Fourier transform, spectral average and binning, as well as spectral matrix computations. Given the programmable nature of the WvFE core architecture the software executed by the processor defines how it operates. This allows future updates to the software to extend or modify the DSP capabilities of the instrument.

In operation, the WvFE core sets up and then executes the digitization of a set of waveforms, controlling the analog to digital converters on the appropriate receiver board(s). The digitized waveforms are then processed by first applying a Hann window and then the FFT operation. The calibration, in both phase and amplitude, is then applied to the spectral components which are summed into bins (based on a programmable binning table). Following this, the complex cross-multiplication is performed and the spectral matrix and/or the waveforms are made available to the CDPU for transmission to telemetry.

6 The Central Data Processing Unit (CDPU)

The CDPU manages coordinated electromagnetic field data for the entire set of EMFISIS instruments: controlling the intra-instrument timing, the data collection scheme and the interface to the spacecraft data system. Time series data from MAG and Waves, as well as

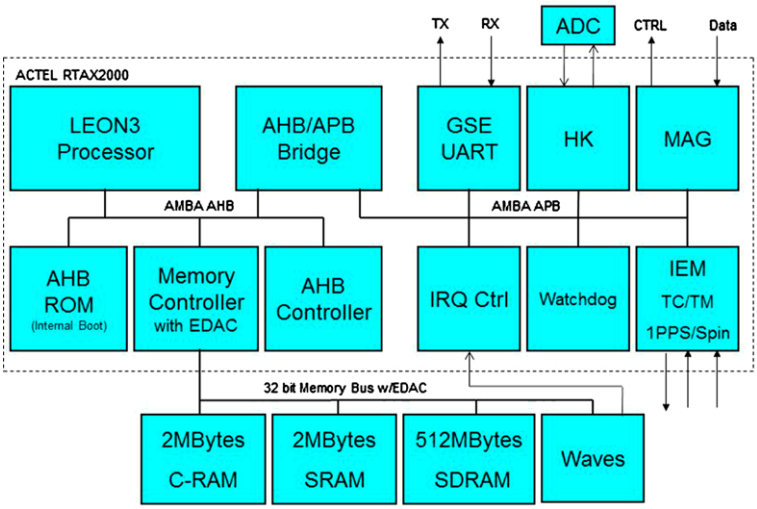

Fig. 21 CDPU block diagram

short burst samples of electric and magnetic field waveforms at higher rates are needed to resolve and identify the detailed physics of wave-particle interactions responsible for radiation belt dynamics, but cannot be transmitted continuously because of telemetry constraints. In addition, spectra are continuously compiled. The Waves FFT boards for both E- and B-field analog data rely heavily on field programmable gate arrays to reduce size and power consumption, yet are radiation tolerant, and will supply both survey and burst data.

The CDPU handles compression of the magnetometer data and intermediate storage of all data before transmission to the spacecraft data system. Data from all EMFISIS components are transmitted digitally across the MEB backplane and are stored in a set of buffers which allows the implementation of both 'survey' mode and 'burst' mode data. The CDPU is capable of detecting trigger signals both from EMFISIS instruments and those external to EMFISIS and manages coordination of data modes with the RBSP particle instruments via BURST messages.

6.1 Heritage

The CDPU is built upon the LEON-III VHDL core implementation of a SPARC processor. The LEON-III core is programmed into an Actel RTAX2000 FPGA which is radiation hardened to >100 krad, latch-up immune (LET > 100 MeV cm^2/mg), and triply-modular-redundant for single event upset (SEU) rejection. The basic design of the system, with 512 Mbytes of volatile burst RAM, is a derivative of units on both ISTP and CLUSTER, but in detail is very similar to units being delivered for the NASA MMS program.

6.2 Functional Description

Figure 21 shows the architecture of the CDPU board. The area inside the box is logic contained inside the RTAX2000. The LEON processor provides the overall control of the data acquisition from the MAG, WAVES, and Housekeeping interfaces. A Finite State Machine (FSM) in the MAG interface directly controls the timing of the mag vector sampling and

presents the vector data to the LEON. The interface to the WAVES system is via memory mapped dual ported SRAM on the FFT boards as well as timing signals to initiate FFT Engine acquisitions. Housekeeping data is measured on the LVPS board and multiplexed to the CDPU's Housekeeping ADC. Spacecraft commands and telemetry as handled by the IEM interface module. FSMs receive telecommands from and transmit telemetry to the IEM. Two telecommands are decoded directly by the receive FSM for system reset with vectored booting, watchdog control, and C-RAM (chalcogenide RAM) write protect. All other telecommands are sent to a FIFO and the LEON is interrupted for processing. Telemetry Instrument Transfer Frames (ITFs) are sent by the LEON to a FIFO and a FSM manages the transmission to the IEM.

The CDPU employs four types of memory: (1) AHBROM, (2) C-RAM, (3) SRAM and (4) SDRAM. A Read Only Memory (AHBROM) is programmed internally to the RTAX2000. The AHBROM contains the boot software for the LEON and a simple interrupt handler which can decode simple telecommands. This provides for a robust operation not requiring any of the external memories of the CDPU. If certain faults occur, the CDPU reverts to this robust mode and waits for ground intervention. The other memories are external to the RTAS2000. 2 Mbytes of BAE C-RAM are used for storage of LEON and FFT Engine programs, as well as tables of control information. C-RAM is a new technology which is a replacement for legacy EEPROM devices. C-RAM has a high radiation tolerance (>1 MRAD) and fast write cycles. Fast write timing precludes the software algorithms required for EEPROMs. 2 Mbytes of SRAM are used for temporary storage and program execution scratch space. 512 Mbytes of SDRAM allow for storage of large quantities of high rate burst data and slow transmission to the ground of high value data. All memories utilize EDAC protection from SEU data corruption. The LEON provides a background task to scrub the volatile memories to detect and correct any SEUs which may occur.

6.2.1 EMFISIS Onboard Data Flow

Command Processing Every second, the IEM transmits an Instrument Transfer Frame (ITF) to EMFISIS. Upon receipt of an ITF, the CDPU triggers a non-maskable interrupt (NMI). The NMI Interrupt service routine (ISR) transfers the ITF from the command FIFO to a buffer in SRAM and sets a flag to announce its arrival. The Real Time Interrupt (RTI) executes at 64 Hz and it checks for the ITF arrival flag. If found, it starts the Command task to process the IFT. The Command task parses and executes commands. Time-consuming commands are handled by the Test Task which is started when such a command is executed. Only one "Test" may be executed at a time. Other "Tests" will be flagged as errors.

Telemetry Generation Telemetry is sent from EMFISIS to the IEM via Instrument Transfer Frames (ITF). Each ITF consists of a header and a series of CCSDS data packets. The ITF format is described in the RBSP IEM to EMFISIS ICD and The EMFISIS Users Manual.

Upon receipt of the 1 PPS interrupt, an ITF is generated containing one HK packet and as many other packets as are available in the Survey or Burst buffers. Each ITF is limited to <4096 bytes and up to 3 ITFs are sent between 1PPS interrupts. Only the first ITF will contain an HK packet and will toggle the Heartbeat Flag. The 64 Hz RTI resumes the Packet task. If any data is ready for packetization the packet task collects the data and places the CCSDS packets in the Survey or Burst Buffers as appropriate. The Survey Buffer is usually emptied on every ITF. There may be a need to buffer Survey data briefly if large Burst packets span ITFs but then the buffered Survey data will catch up on the next ITF. The Survey (WAVES + MAG) telemetry allocation is 9 kbps. Since each ITF can handle 4096 bytes ($= 32$ kbps) of survey data it will not backlog for long.

Data Buffering There are currently 3 data buffers implemented:

1. Survey CCSDS packets
2. Burst CCSDS Packets
3. Burst Waveform Event Capture buffer

The Survey buffer is allocated in SRAM. The Burst Buffer and Event Buffer are allocated in SDRAM. These are circular buffers that are not permitted to overrun. If a Survey Packet spans the ITF then no Burst data is sent. Only Survey or Burst data can span an ITF, not both. When an Event has been captured and is selected for download, it is transferred into the Burst Buffer.

Waves Interface The WAVES programs operate synchronous to the 64 Hz interval and all modes operate on a 6 s cycle divided into 384 intervals. Any WAVES operation can be configured to start on a given phase (0–383) and be repeated after the specified number of intervals. The configuration parameters for a given operation are loaded into a WAVES FFT engine Job Control Block during the interval preceding the desired operation. The FFT engine will execute the configured "program" beginning on the next 64 Hz pulse. When the program is completed, the FFT engine generates an interrupt to the CDPU. The Job Control Block identifies the type of data, size and locations to be fetched from the FFT Engine and packetized for telemetry or Burst buffering.

7 EMFISIS Operational Modes

This section describes the science modes implemented in the CDPU for the EMFISIS investigation. The data consists of two separate types: Magnetometer data and Waves data. The former is simple and constant: 64 vectors per second, in one of three ranges, and are transmitted in losslessly compressed form in all states of instrument operation. The latter is more complex and varied. The various Waves modes span a wide range of telemetry rates, including a basic survey mode which is always running plus a variety of burst modes that provide high time resolution samples. Because the burst modes exceed the average Waves telemetry allocation, these can only be used for limited intervals so that the average Waves telemetry production does not exceed its allocation averaged over a time interval of the order of one week. That is, burst data may be acquired over a relatively short interval of less than an hour, but take as much as a week to be telemetered to the ground. Typically, however, the burst data will be distributed more evenly, with some bursts scheduled each day or perhaps even each orbit. The combination of the Waves FFT engines and EMFISIS CDPU allows for a large range of modes that can be used for various scientific objectives on RBSP and can be updated and changed in flight. The modes listed below represent a reasonable first set and demonstrate the capabilities of the instrument. It is anticipated that variations of these can be defined in-flight by setting various parameters in the CDPU. These Waves modes are summarized in Table 2.

7.1 Common Features of Waves Science Modes

Each of the Waves science modes described here have the following common features:

Table 2 Summary of nominal Waves modes and associated telemetry rates

Mode	Telemetry rate (kbps)	Comments
Survey	7.5	Includes 0.5 s waveforms every 15 minutes
Fast Survey	≈65	Includes 0.5 s waveforms every 30 s
Waveform Burst with Wave Summaries	1260	Includes waveforms with 93.6 % duty cycle
Waveform Burst with Spectral Matrices	1265	Includes waveforms with 93.6 % duty cycle
Continuous Waveform Burst	1300	Waveforms only with 99.4 % duty cycle
30 ms Wave Summaries	190	Includes 0.5 s waveforms every 30 s
30 ms Spectral Matrices	1295	Includes 0.5 s waveforms every 30 s

High Frequency Spectrum Each of the science modes includes a high frequency spectrum every 6 s. The high frequency spectrum is derived from the Wave High Frequency Receiver (HFR) and covers the frequency range from 10 to 500 kHz with limited response above 400 kHz due to roll-off of the EFW signals. A 14-bit A/D converter is used to sample the waveform in this passband at a rate of 1.25 million samples per second (1.25 Msps). Blocks of 4096 samples are collected and analyzed on-board using a fast Fourier transform (FFT), yielding a spectrum with frequency spacing of ≈305 Hz. Subsequently, the samples are binned into quasi-logarithmically-spaced bins with a spectral resolution of about 50 channels per decade. A programmable number of N waveforms (nominally 6) are analyzed within a 0.5 s interval and the results are averaged within the spectral bins to increase the signal-to-noise ratio. All processing is carried out in one of the Waves FFT engines. The results are stored in 16-bit truncated floating point values and packaged by the CDPU for intermediate storage in the EMFISIS Mass Memory (MM) for eventual transmission to the RBSP data system and, subsequently, to the ground.

Compressed Waveforms Since each mode includes survey information relying on on-board processing (either spectral matrices or wave property summaries), all modes periodically include 'dual-routed' compressed waveforms. Dual-routed means that the same waveform data used on-board to compute either spectral matrices or wave property summaries are also included in the downlinked telemetry so that the on-board processing can be validated. The waveforms comprise 6 simultaneously-sampled channels (3 electric and 3 magnetic), each consisting of 16 k samples with 16-bit resolution over a bandpass of 10 Hz to 12 kHz. The sample rate is 35,000 samples per second. Hence, each set of waveforms covers a 0.468 s interval. The spectral resolution afforded by the waveforms is, therefore, approximately 2 Hz if the entire 16-k block is Fourier transformed. Alternately, the blocks can be broken into shorter series (e.g. 1 k blocks) on the ground, allowing greater time resolution for the analysis of, for example, chorus. The waveforms are losslessly compressed by a Rice compression scheme implemented in the Waves FFT engines. The compressed waveforms are delivered to the CDPU for intermediate storage in the EMFISIS mass memory for eventual transmission to the spacecraft and, subsequently, to the ground. For each survey mode, the 0.468 s waveform captures are performed every nth 6 s instrument cycle. For survey modes other than the standard survey mode, the nominal value of n is 5, hence, one waveform data set is returned every 30 s, for a duty cycle of 1.6 %. However, for the standard survey modes, n is 150, hence, one waveform data set is returned every 15 minutes, for a duty cycle of 0.05 %. For the Fast Survey mode, n is 5, or a waveform data set every 30 s, giving a duty cycle of 1.6 %. The value of n is a variable that can be adjusted on the basis of in-flight experience.

Low Frequency Wave Information All instrument modes include information on the spectrum and wave mode of waves in the range of 10 Hz to 12 kHz. While raw waveforms allow for the maximum flexibility in ground processing and analysis, the data rate required for these is prohibitive except for a very small percentage of time in any given day. In fact, the Waves telemetry allocation is geared to allow a continuous set of waveform data covering only 30 minutes every three 9 hour orbits (approximately 1 day). Therefore, a more bit-efficient method of transmitting the wave information is required. There are two options afforded by the EMFISIS instrument.

First, spectral matrices can be calculated on-board and the results binned into quasi-logarithmically-spaced frequency bins at a resolution of about 20 bins per decade in frequency. For the frequency range 10 Hz to 12 kHz, this results in 61 channels (with 4 channels between 2 and 10 Hz). Spectral matrices include auto-correlations of each channel (e.g. $E_i E_i^*$ and $B_i B_i^*$ for $i = U, V, W$) as well as cross-correlations between each pair of sensors resulting in 6 real and 15 complex quantities (since the matrix is symmetric, only half of the off-diagonal terms need be computed; that is, $E_U E_V^* = E_v E_U^*$. Hence, the quantities computed on-board are:

$$
\begin{array}{llllll}
E_U E_U^* & E_U E_V^* & E_U E_W^* & E_U B_U^* & E_U B_V^* & E_U B_W^* \\
E_V E_V^* & E_V E_W^* & E_V B_U^* & E_V B_V^* & E_V B_W^* & \\
E_W E_W^* & E_W B_U^* & E_W B_V^* & E_W B_W^* & & \\
B_U B_U^* & B_U B_V^* & B_U B_W^* & & & \\
B_V B_V^* & B_V B_W^* & & & & \\
B_W B_W^* & & & & &
\end{array}
$$

The quantities in the first column are real and the remaining ones are complex. The real values provide the spectral density in each of the electric and magnetic orthogonal coordinates and can be summed to give the full wave electric and magnetic spectral density as a function of frequency. The off-diagonal terms are used by various algorithms on the ground to determine the wave normal angle, polarization, Poynting flux, etc. Having the spectral matrix on the ground allows for the use of different analysis algorithms. The spectral matrices require a number of computations, including calibration of the signals, despinning of the measurements over the $\approx$0.5 s collection period (since the spacecraft rotates $\approx$15° during the collection period), Fourier transforms, the auto- and cross-correlations, and the binning and averaging within spectral bins. All of these are performed in the Waves FFT engines. Each autocorrelation is represented by a 16-bit value and each complex cross-correlation is represented by a 16-bit real value and 16-bit imaginary value. The binned spectral matrices are sent to the CDPU for intermediate storage in the EMFISIS mass memory for eventual transmission to the spacecraft and, subsequently, to the ground.

All modes with spectral matrices in the mode name plus the Survey mode include spectral matrices at least every 6 s instrument cycle, occurring in the same half-second as the high frequency spectrum. In all survey modes including spectral matrices, the spectral matrices are calculated from 16-k waveform blocks. The 16-k blocks afford reasonable spectral resolution in the lower part of the 10 Hz–12 kHz band, but do not allow for high temporal resolution (sub-half-second) that is required for the proper determination of the propagation characteristics of individual chorus elements (although the matrices include valid information on the chorus spectrum averaged over $\approx$0.5 s). The temporal and spectral resolution, however, is thought to be adequate for EMIC waves, plasmaspheric hiss, and similar emissions displaying a more slowly varying spectrum.

Second, the spectral matrices can be used as input to further on-board processing to calculate a set of wave property summaries for the waves. The primary benefit of this is that

the wave property summaries can be telemetered to the ground with significantly fewer bits (of order 90 % less) than the spectral matrices. However there is no way to apply different analysis algorithms to the measurements once these parameters have been calculated on-board as the computations are irreversible. And, it is known that any given algorithm, e.g. the Means method for wave normal analysis, may not work under certain conditions. This is a primary reason why some waveforms are 'dual-routed' in each mode so that the results of the on-board analysis can be validated for a fraction of the measurements.

The wave parameters included in the wave parameter summaries include E^2, B^2, two wave-normal angles, a measure of the planarity of the waves, the ellipticity and polarization sense (Santolik et al. 2003), and the parallel component of the Poynting flux. The spectral matrices are computed in the Waves FFT engine and the CDPU computes the wave property summaries. All modes with wave summaries in the mode name include wave parameter summaries at least every 6 s instrument cycle, occurring in the same half-second as the high frequency spectrum. In all survey modes including wave summaries, the wave parameters are calculated from 16-k waveform blocks.

7.2 Descriptions of Waves Science Modes

The following descriptions give the details of the primary modes of operation of the EMFISIS investigation.

Survey This mode includes a high frequency spectrum and a set of spectral matrices every 6 s. In addition, it includes a set of compressed waveforms every 150 six-second instrument cycles. All three types of data of this mode are acquired during the same half-second interval. The parameter n (nominally set to 150) which sets the repetition rate for the compressed waveforms is a variable to allow variations in the telemetry rate for this mode, depending on in-flight experience with how often the on-board processing needs to be validated. This mode is expected to be the primary survey mode for the mission.

It should be mentioned that an even lower data rate survey mode could be envisioned that substitutes the wave parameter summaries described in Sect. 7.1 for the spectral matrices, however, it would be necessary to gain significant in-flight experience with the spectral matrices to understand how regularly the on-board computation of the wave summaries yield valid results, based on ground simulation of the on-board algorithms. Should this yield be high, and if the conditions under which the on-board algorithms are successful can be reasonably well understood, then a substitution of wave summaries for the spectral matrices would be considered. Such a mode can be implemented on orbit by minor changes to the mode configuration setup.

Fast Survey This mode includes a high frequency spectrum from the HFR receiver every 0.5 s and a set of spectral matrices from the WFR receivers every second. In addition, its nominal setup includes compressed waveforms every 30 one-second instrument cycles. The rate at which the waveforms are sent is an adjustable parameter, allowing variation from the nominal rate.

Waveform Burst with Wave Summaries This mode includes a high frequency spectrum and a set of wave summaries every 6 s. In addition it includes compressed waveforms every five 6 s instrument cycles. The high frequency spectrum and wave summaries are acquired during the same half-second interval. In addition, a 0.468 s set of compressed waveforms is captured every 0.5 s. Hence, every 12th set of compressed waveforms is obtained simultaneously with

a set of wave summaries. Another version of the mode replaces the continuous waveforms for 5.968 s between each 6 s survey data set. This is referred to as continuous waveform burst mode.

Waveform Burst with Spectral Matrices This mode includes a high frequency spectrum and a set of spectral matrices every 6 s. In addition it includes compressed waveforms every 5 six-second instrument cycles. The high frequency spectrum and spectral matrices are acquired during the same half-second interval. In addition, a 0.468 s set of compressed waveforms is captured every 0.5 s. Hence, every 12th set of compressed waveforms is obtained simultaneously with a set of spectral matrices.

Continuous Waveform Burst Mode This mode is very similar to the Waveform Burst with Spectral Matrices Mode in that it produces a standard survey set of spectral matrices every based on a 0.5 s waveform capture every 6 s. In addition. this mode captures a continuous waveforms for 5.968 s between each 6 s survey data set, leaving a 0.032 s gap between successive captures. This mode can be operated continuously for fixed durations up to several minutes. Alternatively it can be used in conjunction with burst quality flags that retain the best N 5.968 s captures ($N \leq 20$) in a pre-set time interval.

30 ms Wave Summaries This mode is based on the survey with wave summaries mode in that it includes a high frequency spectrum and a set of wave summaries every 6 s. In addition it includes compressed waveforms every 5 six-second instrument cycles. All of the data types in this mode are acquired during the same half-second interval. The parameter n (currently set to 5) which sets the repetition rate for compressed waveforms will be a variable to allow variations in the telemetry rate for this mode, depending on in-flight experience with how often the on-board processing needs to be validated. In addition to the survey data, the mode includes high rate wave summaries at a rate of 1 set per 30 ms. The wave summaries are based on 1k blocks (30 ms) of waveform data and the frequency bins are linear, with spacing of about 150 Hz. The purpose of this mode is to provide high temporal resolution information on the propagation characteristics of chorus, whose individual elements have time scales of order 30 ms. The processing includes tests of planarity and coherency, hence, properties other than E^2 and B^2 need not be returned if these tests fail, reducing the required telemetry. The rates estimated for this mode assume that 75 % of the frequency-time bins fail these tests, hence, only the spectral densities are returned for those bins. With verification that the on-board algorithms are reliable, this mode will provide propagation information on discrete chorus structures over a much longer time interval than afforded by the very high telemetry rates of the waveform burst modes.

30 ms Spectral Matrices This mode is based on the survey mode in that it includes a high frequency spectrum and a set of spectral matrices every 6 s. In addition it includes compressed waveforms every 5 six-second instrument cycles. All of the data types in this mode are acquired during the same half-second interval. The parameter n (currently set to 5) which sets the repetition rate for compressed waveforms will be a variable to allow variations in the telemetry rate for this mode, depending on in-flight experience with how often the on-board processing needs to be validated. In addition to the survey data, the mode includes high rate spectral matrices at a rate of 1 set per 30 ms. The spectral matrices are based on 1k blocks (30 ms) of waveform data and the frequency bins are linear, with spacing of about 150 Hz.

The purpose of this mode is to provide high temporal resolution information on the propagation characteristics of chorus, whose individual elements have time scales of order 30 ms.

Chorus is typically found in the frequency range of 0.1 to 0.7 f_{ce} (f_{ce} = electron cyclotron frequency where f_{ce} [Hz] = 28|B| [nT]). Hence, the telemetry may be reduced by returning only those frequency bins in this frequency range. |B| is a function of radial distance, among other things, therefore, these data volume savings are also a function of position. The telemetry rates assume a worst case spectral range of 1.6 to 12 kHz, or, 69 frequency bins. Since the spectral matrices are more efficient in telemetry than the waveform burst modes, this mode can be used to extend the time interval over which the propagation characteristics of discrete chorus elements are determined. The spectral matrices allow for various types of analysis on the ground that are not afforded by the high time resolution wave summaries in the 30 ms Wave Summaries mode and may allow recovery of wave propagation information where the on-board algorithm fails.

8 EMFISIS Data: Reduction, Products, Distribution, and Archiving

8.1 RBSP EMFISIS/MAG Instrument Data Processing

Telemetry allocations permitted the early adoption of a simple operation model for the RBSP EMFISIS/MAG instrument. Specifically, there is only one instrument mode so that the instrument functions in the same manner collecting data at the same rate at all times. However, there are four different data forms (channels) that are dictated by the needs of the EMFISIS central processor and by the needs of the spacecraft to obtain usable MAG data in the event that the central processor should fail. Each data channel is assigned a unique identifier to ensure proper processing. EMFISIS MAG data is processed in a day-by-day manner without reference to data from prior or subsequent days.

Data Description The EMFISIS/MAG instrument makes 64 vector/s measurements at all times in the unrectified (nonorthogonal) coordinate system known as "MAG sensor" MAG maintains its own internal clock to divide the spacecraft 1 s clock into 64 equal intervals.

MAG Data Reconstruction Although the MAG instrument should run continuously, there may be data gaps in telemetry. The first step in data processing is to reconstruct the true spacecraft clock time as a combination of the spacecraft MET time and the MAG clock time. The second step is to identify data gaps and fill them with data flagged as bad or missing. This adds a processing flag (ifillflag) that marks 1 s packets of missing or fill data. In the process, we check for possible data packets containing time tags but no usable data and data out of range for any reason, both of which are flagged as fill. Compressed data are decompressed. Failsafe data, packets are completed with out-of-range fill values to the extent they are incomplete packets. EMFISIS/MAG data are processed one packet at a time. Any merger of packet types is performed as a post-process only. This first step in data processing is designed to provide the end user with guaranteed contiguous data products.

Application of Calibration and Sensor Axis Alignment The three internal axis sensors are not perfectly rectified or aligned with the nominal UVW axis directions. Two rotation matrices are measured in the lab and applied to the measurements in flight:

$$B_{sensor} = A_1 G R_{ortho}(C - Z)$$

where C is a three-element vector of the 16-bit raw data counts, Z is a three-element vector applied to the counts to remove any offset relative to 0 (range dependent), R_{ortho} is a

3×3 matrix to create an orthogonal coordinate system from the three internal sensor directions (independent of range), G is a three-element vector that converts zero-corrected counts to nT (range dependent), and A_1 is a rigid rotation matrix to rotate the sensor coordinate system to the nominal (UVW) science payload coordinate system assuming perfect magnetometer boom alignment. However, it is not perfectly aligned, and therefore an additional rigid rotation matrix A_2 is required to complete rotation of the measured field to (U, V, W) coordinates:

$$B_{UVW} = A_2 B_{sensor}.$$

All of these matrices are pre-determined in the laboratory before flight. Only the product of these can be determined in flight.

Coordinate Rotation Once the MAG data is obtained in physical units in the (U, V, W) science payload coordinate system it is a simple matter to rotate to other useful coordinate systems. The first of these is the spacecraft payload system (X, Y, Z) which is a 35 degree rotation from (U, V, W). This is useful mainly for diagnostic purposes and will not be made available to the general public unless requested. Science coordinate systems include GSE, GSM, SM, GEI and GEO.

Payload Coordinate Data Products In order to facilitate any magnetic field needs by other instruments on the spacecraft, EMFISIS/MAG will provide data at full 64 vector/sec resolution in (U, V, W) science payload coordinates.

Science Data Products EMFISIS/MAG plans to provide a broad range of data products providing ambient magnetic field data in a variety of coordinate systems and time resolutions. Time resolutions are the full 64 vectors/sec as well as 4 s averages where averaging intervals are aligned with packet boundaries. Daily graphs of the science data are planned using IDL in a fully automated form. These will include spacecraft location and magnetic field predictions for one or more storm time expectations as an aid in assessing the data graphed. Multi-panel spectrograms will also be created including the power, polarization, and ellipticity of the magnetic fluctuations.

8.1.1 MAG Data Example

Figure 22 shows an example of MAG data from October 31, 2013 when the RBSP-A spacecraft was near apogee. The data are in the GSM coordinate system and present an example of a sudden depolarization of the Earth's magnetic field as indicated by rapid increase in the magnitude of the z component around 15:40 UT. This rapid field change is followed by low frequency wave signatures which suggest both ULF and EMIC waves were driven as a result.

8.2 Waves Data Reduction and Products

The Waves data products will be released as a set of files in Common Data Format (CDF) format. The data will be time-ordered and non-duplicating, and the Level 1 and 2 products will be limited to a single data product per file. The following list describes each of the Waves data products, and the types of primary data that will be found in each.

1. 30 ms Spectral Matrices (APID 0x2b5)—component spectrograms, 70 frequencies sampled at 35 kHz.

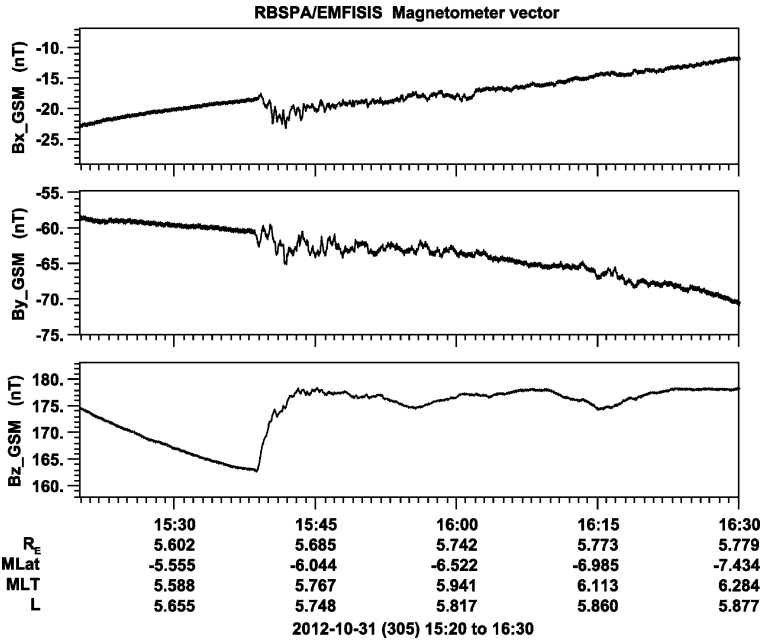

Fig. 22 Example of MAG data from the RBSP-A spacecraft on October 31, 2012 in GSM coordinates

- $B_U B_U$, $B_V B_V$, $B_W B_W$—Autocorrelation of this component, nT^2/Hz
- $E_U E_U$, $E_V E_V$, $E_W E_W$—Autocorrelation of this component, $(V/m)^2$/Hz
- $B_U B_V$, $B_U B_W$, $B_V B_W$—Cross multiply of components, nT^2/Hz (complex)
- $E_U E_V$, $E_U E_W$, $E_V E_W$—Cross multiply of components, $(V/m)^2$/Hz (complex)
- $B_U E_U$, $B_U E_V$, $B_U E_W$, $B_V E_U$, $B_V E_W$, $B_V E_W$, $B_W E_U$, $B_W E_V$, $B_W E_W$—Cross multiply of components, nT (V/m)/Hz (complex)

2. WFR Spectral Matrices (APID 0x2b2)—spectrograms, 65 frequencies
   - Same as 30 ms mode.
3. WFR Spectral Matrices, burst-mode (APID 0x2b3)—spectrograms, 65 frequencies
   - Same as 30 ms mode.
4. HFR Spectra (APID 0x2a1)—spectrograms, 82 frequencies
   - HFR_Spectra—Autocorrelation single E component, $(V/m)^2$/Hz
5. HFR Spectra Burst (APID 0x2a3)—spectrograms, 82 frequencies
   - HFR_Spectra—Autocorrelation single E component, $(V/m)^2$/Hz
6. HFR Waveforms (APID 0x2a0)
   - HFR Samples—Electric field, V/m
7. WFR Waveform (APID 0x2b0)
   - B_U, B_V, B_W—Magnetic field, nT
   - E_U, E_V, E_W—Electric field, V/m

8. WFR Waveform Burst (APID 0x2b4)
   - B_U, B_V, B_W—Magnetic field, nT
   - E_U, E_V, E_W—Electric field, V/m
9. WFR Waveform Continuous Burst (APID 0x2b8)
   - B_U, B_V, B_W—Magnetic field, nT
   - E_U, E_V, E_W—Electric field, V/m
10. Wave Normal Analysis (APID 0x2b6)
   - B^2—Squared magnetic field magnitude, nT^2/Hz
   - E^2—Squared electric field magnitude, $(V/m)^2$/Hz
   - S_x—Poynting Vector , W/m^2
   - S_y—Poynting Vector, W/m^2
   - S_z—Poynting Vector , W/m^2
   - Magnetic eigenvectors and eigenvalues—arbitrary units with component values for vectors.

In addition, each data L0 product contains the following meta-data:

- LWEzGainW—0 = normal, 1 = attenuated (19 dB)
- LWExEyGainUV—0 = normal, 1 = attenuated (19 dB)
- HBGain—0 = normal, 1 = attenuated (19 dB)
- HBSelect—0 = U, 1 = V, 2 = W, 3 = unused
- SCMBW—0 = normal, 1 = limited
- SCMGain—0 = normal, 1 = attenuated (19 dB)
- ADCPWR—0 = on, 1 = off
- waveformChannel—0 = WFR B_X (U), 1 = WFR B_Y (V), 2 = WFR B_Z (W), 3 = WFR E_X (U), 4 = WFR E_Y (V), 5 = WFR E_Z (W), 6 = HFR—Channel selected by HBSelect, 7 = N/A
- sunPulseTimeTag—Bits 21:16 = seconds (6 lsb of MET), Bits 15:0 = subseconds (50 microseconds/bit)
- MET—Mission Elapsed Time

QL files, and higher level files such L2 and L3 files, contain subsets of these meta-data as appropriate for the data contained in the file. For example, WFR attenuator data are not included in higher level HFR files.

8.2.1 Waves Data Examples

Figure 23 shows an example of the three types of survey mode data returned by the EMFISIS Waves instrument on Van Allen Probe B on November 17–18, 2013. The top panel shows the HFR spectral data from 10–400 kHz. Clearly evident is the upper hybrid line which drops rapidly at the plasmapause due to rapidly decreasing plasma density. Several other wave modes are also present during this active time. The middle and bottom panels show the WFR electric and magnetic spectral data for 10 Hz to 12 kHz. The narrow feature above 700 Hz is whistler mode chorus and the lower frequency feature seen within the plasmasphere (before 20:00 and after 01:50) is plasmaspheric hiss.

Figure 24 shows an example of a six-channel waveform capture which has been Fourier transformed into spectrogram form. The data are from a snapshot near apogee when the spacecraft was south of the magnetic equator and located slightly before local dawn. The top

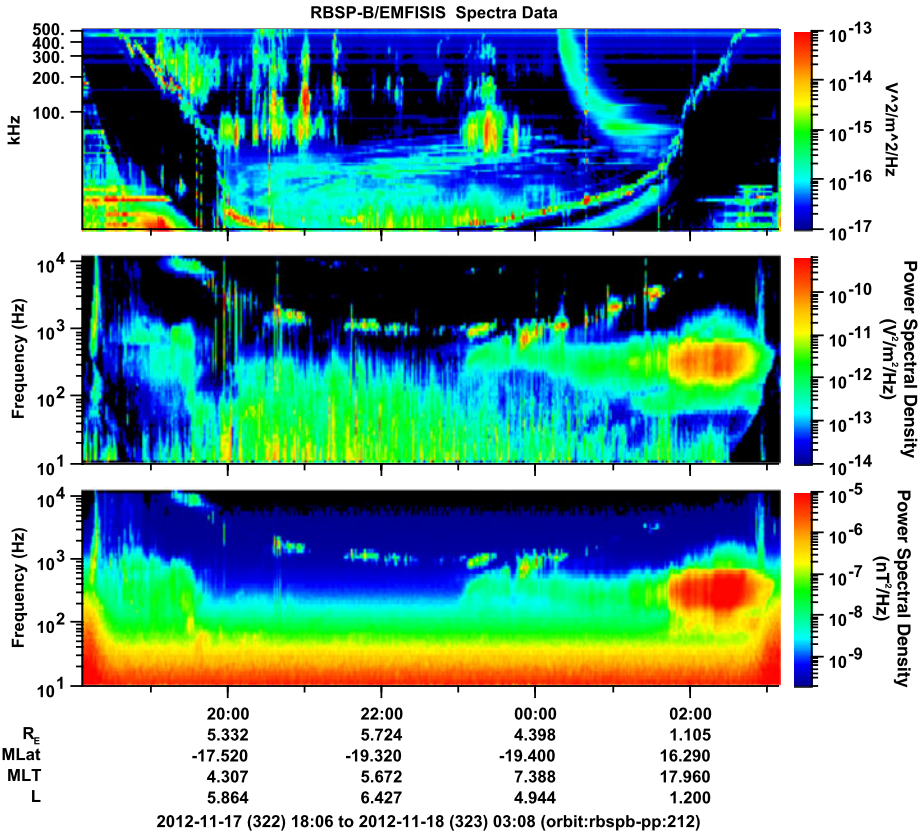

Fig. 23 Example of Waves survey data from November 17–18, 2012. The *top panel* is the HFR data from 10 kHz to 400 kHz, the *middle panel* is the electric field WFR data from 10 Hz to 12 kHz, and the *bottom panel* is magnetic field WFR data from 10 Hz to 12 kHz

three panels show the three components of the magnetic field in spacecraft science coordinates, and the lower three panels show the electric field in spacecraft science coordinates. This high time resolution data reveals whistler mode chorus elements with structure of the order of tens of ms.

Figure 25 shows an example of the derived wave parameters for the same data shown in Fig. 24 The top panel shows the total magnetic field measured by the magnetic search coil and calculated using the sum of the squares of the diagonal elements of the spectral matrix calculated from the waveforms. The middle panel shows the wave-normal vector (k-vector) calculated from the spectral full matrix including both E and B. As can be seen, the wave normal direction is typically less than 20–30 degrees for the chorus elements, but there are some spectral components which have wave normal vectors of up to 60 degrees. The bottom panel of Fig. 25, shows the Poynting flux which is predominantly field-aligned at 180 degrees. This corresponds to propagation in the poleward direction, that is, southward away from the equator.

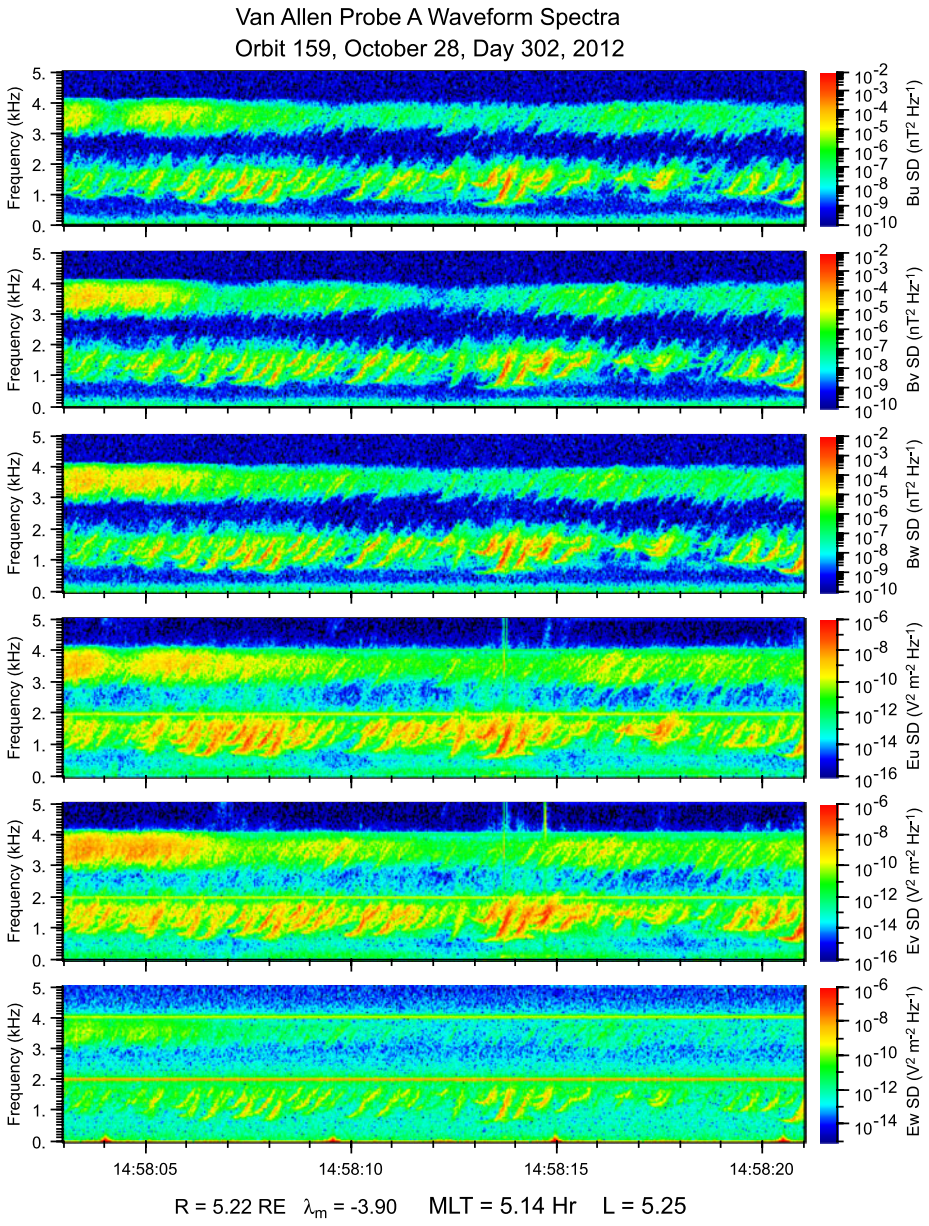

Fig. 24 Example of six-channel waveform data that has been Fourier transformed to produced high time resolution spectrograms

8.3 Data Distribution

Level 0 (L0) data products obtained from the Mission Operations Center (MOC) and base-level calibrated Level 1 (L1) data products created by EMFISIS software at the University of Iowa (see Sect. 8.4, below) are made available to the EMFISIS team members, primarily

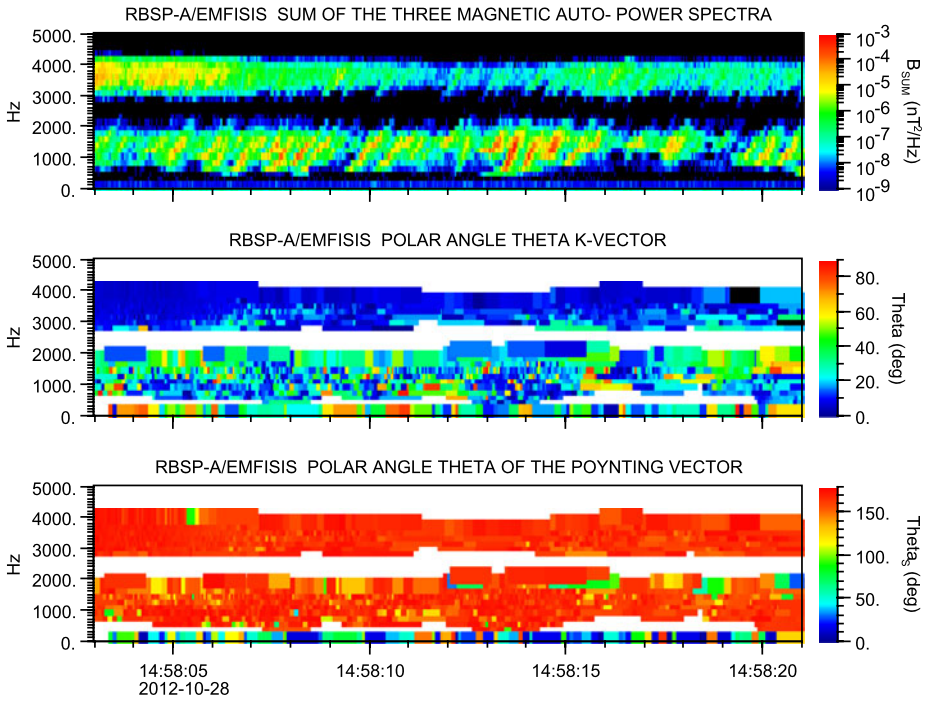

Fig. 25 Wave parameters showing the wave normal direction (*middle panel*) and Poynting vector (*bottom panel*) for the same time interval of the six-channel waveform capture shown in Fig. 24

for the purpose of creating higher-level scientific products, and secondarily for analysis and testing of the EMFISIS instrument and its subsystems.

L0 magnetometer products are sent to Dr. Charles Smith at the University of New Hampshire (UNH) for conversion into quick-look data products and higher-level L2, L3, and L4 products. As part of this process, an internal L1 product is created which remains at UNH. These products are then pulled back to the Science Analysis Science Operations Center (SASOC) at the University of Iowa, and made available to team members and the public on the EMFISIS website.

L0 Waves instrument products are converted from raw PTP products to time-tagged uncalibrated L1 Common Data Format (CDF) data products at the University of Iowa (UI). Calibrations are applied to L1 CDFs at UI to further process them into scientific Level 2 (L2) CDFs. All L2 and higher level data products will be made available to the public on the schedule shown in Table 3.

The primary method of access to the EMFISIS data will be the SASOC web server located at http://emfisis.physics.uiowa.edu/. All data products at those levels will be in the ISTP-compliant Common Data Format (CDF) format, details for which can be found at the NASA Space Physics Data Facility web site.

8.4 Archiving

In addition to storing EMFISIS products indefinitely at the SASOC website listed in Sect. 8.3, all EMFISIS products L2 and higher will be available through the NASA SPDF

Table 3 EMFISIS data definitions

Data level	Product title	Contents	Volume	Format	Latency	Frequency
L0	Raw telemetry	Raw EMFISIS data including both science and HK data	500 Mbytes per day per spacecraft	Binary/ISTP Compliant CDF	Minutes from availability at MOC (T_0)	Daily
L1	Time series and spectra; Burst data, Time series and spectra (relative amplitudes); Burst data	Calibrated DC Magnetic Field values (calibrated and corrected physical units)	750 Mbytes per day per spacecraft	ISTP Compliant CDF	$T_0+ < 8$ days	Daily
L2	Calibrated time series, spectra and burst data	Spectral quantities (calibrated and corrected physical units); Includes low frequency spectra from MAG	850 Mbytes per day per spacecraft	ISTP Compliant CDF	$T_0+ < 60$ days (14 days for MAG)	Daily
L3	Lower level derived products	Magnetic wave parameters	850 Mbytes per day per spacecraft	ISTP Compliant CDF	$T_0+ < 4$ months	Daily
L4	Higher level derived products	Wave propagation parameters (spectral matrices, WNA, polarization, Poynting flux, etc.); Electron densities	1250 Mbytes per day per spacecraft	ISTP Compliant CDF	$T_0+ < 1$ year	Daily

data archive (http://spdf.gsfc.nasa.gov/). Long-term archival through either optical or hard drive media will be evaluated on a yearly basis once RBSP is on-orbit.

8.5 EMFISIS Data Tools

8.5.1 Data-Processing Tools

All EMFISIS data processing code will be made available at the EMFISIS SOC web site (http://emfisis.physics.uiowa.edu) for examination by the public. These programs are used to convert data from low-level telemetry into functional data formats, to apply calibrations, and to produce higher-level derived products.

The primary EMFISIS software library is a collection of Java classes that unpack the PTP telemetry formatted files from the MOC, further decode the CCSDS packets contained therein, and write their EMFISIS data payloads in CDF format. Additionally, the L0 files use Mission Elapsed Time (MET) from the spacecraft, which is converted using SPICE kernels into UTC time. The L1 data products, with the exception of magnetometer data, are in uncalibrated abstract units. L1 to L2 data file conversion primarily applies calibrations

and produces data products in physical units. Additionally, data files containing both survey and burst data may be combined into a single additional data file for ease of data analysis. These programs may be written in a variety of languages, such as Java, Python, and IDL.

Higher level data products will be produced by the schedule listed in Table 3, and the source code for those programs will be made available as they are written.

8.5.2 On-line Tools

A variety of web-based tools will be hosted at the EMFISIS web site (http://emfisis.physics.uiowa.edu), with a focus on tools that provide meta-data about the products, and tools that aid in organizing the data for the user.

The primary data analysis tool for EMFISIS is Autoplot, a free cross-platform data visualization tool. Autoplot can natively read the CDF format, and convert it into a variety of other formats. Autoplot is scriptable, and is capable of working with data sets from a variety of complementary data tools, such as IDL, Matlab, and the THEMIS Data Analysis Software (TDAS).

9 Science Closure and Conclusions

The EMFISIS investigation provides the key set of wave and DC magnetic field measurements needed for significant progress on understanding the detailed physical processes which underlie radiation belt acceleration, loss, and transport as well as the important role that the ring current plays in the inner magnetosphere. As we have demonstrated, EMFISIS has the correct frequency ranges and time resolutions to address the key science questions to be addressed by the RBSP mission. By combining a state-of-the art set of sensors with powerful and flexible central processor and co-processor control, EMFISIS has the needed capability to further our understanding of the Earth's radiation belts.

Acknowledgements We would like to thank the entire Van Allen Probes team who have made this mission the success that it is. We would also like to thank the EFW team, in particular, for their work in supplying electric field signals to EMFISIS as well as supporting cross-calibration of the two sets of instruments. This work was performed under supported on JHU/APL contract no. 921647 under NASA Prime contract No. NAS5-01072.

Appendix A: EMFISIS Key Specifications

A.1 Magnetometer

Cadence: 64 vectors/s

Range ID	Field range	Resolution	Accuracy (sensor only)	Accuracy (deployed on spacecraft)
3	±65536 nT	2 nT	0.1 nT	5 nT
1	±4096 nT	0.16 nT	0.1 nT	5 nT
0	±256 nT	0.001 nT	0.1 nT	5 nT

A.2 Waves

A.2.1 WFR Receiver Performance

MSC Noise Floor best estimate from lab calibrations:

(Noise levels below 100 Hz are difficult to ascertain due to 60 Hz interference)

Frequency	Noise level
100 Hz	$<10^{-8}$ nT^2/Hz
1 kHz	$<10^{-10}$ nT^2/Hz
10 kHz	$<5 \times 10^{-10}$ nT^2/Hz

Dynamic Range: 96 dB (19 dB switchable attenuator)
Maximum amplitude:
no attenuator: 2.1 nT
with attenuator: 9.0 nT (signal begins to distort)
Electric field Noise Floor (100 meter baseline) best estimate from lab calibrations:

Frequency	Noise level
2.5 Hz	$<10^{-14}$ (V/m)^2/Hz
10 Hz	$<10^{-15}$ (V/m)^2/Hz
100 Hz	$<5 \times 10^{-15}$ (V/m)^2/Hz
1 kHz	$<5 \times 10^{-16}$ (V/m)^2/Hz
10 kHz	$< 5 \times 10^{-16}$ (V/m)^2/Hz

Maximum amplitude:
no attenuator: 5.2 mV/m (spin-plane), 37 mV (axial)
with attenuator: 46 mV/m (spin-plane), 330 mV/m (axial)

A.2.2 HFR Receiver Performance

Noise Floor (100 meter baseline) best estimate from lab calibrations:

Frequency	Noise level
10 kHz	$<10^{-17}$ (V/m)^2/Hz
100 kHz	$<10^{-17}$ (V/m)^2/Hz
500 kHz	$<2 \times 10^{-17}$ (V/m)^2/Hz

Dynamic Range: 84 dB (19 dB switchable attenuator)
Maximum amplitude:
no attenuator: 1.4 mV/m (spin-plane), 10 mV (axial)
with attenuator: 14 mV/m (spin-plane), 100 mV/m (axial)

A.3 Standard Survey Products

Note that in what follows the names used are those which correspond to the data products rather than the names of the modes described above. There is a close correspondence, but for data users, the names below match those of files containing the data that is described.

A.3.1 HFR-Spectra

E_U or E_V or E_W:

Cadence: 6 s 4096 samples at 1 MSamples per second (14 bit digitization)
Bin averaged into 82 logarithmically spaced bins between 10 kHz to 500 kHz

A.3.2 WFR-Spectral-Matrix

Three Axis Electric Field (E_U, E_V, E_W) and Three Axis Magnetic field (B_U, B_V, B_W) cross spectral matrix, 6 diagonal components and 15 off-diagonal components:

	E_U	E_V	E_W	B_U	B_V	$\mathbf{B}_W$
E_U	$E_U E_U$	$E_U E_V$	$E_U E_W$	–	–	–
E_V	–	$E_V E_V$	$E_V E_W$	–	–	–
E_W	–	–	$E_W E_W$	–	–	–
B_U	$B_U E_U$	$B_U E_V$	$B_U E_W$	$B_U B_U$	$B_U B_V$	$B_U B_W$
B_V	$B_V E_U$	$B_V E_V$	$B_V E_W$	–	$B_V B_V$	$B_V B_W$
B_W	$B_W E_U$	$B_W E_V$	$B_W E_W$	–	–	$B_W B_W$

Units:

	E_U	E_V	E_W	B_U	B_V	$\mathbf{B}_W$
E_U	$(\mathrm{V/m})^2/\mathrm{Hz}$	$(\mathrm{V/m})^2/\mathrm{Hz}$	$(\mathrm{V/m})^2/\mathrm{Hz}$	–	–	–
E_V	–	$(\mathrm{V/m})^2/\mathrm{Hz}$	$(\mathrm{V/m})^2/\mathrm{Hz}$	–	–	–
E_W	–	–	$(\mathrm{V/m})^2/\mathrm{Hz}$	–	–	–
B_U	(nT V/m)/Hz	(nT V/m)/Hz	(nT V/m)/Hz	$\mathrm{nT}^2/\mathrm{Hz}$	$\mathrm{nT}^2/\mathrm{Hz}$	$\mathrm{nT}^2/\mathrm{Hz}$
B_V	(nT V/m)/Hz	(nT V/m)/Hz	(nT V/m)/Hz	–	$\mathrm{nT}^2/\mathrm{Hz}$	$\mathrm{nT}^2/\mathrm{Hz}$
B_W	(nT V/m)/Hz	(nT V/m)/Hz	(nT V/m)/Hz	–	–	$\mathrm{nT}^2/\mathrm{Hz}$

Cadence: 6 s (E_U, E_V, E_W, B_U, B_V, B_W)
16384 samples at 35 kSamples per second (16 bit digitization)
Bin averaged into 65 logarithmically spaced bins between 2 Hz to 12 kHz

A.3.3 WFR-Waveform

6 channels (E_U, E_V, E_W, B_U, B_V, B_V)
Cadence: ≈once per 15 minutes
16384 samples at 35 kSamples per second (16 bit digitization)

A.4 Waves Burst Mode Products (Commandable and Limited by Memory Allocations)

A.4.1 HFR-Waveform

Cadence: commandable (not a standard product)
4096 samples at 1 MSamples per second (14 bit digitization)

A.4.2 HFR-Spectra-Burst

E_U or E_V or E_W
Cadence: 0.5 s
4096 samples at 1 MSamples per second (14 bit digitization)
Bin averaged into 82 logarithmically spaced bins between 10 kHz to 500 kHz

A.4.3 WFR-Spectral-Matrix-Burst

Similar to the standard survey product described above.
Cadence: 1 s
16384 samples at 35 kSamples per second (16 bit digitization)
Bin averaged into 65 logarithmically spaced bins between 2.14 Hz to 11.2 kHz

A.4.4 WFR-Spectral-Matrix-30 ms

6 channels
Cadence: 0.5 s
16 sets of 1024 samples at 35 kSamples per second (16 bit digitization)

A.4.5 WFR-Spectra-30 ms-Mode

6 channels (E_U, E_V, E_W, B_U, B_V, B_V)
Cadence: 30 ms
1024 samples at 35 kSamples per second (16 bit digitization)
Bin averaged into 70 linearly spaced bins (170 Hz band width) between 102.5 Hz to 11.894 kHz

A.4.6 Wave Normal Analysis Mode (WNA Mode)

Onboard processing of wave normal parameters based on 30 ms mode spectral matrix data. As a function of frequency:

- B^2—Squared magnetic field magnitude, nT^2/Hz
- E^2—Squared electric field magnitude, $(V/m)^2/Hz$
- S_x—Poynting Vector, W/m^2
- S_y—Poynting Vector, W/m^2
- S_z—Poynting Vector, W/m^2
- Magnetic eigenvectors and eigenvalues—arbitrary units with component values for vectors.

A.4.7 WFR-Waveform-Burst

6 channels (E_U, E_V, E_W, B_U, B_V, B_V)
16384 samples at 35 kSamples per second (16 bit digitization) for 0.468 s

A.4.8 WFR-Waveform-Continuous-Burst

6 channels (E_U, E_V, E_W, B_U, B_V, B_V)
208896 samples at 35 kSamples per second (16 bit digitization) for 5.968 s

Appendix B: Acronym List

1PPS	One Pulse Per Second signal
A/D or ADC	Analog to Digital Converter
AC	Alternating Current

AHBROM	Advanced High speed Bus Read Only Memory
APID	Application Identifier
CCSDS	Consultative Committee for Space Data Systems
CDF	Common Data Format
CDPU	Central Data Processing Unity
C-RAM	Chalcogenide Random Access Memory
DSP	Digital Signal Processor
ECH	Electron Cyclotron Harmonic
EDAC	Error Detection and Correction
EEPROM	Electrically Erasable Programmable Read Only Memory
EFW	Electric Field and Waves Instrument
ELF	Extremely Low Frequency
EMFISIS	The Electric and Magnetic Field Instrument Suite and Integrated Science
EMIC	Electromagnetic Ion Cyclotron
FFT	Fast Fourier Transform
FIFO	First In First Out
FPGA	Field Programmable Gate Array
FSM	Finite State Machine
GEI	Geocentric Equatorial Inertial
GEO	Geographic
GSE	Ground Support Equipment
GSE	Geocentric Solar Ecliptic
GSFC	Goddard Space Flight Center
GSM	Geocentric Solar Magnetic
HFR	High Frequency Receiver
HK	Housekeeping
IDL	Interactive Data Language
IEM	Instrument Electronics Module
ITF	Instrument Transfer Frame
LVPS	Low Voltage Power Supply
MAG	Fluxgate Magnetometer
MEB	Main Electronics Box
MET	Mission Elapsed Time
MHD	Magnetohydrodynamics
MI	Magnetosphere-Ionosphere
MLT	Magnetic Local Time
MOC	Mission Operations Center
MSC	Magnetic Search Coil
NASA	National Aeronautics and Space Administration
NMI	Non-Maskable Interrupt
RAM	Random Access Memory
RBSP	Radiation Belt Storm Probes
SAPS	Sub-Auroral Polarization Stream
SASOC	Science Analysis Science Operations Center
SCB	Self-Consistent B
SDRAM	Synchronous Dynamic Random Access Memory
SEU	Single Event Upset
SM	Solar Magnetic
SRAM	Static Random Access Memory

TDAS	THEMIS Data Analysis System
THEMIS	Time History of Events and Mesoscale Interactions during Substorms mission
TLA	Three Letter Acronym
UI	The University of Iowa
ULF	Ultra Low Frequency
UNH	University of New Hampshire
UVW	Spacecraft Science Coordinate System
VHDL	Very high speed integrated circuit (VHSIC) Hardware Definition Language
VLF	Very Low Frequency
WFR	Waveform Receiver

References

B. Abel, R.M. Thorne, Electron scattering loss in Earth's inner magnetosphere. 1. Dominant physical processes. J. Geophys. Res. **103**(A2) (1998a)

B. Abel, R.M. Thorne, Electron scattering loss in Earth's inner magnetosphere. 2. Sensitivity to model parameters. J. Geophys. Res. **103**(A2) (1998b)

M.H. Acuna, Fluxgate magnetometers for outer planets exploration. IEEE Trans. Magn. **10** (1974)

M.H. Acuna, Space-based magnetometers. Rev. Sci. Instrum. **73** (2002)

J.M. Albert, Nonlinear interaction of outer zone electrons with VLF waves. Geophys. Res. Lett. **29**(8) (2002)

J.M. Albert, Evaluation of quasi-linear diffusion coefficients for emic waves in a multispecies plasma. J. Geophys. Res. **108**(A6) (2003)

J.M. Albert, N.P. Meredith, R.B. Horne, Three-dimensional diffusion simulation of outer radiation belt electrons during the 9 October 1990 magnetic storm. J. Geophys. Res. **114** (2009)

R.L. Arnoldy, M.J. Engebretson, R.E. Denton, J.L. Posch, M.R. Lessard, N.C. Maynard, D.M. Ober, C.J. Farrugia, C.T. Russell, J.D. Scudder, R.B. Torbert, S.-H. Chen, T.E. Moore, Pc1 waves and associated unstable distributions of magnetospheric protons observed during a solar wind pressure pulse. J. Geophys. Res. **110** (2005)

J.B. Blake, W.A. Kolasinski, R.W. Fillius, E.G. Mullen, Injection of electrons and protons with energies of tens of MeV into $L < 3$ on 24 March 1991. Geophys. Res. Lett. **19** (1992)

J. Bortnik, R.M. Thorne, The dual role of ELF/VLF chorus waves in the acceleration and precipitation of radiation belt electrons. J. Atmos. Sol. Terr. Phys. **69** (2007)

J. Bortnik, R.M. Thorne, Transit time scattering of energetic electrons due to equatorially confined magnetosonic waves. J. Geophys. Res. **115** (2010)

J. Bortnik, R.M. Thorne, N.P. Meredith, Modeling the propagation characteristics of chorus using CRRES suprathermal electron fluxes. J. Geophys. Res. **112** (2007)

J. Bortnik, R.M. Thorne, U.S. Inan, Nonlinear interaction of energetic electrons with large amplitude chorus. Geophys. Res. Lett. **35** (2008a)

J. Bortnik, R.M. Thorne, N.P. Meredith, The unexpected origin of plasmaspheric hiss from discrete chorus emissions. Nature **452** (2008b)

J. Bortnik, R.M. Thorne, N.P. Meredith, Plasmaspheric hiss overview and relation to chorus. J. Atmos. Sol. Terr. Phys. **71** (2009a)

J. Bortnik, W. Li, R.M. Thorne, V. Angelopoulos, C. Cully, J. Bonnell, O.L. Contel, A. Roux, An observation linking the origin of plasmaspheric hiss to discrete chorus emissions. Science **324** (2009b)

D.H. Brautigam, G.P. Ginet, J.M. Albert, J.R. Wygant, D.E. Rowland, A. Ling, J. Bass, CRRES electric field power spectra and radial diffusion coefficients. J. Geophys. Res. **110** (2005)

A.W. Breneman, C.A. Kletzing, J. Pickett, J. Chum, O. Santolik, Statistics of multispacecraft observations of chorus dispersion and source location. J. Geophys. Res. **114** (2009)

L. Cahill Jr., Inflation of the inner magnetosphere during a magnetic storm. J. Geophys. Res. **71**(19) (1966)

C. Cattell, J.R. Wygant, K. Goetz, K. Kersten, P.J. Kellogg, T. von Rosenvinge, S.D. Bale, I. Roth, M. Temerin, M.K. Hudson, R.A. Mewaldt, M. Wiedenbeck, M. Maksimovic, R. Ergun, M. Acuna, C.T. Russell, Discovery of very large amplitude whistler-mode waves in Earth's radiation belts. Geophys. Res. Lett. **35** (2008)

M.W. Chen, L.R. Lyons, M. Schulz, Simulations of phase space distributions of storm time proton ring current. J. Geophys. Res. **99**(A4) (1994)

M.W. Chen, S. Liu, M. Schulz, J.L. Roeder, L.R. Lyons, Magnetically self-consistent ring current simulations during the 19 October 1998 storm. J. Geophys. Res. **111** (2006a)

Y. Chen, R.H.W. Friedel, G.D. Reeves, Phase space density distribution of energetic electrons in the outer radiation belt during two geospace environment modeling inner magnetosphere/storms selected storms. J. Geophys. Res. **111** (2006b)
Y. Chen, G.D. Reeves, R.H.W. Friedel, The energization of relativistic electrons in the outer Van Allen radiation belt. Nat. Phys. **3** (2007)
L. Chen, R.M. Thorne, R.H. Horne, Simulation of emic excitation in a model magnetosphere including structured high-density plumes. J. Geophys. Res. **114** (2009a)
L. Chen, J. Bortnik, R.M. Thorne, R.B. Horne, V.K. Jordanova, Three-dimensional ray tracing of VLF waves in an asymmetric magnetospheric environment containing a plasmaspheric plume. Geophys. Res. Lett. **36** (2009b)
L. Chen, R.M. Thorne, V.K. Jordanova, C.-P. Wang, M. Gkioulidou, L. Lyons, R.B. Horne, Global simulation of emic wave excitation during the 2001 April 21st storm from coupled RCM-RAM-hotray modeling. J. Geophys. Res. **115** (2010a)
L. Chen, R.M. Thorne, V.K. Jordanova, R.B. Horne, Global simulation of magnetosonic wave instability in the storm time magnetosphere. J. Geophys. Res. **115** (2010b)
F. Chu, M.K. Hudson, P. Haines, Y. Shprits, Dynamic modeling of radiation belt electrons by radial diffusion simulation for a 2 month interval following the 24 March 1991 storm injection. J. Geophys. Res. **115** (2010)
J. Chum, O. Santolik, A.W. Breneman, C.A. Kletzing, D.A. Gurnett, J.S. Pickett, Chorus source properties that produce time shifts and frequency range differences observed on different Cluster spacecraft. J. Geophys. Res. **112** (2007)
S.G. Claudepierre, S.R. Elkington, M. Wiltberger, Solar wind driving of magnetospheric ULF waves: pulsations driven by velocity shear at the magnetopause. J. Geophys. Res. **113** (2008)
S.G. Claudepierre, M. Wiltberger, S.R. Elkington, W. Lotko, M.K. Hudson, Magnetospheric cavity modes driven by solar wind dynamic pressure fluctuations. Geophys. Res. Lett. **36** (2009)
N. Cornilleau-Wehrlin, G. Chanteur, S. Perraut, L. Rezeau, P. Robert, A. Roux, C. de Villedary, P. Canul, M. Maksimovic, Y. de Conchy, D. Hubert, C. Lacombe, F. Lefeuvre, M. Parrot, J. Pincon, P. Decreau, C. Harvey, P. Louarn, O. Santolik, H. Alleyne, M. Roth, T. Chust, O. Le Contel, S. Team, First results obtained by the Cluster STAFF experiment. Ann. Geophys. **21**(2), 437–456 (2003)
J.M. Cornwall, F.V. Coroniti, R.M. Thorne, Turbulent loss of ring current protons. J. Geophys. Res. **75** (1970)
M. Ejiri, Trajectory traces of charged particles in the magnetosphere. J. Geophys. Res. **83** (1978)
S.R. Elkington, M.K. Hudson, A.A. Chan, Acceleration of relativistic electrons via drift-resonant interaction with toroidal-mode PC-5 oscillations. Geophys. Res. Lett. **26** (1999)
S.R. Elkington, M.K. Hudson, A.A. Chan, Resonant acceleration and diffusion of outer zone electrons in an asymmetric geomagnetic field. J. Geophys. Res. **108**(A3) (2003)
C.-G. Fälthammar, M. Walt, Radial motion resulting from pitch angle scattering of trapped electrons in the distorted geomagnetic field. J. Geophys. Res. **74** (1969)
Y. Fei, A.A. Chan, S.R. Elkington, M.J. Wiltberger, Radial diffusion and MHD particle simulations of relativistic electron transport by ULF waves in the September 1998 storm. J. Geophys. Res. **111** (2006)
M.-C. Fok, T.E. Moore, D.C. Delcourt, Modeling of inner plasma sheet and ring current during substorms. J. Geophys. Res. **104**(A7) (1999)
M. Fok, R.B. Horne, N.P. Meredith, S.A. Glauert, Radiation belt environmental model: application to space weather nowcasting. J. Geophys. Res. **113** (2008)
J.C. Foster, H.B. Vo, Average characteristics and activity dependence of the subauroral polarization stream. J. Geophys. Res. **107**(A12) (2002)
B.J. Fraser, R.S. Grew, S.K. Morley, J.C. Green, H.J. Singer, T.M. Loto'aniu, M.F. Thomsen, Stormtime observations of electromagnetic ion cyclotron waves at geosynchronous orbit: GOES results. J. Geophys. Res. **115** (2010)
N. Furuya, Y. Omura, D. Summers, Relativistic turning acceleration of radiation belt electrons by whistler mode chorus. J. Geophys. Res. **113** (2008)
N.Y. Ganushkina, T.I. Pulkkinen, V.A. Sergeev, M.V. Kubyshkina, D.N. Baker, N.E. Turner, M. Grande, B. Kellett, J. Fennell, J. Roeder, J.-A. Sauvaud, T.A. Fritz, Entry of plasma sheet particles into the inner magnetosphere as observed by Polar/Cammice. J. Geophys. Res. **105**(A11) (2000)
J.C. Green, M.G. Kivelson, A tale of two theories: How the adiabatic response and ULF waves affect relativistic electrons. J. Geophys. Res. **106**(A11) (2001)
J.C. Green, M.G. Kivelson, Relativistic electrons in the outer radiation belt: differentiating between acceleration mechanisms. J. Geophys. Res. **109** (2004)
N.M. Haque, M. Spasojevic, O. Santolik, U.S. Inan, Wave normal angles of magnetospheric chorus emissions observed on the Polar spacecraft. J. Geophys. Res. **115** (2010)
M. Hayosh, O. Santolik, M. Parrot, Location and size of the global source region of whistler mode chorus. J. Geophys. Res. **115** (2010)

R.B. Horne, R.M. Thorne, Potential waves for relativistic electron scattering and stochastic acceleration during magnetic storms. Geophys. Res. Lett. **25** (1998)
R.B. Horne, R.M. Thorne, Electron pitch angle diffusion by electrostatic electron cyclotron waves: the origin of pancake distributions. J. Geophys. Res. **105**(A3) (2000)
R.B. Horne, R.M. Thorne, Relativistic electron acceleration and precipitation during resonant interactions with whistler-mode chorus. Geophys. Res. Lett. **30**(10) (2003)
R.B. Horne, G.V. Wheeler, H.S.C.K. Alleyne, Proton and electron heating by radially propagating fast magnetosonic waves. J. Geophys. Res. **105** (2000)
R.B. Horne, R.M. Thorne, N.P. Meredith, R.R. Anderson, Diffuse auroral electron scattering by electron cyclotron harmonic and whistler mode waves during an isolated substorm. J. Geophys. Res. **108**(A7) (2003)
R.B. Horne, R.M. Thorne, S.A. Glauert, J.M. Albert, N.P. Meredith, R.R. Anderson, Timescales for radiation belt electron acceleration by whistler mode chorus waves. J. Geophys. Res. **110** (2005)
R.B. Horne, R.M. Thorne, S.A. Glauert, N.P. Meredith, D. Pokhotelov, O. Santolik, Electron acceleration in the Van Allen belts by fast magnetosonic waves. Geophys. Res. Lett. **34** (2007)
Y. Hu, R.E. Denton, Two-dimensional hybrid code simulation of electromagnetic ion cyclotron waves in a dipole magnetic field. J. Geophys. Res. **114** (2009)
C.L. Huang, H.E. Spence, M.K. Hudson, S.R. Elkington, Modeling radiation belt radial diffusion in ULF wave fields: 2. Estimating rates of radial diffusion using combined MHD and particle codes. J. Geophys. Res. **115** (2010)
M.K. Hudson, S.R. Elkington, J.G. Lyon, V.A. Marchenko, I. Roth, M. Temerin, J.B. Blake, M.S. Gussenhoven, J.R. Wygant, Simulations of radiation belt formation during storm sudden commencements. J. Geophys. Res. **102**(A7) (1997)
M.K. Hudson, S.R. Elkington, J.G. Lyon, M. Wiltberger, M. Lessard, Radiation belt electron acceleration by ULF wave drift resonance: simulation of 1997 and 1998 storms, in *Space Weather*, ed. by P. Song, H. Singer, G. Siscoe. Geophys. Monogr., vol. 125 (AGU, Washington, 2001)
V.K. Jordanova, The role of the Earth's ring current in radiation belt dynamics, in *Dynamics of the Earth's Radiation Belts and Inner Magnetosphere*, vol. 199, ed. by D. Summers, I. Mann, D. Baker, M. Schulz (2012)
V.K. Jordanova, Y. Miyoshi, Relativistic model of ring current and radiation belt ions and electrons: initial results. Geophys. Res. Lett. **32** (2005)
V.K. Jordanova, J.U. Kozyra, A.F. Nagy, G.V. Khazanov, Kinetic model of the ring current-atmosphere interactions. J. Geophys. Res. **102** (1997)
V.K. Jordanova, L.M. Kistler, C.J. Farrugia, R.B. Torbert, Effects of inner magnetospheric convection on ring current dynamics: March 10–12, 1998. J. Geophys. Res. **106** (2001a)
V.K. Jordanova, C.J. Farrugia, R.M. Thorne, G.V. Khazanov, G.D. Reeves, M.F. Thomsen, Modeling ring current proton precipitation by electromagnetic ion cyclotron waves during the May 14–16, 1997 storm. J. Geophys. Res. **106** (2001b)
V.K. Jordanova, A. Boonsiriseth, R.M. Thorne, Y. Dotan, Ring current asymmetry from global simulations using a high-resolution electric field model. J. Geophys. Res. **108**(A12) (2003)
V.K. Jordanova, Y.S. Miyoshi, S. Zaharia, M.F. Thomsen, G.D. Reeves, D.S. Evans, C.G. Mouikis, J.F. Fennell, Kinetic simulations of ring current evolution during the geospace environment modeling challenge events. J. Geophys. Res. **111** (2006)
V.K. Jordanova, M. Spasojevic, M. Thomsen, Modeling the electromagnetic ion cyclotron wave-induced formation of detached subauroral arcs. J. Geophys. Res. **112** (2007)
V.K. Jordanova, J. Albert, Y. Miyoshi, Relativistic electron precipitation by emic waves from self-consistent global simulations. J. Geophys. Res. **113** (2008)
V.K. Jordanova, R.M. Thorne, Y. Miyoshi, Excitation of whistler-mode chorus from global ring current simulations. J. Geophys. Res. **115** (2010a)
V.K. Jordanova, S. Zaharia, D.T. Welling, Comparative study of ring current development using empirical, dipolar, and self-consistent magnetic field simulations. J. Geophys. Res. **115** (2010b)
V.K. Jordanova, D.T. Welling, S.G. Zaharia, L. Chen, R.M. Thorne, Modeling ring current ion and electron dynamics and plasma instabilities during a high-speed stream driven storm. J. Geophys. Res. **117** (2012)
C.F. Kennel, R.M. Thorne, Unstable growth of unducted whistlers propagating at an angle to the geomagnetic field. J. Geophys. Res. **72** (1967)
H.-J. Kim, A.A. Chan, Fully adiabatic changes in storm time relativistic electron fluxes. J. Geophys. Res. **102** (1997)
B.T. Kress, M.K. Hudson, M.D. Looper, J. Albert, J.G. Lyon, C.C. Goodrich, Global MHD test particle simulations of >10 MeV radiation belt electrons during storm sudden commencement. J. Geophys. Res. **112** (2007)

X. Li, I. Roth, M. Temerin, J.R. Wygant, M.K. Hudson, J.B. Blake, Simulation of the prompt energization and transport of radiation belt particles during the March 24, 1991 SSC. Geophys. Res. Lett. **20**(22) (1993)
W. Li, R.M. Thorne, N.P. Meredith, R.B. Horne, J. Bortnik, Y.Y. Shprits, B. Ni, Evaluation of whistler mode chorus amplification during an injection event observed on CRRES. J. Geophys. Res. **113** (2008)
W. Li, R.M. Thorne, V. Angelopoulos, J.W. Bonnell, J.P. McFadden, C.W. Carlson, O. LeContel, A. Roux, K.H. Glassmeier, H.U. Auster, Evaluation of whistler-mode chorus intensification on the nightside during an injection event observed on the THEMIS spacecraft. J. Geophys. Res. **114** (2009a)
W. Li, R.M. Thorne, V. Angelopoulos, J. Bortnik, C.M. Cully, B. Ni, O. LeContel, A. Roux, U. Auster, W. Magnes, Global distribution of whistler-mode chorus observed on the THEMIS spacecraft. Geophys. Res. Lett. **36** (2009b)
M.W. Liemohn, J.U. Kozyra, M.F. Thomsen, J.L. Roeder, G. Lu, J.E. Borovsky, T.E. Cayton, Dominant role of the asymmetric ring current in producing the stormtime Dst*. J. Geophys. Res. **106**(A6) (2001)
W. Liu, T.E. Sarris, X. Li, S.R. Elkington, R. Ergun, V. Angelopoulos, J. Bonnell, K.H. Glassmeier, Electric and magnetic field observations of Pc4 and Pc5 pulsations in the inner magnetosphere: a statistical study. J. Geophys. Res. **114** (2009)
T.M. Loto'aniu, B.J. Fraser, C.L. Waters, Propagation of electromagnetic ion cyclotron waves in the magnetosphere. J. Geophys. Res. **110** (2005)
T.M. Loto'aniu, I.R. Mann, L.G. Ozeke, A.A. Chan, Z.C. Dent, D.K. Milling, Radial diffusion of relativistic electrons into the radiation belt slot region during the 2003 Halloween storm. J. Geophys. Res. **111** (2006)
T.M. Loto'aniu, H.J. Singer, C.L. Waters, V. Angelopoulos, I.R. Mann, S.R. Elkington, J.W. Bonnell, Relativistic electron loss due to ultralow frequency waves and enhanced outward radial diffusion. J. Geophys. Res. **115** (2010)
L.R. Lyons, R.M. Thorne, Equilibrium structure of radiation belt electrons. J. Geophys. Res. **78** (1973)
L.R. Lyons, D.J. Williams, A source for the geomagnetic storm main phase ring current. J. Geophys. Res. **85**(A2) (1980)
L.R. Lyons, R.M. Thorne, C.F. Kennel, Pitch angle diffusion of radiation belt electrons within the plasmasphere. J. Geophys. Res. **77** (1972)
R.A. Mathie, I.R. Mann, A correlation between extended intervals of ULF wave power and storm-time geosynchronous relativistic electron flux enhancements. Geophys. Res. Lett. **27** (2000)
J.P. McCollough, S.R. Elkington, D.N. Baker, Modelling emic wave growth during the compression event of 29 June 2007. Geophys. Res. Lett. **36** (2009)
N.P. Meredith, R.B. Horne, R.M. Thorne, R.R. Anderson, Favored regions for chorus-driven electron acceleration to relativistic energies in the Earth's outer radiation belt. Geophys. Res. Lett. **30**(16) (2003a)
N.P. Meredith, R.M. Thorne, R.B. Horne, D. Summers, B.J. Fraser, R.R. Anderson, Statistical analysis of relativistic electron energies for cyclotron resonance with EMIC waves observed on CRRES. J. Geophys. Res. **108**(A6) (2003b)
N.P. Meredith, R.B. Horne, R.R. Anderson, Survey of magnetosonic waves and proton ring distributions in Earth's inner magnetosphere. J. Geophys. Res. **113** (2008)
N.P. Meredith, R.B. Horne, R.M. Thorne, R.R. Anderson, Survey of upper band chorus and ech waves: implications for the diffuse aurora. J. Geophys. Res. **114** (2009)
R.M. Millan, R.M. Thorne, Review of radiation belt relativistic electron loss. J. Atmos. Sol. Terr. Phys. **69** (2007)
E.V. Mishin, W.J. Burke, C.Y. Huang, F.J. Rich, Electromagnetic wave structures within subauroral polarization streams. J. Geophys. Res. **108**(A8) (2003)
Y. Miyoshi, V.K. Jordanova, A. Morioka, M.F. Thomsen, G.D. Reeves, D.S. Evans, J.C. Green, Observations and modeling of energetic electron dynamics during the October 2001 storm. J. Geophys. Res. **111** (2001)
Y. Miyoshi, V.K. Jordanova, M.F. Thomsen, G.D. Reeves, D.S. Evans, A. Morioka, Y. Kasahara, T. Nagai, J. Green, Simulation of energetic electrons dynamics on the Oct. 2001 magnetic storm. EOS Trans. AGU **84** (2003)
S.K. Morley, S.T. Ables, M.D. Sciffer, B.J. Fraser, Multipoint observations of Pc1–2 waves in the afternoon sector. J. Geophys. Res. **114** (2009)
S.K. Morley, R.H.W. Friedel, T.E. Cayton, E. Noveroske, A rapid, global and prolonged electron radiation belt dropout observed with the global positioning system constellation. Geophys. Res. Lett. **37** (2010)
N.F. Ness, Magnetometers for space research. Space Sci. Rev. **11** (1970)
B. Ni, R.M. Thorne, Y.Y. Shprits, J. Bortnik, Resonant scattering of plasma sheet electrons by whistler-mode chorus: contributions to diffuse auroral precipitation. Geophys. Res. Lett. **35** (2008)
B. Ni, R.M. Thorne, J. Liang, V. Angelopoulos, C. Cully, W. Li, X. Zhang, M. Hartinger, O.L. Contel, A. Roux, Global distribution of electrostatic electron cyclotron harmonic waves observed on THEMIS. Geophys. Res. Lett. **38** (2011)

Y. Nishimura, J. Bortnik, W. Li, R.M. Thorne, L.R. Lyons, V. Angelopoulos, S. Mende, J.W. Bonnel, O. LeContel, U. Auster, Identifying the driver of pulsating aurora. Science **330** (2010)
T.P. O'Brien, R.L. McPherron, D. Sornette, G.D. Reeves, R. Friedel, H.J. Singer, Which magnetic storms produce relativistic electrons at geosynchronous orbit? J. Geophys. Res. **106** (2001)
N. Omidi, R.M. Thorne, J. Bortnik, Non-linear evolution of emic waves in a uniform magnetic field: 1. Hybrid simulations. J. Geophys. Res. **115** (2010)
T.G. Onsager, J.C. Green, G.D. Reeves, H.J. Singer, Solar wind and magnetospheric conditions leading to the abrupt loss of outer radiation belt electrons. Geophys. Res. Lett. **112** (2007)
K.L. Perry, M.K. Hudson, S.R. Elkington, Incorporating spectral characteristics of Pc5 waves into three-dimensional modeling and the diffusion of relativistic electrons. J. Geophys. Res. **110** (2005)
J.S. Pickett, B. Grison, Y. Omura, M.J. Engebretson, I. Dandouras, A. Masson, M.L. Adrian, O. Santolik, P.M.E. Decreau, N. Cornilleau-Wehrlin, D. Constantinescu, Cluster observations of EMIC triggered emissions in association with Pc1 waves near Earth's plasmapause. Geophys. Res. Lett. **37** (2010)
K.G. Powell, P.L. Roe, T.J. Linde, T.I. Gombosi, D.L. de Zeeuw, A solution-adaptive upwind scheme for ideal magnetohydrodynamics. J. Comput. Phys. **153** (1999)
C.E. Rasmussen, S.M. Guiter, S.G. Thomas, Two-dimensional model of the plasmasphere: refilling time constants. Planet. Space Sci. **41** (1993)
A.J. Ridley, M.W. Liemohn, A model-derived storm time asymmetric ring current driven electric field description. J. Geophys. Res. **107**(A8) (2002)
J.G. Roederer, *Dynamics of Geomagnetically Trapped Radiation* (Springer, New York, 1970)
G. Rostoker, S. Skone, D.N. Baker, On the origin of relativistic electrons in the magnetosphere associated with some geomagnetic storms. Geophys. Res. Lett. **25** (1998)
O. Santolik, F. Lefeuvre, M. Parrot, J. Rauch, Complete wave-vector directions of electromagnetic emissions: application to INTERBALL-2 measurements in the nightside auroral zone. J. Geophys. Res. **106**(A7), 13191–13201 (2001)
O. Santolik, M. Parrot, F. Lefeuvre, Singular value decomposition methods for wave propagation analysis. Radio Sci. **38**(1) (2003)
O. Santolik, D.S. Gurnett, J.S. Pickett, M. Parrot, N. Cornilleau-Wehrlin, A microscopic and nanoscopic view of storm-time chorus on 31 March 2001. Geophys. Res. Lett. **31** (2004)
O. Santolik, D.A. Gurnett, J.S. Pickett, J. Chum, N. Cornilleau-Wehrlin, Oblique propagation of whistler mode waves in the chorus source region. J. Geophys. Res. **114** (2009)
M. Schulz, L. Lanzerotti, *Particle Diffusion in the Radiation Belts* (Springer, New York, 1974)
Y.Y. Shprits, B. Ni, Dependence of the quasi-linear scattering rates on the wave normal distribution of chorus waves. J. Geophys. Res. **114** (2009)
Y. Shprits, R.M. Thorne, Time dependent radial diffusion modeling of relativistic electrons with realistic loss rates. Geophys. Res. Lett. **31** (2004)
Y.Y. Shprits, R.M. Thorne, R. Friedel, G.D. Reeves, J. Fennell, D.N. Baker, S.G. Kanekal, Outward radial diffusion driven by losses at magnetopause. J. Geophys. Res. **111** (2006)
Y.Y. Shprits, D. Subbotin, B. Ni, Evolution of electron fluxes in the outer radiation belt computed with the verb code. J. Geophys. Res. **114** (2009)
D.A. Subbotin, Y.Y. Shprits, Three dimensional modeling of the radiation belts using the versatile electron radiation belt (verb) code. Space Weather **7** (2009)
D. Summers, Y. Omura, Ultra-relativistic acceleration of electrons in planetary magnetospheres. Geophys. Res. Lett. **34** (2007)
D. Summers, R.M. Thorne, Relativistic electron pitch-angle scattering by electromagnetic ion cyclotron waves during geomagnetic storms. J. Geophys. Res. **108**(A4) (2003)
D. Summers, R.M. Thorne, F. Xiao, Relativistic theory of wave-particle resonant diffusion with application to electron acceleration in the magnetosphere. J. Geophys. Res. **103** (1998)
X. Tao, A.A. Chan, J.M. Albert, J.A. Miller, Stochastic modeling of multidimensional diffusion in the radiation belts. J. Geophys. Res. **113** (2008)
X. Tao, J.M. Albert, A.A. Chan, Numerical modeling of multidimensional diffusion in the radiation belts using layer methods. J. Geophys. Res. **145** (2009)
R.M. Thorne, Radiation belt dynamics: the importance of wave-particle interactions. Geophys. Res. Lett. **37** (2010)
R.M. Thorne, R.B. Horne, Modulation of electromagnetic ion cyclotron instability due to interaction with ring current o+ during geomagnetic storms. J. Geophys. Res. **102**(A7) (1997)
R.M. Thorne, C.F. Kennel, Relativistic electron precipitation during magnetic storm main phase. J. Geophys. Res. **76** (1971)
R.M. Thorne, T.P. O'Brien, Y.Y. Shprits, D. Summers, R.B. Horne, Timescale for MeV electron microburst loss during geomagnetic storms. J. Geophys. Res. **110** (2005)

R.M. Thorne, X.T. B. Ni, R.B. Horne, N.P. Meredith, Scattering by chorus waves as the dominant cause of diffuse auroral precipitation. Nature **467** (2010)
B.T. Tsurutani, E.J. Smith, Postmidnight chorus: a substorm phenomenon. J. Geophys. Res. **79** (1974)
B.T. Tsurutani, E.J. Smith, Two types of magnetospheric elf chorus and their substorm dependences. J. Geophys. Res. **82** (1977)
B.T. Tsurutani, O.P. Verkhoglyadova, G.S. Lakhina, S. Yagitani, Properties of dayside outer zone chorus during HILDCAA events: loss of energetic electrons. J. Geophys. Res. **114** (2009)
N.A. Tsyganenko, D.P. Stern, Modeling the global magnetic field of the large-scale Birkeland current systems. J. Geophys. Res. **101** (1996)
N.A. Tsyganenko, H.J. Singer, J.C. Kasper, Storm-time distortion of the inner magnetosphere: how severe can it get? J. Geophys. Res. **108** (2003)
W. Tu et al., Storm-dependent radiation belt electron dynamics. J. Geophys. Res. **114** (2009)
A.Y. Ukhorskiy, K. Takahashi, B.J. Anderson, H. Korth, Impact of toroidal ULF waves on outer radiation belt electrons. J. Geophys. Res. **110** (2005)
A.Y. Ukhorskiy, B.J. Anderson, K. Takahashi, N.A. Tsyganenko, Impact of ULF oscillations in solar wind dynamic pressure on the outer radiation belt electrons. Geophys. Res. Lett. **33** (2006)
A.Y. Ukhorskiy, M.I. Sitnov, K. Takahasi, B.J. Anderson, Radial transport of radiation belt electrons due to stormtime Pc5 waves. Ann. Geophys. **27** (2009)
M.E. Usanova et al., Multipoint observations of magnetospheric compression-related emic Pc1 waves by THEMIS and Carisma. Geophys. Res. Lett. **35** (2008)
A.L. Vampola, A. Korth, Electron drift echoes in the inner magnetosphere. Geophys. Res. Lett. **19** (1992)
A. Varotsou, D. Boscher, S. Bourdarie, R.B. Horne, N.P. Meredith, S.A. Glauert, R.H. Friedel, Three dimensional test simulations of the outer radiation belt electron dynamics including electron-chorus resonant interactions. J. Geophys. Res. **113** (2008)
D.R. Weimer, An improved model of ionospheric electric potentials including substorm perturbations and application to the Geospace Environment Modeling November 24, 1996, event. J. Geophys. Res. **106** (2001)
R.A. Wolf, J.W. Freeman Jr., B.A. Hausman, R.W. Spiro, R.V. Hilmer, R.L. Lambour, *Modeling Convection Effects in Magnetic Storms*. Geophys. Monogr., vol. 98 (AGU, Washington, 1997)
J. Wygant, F. Mozer, M. Temerin, J. Blake, N. Maynard, H. Singer, M. Smiddy, Large amplitude electric and magnetic field signatures in the inner magnetosphere during injection of 15 MeV electron drift echoes. Geophys. Res. Lett. **21** (1994)
Y. Yu, V. Jordanova, S. Zaharia, J. Koller, J. Zhang, L.M. Kistler, Validation study of the magnetically self-consistent inner magnetosphere model RAM-SCB. J. Geophys. Res. **117** (2012)
S. Zaharia, V.K. Jordanova, M.F. Thomsen, G.D. Reeves, Self-consistent modeling of magnetic fields and plasmas in the inner magnetosphere: application to a geomagnetic storm. J. Geophys. Res. **111** (2006)
S. Zaharia, V.K. Jordanova, D.T. Welling, G. Toth, Self-consistent inner magnetosphere simulation driven by a global MHD model. J. Geophys. Res. **115** (2010)

DOI 10.1007/978-1-4899-7433-4_6
Reprinted from *Space Science Reviews* Journal, DOI 10.1007/s11214-013-0013-7

The Electric Field and Waves Instruments on the Radiation Belt Storm Probes Mission

J.R. Wygant · J.W. Bonnell · K. Goetz · R.E. Ergun · F.S. Mozer · S.D. Bale · M. Ludlam · P. Turin · P.R. Harvey · R. Hochmann · K. Harps · G. Dalton · J. McCauley · W. Rachelson · D. Gordon · B. Donakowski · C. Shultz · C. Smith · M. Diaz-Aguado · J. Fischer · S. Heavner · P. Berg · D.M. Malsapina · M.K. Bolton · M. Hudson · R.J. Strangeway · D.N. Baker · X. Li · J. Albert · J.C. Foster · C.C. Chaston · I. Mann · E. Donovan · C.M. Cully · C.A. Cattell · V. Krasnoselskikh · K. Kersten · A. Brenneman · J.B. Tao

Received: 21 February 2013 / Accepted: 22 July 2013 / Published online: 11 October 2013

J.R. Wygant (✉) · K. Goetz · C.A. Cattell · K. Kersten · A. Brenneman
School of Physics and Astronomy, University of Minnesota, Minneapolis, MN, USA
e-mail: wygan001@umn.edu

J.W. Bonnell · F.S. Mozer · S.D. Bale · M. Ludlam · P. Turin · P.R. Harvey · R. Hochmann · K. Harps · G. Dalton · J. McCauley · W. Rachelson · D. Gordon · B. Donakowski · C. Shultz · C. Smith · M. Diaz-Aguado · J. Fischer · S. Heavner · P. Berg · C.C. Chaston · J.B. Tao
Space Sciences Laboratory, University of California, Berkeley, CA, USA

F.S. Mozer · S.D. Bale
Department of Physics, University of California, Berkeley, CA, USA

R.E. Ergun · D.M. Malsapina · M.K. Bolton · D.N. Baker · X. Li
Laboratory for Atmospheric and Space Physics, University of Colorado, Boulder, CO, USA

R.J. Strangeway
IGPP and Department of Earth and Space Sciences, University of California, Los Angeles, CA, USA

M. Hudson
Department of Physics and Astronomy, Dartmouth College, Hanover, NH, USA

J. Albert
AFGL/RVBX, Kirkland Air Force Base, NM, USA

I. Mann
Department of Physics, University of Alberta, Edmonton, Alberta, Canada

E. Donovan · C.M. Cully
Department of Physics and Astronomy, University of Calgary, Alberta, Canada

J.C. Foster
Haystack Observatory, MIT, Cambridge, MA, USA

V. Krasnoselskikh
LPC2E, Orleans, France

Abstract The Electric Fields and Waves (EFW) Instruments on the two Radiation Belt Storm Probe (RBSP) spacecraft (recently renamed the Van Allen Probes) are designed to measure three dimensional quasi-static and low frequency electric fields and waves associated with the major mechanisms responsible for the acceleration of energetic charged particles in the inner magnetosphere of the Earth. For this measurement, the instrument uses two pairs of spherical double probe sensors at the ends of orthogonal centripetally deployed booms in the spin plane with tip-to-tip separations of 100 meters. The third component of the electric field is measured by two spherical sensors separated by ∼15 m, deployed at the ends of two stacer booms oppositely directed along the spin axis of the spacecraft. The instrument provides a continuous stream of measurements over the entire orbit of the low frequency electric field vector at 32 samples/s in a survey mode. This survey mode also includes measurements of spacecraft potential to provide information on thermal electron plasma variations and structure. Survey mode spectral information allows the continuous evaluation of the peak value and spectral power in electric, magnetic and density fluctuations from several Hz to 6.5 kHz. On-board cross-spectral data allows the calculation of field-aligned wave Poynting flux along the magnetic field. For higher frequency waveform information, two different programmable burst memories are used with nominal sampling rates of 512 samples/s and 16 k samples/s. The EFW burst modes provide targeted measurements over brief time intervals of 3-d electric fields, 3-d wave magnetic fields (from the EMFISIS magnetic search coil sensors), and spacecraft potential. In the burst modes all six sensor-spacecraft potential measurements are telemetered enabling interferometric timing of small-scale plasma structures. In the first burst mode, the instrument stores all or a substantial fraction of the high frequency measurements in a 32 gigabyte burst memory. The sub-intervals to be downloaded are uplinked by ground command after inspection of instrument survey data and other information available on the ground. The second burst mode involves autonomous storing and playback of data controlled by flight software algorithms, which assess the "highest quality" events on the basis of instrument measurements and information from other instruments available on orbit. The EFW instrument provides 3-d wave electric field signals with a frequency response up to 400 kHz to the EMFISIS instrument for analysis and telemetry (Kletzing et al. Space Sci. Rev. 2013).

Keywords Electric fields · Magnetosphere

1 Introduction

The goal of the Electric Field and Waves (EFW) Investigation on the Radiation Belt Storm Probe (RBSP) mission is to understand the role of electric fields in driving energetic particle acceleration, transport, and loss in the inner magnetosphere of the Earth. The overall EFW instrument development was led by the University of Minnesota under Principal Investigator, John Wygant, and Project Manager, Keith Goetz. The hardware and software development of the RBSP EFW instrument including the Instrument Data Processing Unit (IDPU) and the spin plane and spin axis boom deployment units was carried out by a team led by John Bonnell at the Space Sciences Laboratory at the University of California, Berkeley. A team at the Laboratory for Atmospheric and Space Physics at the University of Colorado led by Robert Ergun provided a signal processing board for digital filtering and on-board calculation of spectral products.

The EFW instrument provides electric field measurements on each of the two RBSP spacecraft focusing on the frequency range from DC to 256 Hz. In addition, the instrument

has the capability to sample large amplitude 3d electric fields and magnetic fields waves and structures at 16.4 k samples/s in special high rate mode. The frequency range of primary focus from dc to 256 Hz includes measurements of the convection electric field, interactions with interplanetary shocks, electric fields associated with particle injection fronts, Alfven waves, magnetosonic waves, electromagnetic ion cyclotron (EMIC) waves, lower hybrid waves. The candidate structures and waves that have been proposed for the acceleration of different particle populations in the inner magnetosphere span over seven orders of magnitude in time and four orders of magnitude in amplitude. The generation of these waves and their ability to accelerate different particle populations is often tied to the dynamics of the inner magnetosphere during geomagnetic storms. During these times, the free energy sources available to drive magnetospheric processes increase by $\sim$2 orders of magnitude (Axford 1976) due to encounters powerful interplanetary shocks, coronal mass ejections, and fast-slow streams in the solar wind. During major geomagnetic storms, the plasma pressure between 2 R_E to 6 R_E is dominated by the development of a hot (20–700 keV) ion ring current torus surrounding the Earth which is generated by intense convection electric fields that appear deep within the magnetosphere. The spatial configuration of the convection electric fields is modified by the development of powerful ring current pressure gradients in a complex interplay of self-consistent dynamics that ultimately controls the cold plasma density structure, the intensity and configuration of the magnetic field, and the ability of the system to support a wide variety of wave modes. A signature feature of major geomagnetic storms is the erosion of the plasmasphere on the night-side to within 2 R_E of the Earth in the equatorial plane. During this massive reconfiguration of the inner magnetosphere, relativistic particle acceleration and loss mechanisms are particularly strong and variable. More than half a dozen different acceleration mechanisms with varying degrees of theoretical and experimental support have been invoked to explain the several order of magnitude increases and decreases in relativistic and near relativistic electrons and energetic ions.

In this section, we present examples of electric field measurements and their limitations from the CRRES spacecraft to illustrate the varied roles of the electric field in the inner magnetosphere. These data motivated the measurement goals of the RBSP EFW instruments. Next we present recently obtained on-orbit data from the first few months of the RBSP mission that illustrate instrument capabilities. In subsequent sections, we present the measurement goals of the instrument, followed by an instrument overview and a more detailed discussion of the instrument subsystems.

Figure 1 presents a pass from the CRRES spacecraft through the inner magnetosphere in the equatorial plane during the major geomagnetic storm of March 1991. These data illustrate three different energization processes that produced dramatic effects on different particle populations. The three processes are: (1) interplanetary shock induced acceleration; (2) anomalously large enhancements in the convection electric field; and (3) large amplitude ULF waves present throughout the inner magnetosphere. This figure shows an abrupt enhancement in the electric field of 40 mV/m on the night-side of the Earth near $L = 2.4$ with a duration of 60 seconds associated with an interplanetary shock induced magnetosonic wave (Wygant et al. 1994). It is estimated that the amplitude of the magnetosonic wave on the dayside, where it was directly incident on the inner magnetosphere, was on the order of 250 mV/m. Energetic electron measurements on CRRES showed (Blake et al. 1992; Blake and Imamoto 1992; Vampola and Korth 1992) that this structure produced a five order of magnitude enhancement in $>$13 MeV electrons over a period of $<$1 minute that evolved into a new radiation belt near 2 R_E that lasted over 2 years. The shock induced prompt acceleration of the relativistic electrons was subsequently reproduced in detail by large-scale test particle simulations (Li et al. 1993; Hudson et al. 1997). Shock induced acceleration of protons was also observed during this event and simulated (Hudson et al. 1995).

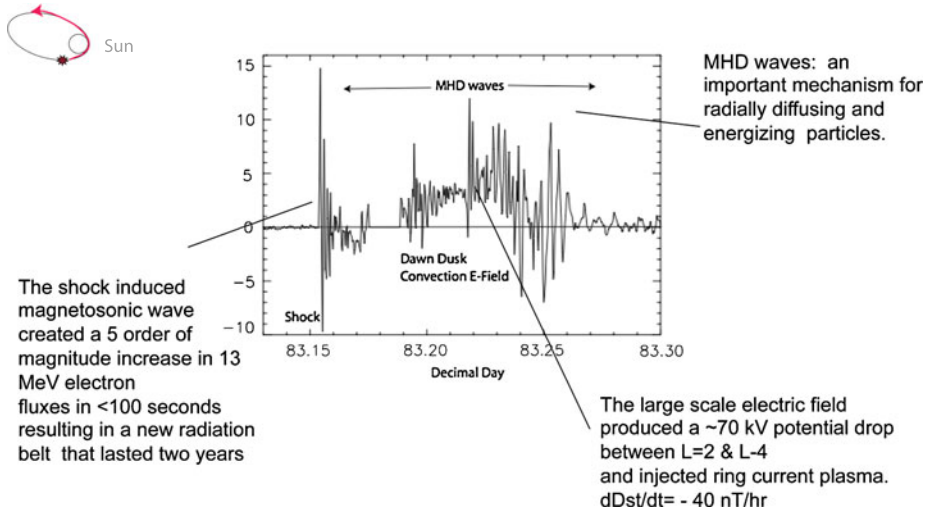

Fig. 1 CRRES measurements during major geomagnetic storm of March 21, 1991 showing interplanetary shock induced electric fields, the enhancement in the large scale electric field, and ULF waves. *Inset* figure shows the CRRES orbit with "explosion symbol" indicating position of spacecraft at time of encounter with shock induced magnetosonic wave and tip of *red arrow* indicating end of plot interval. Text indicates the kinds of energization expected from each structure

Figure 1 also shows an enhancement in the large-scale dawn-dusk convection electric field from quiet time values of 0.1 mV/m to values of 5–7 mV/m during the main phase of the storm. Measurements of the magnetic field perturbations associated with ring current plasma provide evidence that the plasma was injected by this electric field to a radial distance of $\sim 2\ R_E$ over a several hour period (Wygant et al. 1998; Rowland and Wygant 1998). Radar measurements at ionospheric altitudes also provide evidence for similar storm time enhancements of the large-scale convection electric field at low latitudes (Yeh et al. 1991).

Finally, Fig. 1 shows strong MHD fluctuations of $\sim$10 mV/m lasting almost the entire orbit that in principle could interact strongly with $\sim$1 MeV electrons stochastically to produce radial diffusion and energization through conservation of the first adiabatic invariant. Alternatively, the acceleration could proceed through a "coherent" non-linear interaction involving trapping in the quasi-monochromatic large amplitude waves. In order to understand the role of ULF waves in the energization of radiation belt particles, the amplitude of the electric field, its propagation velocity, its azimuthal wave number, and its radial spatial scales must be measured (Hudson et al. 2001, 2004; Brautigam et al. 2005). These properties should be measured as a function of radial position and local time. In addition, the mechanisms responsible for the generation of the waves should be understood. Candidate mechanisms for generating these waves include magnetopause surface perturbations driven by solar wind dynamic pressure variations, reconnection at the front-side magnetopause, large scale shear mode instabilities on the flanks of the magnetopause, the internal free energy in anisotropic ring current ion distribution functions, and stochastic forcing by substorm related electric fields. The existence of the two RBSP spacecraft, upstream solar wind monitors, and the routine presence of the THEMIS spacecraft at larger radial distances will be used to evaluate the driving forces, the structure of the waves, and to distinguish between competing accelerating mechanisms.

Evidence from CRRES and other spacecraft also has shown that substorm injection fronts propagating inward from the tail can also produce electric fields ranging from 1–40 mV/m for periods of 1 to 5 minutes (Rowland 2002; Dai et al. 2011; Li et al. 1998). These fronts could result in the injection and energization of both ring current ions and high-energy electrons (10–700 keV), which are the dominant contribution to the particle energy density and pressure around the Earth during major geomagnetic storms. There is evidence (Ingraham et al. 2001) suggesting that intense substorm injection fronts may be able to energize significant fluxes of electrons up to >1 MeV below $L = 4-5$ over time scales of minutes. However, our understanding of the efficiency of the mechanism is largely based on CRRES, which only saw one very large storm on the night side of the Earth. In addition, because CRRES was a single spacecraft, it could not measure the propagation velocity of the injection event or the radial and azimuthal extent of the region of accelerating electric fields.

Figure 2 presents measurements of the dawn-dusk electric field from the EFW instrument on RBSP-A and of the energetic electron omni-directional fluxes from the MagEIS instrument during an injection event associated with a small storm on January 17, 2013. The fluctuating electric field is significantly enhanced over the four hour time interval from 18:00 UT to 22:00 UT, often exceeding 10 mV/m. There is also am average positive value of the Ey mgse (or dawn-dusk) electric field component of 1–3 mV/m beginning at 14 UT and lasting about two hours until the spacecraft move earthward to lower l-values. The dc field is seen again on the out bound pass from 18 UT to the end of the day. Thus the electric field is observed nearly continuously as the spacecraft moves from midnight to the morning sector. The total period of enhanced dawn-dusk electric fields is nearly eight hours. This period coincides with a decrease in Dst from 33 at 14:00 UT to −53 at 24:00 indicating an injection of ring current plasma during this period of strong electric fields. While there have been a number of studies of large amplitude convection and ULF electric fields in the tail and on the night side near geosynchronous orbit, to our knowledge, these are the first observations showing that such large fields can be nearly continuously present for many hours. A cursory examination of this and similar time intervals provides evidence for a rich phenomenology of magnetic field dipolarizations, plasma-sheet expansions and contractions, encounters with the plasma sheet boundary layers, Alfven waves and other ULF waves, and enhancements in the large scale convection electric field. The second panel of Fig. 2 shows line plots of flux from selected MagEIS electron energy channels ranging between 37 keV and 846 keV. The third panel presents color-coded electron fluxes from the MagEIS instrument (Blake et al. this issue) in an energy time spectrogram format. The data from the second and third panel suggest an abrupt injection of <100 keV electrons during the period of the enhanced quasi-static and fluctuating electric field. At the same time, the particles fluxes with energies larger than 100 keV are decreased by about an order of magnitude. This behavior illustrates the complexity of response of different energy particles to electric fields that vary over different spatial and temporal scales. Much detailed analysis remains to unravel the complicated phenomenology revealed by this data set.

The lower values of the electric field, with magnitude less than 1 mV/m seen over the interval from 9:00 to 12:00 UT in Fig. 2, indicate the sensitivity of the electric field measurement is a fraction of a mV/m. Evaluations of measurements from orbits occurring during especially quiet periods ($Kp < 1$) indicate the spin-plane electric measurement is sensitive to fields of <0.3 mV/m.

The CRRES spacecraft had only limited capability of making high time resolution burst measurements, so that intense small-scale wave fields that might violate the conservation of the first or second adiabatic invariants within the injection front could not be evaluated. The RBSP EFW electric field measurements along with measurements of the magnetic field

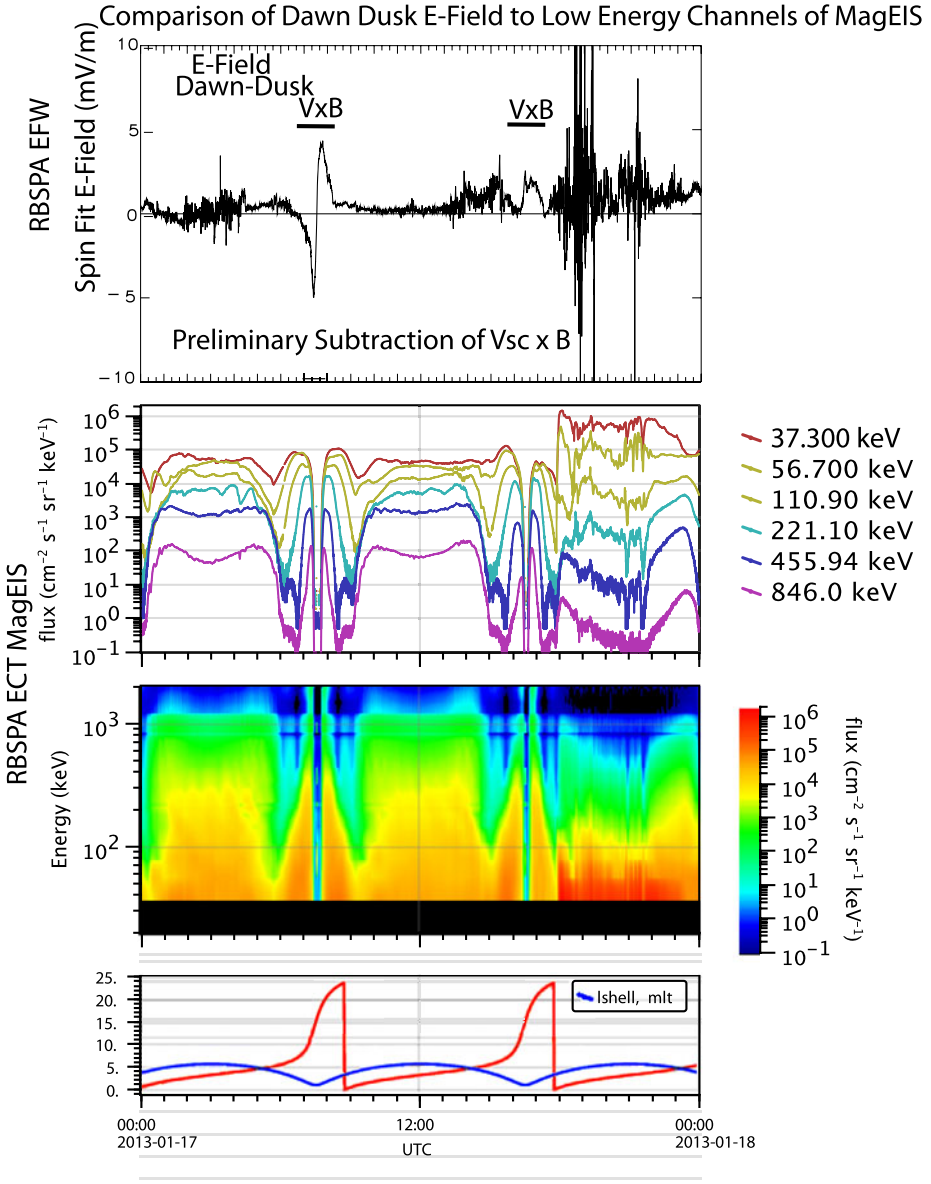

Fig. 2 RBSP-A measurements from January 17, 2013 of the (*upper panel*) dawn-dusk component of the electric field from the spin plane booms at a spin period cadence (11.5 s). The *second panel* presents the omni-directional electron energy flux from selected energy channels (37 keV to 846 keV) from the MagEIS instrument. The *third panel* presents a color-coded omni-directional fluxes in a energy-time spectrogram over the lower energy channels of the MagEIS instrument (MagEIS data courtesy J. Fennell, H. Spence and J.B. Blake). The *bottom panel* consists of line plots of the spacecraft L-value and Magnetic Local Time (MLT) in units of hours

and energetic particles from other instruments will determine, for the first time, the global spatial structure and time evolution of injection events as they propagate through the inner

magnetosphere. This information is crucial for assessing the ability of diverse structures to accelerate particles of different energies and inject them deep into the inner magnetosphere.

At higher frequencies, the EFW instrument will measure electric fields associated with kinetic Alfven waves, lower hybrid waves, ion cyclotron waves, and small-scale discrete structures such as solitary waves. Since CRRES, a number of studies have suggested that whistler mode chorus with amplitudes of 0.1 to several mV/m can be effective in the stochastic energization of electrons over 100 keV to >1 MeV (Roth et al. 1999; Horne and Thorne 1998; Albert 2000; Summers and Omura 2007). It has only been in recent years that the possible role of large amplitude small-scale or high frequency waves in the prompt energization and loss of charged particles over broad energy ranges has been appreciated. High time resolution electron measurements from SAMPEX (Blake et al. 1996; Lorentzen et al. 2002) have provided evidence for relativistic microbursts, which consist of abrupt enhancements of relativistic electron precipitation over periods small compared to an electron bounce period. Measurement of bremsstrahlung x-rays due to precipitating high energy electrons have been provided by balloon-borne detectors and have similarly shown that relativistic electrons can be scattered into the loss cone on rapid time scales (Millan et al. 2002).

Figure 3 from Cattell et al. (2008) presents recent STEREO high time resolution burst measurements of very large amplitude (200 mV/m) obliquely propagating whistler mode waves in the inner magnetosphere just outside the plasmapause. Panel A presents a color-coded frequency time spectrogram showing the over all interval of whistler mode power. The lower plot of panel A is the output of a peak detector that provides the peak amplitude each minute of the whistler mode waves. These measurements indicate large amplitude waves at a frequency of $\sim 0.2 f_{ce}$ (the electron cyclotron frequency, plotted in black) are present for about 30 minutes. Panel B provides a 0.5 second high time resolution measurement of an intense whistler mode pulse from the S/WAVES time domain sampler at a resolution of 35 k samples/s. Panel D provides evidence from SAMPEX of microburst activity on "nearly" conjugate field lines (within 1 hour MLT and 10 minutes) as the STEREO observations. Panel C provides results from a 1-D test particle simulation in which a large amplitude whistler wave is launched along a magnetic field line and interacts with a 1 MeV electron with an initial pitch angle of 30° through a cyclotron resonant interaction. The top panel plots kinetic energy in MeV, the second panel plots the resonance mismatch (see Roth et al. 1999), the third panel plots the equatorial pitch angle, the bottom panel plots the distance along the field line from the equatorial plane in km and the x-axis is time from 0 to 2 seconds, with the electron initially at the equatorial plane. The figure shows that the whistler traps the electron and accelerates it up to 4 MeV in about 0.2 seconds (first panel). The wave also causes strong pitch angle scattering (third panel). The results from these simple test particle simulations indicate that large amplitude whistler mode waves may be capable of nonlinear trapping and acceleration of electrons from initial energies of 100 keV to final energies of 2 MeV over broad portions of phase space in fractions of a second (Cattell et al. 2008) in a single interaction. Over 20 one-half second intervals of large amplitude whistler waves were observed by the STEREO spacecraft during one pass associated with a modest substorm. More evidence for intense whistlers was found by Cully et al. (2008) using the THEMIS spacecraft and, by Kellogg et al. (2010) and Wilson et al. (2011) utilizing Wind data. Evidence for an association of the large amplitude whistler waves with microbursts has been provided by Kersten et al. (2011) using roughly simultaneous measurements from the STEREO spacecraft and the low altitude SAMPEX spacecraft and also measurements between WIND and SAMPEX. An understanding of how the waves are generated and their ability to accelerate particles has been limited by the lack of simultaneous high cadence

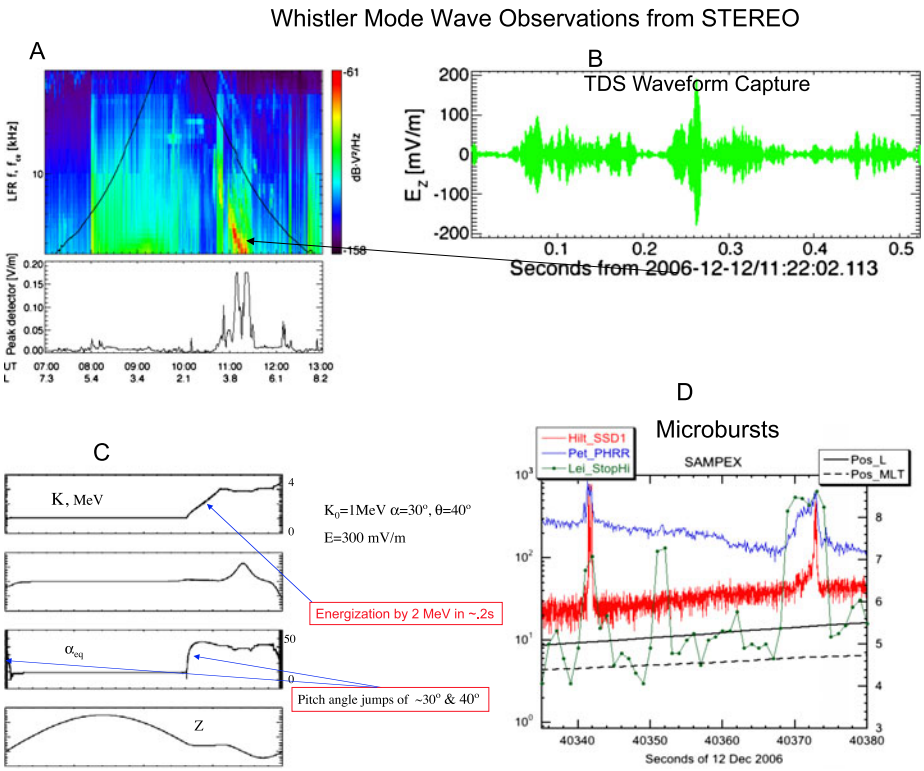

Fig. 3 Wave measurements from STEREO motivating measurements goals of RBPS-EFW. Panel A: *Upper plot* is the electric field spectrogram over frequency range from 2 kHz to 100 kHz (Cattell et al. 2008) from S/WAVES STEREO spacecraft during pass through inner magnetosphere showing strongly enhanced power in whistler band near $L = 3{-}4$ at about 11 UT; Panel **A**, *lower plot* is the peak amplitude in electric field associated with enhanced whistler waves measured once per minute by the peak detector. Panel **B**: High time resolution waveform capture from STEREO showing large (200 mV/m ptp) whistler wave packets from burst recording at time indicated on spectrogram. Panel **C**: Test particle simulations of imposed whistler wave field of amplitude 300 mV/m interacting with an electron with initial energy 1 MeV. The *top plots* is the kinetic energy in MeV, the *second plot* is the resonance mismatch (see Roth et al. 1999), the *third plot* is the equatorial pitch angle, the *bottom plot* is the distance along the field line from the equatorial plane in km and the x-axis is time from 0 to 2 seconds. The *top plot* shows the abrupt coherent nonlinear energization of electrons by 2 MeV and the *third plot* shows the jump in pitch angle through cyclotron resonance during one interaction. Panel **D**: Near simultaneous (within 10 minutes) low altitude SAMPEX observations of relativistic electron microbursts over same L value extent as STEREO whistler displaced 1 hour in magnetic local time

energetic particle measurements and field measurements on the same spacecraft. The EFW instrument provides unambiguous measurements of the occurrence frequency of large amplitude waves, as well as their spatial distribution along magnetic field lines, in radial distance, and in local time. The high time resolution particle measurements will be provided on RBSP by the MAGEIS instrument (Blake et al. this issue) and HOPE instrument (Reeves et al. this issue).

The EFW instrument has the capability of measuring, through burst recordings, large amplitude (requirement $<$500 mV/m; capability $>$4 V/m) waves and structures at frequencies up to 16.4 k samples/s and recording them in burst memory. These will be compared to high time resolution measurements of particles by the HOPE and MagEIS instruments on RBSP

and also to measurements of microburst X-rays detected by balloon-borne instrumentation flown during the BARREL campaign (Millan this issue).

Early measurements from the EFW instruments on RBSP during several major storms illustrate that large amplitude whistler waves routinely have peak values ranging from 10 to >200 mV/m over the entire orbital path outside the plasmasphere during active periods. The incidence of high amplitude whistler waves systematically enhances during major storm periods from apogee at 5.8 Re to radial distances below 3 Re, spanning the position of the outer radiation belts. Figure 4 presents measurements from the main phase of a geomagnetic storm on November 1, 2012. The top panel shows line plots of flux from selected MagEIS electron energy channels ranging between 37 keV and 1942 keV (Spence et al. this issue; Blake et al. this issue); the second panel presents the omidirectional electron fluxes from the MagEIS in an energy time spectrogram format showing a series of injection events (labeled "INJECT"), the outer radiation belts ("OB") and the slot region between the outer and inner belts. Notice that during the final orbit the energetic electrons display a complex signature. Near apogee, between 18:00–20:00 UT, the lower energy (36 and 57 keV) electron fluxes near apogee are strongly enhanced over the previous orbit. The higher energy electrons (100 keV to 2 MeV) fluxes decrease relative to those of the previous orbit. This complex behavior is the consequence of the interplay between a variety of different acceleration and loss mechanisms, including enhancements in the large-scale convection electric field, changes in the magnetic field configuration, current sheet scattering, magnetopause shadowing, and higher frequency wave activity. Here we emphasize observations of the waves. The next two panels present frequency-time spectrograms of the spectral power in the wave electric and magnetic fields (respectively). The wave magnetic field is measured by the magnetic search coil sensor in the EMFISIS instrument (Kletzing et al. 2013) and provided to the EFW instrument via an analog interface. The electric and magnetic spectrograms show that there are enhanced whistler mode waves (labeled "whis"), which extend from near apogee down to radial distances coinciding with the outer radiation belts. Whistler mode chorus is thought to be generated at the magnetic equator and is usually observed in two bands, an upper band and a lower band centered on $f_{ce}/2$ at the equator. The second orbit during this day is near the magnetic equator and provides, as expected, the upper and lower band separated by the measured $f_{ce}/2$. However, during the last orbit, which occurs during the main phase of the storm, the spacecraft is at higher magnetic latitude and the instrument observes only the lower band, and its upper limit frequency is much less than the locally measured $f_{ce}/2$. This suggests the possibility, subject to further analysis and observations from other time intervals, that the value of the magnetic field at the equator where the chorus is generated is much less than the locally measured magnetic field and thus the frequency of the waves, which (to a good approximation) have group velocities along magnetic field lines and propagate to the spacecraft along the field, reflects the equatorial $f_{ce}/2$. These deviations in the frequency of the whistlers occur almost exclusively during storms when field lines are likely to be especially stretched. They may provide information on the accuracy of magnetic field models and on the adiabatic deceleration of energetic particles, which respond to field line stretching. Such stretching might also enhance magnetopause shadowing and current sheet scattering loss mechanisms. Another possibility, that should be investigated with ray tracing programs, is that the whistler mode waves are not propagating along magnetic field lines, in this especially distorted magnetic field configuration. All these issues need further careful study and are beyond the scope of this initial paper.

Electromagnetic emissions seen in both the electric field and the search coil between the hydrogen gyro-frequency (∼100 Hz) and the lower hybrid frequency (∼1 kHz) are enhanced at 14:00 UT during an inbound approach to perigee and again at 23:00 UT during

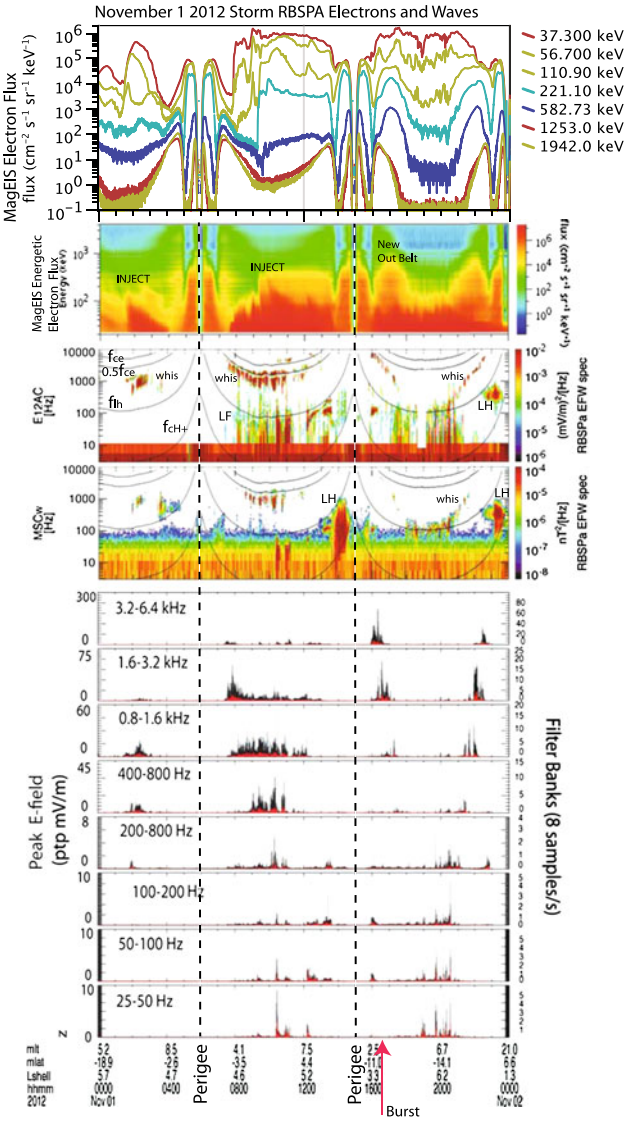

Fig. 4 Measurements during the geomagnetic storm on 11/01/2012 from RBSP-A. *Top panel* is energetic electron omni-directional flux from selected energy channels from the MagEIS instrument and the *second panel* is the color-coded omni-directional fluxes in a energy-time spectrogram format from 37 keV to 4 MeV. The *third* and *fourth panels* are frequency-time spectrograms showing (*third panel*) the power in the wave electric field from a pair of E-field booms and (*fourth panel*) the power in the wave magnetic field from a single search coil magnetometer sensor from the EMFISIS instrument as telemetered through EFW. The subsequent *eight panels* contain line plots of the peak-to-peak value of the electric field at 8 samples/s in each of a series of frequency bins ranging from 25 Hz to 6.4 kHz in order of decreasing frequency. The *vertical scale* is variable for each bin and includes the calibrations of instrument frequency response and effective antenna length. The *vertical red line* coincides with the time of the burst data in the next figure. The wave data from the storm period on 11/01/2012 showing intense average wave power and extra-ordinarily large values of the peak whistler amplitudes over the radial distance from 3 *Re* to 5.8 *Re* (apogee). The *dark curves* superimposed on the wave spectrograms correspond to (in sequence from lowest to highest frequency) the hydrogen ion gyro-frequency, the lower hybrid frequency, one half of the electron gyro-frequency, and the electron gyro-frequency

another inbound approach. These strongly enhanced waves coincide with the position of the "New Outer Belt" which appeared at 14:00 UT. Spacecraft potential measurements (not shown) indicate that these waves are observed inside the plasmasphere. It is worth noting that magnetosonic waves and waves near the lower hybrid frequency inside the plasmasphere are candidate waves for the stochastic acceleration of electrons between 100 keV and several MeV (Horne and Thorne 1998).

Strong electric and magnetic fields are also present at apogee between the ion cyclotron and lower hybrid frequencies. These lower frequency waves (labeled "SS" for "Small Scale") are in the frequency range of lower hybrid waves, ion cyclotron waves, kinetic Alfven waves, and magnetosonic waves. The bottom set of 8 panels in Fig. 4 show the peak electric field measurements in selected frequency bins ranging from 20 Hz to 6.4 kHz. These electric field peak detectors are sampled routinely with unprecedented time resolution; each channel is sampled 8 samples/s compared to 1–2 samples per second or once per spin on previous spacecraft electric field instruments. The RBSP sampling is comparable to the time interval between individual wave pulses and allows us to count high amplitude whistler-mode and other wave mode pulses. These peak measurements will enable assessment of the role of large amplitude whistler waves in the non-linear scattering and energization of energetic electrons and provide context for burst measurements of electric fields (see, for example, burst at time of red arrow shown in Fig. 5). In this plot, they reveal that intense whistler waves with amplitudes exceeding 100 mV/m (peak-to-peak) are present before and during periods of enhanced outer belt fluxes and extend over the entire spatial extent of the outer zone radiation belts down to the slot region. These are necessary conditions for the waves to be important in accelerating outer zone energetic electrons.

Routine high-time resolution burst measurements of electric field waveforms from RBSP allow a detailed examination of wave properties. Figure 5 shows 0.8 seconds of data (from a total burst duration of 5 seconds sampled at 16.4 k samples/second) obtained on the November 1, 2012 storm period at 16:20:26 UT (red arrow in Fig. 4) from the RBSP-A EFW burst memory. The figure shows packets of large amplitude whistler wave with peak to peak amplitudes exceeding 200 mV/m.

As previously discussed, the structure and dynamics of the plasmasphere are important for understanding the dynamics of the inner magnetosphere during major geomagnetic storms. The plasmasphere can be strongly eroded during major geomagnetic storms by the action of the large-scale convection electric field. During these times, the plasmapause can move from its quiet time position of $>5\,Re$ to within $2\,Re$. However, there have been few direct experimental comparisons in the outer magnetosphere between the large-scale electric field and the plasmaspheric structure. Information on cold plasma densities is provided on the RBSP mission by tracking the frequency of the upper hybrid line as determined by the EMFISIS instrument and by the measurement of the spacecraft potential by EFW. The EMFISIS determination of density is more accurate than the density estimated from spacecraft potential and less subject to uncertainties associated with cold electron temperature effects. The spacecraft potential measurement provides higher time resolution ranging up to 16 samples/s in routine survey mode. Figure 6 presents a cross calibration over one day and several orbits between density determined the upper hybrid line and that estimated from the EFW spacecraft potential. The plasmaspheric profile is clearly shown in the spacecraft potential measurements and the cold plasmaspheric density determined to better than the 50 % accuracy of the measurement goal.

The two RBSP spacecraft provide measurements at radially and azimuthally separated points deep in the inner magnetosphere allowing, for the first time, the determination of the spatial extent, velocities of propagation, and temporal evolution of large scale electric field

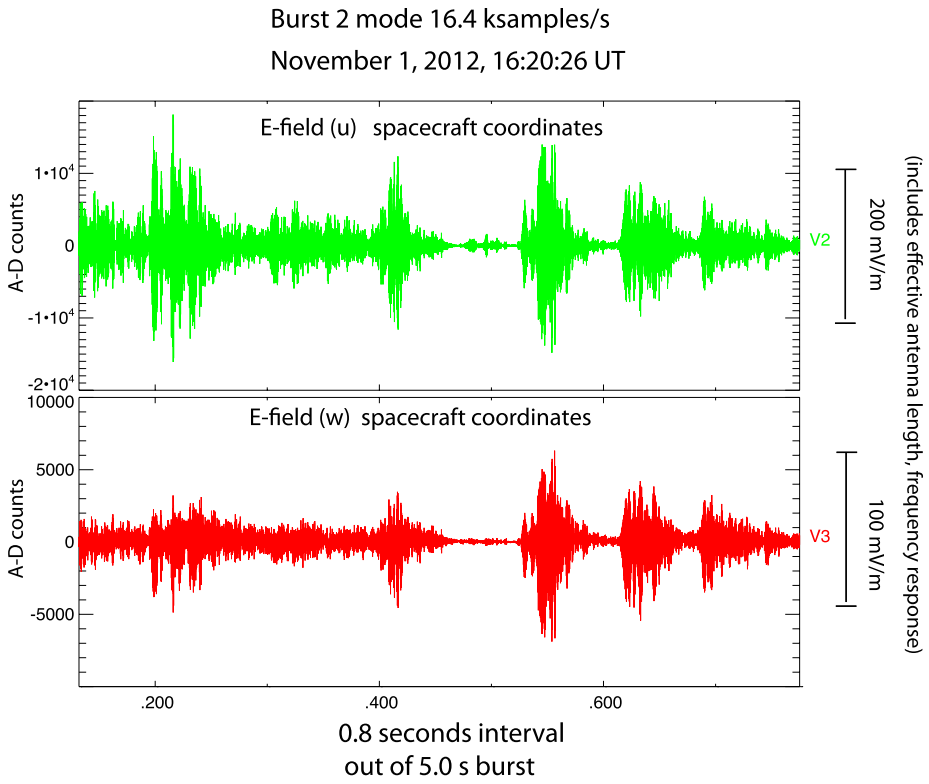

Fig. 5 EFW burst recording on 11/01/2012 16:20:26 of high time resolution measurements of two components of the electric field in the spin plane of the spacecraft showing a whistler waveform over a period of 0.8 seconds. This burst was triggered by the peak power in the electric field determined by the sum over the five highest frequency bins in the filter banks shown in the previous figure. The time of this burst coincides with the *red arrow* labeled "burst" at the bottom of Fig. 4. EFW bursts also include search coil magnetometer data from the EMFISIS instrument (not shown). The total burst duration was 5 seconds

structures associated with shocks, injection fronts, and MHD waves. The two spacecraft measurements will distinguish between temporal and spatial structures in the hot ring current plasma and allow the measurement of ring current pressure gradients that control the configuration of convective flows. This provides a framework for understanding the ability of different mechanisms to selectively energize different particle populations. The two spacecraft mission will determine the radial and azimuthal extent of the higher frequency wave fields thought to be important in energization and scattering. The amplitude structure, occurrence frequency, polarization, direction of propagation, E/B ratios and local density structure will be investigated in detail.

Previous magnetospheric missions missed many of these effects because the spacecraft orbits were not in the equatorial plane, they had apogees outside the region of interest, and they passed through the inner magnetosphere for only short periods of time often missing the intervals of powerful acceleration. They sometimes were not equipped with the necessary complement of electric field, magnetometer, and particle instruments. The CRRES spacecraft, which has provided some of the most interesting measurements in the inner magnetosphere, took measurements when the monitoring of upstream solar wind conditions was sporadic. There were no solar wind observations of the interplanetary shock or the CME that

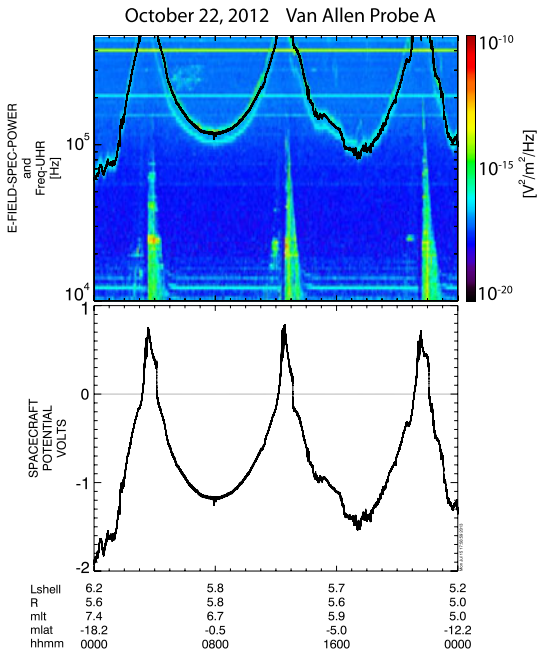

Fig. 6 Comparison of spacecraft potential to the density determined from the upper hybrid line. The *top panel* is the color-coded spectrogram of the wave electric field over the frequency range from about 10 kHz to above 400 kHz in a frequency vs time format (obtained the EMFISIS instrument). The superimposed *dark line* is the prediction of the upper-hybrid line based on an empirical fit to the EFW measured spacecraft potential. The bottom panel is the directly measured spacecraft potential measured as the sum of the potential measurement of the individual probes in the spin plane $(V1 + V2)/2$

drove convective flows and ring current injection for the March 1991 storm or most of the other storms of the CRRES mission. The CRRES electric field instrument had only a small burst memory and a limited capability for high time resolution measurements of electric fields and therefore never saw the large amplitude whistler waves thought to be a major energization candidate. Some of the most important measurements of large amplitude whistler waves came from the WAVES instrument on STEREO and also the WAVES instrument on WIND. The STEREO mission was a two-spacecraft solar wind mission that only orbited through the inner magnetosphere about a half a dozen times on their way out to their respective orbits around the Sun. The observations of numerous large amplitude whistler wave packets were obtained during just one pass during a modest substorm and were not part of the prime science effort of that mission. The WIND spacecraft similarly orbited through the inner magnetosphere only a limited number of times.

Another major NASA asset that will significantly enhance the science return of EFW and other RBSP instruments is the THEMIS spacecraft, which will be able to provide crucial information on electric fields and particles at larger radial positions which provides the source population for many of the inner magnetosphere acceleration processes. The EFW team includes Co-Is associated with the electric field experiment on THEMIS. In order to enhance global coverage of the large-scale electric field and provide insight into the ionospheric effects of major geomagnetic storms, the EFW team has included the Millstone Hill radar, which provides measurements of electric field in the mid-latitude regions. In addition, the EFW team plans to coordinate high time resolution burst electric field measurements with the BARREL investigation (Millan this issue), which will provide balloon-borne measurements of X-rays associated with relativistic electron microbursts.

2 EFW Measurement Requirements

In order to measure the electric fields responsible for the acceleration mechanisms described above, the EFW instrument has been designed to meet a series of demanding measurement requirements and goals. The most important requirements driving instrument design are described below. The instrument meets or exceeds these requirements.

- Measure 2-d quasi-static electric fields in the spin plane of the spacecraft at radial distances $>3\,R_E$ to an accuracy of 0.3 mV/m or 10 % of the maximum electric field amplitude, which ever is larger, over a dynamic range of ±500 mV/m.
- To provide measurements of the quasi-static electric field component along the shorter spin axis booms to an accuracy of 4 mV/m or 20 % of the maximum electric field magnitude at radial distances of $>3\,Re$.
- To provide measurements of cold (<30 eV) plasma variations in the plasmasphere over time scales from DC to <1 s with an accuracy of 50 % over a density range from 0.1 to 50 cm^{-3}.
- To provide burst waveform measurements of large amplitude electric fields up to at least 250 Hz with an accuracy of 0.3 mV/m and a range of 500 mV/m at a cadence of 512 samples/s.
- To include measurements of the 3-d wave magnetic field obtained from the EMFISIS instrument in burst recordings (along with the wave electric field measurements described above) up to at least 250 Hz.
- Provide interferometric timing of the propagation of small-scale waves and structures between opposing sensor pairs using burst recordings with a time cadence of up to 16.4 k samples/s.
- Provide spectral and cross-spectral information on the wave electric fields, magnetic fields, and density fluctuations up to 250 Hz.
- Provide the EMFISIS wave instrument with the three measured components of the electric field over the frequency range from 10 Hz to 400 kHz with a noise level of 10^{-13} V^2/m^2 Hz at 1 kHz and 10^{-17} V^2/m^2 Hz at 100 kHz with a 90 dB dynamic range and a maximum signal of 30 mV/m.

3 Overview

3.1 Instrument Design

The design of the RBSP EFW instrument is based on heritage from a long line of double probe instruments including those on the S3-3 spacecraft (Mozer et al. 1979), ISEE-1 (Mozer et al. 1973), CRRES (Wygant et al. 1992), Viking (Marklund 1993), Freja (Marklund et al. 2004), FAST (Ergun et al. 2001), Polar (Harvey et al. 1995), the Cluster multi-spacecraft mission (Gustafsson et al. 1997), and the THEMIS spacecraft (Bonnell et al. 2008). An extensive discussion of electric field measurements and error sources of this kind of electric field instrument may be found in Bonnell et al. (2008).

On RBSP the three dimensional electric field is measured using spherical sensors at ends of two orthogonal pairs of centrifugally deployed spin plane booms with tip to tip separations of 100 m and a pair of spin-axis stacer booms with an adjustable tip to tip separation of 12–14 m. A schematic of the spacecraft showing the orientation of the booms is presented in Fig. 7. Also shown are the search coil and fluxgate magnetometers. Table 1 presents information on the relation between the spacecraft coordinate system and the measurement

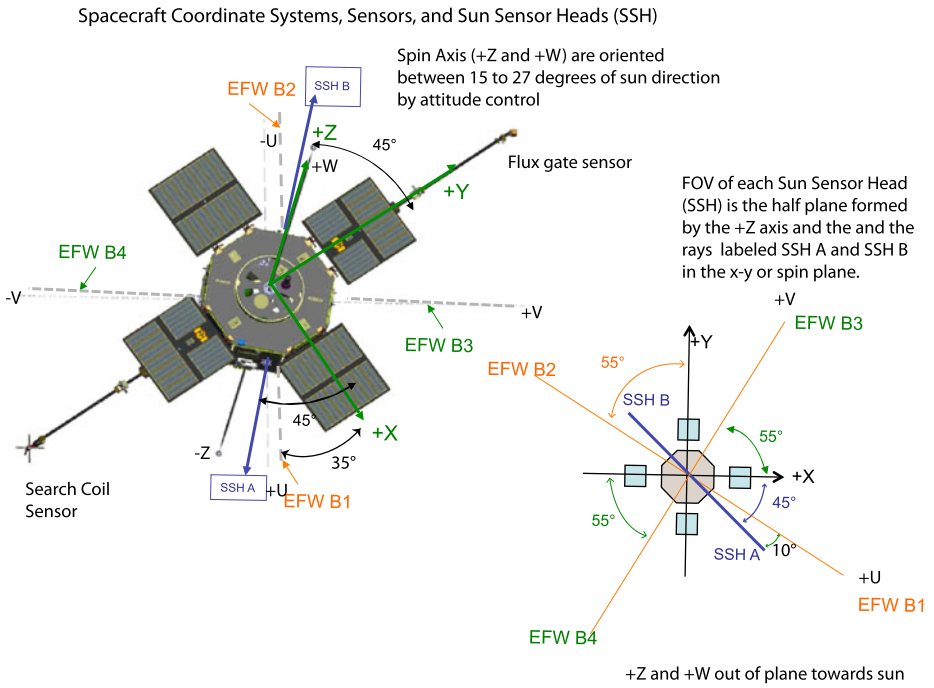

Fig. 7 Overview picture of RBSP spacecraft showing orientation of EFW spin plane boom sensors, EFW axial boom sensors, and EMFISIS 3-D Magnetic Search Coil sensors, spacecraft coordinates (xyz) and sensor coordinates (UVW) are indicated. Also shown are the two Sun Sensor Heads (SSH A and B) FOV directions relative to spacecraft coordinates and EFW spin plane booms. Magnetic Search Coil sensors directions and EFW booms are aligned in a common the UVW coordinate system for ease of analysis

Table 1 Boom locations and telemetry channels relative. To coordinate systems on the spacecraft

EMFISIS Science Coordinates (SCM& FGM)	S/C Coordinates	S/C-ICD Boom#	EFW TM Channel
$+V$	$+X+Y$	3	4
$+U$	$+X-Y$	1	2
$-U$	$-X+Y$	2	1
$-V$	$-X-Y$	4	3
$+W$	$+Z$	6	6
$-W$	$-Z$		5

directions of the electric field, flux gate magnetometer, and search coils. The three orthogonal search coil sensors and the three pairs of electric field probes are aligned with each other to facilitate comparison. Additional images of the spacecraft, coordinate systems, electric and magnetic field sensor booms, and instrument fields of view may be found in Kirby et al. (this issue).

The spacecraft rotates in a right-handed sense about the spacecraft +z axis with a nominal spin rate ~5.5 RPM. The spacecraft spin axis is directed between 15 and 27 degrees of the Sun, so that the spin plane booms rotate approximately in the y–z GSE plane. The

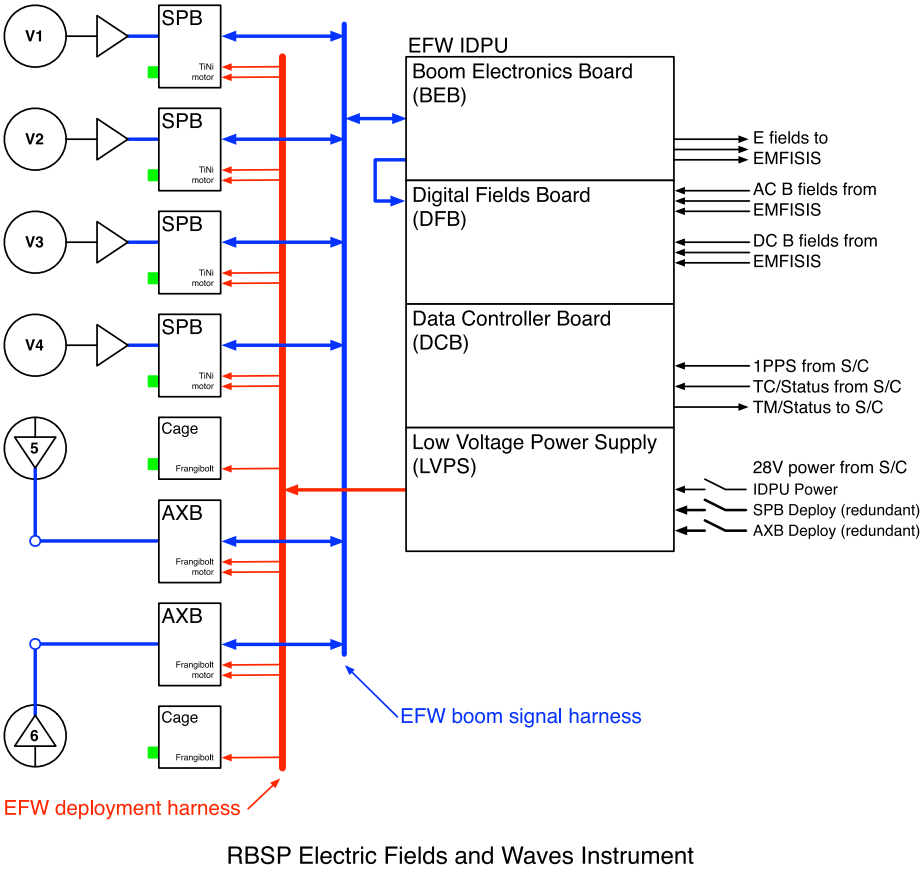

Fig. 8 Block diagram of EFW instrument including Deployment Units, the EFW IDPU, and major interfaces with the spacecraft and with the EMFISIS instrument. The IDPU block shows major functional subsystems, as well as, signal lines (V1–V6), power lines, diagnostic lines (temperature, boom turns counters), and control lines (motor power, door controls) between the IDPU and the Deployment Units

electric field measurement is most accurate in this plane due to the length of the booms and the nearly uniform illumination of the sensors by the Sun.

A functional block diagram of the EFW instrument is presented in Fig. 8. Each EFW instrument consists of an Instrument Data Processing Unit (IDPU) and the six separate boom deployment units. The IDPU consists of a Boom Electronics Board (BEB), a Digital Fields Board (DFB), a Digital Control Board (DCB), and a Low Voltage Power Supply (LVPS) board. The EFW instrument transfers three high frequency analog differential electric field signals to the EMFISIS instrument (Kletzing et al. 2013, this issue). From EMFISIS, EFW receives three axis analog search coil AC magnetometer signals as well as the three axis fluxgate DC magnetometer signals. The EMFISIS search coil sensors are aligned with the electric field booms and are measured in the UVW coordinate system as illustrated in Fig. 7.

Table 2 presents a summary of the mass, power, and telemetry allocations of the EFW instrument and its major subsystems.

Table 2 EFW mass. power, and telemetry

	Mass (kg)	Power (W)	TM
IDPU	6.4	11 (@30V)	12.0 kbits/s
Shielding	2.2		
Spin Plane Booms (×4)	2.04 (8.16)	–	–
Axial Booms (×2)	3.12 (6.24)	–	–
Axial boom tube assembly	1.03	–	–
Harness	3.36	–	–
Total	27.39	10.2	12.0 kbits

4 EFW Design

4.1 Overview of Signal Path, Block Diagram and Science Quantities

This section provides a brief overview of the signal paths and processing through the EFW instrument. A more detailed discussion of the design and functionality appears in subsequent sections.

The potential differences between each of the six spherical sensors and the spacecraft (labeled V1 through V6) are driven by unity gain preamplifiers near the sphere and the signals are sent down their respective boom cables to the Instrument Data Processing Unit (IDPU) where they enter the Boom Electronics Board (BEB). These signals are transferred directly to the Digital Filter Board (DFB) where AC coupled versions of the signals are generated in analog circuitry. The sensor signals from opposing booms are also differenced on the DFB board to provide AC (>10 Hz) and DC coupled versions of the three components of the electric field. The analog signals are digitized with 16-bit cross-strapped A-D converters on the DFB. Higher frequency (10 Hz–400 kHz) wave electric field signals over the amplitude range (± 40 mV/m) are transferred to the EMFISIS wave instrument from the BEB via an analog buffer for wave analysis in that instrument. The digitized sensor and electric field measurements made on the DFB are transferred to the Digital Control Board (DCB) for formatting into Survey and Burst telemetry formats. The DFB provides the three components of the DC electric field from opposite sensors, denoted E12dc, E34dc, E56dc, which are sampled at 32 samples/s and digitally filtered at 10 Hz with a dynamic range of ± 1V/m and the single ended probe-spacecraft potential measurement (V1 through V6) sampled at 16 samples/s with a dynamic range of ± 225 volts. These single sensor measurements when differenced on the ground can provide electric field measurements with a dynamic range up to 4 V/m. The waveform data are telemetered to the ground continuously over the entire RBSP orbit in a survey mode. The DFB also calculates for inclusion in the survey mode a variety of spectral and filter bank products. These include the complex Fast Fourier Transform (labeled SPEC) of selectable EFW field measurements over a frequency range of 1 Hz to 6.4 kHz. In the default mode, a spectrum is telemetered once every 8 seconds and is organized into 64 pseudo-logarithmic frequency bins. The cross spectra between two selected measurements (XSPEC) is also calculated and telemetered to the ground in 64 pseudo-logarithmically spaced frequency bins. The two default measurements used in this calculation are the AC coupled differential electric field measurement from the 1–2 boom pair (E12ac) and the component of the search coil along the spin axis (SCM_W). Continuous

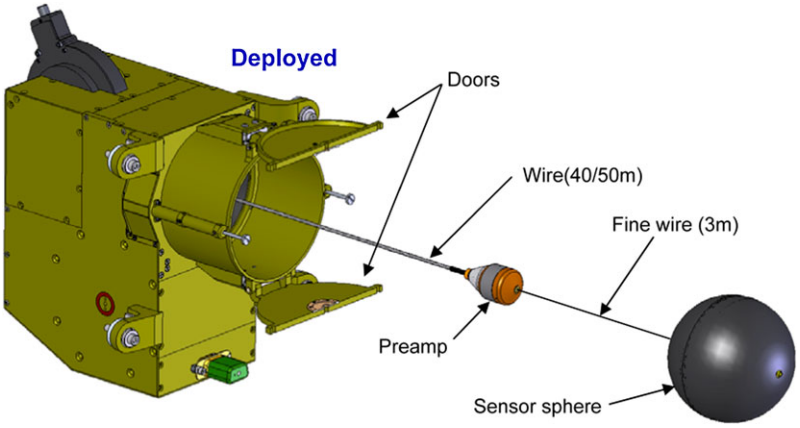

Fig. 9 EFW Spin Plane Boom Deployment Unit in deployed configuration showing deployment unit, cable, pre-amplifier housing, 3-meter thin wire, and spherical sensor

measurements of rapid variations in average power and peak values of waves, is provided in survey mode for two selectable quantities via a bank of broadband filters. These quantities are denoted FBK_1_av, FBK_1_pk, FBK 2_av, and FBK_2_pk respectively. In the default mode, these broad band filters are sampled at a cadence of 8 times per second in seven pseudo-logarithmically spaced frequency bins from 1 Hz to 6.5 kHz.

High time resolution measurements of waveforms, which cannot be continuously telemetered within the allocated EFW telemetry, are provided through two burst modes using two independent burst memories involving different programmable modes of collection and playback controlled by the DCB. The Burst telemetry nominally includes three high frequency versions of the differential electric field measurements, the six sensor-spacecraft potential measurements, and the three components of the search coil magnetometer. These modes will be described in more detail in later sections.

4.2 Sensor System and Measurement Accuracy

Spin Plane Sensors The spin plane sensor and cable system is illustrated in Fig. 9. The sensor is a conducting metal sphere of radius 4 cm coated with DAG 213 in order to minimize work function variations over the sphere and from sphere to sphere. In the deployed configuration, the sphere is connected to a high input impedance preamplifier via a thin 3 m long conducting wire. The sensors are current biased to control their floating potential and to minimize their sheath impedance. Theoretical calculations and comparison of measurements from biased and unbiased probes on ISEE-1, CRRES and Polar have shown that current biasing can reduce errors due to variations in floating potential by three orders of magnitude. In a manner similar to CRRES, Polar and Cluster, diagnostic sweeps in voltage will be used to determine the optimum value of the bias current. The sheath impedance coupling the electric field sensors to the plasma is adjusted through biasing to be $<10^7$ ohms which is much smaller than the input resistance of the PMI OP-15 pre-amplifier input stage (10^{11} ohms). Similarly, the capacitive impedance of the 3-meter bare wire portion of the sensor dominates over the input impedance of the OP-15 preamplifier input stage. This sensor design dramatically limits both DC and AC voltage divider effects on input signals producing a near unity gain out to high frequencies. The frequency response of the electric field instrument ranges

up to 400 kHz. The OP-15 was used on CRRES and on THEMIS. It is radiation tolerant to 50 krads of total dose and is tantalum shielded to 100 krads to meet the 2-year mission specification. The spin-plane boom cables carry power supply and biasing voltages out to the pre-amplifiers. They carry the sensor voltages measured by the pre-amplifiers back to the main electronics box.

An important error source in the measurement of electric fields is associated with the spurious photocurrents flowing between the spherical sensors and neighboring boom and sensor elements. These photocurrents produce fluctuations in the floating potential of the sphere surface relative to plasma potential. The small surface area of the very thin 3 m long wire connecting the sphere to the pre-amplifier is designed to limit the magnitude of such photo-currents to the sensor. In addition, the flow of photocurrents is controlled by voltage biasing of neighboring surfaces relative to the sphere potential. The biasing is controlled by the DCB microprocessor. The in-board surface called the guard is nominally biased at a constant value of $\sim$5 volts negative relative to the sphere in order to limit the flux of photoelectrons to the sensor from the nearby cable and the large spacecraft surface. The out-board surface is typically biased $\sim$1 volt negative to limit the outflow from the pre-amplifier housing to the sensor. Precise values will be determined through processor controlled bias sweeps and evaluation of the measurement accuracy at different points along the orbit during commissioning, as well as periodically during the mission.

The fact that the spin axis of the spacecraft is pointed nearly towards the Sun contributes to an especially sensitive electric field measurement in the spin-plane. This orientation results in nearly uniform solar illumination of the spin plane sensors over a spacecraft rotation. Consequently, the photocurrent to the spin plane sensors is also nearly constant over a spacecraft rotation. The electric field data will be less accurate when (1) the spacecraft is shadowed by the Earth so that the photo-currents necessary to produce a stable potential reference for the probes are not present, (2) during very brief periods when the thrusters on the spacecraft are firing and the spacecraft is surrounded by a thruster plume, (3) and during periods after attitude maneuvers when the boom cables are oscillating about their equilibrium points.

The spin-axis electric field is about an order of magnitude less accurate than the spin plane measurements since the spin axis booms are shorter by a factor of $\sim$7 and have a comparatively greater error contribution from asymmetries in the spatial configuration of the spacecraft potential. A new feature of the spin-axis stacer booms on RBSP is that the length of the booms can be controlled such that, after on-orbit calibration, the sensors are positioned on the same equipotential of the spacecraft potential reducing offset errors to the electric field. Thus, the booms are not "popped" outward to a pre-determined length under the spring force of the stacer, but are restrained during deployment by the tension in the cable, which is slowly played out in a controlled fashion by a motor. The motor does not have a retract capability, but does allow the lengths of the two opposing spin axis booms to be independently adjusted.

Accuracy of the measurement along the spin axis booms is affected if the anti-sunward spin-axis boom is partially shadowed by one of the four solar panels as the spacecraft rotates. At these times, because there will be perturbations per spin period, the spin axis electric field component will be calculated from samples obtained from those intervals when the spin axis boom is not shadowed. In addition, spacecraft attitude is controlled by operators to minimize this shadowing by maintaining at least 15 degree offset of the spin axis from sun pointing.

On CRRES, during some of most intense electron injection events, the spacecraft differentially charged hundreds of volts relative to the plasma. These voltages exceeded the power supply rails of the pre-amplifier electronics and, as a consequence, the electric field

instrument sometimes saturated during interesting electron acceleration events. On RBSP, the project instituted a rigorous program of electrostatic cleanliness to insure that the surface of the spacecraft was conducting and that conductive paths tied all major exterior surfaces together including the solar panels and thermal blankets. The electrostatic cleanliness program was designed to attempt keep spacecraft surfaces electrical equipotentials to within 1 volt and avoid differential charging.

The EFW instrument provides a measurement the spacecraft potential which can be used to estimate of the thermal plasma density in the plasmasphere and identify interval of spacecraft charging. The EFW instrument telemeters "single probe potentials", V1s, V2s, . . . , V6s, which consist of the measured potential differences between individual probe and the spacecraft. The spacecraft potential is calculated on the ground by summing the single probe potentials from sensors on opposite sides of the spacecraft. This sum removes the differential electric signal due associated convection, waves, and other ambient plasma processes. In lower density cold plasmas (<100 cm^{-3}), the spacecraft potential relative to the ambient plasma is primarily determined by the balance between photoemission associated with solar illumination and the thermal current associated with thermal electrons in the plasma. The current-biased probes provide a stable reference (within 1–2 volts of plasma potential) for the measurement of the spacecraft potential relative to the ambient plasma. Interpretation of the spacecraft potential in terms of the properties of the thermal electron plasma must include the fact that the spacecraft is typically in the Langmuir probe "focusing regime" (Pedersen 1995; Pedersen et al. 2008). In these circumstances the spacecraft potential scales as the logarithm of the electron density with a small contribution from temperature effects. The spacecraft potential is typically calibrated periodically against other measures of plasma density. As discussed in the Introduction, Fig. 6 presents a calibration of the spacecraft potential versus density as determined from measurements of the upper hybrid frequency by the EMFISIS instrument (Kletzing et al. 2013) over the density range from 1 to 10^{-3} during one orbit. The spacecraft potential measurements provide a higher time resolution (DC—100 Hz), but less accurate, measurement of the density and thermal plasma structure than the one obtained from the upper hybrid frequency measurement. The spacecraft potential algorithm for calculating density is inaccurate during intervals of negative spacecraft charging induced by very strong fluxes of 10 eV to 1 keV electrons near apogee. Periods of strong spacecraft charging may be identified by comparing the spacecraft potential to the HOPE measurement of H+ and O+ over the 10 eV to 5 keV range (Reeves et al. this issue).

Sensor Frequency Response The frequency response of the spin-plane sensor system is governed by the properties of the plasma sheath around the sensors and by the ability of the preamplifier to drive the long 50-meter cables. The source impedance of the plasma sheath surrounding the sensor forms a voltage divider with the input impedance of the preamplifier system. The switch from resistive to capacitive coupling is associated with a roll-off in frequency response from unity near DC to 0.6 at $\sim$100 Hz. A second higher frequency roll-off in the sensor/cable system occurs as a consequence of the capacitive loading of the preamplifier by the long spin-plane cables. This occurs near 300–400 kHz and defines the upper end of the frequency response for the signals sent to the EMFISIS instrument.

Figure 10 presents plots of the gain and phase shift of the spin plane and spin axis boom pre-amplifier system and cables at the entrance to the EFW IDPU. Note that the spin axis booms have a higher frequency response as a consequence of the decreased attenuation due to the lower capacitance of the shorter spin axis boom. Additional phase shifts for these measurements are associated with the 5 pole Bessel anti-aliasing filters. For Bessel filters

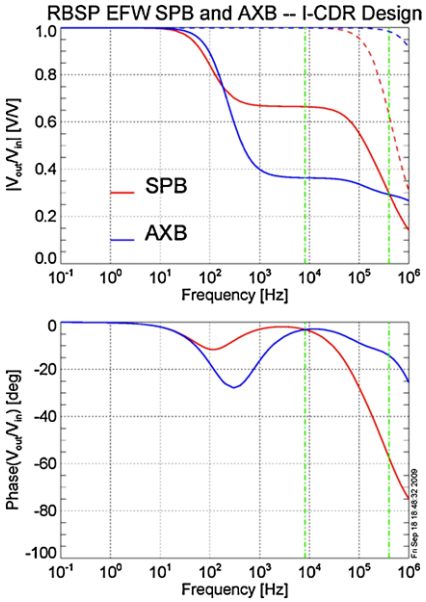

Fig. 10 Panel **A**. Calculated (for low density plasma) SPB sensor frequency response (including phase shift) of signals input to spherical sensors and output at entry to IDPU. Panel **B**: Same as Panel **A** for spin axis sensor. The *first vertical green dotted line* (near 8.2 kHz) indicates the highest frequency signal processed by the EFW instrument. The *second dotted line* at higher frequency indicates the required upper frequency of the signal passed to the EMFISIS wave instrument

Table 3 Time delay due to FIR 5 pole Bessel filters

Sampling rate	Delay (ms)	Sampling rate	Delay (ms)
1	6007.446	256	30.884
2	3007.446	512	19.165
4	1507.446	1024	13.306
8	757.446	2048	10.376
16	382.446	4096	8.911
32	194.946	8192	8.179
64	101.196	16384	7.813
128	54.321		

the phase shift is linear as a function of frequency. For time domain signals this results in a constant time delay for a given roll-off frequency. Table 3 provides the time delays for different anti-aliasing frequencies for the 5 poles Bessel filters appropriate for all quantities in the burst and survey data.

On-orbit Calibration and Analysis of the Electric Field Measurement Calibrations of the electric field instrument can be provided in several ways. During quiet times when geophysical electric fields are small, the electric field measurement should approach $E = -V_{sc} \times B$ where V_{sc} is the spacecraft velocity relative to the rest frame of the Earth and B is the measured magnetic field. For electric fields that are constant over a spin period, the measured signal from orthogonal booms pairs should be 90 degrees out of phase and scale in magnitude with 100 m boom lengths. During periods of strong flows in the near Earth plasma sheet, the velocity moments, V_P, from the HOPE plasma instrument can be used to estimate $E = -V_P \times B$.

Historically it has been found that the most accurate quasi-static electric field determinations are provided by least-squares spin-fits to the electric field measured by the spin plane

sensors in the rotating frame of the spacecraft. In the rotating system, a constant electric field in inertial space appears as a sinusoidal signal. This fit determines the optimum values of the amplitude and phase of this sinusoidal signal, determining the magnitude and direction of the electric field projected into the spin plane. Such spin fits are especially accurate because they use the large number (484) of measurement points gathered over one spin period and because they remove work function voltage differences between the probes and other errors which appear as constant offsets to the sinusoid. After one fit, the fit may be further optimized by removing noise points far from the fit value (i.e. more than 2 standard deviations) and repeating the process as needed to obtained the desired accuracy. Perturbations to the sinusoidal electric field signal observed by the rotating sensors due to angle dependent spurious photo-currents or wake effects can removed by selectively masking data points over those rotation angles most susceptible to the perturbations.

Analysis of data from the CRRES spacecraft, which also had a sun-pointing spin axis, shows that the dominant error source for the quasi-static spin plane electric field is typically due to the effect of attitude uncertainties in the Lorentz transformation from the spacecraft frame to the inertial frame of the Earth. The attitude uncertainty of $<3^0$ will allow EFW to meet or exceed the spin-plane boom measurement sensitivity requirement above 3 R_E radial distance (either of 0.3 mV/m or 10 % of the amplitude of the electric field, which ever is larger). The anticipated Spin plane electric field sensitivity after spin fits and other ground analysis efforts is expected to be 0.1 mV/m (or 10 % of the amplitude) based on CRRES measurements (Rowland and Wygant 1998).

Spin Axis Electric Field Measurement The spin axis measurement is especially accurate for higher frequency wave measurements ($>$100 Hz to 400 kHz) where it provides for a full three-dimensional electric field measurement. However, for quasi-static and low frequency measurements, the measurement is less accurate than the spin plane booms since the spin axis booms provide a shorter measurement baseline. In addition, the spin axis sensors are closer to the spacecraft and sample a larger fraction of the spacecraft charging structure especially at apogee where the Debye length is larger than the spacecraft dimensions and the charging structure has a slower fall-off with radial distance. Since this structure is asymmetric with respect to the Earth–Sun line, a portion of this charging structure appears as a differential signal in the low frequency electric field. These asymmetric contributions to the spin axis measurement are partially mitigated on RBSP, since the lengths of the individual spin axis booms may be incrementally adjusted (outward only) during on-orbit calibrations to remove the contribution from the spacecraft potential to the electric field. Finally, the spin axis booms may be shadowed by solar panels, which rotate and intermittently shadow the anti-sunward boom varying the photoemission and potentials of booms surfaces. This shadowing can produce periodic spikes repeating at the spin period lasting $<1/16$ second, which must be removed from the data. This photoemission variability is strongest for the anti-sunward spin-axis boom when the spin axis of the spacecraft points directly at the Sun. This shadowing near the electric sensors is mitigated on RBSP through on-orbit attitude maneuvers that control the angle between the spin axis of the spacecraft and the Earth sun-line so that it is always larger than 15 degrees. Measurement of the quasi-static spin-axis electric field requires extensive ground analysis and validation. The quasi-static spin axis electric field measurement is most useful for large electric fields associated with ULF waves, shocks, and injection events. In addition, it is designed to provide useful information on the structure of the large-scale convection electric field during major geomagnetic storms when the field is especially strong and penetrates to lower L-value, and higher plasma densities (Wygant et al. 1998; Rowland and Wygant 1998). It is complemented when possible by the derivation of the spin

axis electric field from the measurement of the two spin plane components of the electric field and the full three dimensional magnetic field measurement (from EMFISIS) and the constraint that (for large scale slowly varying fields) $E \bullet B = 0$.

IDPU Electronics: Boom Electronics Board The signals from the six electric field sensors enter the IDPU onto the Boom Electronics Board (BEB). At this point, the DC signal has a gain of near unity and a dynamic range of ∼225 volts. The sensor electric field signal is transferred to the Digital Filter Board (DFB) for signal processing and A-D conversion. Signals from opposing booms are subtracted and sent as buffered wave electric field signals with a frequency response up to 400 kHz to the EMFISIS instrument. The required noise level of the signal to the EMFISIS instrument at the output of this buffer is 10^{-14} V^2/m^2 Hz at 1 kHz and 10^{-17} V^2/m^2 Hz at 100 kHz. This was verified at EFW instrument level testing and also during interface testing with the EMFISIS instrument itself. The required minimum dynamic range is ±30 mV/m. This value is met and exceeded by the actual dynamic range of ∼40 mV/m.

One of the principle functions of the BEB is to generate and transfer the different control voltages that are used for current biasing of the probe and to control the potential of surfaces near the sensors. These signals are transferred to each of the six boom deployment units and then out via wires in the boom cables to each of the sensors. These bias control circuits consist of the current bias circuit, the usher bias circuit, and the guard bias circuit. Each of the sensors is independently controlled by a set of bias circuits.

The current bias circuitry results in the injection of a microprocessor-controlled bias current from the sensor surface into the plasma to control the sensor floating potential and the plasma sensor-sheath resistance. This is achieved by setting the operational point on the current-voltage curve of the sensor/plasma sheath. In low-density plasmas, the bias current is generally adjusted to be a significant fraction of the total photocurrent to the probe. The injected bias current may be adjusted over a range between ±500 nA to an accuracy of 0.2 % by the bias circuitry. The bias circuit has a high frequency roll-off (6 dB) at about 300 Hz. The optimum bias current will be determined by on-orbit bias sweeps during the commissioning phase and also at a lesser cadence throughout the mission. Depending on on-orbit calibration results, the bias current may have different values in the low-density plasma near apogee and in the higher density plasma deep within the plasmasphere.

The usher and guard bias circuits generate voltages that equal the sum of a sphere output plus a microprocessor-controlled voltage offset. The roll-off for the usher signal is 300 Hz and that for the guard circuit is 100 Hz. These circuits control the perturbing sensor-boom photocurrents over the frequency range from DC to somewhat less than 100 Hz where the sensor-plasma sheath impedance is resistive. The usher and guard voltages are transferred via the boom cable to their respective conductive control surfaces on the preamplifier sensor housing. Thus, the potential of these control surfaces relative to the sensor are a constant microprocessor-controlled value. The voltages may be adjusted to a constant value over a range of ±40 volts with a 16-bit DAC. The usher and guard bias potentials will be optimized during the commissioning phase and periodically throughout the mission. Typical values range between zero and several times the photoelectron e-folding energy or ∼5 volts. Typically, once adjusted to their optimum values, the guard and usher voltages remain constant for months to years. The commanded values of the bias, guard, and usher voltages are included in EFW housekeeping telemetry, as are the parameters of the bias sweeps.

Search Coil Signals The three components of the wave magnetic field from the EMFISIS search coils (Kletzing et al. 2013) are provided to the EFW instrument via analog lines

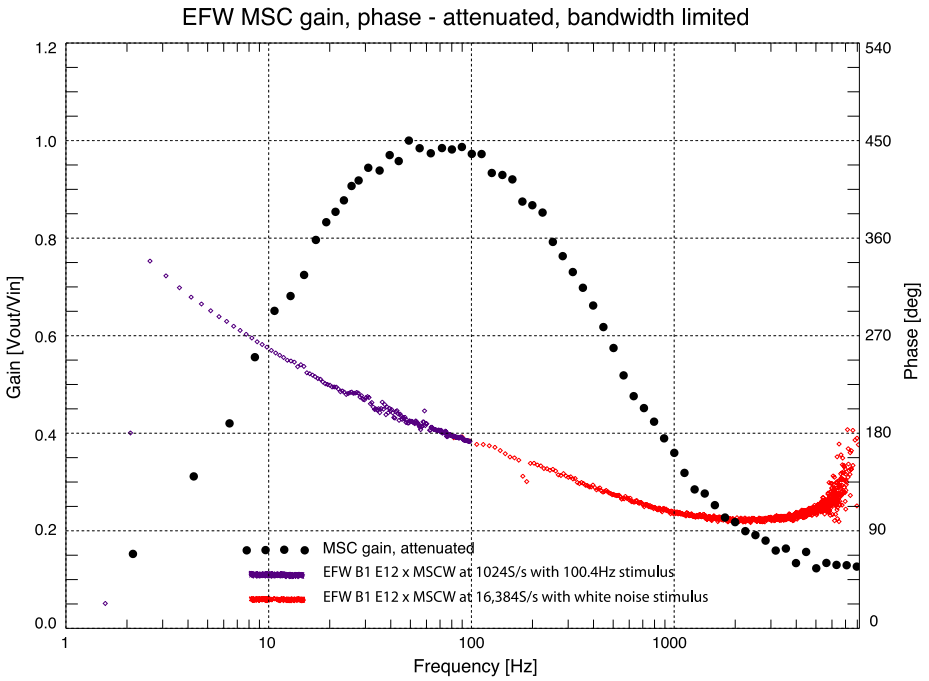

Fig. 11 Magnetic Search Coil gain and phase frequency response through EMFISIS search coil sensors to EFW telemetry from 2 Hz to 7 kHz. The different *colored dots* on the phase curve correspond to different signal generator modes driving the stimulus coils

where they are digitized along with the electric field signals. The EFW instrument science measurements focus primarily on the lower frequency (<250 Hz) portion of the wave signal. The maximum response for the EFW search coil signal is at about 100 Hz but on-orbit measurements indicate that large amplitude waves can be detected in the >2 kHz range. Search coil data is incorporated into EFW spectral products and also burst data collections. The gain (left hand label) and phase (right hand label) responses of the search coil were calibrated relative to the electric field signals during bench tests and also on the spacecraft. The results of these calibrations are shown in Fig. 11. The blue and red traces of the phase response simply refer to the nature of the signal from the signal generator that provided the spectral power for optimum calibration. A sinusoidal signal was used at low frequency (blue) and a broad band "white noise" signal was used for high frequency calibration (red).

4.3 Digital Filter Board

The Digital Filter Board (DFB) and associated firmware was designed, fabricated, and tested by a team from the Laboratory for Atmospheric and Space Physics (LASP) at the University of Colorado led by Robert Ergun. The digital filter board is responsible for analog processing of sensor signals, A-D conversion, and anti-aliasing, as well as onboard calculation of a variety of spectral and cross-spectral products.

Time Domain measurements As indicated by Fig. 8 diagram, and as previously discussed, the analog signals from each of the six spheres are passed to the DFB where the signals from

Table 4 Survey mode time domain measurements (100 % duty cycle)

Survey data	Range	Resolution (A-D)	Samples/s (Default)	Duty cycle	TM bits/s
E12S, E34S, E56S	±1 V/m	30 μV/m	32	100 %	1536
V1, V2, V3, V4, V5, V6	±225 V	6 mV	16	100 %	3072

opposing boom pairs are differenced and filtered in analog circuitry to provide three analog signals proportional to the electric field. In addition, higher gain AC coupled versions of the analog signals are generated to more sensitive wave measurements.

The analog filtering roll-off is performed by 5 pole Bessel filters with a linear phase shift with frequency. This linear phase shift in frequency space corresponds to a constant time delay for signals in the time domain and gives an undistorted waveform.

After A-D conversion, signals are digitally filtered with 5 pole low pass Bessel filters at an adjustable Nyquist frequency. The Bessel filters have a near linear phase shift as a function of frequency. This results in a constant group delay over almost the entire band-pass, which minimizes distortion of the waveform of the analog signal. This property is particularly useful when performing interferometric timing between opposite probes. The digital filtering is implemented in FPGA based firmware. The filtering algorithm consists of a recursive algorithm that allows filtering with programmable (2^N) Nyquist frequencies. The maximum filter frequency is 6.5 kHz. The total group delays for different sampling frequencies are presented in Table 3.

There are three contributions to phase shifts between the "natural" and telemetered electric field waveforms. One is the phase shift due to the sensor-plasma sheath, one is the sensor-cable frequency response/phase shift, and the other is associated with the anti-aliasing filters of the DFB board. The first two contributions are shown in Fig. 10. The last contribution consisting of the constant time delays, due to the linear phase shift of the analog 5 pole Bessel filters set at 6.5 kHz, and also the time delays due to the FIR 5 pole Bessel filters discussed above and presented in Table 3 should be included during ground analysis.

The higher frequency digitized electric field waveforms (up to 16.4 k samples/s) are transferred to the Data Controller Board (DCB) for waveform recordings in either of two burst memory systems. The burst data sampling rates, duration of the burst, and selection of specific time intervals to record into memory, as well as, which of the intervals in memory to telemeter to the ground, are all controlled by the microprocessor in the DCB.

The DFB produces the three components of the 16-bit digitized electric waveform sampled at 32 samples/s (E12_SVY, E34_SVY, and E56_SVY). It provides six single-ended measurements of the potential difference between the individual electric sensors and the spacecraft sampled at 16 samples/s (denoted V1_SVY through V6_SVY). These quantities are described in Table 4. In addition, it provides higher time resolution data inputs for either of the two instrument burst modes. The burst 1 mode includes three components of the electric field (E12_B1, E34_B1, E56_B1), six components of the spacecraft–sensor potential (V1_B1 through V6_B1), and three components of the AC magnetic field from the EMFISIS search coil magnetometer (SCM_U_B1, SCM_V_B1, SCM_W_B1). The burst 2 mode data returns a similar complement of electric field (E_12ac_B2, E34ac_B2, E56ac_B2), search coil (SCM_B2, SCM_2B2, and SCM_B2) and single ended measurements (V1ac_B1 through V6ac_B2) with the exception that in the default mode the single ended and electric field signals are AC coupled with a higher gain.

Table 5 Survey mode spectral and cross spectral products (100 % duty cycle)

Default data selection	Default # Comp	Range	Freq. Bins	Samples/s (Default)	TM bits/s
Spectral Power: E12ac E56ac, SCMpar, SCMprp.	4	100 dB	64 bins	1/8	448
Cross Spectra SCMW × E12ac, V1ac × V2ac	2	Phase difference	64 bins	1/8	768

The DFB receives signals from the EMFISIS search coil magnetometer via an analog interface to provide measurements of the 3-D wave magnetic field. These data may be used as input to the EFW spectral products or filtered and sent to the DCB to be included in EFW time domain burst recordings.

The DFB also receives DC fluxgate magnetometer analog signals from the EMFISIS instrument in order to allow for rotation of EFW data into a magnetic field aligned coordinate system on-orbit. This data stream is not normally included in EFW telemetry. However, for purposes of redundancy, the digitized fluxgate data can be included in EFW telemetry in the event of failure of the EMFISIS digital section. This redundancy is motivated by the important role that the DC magnetometer data play in the RBSP spacecraft attitude determination and analysis of field aligned coordinates for the different science instruments. There is a similar redundant data path for EFW electric field data above 10 Hz via the EMFISIS instrument. The EFW preamplifiers and signal buffers to the EMFISIS instrument will remain powered in the event of a failure of the EFW digital section.

Survey Mode Spectra and Cross Spectra In the survey mode, the DFB provides a continuous stream of electric and magnetic field spectra over the frequency range of ∼1 Hz to 6.5 kHz at a cadence of one spectrum every 8 seconds. It calculates 2048-point complex FFT spectra and cross spectra every 0.125 second over a frequency range from 1 Hz to 6.5 kHz. Prior to the FFT calculation, the waveform data are multiplied by a Hanning window. Subsequent to the FFT calculation, in order to save telemetry, the real (R) and imaginary (I) parts of FFT frequency components are pseudo-logarithmically compressed into 36, 64 or 112 frequency bins. In the default mode, the spectra accumulated over 1/8 second are averaged together over an 8 second period to provide the real and imaginary components of selected wave forms in 64 frequency bins every 8 seconds. The quantities that can be selected for the spectra and cross-spectra are presented in Table 5.

In addition, the complex cross-spectra are calculated for four selected pairs of quantities. This allows us to calculate, on the ground, spectra of the estimated complex E/B ratio, the magnetic field-aligned Poynting flux, wave polarization, or, the correlation (or anti-correlation) between density and the magnetic field magnitude fluctuations. These calculations are especially designed to routinely determine the properties of whistler waves which provide strong signal to noise ratios and have pulse widths nearly comparable to the 125 ms spectral sampling interval The results of these calculations can be compared for brief selected periods of time to similar calculations using the full three dimensional electric and magnetic field obtained from the burst recordings. The number of frequency bins, the sampling interval may be optimized on the basis of these comparisons.

The DFB board uses a CORDIC algorithm to rotate wave electric and magnetic field data into a magnetic field aligned coordinate system based on the direction of the average magnetic field. The rotation is performed in the spin plane of the spacecraft to obtain E_{perp}, which

Table 6 Survey mode: broad band filters banks (FB) (100 % duty cycle)

	Default quantities	Freq. Bins (default)	Range	Sensitivity	Cadence (samples/s)
Power	FB1: E12dc aver	0.8 Hz–6.7 kHz (7 log bins)	1 V/m	20 μV/m	8
Power	FB2 SCMa_ave				8
Peak value	FB1: E12dc_peak				8
Peak value	FB 2 SCMa peak				8

is the component of the electric field perpendicular to the magnetic field direction in the spin plane and E_{par} or the component of the electric field closest to parallel to the magnetic field within the spin plane. The spin axis electric field component is not included in the rotation. The wave magnetic field data is also rotated in order to determine the projection of the wave magnetic field orthogonal to the background magnetic field direction and orthogonal to the direction of E_{perp}. The data from this field-aligned coordinate system may be input into the spectral or cross spectral products in survey mode to provide spectral information on wave Poynting flux parallel to the average magnetic field and also the velocity of propagation of waves along the magnetic field. CORDIC rotated data may also be incorporated in burst formats for playback to the ground. A cross-correlation algorithm allows calculation of the phase-lag between opposite boom pairs, which can provide information on the velocity of propagation of small-scale plasma structures propagating from one sensor to the opposing sensor with a baseline separation of 100 meters. This technique is most feasible for structures with scale sizes of several kilometers or less and travelling at less than 800 km/s. The fidelity of these calculations will be determined by comparison to the full three dimensional electric and magnetic field wave forms which are downloaded from burst mode recording.

Survey Mode Filter Bank Data The DFB also provides measurements of the average power and peak amplitudes from either 7 (default) or 13 logarithmically spaced band-pass filters, implemented in FPGA based firmware, between 0.8 Hz and 6.5 kHz sampled at a cadence of 8 samples/s. Details of the filter banks are summarized in Table 6. Two quantities may be input into the filter banks. In the default mode, V12ac, the AC coupled measurement of the electric field from sensors 1 and 2 in the spin plane is input into filter bank 1 And SCMw, the spin axis component of the search coil magnetic field serves as input into the second filter bank. The broadband filters provide a continuous stream of survey mode measurements over the entire orbit providing information on rapid time variations and bursty wave activity over a broad frequency spectrum. These measurements are also used as an input to burst trigger algorithms.

4.4 Data Controller Board and Burst Memory Modes

The Data Controller Board (DCB) is responsible for the reception of instrument commands, timing and status information from the spacecraft command and data handling system. The DCB implements commands, keeps track of internal data acquisition timing and monitors spacecraft status. It controls instrument data compression, telemetry formatting and sends all EFW telemetry to the spacecraft for transmission to the ground. It controls instrument operational modes including bias sweeps on the BEB board. It also handles burst memory

sampling formats, triggering, recording, playback, and memory management for the DFB. It controls all boom deployments. It calculates space weather products including electric field spin period sine wave fits and the spacecraft potential. It also controls the redundant magnetometer back-up mode in the event of an EMFISIS instrument failure.

The DCB is based on a general purpose microprocessor, the Z80, an 8-bit processor implemented as FPGA firmware. The FPGA chosen for flight is an Actel RTAX2000S. It includes a Z80 processor as an instantiation of the CAST Inc. Z80 IP-core. The CPU in the FPGA is supported by external 32K × 8 boot PROM, 128K × 8 SEU-immune static RAM and 128K × 8 EEPROM. Additional logic within the FPGA handles the processor bus control and provides registers for accessing the various sections of memory. Also included in the FPGA are the instrument interfaces, the SDRAM controller, the FLASH memory controller, error detection and correction logic for SDRAM and FLASH memories, the spacecraft interface logic, DMA and data management control, analog housekeeping control, and timing/time-tagging support.

Like the other EFW IDPU boards, the DCB resides on a 6U VME board, connecting to a custom instrument backplane. Power is received through the backplane connection, which is also used to communicate with the other IDPU boards: the LVPS, the BEB and the DFB (described elsewhere). The DCB receives its operating power from the LVPS as well as a number of analog housekeeping values. The DCB controls the boom deployment power switching in the LVPS. The DCB controls sensor biasing and modes in the BEB. The DCB controls the operating modes of the DFB and directs DFB data products via DMA to DCB memory.

The DCB serves as the EFW interface to the spacecraft command and data handling system. The interface includes a UART based telemetry interface (115.2 KBaud), a timing signal (1 Hz Clock and "Spin Pulse"), and a UART (115.2 Kbaud) based command interface.

For Burst-1 data storage, 32 GBytes of non-volatile FLASH memory is installed on the DCB. This bulk memory is composed of eight 4 GByte memory modules. Each memory module includes eight 512M × 8 Micron FLASH Memory devices. Each of the 4 GB modules is separately powered. FPGA based logic is used to streamline the intensive DMA data-transfer operations between FLASH and the DCB-based random access memory banks including error detection and correction. The CPU is responsible for continuous FLASH memory module management.

For Burst-2 data storage, 256 MBytes of local dynamic RAM memory is installed on the DCB. The SDRAM can be powered on and off to save power and clear problems. FPGA logic manages the SDRAM refreshing.

4.4.1 Burst Memory and Operations

The EFW instrument has two independent burst memory systems, which focus on different aspects of high frequency waves and involve different modes of data selection. The measurement quantity formats, data rates, modes of burst playback and triggers are programmable and are controlled by the DCB. Analog filtering, analog to digital conversion, and digital anti-aliasing occur on the DFB. The solid-state burst memories are located on the DCB. Tables 4–7 present the format, sampling, signal ranges, and A/D resolution of science quantities for burst 1 and burst 2 modes respectively.

Burst Mode 1 The Burst-1 mode uses the 32 GB flash memory for the recording and playback of high time resolution waveform data. Telemetry quantities and sampling rates are summarized in Table 7. In the default mode, the sampled quantities include three components of the DC coupled electric field, three components of the search wave magnetic field

Table 7 Burst 1 data (16 bit quantities)

Measurements (nominal)	Meas. Range	Meas. Res.	Sample/s		Duty cycle	Bits/s orbit Avg.
			Max	Default		
Electric field E12dc, E34dc, E56dc	±1 V/m	30 μV/m	16.4 k	512	4.00 %	983
Sensor-SC potential: V1dc, V2dc, V3dc, V4dc, V5dc, V6dc	±225 V	6 mV	16.4 k	512	4.00 %	1966
Search coil magnetometer SCMU, SCMV, SCMW	12 nT	0.36 pT	16.4 k	512	4.00 %	983
Total telemetry						3932

from the EMFISIS search coil, and the 6 values of the potential differences between each of the 6 sensors and the spacecraft. All these quantities are sampled at 512 samples/s in and low pass filtered at ∼200 Hz with a constant time delay 5 pole anti-aliasing filter in the Burst-1 default state.

An alternative format that could be selected includes ac-coupled versions of the signals with higher gains.

The sampling rate is programmable and with selectable values ranging between the default of 1 sample/s to 16.4 k samples/s in factors of two increments with adjustable low pass anti-aliasing filters near the 80 % of the Nyquist frequency or 6.4 kHz at the highest sampling rate of 16.4 k samples/s.

At the nominal rate with continuous sampling, the 32 GB memory would be filled in ∼20 days. The telemetry allocation for playback is 3932 bits/s. This allows for about 4 % of the orbit averaged total non-compressed burst 1 data to be played back. This corresponds to about 40 minutes of data at the default Burst-1 sampling rate. The minimum size burst is 2 Mbytes or about 5 minutes in the default mode. Higher sampling rates may be used and the corresponding fraction of the data played back is less.

Data compression algorithms implemented in the DCB flight software increase the actual volume of B1 and B2 recorded data played back on orbit by factor of 2–4.

The selection of the "most interesting" time intervals for high time resolution bursts and their relation to time intervals of strong particle energization and to intervals when high time resolution data are not obtained is of crucial importance to the EFW science goals.

In the default Burst-1 playback mode, the time intervals of the Burst-1 mode data to be returned to the ground for analysis may be selected by designated EFW scientists at the EFW SOC and uplinked to the EFW instrument for playback of Burst-1 data intervals on subsequent passes. This "human intervention" allows EFW scientists to identify interesting time intervals on the basis of EFW survey data and any data available from other instruments on the RBSP spacecraft. In addition, information from ground based investigations, other spacecraft, or the BARREL investigation will be incorporated into the burst selection decision as available.

Alternatively, the time intervals of the Burst-1 playback data may be autonomously determined by software algorithms in the DCB flight software. Some of the information from the EFW instrument to be used to decide the burst intervals of the most value include the DC electric and magnetic fields, information on intervals of intense wave activities using

Table 8 Burst 2 data (16 bits)

Measurements (nominal)	Meas. Range	AD Resol.	Cadence sample/s (nominal)	Duty cycle	Bits/orbit (average)
E12AC, E34AC, E56AC	±400 mV/m	12 μV/m	16.4 k	0.100 %	786
V1–V6	±12.5 V	0.4 mV	16.4 k	0.100 %	1573
SCMU, SCMV, SCMW	±11 nT	0.36 pT	16.4 k	0.100 %	786
Total				0.100 %	3146

spectral data and also power in electric fields and magnetic fields measured by broad-band filters which are sampled at 8 samples/s.

Candidate burst intervals of special interest include: (1) Waves observed during substorm injections and dipolarizations; (2) Waves observed during interplanetary shocks impacts on the magnetosphere; (3) Waves observed during observations of energetic electron microburst and other intervals of electron flux enhancements or loss revealed by the RBSP ECT MAGEIS high time resolution measurement of energetic electrons; (4) Intervals of magnetic conjunction with the BARREL balloon campaign designed to investigate microbursts and other modes of electron precipitation and loss; (5) Periods of high wave activity when the two RBSP spacecraft are "closely spaced" sampling the same wave field; and, (6) Science targets of opportunity including compressed front-side magnetopause crossings during major storms when energy transfer into the magnetosphere is the largest.

Burst Mode 2 The second burst waveform mode (Burst-2 or interferometric mode) in the default mode typically samples each of the six individual electric field sensors at nominal rate of ∼16.4 k samples/s. Telemetry formats and sampling options for this mode are summarized in Table 8. The signals from the individual probes provide interferometric timing information of small scale structures as they move over the spacecraft. These measurements allow the determination of the direction and velocity of propagation of the structure. Similar bursts have proven useful in determining the properties of ion phase space holes and other small scale structures (Ergun et al. 2001; Dombeck et al. 2001; Cattell et al. 2001) as they propagate along the magnetic field.

Burst-2 data collection is autonomously triggered with an algorithm in flight software on the DCB that continuously evaluates a quality factor which is a weighted linear combination of a variety of measured wave electric and magnetic field parameters. The most important of these parameters are the measured power and the peak in the electric and magnetic fields in the DFB broadband filters. The weights for the different field parameters used to compute the quality factor are stored in look-up tables that can be updated by ground command. Similar automated burst trigger algorithms have been used by electric field instruments on the FAST, Polar, Cluster, and THEMIS missions.

Burst-2 data are stored in 256 MB of rad-hard SDRAM memory. In the EFW default telemetry mode, this burst mode can playback data covering 0.1 % of the orbit period or for about 300 seconds without data compression. The burst information is played back in a prioritized list based on the value quality factor. This insures that the "best" events are telemetered to the ground. Burst 2 data can also be collected and played back on the basis of time tagged commands.

4.5 Low Voltage Power Supply Board

The function of the Low Voltage Power Supply (LVPS) board is to generate voltages for the analog and digital sections of the IDPU and to controlling boom deployment motors. Receiving an unregulated supply voltage from the spacecraft power bus, the LVPS provides stable fixed (referenced to signal ground) voltages to power analog and digital circuitry throughout EFW. It also produces ± 225 volts for the floating ground reference and ± 15 volts floating power for the sensor pre-amplifiers. In addition, the LVPS receives two additional switched power lines from the spacecraft power bus to allow for deployment of the EFW mechanisms. When the spacecraft activates these primary circuits, the EFW DCB controls power switches within the LVPS to pop pin-pullers, fracture frangibolts and activate deployment motors.

The dynamic range of the electric field measurement in the spin plane must accommodate voltage swings that include the amplitude of the largest anticipated electric fields (1 V/m) integrated over the boom separation distances (50 m) plus the largest (slowly varying) floating potential of spacecraft that is expected in low density plasmas (40 volts) or during electron injection events (<10 volts). This motivates the use of a floating power supply system in which the sensor pre-amplifiers power supplies (± 15 volts) are referenced to a floating ground reference driven by a low pass (<500 Hz) signal at the potential of the pre-amplifier output. This allows low frequency excursions of ± 225 volt power supply which track the sphere outputs for potential variations below 500 Hz. Higher frequency signals are tracked by the ± 12 volt power supply.

This power supply system is used to power the pre-amplifiers at the ends of the booms. Special care in LVPS layout has been taken to insure that the power supplies are especially low in noise. This includes placement of traces and ground planes. The power converter frequency is fixed at 200 kHz so that noise is generated only at this frequency and its integer multiples.

The power supplies for the sensor pre-amplifiers and the buffers to the EMFISIS system are designed to continue to function in the event of a failure of the EFW IDPU digital section. (As discussed, similar precautions have been taken by the EMFISIS team to provide a back-up analog data stream for the fluxgate magnetometer data via the EFW instrument).

Spin Plane Booms and Deployment Units The electric field spin plane boom deployment units were designed, constructed and tested by the Space Science Laboratory at the University of California at Berkeley. Members of the boom engineering team have been responsible for the booms on the Air Force S3-3, ESA GEOS 1 and 2, NASA/ESA ISEE-1, Swedish Viking, Swedish Freja, NASA/USAF CRRES, NASA Polar, FAST, and THEMIS, and ESA/NASA Cluster spacecraft, as well as boom systems on dozens of sounding rockets.

The RBSP spin plane booms consist of two pairs of centripetally deployed booms in the spin plane of the spacecraft. As shown in Fig. 9, the booms are terminated with spherical sensors, which are separated by 100 meters. The boom deployment units are mounted on the periphery of the spacecraft at 90 degree intervals. In the stowed configuration, the spin plane boom cable is wound around a spool within the deployment unit and is deployed under the influence of the "centrifugal force" associated with the spacecraft rotation. The mass of one of the spin plane boom deployment units including sensor and cable is ~ 2.0 kg. The linear mass density of the boom cable is ~ 3.6 gm/m. Each deployment unit contains a rotating wire storage spool, a metering wheel based cable deployment assembly, a DC brush motor, over tension and end of wire indicators. A micro-switch is pulsed on each turn of the cable spool allowing flight software in the DCB to monitor and control the deployed length and to match the deployed lengths of opposing pairs of booms.

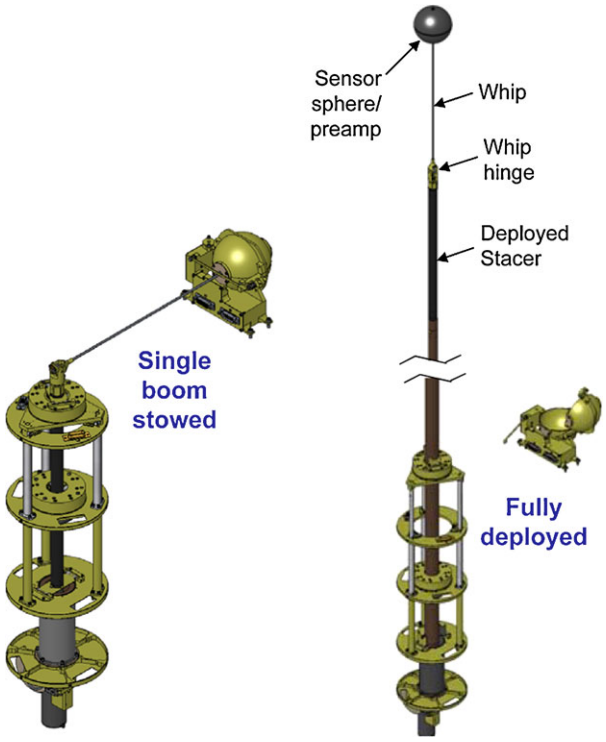

Fig. 12 EFW Spin Axis Booms Deployment Unit in stowed and deployed configurations showing deployment assist device, stacer element, hinge and whip, and spherical sensors and cable

At the end of the deployed multi-conductor cable, a preamp enclosure is attached and contains the preamp electronics board, as well as acting as two of the photoelectron control surfaces (usher and guard). A fine wire exits the preamp housing and connects to a spring-loaded spool enclosed within a spherical probe of radius 4 cm. Three meters of fine wire are wound onto the spool mechanism inside the spherical probe and the wire is intended to deploy by centrifugal force as the boom elements are deployed.

The motor in the base of each unit is shielded with mu metal to limit leakage of stray magnetic fields. Magnetic shielding is external to the motor, and does have some effect on performance, by its magnetic field short-circuiting effects. The drive mechanism is fully enclosed to provide EMI shielding, as well as to keep debris out. EMI filters are used on both power lines.

Spin Axis Booms The electric field axial boom deployment units were designed, constructed and tested by the Space Science Laboratory at the University of California at Berkeley. Members of the boom engineering team have been responsible for the booms on the Air Force S3-3, ESA GEOS 1 and 2, NASA/ESA ISEE-1, Swedish Viking, Swedish Freja, NASA/USAF CRRES, NASA Polar, FAST, and THEMIS, and ESA/NASA Cluster spacecraft, as well as boom systems on dozens of sounding rockets.

The RBSP axial booms consist of one pair of booms to be deployed along the spacecraft spin axis. As shown in Fig. 12, the booms can be deployed to a maximum length of 7 meters each and are terminated with spherical sensors with internal preamplifiers giving a maximum tip-to-tip separation of ∼15 meters. The boom deployment units are mounted back-to-back within a carbon composite tube installed along the center line between the top and bottom decks of the spacecraft structure. In the stowed configuration, the axial probe is

held against the spacecraft deck in a caging mechanism. When released, the probe and whip assembly rotate up along the spacecraft spin axis. At that point the whip/probe assembly can be deployed along the spin axis at the end of a stacer boom element. The stacers are spring loaded helical beryllium-copper coils of metal with an outward spring force. Unlike designs for previous spacecraft, the deployed length of this boom is adjustable. The purpose of this capability is to optimize the position of the sensors relative to the asymmetric electrical equipotential associated with the spacecraft. By placing the sensors on the same spacecraft equipotential surface, error offsets to the electric field measurement may be removed. In this design, the outward spring force of the stacer is restrained by the outer Kevlar braid of a cable through the center and along the length of the stacer tube. The in-board end of this cable is wound around a motor driven spool. Powering the motor allows the spool to unwind under the outward spring force of the stacer element. As a result, the deployed boom length can be adjusted with a resolution of 0.5 cm but only in one direction—there is no retraction capability. The lengths of the booms will be adjusted in stages during the commissioning phase of the mission.

The sensor consists of a 75 cm-long, tapered (4.8 to 7.0-mm) graphite-coated (DAG-213) whip with 4 cm radius sphere at its tip. The preamp enclosure is similar to that found on the spin plane booms, and contains the preamp electronics board, as well as acting as two of the photoelectron control surfaces (usher and guard). The preamp and whip assembly is mounted to the outboard end of the graphite coated (DAG-214) main stacer. A two-stage deployment assist device (DAD) is spring-loaded, and serves to start the stacer deploy. The stacer element is formed during deployment through two sets of roller nozzles to provide for lateral stability of the stacer when fully deployed.

As with the spin plane booms, the motor in each unit is shielded with mu metal to limit leakage of stray magnetic fields. The drive mechanism is fully enclosed to provide EMI shielding, as well as to keep debris out. EMI filters are used on both power lines.

5 Boom Deployment During Commissioning

Following the successful launch of the RBSP spacecraft on 30 August 2012 and the successful turn-on of the EFW instruments, the spin plane boom deployments began on both spacecraft on September 13, 2012. After opening the exterior doors on the deployment units, the DCB was commanded to deploy each of one pair of Spin Plane Booms to a length of 4 meters corresponding to a total tip-to-tip distance between the two pair (including the spacecraft) of 9.8 m. Following that, the other pair was deployed a similar amount. Over the course of many orbits, this alternating pair-wise deployment continued until all four spin plane booms reached a final deployed length of 50 meters on each boom element giving two orthogonal 100-meter tip-to-tip dipoles. When deployed to a length of about 10 m, the fine-wire between the preamplifier housing and the spherical probe deploys to a length of 3 meters. At several points in the deployment process, the spacecraft spin rate was increased to compensate for the increasing moment-of-inertia such that, when the booms reached their final length on 22 September 2012, the spacecraft spin rate was the nominal 5.48 RPM.

Once the spin plane booms were fully deployed, the axial boom deployments began on both spacecraft on September 24, 2012. After opening the caging mechanisms and confirming proper deployment of the whip/sphere assemblies, the DCB was commanded to deploy one axial boom to a length of $\sim$4 meters. Following that, the other boom was deployed a similar amount and then the pair on the other spacecraft. After several orbits, the axial boom lengths were adjusted to provide a tip-to-tip sensors separation of $\sim$14 meters It is expected that further trimming operations will be conducted as needed to optimize the science.

Analyses of the boom dynamics during deployment, Earth shadow entry and exit and attitude maneuvers for a small spinning spacecraft similar to the baseline RBSP spacecraft indicate that booms pose no stability problems. This analysis is consistent with the flight experience from the previously mentioned spacecraft. On-orbit characteristics of RBSP spin plane boom dynamics are consistent with expectations.

Spacecraft Accommodation of EFW The requirement for a sensitive double probe electric field experiment motivates several important properties of the RBSP spacecraft. The near sun-pointing spin axis is needed so that photo-illumination of the spin plane booms and sensors is uniform over the spin period of the spacecraft.

The necessity for a conducting spacecraft has lead to the coating of the solar cell cover glasses and the thermal blankets with a conductive coating of Indium Tin Oxide (ITO). Conductive paths through wiring of solar panels and grouting between panels allowing current to flow from solar cells to the body of the spacecraft have been implemented. There are strict limits on the total surface area of exterior insulating surfaces and instrument apertures, which could to charge to high potentials. These requirements are designed to give a nearly constant floating potential for the electric field sensors and reduce spin dependent errors in the electric field.

Since the front-side of the spacecraft is illuminated by the Sun and the "back" of the spacecraft is not illuminated, unless otherwise prevented, the front side of the spacecraft will charge to potentials of tens of volts positive while the shadowed portion of the spacecraft will charge to the characteristic thermal energy of the plasma electrons. Experience on previous spacecraft missions and modeling indicate this electric potential can range from $\sim$1 volt in the high-density low temperature plasmasphere to several kilovolts during intense substorm electron injection events. This would be a major impact on the electric field measurements since it not only contributes large asymmetries (100 V to several kV) to the spacecraft potential structure around the spacecraft but it is sometimes large enough to saturate the electric field pre-amplifiers. The solution to this problem is to insure that both the shadowed and illuminated surfaces on the spacecraft are conductively tied together such that photo-currents on the illuminated surfaces including solar panels are able to flow to the shadowed surfaces where, they dominate, under typical plasma conditions, over currents associated with high energy electrons in controlling current balance and floating potential.

For the same reason, the spin axis boom measurements are accurate only when the anti-sunward spin axis sensor is not shadowed by the body of the spacecraft or the solar panels. This motivates a pointing strategy in which the spin axis is nominally pointed at least 15 degrees away from the Sun so that the anti-sunward probe and a short section of the adjacent boom element are not shadowed by the spacecraft.

6 EFW Space Weather Products

The EFW instrument flight software incorporates a module for the calculation of space weather products for real time telemetry to the ground. EFW space weather products are: (1) spin fit electric field with a time cadence of $\sim$12 seconds and (2) the spacecraft potential. It should be noted that the electric field data at this level of analysis still includes the motional electric field of the spacecraft ($V_{sc} \times B$) discussed above. These products will provide real time information on the electric fields associated with injection events and interplanetary shock induced waves. The spacecraft potential measurement provides information on thermal structures over the density range from 0.1–50 cm^{-3} for cold plasma regimes

(<10 eV). The spacecraft potential is an important diagnostic for the detecting discontinuities in thermal plasma including the plasmapause and the tail-lobe plasma sheet boundary, and, occasionally, the magnetopause. Calibration files for these products may be found on the EFW SOC website. *This dataset is designed for real time and near real time diagnostics of the space weather of the inner magnetosphere and not for publication purposes.*

Data Collection, Analysis, and Dissemination and Archiving The EFW Science Operations Center (SOC) is located at SSL/UCB. Instrument command loads and mode schedules are generated and verified at the EFW SOC based on the overall RBSP mission plan, the EFW science plan, and other input from the EFW science team. These command loads are sent to the Mission Operations Center (MOC) operated by APL. In addition to its role in monitoring and maintaining instrument health and safety and in instrument commanding, the SOC will provide access to the EFW data and software products. The EFW SOC downloads telemetry data from the RBSP MOC; provides secure and redundant archiving of the all data; produces and validates the EFW Level 1 CDF data products; produces and validate the EFW Level 2 CDF data products; and, makes these data products widely available.

SSL has developed and implemented an automated system for level 0 data acquisition from NASA sites that is currently used to electronically download the THEMIS, STEREO, Wind, and RBSP EFW data sets. The SOC at the SSL electronically downloads the level 0 data and the additional spacecraft housekeeping data and ancillary data products from the RBSP MOC, and produces time tagged level 1 data, and also provides the calibrated science quantities comprising the level 2 processed data in CDF files. The EFW level 2 CDF files are available on-line. The SOC records and archives the EFW data, and produces daily quicklook science survey plots. The survey plots are placed on line for access by the scientific community. The summary plots are designed as a "first step" browse tool to identify events. The summary data is not a final scientific product. It contains known errors associated with incorrect or in-appropriate biasing, episodes of preamplifier saturation associated spacecraft charging, spin axis sensor shadowing by solar panels, and other spurious signals. This data is not to be published in the scientific literature. Researchers are encouraged contact the P-I when using any EFW data for presentations and publications.

Scientists interested in the complete EFW data set can download the analysis software and data set from the SOC website. The SOC web site will contain a complete set of help pages that detail the format and data quantities available in the CDF files, the data available in the complete data set and provide assistance in installation and use of the analysis software. Software analysis tools include IDL based TPLOT, and TDAS software routines first developed at SSL for FAST and THEMIS particle and fields measurements. In addition, the SDT analysis program used in Polar, Cluster and THEMIS data analysis is available. These analysis tools allow electric field data to be rotated into a variety of geophysical coordinates, calculation of spin fit electric field vectors, subtraction of the spacecraft motional electric field, generation of spectra products, as well as, more detailed scientific analysis.

7 Conclusion

Since early commissioning and checkout, measurements from EFW instruments on the two RBSP spacecraft, in concert with the other fields and particle instruments on the spacecraft, have been providing unprecedented capabilities to investigate the physics of energetic particle acceleration and the dynamics of major geomagnetic storms in the inner magnetosphere. The unique insights provided by these measurements should allow a conceptual framework for a central problem in space and astrophysics which is based on direct in-situ observations of the structures and waves controlling the acceleration of energetic particles.

Acknowledgements We would like to acknowledge the many contributions of the RBSP Project team at Johns Hopkins Applied Physics Laboratory. We would like to also thank the EFW team of scientists and engineers at Space Science Laboratory at the University of California, Berkeley and the staff at the Laboratory for Atmospheric and Space Physics at the University of Colorado in the development and test of the instrument. We also thank the efforts of the other instrument teams on the RBSP mission. We would like to acknowledge the contributions of the EMFISIS team, the ECT team (MagEIS, HOPE and REPT), and the RBSPICE team. In this paper, the energetic electron figures were provided by Joe Fennell, J.B. Blake, and Harlan Spence of the MagEIS/ECT teams. This work was supported by RBSP-ECT funding provided by JHU/APL Contract No. 967399 under NASA's Prime Contract No. NAS5-01072. The work by the EFW team was conducted under JHU/APL contract 922613 (RBSP-EFW).

References

J.M. Albert, Gyroresonant interactions of radiation belt particles with a monochromatic electromagnetic wave. J. Geophys. Res. **105**(A9), 21 (2000). 191

W.I. Axford, Flow of mass and energy in the Solar system, physics of solar planetary environments, in *Proceeding of the International Symposium on Solar-Terrestrial Physics*, vol. 1 June 7–18 American Geophysical Union (1976), pp. 270–283

J.B. Blake, W.A. Kolasinski, R.W. Fillius, E.G. Mullen, Injection of electrons and protons with energies of tens of MeV into $L < 3$ on 24 March 1991. Geophys. Res. Lett. **19**, 821 (1992)

J.B. Blake, S.S. Imamoto, The proton switches. J. Spacecr. Rockets **29**, 595 (1992)

J.B. Blake, M.D. Looper, D.N. Baker, R. Nakamura, B. Klecker, D. Hovestadt, New high temporal and spatial resolution measurements by SAMPEX of the precipitation of relativistic electrons. Adv. Space Res. **18**(8), 171–186 (1996)

J.B. Blake et al., The ECT instrument on the Van Allen probes (this issue)

J.W. Bonnell et al., The electric field instrument for THEMIS. Space Sci. Rev. **114**, 303–341 (2008). doi:10.1007/s11214-008-9469-2

D.H. Brautigam, G.P. Ginet, J.M. Albert, J.R. Wygant, D.E. Rowland, A. Ling, J. Bass, CRRES electric field power spectra and radial diffusion coefficients. J. Geophys. Res. **110**, A02214 (2005). doi:10.1029/2004JA010612

C. Cattell et al., Polar observations of solitary waves at low and high altitudes and comparison to theory. Adv. Space Res. **28**, 1631 (2001)

C. Cattell et al., Discovery of very large amplitude whistler-mode waves in Earth's radiation belts. Geophys. Res. Lett. **35**, L01105 (2008). doi:10.1029/2007GL032009

C.M. Cully, J.W. Bonnell, R.E. Ergun, THEMIS observations of large amplitude whistler mode waves in the inner magnetosphere. J. of Geophys. Res. **35**, L17S16 (2008). doi:10.1029/2008GL033643

L. Dai et al., Observations of surface waves in jets from magnetotail reconnection. J. Geophys. Res. **116**, A12227 (2011). doi:10.1029/2011JA017004

J. Dombeck et al., Observed trends in auroral zone ion mode solitary structure characteristics using data from polar. J. Geophys. Res. **106**, 19013 (2001)

R.E. Ergun et al., The FAST satellite field instrument. Space Sci. Rev. **98**, 67–91 (2001)

G. Gustafsson et al., The electric field and wave experiment for the CLUSTER mission. Space Sci. Rev. **79**, 137 (1997)

P. Harvey, F.S. Mozer, D. Pankow, J. Wygant, N.C. Maynard, H. Singer, W. Sullivan, P.B. Anderson, A. Pedersen, C.-G. Falthammar, P. Tanskannen, in *The Electric Field Instrument on the Polar Satellite in the Global Geospace Mission*, vol. 71, ed. by C.T. Russell (Kluwer Academic, Dordrecht, 1995). Reprinted from Space Sciences Rev., **71**, N1-4, 1995

R.B. Horne, R.M. Thorne, Potential waves for relativistic electron scattering and stochastic acceleration during magnetic storms. Geophys. Res. Lett. **25**(15), 3011–3014 (1998)

M.K. Hudson, A.D. Kotelnikov, X. Li, I. Roth, M. Temerin, J. Wygant, Simulation of proton radiation belt formation during the March 24, 1991 SSC. Geophys. Res. Lett. **22**, 291 (1995)

M.K. Hudson, S.R. Elkington, J.G. Lyon, V.A. Marchenko, I. Roth, M. Temerin, J.B. Blake, M.S. Gussenhoven, J.R. Wygant, Simulations of radiation belt formation during storm sudden commencement. J. Geophys. Res. **102**, 14087 (1997)

M.K. Hudson, S.R. Elkington, J.G. Lyon, M.J. Wiltberger, in *Radiation Belt Electron Acceleration by ULF Wave Drift Resonance: Simulation of 1997 and 1998 Storms*, ed. by G. Siscoe, P. Song, H. Singer. AGU Monograph, Space Weather (AGU, Washington, 2001), p. 289

M.K. Hudson, R.E. Denton, M.R. Lessard, E.G. Miftakhova, R.E. Anderson, A study of Pc5 ULF oscillations. Ann. Geophys. **22**, 289 (2004)

J.C. Ingraham, T.E. Cayton, R.D. Belian, R.A. Christensen, R.H.W. Friedel, M.M. Meier, G.D. Reeves, M. Tuszewski, Substorm injection of relativistic electrons to geosynchronous orbit during the great magnetic storm of March 24, 1991. J. Geophys. Res. **106**(A11), 25759–25776 (2001). doi:10.1029/2000JA000458

P.J. Kellogg et al., Electron trapping and charge transport by large amplitude whistlers. Geophys. Res. Lett. **37**, L20106 (2010). doi:10.1029/2010GL044845

K. Kersten et al., Observation of relativistic electron microbursts in conjunction with enhanced radiation belt whistler mode waves. Geophys. Res. Lett. **38**, L08107 (2011). doi:10.1029/2001GL046810

K. Kirby et al., The radiation belt storm probes-observatory and environment (this issue)

C. Kletzing et al., The electric and magnetic field instrument suite and integrated science and integrated science (EMFISIS) on RBSP. Space Sci. Rev. (2013). doi:10.1007/s11214-013-9993-6 (this issue)

X. Li, I. Roth, M. Temerin, J.R. Wygant, M.K. Hudson, J.B. Blake, Simulation of prompt energization and transport of radiation belt particles during the March 24, 1991 SSC. Geophys. Res. Lett. **20**, 2423 (1993)

X. Li, D.N. Baker, M. Temerin, G. Reeves, R. Belian, Simulation of dispersionless injections and drift echoes of energetic electrons associated with substorms. Geophys. Res. Lett. **25**, 3763 (1998)

K.R. Lorentzen, J.E. Mazur, M.D. Looper, J.F. Fennell, J.B. Blake, Multisatellite observations of MeV ion injections during storms. J. Geophys. Res. **107**, 1231 (2002)

G. Marklund, Viking investigations of auroral electrodynamical processes. J. Geophys. Res. **98**, 1691 (1993)

G. Marklund et al., The Swedish small satellite program for space plasma investigations. Space Sci. Rev. **111**(3–4), 377–413 (2004). doi:10.1023/B:SPAC.0000032690.82775.dB

R.M. Millan, R.P. Lin, D.M. Smith, K.R. Lorentzen, M.P. McCarthy, X-ray observations of MeV electron precipitation with a balloon-borne germanium spectrometer. Geophys. Res. Lett. **29**, 2194 (2002)

R.M. Millan (this issue)

F. Mozer, Analysis of techniques for measuring DC and AC electric fields in the magnetosphere. Space Sci. Rev. **14**, 272 (1973)

F.S. Mozer et al., A proposal to measure quasi-static electric fields on the ISEE-1 mother daughter satellite, University of California Berkeley Space Science Technical Note, UCBSSL No. 454 (1973)

F.S. Mozer et al., The dc and ac electric field, plasma density, plasma temperature and field-aligned current experiments on the S3-# spacecraft. J. Geophys. Res. **84**(A10), 5875 (1979)

T.P. O'Brien, K.R. Lorentzen, I.R. Mann, N.P. Meredith, J.B. Blake, J.F. Fennell, M.D. Looper, D.K. Milling, R.R. Anderson, Energization of relativistic electrons in the presence of ULF power and MeV microbursts: evidence for dual ULF and VLF acceleration. J. Geophys. Res. **108**(A8), 1329 (2003). doi:10.1029/2002JA009784

A. Pedersen, Solar wind and magnetospheric plasma diagnostics by spacecraft electrostatic potential measurements. Ann. Geophys. **13**, 118 (1995)

A. Pedersen et al., Electron density estimations derived from spacecraft potential measurements on cluster in tenuous plasma regimes. J. Geophys. Res. **113**, A07S33 (2008). doi:10.1029/2007JA012636

G. Reeves et al. (this issue)

I. Roth, M. Temerin, M.K. Hudson, Resonant enhancement of relativistic electron fluxes during geomagnetically active periods. Ann. Geophys. **17**, 631 (1999)

D. Rowland, J.R. Wygant, The dependence of the large scale electric field in the inner magnetosphere on magnetic activity. J. Geophys. Res. **103**(A7), 14959 (1998)

D. Rowland, The electrodynamics of the inner magnetosphere during major geomagnetic storms. PhD Thesis, University of Minnesota (2002)

O. Santolik, D.A. Gurnett, J.S. Pickett, M. Parrot, N. Cornilleau-Wehrlin, Spatio-temporal structure of storm-time chorus. J. Geophys. Res. **108**, 1278 (2003). doi:10.1029/20002JA009791

H. Spence et al. (this issue)

D. Summers, Y. Omura, Ultra-relativistic acceleration of electrons in planetary magnetospheres. Geophys. Res. Lett. **34**, L24205 (2007). doi:10.1029/2007GL032226

A. Vampola, H. Korth, Electron drift echoes in the inner magnetosphere. Geophys. Res. Lett. **19**, 625 (1992)

L. Wilson et al., The properties of large amplitude whistler mode waves in the magnetosphere: propagation and relationship with geomagnetic activity. Geophys. Res. Lett. **38**, L17107 (2011). doi:10.1029/2011GL048671

J.R. Wygant, P.R. Harvey, D. Pankow, F.S. Mozer, N. Maynard, H. Singer, M. Smiddy, W. Sullivan, P. Anderson, The CRRES electric field experiment/Langmuir probe. J. Spacecr. Rockets **29**, 601 (1992)

J.R. Wygant, F. Mozer, M. Temerin, J. Blake, N. Maynard, H. Singer, M. Smiddy, Large amplitude electric and magnetic field signatures in the inner magnetosphere during injection of 15 MeV drift echoes. Geophys. Res. Lett. **21**, 1730 (1994)

J.R. Wygant, H.J. Singer, M. Temerin, F. Mozer, M.K. Hudson, Experimental evidence on the role of the large spatial scale electric field in creating the ring current. J. Geophys. Res. **98**, JA01436 (1998)

H.-C. Yeh, J.C. Foster, F.J. Rich, W. Swider, Storm-time electric field penetration observed at mid-latitude. J. Geophys. Res. **96**, 5707–5721 (1991)

DOI 10.1007/978-1-4899-7433-4_7
Reprinted from *Space Science Reviews* Journal, DOI 10.1007/s11214-012-9926-9

The Relativistic Proton Spectrometer (RPS) for the Radiation Belt Storm Probes Mission

J. Mazur · L. Friesen · A. Lin · D. Mabry · N. Katz · Y. Dotan · J. George · J.B. Blake · M. Looper · M. Redding · T.P. O'Brien · J. Cha · A. Birkitt · P. Carranza · M. Lalic · F. Fuentes · R. Galvan · M. McNab

Received: 28 March 2012 / Accepted: 27 July 2012 / Published online: 30 August 2012

Abstract The Relativistic Proton Spectrometer (RPS) on the Radiation Belt Storm Probes spacecraft is a particle spectrometer designed to measure the flux, angular distribution, and energy spectrum of protons from ∼60 MeV to ∼2000 MeV. RPS will investigate decades-old questions about the inner Van Allen belt proton environment: a nearby region of space that is relatively unexplored because of the hazards of spacecraft operation there and the difficulties in obtaining accurate proton measurements in an intense penetrating background. RPS is designed to provide the accuracy needed to answer questions about the sources and losses of the inner belt protons and to obtain the measurements required for the next-generation models of trapped protons in the magnetosphere. In addition to detailed information for individual protons, RPS features count rates at a 1-second timescale, internal radiation dosimetry, and information about electrostatic discharge events on the RBSP spacecraft that together will provide new information about space environmental hazards in the Earth's magnetosphere.

Keywords RBSP · Inner radiation belt · CRAND · Trapped protons · Solar energetic protons · Total ionizing dose · Relativistic protons

Acronym List

ASP	Analog Signal Processing
CCSDS	Consultative Committee for Space Data Systems
CRA	Cherenkov subsystem within RPS
CRAND	Cosmic Ray Albedo Neutron Decay
CRaTER	Cosmic Ray Telescope for the Effects of Radiation
CRRES	Combined Release and Radiation Effects Satellite

J. Mazur (✉)
The Aerospace Corporation, 15049 Conference Center Drive, Chantilly, VA 20151, USA
e-mail: Joseph.mazur@aero.org

L. Friesen · A. Lin · D. Mabry · N. Katz · Y. Dotan · J. George · J.B. Blake · M. Looper · M. Redding · T.P. O'Brien · J. Cha · A. Birkitt · P. Carranza · M. Lalic · F. Fuentes · R. Galvan · M. McNab
The Aerospace Corporation, 2310 E. El Segundo Blvd., El Segundo, CA 90245, USA

CRRESELE	CRRES electrons (model)
CRRESPRO	CRRES protons (model)
DPIE	Digital Processing and Interface Electronics
EMI	Electro-Magnetic Interference
ESD	Electro-Static Discharge
Geant4	Geometry and Tracking (4)
HVPS	High Voltage Power Supply
ISTP	International Solar-Terrestrial Physics
JHU/APL	Johns Hopkins University/Applied Physics Laboratory
LEO	Low Earth Orbit
LRO	Lunar Reconnaissance Orbiter
LTD	Limited
LVPS	Low Voltage Power Supply
MAG	Magnetometer
MCP/PMT	Micro-Channel Plate/Photo-Multiplier Tube
MIL-STD	Military Standard
MOC	Mission Operations Center
NASA	National Aeronautics and Space Administration
NRLMSISE	Naval Research Laboratory Mass Spectrometer Incoherent Scatter Radar
NRO	National Reconnaissance Office
PAMELA	Payload for Antimatter Matter Exploration and Light-nuclei Astrophysics
PET	Proton Electron Telescope
PMT	Photo-Multiplier Tube
PPS	Pulse Per Second
PRBEM	Panel on Radiation Belt Environment Modeling
RBSP	Radiation Belt Storm Probes
RPS	Relativistic Proton Spectrometer
SAMPEX	Solar, Anomalous, and Magnetospheric Explorer
SOC	Science Operations Center
SSDA	Solid State Detector Assembly
TRIUMF	Tri-University Meson Facility
UV	Ultra-violet

1 Scientific Goals

Within two Earth radii of the Earth's surface there is an unexplored region of trapped particles that are a challenge to accurately measure, a challenge to engineer for spacecraft design, and a challenge to understand given particle lifetimes that can exceed decades or even centuries. The inner Van Allen belt is a nearby reservoir of charged particles from a multitude of sources. We know the existence of trapped protons with energies beyond 1 GeV, secondary particles such as positrons, electrons, and light ions ^{4}He, ^{3}He, and ^{2}H, electrons that diffuse inward from the outer magnetosphere, and heavy ions that originate as interstellar neutral particles. These particles execute their gyration, bounce, and drift motions in a region with a relatively strong and stable magnetic field that shelters them from transients in the geomagnetic field, yielding the longest trapping lifetimes for particles in the Earth's magnetosphere. The tenuous upper atmosphere is both a source and sink of these populations, whose influence varies over the solar cycle and episodically during times of rapid atmospheric joule heating.

Sorting out the various sources and losses in the Inner belt is challenging but there are particle characteristics that aid the process such as: extremely high proton energies that distinguish these particles as having a galactic cosmic ray origin; heavy ion composition that identifies these as being anomalous cosmic rays whose access to the inner belt is only afforded by their being mostly singly-ionized; and antimatter composition that identifies another branch the products of nuclear collisions between galactic cosmic rays and atmospheric atoms. For electrons the picture is less clear since there is little information about the electron energy spectrum and no identifiable characteristics of an electron that originates from a nuclear interaction versus one that diffused inwards from the outer Van Allen belt.

This paper describes the Relativistic Proton Spectrometer (RPS) whose purpose is to answer scientific and applied questions about the inner Van Allen belt proton population. RPS is government furnished equipment for the RBSP mission. As part of the scientific payload, RPS will measure protons in the energy range of ~60 to 2000 MeV with good energy resolution and with a design that accommodates the challenges of measuring a foreground proton population with a large background due to penetrating protons. It is strictly a proton spectrometer focused on the primary constituent of the inner belt. RPS complements the other energetic proton measurements on RBSP (Baker et al. 2012; Blake et al. 2012) by extending the proton capability of the mission into the GeV range beyond previous investigations from the near-geosynchronous transfer orbit of CRRES (Johnson and Kierein 1992).

The measurement difficulties in a high-background environment of penetrating particles, along with the mission challenges of operating in the inner belt, have allowed us to obtain only glimpses of the entire inner belt proton population, either at the bottom of the field lines in low-Earth orbit (e.g. Baker et al. 1993) or only up to ~100 MeV at higher altitudes (Albert and Ginet 1998). By sampling the protons near where their intensities are greatest and by monitoring outer trapping boundaries on two RBSP vehicles, RPS will provide new insights into this unexplored territory of the inner Van Allen belt.

1.1 Inner Belt Origins

The RPS instrument objectives stem from a modern interest in the dominant inner Van Allen belt proton component. One can trace the RPS investigation to the beginning of the modern space age with the flight of Explorer-1 (Van Allen 1960). There are several compelling historical accounts of the first Explorer missions and the concurrent hypotheses about what later investigations determined were high-energy protons stably trapped in the inner belt (e.g. Chudakov and Gortchakov 1959). Reviews such as Hess (1963, 1968) provide a glimpse of these early measurements and the open questions, some of which remain unanswered today. Ludwig (2011) relates a more recent description of those path-finding space discoveries. An early hypothesis held that the trapped radiation was related to the aurorae, while others found a natural link to albedo particles formed from nuclear interactions of galactic cosmic rays with the upper atmosphere (Singer 1958). The relevant facts to remember here are: the trapped inner belt proton environment saturated the Explorer-1 measurement in 1958 with high penetrating rates; and there was an early appreciation for the stability of the inner magnetosphere to form a strong magnetic bottle for natural and artificial injections of high-energy particles.

The dominant source for protons above ~50 MeV in the inner belt is the decay of albedo neutrons from galactic cosmic ray protons that collide with nuclei in the atmosphere and ionosphere (Cosmic Ray Albedo Neutron Decay, or CRAND); e.g., Singer (1958); Freden and White (1962); Farley and Walt (1971). Free neutrons undergo beta decay with a mean lifetime of ~885 seconds or ~14.75 minutes (Paul 2009). A small fraction of neutrons above

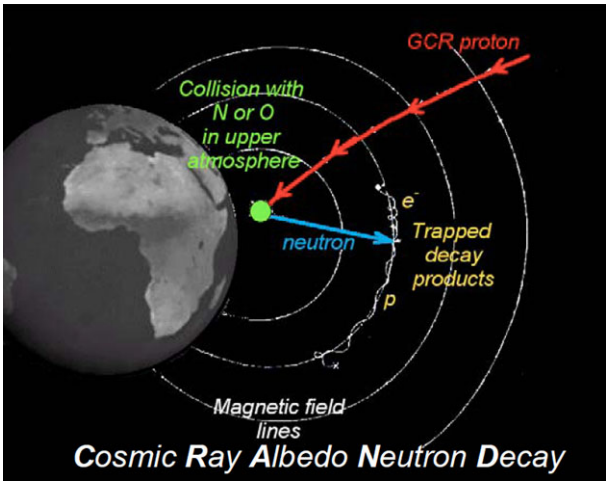

Fig. 1 The cosmic ray albedo neutron decay process (CRAND) is the dominant source of inner belt protons above ∼50 MeV

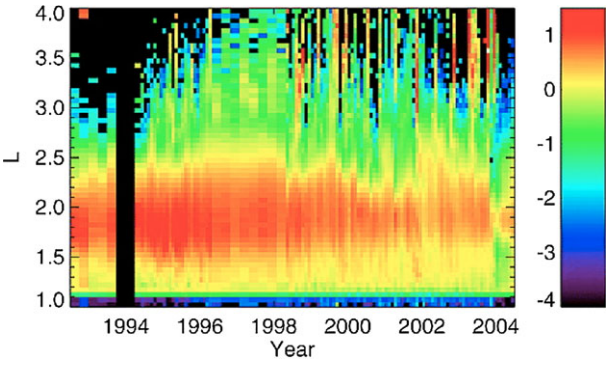

Fig. 2 Monthly averaged count rate of 19–28 MeV protons in the inner belt that mirror at the SAMPEX altitude (Looper et al. 2005). Note the changes in the outer trapping boundary between $L = 2$ and $L = 3$. Episodic solar particle events in 1998 through 2003 created new transient belts inside $L = 3$

50 MeV decay and, within the strong magnetic field inside a MacIIwain L-shell of 2, leave a stably trapped proton with approximately the same kinetic energy as the parent neutron (Fig. 1). The energy spectrum is known to extend beyond 1 GeV, but the spectral details are not well established. These are the highest-energy trapped ions in the inner solar system; their fluxes are orders of magnitude more intense than the galactic cosmic ray protons, which are their ultimate source.

In contrast to the steady and weak source for CRAND protons, there are transient events wherein new radiation belts form above and within the inner belt when interplanetary shocks collide with the magnetosphere as shown in Fig. 2 (Looper et al. 2005). The particle sources in these events can be residual magnetospheric ions and electrons as well as interplanetary solar particles including heavy ions up to Fe. An often-cited example is the 1991 March shock event that created >15 MeV electrons and >50 MeV protons above the inner belt within seconds of its impact on the magnetosphere (Blake et al. 1992; Li et al. 1993; Hudson et al. 1995). Recent measurements have also shown newly trapped radiation belts within $L \sim 2$ that are created from solar energetic particles (Mazur et al. 2006; Lorentzen et al. 2002). There may be multiple mechanisms at work in creating these new belts. It has also become clear that the new belts can be lost quickly during subsequent geomagnetic activity (Selesnick et al. 2010). Below ∼100 MeV, the disagreement between observations and CRAND models suggest the existence of additional sources such as radial

diffusion of newly injected solar protons, although the details of these processes have not been established (e.g. Albert and Ginet 1998).

1.2 Highlights of Inner Belt Measurements

We highlight a few studies of inner belt protons from ∼10 to ∼100 MeV. One quickly finds that the research interest in the inner belt peaked decades ago with only a few successful attempts at quantifying the inner belt proton spectrum over the past 20 years. Sawyer and Vette (1976) listed the missions that operated in the inner belt including observations from Explorer 4 in 1958 through the Azur mission in 1970. While the examples we highlight here reinforce the existence of a high-energy proton population, the next steps in quantifying the details of that population will require the RBSP mission. What was the case decades ago still obtains today: few satellites have spent significant time near the magnetic equator and at the peak intensities of the inner belt. These research examples added to our motivation to settle the unknowns of the proton energy spectrum: its shape, maximum energy, and time dependence.

The 1971-067 mission was a US Air Force Space Test Program mission with 8 space vehicles. The propulsion module called OV1-20 included a Cherenkov counter telescope that orbited for ∼21 days in a 130 km by 1950 km polar orbit. The counter itself operated for about 8 days in August 1971 using an on-board battery for power. A pair of thin scintillators defined the geometry and a Lucite Cherenkov radiator yielded an energy range of ∼65 to >550 MeV (Kolasinski 2012). The limited OV1-20 measurements were not consistent with the AP-8 model of the inner belt (see the model discussion below). There were plans for follow-on missions to measure the inner belt for longer time periods, although those missions did not occur.

RBSP will be the first mission since the Combined Radiation and Release Effects Satellite (Vampola 1992; Johnson and Kierein 1992) to survey the inner belt using a near-equatorial orbit and suites of particle and fields experiments. Although the CRRES orbit itself was sufficient for investigations of the inner belt, the vehicle did not have instruments to measure protons above ∼100 MeV and many relevant CRRES instruments did not perform well in the inner belt because of large backgrounds from penetrating protons (e.g. Gussenhoven et al. 1993).

After the end of the CRRES mission 1992, the only other relevant science data originated from low-Earth orbit (LEO). Continuing LEO observations, though important for situational awareness and refinement of our understanding of atmospheric losses, cannot obtain the information we need to validate our understanding of the inner belt proton sources and losses. The steep flux gradients caused by the atmosphere introduce large uncertainty in the modeling (e.g. Heynderickxs et al. 1999).

The SAMPEX mission provided a long baseline of inner belt proton measurements below ∼600 km (Baker et al. 1993). The PET instrument was a cosmic-ray sensor design that monitored the outer belt electron population in LEO, solar energetic particle precipitation over the polar caps, and the trapped protons in the inner belt. Figure 2 shows changes in the outer boundary of the trapping region from SAMPEX/PET.

The PAMELA magnetic spectrometer is another example of obtaining information about the inner belt from a cosmic ray detector placed in low-Earth orbit, in this case an elliptical 350–650 km orbit (Adriani et al. 2008). PAMELA benefits from a large geometry factor and an extensive energy range designed to address galactic cosmic ray antiparticle abundances. Similar to SAMPEX, their measurements indicate an inner belt energy spectrum above ∼100 MeV that is harder than the AP8 model discussed below.

1.3 Inner Belt Proton Models

Models of the inner belt protons have been developed to predict the penetrating backgrounds in science and engineering instrumentation, for science analysis, and for spacecraft engineering. We briefly discuss them here because they represent an efficient way of comparing new measurements to prior data sets and because we designed RPS to meet the needs of future models.

A host of LEO models address the low-altitude fringes of the Inner Belt, but only two sets of specification models describe the heart of the Inner Belt environment: AE-8/AP-8 (Vette 1991; Sawyer and Vette 1976) and models from the CRRES mission (Brautigham and Bell 1995; Meffert and Gussenhoven 1994).

From 1966 to 1976 there were a series of publications that compiled the available trapped proton (and electron) measurements in empirical models for applications and space science. The last versions called "AP-8" and "AE-8" for protons and electrons respectively are the de-facto standard for spacecraft engineering and are commonly used references for new measurements. We briefly discuss AP-8 and select a few inner belt proton studies since the creation of AP-8. See Ginet et al. (2012) for further details of the AP & AE models and their follow-ons.

The goal of the trapped proton and electron modeling effort by Vette and others was to synthesize a number of datasets with different coverage in energy and spatial location into a single reference model for engineering and research. Episodic updates using short-term datasets of that era, sometimes only a few months in duration, kept the models in step with the new measurements. There were 43 separate missions that contributed to the last version of the proton model, most of which provided little or no coverage of the inner belt.

The actual model took the form of least squares fits to integral energy spectra at various B and L coordinates. The authors drew smooth curves by hand through the data if there were too few points for a least squares fit, sometimes missing the data by a factor of 2 or more in order to constrain the fit to be smooth. The authors remarked that "the spectrum in the inner zone for energies above 150 MeV is not well supported by data in these models" and in fact above 150 MeV the model consists only of extrapolations of the least squares fits. They anticipated using the data from new missions to populate the higher energies but this addition never occurred. Another problem is that the mapping to B-L space for AP-8 took place in a static 1960 Jensen-Cain magnetic field model (Jensen and Cain 1962), limiting its usefulness today given the secular changes in the geomagnetic field.

Data from the CRRES spacecraft were the basis for the CRRESELE/CRRESPRO models. As mentioned above, the relevant instruments did not perform well in the inner belt. The proton datasets extend from 1.1 to 90.4 MeV and are therefore insufficient for questions relating to the exact shape and energy extent of the CRAND energy spectrum.

Heynderickxs et al. (1999) created an inner belt model for LEO using SAMPEX measurements that extended to 500 MeV and found that the SAMPEX data were higher than the AP-8 model by factors of $\sim$2 at several hundred MeV. The authors noted that the secular drift in the geomagnetic field means that data of different epochs such as SAMPEX and the 1970's era AP-8 cannot be compared without transforming both data sets into the same magnetic field model.

Selesnick et al. (2007) reexamined the CRAND with a modern set of tools and knowledge about the process. This theoretical model is the most up to date reference for CRAND and solar energetic particle contributions to the inner belt and forms the hypothesis that the RPS data seeks to test experimentally. They considered two sources for inner belt protons: the neutron albedo using galactic cosmic ray H and He incident on the neutral atmosphere

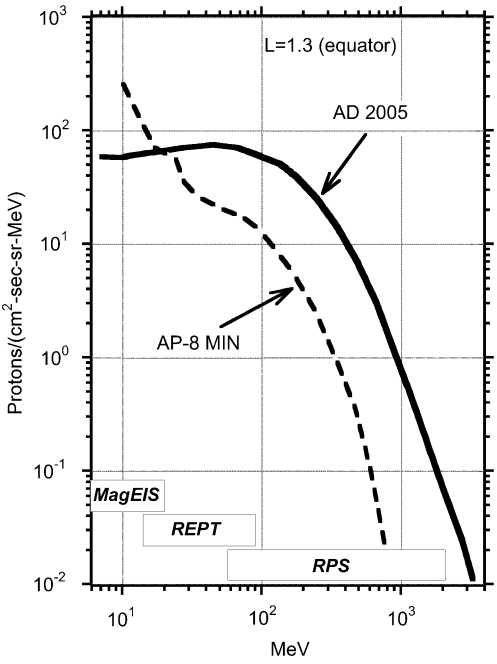

Fig. 3 Comparison of model inner belt energy spectra at $L = 1.3$. AD2005 refers to the model of Selesnick et al. (2007). The *boxes* at the bottom of the figure show the energy ranges of proton instruments onboard the RBSP mission (energy ranges placed at arbitrary proton intensity)

(specified in the NRLMSISE-00 model); and solar energetic particle trapping based upon empirical trapped proton intensities and records of the solar proton fluence during the space age and inferred from polar ice samples for dates prior to 1956. Their use of polar ice proxies indicates a novel challenge for this theoretical treatment of the inner belt: an accurate specification of the current inner belt population must account for histories of the sources, losses, and the trapping field on timescales of hundreds of years or more (e.g. Farley and Walt 1971). Figure 3 is an example of equatorial energy spectra from the Selesnick et al. (2007) model at $L = 1.3$ along with the AP-8 solar minimum model. Most of the energy spectra in the 2007 model (and AP-8) have components below ~50 MeV from solar proton trapping. The 2007 model predicts harder spectra (i.e. smaller spectral slope) above several 100 MeV, but one must realize that the AP-8 model had no data to justify its spectral rollovers. Figure 3 also shows the energy ranges for the relevant RBSP instrumentation that will form the basis of new models and understanding of the inner belt.

1.4 Inner Belt Engineering Hazards

Many space vehicles have inadvertently detected the inner belt though anomalies and performance impacts from the intense penetrating proton environment. Most often these operational problems have occurred in LEO where the weaker geomagnetic field in the region of the southern Atlantic Ocean and South America allows the trapped protons to mirror at lower altitudes than other portions of their drift orbits. For other missions, the impacts had been anticipated. For example, Fig. 4 shows the position of the SAMPEX satellite during re-tries of its MIL-STD-1773 optical fiber bus. The retries occurred when an energetic proton produced secondary particles (multiple delta rays, nuclear fragments, or both) that upset an optical signal receiver (Crabtree et al. 1993). Other reports (e.g. Bedingfield et al. 1996; LaBel 2009) show the same type of impact, namely single event upsets from secondaries when vehicles transit the inner belt.

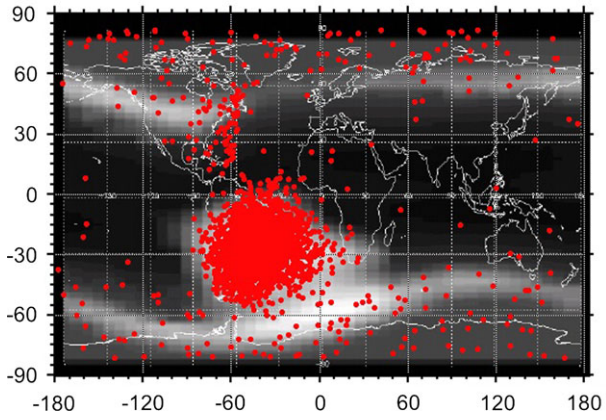

Fig. 4 Location of single-event transients in the optical data bus of the SAMPEX satellite from 1995 to 1996 (*solid symbols*). The *background image* is the count rate of >0.5 MeV protons and electrons, showing the extent of the inner belt at ~600 km altitude as well as the outer electron belt and higher galactic cosmic ray flux over the polar caps

There have also been documented cases of induced radioactivity in materials. This is a potential problem for LEO spacecraft with astrophysics instrumentation that includes large volumes of scintillator material such as sodium iodide (Peterson 1965; Fowler et al. 1968; Fishman 1977). The effect is a tail on the background count rate that impacts the primary measurement for minutes after leaving the inner belt. The mechanism is photon and electron emission as the transmuted nuclei decay into stable elements. See O'Brien et al. (2006) for more details of these and other engineering concerns.

1.5 Primary RPS Science Questions

The instantaneous inner belt proton spectrum therefore is the result of a wide variety of particle source and loss processes that operate over timescales from minutes to centuries. Fundamental questions remain about these processes and the links between them, in part because what we see today in the trapped particles is a snapshot of a longer-term history. Our primary science questions about the inner belt protons are:

1. What is the energy spectrum of the inner belt protons?
2. How does the spectrum compare with the CRAND mechanism above 100 MeV?
3. What are the major sources for protons below ~100 MeV?
4. Can we account for long-lifetime protons of ~GeV energy using our current knowledge of the CRAND process and the secular variations of the geomagnetic field?
5. What are the causes of changes to the outermost limits of the proton-trapping region?
6. What determines whether an interplanetary shock forms a new proton radiation belt?
7. What geomagnetic activity determines how these transient-related belts are lost?

2 RPS Requirements

The RPS instrument requirements flow from the science questions and from the need for a new model of the trapped radiation environment that includes the inner belt protons from ~100 keV to beyond 100 MeV (Ginet et al. 2012). Figure 5 shows what we define as the level-1 AP-9 model requirements mapped to the RPS instrument. Accommodation of RPS on RBSP provides the spatial coverage and the ability to sample the proton pitch angle distribution for the duration of the RBSP mission.

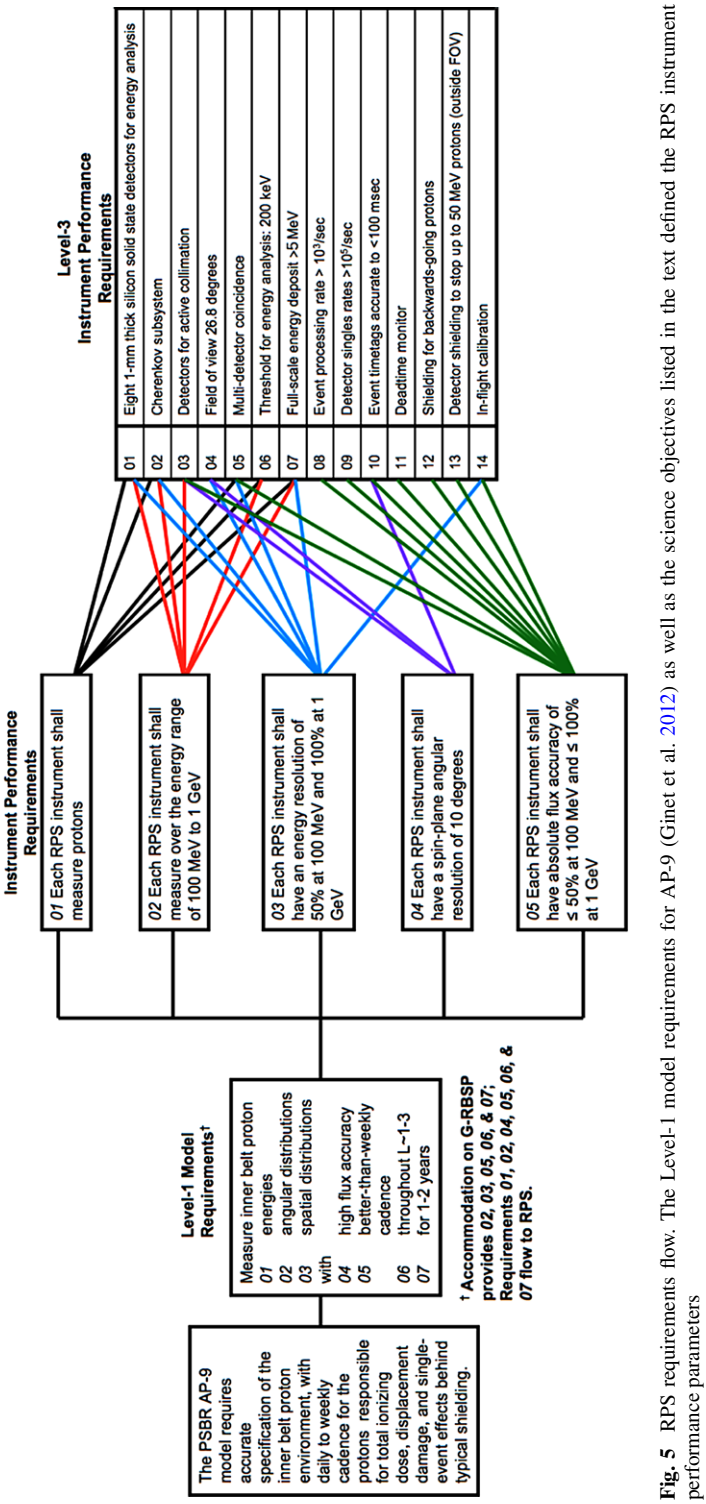

Fig. 5 RPS requirements flow. The Level-1 model requirements for AP-9 (Ginet et al. 2012) as well as the science objectives listed in the text defined the RPS instrument performance parameters

The prime concern for the RPS development is the clean separation of foreground events from the larger rate of penetrating background events. Some previous proton instruments have suffered from insufficient appreciation of the background in the inner belt, hence our need for an instrument that has the minimization of background as a fundamental part of its design. Other major concerns were sufficient margin for particle intensity, both to prevent instrument saturation and to insure sufficient statistics on the spatial scale of 0.1 L; accurate monitoring of instrument deadtime; and accurate in-flight calibration to monitor any changes in the instrument response. Our flux accuracy requirement applies when sufficiently high proton intensity is present so that the error from Poisson counting statistics is negligible and the remaining uncertainty in the flux originates from systematic uncertainties in the instrument itself. This will obtain over short (minutes) timescales in some regions of the RBSP coverage in magnetic coordinates, and over longer (several days) timescales in others.

Figure 5 also indicates the mapping from the higher-level instrument requirements to the detailed RPS attributes captured in level-3 requirements. The following section describes how we addressed these requirements.

3 RPS Instrument Description

3.1 Design Overview

A traditional method of discriminating a penetrating background from desired coincidence events in charged particle telescopes is to use an anticoincidence detector that surrounds the primary detecting elements (e.g. Krimigis et al. 1977). An anticoincidence cup would not work in the inner belt because its trigger rate would be much larger than the rate of valid events leading to a crippling deadtime. Another method is to discriminate against background in the time domain using fast timing coincidence to define valid events; the timing requires fast detectors such as scintillators and corrections for timing walk. The Cherenkov counter on OV1-20 used this timing method. The fast timing method does work in an inner belt environment; however it requires careful and potentially challenging coupling of the scintillator detectors to their light amplifiers and the latter will have gain changes in the environment if one uses traditional photomultiplier tubes, or there may be impacts from single event effects if one uses solid-state photon detectors.

In order to balance the interest in using standard charged particle detection techniques against a large instrument deadtime, the RPS concept requires a 10-fold coincidence in a stack of silicon solid-state detectors for a valid measurement. RPS is therefore not a standard range telescope because it does not measure the range of particles in a silicon stack; rather, we only analyze events that penetrate the entire silicon stack.

Figure 6 is a sketch of the RPS operational principle. Event analysis only occurs after a forward-going proton penetrates a stack of silicon detectors each of whose thickness is sufficient for accurate pulse-height analysis. The energy resolution steadily degrades with increasing proton energy if one only used the silicon detectors, hence the need for another incident energy measurement above several hundred MeV. We employ the proven technique of amplification of Cherenkov light in a solid radiator (Tamm 1939; Getting 1947) to complement the silicon detector measurement at moderate energies in the inner belt and to be the primary measurement up to and beyond $\sim$1 GeV. Non-ideal response of the Cherenkov system arises from knock-on electrons (e.g. Evenson 1975; Grove and Mewaldt 1992) and scintillation in the radiator. As discussed below, these subthreshold light sources exist in the RPS flight instruments. However they do not impact the

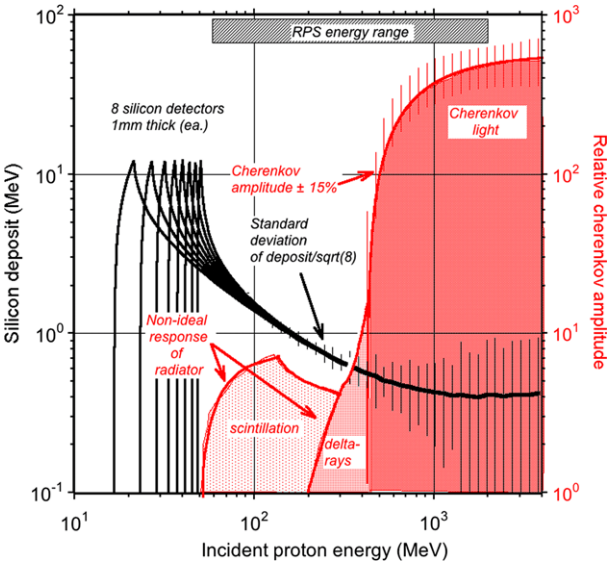

Fig. 6 The RPS measurement principle. Valid coincidence events penetrate all detectors in a series of 1-mm thick silicon detectors. A Cherenkov system provides the incident proton energy for the highest-energies in the RPS range. Non-ideal responses from scintillation and from delta-rays (shown here schematically) in the Cherenkov radiator contribute to photons below the nominal threshold for Cherenkov light (in this case ~423 MeV for an index of refraction of 1.38)

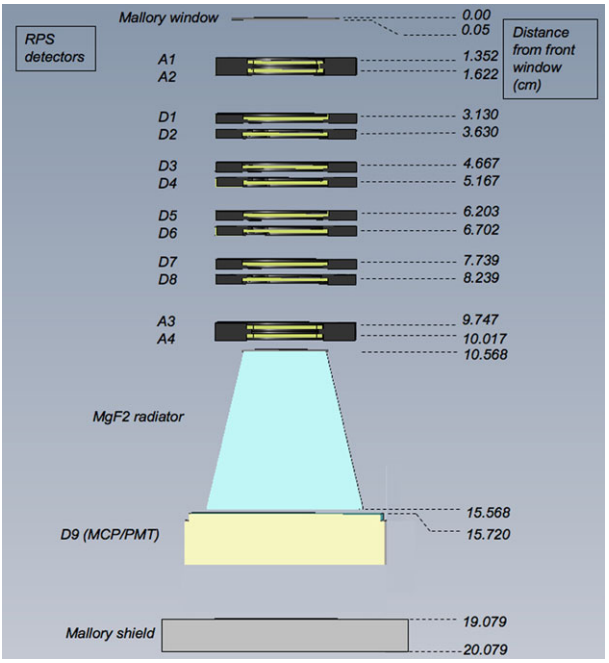

Fig. 7 Schematic of the RPS physics package including all active solid-state detectors, the Cherenkov radiator, and MCP/PMT. The *rightmost values* indicate the distance (cm) from the front of the RPS window

resolution of the spectrometer because they occur in an energy range where the dominant source of information is the array of solid-state detectors.

Figure 7 is a cross section schematic of RPS. Forward-going protons must penetrate and deposit at least 200 keV in each of the 8 energy-measuring detectors labeled D in order to generate a valid event. Pairs of geometry-defining detectors labeled A in the figure are threshold-only detectors with a smaller diameter to guarantee that valid event trajectories

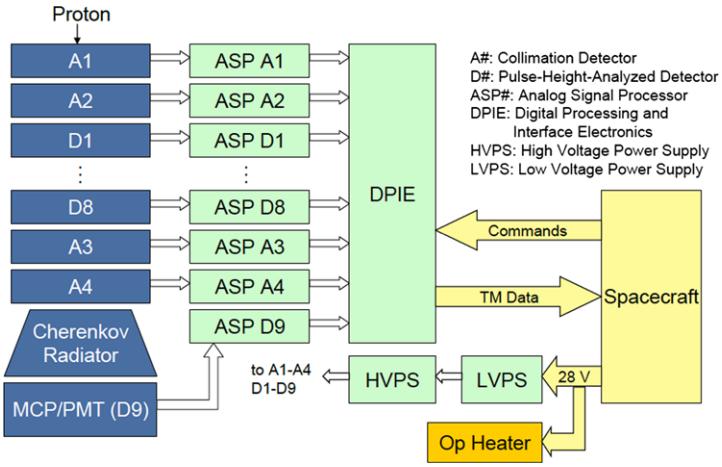

Fig. 8 RPS block diagram. The *block arrows* indicate signal flow and or power connections

are well away from the edges of the D detectors where incomplete charge collection distorts the energy deposits (see Appendix D for more details on edge effects). A front-back pair of A's is also required in the coincidence of a valid event. We use only one pair (A1A3 or A2A4) in the coincidence definition to define the geometry, leaving the other unused pair as a redundant backup. The microchannel plate photomultiplier tube (MCP/PMT) assembly detects and photoconverts the Cherenkov light from the proton's passage through an optical grade conical magnesium fluoride radiator.

3.2 System Block Diagram

Figure 8 shows the primary functional components of RPS. The physics package consists of the 4 geometry-defining detectors, the 8 energy-sensing detectors, and the Cherenkov system. A single high-voltage power supply provides the detector bias voltage and the higher voltage required for the Cherenkov system. Analog detector signals flow from the physics package through the Analog Signal Processing (ASP) boards. A single Digital Processing and Interface Electronics board (DPIE) contains the digital signal conversion, event coincidence, and serves as the interface with the RBSP telemetry and command lines. Figure 9 is a photograph of one of the RPS flight models with the top cover removed with labels for the locations of the major subsystems discussed in more detail below. Figure 10 is a photograph of the completed flight model 1. Both flight models have identical design and function.

3.3 Solid-State Detector Assembly

The solid-state detector assembly (SSDA) consists of a total of twelve silicon solid-state detectors, their mechanical mountings, in-flight alpha sources (for the energy-sensing detectors), and a shielding housing to limit the singles rates due to penetrating protons and electrons. We procured the detectors from Micron Semiconductors, LTD. The technology uses ion-implanted doping to form a p+ junction on n-type silicon with nominal thickness of 1000 ± 50 microns. The junction window is a continuous aluminum layer 0.1 micron thick; the ohmic window is continuous aluminum but 0.3 microns thick. Full depletion obtains at a nominal 70 to 90 volts for the flight RPS detectors; we employed a common bias

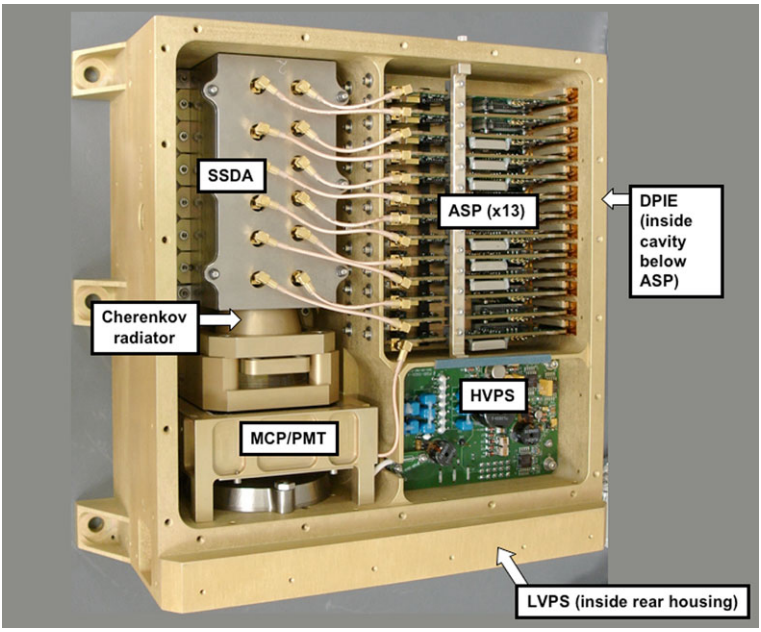

Fig. 9 Photograph of the inner components of RPS. The LVPS and DPIE subsystems are housed in isolated cavities at the rear and bottom of the RPS chassis, respectively

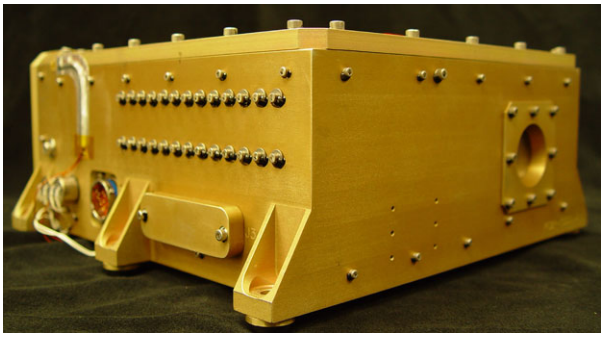

Fig. 10 Photograph of RPS flight model 1. There is one RPS on each of the RBSP vehicles. The *instrument aperture* is the rightmost circular area in the photo

voltage of 170 volts to insure full depletion of the silicon for all the flight detectors. Leakage currents are typically 100 to 200 nA.

The active area diameters are 20 mm and 23 mm for the collimating and energy-sensing detectors, respectively. Figure 11 is a close view of one pair of energy-sensing detectors. To minimize the potential for external noise pickup we mounted the detectors in pairs with their ohmic (signal) sides facing each other. The design also accommodated the potential need to replace a noisy detector at some time during the instrument or spacecraft-level testing, so we made their access relatively simple. To date no detector in either flight instrument has needed replacement.

We also made a provision for continuous alpha particle stimulus of the D detectors during instrument testing, integration, and in-flight, hence the 4-mm diameter extension of the active area outside the circular active area. We attached holders for the alpha sources to ei-

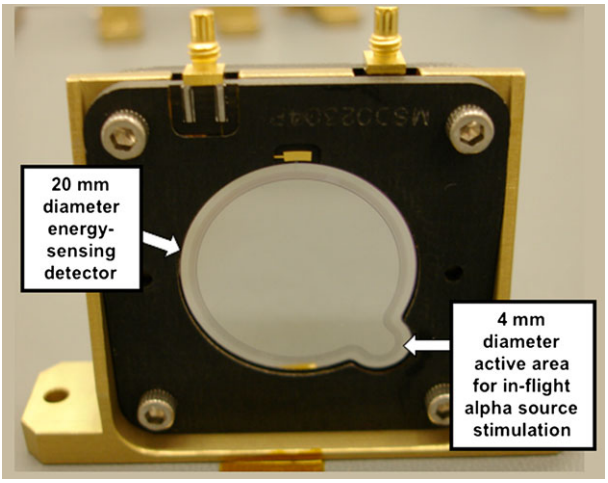

Fig. 11 Photograph of a pair of energy-sensing D detectors (in this case D5 & D6) in their insulating detector mounts and aluminum holder. The view is towards the junction side that is signal ground. *Mini-coax connectors* at the top provide bias and signal connectivity with ASP

ther side of the central aluminum detector mounts. The in-flight calibration section has more specifics on the in-flight alpha sources.

All the paired detector housings mount to a 3 mm thick Mallory base. The SSDA base attaches to an aluminum plate that is electrically and thermally coupled to the RPS chassis. A 3 mm thick Mallory cover fits over the remaining 3 sides of the SSDA providing electromagnetic shielding for the detectors and particle shielding corresponding to the range of 53 MeV protons and 5.3 MeV electrons; these approximate energies include the RPS mechanical housing of 350 mils aluminum.

3.4 Cherenkov Subsystem

The Cherenkov subsystem contains the Cherenkov radiator, its mechanical support, and the microchannel plate photomultiplier tube (MCP/PMT) for conversion of the Cherenkov light to an amplified electronic signal, and the bias network for the MCP/PMT. We refer to the entire subsystem as CRA. The radiator is optical-grade magnesium fluoride (MgF_2). We chose MgF_2 for its index of refraction of 1.38 which yields a threshold energy of ∼432 MeV for protons to generate light in the medium. The actual index of refraction depends on wavelength as described in the Geant4 modeling section below.

The conical shape of the radiator matches the field of view defined by the SSDA geometry. We suppressed internal reflections of light from backwards-going protons by painting the topmost surface of the radiator with a space qualified conducting black paint. A spring-loaded assembly holds the radiator in place; we used this method of pre-loading to mount detectors in the LRO/CRaTER instrument (Spence et al. 2010) and it proved itself useful for RPS. Here the primary concern was possible mechanical damage to the radiator crystal in the vibroacoustic launch environment.

An early design trade considered using a monolithic radiator and conventional PMT in order to eliminate any vacuum gaps or interfaces where internal reflections might cut the light intensity. However there was not sufficient time to pursue development for the RBSP mission, so we procured a UV-sensitive MCP/PMT assembly from Burle Industries. Their 85001 device incorporates a bialkali photocathode deposited onto the backside of a fused silica window; the nominal spectral response is 185 to 660 nm. The window area is 51 mm square. Inside the “tube” is a chevron pair of microchannel plates that amplify the photoelectrons and an anode with 4 equal area quadrants to collect the resulting charge cloud. We

did not use the position information that the separate anodes provide, deciding instead to add the 4 quadrants together with a coupler printed circuit board since the prime measurement for RPS is the total light amplitude.

The Burle design allows for a smaller Cherenkov system than a conventional PMT would require, but there is a vacuum gap between the MgF_2 radiator and the photocathode. Our early design simulations using the Geant4 tool indicated that there would be a negligible loss due to the gap for incident energies near ∼600 MeV, but that this loss would occur well below the 185 nm threshold of the Burle device. The result is that we capture the bulk of the light output from the radiator and the design is insensitive to cutoffs due to total internal reflections.

We potted the tube into an aluminum housing that also houses the resistor divider network that provides the correct bias voltages to the photocathode and to the MCPs. With 500 MeV protons we measured the flight model tube gains to be on the order of 10^5 at nominal high voltage of −1950 volts.

3.5 Analog Signal Processing

The Analog Signal Processing (ASP) subsystem accurately collects the pulse height amplitudes of detection events and provides in-flight electronic stimulus of each of the signal processing chains. There are a total of 13 ASP printed circuit boards in each RPS with one ASP dedicated to one detector element (12 for SSDA and 1 for CRA). Our analog processing follows the standard approaches of modern nuclear signal processing with these attributes: a hybrid charge sensitive preamplifier with a low-noise junction field-effect transistor; pole zero cancellation; active multi-pole shaping amplifier; a gated active baseline restorer; a gated peak stretcher; and a synchronous Wilkinson rundown for the pulse height conversion.

Another feature of the ASP system is the use of a dual-threshold detection. A low 50 keV threshold for the D detectors determines whether a deposit in a detector might be a candidate for pulse-height conversion. A higher threshold of 200 keV must then be triggered for actual pulse height analysis. We discuss the coincidence method more in Appendix A. The use of a lower threshold minimizes the walk in the timing coincidence window that is 260 nsec wide. The full range for energy loss measurement in the D detectors is 0.2 to 10 MeV with approximately 20 keV FWHM of system noise.

The ASPs for the D energy sensing detectors incorporate the full circuitry for the PHA conversion. Each valid deposit is digitized with the Wilkinson rundown circuitry in an Amptek PH300 hybrid with a maximum rundown time of 61.44 microseconds and 10 bit conversion, yielding a channel width of ∼10 keV. We perform the rundown simultaneously on all ASPs. Logic within the programmable gate array on the DPIE (next section) controls the PH300 devices.

The ASPs for the four A collimation detectors do not include the PHA circuitry. The single ASP that is dedicated to the CRA required that we attenuate the input by a factor of 18 in order to make the anode charge pulse amplitudes match the range of charge pulses seen from the SSDA, thus enabling all the critical components for signal amplification and processing to be duplicated across the physics package.

3.6 Digital Processing and Interface Electronics

The digital processing and interface electronics subsystem (DPIE) is the data processing unit for the multiple subsystems within RPS. DPIE is a single printed circuit board that contains

the command and telemetry interface to the RBSP spacecraft, the power and logic interfaces to the ASP subsystem, and the main coincidence event processing logic. DPIE also creates the RPS CCSDS data packets that include pulse height and rate scaler data from the SSDA and CRA as well as all of the instrument voltage, current, temperature, and radiation dose monitoring.

The field programmable gate array contains the detector scalers, the coincidence logic, and the interfaces to the ASP system for the start of the rundown of valid events. The singles counters tally the number of low-threshold (50 keV) triggers in each active detector; there is a unique double coincidence counter for the selected pair of geometry-defining A detectors. When a valid coincidence event occurs (the nominal case is the 2 active A detectors and 8 D detectors), DPIE sends a signal to the ASPs to begin the rundown of stored charge in the PH300 PHA devices. The gate array latches the event time at the time of the coincidence, inserts the peak amplitudes and other information into the event packet, and transmits the packet to the RBSP spacecraft on a 1-second boundary. An internal counter monitors the time spent processing events and reports it every second as the total system deadtime.

DPIE processes all RPS commands received over the RBSP low-voltage differential signal command interface and uses the 1 pulse per second (PPS) interface for packet creation. RPS does not use any other instrument data or spacecraft housekeeping for autonomous operation, nor does RPS contain any software. One last feature worth noting here is that DPIE gate array monitors the command and PPS interfaces for fast ($<$120 nsec width) pulses that might be induced on these lines from electrostatic discharge (ESD) events somewhere on the space vehicle. RPS reports accumulated counts of these fast transients in its routine telemetry. Ground-based testing of RPS with a human-body-model ESD gun verified that the instrument had no anomalies from 5 kV pulses, and that the DPIE counted and rejected the induced pulses on the PPS and command interfaces.

3.7 Power Supplies

The RPS low voltage power supply (LVPS) is the power interface between the instrument and the RBSP spacecraft. A space-qualified EMI filter provides the first interface to the spacecraft LVDS power system, followed by three 5-watt DC to DC converters and other power conditioning and filtering to limit inrush currents on the power return and to satisfy the observatory electromagnetic cleanliness requirements. Typical efficiency for the LVPS is 55 %. The rear of the RPS mechanical structure houses the power supply on a single printed circuit board in its own cavity.

The high voltage power supply (HVPS) provides the SSDA bias and the higher voltage for the CRA on a single printed circuit board. The SSDA bias is 170 volts using a custom transformer and a two-stage Cockroft-Walton voltage multiplier. Note that all silicon detectors derive their bias from a single power supply. On the same board separate circuitry using a four-stage Cockroft-Walton series provides the -1650 volts to -2200 volts required for the CRA. A digital to analog converter on the DPIE provides the control signal for the MCP/PMT bias enabling us to compensate for changes in the MCP/PMT gain on the ground and in orbit with 0.14 volts per command step of 0 to 4095. When the HVPS is armed, then all outputs are nominally 2 volts; a disarm command sets the outputs to 0 volts.

3.8 Mechanical & Thermal Systems

The RPS mechanical housing conforms to the RBSP mission requirement of a minimum of 350 mils Aluminum shielding for internal components. Therefore the instrument is much

stiffer than typical particle spectrometers with a fundamental resonance mode of the structure about 1.3 kHz. We designed the mechanical housing and its components around the main subsystems to allow for easy bench testing and integration of the engineering and flight subassemblies. For example, the SSDA is a self-contained mechanical housing that can be assembled and tested independently of the rest of the instrument.

We were concerned about the mounts for the Cherenkov radiator and the MCP/PMT because of the housing stiffness. For the former, we captured the radiator in an aluminum cone-shaped housing using 8 springs to pre-load the assembly. For the latter, analysis was of little use because of the complexity of the MCP/PMT stack. Phase-A vibration testing of a similar MCP/PMT led the manufacturer to stiffen the washers that hold the MCPs in place. Subsequent vibration testing on the flight models showed increased gains after shaking, which suggested some movement of the MCPs themselves might still be taking place with our design (see Appendix E for further details).

A single purge port allowed for purge during instrument testing and while on the RBSP spacecraft. A vent hole 0.1 inch in diameter vents the instrument via the LVPS cavity with a characteristic venting time of ∼1 second.

RPS is thermally isolated from the bottom deck of the RBSP spacecraft with insulating washers at each of the six mounting feet. A single thermal blanket, designed and provided by JHU/APL, isolates the bottom of RPS from radiation from the spacecraft. There is no direct solar loading of RPS since it sits on the anti-sunward side of the spacecraft. To control its temperature, RPS uses an operational heater located directly under the SSDA, a survival heater under the DPIE cavity, and a passive germanium black-kapton radiator on the space-facing top of RPS. Predicted temperatures for the SSDA on-orbit are between −20 to −10 degrees C.

One unique aspect of the RPS thermal subsystem was a thermal balance test that occurred before we built the flight model instruments. This earlier-than-usual balance test used a flight-like housing, circuit boards, and power dissipation. We performed the test to gain confidence in the thermal design and the thermal model *before* the flight model construction.

3.9 In-Flight Calibration System

RPS has internal calibration systems that enable us to monitor the SSDA and ASP performance. The first system is a commandable electronic pulser that sends precision amplitude pulses simultaneously to each of the 13 ASP boards equivalent up to 5 MeV deposit into the charge-sensitive amplifiers at a rate of 10 kHz. With the pulser we are able to monitor the 200 keV thresholds of the SSDA ASPs and simultaneously quantify the system noise by differentiating the curve of system rate versus input amplitude. The DPIE board houses the pulser; we can command the pulser on and off and adjust its amplitude with a 12-bit digital command level. Part of the routine on-orbit calibration will include stimulating the ASPs with the pulser as has been done with our ground-based functional test procedures.

We wanted a way to monitor the complete SSDA performance throughout the integration and testing of the instrument and observatories. As noted in Sect. 3.3, the detector design and mounts accommodate a holder for an alpha particle emitter to directly stimulate the 1 mm detectors. We procured a custom set of muti-nuclide alpha sources that contain approximately equal activities of 148 Gadolinium (3.18 MeV alpha, 74.6 year half life) and 244 Curium (5.76 MeV and 5.80 MeV alphas, 18.1 year half-life). The sources were unsealed and deposited onto 4 mm diameter titanium-platinum foils. The set of sources had an average activity of ∼3700 decays per second (90 nCi) which we scaled down with a small aperture in the source holder to yield approximately 8 events per second per detector in the flight models.

The alpha sources have been useful for monitoring the end-to-end performance of SSDA, ASP, and DPIE throughout the instrument environmental testing and will provide a useful benchmark for flight operations. It is important to note that only when RPS is commanded into its "alpha" operational mode do we pulse-height analyze the alpha events. The normal mode of operation sees no coincidences between any of the alpha triggers due to their low rates. Also note that the alpha sources will always be present in the quiet-time singles rates of the D detectors and will likely dominate those rates when RPS is not inside the inner belt.

3.10 Microdosimeters

Each RPS contains two micro dosimeters that measure the total ionizing dose and dose rate inside the RPS mechanical housing. These dosimeters are the second generation of the design first flown on board the Lunar Reconnaissance Orbiter (Mazur et al. 2011). For RPS, we telemeter the low and medium ranges that have 13.6 microRad and 895 milliRad resolution, respectively. We tested all four RPS dosimeters using a cobalt-60 gamma irradiator to confirm their dose equivalent gains, and have tested the design with 50 MeV protons (Mazur et al. 2011). The dosimeters accumulate the dose as long as RPS is powered on, requiring ground-based processing in the RPS Science Operations Center to accurately derive the dose rate and account for power-off intervals for the calculation of total mission dose. The dose rate and total dose information will be useful for monitoring the performance of RPS, of other systems on the RBSP vehicles, and for direct comparison with calculations of the dose derived from RPS and the other science measurements.

Within the DPIE cavity, one micro dosimeter has its silicon detector in the same plane as the SSDA detectors and facing the front RPS window, while the other is oriented 90 degrees away to explore for systematic pitch angle effects. To penetrate the RPS housing and micro dosimeter package and trigger the nominal 100 keV dosimeter thresholds it will require protons above ~53 MeV and electrons above ~5.3 MeV. The effective shielding is ~3.25 g/cm^2 for normal incidence, corresponding to an aluminum thickness of 474 mils.

3.11 Resource Summary

Table 1 lists the RPS mass, volume, power, and data resources.

3.12 Geometry Factors

Table 2 lists the RPS geometry factor as calculated from the active areas of the SSDA. We also list the geometry factors (and energy thresholds) of the PEN and CHE coincidence rates that we derived from bow tie analyses of the modeled instrument response. The bow tie method (Fillius and McIlwain 1974) factors an assumed energy spectrum (here a power law) through the instrument response to derive a consistent geometry factor along with a consistent threshold energy.

4 Calibration

The goal of the RPS calibration is to develop quantitative procedures for converting the RPS data (rates, direct events, & housekeeping) into estimates of the proton energy spectrum and angular distribution. Calibration procedures consist of stimulating the instrument with electronic pulsers, particle sources, and particle beams. Calibration for RPS also consists of iterating the instrument Geant4 model to reproduce the particle data and to refine algorithms for

Table 1 RPS instrument resources

Parameter	Value
Mass[a]	9.16 kg
Power	
Operational[b]	13.18 W
Survival[c]	10.22 W
Data rate	
Normal mode (no direct events)[d]	304 bps
Alpha mode[e]	7112 bps
Orbital allocation	2000 bps

[a]Thermal blanket not included

[b]Worst-case operational power includes operational heater. The RPS instrument power without the operational heater is 8.92 W at RBSP bus voltage of 31 volts

[c]Worst-case survival heater power

[d]Normal mode without direct events yields the minimum RPS telemetry rate. The maximum telemetry rate is $304 + 32640 = 32944$ bps if every direct event packet is filled with the maximum number of 339 direct events. On-orbit direct event quotas will throttle the number of direct events to keep the RPS telemetry within the RBSP orbital allocation for RPS

[e]Alpha mode produces approximately 70 direct events per second

Table 2 RPS geometry factor

Method	Geometry factor (cm^2 sr)	Threshold energy (MeV)[d]
Detector active area [a,b]	0.136	–
PEN events; bowtie analysis [c]	0.13	61
CHE events; bowtie analysis [c]	0.11	70

[a]Geometry factor calculated with nominal AlA3Dn ($n = 1$ to 8) coincidence requirement

[b]Field of view is 26.8 degrees half-angle

[c]Bowtie analysis used power law energy spectra E^{-g} with $g = 4$ to 8

[d]Threshold energy refers to conversion of PEN and CHE rates to integral proton fluxes above the indicated threshold

extracting incident proton energy versus incident angle. Finally, in-flight calibration will use internal RPS stimulus and the modeled galactic cosmic ray proton energy spectrum. Hence, calibration for RPS will not stop after launch but is at a sufficiently high level of accuracy prior to the RBSP launch to allow for immediate RPS operations after instrument commissioning. This section briefly reviews the pre-launch and post-launch calibration techniques and their results.

The Level-2 requirements that drive the calibration work for RPS are those for energy resolution (50 % at 100 MeV) and for flux accuracy ($\leq$50 % at 100 MeV). Together these two requirements impact almost every aspect of the RPS design, and we used all aspects of our calibration to verify that the sensors meet the requirements, and to monitor the constituent subsystems so that the instruments always satisfy these performance metrics. We meet the spin-plane angular resolution requirement of 10 degrees via mechanical accommo-

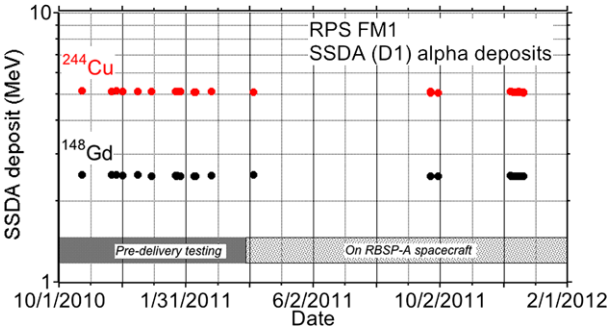

Fig. 12 RPS FM1 alpha source deposit history over 14 months prior to and after integration on the RBSP spacecraft A. The standard deviations were ∼10 keV and all the other detectors had similar histories. There was no systematic trend with time thus verifying the stability of the SSDA system. Measured deposits in air as shown are on the order of ∼10 % lower that those in vacuum due to energy loss in the 2.7 mm gap between the alpha source and the detector

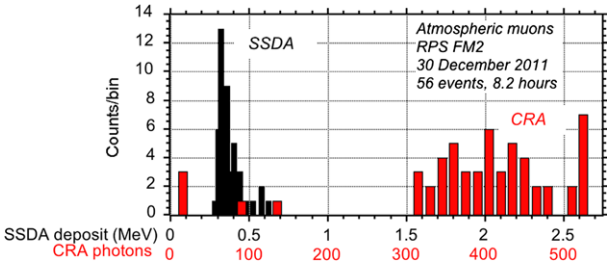

Fig. 13 Example of an RPS collect of atmospheric muons while RPS was integrated with the RBSP-B spacecraft. The figure shows the minimum ionizing SSDA deposits and the Cherenkov light peak. Muons of energies greater than ∼49 MeV will emit Cherenkov light and the sea-level spectrum peaks near ∼500 MeV, hence most events have maximum light output. For this particular HVPS setting some muons saturated the CRA as seen in the highest CRA bin

dation on the RBSP vehicle, the RBSP MAG angular accuracy, and the 1/64 second fine time tags of the RPS direct events relative to the MAG data. Those uncertainties in angular response add to ∼4.3 degrees and are not expected to change with time.

As discussed above in Sect. 3.9, the internal pulser and SSDA alpha emitters allow us to routinely monitor the threshold and noise performance of all 13 ASPs as well as the end-to-end performance of the SSDA (e.g. Fig. 12). Another less frequent yet important calibration effort is the collection of atmospheric muons as a means of monitoring the gain and performance of the CRA. We collected atmospheric muons with RPS during the instrument test phase and periodically during the integration and test phase with the RBSP vehicle. The latter required tilting the vehicles 90 degrees on their test stands which was a unique attitude for the spacecraft ground support equipment and normally used only for the tests of the solar array and boom deployments. Muons with ∼19 MeV penetrate the SSDA and the Cherenkov light threshold is ∼50 MeV. Our observed rate near sea level was approximately 7 muons per hour, which was consistent with a convolution of the sea-level muon energy spectrum (Hagmann et al. 2007) with the RPS geometry factor. Figure 13 shows an example of a muon collect during spacecraft integration and test.

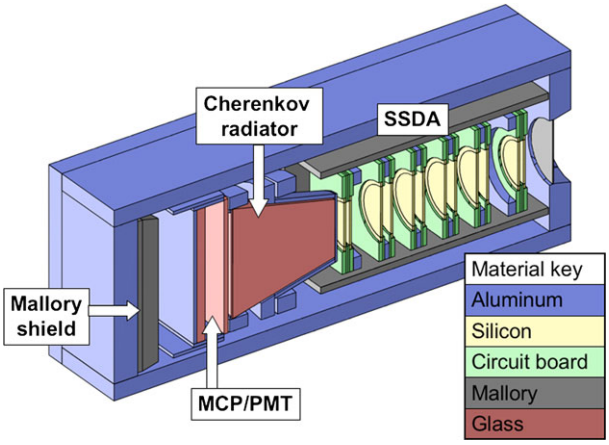

Fig. 14 Solid model of RPS as implemented in Geant4. The glass materials are SiO_2 for the MCP/PMT faceplate and MCP, and MgF_2 for the radiator

4.1 Geant4 Model

Our algorithm for identification of the energy of incident protons after launch relies on a library of simulated responses of the sensor to well-characterized incident particles against which we compare the observed response of the sensor to real particles whose characteristics we wish to determine. We simulated RPS using the Geant4 (GEometry ANd Tracking) radiation-transport code version 9.4 (Agostinelli et al. 2003; Allison et al. 2006). Geant4 models the three-dimensional transport of individual particles of arbitrary species and energy through arbitrary material geometries, allowing the user to log information such as energy deposit and the generation of secondary particles along the trajectory of each primary or secondary particle.

The detector coincidence conditions required to be satisfied in order for a particle event to undergo pulse-height analysis result in a well-collimated response restricted to particles arriving near the axis of the detector stack; thus the geometric model whose response we simulated, shown in Fig. 14, has good fidelity for the physics package of the active elements (SSDA and CRA). We represented the shielding of the surrounding mechanical housing as a simple rectangular box for approximate calculation of the off-axis response of individual detectors.

Geant4 has great flexibility with regard to the choice of physical processes modeled during runs. Often this flexibility can hinder its usefulness. Table 3 lists the physical processes that we selected to capture the relevant physics in RPS. These components, taken together, successfully reproduced the RPS response to protons at the TRIUMF accelerator and to atmospheric muons.

In order to ensure that our simulation represents the response of the actual instrument, ideally we would expose the real sensor to unidirectional, monoenergetic particle beams and compare the observations with models of the response. In practice, our primary proton calibrations used two proton beamlines at TRIUMF (Blackmore 2000). In the first, we used un-degraded 500 MeV and 350 MeV primary beams as well as the same beams degraded to lower energies with stacks of aluminum slabs up to 12″ thick. The other TRIUMF line provided 116 MeV primary beams degraded with Lucite up to 4 cm thick. In both cases a lead scatterer a few mm thick was also in the beamline upstream to lower the event rate. The beamlines included collimators and other inert material near the beam axis for focusing and intensity. This additional material resulted in proton spectra at the sensor that were

Table 3 Physics processes included in the Geant4 simulation of RPS

Physics process	Relevant to these RPS subsystems	Comments
Electromagnetic energy loss	SSDA (primary measurement); CRA (scintillation); all (transport)	Includes scattering and dE/dx fluctuations for realistic straggling of range and energy deposit
Secondary-particle generation	All (transport)	Includes creation of knock-on electrons (delta rays) and bremsstrahlung photons that can carry energy away from detector volumes
Nuclear interactions	All (transport)	Based on Geant4 Binary Cascade model
Cherenkov radiation	CRA; MCP faceplate	Photon spectral distributions are shaped by wavelength-dependent refractive index of optical materials
Scintillation	CRA	Spectral distribution from Viehman et al. (1975)
Optical photon transport	CRA; MCP faceplate	Includes wavelength-dependent absorption and partial and total internal reflection
Quantum efficiency	MCP photocathode	Wavelength dependence from manufacturer specification

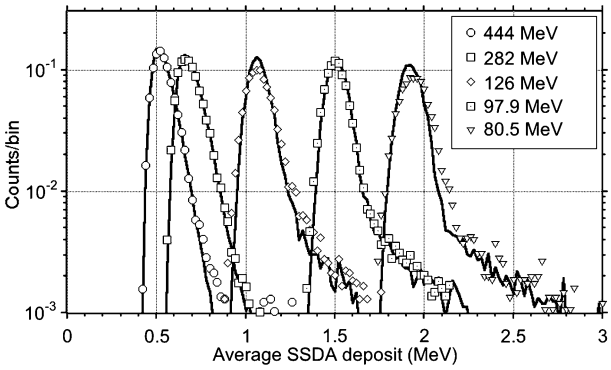

Fig. 15 RPS measurements of the averaged SSDA deposits (*symbols*) compared to the modeled TRIUMF incident proton beam and modeled RPS response (*solid curves*)

broadened rather than monoenergetic. We therefore found it necessary to model the entire beamlines from the points where they entered the test area, placing the RPS sensor model shown above in the appropriate position. Thus the results we show below reflect the accuracy of not only the RPS model but also our models of the TRIUMF beamlines.

Figure 15 compares the measured and modeled distributions of the average energy deposits in SSDA for valid coincidence events. The average energy deposit increased as proton energy decreased as one expects; the curves from left to right represent test conditions (combinations of primary beam energy and set of degraders in the beam) producing energy distributions at the sensor location that peaked at energies from 444 MeV to 80.5 MeV. Note that using the average of the energy deposits in all eight D detectors discards much of the information available from the variation of deposits between the individual detectors, especially for lower-energy protons. The full particle-identification algorithm uses all the SSDA deposit information but we show just the average in Fig. 15 for brevity. Silicon de-

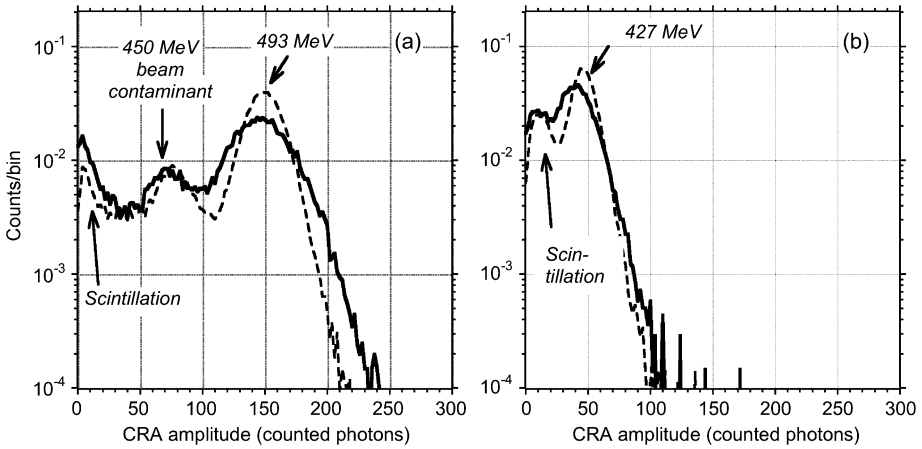

Fig. 16 RPS Cherenkov light amplitude for (**a**) 493 MeV proton beam and (**b**) 427 MeV beam (*solid curves* RPS data; *dashed curves*: Geant4 model). The former beam had a 450 MeV contaminant visible in the histogram. The lower-amplitude peaks originate from scintillation in the MgF_2 radiator

tectors respond in a very nearly ideal manner, efficiently collecting charge from electromagnetic energy deposit throughout their active volumes. Thus, not surprisingly, our simulations were able to accurately reproduce the measured shapes of the SSD responses. The primary differences were for the lowest-energy beams where the simulation was most sensitive to minor errors in the thickness and distribution of inert material such as degraders and beam deflectors in the TRIUMF beamline.

Our simulations had enough fidelity that, for example, we identified a contamination of ∼250 MeV and ∼450 MeV protons in the 500 MeV beam. Consultations with TRIUMF staff suggested non-nominal paths of some protons through the bulk of the collimators rather than through their apertures likely caused the observed lower-energy populations.

The CRA subsystem has a relatively more complex response as seen by the difference between the widths of the simulated and observed peaks for the highest energies in Fig. 16. As examples we show the CRA amplitude for two TRIUMF beam tests in which the dominant CRA signal was from the Cherenkov light. The test reality was a bit more complex as noted above with the presence of lower-energy protons from the beam collimators. Figure 16a shows the main components of the CRA signal: two distributions from the primary protons and a low-amplitude signal from scintillation in the radiator (discussed below). Figure 16b is the response at an energy near the optical wavelength threshold for light generation. In both cases the simulations have enough fidelity that we are able to see the effects of variation of the CRA refractive index with wavelength, which results in Cherenkov response at the shortest transmitted ultraviolet wavelengths to lower-energy protons than at optical wavelengths. The model predicts Cherenkov response at proton energies somewhat below the threshold of about 432 MeV that would be calculated from the optical-wavelength refractive index, and we observed this sub-threshold response in the TRIUMF calibration. Another source for sub-threshold Cherenkov light is the generation of electron delta-rays in SSDA and the radiator (e.g. Grove and Mewaldt 1992); we include this effect in the Geant4 model.

Figure 16 makes clear the presence of a CRA signal at proton energies well below the Cherenkov threshold. These photons result from proton-induced scintillation in the MgF_2 radiator with an intensity of about 5 photons per MeV of energy deposit in our model. Viehmann et al. (1975) estimated a yield of about 20 photons per MeV for UV-grade MgF_2.

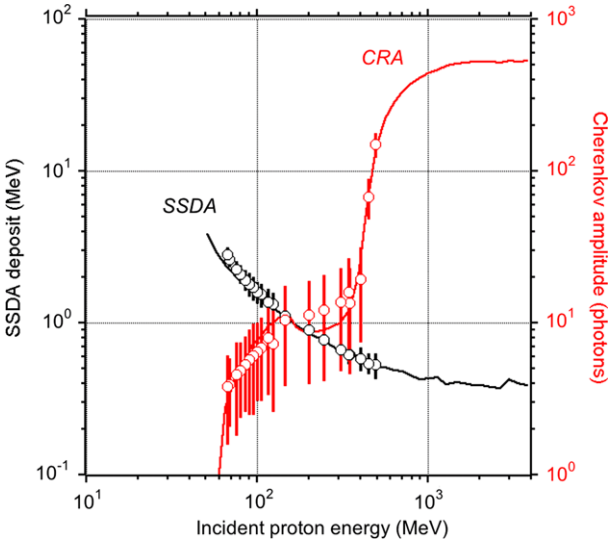

Fig. 17 Comparison of measured RPS response at TRIUMF (*symbols*) with the Geant4 instrument model (*continuous curves*). We show the 8-detector averaged SSDA amplitude and the mean CRA amplitude. The *error bars* are the standard deviations of the measured TRUMF SSDA and CRA pulse distributions

The lower scintillation yield for RPS suggests that the RPS radiator has a higher purity than the material that Viehmann et al. tested. We use the scintillation photon signal as an additional input to the algorithm that calculates the incident proton energy.

Combining the SSDA and CRA signals together is the essence of the RPS measurement. Figure 17 compares the TRIUMF measurements of these detector signals with the Geant4 model for the TRIUMF beams. We show the 8-detector averaged SSDA amplitude and the mean CRA amplitude. The largest discrepancy appears where the model predicts slightly less light from delta rays than observed, but the difference does not warrant further revision because the algorithm to derive incident proton energy is sufficient to meet our requirements across the entire RPS energy range as we discuss below. We attribute the 10–20 % offset in the SSDA responses below 100 MeV to uncertainties in our model of the TRIUMF beam degraders.

Lastly we note that the RPS development schedule prevented a calibration of the flight models at energies higher than 500 MeV. However, early on in the requirements development process we did calibrate an RPS prototype that included the same CRA assembly design as the flight models. There we were able to confirm the roll over of the CRA response, both actual and modeled, to 1 GeV.

4.2 Incident Energy Algorithm

Our process for deriving the incident proton energy from the RPS measurements relies on a pre-computed database of Geant4 test particle interactions with the RPS sensor. Using the modeled event rates as functions of incident energy and angles, we can accurately estimate the energy-angle response of the sensor. To estimate the energy of a single incident particle we constructed an algorithm (called "Enigma") to perform a nearest-neighbors lookup against the database of modeled proton coincidence events. Specifically, we find a variable k nearest neighbors ($k \sim 10$) from the database in a 9-dimensional space defined by the energy deposits in each of D1 through D8 of SSDA and the number of photons detected by the CRA. From these nearest neighbors, we compute an average incident energy and an error metric. We implemented this computation scheme in the RPS Science Operations Center

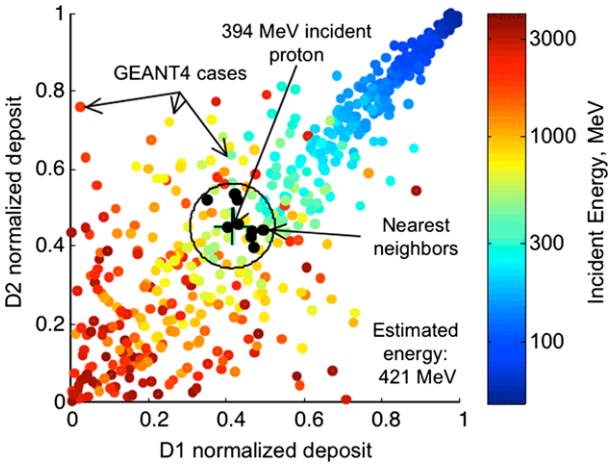

Fig. 18 Example of the incident energy look-up technique. For this illustration we show only the D1–D2 events. The particle of interest had an incident energy of 394 MeV (a 500 MeV incident beam degraded with 6 inches of aluminum), and the algorithm estimated 421 MeV which is well within the RPS Level-2 requirements for energy resolution

and hence all of what follows occurs in the ground-based processing of the data. We briefly discuss the steps in the Enigma algorithm below

Conversion from pulse heights to MeV for D1–D8 in SSDA is a necessary step to account for the slightly different gains of the ASPs and the few percent dependence on instrument temperature. Similarly, we convert the CRA pulse height to a count of photons using a gain factor established with the TRIUMF beam tests and the Geant4 simulations.

We transform each dimension of the 9-dimensional space (8 dimensions are MeV and the 9th is photons) onto [0, 1] domains. The algorithm orders the values for each dimension using the Geant4 model event database: the smallest value maps to $1/(N+1)$, the largest value maps to $N/(N+1)$, and the middle value maps to 0.5, where N is the number of samples in the database. If an observed event falls below the smallest value then the algorithm sets it to zero; events above the largest value get set to 1. The entire transformation follows the empirical cumulative distribution function (or percentile function) of the values in the database for each individual dimension. Therefore, distances in this transformed domain approximate differences in probability or percentile, given the assumed spectrum and angular distribution used to generate the database.

Using the 9 numbers from the observed event transformed onto the [0, 1] domains, we find the k events in the database that are closest in response to the observed event. The algorithm applies a scalable weight to the distance in the D9 (photon) axis that is currently set to a factor of 20 to make the CRA response have the same weight as SSDA. The time it takes the algorithm to find the closest event in the Geant4 model database scales with $\log(N)$. Because k is much less than N, the set of neighbors is independent of the choice of the incident spectrum for the Geant4 particle simulations.

Once the algorithm identifies the k nearest neighbors, it queries the database to determine the original incident energy of those k simulated events and computes the average. We then assign this average incident energy to be the estimated energy for the observed event. Figure 18 illustrates how the Enigma algorithm uses nearest neighbors to estimate the incident energy. In the figure we show only the D1–D2 plane of the look-up space so that the nearest neighbors in the figure were nearest in the total space but not necessarily closest in this plane. Also note that while the spread of events in the D1–D2 plane increases for energies above several hundred MeV (yellow to red in the figure), it is at these high energies that the CRA signal plays the larger role in determining incident energy.

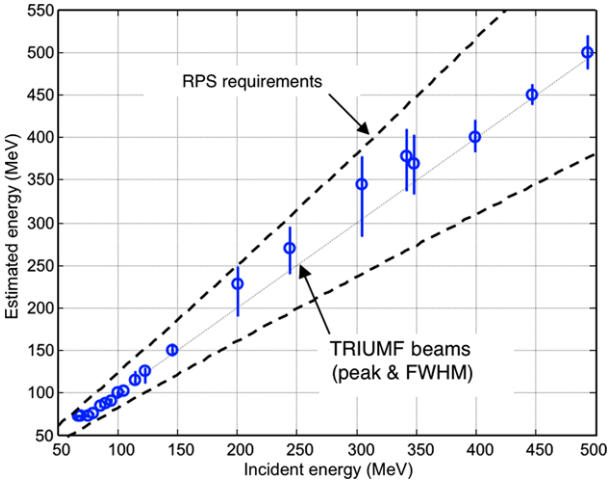

Fig. 19 Comparison of estimated and actual energies for various calibration beams. The *dashed lines* indicate the RPS measurement requirements. The FWHM of the estimated energies is largest in the 200–350 MeV region where the SSDA resolution begins to degrade and before the onset of Cherenkov light

We chose the standard error as the error measurement for the incident energy; this is the sample standard deviation of the k incident energies, divided by the square root of k. This $k^{1/2}$ factor reduces the dependence of the error metric on the choice of k. Figure 19 shows the results of numerous beam tests at TRIUMF. The straight lines correspond to the RPS level-2 energy resolution requirement (e.g. 50 % at 100 MeV) and demonstrate the as-built resolution meets the requirement. Also note the improved energy resolution above several hundred MeV where the Cherenkov light amplitude has the dominant role in energy determination.

As noted above, we were able to inadvertently test the Enigma algorithm at the TRIUMF facility when the efforts to reduce the beam intensity produced near-monoenergetic contaminants in the 500 MeV beam at the level of a few percent of the primary beam intensity. We found the estimated contaminant energies to be consistent with material thicknesses upstream of the instrument.

We lastly note that the Enigma approach of using a nearest-neighbors look-up against a database of simulated events has applications to a broad class of particle sensors.

5 Flight Operations

We designed RPS to require minimal operations support. We rely on the extensive calibration efforts discussed above to produce RPS science in the Science Operations Center (SOC) instead of on-board processing of events. There is no on-board software. Choices such as these simplified the development, test, and integration of the flight models. We also recognize that we benefited from the targeted goal of only measuring inner belt protons. In this section we summarize the RPS telemetry, the main components and functions of the RPS SOC, and the primary data products.

5.1 Telemetry and Commands

RPS telemetry consists of two CCSDS packet types; Appendix B contains the details of both. The instrument produces a 304 bit long rate and housekeeping packet once per second whenever RPS is powered on and the instrument receives the 1 pulse per second signal;

no command is necessary to start the flow of these packets. When integrated with RBSP, we have detailed information about all the RPS operations parameters, including SSDA and CRA rates as well as internal voltages, currents, and the micro dosimetry. Table 5 in Appendix B lists the contents of the rate and housekeeping packet. In addition to its use in RPS science, the RBSP spacecraft will include the entire RPS rate and housekeeping packet in its real-time space weather broadcast.

The second packet type contains the direct events which are the pulse heights for the valid coincidence events. Table 6 in Appendix B lists the contents of the direct event packet. Each event consists of nine 10-bit pulse heights and a 6-bit sub-second counter for more detailed timing analysis. The packet size is variable depending on the incident flux with up to 339 events per packet. RPS creates direct event packets when one or more valid coincidences occur in a second and when the on-board event quotas allow for transmission of the direct events to the RBSP spacecraft. The direct event packets follow the corresponding 1-second rate and housekeeping packet in the telemetry.

The ability of RPS to control its telemetry via event quotas was a simplification for on-orbit operations. A typical orbit will include two passes through the inner belt lasting 10 s of minutes, followed by quiet-time galactic cosmic rays above $L \sim 2$. RPS has a telemetry allocation of 2 kbps averaged across the orbit, and during quiet times we expect that RPS will not exceed this allocation. Of course, RBSP is in some aspects a discovery mission, so the exact nature of the inner belt proton intensity near the magnetic equator will not be known until after launch. However, during intense solar energetic particle events, it is likely that solar protons would exceed our orbital telemetry allocation. These will be scientifically interesting times to monitor the penetration of solar protons to low altitudes and to search for new radiation belts; we do not want to miss collections inside $L = 2$ due to higher-altitude solar particles which will be measured with other sensors. Hence, we implemented 1-second quotas on the coincidence rates of events that trigger the SSDA and those that also have a valid CRA signal. These quotas are commandable in the range of 0 to 650 events per second for the sum of both SSDA and CRA events. The RBSP instrument telemetry data message format limits the size of a packet to 4086 bytes; the result is that RPS cannot send more than 339 direct events per second and quotas larger than 339 events per second will not telemeter more events. Routine operations will use the RBSP ephemeris predictions to estimate the times when each vehicle will cross an L shell of 2.0. On outbound passes at $L = 2.0$ we will lower the event quotas to give priority to the direct events within the inner belt.

RPS has 36 distinct commands. RPS transmits a maximum of one RPS specific command following the spacecraft time and status information within the second. Appendix C lists the RPS commands. Two commands refer to the coincidence mode of the instrument, namely the normal mode in which a pair of A detectors defines the geometry and all D detectors are required for a valid event, and the alpha mode in which any trigger of a D detector creates a valid event. The latter mode is the only means of using the in-flight alpha emitters to create valid events. We can also enable or disable the in-flight pulser, enable and disable the high voltage, and set the CRA high voltage level. The remaining commands are for enabling and disabling individual detectors in SSDA, including the CRA, in order to remove any noisy detector from the nominal coincidence mode.

5.2 Science Operations Center

The RPS Science Operations Center (SOC) is a set of computer algorithms, ground-support equipment software, databases, and desktop computers that operate the RPS instruments in a near-autonomous way and process the RPS telemetry into scientifically useful products.

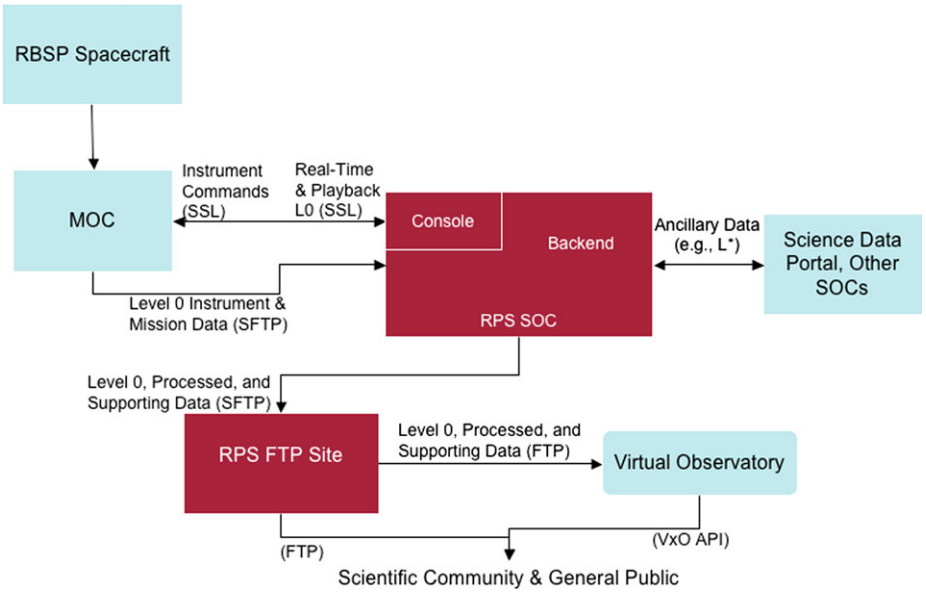

Fig. 20 RPS Science Operations Center architecture

Figure 20 diagrams the two primary SOC components. The console is the interface between the SOC and the RBSP Mission Operations Center (MOC). Functions such as maintaining network connections to the MOC and routine command scheduling occur automatically. We have used the RBSP mission-standard ground support software GSEOS (Hauck 1998–2007) for instrument development, pre and post-delivery testing, and will use the same routines for on-orbit operations.

A governing concern in constructing the SOC was the need to keep the RPS science team aware of the RPS instrument states of health and the status of the SOC data processing. We added a series of scripts that routinely check the instrument status and the volume and contents of the various level-N data against tables and that announce anomalies or abnormalities via emails and text messages to pagers. Fault detection for RPS thus relies on the monitoring of housekeeping and performance in the SOC. Part of the warning message system includes a dead-man timer to insure that a human inspects the top-level functions of the SOC at least once every 2 days. The warnings scripts also automatically construct simple displays of the on-orbit proton flux compared with the AP-8 and -9 models for commissioning and early orbit operations.

5.3 Data Products

The SOC backend is mainly a set of IDL routines that process the RPS telemetry into various data levels as defined in Table 4. All levels of RPS data will be in the form of Common Data Formatted files that conform, as appropriate, to the Panel on Radiation Belt Environment Modeling (PRBEM) standard file format guidelines (http://irbem.svn.sourceforge.net/viewvc/irbem/docs/Standard_File_Format.pdf), which is itself compliant with the ISTP guidelines (http://spdf.gsfc.nasa.gov/sp_use_of_cdf.html).

We will perform the initial data processing with orbit, attitude, and universal time predictions and a model magnetic field. Reprocessing will occur as needed when we obtain the

Table 4 RPS data products

Data Level	Name	Contents	Latency[a,b]	Reprocessing[a,b]
L0	Level 0	RPS CCSDS packets (decoded in CDF version)	1–3 days	By RBSP MOC
L1	Level 1	Nearly all L0 data; universal coordinated time (UTC), SSDA & CRA deposits; singles and coincidence rates, vehicle location, RPS boresight vector, magnetic field vector, estimated incident energy/angle, dead times (including quota effects)	L0 + 1–3 days	Daily up to L0 + 5 days, and on-demand
L2	Energy spectra	Mission elapsed time & UTC; flux versus energy spectrum (once per 5 degrees rotation); pitch-angle and full magnetic coordinates of RPS boresight in Olson-Pfitzer-Quiet and Tsyganenko models	L1 + 1–2 days	Daily up to L0 + 7 days and on-demand
L3	Energy-angle spectra	Mission elapsed time & UTC; energy-pitch angle spectrum (once per spin and once per minute); full magnetic coordinates in Olson-Pfitzer-Quiet and Tsyganenko models	L2 + 1–2 days	Daily up to L0 + 10 days and on-demand
L4	Global maps	UTC; flux versus energy, pitch angle, and L shell; flux vs. other magnetic coordinates; phase-space density maps	L3 + 1–2 days	Daily up to L0 + 14 days and on-demand

[a]Latency applies to data availability schedule after processing is fully automated

[b]Days are business days

input parameters that global magnetic field models require and when the MOC publishes updates or revisions to attitude, time, and magnetic field vectors. We note that we can meet all the RPS science requirements entirely in the absence of external data because pseudo-static (e.g., Olson-Pfitzer quiet) magnetic field models are adequate organizers of the inner zone protons.

For science analysis, the SOC will routinely push the processed data to a location such as the NASA virtual radiation belt observatory. The daily data volume will be approximately 154 Mbytes for each RPS instrument. This yields an estimated data volume for the 60-day checkout plus a 2-year mission of approximately 300 Gb. The RPS SOC will also work with NASA personnel to transfer the RPS data to a long-term archive that NASA will provide.

6 Summary

The RPS instrument is focused on answering decades-old questions about the inner belt proton environment: the proton energy spectrum across a broad energy range and how it compares to the CRAND process, its maximum energy, and how it changes during geomagnetic activity. The observations from RBSP will foster new interest in this nearby yet relatively unexplored region of trapped particles and will raise new questions and insights about the processes that occur there.

We have implemented a robust instrument design that accommodates the lessons from previous measurements in this challenging penetrating background. RPS also incorporates in-flight calibration and subsystem diagnostics so that we can track its performance on-orbit and make any corrections its response. The RPS calibration and modeling efforts proceeded in pace with the instrument design and test, yielding a pre-flight model that meets our requirements for understanding the instrument performance and for producing useful science products immediately after on-orbit commissioning.

Acknowledgements We thank Colonel C. Groves for architecting the PSBR program of which RPS is the space hardware component. R. Selesnick (AFRL) conceived of the RPS measurement concept. W. Olson managed the early phases of the PSBR project for the National Reconnaissance Office (NRO) and D. Byers (NRL/NRO) led PSBR at the NRO through flight model construction and delivery of the RPS flight models. C. Pritt managed the PSBR program office support for The Aerospace Corporation and B. Klatt provided quality assurance guidance for RPS. We thank T. Alsruhe for his contributions to the early project management and E. Blackmore of TRIUMF for his support of the RPS proton calibrations. We greatly appreciate the efforts of the NASA and JHU/APL RBSP mission partners for their cooperation, support, and participation in accommodating RPS on the RBSP spacecraft, specifically: K. Cooper, A. Reiter, D. Myers, J. Stratton, R. Fitzgerald, B. Williams, J. Troll, C. Herrman, N. Mosavi, D. Jones, A. Dolbow, and E. Rodberg (all at JHU/APL); S. Himes, S. Aloezos, and D. Sibeck (all at NASA/Goddard Space Flight Center); and D. Brewer and M. Kessel (NASA/Headquarters).

Appendix A: Event Processing Logic and Count Rates

Each of RPS detectors (A1 through A4 and D1 through D9) provides fast timing logic used in singles counting, pulse height digitization, and deadtime determination. The fast timing logic is found on the associated ASP board, with levels set to approximately 50 keV (low threshold) and 200 keV (high threshold). On the ASP/DPIE interface, these signals are active low; however to simplify the discussion, "low/high threshold triggered" will mean that the input signal is over the associated threshold.

A.1 Normal Mode

This is the nominal operating mode for RPS that requires the 10 or 11-fold coincidence for valid event determination. RPS coincidence event processing in normal mode consists of 5 states: idling, window, gate, valid, and rundown. Below we describe each state and its transition conditions.

Idling: This is the default start-up state for the event processing logic. When in this state, the logic monitors all enabled detectors (nominally a front/back pair of A detectors and D1 through D8 and D9) while watching for a low threshold trigger on any detector. RPS transitions to the window state when DPIE detects *any* low threshold trigger.

Window: The window state is active while the coincidence window is open. In this state, DPIE checks if all enabled detectors trigger the low threshold within the coincidence window; the maximum window length is 260 ns. If the full window period passes without a full coincidence, then processing logic returns to the idling state with no event generated. An immediate transition to gate state occurs when all enabled detectors trigger their low thresholds within the 260 ns window.

Gate: DPIE logic enters the gate state when fast trigger logic (low thresholds) indicates that an event candidate exists in the signal path. While in this state, DPIE sends a signal to the PH300s pulse-height analysis hybrids on the ASPs to track the input waveform for each of D1–D9 detectors. The gate period is fixed at 800 ns and guarantees that the peak amplitudes will be tracked and stored at conclusion of the interval. At the end of the 800 ns interval, transition to the valid state occurs.

Valid: The valid state tests whether all the enabled detectors had their high thresholds triggered to determine if the PH300s captured a valid event. On the valid condition, the next state will be rundown. If the event is not a valid coincidence, then the DPIE logic returns to the idling mode with no rundown. When transitioning to the rundown state, the D9 high threshold condition dictates the type of event to be handled (CHE if D9 active, or PEN if not). DPIE increments the PEN scaler if the event is valid and of type PEN and the CHE scaler if the event is valid and of type CHE (that is, if D9 was triggered). In this way we can separately tally events that have Cherenkov light and those that do not. Note that a CHE event cannot be identified in the logic unless the D9 coincidence mask bit is enabled, therefore the D9 coincidence enable bit should always be enabled.

Rundown: DPIE logic enters the rundown state when the PH300s store a valid event. Here the purpose is to perform the Wilkinson rundown on each ASP as the conversion from pulse height to a digital signal. The "PeakHeld" output from the PH300s is initially asserted on all detectors to show that a peak is held for readout. When the logic transitions to the Rundown state, the gate is released at the PH300s, and ASP logic begins the rundown process. We discharge the pulse peak voltage held by the PH300 at a fixed rate (following a 400 ns delay) and de-assert the PeakHeld when the stored level returns to zero, thereby preparing for the next event. The rundown state lasts a fixed period of 61.84 μs: 400 ns pre-rundown delay +61.44 μs rundown. In the rundown state, the RPS logic monitors the state of all PeakHeld signals while incrementing the rundown count at 25 MHz; de-assertion of a detector's PeakHeld causes the current rundown count to be latched as the pulse height value for that detector.

A.2 Alpha Mode

Alpha mode is a special operational mode designed to allow collection of the energy deposits in the eight D detectors from the in-flight alpha sources. We use alpha mode as discussed above, primarily for calibration and monitoring of the SSDA subsystem. RPS event processing in alpha mode consists of 4 states: idling, gate, valid, and rundown. We describe each state and the transition conditions here:

Idling: this is the default start-up state for the event processing logic in alpha mode. When in this state, the DPIE logic monitors any enabled D detector for a low threshold trigger whereupon the state transitions to the gate state to capture pulse peaks for all of the D detectors.

Gate: DPIE logic enters the gate state when fast trigger logic (low thresholds) indicates that an event exists in the signal path. While in this state, the PH300s on the ASPs are enabled to track the input waveform for each of D1–D9 detectors. The gate period is fixed at 800 ns and guarantees that the peak amplitude will be tracked and stored at conclusion of this interval. At the end of the 800 ns interval, transition to the valid state occurs.

Valid: In alpha mode, the logic always follows a valid event with an immediate transition to the rundown state.

Rundown: The rundown in alpha mode is identical to the rundown process in normal mode, with the exception that typically only one D detector has a measurable pulse height.

A.3 Discriminator Rates

We monitor each detector with a "singles" counter, that is a scaler that increments whenever the high threshold is triggered for the associated detector. Singles counters operate regardless of the state of the associated bit in the coincidence mask. The scalers are 24 bits, allowing for maximum rates of greater than 10^7 counts per second. We also monitor the event rate of particles that are in coincidence as defined by a front/back pair of selected A collimation detectors. We included this doubles coincidence as a consistency check on the total rate of 10 or 11-fold coincidence events. We specify this coincidence rate with commands that enable or disable detectors with the nominal pair being A1A3 and the backup pair being A2A4. If both pairs are not available because of detector noise or other problems, the D1 becomes the front detector and D8 the back element.

A.4 Deadtime Monitor

RPS deadtime occurs whenever any enabled detector triggers its low threshold. The deadtime counter increments on the rising edge of a 12.5 MHz clock using a 24-bit floating point format with 3 exponent bits (most significant portion of output) and 21 mantissa bits (least significant portion of output). Hence the resolution of the deadtime scaler is 80 nsec. RPS reports the deadtime value in the rate and housekeeping packet as a 16-second accumulation that is sufficient for ground-based corrections to the incident particle intensity. The reported value is the number of 80 nsec intervals within 16 seconds during which RPS was busy transitioning from the idle state, hence the time during which new events would not be analyzed.

Appendix B: RPS Data Packet Formats

The RPS rate and housekeeping packet is a total of 38 bytes long and contains all detector scalers, coincidence rate scalers, micro dosimeter values, and other housekeeping information. RPS creates these packets once per second when power is applied and the 1 pulse per second signal exists from ground support equipment or the RBSP spacecraft. Hence the baseline data rate is 304 bits per second. Table 5 lists the contents of the rate and housekeeping packet.

Direct event packets have variable size depending on the number of coincidence events within the second. Table 6 lists the detailed packet contents.

Appendix C: RPS Commands

Table 7 summarizes the RPS commands.

Appendix D: Design Trades and Analyses

During the RPS development we addressed several questions regarding the RPS measurements technique and possible hazards to achieving the Level 1 instrument requirements. We focus here on one effect in order to document some interesting test results regarding the charge collection at the edges of silicon detector active volumes. For future reference, Table 8 summarizes all the major measurement questions that we considered and their answers.

Table 5 Contents of the RPS rate and housekeeping data packet

Start byte	End byte	Bits	On subcom:	Description
0	5	All	n/a	Primary header
0	1	15:13		CCSDS version = 0
0	1	12:12		Packet type = 0 (telemetry)
0	1	11:11		Secondary header flag =1 (set)
0	1	10:0		Application ID = 0x2C1
2	3	15:14		Grouping flags = 3 (not part of group)
2	3	13:0		Sequence count (incremented with each packet output)
4	5	15:0		Packet length = 31 (bytes)
6	9	All	n/a	MET seconds = packet time[a]
10	11	All	n/a	PEN rate[b]
11	12	All	n/a	CHE rate[b]
14	15	15:12	n/a	Subcom (used for output of rate scalers and housekeeping)[c]
		11:0	0	A1 count, 16 second accumulation, 24 to 12 bit compressed
			1	A2 count, 16 second accumulation, 24 to 12 bit compressed
			2	D1 count, 16 second accumulation, 24 to 12 bit compressed
			3	D2 count, 16 second accumulation, 24 to 12 bit compressed
			4	D3 count, 16 second accumulation, 24 to 12 bit compressed
			5	D4 count, 16 second accumulation, 24 to 12 bit compressed
			6	D5 count, 16 second accumulation, 24 to 12 bit compressed
			7	D6 count, 16 second accumulation, 24 to 12 bit compressed
			8	D7 count, 16 second accumulation, 24 to 12 bit compressed
			9	D8 count, 16 second accumulation, 24 to 12 bit compressed
			10	A3 count, 16 second accumulation, 24 to 12 bit compressed
			11	A4 count, 16 second accumulation, 24 to 12 bit compressed
			12	D9 count, 16 second accumulation, 24 to 12 bit compressed
			13	A (active front) A (active back) double coincidence, 16 second accumulation, 24 to 12 bit compressed
			14	High 12 bits of Deadtime counter, 30–24 bit compressed
			15	Low 12 bits of Deadtime counter, 30–24 bit compressed
16	16	All	n/a	Solid state recorder status from RBSP
17	17	7:2	n/a	Count of <120 nsec glitches on command interface[d]
17	18	9:0	n/a	PEN event quota per second
19	19	7:2	n/a	Count of glitches on 1 pps interface[d]
19	20	9:0	n/a	CHE event quota per second
21	21	All	n/a	Command count
22	22	All	n/a	Command error count
23	25	All	n/a	Last command

Table 5 (*Continued*)

Start byte	End byte	Bits	On subcom:	Description
26	27	15:15	n/a	Selftest pulser status (1 = enabled, 0 = disabled)
		14:12	n/a	Unused (= 0)
		11:0	n/a	Selftest pulser level
28	29	15:15	n/a	Commanded HV state (1 = enabled, 0 = disabled)
		14:14	n/a	Arm/safe HV state (1 = enabled, 0 = disabled)
		13:13	n/a	Overall state of HV system (1 = enabled, 0 = disabled)
		12:12	n/a	Unused (= 0)
		11:0	n/a	HV level
30	31	15:15	n/a	A1 detector enable mask (1 = enabled, 0 = disabled)
		14:14	n/a	A2 detector enable mask (1 = enabled, 0 = disabled)
		13:13	n/a	D1 detector enable mask (1 = enabled, 0 = disabled)
		12:12	n/a	D2 detector enable mask (1 = enabled, 0 = disabled)
		11:11	n/a	D3 detector enable mask (1 = enabled, 0 = disabled)
		10:10	n/a	D4 detector enable mask (1 = enabled, 0 = disabled)
		9:9	n/a	D5 detector enable mask (1 = enabled, 0 = disabled)
		8:8	n/a	D6 detector enable mask (1 = enabled, 0 = disabled)
		7:7	n/a	D7 detector enable mask (1 = enabled, 0 = disabled)
		6:6	n/a	D8 detector enable mask (1 = enabled, 0 = disabled)
		5:5	n/a	A3 detector enable mask (1 = enabled, 0 = disabled)
		4:4	n/a	A4 detector enable mask (1 = enabled, 0 = disabled)
		3:3	n/a	D9 detector enable mask (1= enabled, 0 = disabled)
		2:1	n/a	Unused (= 0)
		0:0	n/a	RPS operating mode (0 = normal, 1 = alpha)
32	32	All	0, 4, 8, 12	HV voltage monitor
			1, 5, 9, 13	Bias voltage monitor
			2, 6, 10, 14	+5 VD voltage monitor
			3, 7, 11, 15	+2.5 VD voltage monitor
33	33	All	0, 4, 8, 12	+5 VA voltage monitor
			1, 5, 9, 13	+5 VA current monitor
			2, 6, 10, 14	+2.5 V reference monitor
			3, 7, 11, 15	−5 VA current monitor
34	34	All	0, 4, 8, 12	Micro dosimeter 1 low output (13.65 µRads per step)[e]
			1, 5, 9, 13	Micro dosimeter 1 medium output (3.494 mRads per step)
			2, 6, 10, 14	Micro dosimeter 2 low output (13.65 µRads per step)
			3, 7, 11, 15	Micro dosimeter 2 medium output (3.494 mRads per step)

Table 5 (*Continued*)

Start byte	End byte	Bits	On subcom:	Description
35	35	All	0, 4, 8, 12	Bias current monitor
			1, 5, 9, 13	+5 VD current monitor
			2, 6, 10, 14	+2.5 VD current monitor
			3, 7, 11, 15	DC/DC converter temperature
36	36	All	n/a	Spare = 0xA5
37	37	All	n/a	Packet checksum[f]

[a]The MET value indicates the start time of data collection for this packet, except for subcommed values which are aligned to the previous packet at subcom = 0

[b]PEN and CHE rates are 1-second accumulated values

[c]Singles rates found in bytes 14 and 15 of this packet are 16-second accumulated value. To compute the rate/second, divide the value received, after decompression, by 16. All singles values are latched at the transition from subcom 15 to 0 so that they share the same collection interval

[d]Glitch counters found in bytes 17 and 19 count whenever a glitch (<120 ns wide pulse) is seen on either the 1 pps or command interface (typical pulsewidths >1 μs). The counters are reset at power up and count (modulo 16) whenever a glitch is detected

[e]Microdosimeter 1 is located next to the entrance aperture with its detector co-planar with SSDA; Microdosimeter 2 is located on the side of the DPIE cavity with its detector perpendicular to the SSDA and the RPS boresight

[f]The checksum is computed as the XOR of all bytes in the packet from the start of the primary header to the byte just before the checksum byte. When validating a received packet, XOR-ing all bytes of the packet, including the checksum, should yield a value of 0 for a valid packet

D.1 Silicon Detector Edge Effects

Early in the RPS design we recognized the need to obtain as accurate a measurement of SSDA energy deposits as feasible. Unlike typical range telescopes, RPS analyzes small (<few MeV) deposits from only $Z = 1$ particles, some of which are near minimum ionizing. Therefore one potential source of uncertainty in the determination of incident proton energy is incomplete charge collection in the SSDA silicon detectors at the edges of their active areas. We took two approaches to address potential edge effects.

The first was to quantify the spatial scale over which incomplete collection occurs at the detector edge. One could use actual particle beams that are sufficiently collimated to probe the energy deposit versus location, but it is challenging to collimate an alpha source to a few microns and expensive to use an accelerator facility. Instead we chose to deposit energy within a test detector using a pulsed ultraviolet (800 nm wavelength) laser whose spot size on the silicon was less than 2 microns wide; this same facility is used for single-event effect testing on bare microcircuits. Another benefit to probing the detector with the UV laser was the visual information about where the energy deposit was relative to the complex guard ring structure; one can image the spot with a video camera. The 1/e penetration depth in the silicon was ∼12 microns. We probed a detector design that uses a metallized grid to establish the electric field in the silicon thus allowing a direct stimulation of the bulk silicon except where the thicker guard rings stopped the laser beam. This detector design and the accurate laser spot placement yielded the transect shown in Fig. 21. The relative signal amplitude fell to 30 % of its nominal value at a radial distance equal to the detector thickness, a result consistent with the rule-of-thumb that the incomplete charge collection

Table 6 Contents of the RPS direct event data packet

Start byte	End byte	Bits	Description
0	5	All	Primary header
0	1	15:13	CCSDS version = 0
0	1	12:12	Packet type = 0 (telemetry)
0	1	11:11	Secondary header flag = 1 (set)
0	1	10:0	Application ID = 0x2C1
2	3	15:14	Grouping flags = 3 (not part of group)
2	3	13:0	Sequence count (incremented with each packet output)
4	5	15:0	Packet length = variable (length of data following Packet Length-1)
6	9	All	MET seconds = packet time[a]
10	21	All	DE slot 1 (90 bits of pulse heights, 6 bits of time offset)
10	10	7:2	Event time offset from last second edge (resolution is 1/64 seconds)
10	11	9:0	D1 detector pulse height[b]
12	13	15:6	D2 detector pulse height
13	14	13:4	D3 detector pulse height
14	15	11:2	D4 detector pulse height
15	16	9:0	D5 detector pulse height
17	18	15:6	D6 detector pulse height
18	19	13:4	D7 detector pulse height
19	20	11:2	D8 detector pulse height
20	21	9:0	D9 detector pulse height
22	33	All	DE slot 2 (same format as DE slot 1 above)
34	45	All	DE slot 3 (same format as DE slot 1 above)
...	N	All	...continued for up to $N = 339$ DE slots per packet
$N+1$	$N+1$	All	Unused (random value)
$N+2$	$N+2$	All	Checksum[c]

[a]The MET value indicates the start time of data collection for this packet

[b]Pulse height values output in the DE slot are decompressed as follows: compressed value = 0 to 511, decompressed value = compressed value compressed value = 512 to 1023, decomp. value = (compressed value − 512) ∗ 2 + 512

[c]The checksum is computed as the XOR of all bytes in the packet from the start of the primary header to the byte just before the checksum byte. When validating a received packet, XOR-ing all bytes of the packet, including the checksum, should yield a value of 0 for a valid packet

occurs over a distance comparable to the detector thickness. At twice the detector thickness, the deposit was only about 4 % of its true value.

We thus used the UV laser test data to establish the need for collimation detectors in SSDA and to choose the diameters of the collimators (20 mm) and the energy-sensing detectors (23 mm). The difference in their radii is 1.5 mm corresponding to 1.5 times the nominal detector thickness, thus allowing for 50 % margin away from the detector edge.

D.2 Summary of Other Design Analyses

Table 8 lists the most significant questions that influenced the RPS design.

Table 7 Summary of the RPS commands

Commanded item	Number of commands	Command description
Operational mode	2	Select normal mode
		Select alpha mode
Detector enable & disable	26	Enable *N* detector (where *N* refers to any of the D or A detectors)
		Disable *N* detector (where *N* refers to any of the D or A detectors)
Coincidence event quotas	2	Set maximum PEN events per second (range 0 to 650)
		Set maximum CHE events per second (range 0 to 650)
High voltage	3	Enable MCP/PMT high voltage and SSDA bias
		Disable MCP/PMT high voltage and SSDA bias
		Set high voltage level for MCP/PMT (range 0 to 4095)
In-flight electronic pulser	3	Enable in-flight pulser
		Disable in-flight pulser
		Set in-flight pulser level (range 0 to 4095)

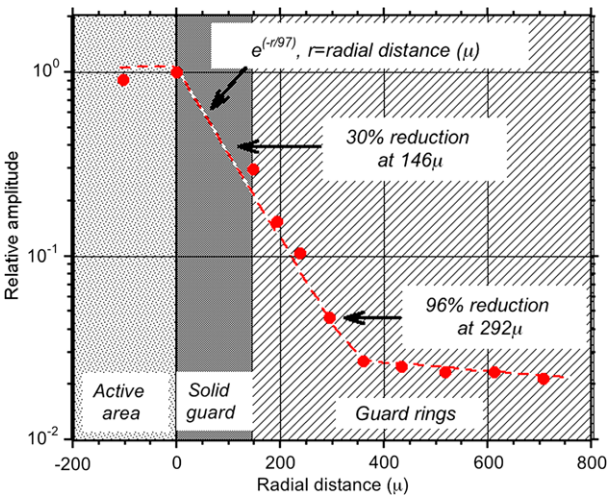

Fig. 21 Signal amplitude in a 146-micron thick Si solid-state detector versus position along the radius of the circular detector. We stimulated the detector with a pulsed UV laser and measured the location of the energy deposition to within a few microns (*solid symbols*) as referenced from the edge of the active area. The *dashed curve* is to guide the eye. The *transect* shown indicates a 30 % reduction of the energy deposit at a radial distance equal to the detector thickness with non-trivial signal amplitude up to twice the detector thickness

Appendix E: RPS Performance Lessons

We highlight here two RPS performance issues that we discovered prior to and during the flight model environmental testing. The issues had been solved before integration on the RBSP space vehicles, but we felt their stories were interesting enough to include in this instrument paper. They may be relevant for future instruments that use similar components.

Table 8 Summary of questions that influenced the RPS design

Question	Potential impact on RPS measurements	Phase-A analysis result
Is the RPS geometry factor sufficient for the AP-9 model needs?	On-orbit rates too low or too high, resulting in poor statistics on timescales of interest or premature filling of event quotas, respectively	RPS geometry factor 0.13 cm^2 sr sized to AP-8 model. Coincidence rates $\sim$1 to 100 Hz, singles rates $\sim 10^4$ Hz with sufficient scaler and telemetry margins
Will elastic proton scattering be a concern?	Measured particle intensity less than actual	Multiple coulomb scattering is negligible as determined with Geant4 modeling
Will inelastic scattering products contaminate the RPS measurement of protons?	Error in inferred incident proton energy	Expect fewer than $\sim$2 % of primary protons to yield products that satisfy coincidence
How will RPS distinguish valid events from the higher rates of protons that penetrate RPS from outside its field of view?	Signal lost in the noise	10-fold (11-fold for events with Cherenkov or scintiillator light) coincidence method eliminates contributions from side-penetrators
How will RPS distinguish forward-going protons from protons that penetrate RPS from the back?	Measured intensity higher than actual	Below the Cherenkov threshold, RPS cannot distinguish front—going from backwards-going protons. Mitigate the effect by: • Increasing the energy at which back and front protons have the same energy deposit signature (i.e. add 1 cm shielding at the back of the MCP/PMT) • Modeling using realistic input spectra
What happens to the RPS measurement when the materials that surround the detectors activate in the inner belt?	Additional source of detector singles counts and therefore deadtime	Expect low singles rates (order of 100 Hz) due to decay gammas of tungsten. No impact on coincidence measurement and small impact on instrument deadtime
How will RPS operations quantify and compensate for gain loss in the MCP/PMT?	Measured proton intensity less than actual	Measurements of galactic cosmic ray spectrum compared to models and contemporary measurements on other vehicles
What is the effect of the vacuum gap between the Cherenkov radiator and the MCP/PMT?	Loss of photons due to total internal reflection at vacuum/material interface	No observable effect. Internal reflection effects are mostly below the 160 nm cutoff of the MCP/PMT SiO_2 entrance window. The reflection effects are therefore not observable because they are below the peak photon output of the Cherenkov process

E.1 MCP/PMT Response During Instrument Environmental Testing

The 85001 Burle MCP/PMT had no spaceflight heritage prior to its use in RPS. We subjected engineering model MCP/PMTs to thermal cycling and vibration prior to the final instrument design to assess their performance before instrument-level testing. We monitored two of the MCP/PMTs with adjustable light inputs and neutral density filters and found that the 28 thermal cycles revealed no performance changes. During early design trades we also vibrated an

engineering model device to qualification vibration levels and found, in coordination with the vendor, that there was a slight (<1 mm) movement of one of the MCP mounting clips. The vendor ruggedized the clips for the flight devices and therefore we proceeded with their integration into the engineering and flight models for further testing.

However, during instrument-level vibration testing we found stepwise increases in the dark current noise of the MCP/PMTs. We conducted functional instrument tests during the switch between vibration axes that allowed us to document the instrument status using the 1-second rate and housekeeping packet information. This method proved to us the usefulness of quick functional tests during a vibration test campaign, not only before and after all the tests, but also between the various vibration directions. We found that the MCP/PMT in flight model 2 showed increases in the dark count rate by factors of ∼10 after each of the last 2 of 3 axis vibrations. After subsequent operation the dark count rate gradually dropped a factor of 10 in one month. Follow-on muon collects verified that the system worked adequately for flight. Also, we saw a more modest increase of a factor of 2 in the dark count rate after spacecraft-level vibration.

For RPS flight model 1, the dark count rate dropped by a factor of ∼1000 after the first instrument-level vibration test and a follow-on muon collect showed that the device had lost most of its gain. We replaced the MCP/PMT and the replacement had a similar pattern of increased dark counts after each vibration test.

Our hypothesis was that there was some material being loosened after each vibration within the sealed MCP/PMT, thus accounting for the increased gain that gradually decays with a month timescale. We were unable to discern a root cause for the failed unit. Most importantly, the decreased sensitivity of the devices to the spacecraft-level vibration testing enforces the view that subsystem-level tests are the most stressing due to extreme margins that programs routinely place on the vibration environment (e.g. Margolies and von Rosenvinge 1998). A contributing factor to the RPS design is the robust housing of 350 mils; other less rigid housings may dissipate the vibrational energy although the details would have to be determined through testing because of the mechanical complexity of the MCP/PMT.

E.2 LVPS Microphonics

Another effect of the rigid RPS housing came into play in the thermal sink for the 3 DC to DC converters on the LVPS circuit board. Upon assembly of the flight models we discovered an unacceptable noise level well above the 50 keV fast timing threshold on the ASPs. The noise had a specific frequency of 500 kHz. The root cause was vibrational energy emitted from the DC-to-DC converters.

Magnetic components on the converter hybrid oscillate at 500 kHz causing a subtle mechanical vibration of the entire part. This mechanical energy coupled through the converter heat sink to the RPS chassis, which being as rigid as it is, efficiently transmitted the energy to the detector coupling capacitor for each of the 13 ASPs. Those input capacitors are ceramic of type XR7 that are known to have piezoelectric properties. Hence, the desire to thermally couple the converters to the chassis had the unintended effect of causing unacceptable electronic noise. We note that the effect was not present in the RPS engineering model likely because of the different thermal coupling used there and the apparent lesser response of the non-flight coupling capacitors to microphonics.

It would have been a large schedule and cost impact to switch the capacitors to a type without any microphonics sensitivity. Instead, we successfully mitigated the problem in the flight models by (1) using a thermally conducting staking compound to fasten the converters, transfer their thermal energy into the chassis, and dampen much of the vibration at its

source; (2) further dampen vibration by using compliant washers on the feet of the converter assembly; and (3) changing the ASP card guides that were closest to the coupling capacitors from beryllium-copper to a spaceflight-qualified polymer which was less efficient at transmitting any residual mechanical energy but provided the necessary clamping force for the printed circuit boards.

The problem was an interesting confluence of a part with a known sensitivity to microphonics and an unknown source of the mechanical energy. Finally, we note that spacecraft-level testing showed that there is no external source of similar high-frequency mechanical energy on the RBSP vehicles.

References

O. Adriani et al., in *Proc. 21st European Cosmic Ray Symp.* (2008)

S. Agostinelli et al., Geant4—a simulation toolkit. Nucl. Instrum. Methods Phys. Res., Sect. A, Accel. Spectrom. Detect. Assoc. Equip. **506**(3), 250–303 (2003). doi:10.1016/S0168-9002(03)01368-8

J.M. Albert, G.P. Ginet, J. Geophys. Res. (1998). doi:10.1029/98JA00290

J. Allison et al., Geant4 developments and applications. IEEE Trans. Nucl. Sci. **53**(1), 270–278 (2006). doi:10.1109/TNS.2006.869826

D.N. Baker, G.M. Mason, O. Figueroa, G. Colon, J.G. Watzin, R.M. Aleman, IEEE Trans. Geosci. Remote Sens. **31**, 531–541 (1993)

Baker et al., The Relativistic Electron-Proton Telescope (REPT) instrument on board the radiation belt storm probes (RBSP) spacecraft: characterization of Earth's radiation belt high-energy particle populations. Space Sci. Rev. (2012, this issue)

K.L. Bedingfield, R.D. Leach, M.B. Alexander, NASA Ref. Publ. 1390, 1996

E.W. Blackmore, in *Radiation Effects Data Workshop* (2000). doi:10.1109/REDW.2000.896260

J.B. Blake, W.A. Kolasinski, R.W. Fillius, E.G. Mullen, Geophys. Res. Lett. (1992). doi:10.1029/92GL00624

Blake et al., MagEIS paper. Space Sci. Rev. (2012, this issue)

D.H. Brautigam, J.T. Bell, CRRESELE Documentation, PL-TR-95-2128, Phillips Laboratory, 1995

A.E. Chudakov, E.V. Gortchakov, Repts. Acad. Sci. USSR **124**, 5 (1959)

C.M. Crabtree, K.A. LaBel, E.G. Stassinopoulos, J.T. Miller, Proc. SPIE (1993). doi:10.1117/12.156592

P. Evenson, in *14th Int. Cosmic Ray Conf*, vol. 9 (1975), p. 3177

T.A. Farley, M. Walt, J. Geophys. Res. (1971). doi:10.1029/JA076i034p08223

R.W. Fillius, C.E. McIlwain, Measurements of the Jovian radiation belts. J. Geophys. Res. **79**(25), 3589–3599 (1974). doi:10.1029/JA079i025p03589

G.J. Fishman, Proton-induced radioactivity in NaI (Tl) scintillation detectors. (NASA CR-150237, 1977). http://ntrs.nasa.gov/archive/nasa/casi.ntrs.nasa.gov/19770016962_1977016962.pdf. Accessed 16 January 2012

W.B. Fowler, E.I. Reed, J.E. Blamont, NASA TM X-63419, 1968

S.C. Freden, R.S. White, J. Geophys. (1962). doi:10.1029/JZ067i001p00025

I. Getting, Phys. Rev. **71**, 123 (1947)

G. Ginet et al., Space Sci. Rev. (2012, this issue)

J.E. Grove, R.A. Mewaldt, Nucl. Instrum. Methods Phys. Res., Sect. A, Accel. Spectrom. Detect. Assoc. Equip. **314**, 495 (1992)

M.S. Gussenhoven, E.G. Mullen, M.D. Violet, C. Hein, J. Bass, D. Madden, IEEE Trans. Nucl. Sci. **40**, 1450 (1993)

C. Hagmann, D. Lange, D. Wright, Monte Carlo simulation of proton-induced cosmic-ray cascades in the atmosphere. (UCRL-TM-229452, 2007). http://nuclear.llnl.gov/simulation/cry_physics.pdf. Accessed 16 January 2012

T. Hauck, GSEOS 6.0 user manual. (GSE Software, 1998–2007). http://www.gseos.com/doc/Gseos6.0/Gseos.pdf. Accessed 16 January 2012

W.N. Hess, NASA Technical Note D-1749, 1963

W.N. Hess, *The Radiation Belt and Magnetosphere* (Blaisdell, Boston, 1968)

D. Heynderickx, M. Kruglansk, V. Piercard, J. Lemaire, M.D. Looper, J.B. Blake, IEEE Trans. Nucl. Sci. **46**(6), 1475 (1999)

M.K. Hudson, A.D. Kotelnikov, X. Li, I. Roth, M. Temerin, J. Wygant, J.B. Blake, M.S. Gussenhoven, Simulation of proton radiation belt formation during the March 24, 1991 SSC. Geophys. Res. Lett. **22**(3), 291–294 (1995). doi:10.1029/95GL00009

D.C. Jensen, J.C. Cain, J. Geophys. Res. **67**, 3568 (1962)
M.H. Johnson, J. Kierein, J. Spacecr. Rockets **29**, 556 (1992)
A. Kolasinski, Energetic Proton Analyzer. (NSSDC, 2012). http://nssdc.gsfc.nasa.gov/nmc/experimentDisplay.do?id=1971-067A-01. Accessed 16 January 2012
S.M. Krimigis, T.P. Armstrong, W.I. Axford, C.O. Bostrom, C.Y. Fan, G. Gloeckler, L.J. Lanzerotti, Space Sci. Rev. (1977). doi:10.1007/BF00211545
K.A. LaBel, In-flight anomalies and radiation performance of NASA missions—selected lessons learned. (NASA Technical Reports Server, 2009). http://ntrs.nasa.gov/archive/nasa/casi.ntrs.nasa.gov/20090004168_2008049644.pdf. Accessed 16 January 2012
X. Li, I. Roth, M. Temerin, J.R. Wygant, M.K. Hudson, J.B. Blake, Geophys. Res. Lett. (1993). doi:10.1029/93GL02701
M.D. Looper, J.B. Blake, R.A. Mewaldt, J. Geophys. Res. (2005). doi:10.1029/2004GL021502
K.R. Lorentzen, J.E. Mazur, M.D. Looper, J.F. Fennell, J.B. Blake, J. Geophys. Res. (2002). doi:10.1029/2001JA000276
G.H. Ludwig, *Opening Space Research: Dreams, Technology, and Scientific Discovery* (AGU, Washington, 2011). doi:10.1029/062SP
D.L. Margolies, T. von Rosenvinge, Advanced Composition Explorer (ACE) lessons learned and final report. (Caltech ACE Science Center, 1998). http://www.srl.caltech.edu/ACE/ASC/DATA/pdf_docs/LessonsLearned.pdf. Accessed 16 January 2012
J.E. Mazur, J.B. Blake, P.L. Slocum, M.K. Hudson, *AGU Geophys. Monogr. Ser.*, vol. 165 (2006), p. 345
J.E. Mazur, W.R. Crain, M.D. Looper, D.J. Mabry, J.B. Blake, A.W. Case, M.J. Golightly, J.C. Kasper, H.E. Spence, Space Weather (2011). doi:10.1029/2010SW000641
J.D. Meffert, M.S. Gussenhoven, CRRESPRO Documentation, PL-TR-94-2218, ADA 284578, Phillips Laboratory, Hanscom AFB, MA (1994)
T.P. O'Brien, J.E. Mazur, J.B. Blake, M.D. Looper, J.T. Bell, G.P. Ginet, A.B. Campbell, Aerospace Report No. ATR-2006(8377)-1, 2006
S. Paul, Nucl. Instrum. Methods Phys. Res., Sect. A, Accel. Spectrom. Detect. Assoc. Equip. **611**, 157 (2009)
L.E. Peterson, J. Geophys. Res. (1965). doi:10.1029/JZ070i007p01762
D.N. Sawyer, J.I. Vette, NSSDC WDC-A-R&S 76-06, 1976
R.S. Selesnick, M.D. Looper, R.A. Mewaldt, Space Weather (2007). doi:10.1029/2006SW000275
R.S. Selesnick, M.K. Hudson, B.T. Kress, J. Geophys. Res. (2010). doi:10.1029/2010JA015247
S.F. Singer, Phys. Rev. Lett. **1**(5), 171 (1958)
H.E. Spence, A.W. Case, M.J. Golightly, T. Heine, B.A. Larsen, J.B. Blake, P. Caranza, W.R. Crain, J. George, M. Lalic, A. Lin, M.D. Looper, J.E. Mazur, D. Salvaggio, J.C. Kasper, T.J. Stubbs, M. Doucette, P. Ford, R. Foster, R. Goeke, D. Gordon, B. Klatt, J. O'Connor, M. Smith, T. Onsager, C. Zeitlin, L.W. Townsend, Y. Charara, Space Sci. Rev. **150**, 243–284 (2010). doi:10.1007/s11214-009-9584-8
I. Tamm, J. Phys. USSR **1**, 439 (1939)
A.L. Vampola, J. Spacecr. Rockets **29**, 555 (1992)
J.A. Van Allen, State Univ. of Iowa S/ui60-13, 1960
J.I. Vette, NSSDC/WDC-A-R&S 91-24, 1991
W. Viehmann et al., Photomultiplier window materials under electron irradiation: fluorescence and phosphorescence. Appl. Opt. **14**(9), 2104–2115 (1975)

DOI 10.1007/978-1-4899-7433-4_8
Reprinted from *Space Science Reviews* Journal, DOI 10.1007/s11214-013-9965-x

Radiation Belt Storm Probes Ion Composition Experiment (RBSPICE)

D.G. Mitchell · L.J. Lanzerotti · C.K. Kim · M. Stokes · G. Ho · S. Cooper · A. Ukhorskiy · J.W. Manweiler · S. Jaskulek · D.K. Haggerty · P. Brandt · M. Sitnov · K. Keika · J.R. Hayes · L.E. Brown · R.S. Gurnee · J.C. Hutcheson · K.S. Nelson · N. Paschalidis · E. Rossano · S. Kerem

Received: 30 June 2012 / Accepted: 1 February 2013 / Published online: 18 April 2013

Abstract The Radiation Belt Storm Probes Ion Composition Experiment (RBSPICE) on the two Van Allen Probes spacecraft is the magnetosphere ring current instrument that will provide data for answering the three over-arching questions for the Van Allen Probes Program: RBSPICE will determine "how space weather creates the storm-time ring current around Earth, how that ring current supplies and supports the creation of the radiation belt populations," and how the ring current is involved in radiation belt losses. RBSPICE is a time-of-flight versus total energy instrument that measures ions over the energy range from ∼20 keV to ∼1 MeV. RBSPICE will also measure electrons over the energy range ∼25 keV to ∼1 MeV in order to provide instrument background information in the radiation belts. A description of the instrument and its data products are provided in this chapter.

Keywords Magnetosphere · Ring current · Time-of-flight · Radiation belt · Space weather

1 Introduction

The idea, or concept, of a "ring current" around Earth and its association with geomagnetic storms began in the early days of the twentieth century. As Stern (1989) relates, Stoermer

D.G. Mitchell · C.K. Kim · M. Stokes · G. Ho · S. Cooper · A. Ukhorskiy · S. Jaskulek · D.K. Haggerty · P. Brandt · M. Sitnov · J.R. Hayes · L.E. Brown · R.S. Gurnee · J.C. Hutcheson · K.S. Nelson · N. Paschalidis · E. Rossano · S. Kerem
Space Department, The Johns Hopkins University Applied Physics Laboratory, Laurel, MD 20723, USA

L.J. Lanzerotti · K. Keika
Center for Solar Terrestrial Research, Department of Physics, New Jersey Institute of Technology, Newark, NJ 07102, USA

J.W. Manweiler (✉)
Fundamental Technologies LLC, Lawrence, KS 66046, USA
e-mail: Manweiler@ftecs.com

(1910, 1911, 1912) proposed this physical phenomenon as a way in which to handle a problem associated with his theory of charged particle motions in the geomagnetic field as related to actual observations. Somewhat later Adolf Schmidt (1924) proposed that such a ring current produced the "bays" (decreases in the ground-level geomagnetic field) measured in magnetogram traces during the main phase of a magnetic storm.

In their series of papers that provided a very early theory of the initiation and life of geomagnetic storms, Chapman and Ferraro (1931, 1932, 1933) postulated that a ring current at several Earth radii distance formed around Earth during the main phase of a storm. The ring current would be transient, being dissipated by interactions of the charged particles with the ambient atmosphere (Parker 1997). In this embodiment, the ring current somehow was the result of a neutral plasma cloud from the Sun that impacted Earth's magnetic field, first producing the short-lived "sudden commencement" enhancement of the ground-level field, and then the ring current. This ring current would be formed inside the Chapman-Ferraro geomagnetic cavity that was formed when the hypothesized plasma cloud encountered Earth's field. A major theoretical difficulty was how the particles from the cloud could penetrate the cavity (as discussed by Gillmor 1997, and by Stern 1989).

Hannes Alfvén published a nearly contemporaneous theory of magnetic storms (Alfvén 1939, 1940) wherein a ring current could be formed by the particles in a solar stream entering the geomagnetic field. These particles could access the field because they were convected by an electric field due to the motion of Alfvén's cloud that had a slight magnetic field embedded within (Stern 1989; Gillmor 1997). Alfvén was employing his "frozen-in" magnetic flux concept that had been largely overlooked by the research community. The disagreements between the Chapman and the Alfvén theories, which persisted for many years, are addressed by Akasofu (1970) and by Dessler (1970).

Prior to the discovery by Van Allen of Earth's radiation belts, S. Fred Singer (1957) had considered what the motions of charged particles would be if they somehow were to exist in the Earth's field, independent as to how they may have gotten there (since Stoermer's calculations of particle trajectories showed particles to be excluded from where a ring current might exist). Singer (1957) proposed that low energy charged particles could produce a ring current due to their longitudinal drift around Earth—"electrons one way, and protons the other—thus creating a completely stable ring current" (Singer 1957).

The particles discovered by Van Allen in his flights of Geiger-Mueller tubes on Explorers 1 and 3 (Ludwig 2011) were of too high an energy and too low in density to produce the hypothesized ring current. As the capabilities of instrumentation improved in the first decade of space flight, the energies of particles trapped in the geomagnetic field that could be measured decreased until particles with sufficient density in the range of the now-known ring current ($\sim$10 keV–$\sim$200 keV) could be detected during geomagnetic disturbances. The Explorer 26 satellite (December 1964–May 1967) flew a magnetometer and three instruments for measuring charged particles. One of these covered the proton energy range from 97 keV to $>$1700 keV and produced excellent data on ring current particles. Data obtained on April 18, 1965, during a magnetic storm demonstrated for the first time the importance of the ring current in the generation of a plasma instability (the drift mirror instability) in the magnetosphere and the acceleration of electrons at L $\sim$ 5 Re (Lanzerotti et al. 1969).

It is now well recognized that the plasma pressure of the inner magnetosphere is dominated by H, He, and O ions in the energy range from a few keV to order 400 keV (e.g., review by Kozyra and Liemohn 2003; Mitchell et al. 2003). Quite frequently the peak energy density is held by the charged particles with energies in the range of order 100 keV to order 200 keV. Ions are injected and energized in the inner magnetosphere during geomagnetic storms, building up hot plasma pressure that drives the electrodynamics of the magnetosphere-ionosphere system.

The hot plasma ring current has many effects, and many potential effects, on the magnetosphere and radiation belt populations as deduced from past measurements and theoretical work. In more recent years with more quantitative models of the geomagnetic field under normal and storm-time conditions (e.g., Sitnov et al. 2008), it has become apparent that the hot plasma can affect radiation belt particle motion in ways not conceived earlier. For example, the diamagnetic effect due to storm-time ring current can produce fast outward expansion of electron longitudinal drift orbits leading to their loss through the magnetopause. This effect can explain rapid depletion of electron fluxes over a broad region of the outer electron belt during storm main phase (e.g., Ukhorskiy et al. 2006; Turner et al. 2012). The hot plasma can produce "islands" in the drift paths of longitudinally-drifting ions (Ebihara and Ejiri 2000, 2003) and electrons (Ukhorskiy et al. 2006). The hot plasma also provides the energy source for multiple instabilities generating wave modes that drive local acceleration and loss (see review Thorne 2010) as well as radial transport of the outer belt electrons (e.g., Lanzerotti et al. 1969; Ukhorskiy et al. 2009).

One scenario, adapted by most of the existing ring-current models (e.g., Wolf et al. 1997; Kozyra et al. 1998; Liemohn et al. 1999; Jordanova et al. 2001; Fok et al. 2001; Ebihara and Ejiri 2003; Chen et al. 2007) is that the buildup of hot pressure is produced by steady-state magnetospheric convection. It is assumed in these models that the strong southward component of the interplanetary magnetic field (IMF), typical of a storm main phase, induces a large duskward electric field across the magnetotail. This cross-tail electric field drives earthward particle convection from the tail to the inner magnetosphere. In this framework the transport rates are directly controlled by the magnitude of the solar wind driver. The larger the southward IMF component, the stronger is the cross-tail electric field and the higher are the convection rates. It is expected that the convection electric field is larger during a storm main phase when the IMF is predominantly southward, and lower in a storm recovery phase when the IMF is mostly northward. This paradigm was questioned by recent statistical analysis of electric field data from the Geotail spacecraft (Hori et al. 2005); no substantial difference in the convection electric field was found between main and recovery phases.

It has also been suggested that the ring current buildup can be produced by the inductive electric field associated with dynamic reconfigurations of the magnetic field in the tail such as observed during magnetospheric substorms (e.g., Lui et al. 1987). Global images of ion injections into the ring current obtained with the use of neutral particle imaging techniques by the HENA instrument on the IMAGE spacecraft (e.g., Roelof et al. 1985; Henderson et al. 1997; Barabash et al. 1997; Mitchell et al. 2001, 2003; Brandt et al. 2002) show the highly dynamic nature of ion injections and the population changes during a geomagnetic storm.

In-situ ion measurements on spacecraft show that the transport and energization of ions in the magnetotail occurs largely in the form of discrete activations such as substorms and bursty bulk flows (Baumjohann et al. 1990; Angelopoulos et al. 1992; Shiokawa et al. 1997, 1998; Fairfield et al. 1998, 1999). Distinctive features of these impulsive events are high-speed plasma flow bursts with strong and steep increases of the tail magnetic field component (Bz) normal to the neutral plane. Such abrupt magnetic field changes, which make the stretched tail field more dipolar-like, are often referred to as dipolarization fronts (Nakamura et al. 2002; Runov et al. 2009).

Dipolarization fronts are routinely observed by the five THEMIS spacecraft in the magnetosphere tail ($X < -10R_E$) (e.g., Runov et al. 2009, 2011). It is not clear, however, whether these dipolarization events are related to the injections observed by IMAGE and whether injected particles can penetrate all the way into the ring current through the regions

Table 1 RBSPICE particle measurements

Level-1 Req.	Measurement	Cadence	Energy Range	Angle Res.	Energy Resolution
4.1.2.4	Medium energy protons	1 measure per minute	H: 10–10000 keV	15° × 12°	40 % at 0.3 MeV
4.1.2.5	Medium energy ions	1 measure per minute	He: 25–10000 keV, O: 40–10000 keV	15° × 12°	40 % at 0.05 MeV

of stronger dipolar magnetic fields of the inner magnetosphere—which may break the flows (e.g., Dubyagin et al. 2011). RBSPICE measurements on the two Van Allen Probes spacecraft will provide unique measurements necessary to differentiate between various mechanisms of the buildup of hot plasma pressure in the inner magnetosphere. The comparison of ions and field measurements at the two satellites will reveal whether the injections have a steady-state or a dynamic nature.

2 RBSPICE Hot Plasma Objectives and Measurement Technique

The three overarching science questions for the Van Allen Probes mission are

(a) Which physical processes produce radiation belt enhancement events?
(b) What are the dominant mechanisms for relativistic electron loss?
(c) How do ring current and other geomagnetic processes affect radiation belt behavior?

The RBSPICE instrument makes critical contributions to all of these science questions by determining how space weather creates the storm-time ring current around Earth and by determining how that ring current supplies and supports the creation of the radiation belt populations, and how it can also quickly reduce radiation belt particle intensities.

As discussed in the Introduction, for the last more-than-a-century, a ring current has been understood to be a critical part of the magnetosphere environment and magnetosphere dynamics. The generation of the hot plasma that comprises the ring current remains a major unknown in space plasma physics; therefore, the effects of this plasma environment on radiation belt particles are quite poorly understood. In order to obtain a comprehensive physical understanding of the radiation belts and their effects on technical systems that fly in them, it is mandatory that a comprehensive understanding of the physics of the hot magnetosphere plasmas be obtained by the Van Allen Probes Mission.

The basic particle measurements made by RBSPICE as required by the Van Allen Probes mission Level-1 science requirements are shown in Table 1.

The RBSPICE instrument is a time-of-flight (ToF) versus energy measurement system as shown schematically in Fig. 1.

The total energy of a particle that transits the detector system is measured with a solid state detector (SSD). Ion velocities are determined by measuring the flight time of a particle through the instrument (the particle's "time-of-flight"). The entry of a particle is recorded by detecting, in a microchannel plate (MCP), the secondary electrons that are emitted when the entering particle passes through the entrance aperture thin foil. The exit of the particle (prior to being measured in the SSD) is recorded by the transiting particle's passage through the exit foil with the detection in the MCP of the produced secondary electrons.

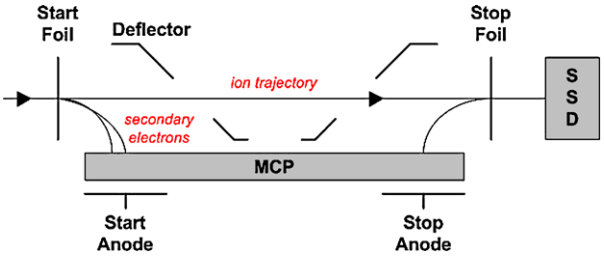

Fig. 1 Schematic illustration of RBSPICE measurement system

Table 2 RBSPICE performance requirements

Parameter	Required	Goal
Electron energies	None	25–1000 keV
Ion energies (measured, not necessarily discriminated)	H: 20–1000 keV, He: 30–1000 keV, O: 50–1000 keV	H: 10–10000 keV, He: 25–10000 keV, O/S: 40–10000 keV
Energy resolution	25 % for required energy range	20 % for required energy range. 50 % above and below required energy.
Time sampling	1/36 spin	1/36 spin
Angular resolution	15° × 12°	15° × 12°
Pitch Angle (PA) coverage	0–90° or 90°–180°	0–90° or 90°–180°
Time for full PA	1 Spin	1 Spin
Ion composition	H above 20 keV, He above 70 keV, O above 50 keV	H above 10 keV, He above 50 keV, O above 45 keV
Electron sensitivity, I = intensity (1 cm^2 sr), G = geometric factor × efficiency (cm^2 sr)	None	Sensor-G: 0,0036–0.00018, Pixel-G: 0.0007–0.000035, Up to 6 × 10^5/s counting
Ion sensitivity	$I = 1 \times 10^4$–1×10^8/cm^2 s sr	Sensor-G: 0.0036–0.00018, Pixel-G: 0.0007–0.000035, Up to 3.5 × 10^5/s count (TOP), Up to 6 × 10^5/s counting (E)

2.1 Science Requirements and Flow to Measurement Requirements

The Van Allen Probes Science Requirements Document provides for the inclusion of the RBSPICE instrument in the Van Allen Probes payload as the

> Radiation Belt Storm Probes Ion Composition Experiment (RBSPICE)—Determine how space weather creates what is called the "storm-time ring current" around Earth and determine how that ring current supplies and supports the creation of radiation populations.
>
> Overall RBSPICE performance requirements are listed in Table 2.

2.2 Relevant Program Level (Level 1) Requirements

Level 1 Requirements for the Van Allen Probes Mission are contained in Appendix C of the NASA *Living With a Star* (LWS) Program Plan.

2.3 RBSPICE-Relevant Mission Level Requirements (Level 2)

Level 2 requirements are maintained at the project level, and higher-level requirements flow from these:

Medium Energy Protons The Mission shall determine medium-energy proton distributions as follows:

- distribution energy range: 100 keV to 1 MeV
- distribution energy resolution (dE/E FWHM): at least 30 %
- distribution cadence: 1 distribution per 30 seconds
- distribution angular resolution: 20 degrees

Medium Energy Ion Composition (Protons) The Mission shall determine medium-energy ion composition (proton) distributions, as follows:

- distribution energy range: 20 keV to 300 keV
- distribution energy resolution (dE/E FWHM): 20 % at 20 keV, 30 % at 50 keV, 30 % at 300 keV
- distribution cadence: 1 distribution per 30 seconds
- distribution angular resolution: 30 degrees

Medium Energy Ion Composition (Helium) The Mission shall determine medium-energy ion composition (helium) distributions, as follows:

- distribution energy range: 20 keV to 300 keV
- distribution energy resolution (dE/E FWHM): 20 % at 20 keV, 30 % at 50 keV; 30 % at 300 keV
- distribution cadence: 1 distribution per 15 seconds
- distribution angular resolution: 30 degrees

Medium Energy Ion Composition (Oxygen) The Mission shall determine medium-energy ion composition (oxygen) distributions, as follows:

- distribution energy range: 40 keV to 300 keV
- distribution energy resolution (dE/E FWHM): 20 % at 40 keV, 20 % at 50 keV, 30 % at 300 keV
- distribution cadence: 1 distribution per 15 seconds
- distribution angular resolution: 30 degrees

2.4 RBSPICE Level 3–4 Performance Requirements

Level 3 and 4 Performance Requirements are maintained at the RBSPICE investigation level.

3 RBSPICE Mission Design Drivers

The Van Allen Probes Mission will intentionally be concentrated in the depths of the intense radiation environment of Earth's radiation belts. As such, the radiation environment imposes severe requirements on parts and system design.

The RBSPICE instrument addresses the intense natural charged particle environment by several techniques:

(a) The natural environment produces a dynamic range of foreground rates in the instrument. These are handled by the employment of very fast timing circuitry and two ranges of pixel size in the solid state detectors (SSD).
(b) The natural environment consists of very high rates of electrons, which produce a background that must be minimized. This is done by using very fast timing circuitry and the two ranges of pixel size in the SSDs. Background counts are measured in both the SSDs and the MCPs. There is an extra 4.5 g/cm^2 shielding around the SSDs. There is a "witness" SSD created by shielding a small pixel in one of the SSDs. Importantly, charged particle trajectory and stopping is modeled using the GEANT4 code and compared to instrument characterizations determined during calibrations.

The science requirements impose additional important mission design drivers:

(a) High temporal and angular resolution is required. This is achieved by fast electronics in binning the detector counts, by multiple view sectors, and by using the telemetry allocation as efficiently as possible.
(b) High energy resolution is required. This is achieved by selecting low noise detectors, by fast electronics for high time-of-flight timing resolution, and by efficiently using the telemetry allocation.

RBSPICE is designed and configured to overcome the challenges of the mission. Addressed here are: (1) visible light and UV; (2) huge dynamic range of input intensities expected for RBSPICE; (3) possibility of high fluxes of "out-of-band" low energy electrons and protons; (4) penetrating radiation.

3.1 Light, UV

The first defense against light and UV is collimation and mounting configuration, both designed to minimize the effects of sunlight. Direct entry of sunlight through the collimator would drive counting rates well above design limits on both the MCP and the SSDs. The second defense against both visible and UV light is filtering. The thin foils that serve to produce secondary electrons for timing pulses also serve to reduce the intensity of UV in the instrument, and the thicknesses of the foils are chosen to satisfy that requirement. In addition, visible light can overdrive the SSDs, raising their noise levels and leakage currents. Therefore the combination of foils and flashings on the detectors are the methods that reduce the light levels below those that result in such detector noise.

Background rejection on RBSPICE further relies, importantly, on valid event logic that requires coincidence among three separate detector signals: the TOF start, TOF stop, and SSD pulses must all fall within narrow timing windows for a valid event to be counted. Based on simulations of penetrating particles and UV, the expected maximum background rates R_{start}, R_{stop}, and R_{SSD} are all $\sim 10^4$ counts/s (the combined Front and Start foil thickness is selected to reduce UV sufficiently to meet this level). The predicted valid event rate is $R_{\mathrm{VE}} = R_{\mathrm{start}} \times R_{\mathrm{stop}} \times R_{\mathrm{SSD}} \times t_{\mathrm{TOF}} \times t_{\mathrm{SSD}}$, where $t_{\mathrm{TOF}} = 100$ ns and $t_{\mathrm{SSD}} < 1$ μs. This yields a false $R_{\mathrm{VE}} \sim 0.1$. Thus, for a typical (low) foreground rate of 1000 counts/s, the foreground/background (F/B) ratio is $\sim 10^4$. Even at a foreground rate of 1 c/s, the predicted F/B ratio caused by UV is 10.

3.2 Dynamic Range

RBSPICE is designed to handle a large dynamic range of ring current intensities, from levels below which the ring current pressure is unimportant to radiation belt dynamics up to the largest conceivable intensities in a super storm (well above any historical measurements).

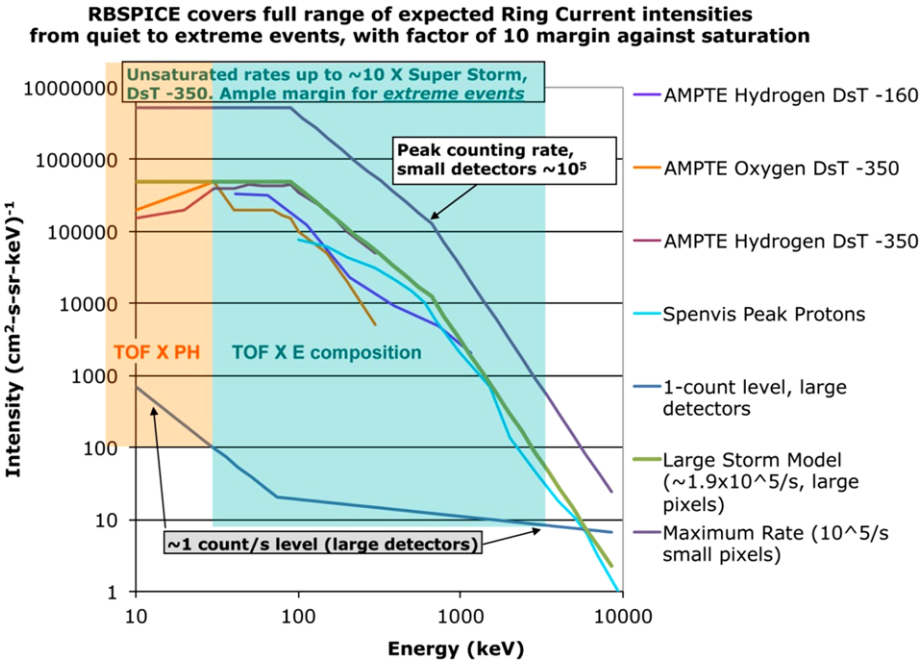

Fig. 2 RBSPICE coverage in intensity and energy

Figure 2 shows Earth ring current intensities and RBSPICE capabilities. Example ring current intensities obtained from measurements on the AMPTE satellite and from models are shown. The curves indicate the intensities corresponding to RBSPICE measurements of 1 count/s in an energy bin (minimum useful measurement), and 10^5 c/s over the full energy range using the small pixels of the SSDs (maximum calibrated intensity). For a "typical" Super Storm (Dst $= -350$ nT) RBSPICE would count at $\sim 1.9 \times 10^5$ in its large pixels (still in the calibrated range), or $\sim 10^4$ in its small pixels.

3.3 Low Energy Plasma

Using relatively thin ($\sim$10 micrograms/cm^2) foils to filter UV and produce secondary electrons for TOF determination, RBSPICE will allow protons as low as $\sim$3 keV to enter its TOF section. Therefore the TOF electronics must be capable of handling high rates generated by these particles, whose energy is below the primary energy range requirements and goals for calibrated characterization of the environment. Likewise, plasma electrons can penetrate the thin foils and either produce secondary electrons or directly strike the MCP, producing counts. Figure 3 provides the efficiencies for secondary electron generation in the Start foil, as a function of electron energy.

To reduce the susceptibility of RBSPICE to plasma electrons, as well as low energy protons, particles entering the instrument encounter two separate, independent foils whose total thickness is driven by the requirements for UV absorption. The first of these two foils is mounted on one of the perforated cylindrical sections (blades) that make up the RBSPICE collimator. Encountering this foil, transmitted low energy particles are typically scattered by large angles into trajectories that are stopped by subsequent collimator blades, and never

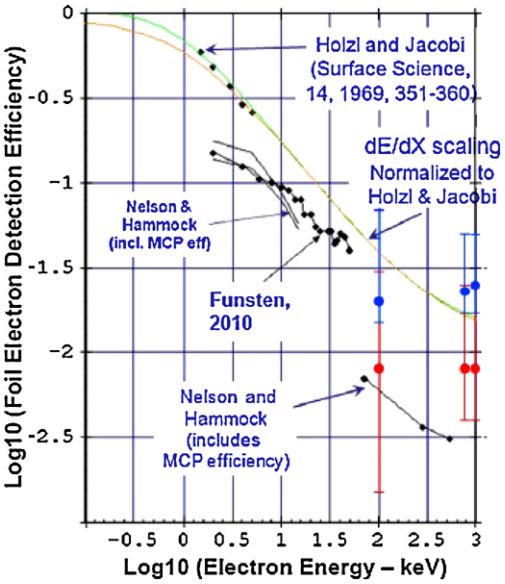

Fig. 3 Efficiency of secondary electron generation from energetic electrons passing through thin carbon foils as a function of primary electron energy

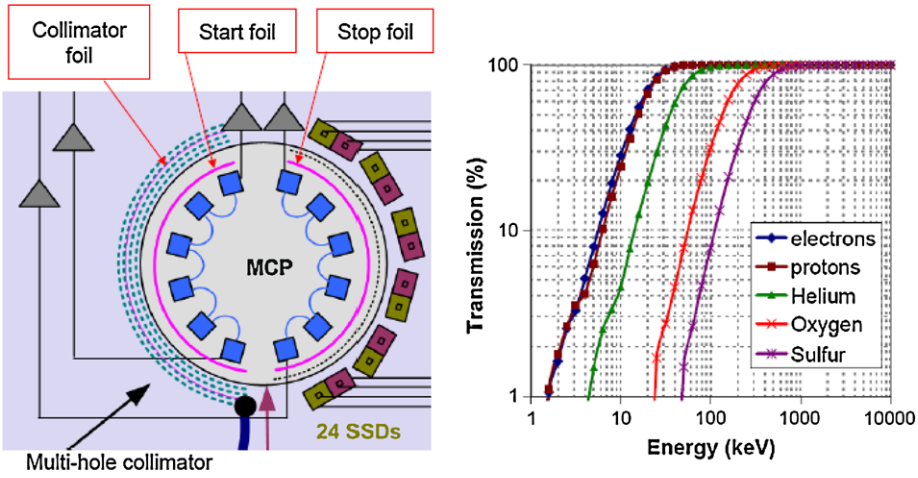

Fig. 4 *Left*: configuration of sensor head; *Right*: transmission efficiency as a function of energy of particle species

strike the second (start) foil. The start foil covers the entrance to the TOF section, but only a small fraction of the original low energy ion and electron intensities reach it, thus limiting background rates.

In the absence of a magnet to sweep out low energy contaminating electrons, the collimator foil suppresses (by scattering into the collimator) the lowest energy electrons (and protons), thereby preventing "start" saturation by the most intense low-energy plasma particles.

The right hand side of Fig. 4 shows the drop off in efficiency to low energy particles that result from scattering in the front foil and the subsequent loss in the collimator. The

figure also includes the effects of scattering in the start foil causing incident particles to miss striking the stop foil and registering a TOF signal. Less than 6 % of the incident protons and electrons are transmitted for particle energies below ∼10 keV.

3.4 Penetrating Radiation

At the high energy end of the spectrum, RBSPICE is designed to minimize the effects of penetrating radiation. RBSPICE includes a minimum of ∼3.8 g/cm^2 WCu shielding, capable of stopping electrons up to about 5 MeV, and protons up to about 40 MeV. This is sufficient to greatly reduce detector rates driven by penetrating particles in all but the heart of the inner radiation belt (where RBSPICE has no measurement requirements). In the outer electron belt, penetrating electrons above 5 MeV will at times produce elevated rates on the individual detectors, but the intensities are not sufficient to drive the rates high enough to produce significant numbers of false valid events (start-stop pairs or TOFs, and TOFs with correlated SSD energy pulses).

Energetic electrons entering through the collimator, for which RBSPICE has no mission requirements, nevertheless will drive high rates in the SSDs (the MCPs have relatively low efficiency response to the electrons). Calculations using a worst case electron spectrum as the input (the so-called Baker-Mitchell-O'Brien spectrum after those who compiled historical data to construct the spectrum) show that under extreme circumstances, the RBSPICE ion system will see rates close to, but not exceeding, the instrument's design maximum. Under these conditions, the false valid event rates will be elevated, but not sufficiently to obscure or distort the measurement of ring current intensities at meaningful (significant distortion of the main geomagnetic field) levels.

RBSPICE also includes a "witness" electron detector. This detector is at one extreme end of the SSD semi-circle and is covered with a copper/tungsten (CuW) shield. This detector sits at an angle already physically blocked by one end of the collimator, which is filled (no holes) in that look direction to avoid entry of sunlight into RBSPICE in flight. This detector serves as a monitor of penetrating background radiation (radiation belt ions and electrons, and cosmic rays).

3.5 RBSPICE Viewing

The Van Allen Probes spacecraft spins about its Z axis, sweeping the RBSPICE fan-shaped field of view through 360° every ∼12 second spin. RBSPICE is mounted at an angle to the spacecraft such that its anti-sunward look direction is approximately centered on the spin axis (see Sect. 4.4). This mounting arrangement provides one angular direction that is unmodulated by the spin, allowing for unaliased detection of changes in the particle environment. The tilt also prevents direct sunlight from entering the RBSPICE Field of View (FOV). The RBSPICE collimator FOV is blocked through an additional 12 degrees from its sunward edge to eliminate off-radial sunlight paths. This blockage also blinds one of the RBSPICE electron SSDs; that SSD is also covered with a copper-tungsten (CuW) shield so that it can serve as a background monitor (Sect. 3.4).

4 RBSPICE Instrument

4.1 Principle of Operation

RBSPICE, shown in Fig. 5, measures ion energy, direction, and composition using Time-of-Flight by Energy (TOF × E) and Time-of-Flight by Pulse Height (TOF × PH) techniques

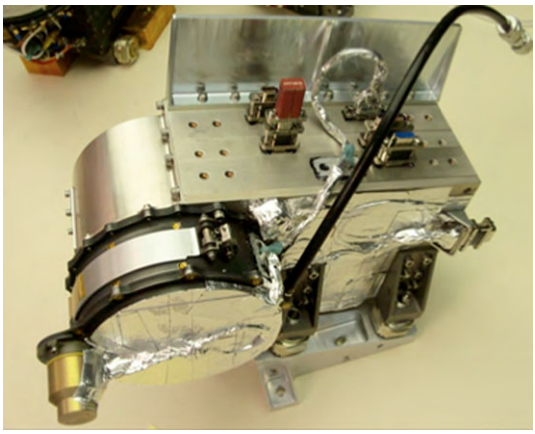

Fig. 5 RBSPICE instrument on spacecraft bracket prior to spacecraft integration

(see Fig. 1). The RBSPICE sensor head contains a Micro Channel Plate (MCP) detector that measures particle TOF and six solid state detectors (SSD) that measure particle energy. Secondary electrons that are generated by ions passing through the entry and exit foils are detected by the timing anodes and their associated pre-amplifiers to measure the ion TOFs. Event energy and TOF measurements are combined to derive ion mass and to identify particle species.

4.1.1 Ion Sensors

Prior to an ion passing through the TOF head, the ion first passes through a thin foil in the collimator. The ion will emerge as an ion or a neutral. If it emerges as an ion, it is accelerated by a negative 2.6 kV potential on the TOF start foil; after passing through the stop foil the ion can have a changed charge state. If the particle remains an ion after the stop foil, the ion is decelerated by 2.5 kV prior to reaching a SSD. (Below about 30 keV a proton has less than a 50 % chance of remaining charged upon exiting either foil. At 10 keV, the probability for remaining charged drops to about 20 %.) Secondary electrons from the foils are electrostatically guided onto the MCP, providing the start and stop signals for the TOF measurements.

The segmented MCP anodes, with two start and two stop anodes for each of the six angular segments determine the direction of travel, a parameter that is required for lower energy ions that do not yield a SSD signal above the detector threshold. A 500-volt accelerating potential between the foil and the MCP surface controls the electrostatic steering of secondary electrons. The dispersion in electron transit time is less than 1 nsec.

Ion energy measurements using the ion detectors are combined with coincident TOF measurements to derive particle mass and identify particle species. Particles are measured from less than 10 keV to above 1 MeV; they are discriminated in the energy system above about 25 keV for protons and above about 80 keV (total energy) for heavy ions (such as the CNO group). Lower-energy ion fluxes are measured using TOF-only measurements; detection of MCP pulse height provides a coarse indication of low-energy particle mass. The sensitivity to higher energy ions (those with energies above the SSD channel thresholds) can be adjusted by selecting large or small SSD pixels.

The RBSPICE acceptance angle is fan-like, and measures 160° by 12° with six 26.7° look directions. The total ion geometric factor for RBSPICE is greater than 0.0003 cm^2-steradian (the large SSD pixels). Particle direction is determined by the particular SSD pixel

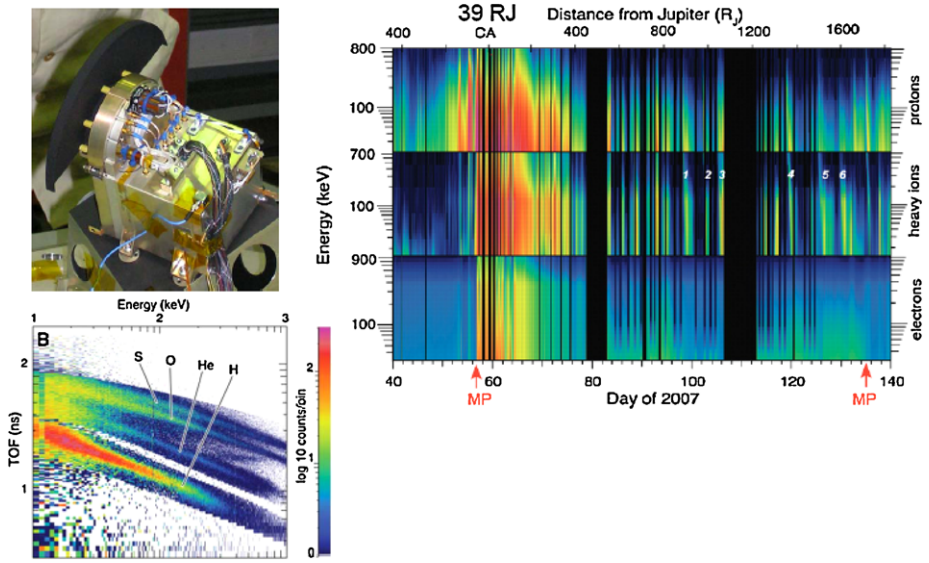

Fig. 6 New Horizons PEPSSI Instrument Heritage

in which it is detected as well as the locations of the TOF start and stop pulses. This direction information is used together with magnetic field data from the EMFISIS instrument to determine the particle pitch angles in the data processing by the RBSPICE Science Operations Center (SOC); see Sect. 7.

4.1.2 Electron Sensors

Although not a science requirement for RBSPICE, the instrument also has the capability (based on heritage designs) to measure electrons. The capability was retained for the Van Allen Probes program because the electron detection feature is essential for monitoring background fluxes in the instrument.

Prior to an electron passing through the TOF head the electron is first decelerated by the 2.6-kV potential. The electron is later reaccelerated by 2.5-kV after exiting the head before reaching the SSDs. Energetic electrons from 25 keV to 1000 keV are measured by the electron SSDs. These detectors are covered with 2-μm aluminum metal flashing to keep out protons and other ions with energies less than about 200 keV. No TOF criterion is applied to the electron measurements.

4.2 Heritage

RBSPICE uses the measurement techniques and technologies demonstrated with the Galileo Energetic Particle Detector and the Geotail Energetic Particle Ion Composition instrument (EPIC), with a configuration similar to the New Horizons Pluto Energetic Particle Spectrometer Science Instrument (PEPSSI). RBSPICE is also nearly identical to the Jupiter Energetic particles Detector Instrument (JEDI) on the Juno Mission (launched August 2010).

The very similar PEPSSI sensor has the most relevant in-flight performance record to date, as it has provided high quality energetic ion composition measurements during the New Horizons Jupiter encounter. These data have demonstrated the capabilities of the TOF $\times$ E

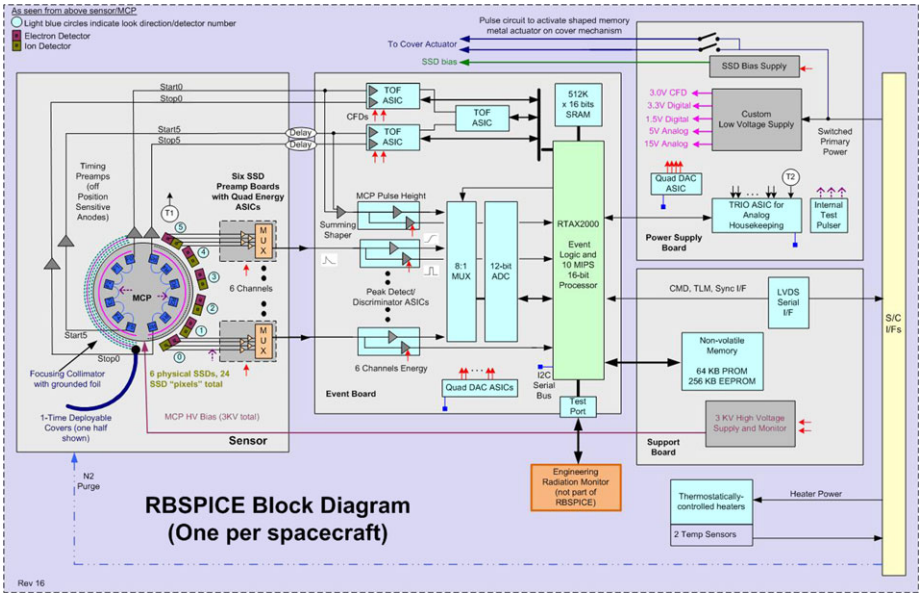

Fig. 7 RBSPICE block diagram

technique in rejecting penetrating energetic particle backgrounds while obtaining high quality ion composition and ion angular distributions. Figure 6 shows the PEPSSI flight instrument (upper left), energy spectrograms for protons, electrons, and heavy ions throughout the Jupiter flyby (upper right), and a TOF $\times$ E scatterplot demonstrating the capability of the instrument to resolve H, He, O, and S (lower left).

4.3 Block Diagram

Following the instrument block diagram from left to right in Fig. 7, the sensor generates analog representations of the particle TOF and SSD energy (left board in Fig. 7). The event board (center board in Fig. 7) directly processes the sensor SSD and anode preamp output signals, and contains all the necessary analog and digital circuitry to process and store event information on an event-by-event basis. Each SSD has an ion detector and an electron detector with both a large and a small pixel. There is only one analog electronics processing chain per SSD. Consequently, to collect both electrons and ions, the hardware is time-multiplexed between the electron and ion detectors. The energy signals from the six SSD preamplifiers and the MCP anode pulse height are processed in parallel peak-detect/discriminator ASIC chains feeding a multiplexed analog-to-digital converter (ADC). The MCP anode signals are processed via constant-fraction discriminators (CFDs) and time-to-digital (TDC) circuitry in the TOF ASICs. These measured time differences are converted into event look direction and particle velocity in the field-programmable gate array (FPGA). The FPGA-based event logic also determines which signals comprise valid ion and electron events and coordinates all event hardware processing timing. An RTX-2010 processor clone is embedded in the FPGA to provide all command, control, telemetry, and data processing functions of the instrument. SRAM and EEPROM support this processor. The software requires access to EEPROM and PROM infrequently so these memories are located on the support board (lower right board in Fig. 7).

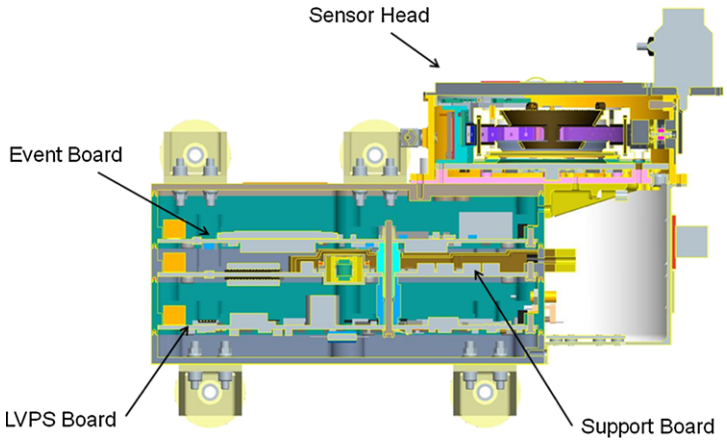

Fig. 8 RBSPICE cross section

In addition, the support board also contains the command and telemetry interface to the spacecraft. This board is designed to support either single-string or redundant LVDS or RS422 with part substitutions: for RBSPICE it is single string LVDS. The support board also generates the necessary high voltage outputs for the sensor MCP and electron optics up to 3300 V.

The power board (upper right board in Fig. 7) contains both the low and high voltage power supplies. The low voltage portion takes spacecraft primary power and generates 1.5 V (for FPGA core), 3.3 V (digital interface logic, memories, and TDCs), and 5 V (analog functions). A 15 V output powers the high voltage electronics on the support board. The power board also switches power to the sensor cover actuator mechanism, generates and filters 100 V bias for the SSD detectors, and uses a TRIO ASIC to measure currents, voltages, and temperatures.

4.4 Mechanical Configuration

RBSPICE is comprised of two subsystems: the sensor head and the main electronics box. The electronics box consists of three $4'' \times 6''$ printed circuit boards that are electrically connected with a custom 152 pin connector; the boards are stacked on top of each other (Fig. 8). The instrument housing is CuW in order to meet Van Allen Probes program radiation and deep dielectric discharge requirements. Total instrument mass is 6.6 kg. The sensor head and main electronics are mechanically integrated together and mounted as a single unit to the spacecraft (Fig. 9).

RBSPICE is mounted on a 16.9° bracket on the bottom spacecraft deck to have a clear FOV and prevent the sun from entering the FOV (Fig. 10). An additional 12° FOV is blocked in the collimator to accommodate sun off-pointing up to 27° Fig. 11). A door stop that prevents the sensor cover (Sect. 4.4.1) from fully opening permits the cover to provide additional sun blockage while not limiting the instrument field of view.

4.4.1 Deployable Cover

RBSPICE includes a deployable cover to prevent acoustic damage to the thin foils and to protect the sensor from contamination. The sensor cover mechanism consists of two curved,

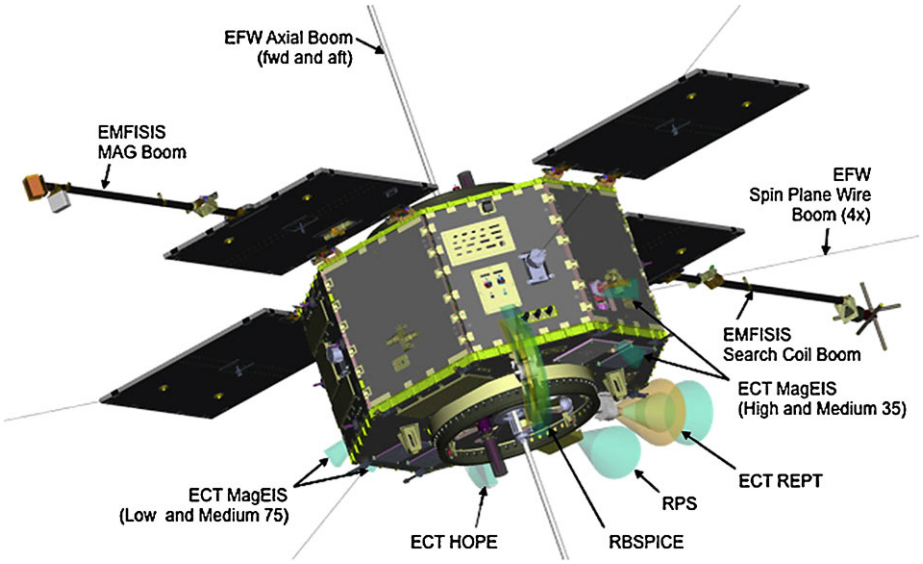

Fig. 9 RBSPICE placement on spacecraft

Fig. 10 RBSPICE on spacecraft mounting bracket

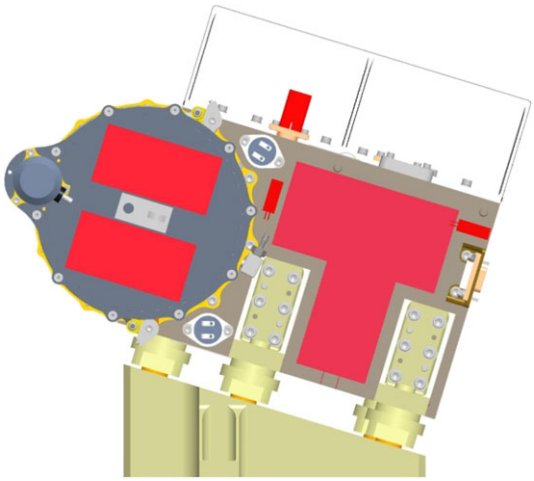

spring-loaded hinged doors that are retained over the aperture opening by a sliding pin. This pin can be pulled away from the doors (thus allowing the doors to swing free) via a pin-puller, shaped, memory actuator device. A sequence of three commands must be sent to fire the doors and, once opened, the covers are maintained in the open position by the springs. During ground testing, a safing plug also prevents accidental actuation; following ground testing activation, the doors are manually re-stowed.

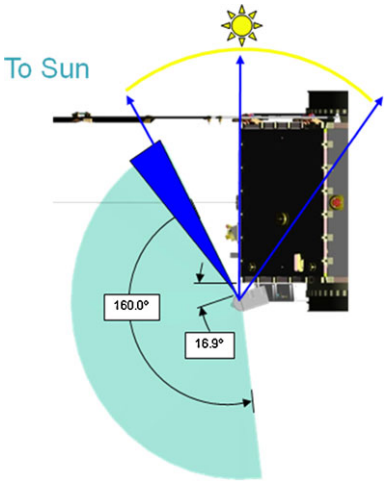

Fig. 11 Accommodation of sun off pointing

4.4.2 Thermal Design

The preferred RBSPICE operating temperature range is −25 °C to 0 °C with an acceptable operation range of −35 °C to +35 °C. The heat transfer between the spacecraft and the instrument is minimized by use of Multi-Layer Insulation (MLI) blanketing and thermal isolators on the mounting feet (Fig. 10). A radiator extension (shown to the rear of the instrument in Fig. 5) and a portion of the electromagnetic interference (EMI) shield serve as a radiator to allow RBSPICE to run colder than the spacecraft deck; a thermostatically controlled heater prevents the instrument from becoming too cold. RBSPICE survival temperature test limits are −40 °C to +60 °C.

4.5 Detectors and Foils

The RBSPICE sensor head and its component parts are shown in Figs. 12 and 13. The component parts are discussed in the following sections.

4.5.1 Microchannel Plates

Secondary electrons emitted by the start and stop foils are amplified by a pair of MCPs in the chevron configuration. Specifications for the individual plates are: 12 μm pore dia., $L/D = 60$, 40 mm sensitive dia., 12 degree bias angle, 10–50 μA bias current, and output electrode penetration of ∼50 μm. The chevron pair was tested, baked, and scrubbed to .03 C/cm^2 by the manufacturer. The MCP was tested for gain, uniformity, and noise in the holder before incorporation in the next assembly step.

4.5.2 Solid State Detectors

Each SSD is 500 μm thick and segmented 4-fold on the particle entrance face. One half of the detector is optimized for ion detection by having a thin dead layer of ∼50 nm while the other half is optimized for electron detection by covering with 2 μm of Al to block ions below several 100 keV (Fig. 14). Each SSD half is segmented further into a small central pixel and a large surrounding pixel. The ratio of the large to small pixel areas is ∼20.

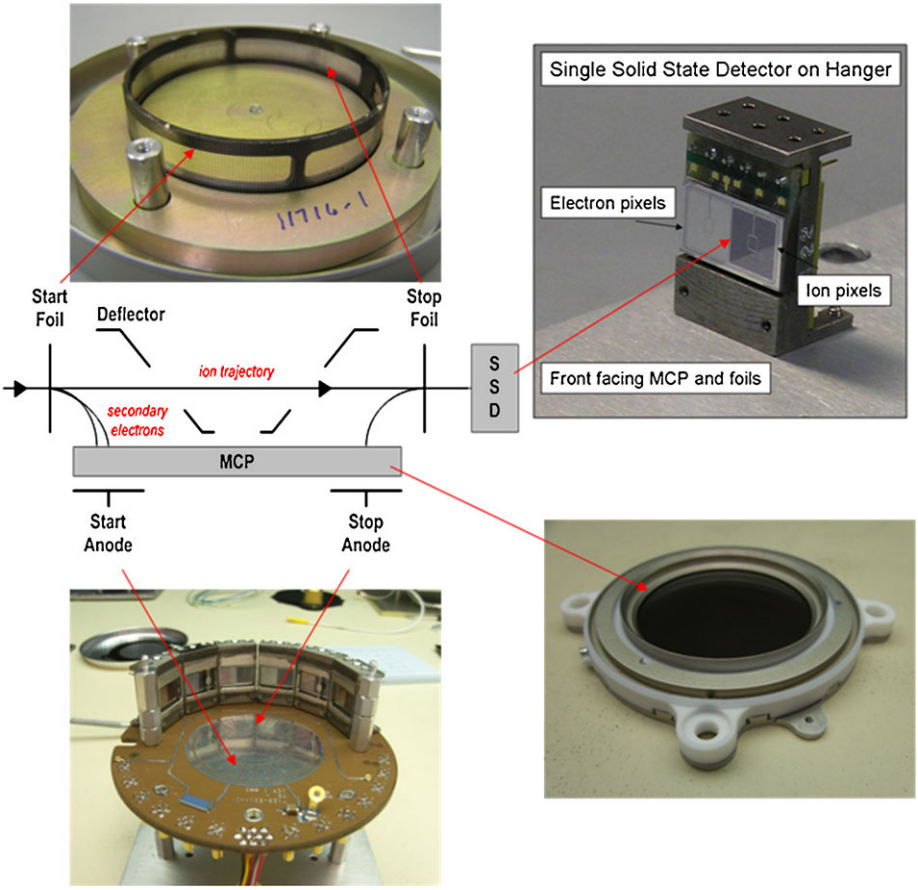

Fig. 12 Sensor components

4.5.3 Foils

The entry look directions are covered by two foils. The outer (collimator) foil is composed of two materials. 62 nm of aluminum covers the entire foil. The sunward-facing half of the foil is covered by an additional 17 nm of palladium to further filter solar EUV emissions. (Adjustments are made in the ground software tables in the RBSPICE Science Operations Center to account for the variable foil thickness as a function of the particle entry direction.) The inner (start) foil is a multilayer structure of 50 Å carbon/350 Å polyimide/50 Å carbon foil. The stop foil covers the exit aperture of the TOF section. It consists of a multilayer structure of 50 Å Carbon/350 Å Polyimide/50 Å C/200 Å Al. As discussed in Sect. 3.1, the collimator foil and the start foil reduce the UV photon background to the TOF section; the stop foil provides additional background reduction for the subsequent solid state detectors. The foils are supported by high transmittance (>80 %) metallic mesh. The start and stop foils are mounted on stainless steel frames while the collimator foil is mounted on a CuW blade of the collimator.

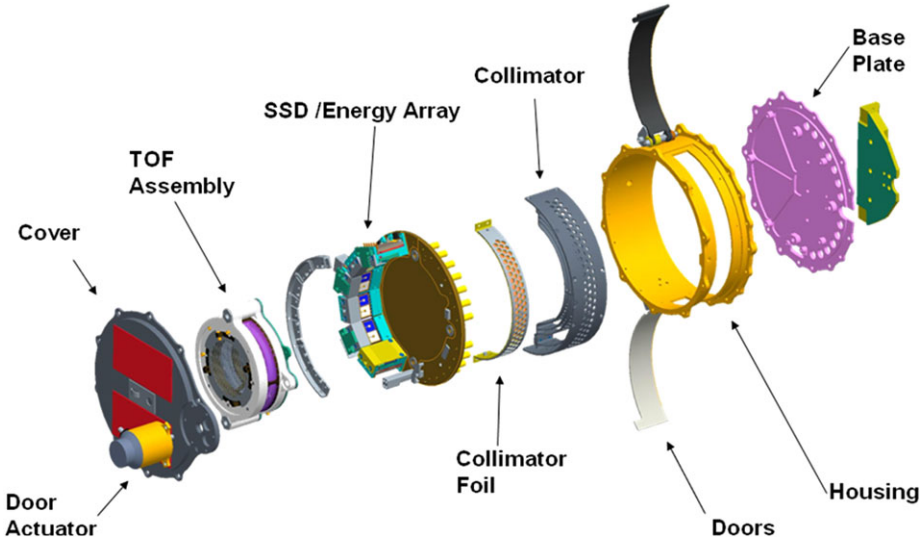

Fig. 13 Sensor exploded view

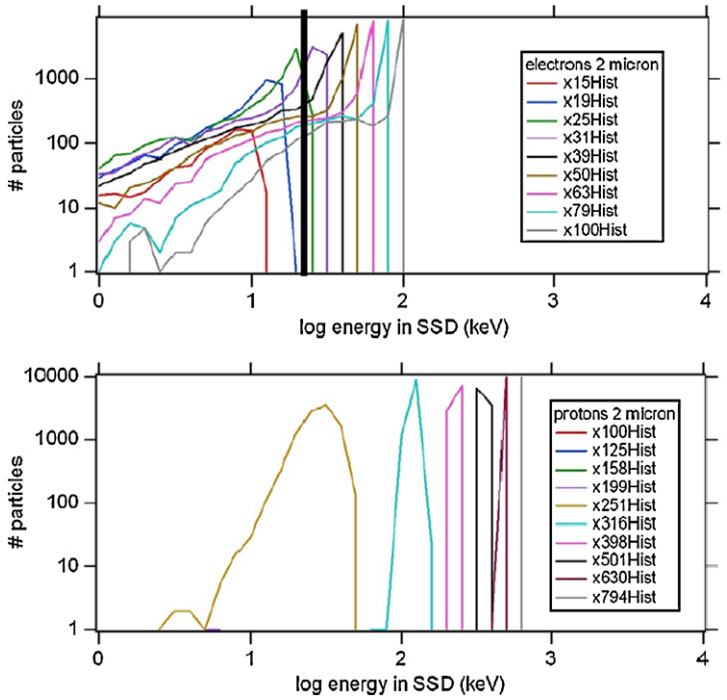

Fig. 14 The 2 micron aluminum flashing on the electron SSD pixels allows >25 keV electrons to be detected (*upper panel*) but strongly suppresses protons with $E < 300$ keV (*lower panel*)

4.6 Event Processing

4.6.1 Signal Flow from Detectors

Particle events stimulate the microchannel plates (MCPs) and solid state detectors (SSDs) as they pass through the sensor. MCP secondary electrons are mapped onto two 1-D position-sensing timing anodes. These anodes, the start anode and the stop anode, generate two timing pulses on each end of each anode. These four timing pulses are processed via the event processing board TOF-C ASICs to produce three timing words, corresponding to the time delay across the start anode, and two measurements of the particle time of flight. Some particles will be energetic enough to register in the SSDs. The derived energy measurement allows detailed categorization of the events; when no SSD signal is present, the MCP pulse height measurement is used.

4.6.2 Event Logic

The hardware is time-multiplexed between three possible modes: ion energy, ion species, and electron energy. The mode determines whether TOF or SSD pulses define an event. In the ion energy and electron energy modes, an SSD energy pulse starts an energy event collection. In the ion species mode, a TOF pulse starts an ion species event collection. Software controls the time-multiplexing of the hardware in order to maintain the illusion of independent electron and ion electronics. In general, RBSPICE does not enter the electron collection mode and time-multiplexes between only ion energy and ion species collection.

The event logic includes parameterized event selection criteria including individual SSD enable/disable, multiple event enable/disable, coincidence window length, and TOF validity flags required. In this way, processing of good events is maximized and noise counts have minimal impact (see Sect. 5.2).

The event processing logic passes valid particle event data to the software for further analysis. The events pass through a First-In First-Out (FIFO) within the FPGA. Each event consists of several parameters. For energy events, only SSD measurements and TOF coincidence flags are valid. For ion species events, TOF measurements and flags are also produced.

4.6.3 On-Board Data Structures

The RBSPICE software divides each spacecraft spin into 36 evenly spaced sectors. As the spin rate varies, the duration of a sector varies accordingly. The spin starts (i.e., sector 0 starts) when the inertial spin phase of the spacecraft is zero. Spin phase angle is zero when the sun line is in the $+Y$ half of the spacecraft YZ plane. The spacecraft provides spin period and phase data to RBSPICE. RBSPICE maintains an internal spin model by updating calculations based on the most recently received spacecraft spin data.

During periods of eclipse, the spin data become inaccurate. If the EMFISIS magnetometer is operational, RBSPICE can use the magnetometer data in lieu of spin data to maintain sector phasing. The RBSPICE software needs an interval when both spacecraft spin data and EMFISIS magnetometer data are valid so that the phase offset to one of the zero-crossings can be determined. If no spacecraft data have been received or if the data are invalid, a nominal 12 second spin period is used. On startup, it will take several spins for the internal spin model to eliminate its phase error with the actual spacecraft spin. Once the spin model and the actual spin are in phase, they will stay in phase as the spacecraft spin rate varies.

Fig. 15 Subsector timing

Table 3 Data products per hardware mode

Electron Energy	Ion Energy	Ion Species
Electron Energy Spectra	Ion Energy Spectra	Ion Energy Spectra and Proton (and Non-Proton) Rates
Basic Rates (Electron Energy)	Basic and Diagnostic Rates (Ion Energy)	Basic and Diagnostic Rates (Ion Species)
Raw Event Data (Electron Energy)	Raw Event Data (Ion Energy)	Raw Event Data (Ion Species)
		Priority Event Data
		Space Weather

Each spin sector is further divided into three subsectors. The first subsector is long, 1/2 of a sector. The last two subsectors are short, 1/4 of a sector each. This is illustrated in Fig. 15. As for sectors, the subsector timing varies with the spin rate.

The sensor hardware can be placed in a different mode during each subsector. The dark bars in Fig. 15 represent a fixed dead-time to switch between hardware modes: the first bar is ∼4.04 ms and the other two bars are ∼3.95 ms. The pattern of modes in each subsector is commandable. Any subsector may collect data in any mode. Each pattern collects different data in different proportions. For example, setting subsector 1 to ion energy and subsectors 2 and 3 to ion species collects ion energy 1/2 of the time and ion species the rest of the time; electron energy is not collected at all. If two adjacent subsectors have the same mode, there will still be a dead-time between the subsectors.

The data products (Table 3) generated by the RBSPICE software depend on the hardware modes commanded for each subsector. For example, if the electron energy mode is selected for all three subsectors, only electron energy spectra, basic rates, and raw event data will be collected.

The data products generated by the RBSPICE software are organized into three types depending on their integration time: fast, medium, or slow (Table 4). Slow RBSPICE data products can be integrated over multiple spins. At the end of its normal integration, if multi-spin integration is enabled, the data product is saved instead of being telemetered. When the spacecraft spin returns to the sector that began the product, integration resumes.

Each of the data products can be enabled or disabled by command. Data products will also be disabled automatically if they are not commanded. For example, if the ion energy mode is not scheduled in any of the subsectors, then Ion Energy Basic Rates will not be produced, regardless of its commanded enable or disable state.

Event analysis varies with the hardware mode, i.e., ion energy, ion species, or electron energy. For electron energy mode events, the RBSPICE software accumulates histograms of the SSD energy. Events are counted as processed by software and included in the basic rate data. Each event is also a candidate for inclusion in the raw event data. Ion energy mode events are processed similarly. For ion species mode events, the RBSPICE software accumulates ion species rate counts. Ion species events are either high energy with TOF and SSD energy measurements (Fig. 16) or low energy with TOF and PH (Fig. 17). Events are counted as processed by the software and included in the basic rate data. Each event is also a candidate for inclusion in the priority event data and raw event data.

Table 4 Data products per integration time

Type	Data Product	Integration Time (Sectors)	Multi-Spin?
Fast	Electron Energy Basic Rates	S	–
	Ion Energy Basic Rates		–
	Ion Energy Diagnostic Rates		–
	Ion Species Basic Rates		–
	Ion Species Diagnostic Rates		–
	Low Energy-Res./High Time-Res. Electron Spectra		–
	TOF × Energy Proton Rates		–
	Low-Res./High Time-Res. TOF × Pulse Height Proton Rates		–
	Priority Events		–
	Raw Electron Energy Event Data		–
	Raw Ion Energy Event Data		–
	Raw Ion Species Event Data		–
	Space Weather (Low Energy Counts)		–
Medium	TOF × Energy Non-Proton Rates	S*N1	–
Slow	High Energy-Res./Low Time-Res. Ion Spectra	S*N1*N2	Yes
	High Energy-Res./Low Time-Res. Electron Spectra		Yes
	TOF × Energy Ion Energy Spectra		Yes
	High-Res./Low Time-Res. TOF × Pulse Height Proton Rates		Yes
	Space Weather (High Energy Counts)		–

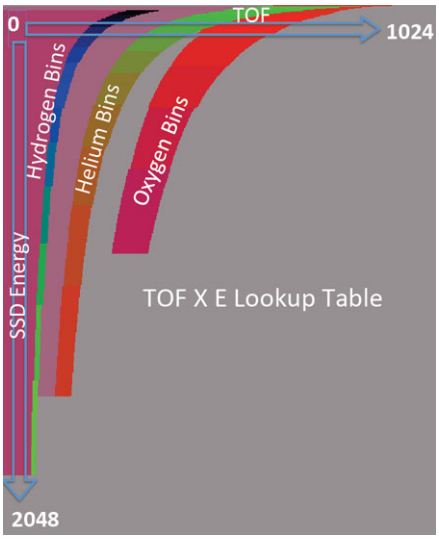

Fig. 16 TOF × *E* lookup table

The RBSPICE software measures basic event rates using hardware and software counters. The basic rates can also be used to automatically select the SSD pixel size. The RBSPICE hardware counts a variety of pulses from the detectors. In addition to valid particle events, these count foreground, background, and noise events. The valid events seen, as well

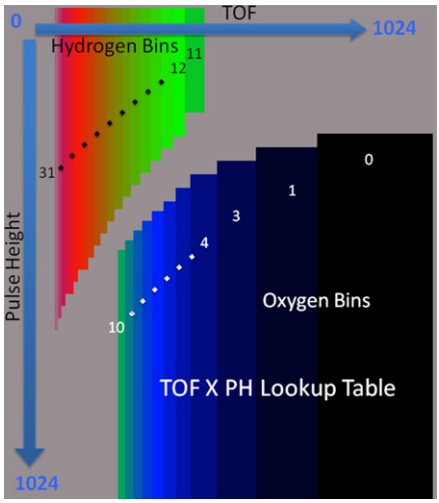

Fig. 17 TOF × PH lookup table

as the valid events placed in the FIFO, are counted. The software also counts the number of events it is able to process. The hardware counters are 24 bits. Every subsector, the counters are read out and accumulated in 32-bit counters in software. A different set of counters are collected in ion energy, ion species modes, and electron modes.

4.6.4 Engineering Radiation Monitor

The Engineering Radiation Monitor (ERM) monitors the total radiation dose received by the Van Allen Probes and is connected to the RBSPICE test port. RBSPICE software reads out one ERM value every second and telemeters the measurements every 3 minutes. RBSPICE also switches +5 V power to the ERM by command.

4.6.5 Diagnostic and Test Support

RBSPICE can inject pulses into the preamps of the TOF start, TOF stop, and SSDs to confirm signal flow through the instrument. The TOF start, TOF stop, and SSD pulses can be enabled or disabled individually by command. The rate of the pulses can be controlled onboard or with an external pulse generator during ground testing. The RBSPICE hardware can be commanded to measure SSD energy channel or MCP pulse height baseline values instead of doing its normal event processing.

4.7 Operational Modes

RBSPICE will normally be commanded on throughout the mission. The standard operational mode multiplexes the collection of ion energy data and ion species data including spectra, counters, and prioritized events. To further characterize the environment, RBSPICE also collects additional diagnostic counters, raw events, and electron energy data.

4.7.1 Boot Mode

During boot mode, RBSPICE supports commanding and telemetry but no macro services, monitoring, safing, or science collection. The boot PROM contains the start-up flight code.

4.7.2 Application Mode

Upon boot command, the flight software is copied from EEPROM into SRAM and the application code starts running. This standby mode has full operational capabilities without operational voltages and requires approximately 1.7 W. Additional commands configure the instrument with proper operational voltages, threshold settings, etc., to collect science data. In application mode, most processor time is spent analyzing event data and formatting telemetry. The processor is able to fully process 40,000 events per second. Full science operation requires less than 2.0 W.

5 RBSPICE Calibration and Performance

Various instrumental factors affect RBSPICE measurements, and all factors must be identified, evaluated, and accounted for prior to interpreting data. These factors include geometric factor of the instrument collimator, various foil thicknesses, and detector and electronics efficiency. These factors are identified and measured throughout the several steps of the instrument build, followed by a final calibration campaign before delivery. Continued instrument assessment in-flight is also used to evaluate all these factors.

Typical calibration procedure involves stimulating the instrument with energetic particles, first from laboratory radiation sources and later from accelerator beams, and recording the response of the instrument to the sources and beams. Calibration tests were conducted at the component, assembly and instrument levels. The functionality and response of the hardware was calibrated at each level to more completely understand the integrated instrument.

The detectors (SSDs, MCPs) were tested and calibrated individually with radioactive sources after arrival from vendors. The detectors were then characterized once again at the assembly level (sensor head, SSD array, etc.) as the flight build progressed. Finally, both flight instruments units were calibrated pre- and post-environmental qualification tests.

The combined calibration efforts focused on the following areas:

A. Collimator performance and geometric factor. The collimator and sensor geometry, and the size of the detectors, define the geometric factor (G) of the sensor. The multi-hole collimator design minimizes the scattering of ions and electrons in the collimator while restricting the FOV of the instrument. However, side lobes can exist in this collimator design. Simulation using the GEANT4 particle model and optical tracing software were used to assess the collimator performance for suppressing electron scattering and the rejection of scattered light, respectively.

B. TOF measurements. When the ions penetrate the start foil and enter the TOF section, secondary electrons are collected from both the start and stop foils by the MCP to measure the velocity of the ion. At low energy (tens of keV), ions lose significant amounts of energy and scatter significantly when going through the foils. Ion scattering, electron optics, and electronics all contribute to error in the measurement of time of flight. All these errors are identified and measured during the calibration.

C. Ion measurement. If an ion has sufficient energy once it transits the foils, it stops in a SSD. Depending on the final energy and mass of the ion, it will produce a measurable electronic signal in a SSD. However, both the dead layer and the pulse height defect of the SSD contribute to undetected energy loss, and both have to be both modeled, and measured during calibration.

D. Efficiencies. The total efficiency for detecting an ion involves combining scattering and consequent losses of ions within the front (collimator) and start foils, and secondary electron efficiencies for generating start and stop pulses to register a TOF within the maximum allowable time of flight window. The system efficiency is calibrated end-to-end for the entire sensor, including flight electronics.

E. Electron measurement. The RBPSICE electron measurement strategy depends on aluminum flashing over the electron SSDs, stopping ions below ∼300 keV. The effect of the flashing thickness on both the ion and electron energy measurements within the electron SSDs requires determination. Dedicated electron accelerator beam tests were used for this measurement.

F. Input rate vs. output rate characterization and photon rejection test. The RBSPICE instrument is tested to characterize its throughput as a function of increasing input flux. Visible and UV photon rejection is tested.

G. Background suppression. The flight-like engineering model unit was subjected to penetrating radiation tests at special high energy particle accelerator facilities (both electron and proton) to characterize the instrument background response in a high radiation environment such as the Earth's inner radiation belt.

5.1 Calibration Procedures and Facilities

A majority of the calibrations at the component and assembly level were performed using a set of National Institute of Standard and Test (NIST) calibrated alpha and beta emitters of known strength and energy. In addition, a custom-built source holder was made to fit onto the RBSPICE collimator that allows the simultaneous stimulation of the response of all RBSPICE detectors at the instrument unit level. During assembly level test, the RBSPICE flight model sensor heads were calibrated both at the APL accelerator facility (ions between 12 and 170 keV) and at the NASA Goddard Space Flight Center (GSFC) Van de Graff Accelerator facility for electrons and ions from 125 keV to 1.6 MeV. The APL particle accelerator is capable of producing beams of H, He, O, N, Ne, Ar with intensities from 10's to 1,000,000 particles/cm^2/s. The accelerator target chamber is custom outfitted with a 4-axis articulation stage designed to accommodate RBSPICE such that all look directions within the instrument field of view can be exposed to the accelerator beam.

5.2 RBSPICE Capabilities Versus Requirements

RBSPICE Level 3/4 science requirements drive the calibration requirements. Particle intensities must be known to relative/absolute accuracy of 20 %/50 %. The RBSPICE calibrations fully satisfy the Level 3 requirements in all areas, and frequently exceed those demanded from the project requirements.

As noted above, RBSPICE is essentially identical to the JEDI instrument on the Juno spacecraft destined for Jupiter, with exceptions for mechanical and accommodation details such as thermal surfaces, data interfaces, collimator field of view, and collimator foil thickness and composition. All of the calibration scopes and procedures described were determined by the JEDI project. Since the instruments on the Van Allen Probes and Juno spacecraft are nearly identical, much of the RBSPICE characterization could be achieved by calibration results derived from the JEDI program.

Since identical start and stop foils are used in both programs, the efficiency of the TOF measurement as a function of species and energy is expected to be the same for the two instruments. Figure 18a shows fits to the calibrations of efficiency for various species and

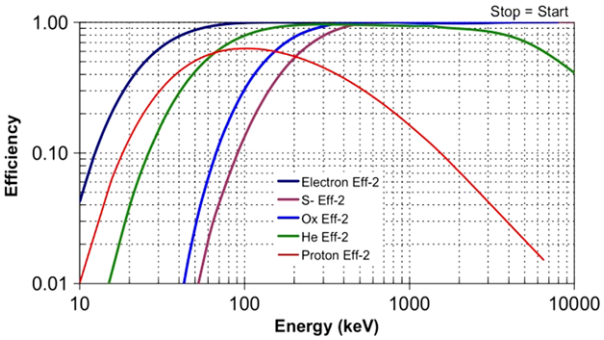

Fig. 18a Fit efficiencies vs energy for various species for required Start position = Stop position

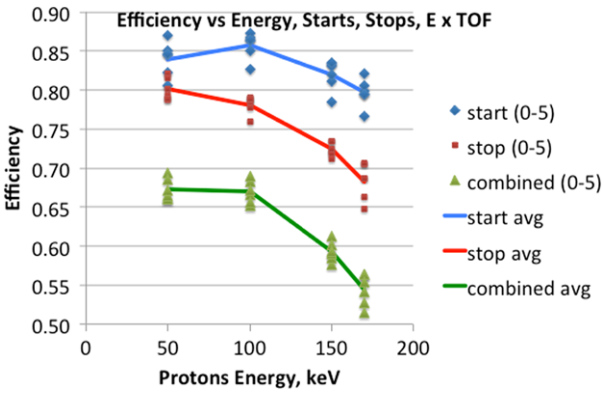

Fig. 18b Measured proton efficiencies for Start = Stop

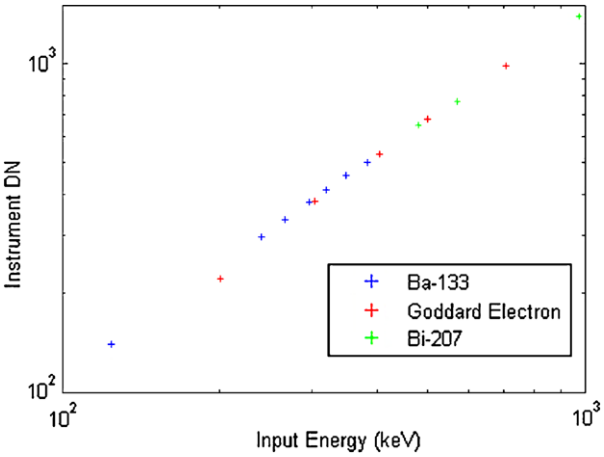

Fig. 19 Calibration of RBSPICE SSD response, Data Number (DN) corresponding to input electron energy in keV

energies under the requirement that the Start position equals the Stop position (meaning the scattering in the Start foil is small enough that the particle crosses the TOF region roughly on a diameter). Figure 18b shows the detailed efficiency (start, stop and total) measurements for protons at different energies on JEDI for $E \times$ TOF under the requirement that Start = Stop positions. On RBPSICE, the efficiencies for several energies were spot-checked, validating the adoption of the JEDI results for RBSPICE.

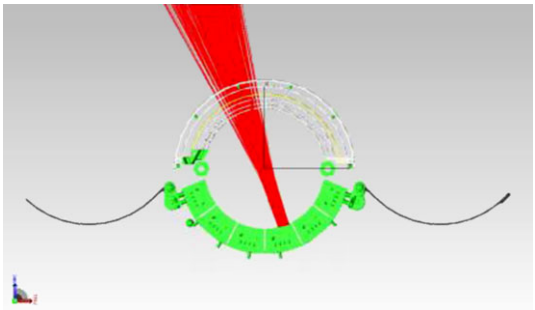

Fig. 20a Subset of isotropic rays leaving the surface of SSD 3 that get out through the collimator

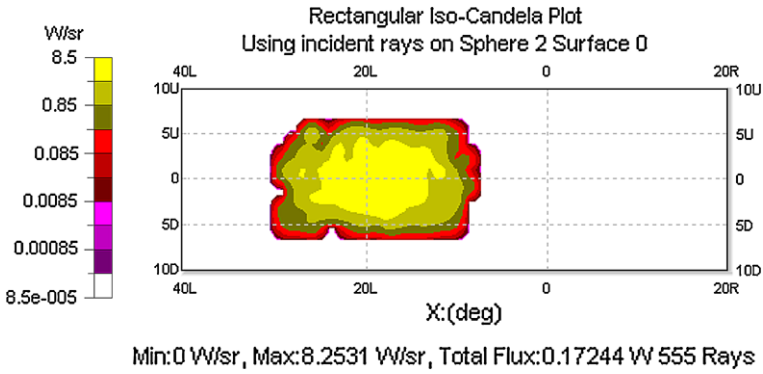

Fig. 20b Angular distribution and relative intensity of rays shown above

Figure 19 shows the calibration of RBSPICE between input energy and data number (DN). Because electrons lose negligible amounts of energy in passing through the foils and dead layers, two beta sources and multiple electron beams from GSFC were used to cover the entire energy range of the instrument.

The results of measurements that establish the RBSPICE capabilities are the following:

A. Collimator performance and geometric factor. The sensor geometric factor was established by two methods: (a) modeling the CAD model of the sensor for its reverse optical paths from the solid state detectors out through the collimator (Figs. 20a, 20b), and (b) actual measurement (both through sweeping the sensor over a range of angles relative to an incident ion beam, and by covering the sensor collimator aperture with a distributed, omnidirectional alpha source that fully covers all of the collimator entrance holes, and recording the relative responses for each angular bin). The first method uses the instrument geometry as captured in the instrument CAD model and computes all possible ray paths from the detector and foil surfaces outward through the collimator. This not only directly determines the solid angle that each surface element of a detector views, but at the same time systematically searches the model for possible side lobes/light leaks. The CAD reverse ray tracing does not include efficiency factors introduced by start and stop foil secondary electron production efficiency (which is a function of species and energy).

Calibration using the distributed alpha source on the collimator aperture includes the start and stop foil efficiencies (since it is an actual measurement of particles), as well as scattering losses and impacts with the grids that support a given foil. For high-energy alpha particles, the secondary electron generation efficiency is quite high and scattering in the

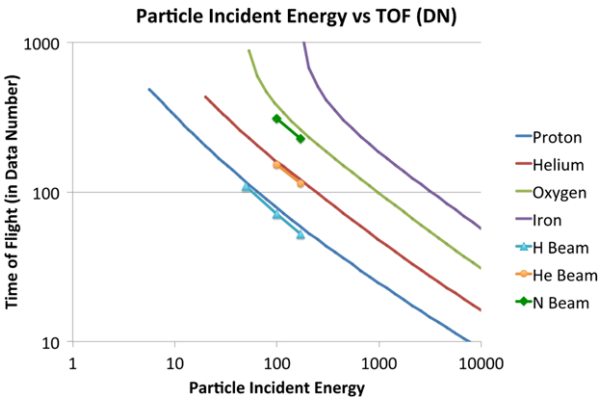

Fig. 21 GEANT4 model of particle incident energy vs TOF in DN, based on modeled energy loss in front and Start foils. Data points from accelerator beam runs are included for comparison with the predicted curves

foils is very low, so most of the differences between the optical modeling and the measurements can be attributed to impact losses of the alpha particles in the foil support grids. The alpha particle measurements also allow estimation of the relative geometric factor between TOF-only and TOF $\times$ E measurements (the TOF-only geometric factor is nominally about a factor of 2.5 times larger than the TOF $\times$ E geometry factor for the large pixels, and about a factor of 50 larger for the small pixels).

B. TOF measurements. When ions penetrate the start foil and enter the TOF section, secondary electrons are collected from both the start and stop foils onto the MCP to measure the velocity of the ion. At low energies (tens of keV), ions lose significant amounts of energy and scatter significantly when going through the foils. Ion scattering, electron optics, and electronics all contribute to error in the measurement of the time of flight. GEANT4 modeling has been done for both the energy losses and the scattering of ions as a function of energy and species to produce predicted RBSPICE TOFs and SSD energies. The results of ion beam and alpha source measurements have been cross-compared with GEANT4 predictions, and the two methods have been found to be in close agreement. Figure 21 indicates the mapping between ion incident energy and the TOF predicted to be measured by the instrument, expressed in data number (DN, which is what is used in-flight to determine the ion velocity). Data points derived from APL Accelerator runs are also included for a few energies. Generally, these results are quite consistent with the predicted curves. In particular, the He data agree very closely; the H data fall slightly below the predicted curve, a departure also observed in the flight data. A correction to the species lookup table on the flight instruments corrects this small departure. Oxygen beam data are not available, but nitrogen beam data have been obtained. These nitrogen data fall below, and nearly parallel with, the oxygen curve, as they should.

Below a species-dependent lower energy bound, ions do not have sufficient energy to generate a signal above a SSD detector threshold. The RBSPICE instrument classifies such ions broadly as either hydrogen or oxygen according to the TOFs and the MCP pulse heights. The third most common magnetosphere ion (helium) can be classified as either species, but is more likely to be either classified as hydrogen or rejected. As RBSPICE is not required to identify helium uniquely at energies lower than 70 keV total energy, these misclassified helium ions simply contribute to uncertainty in the hydrogen and oxygen intensities. However, as the abundance of helium is typically low relative to hydrogen or oxygen, this uncertainty is not important for RBSPICE measurement requirements.

C. Ion energy measurement. If an ion retains sufficient energy once it transits the foils, it will stop in a SSD. Depending on the final energy and mass of the ion, it will produce

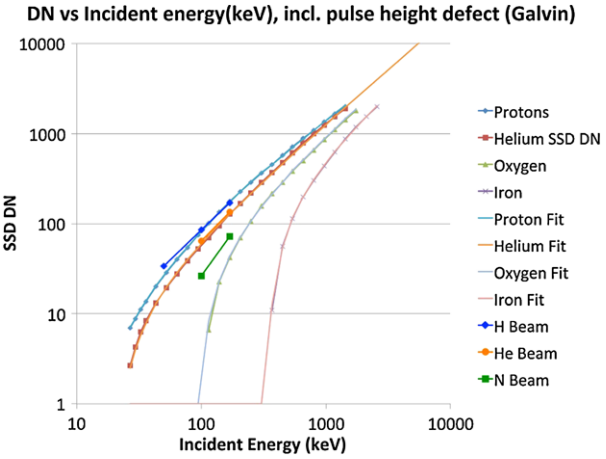

Fig. 22 Curves of particle incident energy versus SSD output Data Number (DN), including modeled energy losses in the front, Start, and Stop foils, in the SSD dead layer, and detector pulse-height defect. Individual points are for discrete energies modeled in GEANT4, curves are fits to those points to allow interpolation to energies not modeled. Data points from accelerator beam runs are included for comparison with the predicted curves

a measurable electronic signal. However, losses in the foils, SSD dead layers, and pulse height defects of the detectors contribute to undetected energy loss. These energy losses are modeled in GEANT4, whereas the pulse-height defect is taken from work by Galvin (private communication). Figure 22 shows the curves for the predicted SSD response (in data number) for a broad range of input energies. Data points from accelerator beam runs are included for comparison. The nitrogen points were measured as a proxy for oxygen, but fall above the oxygen curve as they would be expected to. In general the data agree very closely with the predictions, although there is a tendency for the measured SSD DN to lie above the predictions at lower energies, near the SSD electronic threshold. This is a threshold effect caused by electronic noise, and it has been taken into consideration in the generation of the TOF $\times$ E lookup tables on the flight instruments.

By combining the results in Figs. 21 and 22, the data number (DN) measurements of energy and TOF can be predicted for each species over the RBSPICE energy range. These results are used to construct the TOF $\times$ E lookup table that resides in instrument memory, and by which the DPU assigns the measurement to a particular species. At energies below which the SSD pulse is under threshold, the MCP pulse height is used together with the TOF to assign species via an onboard lookup table. The results of this procedure are captured in Fig. 23a, which shows the classification by the RBSPICE Flight Model1 of calibration data from a degraded alpha source.

Although a small fraction of the particles produce anomalous energy signals, accounting for the out-of-track haze in Fig. 23a, the vast majority of the particles lie along the expected track. The points in red are events that have been classified by the RBSPICE TOF $\times$ E lookup table as being helium events. The lookup classification very successfully eliminates events with spurious parameters from the helium rate bins. The lookup table only extends up to 400 keV, the upper limit for the required helium rate bins in the telemetry. The inset in the upper right of Fig. 23a shows the mapping of events into specific telemetry rate bins, verifying the energy bounds of the helium rate bins (red oval) in flight software.

A small number of events (a small fraction of the scatter in Fig. 23a) are misidentified by the lookup table as hydrogen, and these events are binned into hydrogen rate bins (blue circle). Although this means that in flight a small fraction of the measured helium will be misclassified as hydrogen, the ambient magnetosphere hydrogen will outnumber these few misclassified events by at least 4 orders of magnitude at any particular energy, rendering the misclassified particles negligible. The remaining events are classified as not belonging

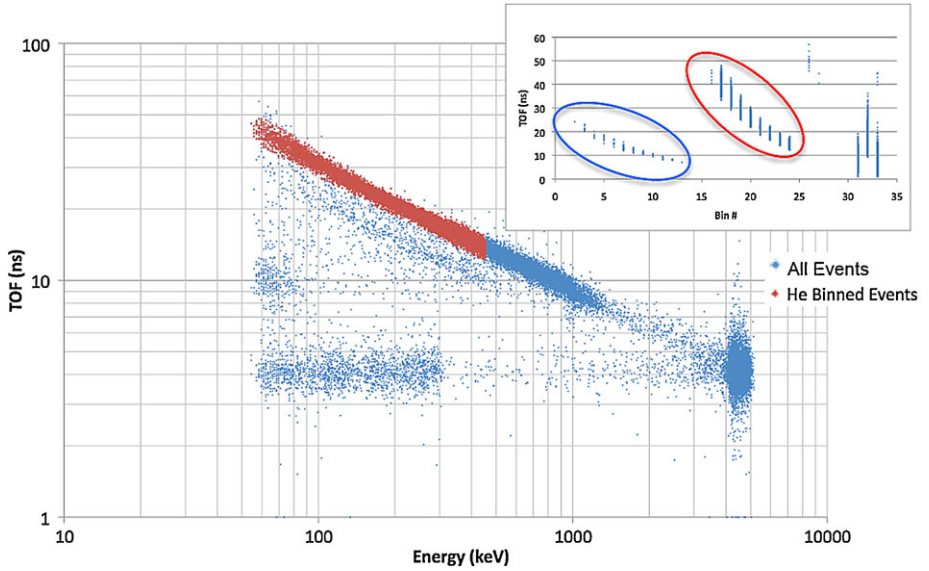

Fig. 23a Scatter plot of events (TOF × E) from degraded alpha source, RBSPICE FM1. *Inset* plots the mapping of the points in the scatter plot into the species energy bins as determined by the flight software lookup tables (protons bins 0–14, helium bins 15–25, oxygen 26–30, and "other" 31–33)

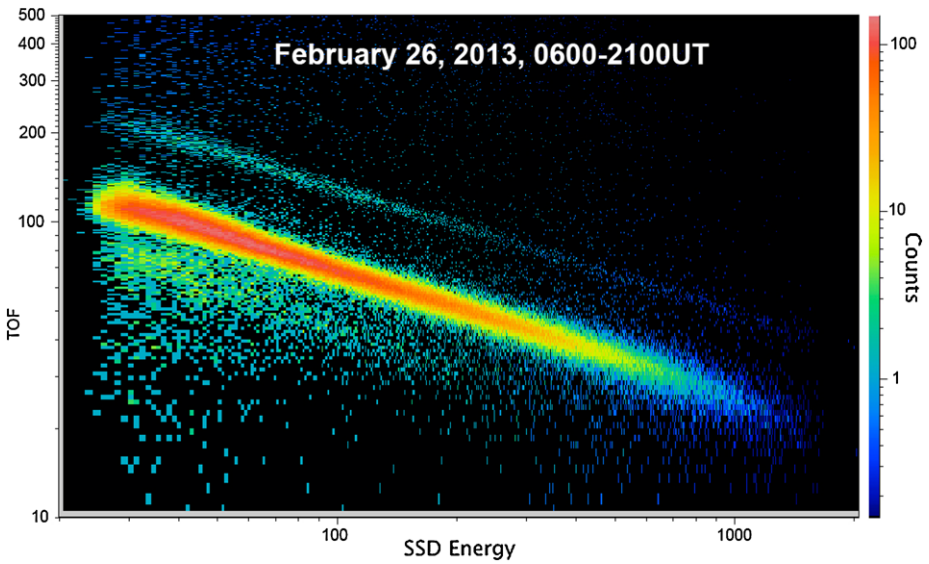

Fig. 23b Scatter plot of events downloaded from RBSPICE-B in flight, day 331, 2012. The brightest track is hydrogen, the faint track is helium. Oxygen is nearly absent, with only a few points in the location of its track

to any of the lookup table identifiable species, and these are binned into non-science rate bins; these are also telemetered to keep track of the fraction of events that are not valid according to the flight software algorithms. The large number of points near 5 MeV comes

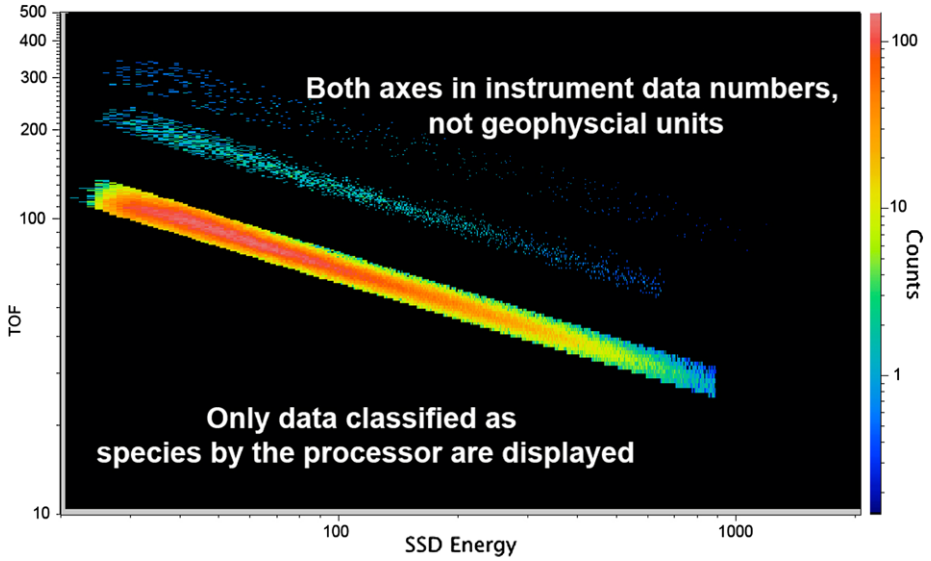

Fig. 23c Same as Fig. 23b, but only including data binned into defined species bins (i.e., bins 0–30; see Fig. 23a). This plots shows that the bin definitions for hydrogen are slightly off, and the hydrogen track is being clipped at high energies (resulting in lower efficiency for those spectral bins). This has since been corrected with a new lookup table

from a portion of the area of the alpha particle calibration source that was not degraded. Figures 23b and 23c show examples of the in-flight performance of RBSPICE B (FM2), and Fig. 23d shows an example energy spectrogram during an energetic particle event seen on orbit for RBSPICE B (FM2) showing electrons in the top panel and ions in the bottom panel.

D. Efficiencies. The total efficiency for detecting an ion involves the combined scattering and consequent losses of ions within the three foils, and secondary electron efficiencies for generating start and stop pulses to register a TOF within the maximum allowable time of flight window. Proton energy efficiencies are shown in Figs. 24a, 24b, 25a and 25b.

E. Electron measurement. RBSPICE has no formal measurement requirements for electrons. However, as discussed above, electrons represent potential sources of background for the ion composition measurements. Furthermore, electron calibration of the SSDs is a necessary step in determining the mapping between keV and DN in the instrument. Example electron calibration data are shown in Figs. 26a, 26b.

F. Input rate vs. output rate characterization and photon rejection test. The RBSPICE instrument was tested to characterize its throughput as a function of increasing input particle flux, and visible and UV photon rejection (Fig. 27). The RBSPICE package includes a large number of hardware and software counters that track detector singles rates, various coincidence rates, state machine idle time, various component dead times, etc. Using these housekeeping data, calibrated intensities can be recovered in spite of various bottlenecks in the sensor through-put at high rates. Such high rates were not generated in accelerator tests for a variety of reasons, most simply understood in considering that with the curved collimator composed of radially aligned paths, the accelerator beam could only enter through a very small fraction of the collimator at any one measurement geometry. Although accelerator rates could be driven fairly high, saturation effects of the MCP, and overdriving of the

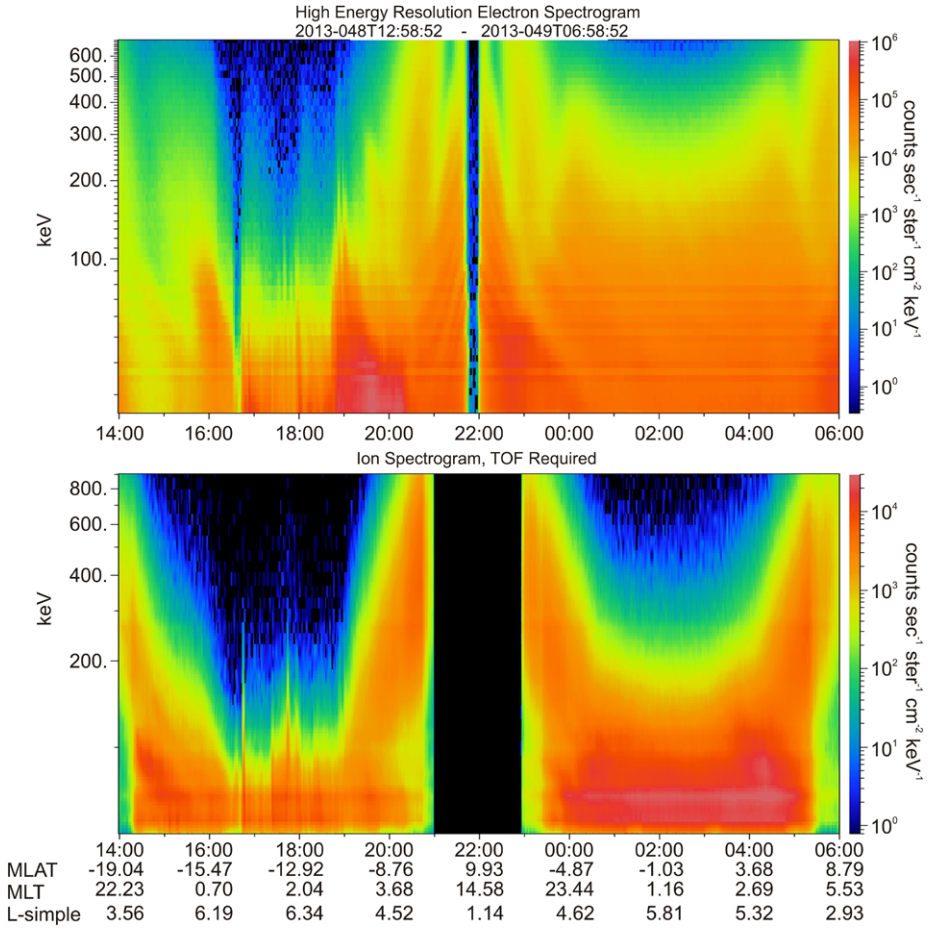

Fig. 23d Example of in-flight energy spectrogram from the detectors showing electrons (*top panel*) and ions (*bottom panel*). The intensities are actually dominated by electrons; ions are cleanly extracted by requiring a TOF, so that the much lower ion intensities represented in Figs. 23b and 23c can be measured in the presence of these electrons

SSD while the other SSDs were not seeing any flux, leads to very unrealistic conditions and in fact does not allow for driving the FPGA logic at particularly high rates. Such high rates are quite readily driven in flight, with all collimator angular directions filled with high intensities. Therefore, high rates were achieved through pulser stimulation of the front-end electronics instead, and it is those results that are shown in Figs. 27, 29, 30, and 31.

G. Background suppression. The flight-like RBSPICE engineering model unit was subjected to penetrating radiation tests at special high-energy particle accelerator facilities (both electron and proton) to characterize the instrument background response in a high radiation environment.

5.3 In-Flight Calibration

In-flight calibration is conducted as needed. The calibration telemetry modes include several data products not normally telemetered, as well as higher time resolution for some data

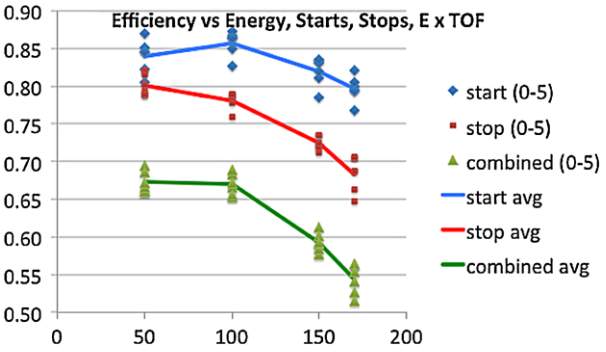

Fig. 24a Efficiency for protons, $E \times$ TOF

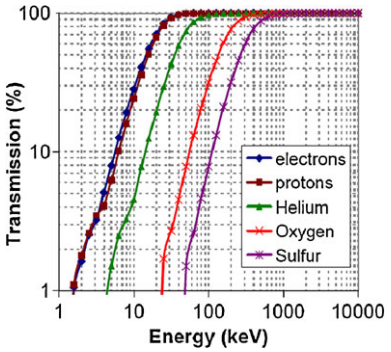

Fig. 24b Transmission as a function of species and energy, losses dominated by scattering in the front (collimator) foil

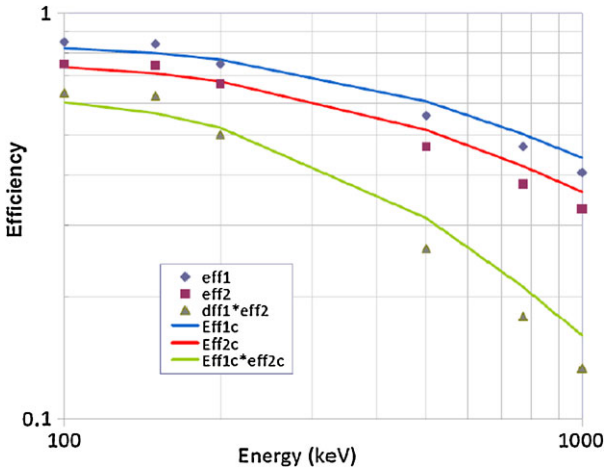

Fig. 25a Proton efficiencies above 100 keV, with functional fits to those efficiencies

products. Among the products that can be included during calibration intervals are diagnostic rates (which include additional information on state machine dead-times, etc.) and raw event data (which provide additional information on various low-level quantities that the instrument typically uses internally to calculate higher level quantities such as energy, time of flight, and species). Depending upon the goals of a calibration, various telemetry modes are available. All of these modes produce data at a higher rate than would fit within the RBSPICE downlink allocation data volume were they to be used continuously. Some modes

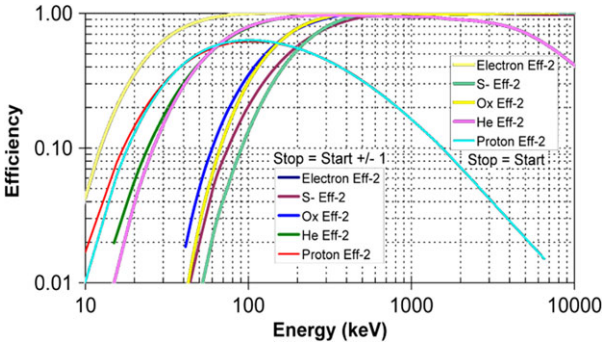

Fig. 25b Fits to over-all efficiency, including secondary electron effects as well as front foil scattering effects. The curves separate at low energy according to valid event logic, i.e. whether the Stop position is required to be equal to the Start, or whether Stop can be within 1 above, equal to, or 1 below the Start position. The latter are modified for positions at the extreme ends of the position chain (since only +1 or −1 is available there)

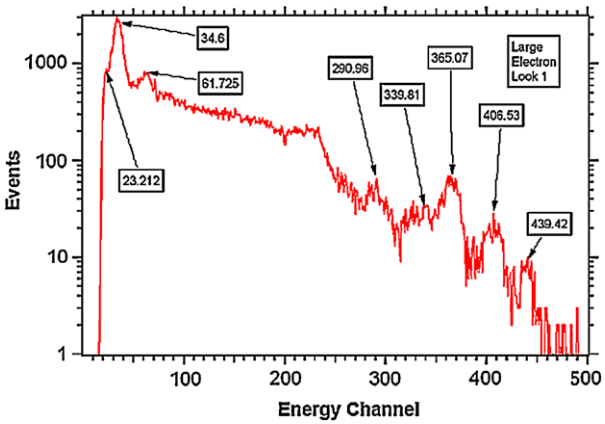

Fig. 26a Calibration of the RBSPICE energy measurement with radioactive sources (Ba133 and Bi207) together with monogenetic electron beams

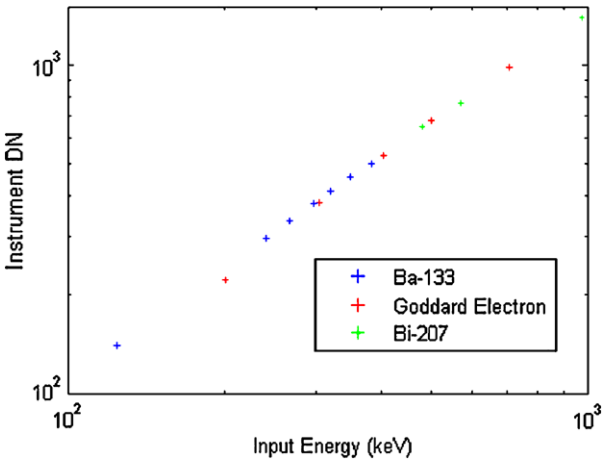

Fig. 26b Linearity of the RBSPICE energy response from 100 keV to 1 MeV

produce only slightly more data (for example, Checkout Mode) whereas others produce up to and more than four times the nominal allocated rate. Therefore, these modes will be used selectively and sparingly during flight.

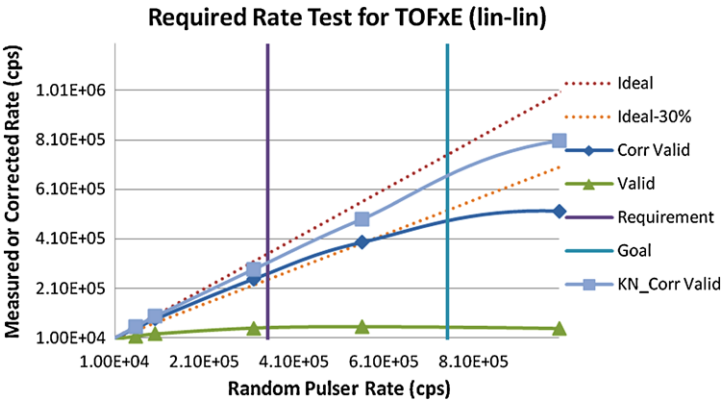

Fig. 27 Data from bench test demonstrating the correction of output rates to match the input rates using instrument-reported idle times and dead times. Output rate corrections are good to about 10 % for input rates to more than 8×10^5

During calibrations, on-board pulsers may be exercised to stimulate the sensor front-end electronics, depending on the goals of the calibration.

A principle concern is determining and setting the efficiency of detection of secondary electrons coming from the start and stop foils, given the changing gain states of the MCP's over time. This is also a concern for the nearly identical JEDI sensors on Juno, and the following paragraphs are excerpted from the JEDI instrument paper to describe how this important consideration is handled. There are two features of RBSPICE that make this process much easier than it has been on heritage instruments. The first feature is that complete detailed pulse height distributions (2048 channels) can be obtained in flight for the start region of the MCP, allowing the detailed response of the start system (start foil, MCP, anodes) to incoming particles. To take advantage of this capability, the so-called event data must be telemetered to ground. The complete diagnostic event data can be sent, but generally to preserve telemetry volume a subset of that information is sent. With several hours of sampling, the individual event data may be sorted according to energy, TOF, Pulse-Height (PH), and look direction, and so the PH distribution for a "standard candle" energy (e.g. 100 keV protons) for each look direction can be generated and compared with ground distributions and with other distributions in space. Because the pulse height distribution is obtained only for the start pulses, this procedure only diagnoses the evolution of secondary electron detection of the start region, not the stop region. However, the start region is where the more rapid changes in efficiency are expected due to the greater flux of particles and UV light onto the start foil than is expected on the stop foil (the geometric factor of just the start foil is a factor of 3–4 greater than the geometric factor of just the stop foil).

The second feature that RBSPICE contains to determine the efficiencies of secondary electron detection, for both the start and the stop regions, is the ability to count various kinds of coincident events. If by choice only "diagnostic rates" (generally not sent to the ground in order to save telemetry) are telemetered, there are counters that report coincident SSD-Start counts and coincident SSD-Stop counts. Total TOF-SSD counts (non-directional), and under some conditions (at relatively low rates) directional TOF-SSD counts can also be reported. These counters can be combined to obtain the efficiencies of secondary electron generation for both the start regions and the stop regions.

The principal responses to changes in the efficiency of secondary electron generation are: (a) to increase the gain of the MCP by increasing its bias voltage, and/or (b) to modify the TOF × PH look-up tables by adjusting a multiplicative parameter.

6 RBSPICE Sensor Operations

The RBSPICE instrument will typically be operated in a single science mode throughout the flight mission. Depending upon in-flight experience, and in order to avoid unnecessary premature aging, during inner radiation belt transits the MCP high voltage may be reduced below the level where the MCP multiplies signals. Periodically (approximately once per month) the instrument will be commanded through a calibration sequence, involving internal pulsers and high resolution diagnostic data modes (Sect. 5.3). Detector status will be tracked (noise levels, MCP pulse-height performance), and any necessary adjustments will be made to thresholds and voltage levels to keep the instrument within its calibrated response.

Downlink health and safety data from the instrument housekeeping data stream, as well as relevant spacecraft housekeeping data will be tracked and reviewed daily. Science data is converted to browse products and will also be examined as an indicator of instrument health and calibration status.

Command loads to maintain proper instrument state will be generated, tested on the Engineering Model, and uploaded as required. This will nominally be no more frequent than once per week.

7 RBSPICE Data: Reduction, Products, Distribution, and Archiving

7.1 Overall RBSPICE Data Handling

An overview of the data flow to and from each RBSPICE instrument into the RBSPICE Science Operations Center (SOC) is provided in Fig. 28. As the diagram indicates, data operations are broken into two specific segments: Commanding and Data Processing, each operating out of different RBSPICE SOC facilities.

Commanding occurs through the spacecraft tracking facilities in the Space Department at Applied Physics Laboratory (APL), where a workstation runs the Ground Support Equipment Operating System (GSEOS). This GSEOS is specifically tailored for the Van Allen Probes mission and managed by the Van Allen Probes project. One workstation is dedicated to each of the two RBSPICE instruments.

Commands are created, tested, and verified against the Spacecraft Emulator and the RBSPICE Engineering Model (EM). Once validated, command sequences are added to a standard commanding library and are available for later use as needed. All commands are sent as CCSDS packets to the Van Allen Probes Mission Operations Center (MOC) through interfaces between the RBSPICE SOC at APL and the Van Allen Probes MOC. (The interfaces are specified in the Van Allen Probes Interface Control Document (ICD) entitled 7417–9050 MOC to SOC). During contact times, the MOC will telemeter the command(s) to the targeted spacecraft. Validation of execution of the commands will be seen in subsequent telemetry received from the instrument (see below specific data products).

Data processing occurs primarily through servers running at Fundamental Technologies (FTECS). The data system is configured to be as automated as possible, providing the means to directly download RBSPICE telemetry for each spacecraft to the RBSPICE

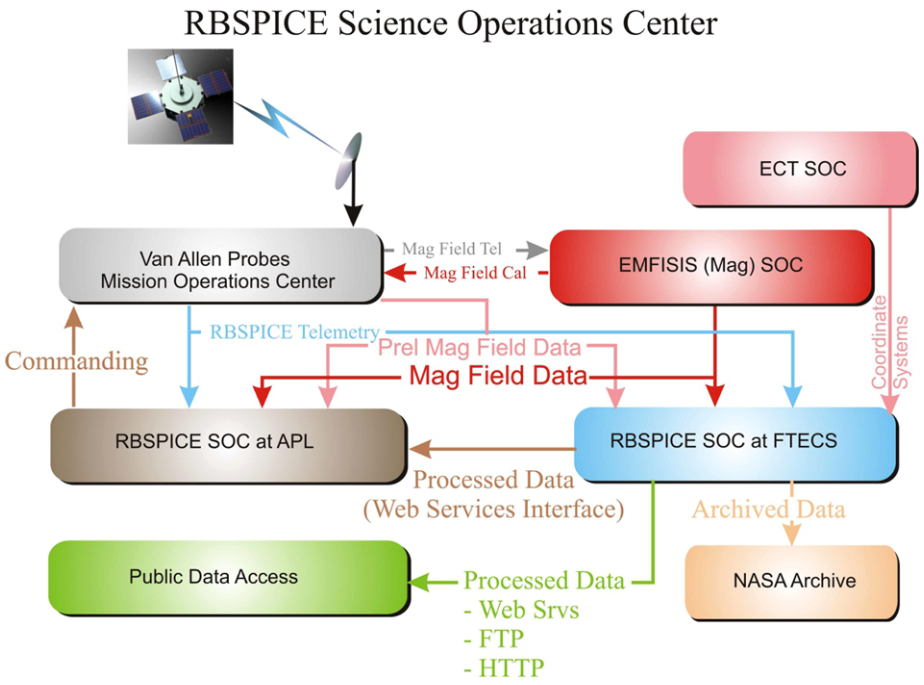

Fig. 28 Schematic diagram of RBSPICE data acquisition and flow

SOC operations at FTECS. In addition, magnetic field data from the EMFISIS instrument is downloaded to the RBSPICE SOC at FTECS to enable the calculation of particle pitch angle-related data products. Finally, the RBSPICE SOC acquires the ephemeris for each spacecraft from the MOC but also acquires spacecraft coordinate system data using various magnetic field models as calculated by the ECT SOC. Coordinate system information is included in the RBSPICE Level 2 and higher data products. Telemetry and other data, such as the magnetic field data, are then categorized and analyzed based upon specific Application ID's (APID) for each product. Each APID is then processed into either auxiliary support information or higher-level data products. Redundant operations are maintained in the Space Department at APL, in the event of significant internet connectivity failures during mission operations. The final RBSPICE data products are hosted at FTECS on a web server, allowing for public access to the data with very short lags from reception of telemetry data to final data products.

The TOF/SSD-based RBSPICE instrument provides a large number of data products based upon specific commanding options provided to the instrument. Table 5 provides a high level summary of the various data products produced in the RBSPICE SOC. All but the raw telemetry will become publicly available through the RBSPICE SOC web site within the latency time frame as identified in the table. The Level 4 data products will only be produced for selected ring current events and are not part of the automatic data processing system. These Level 4 products will be generated through other science software and made available through the RBSPICE SOC web site as the products become available. Each of the data products will be provided as a self-describing CDF formatted data file, as well as an ASCII Comma Separated Value (CSV) data file.

Table 5 RBSPICE data products

Data Level	Product Title	Contents	Daily Volume	Format	Latency	Frequency
L0	Raw telemetry	Raw de-commutated telemetry received at RBSPICE-SOC	~414 MB	Binary, ISTP Compliant CDF & ASCII (CSV)	from Receipt (T_0)	daily
L1	Count Rates	Sorted, time-tagged, instrument separated counts/sec	~750 MB	ISTP Compliant CDF & ASCII (CSV)	$T_0+ < 14$ days	daily
L2	Calibrated Flux	Calibrated and corrected physical units	~1200 MB	ISTP/PRBEM Compliant CDF & ASCII (CSV)	$T_0+ < 1$ month	daily
L3	Pitch Angle and Moments	Pitch angle distributions, 1st adiabatic invariant	~1500 MB	ISTP/PRBEM Compliant CDF	$T_0+ < 3$ months*	daily
L4	Phase Space Density	PSD units, 2nd and 3rd adiabatic invariants, magnetic coordinates	~30 MB	ISTP/PRBEM Compliant CDF	$T_0+ < 1$ year	Selected events

Table 6 lists the data products that can be directly related to the particle counts measured by each of the RBSPICE instruments. The data products are organized by the type of product, the particle species, and the NASA data level.

In general, the basic rate and diagnostic rate data, as well as the auxiliary and critical housekeeping data, are used to guide the production of the other data products. This includes the understanding of cases of very high rates where the Rate_{In} versus Rate_{Out} (R_{In} vs R_{Out}) calibration has to be taken into consideration (Sect. 7.2). The basic rate and diagnostic rate data are produced as rate and flux data, but users will find those particular products less helpful in understanding the overall Phase Space Density distributions (PSD) of the source populations.

Each of the data products are organized by either the Mission Elapsed Time (MET) or the Ephemeris Time of the measurement. The products are also organized by the spacecraft orbit number, spin number, and by the sector number with which the measurement is started. The duration of a measurement for each product is programmable. This permits lower energy products with higher particle counts to be measured over shorter periods of time and higher energy products with much lower particle counts to be measured over longer periods of time.

A description of each of the higher level data products and the controlling variables for the duration is listed in Table 7. Additionally, this table provides short product names mapping from the longer names that relate to how the overall directory structure is organized. The duration variables are S measured in the number of sectors, N1 and N2 as multiplying factors, and "spins" representing the number of integration spins. That is, if a product is identified to have a measurement duration

of S*N1*N2, then the measurement of the product will start in a particular sector and stop at S*N1*N2 sectors later. For products that allow for multiple spins, the measurement from the start sector to the stop sector is repeated for a total of "spins." Each of the S, N1, and N2 variables is configurable in the flight software with the following limits: $1 \leq \text{S} \leq 36$, $1 \leq \text{N1} \leq 36$, and $1 \leq \text{N2} \leq 36$. In general, the values of S, N1, and N2 are used to manage the overall telemetry rate of the RBSPICE data. Using this formulary, the highest energy data products can be measured over multiple spins allowing for better statistics in the data collection, but sacrificing some understanding of the pointing of the instrument.

Table 6 Detailed RBSPICE data products

Product	Species	Energy Bins	L0 Data Type	L1 Data Type	L2 Data Type	L3 Data Type	L4 Data Type
Low Energy Resolution High Time Resolution Electron Species Rate	Electrons	14	Count	Spectra Rate	Spectra Flux	PAD, μ	
High Energy Resolution Low Time Resolution Electron Species Rate	Electrons	64	Count	Spectra Rate	Spectra Flux	PAD, μ	
High Energy Resolution Low Time Resolution Ion Species Rate	Ions	64	Count	Spectra Rate	Spectra Flux	PAD, μ	PSD, Pressure
High Energy Resolution Low Time Resolution TOF $\times$ PH Proton Rate	Protons	32	Count	Spectra Rate	Spectra Flux	PAD, μ	PSD, Pressure
TOF $\times$ E Proton Rate	Protons	14	Count	Spectra Rate	Spectra Flux	PAD, μ	PSD, Pressure
TOF $\times$ E non Proton Rate	Heavy Ions	28	Count	Spectra Rate	Spectra Flux	PAD, μ	PSD, Pressure
Low Resolution High Time Resolution TOF $\times$ PH Proton Rate	Protons	10	Count	Spectra Rate	Spectra Flux	PAD, μ	PSD, Pressure
TOF $\times$ E Ion Species	Ions	64	Count	Spectra Rate	Spectra Flux	PAD, μ	PSD, Pressure
Space Weather Rates	All	NA	Count	Rate	Flux		
Ion Basic Rate	Ions	NA	Count				
Ion Species Basic Rate	Ions	NA	Count				
Electron Basic Rate	Electrons	NA	Count				
Ion Energy Diagnostic Rate	Ions	NA	Count				
Ion Species Diagnostic Rate	Ions	NA	Count				
Priority Events	NA	NA	Event	Event			
Raw Ion Species Events	NA	NA	Event	Event			
Raw Electron Energy Events	NA	NA	Event	Event			
Raw Ion Energy Events	NA	NA	Event	Event			
Auxilary Data	NA	NA	Aux				
Critical Housekeeping Data	NA	NA	HSK				
Magnetic Field and Pitch Angle Data (included as fields in other products)						Pitch Angles	
Spacecraft Coordinates (included as fields in other products)					L, SM	L, GEO, GSM, SM	Others as applicable

Table 7 Higher level data products from RBSPICE

Product	Short Product Name	Duration of Measurement
Electron Energy Basic Rates	EBR	Every S Sectors, if enabled
Ion Energy Basic Rates	IEBR	Every S Sectors, if enabled
Ion Energy Diagnostic Rates	IEDR	Every S Sectors, if enabled
Ion Species Basic Rates	ISBR	Every S Sectors, if enabled
Ion Species Diagnostic Rates	ISDR	Every S Sectors, if enabled
Low Energy Res High Time Res—Electron Spectra	LERHTR-ES	Every S Sectors, if enabled
High Energy Res Low Time Res—Electron Spectra	HERLTR-ES	Every S*N1*N2 Sectors/Spins, if enabled
High Time Res Low Energy Res—Ion Spectra	HTRLER-IS	Every S*N1*N2 Sectors/Spins, if enabled
High Time Res Low Energy Res—TOF × E Ion Energy Spectra	HTRLER-TOF×E-IS	Every S*N1*N2 Sectors/Spins, if enabled
TOF × E Proton Rates	TOF×E-P	Every S Sectors, if enabled
TOF × E Non Proton Rates	TOF×E-nP	Every S*N1 Sectors, if enabled
Low Res High Time Res—TOF × PH Proton Rates	LEHTR-TOF×PH-P	Every S Sectors, if enabled
High Res Low Time Res—TOF × PH Proton Rates	HRLTR-TOF×PH-P	Every S*N1*N2 Sectors/Spins, if enabled
Space Weather Data	SWD	Every Spin—if enabled
Raw Electron Energy Event Data	EEE	Every S Sectors, if enabled
Raw Ion Species Event Data	ISE	Every S Sectors, if enabled
Priority Events Data	Priority	Every S Sectors, if enabled
ERM Data	ERM	Every 180 seconds, if powered

7.2 R_{In} vs R_{Out} Calculations

In general, RBSPICE counts particle events seen by the TOF and SSD systems. The ability of the instrument to count each event is limited by the electronics of the system, causing a failure in counting when counting rates reach approximately 40,000 events per second for the TOF system and 60,000 events per second for the SSD energy mode. When these limits are exceeded, the resulting spectra require scaling to properly represent actual incident event intensities. Scaling is done in four stages.

(1) The TOF system can be commanded to accept a decimation factor of anywhere from each incident event counted to as large as one event counted for every 64 incident events in steps of (incident: count) 1:1, 2:1, 4:1, 8:1, 16:1, 32:1, and 64:1. This factor is adjustable, by command. When the expected incident rates are higher than the TOF system can handle, the decimation factor will be changed, accordingly.

(2) The second scaling stage is modification of the basic counting rates, using the telemetry from the electron (APID: 0 × 312) and ion (APID: 0 × 313) energy basic rates and the ion species (APID: 0 × 315) basic rates. Scaling is done for the start and stop anode rates, as well as for the observed SSD rates, using the following equations:

$$Start_{rate} = \frac{Start0/(Max_{IDLE} * Clk_{period})}{1 - (Start0 * ST_{dead}/Max_{IDLE}) - (Rdt * Rdt_{veto}/Max_{IDLE})} \quad (1)$$

$$Stop_{rate} = \frac{stop0/(Max_{IDLE} * Clk_{period})}{1 - (stop0 * SP_{dead}/Max_{IDLE}) - (R_{dt} * R_{dtveto}/Max_{IDLE})} \quad (2)$$

$$SSDn_{rate} = \frac{SSDn}{(Max_{IDLE} - SSDn_{dt}) * Clk_{period}} \quad (3)$$

where the values of $start0$, $stop0$, $SSDn_{dt}$, SSD, and R_{dt} are taken from the basic counting rate telemetry (either 0×312, 0×313, or 0×315). The other values (except for Max_{IDLE}) are constants of the FPG processor and the value of Max_{IDLE} is derived from the total amount of time allotted for the particular mode of the observation to accumulate counts.

(3) The third scaling stage is a modification of the Energy Mode spectra counts into rates. This stage integrates values from the second stage into the calculation of the rates to adjust the counts due to the inability of the system to identify all incident events. The energy spectrum is a two dimension measurement taken over each of the look directions, i, and for each of the energy bins, j, associated with the particular measurement. This specifically applies to APID's 0×317, 0×318, and 0×319. The equations describing this adjustment are as follows:

$$R_{ij} = \frac{h_{ij}}{Valid_{proc}} * \frac{Valid_{energy}}{IDLE} * C^i_{PKD_{reset}} * C^i_{PUR_{veto}} \quad (4)$$

$$C^i_{PKD_{reset}} = e^{(SSDn_{rate} * PDK_{reset} * Clk_{period})} \quad (5)$$

$$C^i_{PUR_{veto}} = e^{(\frac{SSD_i * PUR_{Veto}}{Max_{IDLE}})} \quad (6)$$

The values of $Valid_{proc}$, $Valid_{energy}$, and $IDLE$ are taken from the basic rate telemetry (either APID 0×312 or 0×313) and used to adjust the counted rate to a more accurate measure of the incident rate.

(4) The final stage of correction is for the Ion Species mode measurements. Again the counts are accumulated in a two dimension array of look directions, i, and "energy bin", j, which is actually the TOF $\times$ E and TOF $\times$ PH ID generated by the event processor for each incident event. The equation describing the modification to the counts is:

$$R_{ij} = \frac{h_{ij}}{Valid_{proc}} * \frac{Valid_{TOF \times E}}{IDLE} * C^i_{PKD_{reset}} * C^i_{PUR_{veto}} * e^{(\frac{Stop0 * SP_{veto}}{Max_{IDLE}})} \quad (7)$$

These equations have been tested using a limited set of laboratory measurements. Random pulsers were used to stimulate the Start and Stop Anodes as well as a single SSD of an Engineering Model. The uncorrelated (background) rates were 1.0×10^6, 5.6×10^5 and 1.0×10^3/sec on the Start, Stop and SSD. Additional random coincident Start, Stop and SSD (foreground) pulses were superimposed on the "background." The foreground pulses were generated with a fixed TOF position on anode and SSD energy. The foreground rates were varied from 1.0×10^3/sec to 7.5×10^6/sec.

The conversion and correction of Start Anode counts (Eq. (1)) and SSD counts (Eq. (3)) for varying input rates are shown in Figs. 29 and 30 with markers indicating the location of the instrument's required and goal rates.

Because a mono-energetic pulse was used to excite only one SSD, the lab data cannot test the formula for correcting the bins of the spectra. Nevertheless, a reduced form of Eq. (7) can be applied, in which the first factor is omitted, to correct the measured Valid event rate. That correction is shown in Fig. 31 for TOF $\times$ E events.

Because the Start Anode pulses start the Event state machine, one sees that in this data set, in which there is a large (>1E6/sec) Start Anode rate, the raw valid rate saturates at a

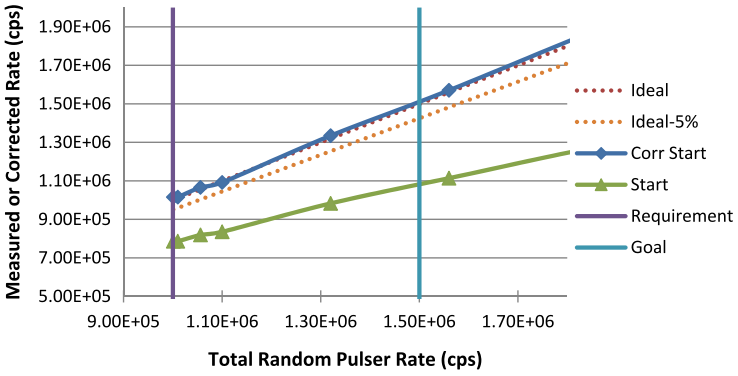

Fig. 29 Start Anode singles rates; raw (*green*) and corrected (*blue*)

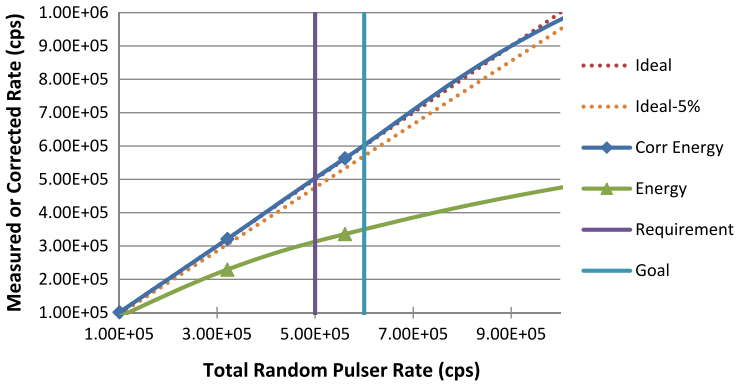

Fig. 30 SSD3 singles rates; raw (*green*) and corrected (*blue*)

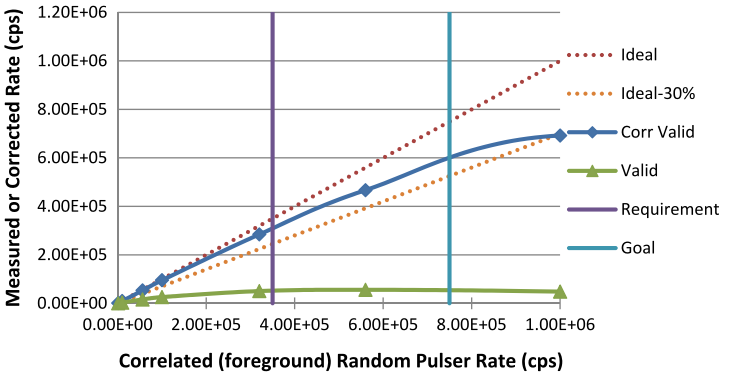

Fig. 31 Valid TOF × *E* rate; raw (*green*) and corrected (*blue*)

somewhat low value due to the state machine deadtime. Nevertheless, after the corrections are made, there is reasonably good tracking of the corrected rate with the foreground input rate.

7.3 Differential Particle Intensity Calculations—Level 2 Data

The conversion of the RBSPICE counting data from rates into differential particle intensities is done in a straightforward method. A calibration file for each of the RBSPICE instruments is used to define the conversion data for each of the data products. The calibration file is an Excel spreadsheet with a worksheet for each of the data products that are to be converted into NASA level 2 data as differential particle intensities. Each worksheet contains a series of entries for each of the energy bins associated with the product. The entries describe the name of the channel, the minimum energy of the bin in units of KeV, the maximum energy of the bin in units of KeV, the mid-point energy of the bin in units of KeV, the geometric factor for the bin if a small pixel is used in units of (cm^2 sr), the geometric factor for the bin if a large pixel is used in units of (cm^2 sr), and finally the efficiency of the channel. Differential particle intensities are then calculated from the derived incident rates (see previous section on R_{In} vs R_{Out} calculations) using the following equation:

$$I = \frac{R}{(\Delta E * G * eff)} \tag{8}$$

with "$\Delta E = E_{\mathrm{High}} - E_{\mathrm{Low}}$" being the channel width.

Which G is used (G_{small} or G_{large}) is determined from the RBSPICE Auxiliary record (APID 0×323) that identifies whether the pixel used is large or small.

7.4 Detailed Discussion of Data Flow

The RBSPICE data processing is done in a series of steps each dependent upon the other with few exceptions.

(1) The most recent data for each of the two spacecraft is downloaded from the Mission Operations Center (MOC) data sites. This process includes a built-in three day delay to allow all of the RBSPICE telemetry to be collected and processed by the MOC. This step also involves downloading all of the Van Allen Probes mission related ephemerids and SPICE kernels that are required for RBSPICE data processing. One aspect of this process is that the SPICE SCLK kernel describing the relationship between Mission Elapsed Time (MET) and Ephemeris Time (ET) is not only downloaded but verified against a MOC-provided time testing web service. If this validation fails, then RBSPICE data processing is stopped until the problem is resolved. This particular time check is a mission requirement that provides a simple means to ensure all of the SOC's data is using the most recent and validated SCLK kernel, thereby ensuring that time stamps on each of the data records are accurately matched from one instrument to another.
(2) A process is executed whereby the downloaded data from the MOC is first moved to a final directory, based upon the APID of the data product. The process then does a full file read to provide a detailed characterization of each file including the actual start and stop times of the included data, the total number of included records, and other relevant information. This information is entered into a processing control database, which is the primary driver for subsequent data processing.
(3) The level 0 (telemetry) data files are then read, and the data is extracted into the database, a Comma Separated Values (CSV) text based data file, and a CDF data file. Not all of the data products are written directly to the database, but instead, only data that must be used by later processing steps (e.g. conversion of counts into rates) is initially stored into the database tables. A prioritization of APID's is done so that Auxiliary and Status data products are read and saved first and then all other data products are processed.

(4) Level 1 processing then continues by converting any data products that include counts into rates. Each of the rate data files is then also written to the file system as both CSV and CDF files. This process also includes a prioritization so that Basic Rate and Diagnostic Rate data products are processed first and then all other files are processed.
(5) Level 2 processing then occurs converting each of the data files from the previous step into particle intensities. Each file written is done as CSV and CDF.
(6) Processing of the magnetic field data is then started. This process includes downloading the most recent magnetic field data from either the EMFISIS or EFW data sites. The files are characterized, and that information is saved in the process control database. The files are then used to generate a look direction data product, which is generated for each of the Level 2 data files at the time cadence of each file. This look direction data product specifies a time stamp, the look direction of each of the RBSPICE telescopes in spacecraft science coordinates, the associated measurement of the magnetic field for the time stamp, and the calculated Pitch Angle of any incident particles measured for each of the RBSPICE telescopes.

This overall processing of the RBSPICE data has been automated so that very little operator intervention should be required. There are a large number of exception—checking steps for each of the processing steps and the processing system is made to compensate for as many of the possible exceptions as possible to allow processing to continue without intervention.

The system has also been built to allow a data operator to follow the processing of each of the data files and verify that the steps of the process succeed. If issues do arise that require intervention, then the system has been built to allow any particular file to be reprocessed at a later time.

7.5 Discussion of Overall Data Organization

The overall RBSPICE data system has been organized to allow a scientist or computer system easy access to any particular data file. The RBSPICE data system is fully described in the document entitled: RBSPICE_SOC_Archive_Dir_Filename_Convention and is available through the RBSPICE SOC web site.

7.6 Discussion of Distribution Protocols Used

The RBSPICE data will be available to the general public through the following web sites: http://rbspicea.ftecs.com and http://rbspiceb.ftecs.com. The data access protocols available are described on each of the web sites, but include data access through standard web ftp protocols for each downloading of each of the data products.

8 RBSPICE Conclusion

The Van Allen Probes Program will provide a transformational view of Earth's space environment, one that has not existed since the discovery of the Van Allen radiation belts more than five decades ago. The comprehensive array of Van Allen Probes instruments with their measurement objectives, combined with the unique two-spacecraft mission, will yield data sets that will provide new understanding of the physics of the radiation belts, including their formation and loss. Importantly, the data sets returned by the Van Allen Probes will be essential for the establishment of new models of the radiation belts and hot plasma environment, models that will be the centerpieces for space program mission design into the future.

The RBSPICE instrument is an essential part of the Van Allen Probes instrument complement. It will provide critical data to answering the three over-arching questions for the Van Allen Probes Program (Sect. 2): that is, RBSPICE will determine "how space weather creates the storm-time ring current around Earth, how that ring current supplies and supports the creation of the radiation belt populations," and how the ring current is involved in radiation belt losses.

Acknowledgements The RBSPICE instrument was supported under a NASA Contract with the New Jersey Institute of Technology, with subcontracts to The Johns Hopkins University Applied Physics Laboratory and to Fundamental Technologies LLC. We thank Heather Mull for her assistance with this paper.

References

S.-I. Akasofu, In memoriam Sydney Chapman. Space Sci. Rev. **11**, 599–606 (1970)

H. Alfvén, A theory of magnetic storms and of the aurorae. K. Sven. Vetenskapakad. Handl., Ser. 3 **18**(3) (1939) (Reprinted in part with comments by Alex Dessler and John Wilcox in Eos **51**, 180–194 (1970))

H. Alfvén, A theory of magnetic storms and of the aurorae, II, The aurorae; III, The magnetic disturbances. K. Sven. Vetenskapakad. Handl., Ser. 3 **18**(9) (1940)

V. Angelopoulos, W. Baumjohann, C.F. Kennel, F.V. Coroniti, M.G. Kivelson, R. Pellat, R.J. Walker, H. Lühr, G. Paschmann, Bursty bulk flows in the inner central plasma sheet. J. Geophys. Res. **97**, 4027 (1992)

S. Barabash, P.C. Brandt, O. Norberg, R. Lundin, E.C. Roelof, C.J. Chase, B.H. Mauk, H. Koskinen, Energetic neutral atom imaging by the Astrid microsatellite. Adv. Space Res. **20**, 1055–1060 (1997). doi:10.1016/S0273-1177(97)00560-7

W. Baumjohann, G. Paschmann, H. Lühr, Characteristics of high-speed ion flows in the plasma sheet. J. Geophys. Res. **95**, 3801 (1990)

P.C. Brandt, S. Ohtani, D.G. Mitchell, M.C. Fok, E.C. Roelof, R. Demajistre, Global ENA observations of the storm main-phase ring current: implications for skewed electric fields in the inner magnetosphere. Geophys. Res. Lett. **29**(20), 1954 (2002). doi:10.1029/2002GL015160

S. Chapman, V.C.A. Ferraro, A new theory of magnetic storms, I, The initial phase. J. Geophys. Res. **36**, 77–97, 171–186 (1931)

S. Chapman, V.C.A. Ferraro, A new theory of magnetic storms, I, The initial phase (continued). J. Geophys. Res. **37**, 147–156, 421–429 (1932)

S. Chapman, V.C.A. Ferraro, A new theory of magnetic storms, II, The main phase. J. Geophys. Res. **38**, 79–96 (1933)

M. Chen, C.-P. Wang, M. Schulz, L.R. Lyons, Solar-wind influence on MLT dependence of plasma sheet conditions and their effects on storm time ring current formation. Geophys. Res. Lett. **34**, L14112 (2007). doi:10.1029/2007GL030189

A.J. Dessler, Swedish iconoclast recognized after many years of rejection and obscurity. Science **170**, 604–606 (1970)

S. Dubyagin, V. Sergeev, S. Apatenkov, V. Angelopoulos, A. Runov, R. Nakamura, W. Baumjohann, J. McFadden, D. Larson, Can flow bursts penetrate into the inner magnetosphere? Geophys. Res. Lett. **38**, L08102 (2011). doi:10.1029/2011GL047016

Y. Ebihara, M. Ejiri, Simulation study on fundamental properties of the storm-time ring current. J. Geophys. Res. **105**, 15843–15859 (2000). doi:10.1029/1999JA900493

Y. Ebihara, M. Ejiri, Numerical simulation of the ring current: review. Space Sci. Rev. **105**(1–2), 377 (2003)

D. Fairfield et al., Geotail observations of substorm onset in the inner magnetotail. J. Geophys. Res. **103**(A1), 103 (1998)

D. Fairfield et al., Earthward flow bursts in the inner magnetotail and their relation to auroral brightenings, AKR intensifications, geosynchronous particle injections and magnetic activity. J. Geophys. Res. **104**(A1), 355 (1999)

M.C. Fok, R.A. Wolf, R.W. Spiro, T.E. Moore, Comprehensive computational model of Earth's ring current. J. Geophys. Res. **106**(A5), 8417–8424 (2001)

C.S. Gillmor, The formation and early evolution of studies of the magnetosphere, in *Discovery of the Magnetosphere*, ed. by C.S. Gillmor, J.R. Sprieter (American Geophysical Union, Washington, 1997)

M.G. Henderson, G.D. Reeves, H.E. Spence, R.B. Sheldon, A.M. Jorgensen, J.B. Blake, J.F. Fennell, First energetic neutral atom images from polar. Geophys. Res. Lett. **24**, 1167–1170 (1997). doi:10.1029/97GL01162

T. Hori, A.T.Y. Lui, S. Ohtani, P.C. Brandt, B.H. Mauk, R.W. McEntire, K. Maezawa, T. Mukai, Y. Kasaba, H. Hayakawa, Storm-time convection electric field in the near-Earth plasma sheet. J. Geophys. Res. **110**, A04213 (2005). doi:10.1029/2004JA010449

V.K. Jordanova, L.M. Kistler, C.J. Farrugia, R.B. Torbert, Effects of inner magnetospheric convection on ring current dynamics: March 10–12, 1998. J. Geophys. Res. **106**(A), 29705 (2001). doi:10.1029/2001JA000047

J.U. Kozyra, M.W. Liemohn, Ring current energy input and decay. Space Sci. Rev. **109**, 105–131 (2003)

J.U. Kozyra, V.K. Jordanova, J.E. Borovsky, M.F. Thomsen, D.J. Knipp, D.S. Evans, D.J. McComas, T.E. Cayton, Effects of a high-density plasma sheet on ring current development during the November 2–6, 1993, magnetic storm. J. Geophys. Res. **103**, 26285 (1998)

L.J. Lanzerotti, A. Hasegawa, C.G. Maclennan, Drift mirror instability in the magnetosphere: particle and field oscillations and electron heating. J. Geophys. Res. **74**(24), 5565–5578 (1969). doi:10.1029/JA074i024p05565

M.W. Liemohn, J.U. Kozyra, V.K. Jordanova, G.V. Khazanov, M.F. Thomsen, T.E. Cayton, Analysis of early phase ring current recovery mechanisms during geomagnetic storms. Geophys. Res. Lett. **26**, 2845 (1999)

G.H. Ludwig, The birth of Explorer I, in *Opening Space Research: Dreams, Technology, and Scientific Discovery* (AGU, Washington, 2011), pp. 245–262. doi:10.1029/2011062SP011

A.T.Y. Lui, R.W. McEntire, S.M. Krimigis, Evolution of the ring current during two geomagnetic storms. J. Geophys. Res. **92**(A7), 7459–7470 (1987)

D.G. Mitchell, K.C. Hsieh, C.C. Curtis, D.C. Hamilton, H.D. Voss, E.C. Roelof, P.C. Brandt, Imaging two geomagnetic storms in energetic neutral atoms. Geophys. Res. Lett. **28**, 1151–1154 (2001). doi:10.1029/2000GL012395

D.G. Mitchell, P.C. Brandt, E.C. Roelof, D.C. Hamilton, K.C. Retterer, S. Mende, Global imaging of O+ from IMAGE/HENA. Space Sci. Rev. **109**, 63–75 (2003). doi:10.1023/B:SPAC.0000007513.55076.00

R. Nakamura, W. Baumjohann, B. Klecker, Y. Bogdanova, A. Balogh, H. Reme, J.M. Bosqued, I. Dandouras, J.A. Sauvaud, K.-H. Glassmeier, L. Kistler, C. Mouikis, T.L. Zhang, H. Eichelberger, A.A. Runov, Motion of the dipolarization front during a flow burst event observed by cluster. Geophys. Res. Lett. **29**(20), 1942 (2002). doi:10.1029/2002GL015763

E.N. Parker, Adventures with the geomagnetic field, in *Discovery of the Magnetosphere*, ed. by C.S. Gillmor, J.R. Sprieter (American Geophysical Union, Washington, 1997)

E.C. Roelof, D.G. Mitchell, D.J. Williams, Energetic neutral atoms ($E \sim 50$ keV) from the ring current—IMP 7/8 and ISEE-1. J. Geophys. Res. **90**, 10991–11008 (1985). doi:10.1029/JA090iA11p10991

A. Runov, V. Angelopoulos, M.I. Sitnov, V.A. Sergeev, M. Bonnell, J.P. McFadden, D. Larson, K.H. Glassmeier, U. Auster, THEMIS observations of an earthward-propagating dipolarization front. Geophys. Res. Lett. **36**, L14106 (2009). doi:10.1029/2009GL038980

A. Runov, V. Angelopoulos, X.-Z. Zhou, X.J. Zhang, S. Li, F. Plaschke, J. Bonnell, A THEMIS multicase study of dipolarization fronts in the magnetotail plasma sheet. J. Geophys. Res. **116**(A5) (2011). doi:10.1029/2010JA016316

A. Schmidt, Das erdmagnetische Aussenfeld. Z. Geophys. **1**, 3–13 (1924)

K. Shiokawa, W. Baumjohann, G. Haerendel, Braking of high-speed flows in the near-Earth tail. Geophys. Res. Lett. **24**(1), 1179 (1997). doi:10.1029/97GL01062

K. Shiokawa, W. Baumjohann, G. Haerendel, G. Paschmann, J.F. Fennell, E. Friis-Christensen, H. Luhr et al., High-speed ion flow, substorm current wedge, and multiple Pi 2 pulsations. J. Geophys. Res. **103**(A), 4491 (1998). doi:10.1029/97JA01680

S.F. Singer, A new model of magnetic storms and aurorae. Eos **38**, 175–190 (1957)

M.I. Sitnov, N.A. Tsyganenko, A.Y. Ukhorskiy, P.C. Brandt, Dynamical data-based modeling of the storm-time geomagnetic field with enhanced spatial resolution. J. Geophys. Res. **113**, A07218 (2008). doi:10.1029/2007JA013003

D.P. Stern, A brief history of magnetospheric physics before the spaceflight era. Rev. Geophys. **27**(1), 103 (1989). doi:10.1029/RG027i001p00103

C. Stoermer, Sur la situation de la zone de fréquence maximum des aurores boréales d'aprés la théorie corpusculaire. C. R. Acad. Sci. **151**, 736–739 (1910)

C. Stoermer, Sur les trajectories des corpuscules electrises dans l'espace sous l'actions des magnetisme terrestre avec application aux auarores boréales, seconde memoire. Arch. Sci. Phys. Nat., Ser. 4 **32**, 117–123, 190–219, 277–314, 415–436, 505–509 (1911)

C. Stoermer, Sur les trajectories des corpuscules electrises dans l'espace sous l'actions des magnetisme terrestre avec application aux auarores boréales, seconde mernoire (continued). Arch. Sci. Phys. Nat., Ser. 4 **33**, 51–69, 113–150 (1912)

R.M. Thorne, Radiation belt dynamics: the importance of wave-particle interactions. Geophys. Res. Lett. **37**(22), L22107 (2010). doi:10.1029/2010GL044990
D.L. Turner, Y. Shprits, M. Hartinger, V. Angelopoulos, Explaining sudden losses of outer radiation belt electrons during geomagnetic storms. Nat. Phys. (2012). doi:10.1038/NPHYS2185
A.Y. Ukhorskiy, B.J. Anderson, P.C. Brandt, N.A. Tsyganenko, Storm-time evolution of the outer radiation belt: transport and losses. J. Geophys. Res. **111**, A11S03 (2006). doi:10.1029/2006JA011690
A.Y. Ukhorskiy, M.I. Sitnov, K. Takahashi, B.J. Anderson, Radial transport of radiation belt electrons due to stormtime Pc5 waves. Ann. Geophys. **27**(5), 2173 (2009). doi:10.5194/angeo-27-2173-2009
R.A. Wolf, J.W. Freeman, B.A. Hausman, R.W. Spiro, R.V. Hilmer, R.L. Lambour, Modeling convection effects in magnetic storms, in *Magnetic Storms*, ed. by B.T. Tsurutani, W.D. Gonzalez, Y. Kamide, J.K. Arballo. Geophysical Monograph Series, vol. 98 (1997), p. 161

DOI 10.1007/978-1-4899-7433-4_9
Reprinted from *Space Science Reviews* Journal, DOI 10.1007/s11214-013-9995-4

ERRATUM

Erratum to: Radiation Belt Storm Probes Ion Composition Experiment (RBSPICE)

D.G. Mitchell · L.J. Lanzerotti · C.K. Kim · M. Stokes · G. Ho · S. Cooper · A. Ukhorskiy · J.W. Manweiler · S. Jaskulek · D.K. Haggerty · P. Brandt · M. Sitnov · K. Keika · J.R. Hayes · L.E. Brown · R.S. Gurnee · J.C. Hutcheson · K.S. Nelson · C.M. Hammock · N. Paschalidis · E. Rossano · S. Kerem

Published online: 11 June 2013

Erratum to: Space Sci Rev
DOI 10.1007/s11214-013-9965-x

Unfortunately, the author C.M. Hammock was not included in the author group in the original published article. The author has now been added.

The online version of the original article can be found under doi:10.1007/s11214-013-9965-x.

D.G. Mitchell · C.K. Kim · M. Stokes · G. Ho · S. Cooper · A. Ukhorskiy · S. Jaskulek · D.K. Haggerty · P. Brandt · M. Sitnov · J.R. Hayes · L.E. Brown · R.S. Gurnee · J.C. Hutcheson · K.S. Nelson · C.M. Hammock · N. Paschalidis · E. Rossano · S. Kerem
Space Department, The Johns Hopkins University Applied Physics Laboratory, Laurel, MD 20723, USA

L.J. Lanzerotti · K. Keika
Center for Solar Terrestrial Research, Department of Physics, New Jersey Institute of Technology, Newark, NJ 07102, USA

J.W. Manweiler (✉)
Fundamental Technologies LLC, Lawrence, KS 66046, USA
e-mail: Manweiler@ftecs.com

DOI 10.1007/978-1-4899-7433-4_10
Reprinted from *Space Science Reviews* Journal, DOI 10.1007/s11214-013-0007-5

Science Goals and Overview of the Radiation Belt Storm Probes (RBSP) Energetic Particle, Composition, and Thermal Plasma (ECT) Suite on NASA's Van Allen Probes Mission

H.E. Spence · G.D. Reeves · D.N. Baker · J.B. Blake · M. Bolton · S. Bourdarie · A.A. Chan · S.G. Claudepierre · J.H. Clemmons · J.P. Cravens · S.R. Elkington · J.F. Fennell · R.H.W. Friedel · H.O. Funsten · J. Goldstein · J.C. Green · A. Guthrie · M.G. Henderson · R.B. Horne · M.K. Hudson · J.-M. Jahn · V.K. Jordanova · S.G. Kanekal · B.W. Klatt · B.A. Larsen · X. Li · E.A. MacDonald · I.R. Mann · J. Niehof · T.P. O'Brien · T.G. Onsager · D. Salvaggio · R.M. Skoug · S.S. Smith · L.L. Suther · M.F. Thomsen · R.M. Thorne

Received: 6 May 2013 / Accepted: 16 July 2013 / Published online: 18 October 2013

Abstract The Radiation Belt Storm Probes (RBSP)-Energetic Particle, Composition, and Thermal Plasma (ECT) suite contains an innovative complement of particle instruments to ensure the highest quality measurements ever made in the inner magnetosphere and radiation belts. The coordinated RBSP-ECT particle measurements, analyzed in combination with fields and waves observations and state-of-the-art theory and modeling, are necessary for understanding the acceleration, global distribution, and variability of radiation belt elec-

H.E. Spence (✉) · S.S. Smith
Institute for the Study of Earth, Oceans, and Space, Univ. of New Hampshire, Durham, NH 03824, USA
e-mail: Harlan.Spence@unh.edu

G.D. Reeves · R.H.W. Friedel · H.O. Funsten · A. Guthrie · M.G. Henderson · V.K. Jordanova · B.A. Larsen · E.A. MacDonald · J. Niehof · R.M. Skoug · M.F. Thomsen
Los Alamos National Laboratory, Los Alamos, NM 87545, USA

D.N. Baker · M. Bolton · S.R. Elkington · X. Li
Laboratory for Atmospheric and Space Physics, University of Colorado, Boulder, CO 90303-7820, USA

J.B. Blake · S.G. Claudepierre · J.H. Clemmons · J.F. Fennell · T.P. O'Brien · D. Salvaggio
The Aerospace Corporation, El Segundo, CA 900009, USA

A.A. Chan
Rice University, Houston, TX 77005-1827, USA

J.P. Cravens
JPC LLC, Port Aransas, TX 78373, USA

J. Goldstein · J.-M. Jahn
Southwest Research Institute, San Antonio, TX 78238-5166, USA

J.C. Green · T.G. Onsager
National Oceanic and Atmospheric Administrations, Boulder, CO 80305, USA

trons and ions, key science objectives of NASA's Living With a Star program and the Van Allen Probes mission. The RBSP-ECT suite consists of three highly-coordinated instruments: the Magnetic Electron Ion Spectrometer (MagEIS), the Helium Oxygen Proton Electron (HOPE) sensor, and the Relativistic Electron Proton Telescope (REPT). Collectively they cover, continuously, the full electron and ion spectra from one eV to 10's of MeV with sufficient energy resolution, pitch angle coverage and resolution, and with composition measurements in the critical energy range up to 50 keV and also from a few to 50 MeV/nucleon. All three instruments are based on measurement techniques proven in the radiation belts. The instruments use those proven techniques along with innovative new designs, optimized for operation in the most extreme conditions in order to provide unambiguous separation of ions and electrons and clean energy responses even in the presence of extreme penetrating background environments. The design, fabrication and operation of ECT spaceflight instrumentation in the harsh radiation belt environment ensure that particle measurements have the fidelity needed for closure in answering key mission science questions. ECT instrument details are provided in companion papers in this same issue.

In this paper, we describe the science objectives of the RBSP-ECT instrument suite on the Van Allen Probe spacecraft within the context of the overall mission objectives, indicate how the characteristics of the instruments satisfy the requirements to achieve these objectives, provide information about science data collection and dissemination, and conclude with a description of some early mission results.

Keywords Radiation belts · Particle senors · Radiation detection · Space weather · Van Allen Probes

R.B. Horne
British Antarctic Survey, Cambridge CB3 0ET, UK

M.K. Hudson
Dartmouth College, Hanover, NH 03755-1404, USA

S.G. Kanekal
NASA Goddard, Greenbelt, MD 20771, USA

B.W. Klatt
Massachusetts Institute of Technology, Cambridge, MA, USA

I.R. Mann
University of Alberta, Edmonton, AB T6G 2R3, Canada

S. Bourdarie
ONERA-CERT, Toulouse, Cedex 04, France

L.L. Suther
Johns Hopkins University/Applied Physics Laboratory, Laurel, MD, USA

R.M. Thorne
University of California, Los Angeles, 90095, USA

B.W. Klatt
University of Calgary, Alberta, T2N 1N4, Canada

1 ECT Science Goals and Objectives

1.1 Introduction

Understanding the acceleration, global distribution, and variability of radiation belt electrons and ions requires a coordinated set of particle measurements analyzed in combination with fields and wave observations and state-of-the-art theory and modeling. The Radiation Belt Storm Probes (RBSP)-Energetic Particle, Composition, and Thermal Plasma (ECT) suite on the Van Allen Probes mission contains a proven complement of particle instruments to ensure the highest quality measurements ever made in the inner magnetosphere.

Instruments in the RBSP-ECT suite were chosen to provide the essential particle measurements needed to achieve science closure on each of eight prime Van Allen Probes mission objectives (see text in Fig. 4 and as outlined below). The suite provides a comprehensive set of particle measurements, optimized to achieve science closure with the fewest instruments and resources. Additionally the RBSP-ECT science team has applied extensive experience in designing, fabricating and operating spaceflight instrumentation for the harsh Van Allen Probes radiation environment.

The HOPE instrument uses an electrostatic top-hat analyzer and time-gated coincidence detectors to measure electrons, protons, helium, and oxygen with energies from 1 eV to 50 keV while rejecting penetrating backgrounds. The MagEIS energetic particle magnetic spectrometer uses magnetic focusing and pulse height analysis to provide the cleanest possible energetic electron measurements over the energy range 20 keV–4 MeV, total ions from 15 keV to ∼1 MeV, and ion composition from a few to ∼50 MeV/nucleon. The REPT telescope covers the challenging electron (proton) energy range above ∼2 (∼8) MeV in order to capture the characteristics of the most intense populations and events using designs adapted from the highly successful SAMPEX mission. These instruments are described respectively in detail in complementary publications of this same special issue (Funsten et al. 2013; Blake et al. 2013; and Baker et al. 2012). The integrated RBSP-ECT suite provides maximum Van Allen Probes science return using a minimum of resources. The RBSP-ECT suite particle measurements are complemented on each Van Allen Probes spacecraft by two other particle sensors which provide additional important information about ion composition in the ring current energy range, RBSPICE (Mitchell et al. 2013), and of the inner zone proton populations, RPS (Mazur et al. 2012).

1.2 Science Objectives and Context

The RBSP-ECT Science Team applies measurements from MagEIS, HOPE, and REPT along with theory, models, and auxiliary measurements to answer four fundamental science objectives. These four science objectives consolidate eight prioritized Van Allen Probes mission objectives. These objectives follow naturally from the accumulated scientific understanding developed by earlier missions which motivate the Van Allen Probes mission (please see the introductory section of Baker et al. (2012) for a concise history of those missions and our progress in understanding.) The four Van Allen Probes mission objectives are to:

(1) Determine the physical processes that produce radiation belt enhancement events,
(2) Determine the dominant mechanisms for relativistic electron loss,
(3) Determine how the inner magnetospheric plasma environment controls radiation belt acceleration and loss, and
(4) Develop empirical and physical models for understanding and predicting radiation belt space weather effects

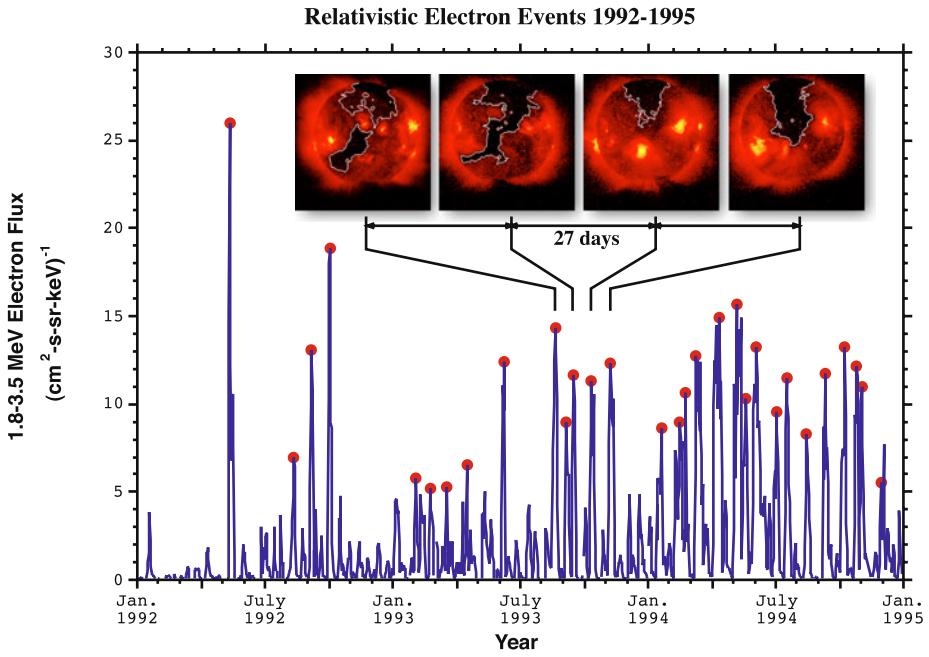

Fig. 1 Daily average geosynchronous electron fluxes 1992–1995 showing quasi-periodic response to high speed solar wind streams from coronal holes (Reeves 1998)

Changes in the Earth's radiation belt environment are primarily caused by two distinct types of solar (interplanetary medium) disturbances: Coronal Mass Ejections (CMEs) and Co-rotating Interaction Regions (CIRs) associated with fast solar wind streams that often originate in solar coronal holes (Fig. 1). Near solar maximum, large geomagnetic storms are frequently initiated by CMEs (Baker et al. 1998). The radiation belt response to CME and non-CME forcing cannot currently be predicted. Storms increase the flux of outer belt electrons only about half the time (Fig. 2). Storms can also decrease relativistic electron fluxes (≈20 %) or change their structure without changing their intensity (≈30 %). This indicates in a given event either acceleration or loss processes can dominate. Acceleration, losses, and adiabatic responses must be understood as a system (Baker et al. 1994). In addition, Blake et al. (1992) have shown that interplanetary shocks can produce 'prompt acceleration' events and combinations of processes under extreme conditions can produce 'slot-filling' events; such observations provide highly-sensitive tests of our physical understanding through theory/model comparisons (e.g. Horne et al. 2005). The RBSP-ECT particle observations will be fully understood only in the context of their connection to the Sun (Mason et al. 2001). We use observations from the LWS Solar Dynamics Observatory (SDO) mission, the ACE satellite, the GOES soft X-ray imagers, and all other relevant available information to fully explore solar and heliospheric sources for all these classes of radiation belt events.

Understanding radiation belt physics requires multi-point measurements of phase space densities. Phase space density is best represented for the radiation belts as a function of the three magnetic invariants—gyro (μ or M), bounce (J or K), and drift (Φ or L^*). Particles with the same invariants measured at different locations (therefore different **B**) have different energies and pitch angles. This fact drives the need for continuous spectral and pitch angle

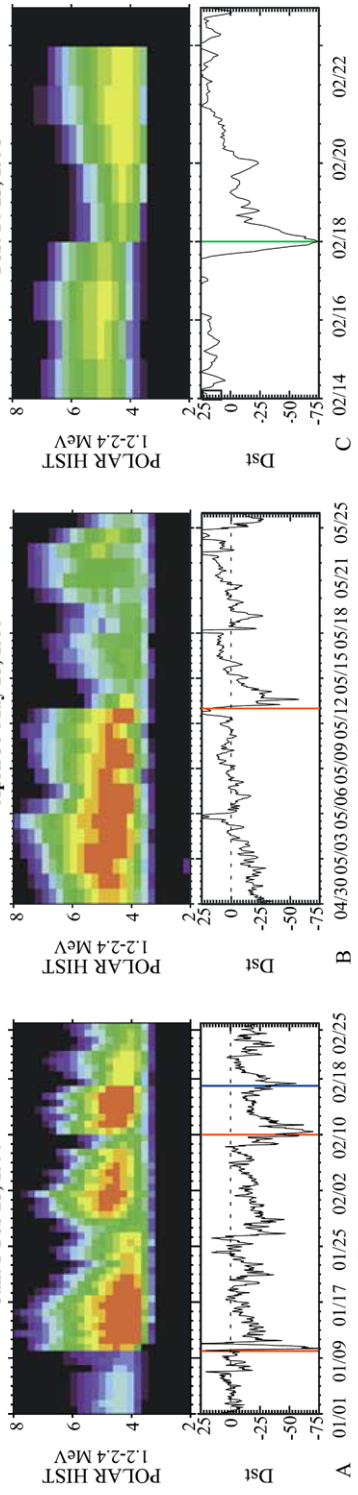

Fig. 2 Radiation belt electron response to geomagnetic storms can produce increases or decreases in flux (after Fig. 2 of Reeves et al. 2003). POLAR HIST 1.2–2.4 MeV electrons plotted as a function of L for three representative storms are shown to illustrate how comparable storms (see Dst index in the *bottom panels*) can yield increases of the electron flux in the outer zone belt (Jan. 1–Feb. 25, 1997), decreases (April 30–May 25, 1999), or essentially no change (Feb. 14–23, 1998). In each of the HIST L-time spectrograms, the log of the differential flux (#/cm^2 keV s) is plotted on a color scale which ranges from 10^2 at the deep blue low intensity end to 10^6 at the bright red high intensity end. The increases and decreases exemplified in the first two plots are dramatic, with electron flux changing by three to four orders of magnitude

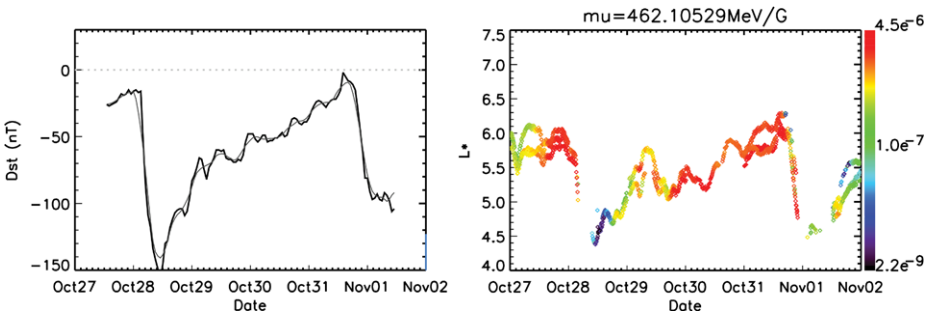

Fig. 3 Dst index and calculated geosynchronous drift shell and phase space densities during a storm using the DREAM model (after Fig. 6 of Reeves et al. 2012). The electron phase space density in units of $(c/MeV/cm)^3$ is color coded as a function of L^* for three geosynchronous satellites (overtraced) during a geomagnetic storm in 2001

coverage with unambiguous instrument energy responses. Temporal and spatial variations will be resolved using the 2-spacecraft Van Allen Probes configuration that produces a full range of radial and azimuthal separations in each local time sector (dawn, dusk, noon, and midnight) over the course of the mission.

The geomagnetic field controls the motion of radiation belt particles. As the field changes during active conditions, large-scale redistribution of radiation belt particles occurs. Recent studies have shown (Reeves et al. 2012), for even a modest storm, that a geosynchronous satellite originally at $L^* \approx 6$ will observe particles from $L^* \approx 4$ that have moved adiabatically outward during the main phase in response to the inflation of the magnetic field. Figure 3 shows color coded electron phase space density (PSD) as a function of L^* for three satellites at geosynchronous orbit during a geomagnetic storm in 2001. As the ring current intensifies (evidenced by the depression in the Dst index) the drift shells "inflate" which produces an "apparent motion" of the satellites to very low L^*. This adiabatic redistribution (sometimes known as the 'Dst effect') is superposed on any other transport, acceleration, or loss processes.

Non-adiabatic processes come into play when one of the three adiabatic invariants is violated leading to energy diffusion, cross-field transport, and pitch angle scattering (Schulz and Lanzerotti 1974). These processes are produced through the action of convective or inductive electric fields and through wave-particle interactions over a variety of frequencies. Large-scale electric fields transport plasma sheet plasma into the inner magnetosphere where it becomes the source or 'seed' population for radiation belt particles. The characteristics (including composition) of the plasma sheet and plasmasphere determine where and how the waves that control radiation belt dynamics are produced.

The LWS Geospace Mission Definition Team (GMDT) (Kintner et al. 2002) recognized that the storm-time ring current produces the biggest adiabatic changes in the geomagnetic field. Additionally, interaction of the ring current and plasmasphere produces electromagnetic ion-cyclotron (EMIC) waves that strongly interact with outer belt electrons; injected plasma distributions produce broadband chorus across the dawn hemisphere that can both accelerate and precipitate relativistic electrons; and plasmaspheric hiss controls the location and dynamics of the "slot" region. Since the GMDT report was written, however, we have seen considerable advances in our understanding of ring current dynamics. When boundary and initial conditions of these ring current models are well-constrained by measurements of the relevant physical parameters, studies (Jordanova et al. 2001, 2003, 2006; Zaharia et al. 2006) have demonstrated the models' ability to accurately predict the global geomagnetic

field configuration, as well as predicting VLF wave properties consistent with statistical surveys of wave observations. The RBSP-ECT and RBSPICE particles suites were selected, with these advances in mind, to directly measure those particles and plasma distributions that produce the ring current as well as those properties that determine how, when, and where critical wave populations that accelerate or precipitate relativistic electron are produced.

The RBSP-ECT instrument suite comprising MagEIS, HOPE, and REPT measures the comprehensive spectrum of electrons and ions needed to: calculate adiabatic invariants in storm-time fields; determine dynamic phase space density profiles; understand production of plasma waves; characterize source populations and their transport; and understand the acceleration and loss of radiation belt particles, their space weather effects, and ultimately their response to the variable Sun as well as to processes internal to Earth's magnetosphere.

- Science Objective #1: Determine the physical processes that produce radiation belt enhancement events

When we consider radiation belt enhancements we distinguish them from "recoveries" following an adiabatic change such as magnetic field stretching or the "Dst effect." True enhancements occur due to the energization of particles when one or more of the magnetic invariants are violated. Betatron/Fermi acceleration (also referred to as "radial" acceleration) occurs when particles are transported from regions of low magnetic field strength to regions of higher magnetic field strength. "Local" acceleration occurs without significant radial transport due to the interaction of particles with local wave populations. "Prompt" acceleration occurs through resonant interaction of a particle's drift motion and the passage of a shock through the magnetosphere. Regardless of type, properties of the resulting enhancement are determined by pre-existing "seed" or source populations as much as by the processes acting on them.

Radiation belt enhancements can occur for both ions and electrons but it is electrons—particularly outer belt and slot electrons—that are the most dynamic. Therefore, while we investigate the electron and ion populations, the primary RBSP-ECT suite emphasis is on understanding electrons. To accomplish this prime suite objective, we will reach closure on four science questions listed below.

Question 1 What processes are responsible for radial transport and acceleration? (Mission priority #1)

Question 2 Where, when, and how do local acceleration processes produce radiation belt acceleration? (Mission priority #2)

Question 3 How does 'prompt acceleration' create new radiation belts? (Mission priority #3)

Question 4 How do plasma 'seed' or source populations influence the characteristics of relativistic electron events? (Mission priority #5)

ECT Closure on Science Objective #1, Question 1 Understanding and predicting radial diffusion and relativistic electron acceleration requires: (1) comprehensive and 'clean' particle measurements over a broad range of energies and pitch angles; (2) measurements of the changing radial phase space density gradients; and (3) correlation with local Van Allen Probes and ground-based wave observations, e.g. CanadianArray for Realtime Investigations of Magnetic Activity (CARISMA; Mann et al. 2008), British Antarctic Survey (BAS), and other magnetometer networks). In conjunction with the Van Allen Probes fields and waves observations and the modeling resources available in the community, the ECT particles suite will provide all the necessary information needed to answer this critical science question.

Multi-spacecraft measurements with broad and continuous *differential* (integral fluxes will not suffice) energy coverage is key to this problem. To compare electrons with energies from 0.5 to 10 MeV at $L = 2$ to electrons at other L-shells that have the same first invariant (μ) it is critical to have continuous differential energy coverage down to at least 20 keV. For non-equatorial particles (J) or for removing adiabatic effects (L^*) energies well below 10 keV become important.

In addition to continuous energy coverage, the ECT instruments have been optimized to provide continuous pitch angle coverage for all expected magnetic field conditions (see Blake et al. 2013, for an extensive discussion of instrument design for optimal pitch angle coverage). This is necessary not only to cover a range of second invariants (J) but also to understand how wave-particle interactions alter the electron pitch angle distributions. Radial diffusion preferentially adds perpendicular momentum producing "pancake" distributions with peaks at 90°, whereas wave-particle interactions can produce a wide range of effects depending on the particular wave properties.

Using the DC magnetic field measurements from EMFISIS (Kletzing et al. 2013) with ECT particle fluxes we will achieve science closure by: (1) measuring the temporal evolution of phase space density gradients over a range of adiabatic invariants, (2) examining the evolution of the pitch angle distributions at different drift shells, (3) correlating with ULF field observations, and (4) looking for drift phase-bunching of electrons that resonate with ULF waves.

ECT Closure on Science Objective #1, Question 2 The most important observations for understanding the role of local acceleration in radiation belt acceleration are radial phase space density distributions. Our previous studies have shown evidence for local peaks but were limited by the range of L-shells (e.g. McAdams et al. 2001; Chen et al. 2005) or by high spacecraft latitudes that limited pitch angle coverage (e.g., Selesnick and Blake 1997; Green and Kivelson 2004). The ECT particles suite (plus magnetic field observations) will provide phase space density gradients over the full range of μ, J, and L^* values that are crucial to understand belt dynamics. As we have seen, this requires differential energy and pitch angle coverage from a few keV to ~1 MeV. The RBSP-ECT phase space density measurements will enable two types of studies. One uses each spacecraft to measure profiles of the gradient as each traverses L-shells in its orbit, at times when we can assume that radial gradients evolve slowly compared to the orbital period. The second technique uses the two spacecraft to obtain instantaneous gradients as well as measurements of the same point separated by the lag time of the trailing satellite. Van Allen Probes mission strategy designed variable separation of the satellites specifically for this purpose—enabling new understanding of acceleration under rapidly changing conditions.

The orbital sweep and instantaneous multi-point measurement strategies are important for understanding and differentiating the spatial and temporal characteristics of changing energy spectra and pitch angle distributions. We correlate those changes with observed wave characteristics, both locally and statistically. Along with wave measurements, understanding where, when, and how, local acceleration occurs requires measuring where and when we observe the characteristic spectral and pitch angle changes discussed earlier.

Over the course of the 2-year Van Allen Probes mission we expect to observe one or two relativistic electron events per month. We will analyze these events in-depth to understand the detailed processes that produce electron acceleration, transport, and loss. Statistical models for the global distribution of all relevant waves, electron spectra, pitch angle distributions, and radial phase space density will be constructed, as a function of MLT, L-shell, latitude, and geomagnetic activity. This resource will be made available to develop statistical, physical, empirical, and data assimilation based models.

ECT Closure on Science Objective #1, Question 3 ECT instruments are specifically designed to discover how prompt acceleration events create new radiation belts and the most extreme space radiation conditions such as the transformational 24 March 1991 event (Blake et al. 1992) REPT will cover the energy range above what is practical using magnetic spectrometer techniques and will measure the differential energy of electrons from several to >10 MeV and ions from 10 to >100 MeV. The shape of the energy spectrum (and the existence of theorized upper energy cutoffs) will test acceleration processes.

Ion telescopes in MagEIS use silicon detectors to measure the differential fluxes, energies, and angular distributions of protons from ∼50 keV to ∼20 MeV, and helium and oxygen ions from a few hundred keV/nuc to a few MeV/nuc. Since the heavy solar ions are not stripped, and the charge state varies from event to event, the change in composition between the pre-existing seed and the newly trapped ions will be invaluable in understanding the injection process. The drift rate and thus resonance conditions should be charge-state dependent. Although MagEIS does not measure charge state, one can infer the charge state of newly injected helium and oxygen populations by observing the drift resonance periodicity and then comparing these ion populations from event to event and also from pre-event through event to learn about the efficiency of the injection and acceleration processes. ECT will make the best measurements to date of this important part of the distribution and will provide the radial and energy distributions of the pre-existing populations, the largest source of error in numerical models. Together the ECT instrument suite will make the measurements necessary to understand how prompt acceleration works, how it affects electrons and ions, how often it occurs, under what circumstances, and how it combines with other processes to create sudden changes in the space radiation environment. Because of the promptness of these acceleration processes, identical measurements on two spacecraft are critically needed in order to improve both spatial structure and temporal evolution.

ECT Closure on Science Objective #1, Question 4 Understanding the energy spectra, pitch angle distributions, and spatial/temporal characteristics of the relativistic electron source populations is as important for predictive understanding of the radiation belts as knowing the acceleration, transport, and loss processes. It reinforces the need for continuous, pitch angle-resolved differential energy coverage—particularly at lower energies. This science objective also benefits strongly from the associated observational and modeling tools of the ECT science team and in the community. Coordinated studies with the THEMIS mission (Angelopoulos 2008), at greater distances from the Earth, will allow us to characterize acceleration and transport of plasma sheet electrons into the inner magnetosphere.

- Science Objective #2: Determine the dominant mechanisms for relativistic electron loss

Relativistic electron losses occur both during strong geomagnetic activity and during quiet periods. The Solar, Anomalous, and Magnetospheric Particle Explorer (SAMPEX) spacecraft (Baker et al. 1993) observations showed that, even during quiet periods, there is a 'drizzle' of electrons into the loss cone that maintains fluxes at low altitude roughly proportional to trapped fluxes (Kanekal et al. 2001). It is, however, dramatic dropouts of relativistic electrons during active times that raise fundamental, unanswered questions. To accomplish the second objective, we will reach closure on two science questions:

Question 1 Where, when, and how are radiation belt electrons scattered into the atmospheric loss cone? (Mission priority #2)

Question 2 What is the contribution of magnetopause shadowing to relativistic electron loss? (Mission priority #2)

ECT Closure on Science Objective #2, Question 1 Missions such as SAMPEX have clarified how wave-particle interactions are the cause of the pitch angle scattering producing atmospheric precipitation and relativistic electron loss (Baker et al. 2007), but quantitative questions remain. Science closure on this topic relies heavily on correlated studies of Van Allen Probes wave observations with ECT measurements of electron and ion pitch angle distributions, and with other contemporaneously operating missions measuring precipitation at low altitudes (Li et al. 2013; Millan et al. 2013; Spence et al. 2012). Using the 2-spacecraft Van Allen Probes observations we will determine the duration of chorus, EMIC, and hiss emissions in a particular region of space and the temporal evolution of the pitch angle distributions as they interact with the waves. Using statistical studies we will determine the spatial and temporal relationships of wave fields and relativistic electron distributions as a function of L-shell, MLT, and activity. We will also determine plasma parameters that control wave growth and amplitude to develop predictive understanding of the magnitude and spatial extent of relativistic electron precipitation.

It is important to note that the RBSP-ECT instruments will not resolve the atmospheric loss cone at most L-shells. While this has been attempted on other spacecraft missions (e.g. POLAR) it was not a realistic use of Van Allen Probes resources. Regardless of the angular size of the loss cone, the loss cone fluxes are orders of magnitude lower than trapped fluxes. Both populations cannot be credibly measured by the same instrument. Fortunately, science closure in this area does not require resolving the loss cone. It requires measuring pitch angle distributions near the loss cone and the evolution of trapped pitch angle distributions that are the 'smoking gun' for pitch angle diffusion. The RBSP-ECT instruments were designed to measure distributions in the vicinity of the loss cone during quiet conditions and during active times when the field can be stretched into near horizontal orientations.

ECT Closure on Science Objective #2, Question 2 Because of their 5.8 R_E apogee, the Van Allen Probes satellites will only encounter the magnetopause when they are observing on the day side during strong magnetopause compressions. However, the Van Allen Probes satellites along with the LANL-GEO, GOES, THEMIS and other satellites can significantly improve our understanding of magnetopause losses. The ECT particle suite will measure the near-equatorial pitch angle distributions that particle drift paths depend upon critically. At the same time advanced numerical models provide global magnetic field configurations for test particle simulations for both magnetopause compressions and storm-time adiabatic changes. Models such as DREAM that use data assimilation and relativistic electron phase space density matching techniques (Chen et al. 2005; Reeves et al. 2012) are particularly powerful tools for combining the pitch angle and energy-resolved measurements from the ECT instruments with geosynchronous observations of magnetopause compressions. Accurate specification of phase space density and radial gradients will allow us to determine loss-related radial diffusion, parallel to studies of acceleration-related radial diffusion. The ECT observations will significantly advance the state-of-the-art specification and prediction of magnetopause losses.

- Science Objective #3: Determine how the inner magnetospheric plasma environment controls radiation belt transport, acceleration, and loss

We have discussed how the global magnetic field configuration has a direct effect on radiation belt structure. In addition, inner magnetosphere plasmas also affect belt structure and dynamics, even though those effects are often indirect. These lower energy populations are controlled not only by the magnetic field, but their drifts are also significantly controlled by the global convective electric fields which are measured on the Van Allen Probes by the

Electric Fields and Waves (EFW) instrument (Wygant et al. 2013). Consequently, to quantify the roles of the inner magnetospheric environment to radiation belt particle transport, acceleration, and loss, we also need to understand the processes that control this environment. To accomplish the third objective, we will reach closure on two science questions:

Question 1 How do we characterize/model adiabatic transport of radiation belt particles? (Mission priority #4)

Question 2 How do the global and local characteristics of plasma sheet and plasmaspheric populations control radiation belt structure, acceleration, and loss? (Mission priority #6 and 7)

ECT Closure on Science Objective #3, Question 1 As discussed in the GMDT report and other publications, specification of the storm-time ring current and changes to the global magnetic field are necessary to understand associated radiation belt changes. Ideally this would be done with energetic ion (H^+, He^+, O^+: $E > 50$ keV) measurements, plasma ion composition (H^+, He^+, O^+: $E < 50$ keV) measurements, energetic neutral atom (ENA) images (Jorgensen et al. 1997; 2001), and self-consistent ring current and magnetic field models. Thermal ($E < 50$ keV) and energetic ($E > 50$ keV) ions in the inner magnetosphere each carry about half the total plasma pressure (Spence et al. 1987); these pressure-bearing ions thereby control the magnetic field configuration. While Van Allen Probes' two-point data will be used to validate or act as input to global models, only models can provide the 3D magnetic field needed to track electron drift orbits.

Comprehensive spectral and pitch angle coverage of electrons and ions provided by RBSP-ECT and by RBSPICE, along with magnetometer measurements on the Van Allen Probes spacecraft, will be used to specify μ for locally-mirroring particles and as an input into global field models. Models such as DREAM will provide a data-driven, self-consistent, physical model of the storm-time field (Zaharia et al. 2006) and a basis for calculating adiabatic invariants.

We developed/validated a technique to test global fields using 2-satellite measurements similar to those of the Van Allen Probes mission (Chen et al. 2005). This procedure identifies times when non-collocated satellites measure electrons with the same invariants. At these times, phase space densities should be identical. Discrepancies indicate magnetic field errors. Combining detailed measurements, improved magnetic field models, and accuracy tests will produce an unprecedented dataset.

As with the current generation of models we will establish boundary conditions given by the Magnetospheric Plasma Analyzers (MPA) on the LANL geosynchronous satellites (e.g. Thomsen et al. 1998; Jordanova et al. 2003; Blum et al. 2009). Additionally, the HOPE instrument will provide ion composition measurements (at the same energies as MPA) currently unavailable to modelers. The RBSP-ECT science team plans to use global ENA images from the two TWINS satellites (McComas et al. 2009), expected to be operating concurrently with Van Allen Probes.

ECT Closure on Science Objective #3, Question 2 The RBSP-ECT particles suite, together with the Van Allen Probes fields and waves measurements and inner magnetosphere models, will provide the necessary elements, not only to understand the general interactions that control radiation belt processes, but also to understand and predict the net effect of those processes in a given relativistic electron event. We will measure the plasma distributions that are responsible for the growth and intensity of EMIC, chorus, and other VLF waves. Those measurements include electron phase space density gradients in the vicinity of the loss cone, plasma densities, ring current ion anisotropies, and the flux of H^+, H_E^+, and

O^+ions. We will use ECT particle measurements to both drive and validate global models of plasma sheet, ring current, and plasmasphere particles to determine their location and dynamics and therefore the regions where waves will be produced. In combination with the physical understanding gained from investigations of radiation belt acceleration and loss and with the specification of phase space densities as a function of magnetic invariants we will determine where, when, and how inner magnetosphere plasmas and waves control radiation belt structure and dynamics.

- Science Objective #4: Develop empirical and physical models for understanding and predicting radiation belt space weather effects

To accomplish the fourth objective, which is at the core of overall LWS program objectives, the RBSP-ECT science team will answer the following science question:

Question 1 How do we predict and model spatial, spectral, and temporal characteristics of radiation belt enhancements, over both long and short times? (Mission priority #8)

ECT Closure on Science Objective #4, Question 1 Empirical modeling conducted by the RBSP-ECT team will take a stepped approach, recognizing that different levels of model sophistication are required for different applications. While a statistical distribution of peak flux and integrated dose over a satellite orbit may be adequate for some applications, other applications require a more specific parameterization of flux levels at a given location based on solar wind and geomagnetic conditions. We will develop empirical models to provide statistical and probabilistic assessments of flux levels as a function of energy and location (radius, longitude, and latitude). We will also develop models that incorporate current solar wind and magnetospheric conditions, including estimates of wave intensities, diffusion rates, and magnetic field configuration (e.g., Huang et al. 2010a, 2010b). These empirical models will serve as accurate and easily useable tools to further understanding of the radiation belts, as well as provide information for a variety of LWS applications. These efforts will leverage ongoing team modeling strengths including related space weather efforts.

2 Science Requirements, Traceability, and Instrument Requirements

In Sect. 1 we identified four overarching RBSP-ECT science objectives, derived from the eight underlying mission priorities that ECT observations will address. Within each objective, we identified one or more science questions that the ECT suite provides closure on, often in concert with other Van Allen Probes measurements, related data sets whether in space or ground-based, and/or with leveraged modeling activities. Within each question, we identified key measurements required to provide closure and discussed how the resultant data analysis answers the science questions.

The RBSP-ECT Instrument Suite Traceability Matrix (see Figs. 4a, 4b) summarizes the Van Allen Probes mission science priorities and their mapping into our ECT measurement goals and science questions, as well as their flow down into science measurement objectives, and finally to instrument requirements. Figure 4c demonstrates in detail the mapping needed to go from the "science driven measurement requirements" (listed according to physical processes and plasma population) to the minimum-required "science driven instrument requirements."

The science flow "down" (left to right of Fig. 4a) culminates with the minimum instrument requirements necessary and sufficient to achieve RBSP-ECT science goals. As

Understand the acceleration, global distribution, and variability of energetic electrons and ions in the inner magnetosphere

Measurement Goals	Science Questions	Science Measurement Objectives	Instrument Requirements	HOPE	MagEIS	REPT
Determine the physical processes that produce radiation belt enhancement events (1, 3, 5)	What processes are responsible for radial transport and acceleration? (1)	Radial PSD distribution	Electron energy and pitch angle 20 keV to 4 MeV			
	Where, when, and how do local acceleration processes produce radiation belt acceleration? (1)	Radial PSD distribution, local PSD gradients, pitch angle distribution, plasma density, composition	Electron energy and pitch angle 10 keV to 4 MeV; plasma density, composition			
	How does "prompt acceleration" create new radiation belts? (3)	Radial PSD distribution, ultrarelativistic population, energetic particle composition	Electron energy and pitch angle 30 keV to >10 MeV; > few MeV/nucleon composition			
	How do plasma "seed" or source populations influence the characteristics of relativistic electron events? (5)	Radial PSD distribution before and after acceleration events	Electron energy and pitch angle 1 keV to few MeV			
Determine the dominant mechanisms for relativistic electron loss (2)	Where, when, and how are radiation belt electrons scattered into the atmospheric loss cone? (2)	Measure full electron energy-dependent pitch-angle distributions and intensities throughout outer zone regions	Electron energy and pitch angle 30 keV to 4 MeV			
	What is the contribution of magnetopause shadowing to relativistic electron loss? (2)	Measure full electron energy-dependent pitch-angle distributions and intensities throughout outer zone regions	Electron energy and pitch angle 30 keV to 4 MeV			
Determine how the inner magnetospheric plasma environment controls radiation belt transport, acceleration, and loss (4, 6, 7)	How do we characterize and model the adiabatic transport of radiation belt particles? (4)	Measure pitch-angle distribution of ions and electrons; energy density of ring current	Ions and electrons <200 keV; composition			
	How do the global and local characteristics of plasma sheet and plasmaspheric populations control radiation belt structure, acceleration, and loss? (6, 7)	Effects of ring current and plasmapause structure on the outer radiation belt	Ions and electrons <20 keV			
Develop empirical and physical models for understanding and predicting radiation belt space weather effects (8)	How do we predict and model the spatial, spectral and temporal characteristics of radiation belt enhancements over both long and short times? (8)	Radial PSD distribution over wide range of solar wind and geophysical input conditions	Electron and ion energy and pitch angle, few eV to 10's MeV			

(a)

Fig. 4 RBSP-ECT Traceability Matrix

	Measurement Goals	Additional RBSP measurements	Ancillary Data	Analysis Product	Science Results	RBSP Priorities 1	2	3	4	5	6	7	8
Understand the acceleration, global distribution, and variability of energetic electrons and ions in the inner magnetosphere	Determine the physical processes that produce radiation belt enhancement events (1, 3, 5)	ULF E, B	GOES, LANL, ground ULF, GPS	Statistical maps of electron PSD as functions of ULF wave power and impulsive variations	Determination of the mechanism(s) and understanding of the underlying physical processes responsible for relativistic electron acceleration during storms and high speed streams (1)	■			▒				
		AC E, B. N_e	GOES, LANL, GPS	Statistical maps of electron PSD as functions of local VLF wave power; detailed event analysis		■			▒				
		DC E, B	Solar wind, GOES	Spatial and temporal evolution of prompt electron acceleration	Comprehensive understanding of the prompt creation of inner zone radiation belts (3)			■	▒				
		DC E, B	GOES, LANL	Statistical model for the global distribution of seed population electrons; mapping of low energy source(s) to energize population(s)	Knowledge of the seed population influence on energization of electrons and wave excitation under varying conditions (5)					■	▒		
	Determine the dominant mechanisms for relativistic electron loss (2)	AC E, B. N_e	LEO precipitating flux	Average electron loss rates versus energy during storms for wave-induced pitch-angle scattering	Comprehensive precipitation/loss model reflecting relative importance of various proposed mechanisms (2)		■		▒				
		DC B	GOES, LANL, solar wind pressure	Disturbed time drift orbits			■						
	Determine how the inner magnetospheric plasma environment controls radiation belt transport, acceleration, and loss (4, 6, 7)	AC and DC E,B	ENA images, LANL	Magnetic perturbation due to ring current; others	Variation in particle drift orbits; adiabatic transport quantification (4)	▒	▒	▒	■	▒	■	■	
		AC and DC E,B	ENA and EUV images, LANL	Statistical maps of wave excitation by ring current injection	Effects of plasmapause and plasma conditions producing chorus and EMIC waves (6, 7)	▒	▒	▒	▒		■	■	
	Develop empirical and physical models for understanding and predicting radiation belt space weather effects (8)	AC and DC E, B	Solar wind, SDO, GOES, etc. as needed to provide context	Statistical maps of electron enhancements as functions of solar wind parameters	Abilitiy for any given event to determine: intensity, spectral hardness, and timescale of enhancement and longetivity (8)								■

(b)

Fig. 4 (*Continued*)

Science Driven Measurement Requirements		Science Driven Instrument Requirements											
		HOPE				MagEIS				REPT			
Process or Population	Energy Range	Energy Range	Energy Resolution (dE/E)	Temporal Resolution	Angular Resolution (degrees)	Energy Range	Energy Resolution (dE/E)	Temporal Resolution	Angular Resolution (degrees)	Energy Range	Energy Resolution (dE/E)	Temporal Resolution	Angular Resolution (degrees)
ULF waves, radial diffusion	e-: 10 keV to 10 MeV	e-: 10 to 50 keV	20%	30 s	40	e-: 20 keV to >4 MeV	30%	30 s	20	e-: > 2 MeV	40%	3 min	30
VLF waves (EMIC, Chorus, Hiss)	e-: 1 eV to 1 MeV p+: 1 ev to 1 MeV ions: <50 keV	e-: 1 eV to 50 keV p+: 1 ev to 50 keV ions: 1 eV to 50 keV	20%	e-: 12 s p+: 12 s ions: 5 min	40	e-: 20 keV to 1 MeV p+: 60 keV to >1 MeV	30%	30 s	20	-	-	-	-
Prompt acceleration	e-: 1 to >10 MeV p+: 20 to 100 MeV	-	-	-	-	e-: 1 MeV to >4 MeV p+: >1 MeV	30%	30 s	20	e-: 2 to >10 MeV p+: 20 to >100 MeV	40%	3 min	30
Adiabatic changes, ring current	e-: <200 keV p+: <200 keV ions: <50 keV	e-: <200 keV p+: <200 keV ions: <50 keV	20%	1 min	40	e-: <200 keV p+: <200 keV	50%	1 min	20	-	-	-	-
Plasmasphere	e-: <100 eV p+: <100 eV ions: <100 eV	e-: 1 eV to 20 keV p+: 1 eV to 20 keV ions: 1 eV to 20 keV	20%	e-: 1 min p+: 1 min ions: 5 min	40	-	-	-	-	-	-	-	-
Plasmasheet	e-: 1 to 100 keV p+: 1 to 100 keV	e-: 1 to 50 keV p+: 1 to 50 keV	20%	1 min	40	e-: 20 to 100 keV p+: 60 to 100 keV	50%	30 s	20	-	-	-	-
Radiation belts	e-: 100 keV to >10 MeV p+: 100 keV to >10 MeV	-	-	-	-	e-: 100 keV to 4 MeV p+: 100 keV to >1 MeV	30%	30 s	20	e-: >2 MeV p+: >20 MeV	40%	3 min	30
Minimum Requirements	**e-: 1 eV to >10 MeV p+: 1 ev to >100 MeV ions: 1 ev to 50 keV**	**e-: 1 eV to 50 keV p+: 1 ev to 50 keV ions: 1 eV to 50 keV**	**20%**	**e-: 12 s p+: 12 s ions: 5 min**	**40**	**e-: 20 keV to >4 MeV p+: 60 keV to >1 MeV**	**<50% / < 30%** <0.3 / >0.3 MeV	**30 s**	**20**	**e-: 2 to >10 MeV p+: 20 to >100 MeV**	**40%**	**3 min**	**30**

(c)

Fig. 4 (*Continued*)

RBSP Prioritized Science Objectives

1. Differentiating among competing processes affecting the acceleration and transport of radiation belt particles
2. Differentiating among competing processes affecting the precipitation and loss of radiation belt particles
3. Understanding the creation and decay of new radiation belts
4. Quantifying the relative contribution of adiabatic and nonadiabatic processes on energetic particles
5. Understanding the role of "seed" or source populations for relativistic particle events
6. Understanding the effects of rind current and other storm phenomena on radiation belt electrons and ions
7. Understanding how and why the ring current and associated phenomena vary during storms
8. Developing and validating specification models of the radiation belts for solar cycle time scales

(d)

Fig. 4 (*Continued*)

is clearly seen in Fig. 4c, the three ECT instruments (HOPE, MagEIS, and REPT) are designed to meet the critical science-driven instrument requirements in terms of species-dependent and energy-dependent overall energy ranges, energy resolutions, temporal resolutions, and pitch angle coverages. In the RBSP-ECT companion papers (Funsten et al. 2013; Blake et al. 2013; Baker et al. 2012), we describe all ECT instruments in great detail and show how the instrument requirements are met economically and efficiently as a suite. Color coding in the rightmost columns of Fig. 4a denotes the primary contribution of each instrument to achieving closure on RBSP-ECT science questions; green indicates a required measurement, yellow a desired measurement, and gray indicating that it is not required.

From the leftmost columns working toward the right, the science traceability matrix shows the flow "up" from the instruments back to science closure in Fig. 4b. To answer every RBSP-ECT question, additional Van Allen Probes measurements are identified. For each question, we identify ancillary measurements. We identify next in the matrix the key science analysis product that is responsive to each science question and which flows from the core ECT measurements combined with the other measurements. Finally, we outline the anticipated science result that follows from each analysis product, thereby demonstrating closure back to an initial science question. The final columns of Fig. 4b map the ECT science questions back into the eight Van Allen Probes mission priorities (defined in Fig. 4d). A black bar indicates primary association of the question(s) with the mission priority, gray a secondary association, and white indicating non-applicability.

2.1 Hope

The as-flown HOPE instrument performance (see Table 2 of Funsten et al. 2013) meets or exceeds the science measurement requirements developed in the traceability matrix.

The energy range (0.001 to 50 keV) follows directly from the science-measurement traceability matrix. Energy resolution is chosen to adequately resolve all known spectral features in these plasma populations based on previous measurements in the radiation belt, for instance those made by the LANL MPA and Polar HYDRA instruments. The angular coverage and resolution are needed to yield pitch angle distributions with accuracy sufficient to track the pitch angle evolution of plasmasheet electrons and ions (see discussion of Table 2 in Funsten et al. 2013). For plasmasphere ions full spatial coverage is more important than resolution. The time resolution is needed to resolve changes on substorm injection timescales

for plamasheet electrons; 5 min resolution for the plasma sheet is sufficient to resolve 0.2 R_E spatial regions. The instrument geometric factors are optimized to cover flux ranges representing the dynamic range of electron and total ion fluxes observed by Polar HYDRA (1 eV to 20 keV) in the region covered by the Van Allen Probes mission.

2.2 MagEIS

The as-flown MagEIS instrument performance (see Tables 1 and 2 of Blake et al. 2013) meets or exceeds the science measurement requirements developed in the traceability matrix. The MagEIS instruments cover three different particle populations: ring current electrons ($\sim$20 to a $\sim$200 keV) and radiation belt electrons ($>\sim$200 keV to $>$3 MeV); ring current protons and radiation beltprotons ($\sim$60 keV to $\sim$20 MeV); and energetic helium and oxygen ions from a few hundred keV/nucleon to a few MeV/nucleon. We stress that Van Allen Probes science closure will not be possible with instrumentation that lacks differential energy resolution across a broad range of energies. That is especially important in the domain of the relativistic electrons, where some techniques (i.e., solid state telescopes) have not observed important spectral features that only a magnetic spectrometer such as MagEIS can observe. The angular and temporal requirements for MagEIS follow from the same arguments mentioned previously for HOPE.

2.3 REPT

REPT provides measurements of the remaining two extreme energy populations needed for closure on ECT science objectives. As with HOPE and MagEIS, the as-flown REPT instrument performance (see Table 1 of Baker et al. 2012) meets or exceeds the science measurement requirements. REPT resolves protons of $\sim$17 MeV to $>$100 MeV and electrons between $\sim$1.6 MeV and to $>\sim$19 MeV, with a geometric factor optimized for the range of fluxes expected for these dynamic particle populations, and with a time cadence sufficient to resolve dynamical features.

3 ECT Suite Science Data Collection, Analysis, and Dissemination

In accordance with the Van Allen Probes mission data policy, the RBSP-ECT instrument team ensures that calibrated high-quality science-grade data, software tools, and related documentation are made available as a public resource to a wide range of end-users including guest investigators (GIs) and members of the space weather community. Our overall plan and timelines for achieving these goals are described in detail below. We anticipate that in many cases science closure on the questions discussed above may be achieved with RBSP-ECT data in studies led by scientists that are not part of the ECT science team.

3.1 ECT SOC (Science Operations Center) Overview

Figure 5 illustrates how the RBSP-ECT data flows from the spacecraft to the various end users. The JHU/APL-run Mission Operations Center (MOC) communicates with the spacecraft and provides command uplink and data downlink. In addition, Near Real Time (NRT) data feeds may also exist as a result of mission-level agreements with external downlink facility operators. The RBSP-ECT Science Operations Center (SOC) is split into two parts—the Command, Telemetry and Ground support part (CTG) and the Science data center part

Table 1 RBSP-ECT generated data products

Data level	Description	Available	Users
$L0$	Raw de-commutated telemetry data from MOC. $L0$ generated by SOC.	Minutes from receipt (Time = T_0)	SDC, Archives
$L1$	$L0$ + sorted, time-tagged, instrument separated, units of count rate	T_0 + <6 Hours	SDC, ECT team, Archives
$L2$	$L1$ + calibrated and corrected (bkg. dead-time, etc.), physical units	T_0 + <2 weeks	SDC, Co-Is, GIs, US & Intl scientific community, Other LWS Missions, Archives, Space weather users, Virtual Observatories
$L3$	$L2$ + B-field derived science products (pitch angles, moments)	T_0 + <2 months	
$L4$	$L3$ + PSD units derived using B-field models, magnetic coordinates	T_0 + <1 year	

(SDC). The SOC-CTG transmits instrument commands to the MOC and receives science data, state of health data, housekeeping data and ancillary data (S/C attitude, ephemeris, time offset and scale factor data) from the MOC. Science data would also be received from NRT downlink facilities. The SOC-CTG retrieves and archives these Level-0 ($L0$) data products and transmits them together with ancillary data to the SOC-SDC where higher-level products are generated and detailed data analysis, dissemination, and archiving occurs. Since both the SOC-CTG and SOC-SDC reside at Los Alamos National Laboratory (LANL), data processing is highly integrated and a number of resources are effectively and efficiently shared. The RBSP-ECT suite maintains a stripped-down fully redundant emergency SOC capability in a separate facility to ensure reliable failsafe operations.

The SOC-SDC creates higher-level data products (see Table 1) and makes them available for dissemination. Level-1 ($L1$) data products are raw instrument-specific, uncalibrated data files and are archived and made available to the ECT instrument teams. Level-2 data ($L2$) products (instrument-specific, calibrated, and validated data) are then generated at the SDC with feedback and validation from the suite instrument teams. Higher level analysis of the particle data requires knowledge of the magnetic field vector at each spacecraft and these data are obtained in a preliminary format directly from the EMFISIS Fields and Waves team SOC (quicklook product). Higher quality magnetic field data (EMFISIS level 2) subsequently flows into the SDC when they become available. Level-3 ($L3$) data are science data products based on these inputs (pitch angles, moments). To enable our science goals, data needs to be folded into adiabatic invariant space with the aid of magnetic field models (Level-4 or $L4$ products). The ECT SDC will also link to a number of other important and relevant ancillary datasets that will be accessible to the team and all interested users in a timely manner. These include the LANL geosynchronous and GPS particle datasets that are being made accessible as they become available. The team will make available the RBSP-ECT data together with these additional datasets via the SOC-SDC website (http://www.rbsp-ect.lanl.gov).

In addition, the ECT SOC has taken on a mission-wide responsibility of producing a set of value-added ephemeris files, called the "MagEphem" files. These files include the Van Allen Probes satellite position information together with magnetic field model derived coordinates that are useful for radiation belt analysis (such as L^* as a function of pitch angle). These files are produced one month ahead based on static field models and orbit predictions, and on dynamic field models once definite orbit files become available. The predict files are also used by the SOC-CTG to plan ahead orbit-specific commanding. All the MagEphem files are provided to the public on the ECT-SOC website.

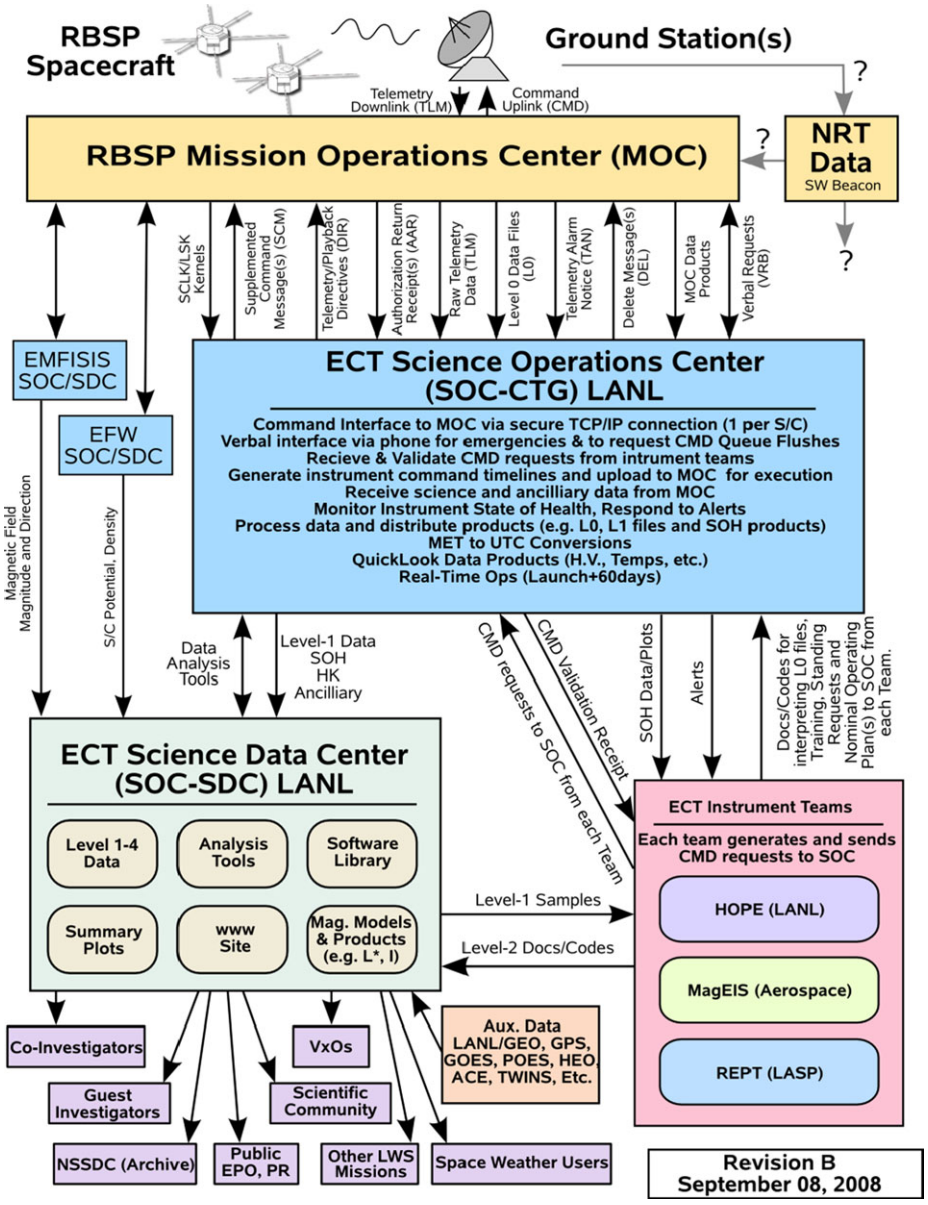

Fig. 5 ECT Data Flow Diagram

The SOC-SDC generates public-domain, science-quality data products available to various end-users in a timely manner: $L1$ data become available within hours of acquisition from the MOC; $L2$ data within two weeks; and, $L3$ data available no later than 2 months. $L4$ data is available within one year with early Phase-E priority given to intervals selected for community-wide investigation. Expected end-users include: RBSP-ECT co-investigators, Van Allen Probes investigator teams and guest investigators (GIs), the U.S. and interna-

tional scientific community, virtual observatories, space weather users, archive operators, E/PO partners and the public.

3.2 Science Operations Center Command, Telemetry and Ground Support (SOC-CTG)

The SOC-CTG operates in two modes—as an automated "Command Scheduler" for normal operations and as a GSEOS (Ground Support Equipment Operating Systems)-based interface for real-time activities. The Command Scheduler provides an easy interface to the three RBSP-ECT suite instrument teams, allowing them to submit command requests simply by email or via a secure SFTP site. The ECT-CTG translates the requests into simple commands, batch commands, or standing requests, uses the predict MagEphem files to schedule orbit specific requests (e.g. "execute at outbound $L = 3$ crossing") and manages the execution time requests and the limited on-board command buffers to ensure timely delivery of commands to each spacecraft. In this mode, all commands are time-tagged for a given execution time, uploaded on passes prior to that time and then executed at the target time—allowing commanding for times outside of spacecraft contact times.

The GSEOS interface is used for real-time commanding, only possible during actual spacecraft contact times. This mode was extensively used during instrument commissioning and is used for instrument code uploads and anomaly resolution tasks. The SOC-CTG uses the RBSP-ECT suite instruments team's existing GSEOS implementations from their laboratory development, which provided an integrated system for each team to access their instrument through the single ECT MOC connection provided.

3.3 Science Operations Center Science Data Center (SOC-SDC)

The primary function of the RBSP-ECT SOC-SDC is to provide scientific processing, analysis, dissemination, and archiving of the data. It is here that Level-1 and higher data products are generated and where a website exists to facilitate detailed scientific analysis and dissemination of these data. All data are provided in ISTP (International Solar Terrestrial Physics)-compliant CDF (Common Data Format; Goucher et al. 1994).

$L0$ science data files and ancillary data files are received from the SOC. $L1$ data are time-sorted and time-tagged in units of count rate. $L2$ data are corrected (background, dead-time, etc.), calibrated and converted into physically meaningful units and include robust numerical estimates of the statistical uncertainties. ECT data products up to $L2$ do not require input from other instruments and can therefore be disseminated quickly. Higher-level data products require the addition of magnetic field measurements and model-dependent assumptions. $L3$ data include pitch-angle sorted data and derived moments. $L4$ data will be highly validated data converted to phase-space density (PSD) with the aid of realistic global magnetic field models (e.g. Tsyganenko-type empirical models).

The MagEphem processing is also integrated into the SOC-SDC. The MagEphem files are produced using a LANL-developed software library, LANLGEOmag (see Morley et al. 2010), that has been extensively used and validated. This library can produce a large number of parameters and derived calculations utilizing a wide range of common and current magnetic field models, using as input satellite position derived from either three-line elements or a simple text file of x,y,z position data.

The SOC-SDC utilizes so called "QinDenton" files (Qin et al. 2007). These files are produced by the JHU/APL MOC team and contain a near real-time set of useful magnetospheric indices and parameters that are used as input for dynamic magnetic field models such as Tsyganenko and Sitnov (TS04) (Tsyganenko and Sitnov 2005); input parameters

include measurements such as $L1$ solar wind properties and geomagnetic indices (Kp and Dst). Apart from using these parameters as input to the MagEphem processing, enabling prompt production of MagEphem files with dynamic magnetic field models, the SOC-SDC also makes them available to the broad scientific community through the RBSP-ECT SOC website.

The RBSP-ECT SOC website also provides an on-line repository for the ECT data products, end-user documentation, and data analysis software. High-quality pre-defined summary plots are generated at the SDC and made available via an efficient web-based browsing tool (Autoplot, www.autoplot.org). Software, documentation and data products served to end-users via the SDC are maintained under strict version control for quality control. This is accomplished with a version control system (e.g., Git; Loeliger and McCullough 2012) and definition and adherence to strict file-naming conventions through an advanced database-driven processing chain. Information on the "providence" of each file (the data inputs, software used and their version) is maintained in a hierarchical SQL (Structured Query Language)-lite data base (Date and Darwen 1997), allowing for the full reconstruction of how each version of a given data product was produced. Code updates, data input updates automatically trigger reprocessing and version number increments.

3.4 Ancillary Data Sets

These data consist of anticipated coincident inner magnetospheric energetic particle datasets, solar wind data and publicly available ground-based resources (e.g. indices). The SDC provides convenient web-based portals also to these ancillary data.

3.5 Data Validation

Primary data validation is the responsibility of the respective RBSP-ECT instrument teams and occurs during the $L2$ generation phase in the two-week period before public release. All $L2$ data and plots are marked "preliminary" until checked and cleared by the SOC-SDC lead. Secondary data validation involves the on-orbit cross-calibration of data between the Van Allen Probes spacecraft and auxiliary datasets. Proper inter-calibration of the two spacecraft is required in order to achieve closure on several of the mission scientific objectives (e.g. goals that require determination of PSD gradients).

3.6 Data Archiving

The RBSP-ECT SOC archives raw telemetry, $L0$, and ancillary files. The SDC archive $L1$ and higher data products. Data, software and documentation generated and stored at the SDC will be prepared for archiving at a site and in a format determined by NASA. $L0$ to $L3$ datasets will be available for archiving within 2 months of data acquisition and $L4$ products within 1 year. Routine local archival operations at LANL will include migration of the datasets to a near-line mass storage facility. Following the mission prime phase, an additional year will be used to complete deep-archiving operations. LANL will also provide a long-term resident archive of the full datasets.

4 Early On-Orbit Performance

The Van Allen Probes spacecraft launched into their nominal orbits at approximately 4 AM local time on 30 August 2012 from NASA's Kennedy Space Center complex. In order to

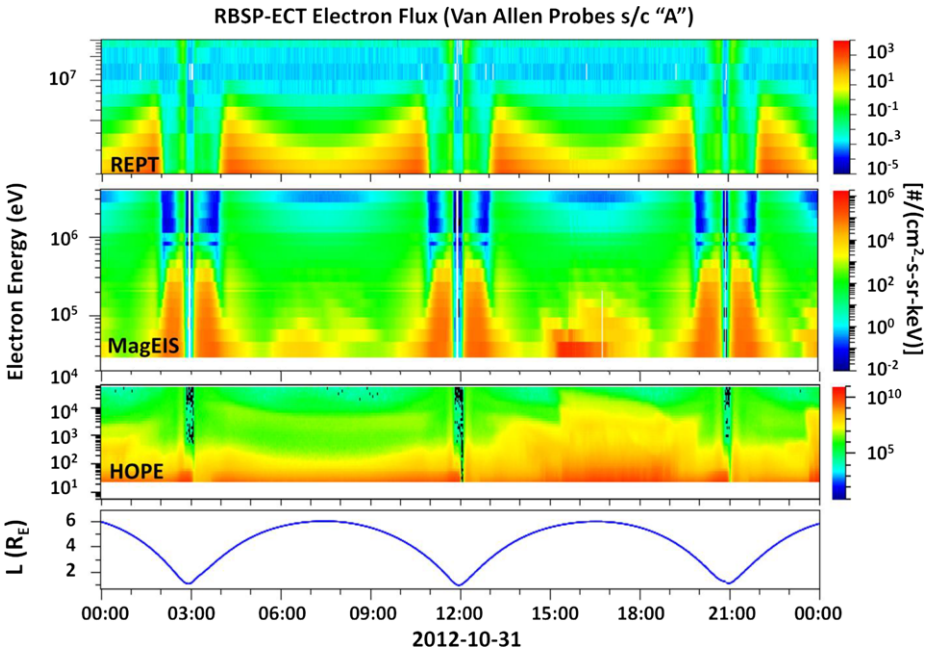

Fig. 6 Early Phase E RBSP-ECT electron energy-time color spectrograms through 2+ orbits on 31 October 2012. Three successive perigee passes of Van Allen Probes spacecraft "A" are seen at 3 UT, ∼12 UT, and ∼21 UT; intervening apogee traversals occur at ∼730 UT and ∼1630 UT. HOPE covers the lowest electron energies (*lower panel*), MagEIS the intermediate energies (*middle panel*), and REPT the highest energies (*top panel*)

maximize overlap in time with the SAMPEX mission, whose orbit was rapidly deteriorating at that time, the two REPT instruments were turned on early during commissioning on 1 and 2 September 2012. The eight MagEIS instruments were powered on starting on 6 September 2012 and the two HOPE instruments were powered on 3 October 2012. The commissioning of the ECT suite ran smoothly, instrument modes were successfully exercised, look-up tables were assessed and adjusted as necessary, and instrument health was monitored. At the end of the 60-day commissioning, 28 October 2012 which also heralded the beginning of the mission Phase E (science), the ECT suite instrument performance met or exceeded the as-delivered performance, which in turn exceeded all mission measurement requirements.

During subsequent months since the beginning of Phase E, instrument settings have been monitored and adjusted to optimize science performance. A record of such changes is tracked and made available through the RBSP-ECT SOC. Preliminary inflight cross-calibration suggests that the ground-level calibrations are very well understood (as detailed in the individual instrument papers in this special issue). Ongoing cross-calibration continues between HOPE and MagEIS, within the MagEIS units, between MagEIS and REPT, and then across the two Van Allen Probes spacecraft. In addition, important cross-calibrations are also underway with REPT and RPS, RBSPICE with both HOPE and MagEIS, and derived plasma properties of HOPE with derived plasma properties from the fields instruments. These cross-calibrations will continuously improve the quality of our observations, which will be documented by the RBSP-ECT SOC, and will form the basis of several upcoming publications.

An example of the comprehensive ECT electron energy-time spectrograms from early Phase E operations is shown in Fig. 6. The bottom (middle, top) panel shows electrons as measured by HOPE (MagEIS, REPT) on 31 October 2012, all on Van Allen Probes spacecraft "A". Perigee passes appear as deep reductions in electrons of all energies at ∼3 UT, ∼12 UT, and ∼21 UT. Intervening apogee passages occur at ∼630 and ∼1730 UT. Figure 6 demonstrates several aspects of the comprehensive ECT electron data: outstanding background rejection from the full range of measurements (∼25 eV to ∼10's MeV); overlapping energy coverage by the three instrument types; and with sufficient energy resolution to study the spatial structure and dynamic evolution of electrons throughout the radiation belts, ring current, and plasmasphere. We note that Fig. 6 shows HOPE performance down to 25 eV but the instrument has capability (not shown) down to a few eV (Funsten et al. 2013), the latter being practically limited by spacecraft potential. Similar measurement capabilities (not shown here) span the ion populations, as well. The high quality of the on-orbit ECT charged particle measurements (electrons, protons, and major ions), both in terms of energy and pitch angle, assures the availability of observations needed to reach science closure on the outstanding questions and science objectives discussed above.

In fact, even though the mission is merely months into Phase E, compelling science progress has already occurred using RBSP-ECT observations. Highlights include: the discovery of a dynamic energetic electron "storage ring" (Baker et al. 2013), demonstrating the remarkable capabilities of the RBSP-ECT measurements and the transformational understanding of how the radiations belts can become so exquisitely structured; the related use of theory and complementary observations to demonstrate convincingly that hiss explains the subsequent intensity and pitch angle evolution of these storage ring particles (Thorne et al. 2013); and finally, we have witnessed strong and compelling evidence that a local wave-particle acceleration process led to the prompt recreating of the outer zone electrons that had previously been wiped out by a powerful belt-emptying process (Reeves et al. 2013). These three highlights alone build high confidence that the RBSP-ECT measurements are already fulfilling and will achieve their full promise to answer the key science questions we have posed, as well as lead to exciting and new scientific discoveries that were unimagined before the mission commenced.

Acknowledgements We gratefully acknowledge the Van Allen Probes mission team at the Johns Hopkins University (JHU)/Applied Physics Laboratory (APL) and the Project Science team at JHU/APL, NASA GSFC, and NASA HQ for their invaluable support during the design, development, testing, and early operations of the mission. This work was supported by RBSP-ECT funding provided by JHU/APL Contract No. 967399 under NASA's Prime Contract No. NAS5-01072.

References

V. Angelopoulos, The THEMIS mission. Space Sci. Rev. (2008). doi:10.1007/s11214-008-9336-1

D.N. Baker, G.M. Mason, O. Figueroa, G. Colon, J. Watzin, R. Aleman, An overview of the SAMPEX mission. IEEE Trans. Geosci. Electron. **31**, 531 (1993)

D.N. Baker, J.B. Blake, L.B. Callis, J.R. Cummings, D. Hovestadt, S. Kanekal, B. Klecker, R.A. Mewaldt, R.D. Zwickl, Relativistic electron acceleration and decay time scales in the inner and outer radiation belts. Geophys. Res. Lett. **21**, 409 (1994)

D.N. Baker, T. Pulkinnen, X. Li, S.G. Kanekal, J.B. Blake, R.S. Selesnik, M.G. Henderson, G.D. Reeves, H.E. Spence, Coronal mass ejections, magnetic clouds, and relativistic magnetospheric electron events: ISTP. J. Geophys. Res. **103**, 17279 (1998)

D.N. Baker et al., Low-altitude measurements of 2–6 MeV electron trapping lifetimes at $1.5 \leq l \leq 2.5$. Geophys. Res. Lett. **34**, L20110 (2007)

D.N. Baker, S.G. Kanekal, V.C. Hoxie, S. Batiste, M. Bolton, X. Li, S.R. Elkington, S. Monk, R. Reukauf, S. Steg, J. Westfall, C. Belting, B. Bolton, D. Braun, B. Cervelli, K. Hubbell, M. Kien, S. Knappmiller, S. Wade, B. Lamprecht, K. Stevens, J. Wallace, A. Yehle, H.E. Spence, R. Friedel, The relativistic electron-proton telescope (REPT) instrument on board the radiation belt storm probes (RBSP) spacecraft: characterization of earth's radiation belt high-energy particle populations. Space Sci. Rev. (2012). doi:10.1007/s11214-012-9950-9

D.N. Baker, S.G. Kanekal, V.C. Hoxie, M.G. Henderson, X. Li, H.E. Spence, S.R. Elkington, R.H. Friedel, J. Goldstein, M.K. Hudson, G.D. Reeves, R.M. Thorne, C.A. Kletzing, S.G. Claudepierre, A long-lived relativistic electron storage ring embedded in earth's outer van Allen belt. Science (2013). doi:10.1126/science.1233518

J.B. Blake, W.A. Kolasinski, R.W. Fillius, E.G. Mullen, Injection of electrons and protons with energies of tens of MeV into $L < 3$ on 24 March 1991. Geophys. Res. Lett. **19**, 821 (1992)

J.B. Blake, P.A. Carranza, S.G. Claudepierre, J.H. Clemmons, W.R. Crain, Y. Dotan, J.F. Fennell, F.H. Fuentes, R.M. Galvan, J.S. George, M.G. Henderson, M. Lalic, A.Y. Lin, M.D. Looper, D.J. Mabry, J.E. Mazur, B. McCarthy, C.Q. Nguyen, T.P. O'Brien, M.A. Perez, M.T. Redding, J.L. Roeder, D.J. Salvaggio, G.A. Sorensen, H.E. Spence, S. Yi, M.P. Zakrzewski, The magnetic electron ion spectrometer (MagEIS) instruments aboard the radiation belt storm probes (RBSP) spacecraft. Space Sci. Rev. (2013). doi:10.1007/s11214-013-9991-8

L.W. Blum, E.A. McDonald, S.P. Gary, M.F. Thomsen, H.E. Spence, Ion observations from geosynchronous orbit as a proxy for ion cyclotron wave growth during storm times. J. Geophys. Res. **114** (2009). doi:10.1029/2009JA014396

Y. Chen, R.H.W. Friedel, G.D. Reeves, T.G. Onsager, M.F. Thomsen, Multi-satellite determination of the relativistic electron phase space density at geosynchronous orbit. I. Methodology and initial results during geomagnetic quiet times. J. Geophys. Res. **110**, A10210 (2005). doi:10.1029/2004JA010895

C.J. Date, H. Darwen, *A Guide to the SQL Standard: a Users Guide to the Standard Database Language SQL*, 4th edn. (Addison Wesley, Reading, 1997). ISBN 978-0-201-96426-4

H.O. Funsten, R.M. Skoug, A.A. Guthrie, J.R. Baldonado, R.W. Harper, K.C. Henderson, K.H. Kihara, J.E. Lake, B.A. Larsen, E.A. MacDonald, A.D. Puckett, V.J. Vigil, R.H. Friedel, M.G. Henderson, J.T. Niehof, G.D. Reeves, M.F. Thomsen, J.-M. Jahn, J. Hanley, D. George, M. Ferris, G. Dunn, M. Freeman, C. Urdiales, A. De Los Santos, C. Nunez, M. Maple, W. Toczynski, T. Taylor, S. Cortinas, E. Edlund, H.E. Spence, J. Cravens, S. Smith, L. Suther (eds.), Helium, Oxygen, Proton, and Electron (HOPE) Mass Spectrometer for the radiation belt storm probes mission. Space Sci. Rev. (2013). doi:10.1007/s11214-013-9968-7

G.W. Goucher, J. Love, H. Leckner, A discipline-independent scientific data management package—the national space science data center's (NSSDC) common data format (CDF), in *Proceedings of the 1992 STEP Symposium/5th COSPAR Colloquium*, Applied Physics Laboratory, Laurel, Maryland, February (1994)

J.C. Green, M.G. Kivelson, Relativistic electrons in the outer radiation belt: differentiating between acceleration mechanisms. J. Geophys. Res. **109** (2004). doi:10.1029/2003JA010153

R.B. Horne, R.M. Thorne, S.A. Glauert, J.M. Albert, N.P. Meredith, R.R. Anderson, Timescale for radiation belt electron acceleration by whistler mode chorus waves. J. Geophys. Res. **110**, A03225 (2005). doi:10.1029/2004JA010811

C.-L. Huang, H.E. Spence, H.J. Singer, W.J. Hughes, Modeling radiation belt radial diffusion in ULF wave fields. 1. Quantifying ULF waves at geosynchronous orbit in data and model. Journal of Geophysical Research **115** (2010a). doi:10.1029/2009JA014917

C.-L. Huang, H.E. Spence, M.K. Hudson, S. Elkington, Modeling radiation belt radial diffusion in ULF wave fields. 2. Estimation of radial diffusion coefficient using combined MHD and particle codes. J. Geophys. Res. (2010b). doi:10.1029/2009JA014918

V.K. Jordanova, C.J. Farrugia, R.M. Thorne, G.V. Khazanov, G.D. Reeves, M.F. Thomsen, Modeling ring current proton precipitation by EMIC waves during the May 14–16, 1997, storm. J. Geophys. Res. **106**, 7–22 (2001)

V.K. Jordanova, L.M. Kistler, M.F. Thomsen, C.G. Mouikis, Effects of plasma sheet variability on the fast initial ring current decay. Geophys. Res. Lett. **30**(6), 1311 (2003). doi:10.1029/2002GL016576

V.K. Jordanova, Y.S. Miyoshi, S. Zaharia, M.F. Thomsen, G.D. Reeves, D.S. Evans, C.G. Mouikis, J.F. Fennell, Kinetic simulations of ring current evolution during the geospace environment modeling challenge events. J. Geophys. Res. **111**, A11S10 (2006). doi:10.1029/2006JA011644

A.M. Jorgensen, H.E. Spence, M.G. Henderson, G.D. Reeves, M. Sugiura, T. Kamei, Global energetic neutral atom (ENA) measurements and their association with the Dst index. Geophys. Res. Lett. **24**, 3173 (1997)

A.M. Jorgensen, M.G. Henderson, E.C. Roelof, G.D. Reeves, H.E. Spence, Charge exchange contribution to the decay of the ring current, measured by energetic neutral atoms. J. Geophys. Res. **106**, 1931 (2001)

S.G. Kanekal, D.N. Baker, J.B. Blake, Multisatellite measurement of relativistic electrons: global coherence. J. Geophys. Res. **106**, 29721 (2001)

P.M. Kintner, R.S. Lebair, R.A. Hoffman, S. Basu, J.F. Fennell, T.J. Fuller-Rowell, G.A. Germany, G.P. Ginet, M.J. Golightly, R.A. Heelis, M.K. Hudson, R.R. Meier, D.J. Mitchell, R.F. Pfaff, G.D. Reeves, R.M. Robinson, R.W. Shunk, H.J. Singer, J.J. Sojka, R.M. Thorne, R.A. Wolf, J.R. Wygant, W.S. Lewis, The LWS geospace storm investigations: exploring the extremes of space weather, living with a star. Geospace Mission definition team report, NASA/TM–2002–NASA/TM-211613 (2002)

C.A. Kletzing, W.S. Kurth, M. Acuna, R.J. MacDowall, R.B. Torbert, T. Averkamp, D. Bodet, S.R. Bounds, M. Chutter, J. Connerney, D. Crawford, J.S. Dolan, R. Dvorsky, G.B. Hospodarsky, J. Howard, V. Jordanova, R.A. Johnson, D.L. Kirchner, B. Mokrzyki, G. Needell, J. Odom, D. Mark, R. Pfaff Jr., J.R. Phillips, C.W. Piker, S.L. Remington, D. Rowland, O. Santolik, R. Schurr, D. Sheppard, C.W. Smith, R.M. Thorne, J. Tyler, The electric and magnetic field instrument suite and integrated science (EMFISIS) on RBSP. Space Sci. Rev. (2013). doi:10.1007/s11214-013-9993-6

X. Li, S. Palo, R. Kohnert, L. Blum, D. Gerhardt, Q. Schiller, S. Califf, Small mission accomplished by students—big impact on space weather research. Space Weather J. (2013). doi:10.1002/swe.20025

J. Loeliger, M. McCullough, *Version Control with Git*, 2nd edn. (O'Reilly, Farnham, 2012). ISBN 978-1-4493-1638-9

I.R. Mann, D.K. Milling, I.J. Rae, L.G. Ozeke, A. Kale, Z.C. Kale, K.R. Murphy, A. Parent, M. Usanova, D. Pahud, E.-A. Lee, V. Angelopoulos, C.T. Russell, H.J. Singer, The upgraded CARISMA magnetometer array in the THEMIS era. Space Sci. Rev. **141**, 413–451 (2008). doi:10.1007/s11214-008-9457-6

G.M. Mason et al., Report on the living with a star (LWS). Science Architecture Team, NASA Headquarters, July 16–18 (2001)

J. Mazur, L. Friesen, A. Lin, D. Mabry, N. Katz, Y. Dotan, J. George, J.B. Blake, M. Looper, M. Redding, T.P. O'Brien, J. Cha, A. Birkitt, P. Carranza, M. Lalic, F. Fuentes, R. Galvan, M. McNab, The relativistic proton spectrometer (RPS) for the radiation belt storm probes mission. Space Sci. Rev. (2012). doi:10.1007/s11214-012-9926-9

K.L. McAdams, G.D. Reeves, R.H.W. Friedel, T.E. Cayton, Multi-satellite comparisons of the radiation belt response to the GEM magnetic storms. J. Geophys. Res. **106**, 10869 (2001)

D. McComas, F. Allegrini, J. Baldonado, B. Blake, P. Brandt, J. Burch, J. Clemmons, W. Crain, R. Delapp DeMajistre, D. Everett, H. Fahr, L. Friesen, H. Funsten, J. Goldstein, M. Gruntman, R. Harbaugh, R. Harper, H. Henkel, C. Holmlund, G. Lay, D. Mabry, D. Mitchell, U. Nass, C. Pollock, S. Pope, M. Reno, S. Ritzau, E. Roelof, E. Scime, M. Sivjee, R. Skoug, T.S. Sotirelis, M. Thomsen, C. Urdiales, P. Valek, K. Viherkanto, S. Weidner, T. Ylikorpi, M. Young, J. Zoennchen, The two wide-angle imaging neutral-atom spectrometers (TWINS) NASA mission-of opportunity. Space Sci. Rev. (2009). doi:10.1007/s11214-008-9467-4

R.M. Millan, M.P. McCarthy, J.G. Sample, D.M. Smith, L.D. Thompson, D.G. McGaw, L.A. Woodger, J.G. Hewitt, M.D. Comess, K.B. Yando, A.X. Liang, B.A. Anderson, N.R. Knezek, W.Z. Rexroad, J.M. Scheiman, G.S. Bowers, A.J. Halford, A.B. Collier, M.A. Clilvert, R.P. Lin, M.K. Hudson, The balloon array for RBSP relativistic electron losses (BARREL). Space Sci. Rev. (2013). doi:10.1007/s11214-013-9971-z

D.G. Mitchell, L.J. Lanzerotti, C.K. Kim, M. Stokes, G. Ho, S. Cooper, A. Ukhorskiy, J.W. Manweiler, J. Jaskulek, D.K. Haggerty, P. Brandt, M. Sitnov, K. Keika, J.R. Hayes, L.E. Brown, R.S. Gurnee, J.C. Hutcheson, K.S. Nelson, N. Paschalidis, E. Rossano, S. Kerem, Radiation belt storm probes ion composition experiment (RBSPICE). Space Sci. Rev. (2013). doi:10.1007/s11214-013-9965-x

S.K. Morley, D.T. Welling, J. Koller, B.A. Larsen, M.G. Henderson, J. Niehof, SpacePy—a python-based library of tools for the space sciences, in *Proceedings of the 9th Python in Science Conference (SciPy 2010)*, ed. by S. van der Walt, J. Millman (2010), pp. 39–45

Z. Qin, R.E. Denton, N.A. Tsyganenko, S. Wolf, Solar wind parameters for magnetospheric magnetic field modeling. Space Weather **5**, S11003 (2007). doi:10.1029/2006SW000296

G.D. Reeves, Relativistic electrons and magnetic storms: 1992–1995. Geophys. Res. Lett. **25**, 1817 (1998)

G.D. Reeves, K.L. McAdams, R.H.W. Friedel, T.P. O'Brien, Acceleration and loss of relativistic electrons during geomagnetic storms. Geophys. Res. Lett. **30**(10), 1529 (2003). doi:10.1029/2002GL016513

G.D. Reeves, Y. Chen, G.S. Cunningham, R.W.H. Friedel, M.G. Henderson, V.K. Jordanova, J. Koller, S.K. Morley, M.F. Thomsen, S. Zaharia, Dynamic radiation environment assimilation model: DREAM. Space Weather **10**, S03006 (2012). doi:10.1029/2011sw000729

G.D. Reeves, H.E. Spence, M.G. Henderson, R.H.W. Friedel, H.O. Funsten, D.N. Baker, S.G. Kanekal, J.B. Blake, J.F. Fennell, S.G. Claudepierre, R.M. Thorne, D.L. Turner, C.A. Kletzing, W.S. Kurth, B.A. Larsen, J.T. Niehof, S.K. Morley, Electron acceleration in the heart of the Van Allen radiation belts, Science (submitted and under review) (2013)

M. Schulz, L.J. Lanzerotti, *Particle Diffusion in the Radiation Belts* (Springer, New York, 1974)
R.S. Selesnick, J.B. Blake, Dynamics of the outer radiation belt. Geophys. Res. Lett. **24**, 1347–1350 (1997)
H.E. Spence, M.G. Kivelson, R.J. Walker, Static magnetic field models consistent with nearly isotropic plasma pressure. Geophys. Res. Lett. **14**, 872 (1987)
H.E. Spence, J.B. Blake, A.B. Crew, S. Driscoll, D.M. Klumpar, B.A. Larsen, J. Legere, S. Longworth, E. Mosleh, T.P. O'Brien, S. Smith, L. Springer, M. Widholm, Focusing on size and energy dependence of electron microbursts from the Van Allen radiation belts. Space Weather **10**, S11004 (2012). doi:10.1029/2012SW000869
M.F. Thomsen, J.E. Borovsky, D.J. McComas, M.R. Collier, Variability of the ring current source population. Geophys. Res. Lett. **25**, 3481–3484 (1998)
R.M. Thorne, W. Li, B. Ni, Q. Ma, J. Bortnik, D.N. Baker, H.E. Spence, G.D. Reeves, M.G. Henderson, C.A. Kletzing, W.S. Kurth, G.B. Hospodarsky, D. Turner, V. Angelopoulos, Evolution and slow decay of an unusual narrow ring of relativistic electrons near $L \sim 3.2$ following the September 2012 magnetic storm. Geophys. Res. Lett. (submitted and under review) (2013)
N.A. Tsyganenko, M.I. Sitnov, Modeling the dynamics of the inner magnetosphere during strong geomagnetic storms. J. Geophys. Res. **110**, A03208 (2005). doi:10.1029/2004JA010798
J. Wygant et al., EFW. Space Sci. Rev. (under review) (2013, this issue)
S. Zaharia, V.K. Jordanova, M.F. Thomsen, G.D. Reeves, Self-consistent modeling of magnetic fields and plasmas in the inner magnetosphere: application to a geomagnetic storm. J. Geophys. Res. **111**, A11 (2006). doi:10.1029/2006ja011619

DOI 10.1007/978-1-4899-7433-4_11
Reprinted from *Space Science Reviews* Journal, DOI 10.1007/s11214-012-9950-9

The Relativistic Electron-Proton Telescope (REPT) Instrument on Board the Radiation Belt Storm Probes (RBSP) Spacecraft: Characterization of Earth's Radiation Belt High-Energy Particle Populations

D.N. Baker · S.G. Kanekal · V.C. Hoxie · S. Batiste · M. Bolton · X. Li · S.R. Elkington · S. Monk · R. Reukauf · S. Steg · J. Westfall · C. Belting · B. Bolton · D. Braun · B. Cervelli · K. Hubbell · M. Kien · S. Knappmiller · S. Wade · B. Lamprecht · K. Stevens · J. Wallace · A. Yehle · H.E. Spence · R. Friedel

Received: 12 April 2012 / Accepted: 9 October 2012 / Published online: 14 December 2012

Abstract Particle acceleration and loss in the million electron Volt (MeV) energy range (and above) is the least understood aspect of radiation belt science. In order to measure cleanly and separately both the energetic electron and energetic proton components, there is a need for a carefully designed detector system. The Relativistic Electron-Proton Telescope (REPT) on board the Radiation Belt Storm Probe (RBSP) pair of spacecraft consists of a stack of high-performance silicon solid-state detectors in a telescope configuration, a collimation aperture, and a thick case surrounding the detector stack to shield the sensors from penetrating radiation and bremsstrahlung. The instrument points perpendicular to the spin axis of the spacecraft and measures high-energy electrons (up to ∼20 MeV) with excellent sensitivity and also measures magnetospheric and solar protons to energies well above

D.N. Baker (✉) · V.C. Hoxie · S. Batiste · M. Bolton · X. Li · S.R. Elkington · S. Monk · R. Reukauf · S. Steg · J. Westfall · C. Belting · D. Braun · B. Cervelli · K. Hubbell · M. Kien · S. Knappmiller · S. Wade · B. Lamprecht · J. Wallace · A. Yehle
Laboratory for Atmospheric and Space Physics, 3665 Discovery Drive, Boulder, CO 80303-7820, USA
e-mail: daniel.baker@lasp.colorado.edu

S.G. Kanekal
Goddard Space Flight Center, Greenbelt, MD 20771, USA

B. Bolton
Ball Aerospace, 1600 Commerce Street, Boulder, CO 80301, USA

K. Stevens
Efficient Logic Designs, 2260 Floral Drive, Boulder, CO 80304, USA

H.E. Spence
Center for Earth, Oceans, and Space, University of New Hampshire, Durham, NH 03824, USA

R. Friedel
Los Alamos National Laboratory, PO Box 1663, Los Alamos, NM 87545, USA

$E = 100$ MeV. The instrument has a large geometric factor ($g = 0.2$ cm^2 sr) to get reasonable count rates (above background) at the higher energies and yet will not saturate at the lower energy ranges. There must be fast enough electronics to avert undue dead-time limitations and chance coincidence effects. The key goal for the REPT design is to measure the directional electron intensities (in the range 10^{-2}–10^6 particles/cm^2 s sr MeV) and energy spectra ($\Delta E/E \sim 25$ %) throughout the slot and outer radiation belt region. Present simulations and detailed laboratory calibrations show that an excellent design has been attained for the RBSP needs. We describe the engineering design, operational approaches, science objectives, and planned data products for REPT.

Keywords Radiation detection · Particle sensors · Radiation belts · Space weather

1 Introduction

The existence of Earth's radiation belts was established in 1958 by James A. Van Allen and co-workers using a simple Geiger counter system on board the Explorer 1 and Explorer 3 spacecraft missions. Since that time, many NASA satellites, combined with observations from other space-based platforms, have provided insight into the phenomenology and range of processes active in the Van Allen belts. A watershed event occurred in 1990–1991 when CRRES (Combined Radiation and Release Effects Satellite) was placed in a near-equatorial, geosynchronous transfer orbit with the express purpose of understanding the effects of the space radiation environment (Johnson and Kierein 1992). CRRES was well instrumented for understanding the nature of the energetic particles and fields in the inner magnetosphere, and observations from CRRES suggested a range of processes acting in the Van Allen belts that obviously were not well understood at that time.

As shown in Fig. 1, researchers were surprised when on Orbit 588 (24 March 1991), there suddenly (on time scales <1 min) appeared very high fluxes of trapped electrons extending in energy up to at least 15 MeV. A solar-driven shock wave had impacted the Earth's magnetosphere and had suddenly produced a new radiation belt deep within the pre-existing confines of the terrestrial magnetic field. This was a pivotal moment in radiation belt science (Blake et al. 1992). The results obtained from the CRRES mission were limited by the single-point nature of the measurements and by the ∼10-hour orbital period which did not allow the spacecraft to view the global evolution of the belts on shorter time scales. Unfortunately, CRRES was lost 14 months into a planned 3-year mission as a result of a battery failure.

Apart from CRRES observations in its geostationary transfer orbit, continuous long-term monitoring of the energetic particle environment at geosynchronous orbit (geocentric radial distant $r = 6.6R_E$) has been accomplished over many years via the NOAA Geostationary Orbit Environmental Satellite (GOES) series of spacecraft (http://www.oso.noaa.gov/goesstatus), as well as through particle detectors on board other geostationary orbit spacecraft (e.g., Baker et al. 1981) instrumented by Los Alamos National Laboratory (LANL). The measurements available from these platforms on the fringes of the outer radiation belt have typically offered only limited energy and time resolution, allowing partial inferences about the evolving energy spectrum and spatial extent of the belts. However, neither the GOES nor the LANL spacecraft measure the electric fields driving particle energization in the magnetosphere, and neither set of platforms is capable of providing information about the radiation environment at radial distances $<6.6R_E$.

Inside geosynchronous orbit, the available measurements near the magnetic equator have been very sparse. Measurements are available from some of the spacecraft comprising the

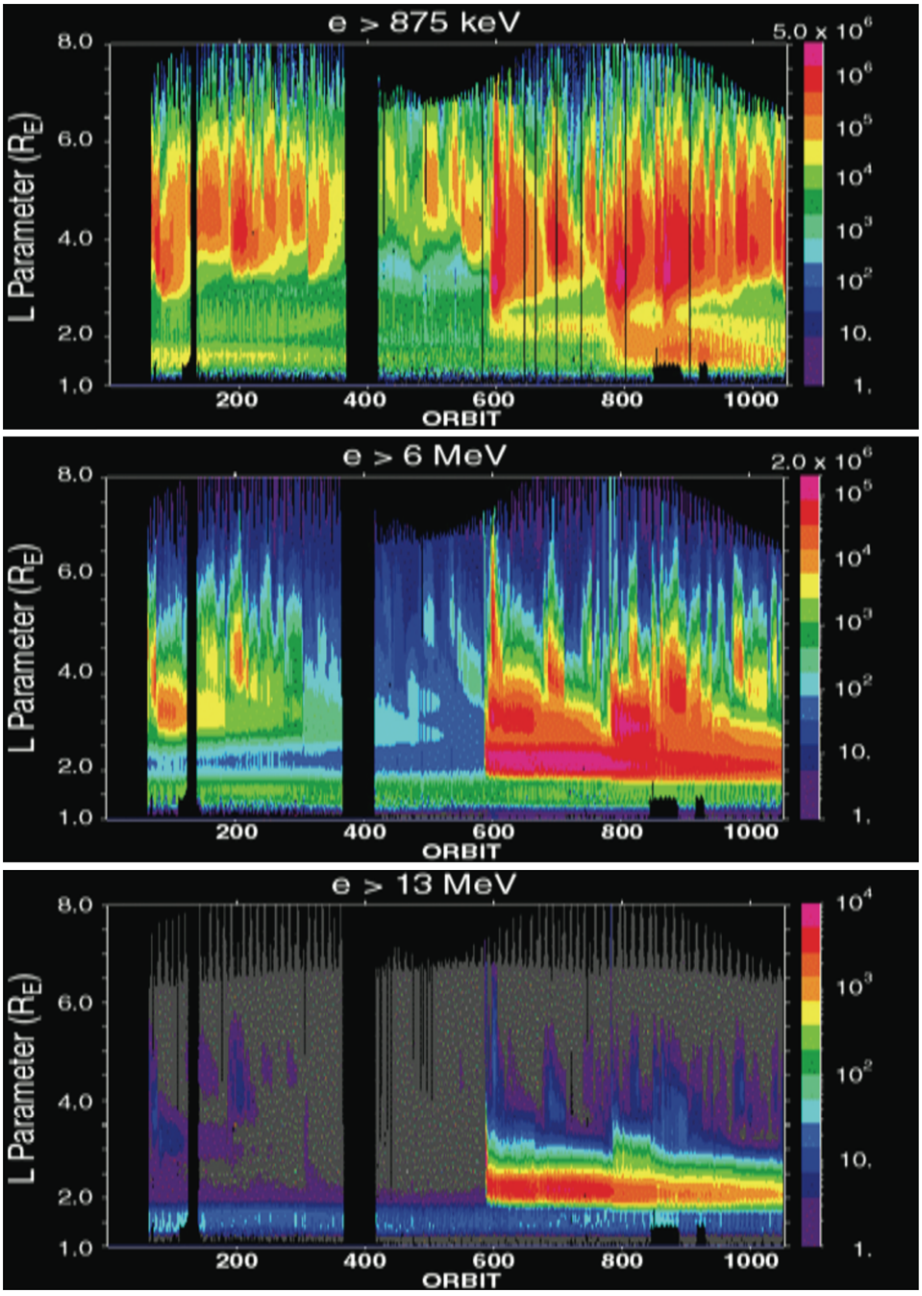

Fig. 1 Summary of the energetic electron flux through the 15 months of the CRRES mission as a function of L-Shell for (*top panel*) >875 keV, (*middle panel*) >6 MeV, and (*bottom panel*) >13 MeV (Blake et al. 1992). Note the very large increase near orbit 588 (24 March 1991), especially at the highest energies

Global Positioning System (GPS) constellation which lie in highly inclined orbits at $4.2 R_E$ radial distance. However, the instruments on these satellites are generally simple and lack high-energy or pitch-angle resolution. On the other hand, key measurements of radiation belt properties have been made since 1992 by the Solar, Anomalous, and Magnetospheric Particle Explorer (SAMPEX) spacecraft (Baker et al. 1993). SAMPEX continues at present to make measurements at low altitudes (∼600 km), but is quite far away from the equatorial acceleration region. The NOAA/POES (Polar-Orbiting Environmental Satellite System) also has made long-term radiation belt measurements in low-Earth orbit. The NASA spacecraft POLAR (1996–2007) carried both electric and magnetic field instruments (Acuña et al. 1996) and was capable of energy-resolved particle measurements at relativistic energies. However, it was placed in a polar orbit that generally only allowed observation of particle populations with relatively small equatorial pitch angles. And, similar to CRRES, the utility of POLAR observations of the radiation belts was limited by the single-point nature of the observations and also its relatively long (∼18-hour) orbital period.

Based on this brief survey of observing platforms, it is evident that there is a clear need for new, comprehensive radiation belt observations from low-inclination satellites. In this paper we describe an innovative high-energy, high-precision particle detection system called the Relativistic Electron-Proton Telescope (REPT). This new sensor system on board the Radiation Belt Storm Probes (RBSP) spacecraft pair will provide crucial new data to help resolve long-standing radiation belt science questions.

2 Requirements and Expected Results

2.1 Science Motivation

REPT will make the measurements necessary to gain fundamental new understanding of the relative importance of different physical acceleration and loss processes that are hypothesized to shape the radiation belt particle populations. REPT provides the basic measurements at a range of altitudes necessary for the development of the next-generation radiation belt specification models. Thus REPT will be an essential component in addressing the science goals of the RBSP mission (see Mauk et al. 2012 and Spence et al. 2012). The instruments will also help monitor the total radiation dose, and will help assess single event upset and deep-dielectric charging of electronic components on-orbit.

While the superstorm of March 1991 mentioned previously provided a striking example of prompt acceleration and deep injection leading to the formation of a new radiation belt, such events are not the norm. Moreover, CRRES happened to be fortuitously located to observe this event. More usual are the smaller storm-related injection events that occur several times per year (Lorentzen et al. 2002). The dual RBSP spacecraft mission will increase the radial visit frequency by 50 % over what CRRES achieved, correspondingly increasing the likely radial range of coverage that may be obtained during a prompt injection of energetic particles.

In contrast to the powerful superstorm acceleration as described above, the response of outer zone electron flux to solar wind variation more typically occurs over a timescale of hours to days (Baker et al. 1998). Increases in flux at higher energies is correlated with increased solar wind speed and southward interplanetary magnetic field (IMF). The former may drive the growth of velocity-shear instability along the magnetopause (in analogy with the way that wind drives surface waves on water). The southward IMF drives up geomagnetic activity, such as substorms, which can provide the seed population for radiation

belt electrons. Low-frequency, long-wavelength perturbations of the magnetopause boundary can transfer energy to ULF (Ultra-Low Frequency) wave modes within the magnetosphere, with periods up to tens of minutes. Enhancement of wave power at these frequencies has been seen both with ground-based and space-borne magnetic field measurements. REPT, in conjunction with the other RBSP particle measurements, will provide key particle observations of these events covering precisely the needed energy ranges.

The REPT instruments will be able to provide information that clearly tests competing models of particle acceleration, and will highlight where and when they are most important. Measurements suggest that the phase space density of $E > 2$ MeV electrons at geosynchronous orbit can be greater than the phase space density of corresponding electrons with the same first adiabatic invariant at greater distances, contrary to the expectations from radial diffusion models (Li et al. 2001a). Magnetopause motion may contribute to this discrepancy. Another possible explanation is that resonant interactions with whistler waves can energize these electrons. In this scenario, electrons are accelerated from several hundred keV to several MeV over periods of hours through multiple interactions with the whistlers (Roth et al. 1999; Horne and Thorne 1998).

Whistler-mode chorus emission excited during enhanced convective injection of plasma sheet electrons into the inner magnetosphere may transfer energy between the suprathermal (tens of keV) and relativistic populations (Horne et al. 2005a, 2005b). The rate of acceleration is strongly dependent on plasma density, specifically, the ratio between the electron gyrofrequency and the plasma frequency. Chorus is primarily excited in the low-density region during enhanced convection events, and has the highest probability of occurrence on the dawnside beyond the plasmapause (Meredith et al. 2003). Using realistic VLF (Very Low Frequency) wave properties, Horne et al. (2005a, 2005b) have shown that the flux of outer zone MeV electrons at $L = 4.5$ can be enhanced by more than a factor of ten during the 1–2 day recovery phase of a storm. During the acceleration, the energy spectrum and pitch-angle distributions of resonant electrons are predicted to evolve in a unique way (Horne et al. 2003). REPT measurements of pitch angle and spectral evolution during the energization will help characterize thisenergization process.

Paulikas and Blake (1979) and Baker et al. (1979, 1990) showed that MeV electrons often appear near geostationary orbit with a delay of about 2 days after the passage of fast solar wind streams. It is now believed these recurring acceleration events may be associated with strong turbulent Alfvenic wave fields in the fast streams. Correlation of electron flux with solar wind velocity fluctuations suggests that dynamic pressure buffeting of the magnetosphere or shear flow instabilities are an important driving force for radial diffusion. A correlation with intense southward IMF over extended periods of time, especially deeper in the magnetosphere ($L \sim 4$), suggests (indirectly) that a necessary condition for strong radial diffusion is the enhancement in large-scale convection electric field or more precisely its fluctuation level. If radial diffusion operates, we must determine what in the magnetosphere or in the solar wind generates the fluctuations that give rise to radial diffusion. In-situ measurements of electric and magnetic fields and particles in the inner magnetosphere, together with upstream solar wind conditions, will enable an assessment of the efficacy and timing of radial diffusion and convection.

The RBSP spacecraft with measurements of electric and magnetic fields, energetic electrons and ions, and plasma density at *spatially separated* points will provide insights into the importance of acceleration mechanisms under different solar wind conditions and at different radial positions inside the magnetosphere. Spacecraft at two separated radial positions will be able to monitor continuously the evolution of the energetic particle spectra and phase space distributions as the acceleration process progresses. Additional prompt acceleration processes due to substorm injection and medium-to-strong interplanetary shocks will

be continuously monitored and easily distinguished from the slower stochastic processes. Information on the azimuthal structure and wave-coherence lengths critical to understanding the radial diffusion problem will be obtained through comparisons between the two RBSP spacecraft, comparisons with the GOES magnetic field measurements at $6.6R_E$ and comparisons to mid-latitude ground magnetometers. Finally, in order to see the "acceleration in action", it is important to have energetic particle measurements on a time scale of about 1–20 seconds since the driving waves have frequencies which vary over periods of 1 minute to 1 hour. Similar requirements obtain for the measurement of energetic particles during shock and substorm induced acceleration. RBSP with REPT will provide this key information.

Determining the rate of loss of radiation belt particles, and the processes responsible for this loss, is also a key component of understanding the overall dynamics of the radiation belts. Fundamental to these efforts is the global measurement of wave activity, particle pitch angle distributions, and global magnetic fields (see Kletzing et al. 2012; Wygant et al. 2012). The dual RBSP mission will significantly enhance the coverage available, allowing observation of wave and particle distributions in local times outside those seen in a single orbit. This is particularly important in the case of scattering through interaction with VLF waves, since the waves involved are expected to be highly localized and may often occur in regions outside the narrow local time region observable from a single orbit. RBSP will increase the instantaneous coverage in radial distance. This will provide crucial information about the radial distribution of the particle losses in the REPT range and suggest the extent to which magnetopause shadowing may be important.

The RBSP mission will provide very important monitoring from MEO (Middle Earth Orbit) altitudes, the data forming a critical input into the development of the next generation radiation belt specification models that will replace AE-8 and AP-8 (see Vette 1991). This work requires coverage of medium energy plasma particles (surface charging), as well as high-energy electrons (>1 MeV; total dose and deep-dielectric charging) and very high-energy protons (>20 MeV) for single event upsets (SEU). Industry has identified the energy bands and orbital requirements as well as the radiation levels and their variability, especially worse case over a variety of integration intervals. The RBSP payload will provide essentially all of the required measurements, especially high-energy electrons and very high-energy protons from REPT through the flight of a payload with extensive energy resolution for both electrons and ions. Especially important are measurements from the under-sampled MEO region, which can provide a link to more extensive measurements at GEO (Geostationary Earth Orbit) and can hence lead to the development of more accurate specification models that are valid into the heart of the outer and inner radiation belts (industry requires MEO satellite lifetimes to be around 10 years).

2.2 REPT Measurement Requirements

The science background and data requirements described above impose significant demands upon the REPT instrument. The proposed sensor elements must fit naturally into the overall RBSP payload and thereby contribute to a complete suite of instruments on the spacecraft. The combination of the REPT instruments and the others on RBSP will address all of the key questions of electron acceleration, electron loss, and ring current effects in a broad space weather context.

Based on long-term observations of SAMPEX and geostationary orbit satellites, the averaged radiation belt intensity has a strong solar cycle variation (Baker et al. 1987, 2007; Li et al. 2001b). REPT must provide pitch angle and energy-resolved particle measurements

near the equatorial plane that can be projected to higher latitude, giving a complete 3-D spatial distribution. The measurements of RBSP will be used to validate existing specification models and calibrate with measurements from spacecraft at other orbits, such as GOES and POES, which have longer mission lives. REPT measurements will aid the global specification of the radiation belts especially at the relativistic and ultra-relativistic energies.

A fundamental goal of the RBSP mission is to differentiate among competing processes affecting the acceleration and transport of radiation belt electrons in the outer zone (Mauk et al. 2012). Crucial to this analysis is obtaining radial profiles of the phase space density of the radiation belts, properly ordering the observations in the three adiabatic invariants μ, K, and L (Roederer 1970). The quantities K and L depend on the global magnetic field configuration, and are particularly sensitive to variations in the model used in their evaluation (Green and Kivelson 2004). Further, these properly-ordered phase space density observations must be made with sufficiently high temporal cadence to capture the sometimes hours-long evolution of the belts and distinguish between features (peaks) in the phase space density profile that result from losses at high L, in contrast to those that result from internal acceleration mechanisms at lower L.

The goal for the REPT design therefore is to measure thoroughly the directional intensities and energy spectra of $\sim$1 to $>$10 MeV electrons throughout the slot and outer radiation belt region. To do this, the instrument requires an adequately large geometric factor to get reasonable count rates above background at the higher energies and yet must not saturate at the lower energy ranges. Thus, there must be a balance between foreground saturation on the one hand and background dominance on the other. There must be fast enough electronics to avert undue dead-time limitations and chance coincidence effects.

Some key features about the REPT design can be described by referring to Fig. 2. As noted previously, the REPT instrument must have an optimized geometric factor in order to

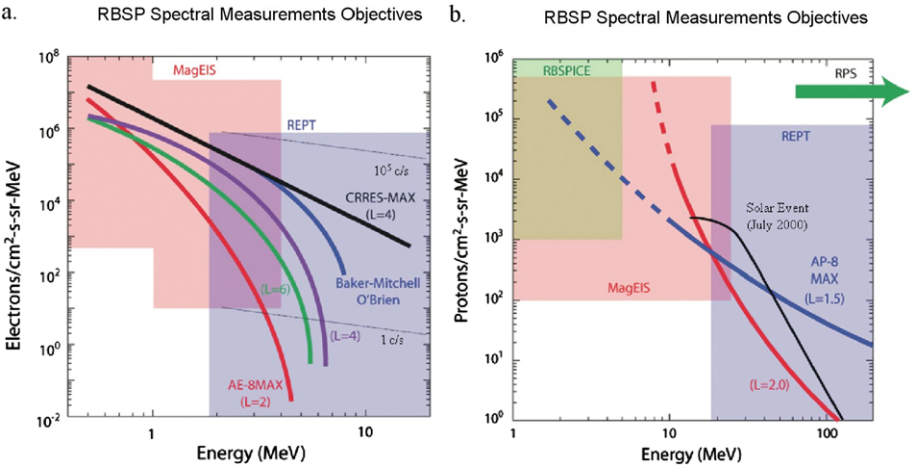

Fig. 2 (**a**) The kind of differential electron energy spectra that REPT will need to measure. The several different colored curves in the plot show model spectra (from AE-8 MAX) and also show two extreme spectra (CRRES-MAX and Baker, 2008), which were derived from the most intense events observed in such periods as the March 1991 case discussed previously. The *blue-shaded rectangle* in the figure shows the flux vs. energy domain that is expected to be measured by REPT in order to cover the requisite energy and intensity ranges (the actual measurement capabilities are described in detail in the instrument section). The *pink shaded rectangles* show for reference the flux-energy intervals that will be covered by the Magnetic Electron Ion Spectrometer (MagEIS) that will also be part of the RBSP payload (see Blake et al. 2012); (**b**) Similar to (**a**) but for protons

cover a wide dynamic range of electron fluxes that may be encountered. As shown in the figure, it is ideally the goal to cover a range from $\sim 10^{-2}$ to over 10^6 electrons/cm^2 s sr MeV. This will give REPT the sensitivity to handle expected fluxes (on the low end) in the radiation belt slot region and also out near spacecraft orbital apogee, while also being able to measure without compromise the most extreme possible spectra that might occasionally occur in the heart of the outer zone ($L \sim 4$) during events such as the March 1991 event.

Other key points to note are that REPT must be designed to avoid substantial deadtime effects in the sensor system. This means that for the highest flux cases (for $L = 3$–4) the electronic signal rates due to electrons in the energy range ~1–5 MeV must be nearly linear (within 10 % or so) in their responses up to at least 2×10^5 counts/second (c/s). It is also clear from Fig. 2 that electron fluxes in the 0.5 to ~1.5 MeV energy range (i.e., the energies just below the REPT energy threshold) could cause significant pileup effects (Vampola 1998) in the REPT sensors. This would probably be worst around the peak flux region at $L \sim 4$. Closely related concerns revolve around having such high single detector counting rates that chance coincidences (Vampola 1998) of counts in the individual detectors lead to false counts in the REPT energy channels. Such chance coincidences can result either from having high background singles rates due to side penetration through physical shielding or it can result from penetration of lower electrons into the detector telescope stack through the front entrance aperture. Finally, a very significant concern is the generation and counting of bremsstrahlung photons (in the X-ray range) generated by incident high-energy electrons. Such bremsstrahlung can itself cause very high and debilitating pulse pileup and side-penetration backgrounds in individual detectors. As will be discussed in detail below, we have carefully designed REPT so as to minimize all of these possible problems with a solid-state detector telescope.

We also have designed REPT to measure the very high-energy proton populations that will be encountered by the RBSP spacecraft. These high-energy protons will be seen primarily in the region known as the "inner" Van Allen radiation zone, which is essentially in the magnetic confinement region at $L \leq 2$. The other situation when very high-energy ($E \geq 20$ MeV) protons will be encountered is when intense solar energetic particle (SEP) events are in progress. Figure 2b illustrates differential directional proton intensities versus proton kinetic energies. Two typical proton spectra, one for $L = 2.0$ and one for $L = 1.5$, are shown by the colored curves based on the AP-8 MAX model (Vette 1991). Also shown by the black curve is the observed proton energy spectrum for an SEP event in July 2000 (Mewaldt 2006). The figure also shows with the blue-shaded rectangle the proton flux-energy domain that REPT will cover. The pink-shaded area shows the domain to be covered by the MagEIS ion sensors (Blake et al. 2012) while the green-shaded area shows the domain to be covered by the RBSPICE instrument on board RBSP (see Lanzerotti et al. 2012).

From Fig. 2b we see that by far the "hardest" proton spectrum expected to be encountered by RBSP will be the inner zone region around $L = 1.5$. In that area—near the perigee for the RBSP orbits—the spacecraft and sensor systems will be exposed to a spectrum of protons extending up to well above 100 MeV in energy. REPT has been designed to have the energy coverage (17–200 MeV) and dynamic range (10^0–10^5 protons/cm^2 s sr MeV) to measure most of the inner zone proton population. REPT will also be able to measure the SEP events likely to be encountered.

As for the electron design considerations discussed in relation to Fig. 2a, we note that similar concerns arise for proton sensor design. Thus, we have chosen a geometric factor which helps assure that neither inner zone proton spectra nor SEP events will ever lead to high enough counting rates to cause nonlinearity due to detector dead time. Also—even for

the worst-case energy spectrum at $L \sim 1.5$—we must assure that lower energy protons (below our designed energy threshold $E \sim 17$ MeV) will not pile up to cause false signals. As for the electron case, we also must design the side shielding and the front sensor aperture to assure that background and single detector rates will never lead to high chance coincidence rates in the proton detection channels. Our discussion of the detailed REPT design (below in Sect. 3) will show that we have carefully dealt with these challenging issues and should have clean proton measurements and acceptable background rates under almost all foreseeable circumstances.

2.3 Anticipated REPT Science Results

As noted above, a well-designed REPT instrument will provide precise and unambiguous measurements of energetic electron fluxes in the energy range ~1.5 to ~20 MeV. By providing accurate energy spectra as well as detailed pitch angle information, it will be possible at each spatial location of RBSP to specify the near-equatorial, directional electron intensity, j. Using concurrent magnetic field strength, B, measured by RBSP, the phase space density (f) can be specified for a given value of the first adiabatic invariant (μ, also known as the magnetic moment):

$$f = j/p^2 \tag{1}$$

where p is the relativistic momentum. This becomes approximately

$$f(\mu) = \frac{j}{\mu B}. \tag{2}$$

This phase space density at constant first invariant (constant μ) is perhaps the single most important derived quantity from the RBSP payload for radiation belt studies (e.g., Roederer 1970). Examining $f(\mu, t)$ allows tremendous insight into radiation belt dynamics, sources and sinks of particles, and mechanisms of acceleration and transport.

Figure 3 is an example of the range of phase space densities that might be encountered for electrons that fall in the REPT kinetic energy range (~1.5–20 MeV). The red colored

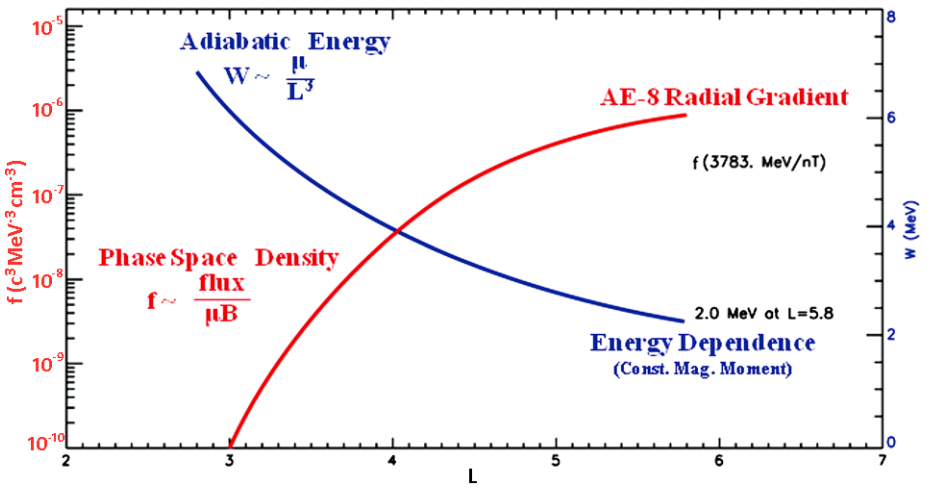

Fig. 3 Phase space density (*red*) and adiabatic energy (*blue*) variations expected over the L-value range to be explored by the RBSP spacecraft (see text)

profile in Fig. 3 shows what a widely adopted radiation belt model (AE-8) would say is the profile of phase space density as a spacecraft such as RBSP went from apogee ($r = 5.8R_E$) near the equator inward to $L \sim 3$. As can be seen, for the particular value of magnetic moment chosen ($\mu = 3783$ MeV/nT), the radial gradient would be such that $f(\mu)$ would go from $f \sim 10^{-6}c^3$ MeV^{-3} cm^{-3} at $L = 5.8$ to $f \sim 10^{-10}c^3$ MeV^{-3} cm^{-3} at $L = 3.0$, where $c = 3 \times 10^8$ m/s (the speed of light).

We also note the corresponding blue curve in Fig. 3. This shows the kinetic energy that an electron moving "adiabatically" along an equatorial pathway from $L = 5.8$ to $L \sim 2.7$ would have. In this case, an electron having $\mu = 3783$ MeV/nT would have a kinetic energy (which we designate here by W) of $W \sim 2.0$ MeV (see vertical axis to the right in Fig. 3) at $L = 5.8$. The electron undergoing adiabatic transport from $L = 5.8$ to $L \sim 3.0$ would gain energy (due to conservation of the first invariant), going as $W \sim \mu/L^3$. At $L = 2.7$, the electron would have an energy $W \sim 7.0$ MeV. Transporting such an electron even more deeply into the magnetosphere, down to $L \sim 2.0$ would bring an electron of this magnetic moment to the upper energy range covered by REPT, i.e., above ~20 MeV.

This figure makes the crucial point that to study consistently and thoroughly the transport, acceleration, and loss of electrons of even relatively modest energies (0.5–2.0 MeV) near geostationary orbit ($r = 6.6R_E$), we must be prepared to follow such electrons up to quite high energies (15–20 MeV) deeper in the magnetosphere. It is most effective and unambiguous to follow such electron transport by using a single detector system that self-consistently measures the electron population transport all the way from RBSP apogee to near RBSP perigee. REPT is designed in this spirit.

A key remaining question that the REPT team has addressed is: "How precisely must we be able to determine phase space densities at various points along the RBSP trajectory?" Figure 4 shows one answer to this question. Underlying the green and blue shaded curves in Fig. 4 is a red profile. This is the same "radial gradient" curve based upon the AE-8 model that was shown in Fig. 3. Using the expected effect of strong radial diffusion (as might result

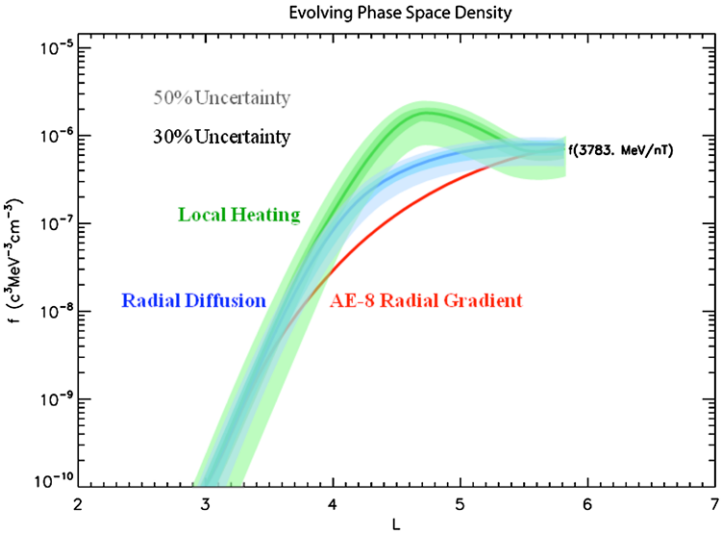

Fig. 4 A figure showing expected equilibrium (*red*) phase space density profile plus the enhanced profiles that might result from enhanced radial diffusion (*blue*) or intense local wave heating (*green*). The effects of REPT measurement uncertainties are shown by the *blue* and *green shading* as described in the text

from ULF wave transport) we show in blue, in Fig. 4, the change that might occur for an enhancement derived from the red curve. Similarly, if we model how VLF waves might locally heat the expected equilibrium (red) electron phase space profile, the green curve shows the "local heating" model curve.

The shaded bands around the main radial diffusion (blue) and local heating (green) curves attempt to show what 30 % and 50 % uncertainties in the REPT electron measurements would imply about derived phase space densities. From such modeling and analysis, we conclude that REPT flux measurement must be made with absolute accuracies in the 20–30 % range. Larger uncertainties in REPT fluxes (i.e., extending up to 50 % uncertainties or greater) would completely prohibit us from distinguishing between radial diffusion and local heating mechanisms. As will be seen below, the REPT science and engineering teams have succeeded in devising REPT flight units for the two RBSP spacecraft that are built and calibrated to a precision ($\leq$20 %) such that the scientific requirements of the mission are more than met.

2.4 Modeling

The RBSP mission will provide an unprecedented view of the dynamics of the radiation belts and the fields and waves associated with those changes. Detailed models of wave/particle interactions (e.g. Horne and Thorne 1998; Bortnik et al. 2009; McCollough et al. 2010; Elkington et al. 1999) and transport processes (Elkington et al. 2005; Li et al. 1998; Sarris et al. 2002) can provide insight into which physical processes are likely to be important in the energization and loss of the particles comprising the radiation belts. However, direct RBSP observation of the important phenomena will still be limited to processes taking place at the satellite locations. As particles drift about the Earth they will encounter and be affected by fields and waves that may be principally occurring in regions away from the spacecraft observation locale at a given moment of time, but still affect the particles that drift across the spacecraft location. Further, many transport processes require knowledge of the large-scale configuration of the waves and fields guiding the radiation belt particle motion, such as is the case with ULF wave mode structure in determining rates of radial diffusion (Elkington et al. 2003). Dynamic models of the global state of the magnetosphere will therefore be necessary to provide context for interpreting changes observed at discrete locations of the RBSP spacecraft.

At present, the most capable physically-based magnetospheric simulation codes are based on the MHD approximation. Global MHD models provide a dynamic, physically-based means of estimating the global configuration of the magnetosphere (e.g. Lyon et al. 2004; Gombosi et al. 2002; Raeder 2003). MHD simulations treat the fields and plasmas surrounding the Earth as a magnetized fluid (Sturrock 1994), allowing a computationally-tractable means of simulating the Earth's magnetosphere as it responds to changes in the solar wind. The MHD approximation does not allow full specification of all the microphysical processes that may affect the radiation belts (e.g. those processes occurring at spatial scales below the ion gyroradius), but does include many important effects known to influence the radiation belts and its boundary populations, including magnetic reconnection, global magnetospheric convection, and the solar wind driving of large-scale waves that can lead to the transport and energization of radiation belt particles. These simulations can be driven by solar wind observations upstream of the bow shock, providing a realistic link between solar wind driving of the magnetosphere the time evolution of the simulated fields.

In Fig. 5 we show how a global MHD simulation may be used to study the effect of differing boundary populations on radiation belt evolution during a hypothetical storm driven

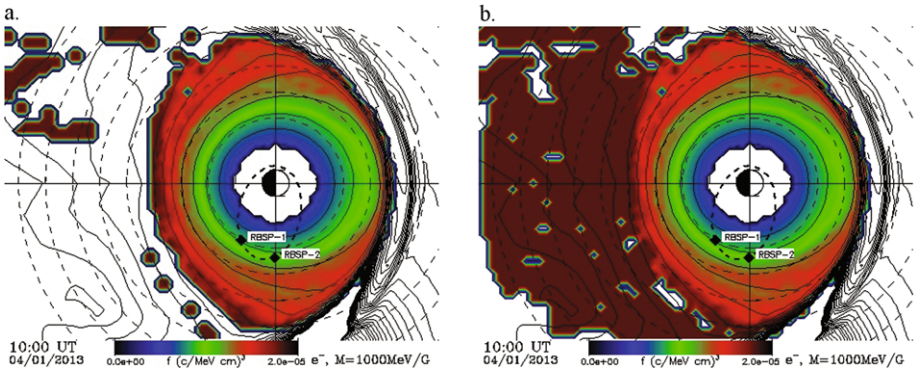

Fig. 5 Global MHD/Particle simulations showing the evolving phase space density in the equatorial plane for energetic electrons of 1000 MeV/G for a hypothetical RBSP orbit configuration. (**a**) Shows conditions where the trapped radiation belt particles are subject to an open boundary condition, allowing particles to be lost from the inner magnetosphere via outward radial diffusion. (**b**) Indicates the effect of plasma sheet particles convectively injected into the inner magnetosphere, augmenting the radiation belt populations in the trapping region

by a high-speed solar wind stream interacting with the magnetosphere. Here we use the LFM MHD simulation (Lyon et al. 2004) coupled with test particle simulations to study the dynamic evolution of the radiation belts in a manner similar to that described by Elkington et al. (2004). In the left hand panel of Fig. 5a we show a snapshot of the simulated state of the radiation belts with an open boundary condition, where trapped energetic electrons are subject to only outward radial diffusion at the trapping boundary, which results in a net loss of particles from the radiation belts (Shprits et al. 2006). In the right-hand panel of Fig. 5b we illustrate a contrasting magnetospheric state where energetic particles from the plasmasheet are convectively transported Earthward, and form a positive boundary population for the radiation belts in the near-Earth tail. In both these figures, the magnetosphere is viewed from the pole, with the phase space density of particles of a given first adiabatic invariant (1000 MeV/G) displayed on the color scale and contours of constant magnetic field strength indicated by solid lines. The locations of the two RBSP spacecraft in this interval are indicated by labeled black diamonds, along with the orbit trajectory (bold dashed line) and contours of constant radial distance (light dashed lines forming concentric circles about the Earth). The trapped population in these figures was modeled as a monotonically-increasing distribution function, with a plasmasheet population exceeding the phase space density at geosynchronous consistent with the observations reported by Taylor et al. (2004). The inner boundary of this simulation is at approximately 2.3 Earth radii from the center of the Earth.

In Fig. 6 we show the simulated magnetic fields (dotted lines) and electron phase space densities (solid lines) observed over several orbits at one of the virtual RBSP spacecraft locations. Over the course of a single orbit the phase space density can be seen to generally rise, and the magnetic field decrease, as the spacecraft moves radially outward, reversing this trend on the inward legs of each orbit and reflecting the outward gradient in the assumed initial radiation belt electron population. Figure 6a indicates that the peak phase space densities decrease over the several orbits comprising this simulation, and suggests the effect of outward radial diffusion on radiation belt losses under these driving conditions. By contrast, Fig. 6b shows peak phase space densities increasing with time, illustrating the

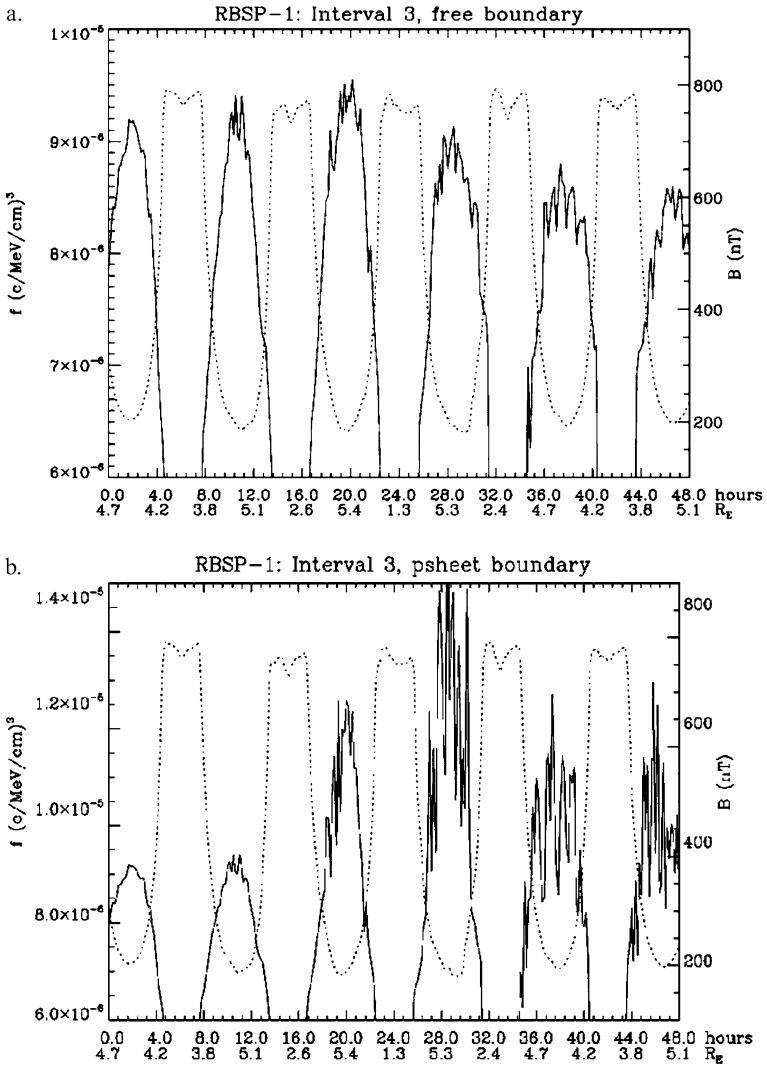

Fig. 6 Virtual phase space densities and magnetic fields observed by the modeled RBSP spacecraft indicated in Fig. 5. (**a**) Shows decreasing phase space densities over several orbits, resulting from particles lost to outward radial diffusion at the open trapping boundary. Increasing phase space densities in the right hand panel (**b**) suggest what might be seen under conditions of plasma sheet access to the inner magnetosphere

effect of plasma sheet particles being trapped in the inner magnetosphere and the resulting contribution to pre-existing radiation belt populations.

At present, the global simulations illustrated here do not include all physical processes currently thought to be important in the dynamics of the radiation belts (e.g. heating via chorus emissions or losses due to EMIC waves); however, they do provide a means of quantifying changes in the distribution function that might occur under the conditions of pure outward radial diffusion and loss through the trapping boundary, or the convective injection of particles from the plasma sheet. The differences between the results of these simulations

and actual observations from the REPT instrument can be used either to infer other physical heating and loss processes that may be occurring in local times and locations beyond the view of the RBSP spacecraft, or to infer that such processes are not required to explain the variations observed during particular events or intervals.

3 Instrument Description

3.1 Instrument Design and Modeling

Obtaining precise spectra and angular distributions is critical for determining the electron and proton phase space densities necessary to answer the important science questions posed above. This is particularly difficult in the inner magnetosphere where the radiation is very penetrating and intense. The high fidelity measurement requirements combined with the hostile environment of the inner magnetosphere has led us to choose passivated ion implanted silicon particle detectors in a particle telescope con-figuration to measure electrons and protons in the energy ranges ∼1–20 MeV and ∼17–200 MeV respectively (the exact energy ranges of all the electron and proton differential channels are listed in Table 7). We employ pulse height analysis techniques to separate electrons from protons and use carefully designed shielding to limit particle background expected in this high radiation environment.

A compact solid-state telescope system is ideal for measuring very high-energy particles, since other approaches such as particle magnetic spectrometers would require high magnetic fields, which result in massive instruments. The REPT therefore consists of a stack of silicon solid-state detectors in a telescope configuration, a collimator, and a thick case surrounding the detector stack to shield the sensor from penetrating radiation and bremsstrahlung. The dimensions of the collimator determine the geometry factor. As mentioned previously (see Sect. 2), REPT measurement requirements constrain the geometry factor. We have optimized the geometry factor based upon electron measurements both at high altitudes and by extrapolating low-altitude observations (Kanekal et al. 1999). The instrument points perpendicular to the spin axis of the spacecraft and will sample all pitch angles of particles during almost all expected magnetic field orientations. The REPT will be used in a closely coordinated way with the MagEIS sensor that is part of the RBSP payload (Blake et al. 2012).

Figure 7 shows the REPT detector system concept in cross-section. The design is based on extensive experience of our team with prior space missions such as CRRES, POLAR, and SAMPEX. The Proton-Electron Telescope (PET) onboard SAMPEX (Cook et al. 1993)

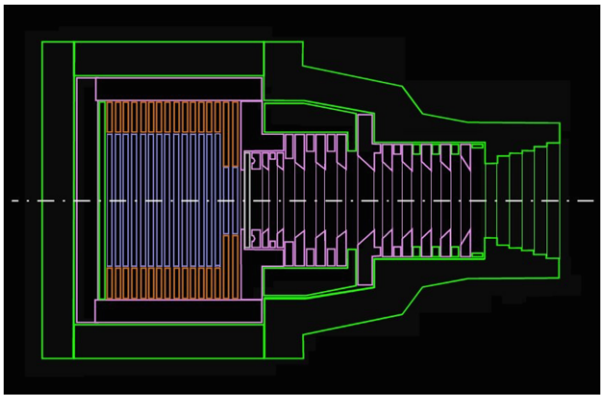

Fig. 7 REPT geometry in cross section implemented in GEANT4. Material marked in *green* is aluminum, *purple* is Hi-Z, *white* is beryllium, *brown* is polyimide and *blue* is the silicon detectors

operated very well for over 17 years from the time of spacecraft launch in 1992. It provided close heritage for the REPT. Lessons learned from the PET/SAMPEX experience (Baker et al. 1993, 1994) helped guide our design on the REPT for the more intense and higher background environment that will be experienced by RBSP near the magnetic equator compared to the low-altitude (∼600 km) SAMPEX orbit. Furthermore, detailed simulation of the instrument response to energetic particles was made using GEANT4 (GEometry ANd Tracking) (Agostinelli et al. 2003) to not only design the basic configuration but also to establish instrument characteristics.

Figure 7 shows the REPT instrument geometry that resulted from optimizations using GEANT4 simulations. The REPT collimator was designed to yield a geometry factor of 0.2 cm^2 sr with a resulting circular conical FOV of 32°. At the back of the collimator is a carefully chosen aperture-covering beryllium (Be) window that excludes lower energy electrons ($\lesssim$1 MeV) and protons ($\lesssim$15 MeV). The silicon detectors (labeled R1 through R9 numbered from the front) are stacked behind the Be window, the first being 1.5 mm thick and 20 mm in diameter with annular concentric designs. The front detector, which is 7 cm from the front of the collimator, determines the geometry factor. The design is analogous to the PET, although the REPT has a narrower field of view (32° for REPT compared to 58° for PET). The geometric factor for REPT is about five times smaller for 1–5 MeV electrons than it was for PET.

It is well known and understood that electrons scatter considerably as they interact within detector systems and deviate considerably from their original direction. Thus, electrons may "leak" out of the detector stack. We have designed the REPT with larger-area detectors R3 to R9, which are 40 mm in diameter and are twice as thick as the front detectors. This results in higher detection efficiency for the 5–20 MeV electrons that are a key target of the RBSP and LWS programs. These larger detectors actually comprise a pair of 1.5 mm thick detectors whose signals are electronically summed.

The REPT detector stack is therefore comprised of 24 mm of Si, which will stop most electrons of energy up to 10 MeV. However, as determined by our GEANT4 simulations, by imposing selection criteria on energy deposition in the detectors comprising the stack, the REPT can detect electrons in differential energy bins up to 20 MeV and protons up to 115 MeV. Higher energy electrons and protons above these values are measured as integral channels. Our goal has been to focus design attention on 1 to 20 MeV electrons. We have set differential energy channels with $\Delta E/E = 0.3$ giving 11 electron energy channels in the target energy range. The designed geometric factor of $g \sim 0.2$ cm^2 sr gives a dynamic range at $E \sim 2$ MeV of ∼100 counts/s for "weak" enhancements near $L = 4.0$ and $>10^5$ counts/s for some of the strongest events we have detected in recent times (cf., Baker et al. 2004 and Fig. 2 above).

An important design consideration is to suppress backgrounds due to directly penetrating radiation and bremsstrahlung. The REPT has been built with gradated side shielding to greatly reduce electrons below ∼20 MeV (and protons below ∼140 MeV). The inner layer of shielding is a high-Z metal (tungsten-copper alloy) to stop bremsstrahlung X-rays, while the outer shielding is aluminum to provide good stopping power while reducing initial bremsstrahlung production. The shielding thickness has been optimized using GEANT4 with a realistic REPT geometry to obtain detection efficiencies for side-penetrating electrons and protons. Singles rates due to side penetrating electrons are about 1 to 2 orders of magnitude lower than the FOV electrons for assumed extreme spectrum (Baker et al. 2008) for the front detectors ($\sim 10^3$ s^{-1}) and are comparable in magnitude for detector R4. Coincidence requirements on the front detectors ensure that the REPT differential energy channels have negligible background even in this extreme scenario. The minimum energy required

to penetrate the shielding varies from ∼100 to ∼150 MeV for protons incident at 0° up to 75° from perpendicular. We have also calculated the expected background from high-energy galactic cosmic ray protons using measured proton spectra (Alcaraz et al. 2000) and found them to negligibly small with singles rates ranging from 20 to 50 s^{-1}, compared to $\sim 10^3$ s^{-1} for the nominal AE8 (Min) FOV electrons at $L = 4$. Our goal has been to maintain high foreground/background ratios even during the most intense radiation belt enhancement events and for passages through the powerful inner zone.

3.2 Sensor Synergy and Proton Detection

The REPT measurement of electrons will have important energy overlap with the MagEIS detector system (Blake et al. 2012). This will afford key redundancy in the crucially important 1.0–4.0 MeV electron energy range. It will also allow good on-orbit cross-calibration between these two highly complementary sensor systems. The REPT will provide the essential measurements of the high-energy portion of the radiation belt electron population with higher sensitivity (larger geometric factor) than MagEIS.

The REPT also has overlapping measurements of protons with the RPS sensor (Mazur et al. 2012, this issue) in the 50–120 MeV range, which is covered by 3 differential channels of REPT. In addition REPT provides integral measurements of protons above ∼115 MeV.

3.3 Design Overview

A cut-away of the REPT instrument layout is shown in Fig. 8. The collimator, beryllium window, detectors and sensor shielding, as previously discussed, are toward the top of the

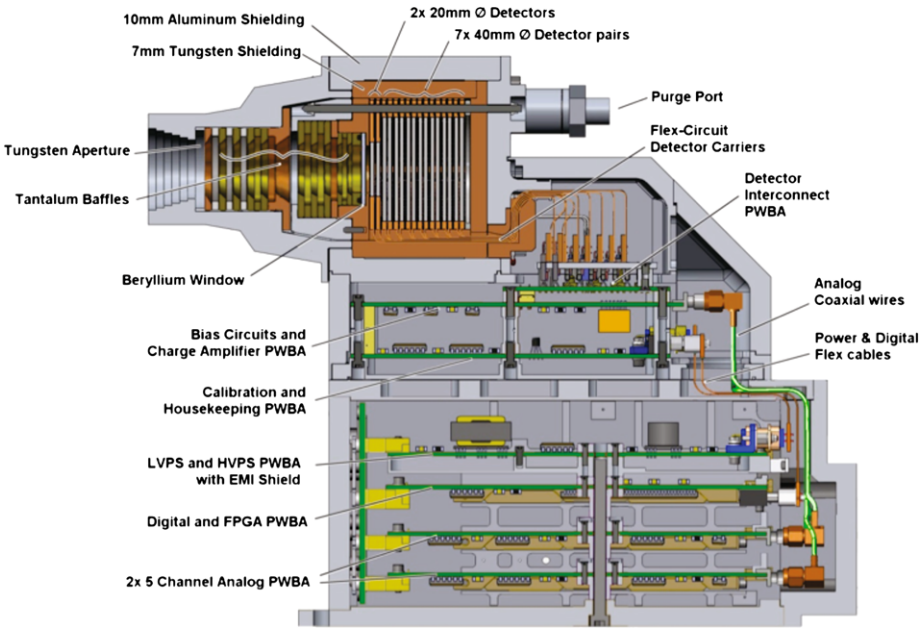

Fig. 8 Cut-away of REPT showing high-Z disk-loaded collimator, detectors and shielding along with the supporting electronics. Charge sensitive amplifiers, bias, and calibration circuitry is located near to the detectors. The balance of the analog circuitry along with the low voltage power supply and FPGA are housed in the lower electronics box

figure. The output signal from each of the detector planes is collected by individual charge sensitive amplifiers (CSA) and the output of each CSA drives parallel fast- and slow-pulse shaping circuits. The fast circuits provide event detection for each detector while the slow circuits provide noise filtering and pulse height analysis (PHA). The fast signals are routed to a field-programmable gate array (FPGA) which implements detector-to-detector coincidence detection monitors for pile-up events to determine the occurrence of valid events, and coordinates the analog to digital conversion (ADC) sampling of each of the slow (PHA) channels.

A valid event occurs when one or more detectors exceed threshold within a coincidence window (see section on Timing, Coincidence and Pile-up). For valid events the FPGA compares the set of PHA values against twenty configurable logic statements, (see Tables 2 and 3) each designed to qualify a particle into a particular species and energy range. Each spin of the spacecraft is divided into 36 sectors. The tally of positive logic statement evaluations is collected over a spin sector and the 36 sector results are reported in primary science telemetry. Along with the energy bin count rates, the primary science includes the individual detector event rate, i.e., singles counts, by sector. A secondary science product, a sampling of PHA data sets with the associated energy bin results, is collected on a nominal 2 sets per second cadence.

All REPT functionality is implemented in an FPGA thereby eliminating the need for a microprocessor and software. Separate state machines support science data processing, housekeeping data collection, data packetization and telemeterization, commanded memory reading and writing, and spacecraft spin synchronization. With only two modes of operation, Safe and Run, REPT operations and commanding is kept to a minimum.

Figure 9 shows the REPT flight model A (FM-A) just prior to integration to the RBSP-A spacecraft. Each REPT instrument is situated on its spacecraft anti-sun deck with electronics box inside the spacecraft and the sensor and collimator passing through the deck. The instrument is aligned to be parallel to the deck and perpendicular to the spacecraft spin axis (see Fig. 10).

The REPT specifications, properties, and requirements are given in Table 1. The energy resolutions for electrons and protons are better than required for science measurements. With the FOV and geometry factor dictated by low-end electron fluxes, meeting the counting rates associated with high fluxes, with acceptable dead time losses, was a driving design factor. The allocated data rates for REPT easily support low volume of fixed rate housekeeping data, and primary science data rate that varies with spacecraft spin rate. A secondary-science PHA data packet is included in the telemetry plan whose length will be adjusted to keep the total rate within allocation. The instrument power requirements are well under the allocated limits and, with generous mission mass allowances to accommodate mandated electron deep dielectric shielding, REPT is heavy but well under its mass limits.

3.4 Sensor Design

The sensor head, the portion of the instrument positioned on the exterior of the spacecraft, includes the detectors, their shielding and the collimator, the beryllium window to block low energy electrons, a dry nitrogen purge port and plenum to keep the detectors dry, and three circuit boards: the Detector Interconnect PWBA, (Printed Wiring Board Assembly) the Bias and CSA PWBA and the Calibration and Housekeeping PWBA.

3.5 Detectors

The detectors, shown in Fig. 11, are ion-implanted high-resistivity 1500 µm thick silicon diodes manufactured by Micron Semiconductor LLC, U.K. Made with Micron's 2M pro-

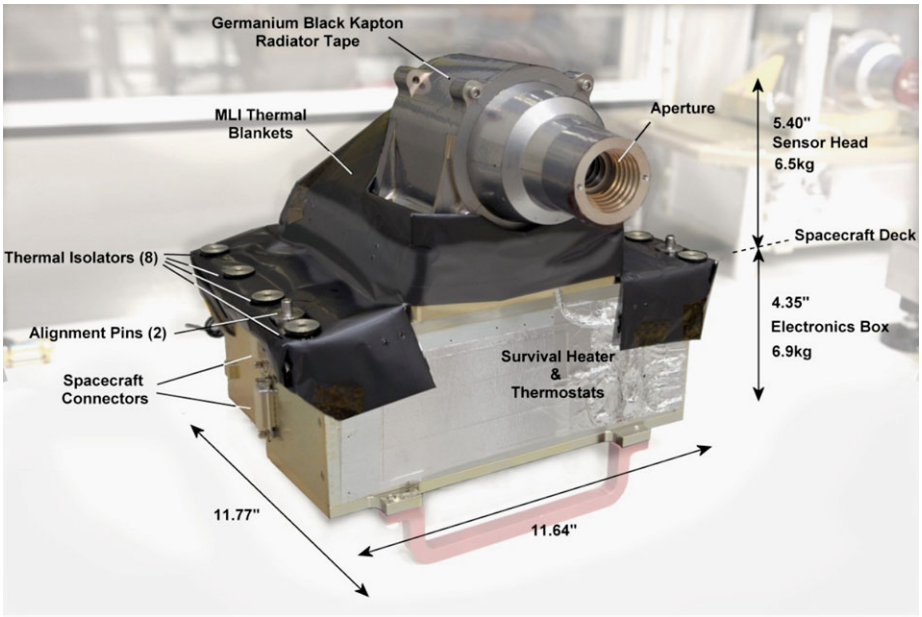

Fig. 9 REPT flight unit 'FM-A'. The upper section, in grey, is the sensor housing with the collimator aperture facing forward. The lower portion is the electronics box sitting on red tag handles that are removed after instrument installation to the spacecraft. The black flight multi-layer insulating (MLI) thermal blankets are seen draped over the box. Spacecraft communication and power cables attach at the left and on the right hand edge of the box front survival heater power and spacecraft monitored temperature sensors attach

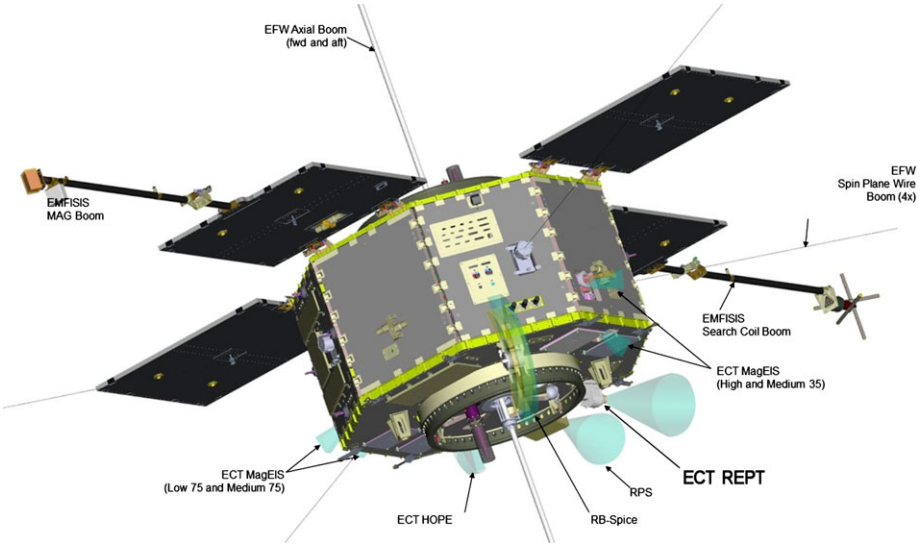

Fig. 10 RBSP Spacecraft showing location of REPT instrument

Table 1 REPT summary specifications

Parameter	Delivered	Level-1 requirements
Proton energy range	17 MeV to >100 MeV	≤40 MeV up to ≥75 MeV
Proton energy resolution ($\Delta E/E$)	30 %	$\Delta E/E < 30$ %
Electron energy range	1.6 MeV to >18.9 MeV	≤4 MeV up to ≥10 MeV
Electron energy resolution ($\Delta E/E$)	25 %	$\Delta E/E < 30$ %
Geometry factor	0.2 cm^2 sr	
Field of view	32° (Full angle)	
Integration cadence	1/3 s nominal (1/36 of spacecraft spin period)	≤1.0 min but an integral number of spins
Spin plane angular resolution	36 sectors	≥8 sectors per spin
Dead time losses	∼20 % at 100 kilocounts s^{-1}, correctable to <5 % 50 % at 350 kilocounts s^{-1}, correctable to <20 %	<30 % including errors at AE8max, $L = 4$, 4 MeV
Mass	13.4 kg	
Power	6.2 W, not including survival heater	
Data volume allocation	1580 bps maximum	
Dimensions	$11.77'' \times 11.64'' \times 9.75''$	

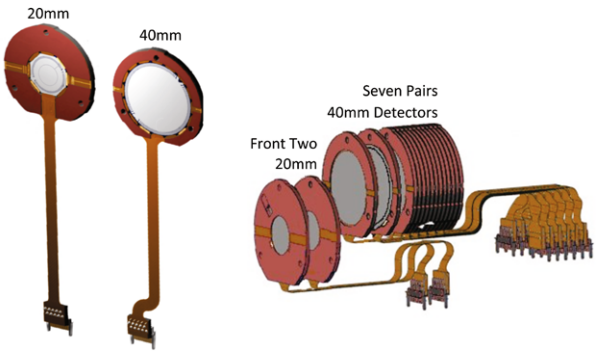

Fig. 11 REPT solid-state detectors in rigid-flex packages. Detector cathode faces are shown in figures at *left*. *Figure on right* shows detector stacking and flex routing out of the shielding

cess, the implantation dead layer is less than 0.5 µm and the full surface sputtered aluminum metallization is nominally 0.3 µm thick. The design includes their proprietary MGR guard ring design that reduces noise from edge leakage paths. The flight detectors came from a number of different silicon boules with different resistivity so depletion voltages varied from 120 V to 300 V. Room temperature leakage currents at full depletion are <0.5 µA on the 40 mm detectors and <0.1 µA on the 20 mm models. Studies show that by the end of RBSP mission life leakage current on the most-irradiated front detector will increase by less than a factor of 10.

The detector packages are multilayer rigid-flex circuits custom designed for the REPT instruments. The rigid detector carrier portion of the package is 2.5 mm thick and precision machined to accurately register the detector silicon and for alignment within the REPT shielding. Electrical contact from the front and back of the silicon to the package is accom-

plished with low-profile triple-redundant bond wires. The approximately 5″ long two-layer flex portion of the package carries the electrical signals through the sensor shielding and to the Detector Interconnect PWBA.

The front two detectors in the sensor stack are 20 mm diameter silicon, custom designed for the REPT instrument. The active area is divided into two concentric regions of equal area with separate electrical connections off-chip to the package. For the second detector in the stack the two active areas are tied together on the Detector Interconnect PWBA but the two active areas on the front-most detector have fully independent electronics channels. The smaller active areas allow much improved pile-up detection at high fluxes. For valid events the PHA values are summed back together in the FPGA, accounting for any charge-sharing of a particle impacting near the boundary of the two active areas. The isolation gaps between the two active areas are ∼100 μm wide and cover less 1 % of the total detector area in order to minimize both the number of particles interacting with them and any charge collection losses. Our studies using electron and proton accelerator beam data, showed that less than 2 % of particle events showed any charge division between the two areas and the reconstructed energy of this group was indistinguishable from the larger population.

The 40 mm diameter detectors are standard devices from Micron Semiconductor mounted in the custom REPT rigid-flex package. Fourteen 40 mm detectors are used as pairs to make up the back 7 detectors. Each pair is electrically connected together in parallel and mounted in the detector stack cathode-to-cathode. This doubles the effective thickness while maintaining the charge collection time of the single thickness. The cathode-to-cathode mounting minimizes differential voltages between adjacent surfaces while also reducing crosstalk between adjacent pairs. Alternating the directions that the detectors face spreads the connectors away from each other for connection in the limited space of the Detector Interconnect PWBA.

All the flight candidate detectors were characterized for depletion voltage, leakage current, alpha particle response, noise and dead layer thickness and uniformity. Flight detectors were selected for in-family leakage current behavior over temperature and for depletion voltages. The 40 mm detector pairs were matched for depletion voltage and the individual bias circuits were adjusted for each pair to provide 30 V to 70 V over depletion from the common bias power supply. Bias voltage was limited to 70 V over depletion as beyond this leakage current became notably more temperature sensitive.

Modeling of charge transport and charge collection times, in the manner of Leroy et al. (1999), compares favorably with collection times measured for REPT detectors with 30 V over-depletion, giving values from 210–380 ns, depending on charge amplitude, temperature and which detector face the particle enters. Our measurements show (Fig. 12) that the time from the inflection point on the CSA waveform to full charge collection is consistently 170 ± 20 ns independent of particle type, incident detector face and temperature.

While the preceding discussion was based on measurements of electrons and alpha particles it was assumed the results would hold for protons. This was confirmed through proton accelerator testing (see Sect. 4), with a notable exception. During early proton beam tests it was observed that, at certain energies, charge collection did not behave uniformly throughout the detector stack. It was determined that high-energy protons penetrating into the stack but stopping after barely penetrating (20–50 μm) in the first of a pair of doubled detectors exhibited notably delayed charge collection. With the detector pairs mounted cathode-to-cathode, the leading face of a pair is the low-electric field n-type region. It was overlooked that ions stopping in this region can exhibit slow charge collection due to the high ionization density (Bragg maximum) shielding most of the charge from the accelerating fields. Charge collection is retarded by the rate of plasma erosion (Ammerlaan et al. 1963). The consequence

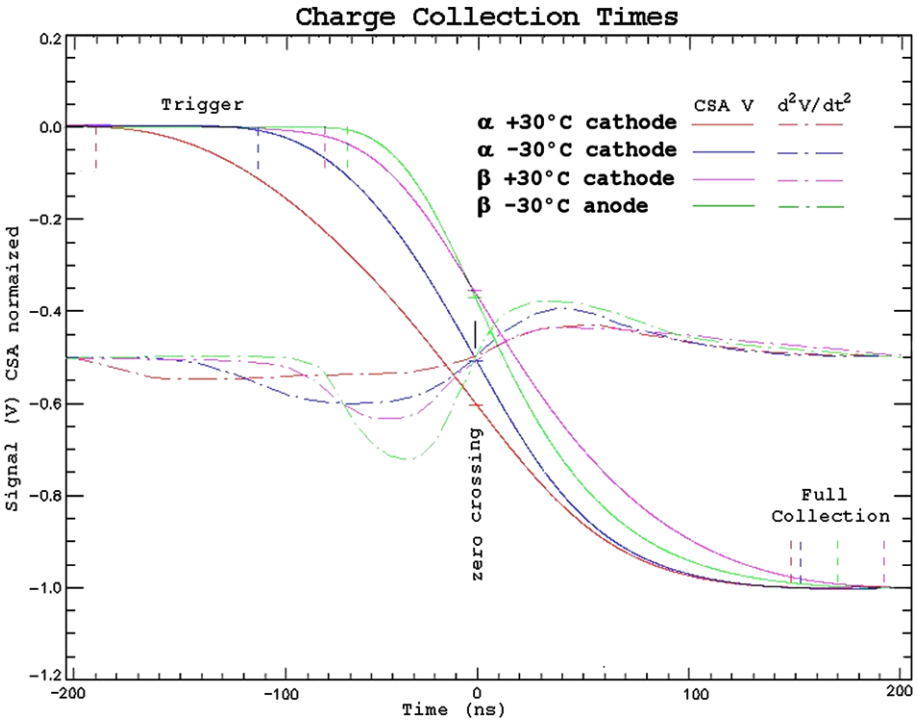

Fig. 12 Charge collection times measured in fully depleted 1500 micron thick solid-state detectors. Collection times from the inflection point of the charge current curve to full collection are roughly constant over particle type, temperature, and detector face

of this was that for a small set of very narrow proton energies REPT was mis-sampling the entire stack based on one delayed channel.

Event timing in the FPGA has since been modified to prevent this mis-sampling of the stack and, as described later, a scheme has been implemented to time any delay and correct the mis-sampling of any detector suffering slow charge collection.

3.6 Collimator

The sensor collimator is a high-Z disk-loaded design developed using GEANT4 modeling to verify scattering and cut-off energies and adjunct ray tracing to establish required material thicknesses for all paths. Disk spacing, edge bevel and aspect ratio were optimized to minimize lower energy range electron scattering (Vampola 1998) while material selection and thickness was chosen to provide a hard aperture for higher energy particles. Most of the collimator rings are made of tantalum. However tantalum is mechanically soft resulting in poor machining tolerance. Where precision is required, as with the front aperture-defining collimator ring, or where the part is structural like the mid-stack clamp, sintered tungsten alloys were used instead (see the following shielding section for a discussion of alloy selection). Toward the front of the collimator the spacers between the high-Z rings are aluminum to prevent scattering back into the collimator, but further down the collimator they change to tantalum to provide the necessary off-axis shielding.

At the back of the collimator, just in front of the detectors, sits the beryllium disk used to stop low energy electrons from overwhelming the front detector. The beryllium window is held in place by a Viton O-ring to provide a light-tight seal to the detector cavity.

3.7 Sensor Shielding

The REPT sensor shielding is made up of the 10 mm aluminum external housing and an inner 7 mm thick layer of sintered tungsten-copper (90 %–10 %) alloy. As pure bulk tungsten is very difficult to machine, the preferred form is one of several sintered alloys with a copper or a nickel/iron mix being the most readily available. A material activation study, undertaken at Brookhaven National Laboratory, showed that the unshielded W/Cu alloys may become activated (when exposed to radiation) but not when behind the 10 mm aluminum outer shielding. For the few tungsten parts in the collimator that do not have full aluminum shielding, we worked with the mission magnetics cleanliness team to fabricate these using a W/Ni/Fe alloy.

The back shielding plate is 9 mm thick to provide extra stopping power for the large surface of the back detector. Pressed into it are three tantalum rods with threaded ends, onto which the detectors are stacked, and which are used to hold the detector stack and shielding together. The detector flex circuits exit the shielding via a two-piece high-Z labyrinth affixed to the back plate. All shielding joints are stepped to eliminate any energetic particle sneak paths.

3.8 Bias, CSA and Calibration Electronics

The Detector Interconnect, Bias & CSA and the Calibration & Housekeeping (Cal & Hskp) PWBAs are mounted in the sensor head near to the detectors. Bias voltages from and detector signals to the Bias & CSA PWBA are routed through the Detector Interconnect PWBA. Electrical power, the common bias voltage and control signals for the sensor head are supplied to the Cal & Hskp PWBA via flex circuits from the Power and Digital PWBAs in the electronics box. The CSA outputs from all ten channels are routed to the two Analog PWBAs in the electronics box over individual 5″–6″ coaxial cables.

The 10 charge sensitive amplifiers on the Bias & CSA PWBA are the AMPTEK A250F that was selected for its speed, low-power characteristics and compact packaging. The CSA gains were adjusted to 36 mV/MeV (Si) with recovery time constants of ∼12 μs. Simulations show that with these values the CSA response remains linear for a 25 MeV (Si) event (expected maximum for a stopping proton) during a sustained 100 kcps 1 MeV (Si) flux. Side penetrating cosmic rays may deposit enough energy to drive the AMPTEKs out of their linear response range but testing shows they recover normally without signs of saturation delay for energies well above 100 MeV (Si).

A charge-injection circuit is part of the Calibration & Housekeeping PWBA for in-flight calibration tracking. The charge level is selectable from 0 to 25 MeV (Si) in increments of ∼83 keV. Upon command, 100 charge pulses are injected at the inputs of one or another set of 5 CSAs. The two sets of calibration channels are physically interleaved on the PWBAs supporting the monitoring of cross-talk. The FPGA collects events immediately following each of the 100 pulses and telemeters them to the ground as calibration data.

3.9 Electronics Box

The REPT electronics box contains the Power Supply PWBA, the Digital PWBA and two identical 5 channel Analog PWBAs and a backplane they all plug into. To mitigate deep

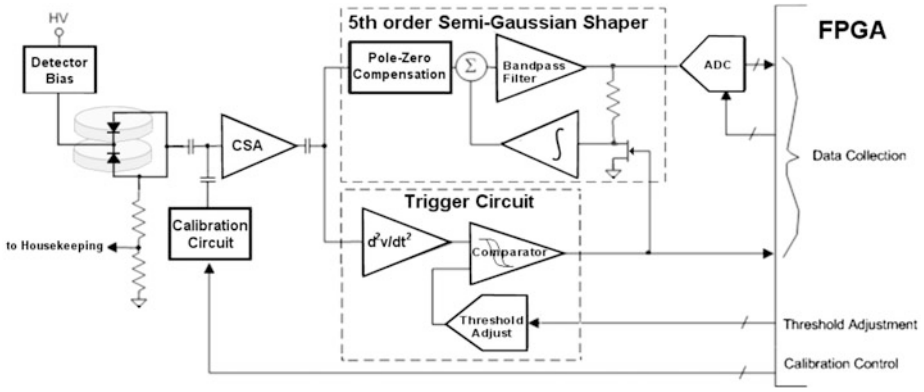

Fig. 13 One of ten REPT analog signal chains. Bias, CSA, and calibration circuitry is located in the sensor head. The shaper and trigger circuits, along with the ADCs are housed in the electronics box

dielectric charging of the PWBAs in the high electron flux environments, the walls of the electronics box, as well as the walls of the electronics portion of the sensor head are a minimum of 0.35″ thick aluminum as mandated by the RBSP mission. The mission provided adequate mass allowance that we were not forced to trade weight-relief against the 0.35″ requirement. All aluminum housing pieces are passivated with a chromate conversion coating and all joints are staggered to provide a seal against electro-magnetic emissions.

3.10 Analog Electronics

Each of the two Analog PWBAs in the electronics box contains five identical analog chains (see Fig. 13) comprising three sections: (1) A fast-channel discriminator performs threshold testing, initiates timing to sample the slow-channel peak, and provides a means to evaluate detector coincidence and pile-up conditions, (2) A slow-channel pseudo-Gaussian shaper creates a pulse whose amplitude is proportional to the charge deposited in the detector. (3) A high-speed ADC provides pulse height measurement of the slow-channel peak.

3.11 Fast-Channel

As mentioned earlier, the time from the inflection point on the CSA waveform to full charge collection is consistently 170 ± 20 ns. This relationship propagates through the slow channel semi-Gaussian shaper so that its peaking occurs at a similarly repeatable time relative to the CSA signal inflection point. The fast-channel discriminator therefore marks the CSA inflection point as a fiducial for FPGA event timing. Figures 14 and 15 illustrate how the fast and slow channel signals are collected for event timing and acquisition.

The fast channel incorporates a double-differentiator, and a zero-crossing discriminator with hysteresis. As implemented, the discriminator triggers (at a threshold that is adjustable) on the leading edge of the initial d^2V/dt^2 excursion and the comparator hysteresis holds-off de-assertion until the subsequent zero crossing. As a consequence the trigger pulse duration varies from 50 ns to 160 ns but the trailing edge of the pulse to full charge collection is relatively constant.

The threshold for each channel's discriminator is adjustable to accommodate variations in CSA gains and increased noise in the detectors from radiation damage. The threshold adjustment range is from about 300–1100 keV (Si) in ∼50 keV (Si) increments.

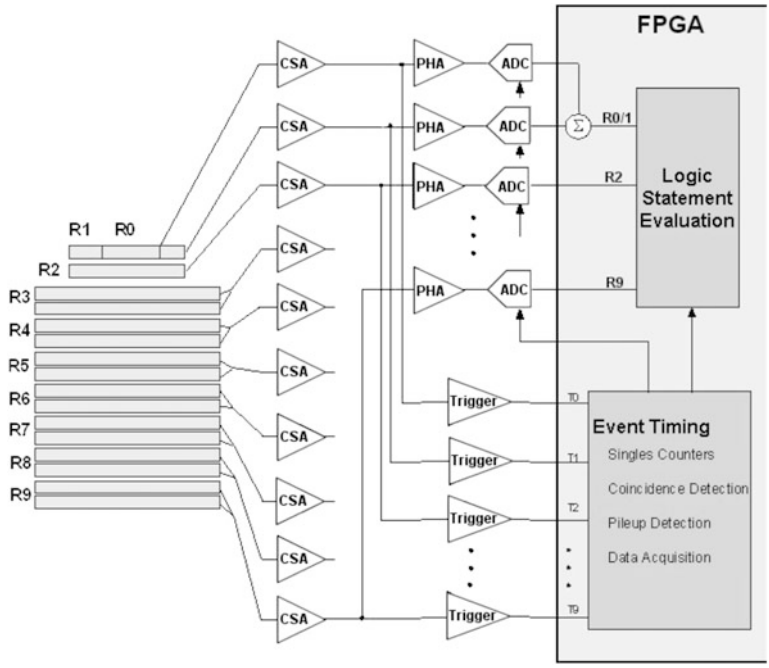

Fig. 14 Slow and fast channel signal flow. The FPGA coordinates slow channel particle event collection based on fast channel timing

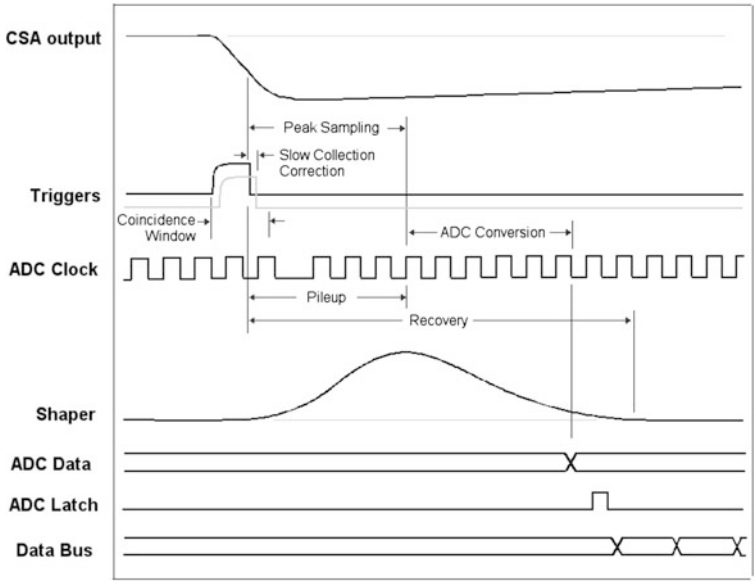

Fig. 15 Particle event timing and data acquisition. *Bold traces* show nominal charge collection and resulting timing events. The *lighter traces* illustrate slow charge collection with the associated timing based correction

3.12 Slow-Channel

The slow channel pulse shaping time is a compromise between long peaking times to minimize ballistic deficit and faster peaking times to support the high-flux environments (Baker et al. 2008). With the measured charge collection times, a 5th order pseudo-Gaussian shaper design was selected with a peaking time on the order of 650 ns (Gornov et al. 2002) and a gain of 60 mV/MeV (Si) with ballistic deficit losses less than 3 % (Loo et al. 1988). The design utilizes methods (Mosher 1976; Beche 2002) for excellent baseline recovery and is implemented with a 4-pole Sallen-Key low pass filter using a low-power, 100 MHz, op-amp. The first stage of the shaper includes a pole-zero cancellation network to compensate for the CSA pole.

The AC coupling of the CSA signal makes the slow channel susceptible to baseline drift, particularly during high flux periods. To correct for this a gated-baseline restore circuit is included which integrates the shaper output between particle events and subtracts that from the shaper input.

3.13 Timing, Coincidence and Pile-up

Using the trigger pulses from the fast channel discriminators, the FPGA based algorithms perform various qualification- and acquisition-related timing functions. In the typical case, triggers from one or more detectors go high and then low within a coincidence window of 250 ns indicating that a single coherent event occurred. When the first of the triggers de-asserts and falls the FPGA adjusts the global ADC sample clock so that a sample edge will occur 475 ns from the trigger trailing edge, to coincide with the slow channel peaking time. From that trailing edge the FPGA also times each of the other trigger trailing edges, so as to apply a mis-sampling correction factor for slow charge collection, as discussed earlier. From the trailing edge of the last trigger to de-assert the FPGA starts a 1000 ns deadtime timer during which the slow channels will be peaking and recovering.

As pile-ups are a critical product of these timing functions, the FPGA detects three classes of pile-up events in the slow channels: immediate pile-up, where a trigger pulse extends outside the coincidence window, primary pile-up where a subsequent particle causes a trigger before a preceding event has been sampled by the ADCs, and secondary pile-up where a second event happens after a preceding event has been sampled but close enough that the second event is riding on the tail of the first. At higher fluxes the separate smaller active areas, R0 and R1, on the front detector provide improved pile-up detection. The FPGA produces a count of all pile-up events but does not sample or analyze them.

Correction of the slow charge collection from shallow penetrating ions is another timing based function carried out by the FPGA. Using the number of 25 ns FPGA clock cycles from the first trigger from a stack event to the each subsequent trigger as indices to a lookup table of multiplication (MLUT) correction factors, the measured energy values are corrected for sampling off of the waveform peak.

3.14 Pulse Height Analysis

The sampling of the slow channel pseudo-Gaussian shaped pulse is carried out by the 12-bit ADC operating at 10 MHz. Input offset and scaling to the ADC is selected such that a 0 MeV (Si) input produces an output of $\sim$20 DN (digital number) and gain is 37 DN/MeV.

The FPGA can shift the ADC clock with 25 ns resolution so as to align the sampling edge with the peak of the slow channel pseudo-Gaussian pulse. The 25 ns resolution arises from the FPGA 40 MHz operation and corresponds to <1 % amplitude error from sampling off the waveform peak.

Table 2 Electron energy bin logic statement parameters

No.	ΔE (MeV)	Logic condition (energy equation)[a]
1	1.6–2.0	$(R_1 \geq 0.4) \cdot (R_2 \geq 0.4) \cdot (R_{12} \leq 1.35) \cdot \bar{R}_{39}$
2	2.0–2.5	$(R_1 \geq 0.4) \cdot (R_2 \geq 0.4) \cdot (1.3 \leq R_{12} \leq 1.7) \cdot \bar{R}_{39}$
3	2.5–3.2	$(R_{12} \geq 0.8) \cdot (1.85 \leq R_{13} \leq 2.25) \cdot \bar{R}_{49}$
4	3.2–4.0	$(R_{12} \geq 0.4) \cdot (2.65 \leq R_{13} \leq 2.95) \cdot \bar{R}_{49}$
5	4.0–5.0	$(R_1 \geq 0.4) \cdot (R_{23} \cdot 0.4) \cdot (3.35 \leq R_{14} \leq 3.95) \cdot \bar{R}_{59}$
6	5.0–6.2	$(R_1 \geq 0.4) \cdot (R_{24} \cdot 0.4) \cdot (4.4 \leq R_{15} \leq 5.0) \cdot \bar{R}_{69}$
7	6.2–7.7	$(0.4 \leq R_1 \leq 1.0) \cdot (0.4 \leq R_{2\_} \leq 2.0) \cdot (R_{34}\_0.4) \cdot (5.5 \leq R_{15} \leq 6.25) \cdot \bar{R}_{69}$
8	7.7–9.7	$(R_1 \geq 0.4) \cdot (0.4 \leq R_{2\_} \leq 1.0) \cdot (R_{34} \geq 2.4) \cdot (5.75 \leq R_{36} \leq 6.6) \cdot \bar{R}_{79}$
9	9.7–12.1	$(R_1 \geq 0.4) \cdot (0.4 \leq R_{2\_} \leq 1.0) \cdot (0.4 \leq R_3 \leq 2.0) \cdot (R_4 \geq 0.4) \cdot (R_{56} \geq 0.4) \cdot (8.0 \leq R_{37} \leq 9.0) \cdot \bar{R}_{89}$
10	12.1–15.1	$(R_1 \geq 0.4) \cdot (R_2 \geq 0.4) \cdot (R_3 \geq 0.4) \cdot (R_4 \geq 0.4) \cdot (R_5 \geq 0.4) \cdot (R_6 \geq 0.4) \cdot (R_7 \geq 0.4) \cdot (10.3 \leq R_{38} \leq 12.5) \cdot (R_9 \leq 0.4)$
11	15.1–18.9	$(0.4 \leq R_1 \leq 1.0) \cdot (R_2 \geq 0.4) \cdot (R_3 \geq 0.4) \cdot (R_{48} \geq 0.4) \cdot (R_{59} \geq 11.0)$
12	18.9–	$(0.4 \leq R1 \leq 1.0) \cdot (0.4 \leq R_2 \leq 1.0) \cdot (0.4 \leq R_3 \leq 1.5) \cdot (R_{48} \geq 0.4) \cdot (R_{59} \geq 15.0)$

[a] $R_{xy} = R_x + R_{x+1} \ldots R_y$
$\bar{R}_{xy} = (R_x < 0.4) \cdot (R_{x+1} < 0.4) \cdot (\cdots) \cdot (R_y < 0.4)$

3.15 Event Processing

The process of classifying particle events by type and energy range proceeds by comparing the PHA data from individual detectors and PHA sums of select detectors against sets of energy bounds, with each set defining an energy bin. The energy bound conditions are written as logic statements with multiple terms that if all evaluate as true the count of the energy bin for that particle type is incremented. The general form of the logic statements is shown below where $\prod$ and $\cdot$ are logical 'And' operators and the δ operator signifies inclusion.

$$E_+ = \prod_{i=1}^{9} (E_{lo_i} \leq R_i \leq E_{hi_i}) \cdot \left(E_{lo_A} \leq \sum_{i=0}^{9} \delta_{A_i} \cdot R_i \leq E_{hi_A} \right) \cdot \left(E_{lo_B} \leq \sum_{i=0}^{9} \delta_{B_i} \cdot R_i \leq E_{hi_B} \right) \quad (3)$$

Each logic statement has up to nine terms comparing each detector PHA against low and high bounds, and two terms where summations of included detector values are compared against low and high bounds.

The specific limits for each of the 12 electron and 8 proton energy bin logic statements are given in Tables 2 and Table 3, respectively.

The diagram in Fig. 16 shows PHA signal flow through the FPGA for particle event processing. On the left, the raw PHA values are adjusted to a zero offset common DN/MeV scale using the MLUT and GCO tables described below; then the results from the separate active areas of the front detector are summed. The scaled PHA values are held in registers where they are gated sequentially into the evaluation circuitry as the various energy bin bounds are also presented. For any given energy bin logic statement, the bounds are evaluated until a term fails or all evaluate true. The result is then noted and the process repeats for the rest of the bins. Because a particle event is evaluated for all bins, a particle can match one

Table 3 Proton energy bin logic statement parameters

No.	ΔE (MeV)	Logic condition (energy equation)[a]
1	18.5–24.0	$(R_1 > 8.0) \cdot (R_2 > 6.8) \cdot \bar{R}_{39}$
2	24.0–31.2	$(R_1 > 0.5) \cdot (R_2 > 5.0) \cdot (R_3 > 11.0) \cdot \bar{R}_{49}$
3	31.2–40.6	$(R_1 > 0.5) \cdot (R_2 > 0.5) \cdot (R_3 > 10.0) \cdot (R_4 > 13.2) \cdot \bar{R}_{59}$
4	40.6–52.8	$(0.5 < R_1 < 4.7) \cdot (0.5 < R_2 < 6.0) \cdot (R_3 > 0.5) \cdot (11.5 < R_{46} < 33.0) \cdot \bar{R}_{79}$
5	52.8–68.6	$(0.5 < R_1 < 5.5) \cdot (0.5 < R_2 < 6.5) \cdot (R_3 > 0.5) \cdot (R_4 > 0.5) \cdot (R_5 > 0.5) \cdot (3.0 < R_{68} < 40.0) \cdot (R_9 < 1.5)$
6	68.6–89.2	$(0.5 < R_1 < 5.0) \cdot (0.5 < R_2 < 5.0) \cdot (R_3 > 0.5) \cdot (R_4 > 0.5) \cdot (R_5 > 0.5) \cdot (R_6 > 0.5) \cdot (R_7 > 0.5) \cdot (R_8 > 0.5) \cdot (37.0 < R_{18} < 65.0) \cdot (R_9 > 0.5)$
7	89.2–116.0	$(0.5 < R_1 < 3.0) \cdot (0.5 < R_2 < 3.0) \cdot (3.0 < R_3 < 5.5) \cdot (3.0 < R_4 < 7.0) \cdot (3.0 < R_5 < 6.0) \cdot (3.0 < R_7 < 6.0) \cdot (4.5 < R_8 < 7.0) \cdot (31.0 < R_{19} < 45.0)$
8	116.0–	$(0.5 < R_1 < 5.0) \cdot (0.5 < R_2 < 5.0) \cdot (5.0 < R_{18} < 28.0)$

[a] $R_{xy} = R_x + R_{x+1} \ldots R_y$
$\bar{R}_{xy} = (R_x < 0.5) \cdot (R_{x+1} < 0.5) \cdot (\cdots) \cdot (R_y < 0.5)$

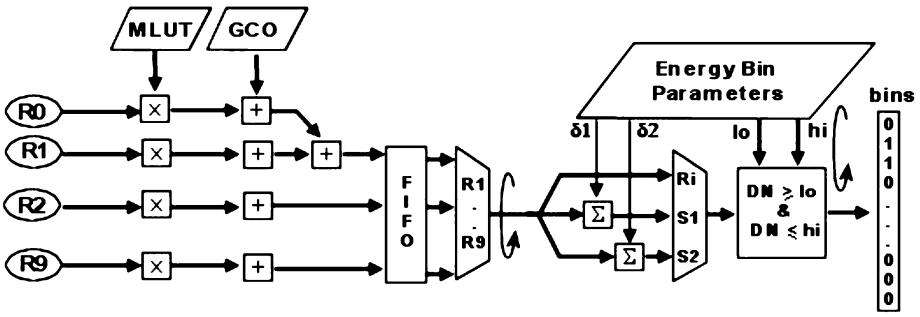

Fig. 16 Data flow in energy bin logic statement evaluation. Detector PHA values are adjusted to a 0 offset common DN/MeV scale and then sequentially compared to the energy bounds of each energy bin logic statement. The results are passed to the FPGA science telemetry block

or more bins; in this case, all matching bins will be tallied. The binning results are passed on to the spin sectoring section of the FPGA. If a particle does not fall into any bin, it is incremented into a 'no-match' counter.

For evaluation by the FPGA, the logic statement bounds and detector PHA values must have the same DN/MeV scale. Although each detector channel was designed to have a nominal gain of 37 DN/MeV and 20 DN offset, variations were unavoidable. To accommodate these variations and any changes that may develop over time, the FPGA uses the MLUT (multiplication lookup table) for channel-by-channel gain normalization and the GCO (gain correcting offset) table to produce zero offset values.

The MLUT contains gain correction terms for each channel convolved with the correction terms for slow charge collection. Using the channel number and any measured trigger delay as indices to the lookup table, the returned value effects both corrections to the PHA values with a single multiplication operation. The values returned by the GCO lookup table are the negative of each channel's characteristic offset. Subtracting them from the PHA produces a zero-offset value.

Due to limitations imposed by the implementation of the MLUT, each REPT instrument has a slightly different optimum common DN/MeV scale. As a consequence the DN values of the energy bin limits must be scaled for each instrument to match. Each instrument's tables of offset, gain and scaled logic bounds are uploaded from the ground each time the instruments are power cycled.

REPT science data collection is synchronized with the spacecraft spin period; each spin is subdivided into 36 equal duration sectors. The FPGA gets the spin period and phase once a second from the spacecraft and interpolates between updates with internal counters. If the internal counters become out of sync with the spacecraft, the FPGA will advance its internal sector counter until it is once again in sync with the spacecraft, flagging the data for each sector with an error. In cases such as spacecraft eclipses where the spin period and phase information are flagged by the spacecraft as invalid, the REPT FPGA propagates its internal sector counters from the last known good spin period and phase information and resynchronizes as described above when the spacecraft indicates the provided spin period and phase data are once again valid.

3.16 Digital Board

The Digital PWBA carries the REPT system FPGA, the spacecraft communications drivers, and the instrument housekeeping collection system. The FPGA is an Actel RTAX2000S operating at 40 MHz. In addition to particle event processing the FPGA handles commanding, collects housekeeping data, and formats and sends telemetry packets to the spacecraft. The details of the FPGA design and operation are given later in the FPGA section.

3.17 Power Supply

The REPT Power PWBA is a custom-built pulse width modulated (PWM) DC-DC power converter using a single-switch, current-mode control, forward converter topology to generate 3.3 V and ±5 V. The 3.3 V secondary is regulated using a discreet magnetic feedback circuit to bridge the isolation barrier. The ±5 V secondaries rely on a coupled inductor to provide cross-regulation. Additional lower voltages, 2.5 V for ADCs and 1.5 V for the FPGA core, are generated using linear regulators powered by the 3.3 V primary and providing better than 1 % regulation.

A second output on the PWM is used to drive the 320 V bias generation. The PWM output is AC coupled to a step-up transformer with the secondary driving a 4-stage series voltage multiplier. The output of the voltage multiplier is series regulated to 320 V and designed to provide ∼500 μA to the Bias & CSA PWBA supporting the worst case end-of-life radiation and elevated temperature.

3.18 Thermal

The REPT instrument, as shown in Fig. 17, utilizes a passive thermal design. It is thermally isolated from the RBSP spacecraft with G-10 spacers and titanium bolts. Multi-layer insulation (MLI) blankets around the electronics box decouple it from the spacecraft interior while radiator surfaces across the sensor housing allow for cooler operating temperatures. The radiator surfaces consist of Germanium Black Kapton sheets attached with an electrically conductive adhesive. The MLI blankets consist of an electrically conductive outer layer of 100XC black Kapton and typical aluminized Kapton inner layers. A single survival heater circuit with series-redundant thermostats maintains REPT temperatures when the instrument

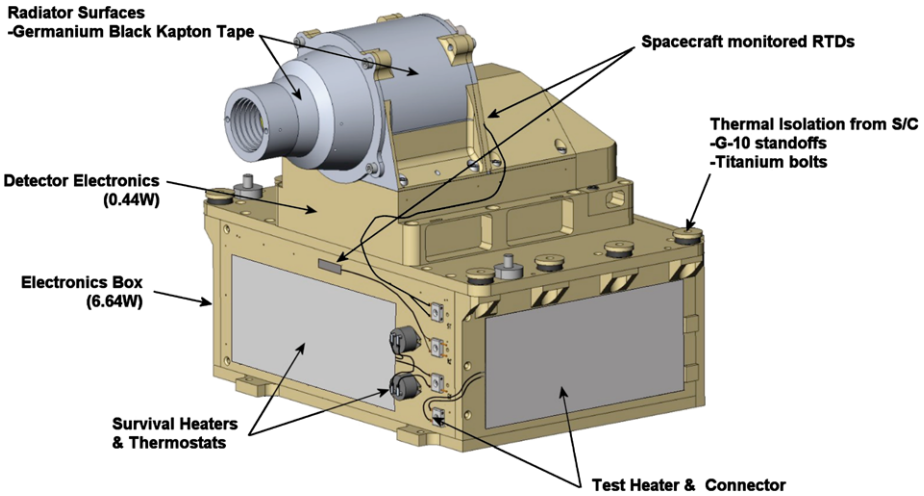

Fig. 17 REPT Thermal Systems. Thermal standoffs and MLI blankets (not shown) isolate the instrument from the spacecraft deck while radiator tape on the sensor head provides a −1 °C nominal detector temperatures

is powered off. Both survival and the test heater elements are a specific magnetically cancelling design. The REPT temperature is monitored through several internal housekeeping thermistors, plus two spacecraft-monitored platinum thermal sensors.

The predicted on-orbit temperatures are: −21 °C to +22 °C for the sensor head with the -1 ± 10 °C being the most likely, and −17 °C to +28 °C for the electronics box with a most likely prediction of $+6 \pm 11$ °C. Variation over any given orbit is expected to be on the order of 1–2 °C. The wide ranges are due to unknowns in the spacecraft operating temperatures.

3.19 Magnetic Compatibility

REPT performance is not affected by spacecraft magnetic fields. The REPT design has been fully reviewed and is compliant with the rigorous RBSP mission magnetic cleanliness requirements, so as to not impact the EMFISIS Search Coil or Magnetometer. All materials were screened for minimal magnetic remanence. For the few cases where the use of non-ideal materials were required, the materials were de-gaussed, tracked, and reported to the mission. All high current paths in the instrument were identified and reviewed. The layout of the electronics PWBA considered low frequency DC current paths to reduce the magnetic loop area. The survival heaters, and the wiring to them, were specially selected and routed to be magnetic-cancelling in the far field.

3.20 Telemetry

REPT telemetry consists of science (energy bins, PHA, space weather), engineering (housekeeping, calibration results) and command responses. The full set of telemetry packets is shown in Table 4. All telemetry is formed in CCSDS packets of less than 256 bytes.

The primary science data, reported in the “Science” packet, consists of particle energy spectral data collected for each of the 36 spin sectors and reported to the spacecraft once each spin. It consists of counts of particle events classified into each of the 20 energy bins, particles not able to be classified, pileup events and counts of triggers on each detector. The

Table 4 REPT telemetry items

Packet name	APID	Size (bytes)	Default RUN rate	Default SAFE rate	Contents
Instrument housekeeping	$0 \times 20A$	80	1/min	1/s	General health and safety info
Critical housekeeping	0×200	18	1/s	1/s	Health and safety info monitored by Mission Operations Center
Space weather	0×201	18	1/spin	None	Real-time space weather info
Science	0×202	1820	1/spin	None	All equations and singles counts
Pulse height analysis (PHA)	0×205	1622	1/50 s	None	Raw signal information
Calibration	0×206	1320	On Cmd	On Cmd	Results of charge injection
Command echo	0×207	14	On Cmd	On Cmd	Opcode and result of last command
Memory read	0×208	254	On Cmd	On Cmd	Memory dump
Checksum	0×209	20	On Cmd	On Cmd	Result of checksum command

data are marked with the instrument ID, Mission Elapse Time (MET) at start of the spin and end of each sector, whether the instrument identifies any potential errors in the sector timing, the state of the bias voltage, and the version of the particle classification logic equations. All counting data are collected in 23 bit counters and reported in an 8 bit mantissa, 4 bit exponent pseudo-log compression providing a dynamic range of over 8 million with less than 1 % loss.

The secondary science data, "PHA," provides a sampling of the collected pulse-height analysis data. Each packet consists of 100 PHA data sets where each PHA set is generated by a particle event and contains 10 bit ADC values for each detector, as well as the energy bin(s) matched by these values. The PHA data are only generated by events that meet validity (timing and coincidence) requirements. The PHA science data are collected at a configurable cadence, with once every 12 ms being the fastest and 500 ms being nominal for flight.

For space weather, the third science data packet, REPT reports the singles counts on detectors R2, R4, and R9, over full spins (all 36 sector counts are combined). These detector single counts correspond roughly with electrons of 2, 5, 10 MeV and protons of 20, 50, 70 MeV.

Housekeeping packets contain information about the state of health of the instrument. REPT has two housekeeping packets, Instrument Housekeeping and Critical Housekeeping. Instrument Housekeeping is a comprehensive set of data points. It contains operating states, packet rates and status, command success/failure counts and codes, other error counters, temperature values from around the instrument, and power supply voltage and current monitors including detector leakage currents. It is typically sent once per second while in SAFE mode, and once per minute when in RUN mode. The Critical Housekeeping packet is a small subset of these data points and is given priority handling both by the spacecraft and by the Mission Operations Center (MOC) as it is among the first data sent down by the spacecraft upon contact with the ground and when received by the MOC its contains will be checked against a set of limits and alarms emailed out as appropriate.

The remaining telemetry packet types are those issued by the instrument in response to a command. The calibration telemetry packet contains the 100 PHA sets resulting from a cali-

Table 5 REPT commands

Command name	Opcode	Description
NOOP	3	No operation
ARM	6	Enter ARM state to allow protected commands
RUN	9	Enter RUN mode
SAFE	12	Enter SAFE mode
CALIBRATE	15	Issue a calibration packet
BIAS_ON	18	Turn on BIAS voltage (Protected)
BIAS_OFF	21	Turn off BIAS voltage
MEM_READ	24	Read FPGA registers/memory
MEM_WRITE	27	Modify FPGA registers/memory
CHECKSUM	30	Request a checksum over a portion of FPGA memory

bration command as described previously, along with a record of the commanded calibration level and analog measurements verifying the actual level.

The telemetry responses to the Checksum and Memory Read commands are discussed below in commanding. The remaining command response packet, Command Echo, is used for communication and commanding diagnostics. When enabled, it repeats each command received back to the ground along with a success/fail indictor. The issuance of the Command Echo response is controlled by writing to a FPGA memory register and is disabled by default.

The total telemetry allocation for REPT is 1580 bits per second. Of this, primary energy bin science uses about 78 %, instrument housekeeping takes up 1 %, and secondary PHA science uses the remaining 21 % but is periodically adjusted down to 17 % to accommodate internal calibration data.

3.21 Commanding

The REPT command set is relatively small. The full set is given in Table 5. Without a microprocessor, commanding of REPT largely entails writing to configuration registers in the FPGA. The registers of particular interest are the following:

- Energy Bin parameters: These registers contain the parameters used for the twenty energy bin logic statements. There is also a separate register that contains the current version of the parameter set.
- Data Processing Registers: These are the registers that contain the GCO and MLUT tables, used to normalize the calibration of each analog chain. There are also separate registers that contain the current GCO and MLUT version.
- Acquisition registers: These registers describe the requirements for valid events, including required triggers, coincidence window duration and timing restrictions.
- Threshold Registers: These registers are used to adjust the trigger sensitivity of each of the detectors.

There is an assortment of other registers for enabling and setting the cadence of telemetry transmission, resetting errors counters and low-level diagnostics. All FPGA registers are configured through the MEM_WRITE command. Each MEM_WRITE command can configure up to 40 separate register addresses. Likewise the MEM_READ command can

request the contents of up to 40 separate registers, which will be reported in the Memory Read telemetry packet.

Aside from the Memory Read/Write commands there are seven explicit commands to the REPT instrument. These are CALIBRATE, NOOP, ARM, SAFE, RUN, BIAS_ON, BIAS_OFF, and CHECKSUM. The CALIBRATE command is discussed above in regard to its operation and telemetry. The NOOP command is the generic null operation that does no action except increment the command success counter and issue an echo packet (if enabled). The SAFE and RUN commands are used to set the REPT operating mode. The CHECKSUM command calculates a CRC checksum over a selected range of memory registers. It is used to verify the integrity of the GCO, MLUT and Energy Bin parameter tables. The calculated checksum comes to the ground in its own telemetry packet.

The ARM command allows the FPGA to accept an immediately subsequent BIAS_ON command which enables the bias voltage supply. The 320 V bias supply poses a risk to personnel and, in some situations, the instrument itself so is protected from being inadvertently enabled. The BIAS_OFF command removes power from the bias supply voltage. It is not protected and can be sent at any time.

4 Instrument Testing, Characterization, and Calibration

REPT calibration was done both at the each individual detector level as well as the instrument level at accelerator beams. For the latter calibration both the flight models as well as the engineering model were calibrated at electron and proton facilities. The details of the calibration are given below.

Each detector comprising both the REPT stacks was calibrated using a trinuclide alpha source in vacuum as well as charge injection to establish the ADC to MeV relationship. Figure 18 shows the ADC counts (DN) as a function of the injected charge for a pair 40 mm detectors comprising the 8th element of one of the flight models of REPT together with a straight line fit to the data. It is clear from the figure that there is excellent linearity between the energy loss and the ADC counts over the entire range of expected energy loss for electrons and protons. Furthermore, the trinuclide alpha source with emitted alpha energies of 5.15, 5.48, and 5.80 MeV lie on the fit straight line further confirming and establishing the ADC to MeV conversion. The number of points scattered along the bottom of the graph

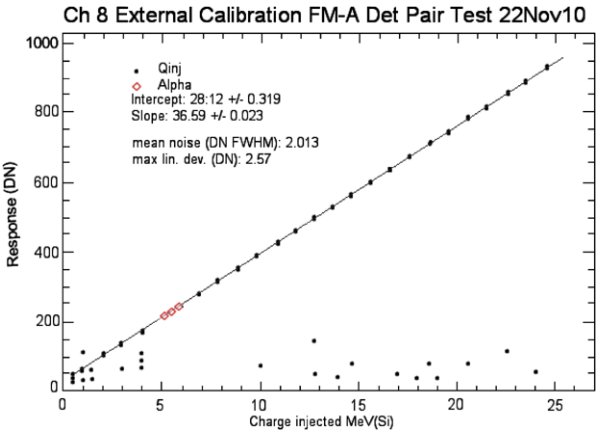

Fig. 18 External charge injection calibration

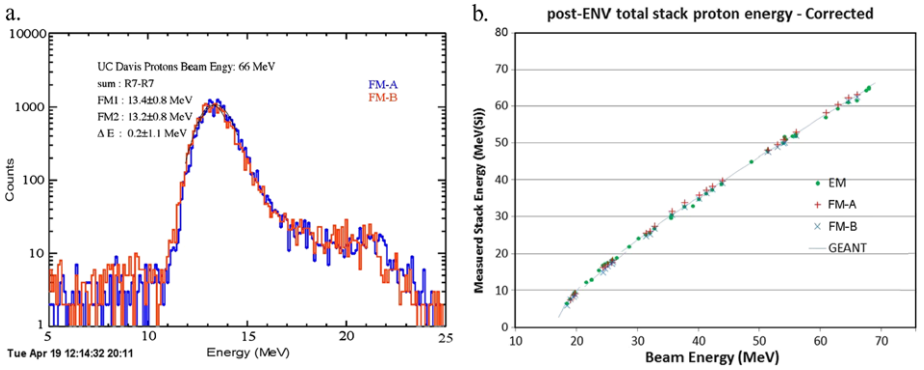

Fig. 19 (**a**) Energy deposited in R7 by 66 MeV protons in R7. The *red* and *blue curves* are for FM-A and FM-B respectively; (**b**) the total energy deposited in the detector stack as a function of the incident proton energy. Proton beam measurements for FM-A, FM-B, EM are shown as *symbols*. Expected total energy from GEANT4 simulations are superposed as a *solid line*

are due to the test setup. The signals from the sensor head were passed through the vacuum chamber wall to the electronics box situated outside.

The offsets and the slopes for all nine channels for each sensor are implemented in the FPGA as an offset and multiplication lookup tables. Each REPT sensor also has an internal calibration circuit to track changes in gain and offset over the period of the mission. This calibration tracking, which takes ∼5 minutes, will be performed periodically to ensure measurement integrity. Sensitivity to threshold changes was also investigated using charge injection. Maximum allowable thresholds accounting for detector/electronics noise were established to be less than 0.365 MeV, which is below the differential channel logic equation threshold of 0.4 MeV. The calibration results were in accordance with GEANT4 simulations, which showed that varying the threshold from 0.35 to 0.41 MeV did not significantly affect singles efficiencies; particularly for the front detector, which is used to trigger pulse height analysis.

The two flight units, FM-A and FM-B, as well as the engineering model (EM), were calibrated and tested at proton and electron accelerators. Calibrations included individual detector response as well as the total stack response and validating differential channel efficiencies. Figure 19a shows the comparison of energy loss in the R7 detector between FM-A and FM-B for an incident proton beam of 66 MeV. The instruments were mounted on a movable platform and exposed sequentially to the beam as it was maintained at the same tune. Figure 19a shows near identical energy response of detector element R7 in both FM-A and FM-B. The mean positions as well as the deposition profiles are in excellent agreement with each other.

Figure 19b shows the summed energy from the entire detector stack as a function of the incident proton energy for all the three instruments as well as the GEANT4 predicted response. The former are shown as symbols and the latter as a solid line. The individual detector pair gains had to be corrected with a factor that varied from 0 to 3 %. This correction factor was obtained from examining proton punch through for the detectors and is included in the energy sums shown in Fig. 19b. The corresponding results for electrons are shown in Figs. 20a and 20b. The former shows the energy deposited in the second detector, R2 of the stack for incident electrons of 10.6 MeV in energy with the red and blue histograms corresponding to FM-B and FM-A respectively. Also shown are Gaussian fits to the primary

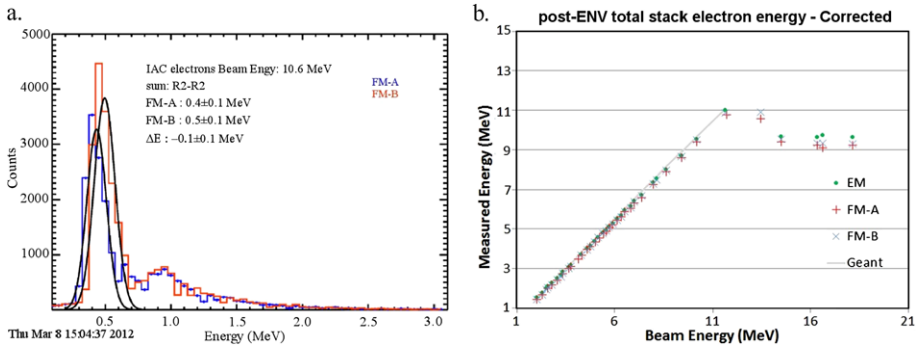

Fig. 20 (**a**) Energy deposited in R2 by 10.6 MeV electrons in R2. The *blue* and *red histograms* are for FM-A and FM-B respectively. The secondary peak to the right is due to 2 electrons per beam pulse (**b**) the total energy deposited in the detector stack as a function of the incident electron energy. Electron beam measurements for FM-A, FM-B, EM are shown as *symbols*. Expected total energy from GEANT4 simulations are superposed as a *solid line*

peak, with the mean and standard deviation indicated in the figure. There is excellent agreement between the two instruments for energy loss in individual detectors (other detectors show similar pattern to that of R2). The smaller peak to the right in Fig. 20a is due to pileup (2 electrons per pulse) from the accelerator beam.

Figure 20b shows the total energy seen in the entire detector stack as a function of the incident electron beam energy. The symbols represent measurements by the EM, FM-A and FM-B units while the solid line is the expected energy according to GEANT4 simulations. The measurements by each of the instruments and GEANT4 predictions are in close agreement. At beam energies from about 10 to 12 MeV, there is a small discrepancy between GEANT4 and measurements, most likely due to not accurately determining beam energy arising from difficulties in tuning the beam with single electron per pulse. Figure 20b also shows that beyond about 12 MeV, most electrons penetrate the full stack and the stack energy is independent of the incident beam. However, due to the fact that electrons straggle, REPT is able to measure electrons differentially up to nearly 20 MeV (see below).

As mentioned before (Sect. 3) REPT measures electrons in 11 differential channels and 1 integral channel and protons in 8 differential channels. The differential channels are obtained using logic conditions (equations) on energy deposits in individual detectors as well as summed energies on specific sets of detectors. GEANT4 simulations were used to determine these equations and all of the three REPT units were calibrated at proton and electron beams. As previously mentioned, Tables 2 and 3 show the logic conditions for electron and proton differential channels.

The logic conditions for electrons and protons yield efficiencies as a function of incident particle energy which are used to obtain particle spectra. The shapes and amplitudes of the channel efficiencies can then be validated at particle accelerators. As noted, all three instruments were calibrated at electron and proton beams. Figures 21a and 21b show the results of beam calibrations for electrons and GEANT4 predicted efficiencies, respectively.

The measured and the calculated efficiencies agree closely both in functional form and in amplitude. The EM, FM-A and FM-B are in good agreement with one another and the small differences arise mainly from lack of absolute counts from the LINAC. Note that for the differential channel measurements, the LINAC had to be operated in dark current mode due to the requirement of a single electron per beam pulse.

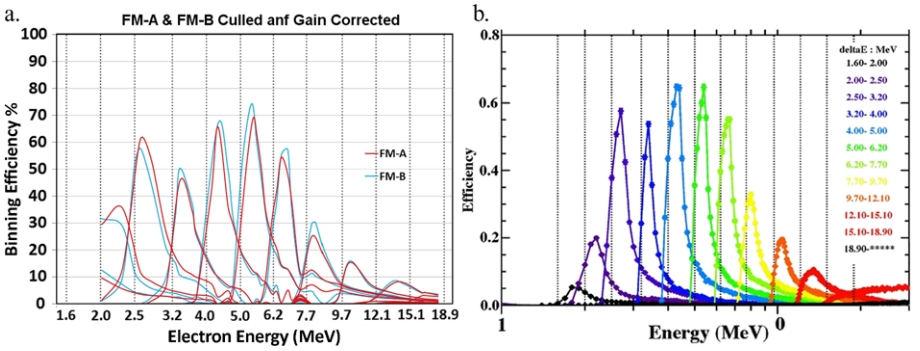

Fig. 21 Electron differential channel efficiencies (**a**) measured and (**b**) GEANT4 simulated. The three REPT units, EM, FM-A and FM-B are shown as *green*, *red* and *blue traces* respectively in panel (**a**). The nominal differential channel energies are indicated in panel (**b**) to the right, which shows GEANT4 efficiencies as different color-coded traces

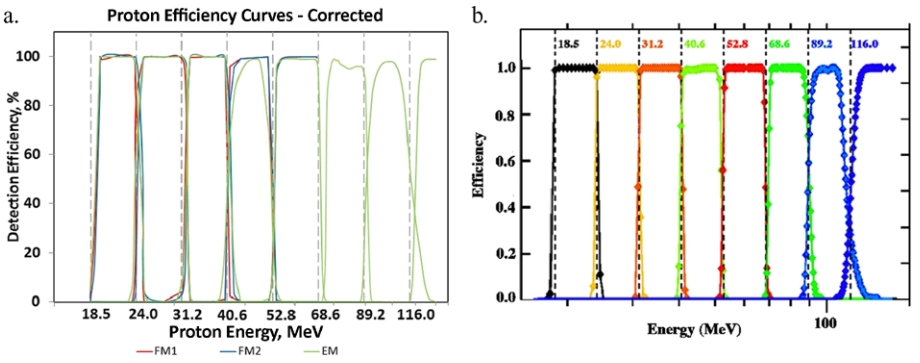

Fig. 22 Proton differential channel efficiencies (**a**) measured and (**b**) GEANT4 simulated. The three REPT units, EM, FM-A and FM-B are shown as *green*, *red* and *blue traces* respectively in panel (**a**). All the channels were not measured at the same beam (see text for details). The nominal differential channel energies are indicated in panel (**b**) to the right that shows GEANT4 efficiencies as different color coded traces

Figure 22 shows the differential channels for protons. As noted for the prior figure, Fig. 22a shows measured efficiencies (at proton beams) and Fig. 22b shows the GEANT4 calculations. The proton channels resemble step functions and are seen to be nearly identical among the three instruments and agree closely with GEANT4 simulations. The two flight models were not exposed to the highest beam energies to limit exposure to radiation and given close agreement with GEANT4 results for the lower energy channels.

It is crucial that REPT be able to measure electrons in the presence of protons, for slot filling (extreme) events that can overlap with the inner belt. To ensure this, we tested the engineering model with a Sr90 source in the 200 MeV beam at the Indiana University proton accelerator. Figure 23 shows the results, with the top histogram showing the combined energy deposit in the front detector and the red trace the Sr90 signal after removing the protons using the expected proton response in the second detector. For comparison, the expected signal for Sr90 alone is shown as a blue trace. It is clear that the electron signal from Sr90 can be separated over backgrounds of less than about 2 %. This accuracy is expected to improve much more for the differential channels as signal from multiple detectors are combined to

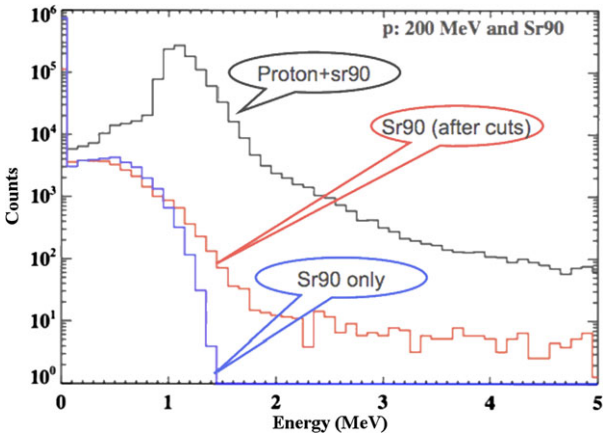

Fig. 23 Separation of electrons and protons in REPT. The histograms show energy deposited in the front detector for (**a**) combined Sr90 and 200 MeV protons (**b**) Sr90 signal over negligible background after removing protons using expected proton response and (**c**) for a purely Sr90 source

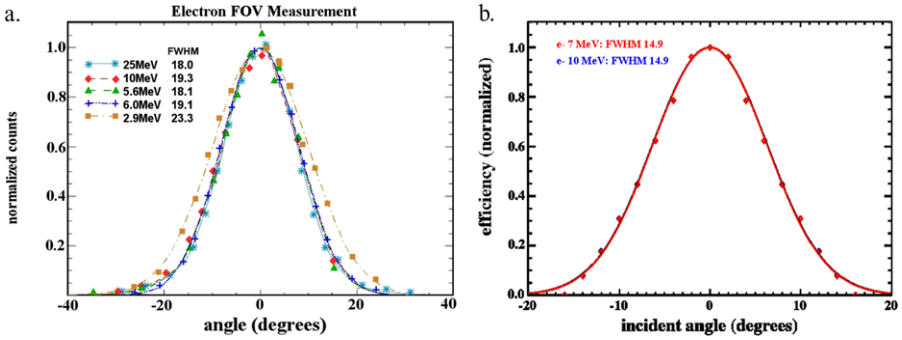

Fig. 24 Angular response of REPT (**a**) at electron beam tests and (**b**) as determined by GEANT4. The response at test beam was measured over a range of energies indicated in (**a**) and at 7.0 and 10.0 MeV for GEANT4

identify electrons. While it is not possible to obtain electrons and protons simultaneously at all energies, we have verified using GEANT4, the ability of REPT to cleanly separate electrons and protons under almost all circumstances.

The REPT field of view set by the collimator determines the geometry factor and therefore the count rates observed. We have measured the field of view for both protons and electrons at test beams and compared to the design set by GEANT4 simulations.

Figures 24a and 24b show the field-of-view for electrons as determined at test beam and GEANT4 simulations, respectively. The measured FWHM is slightly larger than the simulations indicate. This is due to multiple scattering of electrons in air over approximately 2 m-distance that separated the instruments from the beam port (note the FWHM measured at the lowest energy of 2.9 MeV is the highest as expected due to scattering).

In order to minimize background due to side penetrating particles REPT was designed with aluminum-tungsten shielding. The detection efficiencies for both protons and electrons impinging perpendicularly on the instrument were measured in test beams.

Figure 25a shows the measured efficiencies for detectors R3 and R4 with the latter multiplied by a factor of 0.1 to clearly separate the curves. Efficiencies for the two smaller front detectors were also measured (not shown) and were found to be in agreement with GEANT4 results. Due to uncertainty in determining the incident electron flux, the measured efficien-

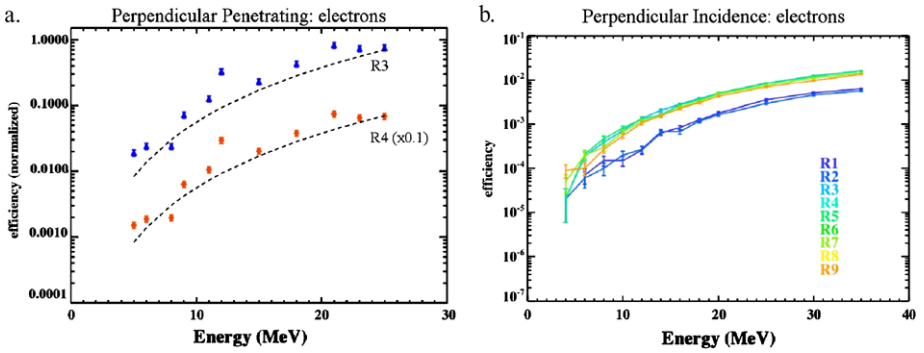

Fig. 25 (**a**) Efficiency of counting side-penetrating electrons in REPT for Detector R3 (*blue*) and Detector R4 (*red*); (**b**) Similar to (**a**) for all detectors in REPT stack and perpendicular (90°) electron incidences

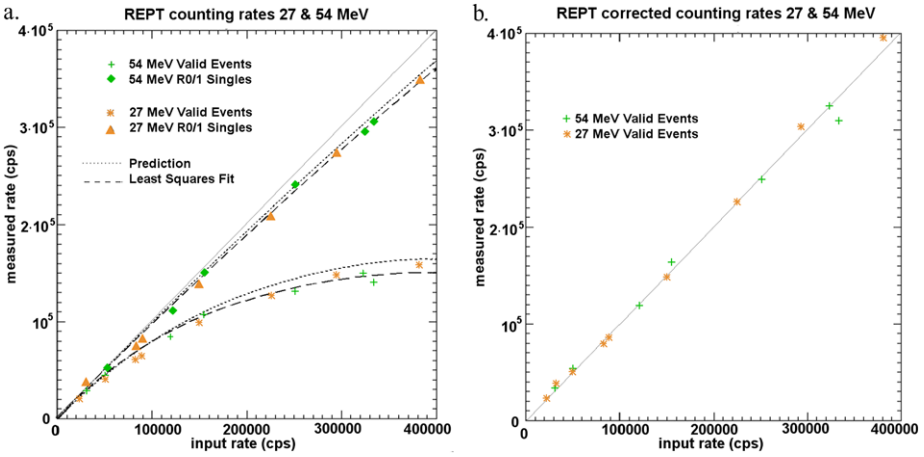

Fig. 26 (**a**) Well-behaved counting rate and dead time performance supports (**b**) excellent dead time correction factor determination

cies are shown normalized with the efficiency set arbitrarily to unity for beam energy of 25 MeV. Figure 25b shows efficiencies for all detectors (color coded as indicated in the figure) as determined by GEANT4. These efficiencies are absolute and were used to estimate background due to side-penetrating electrons. Note that as expected the efficiencies for the two front detectors are systematically less than the rest of the stack since the front detectors are smaller. Most importantly, the functional form of the measured and the GEANT4 efficiencies are in excellent agreement thereby confirming the use of GEANT4 both for design and background estimation aspects.

The proton side penetrating efficiency has a simple step function-like behavior with an efficiency of unity for protons greater than 110 MeV and zero for all energies below. This behavior was confirmed at proton test beam as well.

As described earlier, the division of the front detector into two active areas, coupled with the deterministic timing characteristics of the fast channels, supports excellent counting rate determination. The plot in Fig. 26a shows REPT reported R0/1 singles and valid event (i.e., pile-up free) rates for proton event rates of 0 to >300000 per second for both 27 and 54 MeV

protons. Also included are the plots for predicted singles rates and pile-up free (valid) events rates. The recorded performance is very close to predictions particularly for singles rates.

The REPT slow channels are best considered as paralyzable systems where actual counts m are related to the measured, essentially pile-up free counts n by

$$m = A_m \cdot n \cdot e^{2 \cdot n \cdot \tau_m} \tag{4}$$

with $\tau_m = 1100$ ns, the slow channel dead time, and A_m is the scaling factor coming from a least squares fit.

However the instrument does not provide a direct count of measured events n, and summing the bins is invalid because individual events can be counted in multiple bins. However, an estimate of n can be derived from the singles counts of the front R0/1 detector plane.

The singles counters are paralyzable as well, but not pile-up free, so the measured R0 + R1 singles rate s is related to the actual rate n by

$$s = A_s \cdot n \cdot e^{n \cdot \tau_s} \tag{5}$$

where τ_s, the fast channel dead time measured in particle beams at ~200 ns, and A_s the scaling factor are given by a least squares fit. This relationship is not directly invertible but the 5 term Taylor expansion of the exponent leads to

$$n = \frac{s}{A_s} \cdot \left[1 + \frac{s}{A_s} \cdot \tau_s + \frac{1}{2} \cdot \left(\frac{s}{A_s} \cdot \tau_s \right)^2 + \frac{1}{6} \cdot \left(\frac{s}{A_s} \cdot \tau_s \right)^3 + \frac{1}{24} \cdot \left(\frac{s}{A_s} \cdot \tau_s \right)^4 + \frac{1}{120} \cdot \left(\frac{s}{A_s} \cdot \tau_s \right)^5 \right] \tag{6}$$

The slow channel dead time correction factor b, based on the estimate of the actual event rate n and the slow channel response rate from Eq. (4), is then given by Eq. (7)

$$b = 1 + \frac{n - m(n)}{m(n)} = \frac{e^{2 \cdot n \cdot \tau_m}}{A_m} \tag{7}$$

The dead time correction must be calculated and applied on a sector by sector basis. Figure 26b shows the valid event data sets with dead time correction factors calculated and applied on a point by point basis. Since n is estimated from the singles rates the error bars remain small.

5 Data Analysis and Data Interpretation

5.1 Data Analysis

The data continuously generated by the REPT instruments will be stored on each satellite until a daily contact with a ground station is made. The data will be then downlinked and stored under the control of the Mission Operation Center (MOC), which will transfer the data to the ECT Science Operation Center (SOC) at the Los Alamos National Laboratory (LANL). These data will be in the form of raw telemetry data, containing both science and housekeeping data used to monitor and maintain REPT. The ECT SOC is responsible for the processing and disseminating the data, which will range from raw telemetry to fully calibrated and validated science data with higher-level products resulting from combined ECT suite-wide data (see Table 6). The processing algorithms and software for REPT will be provided and maintained by the REPT team. The REPT team will also receive and process

Table 6 Descriptions of data levels (Adapted from the ECT_SOC_ICD_01A Handbook, April 29, 2009)

Data level	Description	Availability	Users
L0	Raw de-commutated telemetry data from MOC	Minutes from MOC receipt (Time = T0)	SDC, Archives
L1	L0 + sorted, time-tagged, instrument separated units of count rate. CSCI-1, generated by SOC-CTG	T0+ < 6 hours	SDC, ECT team, archives
L2	L1 + calibrated and corrected (bkg. dead-time, etc.), physical units, CSCI-2, generated by SOC-SDC	T0+ < 1 week Quick-Look T0+ < 1 month Final Release	SDC, Co-Is, GIs, US & Intl scientific community, Other LWS Missions, Archives, Space Weather users, Virtual Observatories
L3	L2 + B-field derived science products (pitch angles, moments, L-sorted), CSCI-2, generated by SOC-SDC	T0+ < 1 week Quick-Look T0+ < 1 month Final Release	
L4	L3 + PSD units derived using B-field models, magnetic coordinates, CSCI-2, generated by SOC-SDC	TO+ < 1 year	

the instrument data from the SOC for the purpose of analyzing the health of the instrument and the quality of the science data.

During normal mission operations, the MOC collects all raw telemetry during contact times and combines these data into a daily MET (Mission Elapsed Time) Level zero (L0) files. The ECT SOC obtains these L0 files as soon as they are available at the MOC, on a roughly daily cadence. The first processing step is to produce Level one (L1) data, daily files in UTC, that contain science data in count rates and state of health (SOH) data in engineering units on standard time tags.

Here we adapt the existing process at LASP for use with the RBSP L0 files, which will be run at the LANL ECT SOC. LASP uses an IDL based process that operates on files of CCSDS packets, and produces output in the form of IDL savesets. Here the inputs are APL MOC L0 files and the agreed output format for ECT is ISTP compliant CDF files.

The first task of the L0 to L1 processing step at the SOC is to strip off the MOC file headers, resulting in a raw CCSDS packet file containing the housekeeping and science data in an unmodified form. The decoding software, developed and provided by LASP, simply separates this data from the telemetry stream without modification, allowing access to the individual data points. For the science data, an IDL computer program, produced automatically by a translator application from LASP that uses a telemetry-definitions database as its input, decommutates individual telemetry items from science packets. Time conversions from the Mission Elapsed Time (MET) in packet headers to TAI and UTC are done using SPICE, via the ICY IDL interface. The output of this step is stored in an IDL save file in the form of an IDL structure with appropriate time tags.

The second task of the L0 to L1 processing step is to convert the L0 science data into L1 data. For this step, another IDL computer program from LASP receives the IDL save file containing the L0 data and then converts the L0 data into L1 data. The L1 data are stored in a Common Data Format (CDF) file at the SOC for public access. (As the data are specific

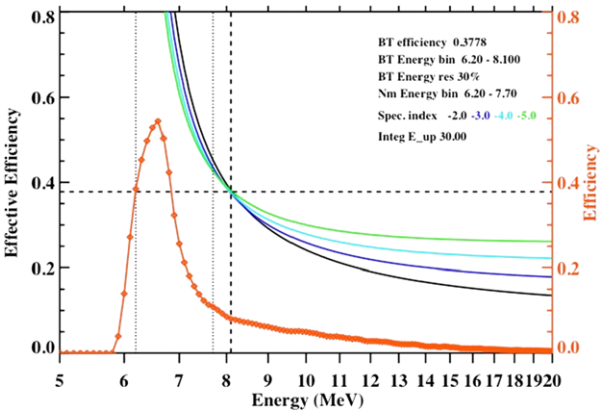

Fig. 27 Bow tie efficiency derived from the full efficiency for the 6.2–7.7 MeV electron differential energy channel

to the instrument, the CDF file does not meet the requirements of the Standard file format guidelines of the COSPAR Panel on Radiation Belt Environment.)

The final task of the L0 to L1 processing step is to re-assemble the daily MET L1 files produced into daily UTC files. This is a processing step that uses a generic process for this task developed at the ECT SOC (since all the ECT instrument L1 data files needed to undergo this step). During this step the ECT SOC also checks, and if necessary, corrects all the MET → UTC time conversions done to enforce consistency in this process across all ECT data products.

After this, the L1 data are converted into Level 2 (L2) data, the first level of useable science data. Codes for the L1 → L2 process are provided by LASP and run at the LANL ECT SOC as part of the ECT data processing chain. The measure count rates are corrected for background and dead time effects. The corrected count rate data are converted to physical flux units (i.e., cm^2 sr s MeV). The conversion from count rates to flux will be a two-step process; in the first step the differential channel efficiencies will be approximated using a bow-tie analysis (Van Allen et al. 1974), which simplifies the energy dependence of the efficiencies to a constant value over an energy range. Figure 27 shows the efficiency as a function of incident electron energy and the corresponding bow tie approximated result for the nominal 6.2–7.7 MeV channel. From the figure it can be seen that the full efficiency can be approximated as a constant of ~0.38 over an energy range of 6.2–8.1 MeV. Table 7 lists the bow tie efficiencies and the energy bin widths for all the electron differential channels. As mentioned earlier, the full efficiency curves are obtained through logic equations that are software commandable and correspondingly bow tie values can be obtained when the logic conditions are changed. To compute the flux determination, the electron spectrum obtained from the bow tie fluxes is used as the input spectrum for an iterative minimization procedure, which uses the full efficiencies to obtain the final fluxes and spectrum.

The procedure is much more straightforward for protons as the full efficiencies for protons are already in the form of a constant value over each energy bin.

The Level 2 output will be saved in a CDF file meeting the PRBEM (Panel on Radiation Belt Environment) standard format guidelines. The data levels higher than Level 2 will combine the data from other RBSP instruments, e.g., local magnetic field direction in order to obtain pitch angles, and will be stored in PRBEM CDF format.

All higher-level data processing beyond L1 will take place at the ECT SOC using a common set of utilities and codes, since all ECT instrument data in L2 format have a high degree of commonality (count rates per detector, spin sector and energy).

Table 7 Electron channel efficiencies and bin widths derived from logic equation efficiencies through bow tie analysis

Electron channel No.	Nominal energy	Bow tie energy	Bow tie efficiency	Bow tie bin width	Bow tie bin center
0	1.6–2.0	1.6–3.0[a]	0.028	1.4	2.30
1	2.0–2.5	2.0–2.6	0.199	0.6	2.30
2	2.5–3.2	2.5–3.2	0.503	0.7	2.85
3	3.2–4.0	3.2–4.0	0.348	0.8	3.60
4	4.0–5.0	4.0–5.0	0.574	1.0	4.50
5	5.0–6.2	5.0–6.2	0.445	1.2	5.60
6	6.2–7.7	6.2–8.1	0.378	1.9	7.15
7	7.7–9.7	7.7–9.9	0.265	2.2	8.80
8	9.7–12.1	9.7–13.6	0.132	3.9	11.65
9	12.1–15.1	12.1–18.6	0.078	6.5	15.35
10	15.1–18.9	15.1–30.0	0.036	14.9	22.55
11	>18.9	18.9–100	0.001	81.1	59.45

[a]Preliminary value

As alluded to previously, the processing of REPT telemetry data will occur in parallel both at the LANL SOC and LASP. During flight, LASP will pull recent, downlinked packet files from the SOC to determine instrument health and the quality of science data. The processing at LASP decommutates housekeeping and science data from packet files and ingests it into a database. Individual data points are then accessible to various standard LASP analysis tools. These tools produce line plots and color-coded limits information for health and safety checking. (The code leverages generic libraries used on many other LASP missions.) If needed, the processing code will be updated to provide new calibrations and corrections. The new versions of the processing codes are kept in sync between LASP and the SOC so that both are always running the same version.

The L2 data are suitable for scientific analyses, such as the characterization of spectral variability, or whether spectra harden during energization events. The data are also useful for synoptic views of the radiation belts such as seen in Fig. 1. Studies of changes in angular distributions of particle flux are also amenable to L2 data, although knowledge of pitch angle requires the sector fluxes be mapped to B field. The Level 3 data incorporates the geomagnetic field direction and thus provide the pitch angle information. Characterization of pitch angle distributions will enable answering key issues in electron energization, such as whether energization and isotropization are nearly simultaneous; energization models have differing predictions regarding evolution of pitch angle distributions and therefore be used to identify the particular mechanism. The highest-level data, Level 4, will combine measurements with global magnetic field models to produce phase space densities. As mentioned before (see Fig. 4) the radial gradient of PSD is the chief discriminator for distinguishing transport vs. in-situ energization of electrons. REPT measurements of PSD then, together with plasma wave data from other RBSP instruments, provide a complete picture of energization and loss mechanisms of relativistic electrons, which is a key goal of the RBSP mission.

6 Discussion and Summary

This paper has provided a comprehensive description of the physical design, engineering characteristics, laboratory calibrations, and expected scientific contributions of the Relativistic Electron-Proton Telescope instruments that are a key part of the scientific payload onboard the RBSP dual-spacecraft mission. As has been detailed in this paper, measurements of the electrons in the energy range $E \sim 1$ MeV to $E \sim 20$ MeV throughout the outer and inner Van Allen belts are absolutely central to the mission objectives of the RBSP program. Careful design efforts based on prior mission heritage (CRRES, SAMPEX, and POLAR) and effective use of the GEANT4 instrument simulation tools have allowed achievement of superior REPT performance properties while using only modest spacecraft resources. Laboratory characterization and high-energy accelerator calibrations have shown that the REPT flight instruments are closely identical to one another and they also have the key performance characteristics that have been demanded by the RBSP mission Level 1 requirements.

The REPT instruments will work in close harmony with the other sensors that make up the overall RBSP scientific payload. While there is some energy overlap of REPT with other particle detectors (e.g., MagEIS and RPS), the REPT measurements will be unique for electrons in the several MeV energy range (and above) and for protons in the 20–50 MeV energy range. These particles are, respectively, of key importance in the outer Van Allen zone and inner Van Allen belt. It is important to always recall that the RBSP mission is a flagship component of the NASA Living With a Star program. As such, it is crucial to complete our understanding of how our active Sun distorts and stresses the near-Earth environs in ways that can efficiently and effectively accelerate charged particles to the immense energies that REPT will observe.

REPT will utilize concurrent magnetic field and plasma wave observations to address long-standing puzzles about the cosmic particle accelerator that operates so remarkably in Earth's magnetosphere. While there will be fascinating scientific studies of low-energy particle processes and wave phenomena using the capable RBSP payload, the central goal of the program is to provide definitive understanding of the highest energy proc-esses. As such, it is clearly the goal of our investigation to look carefully at the connected Sun-Earth system and use the most powerful space weather disturbances to develop effective, predictive models of the magnetospheric response. Our data analysis, visualization tools, and information dissemination methods are all geared toward rapid and efficient infusion of knowledge into our national space weather and LWS systems.

It is both remarkable and sobering that over five decades have passed since the discovery of the Earth's radiation belts by Van Allen and co-workers. With the development, integration, testing and operation of the RBSP mission elements, the space physics community will at long last have the requisite tools to understand the complexities of radiation belt dynamics. It will be a fitting tribute to the pioneering spirit of J.A. Van Allen to return to this first discovery of the Space Age and to address in depth the mysteries of cosmic particle energization.

Acknowledgements We want to express our sincere appreciation to all of our colleagues at the Laboratory for Atmospheric and Space Physics for their support in the successful completion of the REPT instrument. We thank our RBSP and ECT teammates for their assistance, especially J. Bernard Blake, Joseph F. Fennell, Bill Crain, Joseph E. Mazur, John Goldsten, Brian Klatt, and Jim Cravens. We also want to thank the APL payload, spacecraft and mission teams, specifically Lori Suther, Al Reiter, Elliot Rodberg, and Annette Dolbow.

Special thanks to all of the reviewers who contributed their expertise to the improvement of our instrument. In particular we are grateful to Berndt Klecker, Richard Mewaldt, Edward S. Stone, Tycho Von Rosenvinge, Frank B. McDonald, Gary Mullen, Bronislaw Dichter, Gary Galica, Gregory Ginet, and Steve Battel.

This work has been supported by NASA prime contract NAS5-01072 to Johns Hopkins University Applied Physics Laboratory (JHU/APL).

References

M.H. Acuña et al., in *The Global Geospace Mission*, ed. by C.T. Russell (Kluwer Academic, Dordrecht, 1996)

J. Alcaraz et al., Cosmic protons. Phys. Lett. B **490**, 27–35 (2000)

S. Agostinelli et al., Nuclear instruments and methods in physics research section A: accelerators, spectrometers, detectors and associated equipment. Nucl. Instrum. Methods A **506**, 250–303 (2003). doi:10.1016/S0168-9002(03)01368-8

C.A.J. Ammerlaan, R.F. Rumphorst, L.A.Ch. Koerts, Particle identification by pulse shape discrimination in the p-I-n type semiconductor detector. Nucl. Instrum. Methods **22**, 189–200 (1963)

D.N. Baker, P.R. Higbie, R.D. Belian, E.W. Hones Jr., Do Jovian electrons influence the terrestrial outer radiation zone? Geophys. Res. Lett. **6**(6), 531–534 (1979). doi:10.1029/GL006i006p00531

D.N. Baker et al., The Los Alamos geostationary orbit synoptic data set: a compilation of energetic particle data. Los Alamos National Laboratory Report, LA-8843, 1981

D.N. Baker et al., Highly relativistic magnetospheric electrons: a role in coupling to the middle atmosphere? Geophys. Res. Lett. **14**(10), 1027–1030 (1987). doi:10.1029/GL014i010p01027

D.N. Baker, R.L. McPherron, T.E. Cayton, R.W. Klebesadel, Linear prediction filter analysis of relativistic electron properties at 6.6R_E. J. Geophys. Res. **95**, 15,133–15,140 (1990). doi:10.1029/JA095iA09p15133

D.N. Baker, G.M. Mason, O. Figueroa, G. Colon, J. Watzin, R. Aleman, An overview of the SAMPEX mission. IEEE Trans. Geosci. Electron. **31**, 531 (1993)

D.N. Baker, J.B. Blake, L.B. Callis, J.R. Cummings, D. Hovestadt, S. Kanekal, B. Klecker, R.A. Mewaldt, R.D. Zwickl, Relativistic electron acceleration and decay time scales in the inner and outer radiation belts: SAMPEX. Geophys. Res. Lett. **21**, 409 (1994)

D.N. Baker et al., A strong CME-related magnetic cloud interaction with the earth's magnetosphere: ISTP observation of rapid relativistic electron acceleration on May 15, 1997. Geophys. Res. Lett. **25**(15), 2975–2978 (1998). doi:10.1029/98GL01134

D.N. Baker et al., An extreme distortion of the Van Allen belt arising from the 'Hallowe'en' solar storm in 2003. Nature **432**, 878–881 (2004). doi:10.1038/nature03116

D.N. Baker et al., Low-altitude measurements of 2–6 MeV electron trapping lifetimes at $1.5 \leq l \leq 2.5$. Geophys. Res. Lett. **34**, L20110 (2007). doi:10.1029/2007GL03100

D.N. Baker, D. Mitchell, P. O'Brien, RBSP project internal report. JHUAPL, 2008

J.-F. Beche, Second order pseudo-Gaussian shaper. Lawrence Berkeley National Laboratory. LBNL Paper LBNL-52855, 2002

J.B. Blake, W.A. Kolasinski, R.W. Fillius, E.G. Mullen, Injection of electrons and protons with energies of tens of MeV into $L < 3$ on 24 March 1991. Geophys. Res. Lett. **19**(8), 821–824 (1992). doi:10.1029/92GL00624

J.B. Blake et al., The MagEIS/ECT instrument on the RBSP mission. Space. Sci. Rev. (2012, this issue)

J. Bortnik et al., An observation linking the origin of plasmaspheric hiss to discrete chorus emissions. Science **324**, 5928 (2009)

W.R. Cook et al., PET: a proton/electron telescope for studies of magnetospheric, solar, and galactic particles. IEEE Trans. Geosci. Electron. **31**, 565 (1993)

S.R. Elkington, M.K. Hudson, A.A. Chan, Acceleration of relativistic electrons via drift-resonant interaction with toroidal-mod Pc-5 ULF oscillations. Geophys. Res. Lett. **26**(21), 3273 (1999)

S.R. Elkington, M.K. Hudson, A.A. Chan, Resonant acceleration and diffusion of outer zone electrons in an asymmetric geomagnetic field. J. Geophys. Res. **108**(A3), 1116 (2003)

S.R. Elkington, M. Wiltberger, A.A. Chan, D.N. Baker, Physical models of the geospace radiation environment. J. Atmos. Sol.-Terr. Phys. **66**, 1371 (2004)

S.R. Elkington, D.N. Baker, M. Wiltberger, in *The Inner Magnetosphere: Physics and Modeling*, ed. by T.I. Pulkkinen, N.A. Tsyganenko, R.H.W. Friedel. AGU Geophysical Monograph, vol. 155 (American Geophysical Union, Washington, 2005), p. 147

T.I. Gombosi, G. Toth, D.L. de Zeeuw, K.C. Hansen, K. Kabin, K.G. Powell, Semirelativistic magnetohydrodynamics and physics-based convergence acceleration. J. Comput. Sci. **177**, 176 (2002)

M.G. Gornov et al., Selection of the shaping circuits of a multilayer semiconductor spectrometer of charged particles. Instrum. Exp. Tech. **45**(5), 626–630 (2002)

J.C. Green, M.G. Kivelson, Relativistic electrons in the outer radiation belt: differentiating between acceleration mechanisms. J. Geophys. Res. **109**, A03213 (2004). doi:10.1029/2003JA010153
R.B. Horne, R.M. Thorne, Potential waves for relativistic electron scattering and stochastic acceleration during magnetic storms. Geophys. Res. Lett. **25**(15), 3011–3014 (1998). doi:10.1029/98GL01002
R.B. Horne, N.P. Meredith, R.M. Thorne, D. Heynderickx, R.H.A. Iles, R.R. Anderson, Evolution of energetic electron pitch angle distributions during storm time electron acceleration to megaelectronvolt energies. J. Geophys. Res. **108**(A1), 1016 (2003). doi:10.1029/2001JA009165
R.B. Horne, D.N. Baker et al., Wave acceleration of electrons in the Van Allen radiation belts. Nature **437**, 227–230 (2005a). doi:10.1038/nature03939
R.B. Horne, R.M. Thorne, S.A. Glauert, J.M. Albert, N.P. Meredith, R.R. Anderson, Timescale for radiation belt electron acceleration by whistler mode chorus waves. J. Geophys. Res. **110**, A03225 (2005b). doi:10.1029/2004JA010811
M.H. Johnson, J. Kierein, Combined release and radiation effects satellite (CRRES): spacecraft and mission. J. Spacecr. Rockets **29**(4), 556–563 (1992). doi:10.2514/3.55641
S.G. Kanekal et al., Magnetospheric response to magnetic cloud (coronal mass ejection) events: relativistic electron observations from SAMPEX and polar. J. Geophys. Res. **104**, A11 (1999). doi:10.1029/1999JA900239
C.A. Kletzing et al., The electric and magnetic field instrument suite and integrated science (EMFISIS) on RBSP. Space. Sci. Rev. (2012, this issue)
L.J. Lanzerotti et al., Radiation belt storm probes ion composition experiment (RBSPICE). Space Sci. Rev. (2012, this issue)
C. Leroy et al., Study of charge transport in non-irradiated and irradiated silicon detectors. Nucl. Instrum. Methods Phys. Res. **A426.1**, 99–108 (1999)
X. Li et al., Simulation of dispersionless injections and drift echoes of energetic electrons associated with substorms. Geophys. Res. Lett. **25**, 3763 (1998)
X. Li et al., Quantitative prediction of radiation belt electrons at geostationary orbit based on solar wind measurements. Geophys. Res. Lett. **28**(9), 1887–1890 (2001a). doi:10.1029/2000GL012681
X. Li et al., Long term measurements of radiation belts by SAMPEX and their variations. Geophys. Res. Lett. **28**(20), 3827–3830 (2001b). doi:10.1029/2001GL013586
B.W. Loo, F.S. Goulding, D. Gao, Ballistic deficits in pulse shaping amplifiers. IEEE Trans. Nucl. Sci. **35.1**, 114–118 (1988)
K.R. Lorentzen et al., Multisatellite observations of MeV ion injections during storms. J. Geophys. Res. **107**(A9), 1231 (2002). doi:10.1029/2001JA000276
J.G. Lyon, J.A. Fedder, C.M. Mobarry, The Lyon-Fedder-Mobarry global MHD magnetospheric simulation code. J. Atmos. Sol.-Terr. Phys. **66**(15), 1333 (2004)
J.P. McCollough et al., Physical mechanisms of compressional EMIC wave growth. J. Geophys. Res. **115**, A10214 (2010)
B.H. Mauk et al., Science objectives and rational for the Radiation Belt Storm Probes Mission. Space Sci. Rev. (2012). doi:10.1007/s11214-012-9908-y
J.E. Mazur et al., The Relativistic-Proton Spectrometer (RPS) for the Radiation Belt Storm Probes Mission. Space Sci. Rev. (2012). doi:10.1007/s11214-012-9926-9
R.A. Mewaldt, Solar energetic particle composition, energy spectra, and space weather. Space Sci. Rev. **124**, 303–316 (2006). doi:10.1007/s11214-006-909-0
N.P. Meredith et al., Evidence for chorus-driven electron acceleration to relativistic energies from a survey of geomagnetically disturbed periods. J. Geophys. Res. **108**(A6), 1248 (2003). doi:10.1029/2002JA009764
C.H. Mosher, Pseudo-Gaussian transfer functions with superlative baseline recovery. IEEE Trans. Nucl. Sci. **23**(1), 226–228 (1976)
G.A. Paulikas, J.B. Blake, Effects of the solar wind on magnetospheric dynamics: energetic electrons at the synchronous orbit, in *Quantitative Modeling of Magnetospheric Processes*, ed. by W.P. Olson. Geophys. Monogr. Ser., vol. 21 (AGU, Washington, 1979), pp. 180–202
J. Raeder, Global magnetohydrodynamics, a tutorial, in *Space Plasma Simulation*, ed. by C.T. Dum, M. Scholer, J. Buchner. Lecture Notes in Physics, vol. 615 (Springer, New York, 2003), p. 212
J.G. Roederer, *Dynamics of Geomagnetically Trapped Radiation* (Springer, New York, 1970)
I. Roth, M. Temerin, M.K. Hudson, Resonant enhancement of relativistic electron fluxes during geomagnetically active periods. Ann. Geophys. **17**, 631 (1999)
T.E. Sarris, X. Li, N. Tsaggas, N. Paschalidis, Modeling energetic particle injections in dynamic pulse fields with varying propagation speeds. J. Geophys. Res. **107**(A3), 1033 (2002)
Y.Y. Shprits et al., Outward radial diffusion driven by losses at the magnetopause. J. Geophys. Res. **111**, A11214 (2006)
H.E. Spence et al., The ECT investigation on the RBSP mission. Space Sci. Rev. (2012, this issue)

P.A. Sturrock, *Plasma Physics* (Cambridge University Press, Cambridge, 1994)
M.G.G.T. Taylor, R.H.W. Friedel, G.D. Reeves, M.W. Dunlop, T.A. Fritz, P.W. Daly, A. Balogh, Multisatellite measurements of electron phase space density gradients in Earth's inner and outer magnetosphere. J. Geophys. Res. **109**, A05220 (2004)
A.L. Vampola, Measuring energetic electrons—what works and what doesn't, in *Measurement Techniques in Space Plasmas: Particles*, ed. by F. Pfaff, E. Borovsky, T. Young. Geophys. Monogr. Ser., vol. 102 (AGU, Washington, 1998), pp. 339–355. doi:10.1029/GM102p0339
J.A. Van Allen et al., Energetic electrons in the magnetosphere of Jupiter. Science **183**, 309 (1974)
J. Vette, The NASA/National Space Science Data Center trapped radiation environment model program (1964–1991). NSSDC Report 91-29, Greenbelt, MD, 1991
J. Wygant et al., The EFW investigation and instruments on the RBSP mission. Space. Sci. Rev. (2012, this issue)

DOI 10.1007/978-1-4899-7433-4_12
Reprinted from *Space Science Reviews* Journal, DOI 10.1007/s11214-013-9991-8

The *Magnetic Electron Ion Spectrometer* (MagEIS) Instruments Aboard the Radiation Belt Storm Probes (RBSP) Spacecraft

J.B. Blake · P.A. Carranza · S.G. Claudepierre · J.H. Clemmons · W.R. Crain Jr. · Y. Dotan · J.F. Fennell · F.H. Fuentes · R.M. Galvan · J.S. George · M.G. Henderson · M. Lalic · A.Y. Lin · M.D. Looper · D.J. Mabry · J.E. Mazur · B. McCarthy · C.Q. Nguyen · T.P. O'Brien · M.A. Perez · M.T. Redding · J.L. Roeder · D.J. Salvaggio · G.A. Sorensen · H.E. Spence · S. Yi · M.P. Zakrzewski

Received: 15 October 2012 / Accepted: 9 May 2013 / Published online: 7 June 2013

Abstract This paper describes the Magnetic Electron Ion Spectrometer (MagEIS) instruments aboard the RBSP spacecraft from an instrumentation and engineering point of view. There are four magnetic spectrometers aboard each of the two spacecraft, one low-energy unit (20–240 keV), two medium-energy units (80–1200 keV), and a high-energy unit (800–4800 keV). The high unit also contains a proton telescope (55 keV–20 MeV).

The magnetic spectrometers focus electrons within a selected energy pass band upon a focal plane of several silicon detectors where pulse-height analysis is used to determine if the energy of the incident electron is appropriate for the electron momentum selected by the magnet. Thus each event is a two-parameter analysis, an approach leading to a greatly reduced background.

The physics of these instruments are described in detail followed by the engineering implementation. The data outputs are described, and examples of the calibration results and early flight data presented.

Keywords Relativistic electron sensors · Energetic magnetospheric particles · Acceleration · Transport and loss of radiation belt particles

J.B. Blake (✉) · P.A. Carranza · S.G. Claudepierre · J.H. Clemmons · W.R. Crain Jr. · Y. Dotan · J.F. Fennell · F.H. Fuentes · R.M. Galvan · J.S. George · M. Lalic · A.Y. Lin · M.D. Looper · D.J. Mabry · J.E. Mazur · C.Q. Nguyen · T.P. O'Brien · M.A. Perez · M.T. Redding · J.L. Roeder · D.J. Salvaggio · G.A. Sorensen · S. Yi · M.P. Zakrzewski
Space Science Applications Laboratory, The Aerospace Corporation, El Segundo, CA 90245, USA
e-mail: jbernard.blake@aero.org

M.G. Henderson
Los Alamos National Laboratory, PO Box 1663, Los Alamos, NM 87545, USA

B. McCarthy
Environment Test and Assessment Department, The Aerospace Corporation, El Segundo, CA 90245, USA

H.E. Spence
Center for Earth, Oceans, and Space, University of New Hampshire, Durham, NH 03824, USA

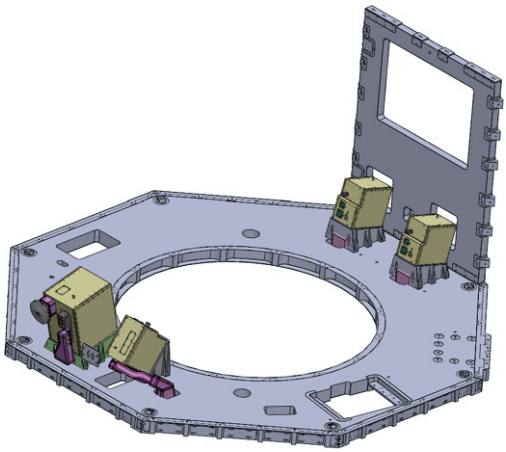

Fig. 1 The four magnetic spectrometers are shown in this cutaway drawing as mounted on the aft deck of a RBSP spacecraft. Each unit is connected to a thermal control surface on the down Sun side of the spacecraft by a thermal strap, shown in purple in the drawing

1 Introduction

An overarching objective of the RBSP mission is to obtain a deep understanding of the physics of the acceleration of electrons to relativistic energies in the radiation belts of the Earth. To this end a suite of four magnetic electron spectrometers aboard each of the two RBSP spacecraft will measure the differential fluxes, energies, and angular distributions of electrons from 20 keV to 5 MeV. They have been designed to do so with only a small, determinable and correctible background during an extreme event such as occurred during March 1991, and to do so with a significant performance margin.

Magnetic electron spectrometers have been fielded by Aerospace aboard several satellite missions since the early 1960s when they were used to measure the intense fission electron fluxes injected into the magnetosphere by the high-altitude nuclear tests of the United States and the Soviet Union. The instrumentation described here is a substantial evolution of the earlier spaceflight investigations using current, vastly improved magnetic materials, silicon detectors and electronic components.

2 Overview

There are four MagEIS spectrometers on each of the two spacecraft. The spectrometers are mounted on the aft deck (anti-solar) of the satellite as shown in the cutaway drawing (Fig. 1). A low-energy, a medium energy, and a high-energy magnetic spectrometer view out a side of the spacecraft at 75 degrees to the satellite spin axis, and a second medium unit views out the bottom of the spacecraft at 35 degrees to the spin axis.

The MagEIS suite also contains a silicon-detector telescope that measures the differential fluxes, energies, and angular distributions protons from 60 keV to 20 MeV, and helium and oxygen ions from a few hundred keV/nuc to a few MeV/nuc. This telescope is contained in the high-energy magnetic spectrometer enclosure.

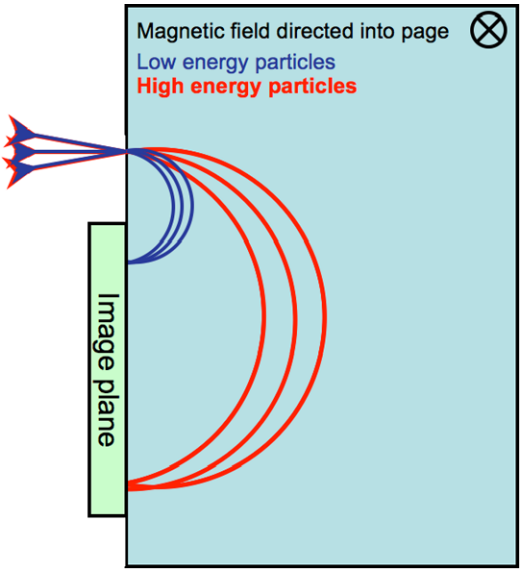

Fig. 2 The basic magnetic spectrometer configuration is shown schematically

3 Instrument Design Details—Magnetic Electron Spectrometers

3.1 Overview

Electrons enter through a collimator defining the field of view of $10° \times 20°$ as shown in Fig. 2. The magnetic field inside the chamber is uniform, and focuses electrons on a linear strip of nine silicon detectors after the velocity vector of incoming electrons has been rotated through 180°. First order focusing occurs in the plane of the spectrometer; there is no focusing in the vertical plane. Focusing in the transverse plane occurs because the chord length subtending angles near 180° in a circle does not change rapidly with change in angle subtended—the chord length is similar to the diameter. Anti-scatter baffling is placed at the top and bottom of the magnetic chamber.

The charge and mass of an electron are unique, and therefore no other magnetospheric particles are focused upon the detector plane. This feature is of paramount importance for instrument performance. No magnetospheric ions can enter through the aperture and strike the electron detectors. Furthermore each detector only sees those electrons in its pass band, unlike the case for a silicon-detector telescope where all electrons pass through the front detector(s) of the telescope. This situation has many critical benefits including removal of unwanted particles, major reduction of system dead time, and a substantial diminution in the radiation damage to the silicon detectors. The distance along the detector plane from the entrance aperture where a given electron is focused is a function of the electron momentum. The energy deposited in the silicon detector upon which the electron is focused determines the incident electron energy. Thus a two-parameter analysis is made for every electron. Only those electrons whose deposited energy is appropriate for the momentum determined by the position along the focal plane are valid events.

3.2 Silicon Detector Configurations

The detector thickness for each of the three-spectrometer types was selected based upon the maximum electron energy measured by a given spectrometer. Micron Semiconductor Ltd.,

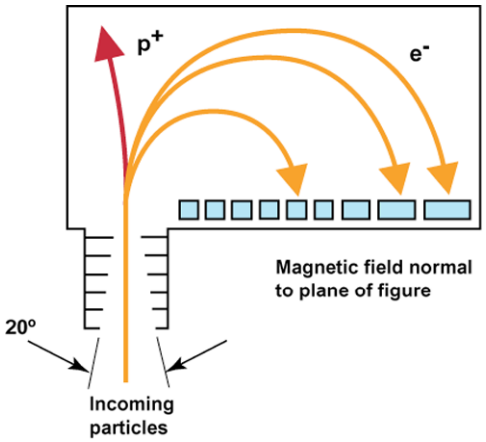

Fig. 3 The Low and Medium Spectrometers have a nine-pixel focal plane

Lancing, England, fabricated all of the electron focal-plane detectors. Detectors consist of one 0.5 mm, and two stacked 1.5 mm thick pieces of silicon for the Low and Medium detectors respectively. Each piece of silicon has nine pixels, that is nine individual sensors. The Low-energy spectrometer covers the electron energy range from ∼20 keV to ∼240 keV and a Medium-energy spectrometer covers the electron energy range from ∼80 keV to ∼1200 keV. The configuration of the low and medium units is shown in Fig. 3.

Representative electron trajectories are shown, with the higher-energy electrons striking further along the focal plane, where the pixels are of increased size. Protons are deflected away from the focal plane.

There are four pixels in a High-energy spectrometer rather than nine pixels as in the Low and Medium units. The front detector is a single piece of silicon, 0.3 mm thick. The rear detector is a sandwich consisting of three pairs of detectors, each pair consisting of two detectors each 1.5 mm thick. Thus there are six pieces of silicon in the stack, giving a total thickness of the rear detector of 9 mm. The configuration of the high units is shown in Fig. 4.

The two detectors for each pixel enable a coincidence measurement as a background reduction measure. The rear pairs are ganged together as needed to stop the maximum energy electrons that can reach a given pixel. Therefore Pixels 1 and 2 use only the first rear pair, Pixel 3 uses two of the pairs and Pixel 4 uses all three pairs. An unused pair, in the Pixel 1 stack, is used as a monitor of penetrating background. The front pixel has a smaller area than the back pixel and is centered upon the back pixel, reducing the percentage of electrons that make a valid coincidence but exit the thick rear detector out of a side rather than stopping. The energy coverage is from 800 keV to 4800 keV.

3.3 Magnet Design

The MagEIS magnetic circuit designs are critical to a successful instrument. The MagEIS magnetic design uses magnetic materials, techniques, and design tools that have advanced considerably since the flight of the early Aerospace magnetic spectrometers. Advanced materials allow creation of the needed field strengths by smaller and lighter packages than possible before. These materials also permit precision magnetization techniques to be used to achieve tight tolerances on the resulting fields. Modern simulation tools allow rapid and accurate modeling of magnetic circuits to take much of the formerly needed guesswork out of the design process.

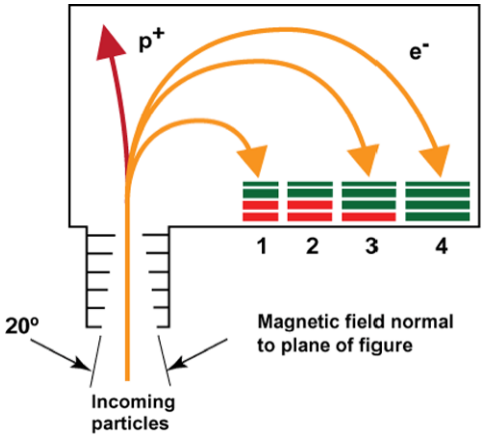

Fig. 4 The High Spectrometer has a four-pixel focal plane consisting of four detector planes. The top plane is 0.3 mm thick and serves as a dE/dx detector. The three rear planes, each 3 mm thick, serve as an E detector in a telescopic arrangement. The number of these planes used in a given pixel is selected according to the range (energy) of an electron that can reach a given pixel, from 1 to 3 going from Pixel 1 to Pixel 4. The unused rear pixels thus are colored red rather than green

The geometric parameters of the MagEIS electron spectrometers are determined by a requirements flow, beginning with the desired energy coverage. The 180° sector geometry specified for the magnets in practice is capable of covering only about one decade of dynamic range in energy (and less in the relativistic regime for an instrument like MagEIS-High) without putting undue constraints on other design parameters, such as size. Therefore MagEIS employs three magnetic chambers to cover the required energy range. The energy ranges for the chambers are thus based on this constraint. The required dynamic range in flux for each chamber is derived from empirically derived models of radiation belt fluxes, including a "worst-case" spectrum derived for the RBSP mission.

The flux-handling requirements then flow down to the geometric factor needed to have the required sensitivity while not being susceptible to saturation during large events. These considerations and design rules of thumb for magnetic spectrometers then establish the geometries for each of the chambers, which in turn produce the specification of the magnetic field in each. One of the design rules of thumb is that the detector pixels should be about the same size as the entrance aperture. Another rule of thumb is that the magnet gap should be kept short to constrain the out-of-plane angular acceptance, keep stray fields low, and make efficient use of magnetic energy. Keeping the gap short also helps keep the energy spread at a given radial detector position low, which is a key MagEIS concept in the pursuit of minimizing the amount of signal registered by penetrating background.

These requirements produce a common geometry for two of the chambers. The low/medium energy chambers have an entrance aperture of 2 mm by 5 mm and an angular acceptance of 20 deg by 10 deg. Nominal field strengths for these designs are 550 G and 1600 G, respectively, with a magnet gap of 7 mm. The high chamber utilizes a larger entrance aperture (10 mm high instead of 5 mm) and has a field strength of 4800 G with a gap of 12 mm. The magnet gaps are larger than the aperture size in order to leave room for internal baffles that reduce scattering from the magnet pole faces. Figure 5 shows the design sensitivity for the three chambers, showing the one-count-per-spin-sector levels and the saturation levels for each.

An important constraint on the magnet chambers is the requirement that stray magnetic fields not interfere with the other RBSP instruments, in particular, the magnetometer. Static stray magnetic fields at the magnetometer location were to be less than a total of 5 nT. The resulting constraint is that the design and fabrication of the MagEIS magnet chambers must pay strict attention to the designs of the entrance and exit apertures and the yokes

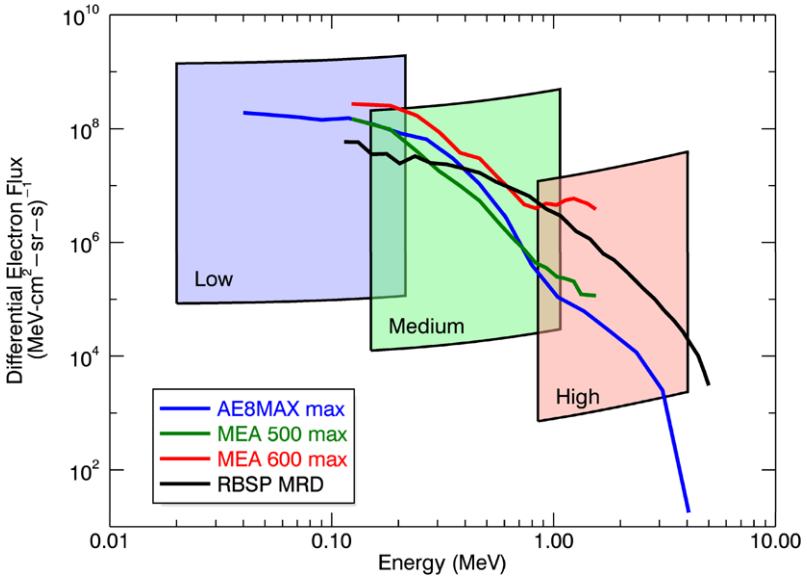

Fig. 5 Design sensitivity for the MagEIS electron instruments. The minimum and maximum are plotted for each of the three chambers based on one-count per sector (min) and electronics saturation (max). Also included for reference are the maximum fluxes that are expected based upon the AE8 radiation model, data from the CRRES mission (MEA), and the mission requirements for the RBSP. MEA 500 means CRRES Orbit 500, and MEA 600 means CRRES Orbit 600

used to close the flux path. A key aspect of the design is driven by this requirement; the detectors are enclosed within the magnet chambers, leaving only a small slit for electrical cabling. The stray field requirement also requires scrupulous attention to be paid to the way the chambers are assembled. Joining seams between yoke pieces are minimized, and the joining surfaces are lapped together before assembly in order to assure a magnetically-tight assembly. Placing a shield of magnetically-soft material around the units was also contemplated as a way to reduce the challenge of creating low-leakage magnetic circuits. However, the polarizability of such shields created a larger problem than it solved, as the dynamic residual fields at the magnetometer that varied with spin phase, and RBSP has a more challenging requirement on dynamic stray fields (less than 0.1 nT). Thus MagEIS does not employ magnetic shields.

MagEIS uses high-performance magnetic materials. The magnets are made of high-energy product materials to enable small magnets to be used. In this way weight is kept relatively low, and, perhaps more importantly, packaging is kept small, keeping the requirements for yoke material low. The use of high-energy product magnets also allows for precise adjustment of the field in the gap, as the magnets are partially magnetized rather than using the maximum energy product available. This approach also allows a common geometry to be used for the low and medium chambers. For the magnets in these chambers a samarium-cobalt (2–17) alloy having an energy product of 18 MGOe is used. A NdFeB alloy with energy product 50 MGOe provides the higher field strength required in the high chamber. In addition to these alloys having higher energy products than older materials such as Alnico, they also have higher intrinsic coercivity, making them easier to work with without their magnetization changing. The yoke material used in all chambers is Hiperco-50, a high-cobalt steel alloy capable of carrying large flux densities without saturating. Unsaturated

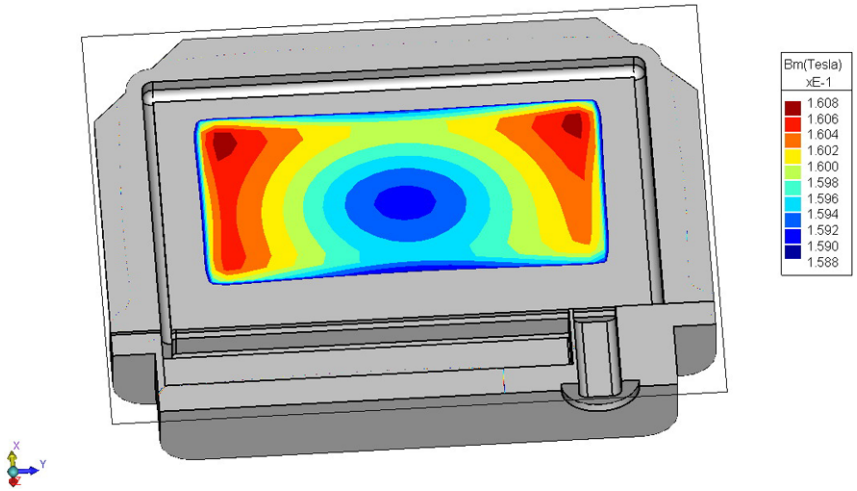

Fig. 6 Section view of the modeled magnetic circuits of the MagEIS medium electron chamber that has a mean field of 1600 G

yokes are important for keeping stray fields low, as well as allowing for efficient use of magnetic energy product.

A valuable product from the modeling is the good visualization of the field made possible, as shown in Fig. 6 for the medium chamber. The fields in all three chambers are quite uniform, with the low/medium chambers being within about 0.5 % of the mean field over most of the volume, while the high chamber exhibits about 5 % variation.

The performance of the magnetic chambers also was simulated by tracing particle trajectories through the modeled magnetic systems. The commercial product *SIMION 8*.0.4 was employed for this purpose due to its ability to compute the trajectories accurately and rapidly. The B-fields were read in from the Lorentz simulation. Note that the simulation does not include the effects of scattering. Figure 7 is an example of tracing some electron trajectories through the medium unit. It illustrates the first-order focus of particles with the same energy. The focusing is not quite ideal, likely owing to the effects of non-idealities in the magnetic field.

More detailed estimates of the instrument performance were obtained by launching large numbers of particles in such a manner for each chamber. A Monte Carlo scheme was used to sample the full gamut of particle trajectory parameters to examine the performance. An example appears in Fig. 8, which shows the distribution of detected energies and angles for Pixel 5 of the detector in the low chamber given an input beam that completely fills the collimator and has a flat energy spectrum. It shows the aggregate effect of the non-ideal field, as the energy-angle mixing should appear as a "smile" for perfect first-order focusing. Instead, only a portion of the "smile" appears. However, the amount of distortion is small enough that MagEIS can still meet its requirements. These simulations also provide accurate estimates for the magnetic chamber performance parameters listed in Table 1.

3.4 Further Design Considerations—Energy Histograms

In order to determine and correct for background in the silicon detectors, we measure the entire pulse-height spectrum in each detector from just above the noise level to amplifier sat-

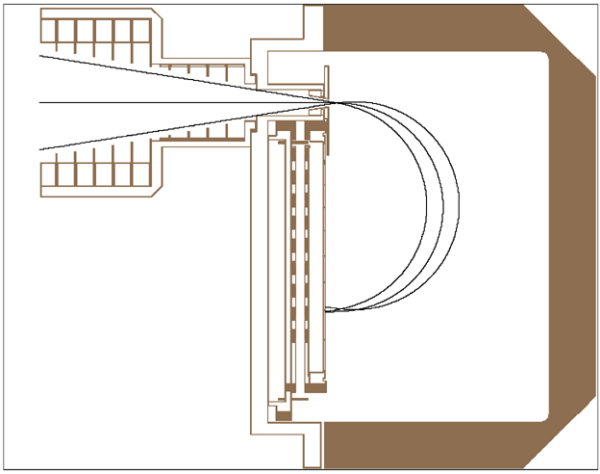

Fig. 7 Illustration of particle trajectory tracing in the modeled magnetic field for the medium chamber. Depicted is a cross-section of the geometry, with 800-keV electrons incident from the left

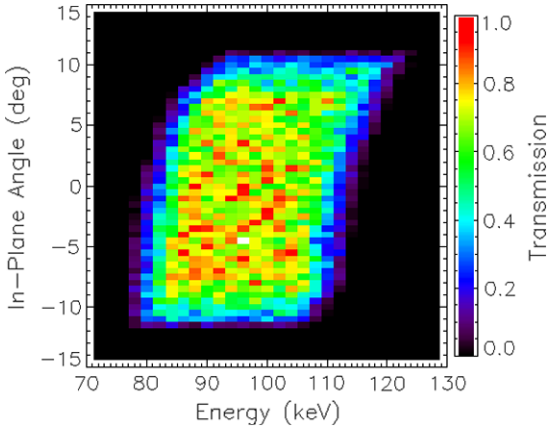

Fig. 8 The distribution of detected energies and angles for Pixel 5 of the detector in the low chamber is plotted

uration, not just those events within the energy pass band of a given detector, cf. Fig. 9. The count rate peak, appropriate to the detector in question, is seen "riding" on a smooth background spectrum, which is largely due to bremsstrahlung from the intense electron fluxes striking the RBSP spacecraft. In those regions of space where energetic trapped protons are found (the inner zone), and during energetic solar particle events, large pulses will result from ions that penetrate the magnetic spectrometer and reach the focal plane detectors. The key point is that with this technique, background events can be unequivocally determined and subtracted from the count rate within the differential energy channel of each detector, giving the true count rate in each channel. Furthermore, should the background swamp the true count rate, this fact will be obvious.

On-orbit data is shown to supplement the idealized discussion of signal and background given above.

In Fig. 10 the pass band of Pixel 4 is clearly seen when the satellite is at $L^* = 5.6$ (red curve) as a nearly rectangular increase in count rate between channel 24 and channel 44. The flat-topped region between channel 27 and channel 38 are the prime data region for Pixel 4 as discussed below. A first order correction for the background can be made by smoothly joining the count rate curve below channel 23 to the section above channel 45,

Table 1 Estimated values for several MagEIS performance parameters derived by simulating particle trajectories through the model magnetic field for each chamber. Values for each detector pixel are shown. Actual telemetered channels do not sum over all PHA energy channels for each pixel and therefore have different effective geometric factors. Energy widths and angular acceptances are full-width-at-half-maximum

Chamber	Pixel	Median energy (keV)	Energy width (keV)	Geometric factor (cm^2 sr keV)	In-plane angular acceptance (deg)	Out-of-plane angular acceptance (deg)
Low	1	19.5	10.6	0.0414	20	9.8
	2	32.7	14.3	0.0526	20	7.8
	3	50.0	18.6	0.0607	20	6.4
	4	71.8	23.0	0.0663	20	5.6
	5	98.1	27.3	0.0703	20	4.7
	6	129	32.2	0.0716	20	4.0
	7	166	37.3	0.0724	20	3.6
	8	207	42.7	0.0726	20	3.2
Medium	1	146	72.4	0.281	20	10
	2	232	89.7	0.328	20	7.9
	3	334	106	0.342	20	6.8
	4	450	121	0.343	20	5.8
	5	580	132	0.332	20	4.7
	6	722	145	0.316	20	4.1
	7	877	151	0.303	20	3.4
	8	1040	163	0.287	20	3.1
High front	1	1200	452	4.53	16	19
	2	1740	452	4.56	16	19
	3	2520	896	8.38	16	16
	4	3770	1170	8.26	16	11
High back	1	1220	489	4.89	16	19
	2	1740	516	5.28	16	19
	3	2510	1030	9.65	16	16
	4	3750	1400	9.57	16	11

and subtracting the values thus obtained from the count rate in the pass band. In this case the background is no more than 10 %.

The background when the spacecraft is at $L^* = 3.5$ can be seen to completely mask any true signal. At $L^* = 2.0$ counts in the pass band lie well above the background. The counts within the pass band drop off markedly within the pass band rather than having a flat top because the energy spectrum is much softer than at $L^* = 5.6$.

Finally at $L^* = 1.3$ the background is large but the true signal can still be seen riding on this background. These data are spin averaged because no magnetic aspect data are available at the time of writing, five months after launch.

The power of the background subtraction system can be further seen by examining the response in a higher energy pixel in the same spectrometer, Fig. 11 data are taken at the same times as in Fig. 10.

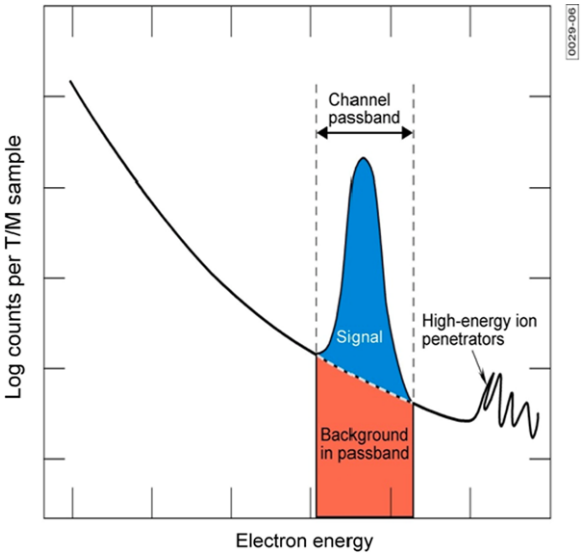

Fig. 9 A valid signal is shown schematically as combined with penetrating background events in a given pixel pass band

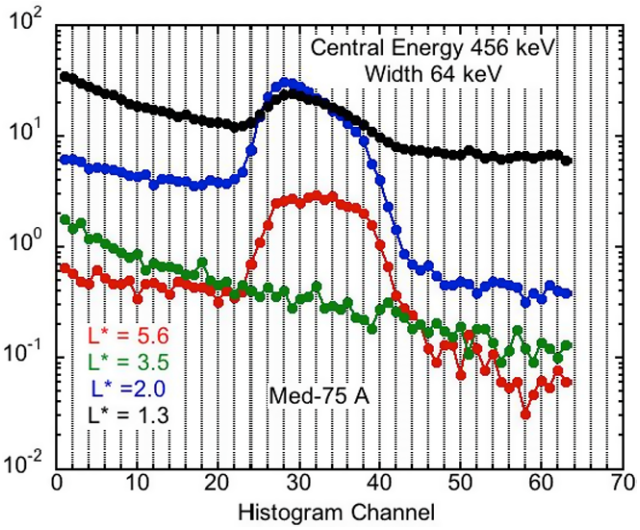

Fig. 10 The histogram data from Pixel 4 of the Med-75 unit of spacecraft A is shown for four values of L^*. Data were acquired on 25 December 2012

Electrons can clearly be seen above the background at $L^* = 5.6$ although the intensity is much lower than in Pixel 4 shown in Fig. 10. However there is no signal in Pixel 7 at the other three values of L^*. This result is in marked contrast to the situation for Pixel 4.

The MagEIS analysis system is even more robust against background than simply as described above. Focal plane detectors are adjacent, and the background energy spectrum will be much the same in adjacent detectors. Deviation from this expectation will provide a direct warning that something is amiss. The superiority of a magnetic spectrometer of this type is clear; not only is a two-parameter analysis made for every electron but the entire gamut of background events is measured as well.

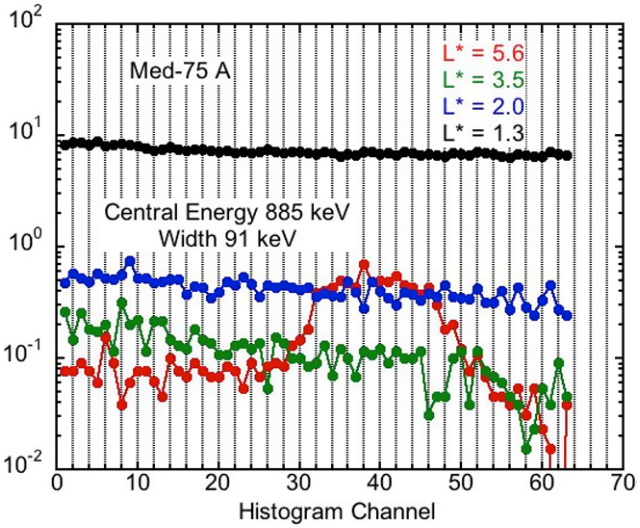

Fig. 11 The histogram data from Pixel 7 of the Med-75 unit of spacecraft 4A is shown for four values of L^*. Data were acquired on 25 December 2012

3.5 Multiple Fields of View

The entrance aperture of each magnetic spectrometer is rectangular, with an opening angle of 10 degrees in the azimuth direction and 20 degrees in the polar direction and the spacecraft rotation provides a pitch-angle scan in the usual manner. There are one low-energy, one medium-energy, and one high-energy spectrometer pointing away from the spacecraft close to the nominal bellyband direction (i.e. close to the direction perpendicular to the S/C spin axis). The field-of-view of each of these sensors is offset by 15 degrees from a perpendicular direction in order to increase the range of observable pitch angles.

In addition, a second medium-energy spectrometer is mounted with a look-direction centered at 35 degrees with respect to the S/C spin axis in order to increase pitch angle coverage during those time periods when the ambient magnetic field is stretched and far from dipolar.

A number of pointing configurations were examined in order to optimize pitch-angle coverage from the two look directions given by the medium energy MagEIS instruments. Since the spin axis of the spacecraft is designed to point approximately toward the sun, small values of beta, the angle between the magnetic field and the spin axis, are indicative of highly stretched field configurations on the day side and night side, while large values of beta result from more dipolar field configurations. On the dusk and dawn sides, stretched fields do not necessarily imply small values of beta because the field direction is typically more perpendicular to the spin axis there. However, very stretched configurations often exist during storm conditions, which is a principal science target for the mission. To ensure reasonable coverage during such events, the detectors were oriented at 75 deg and 35 deg (each with 20 degree field of view). For such a configuration, good pitch angle coverage is maintained for values of beta as low as 10 deg.

Figure 12 shows the pitch angle coverage (and overlap) achieved by the two Medium MagEIS instruments. In the plot, the vertical axis gives the pitch angle (alpha), and the horizontal axis is beta.

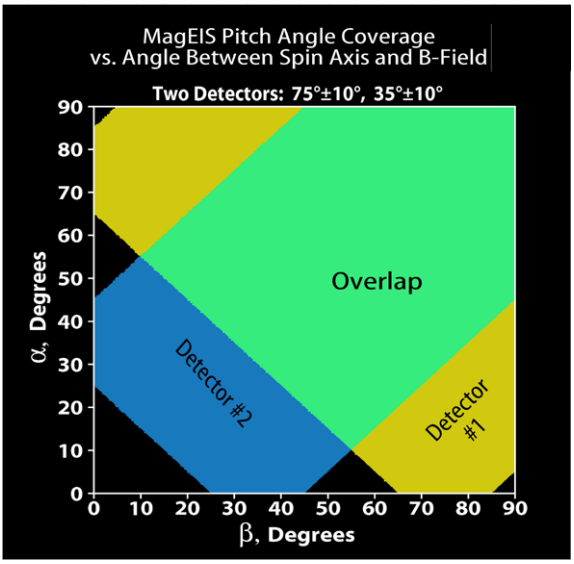

Fig. 12 The pitch-angle coverage of the two Medium MagEIS spectrometers

The coverage in the alpha-beta parameter space from each detector is colored-coded. Blue shows regions covered by the more spin-axis aligned detector (MagEIS-Med35) alone, while yellow shows regions covered by the other detector (MagEIS-Med75) alone. Green shows regions of overlapping coverage.

4 Instrument Design—Ions

4.1 Overview

In addition to a magnetic electron spectrometer, both MagEIS-HI instruments contain a silicon-detector telescope. The first detector in both telescopes measures the fluxes, energy spectra, and angular distributions of protons in the energy range from 50 keV to greater than 1 MeV. These telescopes have no composition discrimination but protons of course will dominate; they are identical in RBSP A and RBSP B.

Two additional detectors follow in both telescopes but are not identical; the configuration differences and measurements made by these detectors are discussed below.

4.2 Low Energy Protons

The proton telescope mechanical configuration is shown in Fig. 13. The front detector is a Micron Semiconductor device that is 50 microns thick, and is totally depleted. The outside diameter of the sensitive area is 8 mm and the inner annulus is 4 mm in diameter. Particles that pass through the annulus strike the rear detectors; the configurations and functions of the rear detectors are discussed below. The detectors are positioned behind a disk-loaded collimation system with a 1.5-kilogauss electron-sweeping magnet in the middle of the collimator. Laboratory testing has shown that this electron sweeper prevents electrons below ∼2 MeV from striking the proton detector and higher energy electrons are largely attenuated.

There are nominally 20 rate (energy) channels, sampled 20 times per spacecraft rotation from the front detector. There are histogram data from both the front and rear detectors.

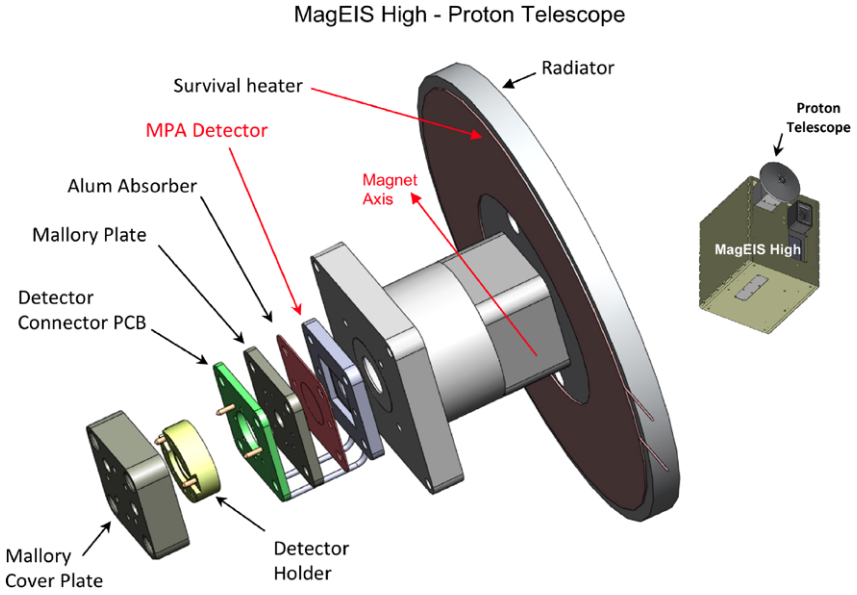

Fig. 13 An exploded view of the mechanical configuration of the proton telescope

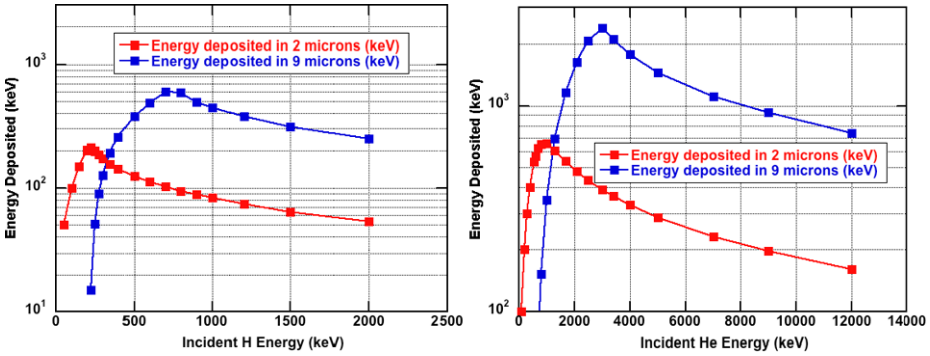

Fig. 14 The figures give the energy deposits in the 2 micron and 9 micron detectors by H and He ions as a function of incident ion energy, in the left and right panels respectively

4.3 Heavy Ions (Telescope in RBSP A—Proton Telescope A)

Two ORTEC surface-barrier detectors are placed inline, and view space through a 3.8 mm diameter collimator placed just behind the 4 mm hole in the center of the front annular proton detector. A 2-micron detector is in front and a 9-micron detector behind. Thus ions striking the 9-micron detector must first pass through the 2-micron detector. There is no coincidence formed between events in these two detectors.

The SRIM 2011 software was used to calculate the energy deposit of H, He, and O ions over the energy ranges of interest, results are shown in Fig. 14.

Table 2 Helium Energy Channels in RBSP A Telescope

He2L	350 keV	350 keV–3500 keV
He2H	500 keV	500 keV–2000 keV
He9L	900 keV	1500 keV–9500 keV
He9H	1500 keV	2000 keV–4800 keV

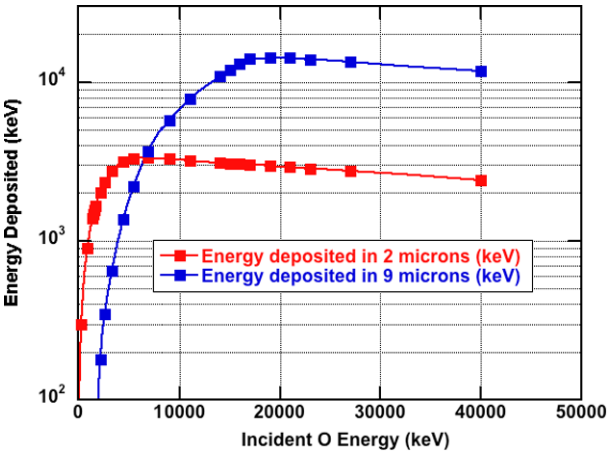

Fig. 15 The calculated response of the 2 micron and 9 micron detectors to O ions is shown

The selected energy thresholds render these detectors insensitive to protons. Each of the two detectors has two energy deposit thresholds; He2L(low); He2H(High); He9L(low); He9H(high). The thresholds and sensitive energy ranges for He ions are given in Table 2.

These two rate (energy) channels, are sampled 20 times per spacecraft rotation in an analogous fashion to the proton data from the front detector.

Oxygen is another ion of high scientific interest for the RBSP mission. Figure 14 shows that He cannot deposit more than ∼700 keV in the 2-micron detector and more than ∼2200 keV in the 9-micron detector. Trapped ions depositing higher energies must be heavier than He, and are expected in general to be due to O ions in the Earth's magnetosphere. An energy deposition plot for O, similar to the two above for H and for He, is shown in Fig. 15.

Because of the expected low rate of oxygen events, there are no rate channels. Histogram data are acquired from both detectors, 64 channels from each detector covering the energy ranges from 400 keV to 4 MeV for the 2-micron detector, and 900 keV to 22 MeV for the 9-micron detector. The histograms are nominally read out every eight spacecraft rotations.

Although the energy/species covered by these two detectors are described by the SRIM software, gains and energy responses were measured using several heavy-ion beams accelerated by the LBNL 88″ cyclotron.

4.4 Energetic Protons and Heavy Ions (Telescope in RBSP B-Proton Telescope B)

Two Micron Semiconductor ion-implanted detectors are stacked inline, and view space through a 3.8 mm diameter collimator placed just beyond the 4 mm hole in the center of the annular proton detector.

The 10-micron detector is used to make heavy-ion measurements much as done with the two thin detectors in the proton telescope in RBSP A. This detector also serves to block

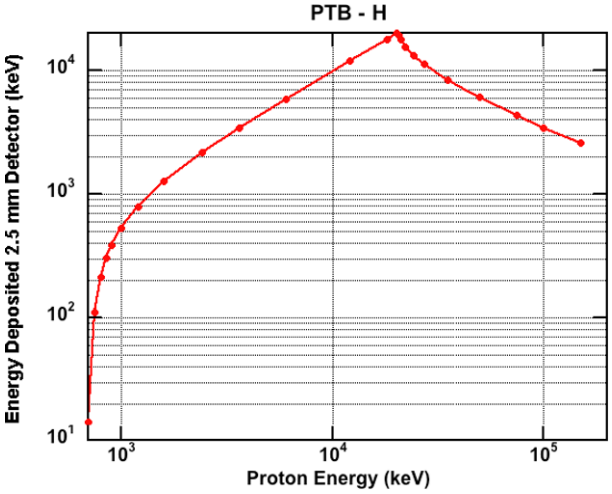

Fig. 16 The calculated response of the telescope to energetic protons is shown

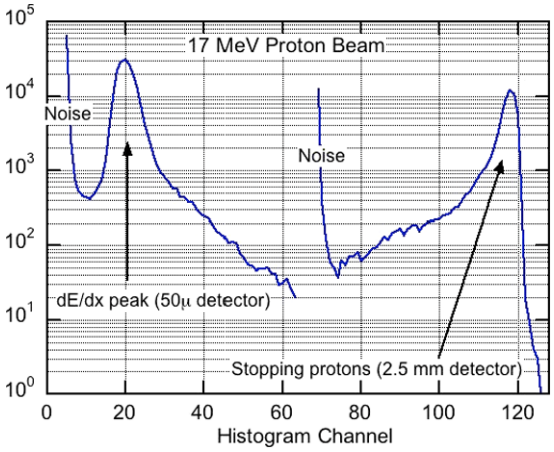

Fig. 17 The response of Proton Telescope B to a 17 MeV proton beam is shown for both the 50 μ and the 2.5 mm detectors. The beam is stopped in the thicker detector giving a total energy peak whereas the 50 μ detector gives a clean dE/dx peak made by the penetrating protons

low-energy protons from being incident upon the 2500-micron detector and thus eliminates a high event rate below the MeV energy range of interest.

The primary function of the 2500-micron detector is to fill the energy gap between ~800 keV and 20 MeV, the latter energy being near the proton threshold of the REPT instrument in the ECT suite. Figure 16 shows the energy deposited in the 2500-micron detector as a function of the incident proton energy.

Near the low-energy threshold, this thick detector augments the measurements made by the primary (front) detectors in both PTA and PTB as can be seen in the following plot. Each detector has a low and a high threshold rate channel. The rate channels are sampled ~20 times per spacecraft rotation. Each detector has a histogram output. The histograms are read out nominally once every 8 spacecraft rotations.

The sensor was calibrated using proton beams between 6 and 50 MeV accelerated by the LBNL 88″ cyclotron. An example of such calibration data is shown in Fig. 17.

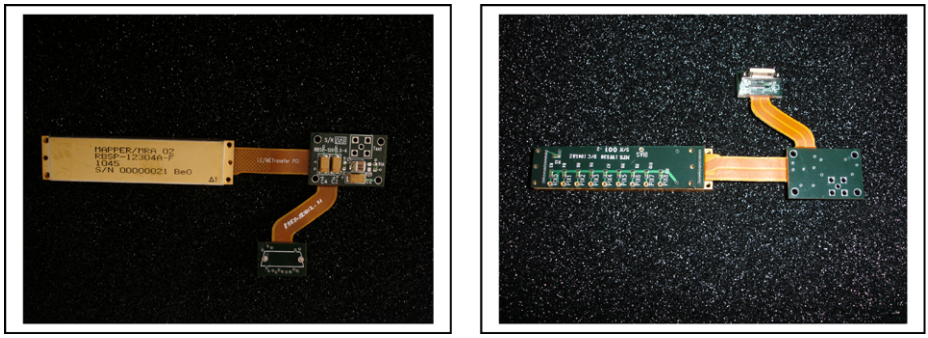

Fig. 18 The MAPPER hybrid attached to Transfer PCB is shown *in the left panel*. The silicon detector array attaches to the sockets on the side of the PCB opposite the MAPPER, *right panel*

5 MagEIS Front-End Electronics

5.1 Electronic Design and Configuration

Each of the MagEIS instruments uses a custom multi-chip module (i.e., hybrid) to amplify and digitize the charge pulse from the silicon detector pixels in the electron spectrometer and proton telescope. The MAPPER hybrid (Multi-Amplifier Pulse Peak Energy Readout) provides an architecture that offers parallel analog processing and digital readout for ten detector pixels. The hybrid is designed to attach to the backside of a detector array with minimal interconnect length, thus minimizing the noise contribution of parasitic capacitance. A rigid-flex circuit board, called the Transfer PCB, is used to provide the detector connection as well as the interface to the digital processing unit (DPU) as shown in Fig. 18.

The analog MAPPER chip and digital MRA chip together form a complete pulse-height analysis (PHA) system. Figure 19 shows the functional block diagram of the hybrid electronics. Each MAPPER amplifier channel contains a charge preamplifier, pole-zero cancellation network, shaping amplifier, scaling amplifier, baseline restorer, and peak-hold amplifier. The front-end is AC coupled to the detector and measures positive charge flowing into the preamplifier feedback capacitance, which can be set to 0.2 pF or 1 pF depending on the gain selection. The preamplifier is continuously reset through a linear-mode FET in the feedback loop. The shaping amplifier produces a 3-pole semi-Gaussian pulse with shaping time of $\sim$1 usec FWHM. This signal is then scaled by another amplifier such that the full-range is approximately 1-volt.

The energy deposited in the detector is linearly proportional to the peak of the shaped detector pulse. A discriminator is used to determine if the peak of the shaped pulse exceeds a pre-stored threshold charge on the peak-hold capacitor. When this happens, a digital peak-detect signal is asserted to indicate that the shaped pulse peak is stored and ready for conversion by the MRA (MAPPER Readout ASIC).

A Wilkinson A/D converter was chosen for its high linearity and low power dissipation, making it suitable for dedicated use on each amplifier channel. The Wilkinson A/D is formed by the way the peak-hold capacitor is discharged. When the peak of the shaped pulse is stored and the peak-detect signal goes active, a constant current source inside the MAPPER chip is activated by the MRA. The current source is pre-tuned by an internal resistor on each MAPPER channel, called the rundown resistor, to give a constant linear decay rate. A buffered form of the peak-hold capacitor voltage is presented to a comparator, which

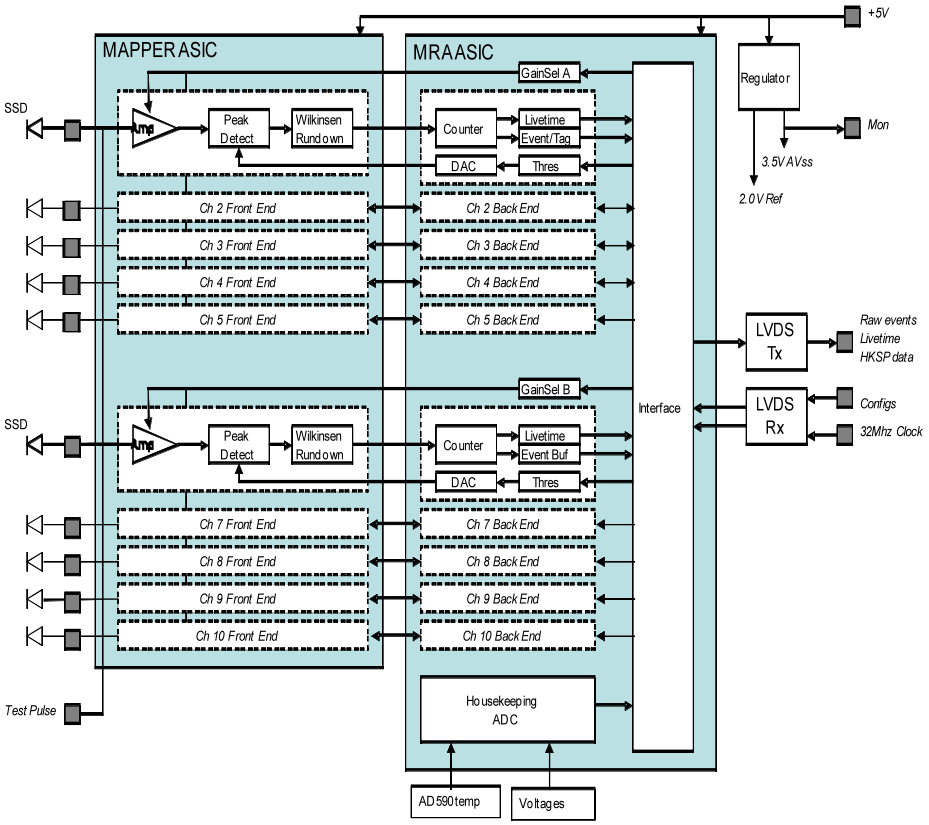

Fig. 19 MAPPER dual-ASIC hybrid functional block diagram

goes active when it drops below the baseline reference, marking the end of the rundown interval and the de-assertion of the peak-detect signal. The width of the peak-detect signal is proportional to the peak of the shaped pulse, and hence the energy deposited in the detector. The MRA chip digitizes this width by counting the number of 32 MHz system clocks between the assertion and de-assertion of the peak-detect signal. Although a much larger dynamic range could be achieved with this A/D converter, only 8-bits are needed to meet the measurement requirements.

The MAPPER hybrid is designed with flexibility to support all the detector requirements. By selecting one of several gain modes (i.e., range modes), the hybrid can be optimized for different energy ranges depending on the targeted instrument. Table 3 gives the nominal energy ranges selected for each of the MagEIS instrument types. In addition, the MRA chip provides a dedicated programmable 12-bit D/A threshold value for each MAPPER channel.

A single MAPPER can also be configured to support two different detectors. This was necessary for the High instrument electron detectors, whereby the front detector and back detector arrays have different required energy ranges. The MAPPER is organized into two banks, each containing five amplifier channels, which share a common range setting.

The MRA chip provides important timing information. Each direct-event is time-tagged and appended to the PHA word. This time-tag is 8-bits and has a resolution of 1-usec. It is used by the DPU to determine coincident events in the High unit detector stack. The MRA

Table 3 MAPPER energy range settings

MAPPER Range Setting	Full-scale Energy	Detectorv System
Low Range	280 keV	Low Electron Array
Medium Range	1.25 MeV	Medium Electron Array, High Front Electron Array
High Range	4.5 MeV	High Back Electron Array

also provides 16-bit live-time counters for each channel, having a resolution of 32 u-secs for monitoring the amount of time the channel is not processing an event (i.e., the opposite of dead-time).

The MAPPER hybrid provides some diagnostic capability. A test pulser input is connected in common to each of the preamplifiers through an on-chip injection capacitor. The DPU activates the pulser during instrument checkout to verify that the gain, offset, and noise of each channel is within specifications. The MAPPER hybrid also provides an 8-bit successive-approximation A/D converter for monitoring the internal temperature, reference voltage, preamplifier source voltage, and baseline levels for both banks.

Bi-directional communication between the MAPPER hybrid and the DPU is established by a synchronous LVDS (Low Voltage Differential Signaling) interface. Direct event data, live-time data, and housekeeping are transmitted to the DPU by a LVDS transmitter chip, while configuration commands are received by a LVDS receiver chip, both of which are internal to the hybrid. LVDS was chosen to minimize digital coupling to the front-end. This choice allowed simultaneous operation of the front-end with digital transmission of events, thus eliminating the dead-time that is encountered by systems that disable the front-end during data transfer. The LVDS operates from a 32 MHz clock, which is also driven as an LVDS signal to minimize noise

5.2 Engineering Calibrations—Gain/Offset Measurements

The gains and offsets of the electronic chains of every pixel were measured over the operational temperature range as well as at room temperature. Every low and medium magnetic spectrometer has a 9 pixel focal plane for a grand total of 54. A high-energy unit has 8 pixels in two planes and each proton telescope in both high units contains 3 detectors. Thus the total number of detectors is 76 in the MagEIS complement. Since gain/offsets of every detector were measured at a least three temperatures, often more, the total number of individual gain/offset measurements made in preparing the eight spectrometers for flight was well over two hundred. Here we will show a few examples and some summaries that are representative of the entire database. Figure 20 is a calibration example that employed a radioactive source.

The Bi-207 source emits electrons at several discrete energies resulting in distinct peaks over the energy range of the focal plane. The channel location was accurately determined by fitting every peak to a Gaussian in channel space. The energies of the various electrons are well known and the peak location can then be plotted vs. peak energy as shown in Fig. 21.

It can be seen that a linear fit is excellent, showing that the electronics have good linearity. The offset of -17.7 keV indicates that zero energy is not at channel 0. Figures 22 and 23 present a summary of the gains and offsets for the nine pixels in the medium energy spectrometer as a function of temperature.

The two plots show that the temperature dependence of both the gains and offsets is small, especially the case of the gains. Furthermore the pixel-to-pixel variation in gain is small also.

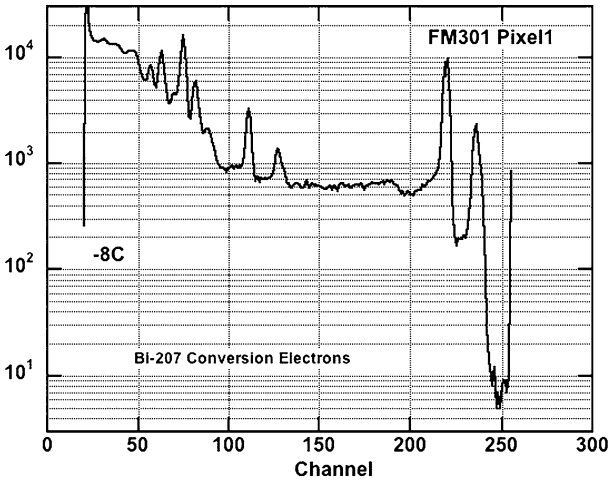

Fig. 20 A plot of the electron energy spectrum of Bi-207 as seen in Pixel 1 of FM301 at −8C is shown

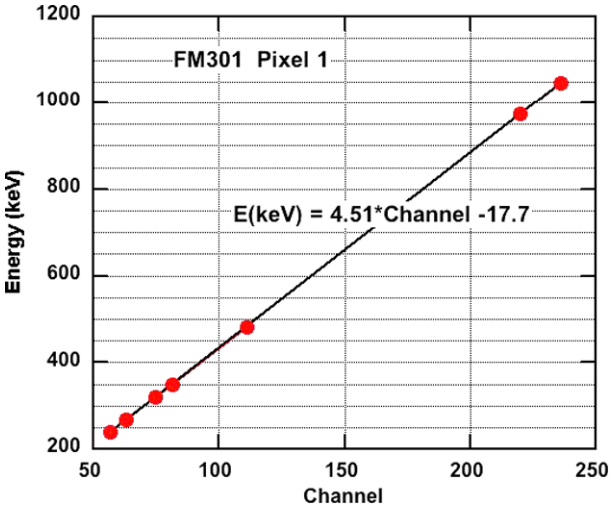

Fig. 21 The channel locations of the energy peaks plotted in Fig. 20 is plotted vs. the energy of the respective peak. The resulting energy vs. channel plot is fitted to a *straight line*

However the pixel-to-pixel variability in offset is sizeable. An average value could not be used in data analysis. The gain/offset measurements summarized here for FM301, a medium energy spectrometer, were carried out for all eight of the flight spectrometers.

6 MagEIS Digital Processing Unit

6.1 Overview

The Digital Processing Unit (DPU) of the MagEIS instrument is the base interface between the spacecraft and the front-end electronics, cf. Fig. 24. The DPU on a very top level converts the raw data from the Mapper Hybrids and sends environment information back to the spacecraft. This level 0 data is properly formatted, compressed, aligned and tagged so the spacecraft can sort it properly. The DPU also controls ancillary functions to the mission such

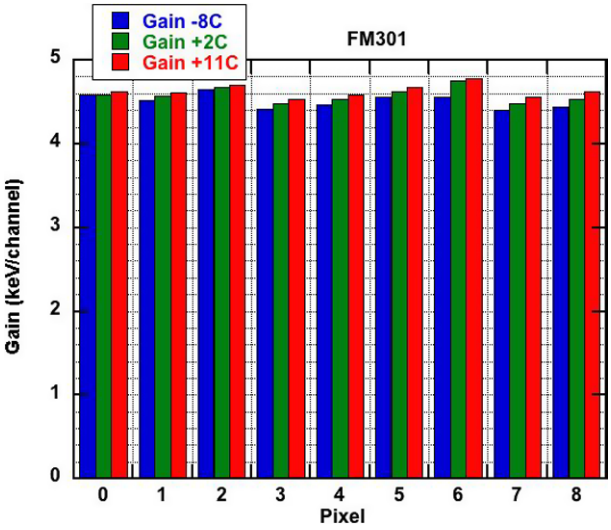

Fig. 22 The temperature dependence of the gains in the nine channels of the FM301 focal plane is summarized

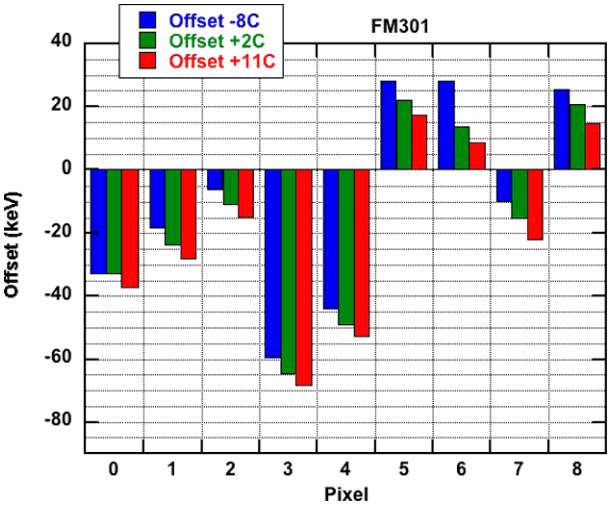

Fig. 23 A summary is plotted of the temperature dependence of the offsets in FM301

as heaters and MAPPER configurations along with collecting various analog housekeeping data throughout the system.

There are two similar yet quite different DPU designs. The Low/Medium design includes only one electron MAPPER interface. It is less complicated but allows for a higher throughput in electron data. The High design has two MAPPER interfaces, one for protons and the other for electrons. In addition, the electrons are processed through a separate coincidence logic function to allow only those events that meet certain coincidence requirements. This lowers the throughput by eliminating data upfront, but improves background reduction in the science data.

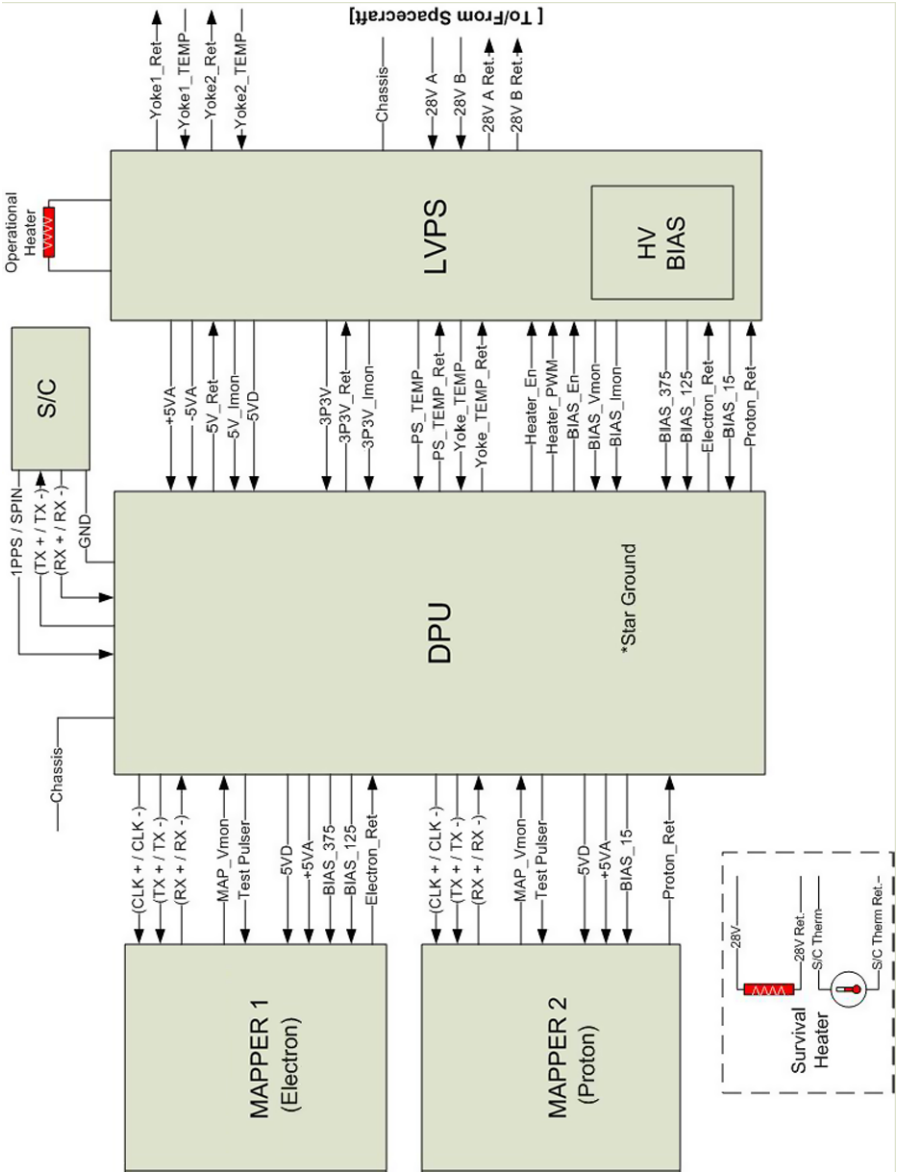

Fig. 24 The Digital Processing Unit of MagEIS is the basic interface between the RBSP spacecraft and the front-end analog electronics of the MagEIS spectrometers

6.2 DPU Design

In essence, the DPU is simply a highly advanced and specific CPU (central processing unit) implemented inside of a radiation hardened FPGA. The main components of the FPGA are the CPU core and the Event Logic. The CPU is a modified 8051 core that has the ability to control all functions of the instrument. This achieved by interfacing to registers and external I/Os. The CPU is connected to an RS232 interface running over LVDS to the spacecraft, allowing real time communication and configuration of the system. The Event logic is responsible for interfacing to the MAPPER ICs, data collection, sorting, summing and storage. Both of these components must share the use of memory spaces. Figure 25 shows a breakdown of the FPGA and DPU functions via a block diagram.

6.3 Software

The CPU runs a custom operating system. This software, by controlling the CPU, allows near unlimited configurability to the entire system. Commands can be sent from the ground to tune and tweak the settings of the DPU to make simple output parameter and threshold changes. Alternatively, new software can be uploaded at any time to drastically reconfigure the instrument to change performance, alter telemetry priorities, or even change packet formatting. In addition Lookup Tables (LUTs) can be uploaded at any time to alter the categorization of the actual event data.

6.3.1 Configurable Parameters

Lookup Tables The lookup tables are the heart of the data "sorting." These tables are configured in such a manner to narrow down the scope of the data to specific areas of scientific interest. This has a twofold benefit. Primarily, regions of data that are superfluous to the mission, considered unimportant or classified as "noise" can be stripped out right at the beginning of the acquisition process. Secondly, this eliminates unnecessary data transmission and reduces the telemetry requirements for each instrument.

MAPPER Settings The MAPPER hybrid is an analog detector front end coupled with digital readout electronics. These Hybrids are commanded through the DPU/spacecraft interface. Changeable parameters include: enabling or disabling individual channels; setting coarse ranges for channel banks; and setting fine threshold ranges for each channel.

Housekeeping Data In addition to flight data, the DPU also collects telemetry from the entire instrument system. This information is gathered once per second and sent to the S/C. This telemetry includes: temperatures throughout the instrument; operating voltages and currents; detector bias voltage settings; calibration test pulser level.

Digital Status The current instrument configuration needs to be known at all times. Once per second, this status information is sent to the S/C. It includes: instrument identification information; software version; spin & pulse per second monitoring; hybrid command monitoring; packet errors; instrument operational modes; and bias, heater and test pulser status.

Auxiliary Controls The DPU also controls other functions that are critical to the mission. The detector BIAS can be turned on or off. The Operational Heaters can be enabled or disabled. Furthermore, the heater set point can be adjusted to allow fine control over the temperature range for the yoke and associated electronics.

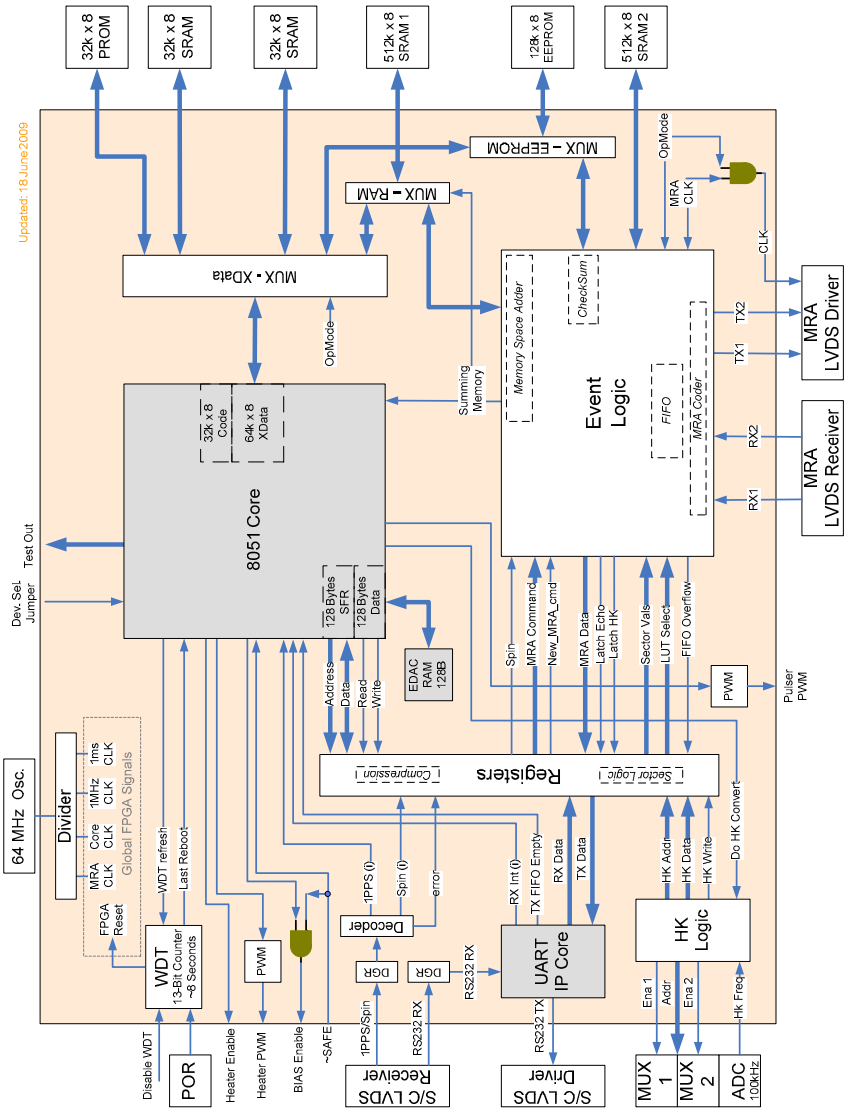

Fig. 25 A breakdown of the FPGA and DPU functions via a block diagram is shown

DPU Memory Management The challenge in designing the DPU system was the storage of data. Only one main component (either the CPU or the Event Logic) can access memory at any given time. Whenever the CPU accesses memory, dead time is present for the instrument as no new events can be stored. The standard operating procedure in such situations is to have two memories and ping pong them, or swap them. As one memory is being written to, the other could be read out eliminating any dead time. This was not possible in our system as different data integration times were programmable. For example, histogram data could acquired for minutes at a time, while singles rates were read out every spin. Ping ponging memories in this instance would be impossible.

The solution was achieved by marrying one memory to the CPU for processing and transmission, and one memory to the Event Logic for data acquisition. Then, once every spin (12 seconds nominal), the front end would be ignored while the data was "summed." This process would read the data from both memories, sum them, and then write the new total to the memory controlled by the CPU. Simultaneously, the Event Logic data would be cleared to allow the acquisition of new event counts. This process, which occurs at the very beginning of a spin, takes 13 ms in the Low/Medium units and 6 ms in the High unit, which leads to an acceptable dead time of no more than approximately 1/10 of 1 %.

DPU Data Flow Each time an electron strikes a detector, a single event is generated inside the MAPPER. This event is processed in an event data flow as described below.

Event Reading The events are transmitted to the DPU each time they are received. It is the responsibility of the DPU to be able to handle simultaneous event readouts from all 10-detector channels for a combined possible maximum of 1 million samples per second. The DPU categorizes each event by its source pixel and places the event into a FIFO. The FIFO buffer allows the writing and reading operations to be independent, divorcing the timing of the two and making the system more flexible.

Lookup Tables When the FIFO is not empty, the events are read out and processed. Based on the type of event and the source, each event has the potential to create multiple data entries. Figure 26 illustrates the process in a HIGH unit. The events are then processed through a lookup table. Each lookup table is a 4K entry into the EEPROM. This table takes in an event pixel number and a PHA value to determine in which "channel" to place the entry. Each memory type has a different number of allowed channels and is stored in separate locations in memory.

Memory Storage Each spin is broken up into sectors so that it can be determined from which spatial direction the event originated. This sector size is independently configurable for each type of data. Once a channel has been determined from the Lookup Table, the event is then combined with the current sector information and written to memory. The storage occurs in the form of a single count. The memory location for that sector/channel combination is read out, incremented, and then written back to the same location. Each location has the ability to store 24 bits of counts, or in excess of 16 million events. The benefit of counters this large is to allow lengthy integration times on the S/C, lowering the size of transmitted telemetry, increasing the scientific value of individual packets, and reducing the effort needed to analyze and consolidate data on the ground.

High Unit—Electrons The High unit, as briefly described before, has significantly different Event Logic from the Low/Medium unit. The first primary difference is the inclusion

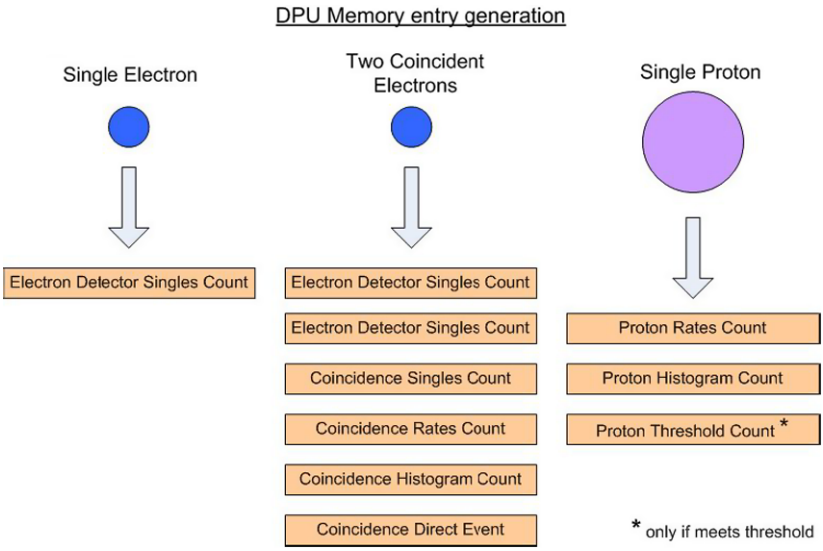

Fig. 26 A block diagram of event generation is shown for the High unit

of a coincidence logic block. This logic determines whether two separate detector events are in coincidence with each other, and therefore the same particle. This is determined by a number of ground programmable parameters such as: time between events; order of events; and channels affected.

Once a particle has been determined to be in time coincidence in the detector stack, processing is enabled and the event is stored in memory. The event is then sorted into a number of categories. A new category in the High unit is the Direct Event Data. This category has the ability to store the actual event PHA data in memory for the last 8 coincidences in a telemetry sample, cf. Fig. 27.

High Unit—Protons With an additional proton MAPPER, a separate Event Logic block is needed. This logic block is similar to the Low/Medium electron processing. However, there are only three detectors and hence only 3 channels available to process. In addition, programmable threshold counters are included to count only events that meet a minimum PHA threshold value. See Fig. 28 for a block diagram of the Proton event processing.

7 Magnetic Spectrometers Data Outputs

The magnetic spectrometers have several types of data output as discussed below.

7.1 Primary and Derived Data—Magnetic Electrons Spectrometers

The primary data are telemetered 20 times per s/c rotation, or nominally 20 times per 12 seconds. These data are from the 9 pixels in the spectrometer focal plane. Figure 29 shows calibration data from one of the flight medium spectrometers taken using a ^{90}Sr–^{90}Y beta source, with data acquired from only 4 pixels shown for clarity.

The primary data are counts within the energy pass band delineated by the colored pillars in the plot. The pass band is selected to encompass those energies in the center of the

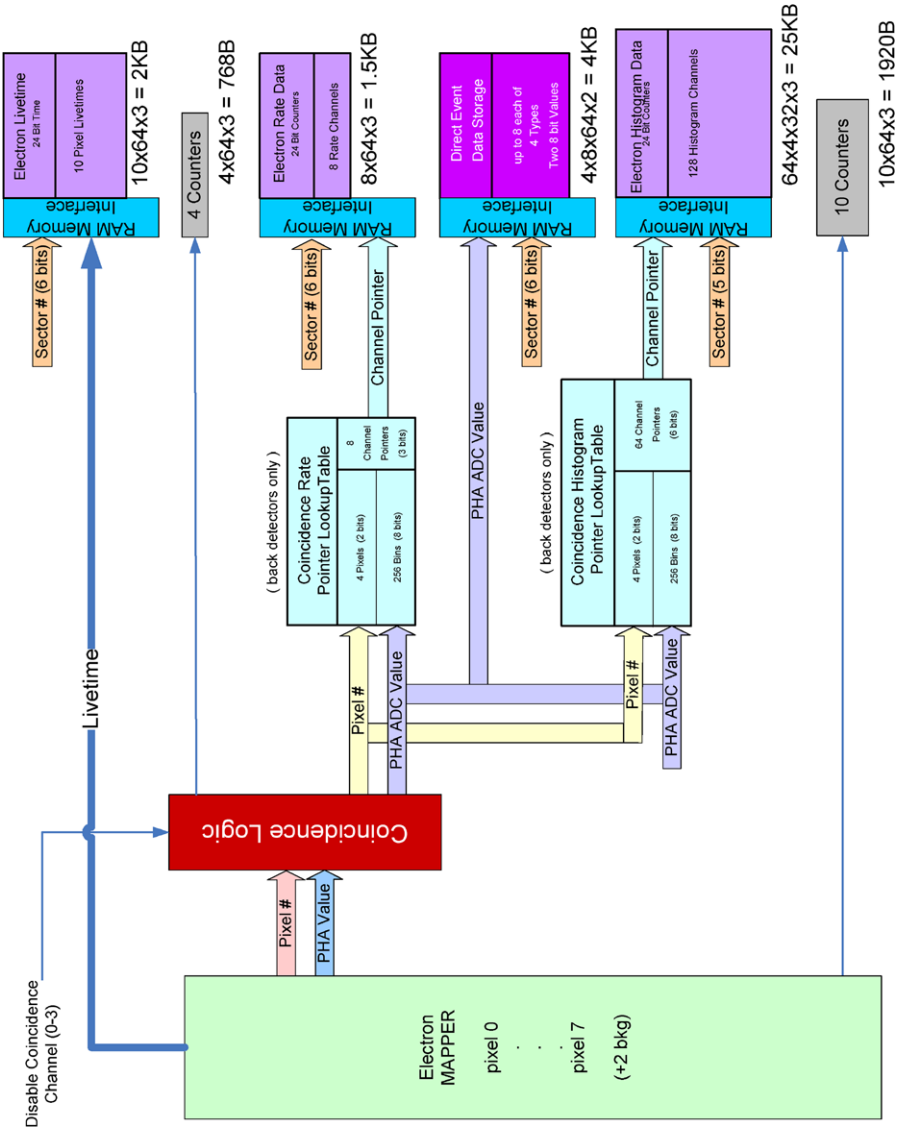

Fig. 27 The coincidence processing in a MagEIS-High unit is shown schematically

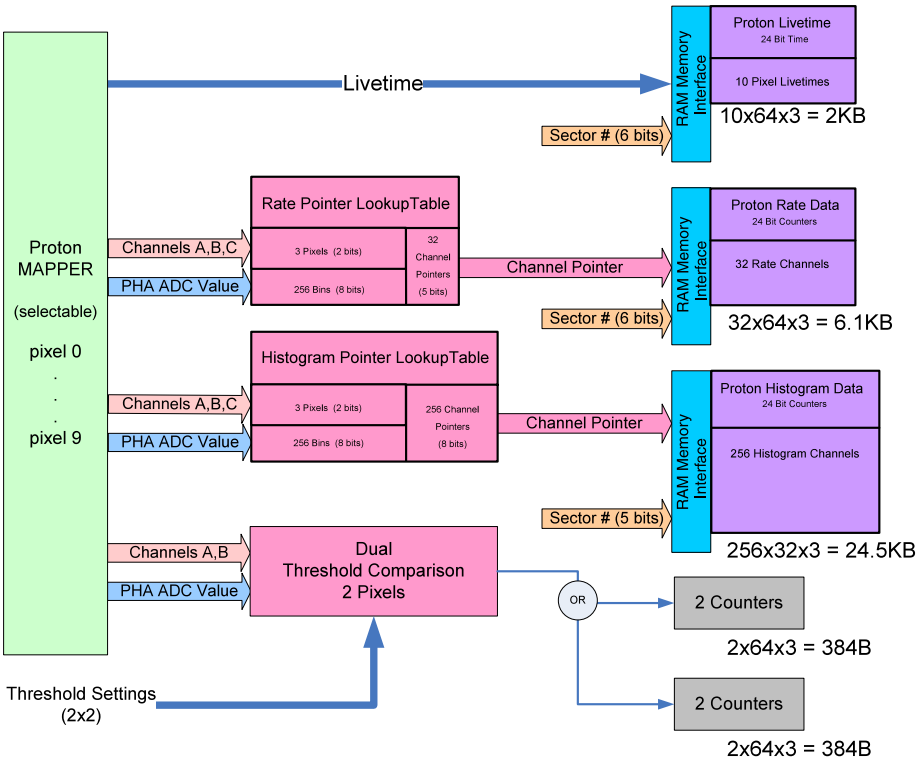

Fig. 28 The proton event processing is shown schematically

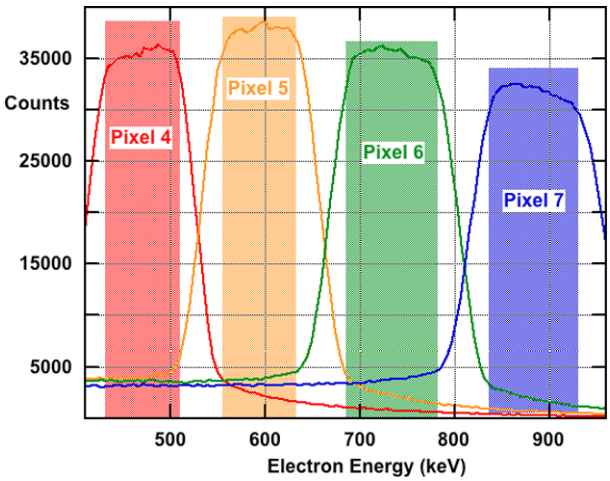

Fig. 29 An example of calibration data acquired with a Medium unit is shown

pass band where the pixel response is quite independent of energy, making conversion from counts to differential flux straightforward.

The derived data are telemetered at the same rate and are derived by combining data from adjacent pixels. Thus all counts, whether in the peak or the skirts of a pixel pass band are

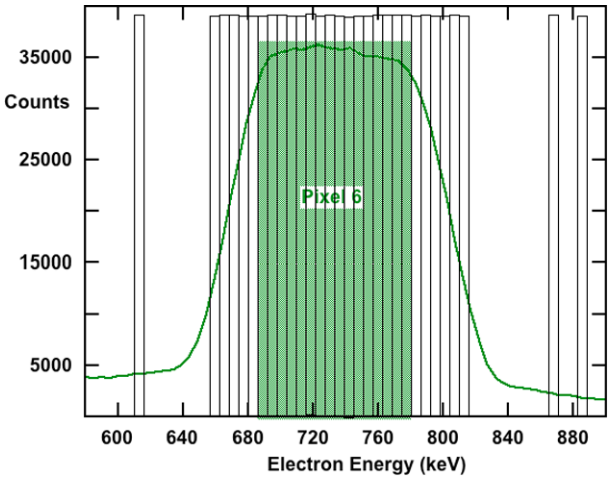

Fig. 30 The figure illustrates schematically how histograms are selected for a given pixel

retained and telemetered. The pixel pass bands stored onboard are based upon calibration data, and may be modified during the mission by ground command.

7.2 Histogram Data—Magnetic Electron Spectrometers

Every event in every pixel is pulse height analyzed into 256 channels between comfortably above the noise to near saturation. In principle all these data could be telemetered. However it would require far greater telemetry resources than are available. So this high-resolution data are combined to provide the primary and derived data described above.

However some histogram data are saved and telemetered at a lower rate than the primary and derived data. To reduce the telemetry burden, only 64 of the 256 histogram bins are saved. Most of these energy bins cover the region in energy space occupied by a given pixel as shown notionally in Fig. 30 for Pixel 6. However some outlier bins are also saved to monitor background in that pixel. These histogram data are collected for the same 20 sectors as the primary data but integrated over 8 rotations of the RBSP spacecraft.

One of the critical reasons to save histogram data is to use it to determine the background level and to use it to remove background from the science data. Data taken during ground testing of a medium spectrometer is shown in Fig. 31. The same data used in Fig. 29 is used in this figure to plot only the Pixel 4 response in red. The curve in blue is the response outside of the Pixel 4 pass band and the dashed red curve the Pixel 4 response with the background subtracted. In this exemplary case the background subtraction is not really needed because of the strength of the true signal. However one can see that were the signal only modestly above the background and especially if the true signal varied over the pixel pass band, the subtraction process would enable extraction of the true signal from a large background.

The silicon detectors have much better energy resolution than the width of the energy channel in momentum space. This pixel width is determined by size of each pixel along the focal plane. In principal many more, smaller pixels could have been employed, but required spacecraft resources, especially telemetry would be substantially increased. The present selection comfortably meets the mission science requirement.

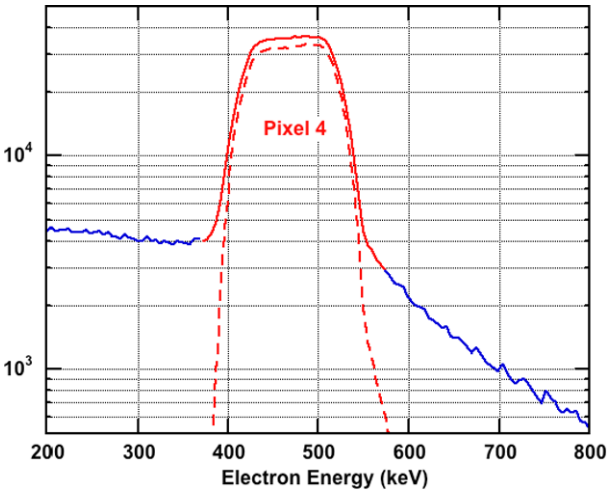

Fig. 31 Calibration data acquired with a flight Medium instrument is plotted, clearly showing the pass band and the high and low energy skirts of the pixel response

Table 4 Proton Telescope data types, number of channels per type, angular sectors per type, spins/set for a data type and resulting TM rates

Proton Telescopes	No. of Counters	Bits	No.† Sects.	bps*	Spins‡ per Set
Main Rates	32	10	24	326	2
Histogram	256	10	24	544	10
Threshold Rates	4	10	24	25	4
Livetime	10	10	24	219	1

* Depends on No. Sects. and Spins/set
†, ‡ Set by command

7.3 Proton Telescope Data Outputs

The process of mapping the telescope detector outputs to data channels is summarized in Fig. 32. In panel [a], the label LP (low proton) is the 10 μ detector in Telescope B while the ORTEC detectors are in Telescope A (see above). The MPA detector is the front detector in both telescopes. The three detectors in each telescope are designated as A, B, and C in panel [a] of Fig. 32 along with their DPU/FPGA identification code (00, 01, 10). These correspond to the A, B, and C designations in panel [b].

Figure 32 panel [b] shows the relationships between the detector/MAPPER outputs (left), the lookup tables (center) and the data outputs (right). 10-bit compressed values, corresponding to the Live times for each of the detector-amplifier-PHA chains, are output to the data stream for each angular sector. The A, B, and C lookup tables are used to define the contents of the Main Rate data (up to 32 channels) and the Histogram data outputs (256 values). The Histogram can be composed of PHA data channels from any combination of the three detectors. Above, we described taking the outputs from A and B detectors to form two 128-channel histograms for each.

The detector outputs labeled A and B in Fig. 32 are used to generate four output data channels based on commandable threshold values, two for each detector as described earlier. These are in addition to the Histogram and Main Rate data.

Typical data output from the telescope is summarized in Table 4 where a satellite spin period of ∼12 sec. was assumed.

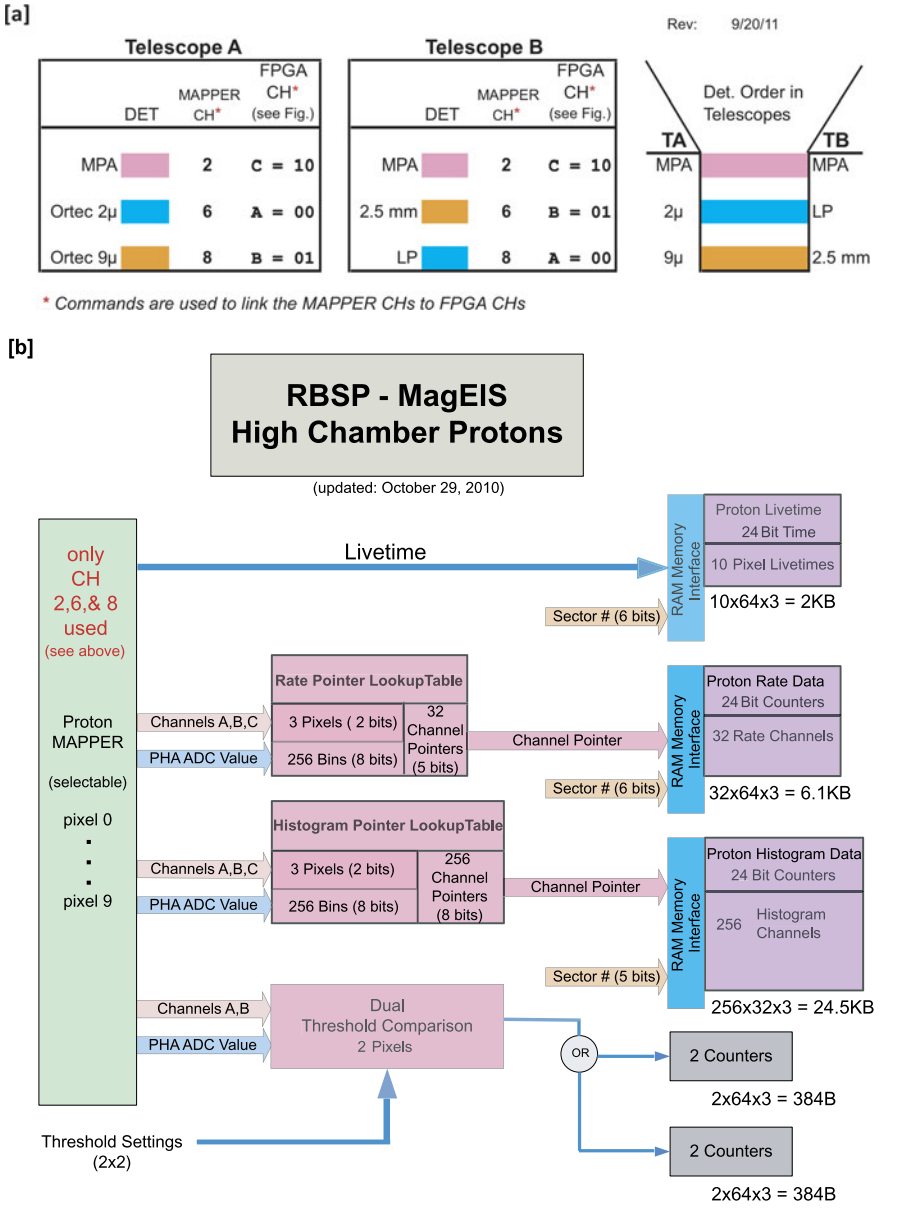

Fig. 32 (**a**) Block diagram of the proton telescopes, A and B identifying the mapper amplifier channels used and the DPU's FPGA code for the channels; (**b**) Block diagram showing the mapping of the telescope detector outputs through the DPU/FPGA logic to the output data counters

In this example, the satellite spin is broken into 24 equal sized angular sectors. The data counters are 24 bits in depth and are compressed to 10 bits (see discussion of compression counters). In this example the data, except for the live times, are accumulated over multiple satellite spins (spins per set) before transmission. The telescope data rates in bits per second are show for each type of data. The number of sectors and spins/set are used to optimize

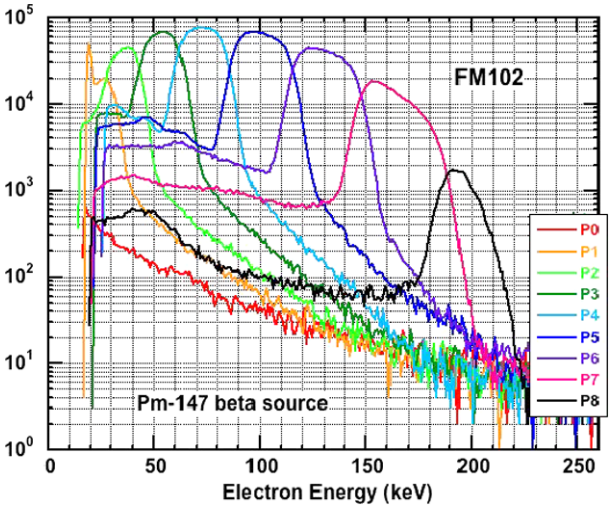

Fig. 33 The energy range of the electrons from Pm-147 covers the entire range of the low unit, with the intensity in the last pixel, P8, much less than the others because of the beta spectrum endpoint of 224 keV. The ordinate is counts per bin over the test and is arbitrary

the data sampling while constraining the telemetry rate required. For example, one could measure the Main and Threshold rates plus Live times every spin by reducing the number of angular sectors for all types and increasing the number of spins per Histogram data set.

8 Electron Spectrometer Performance Verification

A few representative examples of the performance of the magnetic electron spectrometers are shown, beginning with a low unit. A low-energy spectrometer was placed in a vacuum chamber and a Pm-147 beta emitter was placed a few inches in front of the spectrometer aperture, Fig. 33 shows the FM102 unit (Flight Model 102) response. The endpoint of the beta spectrum from Pm-147 is at 224 keV. Data were collected from all pixels. Figure 34 is an expanded plot showing the response of the FM102 lowest four energy channels to the Pm-147 source (see caption). It can be seen at a glance that the response of each pixel is within its respective pass band as designed. As noted elsewhere in this paper, pulse-height analysis removes out-of-band responses, and the histogram data permit removal of the background within the pass band if deemed necessary.

The same test described above was carried out using a Ni-63 source in place of Pm-147, Fig. 35. The endpoint energy of the Ni-63 beta spectrum is 67 keV. Figure 35 shows that the threshold of P0 is below the 20 keV noise threshold and measures only background. It will be used in flight to monitor the penetrating background from energetic protons, and from bremsstrahlung.

The next series of plots show the response of a medium-energy spectrometer. Figure 36 shows the response of FM201 to a Sr-90/Y-90 beta source. The beta spectra from this mother-daughter pair have endpoint energies of 546 keV and 2280 keV respectively. The energy range of the electrons from Sr-90/Y-90 covers much more than the entire range of a medium spectrometer. As a result the count rate in most of the pixels of FM201 are much the same. The modest difference seen in P4 (pixel 4) from its neighbors, P3 and P5, is due to the endpoint of the Sr-90 spectrum at 546 keV, that is, the energy resolution of the spectrometer is such that details in the electron energy spectra emitted by the test source can be seen.

The response of a medium-energy spectrometer can be seen more clearly by using a beta source with a lower endpoint energy, Pm-147. To help illustrate the fact that the responses

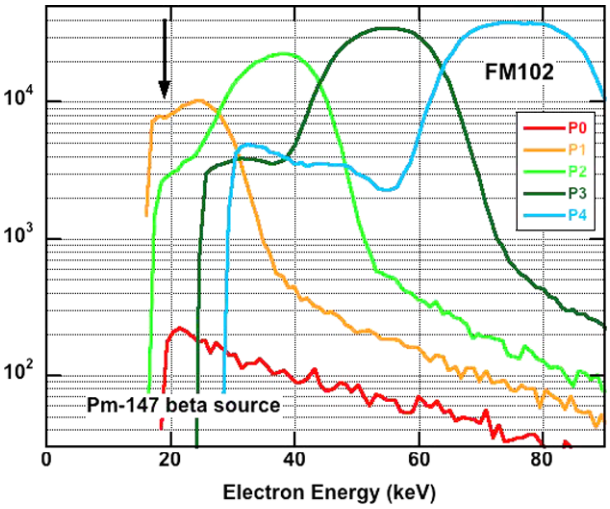

Fig. 34 Data acquired during a Pm-147 test are displayed at lower energies only in order to show the response in pixels 1 through 4 more clearly. The black arrow shows the threshold of P1, which can be seen to be just below 20 keV. The ordinate is counts per bin over the test and is arbitrary. Small differences between Fig. 33 and Fig. 34 are a result of small changes in laboratory temperature. The ordinate is counts per bin over the test and is arbitrary

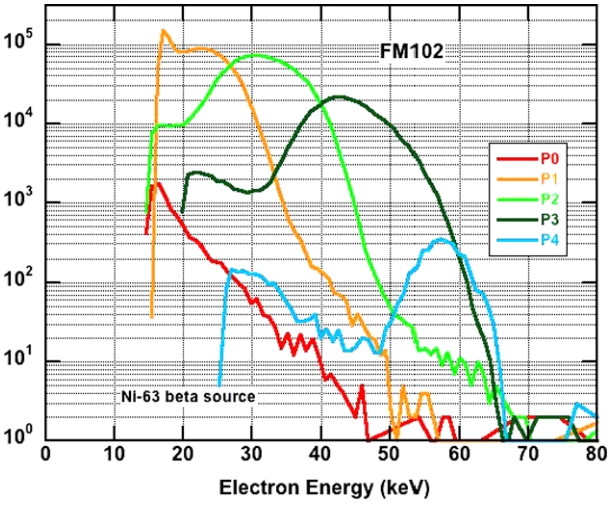

Fig. 35 The response of a low-energy spectrometer to a Ni-63 source is shown. The response in P4 ends at ∼67 keV, the endpoint of the Ni-63 beta spectrum. The ordinate is counts per bin over the test and is arbitrary

of the multiple units of the same type are essentially identical, another medium spectrometer was used to acquire the data used in Fig. 37. (FM302–Med35 in RBSP-B rather than FM201–Med75 in RBSP-A).

The Pm-147 beta spectrum nicely illuminates P0, showing a pass band of ∼75–110 keV. The rapidly falling beta energy spectrum causes the response of P1 to fall substantially over its energy range, and the response in P2 is very small for the same reason. Note the absence of counts in P2 above the Pm-147 endpoint energy of 224 keV. The three higher-energy channels that are plotted show a small background response in channels below their pass bands, counts which would be removed by pulse-height analysis during data analysis if this were flight data.

For this run the source was placed just outside of the aperture of the spectrometer in order to get a high count rate and some pileup. The regions of pileup in P0 and P1 are labeled. The

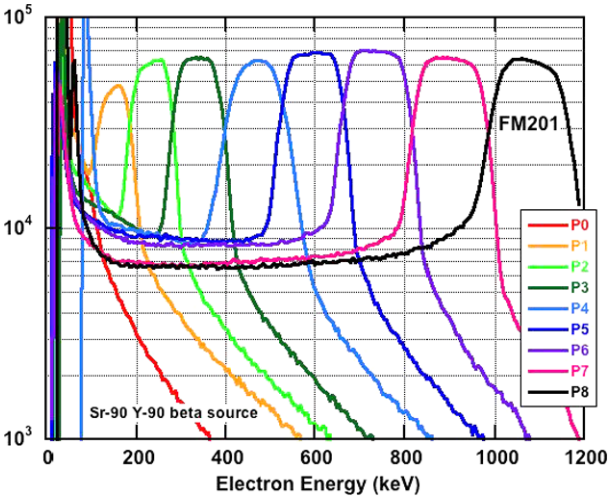

Fig. 36 The response of a medium-energy spectrometer to a Sr-90–Y-90 beta source is shown. The ordinate is counts per bin over the test and is arbitrary

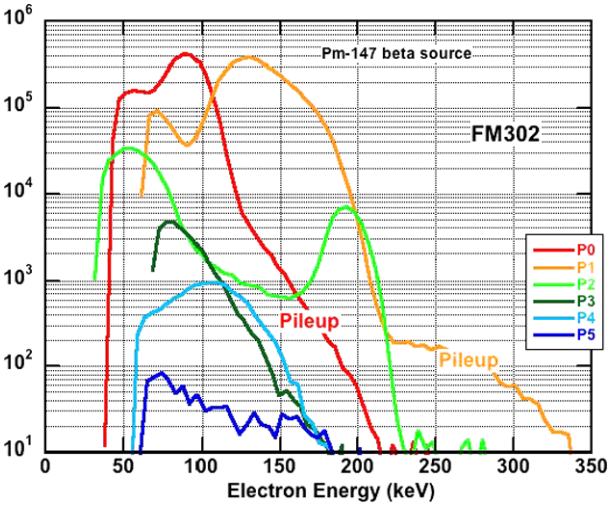

Fig. 37 The response of a medium-energy spectrometer to a Pm-147 beta source is shown. The ordinate is counts per bin over the test and is arbitrary

pileup is orders of magnitude smaller that the signal within the pass band, and what there is would be removed by pulse-height analysis if this were flight data.

The response of high-energy spectrometers was measured in a very similar way. A Ru-106–Rh-106 beta emitter was placed several inches in front of the spectrometer aperture, Fig. 38. The beta spectra from this mother-daughter pair have endpoint energies of 39 keV and 3541 keV respectively. The Rh-106 decay emits many energetic gamma rays that complicate the observed energy spectra in the high-energy spectrometer. This spectrometer has only four pixels rather than nine but has a two-element stack; there is a P1 front and P1 rear and so on, see discussion in Sect. 3.2. Observations are shown using only the four rear pixels in the figures below.

The response of the instrument nicely characterizes the shape of the Rh-106 beta spectrum, with the endpoint electron energy just above 3500 keV clearly revealed. The source completely illuminates the first three pixels, with just a small contribution to P4, whose endpoint is almost 5 MeV. The shoulder in the P4 energy spectrum, labeled Compton edge,

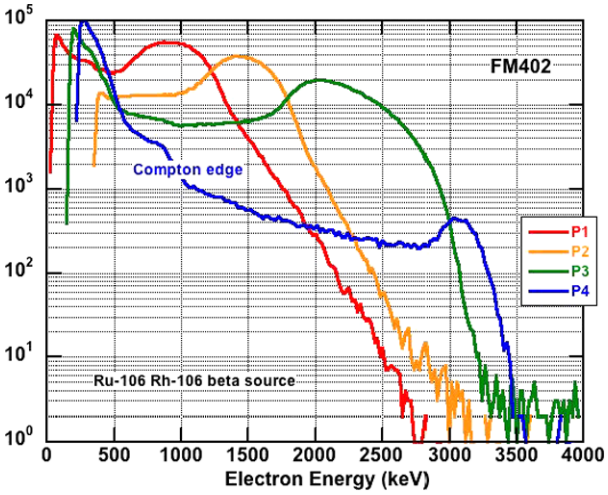

Fig. 38 The response of a high-energy spectrometer to a Ru-106 Rh-106 beta source is shown. The ordinate is counts per bin over the test and is arbitrary

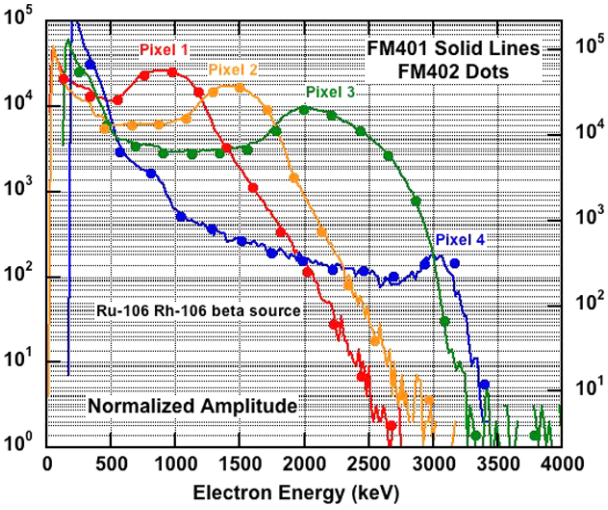

Fig. 39 Data acquired from both high-energy spectrometers are plotted on the same scale with normalized amplitudes. The responses of both units to the Ru-106 Rh-106 beta source are virtually identical. The ordinate is counts per bin over the test and is arbitrary

as well as the general level of background in all channels is due to the energetic gammas emitted by the beta source along with the wanted electrons. In flight no such gammas will be present and the background will be substantially less. Nevertheless this test cleanly delineates the pixel pass bands except for P4.

There was a substantial effort expended to make the same instrument types on both spacecraft perform alike. An example of the comparisons that have been made is shown in Fig. 39 where data from the two high-energy spectrometers have been plotted together after being exposed to the Ru-106–Rh-106 source.

9 MagEIS Data Outputs

All eight MagEIS units utilize a packet-based organization scheme for the raw instrument telemetry data. Each data type (e.g. count rates, livetime, housekeeping) is organized into a

binary Consultative Committee for Space Data Systems (CCSDS) telemetry packet, which consists of a header followed by the raw telemetry bytes. The raw telemetry bytes are of variable length depending on the specific data type. Each CCSDS packet is prepended with a ground annotation and a 3-byte generic header by the Mission Operations Center (MOC) at APL. This combination of the generic header, ground annotation and CCSDS telemetry packet is known as a "payload telemetry packet" (PTP). For each of the eight MagEIS units, one daily level 0 binary data file is produced, which consists of all PTP packets for a given data type, for an entire mission day.

Per spacecraft, all four MagEIS units (low, both mediums, and high) are independently operated in either "science" mode or "maintenance" mode. Science mode data consists primarily of the main and derived channel count rates, the histogram data, the livetime data, and the space weather beacon data. Maintenance mode data consists primarily of the housekeeping data, the digital status data, and command echo data, all of which are also available in science mode. When in science mode, the low and both medium units can be commanded into "sample" mode (e.g. burst-rate mode or high-rate mode). Sample mode uses a larger number of sectors per spin than normal science mode, which increases the temporal resolution of the measurements. To accommodate this increased resolution while meeting the nominal telemetry requirements, the derived channel and histogram data are not recorded in sample mode. It is anticipated that sample mode will be used when the spacecraft traverses the midnight-to-noon region of the equatorial magnetosphere, where electron microbursts are most likely to be observed. The high unit does not utilize a sample mode.

The Science Operations Center (SOC) at the Los Alamos National Laboratory (LANL) receives the binary level 0 MagEIS data, organized into daily (mission day) PTP files for each data type. These files are processed into level 1 data at the SOC, using MagEIS-specific data processing software written in the Interactive Data Language (IDL, version 8.0) a higher-level data analysis and visualization language. The data processing software unpacks the raw level 0 bytes into time-tagged (by mission elapsed time—MET), sorted data products, converted into physical units. The processed data are saved into International Solar-Terrestrial Physics (ISTP) compliant Common Data Format (CDF, version 3.3.1) level 1 files, organized by UTC day. Once level 1 data has been validated by the MagEIS team, the SOC processes the level 1 data into level 2 data, which involves the conversion of raw count rates into calibrated fluxes. The process also involves applying livetime and background corrections, if deemed necessary, to obtain corrected count rates that are then turned into differential unidirectional fluxes.

For a given UTC day, the level 2 data is contained in eight ISTP-Compliant CDF files, one for each of the four MagEIS units on the two RBSP spacecraft. The following naming convention is used for the data files: rbspx_***_ect-mageiszzz-L2_yyyymmdd_vx.y.z.cdf. Here, x = {a, b} is the descriptor for the particular spacecraft and xxx = {LOW, M35, M75} is the descriptor for the particular MagEIS unit. The yyyymmdd descriptor indicates the UTC day. The vx.y.z descriptor indicates the data version number. Increments in x are used for major structural changes to the data file that would require a new version of the data processing software. Increments in y are used if the file contents have been updated to be of better quality (e.g. a calibration change). Increments in z are reserved for minor bug fixes in either the data file or the processing software. In addition to the eight per-unit level 2 files, two additional level 2 data files are produced that combine the spin-averaged electron flux products at a selected number of energy channels across all four MagEIS units on a spacecraft. In all, there are a total of ten level 2 CDF data files from the ECT-MagEIS instruments per day. The naming convention for the two combined data files, providing a continuous electrons energy spectrum over the roughly 30 keV – 4 MeV range, is identical

Table 5 MagEIS data outputs and modes

Resolution Mode

Low & Medium (3 units)	Num PHA chan/ pixel	Num data chan/pixel*	Bits	Num sectors/spin	bps**	Spins /set
Main Rate		9	10	20	172	1
Derived Rate		7	10	20	132	1
Histogram	64	9	10	20	1234	8
Livetime		10	10	20	184	1
High (Electrons)						
Main Rate		8	10	20	146	1
Detector Singles		10	10	20	192	1
Coincidence Singles		4	10	20	79	1
Histogram (rear pixels)	64	4	10	20	567	8
Livetime		10	10	20	184	1
Direct Events		NA	512	20	886	1
High (Protons)						
Main Rate		32	10	24	652	1
Histogram (3 Pixels)	256	1	10	24	680	8
Threshold Rates		4	10	24	91	1
Livetime		4	10	24	91	1

Sample Mode

Low & Medium Units (Support High Sector Rates)						
High Rate (2 Units)		3	8	1000	2036	1
Main Rate (3 units)		9	10	20	172	1
Livetime (3 units)		10	10	20	184	1
High (electrons)	*same as in Resolution Mode*					
High (protons)	*same as in Resolution Mode*					

* pixel for histogram, channel for all other types
** depends on number of sectors/spin and spins/set
values in **red** are changeable by command

to that given above but with the "zzz" unit descriptor omitted. The ISTP-compliant level 2 MagEIS CDF files are fully compatible with standard data visualization software packages, such as Autoplot (autoplot.org) and NASA CDAWeb (cdaweb.gsfc.nasa.gov).

Table 5 shows the nominal telemetry parameters and data bit-rates for the various MagEIS data products from all four electron detectors and the proton telescope on each spacecraft. The first three sub-tables show the nominal telemetry parameters for normal science mode ("resolution mode"), while the last sub-table shows the parameters for the burst mode or high rate mode ("sample mode"). The first column in the sub-tables denotes the data product in question. The second column gives the number of pulse-height analyzer (PHA) channels, which is only defined for the histogram data products. The third column indicates the number of energy channels for the count rate data products (e.g. main and derived) or the number of detector pixels for the histogram and livetime data. The fourth column denotes the bit depth, where the data compression is either 24 to 10 bit or 16 to 8 bit. The direct event data is uncompressed. The fifth column indicates the number of angular sectors per

Table 6 Data characteristics

Instrument	Data Type	Compression	Error
Low/Medium	Electron Rates (main & derived)	24 to 10	3 %
Low/Medium	Electron Samples (high rate)	16 to 8	
Low/Medium	Electron Livetimes	24 to 10	3 %
Low/Medium	Electron Histograms	24 to 10	3 %
High	Electron Coincidence Rates	24 to 10	3 %
High	Electron Coincidence Histograms	24 to 10	3 %
High	Electron Coincidence Singles	24 to 10	3 %
High	Electron Coincidence Direct Events	none	0 %
High	Electron Coincidence Detector Singles	24 to 10	3 %
High	Electron Rate Livetimes	24 to 10	3 %
High	Proton Rates	24 to 10	3 %
High	Proton Histograms	24 to 10	3 %
High	Proton Singles (Threshold)	24 to 10	3 %
High	Proton Livetimes	24 to 10	3 %

spin, where each spacecraft spin is divided into an equal number of sectors. The last column indicates the number spin integrations in a given data set, i.e. how many spins the data is accumulated over. All values shown in red are changeable by ground command and can be adjusted in concert to increase or decrease the telemetry bit rate (shown in column 6) as needed. The values of the number of sectors per spin and number of spins per set (columns 5 and 7) are adjusted to maximize the science return while staying within allotted telemetry constraints.

10 MagEIS Instrument Users Guide—Understanding the Data

This guide documents the operational features of the instrument. Certain settings and conditions can cause unexpected behavioral patterns in the data sets. While the instrument is operating completely within specifications and constraints, the data may not be exactly what is expected. The goal of this section is to provide an understanding of why the data looks the way it does.

10.1 Data granularity

In order to conserve telemetry, data are compressed using one of two schemes: 24 to 10 or 16 to 8. Some data are not compressed at all. Refer to Table 6 for data type and implemented compression scheme. The resulting compression error is the maximum error possible for that data type.

10.2 Spin Pulse/Sectoring

The spin pulse occurs asynchronously to the MagEIS DPU clocks. In order to align the DPU clock with the spin pulse, the DPU samples the spin pulse every $1/4$ ms. All timing and sector sizes are based off of this $1/4$ ms boundary. The minimum delay from the occurrence of the spin pulse until the DPU sector reset is therefore $1/4$ ms. The maximum delay is

1.2 ms. Because of this, the sector resolution and sector error of any given event is $+/-$ 1/4 ms.

The spin pulse time communicated by the spacecraft is divided by the requested number of sectors to create a sector size. This sector size is accurate to 1/4 ms. However, because of rounding, the final sector may end up shorter than the calculated time. As an example: suppose that the previous spin period was 12.03 seconds. The number of sectors desired is 31, that is $12.03/31 = 388.064$ ms/sector. This is rounded *up* to 388.25 ms, as the boundary is 1/4 ms. If the present spin period is exactly the same, this leaves the final sector to be 382.5 ms, or 1.5 % smaller than the first 30 sectors. The discrepancy in counts for the final sector would necessarily coincide with a lower livetime for that sector. However; note that the livetime value itself has an accuracy error of 3 %, and may mask, or exaggerate the smaller sector size.

10.3 Livetime

In order for the Hybrid to latch and read out the Livetime of the instrument, data acquisition must stop for a short period of time. Because data acquisition stopped, the following Livetime that is read out will appear a few clock cycles smaller than expected. This effect depends on the frequency of the Livetime readout, which is based on the size (in ms) of each sector for the main rates.

In addition, just as the data is compressed to conserve telemetry bandwidth, so is the Livetime. The compression scheme used for the Livetime is the same as the data, allowing for an error of up to 3 %. These factors mean changes in sector size will cause a stepped decrease in the Livetime readout.

The current maximum for the Livetime as read out of the Hybrid is a 16 bit counter, or a maximum readout value of 65,536. Each count value represents 32 us. Thus, the maximum possible Livetime is 2.097 seconds. If sectors are defined in such a manner that the resulting sector length is longer than 2.097 seconds, the counter will reach the maximum and stop. It will NOT roll over. This will always result in a specific value of 65,536. If ever a value of 65,536 is shown for the Livetime, the sector should be marked as invalid, because it is impossible to know the true livetime, and most probably it was much higher than that value.

Note that this affects the Hybrid data only. Data stored in the DPU is 24 bits per sector. The instrument will regularly send values larger than 16 bits to the GSE when the data is read out, as multiple sums of the livetime data will be made during flight. The above caveat specifically refers to individual sectors exceeding 2.097 second.

10.4 Summing

At the beginning of a spin (as soon as the instrument receives a spin pulse) summing occurs. Summing is the process of aggregating all counts, data and Livetimes from the hardware memory into the software memory. This is a mandatory operation and cannot be disabled. The length of the summing is as follows: Low & Medium Units, 13 ms; High Unit, 6 ms.

During summing, no data of any kind can be stored, resulting in dead time. To account for the dead time, the summing time should be subtracted from the sector time of the first sector(s), depending on the sector length.

For example: suppose that Low Instrument is running is sample mode, with each sector size set to 10 ms. Because of the summing period of 13 ms, the first sector will not contain any events, regardless of the Livetime readout, as the entire sector occurred during summing. For the second sector, 3 ms will need to be subtracted from the Livetime, as only the final 7 ms of the second sector were available for taking data.

10.5 Direct Events

For Electron Coincidences on the High unit, Direct Event data are stored. Each sector can retain both the front and back PHA values for up to 8 events. If less than 8 events occur in any given sector, the remaining allocation for that sector will return 0s. If more than 8 events occur, you will lose Direct Event data, as the instrument has neither the memory nor the telemetry to retain more. The Direct Events that are transmitted are the *last eight* events to be acquired during that sector. All events prior to the final eight, regardless of the number, are simply discarded.

Acknowledgements This work was supported by the University of New Hampshire under Contract 10-068, the Johns Hopkins Applied Physics Laboratory under Contract 967399, and NASA under contract NAS5-014072.

DOI 10.1007/978-1-4899-7433-4_13
Reprinted from *Space Science Reviews* Journal, DOI 10.1007/s11214-013-9968-7

Helium, Oxygen, Proton, and Electron (HOPE) Mass Spectrometer for the Radiation Belt Storm Probes Mission

H.O. Funsten · R.M. Skoug · A.A. Guthrie · E.A. MacDonald · J.R. Baldonado · R.W. Harper · K.C. Henderson · K.H. Kihara · J.E. Lake · B.A. Larsen · A.D. Puckett · V.J. Vigil · R.H. Friedel · M.G. Henderson · J.T. Niehof · G.D. Reeves · M.F. Thomsen · J.J. Hanley · D.E. George · J.-M. Jahn · S. Cortinas · A. De Los Santos · G. Dunn · E. Edlund · M. Ferris · M. Freeman · M. Maple · C. Nunez · T. Taylor · W. Toczynski · C. Urdiales · H.E. Spence · J.A. Cravens · L.L. Suther · J. Chen

Received: 13 September 2012 / Accepted: 12 February 2013 / Published online: 8 March 2013

Abstract The HOPE mass spectrometer of the Radiation Belt Storm Probes (RBSP) mission (renamed the Van Allen Probes) is designed to measure the *in situ* plasma ion and electron fluxes over 4π sr at each RBSP spacecraft within the terrestrial radiation belts. The scientific goal is to understand the underlying physical processes that govern the radiation belt structure and dynamics. Spectral measurements for both ions and electrons are acquired over 1 eV to 50 keV in 36 log-spaced steps at an energy resolution $\Delta E_{\mathrm{FWHM}}/E \approx 15$ %. The dominant ion species (H^+, He^+, and O^+) of the magnetosphere are identified using foil-based time-of-flight (TOF) mass spectrometry with channel electron multiplier (CEM) detectors. Angular measurements are derived using five polar pixels coplanar with the spacecraft spin axis, and up to 16 azimuthal bins are acquired for each polar pixel over time as the spacecraft spins. Ion and electron measurements are acquired on alternate spacecraft spins. HOPE incorporates several new methods to minimize and monitor the background induced by penetrating particles in the harsh environment of the radiation belts. The absolute efficiencies of detection are continuously monitored, enabling precise, quantitative measurements of electron and ion fluxes and ion species abundances throughout the mission. We describe

H.O. Funsten (✉) · R.M. Skoug · A.A. Guthrie · E.A. MacDonald · J.R. Baldonado · R.W. Harper · K.C. Henderson · K.H. Kihara · J.E. Lake · B.A. Larsen · A.D. Puckett · V.J. Vigil · R.H. Friedel · M.G. Henderson · J.T. Niehof · G.D. Reeves · M.F. Thomsen
Los Alamos National Laboratory, MS-D466, PO Box 1663, Los Alamos, NM 87545, USA
e-mail: hfunsten@lanl.gov

J.J. Hanley · D.E. George · J.-M. Jahn · S. Cortinas · A. De Los Santos · G. Dunn · E. Edlund · M. Ferris · M. Freeman · M. Maple · C. Nunez · T. Taylor · W. Toczynski · C. Urdiales
Southwest Research Institute, 6220 Culebra Road, San Antonio, TX 78238, USA

H.E. Spence · J.A. Cravens
University of New Hampshire, 39 College Road, Morse Hall, Durham, NH 03824, USA

L.L. Suther
Applied Physics Laboratory, Johns Hopkins University, Laurel, MD 20723, USA

J. Chen
Baja Technology, L.L.C., Tuscon, AZ 85721, USA

the engineering approaches for plasma measurements in the radiation belts and present summaries of HOPE measurement strategy and performance.

Keywords Space plasma · Radiation belts · Ion mass spectrometry · Electron spectrometry · RBSP

1 Introduction

The Radiation Belt Storm Probes (RBSP) mission is designed to understand the influence of the Sun on the Earth's space environment by studying the structure and dynamics of the Earth's radiation belts and their response to energy and mass input by the solar wind. The primary scientific objectives of this mission include discovering the physical processes that govern acceleration and transport of radiation belt electrons and ions, understanding the systematic dynamic balance between particle acceleration and loss, and understanding the causal drivers of these processes in the context of geomagnetic storms. By studying and understanding these processes, we will better understand and predict space weather hazards and their impact on the world's space infrastructure as well as for the manned space program. The RBSP mission consists of two sun-pointing, spin stabilized spacecraft (A and B) with a nominal spin period τ_{SC} of $\sim$12 sec. The spacecraft are placed into a 0.1×4.8 R_E altitude orbit at a 10° inclination.

The HOPE mass spectrometers, one for each of the two RBSP spacecraft and designated HOPE-A and HOPE-B, are one of three pairs of instruments of the Energetic Particle, Composition, and Thermal Plasma (ECT) suite (Spence et al., this issue), whose key science objectives in support of the RBSP mission include:

1. Determine the physical processes that produce radiation belt enhancement events,
2. Determine the dominant mechanisms for relativistic electron loss,
3. Determine how the inner magnetospheric plasma environment controls radiation belt acceleration and loss, and
4. Develop empirical and physical models for understanding and predicting radiation belt space weather effects

HOPE was designed to measure the crucial populations of the plasmasphere, plasma sheet, and lower-energy ring current, including the relative composition of the most abundant ion components (H^+, He^+, and O^+) as well as electrons, over the 0.001–50 keV energy range of the core plasma populations. The two other instruments on the ECT Suite, Relativistic Electron Proton Telescope (REPT) (Baker et al., this issue) and Magnetic Electron Ion Spectrometer (MagEIS) (Blake et al., this issue) extend the ion and electron flux measurements to 10 s of MeV. HOPE measurements will be used to understand how, when, and where various types of plasma waves are produced to provide quantitative understanding of their effects on radiation belt particles.

RBSP is the first mission dedicated to the comprehensive study of the physical processes that drive the structure and variability of the radiation belts. In situ measurement of this region of the Earth's space environment presents an extraordinary challenge due to the large fluxes of penetrating radiation. In particular, substantial electron fluxes are typically observed at energies that can exceed 15 MeV in both the inner radiation belt (typically centered near 1.5 R_E) and outer radiation belt (typically most intense near 4–5 R_E at the Earth's magnetic equator), as well as inner belt proton energies that can exceed 100 MeV (Selesnick et al. 2007). The penetrating radiation environment of the RBSP orbit is expected to produce

substantial background counts in conventional plasma and ion mass spectrometers, which presents the primary challenge for the HOPE design and measurement strategy.

Because of the harsh penetrating radiation environment of the radiation belts, a primary driver in the design of HOPE was minimizing the background count rates in the electron multiplier detectors typically used for this type of measurement. Key mitigation strategies incorporated into the design include bulk and spot shielding, use of time-of-flight measurements to reject uncorrelated events associated with penetrating radiation, careful charged particle optical design, and use of channel electron multiplier (CEM) detectors instead of microchannel plate detectors typically used for time-of-flight measurements.

The HOPE mass spectrometer measures the fluxes of H^+, He^+, O^+ and electrons over the energy range 0.001–50 keV. It has five angular pixels coplanar with the spacecraft spin axis, acquires a complete ion or electron measurement each spacecraft spin, and alternates between ion and electron measurements each spin. HOPE consists of four subsystems:

- The Door Subsystem consists of a once-open door that spans the entrance aperture of the instrument to protect the instrument from particulate contamination and to maintain a nitrogen gas purge before launch to prevent contamination from hydrocarbons and humidity to which the detectors are sensitive.
- The Electrostatic Energy Analyzer (ESA) Subsystem incorporates a "top-hat" ESA configuration that selects the charge of the incident plasma particle (ion or electron) as well as the energy-per-charge passband of the incident ion or electron.
- The Time-of-Flight (TOF) Subsystem measures the time τ_{TOF} elapsed when an ion or electron traverses a pathlength $\sim$3 cm between an ultrathin "Start" foil and a "Stop" anode. This measurement provides ion speed that, coupled with the energy measurement of the ESA Subsystem, provides ion mass.
- The Hope Electronics Unit (HEU) incorporates the electronics signal processing from the detectors including TOF, scalars, low voltage power supplies, high voltage power supplies, and communications with the spacecraft.

Because of the complexity of the HOPE measurement technique and strategy, we have developed a comprehensive end-to-end instrument performance model whose subsystem components have been individually and collectively validated through test and calibration. The next section describes the scientific objectives associated with HOPE and measurements needed to meet the scientific objectives. Detailed description of the HOPE mass spectrometer design, performance, and operation follow after this section.

2 Scientific and Measurement Objectives

Many other scientific missions have measured the electrons and/or ions that make up the bulk thermal and suprathermal plasma distributions in the inner magnetosphere. However, three aspects of the HOPE measurements make them unique. First, HOPE is the first mass spectrometer uniquely designed to minimize the effects of penetrating radiation that have severely impacted many other plasma measurements within the most intense portions of the radiation belts. Second, HOPE's measurements on both RBSP spacecraft will enable resolving plasma populations and physical processes in space and time over a large range of spatio-temporal separations. Third, HOPE is part of a comprehensive scientific payload that is, for the first time, capable of resolving the global-scale, local-scale, and meso-scale processes that control radiation belt processes and inner magnetosphere dynamics.

The HOPE science requirements are driven directly by the RBSP mission requirements and, in turn, drive the instrument performance and measurement requirements. We divide the primary science topics that rely on the HOPE measurements into four areas: seed populations, sources of waves, substorms & ring current, and plasmasphere.

2.1 Seed Populations

Unlike solar energetic ions, radiation belt electrons cannot penetrate the magnetosphere directly from the solar wind. Rather, the source of MeV electrons in the radiation belts is lower-energy electrons that obtain MeV energies through the action of one or more energization processes. Therefore the intensity (flux) of MeV electrons in the radiation belts is a product of the strength of the energization process(es) and the number of lower-energy electrons that are available to be energized. These lower-energy electrons are referred to as the "seed population" for radiation belt electrons (Baker et al. 1986; Obara et al. 2000).

However, there is no precise definition of the seed population for radiation belt electrons. Energization is continuous, e.g., 2 MeV electrons were once 1 MeV electrons, 1 MeV electrons were once 500 keV electrons, etc. Of particular interest is the relative importance of low energy electrons to the radiation belt seed populations, for which we must consider phase space densities and the adiabatic invariants defined by guiding center theory (Roederer 1967). The adiabatic (or Hamiltonian) invariants that are typically used in radiation belt physics are the gyro-invariant (μ or M) associated with gyration around the magnetic field, the bounce invariant (J or K) associated with motion along a field line between the mirror points, and the drift invariant (Φ, or L^*) associated with gradient-curvature drift (Schulz and Lanzerotti 1974). Phase space density $f = j/p^2$ (where j is the particle flux and p is the momentum) is conserved along a particle's trajectory (in the absence of additions or losses). The adiabatic invariants are functions of the magnetic field which varies spatially and temporally. For example, the magnetic moment $\mu = p_\perp^2/B$ is conserved, so as a particle moves in a changing magnetic field, B, its momentum changes and the relationship between flux (as a function of position, energy and pitch angle) and phase space density (as a function of μ, K, and L^*) changes. The HOPE instrument (and the entire ECT suite) was designed with the requirement for continuous measurements of phase space density, at a variety of μ and K, over the entire RBSP orbit. The HOPE energy range was required to span from a few eV to ~50 keV with energy resolution $\Delta E_{\mathrm{FWHM}}/E < 20$ % in order to provide contiguous energy coverage with good energy overlap with the MagEIS electron measurements (Blake et al., this issue) and ion measurements from the Radiation Belt Storm Probes Ion Composition Experiment (RBSPICE) instrument (Lanzerotti et al., this issue).

The conservation of adiabatic invariants implies that electrons that are transported over large radial distances can gain large amounts of energy. If we consider only radial transport processes, the energy range that constitutes the source population depends on where the electrons started. MeV electrons in the slot region (~2 R_E) will have a source population energy of 100s of keV if they started at 5 R_E but if they were transported from 7 R_E (as shown for shock-associated events like the March 1991 CRRES event (Li et al. 1993)) the source population is electrons with energies of 10 s of keV. Furthermore, it is not the radial transport *per se* that energizes the electrons, it is the change of magnetic field. Under extreme distortions of the geomagnetic field the radial gradients of field strength can also be extreme and radial transport can produce larger energization than under quiet conditions. The lowest possible energy from which seed populations can be accelerated to radiation belt energies during so-called "super storms" is not yet known. Understanding the dependence

of μ on E and L over the bulk plasma population is a critical result expected from the HOPE measurements.

The above discussion describes the energy of seed populations that are *directly energized* by a single process such as betatron acceleration. An equally important question is the role of seed populations for MeV electrons that are accelerated through a combination of processes. Thermal plasma motion is controlled primarily by plasma ($E \times B$) drift. However, energetic particle motion is controlled primarily by gradient-curvature drift. Intermediate energies undergo both types of motion. Therefore the energy-dependent phase space density profiles provide a powerful tool for analyzing and interpreting multi-step energization and the relationship between seed and radiation belt populations. For example, in one scenario, substorm injection or large scale convection transports electrons from the plasma sheet to the inner magnetosphere, energizing them from 100s of eV to 10s of keV. Radial diffusion further transports and energizes the electrons to 100s of keV near the plasmapause. Finally wave-particle interactions energize the electrons, locally, up to MeV energies. While this is just one, hypothetical, example, a predictive understanding of a radiation belt event relies on the spatial and energy distribution of seed electrons as much as on our ability to quantify the various energization processes.

2.2 Sources of Waves

There is a growing consensus that gyroresonant wave-particle interactions play a key role in the acceleration and loss of radiation belt electrons (Reeves et al. 2009) and, in particular, for equatorially-mirroring electrons (e.g. Taylor et al. 2004; Chen et al. 2007) as evidenced by peaks in the radial profiles of phase space density (e.g. Selesnick and Blake 1997; Green and Kivelson 2004). Gyroresonant wave-particle interactions are frequently referred to as a "local" acceleration (or loss) process because individual wave-particle interactions are temporally brief and spatially localized along a particular magnetic field line. Nevertheless, many of these interactions globally average over the drift motion of the electrons with a large net impact on the radiation belts. When local acceleration or loss occurs in combination with radial diffusion, additional mixing of processes occurs and is averaged over both the radial and azimuthal dimensions.

Generally, five different wave modes can interact strongly with radiation belt electrons (Horne and Thorne 1998) including magnetosonic (Horne et al. 2000) and Z-mode waves (Glauert and Horne 2005). Two of the most important wave populations are whistler mode chorus and electromagnetic ion cyclotron (EMIC) waves. Figure 1 (adapted from Summers et al. 1998; Reeves 2007) schematically shows the production of chorus and EMIC waves. Chorus waves are produced by the injection of plasma sheet electrons into the inner magnetosphere and their subsequent drift around the dawn side of the Earth. The injected electron populations exhibit temperature anisotropies (parallel and perpendicular to B) that are unstable to whistler-mode wave growth. Plasma sheet ions are also injected into the inner magnetosphere but, due to their opposite charge, drift around the dusk side of the magnetosphere where they can produce EMIC waves—particularly in high density regions such as plasmaspheric plumes. The nature of anisotropic energy and pitch angle distributions determines the nature of the waves that are produced which, in turn, determines the nature of interaction with relativistic electrons. Additionally, the characteristics of EMIC waves are strongly controlled by the relative abundances of plasma ions, predominantly H^+, He^+, and O^+.

Plasma data can be used to test the instability conditions for various waves modes (Gary 1993). Instability thresholds for whistler (MacDonald et al. 2008), EMIC (Blum et al. 2009),

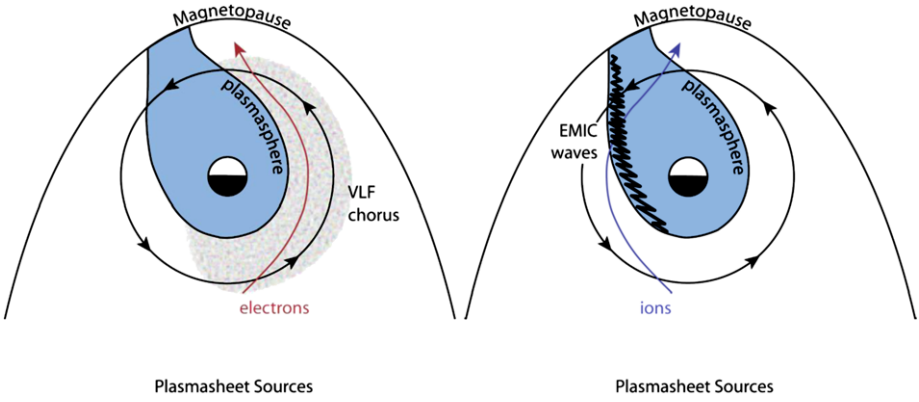

Fig. 1 A schematic showing the expected source of free energy for the generation of VLF chorus waves (*left*) and electromagnetic ion cyclotron waves (*right*) adapted from Reeves (2007). In this view of the equatorial plane, electrons injected from the plasma sheet drift Eastward, believed to be generated through the electron cyclotron instability by an anisotropic temperature distribution. This creates distributions that are unstable to the growth of chorus waves, while injected ions drift west where they can produce EMIC waves, particularly in high-density plasmaspheric plumes. These are only two possible generation mechanisms for a variety of waves that can interact with radiation belt electrons

and magnetosonic mode (Thomsen et al. 2011) waves have been studied using LANL MPA data from geosynchronous orbit. These techniques applied at geosynchronous orbit show good comparison with other measures of waves, either in situ, remote, or from ground-based measurements (e.g. Spasojevic et al. 2011; Blum et al. 2012). Superposed epoch analysis has been used to infer the relative intensity of growth and loss wave processes at geosynchronous orbit (MacDonald et al. 2010). RBSP on-board wave measurements will facilitate detailed comparison with the plasma distributions. In addition, for EMIC mode waves, measurements of the thermal ion composition will reduce assumptions in earlier analyses and enable more detailed discrimination between different bands of EMIC mode waves.

The HOPE mass spectrometer will measure the key plasma distributions (including energy/pitch angle distributions and composition ratios) needed to understand the creation of these waves, their properties (such as frequencies and wave normal), their propagation and damping, and spatial distribution. Detailed comparison of the plasma distributions and the wave properties measured by EMFISIS and EFW will provide critical tests of plasma physics theory including whether wave growth can be explained by quasilinear theory or whether nonlinear dynamics dominate the physics. These questions are particularly important in understanding how large-amplitude chorus (Cattell et al. 2008) is produced, whether it is just an extreme form of "regular" chorus, and what plasma conditions are responsible for such extremes.

The local plasma conditions that HOPE measures also control the propagation of waves away from their generation region, along (or across) magnetic field lines. Relativistic electrons can interact at any point on the field line, and the effects on the radiation belts can be quite different depending on where that interaction occurs. For example, chorus waves are generated at the magnetic equator. Their wave normal angle controls the direction of propagation, but the suprathermal plasma distributions control the Landau damping of the waves and therefore how far off the equator they will propagate (Bortnik et al. 2007) as illustrated in Fig. 2 (from Reeves et al. 2009). Near the equator, wave-particle interactions affect electrons with equatorial pitch angles near 90° where energization dominates. At higher

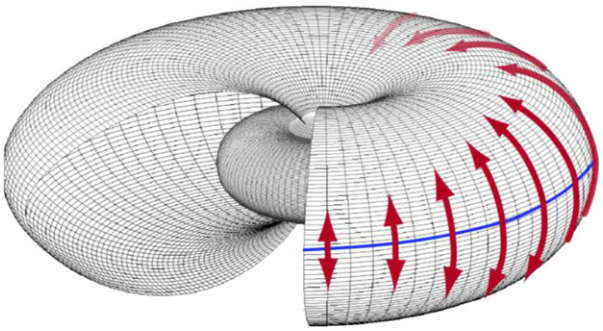

Fig. 2 Chorus waves propagate from the equator following a specific pattern. Electrons that are injected on the nightside drift eastward toward noon. Near midnight (in the gap in the outer torus), chorus waves are strongly damped and stay near the equator. As the electrons drift, their distributions change, allowing chorus waves to propagate to higher latitudes, where they may also further intensify before they eventually lose their energy (see Bortnik et al. 2007). From Reeves et al. (2009)

latitudes, more field-aligned electrons are more strongly affected, and, for those equatorial pitch angles, energization is less rapid but pitch angle scattering is stronger. Therefore whether chorus produces net enhancement or loss of radiation belt electrons may be strongly dependent on the latitudinal extent of the chorus waves as well as the presence and amount of damping.

As discussed above, the net effect on the radiation belts from "local" acceleration and pitch angle diffusion derives from the drift-averaged effect of all local interactions. To date, all theoretical predictions of "global" wave particle interactions take local energy and pitch angle diffusion coefficients and drift-average this ensemble by applying a uniform weighting. A more accurate drift averaging would account for the magnetic local time (MLT), radial distance (since drift paths are not at constant radius) and even temporal dependence of the diffusion coefficients, i.e., $\langle D \rangle = \int D(MLT, R, t)$.

The two-spacecraft configuration of the RBSP mission, assisted by global modeling, is critical for establishing the spatial, temporal, and activity-dependent correlations that enable extrapolation of local measurements to the global scale. Testing competing theories and mechanisms requires measurements that can constrain each step in the complex chain of coupled global plasma dynamics associated with wave generation, propagation, and coupling to radiation belt electrons. Our ability to quantify these steps will ultimately shape our ability to predict, for example, whether a storm will increase or decrease radiation belt fluxes (Reeves et al. 2003).

2.3 Substorms & Ring Current

Geomagnetic storms and substorms have a profound effect on the configuration and dynamics of the inner magnetosphere including the radiation belts. Storms and radiation belt events occur together so often that they are sometimes considered to be synonymous. Figure 3, from Reeves (1998), illustrates the strong *association* between storm activity and geosynchronous MeV electron fluxes. However, that same study as well as subsequent studies showed that this relationship is complex and that stronger storms do not necessarily have a stronger effect on the radiation belts. Nearly all the processes that are thought to strongly affect the radiation belts (radial transport, wave-generation, electron energization, pitch angle scattering, magnetopause losses, etc.) are generally stronger during storms compared to quiet times.

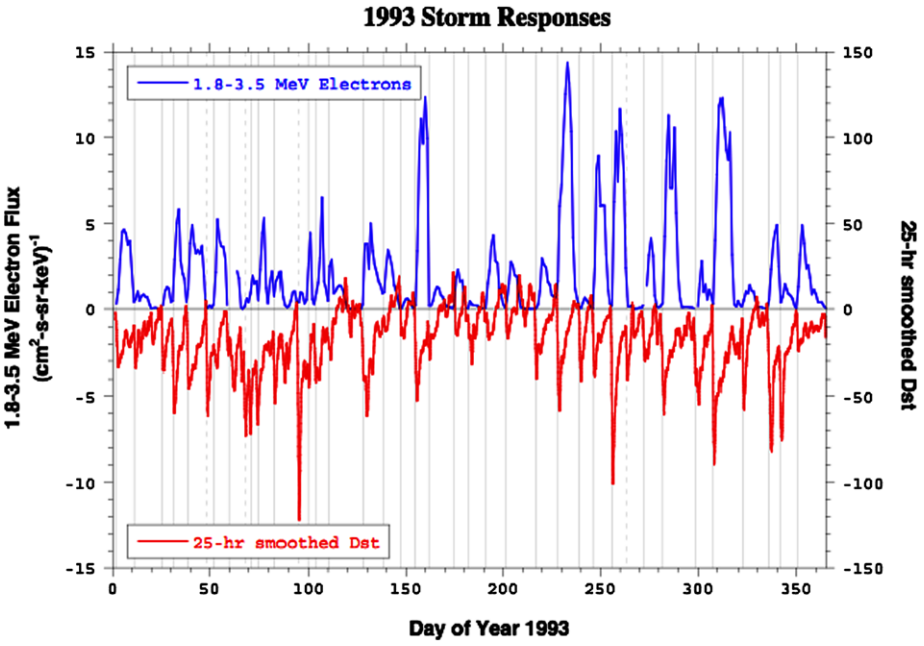

Fig. 3 Geosynchronous relativistic electron fluxes (*blue*) and smoothed Dst (*red*) for the year 1993 show a clear association between storm activity and electron flux enhancements. However, it is apparent that there is not a one-to-one occurrence and that the intensities of electron fluxes and Dst minima are poorly correlated. The precise relationship between radiation belt electron events and geomagnetic storms remains a mystery

Fundamental open questions that will be addressed by the RBSP measurements include the relationship between storms and the radiation belts, whether a storm is a necessary condition for a radiation belt event, and whether and how we can predict the effects of a given storm.

The HOPE and RBSPICE instruments are highly-complementary components of the RBSP mission that will provide continuous and complete measurements of the ring current from essentially 0 to approximately 400 keV. They will both provide information about the ion composition of the ring current that has been a critical, missing input for ring current models (Daglis et al. 1999). The strength of a magnetic storm, as measured by Dst, is proportional to the total energy in the ring current (Dessler and Parker 1959; Sckopke 1966), which is, in turn, a function of the energy density spectrum and the composition. Figure 4 shows an example from the RAM ring current model (Jordanova et al. 1994) for a single point in the ring current with composition ratios that are independent of energy. Observations from HOPE and RBSPICE on the two RBSP satellites will allow us to determine the spatial, temporal, and activity-dependent correlations across the ring current and relate changes in those distributions to the global electric and magnetic fields.

Ring current physics, a critical RBSP science objective, is also profoundly important for interpreting radiation belt observations. As discussed above, the adiabatic invariants of radiation belt particle motion are essential parameters for understanding radiation belt processes. The first invariant, μ, is a function of the local field which can be measured directly, but the second and third invariants, K and L^*, are integrals along a field line and around a drift shell, respectively, and are dependent on a quantitative knowledge of the *global* magnetic field that can only be obtained from models.

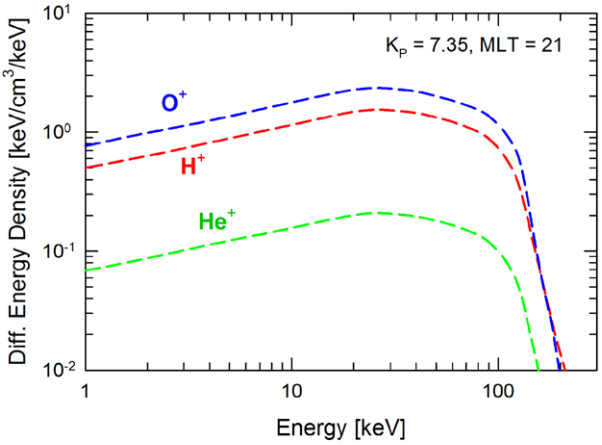

Fig. 4 The differential energy density of ring current ions predicted by the RAM model for an arbitrary geomagnetic storm (courtesy, V. Jordanova). Ions in the HOPE energy range (<∼50 keV) are the source of the high-energy ring current but also comprise a substantial portion of the total energy density in the ring current

Figure 5 shows the profound effect of storm-time magnetic field reconfigurations on relativistic electron phase space density calculations—particularly calculation of the third invariant L^* (Reeves et al. 2012). As the ring current builds up diamagnetic currents, the geomagnetic field "inflates". In order to conserve the third invariant (the total magnetic flux enclosed in a drift shell), particles move outward, simultaneously changing energy and pitch angle to conserve μ and K. This adiabatic rearrangement of particles is often called the "Dst effect" (Kim and Chan 1997). Figure 5 shows the Dst and smoothed Dst indices (top) and phase space density at fixed μ and K (bottom) for three geosynchronous spacecraft. While the geosynchronous satellites orbit at fixed radius, the drift shells move across their fixed positions which is equivalent to a "motion" in the L^* coordinate. Because of these and other factors, the HOPE ring current measurements are intimately linked to studies of phase space density gradients for relativistic electrons and for independently assessing adiabatic and non-adiabatic effects.

Storm-time dynamics cannot be fully studied without including the processes associated with substorms, but non-storm-time (isolated) substorms can also have important effects on the inner magnetosphere and the radiation belts. It has been hypothesized that substorms may directly inject radiation belt electrons (Ingraham et al. 2001), but this mechanism has not yet been fully verified. It is also possible that individual injections can produce the same unstable plasma distributions and wave populations that are produced in storms but with different characteristics (spatial distribution, energies, etc.) and understanding the continuum of activity from isolated substorms to major storms may be key to understanding the balance of competing processes. In addition to the contributions discussed previously, HOPE measurements play a key role in understanding substorms by characterizing the plasma sheet, by measuring the penetration depth and azimuthal extend of substorm injected populations, by tracing the energy-dependent drifts and drift boundaries of electrons and ions, and by measuring the interaction of plasmas with different ionospheric and magnetospheric origins.

2.4 Plasmasphere

The RBSP mission will also provide a unique, new set of observations of the plasmasphere. While plasmaspheric physics is not a direct objective of the RBSP mission, it plays a key supporting role in the primary RBSP science objectives and is a rich target for collateral scientific discovery.

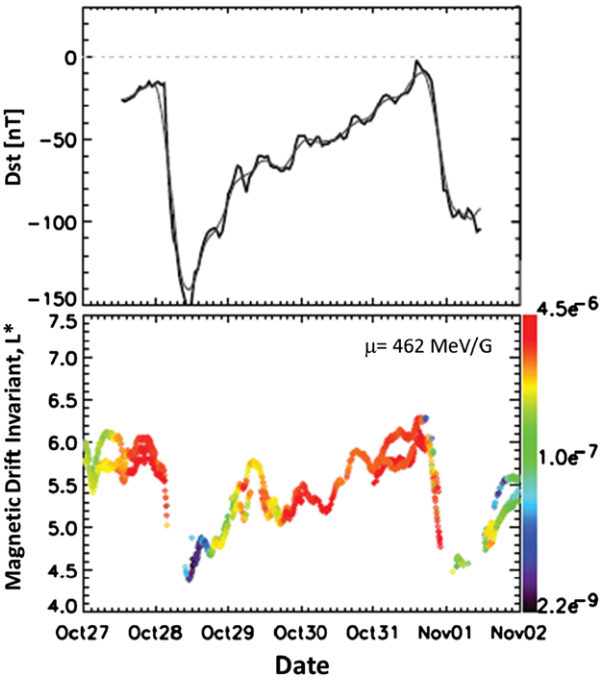

Fig. 5 The phase space density (PSD) (color coded) as a function of L^* for three geosynchronous satellites during a geomagnetic storm in 2001. As the ring current intensifies the drift shells "inflate" which produces an "apparent motion" of the satellites to very low L^*. From Reeves et al. (2012)

Many of the unique aspects of HOPE measurements of plasmaspheric populations come from the two-satellite configuration of RBSP. As the satellites lap one another in their orbits, we will obtain radial profiles of the plasmasphere separated in time by minutes to hours. At the low L-shells of the plasmapause, the inbound and outbound legs of the orbit are separated in MLT by large angles. The plasmapause and structures within it respond to changes in the large-scale convective electric field on a variety of time scales that have yet to be fully investigated (Carpenter 1995).

The dynamics of the plasmasphere also have a direct effect on the structure and dynamics of the relativistic radiation belt electrons. Lyons and Thorne (1973) showed that the equilibrium structure of the electron radiation belts—the inner belt, slot region, and outer belt—could be explained by a balance between radial diffusion rates (as a function of L-shell) and losses due to atmospheric precipitation from whistler hiss inside the plasmasphere. Li et al. (2001) used SAMPEX data to produce a dramatic illustration correlating the inner edge of the outer electron belt with the location of the plasmapause. Figure 6, adapted from their paper, shows MeV electron fluxes from 1992 to 2004 as a function of "McIlwain" L. Also plotted are sunspot number, solar wind velocity, and the plasmapause location based on a statistical model (Carpenter and Anderson 1992). Both the SAMPEX electron flux and plasmapause location were averaged over 30 days to highlight losses consistent with average loss lifetimes in the plasmasphere of roughly 10 days.

Statistical models such as Carpenter and Anderson (1992) or O'Brien and Moldwin (2003) treat the equatorial plasmasphere statistically, considering only large scale features, an inadequate approximation for radiation belt physics applications. As with chorus or EMIC waves, the effects of pitch angle scattering by plasmaspheric hiss must be averaged over the drift path of an electron. For drift paths fully within the plasmasphere, simple models of day-night asymmetry may suffice, but, for drift paths that intersect the plasmasphere

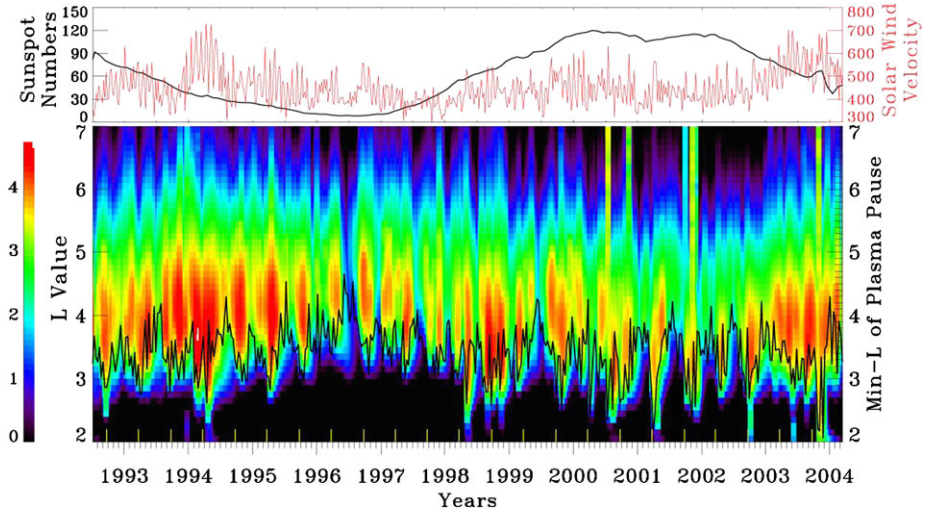

Fig. 6 SAMPEX electron flux measurements (#/cm^2-s-sr) over the energy range 2–6 MeV are shown in the *bottom panel*. The *yellow vertical bars* on the *horizontal axis* are marks of equinoxes. The *color bar* is log scale, and L values are in bins of 0.1 L. Sunspot number and average solar wind velocity for the same period are shown in the top panel. Adapted from Li et al. (2001)

over only part of the orbit, the shape of the plasmasphere is critical. Plasmaspheric plumes drain the outer layers of the plasmasphere to the magnetopause and, when they are present, they intersect all trapped electron orbits (see Fig. 1).

As previously discussed, plasmaspheric plumes play another role in the production, propagation, and effects of EMIC waves. Generally the ring current lies outside the location of the plasmasphere, although they can overlap because the low energy plasmaspheric plasma and higher energy ring current plasma follow different trajectories. Since storms produce both stronger ring currents and plasmaspheric plumes, this overlap typically occurs during storms. This is shown schematically in Fig. 7 from the cover of the AGU monograph on Inner Magnetosphere Physics and Modeling (Pulkkinen et al. 2005) (courtesy J. Goldstein). The figure shows the plasmasphere and drainage plume derived using EUV images and the modeled ring current from ENA observations from the IMAGE mission. This interaction is thought to produce EMIC waves which have been proposed as the cause of the dropout of relativistic electrons seen during the main phase of storms (e.g. Summers et al. 1998). However, questions remain as to whether the interaction always produces EMIC waves and, if so, whether those waves cause radiation belt dropouts (e.g. Meredith et al. 2003; Turner et al. 2012).

2.5 Summary of HOPE Science Objectives

The HOPE measurement requirements traceability starts with the RBSP mission's science objectives. Achieving the mission science objectives depends on answering key science questions such as in Table 1. For example, a key science question needed to determine the physical processes that produce radiation belt enhancement events is knowing where, when, and how local acceleration leads to relativistic electron acceleration. For example: How are

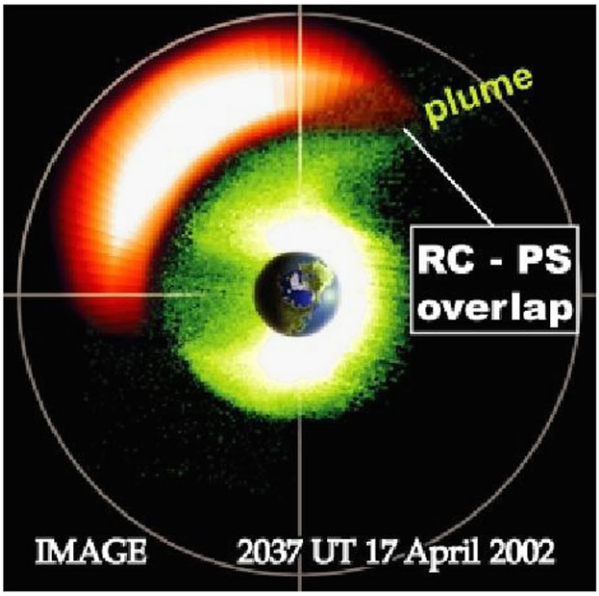

Fig. 7 This figure illustrates the overlap between plasmaspheric drainage plumes (in *green*, derived from IMAGE EUV observations) and energetic ring current ions (in *orange*, derived from inversion of ENA observations)

plasma waves produced? What are the plasma distributions that provide the free energy? How do those waves interact with relativistic electrons? What are the effects on energy and pitch angle distributions? These questions lead to specific science measurement objectives. Those that are specific to the ECT suite include measuring radial phase space distributions and gradients, measuring energy and pitch angle distributions for both plasma and radiation belt particles, and measuring the plasma density and composition. Those measurements enable us to test the cause and effect of specific energization processes. The measurement objectives for the ECT suite drive specific measurement requirements for each instrument in the suite as shown in the final column of Table 1. The implementation of these scientific objectives through the HOPE mass spectrometer is the focus of his paper.

3 HOPE Mass Spectrometer Description

Because of the intensity of the penetrating particle flux in the radiation belts, the overall design and operation philosophy of HOPE was driven toward minimizing the effects of this penetrating radiation on the measurement of plasma ions and electrons. We have incorporated six primary strategies to address this issue. First, substantial resources (including modeling, simulation, and validation as well as instrument mass) were invested in shielding. The interior of the instrument was protected by a minimum wall thickness of 0.89 cm Aluminum and nearly 1.8 cm in the vicinity of the channel electron multiplier (CEM) detectors. Because of the exponential dependence of attenuation of energetic particles on shielding thickness, mating surfaces were stepped at their interfaces, and machined features such as vent holes were strategically placed to prevent a low-shielding pathway for energetic particles to penetrate into the instrument. Second, we exploit the time-of-flight measurement, in which a correlated pair of events from a single incident plasma ion or electron is measured, to reject uncorrelated detected events associated with penetrating radiation. Third, we incorporate CEM detectors instead of microchannel plate (MCP) detectors, which are

Table 1 Key scientific and measurement goals for the HOPE mass spectrometer

Science objectives	Key science questions	Science measurement objectives	HOPE measurement requirements
Determine the physical processes that produce radiation belt enhancement events	What processes are responsible for radial transport and acceleration?	Radial phase space density (PSD) distribution	Electron energy (20–50 keV) and pitch angle
	Where, when, and how do local acceleration processes produce radiation belt acceleration?	Radial PSD distribution, local PSD gradients, pitch angle distribution, plasma density and composition	Electron energy (10–50 keV) and pitch angle; plasma density and composition (H^+, He^+, O^+)
	How does "prompt acceleration" create new radiation belts?	Radial PSD distribution, ultrarelativistic population, energetic particle composition	Electron energy (30–50 keV) and pitch angle
	How do plasma 'seed' or source populations influence the characteristics of relativistic electron events?	Radial PSD distribution before and after acceleration events	Electron energy (1–50 keV) and pitch angle
Determine the dominant mechanisms for relativistic electron loss	Where, when, and how are radiation belt electrons scattered into the atmospheric loss cone?	Full electron pitch-angle distribution and intensities through outer zone regions	Electron energy (30–50 keV) and pitch angle
	What is the contribution of magnetopause shadowing to relativistic electron loss?	Full electron pitch-angle distribution and intensities through outer zone regions	Ions and electrons, 1 eV–50 keV; composition (H^+, He^+, O^+)
Determine how the inner magnetospheric plasma environment controls radiation belt transport, acceleration, and loss	How do we characterize/model adiabatic transport of radiation belt particles?	Pitch angle distribution of ions and electrons; energy density of ring current	Ions and electrons, 1 eV–50 keV; composition (H^+, He^+, O^+)
	How do the global and local characteristics of the plasma sheet and plasmaspheric populations control radiation belt structure, acceleration, and loss?	Effects of ring current and plasmapause structure on the outer radiation belt	Ions and electrons, 1 eV–50 keV
Develop empirical and physical models for understanding and predicting radiation belt space weather effects	How do we predict and model spatial, spectral, and temporal characteristics of the radiation belt enhancements, over both short and long times?	Radial PSD distribution over wide range of solar wind and geophysical input conditions	Ion and electron energy (1 eV–50 keV) and pitch angle

typically used for plasma time-of-flight mass spectrometry. We have found that CEMs are ~20 times less sensitive to penetrating radiation per cm^2 of detection area. Independent pairs of CEM detectors are used for each of the five polar angle pixels; the two CEMs of a pair are separated by 1.96 cm center-to-center to minimize the probability that a single penetrating particle traverses and stimulates counts in both detectors, resulting in a coincidence. This is the first use of CEM detectors for time-of-flight measurement of plasma ions in space. Fourth, the charged particle optics design was carefully constructed so that only secondary electrons generated at locations relevant to the TOF measurement (specifically, the foil backside and the Stop anode) are steered to and collected by the appropriate CEM detector; secondary electrons generated at other surfaces inside the instrument by penetrating radiation cannot reach a CEM and therefore cannot be detected. Fifth, we continuously monitor and report both the count rate of correlated TOF measurements and rates of uncorrelated Start and Stop events. This provides a direct measure of the level of penetrating radiation. Furthermore, during times of low penetrating particle flux, we can calculate from these rates the absolute detection efficiency of the TOF subsystem, enabling quantitative monitoring of the instrument health and performance for the duration of the mission. And sixth, we additionally monitor penetrating radiation by reporting counts registered in long TOF bins in electron mode, which primarily result from coincidences from uncorrelated penetrating radiation, as well as short TOF coincidences in ion mode that are much faster than H^+ and result from individual penetrating particles.

3.1 Overview

The HOPE mass spectrometer is located on the $+\hat{u}$ panel of each RBSP spacecraft as shown in Fig. 8. The HOPE field-of-view (FOV) is fan-shaped, with polar angle θ viewing that extends nearly 180°, from $+\hat{w}$ (the direction of the Sun) to $-\hat{w}$. The center of the HOPE FOV views normal to the panel on which HOPE is attached, such that $\theta = 0°$ corresponds to $+\hat{u}$. Because the HOPE FOV lies in the same plane as the RBSP spin axis, HOPE therefore uses the spin of the spacecraft to sample nearly 4π of space. The panel on which HOPE is placed lies between the panels on which solar panels are attached so that the solar panels do not obstruct the HOPE FOV.

The HOPE mass spectrometer, illustrated in Fig. 9, consists of three sensor subsystems as well as the Hope Electronics Unit (HEU) subsystem. We describe the HOPE spectrometer by following a charged particle through each sensor subsystem. The particle first transits the door subsystem, which consists of a once-open door that spans the entrance aperture and is retracted during instrument commissioning. The particle then enters the toroidal "top-hat" electrostatic energy analyzer (ESA) subsystem, which has a fan-shaped FOV (nearly 180° in polar angle θ and 4.5° FWHM in azimuthal angle ϕ) coplanar with the spacecraft spin axis. The ESA subsystem accepts only charged particles within a specific energy-per-charge (E/q) range as defined by the bipolar, adjustable bias V_{ESA} applied to its inner toroidal dome. Because we expect the preponderance of ions to be singly charged ($q = +1$), we henceforth assume that all ions detected are singly ionized and that the ESA subsystem provides measurement of an ion's energy E. V_{ESA} is defined using an adjustable bipolar power supply with maximum voltage ±7.5 kV that toggles polarity every 12 s (the nominal RBSP spin period) so that ions and electrons are measured during alternate spins.

A charged particle exiting the ESA subsystem enters the TOF subsystem, which has five independent polar pixels, each incorporating a linear, foil-based time-of-flight measurement. The pixels are arrayed at polar angles θ corresponding to 0° (perpendicular to the spin axis), ±36°, and ±72°. The TOF drift boxes for the pixels are together biased to $V_{\mathrm{TOF}} = -11$ kV in

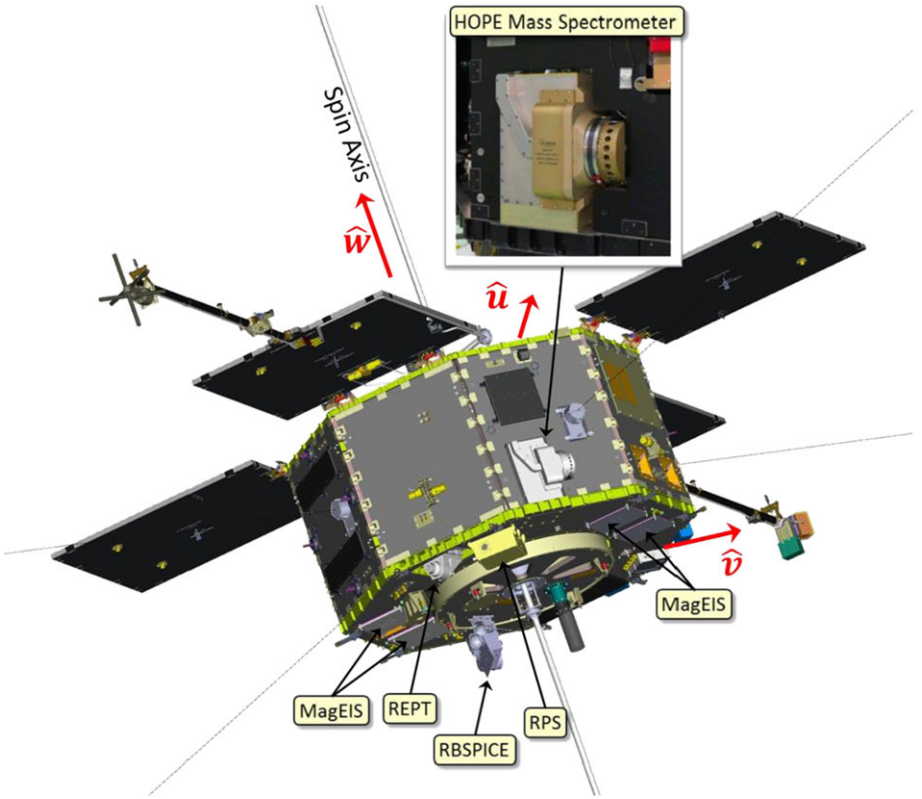

Fig. 8 HOPE is accommodated on the $+\hat{u}$ panel of the RBSP spacecraft, and the center of HOPE's field-of-view is $+\hat{u}$. The sun lies in the $+\hat{w}$ direction. The *inset* photo shows HOPE-A integrated onto the spacecraft, adjacent to the EFW wire boom antenna. The other particle instruments on RBSP, shown in the figure, are the Magnetic Electron Ion Spectrometer (MagEIS), Relativistic Electron Proton Telescope (REPT), Relativistic Proton Spectrometer (RPS), and Radiation Belt Storm Probes Ion Composition Experiment (RBSPICE)

ion mode and $V_{\mathrm{TOF}} = +1.5$ kV in electron mode to accelerate the particles into the foil. This acceleration helps mitigate the energy straggling and angular scattering effects of the foil. This bias scheme also enables constant front and rear CEM detector biases, independent of whether ions or electrons are being measured. In the drift box, a charged particle transits the foil and generates secondary electrons from the foil's exit surface that are detected and start a timer. The charged particle then traverses the drift region of length $\sim$3 cm, whereupon it strikes the Stop anode, generating Stop secondary electrons that are detected and stop the timer. Particle speed is derived from the ratio of the travel distance over the elapsed time. Particle mass is then derived from speed measured in the TOF subsystem and energy measured in the ESA subsystem. A summary of HOPE performance and resources are listed in Table 2.

The instrument response to a charged particle is a function of its species as well as its incident energy E, polar angle (θ) and azimuth angle (ϕ). Our approach to design, characterize and quantify instrument performance has been to first develop performance models for each subsystem and validate these subsystem performance models by testing of prototype and flight subsystems. We then couple these models into an end-to-end performance

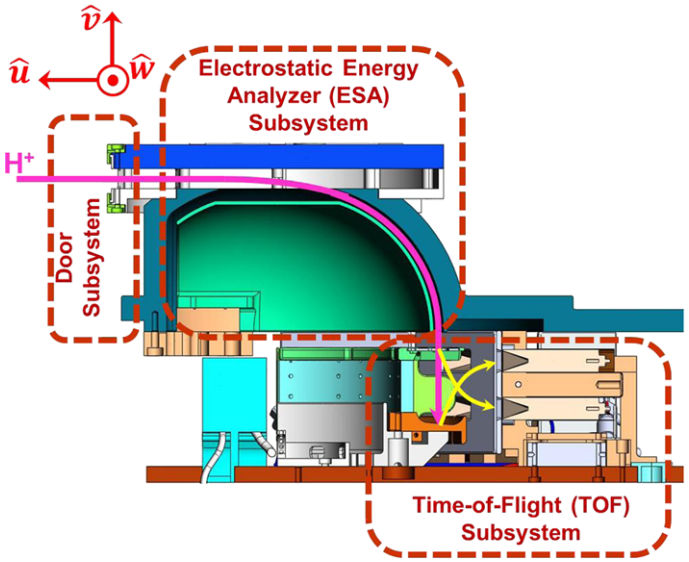

Fig. 9 Cross section of the HOPE mass spectrometer illustrating the three sensor subsystems and the trajectory of a proton through the instrument (*magenta*) and the trajectories of secondary electrons generated by the impact of the proton with the start foil and stop anode (*yellow*). The HOPE Electronics Unit (HEU) subsystem is not shown

model that is validated through flight instrument calibration. This section describes the sensor subsystems as well as the validation testing of the subsystems and their models.

3.2 Sensor Subsystems

The design of the HOPE sensor subsystems was driven by the challenging measurement environment of the radiation belts. We therefore also include a section on radiation analysis of the instrument.

3.2.1 Door Subsystem

The once-open door, successfully opened as one of the first activities of instrument commissioning, provides a barrier to particulate contamination that can cause electrostatic discharge points in regions of high electric fields (such as in the ESA subsystem). It additionally serves as a non-hermetic seal for the N_2 purge of the instrument interior that helps prevent migration of volatile hydrocarbons and water to the CEM detectors, whose performance could be degraded by significant exposure to these species. The door was closed during transport of the flight units, during most spacecraft-level testing, and through launch; the instrument was purged with N_2 up to launch.

Figure 10 schematically shows the door in the closed and opened configurations. The door, made of 0.10-mm-thick 718 Inconel, is self-retracting with a force of 1.6 N around a hub that is located outside of the aperture FOV. The top and bottom edges of the door are captured within channel guides located above and below the entrance aperture of the ESA subsystem. Key surfaces of the guides and door were coated with Dicronite to minimize friction and prevent generation of particulate during testing. The action of the door is similar

Table 2 Summary of HOPE Mass Spectrometer performance and resources

Species	H^+, He^+, O^+, e^-
Energy range	0.001–50 keV
Energy resolution	16 % @1 eV, 12 % @ 50 keV
Energy steps (reported)	36
Energy sweep period	750 ms
Mass resolution, $m/\Delta m$	$\geq$2 FWHM
Polar pixels, center locations (θ)	0^0, $\pm 36°$, $\pm 72°$
Polar angle (θ) resolution	18° Full width
Azim. angle (ϕ) resolution	4.5° FWHM
Azim. sector angle (ϕ_S) width	750 ms/$\tau_{SC} \times 360°$ (22.5° for $\tau_{SC} = 12$ sec)
Dimensions	19.6 cm × 19.6 cm × 33.5 cm
Mass: HOPE A, HOPE B	18.06 kg, 18.07 kg
Power (BOL, predicted EOL)	18.2 W, 23.0 W
Telemetry Rate	9.32 kbps
H^+ Geometric Factor per polar pixel, G_I (cm^2 sr eV/eV)	1.25×10^{-3} cm^2 sr @ 1 eV 1.3×10^{-3} cm^2 sr @ 50 keV
Electron Geometric Factor per polar pixel, G_E (cm^2 sr eV/eV)	2×10^{-4} cm^2 sr @ 1 eV 1.1×10^{-5} cm^2 sr @ 50 keV
Temperature limits (operating, survival)	−25 to +55 °C, −30 to +60 °C

to that of a self-retracting tape measure. The end of the door has a multipurpose tang: it holds the door in closed position, it prevents full retraction of the door around the hub, and it is used as a handle to close the door when it is manually reset.

In its closed position, the door is kept in place by an "L"-shaped pivot arm, with one end connected to a TiNi shaped memory alloy (SMA) pin-puller and a tab at the other end contacting the door tang. The pivot arm uses a constant force (10 lb/in) coil spring. Actuation, performed by command to the instrument, retracts the pin of the pin-puller, allowing the pivot arm to rotate and release the tang. This releases the door, which self-retracts over the entire HOPE entrance aperture. The door and pin-puller must be manually reset after activation. Prototype and engineering models of the door were fabricated and extensively tested to validate the design. The engineering model was deployed in excess of 100 times without a single failure.

3.2.2 Electrostatic Energy Analysis (ESA) Subsystem

The ESA subsystem consists of a toroidal top-hat electrostatic analyzer (ESA) (Carlson et al. 1983; Young et al. 1988) that allows particles of a specific charge (+ or −) and within a specific energy-per-charge (E/q) range and angular range to pass to the TOF subsystem, where they are detected. For our time-of-flight classification scheme, we assume that the ions measured by HOPE are singly ionized, i.e., $q = \pm 1$. The top-hat geometry efficiently rejects ultraviolet light, which can stimulate the CEM detectors, from the instrument interior. The ESAs are blackened by the Ebonol-C process to further enhance UV rejection.

The top hat consists of a parallel plate entrance section that accepts charged particles over a polar angle θ range of nearly 180° and acts as a collimator and restricts the azimuthal (ϕ) field-of-view. The angular field-of-view is thus fan-shaped (180° × 4.5°), with the center of the fan at $(\theta, \phi) = (0°,\ 0°)$ aligned in the $+\hat{u}$ spacecraft direction and perpendicular to the

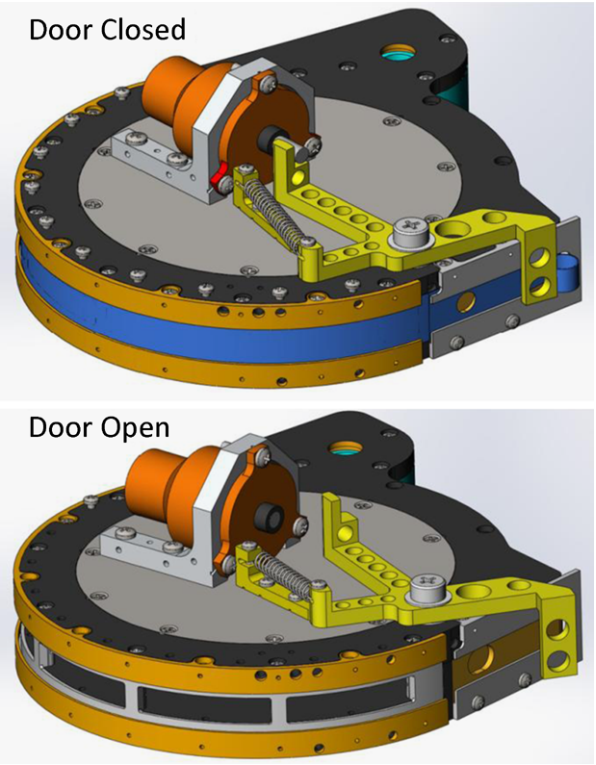

Fig. 10 Door (*blue*) and pivot arm (*yellow*) in closed (*top panel*) and open (*bottom panel*) configurations. The mechanism that releases the pivot arm is a shaped memory alloy pinpuller (*orange cylinder*, above door)

spin axis. As the spacecraft spins, HOPE samples a complete 2π radians in azimuth over each spacecraft spin, forming the fundamental cadence for accumulation of a complete ion or electron histogram (shown in Fig. 38).

A charged particle that transits the top hat entrance section next encounters concentric electrodes in a toroidal geometry with a bending angle of 90°. The outer electrode, which lies at ground potential and serves as an exterior wall for the instrument, has bending radius of 59 mm. The inner electrode, biased to V_{ESA}, has a 7 mm toroidal radius and a central bending radius 55 mm, resulting in a plate separation of 4.0 mm. V_{ESA} is set using an adjustable bipolar power supply with maximum voltage $|V_{\mathrm{ESA}}| = 7.5$ kV; the polarity toggles between spacecraft spins, allowing measurement of ions and electrons for negative and positive polarity, respectively.

The HOPE top hat charged particle optics design was modeled using SIMION (Dahl 2000) in 2.5 D that exploited the cylindrical symmetry of the top-hat. In general, the optics of electrostatic fields scale linearly with applied voltage, are independent of charged particle mass, and are charge-symmetric (particles of opposite charge follow identical trajectories if electrode polarities are reversed). However, this model also includes the closest components of the TOF subsystem (the ultrathin foil and its mounting plate at the entrance of the TOF drift box, all biased to V_{TOF}) to properly couple the performance models of the ESA and TOF subsystems. Because V_{TOF} is different between ion ($V_{\mathrm{TOF}} = -11.0$ kV) and electron ($V_{\mathrm{TOF}} = +1.5$ kV) detection modes and remains constant as V_{ESA} changes, we both expect and observe small variations in the energy, angle, and throughput response of the ESA subsystem to ions and electrons. The ESA and TOF subsystem models are coupled at the planar entrance surface of the foil, and the ion and electron spatial and velocity distributions at

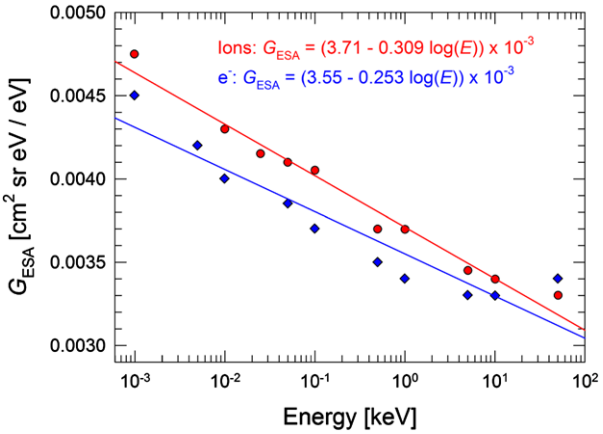

Fig. 11 The geometric factor G_{ESA} per polar pixel for the ESA subsystem varies systematically with energy as $G_{\mathrm{P}} \sim \log(E)$ and exhibits a small difference between incident ions (*black symbols*) and electrons (*blue symbols*). The *lines* are empirical fits

this location derived from the ESA subsystem performance model are input into the TOF subsystem performance model.

SIMION simulations of the ESA were performed for both protons and electrons over the full HOPE energy range of 1 eV–50 keV under two types of incident angle conditions. First, simulations were run with a parallel beam of input particles, corresponding to fixed incident polar and azimuthal directions, which best describes the laboratory ion and electron beams for validation through test and calibration (discussed below in connection with HOPE calibration measurements). Second, simulations were run with incident ions and electrons uniformly distributed over all angles and energies within the acceptance range of the instrument, allowing determination of the instrument geometric factors for an ambient charged particle flux that uniformly fills a pixel in angle and energy, which is more representative of the magnetospheric environment.

These simulations derived the full width at half maximum (FWHM) energy resolution $\Delta E_{\mathrm{FWHM}}/E \approx 15$ % and the azimuth angle resolution $\Delta\phi$ of $\sim$10° full width (FW) and $\sim$5° FWHM. The geometric factor for a toroidal electrostatic is derived using Gosling et al. (1978) and Young et al. (1988). Figure 11 shows the resulting geometric factor G_{ESA} for the ESA subsystem per polar pixel (which each span 18° in polar angle) as a function of incident energy for both protons and electrons. Because particles of the same charge and energy but different mass follow identical trajectories in a static electric field, the proton results apply identically to He^+ and O^+. G_{ESA} is found to depend slightly on energy as $G_{\mathrm{ESA}} \sim \log(E)$, with small differences between ions and electrons. These simulations were used to appropriately size the foil.

The ESA analyzer constant $k = E_{\mathrm{C}}/V_{\mathrm{ESA}}$ is a key parameter describing the central energy E_{C} of an energy passband as a function of the applied bias V_{ESA}. The analyzer constant is based on the ESA geometry but can vary slightly due to factors such as error in the concentricity of the electrodes and fabrication variations within the machining tolerances of the electrodes. The value $k = 7.035$ was derived for both HOPE-A and HOPE-B during calibration, in good agreement with the value of $k = 6.90$ derived using the charged particle optics model for an ideal instrument with no alignment or machining imperfections.

As the spacecraft spins through 360° in azimuthal angle, HOPE systematically acquires ion or electron energy histograms over five swaths of polar angle. Furthermore, V_{ESA} is stepped over the full instrument energy range (1 eV–50 keV) 16 times every 12 seconds, which is the nominal spacecraft spin period. Therefore, HOPE acquires a complete energy spectrum at 80 locations over the full sky; we selectively combine some azimuthal pixels

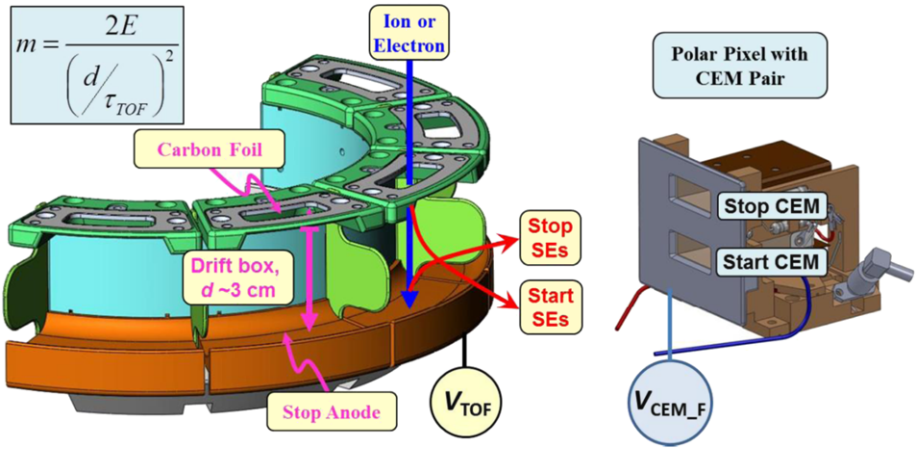

Fig. 12 The TOF subsystem consists of 5 independent polar pixels, each with a TOF drift box and pair of CEM detectors. Ion speed is determined by its time-of-flight τ_{TOF} over ~3 cm between the carbon foil and stop anode

with overlapping fields-of-view at higher polar angles and reduce these to 40 locations that are nearly uniformly distributed over 4π sr from which we derive the full plasma distribution function. Details of this strategy are provided later in Sect. 4.2.1.

3.2.3 Time-of-Flight Subsystem

The TOF Subsystem was designed to allow robust species separation of H^+, He^+, and O^+ as well as a coincidence measurement of incident electrons within a high penetrating background environment. HOPE employs a standard linear, foil-based TOF measurement technique (e.g., Wüest 1998). Because this is a standard technique as a diagnostic for space plasma ions, the physical processes governing almost all aspects of its performance have been individually studied and documented.

A charged particle exiting the ESA subsystem enters the TOF subsystem (Fig. 12), which consists of five independent polar pixels arrayed at polar angles of 0° (perpendicular to the spin axis), ±36°, and ±72°. Each polar pixel has a TOF drift box biased to V_{TOF} and consists of an ultrathin carbon foil at the entrance, a drift region of ~3 cm, and a Stop Anode, which is shaped like a trough. The charged particle transits the foil, generating secondary electrons at the foil's exit surface that are steered to the "Start" CEM detector by the tailored electric field between the TOF drift box and the CEM detectors. Detection of a Start pulse initiates a timer. The particle continues to the Stop Anode, where it generates "Stop" secondary electrons that are optically steered to the Stop CEM detector, generating a Stop pulse that stops the timer. The charged particle's speed is calculated from the measurement of its time-of-flight τ_{TOF} over the drift region. We can calculate the charged particle's mass from knowledge of its speed in the TOF subsystem and its incident energy E from the ESA subsystem. In practice, for each V_{ESA} setting (i.e., each energy passband), the times-of-flight of H^+, He^+, and O^+ uniquely lie within separate TOF ranges; instead of calculating the time-of-flight of individual ions as they are detected, we identify the ion's species at each energy by binning each TOF measurement within these unique TOF windows.

The full TOF window is 160 ns, which is divided into 64 time bins, each of which is 2.5 ns. This window is longer than required, as the slowest ions (incident 1 eV O^+ accelerated by $V_{TOF} = -11$ kV) have a characteristic TOF of ~100 ns; in contrast, the fastest

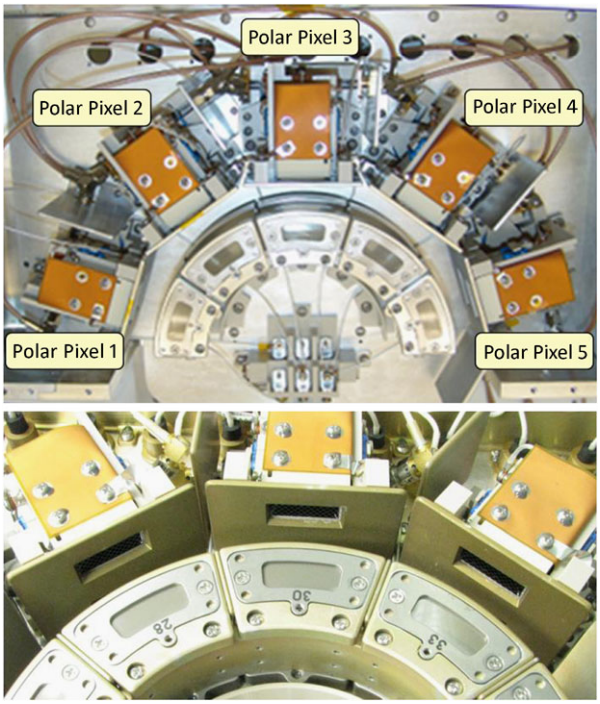

Fig. 13 The HOPE TOF Subsystem consists of five polar pixels each with a pair (Start and Stop) of CEM detectors. Polar pixels are identified from 1 to 5 in a clockwise direction as shown in the top photograph. Polar Pixel 3 is centered on the $+\hat{u}$ spacecraft vector (refer to Figs. 8 and 9). Polar Pixels 1 and 5 lie in the $\hat{u}$–$\hat{v}$ plane, with Pixel 1 located 18° from $-\hat{v}$ (anti-sunward) and Pixel 5 located 18° from $+\hat{v}$ (sunward). A close-up of HOPE-B Pixels 2–4 is shown in the lower photograph. The CEMs are mounted behind a plate electrode that resides at the same bias as the front of each CEM pair, $V_{\mathrm{CEM\_F}}$

ion TOF measurement is 3–4 ns for 50 keV H^+. Because the TOF of incident 1 eV–50 keV electrons is short ($\tau_{\mathrm{TOF}} < 2$ ns), in electron mode we use a short TOF measurement only as a coincidence measurement for electrons and retain longer TOF events to monitor background penetrating radiation. We have incorporated a ~10 ns delay on the Stop pulses to ensure that electrons are all measured with a positive value of τ_{TOF} and, therefore, a valid coincidence.

The bias V_{TOF} of the TOF drift box is nominally -11 kV in ion mode and $+1.5$ kV in electron mode to accelerate the particles before they impact the foil. This mitigates the energy straggling (Allegrini et al. 2006) and angular scattering (Funsten et al. 1993) of the particles in the foil. This bias scheme also enables constant front and rear CEM detector biases, independent of whether ions or electrons are being measured. For each polar pixel, the Start and Stop CEMs are mounted into rectangular apertures in an electrode plate located opposite the drift box, as shown in Fig. 12. Both CEMs are biased at a fixed front voltage $V_{\mathrm{CEM\_F}} = +4.4$ kV, such that secondary electrons generated at the start foil and the stop anode are accelerated into the Start and Stop CEM detectors, respectively. The CEM rear bias is nominally set to $V_{\mathrm{CEM\_R}} = +6.8$ kV and is adjustable up to a maximum of $+9.0$ kV. The assembled TOF subsystem is shown in Fig. 13.

Considerable effort was directed toward the charged particle optics design of the TOF subsystem to efficiently steer and detect secondary electrons emitted only from the foil and anode surfaces, as well as to minimize detection of electrons from all other surfaces in the TOF subsystem. The preliminary optics design was described by MacDonald et al. (2009). Importantly, because (1) the electric field geometry that governs these secondary electron trajectories is solely defined by two electrodes (the TOF drift box at V_{TOF} and plate electrode at $V_{\mathrm{CEM\_F}}$), and (2) Start and Stop secondary electrons are born nearly at rest (<10 eV) compared to the their acceleration energy $q(V_{\mathrm{CEM\_F}} - V_{\mathrm{TOF}})$ into the CEM detectors (minimum of 3.9 keV in electron mode), the secondary electrons follow trajectories that are nearly

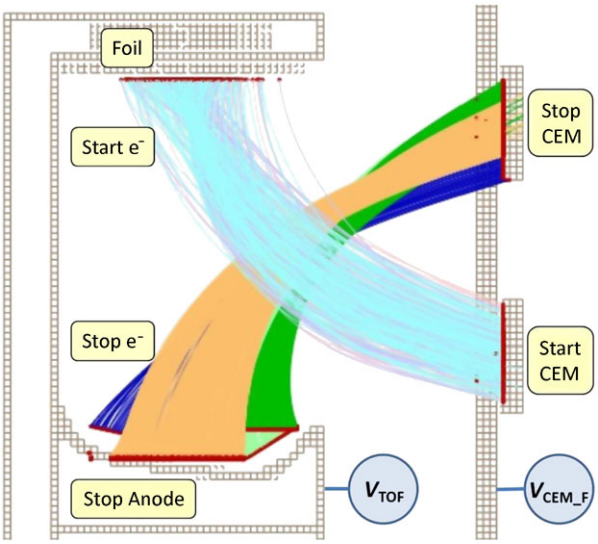

Fig. 14 2.5D electron-optic simulations show the crossing trajectories of Start and Stop secondary electrons generated from the backside of the foil and from different locations along the Stop anode, respectively. The geometry was further refined using full 3D simulations. This geometry enabled efficient secondary electron collection at the Start and Stop CEM detectors using only two voltages, V_{TOF} and V_{CEM_F}, independent of the energy of the incident particle

independent of V_{TOF}, as demonstrated by subsystem testing and flight instrument calibration. This two-electrode design with crossing Start and Stop secondary electron trajectories enabled tremendous simplification of overall design and operation of the TOF subsystem. Furthermore, the separation of the polar angles into five independent polar pixels eliminates electronic cross-talk between pixels or crossing of secondary electron trajectories from one pixel to another.

The TOF subsystem was modeled with SIMION (Dahl 2000) in both 2.5-D and 3-D and validated through prototype testing and flight unit calibration. Charged particle optics optimization was performed through a complex parameter space, defining the foil dimensions, drift box dimensions, stop anode geometry, distance of CEM detectors and detector electrode plate from the drift box, and locations of the Start and Stop CEM detectors relative to the foil and stop anode, respectively. Figure 14 illustrates the trajectories of Start and Stop secondary electron trajectories for ion mode ($V_{TOF} = -11$ kV, $V_{CEM\_F} = +4.4$ kV) using a 2.5D electron-optic simulation with near-flight dimensions of the drift box geometry, CEM detector locations, and plate electrode to which the CEM detectors are attached. Start secondary electrons are emitted at energies of 0.2, 2, and 10 eV, while Stop secondary electrons are emitted at 2 eV; all are emitted within a half cone angle of 45° relative to the emission surface normal. The secondary electrons follow trajectories from the Start foil and Stop anode that accurately map to the appropriate CEM detector and result in a collection efficiency >90 %.

The TOF Subsystem development followed a methodical series of electron-optic modeling and validation steps. Full 3D electron-optic modeling was performed for incident H^+, He^+, O^+, and electrons. For these simulations, the charged particles were initially input at specific locations of the foil to optimize the geometry of individual parts of the drift box; final simulations were performed using ion locations at the foil representative of the output from the ESA subsystem. Secondary electrons, which were generated where the ions exited the Start foil and struck the Stop anode, were modeled using a Gaussian energy distribution (with 2 eV mean and 2 eV FWHM) and random angular emission within a 45° half cone angle relative to the local surface normal. In addition to optimization of the electron-optics

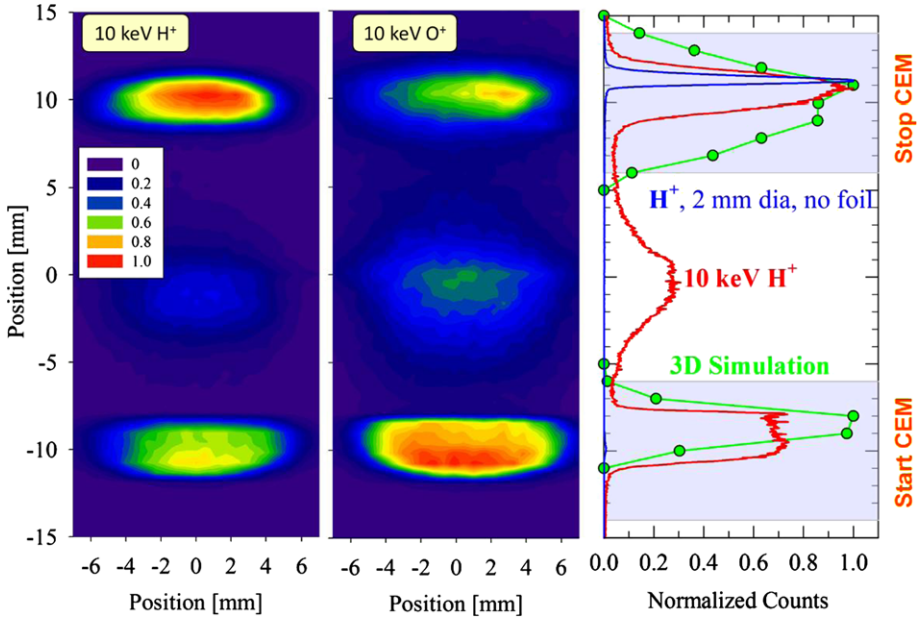

Fig. 15 3D electron-optic simulations were validated using a prototype polar pixel with an imaging MCP detector placed at the location of the CEM detectors. The left and center panels show the spatial distribution of normalized detected secondary electron counts for incident 10 keV H^+ (*left panel*) and O^+ (*center panel*) with $V_{TOF} = -11$ kV. The distributions at vertical positions centered near -10 mm and $+10$ mm correspond to Start and Stop secondary electrons, respectively. The *right panel* shows the vertical distribution of start and stop secondary electrons from incident 10 keV H^+ compared to electron-optic simulations in which the anode is broadly illuminated, showing the extent and positioning of collection required of the Stop CEM detector

of the TOF Subsystem, these models were used to estimate the TOF spectra for each of the charged particle species.

These simulations were initially validated using a polar pixel prototype with an imaging MCP detector placed at the location of the electrode plate to which the CEMs are attached. The left and center panels of Fig. 15 show the distribution of counts (normalized to unity) of secondary electrons emitted from the TOF drift box for incident 10 keV H^+ and O^+ for $V_{TOF} = -11$ kV. Distinct Start and Stop distributions are centered near vertical locations of -10 mm and $+10$ mm, respectively, and each distribution lies within an area of $\sim$5 mm (vertical) $x \sim 12$ mm (horizontal). The peaks observed in each panel near 0 mm vertical are artifacts of the resistive anode of the MCP detector, which centroids the coincident detection (within several 10 s of ns) of start and stop electrons.

Figure 15, right panel, shows the vertical distribution of secondary electrons (red line) for the 10 keV H^+ prototype results in comparison with 3D SIMION simulation results for incident 1 eV O^+ (green points and line). For this worst-case simulation, the Stop anode is fully illuminated due to scattering of O^+ in the foil and results in a broader Stop secondary electron distribution. The funnel dimensions of the flight CEM detectors were 8×20 mm to fully cover this area. The flight CEM detectors are located 19.6 cm apart (center-to-center). The blue line represents the counts (normalized to unity) from the prototype apparatus of a 2-mm-diameter H^+ beam with the Start foil removed so that Start secondary electrons are not generated. The resulting Stop peak is well defined because of no scattering of ions in the absence of the foil; note also the absence of the artifact peak near 0 mm vertical because no

Start pulses (and therefore no Start and Stop coincidences that result in a centroid peak by the MCP resistive anode) are generated.

Further maturing the TOF subsystem design, the MCP detector was then replaced by a polar pixel assembly with CEM detectors, from which TOF spectra were derived and used for performance characterization and validation. A full 5-pixel subsystem was used to validate performance over all pixels, and in particular demonstrating similar performance of the two end polar pixels (Pixels 1 and 5) to the center polar pixel (Pixel 3) as well as negligible cross-talk between polar pixels.

3D SIMION simulations were also used for identifying the areas in the TOF box other than the Start foil and the Stop anode from which secondary and photo-electrons generated by penetrating radiation can or cannot access a CEM. Potential regions in which electrons generated by penetrating radiation might be focused to a CEM detector include the foil frame around the foil's exit surface, the back wall of the TOF drift box, and the side wall electrodes that separate each of the polar pixels. From this analysis, the side wall geometry was modified to a tab geometry (green sidewalls in Fig. 12) to eliminate electron emission from the side walls near the foil and Stop anode that could be steered to the CEM detectors. In the final design, only electrons emitted from the foil frame immediately adjacent to the exit surface of the foil and emitted from the back wall near the Stop anode could be steered to a CEM detector.

We describe each component of the TOF subsystem sequentially in more detail. Each polar pixel has a carbon foil centered at polar angles 0°, ±36°, and ±72°, with inner and outer radii of 60 mm and 68 mm and subtending 18° in polar angle. These foils are nominal 0.6 μg/cm^2 carbon from ACF Metals and are mounted on 333 line per inch (lpi) Ni grids. These grids have a typical transmission of $T_G = 70$ % as measured using a 50 keV H^+ beam and are attached to a stainless steel foil frame with 160 mm^2 open area.

Foils of this thickness have extensive flight heritage (McComas et al. 2004) and are robust to sputtering at typical space plasma fluxes (Funsten and Shappirio 1997). Characterization of each flight foil included thickness measurement through light ion scattering (Funsten et al. 1992a) and pinhole characterization and quantification through heavy ion transmission (Funsten et al. 1992a, 1992b). Carbon foil thicknesses were measured within the range 1.5–1.8 μg/cm^2 and averaged 1.6 μg/cm^2, and each foil had less than 1 % pinholes. The instrument performance model and electron-optic model incorporates foil effects on ions including angular scattering (Funsten et al. 1993), exit charge state (Funsten et al. 1993), and energy loss (Allegrini et al. 2006). Interactions of incident electrons with the foil were simulated using CASINO (Drouin et al. 2007; Demers et al. 2011).

We note that the RBSP mission poses a potential risk to high flux, reactive ion etching of the ultrathin carbon foils near the ∼600 km altitude perigee at which the O^+ density can reach 10^5 cm^{-3} (Nosé et al. 2009). Reactive ions such as O^+ can rapidly etch hydrocarbons, at a much higher rate than physical sputtering by inert ions, by forming volatiles such as CO and CO_2 (Oehrlein et al. 2011); we similarly expect enhanced etch rates of carbon foils from low energy O^+. The RBSP spacecraft speed approaches 10 km/s at perigee, thus encountering an O^+ ram flux of 10^{11} cm^{-2} s^{-1} and O^+ ram energy of ∼8.2 eV. Considering spacecraft charging up to −1.5 V at this altitude (Anderson et al. 1994), care must be taken to ensure that HOPE does not measure ions less than 10 eV in the vicinity of perigee so that the foils in the TOF subsystem are not exposed to the large O^+ flux. Because of the need to avoid this intense O^+ flux near perigee, HOPE nominally operates with a minimum energy of 1 eV in ion mode and 15 eV for electron mode except during a perigee segment (within ±20 min of perigee, below ∼3500 km altitude) in which the minimum energy is at least 15 eV for both ions and electrons.

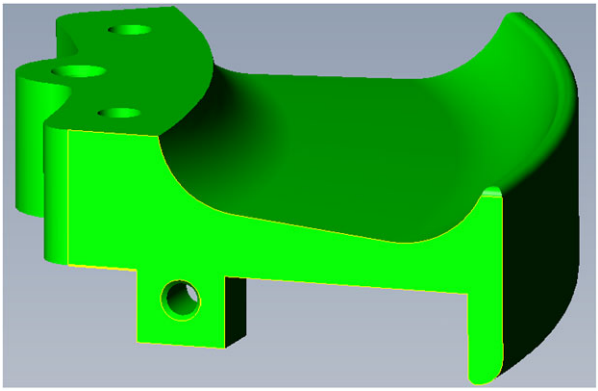

Fig. 16 The Stop anode shape was optimized to minimize the variation of the pathlength of particles in the drift section due to angular scattering in the foil and to maximize the probability that Stop secondary electrons are steered into the Stop CEM detector

In ion mode, Start electron production is the result of forward secondary electron emission from the carbon foil, with a mean forward secondary electron yield $\gamma_F = 0.61E^{0.56}$ for H^+ incident at energy E in keV (Ritzau and Baragiola 1998). For heavier ions at the same energy, the forward secondary electron emission yields are higher. The probability of a non-zero number of electrons emitted can be calculated using a Poisson distribution. In electron mode, due to the lack of studies of electrons transiting carbon foils yields, we approximate the yield using published data of electrons incident on thick targets (e.g., Seiler 1983).

Relative to the HOPE axis of cylindrical symmetry, the envelope of each TOF drift box is 54 mm radius inner wall, 74 mm outer radius (foil frame and Stop anode), and spans ~36°. Partial walls were added between each of the polar pixels to push secondary electrons generated at the outer edges of the foil and Stop anode toward the appropriate CEM detector as well as to provide a barrier to prevent incident ions and electrons that are highly scattered at the foil in one pixel from reaching another pixel. The walls are strategically located and of minimum size to minimize the surface area from which penetrating radiation can generate electrons that might be detected as background.

The Stop anode, shown schematically in Fig. 16, was fabricated using Al 6061, whose native aluminum oxide has been shown to enhance secondary electron emission for incident electrons (Walker et al. 2008) and ions (Dietz and Sheffield 1975; Baragiola et al. 1979). We expect that the native oxide will remain stable far beyond the nominal RBSP mission. The shape of the anode was initially a spherical section with vertex in the middle of the foil to minimize the variation of pathlength of incident particles (and therefore minimize TOF variation of incident particles) in the drift section due to angular scattering in the foil. This general shape was subsequently modified to enhance the electron-optic steering of Stop secondary electrons to the Stop CEM, primarily by introducing a small tilt of the surface toward the Stop CEM detector and a flatter bottom.

Each polar pixel has separate Start and Stop CEM detectors. The CEM detectors, Sjuts KBL series, have a rectangular funnel with an entrance dimension 8 mm × 20 mm. All CEMs were burned in to ~0.1 C output charge to screen for infant mortality. The CEMs are mounted in rectangular holes in the detector electrode plates; both the CEM fronts and the electrode plates were biased to the same potential V_{CEM_F} that is fixed to +4.4 kV using three separate shunt regulators attached to Pixels 1&4, Pixels, 2&5, and Pixel 3. In front of each CEM funnel is a 20 line per inch nickel grid to suppress secondary electrons generated in the funnel. CEMs were selected and matched as pairs for each polar pixel based similarity of gains measured during CEM burn-in as well as similarity of electrical impedance. The gain curves derived before final instrument delivery are shown in the Calibration section.

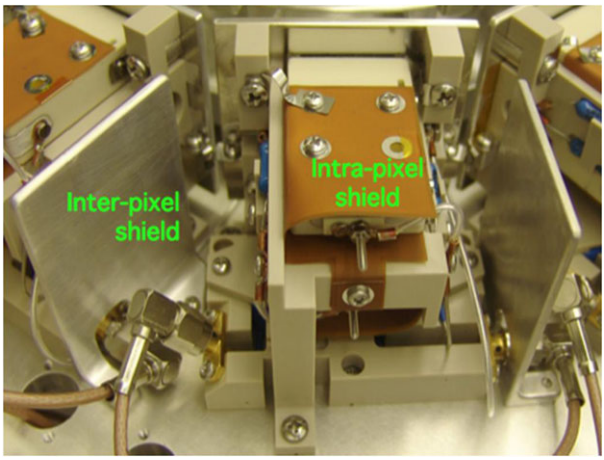

Fig. 17 Electronic shielding within and between polar pixels was found to reduce the level of electronic cross-talk of sufficient magnitude to register noise counts. The intra-pixel shield consisted of a copper sheet sandwiched within Kapton that surrounded a CEM detector as shown in the figure. The inter-pixel shield consisted of an aluminum plate between the polar pixels

Testing of CEMs was performed to assess intrinsic detector timing jitter, which is important for understanding TOF performance limitations and is used to appropriately design the drift box geometry and TOF electronics. An ion beam was directed on a thin carbon foil, generating secondary electrons simultaneously from the entrance surface, which were detected by one CEM detector, and exit surface, which were detected by a second CEM detector. Because electron transport from foil to detector is much shorter than CEM timing jitter, the time difference between detected coincidences provides a measure of the timing uncertainty of the CEM detectors. A delay line was inserted into the electronic chain of one CEM so that all coincidences registered a positive timing difference. The FWHM of this timing difference was found to be 3.5 ns FWHM, which was used to define the drift box length and the required TOF electronics timing accuracy for each polar pixel.

Electronic cross talk was minimized with inter- and intra-pixel shields as shown in Fig. 17. The intra-pixel shield is a sandwiched layer of copper and Kapton to provide grounded signal isolation. Particle crosstalk between pixels was measured with a low energy, heavy ion beam (5 keV O^+) to maximize angular scattering from the foil and therefore maximize the leakage of scattered particles into adjacent polar pixels. No particle crosstalk was observed as will be shown by the polar angle response in the Calibration section.

The performance of the TOF subsystem is governed by numerous complex physical processes, including angular scattering and energy loss of incident charged particles in the foil, secondary electron emission statistics from the foil and the Stop anode, the steering of Start and Stop secondary electrons into the appropriate CEM detector, and probability of detection of these secondary electrons. This ensemble of processes is difficult to model and can change over time, so the subsystem performance model relies heavily on the extensive test and calibration data acquired throughout instrument development and interpolation of these empirical results over energy, angle, and species. We also report as routine HOPE data products both coincidence and non-coincidence count rates from which we monitor the absolute detection efficiencies of each polar pixel of the TOF subsystem over the lifetime of the mission.

3.2.4 Penetrating Radiation Analysis

The fundamental challenge for measuring the plasma environment in the heart of the radiation belts is minimizing the background from the high flux of penetrating radiation. As

previously discussed, HOPE incorporates several strategies to mitigate this background. Of these, shielding has the highest impact for removing this background. Because the penetrating radiation flux exponentially decreases with shielding thickness, small spots of thin shielding can potentially compromise the diligent shielding in all other areas. Therefore, extreme care was taken in the mechanical design to prevent this type of compromise, for example using step mechanical interfaces, strategically locating screw vent holes in any parts used for shielding, and spot shielding key areas identified through simulations.

An empirical scaling analysis compared background count rates from the Magnetospheric Plasma Analyzer (MPA) on LANL satellites (Bame et al. 1993) in geosynchronous orbit to the ambient penetrating particle radiation environment in the radiation belts to develop a basis for estimating detector background count rates over the RBSP orbit (MacDonald et al. 2006). Like HOPE, MPA used CEM detectors, although not in a coincidence configuration. Signal-to-background coincident and non-coincident rates were estimated for HOPE based on scaling of the orbit characteristics, instrument response functions, detector response, and coincident timing window. These results were then used as a basis for simulation studies using a geant4 model (Agostinelli et al. 2003) to understand the susceptibility of HOPE to penetrating radiation. Two studies were performed during development of HOPE design, and a final analysis was performed for verification of the flight design, from which we derived an expected accidental coincidence rate of $\sim$1 Hz. The analysis for the flight instrument design was validated by agreement of the simulated flight instrument response to its measured response from exposure to a 15 mCi ^{60}Co γ-ray source during calibration.

Decay of materials activated by MeV protons can induce backgrounds in instruments (e.g., Väyrynen et al. 2009). HOPE activation analysis focused on materials within the HOPE instrument and, especially, candidate materials for external wall shielding. Slugs of stainless steel, tungsten copper, tantalum, aluminum, G11 fiberglass, copper, and 0.89 cm aluminum shielded copper were exposed over $\sim$30 min to protons from 10–200 MeV in 25 MeV steps using the Alternating Gradient Synchrotron (AGS) (Lowenstein and Rusek 2007) at the NASA Space Radiation Laboratory (NSRL) at Brookhaven National Laboratory (BNL). The proton fluence was the equivalent of one orbit exposure as derived from the AP-8 model (Sawyer and Vette 1976) at worst case at the RBSP orbit. The only material exhibiting any long-term activation was copper, which took $\sim$3 hours to decay to background levels, confirming that significant amounts of copper should be avoided. Stainless steel showed a similar initial specific activity after irradiation, but decayed to background levels in $\sim$10 min; we therefore anticipate slightly enhanced background for up to $\sim$10 min after exiting of the inner belt proton population.

Sensitivity analyses were performed during the design stage and for verification of statistically significant measurements during worst-case flux scenarios in the radiation belts. These analyses used the Sector Shielding Analysis Tool (SSAT) (Santina et al. 2003) based on geant4. The simulated instrument geometry incorporated key HOPE components including all exterior walls, the interface plate between the TOF subsystem and the HEU, and the ESA subsystem. Screws in these components were assumed to uniformly fill their tapped holes with the same material as the component itself. Most small components (e.g., detectors, foils, wires, individual electrical components, door mechanism) and components with comparatively small mass shielding (HEU electronic boards, detector mounting brackets, connectors) were not included in the geometry model. Additionally, the analyses assumed no shielding contribution for the spacecraft, so the analyses represent a worst-case shielding mass density.

The design stage sensitivity analysis derived the shielding mass density integrated along lines-of-slight (LOS) distributed over the complete 4π sr solid angle at various interior locations, primarily in the TOF Subsystem and the HEU. This analysis verified the RBSP

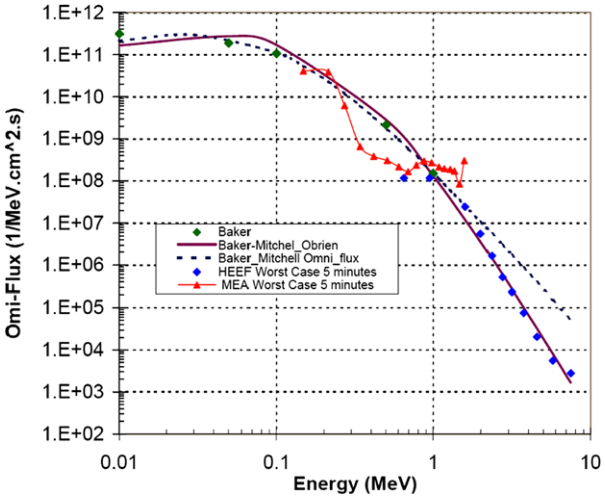

Fig. 18 Ambient penetrating electron spectrum used to characterize worst-case fluxes of penetrating radiation for the RBSP mission

shielding requirement of ≥0.89 cm (0.350 in) aluminum equivalent thickness between any electronics and the instrument exterior.

Another important result was identification and resolution of a set of penetrating particle trajectories that could traverse both CEM detectors of a single polar pixel. Such a particle could register a valid event with a short TOF that may masquerade as detection of a plasma electron or a fast, light ion such as 50 keV H^+. The HEU was found to provide sufficient shielding for penetrating radiation that traverses the Start CEM before the Stop CEM. For penetrating radiation entering HOPE from the opposite direction, traversing the Stop CEM before the Start CEM, the thickness of portions of the exterior wall in the Door subsystem was increased to nearly 1.8 cm (∼0.7 in) aluminum. Additionally, the top of the top-hat ESA on which the door actuator is mounted was changed from aluminum to stainless steel for enhanced shielding with economy of space. We found through simulation with anticipated worst-case radiation belt spectra that the additional thickness blocked almost all penetrating protons or electrons that would otherwise transit the two CEMs of a single polar pixel.

The sensitivity analysis verification evaluated the HOPE penetrating background based on RBSP project-developed spectra. The electron spectrum encompasses the CRRES High Energy Electron Fluxmeter (HEEF) worst case 5 minutes and CRRES Medium Electrons A (MEA) worse case 5 minutes for electrons (Fig. 18). The composite electron spectra, known as Baker-Mitchell-O'Brien worst-case, was constructed by the RBSP project for verification processes across all instruments and subsystems. The proton spectra are derived from the AP-8 peak spectrum. The same HOPE geometry model was used as in the design stage sensitivity analysis, but without the shielding added to minimize radiation that would traverse the two CEMs of a single polar pixel. The simulations derived a maximum 0.7 Hz coincidence count rate from penetrating electrons and ions combined for any polar pixel assuming random coincidence within the 160 ns TOF window in ion mode. We project this background count rate into an equivalent ambient plasma flux outside the instrument using the maximum HOPE geometric factor. This flux can then be compared to a typical stormtime flux, e.g., Krimigis et al. (1985). Figure 19 shows significant (more than an order of magnitude) separation between the anticipated plasma ion signals and the penetrating background signal expected in the HOPE instrument over all except the highest energy He^+ and O^+, for which the separation remains nearly a factor of 10. Considering that most assumptions for

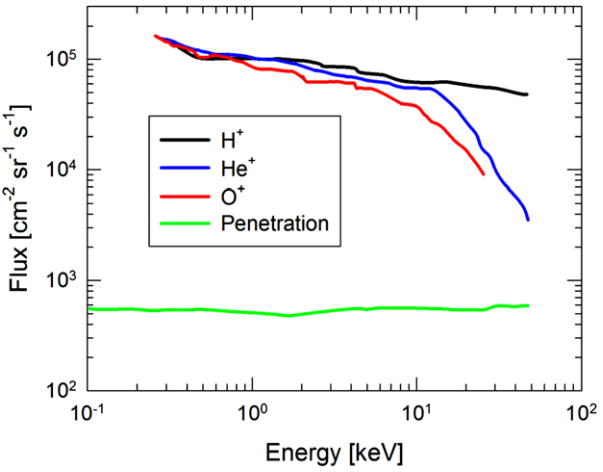

Fig. 19 Penetrating electrons and ions combine to produce background counts in HOPE that might be improperly identified as real plasma ions or electrons. We project the simulated worst-case background count rate from penetrating ions and electrons to an equivalent ion flux at the HOPE entrance aperture (*green line*). Comparison of this background flux with typical stormtime fluxes for H^+ (*black line*), He^+ (*blue line*), and O^+ (*red line*) from Krimigis et al. (1985) shows that backgrounds from penetrating radiation should be negligible

this analysis are worst-case, penetrating background is not expected to be the major source of noise in the HOPE measurements.

3.3 HOPE Electronics Unit (HEU)

The HOPE Electronics Unit (HEU) is multipurpose, designed to communicate with the spacecraft; generate appropriate voltages for operation; receive analog signals from the TOF subsystem and process them into HOPE data products; and monitor housekeeping. The HEU is divided into the following functional elements, shown in Fig. 20: the Low Voltage Power Supply (LVPS) Board that generates conditioned power for the HEU, the High Voltage Power Supply (HVPS) Board that generates high voltages for charged particle optics elements and for detector bias; the Front End Electronics (FEE) Board that receives analog signals from the CEM detectors and converts them into digital signals; and the Digital Board (DB) that processes these digital signals and classifies them as detected events. In addition, the Backplane (BP) serves as the primary communications and interface trunk for all of the HEU boards as well as with the HOPE door and the spacecraft. The HEU interfaces with the spacecraft for +30 V primary power and low-voltage differential signaling (LVDS) communications, which consists of three pairs of interfaces: inbound synchronization, inbound command signals, and outbound telemetry. The synchronization signal from the spacecraft provides both a one-pulse-per-second (1-PPS) signal and a spin pulse signal. We first provide an overview of each board and then provide an overview of HEU operational modes.

3.3.1 Power Supply Boards

The LVPS Board receives spacecraft power (+30 V) and converts it to the following secondary voltages needed throughout the HEU: +3.3 V, ±5 V, ±12 V. The main components are three International Rectifier DC-to-DC converters, one filter, and a slow-start circuit. As with every HEU electronics board, an AD590 temperature transducer is included to monitor temperature. The LVPS Board is mounted directly on the bottom of the HOPE chassis, providing a strong thermal conduction path to the spacecraft. The layout and grounding design is in accordance with RBSP mission requirements with special attention paid to minimizing current loop areas and utilizing a star ground.

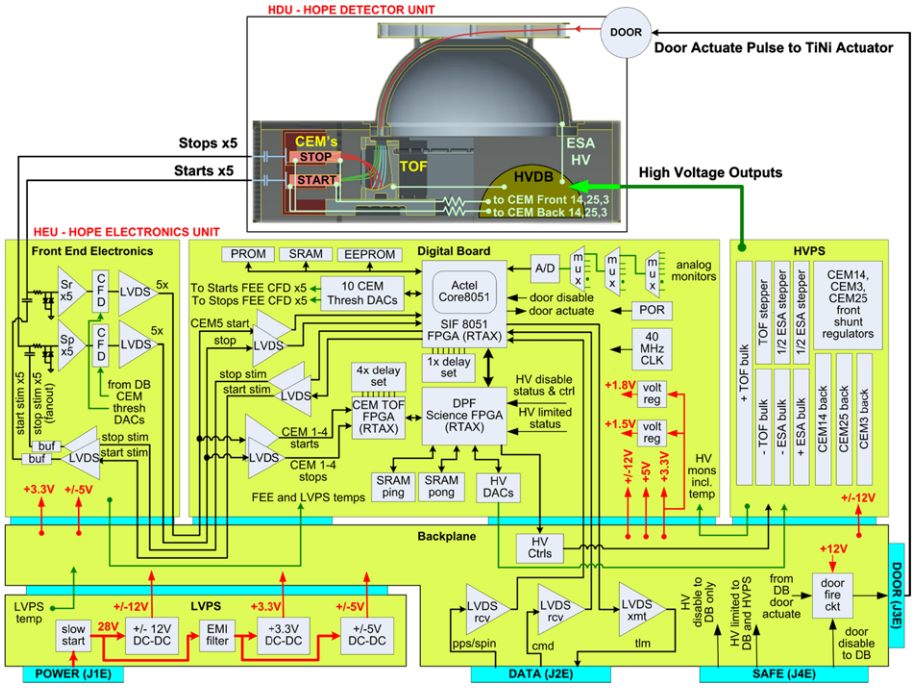

Fig. 20 Block diagram of the Hope Electronics Unit (HEU)

The HVPS Board, powered by ±12 V, provides bipolar ESA (V_{ESA}) and TOF (V_{TOF}) voltages, as well as CEM bias voltages $V_{\mathrm{CEM\_F}}$ and $V_{\mathrm{CEM\_R}}$. To minimize the effect of either a possible HV or CEM failure, three separate CEM supplies provide voltages to polar pixels 1&4, 2&5, and 3. The CEM front voltages $V_{\mathrm{CEM\_F}}$ are obtained from the same supply as the rear voltages $V_{\mathrm{CEM\_R}}$ using a shunt regulator circuit that maintains a fixed +4.4 kV level. To provide the required voltage resolution over the wide dynamic range of HOPE's energy response (1 eV to 50 keV), the ESA supply is dual-range, with low range extending over 0–33 V and high range spanning 0–7500 V. Both the ESA and TOF supplies are bipolar, allowing ion and electron measurements in alternating spins using the same supplies.

HVPS board inputs consist of a series of high-low enables: one overall enable; one for each of the three CEM supplies; and one for each of the following: ESA(+), ESA(−), ESA high/low range, TOF(+), and TOF(−). Also included are digital-to-analog converters (DAC) to control the voltage levels of the three CEM supplies, the ESA supply, and the TOF supply. Scaled analog voltage monitors are provided for all the high-voltage outputs and bulk supplies, along with current monitors for the outputs of the three CEM supplies The supplies use a resonant flyback topology running in the range 100 to 125 kHz. Custom lug connections are used at the detector via a high-voltage distribution block. A $V/10$ function enabled by an external hardware plug limits the output of the high voltage power supplies to a level safe for limited instrument functionality testing at atmospheric pressure. The largest ESA step, between 4077 V and 6440 V, occurs over ∼0.6 ms, which is well within the required transition time of 1.3 ms. The HVPS specifications are summarized in Table 3. All supplies except for the bulk supplies have 12 bit DAC resolution. Table 4 shows additional information for the ESA and TOF stepping supplies.

Table 3 Summary of HOPE high voltage power supply (HVPS) specifications

HVPS name	HVPS type	Voltage (kV)		Max current (μA)	Voltage/current monitor[b]
		Min	Max		
ESA Bulk (+)	Fixed	0	+8.0		Y/N
ESA Bulk (−)	Fixed	−8.0	0		Y/N
ESA (V_{ESA})	Stepping[a]	−7.5	+7.5		Y/N
TOF Bulk (+)	Fixed	0	+2.0		Y/N
TOF Bulk (−)	Fixed	−11.5	0		Y/N
TOF (V_{TOF})	Stepping[a]	−11.0	+1.5		Y/N
CEM Front (V_{CEM_F}), Polar pixels 1 & 4	Fixed	0	+4.4	120	Y/Y
CEM Front (V_{CEM_F}), Pixels 2 & 5	Fixed	0	+4.4	120	Y/Y
CEM Front (V_{CEM_F}), Pixel 3	Fixed	0	+4.4	60	Y/Y
CEM Rear (V_{CEM_R}), Pixels 1 & 4	Programmable[a]	0	+9.0	120	Y/Y
CEM Rear (V_{CEM_R}), Pixels 2 & 5	Programmable[a]	0	+9.0	120	Y/Y
CEM Rear (V_{CEM_R}), Pixel 3	Programmable[a]	0	+9.0	60	Y/Y

[a]Programming voltages are ±5 V (bipolar) or 0 V to +5 V (unipolar) full scale

[b]Monitor voltages are ±4 V (bipolar) or 0 V to +4 V (unipolar) full scale voltage

Table 4 Additional specifications for HOPE stepping high voltage power supplies

Stepping supply	Min/max voltage	Settling time	Time per step	Max step change	Total load capacitance
ESA	−7.5 V/+7.5 kV	1.3 ms	10.4 ms	1.9 kV	150 pF
TOF	−11.0 kV/+1.5 kV	10.4 ms	12 s	12.5 kV	100 pF

3.3.2 Front End Electronics (FEE) Board

The FEE Board is powered by ±5 V and +3.3 V, with the anode outputs of the five CEM pairs (10 channels total) of polar pixels as its primary functional inputs. Each CEM output signal connects to an SMA connector on the FEE and is followed by a zap-trap, comprised of a reversed pair of zener diodes to ground for sinking voltage transients. The signal chain continues with an AD8001 charge amplifier, a constant fraction discriminator (CFD), and digital output to the DB. Each channel has its own isolated reference plane to minimize electrical cross-talk between them. An extra 10 ns delay is added to each of the five Stop CEM channels to ensure that a Stop pulse is preceded in time by its correlated Start pulse, which is especially important in electron mode in which incident electrons produce an extremely short τ_{TOF}. Each charge amplifier has its own analog threshold to provide individual control over a dynamic range of 100; this allows for changes in level sensitivity over the mission for each CEM. Once a threshold is crossed, a channel is activated, and the CFD then provides

triggering at a given percentage level (e.g., 50 %) so that a consistent level crossing of the CEM signal is used for the time-of-flight measurement.

The DB can be commanded to inject artificial pulses into the input of each FEE channel so that end-to-end functional tests of the full electronics chain can be performed without requiring operation of the CEM detectors. The repetition rate and relative timing of pulses injected into correlated Start-Stop channel pairs are both configurable. Each FEE channel demonstrated the processing of periodic pulses exceeding a preiodic injection rate of 2 MHz without pulse pileup. The electronics timing jitter is $\leq$1 ns FWHM for each channel.

3.3.3 Digital Board

The DB is powered by $\pm$12 V, +5 V, and +3.3 V. It receives spacecraft commands, the synchronization pulse, temperature monitors from all boards, HVPS voltage and current monitors, FEE signals, and status signals from the V/10 plug and door interface. The DB outputs are: telemetry to the spacecraft, digital-to-analog converter (DAC) analog signals as input for the HVPS and FEE thresholds, HVPS enable signals, and the door firing signal. The DB is driven by a 40 MHz oscillator which is the primary clock throughout the digital system. The DB contains a 32 kB PROM for the permanent storage of bootup flight software, 128 kB EEPROM for non-volatile (yet in-flight re-writeable) storage of application flight software and tables, 512 kB SRAM for flight software use during code execution, and 2 $\times$ 512 kB SRAM for science data acquisition buffering. Three FPGAs reside on the DB: the Spacecraft Interface (SI) FPGA, the Data Processing (DP) FPGA and the Time-of-Flight (TOF) FPGA. The SI FPGA contains an 8051 core which runs the flight software (FSW), executing at 5 million instructions per second (MIPS). The SI FPGA contains first-in-first-out (FIFO) resources for inbound and outbound communications with the spacecraft. The DP FPGA controls the ESA stepping and ESA and TOF polarity changes during nominal science acquisition, which is illustrated in Figs. 21 and 22.

Because HOPE requires a constant time cadence for stepping through the 72 energy steps, HOPE data acquisition is not synchronized to the spacecraft spin pulse. Instead, acquisition is defined by internal timing, which is an important function for the DB. The time $\tau_{\mathrm{ESA\_STEP}}$ spent at a single ESA level represents the fundamental time cadence for all HOPE data acquisition. As shown in Fig. 21, $\tau_{\mathrm{ESA\_STEP}}$ is constructed from a high voltage settling time during which data is not recorded and a science acquisition period during which data is recorded. Both of these can be independently adjusted as needed and are nominally set to 1.302 ms and 9.115 ms, respectively. The nominal value of $\tau_{\mathrm{ESA\_STEP}}$ is therefore 10.417 ms and can be adjusted in flight over a limited range to allow the HOPE measurement interval to approximately match the final spacecraft spin period.

As shown in Fig. 21 for normal science mode, each ESA sweep of 72 steps constitutes a single azimuthal bin over $72 \times \tau_{\mathrm{ESA\_STEP}} = 750$ ns. As shown in Fig. 22, 16 ESA sweeps over one spacecraft spin constitute a complete electron or ion frame with 16 azimuthal bins acquired for each polar pixel, corresponding to 22.5°. Based on $\tau_{\mathrm{ESA\_STEP}} = 10.417$ ms, an electron or ion frame is acquired every 12 sec, and a Master Frame of one electron frame and one ion frame is acquired every 24 sec. The spacecraft spin pulse timestamp is correlated with the ion and electron frame timestamps to precisely define the azimuthal look direction within each frame. We note that the settling time of the TOF HVPS between electron and ion frames is also adjustable up to 100 ms, if needed.

The TOF FPGA, under the control of the DP FPGA, collects and processes the CEM pulses from each polar pixel at each ESA step. The TOF FPGA classifies each detected event and records events in eight event counters. The TOF measurement concept and its

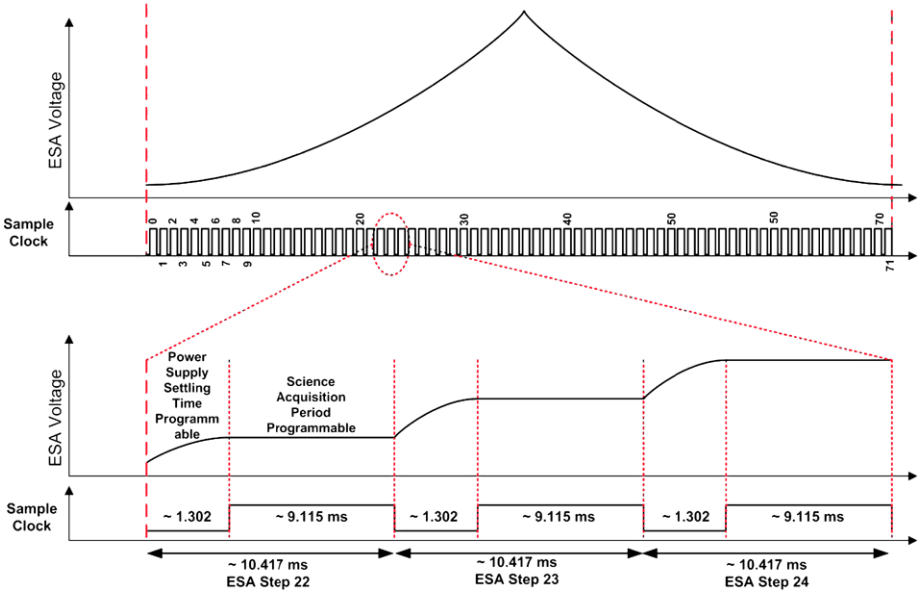

Fig. 21 Timing diagram for one ESA sweep, which traverses 72 discrete energy steps. Each ESA step is nominally $\tau_{\text{ESA\_STEP}} = 10.417$ ms, over which the voltage is allowed to settle for 1.302 ms and data is acquired for the remaining 9.115 ms. Both of these timing values are adjustable, and the net value $\tau_{\text{ESA\_STEP}}$ represents the fundamental timing period for acquisition of all HOPE data. A single ESA voltage sweep based on $\tau_{\text{ESA\_STEP}} = 10.417$ ms is 750 ms

implementation for a single polar pixel with a pair of CEM detectors are shown in Fig. 23. The block diagram (top panel) shows the Start and Stop signals output from the CEMs, represented as Gaussian pulses in the timing diagram. These signals are converted by the FEE to the Start and Stop digital signals. Because of intrinsic timing error within the system, e.g., CEM timing jitter, a 10 ns delay is added to the Stop signal to ensure that a Stop pulse always follows the Start pulse, which is needed for fast particles such as 50 keV H^+ and electrons. The FEE also lengthens the digital signals to ~90 ns, which are easier for the FPGA to process.

The TOF FPGA calculates the elapsed time between the arrivals of the Start and Stop pulses with 2.5 ns time resolution using an innovative approach that does not require the resources needed for traditional precision timing. First, a coarse time measurement τ_{COARSE} is derived (Fig. 23, bottom panel) by counting the number of elapsed 25 ns periods of a 40 MHz clock between the clock's first rising edges after receipt of a Start pulse and after receipt of a Stop pulse. Two fine timing values are then derived: the time $\tau_{\text{FINE\_ST}}$ between the receipt of the Start pulse and the start of the first clock pulse, and time $\tau_{\text{FINE\_SP}}$ between the receipt of the Stop pulse and the start of the last clock pulse. Using this scheme, the measured TOF is derived by adding $\tau_{\text{FINE\_ST}}$ to τ_{COARSE} and subtracting $\tau_{\text{FINE\_SP}}$ from τ_{COARSE}. The particle TOF is therefore

$$\tau_{\text{TOF}} = \tau_{\text{FINE\_ST}} + \tau_{\text{COARSE}} - \tau_{\text{FINE\_SP}} - 10\ \text{ns} \tag{1}$$

where the 10 ns delay line added to the Stop signal is also included.

The fine timing is enabled by inputting the Start or Stop signal into a delay line with 10 taps at intervals of 2.5 ns. As the signal propagates with time along the tapped delay line,

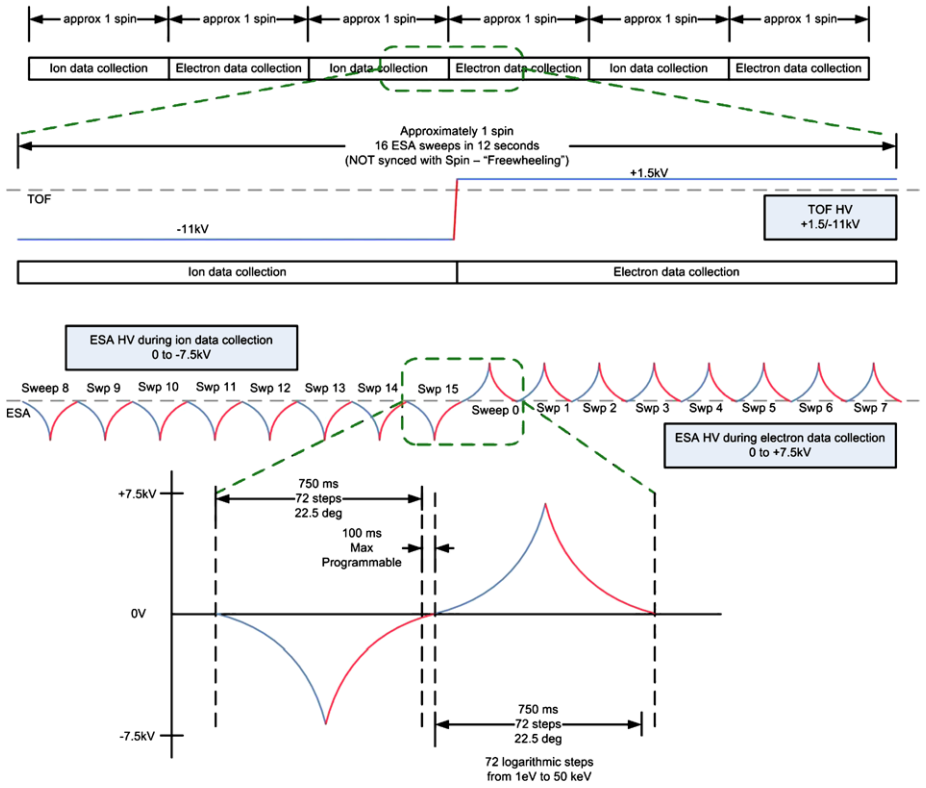

Fig. 22 Timing diagram for a series of HOPE spins and ESA sweeps. Electron and ion frames are acquired over alternating sets of 16 full ESA sweeps. A Master Frame is composed of one electron and one ion frame and is acquired over 24 sec based on $\tau_{\mathrm{ESA\_STEP}} = 10.417$ ms

the taps sequentially register a high state in the FPGA. At each leading edge of the 40 MHz clock pulse, the TOF FPGA polls its tap inputs for high states. If one or more high states are present, the number N_{Hi} of high input states is counted and reported. The fine resolution time measurement is simply $\tau_{\mathrm{FINE}} = 2.5\ \mathrm{ns} \times N_{\mathrm{Hi}}$.

Figure 23 (bottom panel) illustrates the measurement of an ion whose TOF in the Drift Box is $\tau_{\mathrm{TOF}} = 95$ ns. The Start pulse enables coarse counting of the 40 MHz clock pulses. It additionally registers high tap states in the FPGA, which are then counted at the leading edge of the first clock pulse; the six high states at 2.5 ns each yields $\tau_{\mathrm{FINE\_ST}} = 15$ ns. The coarse counting 40 MHz clock pulses continues until a Stop pulse is registered, and the number of counted clock pulses (4×25 ns) yields $\tau_{\mathrm{COARSE}} = 100$ ns. Finally, the number of high states (4×2.5 ns) in the Stop taps at the last rising edge of the clock is counted, providing $\tau_{\mathrm{FINE\_ST}} = 10$ ns. The ion's TOF, including the initial 10 ns time delay applied to Stop signals, is therefore $\tau_{\mathrm{TOF}} = 95$ ns.

An event is registered when a start pulse and/or a stop pulse is registered. Eight event counters are used to track all events at each energy step and each of the five polar pixels. The logical sequences that increment each counter are illustrated in Fig. 24. Every Start and Stop count increments the Start and Stop counters, respectively. Additionally, an event is classified by one of six possible outcomes: valid τ_{TOF} events falling within the H^+, He^+, and O^+ TOF windows; invalid τ_{TOF} events in which a Stop is recorded within 160 ns of the Start

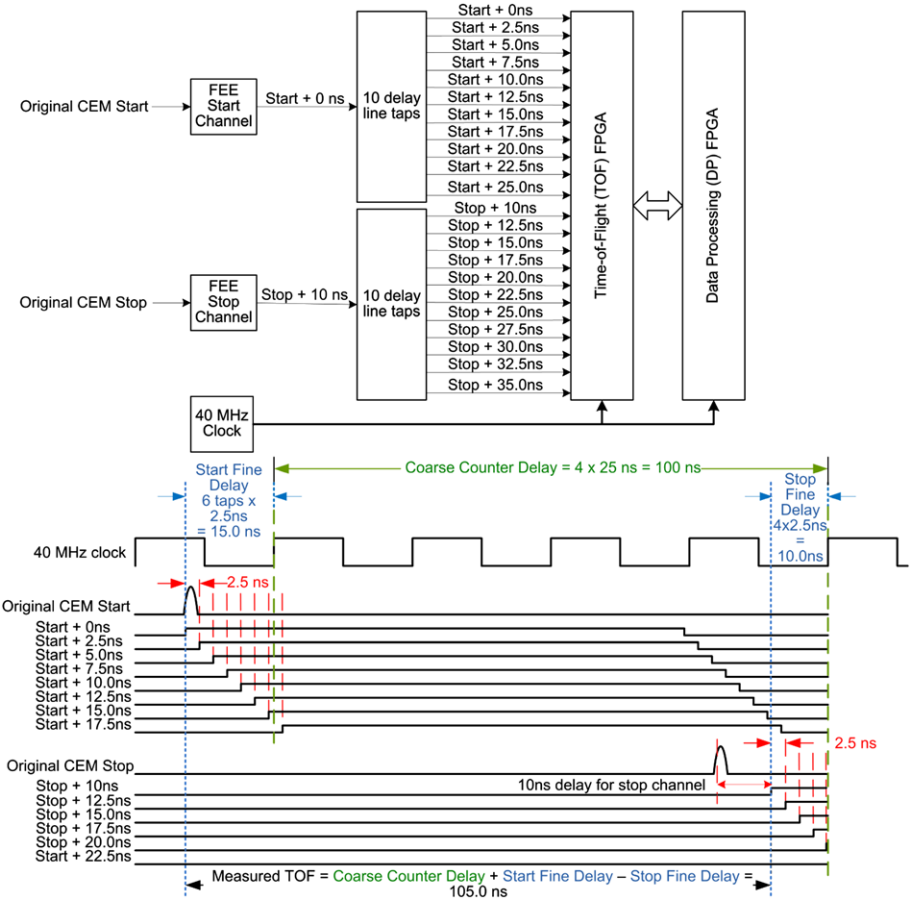

Fig. 23 Block diagram and timing diagram illustrating the time-of-flight calculation algorithm in the TOF FPGA for an ion with a measured 115 ns TOF. The 4 coarse counts of 40 MHz clock periods (25 ns each) and the fine measurements of six and four 2.5 ns intervals registered for the Start and Stop combine to result in a measured TOF of 105 ns. A 10 ns delay is added to the Stop signal before it is input into the TOF FPGA to ensure that the Stop signal is registered after the Start signal; the actual particle TOF in the Drift Box is therefore 95 ns

but does not fall within the H^+, He^+, and O^+ TOF windows; and Starts registered without a Stop within the following 160 ns; and Stops with no Starts registered within the preceding 160 ns. The TOF window for each species is set by the TOF LUT for each energy step. Because τ_{TOF} of incident electrons is short and no other species are present, the classification scheme in electron mode is simpler; electron TOF is short, and all longer TOF events within 160 ns are retained as a measure of penetrating background. This scheme carries redundancy that can be used to check and validate the event electronics, if needed; specifically, the number of events from any three of the four event counters Start, Stop, Start-no-Stop, and Stop-no-Start can be used to calculate what should be observed in the fourth counter.

The range of expected TOF values for valid particles is 0–160 ns based on the length of the drift region and range of ion energies that HOPE will measure. The species is determined from a configurable lookup table (LUT) which outputs the calculated species based

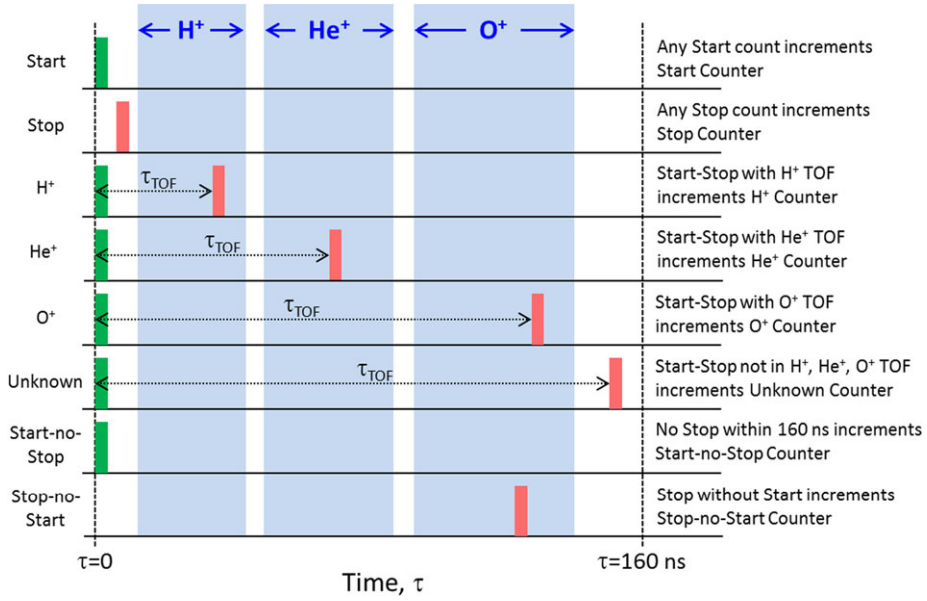

Fig. 24 HOPE uses eight types of counters for classification of events at each energy step for each polar pixel. Ion mode classification is shown. Every event increments either (or both) of the Start and Stop Counters and also increments one of six counters based on classification of the event as shown. The blue time-of-flight regions for H^+, He^+, and O^+ are unique for each energy step and are defined in a LUT

on the current energy step and the TOF value for a valid particle. For each of the five pixels, the TOF FPGA is able to account for all particles up to a 2 MHz constant periodic rate. After every ESA step, the TOF sends its counter information and two histograms to the DP FPGA. The DP FPGA stores the raw data into 2 × 512 kB ping-pong science memories, coordinated with ESA sweeping and ESA and TOF polarity changes that toggle between ion and electron modes.

The DP FPGA is capable of performing summing ("collapse") operations to stay within telemetry limits while retaining all acquired counts. For nominal science mode, adjacent ESA steps are summed so that the number of reported steps is reduced from 72 to 36. Independent of energy collapse, the DP FPGA can also collapse the reported azimuthal angles to reduce that dimension by factors of 2, 4, 8 or 16. In the nominal HOPE azimuth collapse scheme, schematically illustrated later in Fig. 35, polar pixels 1 and 5 (±72° polar angles) are each collapsed into 4 azimuthal bins, polar pixels 2 and 4 (±36°) are each collapsed into 8 azimuthal bins, and polar pixel 3 (0°) is not collapsed, retaining all 16 azimuthal bins. After collapsing, data compression from a 16-bit to 8-bit number can be performed via reconfigurable lookup table. The DP FPGA performs the collapse and compression processes "on-the-fly".

3.3.4 HOPE Operational Modes

The HEU controls the operational mode of HOPE as dictated by spacecraft commands, including the acquisition, processing and telemetering of science data to the spacecraft. The HEU reports health and safety data via engineering telemetry and performs autonomous saving actions. It also controls autonomous recovery from anticipated events such as thruster

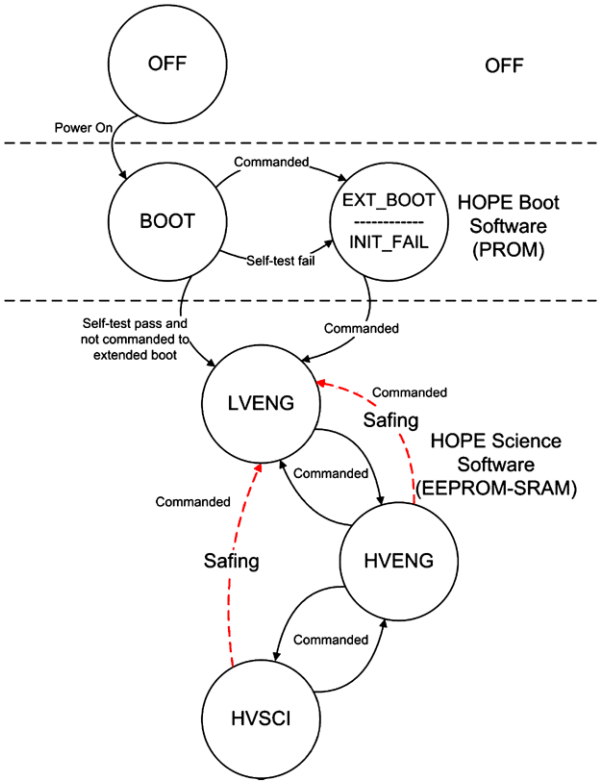

Fig. 25 HOPE mode transition diagram

firing so as to maintain high availability for science acquisition with minimal ground interaction. Timestamping of the science and engineering telemetry is synchronized with the 1-PPS and timestamp messages from the spacecraft. As the mission progresses, the HEU can be updated via configured changes to onboard flight software and lookup tables.

HOPE has four distinct modes of operation, whose relationships are shown in Fig. 25: the bootup phase (called BOOT) after initial power on; low-voltage engineering (LVENG), high-voltage engineering (HVENG) and high-voltage science (HVSCI). During nominal science operation (HVSCI), the HEU sets the bias $V_{\mathrm{CEM\_R}}$ of the CEMs at predetermined levels and controls the sweeping of the ESA and TOF during science acquisition. This activity is coordinated with the collection of the CEM output signals by the FEE, which converts those signals into digital pulses for the DB. The DB calculates the time-of-flight (TOF) between each pair of a start-stop CEM pixel set and organizes the data as various raw histograms, stored as a function of energy step and polar pixel. These raw histograms consist of eight event counters as described in Fig. 24. The flight software, which resides in the DB, coordinates the output of the science data via telemetry by instructing the DB to create a telemetry stream from the raw histograms by specifying a subset to be output. The amount of collapsing (i.e., summing of adjacent energy and azimuthal angle indices in the histogram) and 16-bit to 8-bit compression (via lookup table) are also specified.

Because different operational modes employ different combinations of circuits with different load levels, HOPE power consumption varies, with Boot and LVENG modes using 10.2 W, HVENG at 11.1 W, and HVSCI using 18.4 W.

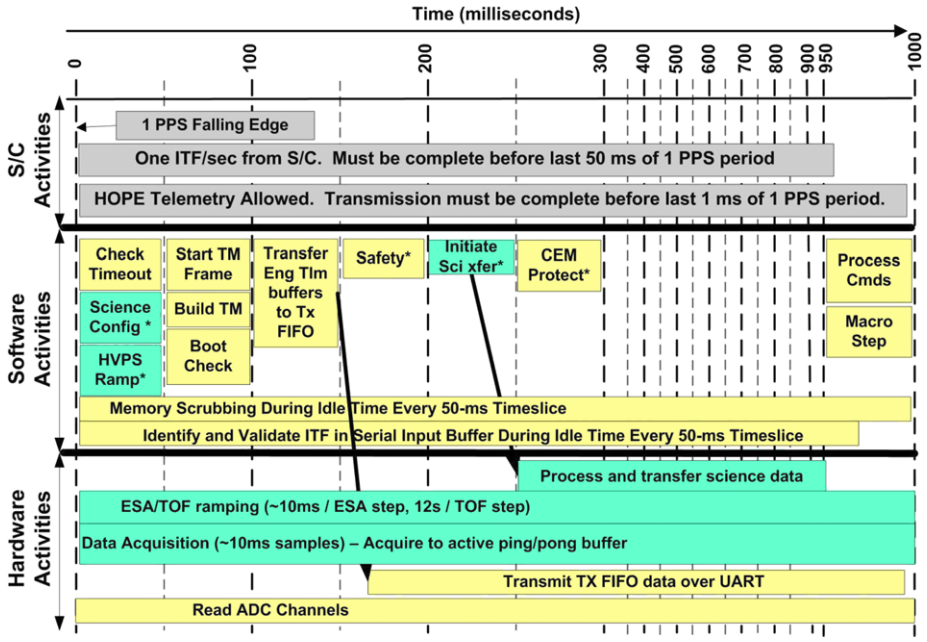

Fig. 26 One-second time-slice used for scheduling HOPE FSW tasks

3.3.5 Flight Software

The HOPE Flight Software (FSW) keeps track of the instrument mode; manages command, telemetry and synchronization interfaces with the S/C; manages science acquisition; maintains instrument integrity through scrubbing the memory and tracking health and safety; and executes recovery operations when applicable. The FSW runs on the Actel 8051 core that resides in the SI FPGA and is written in the C programming language. The code has a time-slice architecture which uses the 1-PPS signal from the spacecraft to synchronize its task timeline with an external reference. FSW tasks are assigned to one of twenty 50-ms time slices within the one-second period. An illustration is shown in Fig. 26.

The HOPE instrument is commanded via CCSDS command packets received through the S/C LVDS command interface.

To maintain configurability without needing to upload new code during ground and flight operations, the FSW manages a lookup table stored within HOPE in non-volatile EEPROM memory which has onboard parameter groups as shown in Table 5.

Data is collected and sent to the spacecraft during HVSCI operations using science acquisition plans and telemetry definitions. These settings include the ESA sweep table, the polarity (ions or electron mode), algorithm for collapse in energy or angle, selection of event counters sent for telemetry, and whether the EFW or EMFISIS burst flags are enabled. When a burst flag is detected and its corresponding burst flag is enabled, a different entry within the science acquisition plan table is chosen to run for a predetermined amount of time from a LUT entry; after this time expires, the operations revert to nominal HVSCI. The HOPE flight software and LUTs are sufficiently flexible that plans can be encoded to control HOPE to execute all currently envisioned HVSCI science acquisition and telemetry scenarios.

Table 5 List of HOPE LUT parameter groups

LUT parameter group	Description
Science acquisition plans	A series of steps executed during HVSCI defining data collection parameters and telemetry products output to the spacecraft
ESA and TOF high-voltage sweep tables	LUTs containing the DAC settings for the ESA and TOF HVPS during HVSCI sweep
Space weather telemetry configuration	Instructions specifying what information (e.g., species, energies) is placed into the Space Weather telemetry packet
Energy-TOF mapping to species	LUT for each polar pixel that associates a measured TOF with an ion species at each energy step.
TOF histogram sampling control	Table that controls the telemetry output of the raw TOF histogram data after all event counters have been telemetered
Data compression table	LUT used by the DB to convert 16-bit values to 8-bit values
Macros	A series of scripts containing sequenced HOPE commands
CEM protection levels	LUT of reduced CEM voltage levels after a thruster warning has been issued by the S/C
Engineering safety	LUT of all onboard engineering parameters and their red levels that can autosafe HOPE
Engineering configurable settings	Default engineering values at power-on

4 HOPE Performance

4.1 Performance Validation: Calibration

End-to-end HOPE performance is derived through a combination of component-level and subsystem-level tests, modeling and simulation that are subsequently empirically validated, and instrument calibration. Although calibration provides the most accurate description of instrument performance, it cannot provide a full picture of the instrument for two reasons. First, the parameter space covered by HOPE is large: 5 polar pixels, 72 energy steps, four species (e^-, H^+, He^+, O^+), and variable response in both polar and azimuth angles. This complexity precludes measurement of each unique parameter combination. In addition, determination of the instrument geometric factor for space plasmas, which uniformly fill a pixel in azimuth angle, polar angle, and energy, is not readily obtained from the monoenergetic, highly collimated ion beams available in the laboratory. Because of these limitations, laboratory measurements are used to validate the electron-optic model of the ESA subsystem, which is then combined with the sensitivity of the TOF subsystem derived from calibration. The instrument response over the full range of input particles (species, energy, polar angle, azimuth angle) is derived by interpolation and extrapolation of the combination of the ESA and TOF subsystem performances.

HOPE calibration was performed in three phases: prior to instrument environmental testing (Phase 1), after instrument-level environmental testing (Phase 2), and after detector refurbishment and flight HVPS installation that followed spacecraft-level testing (Phase 3). Engineering model HVPS were used for Phases 1 and 2; for spacecraft level testing between Phases 2 and 3, the flight detector assemblies were replaced with engineering model assemblies to prevent particulate, hydrocarbon, and water vapor contamination of the flight CEM detectors. Calibration was performed at the Los Alamos calibration facility using ion and electron beams, described in the Appendix. Because of its beam stability over time and

its central location in the HOPE energy range, a 10 keV H^+ beam was selected as the primary calibration fiducial energy and species for testing across all pixels, both instruments, and all calibration phases.

4.1.1 Energy and Angle Response

HOPE energy, polar angle, and azimuth angle responses are characterized using a monoenergetic beam at energy E_0 of electrons or mass-selected ions (H^+, He^+, and O^+). Because the polar angle θ follows the cylindrical symmetry of the ESA subsystem, the energy response is generally independent of polar angle. However, the energy and azimuth angle responses are strongly coupled, and we measure this coupled response by rotating the instrument through azimuth angle ϕ and scanning V_{ESA}. High-resolution scans were performed at azimuthal steps of 0.7° and using V_{ESA} steps of ∼20 V; scans at lower resolution were used to verify performance, e.g., during Phase 3 calibration. From these scans we derive the electrostatic analyzer k factor ($k = E_0/eV_{\mathrm{ESA}}$), energy resolution, azimuth angle resolution, and the coupled energy-azimuth angle response. Results are compared with SIMION model results to validate the electron-optic model used for calculation of the ESA subsystem geometric factor G_{ESA}.

These scans were performed using 10 keV H^+ for each polar pixel. In addition, measurements were made for 5 keV H^+, He^+, and O^+; 30 keV H^+ and O^+; and 45 keV H^+, He^+, and O^+ for a single polar pixel for each instrument. Electron scans were performed at 10 keV for three HOPE-A polar pixels, and at 5, 10, and 20 keV for a single HOPE-B polar pixel.

Figure 27 shows data from the high-resolution scans for HOPE-A and HOPE-B. The ion results are nearly identical to electron results, which are not shown. For each instrument the middle panel shows counts as a function of azimuthal angle ϕ and V_{ESA}. These plots clearly show the coupled energy-angle response characteristic of a top-hat electrostatic analyzer. The left and right panels show these data collapsed as a function of V_{ESA} and ϕ, respectively, and are used to determine the peak location and peak width of the response in both V_{ESA} and ϕ. These panels also show Gaussian fits to the collapsed data, which are used to quantify the response as a function of V_{ESA} and ϕ.

The results of the energy-angle scans are consistent throughout all calibration phases and across all polar pixels of both instruments. Based on average results, with extra weight given to the high-resolution scans, the calibration data yield $k = 7.035$ for both HOPE-A and HOPE-B. For comparison, SIMION simulations of the flight geometry yielded $k = 6.9$. The <2 % difference between calibration and SIMION simulations is consistent with tolerance stack-up in fabrication and assembly of the ESA subsystem, which was measured during flight assembly for both A and B flight units.

Polar angle (θ) scans were performed using a mono-energetic ion or electron beam at a fixed azimuth angle. Figure 28 shows high-resolution polar scan results from HOPE-A and HOPE-B, respectively, for 10 keV H^+ incident at azimuth angle $\phi = 0°$. Measurements were made at polar angle steps of 1°, and ion beam drift was monitored by periodically repeating the measurement at the center of Pixel 3 ($\theta = 0°$). Each panel shows data from both total Starts (black) and valid Coincidence counts (red).

These results show consistency of absolute response across all five polar pixels, as well as no overlap in the polar response between these pixels. Systematic pixel-to-pixel variations are observed at a level <5 %. The peak response of each polar pixel is within 1° of the locations ±72°, ±36°, and 0° predicted by charged particle optics modeling. HOPE-A polar pixels 1–5 were observed to have a maximum response for coincidences at polar angles

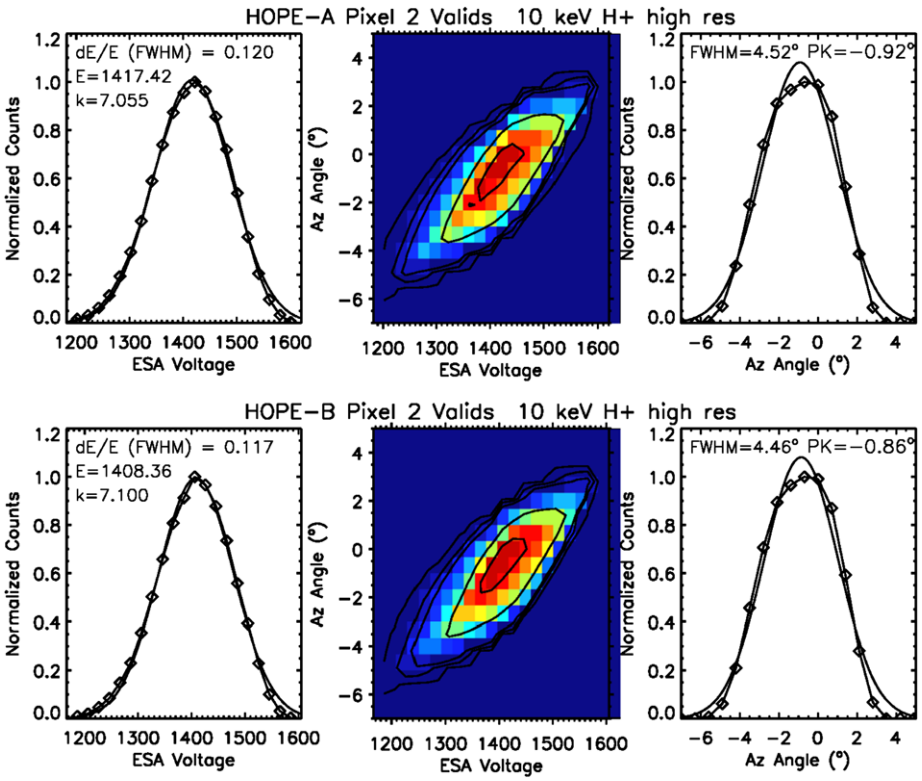

Fig. 27 HOPE-A (*top panels*) and HOPE-B (*bottom panels*) energy-azimuthal angle responses for valid coincidence events from the high-resolution energy-angle scan for incident 10 keV H^+

$+71°$, $+36°$, $0°$, $-35°$, and $-72°$; HOPE-B peak maxima were observed at polar angles $+72°$, $+36°$, $0°$, $-36°$, and $-71°$.

Precision alignment measurements were made for both flight instruments using a theodolite. One reference point was the ion beam, highly collimated by upstream apertures in the calibration facility. The second point was a mirror affixed to an external surface of HOPE and referenced to the HOPE-spacecraft mating surface. The instrument was oriented in the calibration chamber at the location of maximum response to the ion beam, and the orientation of the instrument relative to the ion beam was precisely measured; the resulting alignment offset of HOPE-A was $(\phi, \theta) = (-0.57°,\ -0.06°)$ and of HOPE-B was $(-1.22°,\ -0.15°)$.

4.1.2 Detector Gain

The CEM gain is set such that secondary electrons generated by incident ions or electrons in the TOF subsystem yield a pulse magnitude in the CEM that is larger than the lower level discriminator setting of the amplifier electronics. This level is attained by increasing the CEM bias until the count rate of valid events becomes approximately constant, independent of further increase in CEM bias. However, as a CEM ages, its gain decreases at a rate that primarily depends on the total charge output by the CEM over its lifetime. This gain decrease is typically compensated by periodically increasing the bias applied to the CEM. Regular gain calibration tests are scheduled throughout the RBSP mission. This is performed at a

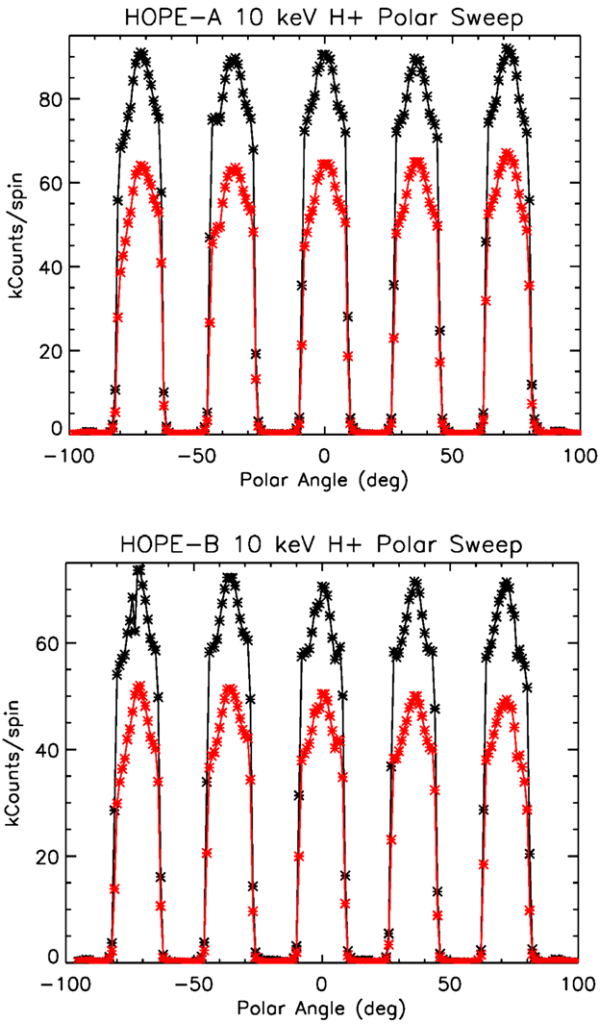

Fig. 28 HOPE-A (*top panel*) and HOPE-B (*bottom panel*) high-resolution polar angle (θ) scans across all five pixels in each instrument for incident 10 keV H^+. In each plot, the Start count rate is shown in *black* and the Coincidence rate in *red*

fixed ESA voltage level in ion and electron modes, with data collected over a range of CEM voltage levels.

Because CEMs can age differently, HOPE utilizes three different CEM bias supplies that service polar Pixels 1 and 4, Pixels 2 and 5, and Pixel 3. While the fronts of the CEMs are fixed at $V_{\mathrm{CEM\_F}} = +4.4$ kV, the adjustable voltage $V_{\mathrm{CEM\_R}}$ applied to the rear of the CEMs can be changed based on the gain calibration tests. The nominal voltage for HVSCI operation at commissioning is $V_{\mathrm{CEM\_R}} = +6.8$ kV. At this voltage, the lower level discriminator (LLD) is set at a value of 100 to retain nearly all real CEM pulses and exclude noise counts of lower pulse magnitudes. The LLDs have a large dynamic range (0-4095) to accommodate variations in CEM gain expected through the RBSP mission; we note that during calibration an LLD setting of 2500 eliminated all CEM pulses from being counted.

The CEMs were originally selected and matched as polar pixels based on similar gain curves and similar intrinsic impedances. The gain curves for each of the CEMs in the flight instruments acquired during Phase 3 Calibration are shown in Fig. 29.

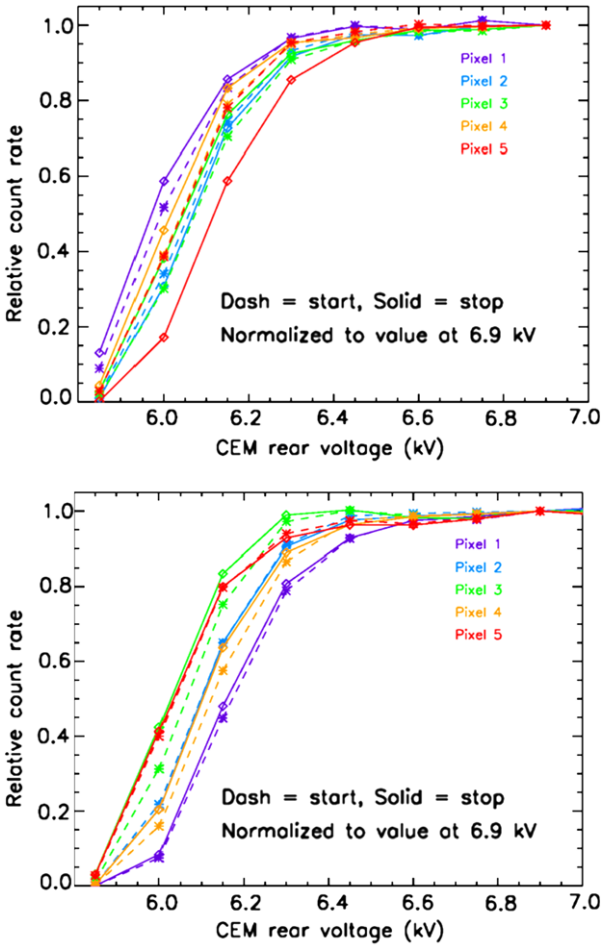

Fig. 29 Gain curves for HOPE A (*top*) and HOPE B (*bottom*). Start counts are shown with *dashed lines* and "*x*" *symbols*, stop counts with *solid lines* and *diamond* "◊" *symbols*. Each curve is normalized to a value of 1.0 at $V_{\mathrm{CEM\_R}} = 6.90$ kV

4.1.3 Sensitivity

Knowledge of the absolute coincidence detection efficiencies for each polar pixel is critical for deriving accurate distribution functions. In spite of the complexity of the TOF subsystem (including the electron-optics and the physical processes that govern secondary electron emission, the trajectories of incident particles in the TOF drift box, and individual CEM detector efficiencies), we can calculate the absolute detector and coincidence detection efficiencies for each polar pixel simply using the total Coincidence, Start and Stop counts over some time interval (Funsten et al. 2005). These values have been measured throughout calibration and will be monitored throughout the mission for each CEM detector. This technique was first incorporated on the IBEX-Hi energetic neutral atom imager (Funsten et al. 2009) and has been an important tool for quantifying, identifying, and monitoring different types of background in IBEX-Hi.

For each polar pixel, HOPE reports the number of total (coincident and non-coincident) Start counts C_{ST}, total Stop counts C_{SP}, and coincidence counts C_{COIN} over a particular time interval. The absolute Start and Stop detection efficiencies are $\varepsilon_{\mathrm{ST}} = C_{\mathrm{COIN}}/C_{\mathrm{SP}}$ and $\varepsilon_{\mathrm{SP}} = C_{\mathrm{COIN}}/C_{\mathrm{ST}}$, respectively. The instrument response is directly proportional to the absolute

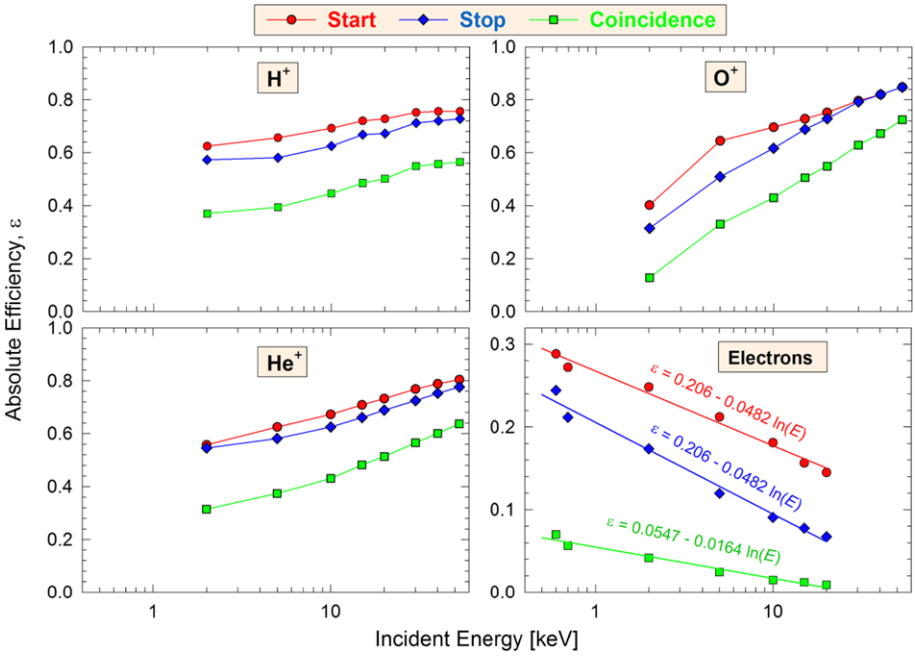

Fig. 30 Typical absolute detection efficiencies for incident ions (Polar pixel 3 of HOPE B) and electrons (Polar pixel 5 of HOPE-A). The Coincidence efficiency is the product of the Start and Stop efficiencies. Detector singles (non-coincident) counts and coincident counts are reported for all detectors throughout the mission, enabling monitoring of TOF subsystem performance and identification and quantification of background from penetrating radiation

coincidence efficiency $\varepsilon_{COIN} = \varepsilon_{ST}\varepsilon_{SP}$, which will likely change as the CEM detectors age during the mission. Typical efficiencies for HOPE are shown in Fig. 30. During times of low penetrating background, ε_{ST}, ε_{SP}, and ε_{COIN} are characteristic of the targeted ions or electrons being measured. In ion mode, the relative abundances of the ion species must be considered because the ion species have different detection efficiencies. To measure and monitor the absolute detection efficiency during the mission, we will target times of high H^+ abundance with low background count rates.

Penetrating background generates mostly non-coincident Starts and Stops, and a coincidence generated by a single penetrating particle will have a short TOF, similar to plasma electrons and fast protons. We therefore use Start and Stop singles rates and Coincidence rates in ion mode to monitor penetrating radiation in general and use long TOF measurements in electron mode as a consistency measurement of random coincidence from events generated by uncorrelated penetrating particles.

Figure 31 shows the measured absolute coincidence efficiencies derived for each polar pixel of HOPE A and B flight units both after environmental testing and after refurbishment of the CEM detectors. A polynomial fit to the measured values was derived for calculation of the absolute HOPE geometric factor. As the incident particle energy approaches 1 eV, the efficiency approaches a constant value because of acceleration into the TOF subsystem by $V_{TOF} = -11$ kV for ions and $V_{TOF} = +1.5$ kV for electrons. The data show consistent results at the two different calibration times across all pixels and between the HOPE A and

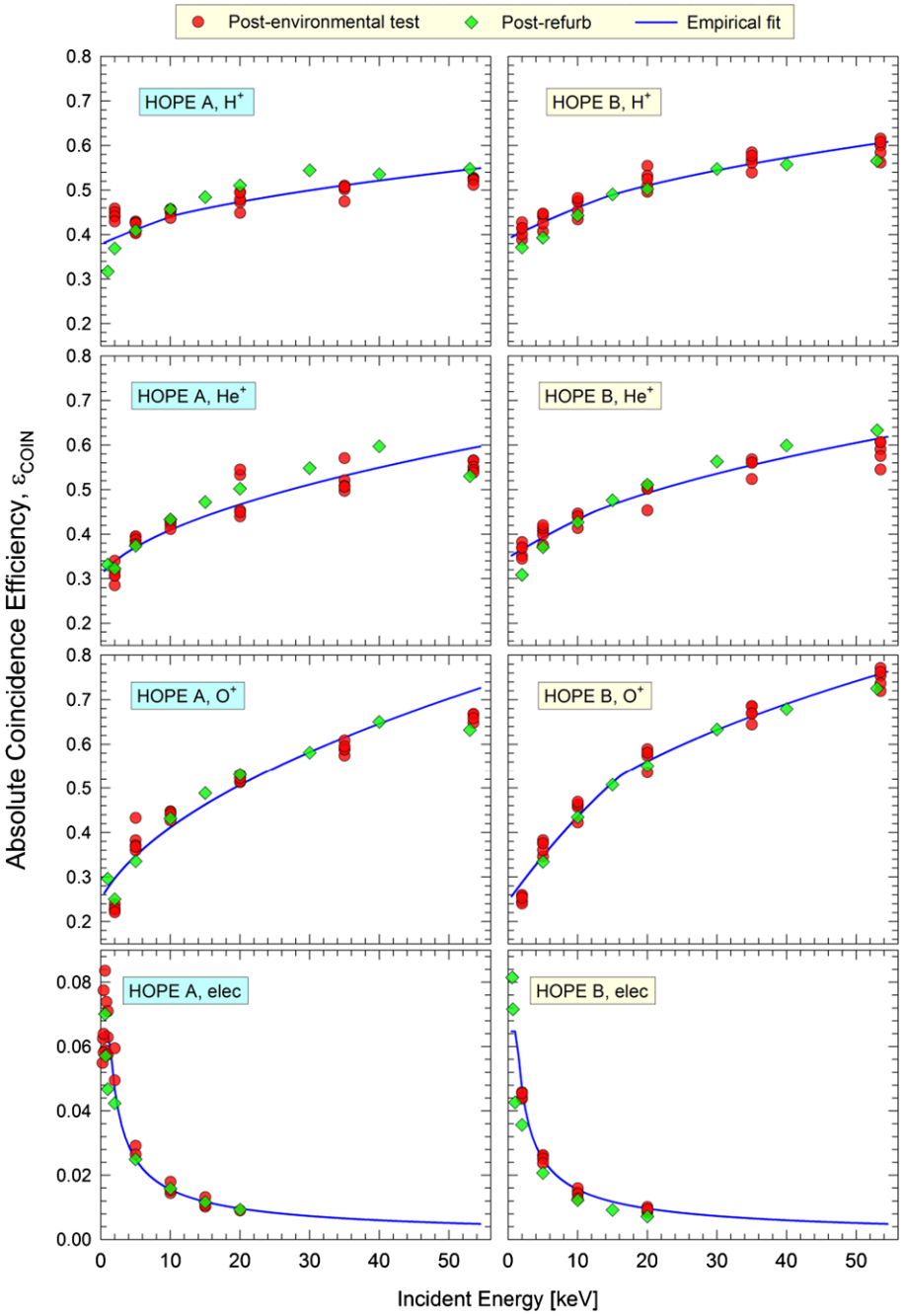

Fig. 31 Absolute coincidence detection efficiencies incident ions (*top three panels*) and electrons (*bottom panels*) for all pixels of HOPE A (*right panels*) and HOPE B (*left panels*). The *red points* are measurements acquired after environmental testing and the *green points* are derived from calibration after CEM detector refurbishment. The *blue lines* are empirical polynomial fits that are used in the calculation of the total HOPE Geometric factor

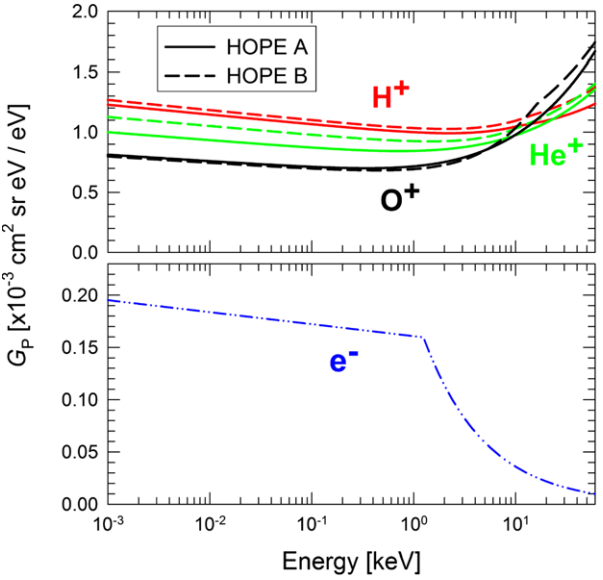

Fig. 32 HOPE geometric factor for each polar pixel is shown for ions (*top panel*) and electrons (*bottom panel*)

B flight units. The electron efficiencies of HOPE A and B were sufficiently similar so that a single polynomial function was used to describe the efficiencies for both instruments.

The HOPE geometric factor per pixel, which is the cumulative instrument response for conversion of instrument counts to ion or electron flux, is derived using

$$G_{\mathrm{P}} = \varepsilon_{\mathrm{COIN}} G_{\mathrm{ESA}} T_{\mathrm{G}} \tag{2}$$

where $T_{\mathrm{G}} = 0.7$ is the geometrical transmission of the grid on which the Start foil is attached, $\varepsilon_{\mathrm{COIN}}$ is obtained from Fig. 31, and G_{ESA} is obtained from Fig. 11. The resulting HOPE A and B geometric factors are shown in Fig. 32 for ions and electrons. Slight variations are observed between A and B flight units.

4.1.4 Species Identification

HOPE identifies species through time-of-flight measurement of species that have been filtered based on energy-per-charge in the ESA Subsystem. As previously described, HOPE represents the first use of CEM detectors for TOF mass spectrometry in space, and the mass identification performance of HOPE is an important validation of this technique. The HOPE mass resolution is a function of three processes: the energy resolution of the ESA subsystem; energy and angular straggling of ions in the foil; and the fundamental, energy-independent time dispersion $\delta\tau_{\mathrm{TOF}}$ of the TOF subsystem that includes secondary electron transport to the detectors, the temporal response of the CEM detectors, and the TOF electronics. We first present calibration data for a monoenergetic ion beam, then quantification of $\delta\tau_{\mathrm{TOF}}$ using commissioning data, and finally TOF spectra from commissioning.

The governing equation for the HOPE mass spectrum for an ion with energy E at the HOPE aperture entrance is:

$$m\ [\mathrm{amu}] = 2u\left(\frac{\tau_{\mathrm{TOF}}\ [\mathrm{ns}] - 10\ \mathrm{ns}}{d\ [\mathrm{cm}]}\right)^2 \left(E\ [\mathrm{keV}] + \left|eV_{\mathrm{TOF}}\ [\mathrm{kV}]\right| - E_{\mathrm{F}}\ [\mathrm{keV}]\right) \tag{3}$$

where τ_{TOF} is the measured particle TOF, 10 ns corresponds to the delay line incorporated into the Stop electronics, d is the pathlength of the particle in the TOF box (~3 cm), $e = 1$ is the electron charge, and the constant $u = 9.58 \times 10^{-4}$ represents all unit conversions. The ion energy at the exit surface of the foil is the sum of its initial energy and additional acceleration by the bias of the TOF, less the energy loss E_F in the foil. Because the ion speeds are generally less than the Bohr velocity, we approximate a velocity-proportional energy loss in the foil (Lindhard et al. 1963) using

$$E_F = k\left(E + \left|V_{TOF}\ [\mathrm{kV}]\right|\right)^{1/2}. \tag{4}$$

which has been shown to reasonably represent energy loss in a foil (Allegrini et al. 2006).

In practice, m is not a discrete function, rather a continuous function driven by uncertainties or dispersion in τ_{TOF}, E, d, and E_F. Figure 33 shows HOPE mass spectra m for incident $^1H^+$, $^4He^+$, and $^{16}O^+$ at incident energies 2, 5, 10, 20, 30, 40, and 53 keV. The TOF spectra were acquired using from HOPE-B, Pixel 3 measured during Calibration Phase 3. We fit and normalize the data using an asymmetric Gaussian distribution (Stancik and Brauns 2008) to the mass spectra derived using (3):

$$m_F = A \exp\left(-\ln(2)\gamma^2\left(\frac{m - m_0}{m_W}\right)^2\right). \tag{5}$$

where m_0 is the location of the peak maximum and m_W is a width parameter of the mass peak. The asymmetry function is $\gamma = 1 + e^{a(m-m_0)}$, and the asymmetry parameter is a. The direction of skewness is reflected in the sign of a, and, when $a = 0$, the peak is Gaussian and m_W corresponds to the full-width-at-half-maximum of the mass peak. The fit to this equation is shown in top panel Fig. 33 using values of $k = 0.2$, 0.7, and 2.6 for H^+, He^+, and O^+, respectively, in Eq. (4). These mass spectra were obtained for monoenergetic ion beams directed into HOPE B, Pixel 3, and thus contain all effects that contribute to uncertainty in the mass spectrum except for the energy response of the ESA subsystem. The peaks are well-resolved over most of the energy range. The precise mass location of the maxima of the peaks varies slightly with energy, which is the result of inaccuracy of the asymmetric Gaussian fit as well as second order effects of energy loss not captured in the generic form of Eq. (4).

The only uncertainty not included in the mass spectra derived using a monoenergetic ion beam (top panel of Fig. 33) is the energy passband of the ESA subsystem. The first order Taylor Series expansion of Eq. (3) (McComas et al. 1990) yields mass uncertainty $\Delta m/m \sim \Delta E/(E + |eV_{TOF}|)$ directly associated with the uncertainty in ion energy at the entrance surface of the foil, which is exclusively due to the ESA energy response. From this equation and noting that $\Delta E_{FWHM}/E \approx 0.12$ for the HOPE ESA subsystem, it is clear that the width and shape of the ESA energy passband, and thus its impact on mass resolution, becomes small at low energies due to the acceleration of the ions by the bias applied to the Drift Box. The bottom panel of Fig. 33 shows the intrinsic HOPE mass resolution derived by convolving the (approximately) Gaussian energy response of the ESA subsystem described in Sect. 4.1.1 with the asymmetric Gaussian fits to the mass peaks derived for a monoenergetic ion beam (top panel). This bottom panel therefore includes all effects that contribute to the HOPE mass resolution. The mass peak corresponding to O^+ is distinct from H^+ and He^+. The H^+ and He^+ peaks are well-separated except at the highest energies. When the H^+ abundance is high relative to He^+ at these higher energies, the He^+ peak becomes a shoulder on the H^+ peak, and the analysis summarized in Fig. 33 forms the basis for determining the

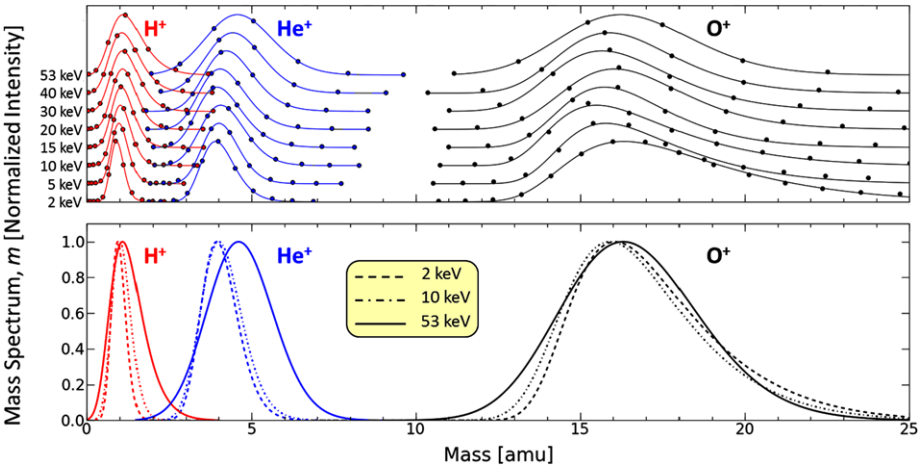

Fig. 33 (*Top panel*) Stacked TOF spectra derived for a monoenergetic beams of 2.0–53.5 keV H^+ (*black*), He^+ (*blue*), and O^+ (*red*) for HOPE B, Pixel 3. TOF spectra for other pixels for both HOPE-A and HOPE-B are similar. TOF data is converted to mass using Eq. (3). The *solid lines* are empirical fits to the data using an asymmetric Gaussian distribution (Eq. (5)). (*Bottom panel*) The convolution of asymmetric Gaussian fits of the mass spectra with the Gaussian energy response function of the ESA subsystem results in mass spectra *m* that include all processes in HOPE that contribute to the instrument mass resolution

He^+ abundance. When compared to the top panel, the slight increase in widths of the H^+ and He^+ mass peaks at 53 keV in the bottom panel is due solely to due to the width of the energy passband.

The dominant effect governing the HOPE mass resolution is the cumulative time dispersion $\delta\tau_{TOF}$ of the TOF subsystem and the timing electrons. While $\delta\tau_{TOF}$ is generally independent of the incident particle mass and energy, a multitude of processes contribute to it, including scatter-induced pathlength differences of particles after exiting the foil, transport time variation of both Start and Stop electrons from their emission to their detection, timing jitter of each CEM detector, variation of propagation times of pulses between detectors of a single polar pixel, and timing variations within the timing electronics for each of the pixels. The TOF time dispersion becomes increasingly important for shorter TOF measurements (i.e., light ions at high energies), for which the time dispersion becomes a significant fraction of the uncertainty, contributing to the observed widening of the mass peaks of both H^+ and He^+ at higher energies in the top panel of Fig. 33.

The time dispersion $\delta\tau_{TOF}$ of the TOF Subsystem and the timing electronics can be derived from the TOF spectra acquired in electron mode. The electron TOF across the 3 cm TOF drift region is short (0.92 ns at 1.5 keV and 0.61 at 52 keV) compared to $\delta\tau_{TOF}$ and has minimal variation from energy lost by transit through the foil. Thus, incident electrons provide a nearly simultaneous stimulation of Start and Stop electrons, and variations in the TOF spectra produced by these electrons reflects the cumulative time dispersion of the entire subsystem. Figure 34 shows a TOF spectrum acquired in electron mode from all HOPE A pixels during commissioning. At each energy, the counts in the TOF spectrum are normalized to a maximum value of one for easier comparison across energies. As expected, the electron peak is clearly observed at $\tau_{TOF} > 10$ ns, which corresponds to the 10 ns time delay of the delay line in the Stop timing electronics that was incorporated to account for $\delta\tau_{TOF}$ and to ensure a Start pulse is registered before a correlated Stop pulse.

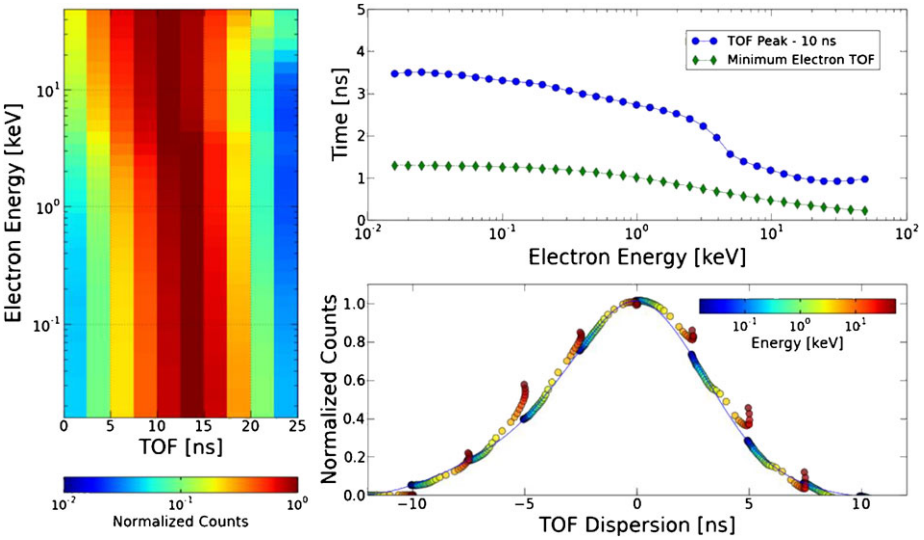

Fig. 34 HOPE TOF performance is demonstrated using TOF spectra in electron mode normalized to unity at each energy (*left panel*) acquired during HOPE commissioning. The location of the TOF peak (*blue curve*) is energy dependent (*top right panel*), and correcting for this time shift yields overlapping TOF spectra (*bottom right panel*) that reflect the fundamental time dispersion $\delta\tau_{\mathrm{TOF}}$ of the TOF subsystem

At each electron energy, we fit a Gaussian peak to the TOF peaks to find the time $\tau_{\mathrm{MAX}}(E)$ corresponding to the maximum counts. The blue curve of Fig. 34, upper right panel, shows $\tau_{\mathrm{MAX}}(E) - 10$ ns, which is a factor of ~2.5 above the calculated electron TOF at its incident energy across the 3 cm of the Drift box (green curve). The difference between the measured TOF of the peak maximum and the calculated location can be attributed to an additional ~1 ns systematically observed over all pixels at the highest electron energies and, at lower energies, energy loss of the incident electron in the foil. After shifting in time the spectrum at each energy by $\tau_{\mathrm{MAX}}(E)$, the TOF spectra at each energy overlap in time as shown in Fig. 34, bottom right panel. The peaks at higher incident electron energy show a slightly wider peak than at lower energies; this likely arises because the higher energy peaks have fewer total counts, and the peak is influenced by the underlying penetrating background which has a similar TOF spectrum and should be uniform in magnitude across all energies. We also note that these TOF peaks include the range in TOF from the different electron energies that are accepted within an individual energy passband; this is a small effect but is largest at the highest energies because the 1.5 keV TOF box bias in electron mode efficiently accelerates low energy ions to nearly the same energy. We fit a single curve to the composite TOF peaks for all incident electron energies less than 11.5 keV using a cubic spline interpolation and obtain the following full widths that characterize $\delta\tau_{\mathrm{TOF}}$: 7.9 ns at half-maximum, 11.8 ns at the 25 % level, and 10 % = 15.7 ns at the 10 % level. This is the primary metric for the mass resolution of the HOPE mass spectrometer.

HOPE commissioning also provided the first complete ion TOF spectra, which are more closely representative of the HOPE performance in space than calibration data because the source ion population is broadly distributed in energy and over incident polar and azimuthal angles. Figure 35 shows an ion TOF spectrum from all five pixels of HOPE B. H^+, He^+, and O^+ are clearly observed. For these spectra, in which the He^+ abundance is low compared to the H^+ abundance, the He^+ peak is distinct from the H^+ peak for energies ≤20 keV; at

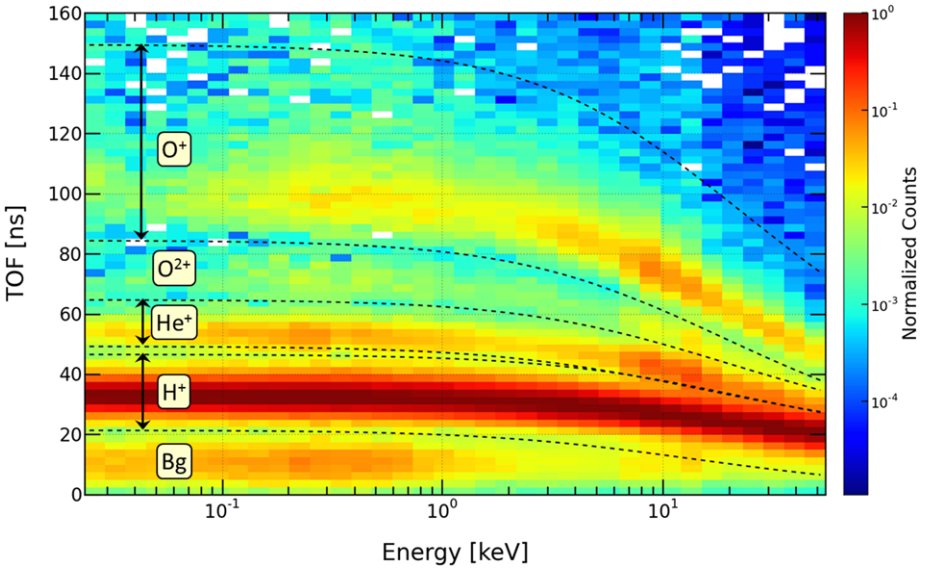

Fig. 35 HOPE A ion TOF spectra acquired over all five pixels. Counts at each energy passband have been normalized to the maximum counts observed for H^+. The upper and lower TOF boundaries for H^+, He^+, and O^+ that are used for defining the TOF LUT are shown as *black dashed lines*. O^{2+} is also clearly observed but is not reported by HOPE as a distinct species. The background (labeled as Bg) from penetrating radiation has a short TOF spectrum similar to electrons

higher energies, the He^+ peak becomes a shoulder of the H^+ peak and thus requires a more sophisticated abundance algorithm, based on calibration results, to quantify the relative H^+ and He^+ abundances. O^{2+} is also clearly observed, but its abundance is comparatively small and is not tracked as a species identified *in situ* by HOPE. Because of the speed at which penetrating radiation traverses the TOF drift region, its TOF is characteristically short and similar to electron TOF spectra. The short TOF peak characteristic of penetrating radiation is also clearly observed in the spectra.

Composition information is obtained *in situ* by binning the data on board the spacecraft by TOF value in three time windows. A unique timing window with minimum and maximum byte values is defined for each of the three ion species H^+, He^+, and O^+. The binning is performed by an onboard look up table (LUT), which allows for different binning for each polar pixel and each energy step. We use the H^+, He^+, and O^+ TOF peaks in Fig. 35 to derive empirical functions that are used to define the minimum and maximum TOF boundaries of the HOPE LUT. These are listed in Table 6 and shown as the dashed lines in Fig. 35 for nominal HOPE operation with $V_{\mathrm{TOF}} = -11.0$ kV. These time values are converted to TOF byte values for incorporation into the LUT.

HOPE routinely provides full TOF spectra such as in Fig. 35 for two polar pixels per spacecraft spin, accumulated over all energies for a single azimuthal sector. TOF spectra are acquired for the other polar pixels over subsequent spins, enabling long-term monitoring of the TOF measurement integrity, monitoring penetrating background at short times-of-flight, and for analysis of, for example, O^{2+} that is not reported as a unique ion species. The TOF byte values in the LUT are identical for both HOPE A and B and have been updated based on analysis of the HOPE commissioning data. These LUTS can be modified in the future

Table 6 Ion species time-of-flight definitions for both HOPE A and B time-of-flight LUTs

τ_{TOF} [ns] $= a_1 + \frac{a_2}{\sqrt{a_3 E \text{ [keV]} \pm V_{TOF}\text{[kV]}}}$

Species	Boundary	a_1	a_2	a_3
H^+	Min	−1.02	74.2	1.630
	Max	11.78	115.4	0.861
He^+	Min	15.65	111.5	1.480
	Max	14.73	166.0	1.120
O^+	Min	8.18	253.0	1.180
	Max	18.18	435.6	0.969

to accommodate any changes needed based on evolving scientific objectives or changes in HOPE operational parameters.

4.1.5 Backgrounds and Noise

The response to UV light was measured using a 5 W, 195 nm mercury lamp. Both HOPE-A and HOPE-B showed fewer than 2.5×10^{-13} singles counts per photon, and no coincidence counts were observed. These count rates meet the HOPE requirements, which assume a geocoronal Ly-a flux of 10^9 photons/cm^{-2} s^{-1} sr^{-1}.

The intrinsic HOPE detector noise during calibration was quantified by examining CEM counts in the absence of particle input. With no incident ions or electrons, each pixel showed 10–100 Hz of singles (Starts or Stops) noise counts. This represents <1 count for each individual 10.4 ms energy step accumulation interval. Start noise counts were generally observed to be slightly higher than Stop noise counts, typically by factors of no more than 2–3. Coincidence counts are even lower, typically <2–30 Hz. These noise rates were monitored throughout instrument testing and calibration for both HOPE-A and HOPE-B. Some temporal variation as well as variation between polar pixels was observed.

The HOPE response to an energetic particle background was determined by measurements in the presence of a radioactive source. This test measured the signature of penetrating radiation in HOPE in electron and ion modes. During calibration, a 15 mCi ^{60}Co source was placed at the exterior surface of a 1.27-cm-thick vacuum chamber glass window, 11.2 cm from HOPE-A. The 1.17 and 1.33 MeV γ-rays are a reasonable proxy for penetrating radiation because they generate photoelectrons and subsequent secondary electron showers deep within the instrument. HOPE-A was operated with the source absent and present in a neutral state in which $V_{TOF} = 0$ kV, in electron mode with $V_{TOF} = +1.5$ kV, and ion mode with $V_{TOF} = -11$ kV.

Figure 36 shows coincident count rates (left panel) and singles count rates (right panel) for these three operational configurations. Measurements when the source was present are indicated by shaded regions; measurements when the source was removed are shown with a white background. The presence of the source clearly has a significant effect on the instrument count rate, although some variation of background independent of source present is observed over the test interval. Count rates were consistent across all five polar pixels and highest in Pixel 3, as expected since it was closest to the source. The presence of the source resulted in additional Start and Stop counts at a rate of 200–500 Hz, with the Start and Stop count rates similar for electron mode and Stops consistently higher than Starts for ion mode. The coincidence rates, typically <5–50 Hz for all pixels, were significantly higher in electron mode than ion mode.

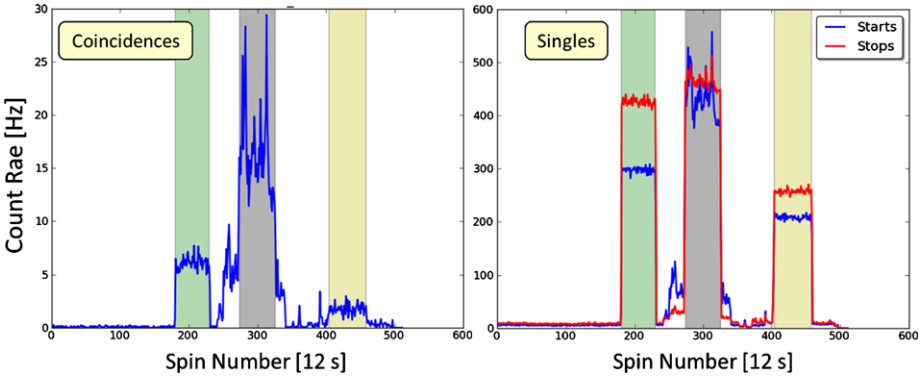

Fig. 36 Coincident (*left panel*) and singles (*right panel*) count rates for HOPE-A Pixel 2 during exposure to a ^{60}Co γ-ray source, which serves as a proxy for penetrating radiation. Neutral state ($V_{\mathrm{TOF}} = 0$ kV) measurements are shown *in green*, electron mode with $V_{\mathrm{TOF}} = +1.5$ kV *in gray*, and ion mode with $V_{\mathrm{TOF}} = -11$ kV *in yellow*. Times with white background are with no source present

Geant4 modeling of HOPE of this test geometry and ^{60}Co source strength (including attenuation in the vacuum window) predicted singles Start and Stop count rates of ∼400 Hz, similar to the observed counts. As described previously in the Penetrating Radiation Analysis section, the same Geant4 modeling of HOPE in the radiation belts predicted a background coincidence rate due to penetrating radiation at <1 Hz. This combination of measurements and analysis thus confirms that HOPE is sufficiently insensitive to the expected energetic particle background of the radiation belts.

4.2 HOPE Observation Strategy

HOPE has several operational modes that we now describe.

4.2.1 HVSCI: Normal Science Mode

Because of the complexity of synchronizing HOPE stepping supplies with a spacecraft-provided spin pulse, HOPE uses its own clock to cycle voltages and to toggle between ion and electron mode. Data are collected on a fixed time cadence that depends on the duration of an energy step $\tau_{\mathrm{ESA\_STEP}}$, with the ∼12 sec electron and ion frame acquisition time designed to be close to the nominal spacecraft spin period. This scheme simplifies the high voltage operations since each plasma measurement always has a fixed duration. Another consequence of this timing cadence is that the HOPE telemetry rate is solely based on the time interval of a HOPE energy step, regardless of spacecraft spin rate. We note that $\tau_{\mathrm{ESA\_STEP}}$ is adjustable over a limited range, and in flight we set this value such that a HOPE data frame is comparable to the actual spacecraft spin (spin rate predicted to be between 4–6 RPM). The following discussion of data projects assumes a nominal 12 sec spacecraft spin period.

The HOPE mass spectrometer measures ions and electrons during alternate spins, and a HOPE Master Frame in nominal science mode is therefore composed of a pair of consecutive ion and electron data frames. A Master Frame is acquired over ∼24 sec.

Each data frame is divided into 16 azimuthal sectors, with data collected over the entire 72-step energy range for each sector (Fig. 37), giving a full energy spectrogram 16 times per data frame. However, because of telemetry limitations, in nominal HVSCI mode data from adjacent energy steps are combined on-board, and data are transmitted for the resulting 36

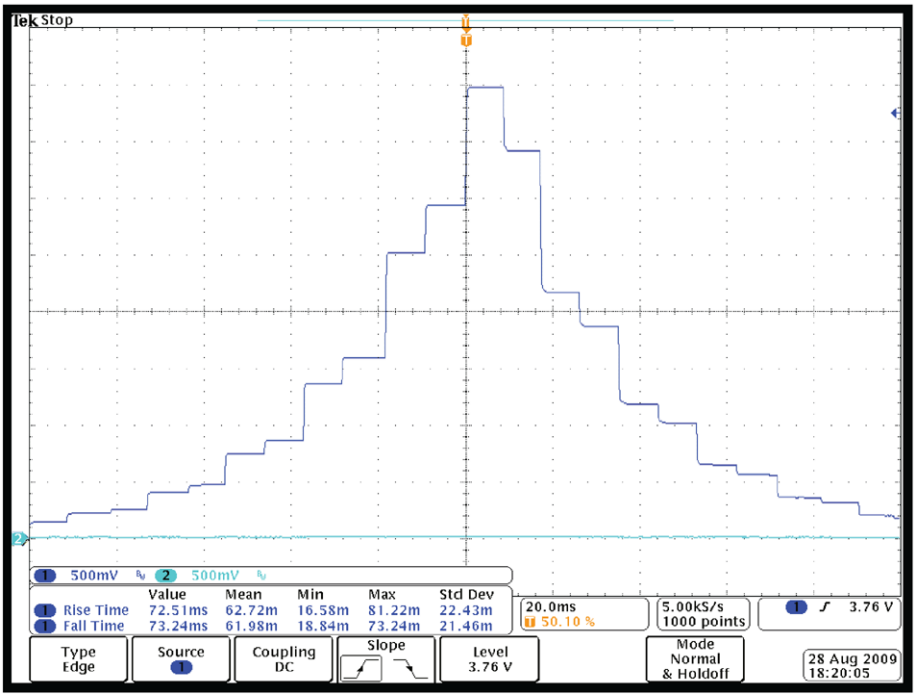

Fig. 37 This snapshot of the ESA voltage sweep in nominal HVSCI mode shows pairing of adjacent energy steps and interleaving of these pairs as the voltage is swept up and down. The time cadence of HOPE data acquisition is based on the time of a single energy step $\tau_{\mathrm{ESA\_STEP}}$

energy steps. Within each sector, voltages are stepped from 0 V to the maximum value (either negative or positive) and back down in an interleaved windshield-wiper mode, to ensure that the power supply is at 0 V when the polarity is changed. Of the 36 transmitted steps, odd-numbered steps are collected on the way up to maximum V_{ESA} and even-numbered steps on the way down as shown in Fig. 37. The 72 energies are thus measured in the order 1–2, 5–6, 9–10, …, 69–70, 72–71, 68–67, …, 8–7, 4–3.

As mentioned above, data from adjacent azimuthal sectors for some pixels are also combined, again for telemetry reasons, with a scheme that provides nearly equivalent solid angle measurements for each pixel as illustrated in Fig. 38. For the ±72° polar pixels, data from the 16 azimuthal sectors are combined in groups of 4, resulting in 4 azimuthal sectors per HOPE data frame. For the ±36° polar pixels, data are combined in groups of 2, resulting in 8 azimuthal sectors per HOPE data frame. Data from the 0° polar pixel retains the complete 16 azimuthal measurements.

The HOPE data collection was designed to be highly flexible to accommodate different measurement strategies that might evolve based on scientific discoveries throughout the mission. A single on-board LUT, which can be changed as necessary, includes voltage levels for each step, combinations of voltage steps for a full scan, and combinations of scans for a larger data collection plan. The LUT also includes energy and azimuthal summing information for each data collection mode. Table 7 shows the primary science data returned by HOPE, whose total telemetry allocation is 9.32 kbps.

For each polar pixel and azimuthal sector, both valid coincident and non-coincident (singles) counts are reported. A valid coincidence count corresponds to a detected particle whose

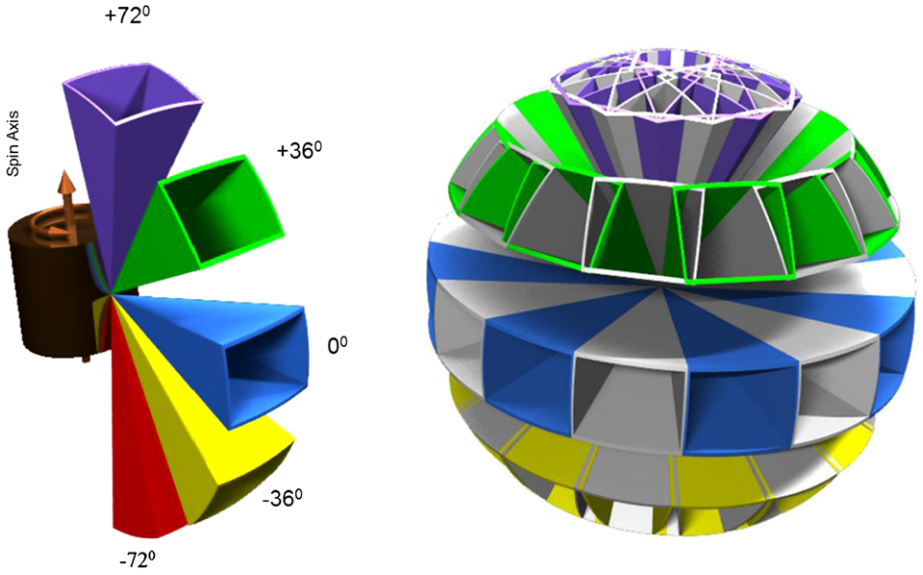

Fig. 38 The HOPE polar pixels (*left panel*) are centered at polar angles 0°, ±36°, and ±72°, where the 0° polar pixel views perpendicular to the spacecraft spin axis. Over a complete spin, measurements over 16 azimuthal sectors are accumulated. At higher polar angles, these azimuthal sectors overlap as shown in the *right panel*

Table 7 Primary HOPE science data

Data frame	Energy bins	Data products	Polar pixels	Average spin/azim sectors	Bits/ sample	No. per master frame[f]	Data rate [kbps]
Electron data frame	36	4[a]	5	8[c]	8	1	1.92
Ion data frame	36	5[b]	5	8[c]	8	1	2.40
Full TOF matrix	36	64	2[e]	1[d]	8	2	3.07

[a]Coincidence events inside and outside of TOF window, Start and Stop singles counts

[b]Coincidence events for H^+, He^+, O^+; total Start single counts; total Stop singles counts

[c]Data is acquired for all 16 azimuthal sectors for each polar pixel; azimuthal pixels are then combined from 16-16-16-16-16 to 4-8-16-8-4 for polar pixels located at −72°, −36°, 0°, +36° and +72°, respectively

[d]Option to select and cycle through specific pixels or azimuthal sectors

[e]1 polar pixel (= one angular sector) per 2 spins; cycles through all CEMs for ions and electrons every 10 spins

[f]Master Frame = 24 sec assuming 12 sec spin period. Complete ion and electron histograms are acquired during alternate spins

TOF lies within a defined TOF window for H^+, He^+, and O^+ in ion mode. In electron mode, valid electron counts correspond to coincident events within the short TOF window that is equivalent to the H^+ TOF bin in ion mode. Also in electron mode, coincidence counts within

a longer TOF window that is far beyond any realistic electron TOF are also reported as a measure of background coincidence rate, likely from penetrating radiation.

Total start and stop counts are also transmitted, and subtraction of valid coincident counts from the start and stop counts yields the singles (non-coincident) counts. Inconsistency of the singles counts relative to the expected valid coincidence counts based on derived composition provides yet another method to monitor background rates. Also, during times of minimal penetrating radiation, the singles and valid coincidence rates are the basis for calculation of the absolute efficiency of each of the detector pixels.

Full TOF spectra (64 TOF bins with 2.5-ns bin width) are transmitted at all 36 energies for a single spin sector per spin for 2 polar pixels. Over time, these spectra step through the polar pixels and over azimuthal sectors 0, 4, 8, and 12 (of the 16 possible sectors), providing TOF information over the full HOPE measurement space every 10 Master Frames. TOF spectra are collapsed in energy and azimuthal angle in the same way as the corresponding counters data. The exact number of reported full TOF spectra can be adjusted by the HEU to fill the available telemetry. All data undergo $15 \rightarrow 8$ bit compression to maximize use of the telemetry allocation. HOPE also routinely transmits housekeeping information, including instrument temperatures, high and low voltage levels, CEM current monitors, and CEM threshold levels.

4.2.2 Burst Support Mode

In addition to the routine data collection described above, HOPE can also collect data in a burst support mode. This mode is designed to enhance wave-particle interaction science by supporting the burst modes of the RBSP wave instruments, EMFISIS and EFW. HOPE burst support mode uses the same data packets and total data rate as nominal science operations, with onboard burst support LUTs used to select electron or ion mode, energy, and angle selection. Burst support mode can be initiated in two ways. In "synoptic" mode burst support data are collected at regular, pre-determined time intervals throughout the orbit. For initial operations, we plan to collect one burst support Master Frame every 633 s (once every 26 Master Frames).

In "triggered" mode, HOPE collects burst support data by responding to requests sent by the EMFISIS or EFW instruments in the shared spacecraft data packet. Requests from the waves instruments are limited to no more than 2 spins out of 60 sequential spins for each of the two instruments, to ensure that sufficient data are collected in normal science mode.

Up to seven unique burst support tables can be stored onboard HOPE, allowing flexibility in the data collection. In addition, these LUTs can be updated in flight if another scheme is deemed more useful. For example, for initial burst support operations, HOPE will operate using a LUT that measures only electrons at 9 energy levels over nearly the full HOPE energy range with high time resolution (0.1875 s per measurement) and with no azimuthal compression for any of the polar pixels. These measurements focus on rapid acquisition of a distribution function with meaningful information on the temperature anisotropy, which requires fitting a pitch angle distribution capable of distinguishing near parallel and near perpendicular energy spectra.

4.2.3 Space Weather Data Support

HOPE will provide data to the real time space weather telemetry stream, consisting of ion and electron counts at 4 energies. Nominal energies for these measurements are 0.25, 0.3, 10, and 40 keV. Measurements from Pixels 1, 2, 4, and 5 will be collapsed over all azimuthal

angles. Measurements from Pixel 3 will be provided in eight 45° azimuthal bins. Space weather data are generated at all times, but are based on energy steps from the nominal energy table. Thus at times when a different table is being used (i.e. burst support mode), these real time data will not represent the expected energies. Although the HOPE space weather data represent only a small fraction of the full HOPE data set, they provide a quick-look overview of particle distributions and their variability in real time. These data will be made available for real-time space weather modeling and forecasting efforts.

4.2.4 Data Processing Levels

The data continuously generated by the HOPE instrument will be stored on the satellite until daily contact with a ground station. The data will be then downlinked and stored under the control of the Mission Operation Center (MOC), which will transfer the data to the ECT Science Operation Center (SOC) at the Los Alamos National Laboratory. These data will be in the form of raw telemetry data, containing both science and housekeeping data used to monitor and maintain HOPE. The ECT SOC is responsible for the processing and disseminating the HOPE scientific data and data products, which includes applying the instrument response function and, with the HOPE team, validating the data. Higher-level products combine the data of all ECT instruments.

During normal mission operations, the MOC collects all raw telemetry during contact times and combines these data into a daily MET (Mission Elapsed Time) Level zero (L0) files. The ECT SOC obtains these L0 files as soon as they are available at the MOC, on a roughly daily cadence. The first processing step is to produce Level one (L1) data, daily files in UTC, that contain science data in count rates and state of health (SOH) data in engineering units on standard time tags.

Level two (L2) data is the first useable science data product and consists of instrument counts of L1 data converted to ion and electron flux as a function of energy, angle, and species by applying the HOPE instrument response function. Also included are estimates of backgrounds from penetrating radiation derived from HOPE. Validation of HOPE data occurs primarily using L2 data.

L3 and L4 data products incorporate data from other RBSP instruments such as local magnetic field direction, enabling higher level data products such as pitch angle distributions, moments, and L-shell association. L4 data products generate phase space distributions and incorporate regional and global models, such as magnetic field models. L3 and L4 use a common set of utilities and codes, since all ECT instrument data in L2 format have a high degree of commonality (count rates per detector, spin sector and energy).

5 Summary

The HOPE mass spectrometer has been designed to measure plasma electron and ion fluxes from 1 eV–50 keV and to distinguish ion composition of the three dominant species H^+, He^+, and O^+ within the harsh environment of the Earth's radiation belts. The HOPE measurement methodology and instrument design have been driven to reduce the potentially enormous background from penetrating radiation in the radiation belts. Measurements made by HOPE will thus enable discovery of the physical processes that drive the dynamics and evolution of the radiation belts.

Acknowledgements The HOPE mass spectrometer is the result of an outstanding collaboration between scientists, engineers, technicians, and support personnel at multiple institutions. In particular, we gratefully appreciate the seamless collaboration with the other instrument teams of the ECT instrument suite (at Aerospace Corporation and University of Colorado) as well as engagement, expertise, and specialty engineering provided by the broader RBSP team, primarily at APL/JHU. Work at Los Alamos National Laboratory was performed under the auspices of the United States Department of Energy under Interagency Purchase Request NNG07EK09I.

Appendix: LANL Space Plasma Instrument Calibration Facility

Los Alamos National Laboratory operates the Space Plasma Instrument Calibration Facility for test and calibration of space physics instrumentation, detector development and characterization, ultrathin foil characterization, and charged particle optics testing and characterization. The Facility consists of an ion accelerator, a Class 10,000 clean room, a nearby Class 1000 clean room, and a supporting lab in which a new electron cyclotron resonance (ECR) ion source, capable of generating ions and charge states characteristic of the solar wind, will be operational. All vacuum systems use hydrocarbon-free vacuum pumps (cryopumps or oil-free turbopumps) to prevent hydrocarbon poisoning of electron multiplier detectors such as microchannel plates (MCPs) and channel electron multipliers (CEMs). The facility has tested and calibrated numerous subsystems and instruments on NASA missions, including SWEPAM on ACE; SWOOPS on Ulysses; IMS and IBS on Cassini; GEM, GIM, and the Solar Wind Concentrator on Genesis; MENA on IMAGE; the TWINS neutral atom imagers; the IBEX-Hi neutral atom imager on IBEX; and the HOPE mass spectrometers on RBSP.

The ion accelerator provides a monoenergetic beam of atomic or molecular ions over a broad energy range 0.4–60 keV/q where q is the ion charge. It's microwave ion source (Leung et al. 1985; Walther et al. 1986) generates primarily $q = +1$ ions and a smaller fraction of $q = +2$ ions from both solid and gaseous sources. Advantages of this source over a duoplasmatron ion source include its high stability (beam current varies <5 % per hr), ease of use, low intrinsic energy spread of <2 eV (Chamberlin et al. 1987), ability to generate (and not fail during) oxygen beam operation (Walther et al. 1987), and extremely low maintenance requirements.

The ion beam is accelerated and focused using an electrostatic Einzel lens embedded in the accelerator column. The beam then enters a water-cooled electromagnet located 137 cm from the exit of the microwave cavity of the ion source. The electro-magnet has 5 exit ports located at bend angles of 0°, ±30°, and ±60° relative to the incident ion beam; two of these ports are dedicated beamlines, instrument calibration chamber (+60°, entrance is 242 cm from the exit of the electromagnet) and an experimental chamber (−60°, entrance is 172 cm from the exit of the electromagnet) for characterizing and testing smaller components and research devoted to development of new detection technologies. Adjustable apertures in the form of vertical and horizontal slits are located 46 cm upstream of the magnet entrance and 82 cm downstream of the magnet exit, in accordance with Barber's rule, i.e., the upstream and downstream transverse-beam focal points and the locus of the bend radius of the sector magnet all lie along the same line (Barber 1933). Quadrupole electrostatic deflection plates (two for vertical deflection and two for horizontal deflection) have inner radii 1.0 cm and length 17.8 cm and are located 100 cm after the exit of the electromagnet and ∼165 cm upstream of the aperture of an instrument in the calibration chamber. A DC voltage applied

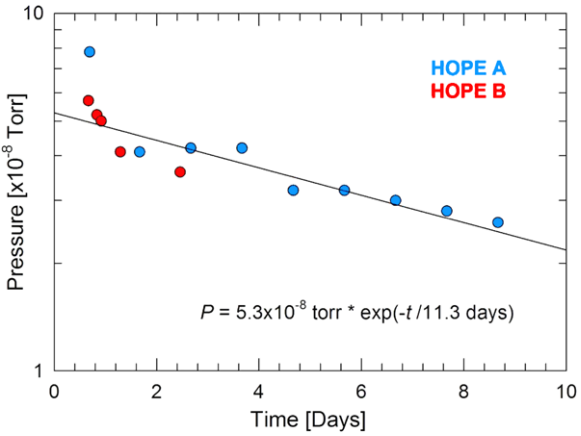

Fig. 39 The calibration chamber pressure is shown as a function of pumpdown time for the HOPE A and B flight units for Phase 3 calibration (after detector refurbishment and flight HVPS installation). After initial pumpdown, the pressure decreased with a characteristic time constant of 11.3 days

to these plates steers the beam, and a periodic bipolar triangular waveform voltage applied on top of this DC level (at slightly different vertical and horizontal frequencies) enables raster scanning of the beam over a broad area. The measured mass resolution of the accelerator is $m/\Delta m > 200$.

The intrinsic angular divergence of a typical ion beam is $\leq 0.07°$ at the instrument calibration chamber, as measured using an imaging microchannel plate detector located in the calibration chamber. The maximum divergence of the beam at the edge of a 2 cm wide aperture at the entrance of an instrument is 0.35°.

An electron source (Henderson et al. 2012) based on UV photoelectron emission from an aluminum photocathode was developed and used for HOPE electron testing and calibration. UV photons with sufficient energy to generate photoelectrons from an Al 6061 plate were generated using a light emitting diode (LED) (Thorlabs Model LED260W) and accelerated through a 12-in-dia aperture. The maximum electron energy attained was 20 keV. Helmholtz coils were installed to cancel the Earth's magnetic field and prevent deflection of the electron beam, enabling calibration at electron energies as low as 0.6 keV.

The calibration chamber is 1.4-m diameter $\times$1.0-m wide ($\sim$1500 liters). Three cryopumps are used for high pumping speed and for cleanliness, especially to minimize hydrocarbon contamination, to which CEM and MCP detectors are particularly susceptible. The chamber pressure was typically at 5×10^{-8} Torr with a flight instrument installed, and the pumpdown rates for the HOPE A and B flight mass spectrometers are shown in Fig. 39. The chamber has an instrument platform with computer-controlled polar, azimuthal, and linear (perpendicular to beam axis) motions. Vibration, shock, thermal, and EMI/EMC testing facilities in the same building complex were used for HOPE.

References

S. Agostinelli et al., Geant4—a simulation toolkit. Nucl. Instrum. Methods Phys. Res., Sect. A, Accel. Spectrom. Detect. Assoc. Equip. **506**(3), 250–303 (2003). doi:10.1016/S0168-9002(03)01368-8

F. Allegrini, D.J. McComas, D.T. Young, J.-J. Berthelier, J. Covinhes, J.-M. Illiano, J.-F. Riou, H.O. Funsten, R.W. Harper, Energy loss of 1–50 keV H, He, C, N, O, Ne, Ar ions transmitted through thin carbon foils. Rev. Sci. Instrum. **77**, 044501 (2006). doi:10.1063/1.2185490

P.C. Anderson, W.B. Hanson, W.R. Coley, W.R. Hoegy, Spacecraft potential effects on the Dynamics Explorer 2 satellite. J. Geophys. Res. **99**(A3), 3985–3997 (1994). doi:10.1029/93JA02104

D.N. Baker, J.B. Blake, R.W. Klebesadel, P.R. Higbie, Highly relativistic electrons in the earth's outer magnetosphere. I. Lifetimes and temporal history 1979–1984. J. Geophys. Res. **91**(A4), 4265–4276 (1986). doi:10.1029/JA091iA04p04265

S.J. Bame, D.J. McComas, M.F. Thomsen, B.L. Barraclough, R.C. Elphic, J.P. Glore, J.T. Gosling, J.C. Chavez, E.P. Evans, F.J. Wymer, Magnetospheric plasma analyzer for spacecraft with constrained resources. Rev. Sci. Instrum. **64**, 1026 (1993). doi:10.1063/1.1144173

R.A. Baragiola, E.V. Alonso, A. Oliva Florio, Electron emission from clean metal surfaces induced by low energy light ions. Phys. Rev. B **19**, 121–129 (1979). doi:10.1103/PhysRevB.19.121

N.F. Barber, Note on the shape of an electron beam bent in a magnetic field. Proc. Leeds Philos. Lit Soc., Sci. Sect. **2**, 427–434 (1933)

L.W. Blum, E.A. MacDonald, S.P. Gary, M.F. Thomsen, H.E. Spence, Ion observations from geosynchronous orbit as a proxy for ion cyclotron wave growth during storm times. J. Geophys. Res. **114**, A10214 (2009). doi:10.1029/2009JA014396

L.W. Blum, E.A. MacDonald, L.B.N. Clausen, X. Li, A comparison of magnetic field measurements and a plasma-based proxy to infer EMIC wave distributions at geosynchronous orbit. J. Geophys. Res. **117**, A05220 (2012). doi:10.1029/2011JA017474

J. Bortnik, R.M. Thorne, N.P. Meredith, Modeling the propagation characteristics of chorus using CRRES suprathermal electron fluxes. J. Geophys. Res. **112**, A08204 (2007). doi:10.1029/2006JA012237.112

C.W. Carlson, D.W. Curtis, G. Paschmann, W. Michael, An instrument for rapidly measuring plasma distribution functions with high resolution. Adv. Space Res. **2**, 67–70 (1983). doi:10.1016/0273-1177(82)90151-X

D.L. Carpenter, R.R. Anderson, An ISEE/Whistler model of equatorial electron density in the magnetosphere. J. Geophys. Res. **97**(A2), 1097–1108 (1992). doi:10.1029/91ja01548

D.L. Carpenter, Earth's plasmasphere awaits rediscovery. Eos **76**(9), 89 (1995). doi:10.1029/95EO00041

C. Cattell et al., Discovery of very large amplitude whistler-mode waves in earth's radiation belts. Geophys. Res. Lett. **35**, L01105 (2008). doi:10.1029/2007GL032009

E.P. Chamberlin, K.N. Leung, S. Walthers, R.A. Bibeau, R.L. Stice, G.M. Kelley, J. Wilson, Measurement of the beam energy spread from a microwave ion source. Nucl. Instrum. Methods Phys. Res., Sect. B, Beam Interact. Mater. Atoms **26**, 227–234 (1987). doi:10.1016/0168-583X(87)90755-5

Y. Chen, G.D. Reeves, R. Friedel, The energization of relativistic electrons in the outer Van Allen radiation belt. Nat. Phys. **3**, 614 (2007). doi:10.1038/Nphys655

D.A. Dahl, SIMION for the personal computer in reflection. Int. J. Mass Spectrom. **200**(1–3), 3–25 (2000). doi:10.1016/S1387-3806(00)00305-5

I. Daglis, R. Thorne, W. Baumjohann, S. Orsini, The terrestrial ring current: origin, formation, and decay. Rev. Geophys. **37**(4), 407–438 (1999). doi:10.1029/1999RG900009

H. Demers, N. Poirier-Demers, A.R. Couture, D. Joly, M. Guilmain, N. De Jonge, D. Drouin, Three-dimensional electron microscopy simulation with the CASINO Monte Carlo software. Scanning **33**, 135–146 (2011). doi:10.1002/sca.20262

A.J. Dessler, E.N. Parker, Hydromagnetic theory of geomagnetic storms. J. Geophys. Res. **64**, 12 (1959). doi:10.1029/JZ064i012p02239

L.A. Dietz, J.C. Sheffield, Secondary electron emission induced by 5–30-keV monatomic ions striking thin oxide films. J. Appl. Phys. **46**, 4361–4370 (1975). doi:10.1063/1.321463

D. Drouin, A.R. Couture, D. Joly, X. Tastet, V. Aimez, R. Gauvin, CASINO V2.42—a fast and easy-to-use modeling tool for scanning electron microscopy and microanalysis users. Scanning **29**, 92–101 (2007). doi:10.1002/sca.20000

H.O. Funsten, D.J. McComas, B.L. Barraclough, Thickness uniformity and pinhole density analysis of thin carbon foils using keV ions. Nucl. Instrum. Methods Phys. Res., Sect. B, Beam Interact. Mater. Atoms **66**, 470–478 (1992a). doi:10.1016/0168-583X(92)95421-M

H.O. Funsten, B.L. Barraclough, D.J. McComas, Pinhole detection in thin foils used in space plasma diagnostic instrumentation. Rev. Sci. Instrum. **63**, 4741–4743 (1992b). doi:10.1063/1.1143626

H.O. Funsten, D.J. McComas, B.L. Barraclough, Ultrathin foils used for low energy neutral atom imaging of the terrestrial magnetosphere. Opt. Eng. **32**, 3090–3095 (1993). doi:10.1117/12.149187

H.O. Funsten, M. Shappirio, Sputtering of thin carbon foils by 20 keV and 40 keV Ar^+ bombardment. Nucl. Instrum. Methods Phys. Res., Sect. B, Beam Interact. Mater. Atoms **127**, 905–909 (1997). doi:10.1016/S0168-583X(97)00079-7

H.O. Funsten, R.W. Harper, D.J. McComas, Absolute detection efficiency of space-based ion mass spectrometers and neutral atom imagers. Rev. Sci. Instrum. **76**, 053301 (2005). doi:10.1063/1.1889465

H.O. Funsten, A.A. Guthrie, R.W. Harper, K.H. Kihara, M.P. Manzo, M.J. Fagan, D.J. McComas, S. Weidner, F. Allegrini, D. Everett, B. Rodriguez, G. Dunn, J. Hanley, M. Maple, K. Mashburn, S. Pope, P. Valek, E. Moebius, J. Nolin, S. Ellis, D. Heirtzler, B. King, H. Kucharek, S. Turco, S. Zaffke, D. Reisenfeld, P. Janzen, S.A. Fuselier, M. Gruntman, E. Roelof, P. Wurz, D. Piazza, L. Saul, P. Bochsler, The interstellar boundary explorer high energy (IBEX-Hi) neutral atom imager. Space Sci. Rev. **146**, 75–103 (2009). doi:10.1007/s11214-009-9504-y

S.P. Gary, *Theory of Space Plasma Microinstabilities* (Cambridge Univ. Press, New York, 1993)

S.A. Glauert, R.B. Horne, Calculation of pitch angle and energy diffusion coefficients with the PADIE code. J. Geophys. Res. **110**, A042046 (2005). doi:10.1029/2004JA010851

J.T. Gosling, J.R. Asbridge, S.J. Bame, W.C. Feldman, Effects of a long entrance aperture upon the azimuthal response of spherical section electrostatic analyzers. Rev. Sci. Instrum. **49**, 1260 (1978). doi:10.1063/1.1135566

J.C. Green, M.G. Kivelson, Relativistic electrons in the outer radiation belt: differentiating between acceleration mechanisms. J. Geophys. Res. **109**, A03213 (2004). doi:10.1029/2003JA010153

K.C. Henderson, R.W. Harper, H.O. Funsten, E. MacDonald, Ultraviolet stimulated electron source for use with low energy plasma instrument calibration. Rev. Sci. Instrum. **83**, 073308 (2012). doi:10.1063/1.4732810

R.B. Horne, R.M. Thorne, Potential waves for relativistic electron scattering and stochastic acceleration during magnetic storms. Geophys. Res. Lett. **25**(15), 3011 (1998). doi:10.1029/98GL01002

R.B. Horne, G.V. Wheeler, H.St.C.K. Alleyne, Proton and electron heating by radially propagating fast magnetosonic waves. J. Geophys. Res. **105**(A12), 27,597–27,610 (2000). doi:10.1029/2000JA000018

J.C. Ingraham, T.E. Cayton, R.D. Belian, R.A. Christensen, R.H.W. Friedel, M.M. Meier, G.D. Reeves, M. Tuszewski, Substorm injection of relativistic electrons to geosynchronous orbit during the great magnetic storm of March 24, 1991. J. Geophys. Res. **106**(A11), 25759–25776 (2001). doi:10.1029/2000ja000458

V.K. Jordanova, J.U. Kozyra, G.V. Khazanov, A.F. Nagy, C.E. Rasmussen, M.-C. Fok, A bounce-averaged kinetic-model of the ring current ion population. Geophys. Res. Lett. **21**(25), 2785–2788 (1994). doi:10.1029/94GL02695

H.J. Kim, A.A. Chan, Fully-adiabatic changes in storm-time relativistic electron fluxes. J. Geophys. Res. **102**(A10), 22107–22116 (1997). doi:10.1029/97JA01814

S.M. Krimigis, G. Gloeckler, R.W. McEntire, T.A. Potemra, F.L. Scarf, E.G. Shelley, Magnetic storm of September 4, 1984: a synthesis of ring current spectra and energy densities measured with AMPTE/CCE. Geophys. Res. Lett. **12**(5), 329–332 (1985). doi:10.1029/GL012i005p00329

K.N. Leung, S.R. Walther, H.W. Owren, A compact microwave ion source. IEEE Trans. Nucl. Sci. **NS-32**, 1803–1805 (1985). doi:10.1109/TNS.1985.4333729

X. Li, I. Roth, M. Temerin, J.R. Wygant, M.K. Hudson, J.B. Blake, Simulation of the prompt energization and transport of radiation belt particles during the March 24, 1991 SSC. Geophys. Res. Lett. **20**(22), 2423–2426 (1993). doi:10.1029/93GL02701

X. Li, D.N. Baker, S.G. Kanekal, M. Looper, M. Temerin, Long term measurements of radiation belts by SAMPEX and their variations. Geophys. Res. Lett. **28**(20), 3827–3830 (2001). doi:10.1029/2001GL013586

J. Lindhard, M. Scharff, H.E. Schiøtt, Range concepts and heavy ion ranges (Notes on atomic collisions II). Mat. Fys. Medd. K. Dan. Vidensk. Selsk. **33**, 14 (1963)

D. Lowenstein, A. Rusek, Technical developments at the NASA space radiation laboratory. Radiat. Environ. Biophys. **46**(2), 91–94 (2007). doi:10.1007/s00411-006-0084-x

L.R. Lyons, R.M. Thorne, Equilibrium structure of radiation belt electrons. J. Geophys. Res. **78**(13), 2142–2149 (1973). doi:10.1029/JA078i013p02142

E.A. MacDonald, M.F. Thomsen, H.O. Funsten, Background in channel electron multiplier detectors due to penetrating radiation in space. IEEE Trans. Nucl. Sci. **53**(3), 1593–1598 (2006). doi:10.1109/TNS.2006.874497

E.A. MacDonald, M.H. Denton, M.F. Thomsen, S.P. Gary, Superposed epoch analysis of a whistler instability criterion at geosynchronous orbit during geomagnetic storms. J. Atmos. Sol.-Terr. Phys. **70**(14), 1789–1796 (2008). doi:10.1016/j.jastp.2008.03.021

E.A. MacDonald, H.O. Funsten, E.E. Dors, M.F. Thomsen, P. Janzen, R.M. Skoug, G.D. Reeves, J.T. Steinberg, R. Harper, D. Young, J.-M. Jahn, D. Reisenfeld, New magnetospheric ion composition measurement techniques, in *Future Perspectives of Space Plasma and Particle Instrumentation and International Collaborations: Proceedings of the International Conference*. AIP Conf. Proc., vol. 1144, (2009), pp. 168–172

E.A. MacDonald, L.W. Blum, S.P. Gary, M.F. Thomsen, M.H. Denton, High speed stream driven inferences of global wave distributions at geosynchronous orbit; relevance to radiation belt dynamics. Proc. R. Soc. A **466**(2123), 3351–3362 (2010). doi:10.1098/rspa.2010.0076

D.J. McComas, J.E. Nordholt, S.J. Bame, B.L. Barraclough, J.T. Gosling, Linear electric field mass analysis: a technique for three-dimensional high mass resolution space plasma composition measurements. Proc. Natl. Acad. Sci. USA **87**(15), 5925–5929 (1990). doi:10.1073/pnas.87.15.5925

D.J. McComas, F. Allegrini, C.J. Pollock, H.O. Funsten, S. Ritzau, G. Gloeckler, Ultra-thin (∼10 nm) carbon foils in space instrumentation. Rev. Sci. Instrum. **75**(11), 4863–4870 (2004). doi:10.1063/1.1809265

N.P. Meredith, R.M. Thorne, R.B. Horne, D. Summers, B.J. Fraser, R.R. Anderson, Statistical analysis of relativistic electron energies for cyclotron resonance with EMIC waves observed on CRRES. J. Geophys. Res. **108**(A6), 1250 (2003). doi:10.1029/2002JA009700

M. Nosé, A. Ieda, S.P. Christon, Geotail observations of plasma sheet ion composition over 16 years: on variations of average plasma ion mass and O^+ triggering substorm model. J. Geophys. Res. **114**, A07223 (2009). doi:10.1029/2009JA014203

T. Obara, T. Nagatsuma, M. Den, Y. Miyoshi, A. Morioka, Main-phase creation of 'seed' electrons in the outer radiation belt. Earth Planets Space **52**(1), 41–47 (2000)

G.S. Oehrlein, R.J. Phaneuf, D.B. Graves, Plasma-polymer interactions: a review of progress in understanding polymer resist mask durability during plasma etching for nanoscale fabrication. J. Vac. Sci. Technol. **29**(1), 010801 (2011). doi:10.1116/1.3532949

T.P. O'Brien, M.B. Moldwin, Empirical plasmapause models from magnetic indices. Geophys. Res. Lett. **30**(4), 1 (2003). doi:10.1029/2002GL016007

T.I. Pulkkinen, N.A. Tsyganenko, R.H.W. Friedel (eds.), *The Inner Magnetosphere: Physics and Modeling* (Am. Geophys. Union, Washington, 2005)

G.D. Reeves, Relativistic electrons and magnetic storms: 1992–1995. Geophys. Res. Lett. **25**(11), 1817–1820 (1998). doi:10.1029/98GL01398

G.D. Reeves, K.L. McAdams, R.H.W. Friedel, T.P. O'Brien, Acceleration and loss of relativistic electrons during geomagnetic storms. Geophys. Res. Lett. **30**(10), 1529–1532 (2003). doi:10.1029/2002gl016513

G.D. Reeves, Radiation belt storm probes: the next generation of space weather forecasting. Space Weather **5**, 11 (2007). doi:10.1029/2007sw000341

G.D. Reeves, A.A. Chan, C. Rodger, New directions for radiation belt research. Space Weather **7**, S07004 (2009). doi:10.1029/2008sw000436

G.D. Reeves, Y. Chen, G.S. Cunningham, R.W.H. Friedel, M.G. Henderson, V.K. Jordanova, J. Koller, S.K. Morley, M.F. Thomsen, S. Zaharia, Dynamic radiation environment assimilation model: DREAM. Space Weather **10**, S03006 (2012). doi:10.1029/2011sw000729

S.M. Ritzau, R.A. Baragiola, Electron emission from carbon foils induced by keV ions. Phys. Rev. B **58**(5), 2529–2538 (1998). doi:10.1103/PhysRevB.58.2529

J.G. Roederer, On the adiabatic motion of energetic particles in a model magnetosphere. J. Geophys. Res. **72**(3), 981–992 (1967). doi:10.1029/JZ072i003p00981

G. Santina, P. Nieminen, H. Evansa, E. Daly, F. Lei, P. Truscott, C. Dyer, B. Quaghebeur, D. Heynderickx, New Geant4 based simulation tools for space radiation shielding and effects analysis. Nucl. Phys. B, Proc. Suppl. **125**, 69–74 (2003). doi:10.1016/S0920-5632(03)90968-6

D.M. Sawyer, J.I. Vette, AP-8 trapped proton environment for solar maximum and solar minimum. NASA STI/Recon Tech. Rep. **77**, 18983 (1976)

M. Schulz, L.J. Lanzerotti, *Particle Diffusion in the Radiation Belts* (Springer, New York, 1974)

N. Sckopke, A general relation between the energy of trapped particles and the disturbance field near the earth. J. Geophys. Res. **71**(13), 3125–3130 (1966). doi:10.1029/JZ071i013p03125

H. Seiler, Secondary electron emission in the scanning electron microscope. J. Appl. Phys. **54**(11), R1–R18 (1983). doi:10.1063/1.332840

R.S. Selesnick, J.B. Blake, Dynamics of the outer radiation belt. Geophys. Res. Lett. **24**(11), 1347–1350 (1997). doi:10.1029/97GL51409

R.S. Selesnick, M.D. Looper, R.A. Mewaldt, A theoretical model of the inner proton radiation belt. Space Weather **5**, S04003 (2007). doi:10.1029/2006SW000275

M.L. Spasojevic, L.W. Blum, E.A. MacDonald, S.A. Fuselier, D.I. Golden, Correspondence between a plasma-based EMIC wave proxy and subauroral proton precipitation. Geophys. Res. Lett. **38**, L23102 (2011). doi:10.1029/2011GL049735

A.L. Stancik, E.B. Brauns, A simple asymmetric lineshape for fitting infrared absorption spectra. Vib. Spectrosc. **47**, 66–69 (2008). doi:10.1016/j.vibspec.2008.02.009

D. Summers, R.M. Thorne, F. Xiao, Relativistic theory of wave-particle resonant diffusion with application to electron acceleration in the magnetosphere. J. Geophys. Res. **103**(A9), 20487–20500 (1998). doi:10.1029/98JA01740

M. Taylor, R.H.W. Friedel, G.D. Reeves, M.W. Dunlop, T.A. Fritz, P.W. Daly, A. Balogh, Multisatellite measurements of electron phase space density gradients in the earth's inner and outer magnetosphere. J. Geophys. Res. **109**, A05220 (2004). doi:10.1029/2003ja010294

S. Väyrynen, J. Räisänen, P. Tikkanen, I. Kassamakov, E. Tuominen, Effects of activation by proton irradiation on silicon particle detector electric characteristics. J. Appl. Phys. **106**(2), 024908 (2009). doi:10.1063/1.3168436

M.F. Thomsen, M.H. Denton, V.K. Jordanova, L. Chen, R.M. Thorne, Free energy to drive equatorial magnetosonic wave instability at geosynchronous orbit. J. Geophys. Res. **116**, A08220 (2011). doi:10.1029/2011JA016644

D.L. Turner, Y. Shprits, M. Hartinger, V. Angelopoulos, Explaining sudden losses of outer radiation belt electrons during geomagnetic storms. Nat. Phys. **8**, 208–212 (2012). doi:10.1038/NPHYS2185

C.G.H. Walker, M.M. El-Gomati, A.M.D. Assa'd, M. Zadrazil, The secondary electron emission yield for 24 solid elements excited by primary electrons in the range 250–5000 eV: a theory/experiment comparison. Scanning **30**(5), 365–380 (2008). doi:10.1002/sca.20124

S.R. Walther, K.N. Leong, W.B. Kunkel, Characteristics of a compact microwave ion source. Rev. Sci. Instrum. **57**, 1531–1535 (1986). doi:10.1063/1.1139197

S.R. Walther, K.N. Leong, K.W. Ehlers, W.B. Kunkel, Generation of oxygen, carbon, and metallic ion beams by a compact microwave ion source. Nucl. Instrum. Methods Phys. Res., Sect. B, Beam Interact. Mater. Atoms **21**, 215–217 (1987). doi:10.1016/0168-583X(87)90830-5

M. Wüest, Time-of-flight ion composition measurement technique for space plasmas, in *Measurement Techniques in Space Plasmas: Particles*, ed. by F. Pfaff, E. Borovsky, T. Young. Geophys. Monogr. Ser., vol. 102 (AGU, Washington, 1998), pp. 141–155. doi:10.1029/GM102p0141

D.T. Young, S.J. Bame, M.F. Thomsen, R.H. Martin, J.L. Burch, J.A. Marshall, B. Reinhard, 2-Pi-radian field-of-view toroidal electrostatic analyzer. Rev. Sci. Instrum. **59**(5), 743–751 (1988). doi:10.1063/1.1139821

DOI 10.1007/978-1-4899-7433-4_14
Reprinted from *Space Science Reviews* Journal, DOI 10.1007/s11214-012-9917-x

The Engineering Radiation Monitor for the Radiation Belt Storm Probes Mission

J.O. Goldsten · R.H. Maurer · P.N. Peplowski · A.G. Holmes-Siedle · C.C. Herrmann · B.H. Mauk

Received: 13 June 2012 / Accepted: 28 June 2012 / Published online: 22 September 2012

Abstract An Engineering Radiation Monitor (ERM) has been developed as a supplementary spacecraft subsystem for NASA's Radiation Belt Storm Probes (RBSP) mission. The ERM will monitor total dose and deep dielectric charging at each RBSP spacecraft in real time. Configured to take the place of spacecraft balance mass, the ERM contains an array of eight dosimeters and two buried conductive plates. The dosimeters are mounted under covers of varying shielding thickness to obtain a dose-depth curve and characterize the electron and proton contributions to total dose. A 3-min readout cadence coupled with an initial sensitivity of ∼0.01 krad should enable dynamic measurements of dose rate throughout the 9-hr RBSP orbit. The dosimeters are Radiation-sensing Field Effect Transistors (RadFETs) and operate at zero bias to preserve their response even when powered off. The range of the RadFETs extends above 1000 krad to avoid saturation over the expected duration of the mission. Two large-area (∼10 cm^2) charge monitor plates set behind different thickness covers will measure the dynamic currents of weakly-penetrating electrons that can be potentially hazardous to sensitive electronic components within the spacecraft. The charge monitors can handle large events without saturating (∼3000 fA/cm^2) and provide sufficient sensitivity (∼0.1 fA/cm^2) to gauge quiescent conditions. High time-resolution (5 s) monitoring allows detection of rapid changes in flux and enables correlation of spacecraft anomalies with local space weather conditions. Although primarily intended as an engineering subsystem to monitor spacecraft radiation levels, real-time data from the ERM may also prove useful or interesting to a larger community.

Keywords Radiation monitor · RadFET · Deep dielectric charging · Space environment

J.O. Goldsten (✉) · R.H. Maurer · P.N. Peplowski · C.C. Herrmann · B.H. Mauk
Applied Physics Laboratory, The Johns Hopkins University, Laurel, MD 20723, USA
e-mail: john.goldsten@jhuapl.edu

A.G. Holmes-Siedle
REM Oxford Ltd., Oxford OX29 4PD, UK

1 Introduction

The RBSP spacecraft must operate in a high-radiation environment consisting primarily of energetic electrons and protons (Mauk et al. 2012, this issue). Most of the spacecraft instruments and subsystems have included significant amounts of shielding around their electronics and detectors to limit the total accumulated dose. The amount of shielding (depth) chosen was based on a conservative determination of the predicted total integrated dose for the mission lifetime using conventional models of the static particle flux (Sawyer and Vette 1976; Vette 1991). The predicted dose is typically obtained using Monte Carlo or ray-tracing radiation transport tools (Calvel et al. 2008). However, several aspects of the design process can be improved with the use of *in-situ* dosimetry. Real-time monitoring of the dynamic radiation dose and dose rate near the location of sensitive electronics can help eliminate inaccuracies associated with static particle environment models and the transport of radiation through simplified spacecraft shielding models. It also allows the direct measurement of space radiation at shielded depths internal to the spacecraft.

Recent studies by Bogorad et al. (2009) presented results of on-orbit particle measurements along with comparisons to the standard AE8 model (Ginet and O'Brien 2009) that suggest a need for updates to the existing static AE8 model. Specifically, analytical estimates from the existing models show long-term radiation rates averaged over six years that are approximately 4X to 10X higher than the measured on-orbit dose for the same time period. This large discrepancy appears to be due primarily to the dynamics of the electron fluence during the period from 1997 to 2003, but could also be due to the use of simplified spacecraft geometry models or calculation methods.

An early design concept of the RBSP spacecraft included an extensive radiation monitoring package that was later descoped along with other proposed spacecraft subsystems (e.g., star trackers) in a necessary cost-cutting exercise. Late in the development cycle (after completion of the Spacecraft Critical Design Review), we proposed recovering some radiation monitoring capability as a balance mass experiment. No longer considered a mission-critical subsystem (i.e., not part of the RBSP Program Level requirements), we were able to obtain approval from NASA to build a simple, inexpensive radiation monitor using a streamlined hardware development process that reduced the documentation and parts screening requirements. As a result, we were able to develop and build the ERM on an accelerated schedule and deliver the qualified flight units to the spacecraft at the same time as other payload elements.

2 ERM Measurement Objectives

As a supplementary experiment, there are no RBSP Program Level (Level-1) requirements levied on the ERM, and its measurement objectives do not feed into the mission success criteria. Nevertheless, we established four challenging objectives for the ERM experiment: (1) Measure all relevant electrical parameters of the RadFET devices in flight to understand better their response to dose in a mixed-particle environment and develop confidence in their long-term application to spacecraft dosimetry; (2) Characterize the actual on-orbit dose-depth curve using an array of dosimeters at different effective shielding depths and compare this result with predictions; (3) Profile the dose and dose rate of the RBSP orbit over a period of two years or longer; (4) Measure the internal charging conditions on each spacecraft ranging from quiescent to the largest, worst-case storm with sufficient sensitivity and time resolution to enable correlation of spacecraft anomalies with local space weather conditions.

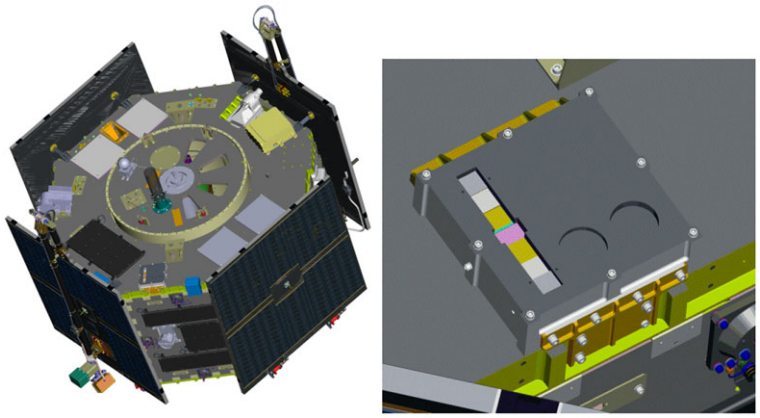

Fig. 1 (*Left*) View of the RBSP spacecraft showing the location of the ERM. The ERM is located toward the edge of the aft deck and mounts near a balance mass location; (*right*) zoom on the mounting detail (MLI blanket not shown for clarity)

A secondary objective of the experiment aims to take advantage of the unique opportunity on RBSP to cross-compare RadFET-based dosimetry data with data collected by the Aerospace dosimeter being flown as part of the Magnetic Electron Ion Spectrometer (MagEIS) (Blake et al. 2012, this issue). The Aerospace dosimeter actively measures the energy deposition of each particle passing through its internal solid state detector. A comparison of results may highlight measurement differences in these two very different technological approaches.

A detailed description of the RBSP mission design may be found in Mauk et al. (2012, this issue). In summary, the two spacecraft are in nearly identical orbits with perigee of ∼600 km altitude, apogee of 5.8 R_E geocentric, and inclination of 10°. The orbital period is ∼9 hr and a slight difference in orbital apogees causes their radial spacing to vary between ∼100 km and ∼5R_E. These orbits allow RBSP to access all of the most critical regions of the radiation belts. The 2-yr nominal mission lifetime allows all local times to be studied.

3 ERM Description

Simplicity, ease of manufacture, and ease of integration and test were driving principles in the design of the ERM. The ERM is contained in a single box that fits on the aft deck of the spacecraft and mounts to an existing balance mass location (see Fig. 1). Because the balance mass plates bolt directly into the edge member of the spacecraft structure, a separate mounting bracket had to be bonded to the spacecraft deck so that both ends of the ERM housing could be properly secured. The ERM dissipates little power (∼0.25 W) and was permitted a generous footprint (17 cm × 17 cm), so no thermal gasket material is required. The box is completely covered with multi-layer insulation (MLI) and the overall profile was kept low (∼6 cm) to limit any intrusion into the field-of-view (FOV) of nearby thermal radiators. The box is not fitted with survival heaters, thermostats, or spacecraft temperature sensors and will simply follow the deck temperature. The mounting location near the edge of the deck assures a clear FOV for the two charge monitors (circular depressions in the cover) and the dosimeter array (rectangular aperture with thinnest absorber at center). The

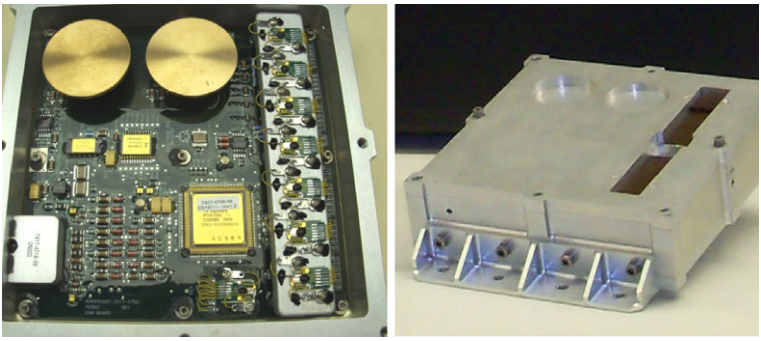

Fig. 2 (*Left*) Flight ERM with its cover removed showing the locations of the individual RadFET dosimeters and the two charge monitors; (*right*) view with cover showing variable thickness absorber

small amount of absorption due to the MLI blanket over the aperture is only significant in comparison to the thinnest part of the cover and has been included in the response model.

Figure 2 provides internal and external views of the ERM. The rectangular aperture in the cover spans the dosimeter array and contains a varying thickness absorber to characterize dose vs. depth. The circular depressions above the charge monitor plates provide two levels of shielding thickness to gauge deep dielectric charging currents over an extended range. The ERM is primarily sensitive to radiation penetrating these defined apertures with thick box walls limiting the exposure from the other sides.

The ERM receives its power and data interface over a single cable (4 wires) that connects to a test port on the Radiation Belt Storm Probes Ion Composition Experiment (RBSPICE) electronics (Lanzerotti et al. 2012, this issue). When the ERM was proposed, there were no more power and data ports available from the spacecraft Integrated Electronics Module (IEM), so the ERM experiment would not have been possible without the foresight of the RBSPICE engineering team to include such a flexible interface in their design. Because the ERM connects to a primary instrument, these interfaces were carefully reviewed and all parts associated with this interface were selected to meet the same reliability standards as other spacecraft components and were fully screened. As further protection, the RBSPICE test port contains a secondary power switch that can turn off the ERM in the event of a fault.

The RBSPICE instrument software collects ERM data and packetizes it for downlink. ERM data will be archived as an RBSPICE data product, but it will also be accessible via the spacecraft Mission Operations Center (MOC). Given the relatively low ERM data rate ($\sim$16 bps), some portion of its data may also be made available through the special RBSP real-time space weather downlink.

Table 1 gives a summary of ERM characteristics and performance. The dosimeter and charge monitor sensitivities exceed the targets assumed for basic engineering measurements and the readout rates are considered sufficient to capture dynamic transients. In general, the ERM design approach is scalable depending on application.

Dosimeter An objective of the dosimeter is to characterize the dose-depth curve and compare the measured results with model predictions. For simplicity, an array of 7 RadFET dosimeters is mounted along a raised aluminum 'bench' that brings them in close proximity to the cover. The RadFETs are spaced $\sim$2 cm apart to form separate pixels, where each pixel sits beneath a different thickness cover (see Fig. 3). An 8th RadFET dosimeter mounted directly to the printed circuit board provides a representative dose for the more heavily shadowed electronics. Given the closeness of the pixels to each other and the penetrating nature

Table 1 ERM characteristics and performance overview

Dosimeter	Range	0–1000 krad Total Integrated Dose (TID)
	Sensitivity	∼0.01 krad; TID <10 krad
		∼0.10 krad; TID <100 krad
		∼1.00 krad; TID <1000 krad
	Configuration	Linear array of 8 redundant RadFET devices
	Shielding	Shield depths: 0.05 mm to 9.0 mm
	Time resolution	3 min
Charge monitor	Range	0–3 pA/cm^2
	Sensitivity	∼0.001 pA/cm^2
	Configuration	Two 3.8-cm dia. × 0.25-cm copper plates (∼11 cm^2 collection area)
	Shielding	Shield depths: 1.0 mm and 3.8 mm
	Time resolution	5 s
General	FOV	∼45°
	Operating temperature	−30 °C to +50 °C
	Envelope	18 × 18 × 6 cm^3
	Mass	2.9 kg
	Power	0.25 W continuous
	Data rate	16 bps continuous

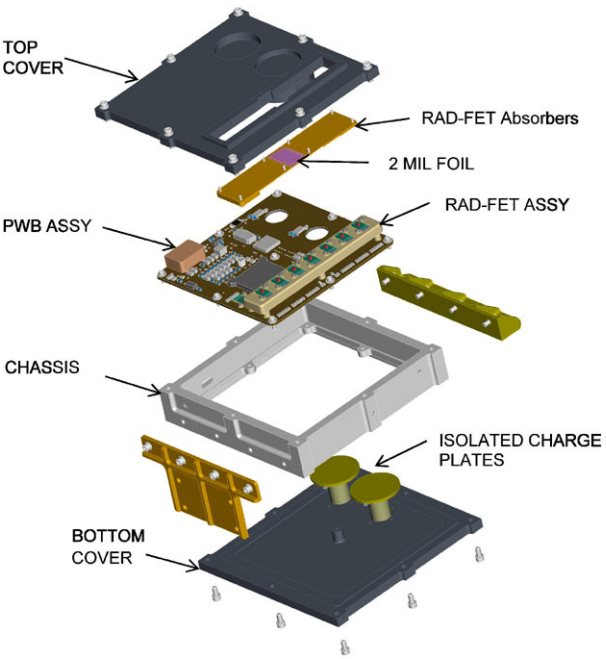

Fig. 3 Exploded view of the ERM. The ERM is a single assembly consisting of an electronics board mounted in a thick aluminum frame with top and bottom covers. A cut-out in the top cover is fitted with a varying thickness absorber that spans an array of 7 RadFETs mounted on a raised aluminum substrate. Two isolated charge plates sit atop pedestals mounted to the bottom cover

Table 2 ERM absorber thickness values

Position	Material	Thickness (mm)
1	Mg	3.00
2	Mg	0.75
3	Mg	0.50
4	Al	0.05
5	Mg	0.25
6	Mg	1.00
7	Mg	1.50
8	Al	9.00

of radiation, there is considerable overlap of dose between adjacent pixels. This result was expected and has been accounted for in the modeling effort. The varying thickness cover (absorber) is thinnest at the center and thicker toward the ends in a v-configuration (see Table 2). The absorber material is primarily magnesium that has been precisely machined to form steps at each pixel boundary. The desired thickness over the center pixel was too thin for accurate machining and was replaced with a piece of 40-micron thick aluminum foil bonded to a framed cut-out.

Each dosimeter is an integrated circuit (IC), type RFT-300CC10G1, developed and manufactured by REM Oxford Ltd. that contains two RadFET sensors and an on-chip diode. The redundant devices are well-matched and can be read out independently with their results averaged to reduce uncertainty. The on-chip diode can be used to monitor the die temperature. Each die is mounted to a small printed circuit carrier board and covered with a low-Z epoxy ("glob top"). A 6-way edge connection permits surface-mount soldering or plugging into a commercial test socket (Kyocera 6207).

RadFETs are p-type Metal Oxide Field Effect Transistors (p-MOSFET) with a thickened gate oxide region. Radiation-induced charge in the insulated gate oxide (SiO_2) region can remain trapped for many years. The presence of this stored space charge produces a threshold voltage shift in the device characteristic vs. the accumulated dose (Holmes-Siedle and Adams 2002). A thicker oxide region increases sensitivity but reduces dynamic range. The ERM employs devices with an oxide thickness of 0.3 microns, which provides an acceptable balance between sensitivity and dynamic range.

Being an IC device, RadFETs have a sensitive micro-volume that mimics those of most spacecraft electronic devices and therefore "sees" the same effects. The oxide is sensitive to all types of ionizing dose and provides a Linear Energy Transfer (LET) type response that is not overly affected by dose rate or particle species (Holmes-Siedle et al. 2007). The response to dose is most sensitive and linear if the gate is biased during irradiation, but an operational constraint of the ERM is that power might be removed at any time, so it was decided to operate the ERM RadFETs under zero bias mode (ZBM) so that they will respond to dose in a predictable manner whether powered on or off. As a consequence, their response is nonlinear, so a careful calibration will be required to convert from threshold shift to dose; however, a benefit of the lower sensitivity and sublinear curvature or "roll-off" is a significantly extended dynamic range (>1000 krad) that will potentially allow operation for several years on-orbit before reaching saturation (see Fig. 4). The shape of the ZBM curve may be approximated as a power law with voltage shift varying as dose to a power n, where n starts near unity and slowly falls with increasing dose. For the high total dose expected during the RBSP mission, the value of n may fall to 0.5 or less. Characteristics of RadFETs

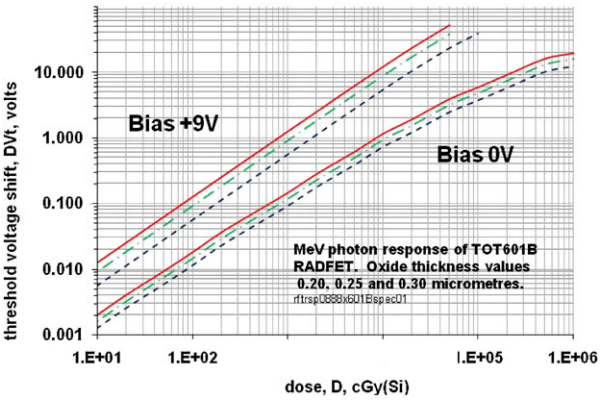

Fig. 4 RadFET specification for shift in threshold voltage with dose of MeV photons (taken from REM Oxford datasheet). The ERM uses the 0.3 micron oxide thickness device biased at 0 V (lower solid red trace). The response of an unbiased RadFET is less sensitive and nonlinear, but extends the useful dynamic range more than an order-of-magnitude and doesn't rely on continuous spacecraft power to maintain calibration

other than threshold voltage vary with dose, such as the device current-voltage transfer characteristic and a transient effect called "drift up", which is related to bias-induced charging of traps in the oxide-silicon interface (Holmes-Siedle et al. 2007). The ERM electronics read out the RadFETs at multiple currents and at multiple time intervals to gauge these additional effects.

Other accepted consequences of operating in ZBM are a larger percentage scatter in responses and increased "fade". Long-term loss of the stored charge in the oxide region ("fade" or room-temperature annealing) occurs as a result of the slow emptying of some charge traps on the oxide. This effect potentially poses a calibration issue but may be less of a problem if the deck temperature runs cold. Most RadFET data for the RFT300 device has been collected under biased conditions, and it has only recently been realized that fade for an unbiased RadFET is more significant. As a result, good accuracy will require a new calibration curve to be captured at dose rates near expected mission values and operating temperatures, which is a planned part of the ground calibration effort.

Charge Monitors The charge monitors are designed to measure the flux of those electrons that penetrate the cover and then stop in buried dielectrics building up potentially hazardous amounts of charge. The ERM has two independent charge monitors beneath different thickness aluminum covers (1.0 mm and 3.8 mm) as a means of providing crude spectrometry ($>$0.7 MeV and $>$2 MeV, respectively) and for extending the dynamic range of intensity measurements in case an unexpectedly large event saturates the more sensitive channel. The two identical charge plates are 38 mm in diameter and 2.5 mm thick. The plates are made of copper (as opposed to aluminum) to reduce the needed thickness to stop electrons penetrating the cover while minimizing the exposure to unwanted background from the sides. The cover itself extends downward to surround the charge plates with a thick baffle that further reduces background from the sides (see Fig. 5). The grounded baffle also reduces susceptibility to Electro-Magnetic Interference (EMI) ensuring measurement capability down to the electronics noise limit.

The charge plates sit atop stainless steel pedestals at their center to bring the charge plates closer to the top cover to maximize their view to space (solid angle $\sim$50 %) and provide the necessary structural support during launch (see Fig. 5). A thin insulating disc between each charge plate and its pedestal, along with an internal bushing inside the pedestal cavity, provides the necessary electrical isolation. The pedestals pass through cut-outs in the electronics board. A short curved wire connects each charge plate to its corresponding

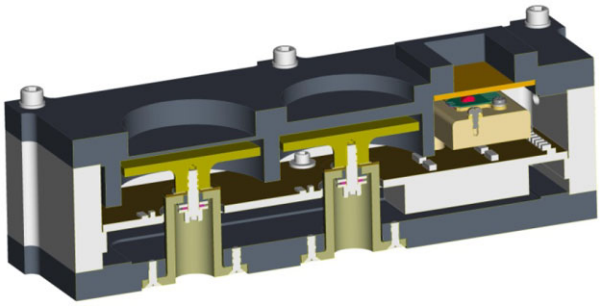

Fig. 5 Cross-sectional view of ERM Charge Monitor plates. Two circular charge collection plates made of copper are mounted close to the top cover. The cover is thinned to two different thicknesses to extend the dynamic range and provide crude spectrometry. The cover extends downward to surround each charge plate to provide additional shielding from the sides

preamplifier located near the cut-out. The charge-plate region is kept clear of extraneous circuits and coatings to minimize parasitic leakage currents and couplings.

The charge monitor preamplifiers are configured as transimpedance (current-to-voltage) amplifiers with resistive feedback. Tying the charge plates to the virtual ground connection keeps the plates operating near zero volts potential and prevents them from charging up to high potentials (and possibly arcing). The preamplifiers convert the incoming electron flux to a voltage representing the instantaneous current. Subsequent filtering provides a time-averaged ($\sim$0.5 s) full-scale range of 30 pA ($\sim$3 pA/cm^2), which exceeds the largest expected signal with 50 % margin.

Response Modeling The RBSP spacecraft will be subject to a challenging high-energy proton and electron radiation environment. The Total Integrated Dose (TID) that any particular component on the spacecraft receives is a function of the thickness of the shielding around that component (and similarly for the amount of radiation-induced charge build up). To provide guidance on the amount of shielding necessary to limit the total dose to electronics and other sensitive components, a general analysis of the RBSP spacecraft was performed using models of the environment along with radiation transport calculations. These simulations assumed two simple shielding geometries: spherical and slab, which may in themselves not be representative of the response for a more complex geometry. The ERM aims to investigate the deviation from these simple cases and evaluate an actual flight configuration.

Using a version of the Geometry and Tracking (Geant4) toolkit for the simulation of the passage of particles through matter using Monte Carlo methods (Agostinelli et al. 2003), a high-fidelity simulation of the ERM experiment was developed to predict the response of the RadFETs and charge collection plates to the expected environment. Details of the ERM mechanical configuration were imported into Geant4 by converting the Computer Assisted Drawing (CAD) files to Geometry Description Markup Language (GDML) using Fastrad (Beutier et al. 2003). The simulation results were then used to understand the directional response of the ERM and optimize the design of the cover.

For the dosimeter, the total mission average proton and electron fluxes were calculated using the SPace ENVIronment Information System (SPENVIS; e.g. Heynderickx et al. 2003) as input to the Geant4 simulations. These fluxes are predictions of the radiation environment in the ERM orbit for the full 2 year, 75 day primary mission. Particles reaching the sensitive volume of each RadFET were tracked and the total energy deposition per second was converted to dose. The design was iterated and a set of cover thicknesses was chosen such that measurements from the RadFET array span much of the range of the dose-depth curve and provide enough well-spaced sample points to characterize its shape (see Fig. 6). Using a range of cover thicknesses from 0.04 mm to 9.0 mm (see Table 2), the simulation

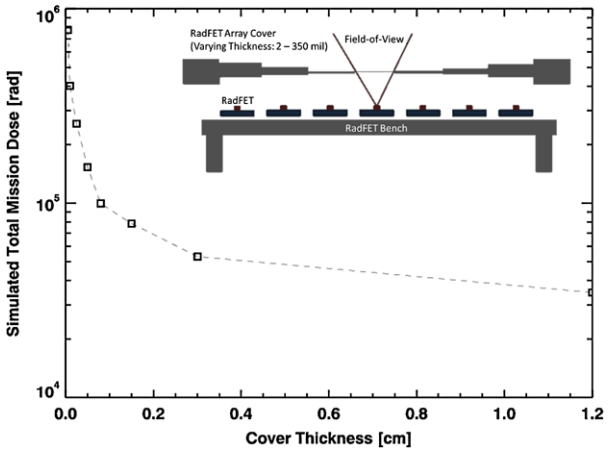

Fig. 6 Cover design of the ERM dosimeter. A detailed modeling effort was used to select the optimal cover thickness over each pixel

effort was able to achieve a factor of ∼30 in total integrated dose between the thinnest and thickest shielded RadFETs.

For the charge monitors, a simulation of the ERM response to the expected worst case electron flux (Mauk 2011, private communication) showed that 3.8-cm diameter plates (as large as would practically fit within the ERM) were sufficiently large to detect environmental signals, but, that without further design effort, "background" electrons from other directions would dominate the overall response. Given this initial result, the ERM design was modified to move the charge plates much closer to the cover (67 % improvement in solid angle) and to increase the amount of shielding around the sides of the plates. Using this modified approach, the change in the measured current from quiescent to worst case is estimated to be ∼20 pA for the plate underneath the thinner 1-mm cover and ∼10 pA behind the 3.8-mm cover.

Electronics Figure 7 shows a functional block diagram of the ERM. The ERM electronics were designed for low-power (<0.25 W) and simple operation with a single operational mode and a fixed-format data interface. There is no internal software and the measurement sequence is controlled by a Field Programmable Gate Array (FPGA). The ERM accepts +5 V power and generates all of its internal voltages from simple charge pumps with unregulated outputs. The critical measurement circuits rely on precision voltage references to maintain accuracy over varying conditions.

The RadFET readout circuit is designed to be responsive to the special features of a solid-state dosimeter based on charge trapping in a glassy material. In all of these materials, there are side effects such as "fade" (slow alteration of trapping), drifts due to interfaces (in this case a Si/SiO_2 interface), and sensitivity to temperature (Holmes-Siedle et al. 2007). The die temperature can be measured directly via the on-chip diode and used for characterization and correction. Precise timing of "reads" can reveal short-term drift effects, and long time-lapse measurements can help determine corrections for "fade". The "read" process itself will affect the field applied to the gate and alter the sensitivity of charge traps in the oxide and will be included in the characterization and calibration of the system.

Most of the time (∼98 %), each RadFET is maintained in an unbiased "irradiate" state in which its gate, drain, and body/source connections are shorted together using a single-pole, double-throw reed relay; a connection scheme consistent with zero bias mode operation where the gate oxide applied field is zero (see Fig. 4). During a measurement cycle, the

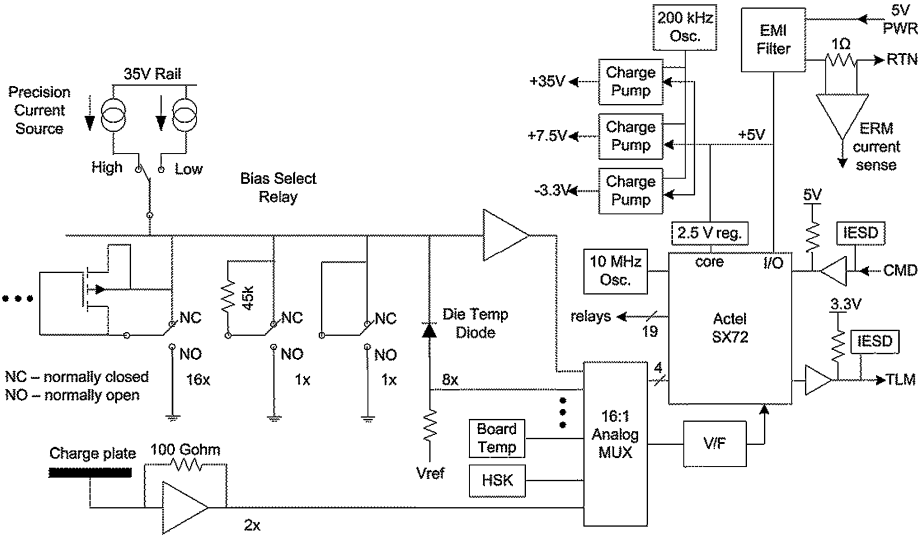

Fig. 7 ERM functional block diagram. The ERM accepts +5 V power and generates all needed voltages internally. When powered, the ERM FPGA sequences through a 3-min repeating cycle of 1-s measurements consisting of staggered readings of 16 RadFETs, 2 charge monitors, calibration references, and general housekeeping parameters. The ERM outputs these data over a protected serial data interface

selected RadFET source terminal is connected to a precision current source while its gate and drain terminals are connected to ground. The RadFET is held in this "read" state for a period of 3 seconds. During the first second, the voltage is measured at a reduced current (167 μA) to allow a two-point measurement of its I–V characteristic. This measurement is then followed by two successive 1-s measurements at a current of 500 μA, which lies much closer to the minimum temperature coefficient point for these devices. The purpose of the two consecutive measurements made at the same current is to characterize any "drift-up" in the device, an effect that also strongly depends on total dose. Since the charge buildup in the oxide during irradiation is very dependent on the gate oxide field, and because it is necessary to apply gate bias during the read cycle, the total amount of read time is held below 2 % so as to minimize the effects of "reads" on the overall calibrated response to dose.

The reed relay associated with each RadFET is a commercial component (Pickering series 101), but was chosen for its compelling attributes: it provides a normally-closed state when unpowered, which may happen at any time and for an indefinite period during spacecraft operations; it acts as an ideal switch, with the ability to tolerate and multiplex voltages in excess of 30 V with no associated leakage current; and it requires very little power to activate (∼15 mW) and draws no power when idle. For ruggedness and reliability, the manufacturer pots these relays using a soft, low-outgassing material that reduces stress on the reed switch under repeated thermal cycling. An internal mu-metal magnetic screen included within the potting shell satisfies the magnetic cleanliness requirement of the RBSP spacecraft. Each of the 16 RadFET devices is assigned a relay. Two more relays are assigned to a precision resistor ("RadFET simulator") and a connection to ground to provide a regular internal calibration of the measurement system. A final relay allows selection between two different precision bias currents.

All voltages to be measured are fed through an analog multiplexer to a central voltage-to-frequency (V/F) converter (Analog Devices AD537), which acts as a low-power, high-

resolution analog-to-digital converter (ADC). The AD537 output frequency, which is set for a nominal full-scale value of ∼100 kHz, drives a 16-bit counter inside the FPGA. The output of a 10-MHz crystal oscillator is divided down to provide a precise 512-ms gate period over which to measure the V/F output frequency. This approach provides nearly 16 bits of resolution in a low-noise measurement system that offers excellent differential non-linearity, an essential feature when looking for small changes in successive readings. The integral non-linearity of this type of system is generally worse in comparison to conventional successive-approximation type converters, but absolute measurement errors less than 0.1 % in either the total dose measurement or the charge monitor measurement are considered negligible. A V/F system may also be more subject to temperature drift than conventional ADCs that have built-in references, but regular measurements of the precision current source in combination with the precision resistor will enable ground correction of drift in both gain and offset that occur due to temperature and/or radiation effects encountered on orbit.

The amount of current applied during the readout of the RadFETs was selected to be close to the minimum temperature coefficient point for these devices, but a residual temperature characteristic will likely remain, which may result in the need for further corrections on the ground to remove this systematic error. Fortunately, each RadFET IC is equipped with an on-chip diode that can be used to track changes in the die temperature. Each of the 8 die temperatures is reported regularly along with a global temperature measurement of the ERM box using a calibrated thermistor.

The two charge monitor outputs are read out much more frequently (once every 5 s) than the RadFETs with these measurements interleaved between RadFET readings. The preamplifier for each charge monitor is a Burr-Brown OPA129 operational amplifier that uses dielectrically-isolated FET inputs to achieve ultra-low input bias currents (<100 fA). While this device is only available in commercial form, a test in our Co-60 irradiator showed its performance meets our 30 krad requirement for electronics inside the shielded portion of the ERM enclosure. The V/F input is configured for positive voltages only, and so a 25 mV dc offset was added to each charge monitor output to allow precision measurements near zero since quiescent currents may be 4 orders down from worst-case conditions. This offset also allows the charge monitors to report small negative currents, which indicates a signal dominated by the collection of protons, a situation that might occur during a solar proton event or passage through the inner belt of trapped protons.

4 Ground Performance and Calibration

The engineering model unit of the ERM closely matches the two delivered flight units and will be used to perform detailed ground performance and calibration measurements at selected beam facilities. These results will be described elsewhere. Here only critical performance parameters are discussed and calibration experiments are described in general terms, with some results given that have been analyzed to date.

Dosimeter Testing and Calibration All of the flight RadFET devices were selected from the same wafer lot and their general characteristics match reasonably well; however, some spread in their response to dose is expected. To assess the amount of spread and establish an initial calibration, each ERM was given a small 100-rad exposure in a Co-60 chamber. The cover (with its integral absorber) was removed so that all of the devices would receive the same dose (see Fig. 8). The dose rate was kept low to simulate the rate expected on-orbit. For this test, we used a 10 Curie source at a separation distance of 300 mm, which provided a dose rate of 2.08e-2 cGy(Si)/s.

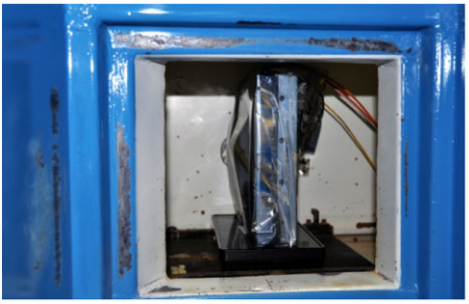

Fig. 8 ERM in calibration chamber. Each ERM flight unit, as shown here with its cover removed and placed in a protective bag, was given a small 100-rad exposure in a Co-60 irradiator to establish an initial calibration

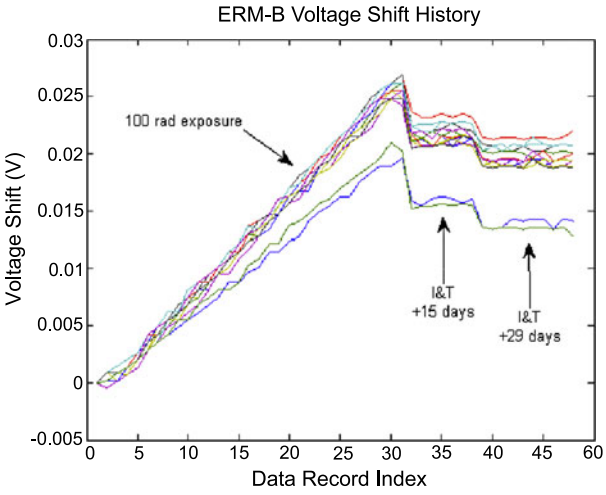

Fig. 9 ERM-B flight unit dosimeter calibration results. The first 32 readings (one every 3 minutes) were captured during the initial 100-rad exposure and show good linearity with a spread between RadFET die of ±5 % or less. The board-mounted RadFET (*lower blue* and *green traces*) received a slightly lower dose as it was slightly further from the source. Subsequent readings, captured after 15 days and 29 days, where the RadFETs were maintained in the shorted condition while sitting on the spacecraft, show two steep downward steps that indicate significant "fade" over a period of weeks. Future tests are planned to evaluate this fade characteristic over temperature. Results for ERM-A are similar

The initial matching in dose response between the RadFET devices was measured to be ±5 %, which is consistent with the manufacturer's claims and is considered acceptable (see Fig. 9). The board-mounted RadFET is positioned slightly further away from the source and therefore received a lower dose. Separating it from the central cluster of measurements also shows the slightly better matching that is achieved between devices on the same die. The initial measured response to dose (∼0.25 mV/rad) is about 50 % higher than was observed for bare RadFETs in the same chamber, which suggests the mounted RadFETs see an enhancement in dose due to backscatter effects from nearby materials (e.g., the thick aluminum substrate and box walls). A Geant4 analysis of the chamber configuration confirmed this result and emphasizes the need to model the calibration setup to obtain accurate results.

Following the irradiation, the covers were re-installed and the qualified units were integrated with the spacecraft. Periodic measurements of the RadFETs during spacecraft Integration and Test (I&T) revealed a fade rate much higher than is normally expected for these devices. A ∼20 % drop in the threshold voltage was observed after about a month's

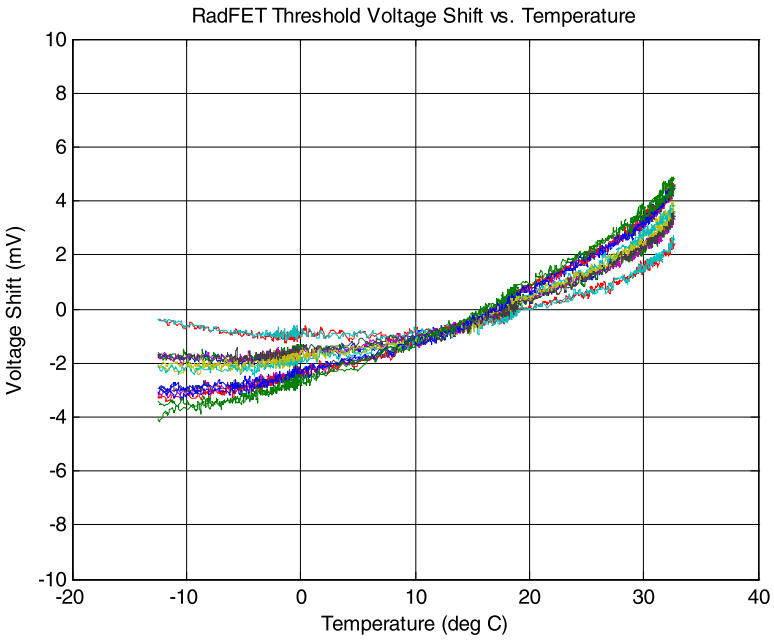

Fig. 10 ERM-B RadFET temperature dependence. The RadFETs are read out using a precision current source with a value close to the minimum temperature coefficient for these devices. The residual variation is less than ±5 mV over a 50 °C range, which corresponds to an error in dose of less than 20 rads. A simple linear correction reduces the variation to ±1 mV. The temperature characteristic may be different from die to die, but RadFETs on the same die match very well. The temperature sensitivity will increase with dose, but this change is predictable and will be allowed for in dose estimates

time, where data collected by the manufacturer using devices under bias exhibit an order-of-magnitude less. Later investigations by the manufacturer confirm that the fade rate for unbiased devices is higher than for biased devices. It also appears that small differences in the fade rate between devices may lead to an increase in the overall uncertainty (note increasing spread in Fig. 9). In general, fade may be less of a problem at colder temperatures (reduced annealing rate) and additional measurements of fade at selected operating temperatures are planned. The effect of fade, in general, will be to reduce dose accuracy. Study of the present case indicates that the effect is predictable and that an appropriate correction can be included in the calibration to determine dose estimates. In the event fade remains a significant source of error, we can perform additional ground calibrations on the EM using the environmental conditions observed in flight.

During spacecraft Thermal Vacuum (TV) testing, each ERM was cycled over a range of operating temperatures. This test provided an opportunity to evaluate the temperature dependence of the RadFET measurement scheme. Figure 10 shows an overlay of the temperature dependence for all 16 RadFET devices in ERM-B. There is some variation in the shape of the dependence from die to die, but devices on the same die match extremely well. In all cases, the magnitude of the variation is small and amounts to a systematic error of less than 20 rads over a 50 °C swing in temperature. At a given dose the characteristic is repeatable, which lends itself to further correction. In this case, it was found that a simple linear correction applied to each die reduced this error by a factor of 5. Previous experience shows, however, that the device temperature coefficient (TC) increases with deposited

dose (Holmes-Siedle et al. 2007); the cause linked to the formation of new interface states (Camanzi et al. 2001). The effect of this change will be to reduce dose accuracy; however, study so far of the change in TC indicates that the effect is predictable, can be calibrated, and will be allowed for in dose estimates.

ERM Charge Monitor Testing and Calibration The charge monitors have not yet been tested in an actual electron beam, which is planned as part of future ground tests on the EM, but their conversion gain was verified using an injected signal via a very high-value resistor (1000 GΩ) and found to be within the precision limit of the feedback resistor (∼1 %). With the injection resistor removed, the output will read close to the added offset (24.8 mV), which was chosen to be an order-of-magnitude larger than the maximum expected input offset voltage of the amplifier along with any stray leakage currents on the board. A guaranteed positive offset voltage allows precision measurements of quiescent currents near zero. Performance testing shows a strong correlation between the amount of stray leakage current and the internal relay state (i.e., which RadFET is selected). As a result, the 36 leakage current measurements within a measurement cycle tend to form "bands" since many of the relay states are similar (see Fig. 11). This effect appears stable and repeatable, which lends itself to a simple offset correction. Without any correction, the maximum difference between readings amounts to less than ∼60 fA, which is less than ∼0.3 % of the expected full-scale signal. With offset corrections applied, this source of systematic error is removed completely and the residual variation reduces to the quantization limit of the ADC. During quiescent periods, additional sensitivity can be achieved at the expense of temporal resolution by averaging together the 36 measurements within a cycle. In this case, the variation reduces to less than ∼0.2 fA, which is 5 orders down from the expected full-scale signal and a full order of magnitude below quiescent levels, thus demonstrating excellent margin.

The output offsets of the charge monitors show some sensitivity to temperature, but the effect is small and will likely be slowly varying on-orbit and thus not likely to confuse the detection of dynamic fluctuations. Figure 12 shows the temperature characteristic for each charge monitor, where the 36 measurements within each 3-min cycle were averaged to reduce the dispersion. The characteristic appears exponential with an effective doubling of stray leakage currents about every 10 °C. Ignoring the very slight amount of hysteresis, the characteristic is repeatable and could be corrected; however, the magnitude of the initial offset and the total change over the expected operating range is relatively small (<100 fA) and can probably be neglected under most conditions.

5 Sensor Operations

The operations plan for ERM is very simple and straightforward as ERM has only a single operating mode. The ERM can be on and generating data whenever the RBSPICE instrument is powered on in at least its low-voltage, standby mode. The operations goal is to remain powered continuously as much as possible, but it is understood that there will be times when it must be switched off to accommodate special RBSPICE operations or to support other instrument or spacecraft operations. The ERM dosimeter is designed to accumulate dose accurately even if powered off for indefinite periods and to report the total integrated mission dose correctly when power is again available (see Sect. 3). The charge monitors can only provide real-time data when ERM is powered. The ERM has a short warm-up characteristic and produces stable data within minutes following a long outage. Short outages have no effect on system performance.

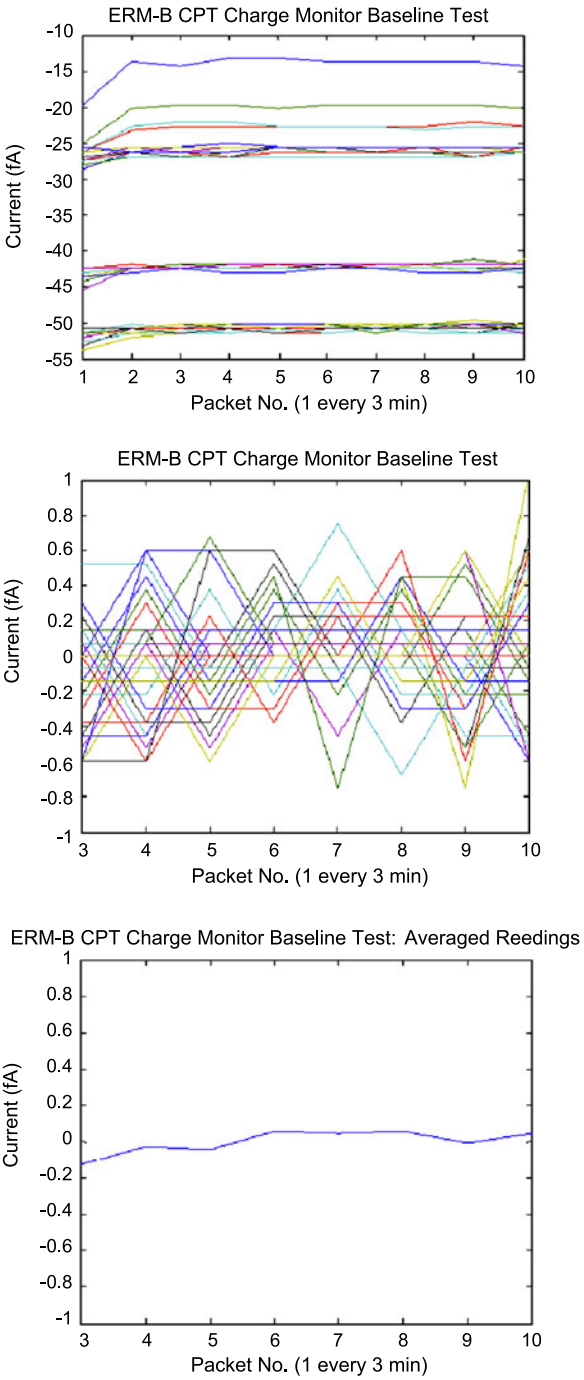

Fig. 11 ERM-B flight unit charge monitor performance test. (*Top panel*) Measurements within a packet tend to form "bands" due to slight differences in offset related to the internal relay state. (*Middle panel*) These systematic offsets can be removed to demonstrate a noise floor consistent with the quantization limit of the ADC. (*Bottom panel*) Additional sensitivity can be achieved by averaging at the expense of temporal resolution

The sensitivity of the RadFETs decreases with the accumulation of dose and will be highest at the start of the mission. The central RadFET (thinnest shielding) is expected to

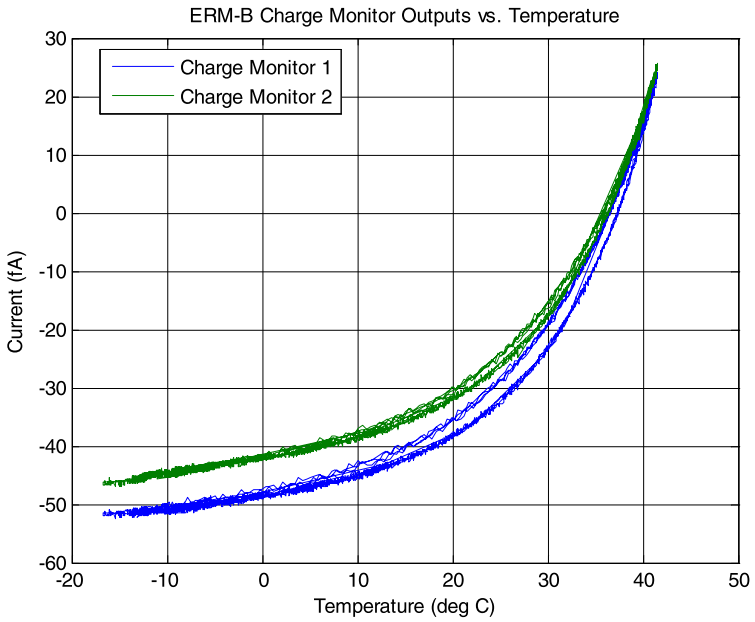

Fig. 12 ERM-B flight unit charge monitor temperature characteristic. As expected, stray leakage currents increase exponentially with temperature with an effective doubling about every 10 °C. Over the expected operating range, the effect is small and repeatable and the slight amount of hysteresis can be ignored

accumulate ∼1 krad/day and the ERM experiment would therefore benefit by being powered on as soon as possible after successful orbit insertion to minimize the data gap since launch and help reduce this initial uncertainty. RBSPICE commissioning activities are scheduled about 18 days into the mission to allow adequate time for outgassing before opening its cover, but an early scheduled turn-on of power rails in low-voltage mode with its cover closed will allow ERM to be powered within the first two days. Pre-irradiation tests show that the fresh sensor array can resolve dose increments well under 100 rads (see Fig. 9), so changes in the threshold voltages before the RBSPICE cover is deployed will be especially meaningful.

6 Telemetry Data Products

The ERM produces a single telemetry packet that contains sensor measurements and housekeeping readings. These packets are assigned a unique RBSPICE application identifier and will be archived as an RBSPICE data product, but ERM data will also be readily accessible via the RBSP Mission Operations Center (MOC) directly. Real-time displays of ERM data have been developed for use by spacecraft operations personnel, but most off-line analysis can ingest the daily Level-0 ERM data files produced by the MOC. This data consists of Payload Telemetry Packet (PTP) files as defined in the RBSP Mission Operations Center (MOC) to Science Operations Center (SOC) Interface Control Document (drawing 7417-9050).

Each Level-0 data file contains all of the raw binary ERM data generated during a Mission Elapsed Time (MET) day. A nominal day will contain 480 ERM data packets. Each packet consists of the MET timestamp followed by a sequence of 178 measurements broken

into 9 groups. The first group contains mostly housekeeping measurements of the internally-generated voltages, total current, board temperature, and oscillator frequency. The next 8 groups are identical in structure and contain measurements corresponding to each of the 8 RadFET die along with calibration checks of the measurement system. The charge monitor readings are interleaved throughout the entire sequence to maintain a constant measurement cadence of one every 5 s.

Given the ERM is a supplementary experiment and not a part of the RBSP Level-1 requirements, conversion of the raw engineering data into calibrated units and higher-level data is planned only on an ad hoc basis. Possible products, as part of a participating scientist program or other funded effort, might include an orbit-by-orbit analysis of accumulated dose and deep dielectric charging for each spacecraft, a cross-comparison of ERM data with other real-time measurements of solar weather, and a general comparison of ERM results with models of the space environment such as AE8.

7 Conclusion

An Engineering Radiation Monitor (ERM) has been successfully built as a balance mass experiment for NASA's Radiation Belt Storm Probes (RBSP) mission that will enable monitoring of total dose and deep dielectric charging at each spacecraft in real time. Each ERM contains an array of RadFET dosimeters with carefully-designed absorbers ranging in thickness from 50 microns to 9 mm. The dosimeters mimic the situation of electronics located at various depths in the spacecraft and the growing doses they receive from the space environment and will obtain a measured dose-depth curve specific to the RBSP orbit for comparison with model predictions. Its high initial sensitivity will enable profiling of RBSP's path through the Earth's trapped radiation belts, which could reveal details not included in current static models. Such data can be used by spacecraft designers when considering the degree of shielding and derating of sensors and electronics that is demanded by the actual environmental conditions in orbit. Two buried conductive plates set behind different thickness covers will measure deep dielectric charging conditions that can be potentially hazardous to sensitive electronic components within the spacecraft. The charge monitors are designed to handle extreme events without saturating and will enable correlation of spacecraft anomalies with local space weather conditions. Beyond its role as a spacecraft engineering subsystem, the ERM may also prove beneficial to the RBSP science investigations by helping to characterize the high-energy background omnipresent in their instruments.

Acknowledgements The authors would like to express our gratitude to the Living With a Star (LWS) Program, the RBSP Project Office, and the RBSPICE Instrument team for enabling the development of this experiment. The authors also wish to thank the ERM engineering team for their dedicated efforts in designing and building a successful ERM on a very short schedule.

References

S. Agostinelli et al., Nucl. Instrum. Methods A **506**, 250 (2003)
T. Beutier et al., in *Proc. 7th Eur. Conf. RADECS* (2003), p. 181
B. Blake et al. (2012, this issue)

A. Bogorad et al., IEEE Trans. Nucl. Sci. **56**, 3429 (2009)
P. Calvel et al., IEEE Trans. Nucl. Sci. **55**, 3106 (2008)
B. Camanzi, A.G. Holmes-Siedle, A.K. McKemey, Nucl. Instrum. Methods A **457**, 476 (2001)
G. Ginet, T. O'Brien, AE-9/AP-9 trapped radiation and plasma models requirements specification (2009)
D. Heynderickx et al., in *Proc. 7th Eur. Conf. RADECS* (2003), p. 643
A.G. Holmes-Siedle, L. Adams, *A Handbook of Radiation Effects*, 2nd edn. (Oxford University Press, Oxford, 2002)
A.G. Holmes-Siedle, F. Ravotti, M. Glaser, in *IEEE Radiation Effects Data Workshop* (2007). doi:10.1109/REDW.2007.4342539L
J. Lanzerotti et al. (2012, this issue)
B.H. Mauk et al. (2011, private communication)
B.H. Mauk et al. (2012, this issue)
D.M. Sawyer, J.I. Vette, Natl. Sp. Sci. Data Cent., NSSDC/WDC-A-R&S 76-06 (1976)
J.I. Vette, Natl. Sp. Sci. Data Cent., NSSDC/WDC-A-R&S 91-24 (1991)

DOI 10.1007/978-1-4899-7433-4_15
Reprinted from *Space Science Reviews* Journal, DOI 10.1007/s11214-013-9971-z

The Balloon Array for RBSP Relativistic Electron Losses (BARREL)

R.M. Millan · M.P. McCarthy · J.G. Sample · D.M. Smith · L.D. Thompson · D.G. McGaw · L.A. Woodger · J.G. Hewitt · M.D. Comess · K.B. Yando · A.X. Liang · B.A. Anderson · N.R. Knezek · W.Z. Rexroad · J.M. Scheiman · G.S. Bowers · A.J. Halford · A.B. Collier · M.A. Clilverd · R.P. Lin · M.K. Hudson

Received: 24 March 2012 / Accepted: 22 December 2012 / Published online: 26 March 2013

Abstract BARREL is a multiple-balloon investigation designed to study electron losses from Earth's Radiation Belts. Selected as a NASA Living with a Star Mission of Opportu-

R.M. Millan (✉) · D.G. McGaw · L.A. Woodger · B.A. Anderson · N.R. Knezek · J.M. Scheiman · A.J. Halford · M.K. Hudson
Dept. of Physics and Astronomy, Dartmouth College, Hanover, NH 03755, USA
e-mail: Robyn.Millan@dartmouth.edu

M.P. McCarthy
Dept. of Earth and Space Sciences, University of Washington, Seattle WA 98195-1310, USA

J.G. Sample · R.P. Lin
Physics Department and Space Sciences Laboratory, University of California at Berkeley, Berkeley, CA 94720, USA

D.M. Smith · A.X. Liang · W.Z. Rexroad · G.S. Bowers
Dept. of Physics, University of California, Santa Cruz, CA 95064, USA

L.D. Thompson
NASA Wallops Flight Facility, Wallops Island, VA 23337, USA

J.G. Hewitt
Department of Physics (DFP), USAF Academy, Colorado Springs, CO 80840, USA

M.D. Comess
Space X, Hawthorne, CA 90250, USA

K.B. Yando
Space Sciences Laboratory, University of California at Berkeley, Berkeley, CA 94720, USA

A.B. Collier
School of Physics, University of Kwazulu-Natal, Durban 4001, South Africa

M.A. Clilverd
British Antarctic Survey, Cambridge CB3 0ET, UK

R.P. Lin
School of Space Research, Kyung Hee University, Yongin, Korea

nity, BARREL augments the Radiation Belt Storm Probes mission by providing measurements of relativistic electron precipitation with a pair of Antarctic balloon campaigns that will be conducted during the Austral summers (January-February) of 2013 and 2014. During each campaign, a total of 20 small (∼20 kg) stratospheric balloons will be successively launched to maintain an array of ∼5 payloads spread across ∼6 hours of magnetic local time in the region that magnetically maps to the radiation belts. Each balloon carries an X-ray spectrometer to measure the bremsstrahlung X-rays produced by precipitating relativistic electrons as they collide with neutrals in the atmosphere, and a DC magnetometer to measure ULF-timescale variations of the magnetic field. BARREL will provide the first balloon measurements of relativistic electron precipitation while comprehensive in situ measurements of both plasma waves and energetic particles are available, and will characterize the spatial scale of precipitation at relativistic energies. All data and analysis software will be made freely available to the scientific community.

Keywords Radiation belts · Wave-particle interactions · Electron precipitation

1 Introduction

The loss of radiation belt particles has long been attributed to scattering into Earth's atmosphere (e.g., Walt and MacDonald 1962). Losses help define the structure of the radiation belts, for example, giving rise to the characteristic slot region between the inner and outer electron zones (Lyons and Thorne 1973). Precipitation into the atmosphere can be significant, completely depleting the radiation belts of electrons during the main phase of some geomagnetic storms (e.g., O'Brien et al. 2004; Selesnick 2006). Such rapid loss places a major constraint on the acceleration rate required to re-populate the belts on the timescale of a few days. Quantifying the electron loss rate is thus critically important for understanding the acceleration processes acting in the belts. Recently, loss to the magnetopause was shown to also be significant, particularly during storms (Ukhorskiy et al. 2006; Ohtani et al. 2009; Turner et al. 2012). The relative importance of magnetopause and atmospheric loss is currently unknown.

Wave-particle interactions are believed to be the main cause of scattering into the atmospheric loss cone (see e.g., Millan and Thorne 2007 and Thorne 2010 for a review). However, there is still very little quantitative comparison between theoretical predictions and observational data. The recent discovery of very large-amplitude whistler-mode waves in the magnetosphere (Cattell et al. 2008) raises questions about the validity of the quasi-linear treatment of wave-particle interactions that is typical of diffusive radiation belt models. It is important to establish when and where this approach is applicable.

The primary objective of BARREL is to understand relativistic electron precipitation. BARREL measures precipitation using an array of stratospheric balloons located in the region that magnetically maps to the radiation belts. Simultaneous measurements of precipitation by multiple balloon payloads distributed in L-value and magnetic local time allow BARREL to measure the electron loss rate across the outer zone, and probe the large-scale spatial structure of high energy precipitation. BARREL will augment the RBSP mission by providing measurements of precipitation which are difficult to obtain from an equatorial platform due to the small size of the equatorial loss cone. Conjunctions between the BARREL payloads and RBSP spacecraft will allow for direct, quantitative tests of theoretical models of precipitation by wave-particle interactions. BARREL is also complementary to other LEO assets that measure precipitation such as the NOAA-POES spacecraft. The

Table 1 BARREL investigation specifications

Attribute	Value
Payload Mass	24 kg
Average Payload Power	4.3 W
Payload Telemetry Rate	2.1 kbits/s
Expected Campaign Durations	1/1/13–2/10/13; 1/1/14–2/10/14
Expected Longitude Coverage	0°–150°W
Expected L-value Coverage	3–7

balloon-based BARREL platform is nearly stationary, allowing for separation of temporal and spatial variations.

A major challenge of BARREL is the manufacture of 45 identical payloads (20 for each campaign and 5 spares) using the resources found at a typical research University. In this sense, BARREL is a pathfinder for future multi-spacecraft space physics missions. Critical to this effort was the production of multiple prototype payloads. This allowed for validation of the payload design, but also for refinement of the procedures for tracking, integrating, and testing payloads in parallel. Improvements to the design necessary for streamlining production were also made possible by building and testing early prototypes of the payload and instruments. Test campaigns, conducted from McMurdo, Antarctica in 2009 and 2010 with support from the NSF and NASA/CSBF, allowed for validation of the payload design in the actual flight environment, and improvement of the operations plans. Science data were also obtained and preliminary results are summarized in Millan (2011).

This paper provides a comprehensive overview of the BARREL investigation. Table 1 gives an overview of the BARREL payload and campaign specifications. In Sect. 2, we provide a more detailed discussion of the science objectives and discuss some mission design considerations for obtaining science closure. BARREL takes advantage of the instrument development done for the NSF-funded MINIS 2005 balloon campaign (Kokorowski et al. 2008). The instrumentation and support systems, described in Sects. 3 and 4 respectively, are largely based on MINIS. Instrument calibration is described in Sect. 5, and BARREL data products and data analysis are described in Sect. 6.

2 Science Objectives and Design Considerations

2.1 Types of Relativistic Electron Precipitation

At least two different types of relativistic electron precipitation have been reported and are thought to be caused by different mechanisms. The two types are differentiated by their temporal profiles and distribution in magnetic local time as described in detail in Millan (2011), and briefly reviewed here.

Rapid (∼250 ms), intense bursts of precipitating electrons, called “microbursts” were first observed in the 10–100 keV energy range using balloon-based instrumentation (Anderson and Milton 1964). Microbursts were later shown to extend to relativistic energies (Imhof et al. 1992), and studied extensively with data from the SAMPEX satellite (e.g., Blake et al. 1996; Nakamura et al. 2000; O’Brien et al. 2004). The top panel of Fig. 1 shows an example of microburst precipitation detected by the MAXIS balloon payload during a geomagnetic storm in January 2000. The occurrence of microbursts peaks between $L = 4$–6 on the dawnside and during geomagnetic storms, similar to the distribution of whistler-mode

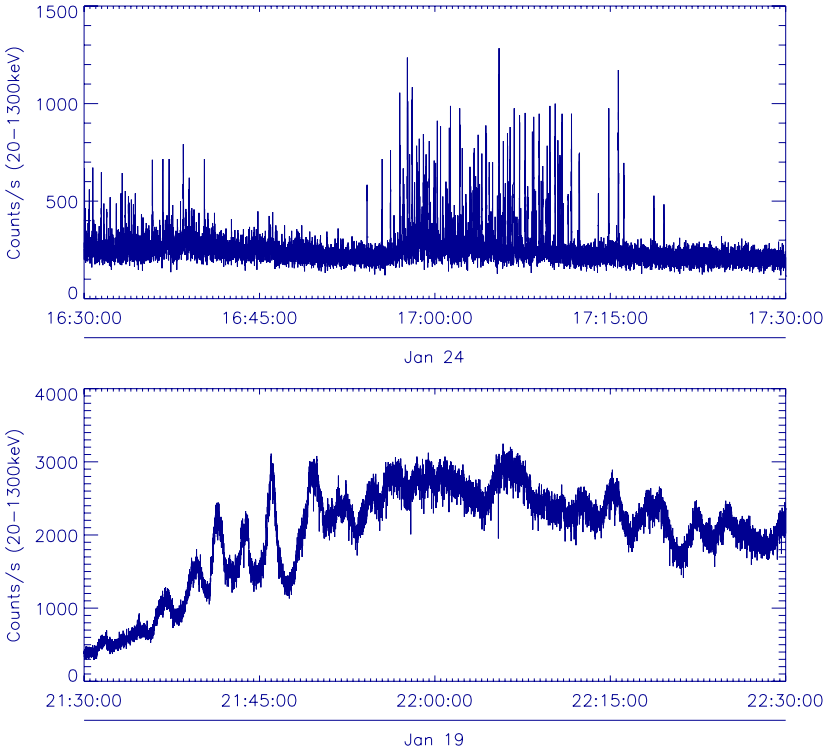

Fig. 1 Microburst precipitation (*top*) and duskside precipitation (*bottom*) observed by the MAXIS balloon experiment on January 24 and January 19, 2000 respectively. Both panels extend over a one hour time interval

chorus (e.g., Lorentzen et al. 2001b). The loss rate due to microbursts was estimated to be fast enough to empty the outer zone in about one day (O'Brien et al. 2004), but this analysis relied on an estimate for the spatial scale of the microburst region based on a statistical distribution. Refinement of this estimate will require knowledge of the instantaneous extent of the microburst precipitation region.

On the duskside, relativistic precipitation occurs with slower time variations, from minutes to hours (Millan et al. 2002). Unlike microbursts, duskside precipitation is not strongly correlated with geomagnetic storms and is known to occur over a range of magnetic activity levels, from small, isolated substorms (Lorentzen et al. 2000) to major CME-driven storms (Kokorowski et al. 2008). The occurrence has a broad radial distribution ranging from $L = 3$–8. Duskside events are often modulated at ULF timescales (e.g., Millan et al. 2007), evident in the bottom panel of Fig. 1 which shows an example of duskside precipitation measured by the MAXIS balloon payload. Pitch-angle scattering by electromagnetic ion cyclotron (EMIC) waves, proposed much earlier on theoretical grounds (Thorne and Kennel 1971), may be the precipitation mechanisms (e.g., Foat et al. 1998; Lorentzen et al. 2000). However, this hypothesis is based primarily on the duskside location, and simultaneous measurements of the waves and precipitation have so far not been available to test it.

Recent work using data from SAMPEX suggests that duskside precipitation dominates over microburst loss at energies above 1 MeV, but that a third type of precipitation that is not localized in local time and does not belong to the two types described above appears to

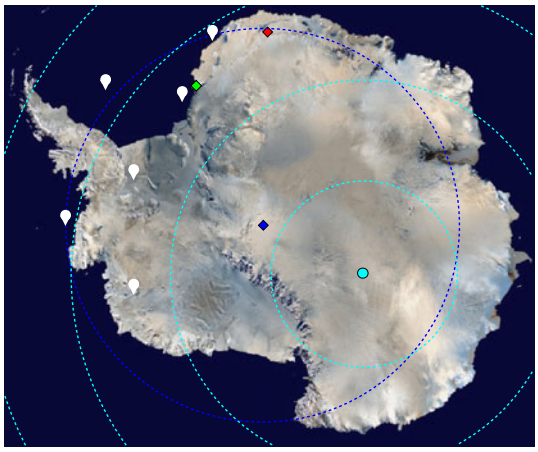

Fig. 2 Schematic of BARREL over Antarctica showing rough locations of SANAE IV (*red diamond*), Halley VI (*green diamond*), South Pole (*blue diamond*), the geomagnetic pole (*cyan dot*) and example balloon locations (*white balloons*). The *blue dashed line* represents 70 °S geographic latitude, and the *cyan dashed lines* are lines of constant geomagnetic latitude at 50°, 60°, 70°, and 80°

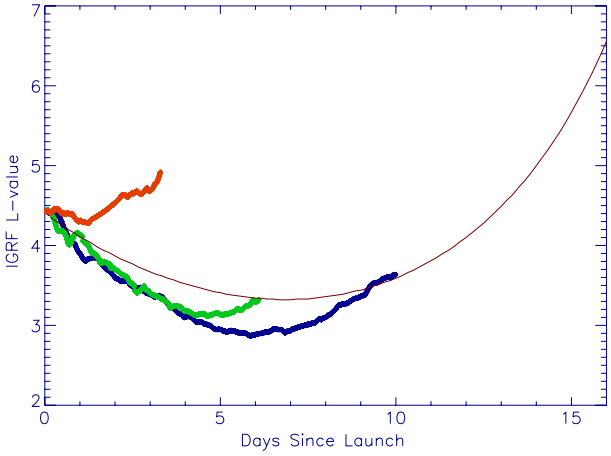

Fig. 3 Balloon trajectory in IGRF L-value assuming constant geographic latitude of −71.7° (*solid thin line*) along with three real trajectories from the MINIS 2005 balloon campaign (*thick red, blue, and green lines*). The payload speed is based on MINIS but can be significantly faster. For example, in January 2000, the MAXIS balloon moved about three times as fast at a similar geographic latitude (−74°)

dominate the overall loss rate, possibly because it represents a constant, low flux "drizzle" (D.M. Smith private comm.). Though further work is required to confirm these preliminary results, it is clear that neither the importance nor the mechanism responsible for relativistic electron precipitation are well understood.

BARREL is designed to measure all types of electron precipitation between 100 keV and a few MeV. To detect microbursts, measurements will be made with 50 ms time resolution. The balloon array will extend across L-values ranging from 3–7, allowing for measurements of precipitation across the outer zone. This is achieved with long duration balloons (LDBs) launched in the polar regions during summer. The circumpolar vortex winds carry each balloon westward away from the launch sites, allowing the array to be established after a few successive launches during the first week of the campaign (Fig. 2). Because of the tilt of Earth's magnetic dipole, each balloon traverses L-shells as it drifts at nearly constant geographic latitude (Fig. 3). Since the balloons move slowly (∼10–30 km/h) relative to the Earth's surface, each payload samples all local times, but when launched 1–2 days apart, provide average separations of 1–2 hours of MLT. Each BARREL payload will remain aloft in the region of interest for 5–10 days, depending on upper level wind speeds. As balloons drift out of the region, new balloons will be launched to maintain the array; a total of 20 pay-

loads will be launched during each campaign. Two Antarctic stations were chosen as launch sites because of their locations and logistical considerations. The South African Antarctic station SANAE IV is located at 2.8W, 71.7S, corresponding to IGRF $L = 4.4$, and Halley VI is located at 26.5W, 75.5S, corresponding to $L = 4.5$. Although only slightly higher in L-value, Halley Bay is at higher geographic latitude and further west, providing greater coverage at higher L-values.

2.2 Wave-Particle Interactions

Precipitation into the atmosphere is generally attributed to wave-particle interactions. The condition for gyro-resonance occurs when the Doppler-shifted plasma wave frequency is equal to the particle gyrofrequency,

$$\omega - k_{\parallel} v_{\parallel} = \frac{n \Omega_e}{\gamma} \tag{1}$$

where ω is the wave frequency, $k_{\parallel}$ and $v_{\parallel}$ are the parallel components of the wave vector and particle velocity respectively, Ω_e is the non-relativistic electron cyclotron frequency, γ is the relativistic factor, and n is a positive or negative integer. When this condition is met, energy can be exchanged between the wave and the particle, leading to acceleration or pitch angle scattering. A more detailed review, including a description of the relevant plasma waves, is given by Millan and Thorne (2007).

Not long after their discovery, low energy microbursts were associated with whistler-mode chorus (e.g., Rosenberg et al. 1971), and more recently the association was made for relativistic microbursts (Lorentzen et al. 2001b). In order for an electron with energy of order 1 MeV to be in resonance with typically observed wave frequencies, the interaction must either occur at off-equatorial latitudes ($\sim 30^{\circ}$) or be a higher order resonance ($n \geq 3$) (e.g., Lorentzen et al. 2001b). As mentioned previously, the distributions in L-value and magnetic local time are strikingly similar for chorus and microbursts. Additionally, Lorentzen et al. (2001b) found that chorus risers, which are whistler mode waves observed to have a frequency rising in time, last for the same length of time as the coincident microbursts, and the occurrence of microbursts and chorus were generally well correlated for the time periods analyzed. However, as the authors point out, "[c]orrelation does not imply causality," and more observations are needed to quantitatively test models. Most theoretical work applies the quasi-linear, bounce-averaged pitch angle diffusion equation (Schulz and Lanzerotti 1974). However, recent observations of microbursts occurring in conjunction with very large amplitude whistler-mode waves suggest that non-linear trapping may play an important role in the interaction (Kersten et al. 2011). Additionally, microbursts occur on the bounce timescale, thus are too fast for bounce-averaging to be appropriate.

Pitch-angle scattering by EMIC waves was also suggested as a primary loss mechanism for relativistic electrons, since observed wave amplitudes exceeding 1 nT imply scattering in the strong diffusion limit (e.g., Summers and Thorne 2003; Albert 2003). A few studies have found correlated ion and electron precipitation, consistent with scattering by EMIC waves (e.g., Bortnik et al. 2006), but the importance of this mechanism has so far not been quantified. EMIC waves can be excited when substorm-injected ions encounter the cold plasmasphere, leading to a temperature anisotropy that is unstable to the generation of the waves. The injected ions drift westward towards dusk, thus there is believed to be some preference for generation of EMIC waves in the dusk sector, although a peak in their occurrence is also observed near noon where the temperature anisotropy is driven by compressions of the magnetopause (Anderson and Hamilton 1993). In addition to wave generation, the interaction

itself is expected to be more effective from afternoon to dusk where a plasmaspheric plume stretches to high L-values (e.g., Goldstein et al. 2004). The high cold plasma density in the plume lowers the minimum resonance energy for the interaction (e.g., Millan and Thorne 2007). The local time of the duskside precipitation, coincident with the location expected for strong interaction between electrons and EMIC waves, prompted further investigation into whether EMIC waves were the scattering mechanism (e.g., Lorentzen et al. 2000). However, quantitative studies have not been carried out to test this hypothesis due to the lack of good wave observations, and the evidence is so far circumstantial.

The BARREL campaigns will be conducted during the RBSP mission, providing a unique opportunity to obtain measurements of relativistic precipitation in conjunction with in situ observations of plasma waves. The combined BARREL-RBSP measurements will be used to directly test models of wave-particle interactions and will quantitatively test whether whistler-mode chorus and EMIC waves are responsible for microburst precipitation and duskside precipitation respectively. This will be crucial for validating the models that will be used to calculate losses based only on in-situ RBSP measurements, for example during times when global precipitation measurements are not available. The array of balloons distributed in local time and L-value maximizes the chance for conjunctions with the two RBSP spacecraft. Two balloon campaigns will be conducted, separated in time by one year. This allows for balloon-spacecraft conjunctions at a range of magnetic local times, since the apogee of RBSP orbits precess at roughly 220° per year. When correlated measurements are obtained, the RBSP measurements will provide wave power, frequency spectrum, background magnetic field, energetic particle energy and pitch angle distributions, and the cold plasma density, all necessary parameters for using as input to wave-particle interaction models. For example, the quasi-linear diffusion rate and precipitating energy spectrum can be predicted and directly compared with the balloon observations of precipitation to determine whether the diffusion model is consistent with the data.

2.3 Precipitation Loss Rate

One of the mysteries of radiation belt variability is the differing electron response for geomagnetic storms that otherwise seem very similar (as characterized by the D_{st} index). A study of 276 storms by Reeves et al. (2003) showed that only 53 % of the storms resulted in an overall increase in the trapped flux over pre-storm levels, while 19 % resulted in a decrease. This suggests that a sensitive balance exists between acceleration and loss processes. Electrons can be lost from the radiation belts very rapidly; large drops in the flux first observed at geosynchronous orbit have been observed down to $L \sim 4$ (e.g., Morley et al. 2010). These rapid electron depletion events may be due to precipitation (Green et al. 2004) or magnetopause losses (e.g., Ohtani et al. 2009; Turner et al. 2012) or a combination of both (e.g., Millan et al. 2010). Attempts to quantify the precipitation loss rate indicate that the loss can be strong enough to empty the radiation belts in a day or less (Lorentzen et al. 2001a; Millan et al. 2002; O'Brien et al. 2004; Selesnick 2006).

BARREL will determine the precipitation loss rate by making measurements over a wide range of local time and L-value. During specific relativistic electron events, the loss rate will be compared to changes in the trapped flux as measured by RBSP and other spacecraft, in order to quantify the role of precipitation relative to magnetopause loss.

2.4 Large-Scale Spatial Structure of Relativistic Precipitation

We currently know very little about the spatial distribution of energetic precipitation. Contrast this with our knowledge of the spatial and temporal evolution of lower energy auroral

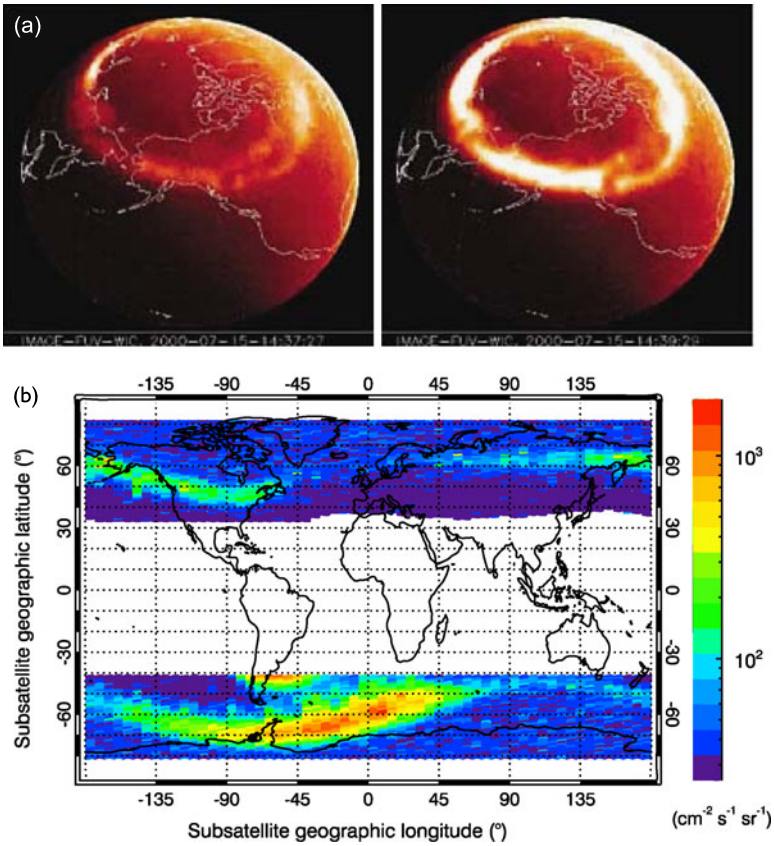

Fig. 4 (**a**) IMAGE FUV time sequence of the auroral oval on July 15, 2000 (Courtesy NASA/IMAGE FUV team), and (**b**) Spatial distribution of > 1 MeV precipitating electrons using data from NOAA POES, averaged over the recovery phase of 69 geomagnetic storm, adapted from Horne et al. (2009), Copyright 2009, American Geophysical Union

precipitation, routinely observed with high spatial and temporal resolution as shown in the IMAGE FUV time sequence in Fig. 4a. At relativistic energies, the primary observational tool has so far been single-point spacecraft measurements such as those from NOAA-POES and SAMPEX. These have provided statistical maps of energetic precipitation such as the map of >1 MeV precipitation shown in Fig. 4b. Such maps reveal important features such as the effects of the South Atlantic Magnetic Anomaly, but the spacecraft revisit a particular location infrequenty, thus limiting the time resolution. Observations from the MINIS balloons revealed complicated temporal and spatial structure of energetic precipitation (Millan 2011) which can only be observed from a nearly stationary platform that does not move quickly through the precipitation region. Untangling the spatial structure of precipitation should reveal information about important boundaries that control or influence precipitation. The spatial scale of the precipitation region is also critical for determining the overall loss rate of electrons discussed in Sect. 2.3.

Another common feature of energetic precipitation is modulation at ULF-timescales, clearly seen in the bottom panel of Fig. 1. Several ideas have been proposed to explain this modulation, but the mechanism is still unknown. It is not clear whether the ULF waves simply modulate the precipitation or whether they play a critical role in causing the scattering.

ULF waves could be modulating the growth rate of waves, which has been proposed to explain Pc1 pearls through several mechanisms (e.g., Demekhov 2007). Alternatively, if EMIC waves are the cause of the precipitation, modulation of the background magnetic field would lead to a modulation of the minimum resonance energy. For a very steeply falling electron energy spectrum, this would lead to a significant modulation of the precipitating flux. A third suggestion is that the azimuthal electric field of a poloidal mode standing wave may violate an electron's second adiabatic invariant, leading to a decrease in pitch angle for those particles decelerated by the wave in the perpendicular direction (M.K. Hudson, priv. comm.). In each of these cases, one can determine whether the precipitation is modulated in phase or out of phase with the wave magnetic field by comparing measurements of precipitation with both the BARREL magnetic field measurements and those of the RBSP spacecraft.

BARREL will characterize the spatial extent and large scale spatial structure of relativistic precipitation, which has been previously addressed only in a statistical sense. The region over which waves scatter electrons is a critical parameter for modeling electron loss timescales. This is particularly important when direct precipitation measurements are not available. BARREL will simultaneously measure precipitation at about 5 different locations. The data can also be combined with other space and ground assets to produce global maps of precipitation. The nearly-stationary balloon platform will allow for separation of temporal and spatial features, and the study of modulation that is so frequently observed. In particular, the multi-point measurements will allow us to determine the azimuthal mode number of the ULF waves responsible for the modulation. Comparison with RBSP and other spacecraft data will determine whether the modulation is, for example, in phase with the electric or magnetic field, allowing us to constrain the mechanism.

3 Science Instruments

3.1 X-Ray Spectrometer

BARREL measures relativistic electron precipitation by detecting the bremsstrahlung X-rays produced when electrons collide with atmospheric neutrals. This technique has been used for observing lower energy auroral precipitation for many years (e.g., Winckler et al. 1958; Parks et al. 1993), including the discovery of microburst precipitation (Anderson and Milton 1964). More recently this technique has proved useful for detecting relativistic precipitation (e.g., Foat et al. 1998; Millan et al. 2002). Since relativistic electrons produce X-rays with energies as high as the parent electron energy, the detectors must be efficient at stopping high energy (up to several MeV) photons. The BARREL spectrometer system is shown in a block diagram (Fig. 5) with specifications outlined in Table 2, and described in more detail below. The spectral inversion process used to obtain flux and energy information about the parent electrons from the X-ray measurements is discussed in Sect. 6.2.2.

3.1.1 Instrument Description

Each BARREL payload includes a single 3 in high × 3 in diameter NaI scintillator which provides a good compromise between energy resolution, detector efficiency (stopping power) and cost. The scintillator crystal is coupled to a photomultiplier tube (PMT), followed by signal processing electronics. The scintillator crystal, the PMT, a high voltage converter and a preamplifier, are all housed in a light-tight aluminum tube (Fig. 6). The assembly is wrapped with a layer of mu-metal shielding to prevent Earth's magnetic field from modulating the PMT gain as the balloon payload rotates or swings.

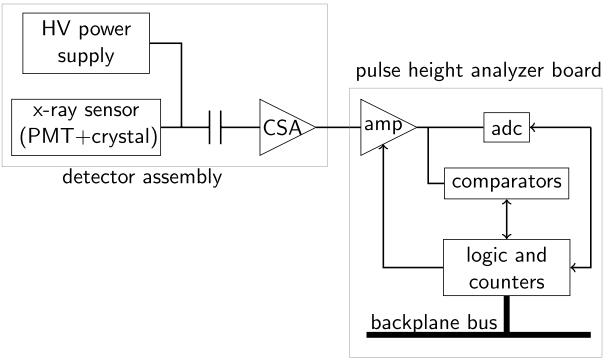

Fig. 5 Block diagram of the BARREL X-ray spectrometer

Table 2 Spectrometer specifications

Attribute	Value	Comments
Mass	2.8 kg	includes insulation and harness
Energy range	20 keV–10 MeV	
Electronic resolution	2.4 keV/channel	reduced by binning
System resolution	7 % at 662 keV	
Effective Area	16 cm^2 at 1 MeV	photopeak
Dead time per event	52 µs	
Operating temperature	−10 °C–40 °C	efficiency decreases below ∼15 °C
Voltage requirement	±5 V	
Current requirement	∼40 mA on plus; ∼15 mA on minus	depends on count rate

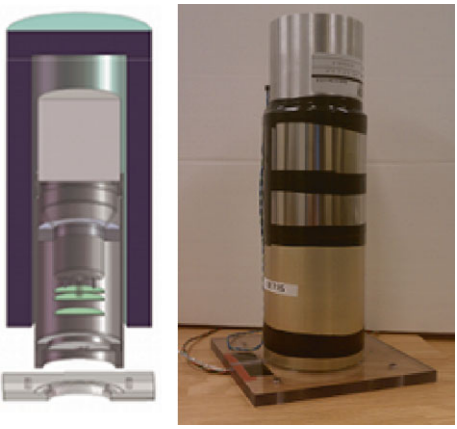

Fig. 6 Cutaway drawing (*left*) and photo (*right*) of the detector assembly

X-rays deposit energy in the scintillator crystal, with a fraction of that energy appearing as a visible light pulse. The PMT converts the light pulse proportionally into a charge pulse, and a charge-sensitive amplifier converts the charge into a voltage pulse. A pulse analyzer board accepts the preamp output and outputs a digital word, whose value is linearly related to the original X-ray energy. The pulse analyzer board contains analog signal processing circuits, an analog to digital converter (ADC), event selection logic, counters, and interface

logic. Data from the pulse analyzer board is read into the instrument controller board (DPU) described in Sect. 4.1 below.

The BARREL X-ray spectrometer assembly (including scintillator, photomultiplier, signal-processing electronics, and high voltage power supply) is fabricated at the University of Washington and is identical to that flown during the 2005 MINIS balloon campaign, and more recently during the BARREL test flights. The spectrometer assembly design has over 2000 instrument hours of operation at balloon altitude.

3.1.2 Effective Area and Field of View

The effective area of the BARREL spectrometer is 16 cm^2 (full energy deposited) or 35 cm^2 (any fraction of the energy deposited) at 1 MeV. The spectrometer is essentially uncollimated and accepts photons over 4π steradians. However, the field of view is effectively limited by atmospheric absorption at large angles; Monte Carlo simulations using GEANT3 indicate that the instrument is sensitive to electron precipitation over a 55–60° cone, corresponding to a 200 km circle at an altitude of 70 km, typical of where the bremsstrahlung at these energies is created. The spectrometer is oriented such that the field of view is centered on the zenith, and the effects of the balloon in the field of view are negligible since the X-rays easily pass through the very thin (0.3 mil) plastic. Using simulations of the response of NaI detectors to incoming gamma rays, and of the conversion efficiency of electrons to gammas by the atmosphere, we estimate that the BARREL 3 in × 3 in detectors have an equivalent area/angle product to a perfectly efficient relativistic electron detector, in orbit, of 3 cm^2-sr. This is, for example, over twice the factor of the energetic particle detector on the DEMETER spacecraft, although much smaller than the extremely large HILT detectors on SAMPEX. This sensitivity assumes that the precipitation occurs over the entire field of view.

3.1.3 Energy Resolution

The spectrometer resolution required to measure and invert the continuum bremsstrahlung spectrum produced by precipitating electrons is about 10 % FWHM at 1 MeV. This requirement is met with the readily available standard 3 in × 3 in NaI scintillator described above. The intrinsic energy resolution is measured to be 7 % at 662 keV. Resolution and linearity are shown in Fig. 7, an X-ray spectrum of uranium ore. Spectral data are binned to coarser resolution for telemetering as described in Sect. 3.1.5 below.

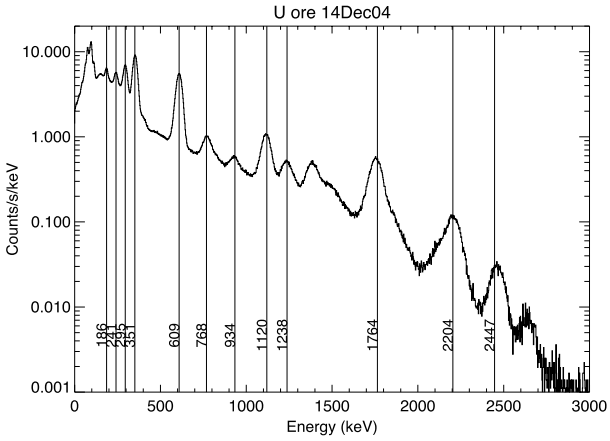

Fig. 7 Energy spectrum of uranium ore calibration source showing intrinsic spectrometer resolution

3.1.4 Time Resolution and Maximum Count Rate

The time required to analyze a single detector event depends on shaping time constants and the analog to digital conversion time, which is 2 μs. The analysis time determines the system dead time and maximum allowable counting rate. The total dead time is nominally 5 μs, corresponding to a few times 10^5 s^{-1} peak counting rate. The expected maximum count rate based on previous observations is a few times 10^4 s^{-1}, well within the instrument capabilities.

Because the arrival time of photons follows Poisson statistics, a small fraction of X-rays are missed due to a small time separation. Correcting for instrument dead time is a well-understood procedure (e.g., Knoll 1989). Pulse pile-up can also occur where two pulses are added together into a single large pulse. When this happens, low energy events are undercounted and high energy events are overcounted. However, the time window for this to occur is very small. The instrument electronics are designed such that, once a peak has been detected, an analog switch disconnects the shaping amplifier from the peak-holding capacitor. This prevents a second event from piling onto an earlier event, unless the second event arrives early enough to obscure the peak of the first event.

The spectrometer produces several data products with differing time resolution as described in the next section. The highest time resolution is 50 ms, sufficient for resolving microbursts which have typical durations of 250 ms.

3.1.5 Spectrometer Data

The spectrometer produces two kinds of data products: rate counters for monitoring instrument health, and digitized energies of individual X-ray photons, which are further binned into fast-, medium-, and slow-rate spectra before being telemetered. The rate counters include lower and upper discriminator counters, an interrupt counter, and a valid peak detect counter. Each of these count over a four second interval and is telemetered once every four seconds.

X-ray photons arrive at random times and must be read on demand. This is accomplished by having the spectrometer interrupt the DSP when it has acquired an X-ray. Individual X-ray events are binned into three spectral products (Table 3) which trade between energy and time resolution. As shown in Fig. 8, fast spectra are binned into four broad energy channels at 50 ms, providing the highest time resolution, but it should be noted that the energy ranges will shift with instrument temperature due to gain changes.

Medium-rate spectra are accumulated every four seconds into 48 bins spanning an energy range of approximately 100–4000 keV. Slow spectra covering the full energy range are accumulated into 256 bins every 32 seconds. Slow spectra bin widths increase geometrically from roughly 2.4 keV/bin (first 64 bins), to 154 keV/bin (last 32 bins). These bin widths will also shift with temperature, a fact especially important when accumulating spectra over long

Table 3 Spectrometer data products

Product	Cadence (s)	Energy Range (keV)	# Energy Channels
Rate Counters	4	–	–
Fast Spectra	0.05	20–1500	4
Medium Spectra	4	100–4000	48
Slow Spectra	32	20–10000	256

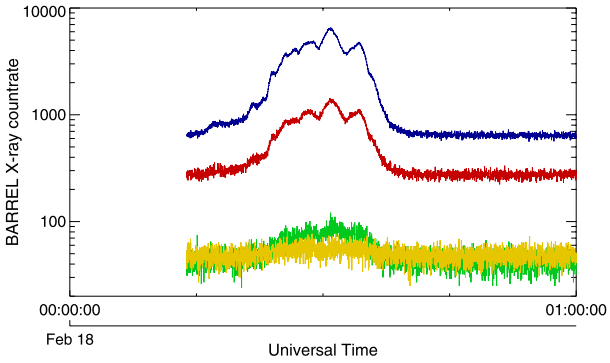

Fig. 8 Example of fast spectra taken during the 2008/2009 BARREL Antarctic test flight, adapted from Millan (2011). X-ray count rate is shown in four energy channels corresponding to <180 keV (*blue*), 180–550 keV (*red*), 550–840 keV (*green*), and 840–1500 keV (*yellow*)

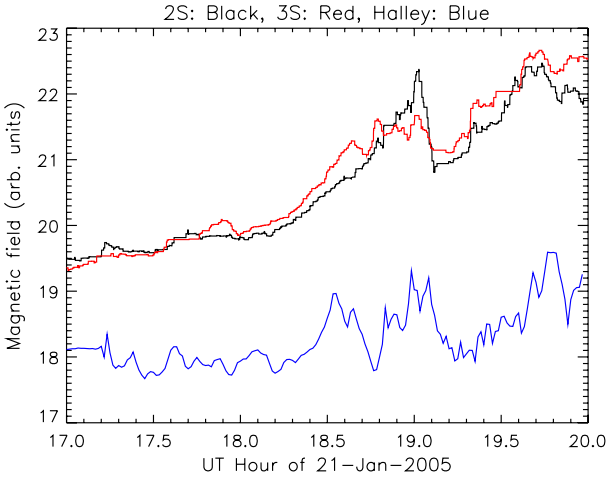

Fig. 9 Smoothed DC Magnetometer data taken showing total magnetic field during 2005 MINIS flights 2/South and 3/South (*red and black*) along with data from Halley Bay (*blue*)

time intervals (hours). Except for the lowest 25 energy bins of the slow spectrum, deltaE/E is near 3 %. At low energy, the bins are relatively wider, concomitant with the larger uncertainty in energy measurement. As described in Sect. 6.2, the Level 2 spectral products are accumulated into standardized energy bins after correcting for gain changes.

3.2 DC Magnetometer

Each BARREL payload also carries a three-axis magnetometer mounted on a 42″-long boom. Since ground-based magnetometers are often not available near the balloon locations, the on-board magnetometer is useful for identifying magnetic activity such as shown in Fig. 9. The magnetometer is also sensitive to ULF oscillations of the magnetic field, and will be used to investigate the ULF-timescale modulation of precipitation. The baseline requirements are to measure horizontal and vertical magnetic field components separately to 100 nT (3 sigma) with 1 minute temporal resolution, and total magnetic field over the range 0.2–0.5 Gauss to 50 nT precision with 1 second temporal resolution. The actual instrument exceeds these requirements, as described below.

Fig. 10 Bartington Mag648

3.2.1 Sensor

BARREL uses a Bartington Mag648 Series three-axis fluxgate magnetometer with full scale range of ±100 μT (Fig. 10), read out as three balanced differential outputs over 0 to ±3 V. The manufacturer's specification for the sensor internal noise level ranges between 10–20 $\mathrm{pT}_{rms}/\sqrt{\mathrm{Hz}}$ @ 1 Hz.

3.2.2 Electronics

The three analog signals from the Bartington sensor are sampled at 4 Hz by a 24-bit, 4-channel analog-to-digital converter (Analog Devices AD7193). The ADC includes a low-pass digital filter with a sinc^4 shape and 40 ms settling time. The sequencing of measurements from each of the three axes is handled within the chip. Each output consists of the 24-bit conversion (Data Register) and 12-bits of information about the conversion (Status Register) creating a 36-bit word per channel. The status register contains useful information for processing such as the channel that supplied the data. The magnetometer data are passed to the BARREL Data Processing Unit (DPU) via an RS-232 serial interface consisting of an 8-bit microcontroller (Microchip Technology PIC16F84A) and driver (Analog Devices ADM3222).

3.2.3 Performance

The ultimate noise performance of our magnetometer system (including the electronics) has not been reached either in laboratory tests or test flights due to magnetic noise from laboratory electronics and the payload. The lowest noise figure in our best-controlled environmental test has been 0.1 nT rms in the final 4 Hz data. In test flight conditions, the noise per axis has varied from approximately 0.2 to 3.0 nT rms, due to currents in the payload. A variety of boom configurations were tested to minimize this noise, subject to the constraint that the boom doesn't make it difficult to balance the payload. The system gain has a small temperature dependence that varies from unit to unit and axis to axis. This gain drift is measured by placing the magnetometer in a thermal chamber that is surrounded by a large three-axis Helmholtz coil.

3.2.4 Magnetometer Data Products

The raw (Level 0) magnetometer data consist of three orthogonal magnetic field values every 0.25 seconds. Because of the orientation of the sensor relative to the payload, what the sensor reports as B_y corresponds to the vertical magnetic field (positive upwards), positive B_z is along the boom, outward from the payload, and B_x is perpendicular to B_y and B_z, all measured relative to the payload. Practially speaking, the payload exhibits pendulum motions, thus it is necessary to transform the data into a geophysical coordinate system. Since we have no independent azimuthal aspect sensor, the data products that will be of most use will be B_{vert} and B_{horiz}; these will be the primary scientific product, although users will have access to the raw B_x, B_y, B_z values, as measured in the payload coordinate system.

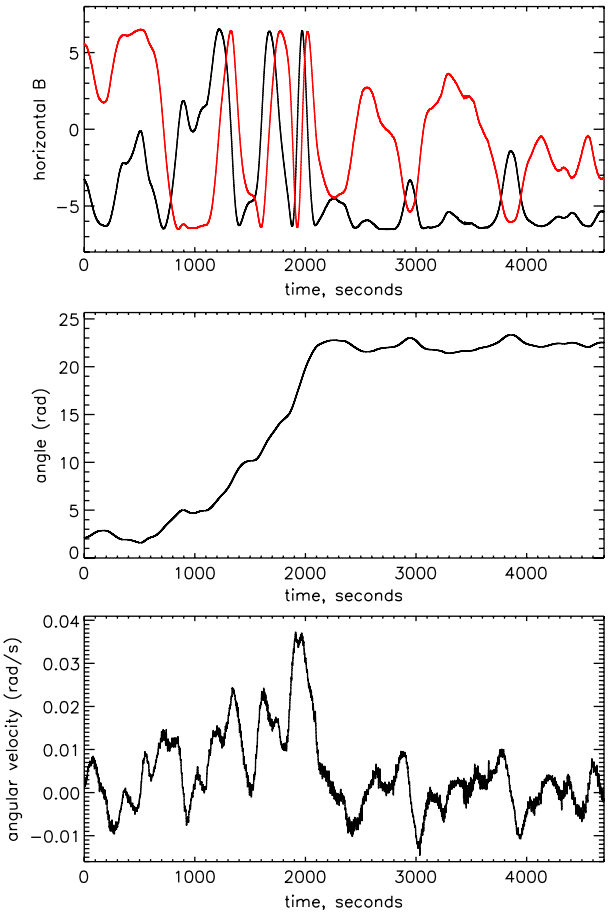

Fig. 11 Data taken during 2010 BARREL test flight: two horizontal components of the magnetic field in μT (*top*), the derived walk in angle (*middle*), and the angular speed (*bottom*)

3.2.5 Interpretation of Magnetometer Data

Since the BARREL payloads are freely rotating and swinging, both of these motions will appear in the raw data. The torsional behavior at float is a sort of smoothed random walk in angle, presumably driven by horizontal wind gradients at the balloon, creating torsion transmitted through the load line to the payload. For the most part, this input is slow compared to the natural torsional oscillation period of the balloon on the load line, so periodic oscillations are not expected to be prominent. Figure 11 shows an interval of data from a 2010 BARREL test flight. From top to bottom, the plots are of the two horizontal components of the field, the derived walk in angle, and the angular speed. We will use closer analysis of such data to identify the torsional and pendulum frequencies of the payload so that they are not mistaken for waves in the magnetic field. Our analytical estimates of the periods are approximately 5 seconds for simple pendulum motion and 40 seconds for torsional motion.

While the temperature variation of gain in each axis of each magnetometer will be known from ground calibration, other parameters of the magnetometers can only be determined to sufficient precision using in-flight data. These are the tilt of the vertical magnetometer axis from true vertical, non-orthogonalities among the three axes (expected to be less than 0.5 degrees according to the manufacturer's specification), constant DC offsets in each axis (due

to both the payload's field and the ADC), and differences in gain among the three axes at fixed temperature. The random motions of the payload during times of relatively constant temperature (noon and midnight) will allow us to define these parameters for each payload by forcing the derived B_z and B_{horiz} to be nearly constant and consistent with geomagnetic models. The calibration will be done using data during geomagnetically quiet times, so that the resulting parameters can be applied to times when the field itself is not expected to be constant.

4 Payload Design and Support Systems

4.1 Data Processing Unit

4.1.1 Instrument Controller Board

The BARREL DPU acquires data from the X-ray spectrometer, magnetometer, a GPS module, and an engineering data interface (EDI). It outputs formatted data frames to an Iridium modem for downlink, and controls the command-cutdown system. The DPU is a general purpose instrument controller board, which communicates with other boards through a backplane and a memory-type interface. Flexibility is achieved through the use of an FPGA that contains interface logic for the backplane signals. The instrument controller board has flown successfully on three sounding rocket experiments, and about 26 balloon flights, most recently in the 2010 BARREL test flights.

4.1.2 Navigation and Timing

Time and positioning are provided by a GPS module, model Lassen SQ manufactured by Trimble, which resides in the DPU box. Each second, GPS time and position data are passed to the DPU through a backplane-connected UART. In addition, the GPS module emits an accurate timing pulse, which signals the DPU to save a free-running 1 kHz clock. By saving this clock value on each GPS second, and injecting GPS second of the week into the telemetry stream, the payload clock is synchronized to GPS time with 1 ms accuracy. Regular synchronization is necessary because the DPU's crystal oscillator undergoes a temperature drift.

4.1.3 Engineering Data

The engineering data interface (EDI) performs analog to digital conversion of key temperatures, voltages, and currents. There are 8 inputs of voltage and current pairs, 4 inputs of voltage only and 16 inputs nominally for temperature sensors. Temperature inputs can also be configured to monitor voltage. All inputs are scaled to the nominal 5 V ADC full-scale range and converted 2 channels at a time with 16-bit precision.

Each of the 8 voltage/current inputs has a voltage divider to scale the input and a differential current-sense amplifier to measure the voltage across an external resistor in series with the current flow. Two inputs employ inverting amplifiers for sensing voltage/current from negative supplies. The 4 voltage-only inputs employ a voltage divider to scale the input. Thirteen of the sixteen temperature sense inputs have a resistor to 5 V to supply approximately 1 mA of current to LM335 temperature sensors, which provide 10 mV/°K output. Three remaining temperature inputs are configured as voltage inputs. All inputs are referenced directly to DPU ground. All housekeeping output digital words are linearly related to physical units such as temperature, voltage, or current.

4.1.4 Flight Software

The BARREL DPU contains a digital signal processor (ADSP-2101) which runs the flight software, and a boot flash memory chip to store the flight software when power is off. The BARREL software is a simple real-time operating system. The main functions are to control and read data from several peripheral devices, format the data into frames, and emit a stream of data frames to the telemetry system.

The software consists of two stages. The first stage initializes memory (RAM) and configuration registers, the internal clock, and the UART and peripheral devices. The second stage is the main software loop, in which the DPU sleeps until interrupted. On an interrupt, the DPU services the interrupt, traverses the main loop, checking on events flagged for attention, and then goes back to sleep. Scheduled interrupts arrive every millisecond, generated by an internal timer. Asynchronous interrupts arrive mostly from the X-ray spectrometer (1000's per second), upon acquisition of an X-ray. For each X-ray, interrupt handling software increments a bin in the accumulating slow, medium, and fast spectra. The minimum time between two X-ray interrupts, including the signal processing and analog to digital conversion time, is about 6 μs. The interrupt service time is from 1.1 to 4.2 μs, with higher energy photons taking more time to bin. The GPS interrupts at one second marks, to provide an accurate timing pulse.

With regard to telemetry and command, the DPU software has two functions: (1) produce data frames and send them to the modem; (2) receive and execute commands from the ground. Ground software is described in Sect. 6 below. Flight software constructs data frames which are accumulated in a toggling buffer pair and transmitted at the rate of one frame per second (currently 214 bytes/second). Housekeeping data, including the EDI measurements, as well as additional GPS data (GPS week, number of satellites, UTC seconds offset), and miscellaneous information (number of dropped calls, number of modem resets, command counter) is sub-commutated on a 40-frame cycle. Four commands are recognized: three for the cutdown system (arm, disarm, cut), and a no-op command. The ARM command stores energy in capacitors which will supply high current to the termination squib. The DISARM command drains the stored energy through resistors. The CUTDOWN command activates a relay to fire a squib and terminate the flight.

4.2 Power System

The BARREL power system is based on a solar-charged nickel metal hydride (NiMH) battery that powers a box of DC/DC converters which provide isolated regulated voltages to payload components. The use of solar power is typical for long duration balloon flights in the polar regions which experience 24 hours of sunlight. The power system was developed for BARREL, based on the same solar panels that CSBF uses, and on a UC Berkeley flight-heritage charge controller (from the HIREGS LDB payload) and DC/DC converters. The only significant change is the choice of battery chemistry. BARREL uses NiMH batteries, chosen for having a higher capacity-to-weight ratio than lead-acid and for its greater robustness in comparison to lithium-based systems in response to charge cycles over a wide range of temperatures. Each BARREL payload requires less than 5 W average total power. A summary block diagram of the complete power system is shown in Fig. 12, followed by a more detailed specification of the individual power system components.

4.2.1 Solar Panels

The BARREL payloads are freely spinning, thus the power system relies on 4 identical solar panels, one for each side of the payload. In addition to satisfying the payload power

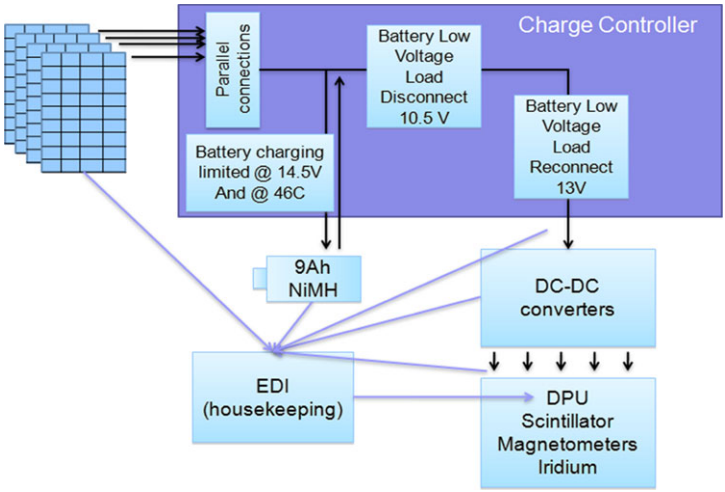

Fig. 12 Power system block diagram

requirements at any orientation to the sun, this provides for some redundancy should a panel be damaged during launch.

BARREL uses custom-built solar panels (Suncat Solar, LLC) to ensure sufficient panel voltage at the high panel temperatures experienced in the balloon environment (up to 100 °C). The four BARREL panels consist of a laminated honeycomb structure 16.25″ × 21.5″ × 0.5″ with 40 series-connected Sunpower cells which have been cut to the minimum size allowed by the all-back-contact cells (1.5″ × 4.875″). Each panel is ∼400 g without mounting structure. Expected performance is V_{mp} of 19 V at 25 °C. Based on flight data from the BARREL test flights, we expect ∼2.5 A from any panel that is close to fully illuminated.

4.2.2 Charge Controller and Battery

The BARREL charge controller is designed to accept 4 parallel solar panel inputs and maintain a battery voltage between 10.5 and 14.5 V. Fundamentally it is a pair of switches (implemented with a pair of IRF5305 FETs), that (1) connect the load when the battery voltage is high enough, and (2) disconnect the solar panels if the battery voltage is approaching its maximum. Hysteresis is present on both switches to avoid oscillation. Panel power is used at whatever current the panels can supply whenever the panel voltage is above the battery voltage (minus a small FET and Shottky diode drop) up to a maximum voltage of 36 V (LM293 limits). When total panel current is above the payload requirements, excess current is stored in battery charge up to the point where the battery is fully charged. When panel current is below the payload required current, the battery makes up the deficit by discharging to its minimum allowed voltage. A thermistor is also included in the battery pack which allows the charge controller to cut battery charging at 46 °C and resume below 42 °C. A backup snap action bimetal cutoff is also present in the battery packs with a 60 °C trip point. This simple charge/discharge arrangement is suitable for nickel chemistry rechargeable batteries with small internal resistances and large capacity.

The battery itself is made of 10 series connected GP9000 NiMH cells (rated at 9 A h) with nominal voltage of 12 V and a range from 10.5–14.5 V. The payload requires ∼500 mA,

which implies about 2/3 of a day in maximum battery capacity, or with derating, about 12 hours. Under typical operations (in full sun), the battery generally remains at full charge, but the excess battery capacity allows for continued operation if sunset is experienced late in the season.

In addition to maintaining battery charge the charge controller outputs to the EDI 6 voltages and 2 currents (measured as voltages across series resistance of 0.025 Ω) for housekeeping purposes.

4.2.3 DC/DC Converter Box

Each DC/DC converter accepts 9–18 V DC from a power supply, the BARREL charge controller, or a battery, and outputs voltages for the rest of the payload. In addition to supplying payload power, the DC/DC converter box outputs voltages and currents to the EDI (measured as voltages across series resistance 100 mV full scale) for housekeeping purposes. DC/DC conversion is accomplished using the isolated CALEX 12s5.1000HW with moderate filtering. The Iridium modem has its own internal DC/DC converter and accepts a wider range of voltages than the rest of the BARREL payload. The DC/DC converter box passes its input voltage to the Iridium after minimal filtering and a current sense resistor.

4.3 Telecommunications

Long-duration balloon flights require either data storage or an over-the-horizon telemetry system for real-time communications, since the payload generally moves out of line-of-sight range within about one day. In the case of BARREL flights from Antarctica, recovery of payloads may be difficult due to the remote location. Therefore, a data storage system is not a practical nor reliable way to retrieve data; a real-time telemetry system is thus required.

The BARREL telemetry needs are primarily driven by the required energy and time resolution of X-ray data. The baseline telemetry requirement for BARREL is a data rate of 214 bytes/s which can be achieved using the Iridium satellite network. Iridium provides real-time communications at up to $\sim$3 kbits/s with both downlink and uplink capabilities. BARREL uses the Iridium Satellite Modem Model A3LA-X from NAL Research, weighing 340 g (0.75 lb) and drawing an average of 800 mA at 5.0 V. The modem operates with the Iridium network at 1616–1626.5 MHz and interfaces with the DPU via serial RS-232 using standard modem AT commands. The flight modem operates in auto-answer mode; if the connection is lost, a new call is automatically initiated by the ground station which includes an identical modem. Flight data are not saved in memory when a call is dropped; the reconnect time is typically 30 seconds or less, based on test-flight data. In the event that the flight modem doesn't recognize a lost connection, the DPU can do a soft modem reset (after 1 hour), or power cycle the modem (after 4.5 hours).

4.4 Flight Train and Termination System

Each payload is carried to a float altitude of about 37 km by an Aerostar Model SF-0.300-.3/0-TA zero-pressure helium-filled balloon. Due to the remote launch site and need for launching payloads at a rate of about one every two days, this balloon size was chosen because it is "hand-launchable" (Fig. 13). The 0.3 mil-thick 300,000 cubic ft. balloon is made of polyethylene and can carry a maximum payload weight of 72 pounds. The payload is suspended from the balloon by the flight train, which includes an 8 ft diameter parachute and a 16 ft long ladder made from 4800 lb nylon rope. Termination of each flight is achieved

Fig. 13 Balloon launch over Halley VI Research station during 2013 BARREL Campaign

with a small explosive guillotine cutter, fired by the terminate system which is suspended at the apex of the parachute. The terminate can be commanded from the ground through the Iridium telemetry system or autonomously in the event that the payload altitude drops below 60,000 feet and contact with the ground has been lost.

4.5 Mechanical Design

The BARREL mechanical design was largely driven by the requirement to fabricate 45 payloads quickly and at low cost. The structure must also be as light as possible, but strong enough to survive chute-shock, and must provide easy access to each subsystem. In order to meet an ambitious operations schedule of one launch every two days, the payloads are shipped fully assembled, with the exception of the science instruments and solar panels which are attached at the launch site. The payload design consists of an internal frame constructed of aluminum angle, a foam enclosure, and an external aluminum frame for attaching the flight train and solar panels and to allow for easy launch. Handles made of square rails allow for easy transport and launch. Improvements to the design were made primarily to the external frame after the first BARREL test campaign. These allowed for a simplification of the manufacturing process and improved accessibility to the instrument subsystems while at the launch site.

4.5.1 Internal Structure

The internal frame is 23″ tall and just over 8″ wide and is made of four aluminum angle "legs" attached with aluminum angle cross-bars. The scintillator is housed in the middle of the frame and sits in a plexi-glass flange that is bolted to a 0.08″ thick aluminum plate. The electronics boxes are mounted to each side of the frame (Fig. 14a), and the battery sits beneath the payload. Cable harnessing is secured to the frame with cable ties. The frame slips into a 2″ thick foam enclosure for passive thermal control (described below). Cut-outs

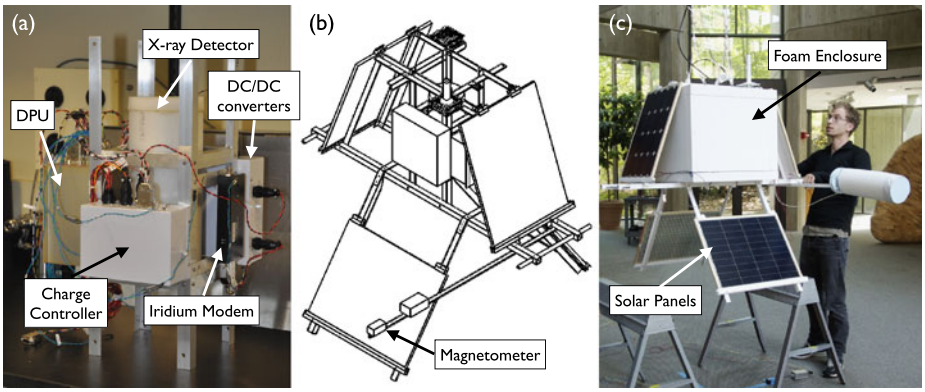

Fig. 14 (**a**) Internal payload structure, (**b**) mechanical cutaway drawing, and (**c**) fully assembled payload, including foam enclosure and solar panels

in the foam allow the GPS antenna cable, Iridium antenna cable, magnetometer serial cable, and solar panel cables to run to the outside.

4.5.2 External Structure

Figure 14b shows the external frame attached to the internal structure. Two 50″ long aluminum square rails run parallel beneath the internal structure outside the foam enclosure and are attached to the internal structure legs with 1/4″ bolts. A 1/2″ diameter aluminum tube passes through the square rails on each side, serving as handles to carry and launch the payload. The square rails support the 42″ magnetometer boom as well as the aluminum H-channel used to suspend the solar panels, two above the square rails on opposite sides of the payload and two below the payload on the other sides. On top of the payload, outside the foam enclosure, a "tic-tac-toe"-shaped structure is attached to the four payload legs and allows for mounting of the Iridium and GPS antennas. This structure also aids in keeping the upper solar panels held in place. The fully assembled payload, including foam thermal enclosures and solar panels is shown in Fig. 14c.

4.5.3 Manufacturing

Manufacturing of mechanical parts was primarily carried out by students at Dartmouth College with the oversight and assistance of the professional machinists. A series of jigs—one jig for each unique part—was fabricated in order to streamline and insure precision in the drilling of holes. This allowed for an assembly-line approach whereby different people could reliably perform the same tasks in a repeatable way. Parts were machined and painted en masse, and then assembled as needed.

4.6 Thermal Control

Balloon payloads are subjected to temperatures ranging from very cold (−50 °C) on ascent through the tropopause to very hot (+50 °C) at float altitude due to a lack of convection at those altitudes and the high level of sunlight reflected off the snow/ice surface of Antarctica. Thermal control of balloon payloads can usually be achieved with simple passive measures such as foam thermal enclosures, thermal coupling of components, and appropriate choice

of surface properties (e.g., aluminized mylar or white paint) since thermal energy transfer is generally dominated by radiation. The majority of BARREL subsystems have temperature operating ranges of or exceeding $-40°$ to $+60$ °C. The thermal design is primarily driven by the scintillator which requires a thermal rate of change less than 8 °C per hour (to prevent the crystal from cracking) and preferred temperature above 0 °C to maintain the instrument efficiency.

Thermal design was aided by the Thermal Desktop package, which is an overlay module to AutoCAD, performing radiative and conductive heat transfer calculations. The thermal model was validated during the BARREL test flights in 2009 and 2010. Each BARREL payload is enclosed in a $2''$ thick foam box which is painted white (Fig. 14b). All exterior metal surfaces are also painted white to reflect sunlight. To reduce its rate of temperature change, the scintillator is conductively isolated from the rest of the payload structure using a plexiglass mounting plate, and is surrounded by an additional inch of foam. The magnetometer is also insulated with $1''$ of white foam since it is mounted on an exterior boom. Two of the four solar panels hang below the payload where they can radiate to open space rather than the main payload, thus reducing the internal payload temperatures.

5 Instrument Calibration

5.1 X-Ray Spectrometer

For the spectrometer, the most important calibration is the energy scale. The standard ^{137}Cs 662 keV line is used to set the PMT nominal operating high voltage and overall gain. After making this adjustment, spectra are collected from background and several radioactive sources to provide a set of energy calibration points. The gain, which determines the relation between channel number and energy bin, depends on temperature, and has been characterized between 5 °C and 30 °C in the laboratory. From these line measurements, a gain model is constructed, and the overall system energy resolution obtained. Because the relation between channel and energy is not quite linear, multiple lines are needed to characterize it in the laboratory. Because the form of the nonlinearity is predictable and reproducible for a given scintillator crystal design, once it has been measured using a number of lines, a single measurement of a single line is enough to establish the entire channel–energy relation to better than 5 %. During flight, the 511 keV annihilation line produced by cosmic rays, is readily observable and usable for in-flight calibration. Atmospheric gamma lines from ^{14}N can also have sufficient intensity during intense precipitation events or solar proton events. Temperature measurements in flight provide a cross-check by giving an independent means to estimate which channel the 511 keV line should occupy.

Measurements of the dead-time response of the detectors at extremely high count rates are made using bright radioactive sources at gradually decreasing (and carefully measured) distance from the detectors. GEANT3 simulations are used to predict what rates the detectors should be seeing and will be made to agree with the data at large distances, where detector dead-time is negligible, by adjusting the source strength in the simulation. The ratio between the predicted and observed count rates as they start to saturate at high rates will be recorded and used to correct observed count rates in flight should a particularly bright precipitation event (or solar flare, or solar particle event) occur. For most of the duskside relativistic electron precipitation and relativistic microburst events that make up the primary BARREL science, this dead-time correction should be minor or negligible.

5.2 Magnetometer

Gain calibration for the magnetometer is carried out at UCSC using a Helmholtz coil surrounding a thermal chamber. A chopped current put through the coil allows the gain to be measured with a known signal, even when the background field in the laboratory is changing. Data are collected in 10°–20° increments, between −40° and +50 °C while chopping the Helmholtz field amplitude between 25–50 μT. The thermal chamber is turned off during data collection, after the desired temperature is reached. From the data, a gain calibration parameter is determined for each axis. A typical value for the gain drift with temperature is 0.02 % per degree C. The sense is usually toward increasing gain with increasing temperature, although some axes reverse this trend. During flight, a temperature sensor is mounted to the case of the magnetometer. The temperature sensor is itself calibrated during I&T. Gain corrections can then be applied in post-processing.

The magnetometer is mounted to a 42″ long boom to reduce the effects of stray currents in the payload, particularly the varying currents of the solar panels. Residual effects of payload currents are measured during an outdoor/full-sun Comprehensive Performance Test. In a separate test, the payload is suspended from the entire flight train and magnetometer data are analyzed to determine the payload natural pendulum frequencies. However, it is anticipated that in-flight data will provide the best characterization of payload motions.

5.3 Clock Synchronization

Since each BARREL payload carries a GPS clock, time synchronization should be straightforward. Test flights have shown tracking of GPS time to better than 10 ms using only the time stamp that is transmitted at a 4 second cadence. Nevertheless, it is important to verify timing between payloads, because multi-point measurements are critical to BARREL science. To verify the synchronization at a sub-second level, the following test is carried out in the laboratory. A set of four operating payloads is exposed to a simultaneous impulsive radiation signal by rapidly moving the cover of a bright radioactive source that illuminates the payloads. The data are recorded and analyzed at UCSC MOC to verify that the event appears simultaneous in all payloads to better than 0.25 s.

6 Operations and Data Analysis

6.1 Mission Operations and Ground Systems

The BARREL ground segment is managed by University of California, Santa Cruz. During normal operations, Iridium downlink is received at the UCSC Mission Operations Center (MOC). Backup downlink capabilities are located at U.C. Berkeley and Dartmouth College.

A schematic of the BARREL ground systems is shown in Fig. 15. The MOC hardware consists of a collection of five laptop computers running Windows XP. Four of the computers are configured to run up to four instances of the ground station software simultaneously, and one computer serves as a backup. Four Iridium modems (NAL research model AL3A-X), are connected to each of the primary computers via a 4-channel serial/ USB converter, supporting satellite communication to four payloads per computer. Each modem is connected via an RF cable to an Iridium antenna (NAL research model SAF5350-CX) bolted to a fixture on the roof of the Natural Sciences II building at UCSC. MOC computers are all networked to a common storage device, the MOCs network attached storage (MOC-NAS).

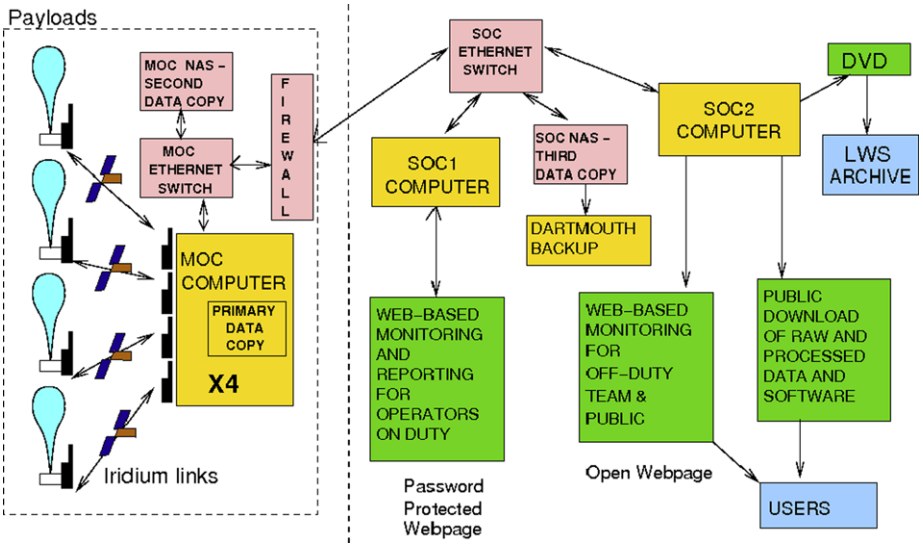

Fig. 15 Schematic of BARREL MOC/SOC

The connection is made through an Ethernet switch which also provides a connection to the UCSC network via a hardware firewall. The only connection allowed through the firewall is for the Science Operations Computer, SOC1, (see below) to read data from the MOC-NAS. The MOC hardware (MOC-NAS, switch, firewall, laptops, and Iridium modems) are powered through a UPS sized for at least 3 hours during an outage.

The GSE software on the MOC computers is C code written in the LabWindows environment, and an associated user interface for displaying science and housekeeping data. The code is a significantly revised version of the GSE software used during the MINIS 2005 balloon campaign. Each instance of the software supports a single flight payload. The software auto-detects when new data are not being received and automatically initiates a new Iridium call to the payload. A binary data file is opened locally and on the NAS for each new Iridium call that is initiated. Raw data frames are written to this file as received, with no further processing by the MOC. Although the flights will be monitored continuously, the software is designed to operate autonomously and very little human intervention is required.

Flight monitoring and science operations are handled by two computers separate from the MOC (SOC1 and SOC2). An Ethernet switch connects SOC1, SOC2, and the SOC-NAS to the UCSC network. SOC1 and SOC2 are server-style tower computers running Linux. SOC1 is primarily used to process the data found on the MOC-NAS and store it on the SOC-NAS. SOC1 also serves a special, password-protected version of the web interface that allows some administrative control. The web server responsible for the bulk of web traffic is hosted on SOC2. This separation ensures that excessive web traffic will not interfere with processing real-time data.

The BARREL SOC software package is used to collect, archive, and disseminate the information from the MOC-NAS raw data files. Local and remote users can see a live feed of the raw data files as they are written and use a number of visualization tools to analyze past data (Fig. 16). This is done by providing three main functions: near real-time conversion of incoming binary data files into ASCII and CDF archive files; data monitoring and text message notification of values that exceed maximum limits; and a web interface for viewing

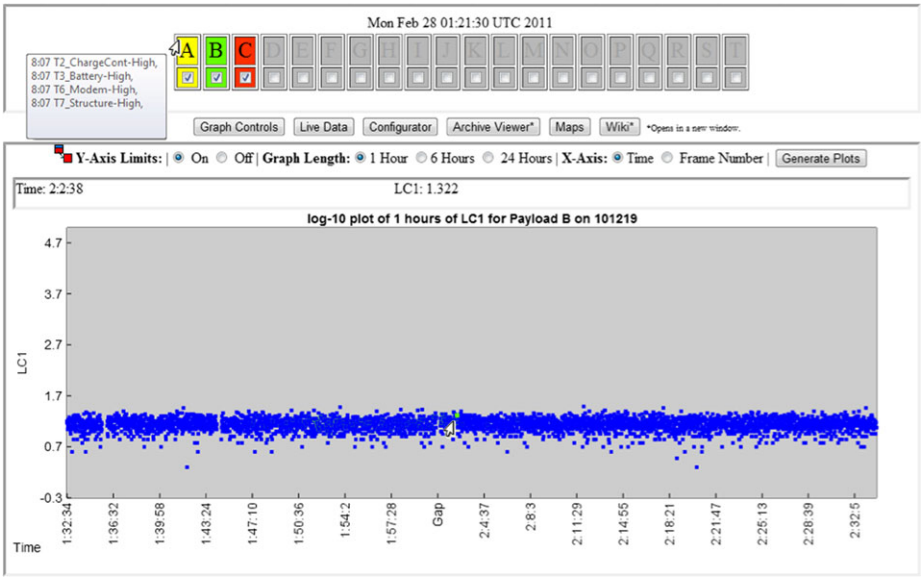

Fig. 16 Screenshot of SOC web interface

live and archived data in a number of different ways. Data products are described in more detail in Sect. 6.2 below.

Mission operations are staffed 24/7, with one mission monitor working a three-hour shift at any given time. Monitoring is carried out via the web interface to SOC1, which allows for monitoring by geographically distributed team members. A report is generated on a team wiki site by the mission monitor at the end of each shift. The mission monitor also notifies a duty scientist in the event of any payload or GSE anomalies. SOC2 is available for data viewing by other team members or the public.

6.2 Science Data Products and Analysis

6.2.1 Data Products

BARREL summary data will be made available to the public in near real-time. Summary plots and a map of payload locations can also be viewed from the BARREL SOC website during the BARREL flights. Archived data will be released as Level 0–3 products about 24–48 hours after collection, summarized in Table 4. The Level 0 data product is a cleaned version of the raw binary data (i.e. with duplicate or corrupt frames removed). One Level 0 data file will be produced for each payload each day. Level 1 data are CDF files of time-tagged uncalibrated data. Calibrated data will be released as Level 2 files in CDF and in IDLSAVE formats. These include energy-scale calibrated X-ray spectra, magnetometer data, ephemeris files, and other housekeeping information. Higher level (Level 3) data products may be released for specific event intervals. For current information about data products and analysis tools, visit the BARREL project website (http://www.dartmouth.edu/~barrel).

6.2.2 Data Analysis

In addition to CDF data files, analysis tools written in the IDL language will be made available through the BARREL SOC website. These will include basic plotting tools used to

Table 4 BARREL Data Products

Level	Description	Format
L0	TM file (1/payload/day), good frames only	binary (BARREL)
L1	Time-tagged, uncalibrated (e.g., counts/s)	CDF
L2	Calibrated (physical units)	CDF, IDLSAVE
L3	Higher level products (e.g., spectrograms)	CDF

display X-ray count rates and magnetic field data versus time, routines for creating Fourier power spectrograms, and routines for creating X-ray count spectra over specified time intervals.

The conversion between the spectrum of counts observed in balloon-borne X-ray detectors and the spectrum of electrons incident on the atmosphere is a well-established one, and not a new development (e.g., Berger and Seltzer 1972; Foat et al. 1998). Nonetheless, we describe it here because it is the primary BARREL measurement. Monte Carlo simulations using GEANT4 are carried out to simulate the conversion of electrons to detector counts. In a sense, one can consider Earth's atmosphere as part of the instrument, responsible for converting the incident electrons into photons that are detected by the scintillator. Incident precipitating electrons are Coulomb scattered and produce bremsstrahlung X-rays in the atmosphere. The photons are scattered in both the atmosphere and the instrument before ultimately being absorbed (or exiting the detector if not fully absorbed). The effects of Compton scattering, photoelectric absorption, and, at the highest energies, pair production and the production of secondary bremsstrahlung; are included in the simulations. A mass model of the payload was constructed along with a model of the atmosphere. GEANT4 also allows for inclusion of Earth's magnetic field. The entire process is modeled for mono-energetic electrons between 40 keV–4 MeV to obtain a response matrix which provides detector counts as a function of energy for each incident electron energy and for a given balloon altitude.

Event count spectra are analyzed using a "forward-folding" technique: a model energy spectrum is assumed for the incident electrons, and the known response based on the Monte Carlo simulations is used to predict the expected count spectrum in the detector at its known altitude. The model count spectrum is normalized to minimize chi-square with the data—the normalization then telling us the intensity of the initially assumed electron spectrum. The process can be repeated, varying the parameters and form of the incident electron spectrum until the best fit is obtained and the range of incident spectral parameters that are allowed by the data to a certain level of confidence are determined. Thus, for example, we might conclude that a given precipitating electron spectrum is consistent with an exponential form with folding energies between 600 and 700 keV, but not consistent with a power law of any index. The BARREL instrument response matrix will be provided along with tools for using it to invert the X-ray spectrum to obtain information about the precipitating parent electrons.

7 Summary

We have discussed known types of relativistic electron precipitation and shown that there are many unanswered questions about the mechanisms causing energetic electron loss. The spatial-temporal evolution of precipitation at relativistic energies is largely unexplored, and the temporal modulation of precipitation at ULF timescales that has been observed routinely remains unexplained. Finally, the relative importance of losses to the atmosphere versus losses to the magnetopause is not currently known. To address all of these questions,

the BARREL Investigation will consist of two balloon campaigns carried out in January 2013 and 2014, during the RBSP mission. The combination of in situ RBSP measurements and low altitude BARREL measurements of precipitation provides a unique opportunity to quantitatively test models of wave-particle interactions thought to be responsible for precipitation.

Acknowledgements BARREL is supported by the NASA Living With a Star program through NASA grant NNX08AM58G at Dartmouth College. Support for operations was provided by the Columbia Scientific Balloon Facility, the NASA Balloon Program Office, and the National Science Foundation's Office of Polar Programs. MAC has received funding from the Natural Environmental Research Council under the Antarctic Funding Initiative (AFI/11/22). The BARREL science campaigns were supported by NERC/British Antarctic Survey, SANSA Space Science, and the University of KwaZulu-Natal.

References

J.M. Albert, Evaluation of quasi-linear diffusion coefficients for EMIC waves in a multispecies plasma. J. Geophys. Res. **108**(A6), 1–9 (2003)

B.J. Anderson, D.C. Hamilton, Electromagnetic ion cyclotron waves stimulated by modest magnetospheric compressions. J. Geophys. Res. **98**, 11369 (1993)

K.A. Anderson, D.W. Milton, Balloon observations of X rays in the auroral zone. J. Geophys. Res. **69**, 4457–4479 (1964)

M.J. Berger, S.M. Seltzer, Bremsstrahlung in the atmosphere. J. Atmos. Terr. Phys. **34**, 85–108 (1972)

J.B. Blake, M.D. Looper, D.N. Baker, R. Nakamura, B. Klecker, D. Hovestadt, New high temporal and spatial resolution measurements by SAMPEX of the precipitation of relativistic electrons. Adv. Space Res. **18**(8), 171–186 (1996)

J. Bortnik, R.M. Thorne, T.P. O'Brien, J.C. Green, R.J. Strangeway, Y.Y. Shprits, D.N. Baker, Observation of two distinct, rapid loss mechanisms during the 20 November 2003 radiation belt dropout event. J. Geophys. Res. **111**(A12), 12216 (2006)

C. Cattell, J.R. Wygant, K. Goetz, K. Kersten, P.J. Kellogg, T. von Rosenvinge, S.D. Bale, I. Roth, M. Temerin, M.K. Hudson, R.A. Mewaldt, M. Wiedenbeck, M. Maksimovic, R. Ergun, M. Acuna, C.T. Russell, Discovery of very large amplitude whistler-mode waves in Earth's radiation belts. Geophys. Res. Lett. **35**, 01105 (2008)

A. Demekhov, Recent progress in understanding Pc1 pearl formation. J. Atmos. Sol.-Terr. Phys. **69**, 1609 (2007)

J.E. Foat, R.P. Lin, D.M. Smith, F. Fenrich, R. Millan, I. Roth, K.R. Lorentzen, M.P. McCarthy, G.K. Parks, J.P. Treilhou, First detection of a terrestrial MeV X-ray burst. Geophys. Res. Lett. **25**(22), 4109–4112 (1998)

J. Goldstein, B.R. Sandel, M.F. Thomsen, M. Spasojević, P.H. Reiff, Simultaneous remote sensing and in situ observations of plasmaspheric drainage plumes. J. Geophys. Res. **109**(A), 03202 (2004)

J.C. Green, T.G. Onsager, T.P. O'Brien, D.N. Baker, Testing loss mechanisms capable of rapidly depleting relativistic electron flux in the Earth's outer radiation belt. J. Geophys. Res. **109**, 12211 (2004)

R.B. Horne, M.M. Lam, J.C. Green, Energetic electron precipitation from the outer radiation belt during geomagnetic storms. Geophys. Res. Lett. **36**, 19104 (2009)

W.L. Imhof, H.D. Voss, J. Mobilia, D.W. Datlowe, E.E. Gaines, J.P. McGlennon, U.S. Inan, Relativistic electron microbursts. J. Geophys. Res. **97**, 13829 (1992)

K. Kersten, C.A. Cattell, A. Breneman, K. Goetz, P.J. Kellogg, J.R. Wygant, L.B.I. Wilson, J.B. Blake, M.D. Looper, I. Roth, Observation of relativistic electron microbursts in conjunction with intense radiation belt whistler-mode waves. Geophys. Res. Lett. **38**, 08107 (2011)

G.F. Knoll, *Radiation Detection and Measurement*, 2nd edn. (Wiley, New York, 1989)

M. Kokorowski, E.A. Bering, M. Ruohoniemi, J.G. Sample, R.H. Holzworth, S.D. Bale, J.B. Blake, A.B. Collier, A.R.W. Hughes, E.H. Lay, R.P. Lin, M.P. McCarthy, R.M. Millan, H. Moraal, T.P. O'Brien, G.K. Parks, M. Pulupa, B.D. Reddell, D.M. Smith, P.H. Stoker, L. Woodger, Magnetospheric electric field variations caused by storm-time shock fronts. Adv. Space Res. **42**, 181 (2008)

K.R. Lorentzen, M.D. Looper, J.B. Blake, Relativistic electron microbursts during the GEM storms. Geophys. Res. Lett. **28**(1), 2573–2576 (2001a)
K.R. Lorentzen, M.P. McCarthy, G.K. Parks, J.E. Foat, R.M. Millan, D.M. Smith, R.P. Lin, J.P. Treilhou, Precipitation of relativistic electrons by interaction with electromagnetic ion cyclotron waves. J. Geophys. Res. **105**(A), 5381–5390 (2000)
K.R. Lorentzen, J.B. Blake, U.S. Inan, J. Bortnik, Observations of relativistic electron microbursts in association with VLF chorus. J. Geophys. Res. **106**(A), 6017–6028 (2001b)
L.R. Lyons, R.M. Thorne, Equilibrium structure of radiation belt electrons. J. Geophys. Res. **78**, 2142–2149 (1973)
R.M. Millan, Understanding relativistic electron losses with BARREL. J. Atmos. Sol. Terr. Phys. (2011)
R.M. Millan, R.M. Thorne, Review of radiation belt relativistic electron losses. J. Atmos. Sol.-Terr. Phys. **69**(3), 362–377 (2007)
R.M. Millan, R.P. Lin, D.M. Smith, K.R. Lorentzen, M.P. McCarthy, X-ray observations of MeV electron precipitation with a balloon-borne germanium spectrometer. Geophys. Res. Lett. **29**, 2194 (2002)
R.M. Millan, R.P. Lin, D.M. Smith, M.P. McCarthy, Observation of relativistic electron precipitation during a rapid decrease of trapped relativistic electron flux. Geophys. Res. Lett. **34**(10), 1–5 (2007)
R.M. Millan, K.B. Yando, J.C. Green, A.Y. Ukhorskiy, Spatial distribution of relativistic electron precipitation during a radiation belt depletion event. Geophys. Res. Lett. **37**(2), 20103 (2010)
S.K. Morley, R.H.W. Friedel, T.E. Cayton, E. Noveroske, A rapid, global and prolonged electron radiation belt dropout observed with the Global Positioning System constellation. Geophys. Res. Lett. **37**, 06102 (2010)
R. Nakamura, M. Isowa, Y. Kamide, D.N. Baker, J.B. Blake, M. Looper, SAMPEX observations of precipitation bursts in the outer radiation belt. J. Geophys. Res. **105**(A), 15875–15886 (2000)
T.P. O'Brien, M.D. Looper, J.B. Blake, Quantification of relativistic electron microburst losses during the GEM storms. Geophys. Res. Lett. **31**(4), 04802 (2004)
S. Ohtani, Y. Miyoshi, H.J. Singer, J.M. Weygand, On the loss of relativistic electrons at geosynchronous altitude: its dependence on magnetic configurations and external conditions. J. Geophys. Res. **114**, 01202 (2009)
G.K. Parks, T.J. Freeman, M.P. McCarthy, S. Werden, The discovery of auroral X-rays by balloon-borne detectors and their contributions to magnetospheric research, in *Auroral Plasma Dynamics*. Geophysical Monograph, vol. 80, (American Geophysical Union, Washington, D.C., 1993), pp. 17–23
G.D. Reeves, K.L. McAdams, R.H.W. Friedel, T.P. O'Brien, Acceleration and loss of relativistic electrons during geomagnetic storms. Geophys. Res. Lett. **30**, 36 (2003)
T.J. Rosenberg, R.A. Helliwell, J.P. Katsufrakis, Electron precipitation associated with discrete very low frequency emissions. J. Geophys. Res. **76**, 8445 (1971)
M. Schulz, L.J. Lanzerotti, *Particle Diffusion in the Radiation Belts*. Springer, Heidelberg (1974)
R.S. Selesnick, Source and loss rates of radiation belt relativistic electrons during magnetic storms. J. Geophys. Res. **111**(A), 04210 (2006)
D. Summers, R.M. Thorne, Relativistic electron pitch-angle scattering by electromagnetic ion cyclotron waves during geomagnetic storms. J. Geophys. Res. **108**, 1143 (2003). doi:10.1029/200JA009489
R.M. Thorne, C.F. Kennel, Relativistic electron precipitation during magnetic storm main phase. J. Geophys. Res. **76**, 4446–4453 (1971)
R.M. Thorne, Radiation belt dynamics: the importance of wave-particle interactions. Geophys. Res. Lett. **37**, 22107 (2010)
D.L. Turner, Y. Shprits, M. Hartinger, V. Angelopoulos, Explaining sudden losses of outer radiation belt electrons during geomagnetic storms (2012)
A.Y. Ukhorskiy, B.J. Anderson, P.C. Brandt, N.A. Tsyganenko, Storm time evolution of the outer radiation belt: transport and losses. J. Geophys. Res. **111**, A11S03 (2006)
M. Walt, W.M. MacDonald, Diffusion of electrons in the van Allen radiation belt, 1, Treatment of particles with mirroring points at high altitude. J. Geophys. Res. **67**, 5013–5024 (1962)
J.R. Winckler, L. Person, R. Arnoldy, R. Hoffman, X-rays from visible aurora at Minneapolis. Phys. Rev. **110**, 1221 (1958)

DOI 10.1007/978-1-4899-7433-4_16
Reprinted from *Space Science Reviews* Journal, DOI 10.1007/s11214-012-9953-6

The Radiation Belt Storm Probes (RBSP) and Space Weather

R.L. Kessel · N.J. Fox · M. Weiss

Received: 13 March 2012 / Accepted: 27 November 2012 / Published online: 28 December 2012

Abstract Following the launch and commissioning of NASA's Radiation Belt Storm Probes (RBSP) in 2012, space weather data will be generated and broadcast from the spacecraft in near real-time. The RBSP mission targets one part of the space weather chain: the very high energy electrons and ions magnetically trapped within Earth's radiation belts. The understanding gained by RBSP will enable us to better predict the response of the radiation belts to solar storms in the future, and thereby protect space assets in the near-Earth environment. This chapter details the presently planned RBSP capabilities for generating and broadcasting near real-time space weather data, discusses the data products, the ground stations collecting the data, and the users/models that will incorporate the data into test-beds for radiation belt nowcasting and forecasting.

Keywords Space weather · Radiation Belt Storm Probes · RBSP · Geomagnetic storms

1 Introduction

Space weather is the state of the plasma, radiation, and magnetic environment in space driven by changes originating at the Sun and carried through interplanetary space by the solar wind. Space weather encompasses the solar environment where changes are initiated in the chromosphere or corona through to the near space environment above Earth (or any magnetized body). Space weather can cause large variations in Earth's upper atmosphere and ionosphere, and in Earth's radiation belts, and can prevent the reliable operation of technologies in space as well as on the ground. Our society is increasingly dependent on

R.L. Kessel
SMD, Heliophysics Division, NASA Headquarters, 300 E St. SW, Washington, DC 20546-0001, USA
e-mail: mona.kessel@nasa.gov

N.J. Fox (✉) · M. Weiss
Applied Physics Laboratory, The Johns Hopkins University, Laurel, MD 20723, USA
e-mail: nicola.fox@jhuapl.edu

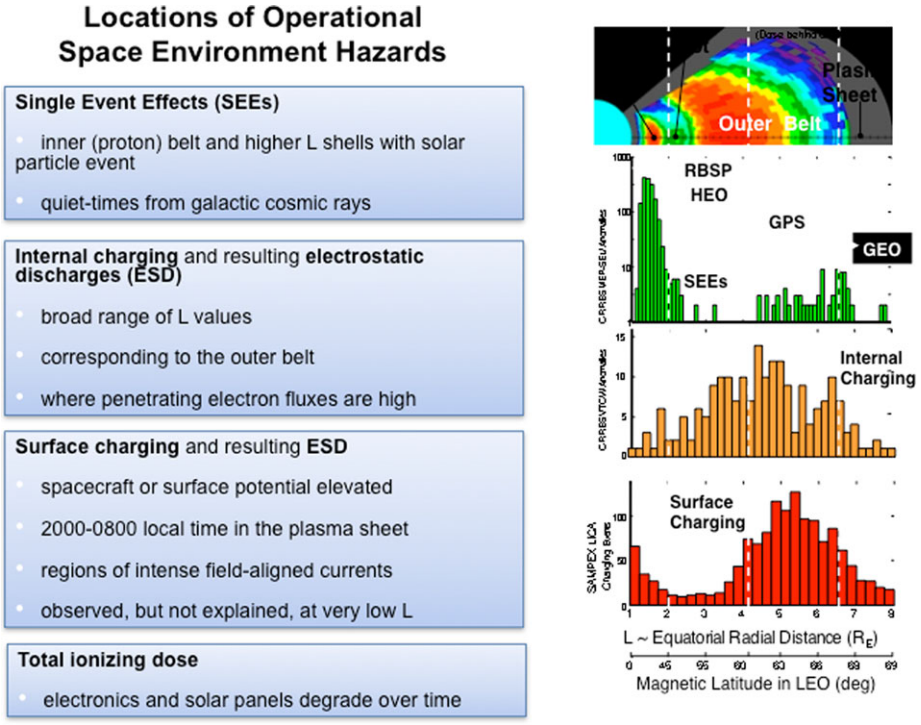

Fig. 1 Location of operational space environment hazards (courtesy of Aerospace Corporation)

these technologies, and their vulnerabilities to space weather need careful assessment, monitoring, and mitigation. Lanzerotti (2001, 2004) provide excellent reviews that describe the effects of space weather on past and current technologies.

The National Space Weather Program (NSWP) began in 1994 to help coordinate space weather activities and promote an increased awareness of space weather. An interagency working group within NSWP recognized early that modeling would play a key role in interpreting space weather data. The interagency working group recommended a modeling center that could transition research models to operations, as well as provide testing and validation. This recommendation led to the founding of the Community Coordinated Modeling Center (CCMC) (Robinson and Behnke 2001). Today the CCMC supports over 20 space weather models. NOAA's Space Weather Prediction Center (SWPC) is the U.S. official source for space weather forecasts, working with the CCMC and others to get the latest, most robust models enabling space weather prediction.

Recent interest at NOAA has focused on identifying space weather impacts to satellite infrastructure and defining services to mitigate those impacts. Figure 1 shows the locations of hazards within the operational space environment (courtesy of Aerospace, T.P. O'Brien). Single event effects predominate at low L shell in the inner belt due to solar particle events, but can also be found from $L = 4$ to 7 due to quiet time galactic cosmic rays. Internal charging and subsequent electrostatic discharges (ESD) can be found over a broad range of L shells with a peak around $L = 4.2$, likely where and when penetrating electron fluxes are high. Surface charging and ESD effects are largest in the outer belt with a peak at about

$L = 5.5$, probably due to intense field-aligned currents. At very low L, surface charging is also observed, but no explanation has yet been found.

NASA's Radiation Belt Storm Probes (RBSP) mission, launched on 30 August 2012, targets one part of the space weather chain: Earth's radiation belts of magnetically trapped, very high-energy electrons and ions. The unusual orbit of the RBSP spacecraft will provide great insight into many regions of the radiation belts. The highly elliptical orbit of RBSP (600 km altitude $\times$ $5.8R_E$ geocentric; and 10° inclination) is non-traditional—most communication and monitoring satellites operate at fixed radial distance, for example at or near geosynchronous orbit at $\sim 6.7R_E$ geocentric. For 3-D specification models, the altitude-varying profiles returned by RBSP will provide greater sampling of Earth's radiation environment. For RBSP this orbit is occupied by two identical spacecraft that lap each other every $\sim$2.5 months. Detailed information about the RBSP science, mission and spacecraft design is described elsewhere in this special issue (Mauk et al. 2012; Stratton et al. 2012, and Kirby et al. 2012).

In addition to scientific data (provided at a mean rate of about 100 kilo bits per second—kbps), each RBSP spacecraft will provide a continuous 1 kbps of space weather broadcast data in support of near real time space weather modeling, forecast and prediction efforts. The real-time data from RBSP also will be available to monitor and analyze current environmental conditions, forecast natural environmental changes and support anomaly resolution. RBSP real-time data will be input into the DREAM model (Sect. 4.4), the output of which will be made available through NOAA (Sect. 4.3). This will provide a simple and very quick visual for displaying the current state of the inner and outer radiation belts and the spacecraft charging environment.

Following the commissioning of RBSP in 2012, the RBSP instruments will generate real-time space weather observations to be broadcast by both RBSP spacecraft. This chapter describes presently planned RBSP capabilities for generating and broadcasting the real-time space weather data (Sect. 2). These data will be collected by ground station partners (Sect. 4.1), and gathered and processed at the Johns Hopkins University Applied Physics Laboratory (Sect. 3). The RBSP Science Gateway website (http://rbspgway.jhuapl.edu) will host and continuously update the Space Weather products that will be used to feed into models and assess space weather conditions. Modeling capabilities are discussed in Sect. 4, and concluding remarks are provided in the final section.

2 Generation and Broadcast of Space Weather Data

Each spacecraft will broadcast space weather data in real-time through the primary spacecraft radio frequency (RF) science downlink system, whenever it is not engaged in a primary mission-related ground contact. The data will be received by users who maintain and fund their own ground station antennas. This scenario is limited by the availability of space weather ground stations and antenna coverage. The real time coverage will be reduced by an average of 2.5 hours for each spacecraft per day due to primary mission contacts, or about 10 % of the time. Often when one of the spacecraft is broadcasting the primary science data, and therefore not broadcasting space weather data, the other spacecraft will still be broadcasting space weather data because many of the contacts with each spacecraft do not overlap in time.

Each of the RBSP payload instruments will participate in the real-time space weather broadcast. The data will include particle intensities at a variety of energies, as well as magnetic and electric field data. In addition to the real-time products, it is a goal for the project

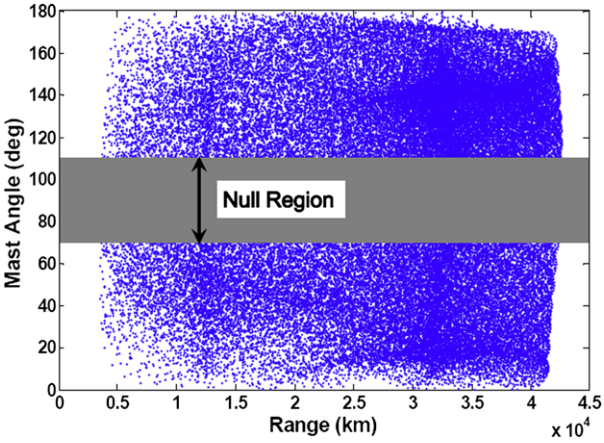

Fig. 2 Statistical distribution with uniform time sampling of RBSP downlink acquisitions plotted as a function of the angle between the RBSP Spin axis (the axis along which the onboard communications antennas are aligned—Fig. 3; called the Mast Angle) and the distance between the spacecraft and the ground station. The antenna pattern for the two antennas on each spacecraft is such that the transmission power is very low within the "null region". It is conservatively assumed that communications may not take place within that region

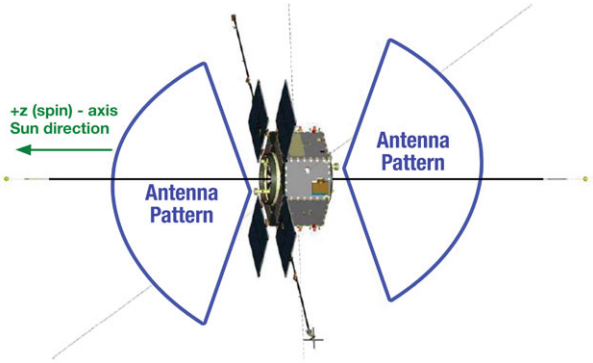

Fig. 3 Schematic of the RBSP radio frequency communications antenna coverage. The sketched patterns are rotationally symmetric with respect to rotations about the horizontal (spacecraft "z") axis

to create "quick look" products to be produced by each of the individual instrument Science Operations Centers (SOC). These products will essentially "fill in the gaps" caused by times when the broadcast data cannot be received and also provide a more complete data set for use in diagnosing anomalies in low (LEO) and mid (MEO) Earth orbit.

The RBSP mission spacecraft will communicate with the ground via S-Band using 8 W Solid State Power Amplifier (SSPA) transmitters. The spacecraft pointing geometry, orbit, and spin stabilization determine communication system requirements. Earth location, as viewed from the spacecraft, covers a very broad angle space (mast angle) as shown in the RBSP communications antenna angle coverage plot in Fig. 2. Contact geometry necessitates onboard antennas that have broad angular coverage and thus relatively low gain.

The coverage is maximized within practical limits using two low gain antennas. The two RF antennas' boresights are aligned with the spacecraft spin- and anti-spin-axes, providing coverage from each boresight to 70° (Fig. 3). Despite maximizing the antenna coverage, there is still a 40° null band, depicted in Fig. 2 as the gray patch in the antenna angle coverage plot. Both antennas are active at all times, as there is no active switching between antennas, but only one will have a line-of-sight to the Earth at any given time (Srinivasan et al. 2009). The top antenna and bottom antenna generate circularly polarized emissions with one spacecraft, RBSP A, using Right Hand Circular Polarization and for the other spacecraft, RBSP B, using Left Hand Circular Polarization. The spacecraft and antenna patterns are illustrated in Fig. 3.

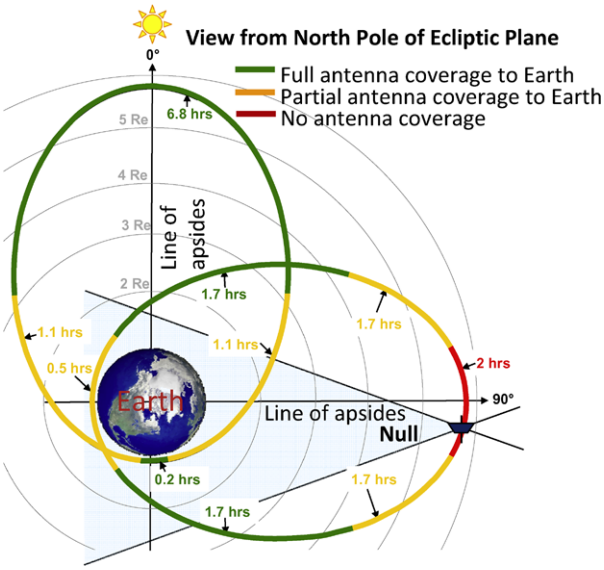

Fig. 4 Regions of the RBSP Orbits where communications downlinks are robust, variable, and impossible. The communications configuration changes over time because of the roughly 220° per year of clockwise (from the north) local time precession of the line of apogee

The possibility of users on Earth receiving the space weather broadcasts depends on an orbit geometry that varies with mission epoch as illustrated in Fig. 4—a view of the orbit changes as seen from a vantage pointing looking down on the Earth from above the North Pole. Although antenna coverage is large, there are times when the antenna patterns are not aligned with the Earth. The large eccentricity of the orbit causes longer periods of time when antennas are not in view during certain times of the year because the relative angle between the spacecraft and Earth changes slowly over long periods of time. Spacecraft orbits are at a low inclination (10°) and the orbit harmonics cause the apogee and perigee to drift between northern and southern hemispheres. Stations near the equator will have the best year-around coverage while high latitude stations may have some limits in coverage over portions of the orbit for parts of the year.

By employing multiple stations at diverse longitudes, we can maximize potential spacecraft contact duration as a function of the number of ground stations. Figure 5 shows the coverage for 1, 2, 3 and 4 ground stations with maximum angular separation—i.e. 2 separated by 180°; 3 by 120°; and 4 by 90°. The peaks and valleys in potential contact periods are primarily due to orbit epoch effects on spacecraft antenna coverage. Normal spacecraft contacts (i.e. downlinking of science data and uplinking commands etc.) would reduce available time for space weather by an average of 2.5 hours per spacecraft per day (∼10 % per spacecraft).

3 RBSP Space Weather Data Products and Services

The space weather data products were chosen to provide a quick look at the state of the radiation belts. The data subset includes particle intensities at a variety of energies, and magnetic and electric field data, both quasi-time-stationary parameters and wave parameters. Current data products can be found in Table 1 and at http://rbspgway.jhuapl.edu. The exact energy and frequency ranges are subject to refinement as the instrument teams plans continue to mature.

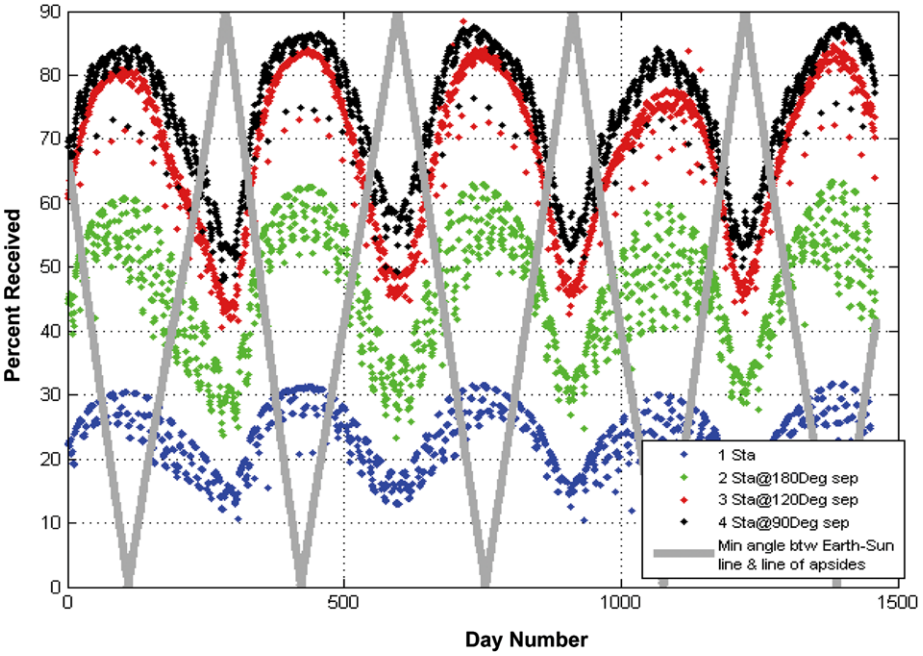

Fig. 5 Average contact time per day (%) of the RBSP spacecraft to 1 or more ground stations distributed around the world plus the minimum angle between Earth-Sun line and line of Apsides (deg). Assumptions: (1) Visibility averaged over 3 day increments. (2) Two 70° half angle antennas. (3) Generic ground stations assumed at 35 °N latitude

The energies within the space weather data by the particle detectors span the ranges expected for the two belts, 25 eV to > 400 MeV for protons, 25 eV–10 MeV for electrons. ECT/HOPE (Funsten et al. 2012—this issue) provides the lower range of both the inner belt ions and outer belt electrons, and the ion composition for the lower energy ions. ECT/MagEIS (Blake et al. 2012—this issue) provides the mid and upper range of outer belt electrons. ECT/REPT (Baker et al. 2012—this issue) provides the upper range of inner belt protons and high range of outer belt electrons, while PSBR/RPS (Mazur et al. 2012—this issue) cover the extreme upper range of inner belt protons. RBSPICE (Lanzerotti et al. 2012—this issue) provides the mid-energy protons intensities.

The EFW instrument (Wygant et al. 2012—this issue) provides the large-scale electric field, and the magnetometer on EMFISIS (Kletzing et al. 2012—this issue) provides the large-scale magnetic field. The Waves instrument portion of EMFISIS on RBSP will provide three values of the high frequency electric and magnetic field observations every 12 seconds for the RBSP space weather data set. The three bands chosen, based on present understanding about which waves propagating within the regions of the radiation belts have the most impact, are defined as follows:

- fce to 0.5 fce (lower band chorus)
- 0.5 fce to 0.7 fce (upper band chorus)
- 10 Hz to fce/$(1837)^{1/2}$ (magnetosonic waves)

Here fce is the so-called electron cyclotron frequency and 1837 is the proton to electron mass ratio. Each band, then, can provide the intensity of the chorus band or magnetosonic waves

Table 1 Space weather broadcast data products

Instrument	Measurement	Energy	Cadence
EMFISIS/MAG	Vector Magnetic Field	N/A	1 vector/12 seconds
EMFISIS/Waves	VLF Wave Power	N/A	E-field spectral density: 3 frequencies every 12 s. B-field spectral density: 3 frequencies every 12 s
EFW	Vector Electric Field	N/A	1 vector/spin
	Spacecraft Potential	N/A	Once/spin
ECT/HOPE	Electrons	24.54 eV, 281 eV, 10.9 keV, 42.9 keV	Once/24 seconds*
	Protons	24.54 eV, 281 eV, 10.9 keV, 42.9 keV	
	Oxygen Ions	24.54 eV, 281 eV, 10.9 keV, 42.9 keV	
	Helium Ions	24.54 eV, 281 eV, 10.9 keV, 42.9 keV	
ECT/MagEIS	Energetic Electrons	30 keV, 60 keV, 100 keV, 300 keV, 600 keV, 1 MeV, 2 MeV	Once/spin
	Energetic Protons	1 MeV	
ECT/REPT	Very Energetic Electrons	2 MeV, 5 MeV, 10 MeV	Once/spin
	Energetic Protons	>20 MeV, >50 MeV, >70 MeV	
RBSPICE	Energetic Protons	50 keV, 100 keV, 150 keV, 300 keV, 1 MeV, 10 MeV	Once/spin
PSBR/RPS	Energetic Protons	>50 MeV, >400 MeV	Once/1 seconds
	Dosimeter Data	Linear & Log Volts	

*Ions and electrons are sampled alternately every other spin

as a function of time (hence, position, as well). By themselves, these observations form the basis of a statistical sampling of the intensity of these phenomena as a function of position. When compared with a model of the occurrence of these phenomena, the parameters allow for instantaneous determination of wave levels relative to the model.

The display of the space weather data is still under discussion, but will likely include products such as: (i) 3-dimensional L-shell-position (y-axis) versus orbit or time (x-axis) versus selected parameters such as particle intensity (represented in the 3rd dimension with a color scale), with the latest data plotted on the right hand side (an example using CRRES data is shown in Fig. 6), (ii) selected parameters such as particle intensity over-layed on the orbit path with the value of that parameter indicated with variable colors or line thicknesses, (iii) line plots of such selected parameters as magnetic field vector and electric field vector, spacecraft charging values, as well as individual team summary plots. The plots will be updated approximately every 12 minutes when space weather data is available. The RBSP space weather telemetry mode is a very low rate, highly compressed data stream broadcast by the spacecraft 24 hours per day. Because of the large compression factors used, the images

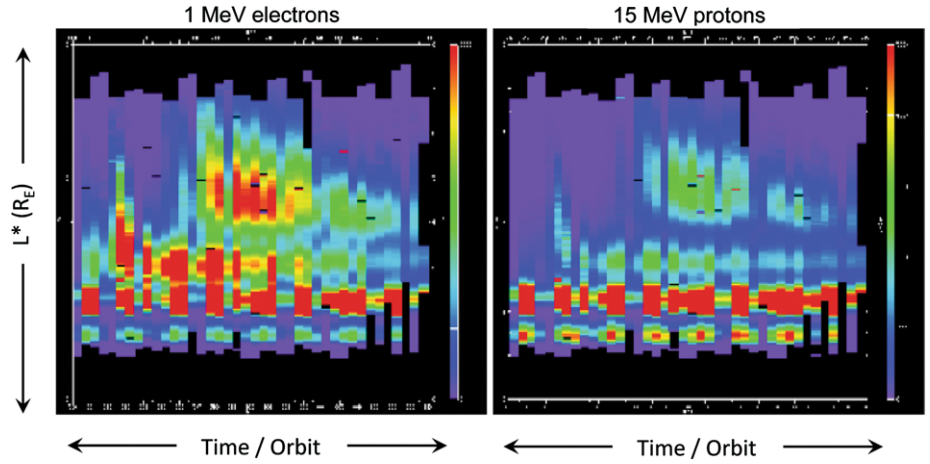

Fig. 6 Images created from CRRES mission showing L^* (y-axis; in R_E) versus time or orbit (x-axis; each vertical stripe will be $\frac{1}{2}$ of a 9 hour orbit for RBSP; x axis) versus intensity (color scale) of 1 MeV electrons (*left*) and 15 MeV protons (*right*). When RBSP launches, the RBSP instruments will be generating and broadcasting real-time space weather data. The RBSP Space Weather images will be created from that data and available at http://rbspgway.jhuapl.edu/weather_currentdata

like that shown in Fig. 6 are of much lower quality and fidelity than those that will be generated by the teams with the actual science data. The raw space weather data will be archived at APL.

The space weather processing uses legacy APL MOC (Mission Operations Center) software developed for the STEREO mission and the LRO/Chandrayaan-1 Mini-RF project. The space weather processing software flow is notionally depicted in Fig. 7. The MOC software will routinely run and automatically ping on the external ground stations to see if new data is available. When available, it will retrieve the data from the external ground stations, strip out the headers put into the Space Weather packets by the external ground stations, extract the variable length packets from the data, clean and merge the space weather Level 0 data and store the raw data in a telemetry archive.

The space weather processing system will periodically ping on the MOC telemetry archive and when new data is available; it will retrieve that data from the archive, decommutate the data and then apply calibration algorithms to generate space weather data products for all of the RBSP instruments. The current space weather data products will be publicly available at http://rbspgway.jhuapl.edu/weather_currentdata. The space weather products will be archived; the most recent 15 days will be publicly available on the RBSP Science Gateway at http://rbspgway.jhuapl.edu/weather_archive.

4 Partners and Customers

The RBSP mission will provide space weather parameters to the user community for integration into nowcast and forecast models. In order to collect these data, a network of ground stations needs to be identified.

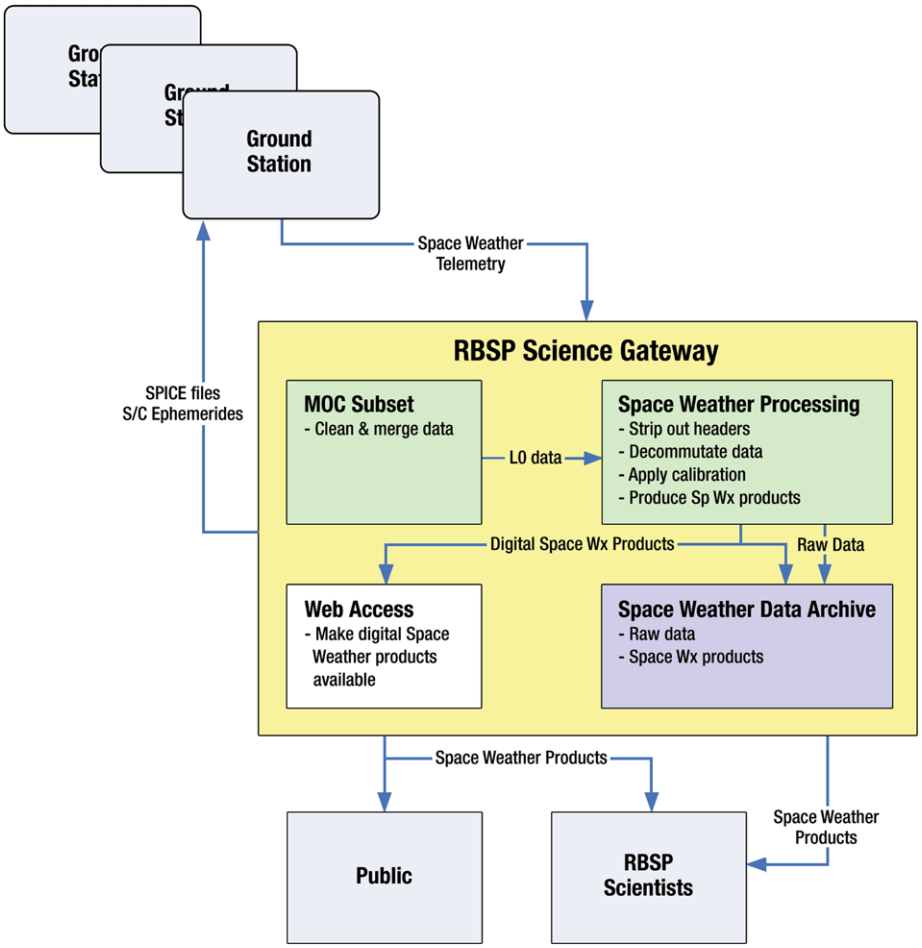

Fig. 7 RBSP space weather data acquisition and processing plan. The ground stations are contributed assets distributed around the world, and the rest of the processing occurs at APL and will be available at http://rbspgway.jhuapl.edu/weather_currentdata

4.1 Ground Stations

Ideally, ground stations should be distributed around the globe at longitudinal separations of about 120° for an optimized 3-station configuration. The telemetry link is subject to orbit geometry, season, and location of each ground station. It is estimated that with an ideal ground network, the link could be operational for about 65 % of the time (assuming 3 longitudinally spaced stations). The normal spacecraft contacts will reduce available time for space weather by an average of 2.5 hours per spacecraft per day.

Ground stations are supplied, operated, and funded by interested parties external to the RBSP Program and Project. Currently, two international ground station partners have been identified and agreements are in place:

– Korea Astronomy and Space Science Institute
– Institute of Atmospheric Physics, Czech Republic

Discussions are underway with other possible international partners including Brazil, Japan, Argentina, Australia, South Africa, and India.

APL regularly provides the participating ground stations with the spacecraft ephemerides and will routinely retrieve the Space Weather data from those ground stations using either socket connections or using ftp/sftp protocols. The APL processing flow for the space weather processing is described in Sect. 3 above.

The RBSP Space Weather ICD contains specific downlink and telemetry formats and is available to partners on request.

4.2 CCMC

The Community Coordinated Modeling Center (CCMC) is a US inter-agency activity, located at GSFC, aimed at research in support of the generation of advanced space weather models (http://ccmc.gsfc.nasa.gov/). The first function of the CCMC is to provide a mechanism by which research models can be validated, tested, and improved for eventual use in space weather forecasting. Examples include NASA's Vision for Space Exploration Models. These models, which have completed their development and which have passed metrics-based evaluations and science-based validations, are being prepared for space weather applications. In this function, CCMC acts as an unbiased evaluator, which bridges the gap between space science research and space weather applications.

As a second equally important function, the CCMC provides to space science researchers the use of space science models, even if those researchers are not model owners themselves. This service to the research community is implemented through the execution of model "runs-on-request" for specific events of interest to space science researchers at no cost to the requestor. Model output is made available to the science customer by means of tailored analysis tools, and by means of data dissemination in standard formats. Through this activity and the concurrent development of advanced visualization tools, CCMC provides unprecedented access to a large number of state-of-the-art research models to the general science community. The continuously expanding model set includes models in all scientific domains from the Solar Corona to the Earth's upper atmosphere. Data received from RBSP will be available for scientific comparisons with model calculations, and as inputs to model calculations performed following requests from the scientific community.

Models tested and evaluated at CCMC are being used at NASA's Space Weather Research Center (SWRC) for providing critical space weather notification for NASA's robotic missions. The SWRC provides a broad range of tools, products, and services including routine experimental research forecasts, notifications, space weather analysis, and spacecraft anomaly resolution support. The SWRC also makes advanced model results and data streams available for public education and information purposes. The SWRC will be receiving RBSP space weather data for situational awareness, model validation, and for ingestion into specification and forecasting models.

4.3 NOAA

NOAA's Space Weather Prediction Center (http://swpc.noaa.gov) is the United States government official source for space weather forecasts. SWPC provides real-time monitoring and forecasting of solar and geophysical events that impact satellites, power grids, communications, navigation, and many other technological systems. There is a range of online data products and services including: Alerts and Forecasts, Models, Indices, and real-time or near-real time instrument measurements. RBSP data will augment their current capabilities

of understanding the space radiation environment, primarily through display of the DREAM model (discussed below) into which near-real time and retrospective MagEIS data has been ingested. This would provide a simple visual for the current level of charged particles in the radiation belts, and hence current internal charging conditions. A new service is under development within the National Geophysical Data center (NGDC) that will combine near-real time and retrospective data for post satellite anomaly analysis. A web page will provide interactive plots of data and models for GEO and LEO orbits for determining whether an anomaly is likely related to surface charging, internal charging, single event effects or total ionizing dose. This will help SWPC and NGDC to deliver space weather products and services that meet the evolving needs of its government and industry stakeholders.

4.4 DREAM

A particularly relevant model for analysis of space weather data from the RBSP mission is the Dynamic Radiation Environment Assimilation Model (DREAM). It was developed to provide accurate, global specification of the Earth's radiation belts and to better understand the physical processes that control radiation belt structure and dynamics (Reeves et al. 2012). DREAM will be used in the RBSP science analysis in two major roles: (a) as a global context for understanding the local 2-satellite measurements and (b) as a testbed for real-time space weather forecasting for the radiation belts. As the name implies, DREAM uses a powerful data assimilation technique (specifically ensemble Kalman Filtering) to calculate a global specification of the radiation belt environment that optimizes the match between model and observations. Unlike traditional models that use "inputs" or "boundary conditions", data assimilation considers uncertainties in both model and observation, it includes observations as part of the internal state of the system, and observations (through a covariance matrix) that affect extended regions around the location of observations.

DREAM uses a Fokker-Planck diffusion formulation (Reeves et al. 2012; see also Ukhorskiy and Sitnov 2012—this issue) as the physics engine that advances the forecast in time. At the time of this writing, data assimilation has only been implemented in the 1D (radial diffusion) version but a 3D-version with radial, energy, and pitch angle diffusion is undergoing testing. The radial diffusion calculation solves for phase space density (PSD) as a function of three magnetic invariants: μ, K, and L^* (invariants of gyration, bounce and drift; again see Ukhorskiy and Sitnov 2012—this issues). DREAM first preprocesses data from intensity (as a function of energy, E, and pitch angle, α) to PSD as a function of μ, K, L^*. [As part of the standard RBSP data processing, μ, K, and L^* will be calculated along the satellite orbits using a variety of different magnetic field models and values, and will be made available for analysis.] Data assimilation runs are done at each time step for each μ, K pair (typically 324 independent assimilations). In an asymmetric (and time varying) magnetic field, each point in space and time has a unique transformation from physical to magnetic coordinates. The same is true for the reverse transformation that takes the DREAM assimilation and converts back to intensity (vs. E and α). Figure 8 (from Reeves et al. 2012) shows an example of the incorporation of the Phase Space Density measurements shown on the left to create a prediction (on the right) for the Phase Space Densities throughout the radiation belt regions. RBSP will give the predictions a lot more fidelity by filling in a lot of the gaps between and inside of the present measurement positions.

The result is a model that gives the space weather forecast for the radiation belts—intensity, flux and fluence, or dose—at any point in the radiation belts based on a very limited set of observations. For space weather forecasting the model can be relatively simple with few (or no) free parameters—for example 1D radial diffusion with D_{LL}(Kp), such

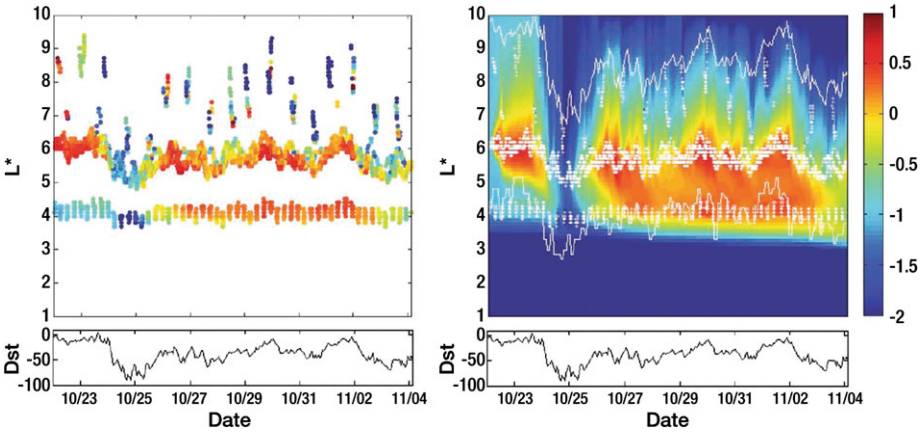

Fig. 8 Example of the capability of the DREAM model (Reeves et al. 2012) to assimilate sparse spacecraft measurements (*left*) together with empirical particle transport and energization algorithms to generate predictions of the overall state of Earth's electron radiation belt. The plots show the magnetospheric parameter L^* (y-axis) versus time (x-axis) versus particle phase space density (color scale), calculated from the particle intensity and the particle momentum. Figures from Reeves et al. (2012)

as is now available with the DREAM model. For detailed scientific analysis more complex models with 3D diffusion and many free parameters will likely be needed with, for example, spatial and temporal distributions of wave power, frequency, and wave normal angle for a variety of wave modes). One of the goals of the RBSP project is to evolve space weather products from the current state of nowcasting with simple models to more sophisticated products that use more complex physics models (balancing accuracy and complexity) and that provide forecasts days or more into the future.

5 Concluding Remarks

The two spacecraft that comprise NASA's LWS RBSP mission will continuously broadcast space weather data, except during prime science download and maneuvers. These data were selected to monitor the state of the radiation belts and will be incorporated into models such as DREAM that could lead to better space weather forecasts.

Currently two international partners have agreed to download this data and make it available for space weather data products. With only two ground stations, portions of the data stream will be lost, but NASA is actively pursuing other ground station partners to fill in the gaps.

RBSP has been designed to operate throughout the worst conditions expected in the hazardous radiation belt environment (Stratton et al. 2012 and Kirby et al. 2012—this issue). By design, the mission will make observations over the full range of particle energy levels and frequencies needed to decipher the mysteries described elsewhere in this volume (Mauk et al. 2012—this issue). RBSP is poised to significantly enhance our understanding of radiation belt dynamics with changing solar wind conditions. RBSP will enable the prediction of extreme and dynamic space conditions, and will provide the understanding needed to design satellites to survive in space for future missions.

Acknowledgements The authors gratefully acknowledge contributions from M. Hesse, G. Reeves, W. Kurth, J. Green, and T.P. O'Brien.

References

D.N. Baker et al., Space Sci. Rev. (2012, this issue). doi:10.1007/s11214-012-9950-9
J.B. Blake et al., Space Sci. Rev. (2012, this issue)
H. Funsten et al., Space Sci. Rev. (2012, this issue)
K. Kirby et al., Space Sci. Rev. (2012, this issue). doi:10.1007/s11214-012-9949-2
C. Kletzing et al., Space Sci. Rev. (2012, this issue)
L.J. Lanzerotti, Solar and solar radio effects on technologies, in *Solar and Space Weather Radiophysics*, ed. by P. Gary, P. Keller (Kluwer Academic, Dordrecht, 2004), p. 1
L.J. Lanzerotti, Space weather effects on technologies, in *Space Weather*, ed. by Song, Singer, Siscoe. Geophysical Monograph, vol. 125 (American Geophysical Union, Washington, 2001), p. 11
L.J. Lanzerotti et al., Space Sci. Rev. (2012, this issue)
B.H. Mauk, N.J. Fox, S.G. Kanekal, R.L. Kessel, D.G. Sibeck, A. Ukhorskiy, Science objectives and rationale for the Radiation Belt Storm Probes mission. Space Sci. Rev. (2012). doi:10.1007/s11214-012-9908-y
J. Mazur, L. Friesen, A. Lin, D. Mabry, N. Katz, Y. Dotan, J. George, J.B. Blake, M. Looper, M. Redding et al., The Relativistic Proton Spectrometer (RPS) for the Radiation Belt Storm Probes mission. Space Sci. Rev. (2012). doi:10.1007/s11214-012-9926-9
G.D. Reeves, Y. Chen, G.S. Cunningham, R.W.H. Friedel, M.G. Henderson, V.K. Jordanova, J. Koller, S.K. Morley, M.F. Thomsen, S. Zaharia, The Dynamic Radiation Environment Assimilation Model: DREAM. Space Weather (2012). doi:10.1029/2011SW000729
R.M. Robinson, R.A. Behnke, The U.S. National Space Weather Program: a retrospective, in *Space Weather*, ed. by P. Song, H. Singer, G. Siscoe. Geophysical Monograph, vol. 125 (American Geophysical Union, Washington, 2001), p. 1
D. Srinivasan, B. Wallis, B. Baker, D. Artis, RF communications subsystem for the Radiation Belt Storm Probes mission. Acta Astron. **65**(11–12) (2009)
J. Stratton et al., Space Sci. Rev. (2012, this issue). doi:10.1007/s11214-012-9933-x
A. Ukhorskiy, M. Sitnov, Space Sci. Rev. (2012, this issue)
J. Wygant et al., Space Sci. Rev. (2012, this issue)

DOI 10.1007/978-1-4899-7433-4_17
Reprinted from *Space Science Reviews* Journal, DOI 10.1007/s11214-012-9938-5

Dynamics of Radiation Belt Particles

A.Y. Ukhorskiy · M.I. Sitnov

Received: 13 March 2012 / Accepted: 26 September 2012 / Published online: 30 November 2012

Abstract This paper reviews basic concepts of particle dynamics underlying theoretical aspect of radiation belt modeling and data analysis. We outline the theory of adiabatic invariants of quasiperiodic Hamiltonian systems and derive the invariants of particle motion trapped in the radiation belts. We discuss how the nonlinearity of resonant interaction of particles with small-amplitude plasma waves, ubiquitous across the inner magnetosphere, can make particle motion stochastic. Long-term evolution of a stochastic system can be described by the Fokker-Plank (diffusion) equation. We derive the kinetic equation of particle diffusion in the invariant space and discuss its limitations and associated challenges which need to be addressed in forthcoming radiation belt models and data analysis.

Keywords RBSP mission · Radiation belts · Quasi-linear diffusion · Chaos · Particle dynamics

1 Introduction

The stability of charged particles trapped in Earth's magnetic field was well established by 1960 (e.g., Northrop and Teller 1960) providing a theoretical basis for the existence of radiation belts discovered by pioneering space missions (Van Allen 1959; Vernov et al. 1959). It was shown that in the approximately dipole field of the inner magnetosphere charged particles undergo three quasiperiodic motions each associated with an adiabatic invariant. A set of three invariants defines a stable drift shell encircling Earth. Subsequent experiments revealed that particle intensities across the belts can vary significantly with time (see review by Roederer 1968), which requires violation of one or more of the adiabatic invariants. Theoretical interpretation of the variability of radiation belt intensities was largely inspired by experiments in particle acceleration by random-phased electrostatic waves in synchrocyclotron devices (e.g., Burshtein et al. 1955; Keller and Schmitter 1958) and the development of quasi-linear theory of weak plasma turbulence (e.g., Drummond and Pines 1961;

A.Y. Ukhorskiy (✉) · M.I. Sitnov
Applied Physics Laboratory, Johns Hopkins University, 11100 Johns Hopkins Rd, Laurel, MD 20723, USA
e-mail: ukhorskiy@jhuapl.edu

Romanov and Filippov 1961; Vedenov et al. 1961). It was concluded that in the absence of large-amplitude perturbations in the electric and magnetic fields the adiabatic invariants of trapped particles can be violated by waves, which can resonantly interact with the quasiperiodic particle motions. Since both the density and energy density of radiation belt particles is negligible compared to other plasma populations, their motion does not affect the fields that govern it. Thus, in accordance with the quasi-linear theory it was suggested that the evolution of radiation belt intensities can be described as a diffusion in the adiabatic invariants under the action of prescribed wave fields, with the diffusion coefficients determined by resonant wave-particle interactions (see reviews Dungey 1965; Trakhtengerts 1966; Tverskoy 1969). While the diffusion framework of radiation belt particle acceleration and loss was well developed within the first decade after the discovery of the belts (e.g., Falthammar 1965; Kennel and Engelmann 1966), the micro-physical origins of particle diffusion and the limitations of the diffusion framework were not fully realized until the development of nonlinear dynamics in 1980–90s.

The goal of this paper is to review basic physical concepts of particle dynamics underlying theoretical apparatus of radiation belt modeling and data analysis. The review is intended primarily for graduate students and non-experts in radiation bet physics who wish to have a brief yet systematic introduction into the field. The material for this review is based on classical monographs on radiation belt particle dynamics such as Roederer (1970) and Schulz and Lanzerotti (1974), several monographs on nonlinear dynamics including (Lichtenberg and Lieberman 1983; Sagdeev et al. 1988; Zaslavsky 2005), as well as a number of original research papers referenced in the text.

We start with outlining the theory of adiabatic invariants of quasiperiodic Hamiltonian systems, then we discuss the motion of charged particles trapped in a quasi-dipole magnetic field of the inner magnetosphere and derive the adiabatic invariants for each of the three quasiperiodic motions of trapped particles. In Sect. 3 we discuss resonant interaction of particles with small-amplitude regular wave fields. We show that particles at resonance with a given harmonic of the spectrum can be trapped in the wave potential where they undergo nonlinear oscillations and phase mixing. The overlap of particle populations at resonance with adjacent harmonics of the spectrum results in stochasticity of particle motion. In the space of adiabatic invariants particle dynamics then resembles random motion of Brownian particles due to collisions with gas molecules. In Sect. 4 we derive the equation of quasi-linear diffusion in the invariant space, often used in radiation belt models, and discuss its relation to the Fokker-Plank kinetic equation of long-term evolution of stochastic systems governed by Markov processes. In Sect. 5 we focus on some limitations underlying the diffusion approximation and associated challenges which need to be addressed in forthcoming radiation belt models and data analysis. In summary we provide a reference table of the most commonly used formulas discussed in this review.

2 Quasiperiodic Motion and Adiabatic Invariants

Adiabatic invariants are approximate constants of motion of a slowly changing system. The change of an adiabatic invariant approaches zero asymptotically as some physical parameter approaches zero. Adiabatic invariants are of great importance for the analysis of stability of the quasiperiodic particle motion in radiation bets in the presence of small perturbation forces, such as various plasma waves or slow variation of the ambient magnetic field due to changing solar wind and geomagnetic conditions.

2.1 General Considerations

Rigorous theory of adiabatic invariants was developed for Hamiltonian systems (e.g., Landau and Lifshitz 1976; Goldstein 1980; Arnold et al. 2010), which in a one-dimensional case are described by equations:

$$H = H(p, q, t); \qquad \dot{p} = -\frac{\partial H}{\partial q}; \qquad \dot{q} = \frac{\partial H}{\partial p}, \tag{1}$$

where H is the Hamiltonian function, p and q are the canonically conjugate momentum and coordinate variables.

If the Hamiltonian of a system does not depend on time explicitly, then the energy $\mathcal{E} = H(p, q)$ is an invariant of motion, i.e. $\mathcal{E} = \text{const}$. For an integrable[1] system with periodic motion the *action-angle* variables are defined by:

$$I = \frac{1}{2\pi} \oint p(q, H) dq = I(H), \tag{2}$$

where the integration is carried out over one period of motion. And by:

$$\theta = \frac{\partial S(q, I)}{\partial I}; \quad S(q, I) = S\big(q, I(H)\big) = \int_{q_0}^{q} p\big(q', H\big) dq', \tag{3}$$

where $S(q, I)$ is a generating function of canonical transformation from the original (p, q) to the new (I, θ) space. The equations of motion in new variables assume the following form:

$$\begin{cases} \dot{I} = -\dfrac{\partial H(I)}{\partial \theta} = 0 \\ \dot{\theta} = \dfrac{\partial H(I)}{\partial I} \equiv \omega(I). \end{cases} \tag{4}$$

From the above equations it follows that the action is an integral of motion, which determines its nonlinear frequency $\omega(I)$:

$$I = \text{const}; \qquad \theta(t) = \omega(I)t + \theta_0. \tag{5}$$

Consider now a slow varying one-dimensional system with a Hamiltonian:

$$H = H\big(p, q, \lambda(t)\big), \tag{6}$$

where the control parameter λ exhibits slow time dependence:

$$\varepsilon \equiv \frac{1}{\omega} \frac{d \ln \lambda}{dt} \ll 1, \tag{7}$$

where ω is a characteristic frequency of the periodic motion at $\lambda = \text{const}$. If in the case when $\lambda = \text{const}$ the system is integrable, then the action (2) is an adiabatic invariant of motion. The integration in this case is carried out over one cycle of motion along unperturbed trajectories specified by $\lambda = \text{const}$.

[1] An N-dimensional Hamiltonian system is integrable, if and only if it has N independent integrals of motion (for a detailed discussion see Lichtenberg and Lieberman 1983).

To examine adiabatic invariance of action we make a canonical transformation from the original variables p and q to the action-angle space (I, θ) using the generating function from Eq. (3):

$$S(q, I, \lambda) = \int_{q_0}^{q} p dq', \tag{8}$$

where momentum $p = p(q, I, \lambda)$ is specified at $\lambda = \text{const}$ by:

$$H(q, p, \lambda) = H(I, \lambda) = \text{const}. \tag{9}$$

Transformation of the Hamiltonian in this case is given by:

$$\widetilde{H} = H + \frac{\partial S}{\partial t} = H + \dot{\lambda}\frac{\partial S}{\partial \lambda}. \tag{10}$$

Since $H = H(I, \lambda)$ and $S = S(q(I, \theta), I, \lambda)$, the canonical equations of motion in new variables have the following form:

$$\begin{cases} \dot{I} = -\dfrac{\partial \widetilde{H}}{\partial \theta} = -\dot{\lambda}\dfrac{\partial^2 S}{\partial \theta \partial \lambda} \\ \dot{\theta} = \dfrac{\partial \widetilde{H}}{\partial I} = \omega(I, \lambda) + \dot{\lambda}\dfrac{\partial^2 S}{\partial I \partial \lambda}, \end{cases} \tag{11}$$

where $\omega(I, \lambda) = \partial H(I, \lambda)/\partial I$ is the frequency of periodic motion at $\lambda = \text{const}$. Since θ is a cyclic variable, the generating function can be expanded in a Fourier series:

$$S(I, \theta, \lambda) = \sum_{k=-\infty}^{+\infty} S_k(I, \lambda) e^{ik\theta}, \quad S_{-k} = S_k^*. \tag{12}$$

To estimate the invariant change over long-term evolution of the system we insert the above expansion into the right hand side of the first equation in system (11) and integrate it over time:

$$\Delta I = I(+\infty) - I(-\infty) = -\sum_{k=-\infty}^{+\infty} ik \int_{-\infty}^{+\infty} dt \dot{\lambda} \frac{\partial S_k(I, \lambda)}{\partial \lambda} e^{ik\theta}, \quad k \neq 0, \tag{13}$$

where $\dot{\lambda}\partial S_k/\partial \lambda = F(\varepsilon t)$ is a slow varying function and the phase θ in the exponent is given by:

$$\theta(t) = \int_0^t \omega(I, \lambda) dt'. \tag{14}$$

The frequency, which is also a slow varying function $\omega = \omega(\varepsilon t)$, usually has zeros only in the complex plane (e.g., Birmingham 1984). To estimate the integrals in expression (13) in this case they are analytically continued over the complex plane. According to the stationary phase method (e.g., Olver 1974) the only non-zero contributions to the integrals occur in the regions of the stationary phase, $\dot{\theta}(t_0) = 0$, given by $\omega(\varepsilon t_0) = 0$ with $\varepsilon t_0 \equiv \tau_0 = \mathcal{O}(1)$. The integrals on the right hand side of expression (13) can then be approximated as:

$$\sqrt{\frac{2\pi}{ik\ddot{\theta}(t_0)}} F(\varepsilon t_0) e^{ik\theta(t_0)}. \tag{15}$$

According to the above expression the invariant change is determined by the imaginary part of the phase at the stationary point:

$$\mathrm{Im}\,\theta(t_0) = \frac{1}{\varepsilon}\,\mathrm{Im}\int_0^{\tau_0}\omega(\tau)d\tau \sim \frac{1}{\varepsilon}\bar{\omega}\tau_{0i}, \tag{16}$$

where $\bar{\omega}$ is the average frequency and τ_{0i} is the imaginary part of τ_0. Consequently the invariant change can be approximated as:

$$\Delta I \sim \exp(-k\bar{\omega}\tau_{0i}/\varepsilon) \sim \exp(-1/\varepsilon). \tag{17}$$

This means that the average (over many periods of fast oscillatory motion) change of the adiabatic invariant is exponentially small, i.e. approaches zero faster than any power of ε. As was proved by Kruskal (1962) the action integral is an adiabatic invariant (i.e. is conserved to all orders in ε) of any Hamiltonian system with quasiperiodic solutions.

It has to be noted that the change in the invariant is no longer exponentially small if the oscillation frequency goes to zero, $\bar{\omega} \sim \varepsilon$. This corresponds to the case when the system crosses a phase space separatrix, which can result in non-negligible violation of the invariant (e.g., Cary et al. 1986; Neishtadt 1986). Implications of invariant violation at separatrix crossings to dynamics of the outer belt particles is discussed in some detail in Sect. 5.3, until then we assume that the estimate (17) holds.

2.2 Adiabatic Invariants of Radiation Belt Particles

The motion of a charged particle in time-varying electromagnetic field of the inner magnetosphere is described by the Hamiltonian function (e.g., Landau and Lifshitz 1959):

$$H = \sqrt{m^2c^4 + c^2\left(\mathbf{P} - \frac{e}{c}\mathbf{A}(\mathbf{r},t)\right)^2} + e\varphi, \tag{18}$$

where e is the electric charge of the particle, m is its mass, c is the speed of light, $\mathbf{A}$ is the vector potential of the magnetic field, φ is the electrostatic potential, and $\mathbf{P}$ and $\mathbf{r}$ are the canonically conjugate variables:

$$\mathbf{P} = \mathbf{p} + \frac{e}{c}\mathbf{A} = m\gamma\mathbf{v} + \frac{e}{c}\mathbf{A}, \tag{19}$$

where γ is the relativistic factor, and $\mathbf{v}$ is the particle's velocity. We assume charge neutrality, so the electromagnetic field is given by:

$$\mathbf{B} = \nabla \times \mathbf{A}; \qquad \mathbf{E} = -\nabla\varphi - \frac{1}{c}\frac{\partial \mathbf{A}}{\partial t}. \tag{20}$$

Canonical equations of motion can then be written in the familiar Lorentz form:

$$\begin{cases} \dfrac{d\mathbf{r}}{dt} = \mathbf{v} \\ \dfrac{d\mathbf{p}}{dt} = e\mathbf{E} + \dfrac{e}{c}\mathbf{v} \times \mathbf{B}. \end{cases} \tag{21}$$

In a static quasi-dipole field of the inner magnetosphere the quasiperiodic motion of trapped particles (Fig. 1a) is a superposition of three independent motions (e.g., Northrop

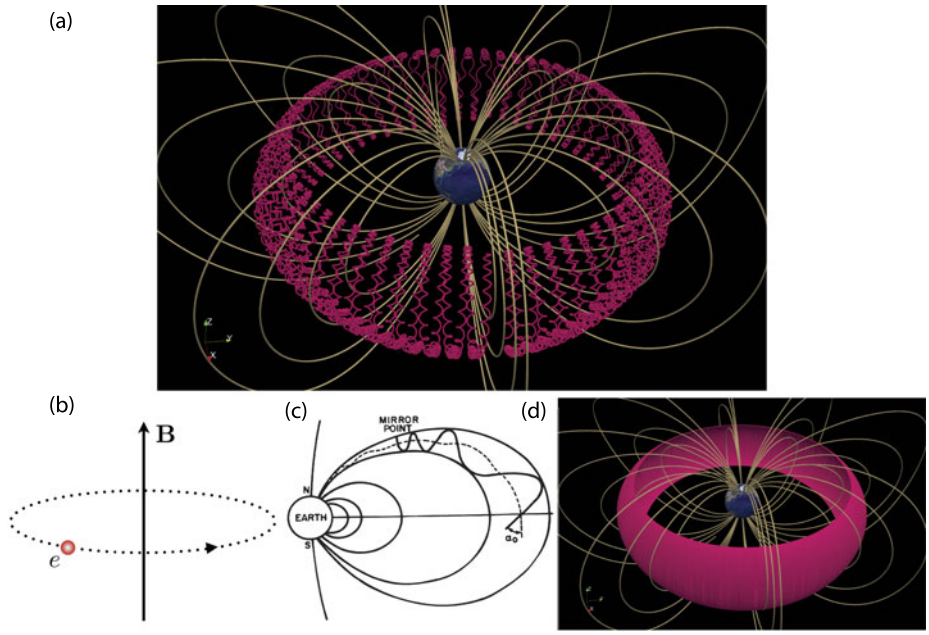

Fig. 1 Quasiperiodic motion of charged particles in the inner magnetosphere. Panel (**a**) shows a trajectory of a 1 MeV particle with electron charge and the mass of 20 m_e (necessary to resolve the gyromotion) over one drift period around Earth. Three components of the quasiperiodic motions are illustrated by subsequent panels. Panel (**b**): particle gyration in a homogeneous magnetic field. Panel (**c**): bounce gyrocenter motion along the field lines. Panel (**d**): drift-bounce gyrocenter motion around Earth, computed for a 1 MeV electron

and Teller 1960): (1) particle gyromotion about its guiding center (Fig. 1b), also referred to as the Larmor motion; (2) the bounce motion of particle guiding center along the field lines between the conjugate reflection points in the northern and southern hemispheres (Fig. 1c); and (3) the longitudinal gradient-curvature drift motion of particle guiding center around Earth (Fig. 1d). Each motion is associated with its own adiabatic invariant.

The first adiabatic invariant is associated with the particle gyromotion. If the characteristic time of field variations (τ) is slow compared to the particle gyration period ($T = 2\pi/\Omega$): $\tau \gg T$, and the spatial scales of field variations (L) greatly exceed the Larmor radius (ρ): $L \gg \rho$, particle gyration $\boldsymbol{\rho}(\mathbf{R}, t, \psi)$ can be separated from the motion of its guiding center $\mathbf{R}(t)$, which can be considered independent of this gyration:

$$\mathbf{r} = \mathbf{R}(t) + \boldsymbol{\rho}(\mathbf{R}, t, \psi), \tag{22}$$

where ψ is the gyration phase: $d\psi/dt = \Omega/\gamma$. The first adiabatic invariant I_1, in this case, can be estimated from expansion of field quantities about the particle guiding center. After expressing an element of Larmor orbit as:

$$d\mathbf{r} = \frac{\partial \boldsymbol{\rho}}{\partial \psi} d\psi = \frac{\mathbf{p}_\perp}{m\Omega} d\psi, \tag{23}$$

where $\mathbf{p}_\perp$ is the momentum associated with the gyromotion, and expanding the magnetic field vector potential in (19) in Taylor series up to the first order about the guiding center,

we obtain the following estimate for the action integral:

$$I_1 \simeq \frac{1}{2\pi}\oint \frac{\mathbf{p}_\perp}{m\Omega}\cdot\left[m\dot{\mathbf{R}}+\mathbf{p}_\perp+\frac{e}{c}\big(\mathbf{A}+(\boldsymbol{\rho}\cdot\nabla)\big)\mathbf{A}\right]d\psi = \frac{p_\perp^2}{m\Omega}+\frac{e}{c}\left\langle\frac{\mathbf{p}_\perp}{m\Omega}\cdot(\boldsymbol{\rho}\cdot\nabla)\mathbf{A}\right\rangle, \quad (24)$$

where $\langle\cdots\rangle = \frac{1}{2\pi}\oint d\psi\cdots$. To estimate the second term on the right hand side of (24), we use the identity $\mathbf{p}_\perp = m\Omega\boldsymbol{\rho}\times\hat{\mathbf{b}}$, where $\hat{\mathbf{b}} = \mathbf{B}/B$, which yields:

$$\frac{e}{c}\big\langle(\boldsymbol{\rho}\times\hat{\mathbf{b}})\cdot(\boldsymbol{\rho}\cdot\nabla)\mathbf{A}\big\rangle = -\frac{e}{c}\frac{\rho^2}{2}\hat{\mathbf{b}}\cdot\nabla\times\mathbf{A} = -\frac{p_\perp^2}{2m\Omega}. \quad (25)$$

After substituting the above expression into (24), and using $\rho = p_\perp/m\Omega$ for the Larmor radius, we obtain the following estimate for the first adiabatic invariant:

$$I_1 = \frac{c}{e}\frac{p_\perp^2}{2B} = \frac{cm}{e}\mu, \quad \text{where } \mu = \frac{p_\perp^2}{2mB}. \quad (26)$$

A charged particle gyrating in strong magnetic field is equivalent to a closed loop of electric current $j = e\Omega/2\pi\gamma$ with the area $\pi\rho^2$. It therefore has a magnetic moment equal to:

$$M = \frac{1}{c}j\pi\rho^2 = \frac{p_\perp^2}{2mB\gamma} = \frac{\mu}{\gamma}. \quad (27)$$

Thus, the first adiabatic invariant of a guiding-center particle is related to its magnetic moment; they become equal in the limit of particle velocities much smaller than the speed of light ($\gamma = 1$).

It has to be noted that μ is a constant of motion only in the guiding-center approximation. If the guiding-center approximation does not hold, i.e. when the magnetic field changes over one gyroperiod become non-negligent, particle orbits can be considerably more complex than in a stably trapped example shown in Fig. 1. In stretched magnetic field configurations, such as in the magnetotail, MeV electrons and keV ions exhibit complex trajectories illustrated in Fig. 2, which shows a Speiser orbit (e.g., Speiser 1965) of an energetic proton in the magnetotail. While the first adiabatic invariant still exists for such orbits, as long as their motion remain quasiperiodic, it is no longer related to μ or the magnetic moment (e.g., Büchner and Zelenyi 1989).

Even in the guiding-center approximation the first invariant is a non-local quantity, which can significantly complicate its derivation from *in situ* particle measurements. While the perpendicular momentum in expression (26) is defined at the location of particle measurements, the magnetic field intensity has to be estimated at the gyrocenter, not sampled by the measurement.

The guiding-center approximation holds well for particles inside the electron and the inner proton belts. The description of particle motion, in this case, can be significantly simplified. Equations for the guiding-center motion were originally derived by expanding the Lorentz equation of motion about the guiding center and then removing fast oscillations by the gyrophase averaging (e.g., Landau and Lifshitz 1959; Sivukhin 1965; Northrop 1963). This procedure, however, has two fundamental shortcomings. First, the equations obtained by the gyrophase averaging do not have the Hamiltonian structure of the original Lorentz equation (e.g., Balescu 1988). As a result they do not conserve the phase space density and therefore are in violation of the Liouville's theorem. Consequently these equations cannot be used for the description of collective phenomena in plasmas. Second,

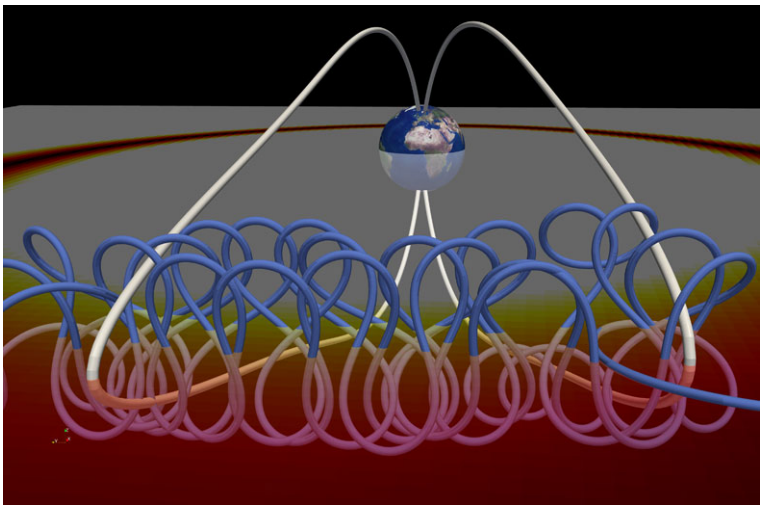

Fig. 2 Speiser motion of a 100 keV proton across the magnetotail. Particle motion was computed in the Tsyganenko (1996) magnetic field model at $P_{dyn} = 4$ nPa and zero tilt angle from the initial location $r = (-15, -5, 0)\ R_E$ and the equatorial pitch angle of 87°

the obtained equations do not conserve energy in time-independent fields. Nonconservation appears in second order terms in the Larmor radius expansion (e.g., Cary and Brizard 2009) and can present difficulties in modeling long-term effects in particle dynamics.

Both problems are successfully solved in a Hamiltonian theory of the guiding-center motion (see review, Cary and Brizard 2009). The six dimensional guiding-center phase space is given by $(\mathbf{R}, \psi, p_\parallel, \mu)$. In the absence of potential electric field and when $E \ll B$ (which is generally true for the inner magnetosphere) and $u_E \ll v_\perp$ (where u_E is the $\mathbf{E} \times \mathbf{B}$ drift velocity: $\mathbf{u}_E = c\mathbf{E} \times \hat{\mathbf{b}}/B$), relativistic guiding-center Hamiltonian function can be written as:

$$H(\mathbf{R}, p_\parallel, \mu, t) = mc^2\gamma(\mathbf{R}, p_\parallel, \mu; t) = mc^2\sqrt{1 + \frac{2\mu B(\mathbf{R}, t)}{mc^2} + \left(\frac{p_\parallel}{mc}\right)^2}. \tag{28}$$

The following noncanonical guiding-center equations of motion are then derived from the variational principle with the use of the above Hamiltonian function (Cary and Brizard 2009; Ukhorskiy et al. 2011):

$$\begin{cases} \dot{p}_\parallel = e\dfrac{\mathbf{E}^* \cdot \mathbf{B}^*}{B_\parallel^*} \\ \dot{\mathbf{R}} = \dfrac{p_\parallel}{m\gamma}\dfrac{\mathbf{B}^*}{B_\parallel^*} + c\dfrac{\mathbf{E}^* \times \hat{\mathbf{b}}}{B_\parallel^*}, \end{cases} \tag{29}$$

where the effective electromagnetic field:

$$\begin{cases} \mathbf{E}^* = -\nabla\Phi^* - \dfrac{1}{c}\dfrac{\partial \mathbf{A}^*}{\partial t} \\ \mathbf{B}^* = \nabla \times \mathbf{A}^*, \end{cases} \tag{30}$$

is defined in terms of the effective electromagnetic potentials:

$$\begin{cases} \Phi^* = \phi + \dfrac{mc^2}{e}\gamma \\ \mathbf{A}^* = \mathbf{A} + \dfrac{cp_\parallel}{e}\hat{\mathbf{b}}. \end{cases} \tag{31}$$

In the absence of large electric currents $\nabla \times \mathbf{B}/B \simeq 0$ and $\mathbf{B}^* = \mathbf{B} + \frac{cp_\parallel}{eB}\hat{\mathbf{b}} \times \nabla B$. For a static magnetic field equations (29) are then reduced to:

$$\begin{cases} \dot{p}_\parallel = -\dfrac{\mu}{\gamma}\hat{\mathbf{b}} \cdot \nabla B \\ \dot{\mathbf{R}} = \dfrac{p_\parallel}{m\gamma}\hat{\mathbf{b}} + \mathbf{U}_D \\ \mathbf{U}_D = \dfrac{c}{\gamma e}\left(\dfrac{p_\parallel^2}{mB} + \mu\right)\dfrac{\hat{\mathbf{b}} \times \nabla B}{B}. \end{cases} \tag{32}$$

The first equation in (32), which describes the motion of particle guiding center along the magnetic field lines, can be written as:

$$\ddot{s} = -\frac{\mu}{m\gamma^2}\frac{\partial B}{\partial s}, \tag{33}$$

where s measures the distance along filed lines from the magnetic equator (minimum of $B(s)$ in a dipole-like magnetic field). From conservation of kinetic energy and the first adiabatic invariant it follows that particle motion along magnetic field lines also satisfies:

$$\frac{\sin^2\alpha}{B} = \text{const}, \tag{34}$$

where α is the particle pitch angle: $\sin\alpha = p_\perp/p$. From Eq. (34) it follows that the particle pitch angle, increases while it moves along a field line from the equator to higher latitudes, where the magnetic field intensity is higher. If at the equator a particle had the pitch-angle α_{eq}, then the parallel component of its velocity will become zero ($\alpha = \pi/2$) at the point s_m: $B(s_m) = B(0)/\sin^2\alpha_{eq}$, and the particle will get reflected back towards the equator. To demonstrate that Eq. (33) describes particle oscillations between the conjugate reflection points, consider particle motion in the vicinity of the magnetic equator, where the field can be approximated by the first two non-zero terms of the Taylor expansion:

$$B(s) = B(0) + \frac{s^2}{2}\frac{\partial^2 B}{\partial s^2} = c_1 + \frac{c_2}{2}s^2. \tag{35}$$

After substituting expression (35) into Eq. (33) we obtain a harmonic oscillator equation:

$$\ddot{s} + \omega_b^2 s = 0, \quad \omega_b^2 = \frac{\mu c_2}{m\gamma^2}, \tag{36}$$

with ω_b angular frequency of particle oscillations across the equator.

The second adiabatic invariant is computed by integrating the parallel component of particle canonical momentum along a guiding-center bounce orbit:

$$I_2 = \oint P_\parallel ds = \oint p_\parallel ds + \frac{e}{c}\oint \mathbf{A} \cdot d\mathbf{s}, \tag{37}$$

where following common convention we multiplied definition (8) by 2π. The integral in the second term on the right hand side is the total magnetic flux enclosed by the unperturbed orbit, which, in this case, is zero since bounce motion is along magnetic field lines. Since the second invariant is calculated for a fixed magnetic field configuration, the kinetic energy is conserved and the invariant can be expressed as:

$$I_2 = 2p\int_{s_m}^{s'_m} ds\sqrt{1-\frac{p_\perp}{p}} = 2pJ; \quad J = \int_{s_m}^{s'_m} ds\sqrt{1-\frac{B(s)}{B(s_m)}}, \tag{38}$$

where the integration is carried out between the conjugate bounce points s_m and s'_m along a fixed magnetic field line. It has to be noted that some textbooks such as Roederer (1970), for example, and papers use different notation: J for I_2 and I for J, which we chose not to follow to avoid confusion with other notations in the paper.

The third equation of (32) describes the longitudinal guiding-center drift across the magnetic field lines around Earth, which is referred to as the gradient-curvature drift. This motion corresponds to the third adiabatic invariant:

$$2\pi I_3 = m\oint \mathbf{U}_D \cdot d\mathbf{R} + \frac{e}{c}\oint \mathbf{A}\cdot d\mathbf{R} \simeq \frac{e}{c}\Phi, \tag{39}$$

where Φ is the magnetic flux across the drift orbit. The above expression is dominated by the second term, since the gradient-curvature drift velocity is small $p_\perp/m\gamma \gg U_D$. The magnetic flux can be computed by shifting the integration contour to any contour C on the drift-bounce surface closed around Earth:

$$\Phi = \oint_C \mathbf{A}\cdot d\mathbf{l} = \oint_C \nabla\times\mathbf{B}\cdot d\mathbf{l} = \int_S \mathbf{B}\cdot d\mathbf{S}, \tag{40}$$

$d\mathbf{l}$ is the contour element, and $d\mathbf{S}$ is the element of a surface encircled by the contour. In the axisymmetrical dipole magnetic field particles gradient-curvature drift along $L = \text{const}$ surfaces, where L is a dipole coordinate which is constant along a given magnetic field line, and is equal to the distance from the dipole center to the field line at the equator measured in Earth radii. The magnetic flux through a drift orbit in this case is equal to:

$$\Phi = -\frac{2\pi B_0 R_E^2}{L}, \tag{41}$$

where $B_0 \simeq 31000$ nT is the magnetic field intensity on Earth's surface at the equator, and $R_E \simeq 6380$ km is the Earth's radius.

In a realistic nondipolar field of the inner magnetosphere the third invariant of trapped particles is often quantified with the use of the *generalized L-value* or *L-star* based on relation (41) for a dipole field:

$$L^* = -\frac{2\pi B_0 R_E^2}{\Phi}. \tag{42}$$

Physically L^* is the radial distance (in Earth radii) to the equatorial points of the drift-bounce shell on which the particle would be found if all nondipolar contributions to the magnetic field would be adiabatically turned off.

Energy and spatial dependencies of the gyration, bounce, and the gradient-curvature drift frequencies in a dipole magnetic field is shown in Fig. 3. Characteristic frequencies of relativistic (~1 MeV) electrons in the center of the outer belt ($L \sim 4$–5) are separated by approximately three orders of magnitude: gyration frequency ~kHz, bounce frequency ~Hz,

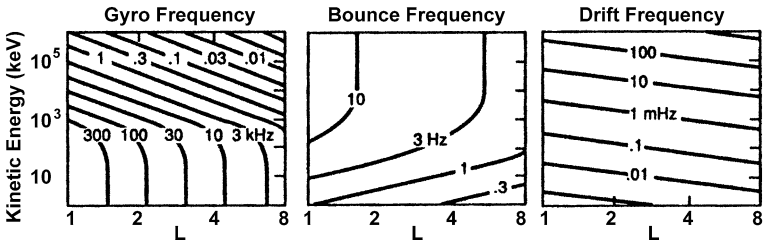

Fig. 3 Contours of constant adiabatic gyration, bounce, and gradient-curvature drift frequencies of equatorially mirroring electrons in a dipole field (adapted from Schulz and Lanzerotti 1974)

while the gradient-curvature drift frequency ∼mHz. This means that in a dipole or an approximately dipole field the quasiperiodic motions corresponding to the three adiabatic invariants are well decoupled. The gradient-curvature drift does not affect the bounce motion, which does not alter the gyration. It also means that it is possible to violate higher invariants without changing lower invariants. For instance, in the process of resonant wave-particle interaction with the gradient-curvature drift motion an ultra-low frequency (ULF) wave can violate the third invariant without altering either the first or the second invariants.

3 Particle Dynamics in Wave Fields

In this section we discuss resonant interaction of particles with small amplitude waves. We show that even if wave fields are regular and no external randomness is introduced into the system, the nonlinearity of resonant wave-particle interaction combined with the overlap of particle populations in resonance with adjacent harmonics of the wave spectrum result in a stochastic particle motion. In the space of adiabatic invariants particles exhibit random walk motion similar to the Brownian motion of heavy particles due to collisions with light molecules in gasses. In our consideration we use a specific example of resonant interaction between the drift motion of the outer belt electrons and the ULF waves, resulting in a stochastic radial motion of electrons across the drift shells. However, the discussed properties of the stochastic motion are general and are equally applicable to resonant interaction of waves with the bounce and the gyromotion of trapped particles.

Consider an electron bouncing at the magnetic equator ($I_2 = 0$) and drifting around Earth due to the gradient of its dipole magnetic field, which in the equatorial plane is given by: $\mathbf{B}(L) = \hat{\mathbf{z}} B_0/L^3$. According to Eqs. (32), $\mathbf{U}_D = 3\hat{\boldsymbol{\varphi}}\mu c/\gamma e R_E L$, and the unperturbed motion of the electron guiding center is the rotation around Earth at constant L:

$$\begin{cases} \dot{L} = 0 \\ \dot{\varphi} = \omega_D(L,\gamma) = \dfrac{3\mu c}{\gamma e R_E^2}\dfrac{1}{L^2}, \end{cases} \tag{43}$$

where φ is the azimuthal angle and $\hat{\boldsymbol{\varphi}}$ is the unitary vector in the azimuthal direction. For relativistic particles with $\gamma^2 \gg 1$, the first invariant can be approximated by: $\mu = mc^2\gamma^2 L^3/2B_0$, and the drift frequency can then be written as function of L: $\omega_D(L) = aL^{-5/2}$, where a includes all constant terms.

Consider now a perturbation of the periodic drift motion due to a small-amplitude azimuthal ULF wave field of the following form:

$$E_\varphi = -E_0 \sum_{m=1}^{M} \sin(\varphi - m\Delta\omega t + \psi_m), \tag{44}$$

where E_0 is the wave amplitude, $\Delta\omega$ is the frequency spacing between adjacent spectral harmonics, M is the number of harmonics, and ψ_m are their phase shits. In the wave field, the particle guiding center will also experience radial motion due to the $\mathbf{E} \times \mathbf{B}$ drift, $\mathbf{u}_E = \hat{\mathbf{r}} c E_\varphi L^3 / B_0$:

$$\begin{cases} \dot{L} = -AL^3 \sum_{m=1}^{M} \sin(\varphi - m\Delta\omega t + \psi_m) \\ \dot{\varphi} = \omega_D(L) = aL^{-5/2}. \end{cases} \tag{45}$$

After introducing a new variable $I = L^{-2}$, assuming that the change $\Delta I = I - I_0$ is small, and approximating the frequency as: $\omega_D(I) = aI^{5/4} \simeq \omega_0 + \omega_D' \Delta I$, where $\omega_0 = \omega_D(I_0)$ and $\omega_D' = 5\omega_0/4I_0$, the above equations can be written as:

$$\begin{cases} \Delta\dot{I} = 2A \sum_{m=1}^{M} \sin(\varphi - m\Delta\omega t + \psi_m) \\ \dot{\varphi} = \omega_0 + \omega_D' \Delta I. \end{cases} \tag{46}$$

Finally, after the following substitutions:

$$t \to t\Delta\omega; \qquad I \to \frac{\omega_D'}{\Delta\omega}\Delta I; \qquad \theta = \varphi - \omega_0 t; \qquad K = \frac{8\pi^2 A \omega_D'}{(\Delta\omega)^2}, \tag{47}$$

dynamical system (46) can be written as:

$$\begin{cases} \dot{I} = \dfrac{K}{4\pi^2} \sum_{m=-M_1}^{M_2} \sin(\theta - mt + \psi_m) \\ \dot{\theta} = I, \end{cases} \tag{48}$$

where $M_1 + M_2 + 1 = M$. The above system corresponds to the following Hamiltonian function:

$$H = \frac{I^2}{2} + \frac{K}{4\pi^2} \sum_{m=-M}^{M} \cos(\theta - mt + \psi_m). \tag{49}$$

While the above derivation was carried out for electron interaction with azimuthal ULF waves (see also Elkington et al. 1999, 2003; Ukhorskiy et al. 2005; Ukhorskiy and Sitnov 2008), the final form of Hamiltonian function (49) is quite general and describes a wide class of wave-particle interactions including interactions with particle gyration and the bounce motion (e.g., Southwood et al. 1969; Smith and Kaufman 1978; Jaekel and Schlickeiser 1992; Shklyar and Matsumoto 2009).

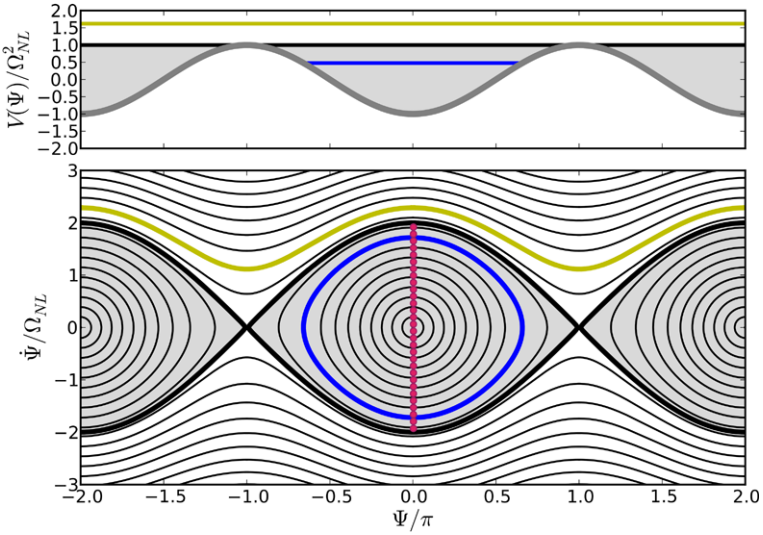

Fig. 4 The potential (*upper panel*) and the phase portrait (*bottom panel*) of particle motion in a single wave

3.1 Nonlinear Resonance

For a particle with a given value of I, the sum on the right hand side of the first equation in (48) is dominated by the term m_0 closest to the resonance: $|I - m_0| \to min$. Neglecting for now contributions of non-resonant terms and introducing a new angle variable, $\Psi = \theta - m_0 t + \psi_{m0} + \pi$, we obtain the following equation for particle oscillations in resonance vicinity:

$$\ddot{\Psi} + \Omega_{NL}^2 \sin\Psi = 0, \tag{50}$$

where $\Omega_{NL}^2 = K/4\pi^2$ is the frequency of nonlinear oscillations. The above equation describes dynamics of a nonlinear pendulum with the Hamiltonian:

$$H = \frac{\delta I^2}{2} + V(\Psi) = \frac{\dot{\Psi}^2}{2} - \Omega_{NL}^2 \cos\Psi, \tag{51}$$

where $\delta I = I - m_0$. Its phase portrait is shown in Fig. 4. Singular points of the motion are defined by the conditions: $\dot{\Psi} = 0$ and $\frac{d}{dt}\delta I = -\partial V/\partial\Psi = 0$, i.e.:

$$\dot{\Psi}_s = 0; \qquad \sin\Psi_s = 0. \tag{52}$$

This yields: $\dot{\Psi}_s = 0$, $\Psi_s = \pi n$, $n = 0, \pm 1, \ldots$. At singular points the velocity $\dot{\Psi}_s$ is zero, and the potential $V(\Psi_s)$ has minima (even n) or maxima (odd n). Thus the singularities are of the elliptic type at $n = 2k$ and saddles at $n = 2k + 1$, where $k = 0, \pm 1, \ldots$. The system has two different types of solutions. When $H < \Omega_{NL}^2$ the solutions correspond to particles trapped in the potential well of the wave and oscillating about the elliptical singular points (blue trajectory in Fig. 4). At $H > \Omega_{NL}^2$ the solutions correspond to untrapped particles with unbounded trajectories (yellow trajectory in Fig. 4). The trajectory separating the phase space regions corresponding to the different types of solutions is called the *separatrix*. It passes through the point $\dot{\Psi} = 0$, $\Psi = \pi$ and therefore corresponds to $H_s = \Omega_{NL}^2$.

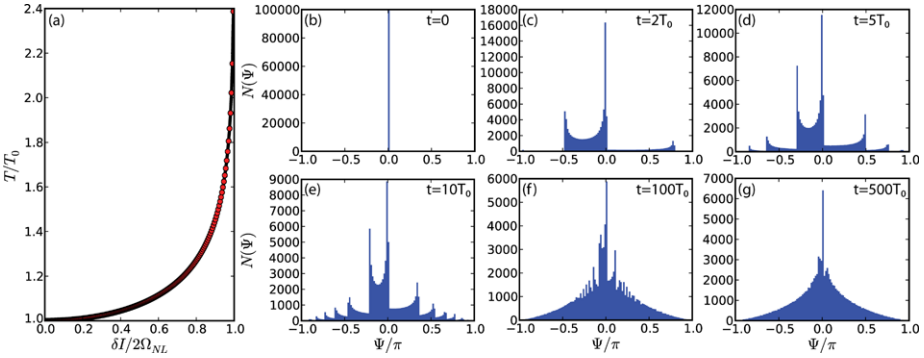

Fig. 5 Panel (**a**): The period of trapped particle oscillations as function of the distance $\delta I(\Psi = 0)$ from the center of the resonance island. Panels (**b**)–(**g**): evolution of an ensemble of 10^5 particles trapped at wave resonance initially at $\Psi = 0$ and $\dot{\Psi} = \delta I$ evenly distributed between the center of the resonance island ($\delta I = 0$) and the separatrix ($\delta I = 2\Omega_{NL}$). The initial conditions are indicated by *red dots* in Fig. 4. Particle dynamics were numerically simulated with the use of a leapfrog integrator

From Eq. (51) it follows that the maximum separatrix width in action space, which is also referred to as the resonance width, is equal to:

$$\Delta I = 2(\delta I)_{max} = 4\Omega_{NL} = \frac{2}{\pi}\sqrt{K}. \tag{53}$$

It specifies the maximum deviation of I from the resonance value m_0 at which particles can still be trapped at resonance with a wave of the amplitude $K/4\pi^2$. Expression (53) also gives the upper limit for the change in action due to nonlinear resonance with one wave harmonic.

The period of trapped particle oscillations in the potential well of the wave depends on the proximity to the resonance. Close to the resonance, i.e. at small $\delta I(\Psi = 0)$ values, particles exhibit harmonic oscillations with the period $T_0 = 2\pi/\Omega_{NL}$, as directly follows from Eq. (50) for small Ψ values. With increase in $\delta I(\Psi = 0)$, oscillations become nonlinear and their period grows. As trajectories approach the separatrix the period goes to infinity logarithmically (see panel (a) in Fig. 5). To elucidate it, let us consider a trapped particle oscillating in close proximity of the separatrix such that: $\Delta/H_s \ll 1$, $\Delta = H_s - H$. From Eq. (51) it follows that the action integral of the trapped particle motion is given by:

$$I_{tr} = \frac{1}{2\pi}\oint \dot{\Psi} d\Psi = \frac{1}{2\pi}\oint \sqrt{2\big(H + \Omega_{NL}^2 \cos\Psi\big)}d\Psi. \tag{54}$$

The oscillation period can then be computed as:

$$T = \frac{2\pi}{\omega} = 2\pi\frac{dI_{tr}}{dH} = \oint \frac{d\Psi}{\sqrt{2(H + \Omega_{NL}^2 \cos\Psi)}}. \tag{55}$$

As H approaches $H_s = \Omega_{NL}^2$, the turning points ($\dot{\Psi} = 0$) approach $\Psi = \pm\pi$ and the expression in the denominator on the right hand side of expression (55) goes to zero. Thus, the largest contributions to the integral in (55) is given by vicinities of the turning points. To evaluate the integral, we can therefore use Taylor expansion of the potential function in the denominator about the reflection points. After introducing a new variable: $x = \Psi - \pi$, and

expanding up to the first non-vanishing, non-constant term we obtain:

$$T = 4\int_{x_2}^{x_1} \frac{dx}{\sqrt{\Omega_{NL}^2 x^2 - 2\Delta}}, \tag{56}$$

where the integration goes from the reflection point: $x_2 = \sqrt{2\Delta/H_s}$, to the center of the resonance island: $x_1 = \pi$. After integrating and taking the limit $\Delta \to 0$ we obtain the following expression for the oscillation period:

$$T = \frac{2}{\Omega_{NL}} \ln \frac{H_s}{2\Delta}, \tag{57}$$

which goes to infinity as the trajectory approaches the separatrix.

As a result of nonlinear dependence of the oscillation period on the resonance proximity, trapped particles undergo phase mixing. Particles who originally had the same phase but slightly different values of δI oscillate about the center of the resonant island at different frequencies. Consequently their phases gradually separate and the motion becomes eventually uncorrelated. Phase mixing is illustrated in Fig. 5. Panels (b)–(g) of the figure show evolution of the phase distribution function computed for an ensemble of 10^5 particles trapped at resonance with a single wave. Initially all particles have the same phase ($\Psi = 0$) but were evenly distributed over δI from $-2\Omega_{NL}$ to $2\Omega_{NL}$. After first several oscillation periods, T_0, particles spread over almost entire phase range from $-\pi$ to π, but still exhibit strong phase bunching indicated by multiple pronounced peaks in the distribution function. Eventually the peaks break down and spread over the phase interval. After a large number of drift periods the process produces a smooth distribution function accept for a singular peak around $\Psi = 0$ corresponding to the particles at exact resonance $\Psi = \dot{\Psi} = 0$.

3.2 Resonance Overlap

Wave perturbation in the Hamiltonian (49) consists of multiple wave harmonics. From our previous considerations it follows that there is a layer of trapped particles of the width ΔI centered at each of the spectral harmonics. The larger is the wave amplitude K the wider are these layers (see Eq. (53)). If the amplitude increases to the point when the resonant width ΔI exceeds the spacing $\Delta\omega$ between spectral harmonics m_0 and $m_0 \pm 1$, the resonant populations trapped by adjacent harmonics overlap, and the particle motion is no longer bounded to a single resonance. From this qualitative consideration it follows that resonances overlap, if $K \gtrsim \pi/2$ (Chirikov 1960). Particle population initially at resonance with one wave harmonic can then spread over the entire system (maximum spread restricted only by the width of the spectrum: $\Delta I = M$). Phase mixing in this case results in exponential divergence of particle trajectories with similar initial condition, which is an attribute of *chaotic* dynamics. Generally speaking, chaotic systems are the systems described by regular dynamical equations (the Lorentz equations (21) in this case) with no stochastic coefficients, but at the same time with solutions that are similar to some stochastic processes.

Transition to stochasticity due to resonance overlap is best illustrated with a special case of a regular broad-band wave field, i.e. when all phase shits in (48) are zero $\psi_m = 0$ and $M_{1,2} \to \infty$. The following identity:

$$\sum_{m=-\infty}^{\infty} \cos(m\nu t) = \sum_{m=-\infty}^{\infty} \delta\left(\frac{t}{T} - m\right), \quad T = \frac{2\pi}{\nu} \tag{58}$$

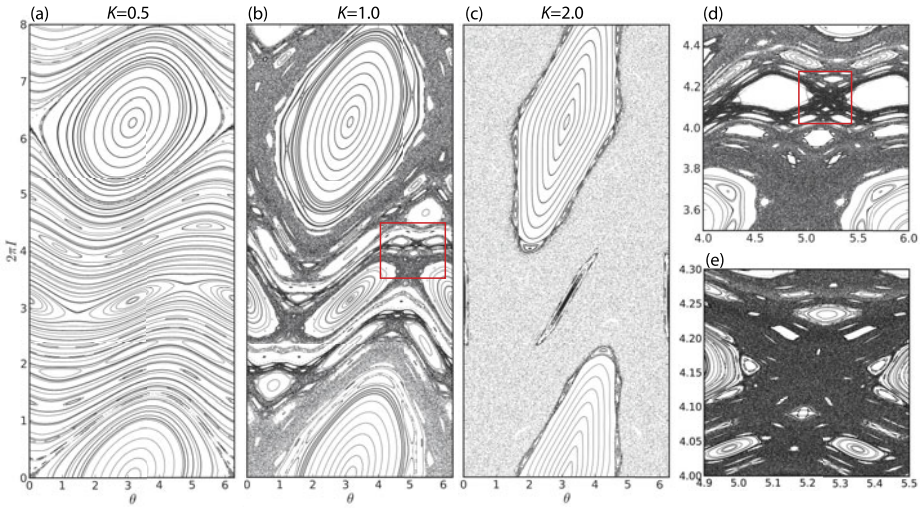

Fig. 6 Phase portrait of the standard map for different values of the nonlinearity parameter K (panels (**a**)–(**c**)). The $K = 1$ portrait in panel (**b**) illustrates the onset of global stochasticity according to the modified Chirikov criterion. Panels (**d**) and (**e**), showing magnifications of regions bounded by *red rectangles* in panels (**b**) and (**d**), illustrate the existence of resonant island structures at all scales

with $\nu = 1$ can then be applied to the right hand side of the first equation (48), which yields:

$$\begin{cases} \dot{I} = \dfrac{K}{2\pi} \sin\theta \displaystyle\sum_{m=-\infty}^{\infty} \delta(t - 2\pi m) \\ \dot{\theta} = I. \end{cases} \tag{59}$$

It means that at time moments $t_m = 2\pi m$ particle experience sharp kicks in action I, while between t_m and t_{m+1} the action is conserved and particles move at constant angular frequency $\dot{\theta} = I = \text{const}$. After defining $I_m = I(t_m - 0)$ and $\theta_m = \theta(t_m - 0)$ Eqs. (59) can be reduced to an algebraic map:

$$\begin{cases} I_{m+1} = I_m + \dfrac{K}{2\pi} \sin\theta_m \\ \theta_{m+1} = \theta_m + 2\pi I_{m+1} \bmod 2\pi, \end{cases} \tag{60}$$

where the change in action was computed by integrating over a small vicinity of t_m.

To illustrate the dynamics described by map (60), which is commonly referred to as the standard map, its phase portrait was computed for different values of the nonlinearity parameter K (see Fig. 6). At $K = 0.5$ most of phase space trajectories are stable. Primary resonant islands are centered at $I = 0, 1$ and $\theta = \pi$. The space between the primary islands has a complex structure. It is populated by chains of smaller islands of various sizes and periodicities associated with higher-order resonances, such as the resonances between trapped particle oscillations and the wave field: $k\omega(I) - m\Delta\omega = 0$, where $\omega(I)$ is the frequency of particle motion about a primary resonant island. Each island chain is bounded by a separatrix. The area near a separatrix is most susceptible for the onset of chaos, since particle velocity near saddle points approaches zero and their dynamics becomes sensitive to small perturbations. An arbitrary small periodic perturbation destroys the separatrix and creates

a stochastic layer of extremely complicated phase space topology where chaotic trajectories are embedded with infinite number of islands (Figs. 6c, d). Even at $K \ll 1$ there is a thin stochastic layer in the vicinity of each separatrix. With an increase in K the width of stochastic layers grows until stochastic layers connect across all values of I, which results in transition to *global stochasticity*. A detailed analysis which takes into account higher order resonances (Chirikov 1979) shows that transition to global stochasticity in the standard map corresponds to $K = 1$, which is known as the *modified Chirikov criterion* (Fig. 6b). With further increase K the area of stochastic phase space region keeps growing, while the area of stable islands keeps shrinking (Fig. 6c).

4 Transition to Kinetic Description

The motion of individual charged particles is described by the Lorentz equations of motion (21). Particle distribution function or the *phase space density* evolves in accordance with the *Liouville's theorem*. If particle motion becomes stochastic, which in a collision-free plasma can be caused by interactions with waves, then correlations among dynamics of individual particles decay. Consequently, the description of long-term evolution of particle distribution function can be reduced to a Fokker-Planck equation, similar to the description of diffusion in gas, which we discuss in this section.

4.1 Phase Space Density

For a system of large number of particles one can introduce the phase space density:

$$\int f(\mathbf{p}, \mathbf{q}, t) d\mathbf{p} d\mathbf{q} = N, \tag{61}$$

where N is the total number of particles, and $f(\mathbf{p}, \mathbf{q}, t) d\mathbf{p} d\mathbf{q}$ is the number of particles in the volume $d\mathbf{p} d\mathbf{q}$ centered at $\mathbf{z} = (\mathbf{p}, \mathbf{q})$ at time t. If particles are not lost or introduced into the system, their evolution in phase-space satisfies the continuity equation:

$$\frac{\partial f}{\partial t} + \nabla_{\mathbf{z}} \cdot (\dot{\mathbf{z}} f) = 0. \tag{62}$$

If $\mathbf{p}$ and $\mathbf{q}$ are the canonically conjugate momentum and coordinate variables corresponding to a Hamiltonian function (Eq. (1)), then $\nabla_{\mathbf{z}} \cdot \dot{\mathbf{z}} = 0$, and the last equation can be written as:

$$\frac{\partial f}{\partial t} + \dot{\mathbf{q}} \cdot \frac{\partial f}{\partial \mathbf{q}} + \dot{\mathbf{p}} \cdot \frac{\partial f}{\partial \mathbf{p}} = 0, \tag{63}$$

which is known as the Liouville's theorem stating that the phase space density is conserved along particle trajectories.

The phase space density is directly related to observable quantities such as particle flux and intensity. The intensity $j_\alpha(\mathcal{E}, \mathbf{r})$ of particles of a given class and kinetic energy is defined as the number of particles coming from a given direction which impinge per unit time, unit solid angle and unit energy, on a surface of unit area oriented perpendicular to their direction of incidence. If δN is the number of particles with kinetic energies between $\mathcal{E}$ and $\mathcal{E} + \delta\mathcal{E}$ impinging on the area δA with normal $\hat{\mathbf{n}}$ during time interval δt, and whose direction of incidence lie in the solid angle $\delta\Omega$ oriented along $\mathbf{p}$ (see Fig. 7), then:

$$\delta N = j_\alpha(\mathcal{E}, \mathbf{r}) \delta A \cos\alpha \delta\Omega \delta\mathcal{E} \delta t. \tag{64}$$

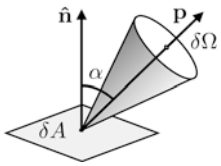

Fig. 7 Definition of particle intensity

At the same time from the definition of the phase space density we have:

$$\delta N = f(\mathbf{p},\mathbf{r})\delta\mathbf{p}\delta\mathbf{r} = f(\mathbf{p},\mathbf{r})p^2\delta p\delta\Omega\delta A\delta t\frac{p}{\gamma m}\cos\alpha. \tag{65}$$

After comparing expressions (64) and (65) we obtain:

$$j_\alpha(\mathcal{E},\mathbf{r})d\mathcal{E} = f(\mathbf{p},\mathbf{r})\frac{p^3dp}{\gamma m}. \tag{66}$$

Kinetic energy and momentum of a relativistic particle are related as:

$$\left(mc^2\gamma\right)^2 = \left(\mathcal{E}+mc^2\right)^2 = p^2c^2+m^2c^4, \tag{67}$$

from which we obtain that $m\gamma d\mathcal{E} = pdp$. Therefore the intensity and the phase space density are related as:

$$j_\alpha(\mathcal{E},\mathbf{r}) = p^2 f(\mathbf{p},\mathbf{r}). \tag{68}$$

4.2 Diffusion in Action Space

In the action-angle coordinates the Liouville's equation can be written as:

$$\frac{\partial f}{\partial t}+\dot{\boldsymbol{\theta}}\cdot\frac{\partial f}{\partial\boldsymbol{\theta}}+\dot{\mathbf{I}}\cdot\frac{\partial f}{\partial\mathbf{I}} = 0. \tag{69}$$

To illustrate derivation of the diffusion equation we as previously use a one-dimensional example. Consider evolution of plasma with small-amplitude waves described by the following Hamiltonian:

$$H(I,\theta,t) = H_0(I)+\varepsilon V(I,\theta,t) = H_0(I)+\varepsilon\sum_m V_m(I,t)e^{im\theta}, \tag{70}$$

where H_0 corresponds to the unperturbed system without waves, V is the perturbation due to waves, and the dimensionless parameter ε indicates that wave amplitudes are small. The corresponding equations of motion are:

$$\begin{cases}\dot{I} = -i\varepsilon\sum_m mV_m e^{im\theta}\\ \dot{\theta} = \omega_0(I)+\varepsilon\sum_m\frac{\partial V_m}{\partial I}e^{im\theta},\end{cases} \tag{71}$$

where ω_0 is the frequency of the unperturbed motion.

The above system evolves at two characteristic time scales. It exhibits rapid oscillations in the angle variable θ and slow change in the action I due to resonant wave-particle interactions. An ensemble of particles with initially same values of I but distributed in θ will

initially rotate coherently, since $\dot{\theta} \simeq \omega(I)$. However, if the system is stochastic, then I of different particles will undergo different small variations due to their interactions with the wave field (see previous section). After some time the ensemble will spread in I and will rotate at different frequencies. Consequently the ensemble will exhibit phase mixing, i.e. correlations between particle $\theta(t)$ and its initial values will decay, and eventually particle distribution in I will become independent of the initial distribution in θ. On timescales longer than the phase correlation decay time (τ_c), it then become possible to derive a reduced description of long-term evolution of the system by averaging the Liouville's equation over the fast angular variable θ.

We start with expanding the distribution function up to first order in ε:

$$f(I,\theta,t) = F\left(I,\varepsilon^2 t\right) + \varepsilon f_1(I,\theta,t) = F\left(I,\varepsilon^2 t\right) + \varepsilon \sum_m f_m(I,t) e^{im\theta}, \tag{72}$$

where in accordance to quasi-linear theory the ε^2 factor insures that slow variations in the distribution function F appear only as a second order term: $dF/dt = \mathcal{O}(\varepsilon^2)$. We then expand the Liouville's equation up to second order and find solutions order by order. Assuming that the wave frequency is related to the wave number by dispersion relationship of the plasma ($\omega_m = \omega(m)$) and $f_m \sim e^{-i(\omega_m t - m\theta)}$ we find in first order:

$$f_m = -\frac{mV_m}{\omega_m - m\omega_0}\frac{\partial F}{\partial I}. \tag{73}$$

The angular dependence appears in second order,

$$\frac{\partial F}{\partial t} + \frac{\partial V}{\partial I}\frac{\partial f_1}{\partial \theta} - \frac{\partial V}{\partial \theta}\frac{\partial f_1}{\partial I} = 0, \tag{74}$$

which we remove by averaging:

$$\langle \cdots \rangle = \frac{1}{2\pi}\int_0^{2\pi} \cdots d\theta. \tag{75}$$

With the use of integration by parts we obtain:

$$\frac{\partial F_0}{\partial t} = \frac{\partial}{\partial I}\left\langle f_1 \frac{\partial V}{\partial \theta}\right\rangle = i\frac{\partial}{\partial I}\sum_m m f_m^* V_m. \tag{76}$$

After inserting expression (73) we obtain the diffusion equation for slow evolution of phase averaged distribution function:

$$\frac{\partial F}{\partial t} = \frac{\partial}{\partial I} D_{QL} \frac{\partial F}{\partial I} \tag{77}$$

with the quasi-linear diffusion coefficient:

$$D_{QL} = \pi \sum_m m^2 |V_m|^2 \delta(\omega_m - m\omega_0), \tag{78}$$

where we used the identity: $\mathrm{Im}(\omega_m - m\omega_0)^{-1} = i\pi\delta(x - x_0)$, which indicates that quasi-linear diffusion is produced by resonant wave-particle interactions.

Alternatively, for systems described by maps, such as standard map (60) discussed in the previous section, the kinetic equation is based on the Fokker-Plank equation of Markov

processes. It is assumed that on time scales longer than the correlation decay time τ_c the transition probability $W_t(\mathbf{I}-\Delta\mathbf{I}, t, \Delta\mathbf{I}, T)$, which is the probability that an ensemble of phase points having an action $\mathbf{I}$ at time t suffers an increment in action $\Delta\mathbf{I}$ after a time T, does not depend on the angle variable and that:

$$F(\mathbf{I}, t+T) = \int F(\mathbf{I}-\Delta\mathbf{I}, t) W_t(\mathbf{I}-\Delta\mathbf{I}, t, \Delta\mathbf{I}, T) dT. \tag{79}$$

Long-term evolution of the distribution function F is then described by the Fokker-Plank equation (see for example Lichtenberg and Lieberman 1983):

$$\frac{\partial F}{\partial t} = -\sum_i \frac{\partial}{\partial I_i}\mathcal{A}_i F + \frac{1}{2}\sum_{ij}\frac{\partial^2}{\partial I_i \partial I_j}\mathcal{B}_{ij} F, \tag{80}$$

with the coefficients defined as:

$$\mathcal{A}_i = \frac{1}{T}\langle \Delta I_i \rangle; \qquad \mathcal{B}_{ij} = \frac{1}{T}\langle \Delta I_i \Delta I_j \rangle \tag{81}$$

where T is a characteristic time scale, such that $T > \tau_c$. Derivation of (80) also implies that moments $\langle \Delta I_i \Delta I_j \Delta I_k \rangle$ and higher are 0. Coefficients of the Fokker-Planck equation are related as:

$$\frac{1}{2}\frac{\partial \mathcal{B}_{ij}}{\partial I_j} = \mathcal{A}_i. \tag{82}$$

Following Landau (1937) let us show it for a one dimensional system by expanding the change in action ΔI up to the second order in time:

$$\Delta I = I(t+\Delta t) - I(t) = \dot{I}\Delta t + \frac{1}{2}\ddot{I}(\Delta t)^2, \tag{83}$$

where:

$$\dot{I} = -\frac{\partial H}{\partial \theta}; \qquad \ddot{I} = -\frac{\partial^2 H}{\partial \theta \partial t} - \frac{\partial^2 H}{\partial \theta \partial I}\dot{I} - \frac{\partial^2 H}{\partial \theta^2}\dot{\theta}. \tag{84}$$

With the use of Hamiltonian equations and after regrouping terms we obtain:

$$\Delta I = -\frac{\partial H}{\partial \theta}\Delta t + \frac{1}{2}(\Delta t)^2\left[\frac{\partial}{\partial I}\left(\frac{\partial H}{\partial \theta}\right)^2 - \frac{\partial}{\partial \theta}\left(\frac{\partial H}{\partial \theta}\frac{\partial H}{\partial I} + \frac{\partial H}{\partial t}\right)\right]. \tag{85}$$

After averaging over the angle variable θ we obtain:

$$\langle \Delta I \rangle = \frac{1}{2}(\Delta t)^2 \frac{\partial}{\partial I}\left\langle \left(\frac{\partial H}{\partial \theta}\right)^2 \right\rangle, \tag{86}$$

all other terms vanish since H is a periodic function of θ. Similarly, for the second moment we obtain:

$$\left\langle (\Delta I)^2 \right\rangle = (\Delta t)^2 \left\langle \left(\frac{\partial H}{\partial \theta}\right)^2 \right\rangle. \tag{87}$$

By comparing (86) and (87) we find the relation (82) in a one dimensional case.

The Fokker-Plank equation (80) can therefore be recast in the form of quasi-linear diffusion equation (77):

$$\frac{\partial F}{\partial t} = \sum_{ij} \frac{\partial}{\partial I_i} D_{ij} \frac{\partial F}{\partial I_j}, \tag{88}$$

where the diffusion coefficient $D_{ij} = \mathcal{B}_{ij}/2$.

Trapped particle motion in the inner and the outer radiation belts often conserve both the first and the second adiabatic invariants. Equation (88), in this case, reduces to a one dimensional equation in the third invariant, which is often written in terms of L^*. Recalling that $I_3 \propto \Phi \propto 1/L^*$ (see Eq. (42)), we obtain:

$$\frac{\partial f}{\partial t} = \frac{\partial}{\partial \Phi} D_{\Phi\Phi} \frac{\partial f}{\partial \Phi} = L^{*2} \frac{\partial}{\partial L^*} \frac{1}{L^{*2}} D_{L^*L^*} \frac{\partial f}{\partial L^*}. \tag{89}$$

Since L^* has the physical meaning of the dimensionless distance to the equatorial points of the drift-bounce shell particles would have in a dipole field, written in this form the diffusion equation in the third invariant is known as the *radial diffusion equation*. In radiation belt models, Eq. (88) is usually written in terms of L^*, energy, and pitch-angle. When all three invariants are violated, the diffusion equation cast in these variables can have a complicated structure, even if additional assumptions are made, such as that the pitch-angle and energy diffusion are uncoupled from radial transport and that the cross-diffusion terms in energy and pitch angles can be neglected (for a detailed discussion see for example Schulz and Lanzerotti 1974).

Let us go back to our example Hamiltonian (49), which we derived for radial transport of radiation belt electrons due to interaction with ULF waves. In the case of a standard map ($\psi_m = 0$) the correlation decay time for $K \gg 1$ can be estimated as (e.g., Zaslavsky 2002):

$$\tau_c = \frac{2T}{\ln K}; \quad T = \frac{2\pi}{\Delta\omega}, \tag{90}$$

where the time step T of the map defines the characteristic time scales of changes in the action variable due to the resonant wave-particle interaction. It has physical meaning similar to the time interval between random weak collisions experienced by a heavy Brownian particle in a gas. The fact that individual steps of the map are small, i.e. $\Delta I/I \ll 1$, makes this analogy even closer.

From estimate (90) it follows that for large K the diffusion coefficient of map (60) can be estimated from a single step, $\Delta I = \frac{K}{2\pi} \sin\theta$, $T = 2\pi$. This yields:

$$D_{QL} = \frac{1}{2T} \frac{1}{2\pi} \int_0^{2\pi} (\Delta I)^2 d\theta = \frac{K^2}{32\pi^3}, \tag{91}$$

which is often referred to as the quasi-linear estimate because it does not include higher-order corrections due to subsequent steps (see for example, Lichtenberg and Lieberman 1983). It can be expected that the deviations of the diffusion coefficient $D_{QL}(K)$ from this one-step estimate is the highest for moderate values of K, when according to Eq. (90) it takes more than one effective collision to randomize particle phases. Additionally, in the standard map case, there are islands of regular particle motion embedded into stochastic regions of phase space at any finite value of K, where particle trajectories are stable. Particle trajectories can be trapped in vicinity of the boundary between the stochastic and regular phase space regions, where the action variable changes almost linearly causing deviations of

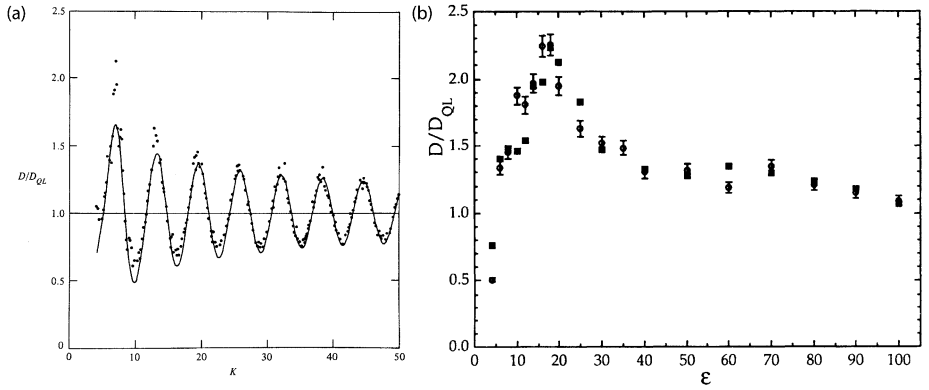

Fig. 8 Panel (**a**): Diffusion coefficient of a standard map ($\psi_m = 0$) computed. The *dots* are the numerically computed values and the *solid lines* is the theoretical result (Rechester and White 1980). Panel (**b**): Diffusion coefficient for a system with Hamiltonian (55) with random shifts among frequency harmonics ($\psi_m \in [0, 2\pi)$). The nonlinearity parameter ε corresponds to K in our notations (Cary et al. 1990)

transport from pure diffusion (e.g., Zaslavsky 2002). Rechester and White (1980) analyzed transport properties in the standard map at different values of K by calculating the diffusion coefficient both numerically and analytically including higher-order correlations due to finite correlation decay time. Their results are shown in Fig. 8a. The diffusion coefficient oscillates about its quasi-linear value with the maximum value exceeding D_{QL} by more than factor of 2, and minimum around $D_{QL}/2$. Since the correlation time becomes shorter and the phase space area occupied by stable islands decreases, deviations become smaller with increase in K.

The existence of random phase shits $\psi_m \in [0, 2\pi)$ between different harmonics of the wave spectrum in Eq. (49), considerably changes the dynamic properties of the system. If resonances overlap ($K > 1$), the islands of regular motion are completely destroyed by random shifts, and the system becomes stochastic everywhere across the phase space. The analysis of particle transport at different values of K (Cary et al. 1990; Helander and Kjellberg 1994) show that the diffusion coefficient in this case can still exhibit large deviations from the quasi-linear value, D_{QL}: while it never gets smaller than D_{QL}, at $K \simeq 18$ it reaches the maximum of $2.3 D_{QL}$ (see Fig. 8b).

In reality, additional stochasticity may be introduced into the system due to random nature of the wave fields. Phase shifts ψ_m at different harmonics of the spectrum in Eq. (49) may no longer be stationary in this case. Their values can change in some characteristic time intervals T corresponding to the spatial or temporal coherence of the problem. For instance, variations of the solar wind dynamic pressure is one of the dominant drivers of the ULF waves in the inner magnetosphere (e.g., Takahashi and Ukhorskiy 2007). ULF waves can violate the third adiabatic invariant of trapped electrons in the process of resonant interaction with their drift-bounce motion discussed in Sect. 3. Oscillations in dynamic pressure are attributed to the Alfvén turbulence in the solar wind. The phase shifts between different harmonics of the ULF wave spectrum therefore change on the time scales of the autocorrelation time of the solar wind turbulence, ~3 hr (e.g., Jokipii and Coleman 1968).

Electromagnetic ion cyclotron (EMIC) waves are considered to be one of the dominant local mechanism of electron losses from the outer radiation belt (e.g., Thorne and Kennel 1971; Horne and Thorne 1998; Summers et al. 1998; Ukhorskiy et al. 2010). Resonant interaction of EMIC waves with electron gyromotion breaks the first adiabatic invariant and

can cause electron scattering into the atmospheric loss cone and their subsequent loss via precipitation. Free energy for the EMIC wave growth is supplied by the positive temperature anisotropy ($T_\perp > T_\parallel$) of energetic (~10–100 keV) ions (e.g., Cornwall 1965; Kennel and Petscheck 1966). EMIC waves grow to observable amplitudes at frequencies of maximum growth rate out of small-amplitude electromagnetic noise propagating along the field lines through the regions of positive anisotropy (e.g., Gomberoff and Neira 1983; Horne and Thorne 1994). EMIC wave activity can extend over $>10°$ about the magnetic equator (e.g., Erlandson and Ukhorskiy 2001) and last for tens of minutes producing pitch-angle scattering of radiation belt electrons over many bounce periods. Detailed spectral analysis (Anderson et al. 1996; Denton et al. 1996) revealed that wave events consist of many short (~30 sec) wave packets. Consequently phase shits among the harmonics of EMIC spectra vary at time scales comparable to the duration of individual wave packets.

Numerical simulations (Ukhorskiy and Sitnov 2008) showed that if additional extrinsic stochasticity is introduced into the system by varying phase shifts ψ_m among spectral harmonics of the wave perturbation (49) at time intervals comparable to the time T between effective collisions (90), then particle motion becomes stochastic even if resonances do not overlap. The diffusion coefficient in this case agrees well with its quasi-linear estimate (91). At the time scales longer than the correlation decay time τ_c the system can then be described by diffusion equation (88) with quasi-linear diffusion coefficients. The correlation decay time τ_c in this case depends on both the collision time and wave amplitude similar to expression (90).

5 Limitations and Challenges

During over five decades since the discovery of radiation belts the concept of diffusion in the invariant space has been successfully applied for the analysis of transport, acceleration, and loss of radiation belt particles. Radial diffusion due to drift-resonant interaction with solar-wind driven ULF fields was the first mechanism proposed to explain acceleration of electrons and protons in radiation belts (Kellog 1959; Tverskoy 1964; Dungey 1965; Falthammar 1965). Subsequent analysis showed that radial diffusion causes not only acceleration but loss of particles from the outer belt (e.g., Bortnik et al. 2006; Shprits et al. 2006) and can be driven by variety of plasma waves including waves excited internally by instabilities in ring current plasma such as stormtime Pc5 waves (Lanzerotti et al. 1969; Ukhorskiy et al. 2009). Local resonant interaction of electron gyromotion with whistler waves was initially considered to be primarily responsible for electron losses from the belts (Dungey 1963; Cornwall 1964; Kennel and Petscheck 1966). Local wave-particle interactions are now recognized as both loss and acceleration mechanisms. As was mentioned in the previous section EMIC waves are considered to be one of the primary mechanism of local losses outside of the plasmasphere. Whistler chorus (e.g., Horne and Thorne 1998; Summers et al. 1998) and magnetosonic (e.g., Horne et al. 2007) waves were identified as mechanisms of local acceleration of radiation belt electron, more efficient than energization due to radial diffusion (e.g., Horne 2007). A number of recent review papers (Hudson et al. 2008; Shprits et al. 2008a, 2008b; Thorne 2010) provide detailed discussions and reference lists on diffusion theory of the radiation belt processes. In this section we discuss to what extent particle motion in the belt can be described in terms of three adiabatic invariants, some limitations of the diffusion approximation and associated challenges which need to be addressed in forthcoming radiation belt models and data analysis.

Diffusion approximation applies to the situations when in zero order radiation belt particles are stably trapped in quasiperiodic motion associated with three adiabatic invariants.

This implies that the magnetic field has a slow-varying quasi-dipole configuration, such that the time scales of the three periodic motions are well separated, and the electric field is small, such that the $\mathbf{E} \times \mathbf{B}$ drift is negligible compared to the gradient-curvature drift. In this case particle invariants can be violated only in the process of resonant wave-particle interaction. Reducing the description from the full Vlasov equation to a Fokker-Plank equation in the invariant space also requires that waves have small enough amplitudes, such that nonlinear phase-dependent effects can be neglected, and the characteristic time scales of the described processes are longer than the phase correlation decay time. Variability of radiation belt intensities do not always satisfy these conditions.

5.1 Large Perturbations

The beginning of large geomagnetic storms driven by coronal mass ejections (CMEs) is typically marked by a sudden storm commencement (SSC), a few tens of nT intensification in the low-latitude ground-based magnetic field intensity, lasting typically for some tens of minutes. SSCs are produced by interplanetary shocks on the front end of CMEs, which can compress the magnetopause inside geosynchronous orbit. As an interplanetary shock impacts the magnetosphere it launches a large-amplitude fast magnetosonic wave. The leading portion of the bipolar electric field pulse associated with the wave can exceed 200–300 mV/m (Wygant et al. 1994) and is predominantly westward. According to spacecraft observations large SSC events produce injections of tens of MeV electrons and protons all the way into the inner radiation belt (Blake et al. 1992; Wygant et al. 1994; Looper et al. 2005). A number of test-particle simulations of the effects of shock-induced waves on the radiation belts were conducted with the use of empirical field models (e.g., Li et al. 1993; Gannon et al. 2005) as well self-consistent electromagnetic fields from global MHD models (e.g., Hudson et al. 1997; Kress et al. 2007, 2008). Simulations showed that trapped particles can $\mathbf{E} \times \mathbf{B}$ drift inward with the wave front through multiple L-shells, undergoing significant energization in a fraction of a drift period due to conservation of the first adiabatic invariant (see Fig. 9a). Particles are energized as long as they stay in phase with the azimuthally propagating wave front. This process, therefore, depends on the azimuthal phase of particle gradient-curvature drift motion and cannot be described with a phase-averaged Fokker-Planck equation (80). Full Liouville's equation (69) must be solved to model rapid particle energization by shock-induced electric field pulses.

Early observations of depletions of the outer belt intensities during storm main phase (Dessler and Karplus 1960; McIlwain 1966) were attributed to an adiabatic response of relativistic electrons to a slow (compared to electron drift period) increase in ring current intensity, which is referred to as the D_{st} *effect*. An increase in ring current intensity decreases the magnetic flux Φ enclosed by electron drift-bounce orbits. To conserve Φ electrons move outward to regions of lower magnetic field intensity. Since $\mu = p_\perp^2/2mB$ is also conserved, the outward motion decreases electron energies. Thus, measurements of electrons within a fixed energy at a fixed radial location after increase in ring current register electrons previously located at lower radial distances where their energy was higher and their phase space density lower so that a lower intensity is measured. In recent years with the development of more quantitative empirical models of storm-time magnetic field (e.g., Tsyganenko and Sitnov 2005, 2007; Sitnov et al. 2008), it became apparent that the ring current has much more profound effect on the outer radiation belt. Test particle simulations (Ukhorskiy et al. 2006b) show that storm-time intensification of highly asymmetric partial ring current produces fast outward expansion of electron gradient-curvature drift orbits leading to their loss through the magnetopause. Depending on the storm magnitude, particles from a broad L-range of outer belt can be permanently lost. These theoretical predictions were recently

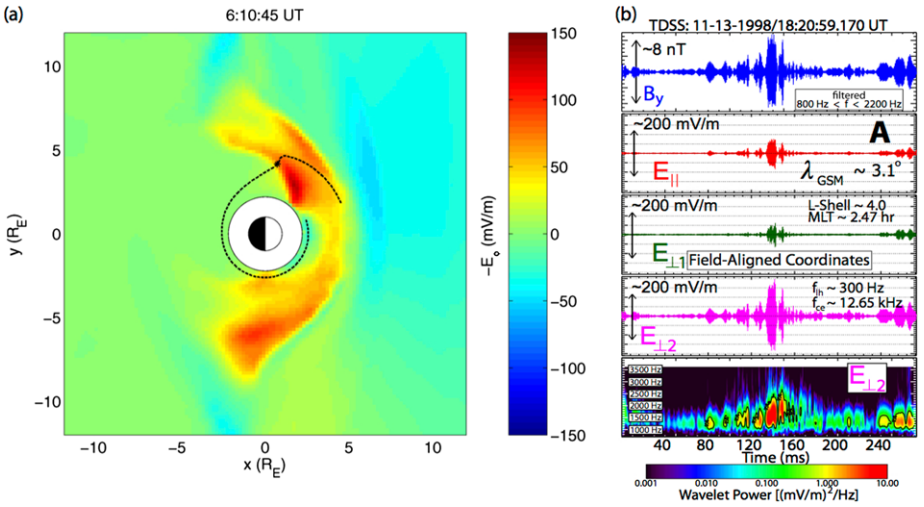

Fig. 9 Panel (**a**): Equatorial snapshot of the azimuthal component of electric field pulse triggered by an interplanetary shock arrival from a global MHD simulation. The *dashed line* shows the trajectory of a single guiding-center electron in drift resonance with the pulse as it propagates from the dayside to nightside. The initial and final energies of the particle are ∼5 and 15 MeV, respectively (Kress et al. 2007). Panel (**b**): An example of large-amplitude (>200 mV/m) whistler waves in the inner magnetosphere (Wilson et al. 2011)

confirmed by the observational analysis of multi-spacecraft data (e.g., Millan et al. 2010; Turner et al. 2012). Due to its rapid nature and dependence on the magnetic local time (azimuthal angle) this effect can be described only with full Liouville's equation (69).

Typically pitch-angle and energy diffusion coefficients in radiation belt models are computed based on statistical properties of waves derived from time-averaged spectral intensity data. For whistler chorus waves characteristic time-averaged wave amplitude is ∼0.5 mV/m (Meredith et al. 2001). Recent analysis of instantaneous wave data (Cattell et al. 2008; Kellog et al. 2011; Wilson et al. 2011) showed that whistler chorus waves can have very large amplitudes >200 mV/m (Fig. 9b). Such large-amplitude whistler waves can accelerate electrons by more than an MeV in less than a second (Cattell et al. 2008), trap electrons (Kellog et al. 2010), and cause their prompt scattering into the loss cone and consequent precipitation into the atmosphere (Kersten et al. 2011). While it was suggested that some aspects of particle response to large-amplitude coherent waves can be described with a Fokker-Planck equation (Albert 2010), bounce and gyrophase dependent aspects of wave particle interactions require fully kinetic treatment.

5.2 Non-diffusive Transport

In the previous section we showed that the diffusion approximation (80) is valid only on time scales τ_D much longer than the correlation decay time τ_c. Regardless of whether the stochasticity in the system has an extrinsic (noise) or intrinsic (nonlinearity) nature, for moderate wave amplitudes $K < 10$, typical for the inner magnetosphere, there is the following hierarchy of time scales:

$$\tau_D \gg \tau_c \gtrsim T, \tag{92}$$

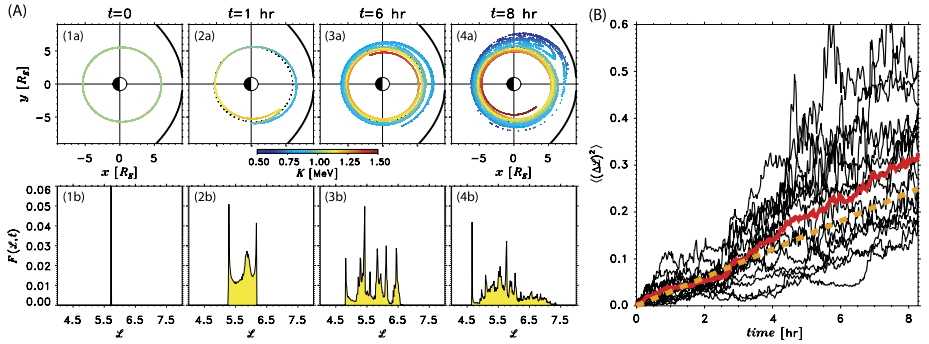

Fig. 10 Panel (**A**): Test-particle simulation of electron motion in ULF fields induced by global magnetospheric compressions. Panels (**1a**)–(**4a**) show snapshots of the position of 10^4 electrons in the equatorial plane at different times during the simulation process. Electron energy is shown with color. Panels (**1b**)–(**4b**) show electron radial distribution functions $F(\mathcal{L};t)$ for snapshots (**1a**)–(**4a**), where $\mathcal{L}=L^*$. Panel (**B**): Radial transport of the outer belt electrons due to global magnetospheric compressions calculated from full test-particle simulations. *Black curves*: $\langle(\Delta L^*(t))^2\rangle$ at statistically identical realizations of electron motion. *Red line*: average of $\langle(\Delta L^*(t))^2\rangle$ over all realization of electron motion. *Dashed yellow line*: radial diffusion $\langle(\Delta L^*(t))^2\rangle = 2D_{QL}t$ (Adapted from Ukhorskiy and Sitnov 2008)

where T is the time between effective collisions in the system. While τ_D always exists for an unbounded system, for a bounded system there is an additional requirement:

$$v_T \tau_c \ll L, \tag{93}$$

where v_T is the characteristic velocity of stochastic transport and L is the system size. This requirement means that phase correlations must decay before particle distribution spreads over the entire system.

Theoretical estimates and detailed numerical simulations (Ukhorskiy et al. 2006a; Ukhorskiy and Sitnov 2008) suggest that condition (93) may never be satisfied for radial transport in the outer electron belt. As a result radial transport always exhibits large deviations from the radial diffusion approximation. The consequences of non-diffusive electron transport are illustrated by Fig. 10 showing results of test-particle simulations of radial transport under typical magnetospheric conditions. Panel (A) in Fig. 10 shows snapshots of an ensemble of particles at various stages of radial transport driven by quiet-time oscillations in the solar wind dynamic pressure. Initially all particles had the same value of the third invariant, but were evenly distributed over the drift phase. Last snapshots (panels (A)4a and (A)4b in Fig. 10) correspond to the time moment when the ensemble expanded up to the magnetopause. Particle distribution function (bottom panels) at this point still exhibits large number of pronounced peaks indicative of persistent phase correlations (compare with Fig. 5). Panel (B) in Fig. 10 shows time evolution of ensemble-averaged $\langle(\Delta L^*)^2\rangle$ (black lines) computed for 15 statistically identical time intervals. Had the diffusion approximation been valid, all transport curves would have been very close to each other and monotonically grow in time. However individual transport curves exhibit large deviations from each other and from the straight line corresponding to diffusion with locally estimated quasi-linear diffusion coefficient, indicating that the diffusion approximating has not been attained over the time by which particle ensembles spread over the entire system.

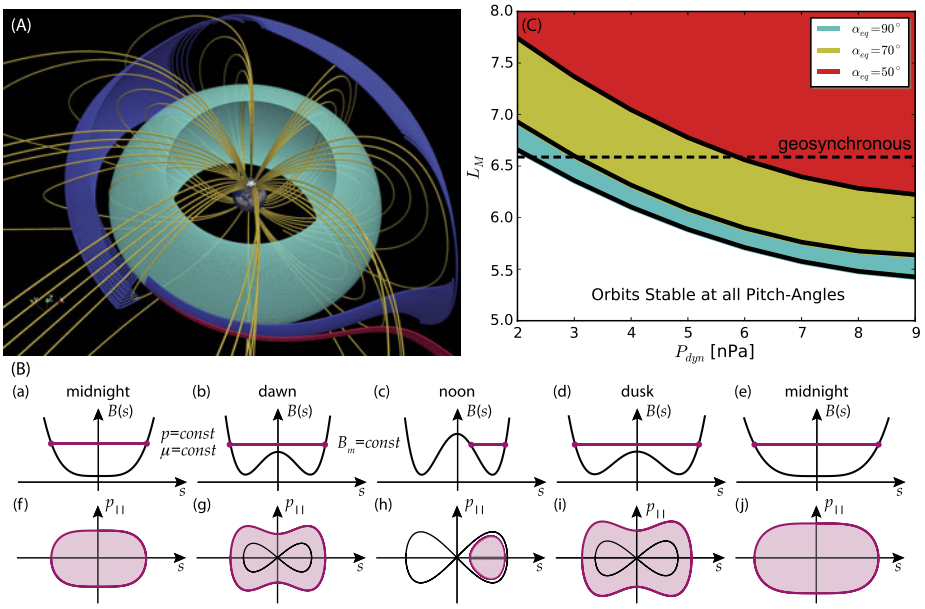

Fig. 11 Panel (**A**): Three types of drift-bounce trajectories in a dayside compressed magnetic field. The trajectories were computed in the Tsyganenko and Sitnov (2007) magnetic field at $P_{dyn} = 3$ nPa. Test particles were launched at $r = (8, 0, 0)$ with equatorial pitch angles of 80°(*red*), 59° (*blue*), and 20° (*cyan*) (adapted from Ukhorskiy et al. 2011). Panel (**B**): Schematic illustration of bifurcating particle dynamics in a simplified case of a symmetric (north-south and east-west) dayside compressed magnetic field. Field-aligned profiles of magnetic field intensity (panels (**a**)–(**e**)), and phase portraits of bounce motion (panels (**f**)–(**j**)) at different points of electron drift orbit around Earth (adapted from Ukhorskiy et al. 2011). Panel (**C**): Earthward boundary (L_M is the L value at midnight) of the bifurcating orbit region at different values of the solar wind dynamic pressure P_{dyn} computed with guiding-center simulations in the Tsyganenko (1996) magnetic field model for different values of the equatorial pitch angle and midnight

5.3 Drift Orbit Bifurcations

Many observational techniques rely on computing electron phase space density as a function of three adiabatic invariants. In particular, radial (L^*) profiles of electron phase space density computed at constant values of the first and second invariants are used as a diagnostic of relative roles of local and global acceleration mechanisms across the outer electron belt (e.g., Green and Kivelson 2004; Chen et al. 2007). If the phase space density has a local peak at some L^* value, much exceeding the phase space density value at the outer boundary of the belt, it is considered to be an indication of additional electron acceleration process operating locally at this L^* value. Recent studies (e.g., Öztürk and Wolf 2007; Wan et al. 2010; Ukhorskiy et al. 2011) suggest that this argument should be used with great caution.

In a dayside compressed magnetosphere electrons can exhibit three types of trajectories (Fig. 11(A)). As was discussed in Sect. 2, stably trapped particles (shown in cyan color) participate in three distinct quasiperiodic motions, timescales of the motion are separated by multiple orders of magnitude, and all three adiabatic invariants are conserved. Particles from the magnetopause loss cone intersect the magnetopause and escape the belt before completing a full circle around Earth (red color). Since the drift trajectories are not closed in this case, only the first and the second invariants exist and are conserved (before particles are lost). The third type of trajectories that undergo bifurcations is shown in blue. The existence of bifurcating orbits has been known for a long time (e.g., Northrop and Teller 1960;

Northrop 1963; Roederer 1970; Shabansky 1971). More recently though it was realized that at drift orbit bifurcations particle trajectory crosses a separatrix in the phase space plane associated with particle bounce motion. According to the general theory (Cary et al. 1986; Neishtadt 1986) its second invariant is violated at each of the separatrix crossings. This follows from the fact that at the approach to the separatrix particle frequency goes to zero and according to Eq. (17) the change in the adiabatic invariant is no longer exponentially small.

If a guiding-center particle is trapped in a stationary magnetic field, both its energy and the first invariant are conserved:

$$p = \text{const}; \qquad \mu = \frac{p_\perp^2}{2mB} = \frac{p^2}{2mB_m} = \text{const}, \tag{94}$$

which means that the magnetic field intensity at the bounce points ($B(s_m) = B_m$) is also constant. In a compressed geomagnetic field the distribution of $B(s)$ along the field lines can exhibit two qualitatively different profiles (Figs. 11(B)a and 11(B)c). On the night side, $B(s)$ has a single minimum at the equator similar to a dipole field (U profile) (Figs. 11(B)a, 11(B)e). On the dayside, adjacent to the magnetopause, however, $B(s)$ has a local maximum at the equator and two minima below and above the equator (W profile) (Figs. 11(B)b–d). Consider a particle initially bouncing across the equator from points with some value B_m of the magnetic field intensity and gradient curvature drifting from the nightside to the dayside into the region where the magnetic field is compressed and has a local maximum at the equator. At some point of the drift trajectory the $B(s)$ profile changes from the U to the W shape (Figs. 11(B)a and 11(B)b). As the particle drifts further into the dayside, the height of the equatorial maximum in the W profile grows. If the magnetic field intensity at the maximum increases up to B_m, the particle can no longer cross the equator and its drift orbit exhibits a bifurcation. To conserve the magnetic field intensity at the bounce points, the particle branches off the equator into one of the local $B(s)$ minima pockets (Figs. 11(B)b and 11(B)c). The trajectory traverses the dayside region either below or above the equator never crossing it until the point where the field at the equator decreases back to the B_m value at the bounce points. The trajectory then bifurcates again and the particle resumes bouncing across the equator (Figs. 11(B)c and 11(B)d).

At drift orbit bifurcations the particle phase space trajectory crosses a separatrix (Figs. 11(B)g and 11(B)h), which divides the $(p_\parallel, s)$ phase plane into three distinct regions. The region outside the separatrix corresponds to the bounce motion across the equator, while two lobes connected at a saddle point correspond to trajectories trapped below and above the equator. As the particle approaches the separatrix, its instantaneous bounce period increases logarithmically (as discussed in Sect. 2) and in some small vicinity of the separatrix becomes comparable to the drift period. In this vicinity the quasiperiodic character of the bounce motion is broken, since the effective potential of the motion there is changing at the time scales of the instantaneous bounce period and can no longer be considered slowly varying (ε in Eq. (8) is no longer small). Close to the separatrix the second invariant is therefore not conserved. At two consecutive separatrix crossings corresponding to bifurcations off the equator and back, the invariant exhibits jumps. As a result by the time the particle resumes its motion across the equator it accumulates a nonzero change in the second invariant. Each bifurcation also leads to radial and pitch angle jumps. Consequently when the particle drifts back to its initial location on the nightside, the drift orbit does not close on itself as in the case of stably trapped particles (Fig. 11(A)).

The range of the second invariant (or equatorial pitch-angle) values affected by bifurcations at given radial locations depends on the degree of the day-night asymmetry in the geomagnetic field, which is mostly controlled by the solar wind dynamic pressure (P_{dyn}).

To quantify the extent of the phase space region affected by bifurcations, we calculated the Earthward boundary of the bifurcating orbits at three different values of equatorial pitch angle as function of P_{dyn} using guiding-center simulations in the Tsyganenko 96 magnetic field model (Tsyganenko 1996) at moderate values of the dynamic pressure ($P_{dyn} < 10$ nPa). The radial location of the boundary was quantified by L at midnight, L_M. The results are shown in Fig. 11(C). As can be seen from the figure, a broad range of the outer belt trajectories is affected by bifurcations. At geosynchronous orbit, for instance, at $P_{dyn} > 6$ nT all orbits with the equatorial pitch angles $\alpha_{eq} > 50°$ (which constitutes most of the pitch-angle distribution) exhibit bifurcations.

In the bifurcating region particle drift motion around Earth is no longer quasiperiodic (i.e. does not have three independent integrals of motion): there is no slow varying control parameter λ in the Hamiltonian function (see Eqs. (6) and (7)), which can be adjusted to turn the bifurcations off. For the drift motion, bifurcations are a property of the unperturbed Hamiltonian. The third adiabatic invariant therefore is undefined for bifurcating orbits and particle phase space density cannot be transformed into the invariant space. An alternative methodology is required for the analysis of relative roles of various acceleration mechanisms extending into the bifurcation region of the outer belt phase space.

6 Summary

In summary we provide a reference table (Table 1) of relativistic formula from this chapter, which are most commonly used in modeling, theory, and the analysis of radiation belt particle data.

Table 1 Reference table

	Definition (cgs)	Comments	Eqn.
Relativistic factor	$\gamma = [1 - (v/c)^2]^{-1/2}$	v is the velocity magnitude, c is the speed of light	
Energy and (mechanical) momentum	$\mathcal{E} + mc^2 = m\gamma c^2$; $\mathbf{p} = m\gamma\mathbf{v}$	$\mathcal{E}$ is the kinetic energy, m is the rest mass, $\mathbf{v}$ is the velocity	
Electromagnetic field	$\mathbf{E} = -\nabla\varphi - \frac{1}{c}\frac{\partial \mathbf{A}}{\partial t}$; $\mathbf{B} = \nabla \times \mathbf{A}$	φ is the electrostatic potential, $\mathbf{A}$ is the magnetic field vector potential	(20)
Canonical momentum	$\mathbf{P} = \mathbf{p} + \frac{e}{c}\mathbf{A}$	e is the electric charge	(19)
Lorentz equation	$\frac{d\mathbf{p}}{dt} = e\mathbf{E} + \frac{e}{c}\mathbf{v} \times \mathbf{B}$	Hamiltonian equation of charged particle motion in electromagnetic field	(21)
Adiabatic invariant (action)	$I = \frac{1}{2\pi}\oint \mathbf{p}(\mathbf{q}, H) \cdot d\mathbf{q}$	Integration is carried out along an unperturbed periodic orbits, such that the Hamiltonian $H = \text{const}$	(2)
First invariant	$\mu = \frac{p_\perp^2}{2mB}$	$p_\perp$ is the relativistic momentum component perpendicular to magnetic field	(22)
Magnetic moment	$M = \mu/\gamma$	Magnetic moment is an adiabatic invariant of motion only in non-relativistic limit ($\gamma \simeq 1$)	(23)

Table 1 (*Continued*)

	Definition (cgs)	Comments	Eqn.
The guiding-center motion in static magnetic fields	$\begin{cases} \dot{p}_{\parallel} = -\frac{\mu}{\gamma}\hat{\mathbf{b}}\cdot\nabla B \\ \dot{\mathbf{R}} = \frac{p_{\parallel}}{m\gamma}\hat{\mathbf{b}} + \mathbf{U}_D \\ \mathbf{U}_D = \frac{c}{\gamma e}\left(\frac{p_{\parallel}^2}{mB} + \mu\right)\frac{\hat{\mathbf{b}}\times\nabla B}{B} \end{cases}$	This approximation assumes that the magnetic field is curl-free, a more general case is treated by (29)–(32); $p_{\parallel}$ is the momentum component and $\hat{\mathbf{b}}$ is the unit vector parallel to magnetic field, $\mathbf{U}_D$ is the guiding-center velocity perpendicular to magnetic field	(32)
Second invariant	$I_2 = 2pJ;\ J = \int_m^{m'} \sqrt{1 - \frac{B(s)}{B_m}}\,ds$	The integration is carried out along a fixed magnetic line between conjugate bounce points	(38)
Third invariant	$\Phi = \oint_C \mathbf{A}\cdot d\mathbf{l}$	C is any contour on the drift-bounce surface closed around Earth	(40)
Dipole L	$r = LR_E\sin^2\vartheta$	Is constant along a dipole field line, it measures the distance from the dipole center to the field line at the equator in Earth radii ($R_E \simeq 6380$ km); r is the radial distance and ϑ is the co-latitude	
Generalized L value	$L^* = -\frac{2\pi B_0 R_E^2}{\Phi}$	L^* is the radial distance (in R_E) to the equatorial points of the drift-bounce shell on which the particle would be, if all nondipolar contributions to the magnetic field would be adiabatically turned off; $B_0 \simeq 31000$ nT is the magnetic field intensity on Earth's surface at the equator	(41)
Liouville's equation	$\frac{\partial f}{\partial t} + \dot{\mathbf{q}}\cdot\frac{\partial f}{\partial \mathbf{q}} + \dot{\mathbf{p}}\cdot\frac{\partial f}{\partial \mathbf{p}} = 0$	$f = f(\mathbf{p},\mathbf{q})$ is the density of particles in the phase space (PSD), $(\mathbf{p},\mathbf{q})$, conserved along particle trajectories	(63)
Intensity	$j_\alpha(\mathcal{E},\mathbf{r}) = p^2 f(\mathbf{p},\mathbf{r})$	Is the number of particles with kinetic energy $\mathcal{E}$ coming from a given direction α which impinge per unit time, unit solid angle and unit energy, on a surface of unit area oriented perpendicular to their direction of incidence	(68)
Course-grained phase space density	$F(I,t) = \langle f(I,\theta,t)\rangle = \frac{1}{2\pi}\int_0^{2\pi} f(I,\theta,t)d\theta$	Variable reduction valid on the time scales longer than the phase correlation decay time τ_c	(75)
Diffusion equation	$\frac{\partial F}{\partial t} = \sum_{ij}\frac{\partial}{\partial I_i}D_{ij}\frac{\partial F}{\partial I_j}$	Averaging over the fast angular variable reduces the Liouville's equation for the exact PSD to a Fokker-Planck equation for course-grained PSD	(88)
Diffusion coefficient	$D_{ij} = \frac{\langle \Delta I_i \Delta I_j\rangle}{2T}$	$T > \tau_c$ is the characteristic time of diffusion, ΔI_i is the adiabatic invariant change over T	(81)
Radial diffusion	$\frac{\partial f}{\partial t} = L^{*2}\frac{\partial}{\partial L^*}\frac{1}{L^{*2}}D_{L^*L^*}\frac{\partial f}{\partial L^*}$	Implies conservation of the fist and the second adiabatic invariants	(89)

References

J.M. Albert, Diffusion by one wave and by many waves. J. Geophys. Res. **115**, A00F05 (2010). doi:10.1029/2009JA014732

B.J. Anderson, R.E. Denton, S.A. Fuselier, On determining polarization characteristics of ion cyclotron wave magnetic field fluctuations. J. Geophys. Res. **101**, 13195 (1996)

V.I. Arnold, V. Kozlov, A.I. Neishtadt, *Mathematical Methods of Classical Mechanics*. Encyclopedia of Mathematical Sciences, vol. 3 (Springer, New York, 2010)

R. Balescu, *Transport Processes in Plasmas. 1. Classical Transport Theory* (Elsevier, Amsterdam, 1988)

T.J. Birmingham, Pitch angle diffusion in the Jovian magnetodisc. J. Geophys. Res. **89**, 2699 (1984)

J.B. Blake, W.A. Kolasinski, R.W. Fillius, E.G. Mullen, Injection of electrons and protons with energies of tens of MeV into $L < 3$ on 24 March 1991. Geophys. Res. Lett. **19**, 821 (1992)

J. Bortnik, R.M. Thorne, T.P. O'Brien, J.C. Green, R.J. Strangeway, Y.Y. Shprits, D.N. Baker, Observation of two distinct, rapid loss mechanisms during the 20 November 2003 radiation belt dropout event. J. Geophys. Res. **111**, 12216 (2006). doi:10.1029/2006JA011802

J. Büchner, L.M. Zelenyi, Regular and chaotic charged particle motion in magnetotaillike field reversals. I—Basic theory of trapped motion. J. Geophys. Res. **94**, 11821 (1989)

E.L. Burshtein, V.I. Veksler, A.A. Kolomensky, A stochastic method of accelerating particles, in *Some Problems in the Theory of Cyclic Accelerators* (Akad. Nauk USSR, Moscow, 1955)

J.R. Cary, A.J. Brizard, Hamiltonian theory of guiding-center motion. Rev. Mod. Phys. **81**, 693 (2009)

J.R. Cary, D.F. Escande, J.L. Tennyson, Adiabatic-invariant change due to separatrix crossing. Phys. Rev. A **34**(5), 256 (1986)

J.R. Cary, D.F. Escande, A.D. Verga, Nonquasilinear diffusion far from the chaotic threshold. Phys. Rev. Lett. **65**, 3132 (1990)

C. Cattell, J.R. Wygant, K. Goetz, K. Kersten, P.J. Kellogg, T. von Rosenvinge, S.D. Bale, I. Roth, M. Temerin, M.K. Hudson, R.A. Mewaldt, M. Wiedenbeck, M. Maksimovic, R. Ergun, M. Acuna, C.T. Russell, Discovery of very large amplitude whistler-mode waves in Earth's radiation belts. Geophys. Res. Lett. **35**, 01105 (2008). doi:10.1029/2007GL032009

Y. Chen, G.D. Reeves, R.H. Friedel, The energization of relativistic electrons in the outer Van Allen radiation belt. Nat. Phys. **3**, 614 (2007)

B.V. Chirikov, Resonance processes in magnetic traps. J. Nucl. Energy, Part C Plasma Phys. Accel. Thermonucl. Res. **1**, 253 (1960)

B.V. Chirikov, A universal instability of many-dimensional oscillator systems. Phys. Rep. **52**, 263 (1979)

J.M. Cornwall, Scattering of energetic trapped electrons by very-low-frequency waves. J. Geophys. Res. **69**, 1251 (1964)

J.M. Cornwall, Cyclotron instabilities and electromagnetic emission in the ultra low frequency and very low frequency ranges. J. Geophys. Res. **70**, 61 (1965)

R.E. Denton, B.J. Anderson, G. Ho, D.C. Hamilton, Effects of wave superposition on the polarization of electromagnetic ion cyclotron waves. J. Geophys. Res. **4**, 271 (1996)

A.J. Dessler, R. Karplus, Some properties of the Van Allen radiation. Phys. Rev. Lett. **4**, 271 (1960)

W.E. Drummond, D. Pines, Non-linear Stability of Plasma Oscillations, in *General Atomic, GA-2386* (1961)

J.W. Dungey, Loss of Van Allen electrons due to whistlers. Planet. Space Sci. **11**, 591 (1963)

J.W. Dungey, Effects of the electromagnetic perturbations on particles trapped in the radiation belts. Space Sci. Rev. **4**, 199 (1965)

S.R. Elkington, M.K. Hudson, A.A. Chan, Acceleration of relativistic electrons via drift-resonant interaction with toroidal-mode Pc-5 ULF oscillations. Geophys. Res. Lett. **26**, 3273 (1999)

S.R. Elkington, M.K. Hudson, A.A. Chan, Resonant acceleration and diffusion of outer zone electrons in an asymmetric geomagnetic field. J. Geophys. Res. **108**, 1116 (2003)

R.E. Erlandson, A.Y. Ukhorskiy, Observations of electromagnetic ion cyclotron waves during geomagnetic storms: wave occurrence and pitch angle scattering. J. Geophys. Res. **106**, 3883 (2001)

C.-G. Falthammar, Effects of time-dependent electric fields on geomagnetically trapped radiation. J. Geophys. Res. **70**, 2503 (1965)

J.L. Gannon, X. Li, M. Temerin, Parametric study of shock-induced transport and energization of relativistic electrons in the magnetosphere. J. Geophys. Res. **110**, 12206 (2005). doi:10.1029/2004JA010679

H. Goldstein, *Classical Mechanics*, 2nd edn. (Addison-Wesley, Reading, 1980)

L. Gomberoff, R. Neira, Convective growth rate of ion-cyclotron waves in a H^+–He^+ and H^+–He^+–O^+ plasma. J. Geophys. Res. **88**, 2170 (1983)
J.C. Green, M.G. Kivelson, Relativistic electrons in the outer radiation belt: differentiating between acceleration mechanisms. J. Geophys. Res. **109**, 03213 (2004). doi:10.1029/2003JA010153
P. Helander, L. Kjellberg, Simulation of nonquasilinear diffusion. Phys. Plasmas **1**, 210 (1994)
R.B. Horne, Plasma astrophysics: acceleration of killer electrons. Nat. Phys. **3**, 590 (2007)
R.B. Horne, R.M. Thorne, Convective instabilities of electromagnetic ion-cyclotron waves in the outer magnetosphere. J. Geophys. Res. **99**, 17259 (1994)
R.B. Horne, R.M. Thorne, Potential waves for relativistic electron scattering and stochastic acceleration during magnetic storms. Geophys. Res. Lett. **25**, 3011 (1998)
R.B. Horne, R.M. Thorne, S.A. Glauert, N.P. Meredith, D. Pokhotelov, O. Santolík, Electron acceleration in the Van Allen radiation belts by fast magnetosonic waves. Geophys. Res. Lett. **34**, 17107 (2007). doi:10.1029/2007GL030267
M.K. Hudson, S.R. Elkington, J.G. Lyon, V.A. Marchenko, I. Roth, M. Temerin, J.B. Blake, M.S. Gussenhoven, J.R. Wygant, Simulations of radiation belt formation during storm sudden commencements. J. Geophys. Res. **102**, 14087 (1997)
M.K. Hudson, B.T. Kress, H.-R. Mueller, J.A. Zastrow, J.B. Blake, Relationship of the Van Allen radiation belts to solar wind drivers. J. Atmos. Sol.-Terr. Phys. **70**, 708 (2008)
U. Jaekel, R. Schlickeiser, The Fokker-Planck coefficients of cosmic ray transport in random electromagnetic fields. J. Phys. G, Nucl. Part. Phys. **18**, 1089 (1992)
J.R. Jokipii, P.J. Coleman, Cosmic-ray diffusion tensor and its variation observed with Mariner 4. J. Geophys. Res. **73**, 5495 (1968)
R. Keller, K.H. Schmitter, Beam storage with stochastic acceleration and improvement of a synchrocyclotron beam, in *CERN Rept. 58-13*, Geneva, Switzerland (1958)
P.J. Kellog, Van Allen radiation of solar origin. Nature **183**, 1295 (1959)
P.J. Kellog, C.A. Cattell, K. Goetz, S.J. Monson, L.B. Wilson III, Electron trapping and charge transport by large amplitude whistlers. Geophys. Res. Lett. **37**, 09224 (2010). doi:10.1029/2010JA015919
P.J. Kellog, C.A. Cattell, K. Goetz, S.J. Monson, L.B. Wilson III, Large amplitude whistlers in the magnetosphere observed with Wind–Waves. J. Geophys. Res. **116**, 09224 (2011). doi:10.1029/2010JA015919
C.F. Kennel, F. Engelmann, Velocity space diffusion from weak plasma turbulence in a magnetic field. Phys. Fluids **9**, 2377 (1966)
C.F. Kennel, H.E. Petscheck, Limit on stably trapped particle fluxes. J. Geophys. Res. **71**, 427 (1966)
K. Kersten, C.A. Cattell, A. Breneman, K. Goetz, P.J. Kellogg, J.R. Wygant, L.B. Wilson III, J.B. Blake, M.D. Looper, I. Roth, Observation of relativistic electron microbursts in conjunction with intense radiation belt whistler-mode waves. Geophys. Res. Lett. **38**, 08107 (2011). doi:10.1029/2011GL046810
B.T. Kress, M.K. Hudson, M.D. Looper, J. Albert, J.G. Lyon, C.C. Goodrich, Global MHD test particle simulations of >10 MeV radiation belt electrons during storm sudden commencement. J. Geophys. Res. **112**, 09215 (2007). doi:10.1029/2006JA012218
B.T. Kress, M.K. Hudson, M.D. Looper, J.G. Lyon, C.C. Goodrich, Global MHD test particle simulations of solar energetic electron trapping in the Earth's radiation belts. J. Atmos. Sol.-Terr. Phys. **70**, 1727 (2008)
M. Kruskal, Asymptotic theory of Hamiltonian and other systems with all solutions nearly periodic. J. Math. Phys. **23**, 742 (1962)
L. Landau, E. Lifshitz, *The Classical Theory of Fields*, vol. 2 (Pergamon, London, 1959)
L. Landau, E. Lifshitz, *Mechanics*, vol. 1, 3rd edn. (Pergamon, New York, 1976)
L.D. Landau, Kinetic equation for the case of Coulomb interaction. Zh. Eksp. Teor. Fiz. **7**, 203 (1937)
L.J. Lanzerotti, A. Hasegawa, C.G. Maclennan, Drift mirror instability in the magnetosphere: particle and field oscillations and electron heating. J. Geophys. Res. **74**, 5565 (1969)
X. Li, M. Temerin, J.R. Wygant, M.K. Hudson, J.B. Blake, Simulation of the prompt energization and transport of radiation belt particles during the March 24, 1991 SSC. Geophys. Res. Lett. **20**, 2423 (1993)
A.J. Lichtenberg, M.A. Lieberman, *Regular and Chaotic Dynamics*. Applied Mathematical Sciences, vol. 38 (Springer, New York, 1983)
M.D. Looper, J.B. Blake, R.A. Mewaldt, Response of the inner radiation belt to the violent Sun–Earth connection events of October–November 2003. Geophys. Res. Lett. **32**, L03S06 (2005). doi:10.1029/2004GL021502
C.E. McIlwain, Ring current effects on trapped particles. J. Geophys. Res. **71**, 3623 (1966)
N.P. Meredith, R.B. Horne, R.R. Anderson, Substorm dependence of chorus amplitudes: implications for the acceleration of electrons to relativistic energies. J. Geophys. Res. **106**, 13165 (2001). doi:10.1029/2000JA900156
R.M. Millan, K.B. Yando, J.C. Green, A.Y. Ukhorskiy, Spatial distribution of relativistic electron precipitation during a radiation belt depletion event. Geophys. Res. Lett. **37**, 20103 (2010). doi:10.1029/2010GL044919

A.I. Neishtadt, On change in adiabatic invariant at a passage through a separatrix. Fiz. Plazmy **12**, 992 (1986)
T.G. Northrop, *The Adiabatic Motion of Charged Particles* (Interscience, New York, 1963)
T.G. Northrop, E. Teller, Stability of the adiabatic motion of charged particles in the Earth's field. Phys. Rev. **117**, 215 (1960)
F.W.J. Olver, *Asymptotics and Special Functions* (Academic Press, New York, 1974)
M.K. Öztürk, R.A. Wolf, Bifurcation of drift shells near the dayside magnetopause. J. Geophys. Res. **112**, 07207 (2007). doi:10.1029/2006JA012102
A.B. Rechester, R.B. White, Calculation of turbulent diffusion for the Chirikov-Taylor model. Phys. Rev. Lett. **44**, 1586 (1980)
J.G. Roederer, Experimental evidence on radial diffusion of geomagnetically trapped particles, in *Earth's Particles and Fields*, ed. by B.M. McCormac (1968), p. 143
J.G. Roederer, Dynamics of geomagnetically trapped radiation, in *Physics and Chemistry in Space*, ed. by J.G. Roederer, J. Zahringer, vol. 2 (Springer, Berlin, 1970)
Y.A. Romanov, G.F. Filippov, The interaction of fast electron beams with longitudinal plasma waves. Sov. Phys. JETP **13**, 87 (1961)
R.Z. Sagdeev, D.A. Usikov, G.M. Zaslavsky, *Nonlinear Physics: From the Pendulum to Turbulence and Chaos* (Harwood Academic, New York, 1988)
M. Schulz, L.J. Lanzerotti, Particle diffusion in the radiation belts, in *Physics and Chemistry in Space*, vol. 7 (Springer, New York, 1974)
V.P. Shabansky, Some processes in magnetosphere. Space Sci. Rev. **12**(3), 299 (1971)
D.R. Shklyar, H. Matsumoto, Oblique whistler-mode waves in the inhomogeneous magnetospheric plasma: resonant interactions with energetic charged particles. Surv. Geophys. **30**, 55 (2009)
Y.Y. Shprits, R.M. Thorne, R. Friedel, G.D. Reeves, J. Fennell, D.N. Baker, S.G. Kanekal, Outward radial diffusion driven by losses at magnetopause. J. Geophys. Res. **111**, 11214 (2006). doi:10.1029/2006JA011657
Y.Y. Shprits, S.R. Elkington, N.P. Meredith, D.A. Subbotin, Review of modeling of losses and sources of relativistic electrons in the outer radiation belt I: radial transport. J. Atmos. Sol.-Terr. Phys. **70**, 1679 (2008a). doi:10.1016/j.jastp.2008.06.008
Y.Y. Shprits, S.R. Elkington, N.P. Meredith, D.A. Subbotin, Review of modeling of losses and sources of relativistic electrons in the outer radiation belt II: local acceleration and loss. J. Atmos. Sol.-Terr. Phys. **70**, 1694 (2008b). doi:10.1016/j.jastp.2008.06.014
M.I. Sitnov, N.A. Tsyganenko, A.Y. Ukhorskiy, P.C. Brandt, Dynamical data-based modeling of the storm-time geomagnetic field with enhanced spatial resolution. J. Geophys. Res. **113**, 07218 (2008). doi:10.1029/2007JA013003
D.V. Sivukhin, Motion of charged particles in electromagnetic fields in the drift approximation. Rev. Plasma Phys. **1**, 1 (1965)
G.R. Smith, A.N. Kaufman, Stochastic acceleration by an obliquely propagating wave—an example of overlapping resonances. Phys. Fluids **21**, 2230 (1978)
D.J. Southwood, J.W. Dungey, R.L. Eherington, Bounce resonant interaction between pulsations and trapped particles. Planet. Space Sci. **17**, 349 (1969)
T.W. Speiser, Particle trajectories in a model current sheet, based on the open model of the magnetosphere, with applications to auroral particles. J. Geophys. Res. **70**, 1717 (1965)
D. Summers, R.M. Thorne, F. Xiao, Relativistic theory of wave particle resonant diffusion with application to electron acceleration in the magnetosphere. J. Geophys. Res. **103**, 20487 (1998)
K. Takahashi, A.Y. Ukhorskiy, Solar wind control of Pc5 pulsation power at geosynchronous orbit. J. Geophys. Res. **112**, 11205 (2007). doi:10.1029/2007JA012483
R.M. Thorne, Radiation belt dynamics: the importance of wave-particle interactions. Geophys. Res. Lett. **37**, 22107 (2010). doi:10.1029/2010GL044990
R.M. Thorne, C.F. Kennel, Relativistic electron precipitation during magnetic storm main phase. J. Geophys. Res. **76**, 4446 (1971)
V.Y. Trakhtengerts, Stationary states of the Earth's outer radiation zone. Geomagn. Aeron. **6**, 827 (1966)
N.A. Tsyganenko, Modeling the global magnetic field of the large-scale Birkeland current systems. J. Geophys. Res. **101**, 27187 (1996)
N.A. Tsyganenko, M.I. Sitnov, Modeling the dynamics of the inner magnetosphere during strong geomagnetic storms. J. Geophys. Res. **110**, 03208 (2005). doi:10.1029/2004JA010798
N.A. Tsyganenko, M.I. Sitnov, Magnetospheric configurations from a high-resolution data-based magnetic field model. J. Geophys. Res. **112**, 06225 (2007). doi:10.1029/2007JA012260
D.L. Turner, Y. Shprits, M. Hartinger, V. Angelopoulos, Explaining sudden losses of outer radiation belt electrons during geomagnetic storms. Nat. Phys. (2012). doi:10.1038/nphys2185
B.A. Tverskoy, Dynamics of the radiation belts of the Earth, 2. Geomagn. Aeron. **4**, 436 (1964)

B.A. Tverskoy, Main mechanisms in the formation of the Earth's radiation belts. Rev. Geophys. Space Phys. **7**, 219 (1969)
A.Y. Ukhorskiy, M.I. Sitnov, Radial transport in the outer radiation belt due to global magnetospheric compressions. J. Atmos. Sol.-Terr. Phys. **70**, 1714 (2008)
A.Y. Ukhorskiy, K. Takahashi, B.J. Anderson, H. Korth, The impact of toroidal ULF waves on the outer radiation belt electrons. J. Geophys. Res. **110**, 10202 (2005). doi:10.1029/2005JA011017
A.Y. Ukhorskiy, K. Takahashi, B.J. Anderson, N.A. Tsyganenko, The impact of ULF oscillations in solar wind dynamic pressure on the outer radiation belt electrons. Geophys. Res. Lett. **33**, 06111 (2006a). doi:10.1029/2005GL024380
A.Y. Ukhorskiy, B.J. Anderson, P.C. Brandt, N.A. Tsyganenko, Storm-time evolution of the outer radiation belt: transport and losses. J. Geophys. Res. **111**, A11S03 (2006b). doi:10.1029/2006JA011690
A.Y. Ukhorskiy, M.I. Sitnov, K. Takahashi, B.J. Anderson, Radial transport of radiation belt electrons due to stormtime pc5 waves. Ann. Geophys. **27**, 2173 (2009)
A.Y. Ukhorskiy, Y.Y. Shprits, B.J. Anderson, K. Takahashi, R.M. Thorne, Rapid scattering of radiation belt electrons by storm-time EMIC waves. Geophys. Res. Lett. **37**, 09101 (2010). doi:10.1029/2010GL042906
A.Y. Ukhorskiy, M.I. Sitnov, R.M. Millan, B.T. Kress, The role of drift orbit bifurcations in energization and loss of electrons in the outer radiation belt. J. Geophys. Res. **116**, 09208 (2011). doi:10.1029/2011JA016623
J.A. Van Allen, The geomagnetically trapped corpuscular radiation. J. Geophys. Res. **64**, 1683 (1959)
A.A. Vedenov, E.P. Velikhov, R.Z. Sagdeev, Stability of plasma. Usp. Fiz. Nauk **73**, 701 (1961)
S.N. Vernov, A.E. Chudakov, P.V. Vakulov, Y.I. Logachev, Study of terrestrial corpuscular radiation and cosmic rays during flight of the cosmic rocket. Dokl. Akad. Nauk SSSR **125**, 304 (1959)
Y. Wan, S. Sazykin, R.A. Wolf, M.K. Öztürk, Drift shell bifurcation near the dayside magnetopause in realistic magnetospheric magnetic fields. J. Geophys. Res. **115**, 10205 (2010). doi:10.1029/2010JA015395
L.B.I. Wilson, C.A. Cattell, P.J. Kellogg, J.R. Wygant, K. Goetz, A. Breneman, K. Kersten, The properties of large amplitude whistler mode waves in the magnetosphere: propagation and relationship with geomagnetic activity. Geophys. Res. Lett. **38**, 17107 (2011). doi:10.1029/2011GL048671
J.R. Wygant, F. Mozer, M. Temerin, J. Blake, N. Maynard, H. Singer, M. Smiddy, Large amplitude electric and magnetic field signatures in the inner magnetosphere during injection of 15 MeV electron drift echoes. Geophys. Res. Lett. **21**, 1739 (1994)
G.M. Zaslavsky, Chaos, fractional kinetics, and anomalous transport. Phys. Rep. **371**, 461 (2002)
G.M. Zaslavsky, *Hamiltonian Chaos and Fractional Dynamics* (Oxford University Press, New York, 2005)

DOI 10.1007/978-1-4899-7433-4_18
Reprinted from *Space Science Reviews* Journal, DOI 10.1007/s11214-013-9964-y

AE9, AP9 and SPM: New Models for Specifying the Trapped Energetic Particle and Space Plasma Environment

G.P. Ginet · T.P. O'Brien · S.L. Huston · W.R. Johnston · T.B. Guild · R. Friedel · C.D. Lindstrom · C.J. Roth · P. Whelan · R.A. Quinn · D. Madden · S. Morley · Yi-Jiun Su

Received: 10 September 2012 / Accepted: 10 January 2013 / Published online: 9 March 2013

Abstract The radiation belts and plasma in the Earth's magnetosphere pose hazards to satellite systems which restrict design and orbit options with a resultant impact on mission performance and cost. For decades the standard space environment specification used for spacecraft design has been provided by the NASA AE8 and AP8 trapped radiation belt models. There are well-known limitations on their performance, however, and the need for a new trapped radiation and plasma model has been recognized by the engineering community for some time. To address this challenge a new set of models, denoted AE9/AP9/SPM, for energetic electrons, energetic protons and space plasma has been developed. The new models offer significant improvements including more detailed spatial resolution and the quantification of uncertainty due to both space weather and instrument errors. Fundamental

G.P. Ginet (✉)
MIT Lincoln Laboratory, 244 Wood Street, Lexington, MA 20420, USA
e-mail: gregory.ginet@ll.mit.edu

T.P. O'Brien · T.B. Guild
The Aerospace Corporation, 15409 Conference Center Drive, Chantilly, VA 20151, USA

S.L. Huston · D. Madden
The Institute for Scientific Research, 400 St. Clement's Hall, Boston College, 140 Commonwealth Avenue, Chestnut Hill, MA 02467, USA

Present address:
S.L. Huston
Atmospheric and Environmental Research, Incorporated, 131 Hartwell Avenue, Lexington, MA 02421, USA

W.R. Johnston · C.D. Lindstrom · Y.-J. Su
Space Vehicles Directorate, Air Force Research Laboratory, Kirtland AFB, NM 87117, USA

C.J. Roth · P. Whelan · R.A. Quinn
Atmospheric and Environmental Research, Incorporated, 131 Hartwell Avenue, Lexington, MA 02421, USA

R. Friedel · S. Morley
Los Alamos National Laboratory, PO Box 1663, Los Alamos, NM 87545, USA

to the model design, construction and operation are a number of new data sets and a novel statistical approach which captures first order temporal and spatial correlations allowing for the Monte-Carlo estimation of flux thresholds for user-specified percentile levels (e.g., 50th and 95th) over the course of the mission. An overview of the model architecture, data reduction methods, statistics algorithms, user application and initial validation is presented in this paper.

Keywords Radiation belt modeling · Energetic trapped particles · Space environment climatology · Space weather

1 Introduction

Since the launch of simple Geiger counters into space on the first Explorer satellites in 1958 and the subsequent discovery of the Van Allen radiation belts, there have been ongoing efforts to model the space radiation environment. These efforts were—and still are—driven not only by scientific curiosity, but also by the practical need of engineers to understand better and mitigate the significant radiation hazards to spacecraft reliability and survivability. Many anomaly resolution reports and several scientific studies have shown that there is a direct association between the dynamic radiation environment and system or sub-system performance (e.g. Wrenn and Sims 1996; Koons et al. 2000; Brautigam 2002). Spacecraft systems and discrete component performance may gradually deteriorate with accumulated dose or may experience abrupt failure (temporary or permanent) due to discrete events associated with Single Event Effects (SEEs) or electrostatic discharge. The radiation environment specification to which system engineers design is a critical factor driving capability versus survivability tradeoffs. Spacecraft flown in orbits where a more severe radiation environment is anticipated require more expensive radiation hardened components and/or greater shielding mass which constrain launch options, limit performance and drive costs higher.

The first definitive empirical models of the radiation belts were sponsored by the National Aeronautics and Space Administration (NASA) and developed in the 1960s–1970s to represent the average radiation environment during the minimum and maximum phase of the solar cycle. They have been incrementally updated since then, the most recent proton and electron models being AP8 and AE8, respectively (Sawyer and Vette 1976; Vette 1991a, 1991b; Fung 1996). These radiation belt models are still widely used, having enjoyed close to three decades as industry's de facto standard. However, there are well-known limitations on their validity including the under-prediction of dose for orbits in the "slot region", i.e. low inclination orbits between about 6000–12000 km, and no coverage of the hot and cold plasma populations below 0.1 MeV (Fung 1996; Gussenhoven et al. 1994; Daly et al. 1996; Armstrong and Colborn 2000; Fennell et al. 2003; Brautigam et al. 2004). The former limitation is especially relevant to dose arising from long-lived higher energy protons ($>$40 MeV) and electrons ($>$1 MeV) injected during geomagnetic storms. In addition, the models are simple averages representing either solar maximum (AP8/AE8 MAX) or minimum (AP8/AE8 MIN) with no error bars or cumulative probability distributions provided. A broad consensus has been building over the past decades among both engineers and scientists that a more accurate, comprehensive, and up-to-date space radiation environment model is needed. Modern design and systems engineering techniques require models with error bars, finite-time duration probability distributions, and a larger spectral range, especially as increasingly complex technologies are flown and missions are being considered for non-traditional orbit regimes.

The development of a global space radiation model such as the AP8 or AE8 is a tremendous effort involving the analysis and combination of data sets from numerous missions over periods of time measured in solar cycles. Progress has been made on some fronts by developing models using data acquired onboard the CRRES (Meffert and Gussenhoven 1994; Brautigam and Bell 1995), NOAA/TIROS (Huston et al. 1996; Huston 2002), LANL-GEO (Boscher et al. 2003; Sicard-Piet et al. 2008), SAMPEX (Heynderickx et al. 1999) and Polar (Roeder et al. 2005) satellites. Data assimilative techniques that ingest a variety of data sets to drive physics-based models have also been developed (Bourdarie et al. 2009; Reeves et al. 2012). Whereas the NASA models span the entire inner magnetosphere over a very wide range of energies, these more recent models face various limitations, either in energy range, spatial range (e.g., exclusively at geosynchronous orbit (GEO), medium-Earth orbit (MEO) or low-Earth orbit (LEO)), temporal range (limited to a small portion of the solar cycle), or possibly all three. Although newer individual models may be an improvement for the restricted parameter range to which they apply, it is likely that the NASA models will remain the industry standard until the space physics community develops a single, comprehensive and engineer-friendly replacement model with increased functionality addressing the known deficiencies.

To meet this need the National Reconnaissance Office (NRO) and the Air Force Research Laboratory (AFRL) have supported an effort to develop a new set of models. Denoted "AE9" for trapped energetic electrons, "AP9" for trapped energetic protons and "SPM" for space plasma, the naming continues the "AE", "AP" convention to maintain an association of functional purpose, i.e. use in space system design. The project has been led by principal investigators from the Aerospace Corporation and MIT Lincoln Laboratory and has involved personnel from AFRL, Boston College, Atmospheric and Environmental Research (AER) and Los Alamos National Laboratory. Development of Version 1.0 (V1.0) of AE9/AP9/SPM was under the auspices of the NRO Proton Spectrometer Belt Research (PSBR) program which also supported the development of the Relativistic Proton Spectrometer (RPS) instruments (Mazur et al. 2012) currently flying on the Van Allen Probes (formerly Radiation Belt Storm Probes, or RBSP). Future versions of the model are expected to include data from RPS as well as the many other particle and plasma detectors on the Van Allen Probes. Furthermore, with AE9/AP9/SPM source code and data sets released in the public domain it is hoped that the national and international radiation belt communities will participate in expanding the data sets and analysis, perhaps working together through an organization such as the National Geophysical Data Center or the Committee on Space Research (COSPAR) Panel on Radiation Belt Models (PRBEM), so as to truly maintain a continually improving standard radiation belt model (perhaps with a new name).

The purpose of this document is to present an overview of AE9/AP9/SPM V1.0 (publicly released in September 2012) for a general audience including both engineers interested in understanding what is behind the application and space scientists interested in contributing data sets and algorithms for future versions. Over five years in development (O'Brien 2005; Ginet et al. 2008; Huston et al. 2009) the model comprises 33 satellite data sets, is comprehensively cross-calibrated, makes extensive use of spectral inversion techniques and introduces a new statistical methodology for combining the data to produce realistic probabilities of occurrence for varying flux levels along a user-defined orbit. Section 2 reviews the requirements for the model as gleaned from the satellite design community. Coordinate systems and associated grids used in the model are discussed in Sect. 3. Data set processing techniques and cross-calibration are outlined in Sect. 4. The architecture and construction of the model is described in Sect. 5 to include discussion of flux maps, the time-evolution algorithm and user-application. A comparison of V1.0 output to other models and data sets

Table 1 Prioritized list of space particle specification requirements for AE9/AP9/SPM. Parentheses indicate higher priority subsets

Priority	Species	Energy	Location	Period	Effects
1	Protons	>10 MeV (>80 MeV)	LEO & MEO	Mission	Dose, SEE, DD, nuclear activation
2	Electrons	>1 MeV	LEO, MEO & GEO	5 min, 1 hr, 1 day, 1 week & mission	Dose, internal charging
3	Plasma	30 eV–100 keV	LEO, MEO & GEO	5 min, 1 hr, 1 day, 1 week & mission	Surface charging, dose
4	Electrons	100 keV–1 MeV	MEO & GEO	5 min, 1 hr, 1 day, 1 week & mission	Internal charging, dose
5	Protons	1 MeV–10 MeV (5–10 MeV)	LEO, MEO & GEO	Mission	Dose

is presented in Sect. 6 and the paper concludes with a summary in Sect. 7. A comprehensive discussion of all the components can be found in the V1.0 Requirements Specification (Ginet and O'Brien 2010), Technical Documentation (Johnston et al. 2013) and User's Guide (Roth et al. 2013).

2 Requirements

To determine the specific requirements for AE9/AP9/SPM, input was avidly solicited from the spacecraft engineering community. Several workshops and meetings on the topic were held to include a series of Space Environment Effect Working Groups (SEEWG) sponsored by the Space Technology Alliance, the NASA Living with a Star Working Group Meeting on New Standard Radiation Belt and Space Plasma Models for Spacecraft Engineering (Lauenstein et al. 2005) and a special session at the 2007 NOAA Space Weather Workshop (Radiation Models 2007). In addition, feedback has been received via email and through the Radiation Specifications Forum Website (Radiation Specifications 2007) hosted by NASA to support the effort. Results from the outreach efforts have been integrated, refined and prioritized by the AE9/AP9/SPM team. Table 1 summarizes the findings in terms of priority, species, energy, location and time resolution. Energy ranges in parentheses indicate areas with especially poor coverage in current models. More details can be found in Ginet and O'Brien (2010).

There has been a universal emphasis from the workshops on the need for an authoritative new model recognized by spacecraft buyers and relatively easy-to-use by spacecraft engineers. Given their role in limiting total system lifetimes, energetic ions (10–500 MeV) and electrons (>1 MeV) in the inner magnetosphere (~400–15000 km altitude) were the primary concern. Models of the poorly characterized lower energy plasma environment (<10 keV) were also a high priority considering the large surface areas and novel materials and coatings under consideration for use in modern space systems. Better characterization of the dynamic MeV electrons (>0.5 MeV) in the slot and outer zone (6000–36000 km altitude) was also universally recognized as important for improving designs to withstand deep dielectric charging events. Relatively low energy protons (1–10 MeV) can cause dose degradation of solar panels and are not yet adequately specified.

In addition to the extended spectral ranges, the new model must also improve upon the statistical description of the space particle distributions. Some regions of energy-location-geophysical activity phase space will be much more accurately described than others and error bars and confidence levels are needed to reflect the uncertainties. Cumulative probability distributions of the flux values time-averaged over different periods (e.g. the 95th percentile of the >1.0 MeV, 12 hour averaged electron flux) are a necessity. The periods of interest are listed in column 5 of Table 1. This is a challenging task considering that the specification must be produced for an arbitrary orbit within the magnetosphere from a model constructed with data from a relatively small number of satellites. Indeed, for V1.0 the resolution for modeling temporal variations at a fixed location is limited to 1 day for electrons, 1 week for protons and is not explicitly captured (other than in the spread of the distribution function) for the plasma. Techniques such as the "sample solar cycle" (see Sect. 7) need to be considered for future versions of the model. For most orbits, variation on finer time scales is dominated by vehicle motion, which is accounted for in the model application at run time.

3 Reference Grids

The empirical basis of the AE9/AP9/SPM models is a set of flux maps derived from data measured by particle detectors and dosimeters onboard satellites traversing the radiation belts. Flux map construction requires that many individual flux measurements taken over a large extent of space and a long time span be mapped to a reference grid defined in the context of a specific coordinate system or systems. A judicious choice of coordinate system facilitates the systematic comparison and combination of the data and can significantly reduce spread of flux distribution functions within each grid bin. In particular, coordinates that are invariant over the drift-bounce motion of a particle allow a local angle-resolved flux measurement to be mapped to a 3-D surface, and measurements along an elliptical satellite orbit can therefore cover a 3-D volume.

A wide variety of coordinate systems are available, each with advantages and disadvantages (cf. Cabrera and Lemaire 2007). For AE9/AP9/SPM the primary coordinates are:

(a) the particle energy E,
(b) the modified second adiabatic invariant K capturing the particle's bounce motion,

$$K = \int_{s_m}^{s_{m'}} \left[B_m - B(s) \right] ds, \tag{1}$$

where B is the magnitude of the magnetic field along the particle trajectory s following a magnetic field line and B_m is the magnetic field at the particle mirror points s_m, $s_{m'}$,
(c) the third adiabatic invariant Φ capturing the particle's drift motion,

$$\Phi = \oint_C d\mathbf{L} \cdot \mathbf{A} = \oint_S d\mathbf{a} \cdot \mathbf{B} \tag{2}$$

where $\mathbf{A}$ is the magnetic vector potential, C is a curve encompassing the entire drift shell of the particle, $\mathbf{B}$ is the magnetic field and S is the area outside the drift shell (Roederer 1970; Schulz 1996).

To more accurately map variations in particle distributions across the Earth's magnetic epochs the (K, Φ) coordinates were chosen. However, the energy E was chosen instead of the first adiabatic invariant μ ($\mu = p_\perp^2/(2mB)$, where $p_\perp$ is the particle perpendicular momentum and m the mass) since most detector channels measure a range of both energy

and pitch-angle α, making the spread of measured μ much wider than just the spread in E. The more intuitive Roederer L-shell L^* is calculated from Φ at a given magnetic epoch according to,

$$L^* = \frac{2\pi k_0}{\Phi}, \tag{3}$$

where k_0 is the magnetic dipole parameter equal to $\mu_0 M_E/(4\pi)$ with μ_0 the magnetic permeability of free space and M_E the Earth's dipole moment.

For all coordinate and mapping calculations, the Olson-Pfitzer Quiet model (OPQ77) (Olson and Pfitzer 1977) was used for the external magnetic field and the International Geophysical Reference Field (IGRF) model (IGRF 2012) was used for the internal magnetic field. The IGRF was evaluated at the epoch appropriate for when the data was taken (for model construction) or for the orbit of interest (for user application). The OPQ77 model represents all major magnetospheric current systems and is valid for all tilt angles, i.e., angles of incidence of the solar wind on the dipole axis, and accurately represents the total magnetospheric magnetic field for conditions of low magnetic activity and to a geocentric distance of 15 R_E or to the magnetopause. OPQ77 has been shown to be a good average model for the inner magnetosphere (Jordan 1994; McCollough et al. 2008). Although the data used in AE9/AP9/SPM were taken at all levels of magnetospheric activity, it was decided that using an activity-dependent model would be inappropriate. If an activity-dependent field model were used to map the data, the same field model would be required to "un-map" the data for a specific application. Since a user would not know *a-priori* what the activity level would be for a future mission, using such a field model would not have any practical benefit. Therefore, any deviations associated with calculating the mapping coordinates with the OPQ77 model compared to a "truer" magnetic field model are manifested in the spread in the particle distribution within each grid bin and captured by the distribution function parameterization of the flux maps (Sect. 5.1).

There are many advantages to using the adiabatic invariants as coordinates but there are also several disadvantages. For example, at low altitudes the particle flux is controlled more by the thermospheric neutral density than by the magnetic field; thus the flux is a strong function of altitude and is also affected by the density variation over the solar cycle. Another complication is the difference between the drift loss cone and the bounce loss cone. Electrons in particular can be scattered onto drift shells which intersect the surface of the Earth at some point. As the electrons drift eastward eventually they are lost due to atmospheric interactions when the local bounce loss cone becomes equal to the drift loss cone. Although these electrons are not permanently trapped, they are a persistent population and should be included in the trapped particle models. For these reasons the (E, K, Φ) coordinate system does a poor job representing flux variations in and near the loss-cone. To overcome this limitation an additional coordinate h_{min}, defined as the minimum altitude a particle reaches during its drift-bounce orbit, has been introduced in AE9/AP9/SPM to map the region below 1000 km. Obtained as a by-product of the Φ computation, h_{min} is much better than Φ for tracking variations in the particle distributions at low altitudes where the flux gradients are large.

Adiabatic coordinates are also less useful for the lower energy plasma where there is a strong magnetic local time (MLT) dependence and effects from electric fields and plasma waves. Consequently, the more traditional McIlwain L-shell L_m (McIlwain 1961) and equatorial pitch angle α_{eq} will be used for the space plasma models instead of (K, Φ). Though MLT variations are substantial for energies less than approximately 100 keV, the main purpose of the SPM is to establish the statistics of particle flux exposure for satellites on mission

time scales, i.e. usually much longer than one day. To avoid the overhead of tracking another degree of freedom in V1.0, the MLT variations of the plasma have not been included in the SPM and are left to future versions. Because the data and simulation capabilities are not yet available to represent the spatiotemporal covariances of plasmas, the statistical linear regression model (Sect. 5.2) has also not been developed for plasmas in V1.0.

Table 2 summarizes parameters for the (E, K, Φ), (E, K, h_{min}) and (E, L_m, α_{eq}) reference grids used in V1.0. The bin size (i.e. distance between grid points) was chosen to be small enough to provide adequate spatial and spectral resolution, yet large enough to contain a statistically significant number of measurements. Grid spacing for (K, Φ) was selected to be uniform in $K^{1/2}$ and $\log_{10}(\Phi)$ to improve resolution near the magnetic equator (small values of K) and at large values of Φ (the inner zone). Note that h_{min} includes negative values to accommodate particles not in the bounce loss cone for some range of longitudes, but definitely in the drift loss cone. Energy resolution is a mix of both linear and logarithmic with the specific grid values chosen to be consistent with the AP8, AE8, and CAMMICE/MICS models. Component models of SPM are denoted SPMH, SPMHE, SPMO and SPME representing the hydrogen, helium, oxygen and electron constituents, respectively. For SPME the grid is consistent with the LANL/MPA data set (Sect. 4).

As an illustration of the reference grid coverage Fig. 1 shows the median 0.5 MeV electron flux from the AE9 model mapped in the (E, K, Φ) and (E, K, h_{min}) grids. In Fig. 1a the y-axis ($K = 0$) is the magnetic equator, and the loss cone is the boundary with the white region, where fluxes are zero. The inner and outer zones are clearly visible as regions of high flux centered at $\log_{10} \Phi$ values of about 0.05 and -0.4, respectively, with the slot region in between. The grey lines indicate the approximate location of the $h_{min} = 0$ (upper) and $h_{min} = 1000$ km (lower) contour, the latter being the upper boundary of Fig. 1b. Also shown in the figures are contours of the traditional $(L_m, B/B_0)$ coordinates (used in the AP8/AE8 and CRRES models, for example), where B is the magnitude of the magnetic field at a point along the field line corresponding to L_m and B_0 is the magnitude of the field at the magnetic equator along the same field line. It can be seen from Fig. 1b that using h_{min} as a coordinate gives much better resolution of the fluxes at low altitudes (or near the loss cone) where the neutral density and consequently altitude becomes a dominant ordering parameter.

To compute the reference coordinates along the ephemerides of the satellites supplying data to the model the IRBEM-LIB (IRBEM 2012) library of functions was used. Ephemeris data (latitude, longitude, altitude, universal time) were input and the K, Φ, h_{min}, L_m and α_{eq} parameters were output. A modification of IRBEM-LIB was required to calculate h_{min} in addition to Φ and to perform the calculation even if the drift shell dipped below the surface of the Earth. The parameters were calculated for discrete local pitch angles at 10 degree increments between 0 and 90 degrees. If higher resolution was required (e.g. for high pitch-angle resolution sensors) the above computed values were interpolated.

Calculation of the drift shells needed to evaluate Φ and h_{min} is a computer time-consuming process. Direct computation with the IRBEM-LIB routines was sufficient for construction of the flux maps since there are a relatively small number of ephemerides to compute (Sect. 4). However, in the general application where a user might evaluate many orbits for long periods of time the computational load to convert the flux map coordinates can quickly become unrealistic. A neural network interpolation algorithm was therefore developed to produce Φ and h_{min} without the computational expense of integrating over an entire drift shell. For a given satellite position and detector look direction the inputs include the Universal Time (UT), day of year, modified Julian day, I $(= K/\sqrt{B})$ and B_m thus requiring a trace of the field line only. A similar approach was used by Koller et al. (2009) and Koller and Zaharia (2011) for active magnetic field models. The neural network is an integral part

Table 2 Summary of the coordinate grids used in AE9/AP9/SPM. Square brackets denotes the units of the quantity inside

Model	Species	Energy	High Altitude Grid		Low Altitude Grid	
			2nd Inv.	3rd Inv.	2nd Inv.	3rd Inv.
AE9	e^-	0.04–10 MeV 21 channels	$0 \le K^{1/2} \le 4.5$ $\Delta(K^{1/2}) = 0.1$ $[K] = G^{1/2} R_E$	$0.8 \le \log_{10} \Phi \le 0.3$ $\Delta(\log_{10} \Phi) = 0.025$ $[\Phi] = G R_E^2$	$0 \le K^{1/2} \le 4.5$ $\Delta(K^{1/2}) = 0.1$ $[K] = G^{1/2} R_E$	$-500 < h_{min} < 1000$ km $\Delta h_{min} = 50$ km
AP9	H^+	0.1–400 MeV 22 channels				$0 < h_{min} < 1000$ km $\Delta h_{min} = 50$ km
SPME	e^-	1–40 keV 16 channels	$5 \le \alpha_{eq} \le 85°$ $\Delta \alpha_{eq} = 10°$	$2 \le L_m \le 10$ $\Delta L_m = 0.5$	N/A	
SPMH	H^+	1.15–164 keV 12 channels				
SPMHE	He^+					
SPMO	O^+					

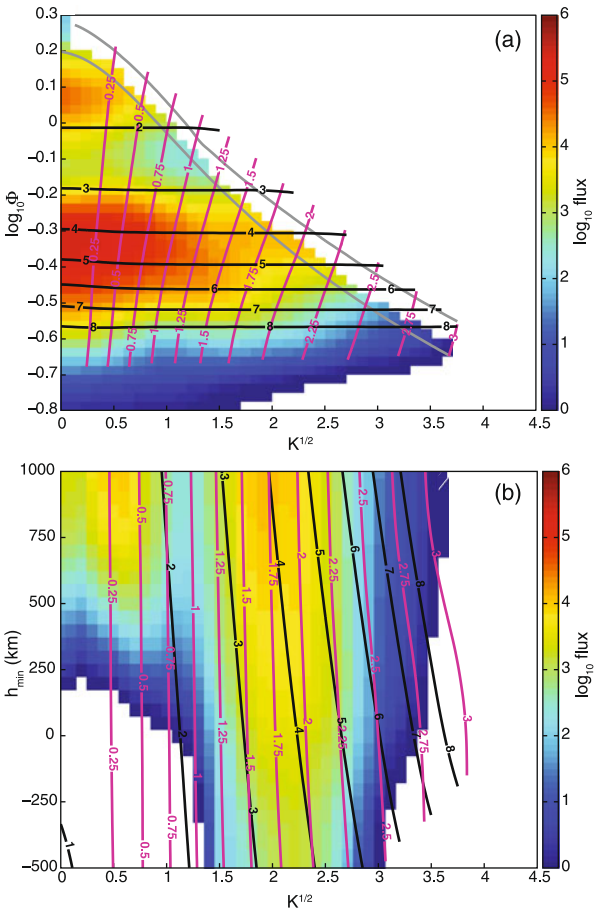

Fig. 1 The (**a**) (K, Φ) and (**b**) (K, h_{min}) grids used in AE9/AP9 with the median fluxes of 0.5 MeV electrons from AE9 shown. For reference the *black* and *purple lines* represent contours of constant $(L_m, B/B_0)$, i.e. the coordinates used in many historical models. *Grey lines* in (**a**) are contours of $h_{min} = 0$ and $h_{min} = 1000$ km in (K, Φ) space

of the AE9/AP9 software allowing Φ and h_{min} to be calculated almost as quickly as L_m. The algorithm is augmented with boundary models that specify the location of the loss cone at low altitudes and the onset of anomalous high altitude orbits not modeled, i.e. Shabansky orbits appearing on field lines with multiple magnetic minima (Shabansky 1971) and drift orbits intersecting the magnetopause.

4 Data

The AP9/AE9/SPM models are derived from measurements made over an extended period of time by particle detectors and dosimeters on board many satellites in a variety of orbits. Table 3 lists the satellites utilized and for each gives the particular sensor, orbital regimes spanned by the measurements, detector energy ranges and periods of coverage. Acronyms are defined in Appendix A. The raw data for each satellite typically comes as a set of counts per second recorded over a relatively small measurement interval (seconds to several minutes) for several differential or integral energy channels and perhaps several narrow or wide

Table 3 Satellites and sensors used in AE9 (Electrons), AP9 (Protons) and SPM (Plasma). The columns from left to right give the satellite/sensor (see Appendix A for acronym definitions), approximate orbital parameters (perigee × apogee, inclination), period from which data was taken and the energy range covered by the processed sensor data on the standard model grids. A * indicates very sparse data coverage

Satellite/Sensor	Orbit	Temporal range	Energy range
Protons			(MeV)
CRRES/PROTEL	350 km × 33000 km, 18°	07/1990–10/1991	2.0–80
S3-3/Telescope	236 km × 8048 km, 97.5°	07/1976–07/1979	0.1– 2.0
HEO-F1/Dosimeter	500 km × 39000 km, 63°	05/1994–02/2011*	10–400
HEO-F3/Dosimeter	500 km × 39000 km, 63°	11/1997–02/2011	10–400
ICO/Dosimeter	1000 km circular, 45°	06/2001–12/2009	10–400
TSX5/CEASE	410 km × 1710 km, 69°	06/2001–07/2006	10–400
POLAR/IPS	5100 km × 51000 km, 86°	02/1996–04/2008	0.1–1.0
POLAR/HISTp	5100 km × 51000 km, 86°	02/1996–04/2008	6.0–15.0
Electrons			(MeV)
CRRES/MEA/HEEF	350 km × 33000 km, 18°	07/1990–10/1991	0.1–7.0
SCATHA/SC3	28000 km × 43000 km, 7.8°	01/1979–05/1991	0.25–4.5
HEO-F1/Dos/Tel	500 km × 39000 km, 63°	05/1994–02/2011*	1.5–10.0
HEO-F3/Dos/Tel	500 km × 39000 km, 63°	11/1997–02/2011	0.5–5.0
ICO/Dosimeter	1000 km circular, 45°	06/2001–12/2009	1.0–7.0
TSX5/CEASE	410 km × 1710 km, 69°	06/2001–07/2006	0.07–3.0
SAMPEX/PET	550 km × 675 km, 82°	08/1992–07/2004	2.0–3.5
POLAR/HISTe	5100 km × 51000 km, 86°	02/1996–04/2008	1.0–6.0
GPS/BDDII ns18	20200 km circular, 55°	01/1990–05/1994	0.25–1.0
GPS/BDDII ns24	20200 km circular, 55°	08/1991–12/2000	0.25–1.0
GPS/BDDII ns28	20200 km circular, 55°	05/1992–09/1996	0.25–1.0
GPS/BDDII ns33	20200 km circular, 55°	04/1996–05/2004	0.25–1.0
LANL-GEO/SOPA 1989-046	36000 km circular, 0°	09/1989–01/2008	0.05–1.5
LANL-GEO/SOPA 1990-095	36000 km circular, 0°	11/1990–11/2005	0.05–1.5
LANL-GEO/SOPA LANL-97A	36000 km circular, 0°	07/1997–01/2008	0.05–1.5
LANL-GEO/SOPA LANL-02A	36000 km circular, 0°	01/2002–01/2008	0.05–1.5
Plasma			(keV)
POLAR/CAMMICE/MICS	5100 km × 51000 km, 86°	03/1997–09/1999	1.2–1.64
POLAR/HYDRA	5100 km × 51000 km, 86°	03/1997–09/1999	1.0–40.0
LANL-GEO/MPA 1990-095	36000 km circular, 0°	11/1990–11/2005	1.0–63.0
LANL-GEO/MPA 1991-080	36000 km circular, 0°	11/1991–11/2004	1.0–63.0
LANL-GEO/MPA 1994-084	36000 km circular, 0°	12/1994–01/2008	1.0–63.0
LANL-GEO/MPA LANL-97A	36000 km circular, 0°	07/1997–01/2008	1.0–63.0

field of view pitch angle channels. Each interval is assigned a unique Universal Time (UT) t and geographic position $\mathbf{x}$ and the set of $(\mathbf{x}, t)$ over the entire mission forms the satellite ephemeris. An expanded satellite ephemeris to include K, Φ, h_{min}, L_m and other reference grid coordinates is computed as described in Sect. 3 with $(\mathbf{x}, t)$, energy and local pitch angle used as input.

Flux maps, correlation matrices and other statistical quantities underlying the model (Sect. 5) are all computed from sets of unidirectional fluxes j (# $\mathrm{cm}^{-2}\,\mathrm{s}^{-1}\,\mathrm{MeV}^{-1}\,\mathrm{sr}^{-1}$) derived from the measurements of each satellite sensor tagged to the reference grid via the expanded ephemeris. The standard deviation of the natural logarithm of the flux $d\ln j$ is used as the estimate of the uncertainty. Transformation of the typical raw sensor output, e.g. counts/sec, into an estimate of the differential flux with error occurs through an often lengthy process. Data cleaning, spectral inversion, angular mapping, interpolation and cross-calibration are essential components and their application is discussed in this section.

4.1 Cleaning

During the course of a mission data from a given sensor can be corrupted due to a variety of issues including design imperfections, fabrication flaws, degradation of components, telemetry errors, background contamination and saturation. Some simple examination procedures can often be used to examine the entire data set and generate rules that define ranges of measurement values, regions of coordinate space or periods of time where the data is suspect and not to be used for model development. Such procedures are applied to the raw data before any sophisticated reduction algorithms (e.g. spectral inversion) which might obscure the problems. The procedures considered for the AE9/AP9/SPM data sets are extensions of those discussed in the PRBEM Data Analysis Procedure document (Bourdarie et al. 2008) and discussed in O'Brien (2012b). Included are (a) scatter plots of measurements in one channel (usually color-coded by time or coordinate, for example) against measurements of another correlated measurement channel such as an adjacent energy or pitch angle channel (identifies single channel problems of all sorts and contamination when the correlated channel is the protons in an electron dosimeter channel, for example); (b) scatter plots of measurements in one channel against measurements in the same channel offset in time (identifies transient spikes); and (c) histograms of the number of occurrences of every possible value of the raw measurement (identifies saturation and bit errors). It is also helpful to plot the data as a function of time for the entire mission with different coordinates color-coded to identify potential time-dependent sensor degradation.

All of the data sets in AE9/AP9/SPM were cleaned with at least one of the procedures and in many cases (e.g. the dosimeters) several of them. Ultimately it is the judgment of the analyst as to how to generate rules on which points to exclude; however, in most cases there are clear anomalies unambiguously associated with certain spatial regions, temporal periods or background flux levels. Once the rules were generated, a new data set for each sensor was created with flags to indicate the bad measurements to be rejected in further analysis.

For the CRRES/PROTEL proton data an explicit background contamination correction was implemented similar to that done by Gussenhoven et al. (1993) but in (K, h_{min}) coordinates instead of $(L_m, B/B_0)$ coordinates. Unlike the cleaning procedures mentioned above, which simply remove bad points from further analysis, the contamination correction goes further and corrects measured values based on an estimated background. At each measurement interval the (K, h_{min}) values are computed for all measured pitch angles. The flux value of the first pitch angle bin with $h_{min} < 100$ km (a nominal altitude within the loss cone where the trapped proton flux is zero) is then subtracted from the flux values of all bins with $h_{min} > 100$ km (the correction) and the entire set of flux values for $h_{min} < 100$ km is set equal to zero (the cleaning). Corrections were significant only within the inner zone $L^* < 1.7$ and the resulting flux maps were insensitive to different methods for estimating the loss cone.

The CRRES/HEEF and CRRES/MEA sensor data provide a unique LEO-to-GEO view of the trapped energetic electrons and are important in the development of AE9. Both sensors

have been analyzed in some detail (e.g. Hanser 1995; Dichter et al. 1993; Cayton 2007 and Vampola 1996) and the data is found in other models, e.g. CRRESELE. Significant additional work was done for AE9 to include more extensive proton contamination removal, spectral correction of MEA data and adjustment of HEEF data at high flux levels (Johnston et al. 2011).

4.2 Spectral Inversion and Pitch-Angle Mapping

It is straightforward to assign flux measurements made by sophisticated particle detectors with high spectral and pitch angle resolution (e.g. CRRES/PROTEL and POLAR/HISTp) to specific (E, K, Φ or h_{min}) bins by simple interpolation, usually of the log of the flux. These types of detectors are relatively few and far between, however, and spatial and temporal coverage of the radiation belts can be expanded considerably by using measurements from dosimeters. With wide fields-of-view and relatively small numbers of integral energy channels, dosimeters produce data that require a substantial amount of processing in order to assign a unidirectional flux value to a reference grid bin. Sensors listed in Table 3 falling into this category are the ICO/Dosimeter, the HEO-F1/Dosimeter, the HEO-F3/Dosimeter, the TSX5/CEASE dosimeter and broad-channel particle telescope, the LANL-GEO/SOPA telescopes and the GPS/BDDII dosimeters. Given the extensive use of dosimeter data sets in V1.0 and the uniqueness of the processing methods as applied to radiation belt models a brief description is given here.

Converting the measured counts/sec C_i in $i = 1, \ldots, N$ dosimeter channels into unidirectional flux j involves inverting in some manner the following relation (e.g. Sullivan 1971),

$$C_i = \int_0^\infty dE \int_0^{2\pi} d\varphi \int_0^\pi d\theta \sin\theta \varepsilon_i(E) A_i(E;\theta) j(E;\theta,\varphi), \tag{4}$$

where (θ, φ) are spherical coordinate angles describing the field of view in the frame where the z axis is along the detector bore sight, $\varepsilon_i(E)$ is the detector efficiency and $A_i(E, \theta)$ is the effective area of the detector channel assuming symmetry in azimuth. For V1.0 a two-step process was employed separating out the spectral inversion and angular mapping parts.

First, the flux was assumed to be isotropic, i.e. $\bar{j}(E) = j(E, \theta, \varphi)$, and was obtained using standard non-linear optimization techniques (cf. Press et al. 1992; O'Brien 2010) from the angular integrated form of Eq. (4),

$$C_i = \int_0^\infty dE R_i(E) \bar{j}(E), \tag{5}$$

where $R_i(E)$ is the known channel response function defined as,

$$R_i(E) = 2\pi \int_0^\pi d\theta \sin\theta \varepsilon_i(E) A_i(E;\theta). \tag{6}$$

Detailed response function models based on Monte-Carlo simulations of energy deposition in materials were available for the TSX5/CEASE (Brautigam et al. 2006) and LANL-GEO/SOPA (Cayton and Belian 2007) sensors. Accurate geometric factors were also measured prior to launch for the electron response of the HEO and ICO dosimeters. Such information was not available for the proton response of the ICO and HEO dosimeters, and an alternative method to determine the geometric factors was developed using on-orbit observations of solar proton events and inter-calibration with GOES/SEM observations (Guild et al. 2009). Principal component analysis was used to *a-priori* parameterize the spectral shapes by generating L^*-dependent basis components derived from the Selesnick Inner Zone Model

for protons (Selesnick et al. 2007) and the CRRES/HEEF/MEA data for electrons (Johnston et al. 2010). In the LANL-GEO/SOPA analysis a double relativistic Maxwellian was assumed as the parameterized spectral function.

For the GPS/BDDII, the flux conversion factors were determined through a cross-calibration analysis with CRRES/MEA data (Friedel et al. 2005). Gain settings for each channel were varied as a function of time throughout the mission to maximize the count statistics. This changed the channel energy threshold and consequently a set of fixed 'virtual' energy channels was created through interpolation for use in AE9.

A second step of angular mapping is needed to estimate a value for the locally-mirroring unidirectional flux j_{90} from the measurements made over the wide fields-of-view characteristic of the dosimeters. This was accomplished by finding the value of j_{90} which best generates the measured flux using an *a-priori* model for the local pitch angle distribution. Electron pitch-angle distributions were modeled using the work of Vampola (1996) based on the CRRES/MEA data. Proton pitch-angle distributions were taken from the CRRESPRO model (Meffert and Gussenhoven 1994) with East-West effect directionality corrections applied to the TSX5/CEASE data using the model of Lenchek and Singer (1962). For the HEO, ICO and GPS sensors the look direction of the detector was not known and therefore assumed to be random. Look direction information was available for CEASE/TSX5 and consequently a more accurate mapping to j_{90} was obtained.

After the inversion process is complete the net result for a single measurement interval is the flux amplitude j_{90} (E, K, Φ or h_{min}) where the value of K corresponds to locally mirroring particles, and E spans the range of standard energy bins where the spectral inversion is valid. Also output is the standard deviation $d \ln j$ which combines the errors of the spectral inversion and angular determination processes. Note that the uncertainty of the initial measurements (Sect. 4.3) is an input to the spectral inversion algorithm. In principle algorithms could be developed which, given knowledge of A_i and the look direction, determine j from the known count rates by simultaneously optimizing over both the E and θ coordinates. In LEO, where pitch-angle distributions can be sharply peaked, the combined inversion is very sensitive to the pitch-angle distribution models and successful implementation awaits more accurate characterization.

A different angle determination problem arises with the LANL-GEO/SOPA and MPA sensors. Though these sensors have relatively good angular resolution, the LANL-GEO satellites on which they are situated do not have magnetometers. Pitch-angle determination must be made with algorithms which exploit the asymmetries observed in the different angular bins over the course of a spin period (Chen et al. 2005; Thomsen et al. 1996). Not all LANL-GEO satellite data sets have been processed yet to yield the pitch-angle resolved data thereby limiting the data sets available for V1.0 to those listed in Table 3.

4.3 Cross-Calibration

Flux measurements exhibit considerable uncertainty due to a wide variety of effects including imperfect sensor electronics, materials degradation, contamination, inadequate calibration and error in spacecraft location, orientation and magnetic environment. Deriving an error budget for each sensor from a detailed bottom-up analysis is an impossible task in most cases. The response of key detector elements was often never measured or recorded, and detailed performance models are rare. Instead, for AE9/AP9/SPM errors were estimated using an on-orbit cross-calibration technique whereby the data from two sensors nominally measuring the same environment (a "conjunction event") were compared, the average bias determined and the residual error (after removing the bias) computed. Starting, for each

species, with a "reference sensor" deemed to be the most accurate (call this sensor A) the data from a sensor (Sensor B) cross-calibrated with A was adjusted by the bias value and the residual error in the natural log of the flux was assigned as the variance for Sensor A and Sensor B. The next sensor in the chain (Sensor C) was cross-calibrated with Sensor B, and the error assigned to Sensor C was the residual between B and C. A bias was then assigned to Sensor C equal to the product of the A-B and B-C biases so as to put the Sensor C measurements on the same level, on average, as Sensor A. Progressing through a series of conjunction events, as described below, all the sensors were compared and corrected. Data sets of j (E, K, Φ or h_{min}) with errors $d \ln j$ were derived for each sensor as inputs to the flux map process (Sect. 5.1). There were a few sensor data sets where conjunctions did not exist with other sensors, e.g. S3-3/TEL, in which case a self-calibration was performed using sequential revisits to the same region of phase space to estimate the error with no applied bias corrections. The cross-calibration technique is an extension of Friedel et al.'s (2005) method with the addition of the residual error.

Prior to this inter-comparison the sensor data was processed at the lowest level required to produce a meaningful result. Differential energy channels on one sensor were sometimes summed and interpolated to produce matches with another sensor with different energy channel values or integral response channels. Detailed pitch-angle data was spin-averaged to estimate omni-directional fluxes which were used for comparison. Channels were combined so that for a given sensor-to-sensor pairing the manipulation was done, to the extent possible, on the most accurate sensor to reconstruct the energy channel on the least accurate sensor. Dosimeter channels were compared using geometric factor approximations of the response to turn count rates into integral fluxes, rather than the more complex spectral inversion that was performed after the measurement uncertainties were estimated (Sect. 4.2).

Solar particle events (SPEs) simplify cross-calibration of the proton sensors by providing a relatively homogeneous environment in LEO, HEO, MEO and GEO, at least at high latitudes and altitudes. Conjunction events were defined as the simultaneous observation of an SPE by more than one sensor. The reference sensor was taken to be the much-studied GOES/SEM detector (GOES I-M 1996) with a correction made to the differential energy values assigned to the published channel values to better account for the monotonically decreasing spectra across the channel bins (Ginet et al. 2010). Figure 2 summarizes the cross-calibration chain for the proton data used in V1.0. Data from the sensors GOES7/SEM, GOES8/SEM, GOES11/SEM, ACE/EPAM and IMP8/CPME were crucial for SPE cross-calibration but were not used in the model since all were outside the region of trapped energetic protons. S3-3/TEL was self-calibrated since it measured the low proton energy range (~0.1–2 MeV) not adequately covered by the GOES/SEM sensor. Similar low energy coverage restrictions apply to the POLAR/IPS sensor but conveniently the ACE/EPAM sensor was available during the POLAR mission to enable cross-calibration during SPEs.

Since there does not exist the equivalent of SPEs bathing the entire high-L shell magnetosphere in a relatively uniform flux of energetic electrons for extended periods of time, the cross-calibration of the electron sensors has to be done through magnetic conjunctions (Friedel et al. 2005). Measurements from two sensors are compared when they are made in close magnetic proximity at the same time, i.e. the ΔL_m, $\Delta B/B_0$, ΔMLT and Δt between the sensors are all small, where MLT is the magnetic local time, and the conjunction occurs in a period of magnetic stability, i.e. $K_p < 2$ for an extended period of time preceding the measurement, where K_p is the planetary magnetic index. In reality, the exact values defining the small Δ criteria have to be adjusted on a case-by-case basis in order to maintain a statistically significant number of comparison points. Typical values chosen were $\Delta L_m < 0.1$, $\Delta B/B_0 < 0.1$ and $\Delta t < 4$ hours with measurements made between 4:00

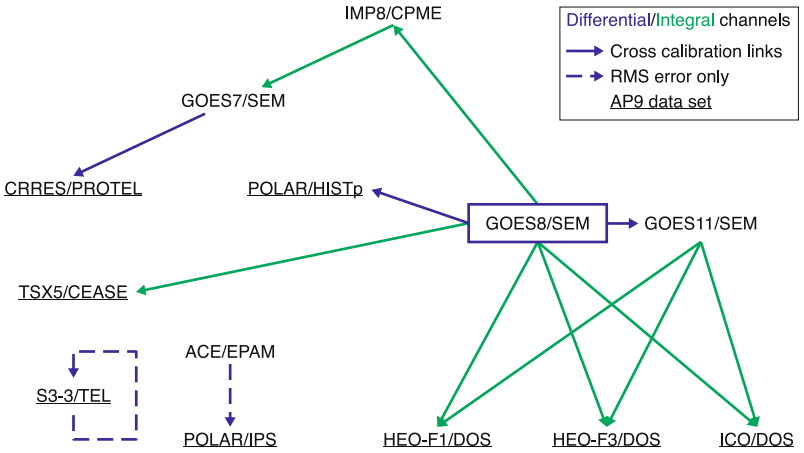

Fig. 2 Cross-calibration chain for the proton data sets in AP9. The *blue box* encloses the reference satellite/sensor data set, while satellite/sensor data sets included in the model are underlined. *Solid blue* and *green lines* are differential and integral channel comparisons, respectively, and *dotted lines* represent RMS error determination only

< MLT < 8:00 (dawn) or 16:00 < MLT < 20:00 (dusk) with $K_p < 2$ for the prior 48 hours. The reference sensor was taken to be the combined CRRES/HEEF and CRRES/MEA data set given its broad L-shell coverage and the extensive work that has been done trying to understand the response and correct for contamination (Sect. 4.1). Figure 3 shows the chain of calibration employed in V1.0 for the energetic electron sensors. The choice of conjunctions is not unique in that a single satellite could have conjunctions with several others. In these cases the conjunctions having the most points were used, which were usually the ones giving the best agreement over the entire spectrum. SAMPEX/PET was self-calibrated because even though there were conjunction events with TSX5/CEASE, SAMPEX/PET was a much more accurate sensor requiring no error-inducing spectral inversion.

The cross-calibration chains for plasma ions and electrons are illustrated in Fig. 4. No bias corrections were applied since the observed differences between LANL-GEO/MPA series were small and the residuals between the POLAR sensors and LANL-GEO/MPA were much larger than the bias. Two versions of the POLAR/CAMMICE/MICS data were used, the first from Roeder et al. (2005) and the second from Niehof (2011). Different processing methods were used which yielded flux estimates that were not always in agreement. Since it was not clear which method was superior, both data sets were used as independent inputs to the flux map building routine (Sect. 5.1) where the bootstrapping algorithm melded the uncertainties.

5 Architecture

5.1 Flux Maps

Underlying AE9/AP9/SPM is a set of empirical flux maps constructed from the collection of multi-satellite differential flux measurements cleaned, cross-calibrated and sorted into reference grid bins as described in the previous sections. Maps are made for two statistical quantities: the 50th (median) and 95th percentile flux values in each reference grid bin, hereafter

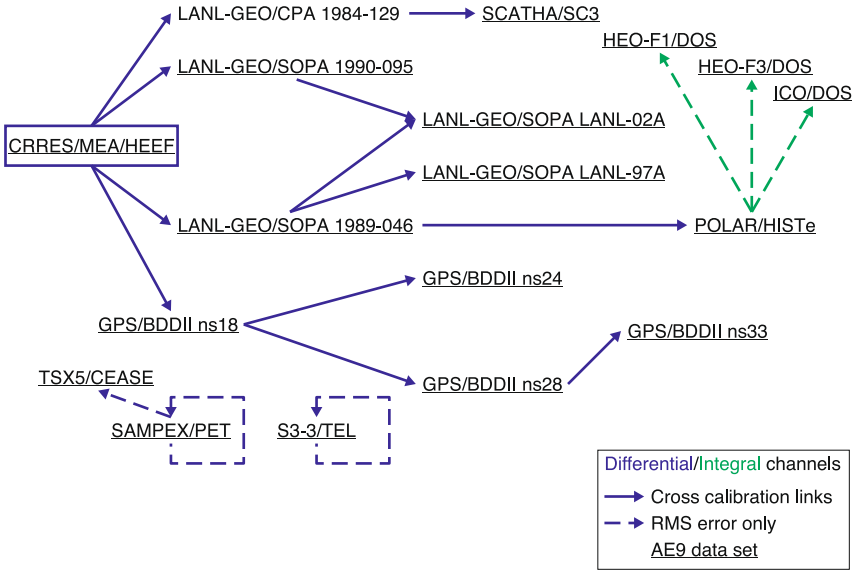

Fig. 3 Cross-calibration chain for the electron data sets in AE9. See Fig. 2 caption for a description

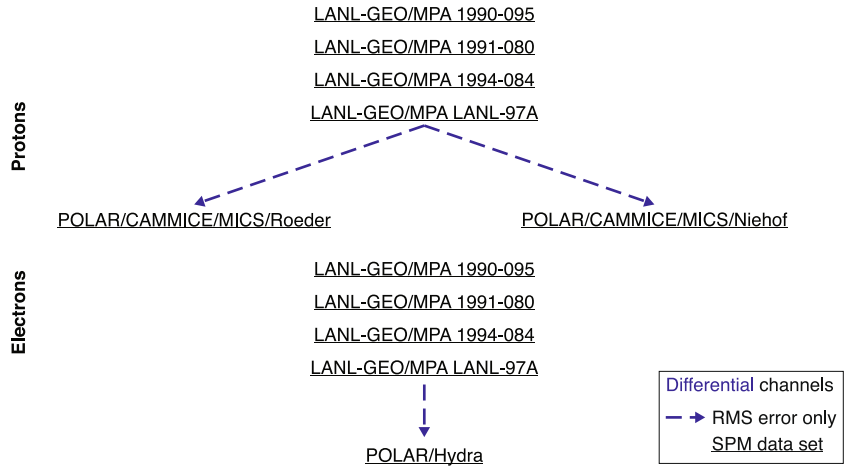

Fig. 4 Cross-calibration chain for the plasma data sets in SPM. See Fig. 2 caption for a description

labeled $m50$ and $m95$, respectively, or together as the vector $\underline{\theta} = (m50, m95)$. An estimate of the uncertainty $\delta\underline{\theta}$ in each bin is also made. The map generation procedure is illustrated on the left-hand side of Fig. 5 and described in some detail in Appendix B. Both uncertainty in measurement and space weather give rise to the spread of the distribution as quantified by $\underline{\theta}$. Even if the measurements were perfect there would still be a difference between $m95$ and $m50$ due to the natural variations caused by geomagnetic storms, atmospheric heating, co-rotating interaction regions, and other space weather effects over the course of the solar cycle. These variations are implicitly captured in the model by independently tracking flux values corresponding to these two percentiles.

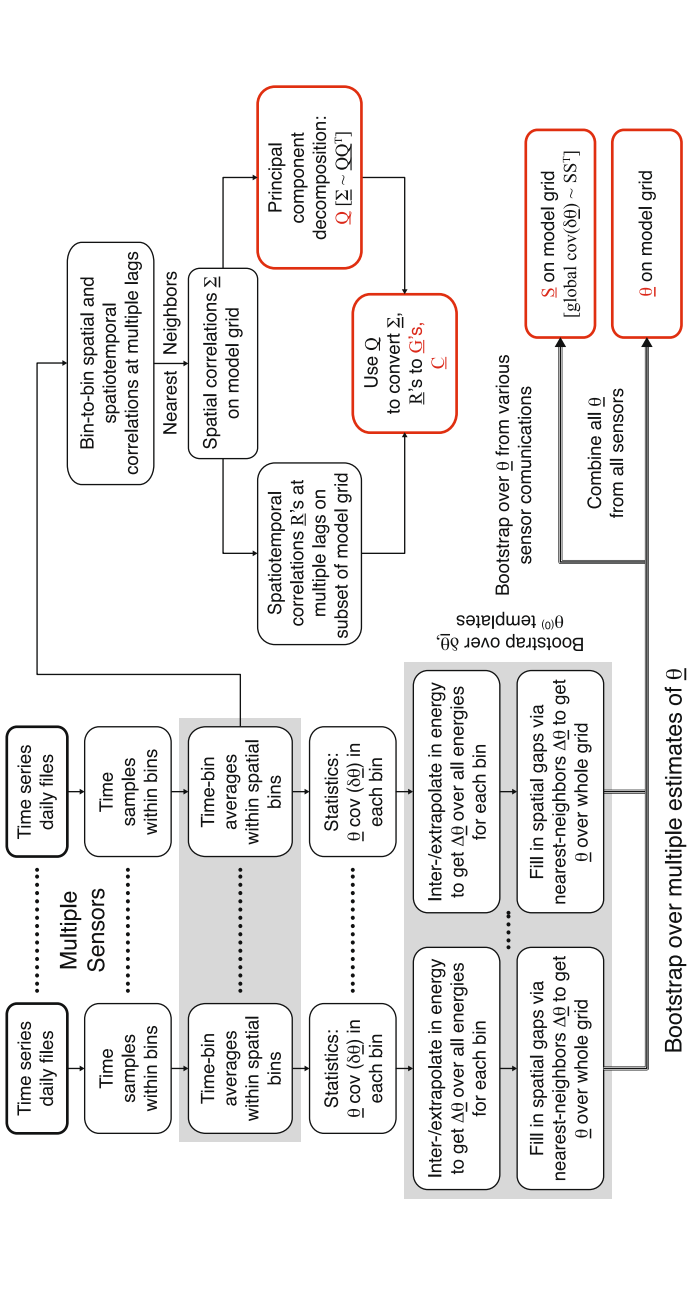

Fig. 5 Schematic of the processes for building the flux map (*left side*) and spatiotemporal covariance matrices (*right side*). See Sect. 5 and Appendix B for details

Table 4 Sources for templates used in developing AE9, AP9, and SPM

AE9	AP9	SPM
• AE8 profiles • CRRES/MEA + HEEF	• S3-3/TEL + CRRES/PROTEL + TSX5/CEASE ($K - h_{min}$ grid) • POLAR/IPS + CRRES/PROTEL + TSX5/CEASE ($K - \Phi$ grid)	• POLAR/CAMMICE/ROEDER + POLAR/CAMMICE/NIEHOF data (ions) • Milillo model (Milillo et al. 2001) (ions) • POLAR/HYDRA (electrons)

Two elements are crucial for map building: bootstrapping and gap-filling. The former process is a well-established technique whereby statistical quantities (e.g. $\underline{\theta}$) are computed by re-sampling with replacement from the observed sample (e.g. Efron and Tibshirani 1993). Besides an estimate for the quantity itself, bootstrapping provides an estimate for the standard deviation of the quantity (e.g. $\delta\underline{\theta}$) and is very useful in "rolling up" uncertainties at lower levels of the analysis (e.g. uncertainties in the flux values, interpolation algorithms, etc.) when applied properly.

For the gap-filling process a template technique is employed. Templates are defined as *a-priori* estimates of the shape of the $\underline{\theta}$ dependence on the model coordinates derived from the examination of data sets, physics-based modeling and the judgment of an experienced space physicist. There is not a single best template for each species, rather, there are a variety of templates characterizing different dynamic states of the radiation belts. As an extreme example, the distributions of energetic protons and electrons in the slot region look much different before and after the March 1991 geomagnetic storm (Brautigam et al. 1992; Gussenhoven et al. 1993). In V1.0 a number of templates were created by team members based on different combinations of data sets and models as summarized in Table 4. Full reference grid maps for each satellite data set are obtained by using the templates and applying bootstrapping techniques (Appendix B) to capture both the uncertainty in the measurements and that arising from non-unique templates. Templates are very much an art involving data, experience and intuition. More diverse and hopefully accurate templates can easily be accommodated in future builds of the model.

Transforming the maps of the percentile values and associated uncertainties into maps of flux j and uncertainty $d \ln j$ requires the choice of a two-parameter distribution function for each species. Examination of the data from some of the higher resolution sensors (e.g. CRRES/HEEF, CRRES/PROTEL and LANL/MPA) indicates that the Weibull distribution (O'Brien and Guild 2010) is a reasonable choice for the electrons and the lognormal distribution (Evans et al. 2000) is satisfactory for the energetic protons and plasmas. Armed with the functional form of the distribution function the values of ($m50$, $m95$) in each reference grid bin can be readily translated into a distribution of j. At this point the model already provides a capability to the user superior to existing models: a map of the flux distribution on the reference grid with an estimate of measurement and mapping uncertainties. Many recalculations of the j distribution using values of $\underline{\theta}$ randomly perturbed by a small amount consist with the deviation $\delta\underline{\theta}$ provide estimates of the uncertainty in j, or any quantity computable from j, arising from the imperfect measurements, data processing and mapping processes.

5.2 Time Evolution

To model variations of the flux on time scales less than a solar cycle an auto-regressive time-evolution model has been developed. The dynamics are governed by the relation,

$$\mathbf{q}(t) = \sum_{k=1}^{N_G} \mathbf{G}_k \mathbf{q}(t - \tau_k) + \mathbf{C}\boldsymbol{\eta}(t), \tag{7}$$

where $\mathbf{q}$ represents the principal component amplitudes of the spatial variation of the flux over the reference grid, $\mathbf{G}_k$ is the time evolution matrix defined for $k = 1$ to N_G specific time lags τ_k and $\mathbf{C}$ is the "innovation" term allocating the white-noise driver to the principal components. The right-hand side of Fig. 5 schematically illustrates how the aforementioned vectors and matrices are constructed from the satellite flux data and Appendix B delves into the details. Suffice it to say that a map of the flux j at time t on the reference grid is uniquely determined by the principal component $\mathbf{q}(t)$, the values of the percentile flux map $\underline{\theta}$ and the choice of distribution function. A random but statistically realistic time-history of flux can be generated from Eq. (7) by choosing a random number seed at $t = 0$ which generates the initial principal component amplitudes $\mathbf{q}(0)$ and the percentile parameters $\underline{\theta}$ constrained by the uncertainty $\delta\underline{\theta}$.

For AE9 $N_G = 6$ and for AP9 $N_G = 4$ with the time lags chosen to be 1 day (electrons only), 1 week, 2 weeks (electrons only), 27 days, 6 months and 1 year, i.e. values that capture geomagnetic storm (albeit at low-resolution), solar rotation, seasonal and solar cycle space weather variations. There is no solar-cycle phase dependence in the model, i.e. statistics are computed from all of the data sets independent of phase. The reasoning behind this is (a) missions often last longer than a solar cycle, (b) launch dates are often uncertain in the design phase and (c) solar activity is notoriously unpredictable on solar-cycle time scales. It would simply not be prudent for an engineer to design to a particular phase of the solar cycle. As mentioned in Sect. 3, the plasma models do not contain a dynamic component because an adequate description involves time scales (minutes) and spatial coordinates (MLT) requiring a more sophisticated analysis than undertaken for V1.0.

5.3 Application

The primary functionality of AE9/AP9/SPM is a "fly-in" software function. A user inputs the satellite ephemeris, energy range of interest, model selection and "specification mode" and is returned a time series of the flux values for the requested energy channels along the orbit. There are three specification modes delineated by the method by which the flux values are determined in each coordinate bin along the orbit: (a) mean—using only the average values for $\underline{\theta}$ to compute the mean flux in each reference grid bin; (b) perturbed mean—using the average $\underline{\theta}$ plus a random perturbation consistent with $\delta\underline{\theta}$ to compute the mean flux in each bin and (c) full Monte-Carlo using the autoregressive time-evolution model with a random initial condition $\mathbf{q}$ and perturbed $\underline{\theta}$ for flux conversion. The mean fly-in mode captures the mean behavior of the model with no uncertainty added while the perturbed mean adds the uncertainty in the flux maps due to measurement and gap-filling errors. A full Monte-Carlo run contains all of the perturbed mean uncertainty plus an estimate of the dynamic variations due to space weather processes.

Meaningful information on average or worst cases fluxes and percentile levels can be derived from multiple applications of the fly-in routines in either perturbed mean or Monte-Carlo mode. By aggregating the results of a large number of mission scenarios, each scenario run with the same ephemeris but with a different random number seed, the percentile flux

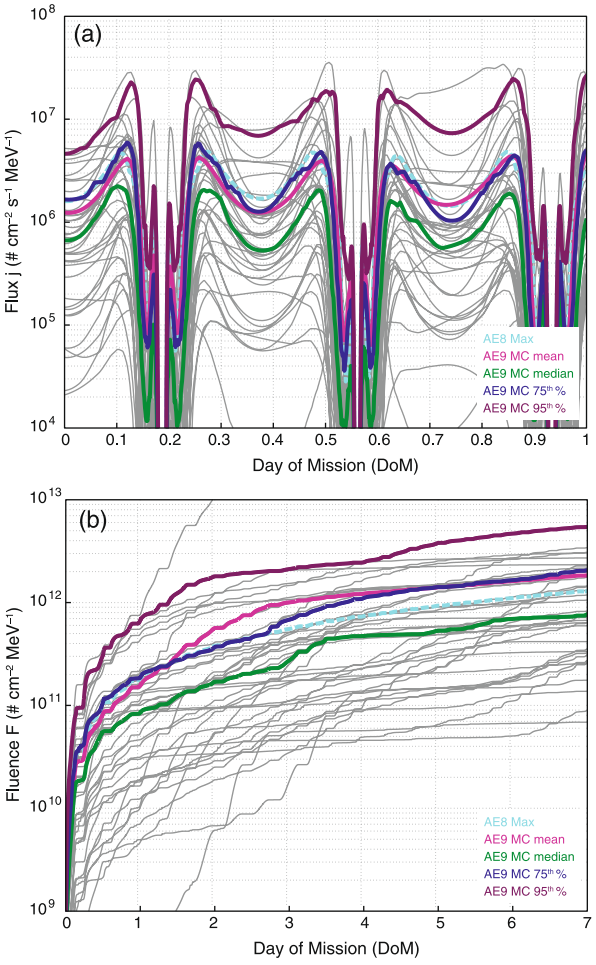

Fig. 6 Flux profiles of >1 MeV electrons from AE9. *Light grey lines* are individual MC scenarios and the mean, median, 75th and 95th percentile aggregates are the *pink*, *green*, *blue* and *maroon lines*, respectively. AE8 MAX as shown as the *light blue dotted line*

levels of any quantity derivable from the flux spectrum, e.g. fluence (time integrated flux) or total dose, can now be specified in terms of probabilities of occurrence during the course of the mission. Dose calculations require, of course, a code such as SHIELDOSE-2 (Seltzer 1994) that takes flux as input and outputs energy deposited in various materials behind user-defined Aluminum shielding thicknesses. An example of aggregation is given in Fig. 6 where the time profiles of the 1 MeV electron flux and fluence as output by AE9 are plotted for 40 Monte-Carlo scenarios (grey lines) run for a geosynchronous transfer orbit. The aggregated mean (pink), median (green), 75th percentile (blue) and 95th percentile (maroon) are shown as well as the output from AE8 MAX (light blue) for comparison. More examples will be discussed in Sect. 5.

The fly-in function in V1.0 is provided by a C++ object with wrappers available in C and Fortran. An application tool has also been built by the AE9/AP9/SPM team which provides an orbit propagator, scenario generator and aggregator for sets of perturbed mean and Monte-Carlo runs. It is accessible by both a command line and graphical user interface. Output is in the form of simple plot and text files. The SHIELDOSE-2 application is included as well as the historical AE8/AP8 (Sawyer and Vette 1976; Vette 1991b),

Table 5 Computer runtimes for AP9/AE9/SPM V1.0 in mean, perturbed mean (40 scenarios) and Monte-Carlo (40 scenarios) modes covering different orbit regimes. Benchmarks were done on a standard desktop 3.4 GHz Intel Core i7-2600 CPU

		Run time (minutes)					
		1 day mission			1 year mission		
Orbit	Time step (sec)	Mean	Pert. Mean (40 Scenarios)	Monte-Carlo (40 scenarios)	Mean	Pert. Mean (40 Scenarios)	Monte-Carlo (40 Scenarios)
GEO	3600	6.7E−03	1.7E−02	1.4E−01	2.5E+00	6.2E+00	4.9E+01
MEO	300	8.1E−02	2.0E−01	1.6E+00	3.0E+01	7.4E+01	5.9E+02
HEO	60	4.0E−01	1.0E+00	8.1E+00	1.5E+02	3.7E+02	3.0E+03
LEO	10	2.4E+00	6.1E+00	4.9E+01	8.9E+02	2.2E+03	1.8E+04

CRRESELE (Brautigam and Bell 1995), CRRESPRO (Meffert and Gussenhoven 1994) and CAMMICE/MICS (Roeder et al. 2005) models. Plans are underway to ultimately host the project on an open source repository to facilitate broad collaboration.

6 Verification and Validation

Verification and validation are essential for any model aspiring to be an engineering application. That is, the model must run according to design and produce results consistent with independent data. These steps are especially important for AE9/AP9/SPM given the uniqueness and complexity of the algorithms and the diversity of the data sets.

With any Monte-Carlo (MC) type model, the statistics always improve with the number of runs performed. In testing V1.0 each perturbed mean or MC demonstration consists of 40 scenarios. Though somewhat arbitrary, this number is computationally realizable (see below) and dictates that the scenario with the 2nd largest magnitude defines the 95th percentile. The primary test suite runs the full set of models AE9, AP9, SPMH, SPMHE, SPMO and SPME in mean, perturbed mean and MC (where applicable) modes for 8 different orbits to include 3 in LEO (400 km, 800 km and 1200 km, circular, 90° inclination), GTO (500 km × 30600 km, 10° inclination), HEO (1475 km × 38900 km, 63.4° inclination), MEO (3900 km × 14100 km, 120° inclination), GPS (20200 km, circular, 55.0° inclination) and GEO (35786 km, circular, 0° inclination). The mission time was taken to be one week, certainly shorter than a typical real-world mission but long enough to observe the dynamic effects in the model. Several examples from the test suite will be presented in Sect. 6.1 and compared with historical data. Other runs were done for much longer periods and are compared to data in Sect. 6.2. As might be expected, execution of the test suite uncovered a number of data set and algorithm issues, many which have been fixed but some which have not (Sect. 7).

As might be expected, the full Monte-Carlo execution of many AP9 and AE9 scenarios for multi-year missions in certain orbits can lead to fairly large computational times. Table 5 displays a representative set of computer run times for V1.0 in various modes derived from the test suite and benchmarked on a typical high-end desktop computer circa 2011 (specifically one with a 3.40 GHz Intel Core i7-2600 CPU). The time steps were chosen to ensure that the spatial structures and temporal variation of the belts in each orbit regime are adequately sampled. Time steps larger than these risk undersampling the flux spatial structure. Summarizing the far right-hand column in units of hours and days a 1 year mission at

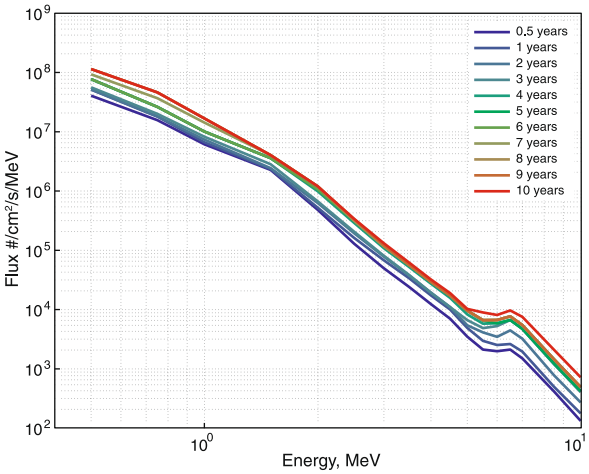

Fig. 7 Spectra of the 95th percentile 24 hour averaged electron flux along a HEO orbit for different mission simulation periods ranging from 0.5–10 years (see key). All simulations comprised 40 MC runs

GEO, MEO, HEO and LEO can be run in 0.8 h, 10 h, 2.1 days and 12.8 days, respectively. Run times can be large, especially when considering a 10 year mission in LEO, but the MC processing can easily be split onto a large number of machines. Unfortunately, a 10 year mission does have to be simulated for the full 10 years because the 11-year solar cycle driving space weather imparts substantial dynamical variations on long time scales and these are statistically captured in the model. Figure 7 illustrates this by showing a spectrum of the 95th percentile, one-hour averaged electron flux along a HEO orbit computed for mission durations ranging from 0.5–10 years with 40 MC scenarios for each mission. Worst case values (e.g. the 95th percentile of the 24 hour average) do not necessarily converge, even after 10 years, but long term averages (not shown) do converge to the perturbed mean.

6.1 Comparison to Models

Outputs from the AE9 Monte-Carlo (MC) runs at GEO are shown in Fig. 8 to include a time history of the 2 MeV flux (Fig. 8a) over the course of 2 days, a time history of the 2 MeV fluence over the course of 7 days (Fig. 8b), the 7 day fluence spectra for the AE9 mean with output from historical models (Fig. 8c) and the 7 day fluence spectra for the entire set of MC scenarios (Fig. 8d). In Figs. 8a, 8b and 8d each grey curve represents one of the 40 MC scenarios and the pink, green, blue and maroon curves represent the aggregated mean, median, 75th and 95th percentile, respectively. The AE8 MAX prediction is shown as the dotted light-blue curves in all panels of Fig. 8. Predictions from the CRRESELE average model (Brautigam and Bell 1995) and the combination of the LANL-2007 plasma model (Thomsen et al. 2007) and the IGE-2006 energetic electron model (Sicard-Piet et al. 2008) are shown in Fig. 8c.

It is clear that AE9 indicates significant uncertainty in the levels of energetic electrons at GEO as demonstrated by the wide spread in the MC scenario runs. This is not surprising, since this population is known to be highly variable at GEO, existing at the whim of dynamic processes in the plasma sheet and the impact of high-speed solar wind streams. The amplitude of the spectra for the AE9 mean is often higher than the historic models (Fig. 8c) though the median value is in closer agreement and all the models are within the uncertainty of the 40 MC scenarios (Fig. 8d). There can also be differences between the historical models of similar or greater magnitude than their disagreement with AE9.

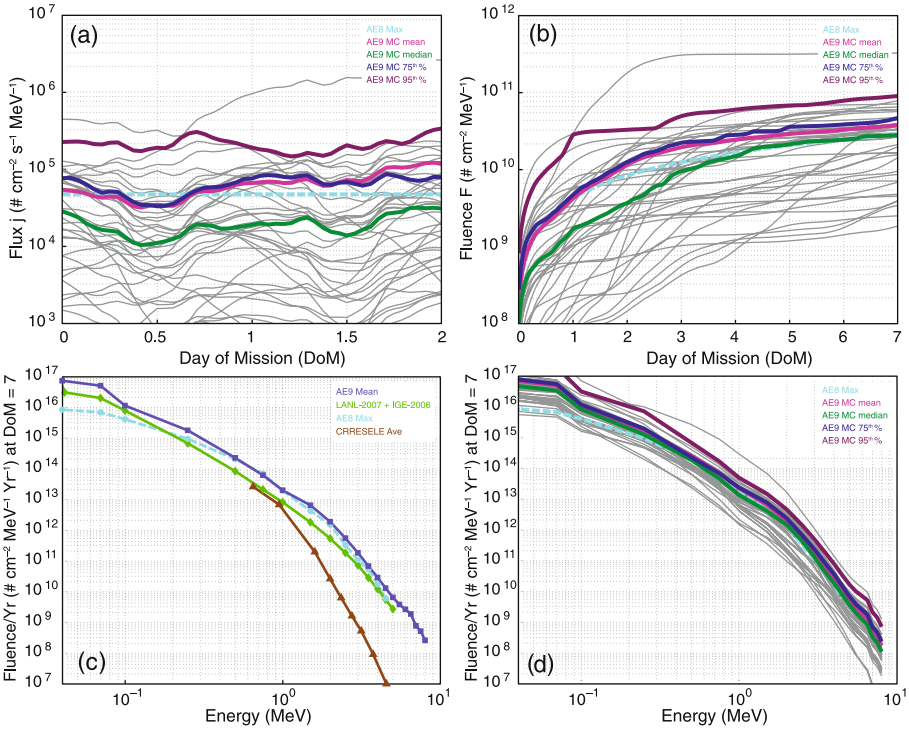

Fig. 8 Flux (**a**) and fluence (**b**) histories of >2 MeV electrons in GEO from AE9. *Light grey lines* are individual MC scenarios and the mean, median, 75th and 95th percentile aggregates are the *pink*, *green*, *blue* and *maroon lines*, respectively. Output from AE8 MAX is shown as the *light blue dotted line*. Shown in (**c**) is the fluence spectra after 7 days from the AE9 median (*dark blue*), AE8 MAX (*light blue*), CRRESELE Average (*brown*) and the LANL-2007—IGE (*green*) models. The full set of 7 day MC fluence spectra is shown in (**d**) with the same color convention as (**a**)

Figure 9 shows time series and spectra relevant to 20 MeV protons for the 800 km LEO orbit as specified by AP9. The format is the same as in Fig. 8 but the comparison models are now AP8 MAX and CRRESPRO Active (Meffert and Gussenhoven 1994) and the span of the flux time series is limited to 0.2 days to better observe the passage through the South Atlantic Anomaly (SAA). Values of the AP9 mean are well above AP8 and closer to CRRESPRO except at the highest energies. Both historical models are within the 40 MC scenario uncertainty except for energies greater than ∼25–40 MeV where CRRESPRO is smaller and AP8 is larger than AP9. The tendency for AP8 to predict lower proton fluxes than what is measured in LEO has been noted previously (e.g. Huston 2002; Ginet et al. 2007).

The results of running the SPMH model for a GPS orbit are shown in Fig. 10 using the same format as Fig. 8 but with a 1 day duration for the flux versus time profile. Here CAMMICE/MICS (Roeder et al. 2005) is the historical model for comparison. The fluence spectra of CAMMICE/MICS is 2–3 times smaller than the SPMH mean (Fig. 10c) and does not appear to be within the uncertainty. However, in the data reduction process the error in SPMH has been clamped to a relatively small value to eliminate the unrealistically large swings in spectral shape that were manifest if the empirical uncertainties were used. Such large empirical uncertainties and the necessity to artificially suppress them should disappear

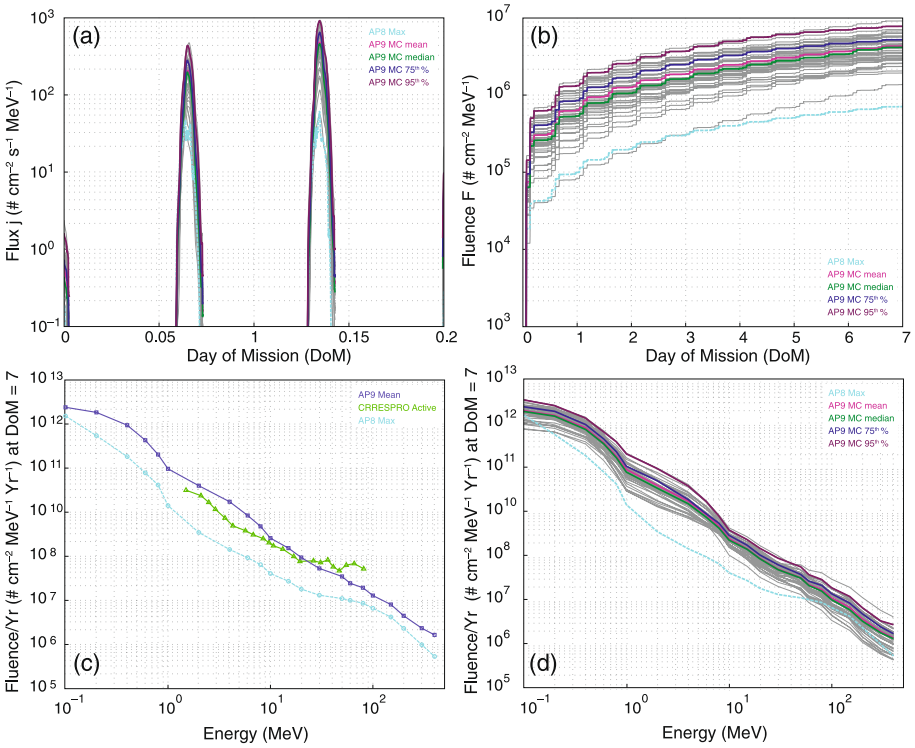

Fig. 9 Flux (**a**) and fluence (**b**) histories of >20 MeV protons in LEO (800 km) from AP9. See Fig. 8 caption for the color convention. AP8 MAX model predictions are shown as the *light blue dotted line*. Shown in (**c**) is the fluence spectra after 7 days from the AP9 median (*dark blue*), AP8 MAX (*light blue*), and the CRRESPRO Active (*green*) models. The full set of 7 day MC fluence spectra is shown in (**d**) with the same color convention as (**a**)

when a larger quantity of data is used in future versions. Including an MLT dependence should also improve accuracy.

6.2 Comparison to Data

Validating AE9/AP9/SPM with independent measurements is a challenge because good data in the radiation belts are scarce and the temptation to include it all in the model is strong. Nevertheless, the temptation was resisted and several data sets were excluded to serve as a check on the final V1.0 product. Data cleaning and cross-calibration of the type discussed in Sect. 4 were not performed on the validation data and the nominal energy channels and geometric factors available publicly or from the instrument Principal Investigators were used without modification. Consequently, comparison of the model predictions to the observations presented in this section should be taken with a grain of salt—the model is certainly not perfect but the data are imperfect as well. Similar to the test suite and model-to-model comparisons, the validation served its purpose by uncovering a number of issues in preliminary versions of AE9/AP9/SPM.

The primary comparisons for AP9 were made with data from the POES/SEM sensor (Evans and Greer 2004). The POES satellites fly in an ∼815 km, circular, 98° inclination

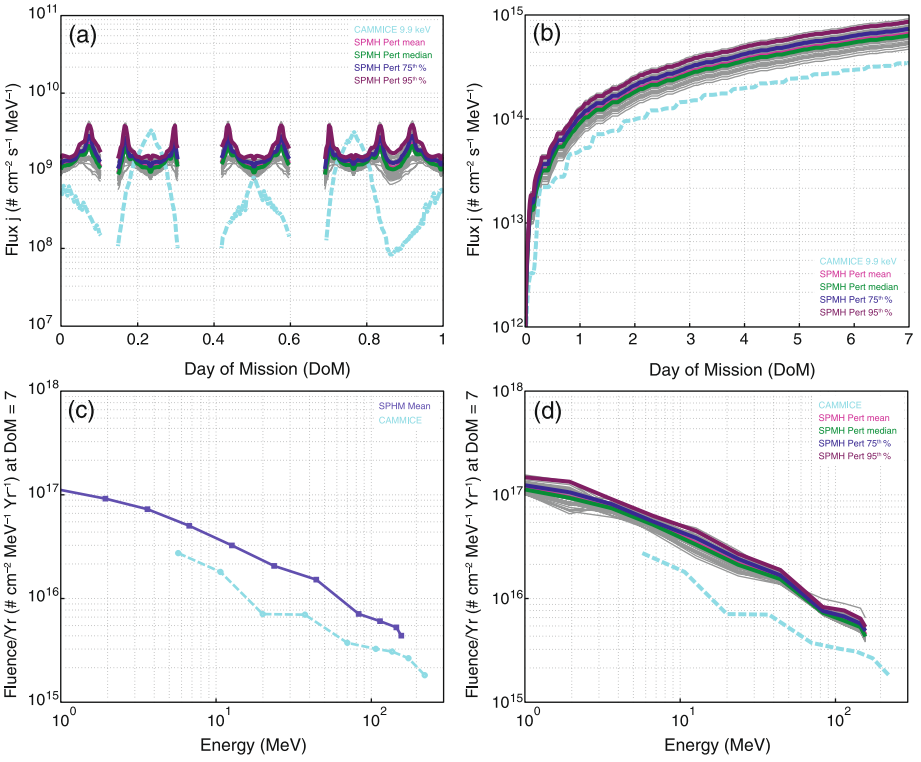

Fig. 10 Flux (**a**) and fluence (**b**) histories of 11.55 keV hydrogen in a GPS orbit from SPMH. See Fig. 8 caption for the color convention. CAMMICE/MICS predictions are shown as the *light blue dotted line*. Shown in (**c**) is the fluence spectra after 7 days from the SPMH median (*dark blue*) and CAMMICE/MICS model (*light blue*). The full set of 7 day MC fluence spectra is shown in (**d**) with the same color convention as (**a**)

orbit and the constellation has been operational since 1978. Data from POES N15 in the 13 year interval from Jul 1998–Dec 2011 were used as illustrated in Fig. 11 showing the >36 MeV channel data in the form of latitude-longitude maps for the median (Fig. 11a) and 95th percentile (Fig. 11c) flux values. Figures 11b and 11d show the corresponding AP9 median and 95th percentile maps, respectively, computed for a 3.5 year interval with 40 MC runs. Computer runtime restrictions precluded a direct 13 year AP9 simulation with 40 MC runs. Agreement is reasonable both in location and intensity with the POES data tending to be somewhat more intense. This can be seen in Fig. 12 where the >36 MeV fluence for each year of the POES data is plotted against one year of AP9 output. Most of the POES curves are between the median and 95th percentile of AP9, and the AP9 median is above the AP8 MIN curve as discussed previously.

AE9 electron flux predictions in LEO were compared to the data from the IDP sensor on the DEMETER satellite which flew in a 660 km, circular, 98° orbit during the period Jan 2005–Dec 2010 (Sauvaud et al. 2006). Figure 13 contains maps of the median and 95th percentile >0.322 MeV electron flux as measured by the DEMETER/IDP over 6 years (Figs. 13a and 13c) and computed from 40 MC AE9 runs for 1 year (Figs. 13b and 13d). The similarity of the general morphology of the SAA and the outer belt horns is comforting but there are some substantial differences. For example, AE9 underpredicts the median in and around the SAA, it overpredicts the 95th percentile in the same areas and it does not

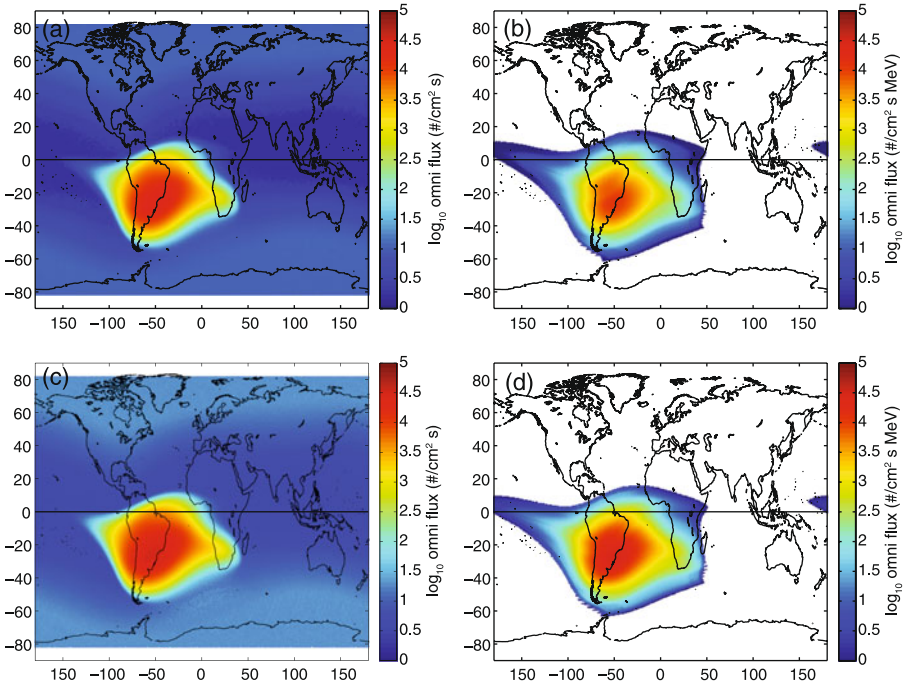

Fig. 11 Median (**a**) and 95th percentile (**c**) >36 MeV flux maps constructed from 13 years of POES N15/SEM data. Similar median (**b**) and 95th percentile maps (**d**) determined from 40 MC AP9 scenarios of 3.5 years duration each

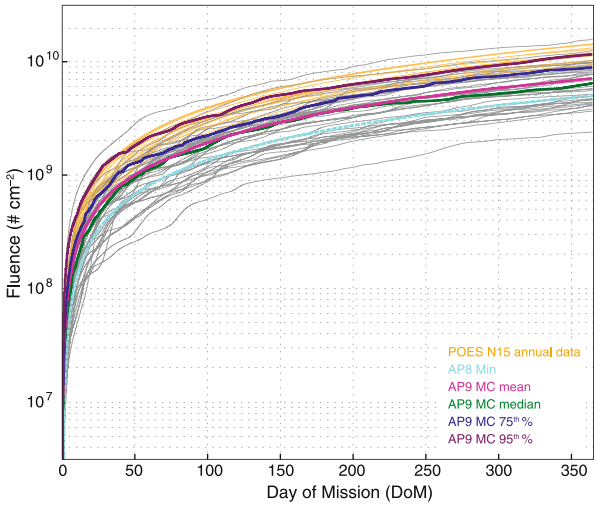

Fig. 12 One year >36 MeV fluence profiles from each of the 13 years of POES/SEM data (*tan lines*) compared to AP9 aggregate predictions and 40 MC scenarios (see Fig. 8 for color code). AP8 MIN is the *light blue line*

capture some of the 95th percentile activity in the slot regions. Indeed, AE9 suffers from a lack of electron data near the SAA manifesting itself though interpolation with templates inspired by CRRES/HEEF/MEA data with TSX5/CEASE and HEO/DOS data at higher (K, Φ) and lower h_{min} values. Comparing DEMETER/IDP higher energy channels to AE9

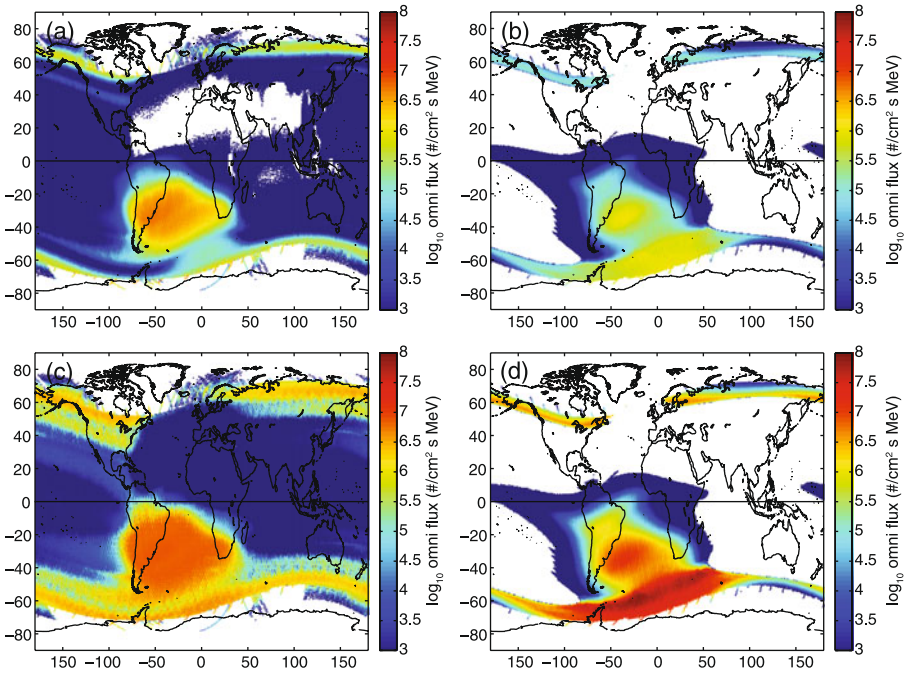

Fig. 13 Median (**a**) and 95th percentile (**c**) >0.322 MeV flux maps determined from 6 years of DEMETER/IDP data. Similar median (**b**) and 95th percentile maps (**d**) determined from 40 MC AE9 scenarios each run for 3.5 years

the differences are most apparent in the energy range <700 keV and decrease in magnitude with increasing energy.

The differences are also apparent in the one-year (2005) fluence plot of Fig. 14 where DEMETER/IDP data is compared to AE9 aggregates and AE8 MAX for a >300 MeV equivalent channel estimated by interpolating the IDP >0.322 MeV and >0.108 MeV native channels. Channel interpolation was done to match the >0.300 keV electron channel on the POESN15/SEM which is also shown in Fig. 14. DEMETER/IDP is above the 95th AE9 percentile level while the POES/SEM is near the mean. However, though at a higher altitude of 800 km the POES/SEM fluences are *less* than DEMETER, indicating a large uncertainty in one or both data sets. With contamination always an issue in the proton-rich SAA and detector fields-of-view an issue for pitch-angle distributions peaked near 90° local (Rodger et al. 2010) it is not surprising that in the absence of detailed response function level analysis the data sets do not agree.

At geosynchronous orbit the time step restrictions on AE9/AP9/SPM are relaxed and it is possible to quickly run extended missions. Figure 15 compares AE9 electron fluence over a period of 8.5 years starting in Aug 2001 to measurements from the CEASE sensor on the DSP21 satellite for the >0.37 MeV (Fig. 15a), >1.51 MeV (Fig. 15b) and >2.02 MeV (Fig. 15c). The CEASE sensor is nearly identical to the one flown on TSX5 used in AE9 and has been well studied (Brautigam et al. 2006). Periods of intense solar proton events, a source of contamination, were removed when integrating both the model and data fluxes. Shown in Fig. 15d is the output from the GOES/SEM >2 MeV channel for a period of 10 years starting in Jul 1998 compared to AE9 fluence predictions. Over the nearly solar-cycle length time period, the flux integral over time (= fluence) averages out the dynam-

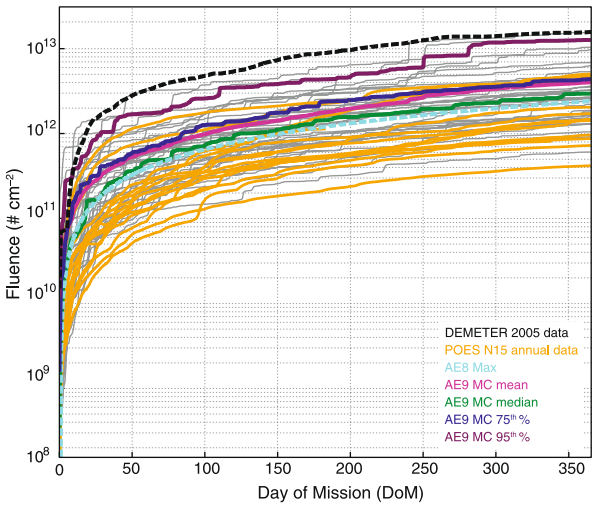

Fig. 14 One year >0.3 MeV fluence profiles from the POESN15/SEM data (*tan lines*) compared to AE9 aggregate predictions and 40 MC scenarios (see Fig. 8 for color code). AE8 MAX is the *light blue curve*. DEMETER/IDP data is also shown (*dotted brown line*), albeit measured at a lower altitude

ical variations and the data converges to close to the AE9 median for all channels but the CEASE/DSP21 >1.51 MeV channel, where it is close to the 95th level. Not surprisingly the dip in both the CEASE/DSP21 data observed prior to year 2 and the dip in the GOES/SEM data prior to year 7 represent the relatively weak electron environment at GEO during the maximum of Solar Cycle 23 prior to the large buildup on the downside of the solar cycle.

7 Summary

The AE9/AP9/SPM V1.0 suite of models represents a transformational approach to specifying the radiation environment for modern satellite design applications. Uncertainties in the model predictions are explicitly included yielding a capability to generate arbitrary percentile flux levels (e.g. mean, median, 95th percentile) from either perturbed mean maps capturing mostly the sensor and data reduction uncertainties, or the full Monte-Carlo autoregressive scheme capturing the statistical space weather variations as well. Included in V1.0 are novel statistical algorithms, spectral inversion techniques, multiple coordinates systems and a diverse set of satellite data cleaned and cross-calibrated to the extent realistically achievable given the development program's finite resources and schedule. Hopefully, the architectural and operational details outlined in this paper are all "under the hood" as far as the design engineer is concerned. Running V1.0 as part of a radiation effects analysis produces a probabilistic assessment that can be traded off at the system level with other bus, payload and mission risks. To a design engineer uncertainty in the environment specification is just uncertainty whether it is rooted in imperfect sensors, interpolation algorithms or the dynamic environment.

There are a number of known issues in the model and, most certainly, issues that have yet to be uncovered. Below is a summary of the major issues, some of which have been previously mentioned:

- There are no reliable data for inner zone electrons at lower energy (<∼600 keV). Spectral and spatial extrapolation of the existing data set can lead to large deviations (e.g., comparison to POES and DEMETER data). However, the problem appears to be no worse than in AE8.

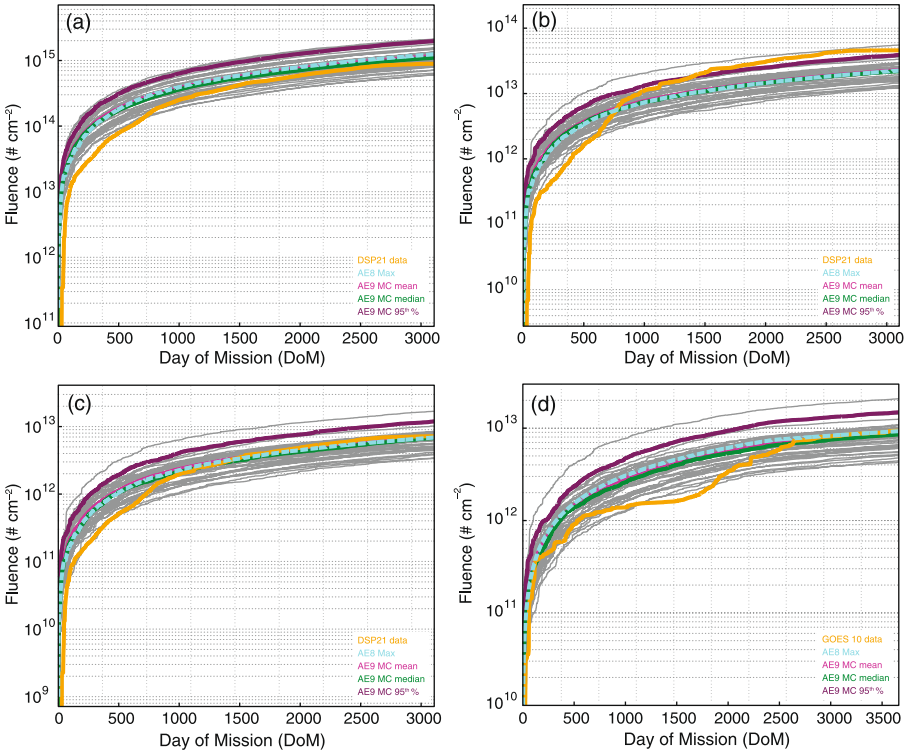

Fig. 15 Fluence vs time profiles as measured by DSP21/CEASE in GEO over 8.5 years in the (**a**) >0.37 MeV, (**b**) >1.51 MeV and (**c**) >2.02 MeV channels (*tan lines*) compared to AE9 aggregate predictions and 40 MC scenarios (see Fig. 8 for color code). Panel (**d**) shows a similar comparison using the >2 MeV measurements from GOES10/SEM over 10 years

- There are no data for high energy protons (>∼200 MeV). AP9 goes out to 400 MeV using a physics-based model extrapolation. Lack of high-energy proton data, a regime especially affecting on-board electronics, is the primary reason for flying the Relativistic Proton Spectrometer (RPS) on the Van Allen Probes (Mazur et al. 2012).
- SPMH (plasma hydrogen), SPMHE (plasma helium), SPMO (plasma oxygen) and SPME (plasma electron) models have small error bars which do not adequately reflect the uncertainty in the measurements. There were limited data and spectral smoothness was imposed at the expense of reducing the error bar.
- Errors in the primary flux map variables $m50$ (log 50th percentile) and $m95'$ (log 95th–50th percentile) were capped at factors of 100 (electrons) and 10 (protons). Large variations in these quantities can quickly lead to obviously unrealistic variations in fluxes derived from our assumed non-Gaussian Weibull and lognormal distributions. This capping does not limit the representation of space weather variation which is captured in $m95'$ and the spatiotemporal covariance matrices.
- Run times are slow for large numbers of MC runs, especially for LEO.

To resolve many of these issues and to improve the overall accuracy of the model more data are crucial. The architecture of AE9/AP9/SPM allows for easy incorporation of new data. All that is required is a cleaned, unidirectional differential flux (j) data set mapped to the model coordinates along the satellite ephemeris, with an estimate of measurement error ($d \ln j$).

The error can be determined by direct observation and modeling of detector performance or by cross-calibration. This new data set becomes just another element of the collection of all data sets on which the automated process building the flux maps and covariance matrices (denoted together as the "runtime tables") operates. Much hope is riding on the NASA Van Allen Probe mission to provide a rich set of energetic particle and plasma data from the many well-calibrated instruments of good pitch angle and energy resolution. With two satellites in a GTO orbit slated for 2–4 years of operation the coordinate coverage should be excellent. Van Allen Probe data will be used first to validate the performance of V1.0 before being incorporated into a new version of the model.

Even with the planned future data sets there will always be a need for templates (Sect. 5) to extrapolate and interpolate the data across spectral and spatial coverage gaps. Significant effort went into building the templates (Table 4) used in AE9/AP9/SPM but they are by no means unique. Additional templates based on both empirical and physics-based analysis are needed and can be easily integrated into the flux map bootstrap construction process.

The model is also fundamentally limited in that it does not capture the MLT dependence of the plasma nor the space weather variations on time scales of less than a day. Future versions can remedy the former problem in a straightforward manner by incorporating an MLT coordinate. However, the latter problem is likely beyond the capabilities of the current empirically based statistical algorithms given the required spatial and temporal data coverage. A more promising approach is to build a "sample solar cycle (or cycles)" that attempts to reconstruct past particle flux distributions using data, physics-based models, data-assimilation and other statistical techniques (O'Brien and Guild 2010; Bourdarie et al. 2009). Such a reanalysis could provide an environment with variations on time scales limited only by the fidelity of the physics-based models. A user might then fly a mission through the reference cycle and accumulate model data in order to build the required statistical distribution on any time scale greater than the model resolution. Reanalysis introduces uncertainty through the statistical and physics-based modeling processes in addition to what is already in the data, but such a description might be far better than none when knowledge of the flux statistics for small time-averaged intervals is essential.

Solar proton events were not included in AP9, though they can be the dominant particles providing dose over time periods of hours to days at high altitudes. Merging AP9 with existing statistical models of solar proton events (e.g. Xapsos et al. 1998, 1999) is a worthwhile endeavor which would provide an integrated application of clear value to the satellite design engineers.

Perhaps the most important consideration concerning the future of AE9/AP9/SPM is the necessity of enlisting the effort of other agencies and countries in the development processes. To build a model of the scope of AE9/AP9/SPM V1.0 required a focused effort with a relatively small team and a level of resources that the NRO and AFRL were able to provide. With V1.0 built and released to the public it is the sincere hope of the V1.0 developers that the radiation belt community will eventually take ownership, incorporating new data sets, algorithms (and maybe a new name) to make the model a true global standard.

Acknowledgements Many people have been involved in building AE9/AP9/SPM. Much credit is due Clark Groves for getting the project started. The authors especially wish to thank Joe Mazur, Bern Blake, Jim Roeder and Joe Fennell for technical advice on the HEO, ICO and POLAR/CAMMICE data; Richard Selesnick for cleaning and analysis of the SAMPEX/PET and POLAR/HISTp data and for his physics-based proton belt climatology model; Jon Niehof and Jack Scudder for access to their versions of the POLAR/MICS and POLAR/HYDRA data; Jean-Andre Sauvaud for use of the DEMETER data; Don Brautigam, Sebastien Bourdarie, Daniel Boscher, Jay Albert, Kara Perry, Brian Wie and Seth Claudepierre for technical assistance; Bill Olson, Dave Byers, James Metcalf, Michael Starks, Tim Alsruhe and Geoff Reeves for project management; Bob Weigel and Mike Xapsos for ViRBO and LWS-SET website support; Sharon Benedict for graphics

support; Dave Chenette and Michael Bodeau for helping define the requirements; and the "short list" of engineers and scientists who tested the beta versions and provided valuable feedback all along the way. This work was supported through Air Force contracts FA8718-05-C-0036, FA8718-10-C-001, FA8721-05-C-0002 and FA8802-09-C-0001 and NASA grant NNG05GM22G.

Appendix A: Acronyms

ACE	Advanced Composition Explorer (satellite)
BDDII	Burst Detector Dosimeter II
CAMMICE	Charge and Mass Magnetospheric Ion Composition Experiment
CEASE	Compact Environment Anomaly Sensor
CPME	Charged Particle Measurement Experiment
CRRES	Combined Radiation and Release Experiment (satellite)
DD	Displacement Damage
DEMETER	Detection of Electro-Magnetic Emissions Transmitted from Earthquake Regions (satellite)
Dos	Dosimeter
EPAM	Electron, Proton, and Alpha Monitor
GEO	Geosynchronous Orbit
GPS	Global Positioning System (satellite)
HEEF	High Energy Electron Fluxmeter
HEO-F1	Highly Elliptical Orbit—Flight 1 (satellite)
HEO-F3	Highly Elliptical Orbit—Flight 3 (satellite)
HISTe	High Sensitivity Telescope—electrons
HISTp	High Sensitivity Telescope—protons
HYDRA	Hot Plasma Analyzer
ICO	Intermediate Circular Orbit (satellite)
IGE	International Geostationary Electron (model)
IDP	Instrument for Particle Detection
IPS	Imaging Proton Spectrometer
LANL-GEO	Los Alamos National Laboratory-Geosynchronous Orbit satellite
LEO	Low-Earth Orbit
MEA	Medium Energy Analyzer
MEO	Medium-Earth Orbit
MICS	Magnetospheric Ion Composition Sensor
MPA	Magnetospheric Plasma Analyzer
PET	Proton/Electron Telescope
PROTEL	Proton Telescope
SAMPEX	Solar Anomalous and Magnetospheric Particle Explorer (satellite)
SCATHA	Spacecraft Charging at High Altitudes (satellite)
SC3	High Energy Particle Spectrometer
SEE	Single event effects
SEM	Space Environment Monitor
SOPA	Synchronous Orbit Particle Analyzer
Tel	Telescope
TIROS	Television Infrared Observation Satellite (satellite)
TSX5	Tri-Services Experiment-5 (satellite)

Appendix B: Construction of the Flux Maps, Principal Components and Time Evolution Matrices

Described in this appendix are the methods used to build the flux maps and components of the auto-regression scheme (Eq. (7)) introduced in Sect. 5 and illustrated in Fig. 5. Much of the theory underlying the V1.0 architecture can be found in O'Brien (2005), O'Brien and Guild (2010) and Johnston et al. (2013). A good deal of statistical analysis is needed to build the autoregressive model and only a cursory overview is given here. Interested readers are referred to Wilks (2006) for information on the basic techniques and O'Brien (2012a) for the application to radiation belt models.

As mentioned in Sect. 5 the statistical quantities tracked in the flux maps are the 50th and the 95th percentile unidirectional flux values $m50$ and $m95$, respectively. Actually, the variable $m95' = m95 - m50$ is used instead of $m95$ so the restriction that $m95 > m50$ imposed on the analysis takes the simple form $m95' > 0$. Hereinafter the $'$ will be dropped. From these two quantities the entire particle distribution can be determined by assuming a two-parameter functional form for the distribution function.

For each satellite data set the unidirectional flux measurements are sorted into a set of time sequential maps where the spatial bins are defined by the coordinate grid and the time bin for each map is one day for electrons and 7 days for protons. Note that the term "spatial" is used in a general sense to denote all the non-temporal coordinates including energy. For each satellite pass through a spatial bin during the time bin a value for the flux and variance is computed as a weighted average of the j and $d \ln j$ measurements during the pass. Weights are determined by the relative values of $d \ln j$ which themselves are computed from a cross-calibration procedure discussed in Sect. 4.3. Bin pass average values are then averaged for each time bin. These preliminary maps can be spatially sparse as only coordinate bins through which the satellite passes will contain values. With the tracked percentile values defined as the vector $\underline{\theta} = (m50, m95)$ and their deviations about the average $\underline{\bar{\theta}}$ as $\delta\underline{\theta} = \underline{\theta} - \underline{\bar{\theta}}$, the average value and the covariance matrix $\mathrm{cov}(\delta\underline{\theta})$ are computed for each bin by using a bootstrap technique over the set of time averaged values. With the bootstrap a random selection of time binned values is chosen, with replacement, to equal the original set size. Each selected value is perturbed randomly in a manner constrained by its standard deviation (in a lognormal sense) and the resultant set sorted to obtain a value for $\underline{\bar{\theta}}_i$ in each spatial bin i (hereafter the subscript i will be dropped to avoid notational overload). Repeating this process 200 times yields a distribution of $\underline{\bar{\theta}}$ estimates that are used to compute an average $\underline{\bar{\theta}}$ and a 2×2 local $\mathrm{cov}(\delta\underline{\theta})$. This process is performed for each spatial bin for each sensor data set.

The filling-in procedure using the templates is as follows. A realization of $\underline{\bar{\theta}}$ on the sparse grid described above is constructed by randomly perturbing the original $\underline{\bar{\theta}}$ values consistent with a normal distribution characterized by $\mathrm{cov}(\delta\underline{\theta})$ in each bin. From this realization the quantity $\Delta\underline{\theta} = \underline{\bar{\theta}} - \underline{\theta}^{(0)}$, where $\underline{\theta}^{(0)}$ is the template estimate, is computed. The $\Delta\underline{\theta}$ grid is filled in first by using energy interpolation and extrapolation, and then applying nearest-neighbor averaged and smoothed before being added to the original sparse $\underline{\bar{\theta}}$ grid to produce an estimate for the full $\underline{\bar{\theta}}$ grid. This process is repeated 10 times for each template and the distribution of $\underline{\bar{\theta}}$ obtained is used to compute a new best estimate of the $\underline{\bar{\theta}}$ and $\mathrm{cov}(\delta\underline{\theta})$ over the entire grid for each satellite.

To compute the final $\underline{\bar{\theta}}$ map, denoted as the generalized vector $\underline{\bar{\boldsymbol{\theta}}}$ with a single index covering all the $(E, K, \Phi$ or $h_{min})$ grid, the individual satellite $\underline{\bar{\theta}}$ maps are averaged with weighting by the standard deviations computed from $\mathrm{cov}(\delta\underline{\theta})$ in each bin. The maps are then smoothed. The final covariance $\mathrm{cov}(\delta\underline{\boldsymbol{\theta}})$ is then captured by computing the "anomaly

matrix" **S** where the number of rows in **S** are the number of grid points (i.e. equal to the number of values in $\underline{\bar{\boldsymbol{\theta}}}$) and each column of **S** is a normalized bootstrap realization of $\underline{\bar{\theta}}$ on the grid obtained by selecting a set of random sensor groups, randomly perturbing $\underline{\bar{\theta}}$ in each bin assuming a normal distribution of $\underline{\bar{\theta}}$ characterized by $\mathrm{cov}(\delta\underline{\theta})$ and averaging the result. This layer of bootstrapping captures the uncertainties of measurement errors, spatial interpolation and extrapolation and the temporal coverage limitations of a finite set of sensors. By construction, $\mathrm{cov}(\delta\underline{\theta}) = \mathbf{S}\mathbf{S}^T$ where T represents the transpose operation. Nominally, $\mathrm{cov}(\delta\underline{\bar{\boldsymbol{\theta}}})$ would be a very large matrix of size $N \times N$, where N is twice the number of grid points (∼50,000 for AE9/AP9). By constructing **S** of 50 bootstrap realizations, a number found to be sufficient, only an $N \times 50$ matrix need be computed and stored. Singular value decomposition of **S** keeping only the number of dimensions needed to re-compute 90 % of the total variance further reduces the stored matrix size to $N \times 10$.

The end result of the process is a flux map $\underline{\bar{\boldsymbol{\theta}}}$ of the 50th and 95th percentile unidirectional flux values with the anomaly matrix **S** allowing for computation of the spatial error covariance across the entire grid. With the assumed Weibull or lognormal distribution functions the mean or any percentile level flux can be computed from $\bar{\boldsymbol{\theta}}$. Uncertainties in these values can be calculated from $\mathrm{cov}(\delta\underline{\theta}) = \mathbf{S}\mathbf{S}^T$ and represent estimates of the combined uncertainty imposed by imprecise measurements, lack of spatial and temporal coverage, and the templates used for interpolation and extrapolation.

To determine the quantities involved in auto-regression equation (Eq. (7)) it is first necessary to estimate the spatial ($\boldsymbol{\Sigma}$) and spatiotemporal ($\hat{\mathbf{R}}$) covariance matrices for the flux. Although there is certainly considerable error in computing the spatial and spatiotemporal covariance matrices it will be neglected hereinafter because only a low-order model of the dynamics is sought and the uncertainty in the flux values due to measurement and space weather is tracked through flux maps and associated covariance.

The starting point is the set of time-average fluxes in each spatial bin for each satellite. Randomly selecting two bins (possibly from different sensors), we compute a "Gaussian" correlation coefficient at several different time lags. The time-averaged flux values in each bin are transformed to Gaussian-equivalent variables z_i according to the relation,

$$\Psi(z_{i,k}) = F_i(j_{i,k}) \approx \frac{k}{1+N_i} \tag{8}$$

where Ψ (often denoted Φ in the statistical literature) is the cumulative distribution of a standard Gaussian with unit variance and a zero average, F_i is the empirical cumulative distribution within the ith bin, and k is the index of the sort list of $k = 1$ to N_i fluxes $j_{i,k}$ within the bin. This transformation is independent of the choice of Weibull or lognormal distributions. By transforming to the Gaussian-equivalent variables the formalism of multivariate normal distributions can be used to develop the autoregressive prediction model. In particular, the spatial and temporal covariance matrices are defined as,

$$\boldsymbol{\Sigma} = \left\langle \mathbf{z}(t)\mathbf{z}^T(t) \right\rangle, \tag{9}$$

$$\hat{\mathbf{R}}(\tau) = \left\langle \mathbf{z}(t)\mathbf{z}^T(t+\tau_k) \right\rangle, \tag{10}$$

where $\mathbf{z}$ is the vector of z_i values spanning the entire grid, τ_k is the kth time lag and the $\langle\cdots\rangle$ notation represents the average. Because of limited spatial and temporal coverage, the initial estimates of the covariance matrices is incomplete. They are filled in using a 100-point nearest neighbors average.

To reduce the substantial storage requirements of what is nominally a $N \times N$ dimensional matrix a principal component decomposition of $\boldsymbol{\Sigma}$ is employed, i.e.,

$$\mathbf{z} = \mathbf{Q}\mathbf{q}, \tag{11}$$

$$\mathbf{\Sigma} = \mathbf{Q}\mathbf{Q}^T, \tag{12}$$

where $\mathbf{Q} = [\hat{\mathbf{q}}_1, \hat{\mathbf{q}}_2, \ldots, \hat{\mathbf{q}}_{N_q}]$ is a matrix of the $i = 1, 2, \ldots, N_q$ principal component eigenvectors $\hat{\mathbf{q}}_i$ and $\mathbf{q}$ is the state vector of principal component amplitudes representing a particular realization of $\mathbf{z}$. $\mathbf{\Sigma}$ contains many noise factors, which we remove by excluding any principal component that explains less than 1 % of the variance. Using the remaining $N_q \sim 10$ principal components the spatiotemporal covariance can be expressed as,

$$\hat{\mathbf{R}}_k = \mathbf{Q}\left\langle \mathbf{q}(t)\mathbf{q}^T(t-\tau_k)\right\rangle \mathbf{Q}^T = \mathbf{Q}\mathbf{R}_k\mathbf{Q}^T, \tag{13}$$

where $\mathbf{R}_k = \langle \mathbf{q}(t)\mathbf{q}^T(t-\tau_k)\rangle$. When $k = 0$ then $\tau_k = 0$ by definition and $\mathbf{R} = \mathbf{I}$, the identity matrix, so that $\mathbf{R}_0 = \mathbf{\Sigma}$. In summary, the procedure to obtain the spatiotemporal covariance matrices from the data is to (a) compute elements of $\mathbf{\Sigma}$ and each $\hat{\mathbf{R}}$ from time averages in spatial bins (Eqs. (9) and (10)), (b) fill in the missing elements of $\mathbf{\Sigma}$ and $\hat{\mathbf{R}}$ via nearest neighbors averaging, (c) determine the principal components $\mathbf{Q}$ of $\mathbf{\Sigma}$ (Eq. (12)), and (d) determine each $\mathbf{R}_k$ using Eq. (13).

The autoregressive time-evolution equation (Eq. (7)) of order N_G is used to advance the N_q principal component amplitudes in time. An expression for the expectation value $\langle \mathbf{q}(t)\mathbf{q}^T(t-\tau)\rangle$ can be derived from the time-evolution equation,

$$\left\langle \mathbf{q}(t)\mathbf{q}^T(t-\tau_m)\right\rangle = \mathbf{R}_m = \sum_{k=1}^{N_G} \mathbf{G}_k\mathbf{R}_{m-k} + \begin{cases} \mathbf{C}\mathbf{C}^T, & m = 0 \\ 0, & \text{otherwise} \end{cases} \tag{14}$$

where $\mathbf{R}_{m-k} = \langle \mathbf{q}(t-\tau_m)\mathbf{q}^T(t-\tau_k)\rangle$ and the $\mathbf{C}\mathbf{C}^T$ term arises from $\langle \boldsymbol{\eta}(t)\mathbf{q}^T(t)\rangle$ because $\boldsymbol{\eta}(t)$ is uncorrelated with all prior $\mathbf{q}(t)$. With the $\mathbf{R}$ matrices determined from the data, Eq. (14) can be inverted to obtain $\mathbf{G}$ and $\mathbf{C}$ (O'Brien 2012a).

Statistically realistic flux profiles are generated by choosing at $t = 0$ a scenario-specific random seed which determines the initial principal component amplitudes $\mathbf{q}(0)$ and a set of flux conversion parameters, i.e. the $\underline{\boldsymbol{\theta}}$ percentiles characterizing the distribution computed from the flux map $\underline{\bar{\boldsymbol{\theta}}}$ with a random perturbation added consistent with the global spatial error covariance $\mathrm{cov}(\delta\boldsymbol{\theta})$ encoded in the anomaly matrix $\mathbf{S}$. A time history of the $\mathbf{q}(t)$ is generated with Eq. (7), the Gaussian equivalent fluxes $\mathbf{z}(t)$ determined from Eq. (11) and the physical flux values $\mathbf{j}(t)$ from the left-side of Eq. (8) using the conversion parameters given by $\underline{\boldsymbol{\theta}}$.

References

T.W. Armstrong, B.L. Colborn, Evaluation of trapped radiation model uncertainties for spacecraft design, NASA/CR-2000-210072, 2000

D.M. Boscher, S.A. Bourdarie, R.H.W. Friedel, R.D. Belian, Model for the geostationary electron environment: POLE. IEEE Trans. Nucl. Sci. **50**, 2278–2283 (2003)

S.A. Bourdarie et al., PRBEM data analysis procedure V1.2, COSPAR Panel on Radiation Belt Environment Modeling (PRBEM), 2008, available at http://craterre.onecert.fr/prbem/Data_analysis.pdf

S.A. Bourdarie, A. Sicard-Piet, R. Friedel, T.P. O'Brien, T. Cayton, B. Blake, D. Boscher, D. Lazaro, Outer electron belt specification model. IEEE Trans. Nucl. Sci. **56**, 2251–2257 (2009)

D.H. Brautigam, CRRES in review: space weather and its effects on technology. J. Atmos. Sol.-Terr. Phys. **64**, 1709–1721 (2002)

D.H. Brautigam, J. Bell, CRRESELE documentation, PL-TR-95-2128, ADA 301770, Air Force Research Laboratory, Hanscom AFB, MA, 1995

D.H. Brautigam, M.S. Gussenhoven, E.G. Mullen, Quasi-static model of outer zone electrons. IEEE Trans. Nucl. Sci. **39**, 1797–1803 (1992)

D.H. Brautigam, K.P. Ray, G.P. Ginet, D. Madden, Specification of the radiation belt slot region: comparison of the NASA AE8 model with TSX5/CEASE data. IEEE Trans. Nucl. Sci. **51**, 3375–3380 (2004)
D.H. Brautigam, B. Dichter, S. Woolf, E. Holeman, A. Ling, D. Wrazen, Compact environmental anomaly sensor (CEASE): response functions, AFRL-VS-HATR-2006-1030, Air Force Research Laboratory, 2006
J. Cabrera, J. Lemaire, Using invariant altitude (hinv) for mapping of the radiation belt fluxes in the low-altitude environment. Space Weather **5**, S04007 (2007). doi:10.1029/2006SW000263
T.C. Cayton, Objective comparison of CRRES MEA electron spectra using response functions for the SOPA aboard S/C 1989-046, LA-UR-07-8023, Los Alamos National Laboratory, Los Alamos, NM, 2007
T.E. Cayton, R.D. Belian, Numerical modeling of the synchronous orbit particle analyzer (SOPA, Version 2) the Flew on S/C 1990-095, Los Alamos Technical Report, LA-14335, Los Alamos National Laboratory, Los Alamos, NM, 2007
Y. Chen, R.H.W. Friedel, G.D. Reeves, T. Onsager, M.F. Thomsen, Multisatellite determination of the relativistic electron phase space density at geosynchronous orbit: methodology and results during geomagnetically quiet times. J. Geophys. Res. **110**, A10210 (2005). doi:10.1029/2004JA010895
E.J. Daly, J. Lemaire, D. Heynderickx, D.J. Rodgers, Problems with models of the radiation belts. IEEE Trans. Nucl. Sci. **43**, 403–415 (1996)
B.K. Dichter, F.A. Hanser, B. Sellers, J.L. Hunerwadel, High energy electron fluxmeter. IEEE Trans. Nucl. Sci. **40**, 242–245 (1993)
B. Efron, R. Tibshirani, *An Introduction to the Bootstrap* (Chapman & Hall/CRC, Boca Raton, 1993)
D. Evans, M.S. Greer, Polar orbiting environmental satellite space environment monitor—2. Instrument descriptions and archive data documentation, NOAA Tech. Mem. 1.4, Space Environ. Lab., Boulder, CO, 2004
M. Evans, N. Hastings, B. Peacock, *Statistical Distributions*, 3rd edn. (Wiley, Hoboken, 2000)
J.F. Fennell, J.B. Blake, D. Heynderickx, N. Crosby, HEO observations of the radiation belt electron fluxes: comparison with model predictions and a source for model updates. Eos Trans. AGU **84**, #SH52A-05 (2003)
R.H.W. Friedel, S. Bourdarie, T. Cayton, Intercalibration of magnetospheric energetic electron data. Space Weather **3**, S09B04 (2005). doi:10.1029/2005SW000153
S.F. Fung, Recent developments in the NASA trapped radiation models, in *Radiation Belts: Models and Standards*, ed. by J.F. Lemaire, D. Heynderickx, D.N. Baker. Geophys. Monogr. Ser., vol. 97 (AGU, Washington, 1996), pp. 79–91
G.P. Ginet, T.P. O'Brien, AE-9/AP-9 trapped radiation and plasma models requirements specification, Aerospace Technical Report, TOR-2010(3905)-3, 2010
G.P. Ginet, S.L. Huston, C.J. Roth, T.P. O'Brien, T.B. Guild, The trapped proton environment in Medium Earth Orbit (MEO). IEEE Trans. Nucl. Sci. **57**, 3135–3142 (2010)
G. Ginet, T. O'Brien, J. Mazur, C. Groves, W. Olson, G. Reeves, AE(P)-9: the next generation radiation specification models, in *Proceedings of the GOMACTech-08 Conference*, 17–20 March, Las Vegas, NV (2008)
G.P. Ginet, B.K. Dichter, D.H. Brautigam, D. Madden, Proton flux anisotropy in low Earth orbit. IEEE Trans. Nucl. Sci. **54**, 1975–1980 (2007)
GOES I-M Data Book, DRL 101-0801 ed. Space Systems Loral, Aug. 31, 1996, GOES/SEM information [online]. Available: http://rsd.gsfc.nasa.gov/goes/text/goes.databook.html
T. Guild, T.P. O'Brien, J. Mazur, M. Looper, On-orbit inter-calibration of proton observations during solar particle events, Aerospace Report No. TOR-2007(3905)-22, Aerospace Corporation, 2009
M.S. Gussenhoven, E.G. Mullen, M.D. Violet, C. Hein, J. Bass, D. Madden, CRRES high energy proton flux maps. IEEE Trans. Nucl. Sci. **40**(6), 1450–1457 (1993)
M.S. Gussenhoven, E.G. Mullen, D.H. Brautigam, Near-Earth radiation model deficiencies as seen on CRRES. Adv. Space Res. **14**, 927–941 (1994)
F.A. Hanser, Analyze data from CRRES payloads AFGL-701/Dosimeter and AFGL-701-4/Fluxmeter, PL-TR-95-2103, Phillips Laboratory, AFMC, Hanscom AFB, MA, 1995
D. Heynderickx, M. Kruglanski, V. Pierrard, J. Lemaire, M.D. Looper, J.B. Blake, A low altitude trapped proton model for solar minimum conditions based on SAMPEX/PET data. IEEE Trans. Nucl. Sci. **46**, 1475–1480 (1999)
S.L. Huston, Space environment and effects: trapped proton model, NASA/CR-2002-211784, NASA Marshall Spaceflight Center, Huntsville, AL, 2002
S.L. Huston, G.A. Kuck, K.A. Pfitzer, Low altitude trapped radiation model using TIROS/NOAA data, in *Radiation Belts: Models and Standards*, ed. by J.F. Lemaire, D. Heynderickx, D.N. Baker. Geophys. Monogr. Ser., vol. 97 (AGU, Washington, 1996), pp. 119–124
S. Huston, G. Ginet, T.P. O'Brien, T. Guild, D. Madden, R. Friedel, AE/AP-9 radiation specification model: an update, in *Proceedings of the GOMACTech-08 Conference*, 17–18 March, Orlando, FL (2009)

IGRF, The international geomagnetic reference field, 2012. Available at http://www.ngdc.noaa.gov/IAGA/vmod/

IRBEM, The international radiation belt environmental modeling library, 2012. Available at http://irbem.svn.sourceforge.net/viewvc/irbem/web/index.html

C.E. Jordan, Empirical models of the magnetospheric magnetic field. Rev. Geophys. **32**, 139–157 (1994)

W.R. Johnston, C.D. Lindstrom, G.P. Ginet, Characterization of radiation belt electron energy spectra from CRRES observations, Abstract #SM33C-1925, American Geophysical Union Fall Meeting, San Francisco, CA, 2010

W.R. Johnston, C.D. Lindstrom, G.P. Ginet, CRRES medium electron sensor A (MEA) and high energy electron fluxmeter (HEEF): cross-calibrated data set, AFRL, 2011, available at ftp://virbo.org/johnston/crres/MEAHEEFCC.pdf

W.R. Johnston et al., AE9/AP9/SPM radiation environment model, Technical Documentation, in preparation to be released as an Air Force Research Laboratory Technical Report, 2013

J. Koller, S. Zaharia, LANL* V2.0: global modeling and validation. Geosci. Model Dev. **4**, 669–675 (2011). doi:10.5194/gmd-4-669-2011

J. Koller, G.D. Reeves, R.H.W. Friedel, LANL* V1.0: a radiation belt drift shell model suitable for real-time and reanalysis applications. Geosci. Model Dev. **2**, 113–122 (2009)

H.C. Koons, J.E. Mazur, R.S. Selesenick, J.B. Blake, J.F. Fennell, J.L. Roeder, P.C. Anderson, The impact of the space environment on space systems, in *6th Spacecraft Charging Technology Conference*, AFRL Tech. Report No. AFRL-VS-TR-20001578, pp. 7–11, Air Force Research Laboratory, Hanscom AFB, MA, 2000

J.-M. Lauenstein, J.L. Barth, D.G. Sibeck, Toward the development of new standard radiation belt and space plasma models for spacecraft engineering. Space Weather **3**, S08B03 (2005). doi:10.1029/2005SW000160. Presentations from the workshop are available online at http://lwsscience.gsfc.nasa.gov/RB_meeting1004.htm

A.M. Lenchek, S.F. Singer, Effects of the finite gyroradii of geomagnetically trapped protons. J. Geophys. Res. **67**, 4073–4075 (1962)

J. Mazur, L. Friesen, A. Lin, D. Mabry, N. Katz, Y. Dotan, J. George, J.B. Blake, M. Looper, M. Redding, T.P. O'Brien, J. Cha, A. Birkitt, P. Carranza, M. Lalic, F. Fuentes, R. Galvan, M. McNab, The relativistic proton spectrometer (RPS) for the radiation belt storm probes mission. Space Sci Rev. (2012, this issue). doi:10.1007/s11214-012-9926-9

J.P. McCollough, J.L. Gannon, D.N. Baker, M. Gehmeyr, A statistical comparison of commonly used external magnetic field models. Space Weather **6**, S10001 (2008). doi:10.1029/2008SW000391

C.E. McIlwain, Coordinates for mapping the distribution of magnetically trapped particles. J. Geophys. Res. **6**, 3681 (1961)

J.D. Meffert, M.S. Gussenhoven, CRRESPRO documentation, PL-TR-94-2218, ADA 284578, Phillips Laboratory, Hanscom AFB, MA, 1994

A. Milillo, S. Orsini, I.A. Daglis, Empirical model of proton flux in the equatorial inner magnetosphere: development. J. Geophys. Res. **106**, 25713–25729 (2001)

J. Niehof, Diamagnetic cavities and energetic particles in the Earth's magnetospheric cusps. PhD Thesis, Boston University, 2011

T.P. O'Brien, A framework for next-generation radiation belt models. Space Weather **3**, S07B02 (2005). doi:10.1029/2005SW000151

T.P. O'Brien, Documentation of C inversion library, 2010, available as part of IRBEM-LIB at http://irbem.svn.sourceforge.net/viewvc/irbem/web/index.html

T.P. O'Brien, Adding multiple time lags to AE9/AP9 V1.0, Aerospace Report No. TOR-2012(1237)-3, 2012a

T.P. O'Brien, Data cleaning guidelines for AE-9/AP-9 data sets, Aerospace Report No. TOR-2012(1237)-4, 2012b

T.P. O'Brien, T.B. Guild, Trapped electron model 2 (TEM-2), Aerospace Report No. TR-2010(3905)-2, Aerospace Corporation, El Segundo, CA, 2010

W.P. Olson, K.A. Pfitzer, Magnetospheric magnetic field modeling, Annual Scientific Report, Air Force Office of Scientific Research contract F44620-75-C-0033, McDonnell Douglas Astronautics Co., Huntington Beach, CA, 1977

W.H. Press, S.A. Teukolsky, W.T. Vetterling, B.P. Flannery, *Numerical Recipes in C*, 2nd edn. (Cambridge University Press, Cambridge, 1992)

Radiation models for engineering and operations, session at the 2007 NOAA Space Weather Workshop. Presentations from the workshop are available at: http://helios.sec.noaa.gov/sww/index.html, 2007

Radiation Specifications Forum, 2007. Website at: http://lws-set.gsfc.nasa.gov/RadSpecsForum.htm

G.D. Reeves, Y. Chen, G.S. Cunningham, R.W.H. Friedel, M.G. Henderson, V.K. Jordanova, J. Koller, S.K. Morley, M.F. Thomsen, S. Zaharia, Dynamic radiation environment assimilation model: DREAM. Space Weather **10**, S03006 (2012). doi:10.1029/2011SW000729

C.J. Rodger et al., Use of POES SEM-2 observations to examine radiation belt dynamics and energetic electron precipitation into the atmosphere. J. Geophys. Res. **115**, A04202 (2010). doi:10.1029/2008JA014023
J.L. Roeder, M.W. Chen, J.F. Fennell, R. Friedel, Empirical models of the low-energy plasma in the inner magnetosphere. Space Weather **3**, S12B06 (2005). doi:10.1029/2005SW000161
J.G. Roederer, *Dynamics of Geomagnetically Trapped Radiation* (Springer, New York, 1970)
C.J. Roth et al., AE9/AP9/SPM radiation environment model. User's guide, in preparation to be released as an Air Force Research Laboratory Technical Report, 2013
J.A. Sauvaud, T. Moreau, R. Maggiolo, J.-P. Treilhou, C. Jacquey, A. Cros, J. Coutelier, J. Rouzaud, E. Penou, M. Gangloff, High-energy electron detection onboard DEMETER: the IDP spectrometer, description and first results on the inner belt. Planet. Space Sci. **54**, 502–511 (2006)
D.M. Sawyer, J.I. Vette, AP-8 trapped proton model environment for solar maximum and minimum, NSSDC/WDC-A-R&S 76-06, Natl. Space Sci. Data Cent., Greenbelt, MD, 1976
M. Schulz, Canonical coordinates for radiation belt modeling, in *Radiation Belts: Models and Standards*, ed. by J.F. Lemaire, D. Heynderickx, D.N. Baker. Geophys. Monogr. Ser., vol. 97 (AGU, Washington, 1996), pp. 153–160
R.S. Selesnick, M.D. Looper, R.A. Mewaldt, A theoretical model of the inner proton radiation belt. Space Weather **5**, S04003 (2007). doi:10.1029/2006SW00275
S.M. Seltzer, Updated calculations for routine space-shielding radiation dose estimates: SHIELDOSE-2. Gaithersburg, MD, NIST Publication NISTIR 5477, 1994
V.P. Shabansky, Some processes in the magnetosphere. Space Sci. Rev. **12**(3), 299–418 (1971)
A. Sicard-Piet, S. Bourdarie, D. Boscher, R.H.W. Friedel, M. Thomsen, T. Goka, H. Matsumoto, H. Koshiishi, A new international geostationary electron model: IGE-2006, from 1 keV to 5.2 MeV. Space Weather **6**, S07003 (2008). doi:10.1029/2007SW000368
J.D. Sullivan, Geometrical factor and directional response of single and multi-element particle telescopes. Nucl. Instrum. Methods **95**(1), 5–11 (1971)
M.F. Thomsen, D.J. McComas, G.D. Reeves, L.A. Weiss, An observational test of the Tsyganenko (T89a) model of the magnetic field. J. Geophys. Res. **101**, 24827–24836 (1996)
M.F. Thomsen, M.H. Denton, B. Lavraud, M. Bodeau, Statistics of plasma fluxes at geosynchronous orbit over more than a full solar cycle. Space Weather **5**, S03004 (2007). doi:10.1029/2006SW000257
A.L. Vampola, The ESA outer zone electron model update, in *Environment Modelling for Space-Based Applications, Symposium Proceedings (ESA SP-392)*, ed. by W. Burke, T.-D. Guyenne, 18–20 September 1996 (ESTEC, Noordwijk, 1996), p. 151
J.I. Vette, The NASA/National Space Science Data Center Trapped Radiation Environment Model Program (TREMP) (1964–1991), NSSDC/WDC-A-R&S 91-29, Natl. Space Sci. Data Cent., Greenbelt, MD, 1991a
J.I. Vette, The AE-8 trapped electron model environment, NSSDC/WDC-A-R&S 91-24, NASA Goddard Space Flight Center, Greenbelt, MD, 1991b
D.S. Wilks, *Statistical Methods in the Atmospheric Sciences*, 2nd edn. (Academic Press, Burlington, 2006)
G.L. Wrenn, A.J. Sims, Internal charging in the outer zone and operational anomalies, in *Radiation Belts: Models and Standards*, ed. by J.F. Lemaire, D. Heynderickx, D.N. Baker. Geophys. Monogr. Ser., vol. 97 (AGU, Washington, 1996), pp. 275–278
M.A. Xapsos, G.P. Summers, E.A. Burke, Probability model for peak fluxes of solar proton events. IEEE Trans. Nucl. Sci. **45**(6), 2948–2953 (1998)
M.A. Xapsos, G.P. Summers, J.L. Barth, E.G. Stassinopoulos, E.A. Burke, Probability model for worst case solar proton event fluences. IEEE Trans. Nucl. Sci. **46**(6), 1481–1485 (1999)

DOI 10.1007/978-1-4899-7433-4_19
Reprinted from *Space Science Reviews* Journal, DOI 10.1007/s11214-012-9945-6

Radiation Belt Storm Probes (RBSP) Education and Public Outreach Program

D. Turney · A. Matiella Novak · K. Beisser · N. Fox

Received: 15 February 2012 / Accepted: 16 October 2012 / Published online: 11 January 2013

Abstract The Radiation Belt Storm Probes (RBSP) Education and Public Outreach (E/PO) program serves as a pipeline of activities to inspire and educate a broad audience about Heliophysics and the Sun-Earth system, specifically the Van Allen Radiation Belts. The program is comprised of a variety of formal, informal and public outreach activities that all align with the NASA Education Portfolio Strategic Framework outcomes. These include lesson plans and curriculum for use in the classroom, teacher workshops, internship opportunities, activities that target underserved populations, collaboration with science centers and NASA visitors' centers and partnerships with experts in the Heliophysics and education disciplines. This paper will detail the activities that make up the RBSP E/PO program, their intended audiences, and an explanation as to how they align with the NASA education outcomes. Additionally, discussions on why these activities are necessary as part of a NASA mission are included. Finally, examples of how the RBSP E/PO team has carried out some of these activities will be discussed throughout.

Keywords Education · Outreach · Radiation Belt Storm Probes · NASA · STEM · Space weather · Van Allen

1 Introduction

Education and Public Outreach (E/PO) efforts have long been a significant aspect to NASA Science Mission Directorate missions and have been used to inspire, engage and educate Americans with mission science and NASA's mission objectives. Although shifts in policy have at times both decreased and increased the role of E/PO within specific missions, the current guiding principle is to devote a small percentage (about 1 %) of mission funds, excluding launch costs, to support E/PO activities and efforts. With this in mind, the Radiation Belt Storm Probes (RBSP) E/PO program has been actively engaged in a robust plan aimed

D. Turney (✉) · A. Matiella Novak · K. Beisser · N. Fox
Applied Physics Laboratory, The Johns Hopkins University, 11100 Johns Hopkins Rd., Laurel, MD 20723, USA
e-mail: dawn.turney@jhuapl.edu

at achieving the outcomes highlighted in the NASA Education Portfolio Strategic Framework (NASA 2007).

The goals of E/PO, as specified by NASA, align with a pipeline strategy that first inspires and engages audiences through public outreach and informal education activities, then educates through formal education activities, culminating with training America's future scientists and engineers through higher education activities. Beginning in 2006, NASA committed to pursuing three major education goals (NASA 2010):

- Strengthen NASA and the Nation's future workforce;
- Attract and retain students in Science, Technology, Engineering, and Mathematics (STEM) disciplines;
- Engage Americans in NASA's mission.

The need for pursuing these goals has always been a part of NASA's overall mission. With NASA's founding legislation, the Space Act of 1958, the Agency was directed to expand the human knowledge of Earth and space phenomena and to preserve the role of the United States as a leader in aeronautics, space science and technology (NASA 2010). To achieve this, NASA must utilize some of its resources and invest them in STEM education, ensuring that the United States remains a leader in space exploration and science—not just presently, but throughout future generations as well. Additionally, it is not just for the benefit of producing top-quality scientists and engineers that NASA invests in STEM education, but also to ensure that the Nation is comprised of a scientifically literate electorate.

A report written by the National Science Board in 2004 contained results from a survey concerning Americans' science literacy. This report stated that although Americans express strong support for science and technology, they are not very well informed about these subjects. Furthermore, the Program for International Student Assessment (PISA), sponsored by the Organization for Economic Cooperation and Development (OECD), conducted a global survey of the science literacy of 15-year-old students in 2006. The results of the survey showed that U.S. students consistently scored lower in science literacy than other OECD countries. For identifying scientific issues, U.S. students ranked 18 out of 29 countries; for explaining phenomena scientifically, U.S. students ranked 22; for using scientific evidence, U.S. students ranked 21 (USDE 2008). These results showed an alarming need to achieve better results in STEM education and NASA is dedicated, through education and public outreach programs, to counteract the decrease in science literacy currently experienced by the United States. To date, NASA lists over 80 education program opportunities which can be found from the NASA education website http://www.nasa.gov/offices/education/programs/index.html. RBSP is a part of the larger Living With A Star program which strives to offer Heliophysics education material and programs for the education community.

Education and public outreach programs are also a useful way to engage NASA and partnering institutions' scientists and engineers with the public as well as the U.S. education system. It's been well documented that scientists face many challenges when communicating their research to the public, especially when dealing with complex systems (Sommerville and Hassol 2011). Education and public outreach programs help to fill the communication gap between scientists and the public and students. With this in mind, it is critical that education and public outreach programs are run not only by education experts, but also by experts in the science and engineering fields. More scientist participation in education and public outreach will ensure that the public and students are engaged with the most up-to-date scientific research and practices. Likewise, scientist participation in the education community will help guide education policy so that today's students are gaining the most effective STEM education for future employment in the STEM workforce (Morrow and Dusenbery 2004).

The RBSP mission E/PO program strives to excite and inspire the next generation of space explorers by creating hands-on, minds-on learning experiences for students, educators and the general public. The goal is to make mission science and engineering concepts accessible to a wide range of diverse audiences, including people that may not have necessarily considered themselves to be a part of the science community in the past as well as to those that have some background knowledge, but would like to know more about RBSP. The overarching goal of the E/PO program is to generate excitement and awareness about the mission, highlighting the fundamental science of the Van Allen Radiation Belts, showing how RBSP directly impacts our modern way of life; engaging, and inspiring people to want to know more and perhaps join in the mission's search for answers to the dramatic and puzzling aspects of the Earth's radiation belts.

The various E/PO programs: (1) include collaboration with leading E/PO professionals; (2) ensure alignment with national standards; (3) provide product and activity evaluation; (4) guarantee effective implementation; and (5) create relationships reaching all ages and education levels. The E/PO programs all follow both National Science Education Standards (NSES) (NRC 1996) and NASA Implementation Strategy (NASA 1996), and work closely with NASA's Science Mission Directorate (SMD) E/PO framework and infrastructure, specifically the NASA SMD E/PO Heliophysics Forum. The programs implemented by the RBSP E/PO team are using best practices for professional development, curriculum design and informal education (NRC 1996; NASA 1996; NSB 2004), as well as for involving the scientific community with the program (Morrow and Dusenbery 2004; Buxner et al. 2012). Instrument teams are invited and encouraged to propose and carry out their own E/PO programs under the umbrella of the overall RBSP E/PO program. As part of NASA's education efforts, all of the E/PO programs are designed to be aligned with NASA's Education Portfolio Strategic Framework. The overarching RBSP E/PO program strives to inspire, educate, engage and employ the nation's next generation of explorers (Fig. 1).

E/PO specialists work together with mission and instrument scientists and engineers to create products and activities consistent with the key messages of the mission, while staying true to the needs of diverse audiences. The key mission messages that are addressed within the components of the program are:

(1) RBSP advances our understanding of the dramatic and puzzling aspects of Earth's radiation belts. The "Van Allen Radiation Belts," named for their discoverer James Van Allen, are two donut-shaped regions encircling the Earth, where high energy particles from the Sun and space are trapped by our planet's magnetic field.
(2) RBSP enables the prediction of extreme & dynamic space conditions. Changes in the Sun's energy flow cause changes in space. These changes are referred to as space weather and have broad impacts on Earth's systems and inhabitants.
(3) RBSP provides understanding needed to design satellites to survive in space. RBSP will explore space weather especially its extreme conditions, which can disable satellites, cause power grid failures, and disrupt GPS services.

The E/PO program provides training and materials to teachers to enhance their classroom activities, creates opportunities that directly engage students, and implements events and programs for members of the general public. Additionally, the Radiation Belt Storm Probes E/PO program makes a contribution to the nation's scientific and technical literacy, aligning the materials created specifically for this mission with current national education efforts and standards and addressing identified needs of educators, students, and the public. Components of the RBSP E/PO program are broken down into three categories which are aligned with NASA's Education Goals and Outcomes within the Education Portfolio Framework (see Fig. 1). These categories are:

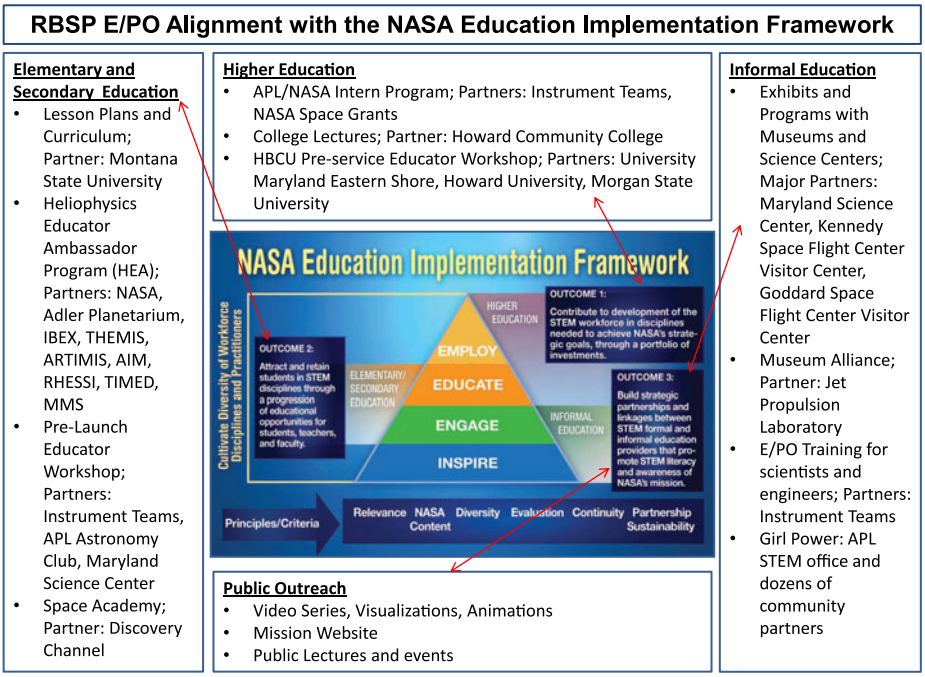

Fig. 1 NASA Education Implementation Framework and the RBSP E/PO Approach. E/PO plan aligns with NASA Education Goals and Outcomes. NASA Education Implementation Framework, **NASA Education Communication Strategy (NP-2008-02-496-HQ)* (NASA 2008)

(1) Formal Education (educating and providing resources for the classroom educator and student),
(2) Informal Education (inspiring museum and science center attendees) and
(3) Public Outreach (engaging the public with the mission and engaging scientists with the public).

Each category contains multiple programs designed to inspire, engage, educate and employ the next generation of space explorers. These components lend themselves to a natural pipeline of education and outreach activities; from lesson plans that begin in elementary education, then progress to secondary education, to higher education activities that progress into employment opportunities. They also seek opportunities to engage minorities and women in science and engineering associated with NASA space science investigations. Overall, the goal of the RBSP E/PO Program is to strengthen NASA and the nation's future workforce, attract and retain students in the STEM disciplines, and engage Americans in the RBSP mission.

2 Formal Education

The formal education program strives to promote careers in science, technology, engineering and mathematics (STEM), fusing a pipeline of future scientists and engineers with a science literate community. A review of literature in a National Science Board (2010) report

titled, "Science and Engineering Indicators: 2010," reported student enrollment in certain high school courses, such as advanced mathematics, is linked to college enrollment and success. Additional studies cited found that a critical factor for successful teaching was the educator's level of skill and knowledge in the subject matter. Another NSB (2007) report states, "No Child Left Behind mandates that all students be taught by teachers who not only are fully certified and possess at least a bachelor's degree, but also demonstrate competence in subject knowledge and teaching." In its 2007 policy recommendations regarding STEM education, the NSB emphasized that STEM teachers should receive adequate STEM content knowledge that is aligned with what they are expected to teach. Similarly, a report from the National Research Council of the National Academies (2007) advocated that teacher preparation and professional development programs focus on boosting teachers' knowledge of science, how students learn the subject, and methods and technologies that aid science learning for all. To fulfill these needs, the RBSP formal education program strives to provide quality professional development opportunities and resources that are tied to national standards to support and assist educators teaching critical STEM courses that will lead to student success in these areas.

The Radiation Belt Storm Probes E/PO formal education programs (grades 5–12) is designed to engage teachers and students by using the excitement of this current NASA program to contribute to a greater understanding of science, mathematics, engineering and technology concepts—ultimately inspiring the next generation of explorers. These programs align with the National Research Council's National Science Education Standards and focus on the key messages of the RBSP mission. RBSP formal education efforts such as creation of lesson plans and teacher training strives to contribute to the broader educational community's confidence in their ability to find and use resources and teach about fundamental science concepts of space weather phenomena and how those processes influence Earth and people. Materials are tailored to be RBSP specific with the goal of complementing the existing NASA formal education efforts.

The formal education program focuses on the fundamental science of Van Allen Radiation Belts as well as the process of designing and building the RBSP spacecraft to operate in such an extreme environment. Key concepts focus around the strange and fascinating behavior in the radiation belts, how we are discovering the drivers behind these phenomena and the importance of gaining a better understanding of this critical region of near Earth space. Another main idea is that the discoveries made here in our "back yard," can be applied to other places and phenomena in the universe; that in many ways this region serves as a near Earth laboratory for discovering the mysteries of not only our own Van Allen belts, but of the universe.

Additionally, our program is aligned with recommendations made by the National Research Council's National Science Education Standards Content Standards. For example standards for grades 5–8 state that at this level, "Students begin to see connections between light, heat, sound, electricity, and magnetism. Focus is on macro view of atomicity, i.e. density. Few students can comprehend the idea of atomic and molecular particles, but it can be discussed on a macro level." Therefore, RBSP programming for middle school students and educators is primarily aligned with content standards which address Science and Technology, Science in Personal and Social Perspectives, Science and Technology in Society, and History and Nature of Science.

Higher level physical science concepts relating to the RBSP mission such as the type, movement and density of electrically charged atomic particles and the influence of electric and magnetic waves upon them are most appropriate for high school and undergraduate programming. According to the National Science Education Standards, students in grades 9–12

Fig. 2 Educators participating in a Sun-Earth education activity during the annual Heliophysics Educator Ambassador (HEA) workshop at the Adler Planetarium, Chicago, IL. HEA is a partnership between several Universities, the Adler Planetarium, and NASA centers. Image credit: Nancy Fiegel

"develop the ability to relate macroscopic properties of substances to microscopic structure of substances." The Physical Science Content Standard for grades 9–12 calls for student understanding of the structure of atoms, the structure and properties of matter, motions and forces, the conservation of energy and increase in disorder, and interactions of energy and matter. Much of RBSP science content is aligned with these fundamental concepts as well as concepts found in the other content standards for grades 9–12. Although there are some connections with K-4 educational content, RBSP mission concepts most appropriately align with the needs of students and teachers of grade levels 5–12, therefore most of the formal education programming is geared toward this audience. For a chart detailing RBSP content ties to the National Education Science Standards please see Table 1.

The formal education program is designed to provide educators and students with experiences and opportunities to enhance their interest in STEM disciplines. The higher education program will provide educational programming designed to encourage opportunities for future employment for undergraduate students, including internships during the integration and test phase of missions and instruments.

The Radiation Belt Storm Probes E/PO formal education program builds on existing partnerships with professional educators and organizations. These partnerships provide nationwide coverage as well as the opportunity to reach a broader number of students and educators. E/PO partners have well-defined roles and bring their experience to various areas of the E/PO program such as design, development and dissemination of curriculum and exhibits. These partnerships also ensure implementation and evaluation of the professional development programs. Forging and maintaining high leverage partnerships is key to the success of the E/PO programs as they ensure broad nationwide dissemination of the E/PO programs. Teachers participating in a workshop that is possible due to such a partnership are shown in Fig. 2.

2.1 Lesson Plans and Curriculum

The E/PO team has contracted with a dedicated team from Montana State University-Bozeman (MSU) Department of Physics to develop classroom-ready learning modules exploring concepts relevant to Earth's radiation belts, geomagnetic storms, and the dynamic solar wind interaction. Care has been taken to avoid redundancy in education materials. The curriculum design team has worked with multiple NASA education initiatives and is aware

of and attentive to the needs of the education community. The design team also works under the supervision of the RBSP E/PO team who are members of the Heliophysics Forum and the Heliophysics Educator Ambassador communities. In addition, the team regularly checks the NASA education materials website to survey Heliophysics related curricula and how they may be leveraged. Module topics may include, but are not limited to: the interaction between charged particles and a magnetic field, general magnetism concepts, the radiation belts and their effect on communication satellites, and the purpose for twin spacecraft in this mission. Modules will be web-accessible for both students and teachers, and will be aligned with

Table 1 RBSP content alignment to the National Science Education standards

Content standard	RBSP tie to content standard
Grades K-4	Grades K-4
B: Physical Science: Light, heat, electricity, and magnetism	B: Electric currents can create magnetic effects-RBSP is investigating electric and magnetic fields
E: Science and Technology: Understanding About Science and Technology	E: RBSP scientists and engineers use tools to solve problems and work in teams with many different types of people
F: Science in Personal and Social Perspectives: Science and Technology in Local Challenges	F: Information gained by RBSP will be used to improve space weather forecasting and design new technologies
G: History and Nature of Science: Science as a human endeavor	G: Scientists and engineers working on the RBSP mission build on the contributions of other scientists and engineers, especially James Van Allen and his team
Grades 5–8	Grades 5–8
B: Physical Science: Transfer of Energy	B: RBSP science addresses many concepts in this standard, including but not limited to: the sun as a major source of energy; energy is associated with heat, light, electricity, motion, sound, nuclei, and nature of chemicals; energy is transferred in many ways
C: Earth and Space Science	C: RBSP content can be used to expand the concepts in the Structure of Earth System section to include geospace, Sun/Earth connections fits well in Earth in the Solar System
D: Science and Technology: Students begin to differentiate between science and technology	D: Special engineering design of the RBSP spacecraft, as well as the need for two spacecraft apply to the concepts addressed in Understandings about Science and Technology; Abilities of Technological Design
E: Science in Personal and Social Perspectives: Role of technology in relation to personal and societal issues	E: Solar storms, risk analysis and how these relate to the RBSP mission can be discussed in the Natural Hazards section of this standard
F: Science and Technology in Society: Societal challenges inspire questions for scientific research and social priorities often influence research priorities through availability of funding for research. Science and technology have advanced through the contributions of many different people, cultures, and times in history. Scientists and engineers work in many settings	F: The Van Allen Belts were discovered years ago, but there is now a greater need to expand our understanding due to an increased societal dependence on technologies in this region. As a result there are additional resources allocated to gain greater understanding. The contributions of many individuals and teams working in a variety of settings and disciplines make this mission successful

Table 1 (*Continued*)

Content standard	RBSP tie to content standard
Grades 9–12	Grades 9–12
B: Physical Science: Structure of Atoms particles, waves, and radiation Motions and Forces; Conservation of Energy and Increase in Disorder; Interactions of Energy and Matter	B: RBSP is investigating the type and energies of particles in the Van Allen Radiation Belts as well as how the particles are influenced by electric and magnetic waves. RBSP science directly addresses many of the concepts in the physical science content standard
D: Earth and Space Science: Energy in the Earth System: Earth systems have internal and external sources of energy. The Sun is the major external source of energy	D: RBSP is a Living With a Star (LWS) mission. "The LWS Program provides missions to improve our understanding of how and why the Sun varies, how the Earth and Solar System respond, and how the variability and response affects humanity in Space and on Earth."—NASA
E: Science and Technology Understandings About Science and Technology	E: Many of the principles and concepts central to end to end RBSP mission planning, design, building, testing, launching, data collection and analysis can be applied. Examples of applicable content topics include but are not limited to: system design, cost, risk, benefit, and tradeoffs
F: Science in Personal and Social Perspectives Natural and Human Induced Hazards	F: Space and ground based systems which our society depends upon are vulnerable to solar storms and changes in the radiation belts. The hazards of the radiation belts and the precautions taken to protect astronaut and airline passengers' health during solar events may be applied here as well
G. History and Nature of Science Science As a Human Endeavor: Individuals and teams have contributed and will contribute to scientific enterprise Nature of Scientific Knowledge: Science and Culture	G: Each instrument team's contribution is essential to the understanding of the radiation belts. Greater understanding of the Van Allen Belts will result from individual and team contributions, in the future as they have in the past Comparison of cultural explanations and scientific explanations of various Heliophysics phenomena such as the Aurora and "whistlers" may be discussed

the NRC National Science Education Standards (NRC 1996), AAAS Benchmarks (AAAS 1993), the NCTM Principles and Standards for School Mathematics (NCTM 2000), and the ITEEA Standards for Technological Literacy (ITEEA 2007). Each module will include an educator guide with a background science section, student handouts, suggested activities, cross-curricular references, adaptations for students with disabilities, and specific standards addressed. At least one module will be accompanied by an online interactive learning tool to engage learners by conveying complex and dynamic concepts in an interactive web-based environment. Another module will employ problem-based learning to challenge students to apply science, technology, and engineering concepts to real life problems.

The RBSP team is also collaborating with Dr. Sten Odenwald of SpaceMath @ NASA. Dr. Odenwald is creating standards based RBSP mathematics problems for middle school and high school level students which will be housed on the SpaceMath @ NASA website, the RBSP website, and will be distributed through educator networks.

Students in grades 5–8 will develop a greater appreciation of RBSP science and the Sun/Earth system with programming designed to align with the National Science Education Standards' Transfer of Energy section of the Physical Science standard, as well as the con-

tent standards for Earth and Space Science and Science and Technology. Other important mission concepts, such as our reasons for studying the Van Allen Radiation Belts, how our discoveries will influence future space science studies and understanding, technological advances, as well as our modern way of life, are aligned well with Science and Technology in Society, and Science in Personal and Social Perspectives content standards.

As discussed previously, investigations of the physical properties of the radiation belts are best aligned with the 9–12 content standards although some concepts may be applied to other grade levels (Table 1). The understanding of atoms past early large scale notions typically develops after middle school (NRC 1996). The structure of atoms, structure and properties of matter, interactions of energy and matter, conservation of energy and increase in disorder fall within the required physical science content guidelines at this level. These topics provide opportunity to incorporate lessons specific to RBSP, such as the types and movement of particles within the radiation belts, energy fluxes, the influence of magnetic fields and the methodology of measuring data over space and time into the framework of the Physical Science content standard. Students further develop their understanding of RBSP mission concepts with lessons that fit within the Earth and Space Science, Science and Technology, and Science in Personal and Social Perspectives content standards.

The RBSP progression of lesson plans is created to address science standards for grades 5–12 and is aligned with NASA's Education Outcome #2: "attract and retain students in STEM disciplines through a progression of educational opportunities for students, teachers and faculty." These lesson plans and curriculum will offer exciting and educational opportunities in which teachers and their students can engage with RBSP mission science and engineering concepts as well as learn more about the human involvement and impact of the mission. Educators learning activities which align with RBSP programming and the National Science Education Standards are shown in Fig. 3.

All modules will be formally reviewed through the NASA Earth and Space Science Education Product Review (ESSEPR) process, the outcome of which includes their identification as exemplary products in the NASA Space Science Education Resource Directory (SSERD). After the modules and activities are approved through NASA's review process, they will be widely disseminated through NASA's space science education resource directory, the RBSP website, as well as through educator networks and educational partners.

2.2 Heliophysics Educator Ambassador Program and Teacher Workshops

RBSP has partnered with other NASA missions in the Heliophysics community (IBEX, ARTEMIS, MMS, TIMED, AIM, Cluster and RHESSI) for the Heliophysics Educator Ambassador (HEA) Program. The RBSP E/PO team will continue to sponsor five educators per year to participate in the HEA program through the life of the program as they have in the years 2009–2011. The RBSP team will also continue to fully participate in the annual HEA educator workshop, and participate as needed in the planning sessions, follow up meetings, and evaluative discussions. During the 2009 and 2010 workshops information and classroom resources were presented to the educator group as a whole with a question and answer session following the presentation. During the July 2011 HEA workshop, the story of the RBSP mission was presented to 28 educators broken up into 3 smaller groups to allow for in depth discussions. RBSP science, engineering, and classroom resources relating to the mission were presented during each presentation, keeping in mind the educational needs of the participants. The HEA workshop format is aligned with the numerous studies that have found that the most effective professional development opportunities: "Focus on subject content, provide an intensive and sustained approach, are presented in a format of

Fig. 3 Educators learning activities which align with RBSP programming and the National Science Education Standards during the National Science Teachers Association Regional Conference in Baltimore, MD. Teachers heard about RBSP mission objectives, science, and engineering then participated in activities that align with the mission objectives and the science standards they need to cover in their classrooms. Image credit: JHU/APL

teacher network, study group, mentoring, and coaching as opposed to a traditional workshop or conference, is connected or related to teachers' daily work, emphasizes a team approach and collaboration, and provides opportunities for active learning" (NSB 2007).

The workshop is aligned with the National Science Education Standards, especially Professional Development Standards A and B. Standard A, subcategory two states, learning experiences for teachers must "address issues, events, problems, or topics significant in science and of interest to the participants." A focus of the oral presentation is the explanation of how the events in the Van Allen Radiation Belts directly affect the modern way of life of the participants and their students. Teachers are given resources and direction to locate additional resources, meeting the third subcategory of Standard A: "Introduce teachers to scientific literature, media, and technological resources that expanded their science knowledge and their ability to access further knowledge." A primary goal of participation in the workshop as a whole is to meet Professional Development Standard B, subcategory three: "Address teachers' needs as learners and build on their current knowledge of science content, teaching, and learning."

The RBSP E/PO team provides access to current science and engineering concepts as it relates to RBSP through dissemination of materials and classroom activities and presentation of information. Additionally, the RBSP E/PO team participated in several mentoring sessions throughout the HEA workshops and will continue to participate fully at future workshops. During the mentoring segments of the workshop, educators have the opportunity to interact with the team members to ask questions of "mission experts" as they create an outline of the workshops they will be presenting to other educators. Through this experience the fourth subcategory of Professional Development Standard D is addressed: "Quality

pre-service and in-service programs are characterized by collaboration among the people involved in programs, including teachers, teacher educators, teacher unions, scientists, members of professional and scientific organizations, parents, and business people, with a clear respect for the perspectives and expertise of each."

The Heliophysics Educator Ambassadors program is aligned to NASA's Education Outcome #2: "attract and retain students in STEM disciplines through a progression of educational opportunities for students, teachers and faculty." Professional development experiences for the nation's teachers will support the ultimate goal of helping them attract, retain, engage, and educate students in STEM disciplines, and creating a more science and technology literate workforce. Because this program not only reaches the teachers that participate directly in HEA workshops, but also has the ripple effect of educator to peer dissemination around the country, it represents a unique and particularly significant opportunity to impact a large audience. *The Heliophysics Educator Ambassadors Program Alaska 2009 and Chicago 2010 Final Evaluation Report* shows the 58 HEAs trained in these two workshops went on to conduct 141 workshops with 2102 participants, known as Tier 2 educators, and reached 8095 students. The Tier 2 educators trained by HEAs then reached over 296,000 students and nearly 19,000 additional educators (Cornerstone Evaluation Associates LLC 2012). As future HEA workshops are planned and executed, the logistics and the format of the programming may change, but the RBSP E/PO team's level of participation and the focus on the needs of the teacher participants during this important program will remain constant. Further information about the HEA program can be found on the HEA website http://cse.ssl.berkeley.edu/HEA/. An image taken during the 2010 HEA educator workshop is shown in Fig. 4.

2.3 Pre-launch Teacher Workshop

The Radiation Belt Storm Probes E/PO team conducted a pre-launch teacher workshop at Johns Hopkins University Applied Physics Laboratory. The two and a half day workshop gave 31 middle school, high school, undergraduate and informal educators from 21 states an opportunity to be trained on the mission by key mission team members, addressing the fourth component of the Professional Development Standard D; "Quality pre-service and in-service programs are characterized by collaboration among the people involved in programs, including teachers, teacher educators, teacher unions, scientists, members of professional and scientific organizations, parents, and business people, with a clear respect for the perspectives and expertise of each." It also aligns with Professional Development Standard C: "Professional development activities must provide opportunities to know and have access to existing research and experiential knowledge."

The workshop was truly a collaborative effort. Representatives of each of the five instrument suites gave tutorials and a hands-on demonstration of activities that could be adapted for the formal or informal classrooms. Twenty-two RBSP science, engineering, mission operations, and launch services team members participated. The planning and implementation of this workshop was carried out by the APL RBSP E/PO team.

The first day of the workshop offered an overview of the mission science and engineering. The focus of day two was a more in depth look at the mission instrument science. The third day was open for the educators to present their ideas and work toward creating new RBSP education materials. Participants also saw the cleanrooms where RBSP was built, toured integration and test facilities where RBSP put through the rigors of the space environment, and visited the APL mission operations center where RBSP will be controlled. Each day was comprised of a mixture of lectures, question and answer sessions, hands-on activities,

Fig. 4 Heliophysics Educator Ambassadors work together to map out magnetic field lines as part of an activity related to RBSP. Throughout the weeklong workshop, teachers hear from experts of various NASA Heliophysics missions and participate in mission related hands on activities, Adler Planetarium, Chicago, IL. Image credit: Nancy Fiegel

and time for educators to interact with one another. This time allowed them to discuss the content learned and how they would modify for their audiences and integrate it into their individual educational settings. Many mission representatives remained to interact with the teachers informally and be on hand to answer questions. Summative reports have not yet been compiled, however preliminary formative daily feedback indicate the teachers found the interaction with mission experts and the time to work with peer educators to be valuable aspects of the workshop.

The goal of this workshop was for educators from a wide range of backgrounds to gain an appreciation for the importance of the RBSP mission, comfort with the materials and mission concepts, and confidence in their ability to modify the materials to bring the mission concepts to their own students. The format was designed to give educators the opportunity to be students, to learn mission concepts through lecture, question and answer, hands on activities, and peer to peer education. The workshop addressed the third component of Professional Development Standard B of the National Standards: "Learning experiences for the teachers of science must address teachers' needs as learners and build on their current knowledge of science content, teaching, and learning." This opportunity was open to educators nationwide and provided a $750 stipend for travel expenses for each teacher. Backgrounds and audiences were diverse. There were eight middle school teachers, twelve high school, three undergraduate, and eight informal educators that participated. Photos taken at the Pre-Launch workshop are shown in Figs. 5a–c.

(a)

(b)

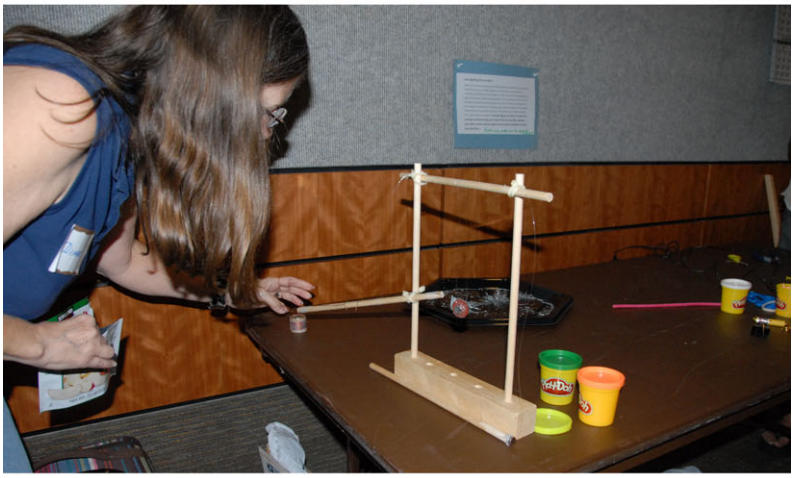

(c)

Fig. 5 Photos taken at the RBSP pre-launch teacher workshop held at Johns Hopkins University Applied Physics Laboratory, July 31–August 2, 2012. Thirty-one middle school, high school, undergraduate and informal educators from twenty-one states participated. Image credits: (**a**) Frank Morgan; (**b**, **c**) Dawn Turney

Like the HEA program for teachers, the launch site teacher workshop is aligned to NASA's Education Outcome #2: "attract and retain students in STEM disciplines through a progression of educational opportunities for students, teachers and faculty." The unique opportunity of providing a professional development workshop at the location where RBSP was built, tested and will be operated, while involving RBSP mission scientists and engineers, was an important aspect of generating excitement for the RBSP mission among middle and high school teachers.

2.4 Pre-service Teachers Heliophysics Workshop

The RBSP E/PO team will partner with historically black colleges and universities (HBCUs) in the Maryland and DC areas to recruit participants for a Pre-Service Teachers Heliophysics Workshop (PTHW). Faculty from the Education Departments for Howard University, Morgan State University, and the University of Maryland, Eastern Shore, were approached to assist the RBSP E/PO team in recruiting students in their programs for the workshop. These workshops will provide professional development opportunities to pre-service teachers close to finishing their education degrees at HBCUs in an effort to target participants that are underrepresented in STEM fields. Conversations with faculty from the HBCUs involved have led to the idea that the students will participate in a 1-day workshop that will take place at APL, followed by campus visits and/or web-seminars by the RBSP scientists and engineers. The content will include the RBSP key messages, fundamental science and engineering highlights, as well as a general overview of the Sun-Earth relationship. Techniques for incorporating this content into current National Science Education Standards will also be addressed so that the teachers can easily incorporate workshop themes into their future classroom curriculum. Pre-service teachers that are pursuing their education degrees in STEM disciplines will be given priority, but pre-service teachers that will be teaching non-STEM disciplines will also be considered if room is available.

The goal of the PTHW is to enhance awareness and understanding of RBSP mission science and engineering among historically underrepresented groups in the sciences. Additionally, engaging teachers early in their education career may give them confidence in teaching these topics as they begin to build a repertoire of lessons they are comfortable integrating into future classroom curriculum. Workshop facilitators will also emphasize to the participants that continuing to look to NASA for future teacher professional development opportunities and resources will benefit their classroom experience, and a list of these types of opportunities and resources will be shared.

An added benefit from the partnership with the faculty at Howard University (HU) is that involvement of HU students with this workshop will help support research for a NSF grant awarded to the HU Education Department titled, "What Works in Producing African American Science and Math Teachers at HBCUs." Dr. Kimberly Freeman, the PI for this grant and an RBSP E/PO partner, expects the investigation to yield data that can be used to strengthen science and math teacher preparation programs at HBCU's; improve recruitment of prospective science and math teachers; and inform higher education policy. Dr. Freeman has expressed interest in using the experiences and outcomes of the PTHW to add to the body of data for this critical study. Better preparation of minorities to teach STEM disciplines is critical in increasing the effectiveness of the K-12 education system to prepare minority youth in the STEM disciplines. According to a AAAS article published in 2008 titled, "African Americans Studying STEM: Parsing the Numbers" (Sasso 2008), it is not a lack of interest in science that is holding minority students back from STEM careers, rather that it is a cumulative effect of not attaining the prerequisites in their K-12 education needed to

continue onto a successful STEM career. Compounding this effect is that minority students are missing STEM teachers and role models with whom they can identify with. In essence, the presence of African American STEM teachers and role models needs to increase in order to overcome these challenges.

This program, like the other teacher workshops planned and facilitated by the RBSP E/PO team is aligned with the National Science Education Professional Development Standards. Specifically, the workshop will "address issues, events, problems, or topics significant in science and of interest to participants, introduce teachers to scientific literature, media, and technological resources that expand their science knowledge and their ability to access further knowledge, build on the teacher's current science understanding, ability, and attitudes, and encourage and support teachers in efforts to collaborate." These aspects of Professional Development Standard A will be of particular significance as the pre-service teachers begin their careers and have a heightened need for support and resources. Throughout the workshop, the facilitators will be mindful to "address teachers' needs as learners and build on their current knowledge of science content, teaching and learning," as well as "provide an opportunity to have access to existing research," as recommended in Professional Development Standards B and C. In addition, the E/PO team will provide a quality pre-service program as characterized by meeting many of the components cited in Professional Development Standard D, "conducting the program in a way that recognizes the developmental nature of teacher professional growth as well as the needs of teachers who have varying degrees of expertise, professional expertise, and proficiency." This characterization will be evident to an even greater degree if teachers from disciplines outside the STEM fields are participants. As an integral part of the workshop, teachers will interact and "collaborate with mission experts, other teachers, teacher educators, and members of professional and scientific organizations." The program will be assessed by Cornerstone Evaluation ensuring that the "assessment captures the perspectives of all involved, uses a variety of strategies, focuses on the process and effects of the program and feeds directly into the program improvement and evaluation" as recommended by the National Science Standards.

This workshop is unique because it simultaneously is aligned to NASA's Education Outcome #2: "attract and retain students in STEM disciplines through a progression of educational opportunities for students, teachers and faculty," as well as NASA's Education Outcome #3: "Contribute to the development of the STEM workforce," where the STEM educators are a significant part of the future STEM workforce.

2.5 Space Academy

The APL Space Department E/PO office created the Space Academy series where students go behind the scenes of current space missions and are introduced to scientists and engineers working on these projects. These educational events are sponsored by Johns Hopkins Applied Physics Laboratory (APL) and Discovery Education. Radiation Belt Storm Probes is a regular topic of these programs.

Space Academy gives middle school students a close-up look at NASA's missions such as the Radiation Belt Storm Probes mission. They are designed to engage, inspire, and influence attitudes about space science and STEM careers. They also provide an opportunity to engage and attract underserved populations and emphasize that space science is for everyone. Space Academy includes a student press conference with mission experts as panelists and students as "reporters." The panelists represent varying backgrounds, careers, and roles on the mission. For example, panelists may include engineers, scientists, the Mission Operations Manager, Project Manager or other integral roles on the mission. Speakers take

Fig. 6 Space Academy allows Maryland school students to enjoy a full day of activities including hearing from RBSP mission experts, participation in a student press conference modeled after a NASA press conference, science demonstrations and activities, and a behind the scenes tour of spacecraft testing laboratories. Image Credit: JHU/APL

turns describing different aspects of the mission and their role on the project, and then students have an opportunity to interview them as if they were part of an official NASA press conference. The event is moderated by an APL public relations representative.

After the press conference, students learn why spacecraft engineers wear white outfits called "cleanroom suits" during spacecraft integration and testing, participate in a lively science demonstration as shown in Fig. 6, and dine with Radiation Belt Storm Probes' scientists and engineers. Lunch with the team gives students a chance to continue conversations, ask questions they may not have had time to ask during the press conference, and gives mission experts an opportunity to change attitudes about what a career in space science may be like. After lunch students put on specially-designed souvenir cleanroom suits and tour APL's space facilities. Spacecraft and instrument team members lead student groups through a series of "exploration stations" that may include a mission operations center used to control the spacecraft; a satellite communications facility used to communicate with the spacecraft; the thermal and vibration laboratories used to test spacecraft; view spacecraft and instruments being assembled in APL's clean rooms, and participate in a variety of mission-related hands-on science demonstrations. In preparation for their visit, students study the mission and space-related careers through a series of classroom activities and videos developed by APL and Discovery Education. They also engage in post-visit activities about the mission including their experiences during Space Academy. Schools from Baltimore City and seven

diverse Maryland counties have attended RBSP Space Academy events in the past. The E/PO office plans to feature RBSP at Space Academy once per year until 2015.

Activities throughout the day develop student understanding about science and technology and address the fundamental concepts that fall under the National Science Education Content Standards: Science and Technology; Understandings about Science and Technology. Topics are also aligned with concepts which fall under the Content Standard: Science in Personal and Social Perspectives, particularly concepts in Natural Hazards, Risks and Benefits, and Science and Technology in Society. Students are immersed in a hands-on experience designed to facilitate understanding of the concepts outlined in the Content Standard: History and Nature of Science. Throughout the day students interact with people of diverse backgrounds and interests while hearing about the specific ways various individuals and teams of people, past and present contribute to the science and technology of the mission, addressing the concepts which fall under the headings of: Science as a Human Endeavor, Nature of Science, and History of Science.

Space Academy is aligned to NASA's Education Outcome #2: "attract and retain students in STEM disciplines through a progression of educational opportunities for students, teachers and faculty." Having students come to the Applied Physics Laboratory and engage with scientists and engineers outside the classroom is an exclusive opportunity and previous Space Academies have been successful in getting students excited about mission science and engineering as well as careers in the space industry. Likewise, exposing students to a diverse group of scientists and engineers may help to alleviate some common stereotypes about these types of careers. In Chap. 15 of the Project 2016: Benchmarks for Science Literacy (AAAS 1993), many stereotypes of scientists are listed, including that they are perceived by students to be bearded, balding, working alone in the laboratory, isolated and lonely. When students engage with the scientists and engineers at APL, they see first-hand that this is absolutely not the case and that successful science and engineering requires a diverse team with multi-disciplinary background. The pre-visit classroom activities are also aligned to National Science Education Standards, so the material is appropriate for use in the classroom. More information can be found on the Space Academy website: http://www.spaceacademy.jhuapl.edu/.

2.6 APL/NASA Undergraduate Internships

The APL Space Department E/PO office partners with NASA in support of the NASA/APL internship program to provide meaningful summer positions in the Space Department. Each summer, up to 20 competitively selected undergraduate students from around the country intern at APL for a 10-week hands-on educational research experience. Students from a wide variant of backgrounds are recruited, in the tradition of encouraging multi-disciplinary student collaborations. Throughout the summer, the E/PO office provides tours and mission-related educational "brown-bag" lunchtime talks on various NASA missions. A special end-of-summer program in which interns present their summer projects and internship experiences to peers, project supervisors, and upper management at APL, affords them an opportunity to experience yet another aspect of working in a STEM career, as well as providing additional exposure to the APL community. The RBSP E/PO office has a continuing commitment to support internships dedicated to training undergraduate students in RBSP mission science and engineering. Several former NASA/APL interns have recently become full-time employees in the APL Space Department; a few specifically came back to resume their work on RBSP. Likewise, many NASA/APL interns go on to work at NASA Centers.

Students are recruited on a national scale. In order to engage the greatest talent from across the nation, the program is advertised through multiple channels with the help of critical partners. Announcements are sent out to the NASA Academy alumni as well as AIAA Mid-Atlantic members. In addition, Space Grant Consortiums partner with APL to advertise at their universities across the country. The link to the NASA/APL Internship Program is www.aplapp.com.

Interns have worked on the RBSP mission under the direction of Space Department scientists and engineers at APL, 2007 to present. 2011: 3 NASA/APL interns and 5 interns from other APL internship programs; 2010: 4 NASA/APL interns; 2009: 4 NASA/APL interns; 2008: 4 NASA/APL interns; 2007: 3 NASA/APL interns and 3 interns from the Minority University-Space Interdisciplinary Network (MU-SPIN) internship program.

Partnerships with NASA Space Grant Consortiums from around the country have supported the funding obligations of this program. Instrument teams are invited to apply for E/PO funds for their own internship opportunities or volunteer applicants from their institutions and universities.

The need for undergraduate research and internship opportunities has been well-documented. More recently, in a 2011 article published in the Journal of Higher Education titled, "Cross-Discipline Perceptions of the Undergraduate Research Experience" (Craney et al. 2011), the undergraduates who participated in the study stated that these types of research opportunities address their needs for research specific skills and clarification/confirmation of career paths. Additionally, female researchers were more likely than the male researchers to report that these types of research opportunities gave them prestige during college and would allow them to develop their communication and presentation skills.

The NASA/APL Internship Program is aligned to NASA's Education Outcome # 1: "contribute to the development of the STEM workforce in disciplines needed to achieve NASA's strategic goals, through a portfolio of investments." The program provides practical work experience and an introduction to space science and engineering. Students spend the summer working with APL scientists and engineers, conducting research, developing leadership skills, and growing professionally. Finally, the high percentage of interns who commit to a career in the STEM workforce supports NASA's goals.

3 Informal Education

The NSB (2004) suggests that the American public expresses strong support for science and technology but is not very well informed about these subjects. The attendance at science centers and museums across the country shows the public is interested in science, although they may not be following science studies in the news. For this reason the RBSP public outreach program creates opportunities to tap into this interest, reaching out to the public and increasing their awareness of RBSP mission science, such as the event shown in Fig. 7. A wide ranging informal education effort is designed to increase public interest and understanding of science, technology, engineering and mathematics activities—using the excitement of the mission to capture their attention and imaginations. This effort includes partnering with informal educators, building their skills, and contributing to the collection of informal education resources for Heliophysics. Many informal education centers, such as science centers and museums, have a wide variety of existing programs that can be leveraged for new RBSP content. These programs also compliment the RBSP mission and instrument exhibits that will be permanently housed at the partner museum and science centers.

Fig. 7 A Maryland boy scout troop has a special and rare opportunity to go behind the scenes to view the Radiation Belt Storm Probes being built in the clean rooms while learning about engineering for an extreme environment from RBSP engineers. Image Credit: Dawn Turney

The APL E/PO office has built strong partnerships with museums and science centers across the country. The programs provide a wide range of services from full exhibits with spacecraft models and artwork for guest speakers and lectures to the development of planetarium shows. RBSP E/PO partners with these informal educators to inspire and engage a broad audience with RBSP mission science and engineering, while at the same time promoting Heliophysics and the Sun-Earth relationship information. All Informal Education programs described align with NASA's Education Outcome #3: "build strategic partnerships and linkages between STEM formal and informal education providers that promote STEM literacy and awareness of NASA missions."

3.1 Maryland Science Center

The Maryland Science Center (MSC) is conveniently located in Baltimore's Inner Harbor, a tourist attraction for visitors from around the country, as well as a field trip destination for school groups. RBSP E/PO partners with MSC utilizing their SpaceLink exhibit, which is part media center, part discovery room, and part newsroom focusing on the "latest and greatest" in space science and aerospace technology. RBSP scientists and engineers support these programming efforts as well as special live events to highlight mission milestones and space-related anniversaries. This allows the guest scientists and engineers to interact directly with the public at MSC. Another opportunity for direct scientist-to-public engagement is through a scientist lecture series sponsored by MSC that includes five to six lectures per year, and an RBSP scientist will be one of these lecturers. These public engagement opportunities

Fig. 8 Partnership with the Maryland Science Center and other science museums and visitor centers allow opportunities for quality public programming and outreach where scientists and engineers have opportunities to share their excitement and knowledge with the public. Image Credit: Maryland Science Center

for RBSP scientists and engineers provide a venue in which they can put into practice the training they have received for public outreach (see Sect. 4.1).

A partnership with MSC also allows for training of other informal educators. MSC is a member of the International Planetarium Society (IPS) and will present RBSP content at IPS conferences and meetings in order to engage other informal educators with RBSP mission science and engineering. The RBSP E/PO team will be involved in creating presentations and posters alongside staff at MSC, for dissemination to other museums, science centers and planetariums. MSC will tailor the content to be fit for an informal education audience, and the RBSP E/PO team will provide scientific guidance and visualizations.

A strategic partnership with MSC engages more Americans with RBSP mission science and supports their existing efforts in offering local and regional NASA-themed educational activities and exhibits, as well as training for other informal educators. The diversity of the Baltimore area also ensures that underrepresented groups in the sciences will have direct access to RBSP scientists, engineers and content. Sixty-eight percent of Baltimore City residents are African American, American Indian, Asian and Hispanic (Source: 2010 U.S. Census, State and County Quick Facts) and Baltimore City schools, many of which are underserved Title I Schools, frequently visit MSC for school field trips (Fig. 8).

3.2 Partnerships with NASA Visitor Centers—KSC and GSFC

RBSP launched from Kennedy Space Center (KSC) and the E/PO program partnered with NASA's KSC Visitor Center to take advantage of the excitement naturally surrounding the launch of a spacecraft. Exhibits included, a large mission booth where visitors participated in multiple hands-on RBSP related activities and received material handouts, a model of

one of the RBSP spacecraft, and an interactive kiosk, and an exhibit along the KSC bus tour route which focused on the RBSP launch vehicle. Other launch events included the Pre-Launch Teachers Workshop (see Sect. 2.3) and visits to Brevard County elementary, middle and high schools by RBSP science team members. Contacts with local school officials were obtained through the partnership with the KSC Education Office. The number of visitors engaged during the KSC and NASA visitor center efforts were recorded and categorized to include coinciding formal education activities.

Formal Education—approximately 2,560 students and teachers reached

- Pre-launch Educator Workshop—31 educators from 21 States
- Distance Learning Network (DLN)—60 students & 2 teachers
- High schools—575 students & 15 teachers
- Middle schools—250 students & 12 teachers
- Elementary schools—500 students & 11 teachers
- INSPIRE Un-Conference at KSC—70 students & parents
- Educator Resource Center at KSC—approximately 1,000 educators

Informal Education—over 16,000 during launch week

- Four RBSP Exhibits throughout KSC Visitors Complex
- Main RBSP Exhibit in IMAX Theater with 5 hands-on activity stations
- Direct interactions and materials passed out at IMAX Exhibit—approx. 4,000
- RBSP Exhibit and video at LC 39 Tour Stop
- Interactive kiosk in Exploration Space
- Twelve Astronaut Encounter Auditorium Briefings—approximately 100 attendees
- Museum Alliance Pre-launch Training—25 informal educators
- Public Lecture at Brevard County Planetarium
- Two Guest Briefings at KSC

An RBSP mission science and engineering exhibit will be coordinated with Goddard Space Flight Center (GSFC). This exhibit will include models of the RBSP spacecraft, videos and visualizations, fact sheets and tactile models that will reinforce the understanding of Heliophysics and the Earth-Sun relationship. Exhibits at both the KSC and GSFC Visitor Centers will highlight the RBSP key messages using both visual and audio resources that will engage and inspire a broad and diverse audience. Likewise, a strategic partnership with both the KSC and GSFC Visitor Centers will support their existing efforts in providing informal education resources and tools that use NASA's unique content to connect NASA's missions to self-directed learners, and to attract individuals to STEM careers.

3.3 Museum Alliance

The Museum Alliance is a partnership between NASA's Solar System Exploration Program and museums, science centers, and planetariums across the country bringing the adventure of space exploration to students, educators, and the public. It is intended to bring real-time data and current science and technology to museum visitors through visualizations and professional development of the museums' staff.

The RBSP E/PO program partners with the Museum Alliance, managed by the Jet Propulsion Laboratory (JPL). Members of the Museum Alliance will be trained on the science and engineering of the RBSP mission by key project personnel and will be equipped with mission materials to conduct their own regional RBSP events and workshops at their

home museums, science centers, and planetariums. The strategic partnership with the Museum Alliance network embeds NASA expertise and content among members of the Museum Alliance who create or offer local, regional or national NASA-themed educational activities and exhibits. Additionally, the RBSP E/PO office will also support opportunities and activities that may come about through these partnerships.

3.4 Launch Events

RBSP launched window opens in August of 2012. The instrument sites and the entire E/PO office was involved with launch efforts on behalf of the mission. All of the RBSP E/PO partners, RBSP Educator Ambassadors, and instrument teams were invited and encouraged to host and conduct regional outreach at their home institutions during launch or participate in launch efforts held at Kennedy Space Flight center and surrounding counties. The Museum Alliance members, Solar System Ambassadors, HEAs, and Solar System Educators were also encouraged to conduct their own regional events and activities.

4 Public Outreach

The RBSP E/PO program engages the public in shaping and sharing the experience of space exploration through its Public Outreach programs. These programs strive to allow the public access to real-time data, milestone events, and general mission and instrument information in easily accessible formats such as videos and animations, a mission website, printed materials, and at times direct scientist/engineer interaction. There will also be an E/PO training workshop for RBSP scientists, engineers and project management so that the public may have greater access to the expertise of the RBSP mission. The goal is to contribute to the overall advancement of the nation's scientific and technical awareness of the RBSP mission.

Like Education Portfolio Strategic Framework Outcome #3—Informal Education—the Public Outreach programs will inspire and engage the public with STEM disciplines as they are applied to RBSP mission science.

4.1 Education and Public Outreach Training for Scientists, Engineers and Project Management

Educational research and first-hand experience demonstrates that involving more scientists and engineers in E/PO activities increases audience interest and learning about scientific topics (Buxner et al. 2012; Morrow and Dusenbery 2004; Ecklund et al. 2012; Morrow 2003; Young 2007). Many opportunities exist within the RBSP E/PO plan for scientists and engineers to get involved with education and public outreach activities. More direct interaction between audiences in the E/PO field (K-12 students, educators, public, etc.) with scientists and engineers is beneficial for both parties. The audiences are excited to interact with real-life scientists and engineers and are exposed to subject expertise, while the scientists and engineers gain first-hand experience in building relationships with the public and sharing their knowledge as seen in Fig. 9. In a document titled, "Workshops for Scientists and Engineers on Education and Public Outreach," by C.A. Morrow and P.B. Dusenbery, the authors state that space scientists and engineers offer much that is needed to contribute to education and public outreach. This includes: (1) respect and influence in their communities; (2) expertise in science and the scientific process; (3) exciting connections to real world exploration and discovery; (4) education access to data and facilities,

(a)

(b)

Fig. 9 Scientist Dan Smith (**a**) and engineer Elliot Rodberg (**b**) share their knowledge and enthusiasm about the RBSP mission with students and the public. Team members support is integral to the success of the E/PO program. Image Credit: (**a**) Dawn Turney; (**b**) Ed Whitman, JHU/APL

and (5) role modeling for students and teachers. For these reasons, the RBSP E/PO Public Outreach program will include a workshop focusing on E/PO training for RBSP mission scientists, engineers and project management. Heliophysics, and the science and engineering behind the RBSP mission, are complex topics, but topics that the public can understand and relate to their everyday lives. In order to make these topics more accessible to education and public outreach audiences, subject matter experts are given the opportunity to learn how to communicate topics effectively using language that is appropriate at various levels of science literacy (Morrow and Dusenbery 2004; Ecklund et al. 2012; Young 2007).

The workshop will be held in conjunction with the RBSP Science Working Group meeting in order to ensure maximum attendance by mission scientists and engineers. The workshop include topics such as best practices for communicating science to a broad audience (Morrow and Dusenbery 2004 and Young 2007) and an overview of National Science Education Standards as they relate to RBSP, Heliophysics, and the Sun-Earth system for presenting these topics in the classroom. Additionally, an overview and discussion on current astronomical and space science misconceptions will be included (Sadler et al. 2010). At the end of the workshop the E/PO team recruits RBSP mission scientists and engineers for participation in upcoming E/PO opportunities (for example interviews for mission videos, speakers for Space Academy, teacher workshops, etc.). The scientists and engineers are encouraged to participate in RBSP E/PO Formal Education, Informal Education, and Public Outreach programs either as an advocate, a resource or a partner, as described in Appendix C of the NASA Explanatory Guide to NASA Science Mission Directorate Education and Public Outreach Evaluation Factors (2010).

This workshop aims to inspire and prepare RBSP mission scientists and engineers to get more involved with education and public outreach opportunities, while also training them in effective techniques for conducting education and public outreach. Sharing their enthusiasm for mission science with students, educators, families and the general public will ultimately increase Americans' science and technology literacy.

4.2 "Girl Power" Event at APL

The Girl Power event at APL is an annual public outreach activity that invites middle and high school girls to be inspired by the science, mathematics, engineering and technology activities at APL. Among the many booths displaying research in high impact STEM fields, RBSP is highlighted. RBSP mission scientists and engineers staff the booth and interact with the girls, even encouraging them to stay in contact after the event. The interactive activities at the RBSP booth have included dressing up in cleanroom suits as seen in Fig. 10, and a hands-on magnetic field line activity that demonstrates the shape of the Earth's magnetic field. Activities that highlight other APL Solar System exploration missions are demonstrated alongside the RBSP mission activities to emphasize the multi-disciplinary nature of space science. Throughout the event girls and their families interact with scientists and engineers of diverse backgrounds and interests while hearing about the specific ways various individuals and teams of people, past and present contribute to the science and technology of the mission. In this way, the event is aligned with the concepts of the National Science Education Content Standard: Science as a Human Endeavor, Nature of Science, and History of Science. Each year, the number of participants has grown. Last year, over 500 middle and high school girls and their families participated in Girl Power, engaging with 155 mostly female scientists and engineers. RBSP will continue to support this outreach activity throughout the mission's lifetime. The need to target girls for STEM education and careers has been

Fig. 10 Three future engineers show off their new fashion sense after spending time learning about building RBSP from APL's Safety and Quality Assurance Group Supervisor, Emily Broderick, a volunteer at the Girl Power event. Image Credit: Connie Finney

well-documented. A literature review in the Journal of Women and Minorities in Science and Engineering titled, "Collaboration as a Means to Building Capacity: Results and Future Directions of the National Girls Collaborative Project" (Marra et al. 2008), noted that factors such as perceptions of careers, confidence, role models, and career advice have been highlighted in the literature as contributing to the lack of females in STEM. The high number of RBSP female scientists and engineers who participate in Girl Power illustrates to the female students that careers in science and engineering are for everyone. Additionally, contact information for each female scientist and engineer is given to each student participating in Girl Power. The participants are encouraged to keep in touch with the role models they have met that day.

4.3 RBSP Video Series/Visualizations/Animations

Easy access to high quality videos, visualizations and animations guarantees that the public will be exposed to exciting science and engineering topics related to the RBSP mission. These products are for educational and public outreach use covering the development of the RBSP mission from instrument delivery through launch and showcasing science returns. Segments of the program also appear on the web. APL creates all of the mission animations and visualizations in both HD and standard definitions for multi-use purposes. They are integrated into produced video products, incorporated into Magic Planet programming, which is an interactive digital video globe and placed on the mission web site. There were

approximately 52,750 views of video and animation accessed from the RBSP website between January and September, 2012 (JHU/APL). The video series and animations are 508 compliant and are made available to media outlets as well as museums and science centers ensuring maximum exposure to the general public.

The pre-launch video series will include an RBSP movie trailer (currently posted on the RBSP website), a short mission video of about three minutes, and a longer follow-up video of about three to five minutes which will include interviews from mission scientists and engineers. Post-launch, three to five new animations will be created per year that highlight new discoveries in radiation belt science and the interaction of the RBSP spacecraft with the radiation belts.

4.4 Mission Web Site

According to NSB (2004), the Internet has had a major impact on how the public gets information about science and technology, and is the preferred source when people are seeking information about specific scientific issues. For this reason, the RBSP website is designed to engage and inspire excitement about the mission and to help people understand its significance through formal and informal education resources. General awareness includes mission updates and interest pieces. Instrument team news as well as spacecraft news and highlights are showcased here. There were approximately 2,460,500 hits and 169,600 pages visited on the RBSP website between January and September 2012. About 28 % of the total number of hits and 25 % of pages visited were accessed by United States educational institutions (JHU/APL).

The RBSP mission website is http://rbsp.jhuapl.edu. It features the latest news about the mission and a monthly spacecraft team perspective column. Features include sections on the following: overview; science; mission, spacecraft; education; news center; gallery and links, among other special elements (Fig. 11). The main RBSP mission website will also include links to RBSP instrument team websites. Leveraging off our strong public affairs partnership, the APL Public Affairs office oversees daily updates for the website, focusing on news and other releases. The E/PO office maintains the website education pages and will coordinate with Public Affairs office as necessary when new items become available. The E/PO team is responsible for the education webpage.

5 Product and Program Evaluation

Both a systematic product evaluation/review and a comprehensive program evaluation plan are critical elements for ensuring that the RBSP E/PO effort is built on a sound foundation and is successful in achieving its objectives. The purpose of the product evaluation is to ensure the pedagogical and scientific merit of lesson plans, curriculum and other materials developed as part of the RBSP E/PO project. Program evaluation involves a multi-method approach for gathering both quantitative and qualitative information to provide the RBSP E/PO team with continual feedback for making data-driven decisions and improvements and to determine the effectiveness and impact of RBSP's E/PO effort.

5.1 Product Evaluation

To ensure the pedagogical soundness and scientific accuracy of products and materials developed under the umbrella of the RBSP E/PO project, products undergo expert reviews

Fig. 11 The Conversation with the Team portion of the website features scientists and engineers answering questions of their choice from a menu of space science and mission questions. This section is especially useful for those who are just discovering the RBSP mission and/or the science of Heliophysics, as well as for those who want to enhance their knowledge. Image Credit: JHU/APL

(both for 'best practices' pedagogy and scientific content), field testing, and the NASA education product review. The majority of lesson plans, activities and curriculum that will be used throughout RBSP's formal education programs will be produced by Montana State University (MSU). MSU will carry out expert pedagogical reviews and field testing on the materials they develop. Reviews of scientific accuracy will be conducted by a team of APL scientists, engineers and program managers (N. Fox, D. Smith, R. Fitzgerald, A. Santo, B. Mauk, J. Stratton) on all lesson plans and curriculum designed by MSU as well as all other products and activities developed as part of the RBSP E/PO project.

Additionally, RBSP E/PO partners coordinate with the APL RBSP E/PO team prior to the public release of any materials, products, curricula or deliverables (either electronic or print) produced under the mission's E/PO effort. E/PO partners and team members field test the materials they develop on their suggested target audiences. Feedback from this testing is integrated into the final products.

5.2 Program Evaluation

An external evaluator is charged with designing and carrying out an evaluation plan in order to determine the effectiveness of RBSP E/PO in meeting its objectives/goals and the overall impact of the RBSP E/PO effort. Cornerstone Evaluation Associates LLC is collaboratively partnering with the RBSP team in tailoring evaluation activities to fit the needs of each of RBSP's programs. Cornerstone takes the primary responsibility for (1) designing all data

collection instruments, (2) facilitating the collection of all data, (3) managing, analyzing and interpreting all data and (4) providing 'as needed' feedback for informed decision-making and a final summary report focused on RBSP's outcomes. This evaluation also assesses the impact of RBSP's programs within the broader context of educational goals outlined by NASA's Science Mission Directorate (SMD), demonstrating how RBSP's outcomes address SMD's overarching goals to engage Americans in NASA's mission, attract and retain students in STEM disciplines and strengthen NASA and the nation's future workforce. The evaluation provides evidence of the E/PO project's success in achieving other strategic SMD goals including: avoiding duplication of effort and tapping existing dissemination networks; coordinating with key players within NASA Space Science and NASA Education and with interested institutions outside of NASA; involving mission scientists and engineers throughout the effort and reaching out to underserved and underrepresented communities. It demonstrates both quantitative and qualitative metrics for measuring program participants' change in knowledge, attitudes, behaviors and skills with regard to RBSP science-related content being conveyed by its formal, informal and public outreach efforts.

Collaboration and Coordination Efforts The RBSP E/PO team is a fully participating member of the Heliophysics Science Education and Public Outreach Forums (SEPOF), attending monthly SEPOF teleconferences, annual retreats and meetings of opportunity in an effort to share and leverage efforts with members of the NASA Heliophysics E/PO community. RBSP team activities have been highlighted during the SEPOF teleconferences as well on the SMD Heliophysics workspace. In addition to collaboration efforts with the Heliophysics community during the planning, implementation, and follow up of the HEA program, the RBSP team coordinates and participates in multiple NASA E/PO activities. Some of these include: support for NASA's Sun Earth Day Celebration, participation in NASA's Explore @ NASA Goddard, participation in Exploration Station alongside other Heliophysics missions such as the Solar Dynamic Observatory, and highlighting NASA's Heliophysics E/PO program links on the RBSP education webpage. The RBSP E/PO team collaborates with Sten Odenwald of NASA Goddard to create SpaceMath@NASA activities to be placed on the SpaceMath@NASA website, the RBSP website, and distributed directly to educators. We invited team members from NASA centers and universities to participate in the pre-launch teachers workshop and plan to collaborate on the HBCU pre-service teacher workshops. The RBSP exhibit that will be created for the NASA Goddard Visitor Center will be integrated with an existing NASA Heliophysics E/PO display.

Summary—Making an Impact The fundamental science research that is being done in the dynamic "laboratory" of the Van Allen Radiation Belts can and will be applied to our study of many other locations and processes throughout the cosmos. The discoveries made during this mission will bolster our understanding of how the universe operates and behaves. Understanding the mysteries and fundamental science of the Van Allen Radiation Belts is also key to our modern way of life: from protecting our current technologies and the health of the people that work in this region of near Earth space, to reaching into the future and building new space based innovations. The E/PO team members and partners strive to share this knowledge through a nationwide program which is based on research and best practices learned from experience working with the education community.

For more information or to become involved in Education/Public Outreach Opportunities please see http://rbsp.jhuapl.edu/.

Acknowledgements The RBSP E/PO team would like to thank NASA's Radiation Belt Storm Probes mission which funded and supported the E/PO efforts. Dawn Turney would like to thank Dan Smith and Tom Sotirelis for help with edits of this paper.

References

American Association for the Advancement of Science (AAAS), *Project 2061: Benchmarks for Science Literacy* (AAAS, Washington, 1993)

S. Buxner, M. Sharma, B. Hsu, L. Peticolas, M.A. Matiella Novak, E. CoBabe-Ammann, Barriers, lessons, learned, and best practices in engaging scientists in education/public outreach, in *Conference Proceedings of the Astronomical Society of the Pacific*, vol. 457 (2012), pp. 81–87

Cornerstone Evaluation Associates LLC, The Heliophysics Educator Ambassadors Program Alaska 2009 and Chicago 2010, Final Evaluation Report, 2012

C. Craney, T. McKay, A. Mazzeo, Cross-discipline perceptions of the undergraduate research experience. J. High. Educ. **82**(1), 92–113 (2011)

E.H. Ecklund, S.A. James, A.E. Lincoln, How academic biologists and physicists view science outreach. PLoS ONE **7**(5) (2012)

International Technology and Engineering Educators Association, Standards for Technological Literacy: Content for the Study of Technology, 2007

Johns Hopkins University Applied Physics Laboratory (JHU/APL), Index of /stats/geospace. http://sd-www.jhuapl.edu/stats/geospace/. Accessed 3 October 2012

R.M. Marra, K. Peterson, B. Britsch, Collaboration as a means to building capacity: results and future directions of the national girls collaborative project. J. Women Minor. Sci. Eng. **14**, 119–140 (2008)

C.A. Morrow, Misconceptions scientists often have about the K-12 national science education standards. Astronomy Education Review **1**(2), 85–94 (2003)

C.A. Morrow, P.B. Dusenbery, Workshops for scientists and engineers on education and public outreach. Adv. Space Res. **34**(10), 2153–2158 (2004)

National Aeronautic and Space Administration (NASA), NASA Implementation Strategy, 1996

National Aeronautic and Space Administration (NASA), Strategic Coordination Framework: A Portfolio Approach, NP-2007-01-456-HQ, 2007

National Aeronautic and Space Administration (NASA), NASA Education Communication Strategy, NP-2008-02-496-HQ, 2008

National Aeronautic and Space Administration (NASA), Explanatory Guide to NASA Science Mission Directorate Education and Public Outreach Evaluation Factors, 2010

National Council of Teachers of Mathematics, *Principles and Standards for School Mathematics* (National Council of Teachers of Mathematics, Reston, 2000)

National Research Council (NRC), *National Science Education Standards* (National Academy Press, Washington, 1996)

National Research Council (NRC), *Taking Science to School: Learning and Teaching Science in Grades K-8* (The National Academies Press, Washington, 2007)

National Science Board (NSB), *Science and Engineering Indicators* (National Science Foundation, Arlington, 2004)

National Science Board (NSB), *National Action Plan for Addressing the Critical Needs of the U.S.—Science, Technology, Engineering and Mathematics Education System* (National Science Foundation, Arlington, 2007)

National Science Board (NSB), *Science and Engineering Indicators* (National Science Foundation, Arlington, 2010)

P. Sadler, H. Coyle, J.L. Miller, N. Cook-Smith, M. Dussault, R.R. Gould, The astronomy and space science inventory: development and validation of assessment instruments aligned with the K-12 national science standards. Astronomy Education Review **8**, 010111 (2010). doi:10.3847/AER2009024

A. Sasso, African Americans Studying STEM: Parsing the Numbers. Science, AAAS (2008). http://sciencecareers.sciencemag.org/career_magazine/previous_issues/articles/2008_05_16/caredit.a0800070. Accessed 2 February 2012

R.C.J. Sommerville, S.J. Hassol, Communicating the science of climate change. Phys. Today **64**(10), 48 (2011)

U.S. Census Bureau, State and County Quick Facts. http://quickfacts.census.gov/qfd/states/24/24510.html. Accessed 1 October 2012

U.S. Department of Education, Highlights from PISA 2006: Performance of U.S. 15-Year-Old Students in Science and Mathematics Literacy in an International Context, 2008. http://nces.ed.gov/pubsearch/pubsinfo.asp?pubid=2008016. Accessed 2 February 2012

K.L. Young, Recruiting future engineers through effective guest speaking in elementary school classrooms, in *Meeting the Growing Demand for Engineers and Their Educators 2010–2020 International Summit, IEEE*, 9–11 November 2007, vol. 50 (2007), pp. 1–14. doi:10.1109/MGDETE.2007.4760352